Transactions of the ASME®
Journal of Heat Transfer

Published Quarterly by The American Society of Mechanical Engineers

VOLUME 112 • NUMBER 4 • NOVEMBER 1990

HEAT TRANSFER DIVISION
Chairman, **W. J. MARNER**
Secretary, **O. A. PLUMB**
Technical Editor, **R. VISKANTA**
Associate Technical Editors,
R. O. BUCKIUS (1993)
W. A. FIVELAND (1992)
L. S. FLETCHER (1992)
F. P. INCROPERA (1993)
H. R. JACOBS (1992)
J. H. KIM (1993)
J. R. LLOYD (1992)
D. M. McELIGOT (1992)
R. J. SIMONEAU (1993)
W. A. SIRIGNANO (1992)
L. C. WITTE (1992)

BOARD ON COMMUNICATIONS
Chairman and Vice President
M. E. FRANKE

Members-at-Large
W. BEGELL
T. F. CONRY
T. DEAR
R. L. KASTOR
R. MATES
E. M. PATTON
R. E. REDER
R. D. ROCKE
A. VAN DER SLUYS
A. J. WENNERSTROM
W. O. WINER
B. ZIELS

President, **A. E. BERGLES**
Executive Director,
D. L. BELDEN
Treasurer,
ROBERT A. BENNETT

PUBLISHING STAFF
Mng. Dir., Publ.,
CHARLES W. BEARDSLEY
Managing Editor,
CORNELIA MONAHAN
Sr. Production Editor,
VALERIE WINTERS
Production Assistant,
MARISOL ANDINO

ANNOUNCEMENTS

TECHNICAL PAPERS

Transactions of the ASME, Journal of Heat Transfer (ISSN 0022-1481) is published quarterly (Feb., May, Aug., Nov.) for $160.00 per year by The American Society of Mechanical Engineers, 345 East 47th Street, New York, NY 10017. Second class postage paid at New York, NY and additional mailing offices. POSTMASTER: Send address changes to Transactions of the ASME, *Journal of Heat Transfer*, c/o THE AMERICAN SOCIETY OF MECHANICAL ENGINEERS, 22 Law Drive, Box 2300, Fairfield, NJ 07007-2300.
CHANGES OF ADDRESS must be received at Society headquarters seven weeks before they are to be effective. Please send old label and new address.
PRICES: To members, $36.00, annually: to nonmembers, $160.00.
Add $15.00 for postage to countries outside the United States and Canada.
STATEMENT from By-Laws. The Society shall not be responsible for statements or opinions advanced in papers or . . . printed in its publications (B7.1, para. 3).
COPYRIGHT © 1990 by The American Society of Mechanical Engineers. Reprints from this publication may be made on condition that full credit be given the TRANSACTIONS OF THE ASME, JOURNAL OF HEAT TRANSFER, and the author, and date of publication be stated.
INDEXED by Applied Mechanics Reviews and Engineering Information, Inc.

Downloaded 04 Feb 2011 to 194.85.80.107. Redistribution subject to ASME license or copyright; see http://www.asme.org/terms/Terms_Use.cfm

(Contents continued)

TECHNICAL NOTES

B. D. Vujanović
Faculty of Technical Sciences,
University of Novi Sad,
21000 Novi Sad, Yugoslavia

S. E. Jones
Department of Engineering Mechanics,
The University of Alabama,
Tuscaloosa, AL 35487-0278

Approximate Solutions of Canonical Heat Conduction Equations

We consider three analytical methods for finding the approximate solutions of one-dimensional, transient, and nonlinear heat conduction problems based upon the canonical equations of heat transfer. The first method can be considered as a generalization or refinement of the integral method. The second is an iterative method similar to that of Targ utilized in boundary layer theory. The third method is a variational procedure introduced in the spirit of Gauss' variational principle of least constraint.

1 Introduction

Let us consider one-dimensional transient heat transfer problems, which are governed by partial differential equations of the form

$$\rho c \partial T/\partial t = \partial/\partial x[k(T)\partial T/\partial x] \tag{1.1}$$

where $T=T(t, x)$ denotes temperature, ρ is density, c is the constant heat capacity, t is time, x denotes the Cartesian spatial coordinate, and k is the thermal conductivity, which can depend upon temperature. This second-order parabolic differential equation can be replaced by a pair of partial equations of the first order in the following two ways:

$$\begin{aligned} \partial H/\partial t &= -k(T)\partial T/\partial x \\ \partial H/\partial x &= -\rho c T \end{aligned} \tag{1.2}$$

and

$$\begin{aligned} Q &= -k(T)\partial T/\partial x \\ \partial Q/\partial x &= -\rho c \partial T/\partial t \end{aligned} \tag{1.3}$$

where $H=H(t, x)$ denotes the so-called heat displacement function and $Q=Q(t, x)$ represents a conjugated function of H. In both pairs of these equations, the first equation represents the law of heat conduction, and the second equation represents the law of conservation of energy of the thermal process. We shall conditionally refer to the systems (1.2) and (1.3) as the "canonical" differential equations of transient heat conduction, alluding to the well-known analogy between the Lagrangian and Hamilton differential equations of motion in ordinary analytical mechanics. We believe that at least the canonical equations (1.2) have been introduced by Biot (see, for example, Biot, 1970). In fact, for two and three-dimensional cases, the functions H and Q are of vectorial character. Since we are only interested in cases having just one space dimension, our attention is focused on the simple scalar form of these equations. It must be noted that numerous authors have appreciated the use of the canonical equations (1.2) and (1.3) as an alternative to attacking the single equation of heat transfer (1.1) directly. As pointed out by Biot (1970, p. 5), ". . . in many cases it is preferable to use two separate equations (1.2)." For example, Biot's variational principle, widely used in linear and nonlinear heat transfer problems, employs as a starting point both sets of canonical equations. Recently, a new approximate method suitable for the study of phase-transition problems with time-varying boundary conditions was developed by Menning and Ozisik (1985) starting from these canonical equations. A hyperbolic version of the canonical equations has also been employed by Glass et al. (1985) for the numerical study of heat conduction with a finite velocity for the thermal disturbance in a semi-infinite medium. Based on the canonical equations (1.2) and (1.3), we discuss in this report three new methods, which are simple but rather accurate and can be utilized in the solution of a wide variety of transient linear and nonlinear heat conduction problems. Before describing these methods, we suppose that in each particular problem we are able to represent in advance the approximate temperature field as a polynomial depending on time t, the space coordinate x, and some finite number of unknown functions $q_1(t)$, $q_2(t)$, . . . , known as generalized coordinates

$$T=T(t, x, q_1, q_2, \ldots) \tag{1.4}$$

The physical significance of these coordinates can vary. For example, the generalized coordinate can represent the depth of the thermal penetration into a medium, the value of the time-dependent surface temperature, the value of the temperature flux at a given place, etc. We also suppose that the temperature field (1.4) is selected in such a way that some of the prescribed initial and boundary conditions are identically satisfied. The selection process for the approximate trial solutions (1.4) generally follows from numerous approximate methods used in engineering study of linear and nonlinear heat conduction problems, for example, the heat-balance integral method, the partial integration method, Galerkin's method, etc.

2 A Generalized Integral Method

The essence of this method is to take, as a basis, the mutual product of the canonical equations (1.2) or (1.3). Supposing for simplicity that the thermal conductivity is temperature independent, we have from (1.2) and (1.3), respectively,

$$\rho c k \partial/\partial x(T^2/2) = (\partial H/\partial x)(\partial H/\partial t) \tag{2.1}$$

and

$$\partial/\partial x(Q^2/2) = \rho c k(\partial T/\partial x)(\partial T/\partial t) \tag{2.2}$$

Each of these equations should be integrated over the space domain, which is involved in the thermal process. The question of which of these two equations shall be taken as a basis for approximate analysis will depend on the initial and boundary

---

Contributed by the Heat Transfer Division for publication in the JOURNAL OF HEAT TRANSFER. Manuscript received by the Heat Transfer Division June 12, 1989; revision received January 4, 1990. Keywords: Conduction, Moving Boundaries, Transient and Unsteady Heat Transfer.

conditions of the problem in question. If we take as a basis equation (2.1), we have to solve the second partial differential equation (1.2) first to find the heat displacement function $H=H(t, x, q_1, q_2, \ldots)$. In doing this we suppose that the rest of the initial and boundary conditions, which have not been satisfied by the primary selection of the trial solution (1.4), are identically satisfied. If we start from equation (2.2) by supposing that all initial and boundary conditions are satisfied by selecting (1.4), we simply substitute this into (2.2) and perform the integration over the given space domain. In both cases we arrive at a single ordinary differential equation of the first order with respect to the q's, which should be integrated subject to the given initial conditions. If the problem contains more than one generalized coordinate, additional differential equations with respect to the q's must be provided by some other means. In this respect, the method proposed is similar to the well-known integral method, which provides only one relation obtained by direct space integration of equation (1.1). The practical use of this method can best be illustrated by the following concrete examples.

Example 2.1 Consider a semi-infinite slab initially at zero temperature whose face at $x=0$ is subject to the power-law boundary temperature condition

$$T(t, 0)=f(t)=\alpha t^{n/2} \tag{2.3}$$

where α is a given constant and n is a positive integer. Assuming that ρ, c, and k are temperature independent, the temperature profile is taken to be of the form

$$T=f(t)(1-x/q)^3 \tag{2.4}$$

where $q=q(t)$ denotes the depth of the thermal penetration into the medium. Observe that this form of the approximate temperature field identically satisfies the boundary condition (2.3), and also the boundary conditions

$$T(t, x)_{x=q}=0, \qquad (\partial T/\partial x)\,|_{x=q}=0 \tag{2.5}$$

Using equation (2.4) and integrating the second equation (1.2) with respect to x, we find

$$H=(1/4)\rho c f(t) q (1-x/q)^4+K(t) \tag{2.6}$$

where $K(t)$ is an arbitrary function of time. To find $K(t)$, we substitute equation (2.6) into the first of equation (1.2)

$$\begin{aligned}-k(\partial T/\partial x) &= (cfnq/8t)(1-x/q)^4+(cf\dot{q}/4)\\ &\quad\times(1-x/q)^3+cf\dot{q}(x/q)(1-x/q)^3+\dot{K}\end{aligned} \tag{2.7}$$

where an overdot denotes the time derivative. Using the second boundary condition in (2.5), we conclude from the last relation that under the condition

$$-k(\partial T/\partial x)\,|_{x=0}=cfnq/8t+cf\dot{q}/4 \tag{2.8}$$

the function K is equal to zero. Substituting equation (2.6) into (2.1), integrating from $x=0$, taking into account (2.3) and the first boundary condition in (2.5), we obtain

$$-\alpha f^2/2=-f^2q[(11/224)\dot{q}+nq/64t] \tag{2.9}$$

where $\alpha=k/\rho c$ denotes the thermal diffusivity. This means that q satisfies the differential equation

$$(11/112)q\dot{q}+nq^2/32t=\alpha \tag{2.10}$$

whose solution, subject to the obvious initial condition $q(0)=0$, is found to be

$$q=[224/(11+7n)]^{1/2}(\alpha t)^{1/2} \tag{2.11}$$

The dimensionless heat flux at the surface $x=0$ can be determined from equation (2.8)

$$Q_{s(\text{approx})}=\left(-k\frac{\partial T}{\partial x}\bigg|_{x=0}\frac{\sqrt{\alpha t}}{kf}\right)=[7(n+1)^2/(22+14n)]^{1/2} \tag{2.12}$$

while the exact expression for the same quantity (see Carslaw and Jaeger, 1959) is given by

$$Q_{x(\text{exact})}=\frac{\Gamma(1+n/2)}{\Gamma(n+1)/2} \tag{2.13}$$

The present solution (2.12) is compared with the exact solution in Table 2.1. Observe that the approximate solution compares very well with the exact solution of the problem. The error does not exceed 0.5 percent in the entire range of the exponential parameter n.

Nomenclature

a = constant coefficient defined in text
B = given constant
c, c_0 = specific heat
D = dissipation function
$f(t)$ = time-dependent surface temperature
$F(t)$ = time-dependent surface heat flux
F = constant heat flux
G = constant nonlinear parameter
H = heat displacement function
$\mathbf{H}$ = heat displacement vector
$h(T)$ = heat constraint
$K(t)$, $K_1(t)$ = arbitrary functions of time
k = heat conductivity
L = latent heat
n = constant time exponent
$\mathbf{n}$ = unit vector normal to the boundary surface S^*
p = $q-s$
P = parameter p in dimensionless form
Q = heat flow per unit time and area (specific rate of heat flow); the function conjugate to H
Q_α = generalized thermal force
q, q_1, q_2 = generalized coordinates
R = function of temperature defined by equation (4.19)
S = dimensionless position of melt line
S^* = boundary surface
s = position of melt line
T = temperature
T_0 = constant surface temperature
T_m = melting temperature
t = time
t_m = the time when the ablation process commences
v = constant velocity of the ablation front
W = spatial optimization complex
x, y, z = coordinates
z_t = the surface temperature
Z, $\bar{Z}$ = Gauss constraint
α = thermal diffusivity
Γ = gamma function
$\overset{G}{\delta}$ = Gaussian variation symbol
μ = parameter defined by equation (3.10)
ν = melting parameter defined by equation (2.32)
Π = thermal potential
ρ = density
τ = dimensionless time

Table 2.1 **Dimensionless boundary heat flux Q_s for various values of the exponential parameter n**

n	$Q_{s(\text{exact})}$	$Q_{s(\text{approx})}$	% Error
0	0.5642	0.5640	0.00
1	0.8862	0.8819	0.48
2	1.1284	1.1225	0.52
3	1.3293	1.3229	0.48
4	1.5045	1.4979	0.44
5	1.6617	1.6550	0.40
6	1.8048	1.7988	0.32
7	1.9386	1.9322	0.33

Table 2.2 **Dimensionless boundary temperature z for various values of the parameter n**

n	z_{exact}	z_1 (2.20)	% Error	z_2 (2.21)	% Error
0	1.1284	1.1180	0.92	1.1339	-0.49
1	0.8862	0.8771	1.02	0.8908	-0.52
2	0.7523	0.7454	0.92	0.7559	-0.48
3	0.6647	0.6594	0.80	0.6676	-0.44
4	0.6018	0.5976	0.70	0.6042	-0.40
5	0.5539	0.5505	0.61	0.5559	-0.36
6	0.5158	0.5130	0.54	0.5175	-0.33
7	0.4847	0.4822	0.52	0.4861	-0.29

Example 2.2. Consider a semi-infinite slab initially at zero temperature whose face at $x=0$ is subject to the boundary condition

$$-k(\partial T/\partial x)|_{x=0}=F(t)=at^{n/2} \qquad (2.14)$$

where a, k, and n are given constants. We again take the trial solution in the form of a cubic polynomial

$$T=q_2(1-x/q_1)^3 \qquad (2.15)$$

where $q_2(t)$ denotes the surface temperature at $x=0$, and $q_1(t)$ is the penetration depth. Since the temperature gradients are prescribed at $x=0$ and $x=q_1$, it is suitable to use as a basis equation (2.2) (although the use of equation (2.1) as a basis is quite possible and would produce slightly better results). Substituting equation (2.15) into (2.2) and integrating with respect to x from $x=0$ to $x=q_1$, and taking into account that $Q|_{x=0}=F(t)$ and $Q|_{x=q_1}=0$, we arrive at the differential equation

$$5\rho ckq_1q_2\dot{q}_2+3\rho ck\dot{q}_1q_2^2=5F^2q_1 \qquad (2.16)$$

To find another differential equation for q_1 and q_2, we substitute (2.15) into the second canonical equation of the system (1.3) and integrate with respect to x over the same range. Thus, we obtain

$$\rho c(q_1\dot{q}_2+\dot{q}_1q_2)=4F(t) \qquad (2.17)$$

The solution of equations (2.16) and (2.17), subject to $q_1(0)=q_2(0)=0$, is

$$q_1=A(\alpha t)^{1/2}, \qquad q_2=(B/k)F(t)(\alpha t)^{1/2} \qquad (2.18)$$

where the constant coefficients A and B are

$$A=[(40n+64)/5]^{1/2}, \qquad B=[10/(5n+8)]^{1/2} \qquad (2.19)$$

The surface temperature in dimensionless form is, therefore,

$$z_1=[T(0,\ t)k/F(t)(\alpha t)^{1/2}]=[10/(5n+8)]^{1/2} \qquad (2.20)$$

Note that if we take as the basis of approximation equation (2.1), by using the same temperature profile (2.15), the approximate surface temperature is found to be

$$z_2=[(14n+36)/7(n+2)^2]^{1/2} \qquad (2.21)$$

The exact expression for the surface temperature is also available (see Carslaw and Jaeger, 1959) and is given by

$$z_{\text{exact}}=\frac{\Gamma(1+n/2)}{\Gamma(n/2+3/2)} \qquad (2.22)$$

The present solutions are exhibited in Table 2.2 and compared with the exact solution. It is seen that the solutions obtained by the method presented here are in very good agreement with the exact solutions of the same problem.

Both problems treated here have been solved by Zien (1976) by employing an exponential temperature profile and using another integral method. The results obtained by Zien are also in excellent agreement with the exact solution. However, the results obtained by means of equation (2.21) are in better agreement with the exact solution for small n than those obtained by Zien. For subsequent considerations, it will be useful to know the value of the penetration depth q_1 at the instant t_m when the surface temperature attains a fixed value $q_2=T_m$. This will be especially important for $n=0$ and $F=\alpha=\text{const}$. From equations (2.18), (2.19), and (2.20), we have

$$q_1(t_m)=(8/\sqrt{5})(\alpha t_m)^{1/2}=(16/5)T_mk/F \qquad (2.23)$$

where

$$t_m=(4/5)T_m^2k^2/\alpha F^2 \qquad (2.24)$$

and where T_m is the time at which $T(0,\ t_m)=t_m$ occurs.

Example 2.3. To conclude this section, consider a semi-infinite solid slab initially at zero temperature. The solid has been heated by a constant heat flux F at the boundary $x=0$. At time $t=0$, the constant melting temperature T_m is reached on the boundary and at that time, the depth of thermal penetration q is given by equation (2.23). For positive time the solid melts and all the melted material is removed from the boundary as soon as the melting begins (ablation). Let us denote by $x=s(t)$ the unknown position of the melting line (which is at the same time the location of the boundary of the body). Let us denote the thermal penetration depth by $q(t)$ measured from $x=0$. The boundary condition at the melting line is prescribed by

$$F+k(\partial T/\partial x)=\rho L ds/dt, \qquad x=s(t) \qquad (2.25)$$

where L denotes the coefficient of latent heat of melting. We suppose that the coefficients ρ, c, and k are constant. Let us approximate the transient distribution by the cubic polynomial

$$T=T_m[1-(x-s)/(q-s)]^3 \qquad (2.26)$$

Integrating the second canonical equation in (1.2) and selecting the function of integration in such a way that the first canonical equation in (1.2) is satisfied at $x=s$, we find the heat displacement function to be

$$H=(1/4)\rho cT_m(q-s)[1-(x-s)/(q-s)]^4 \qquad (2.27)$$

and the heat flux at $x=s$ is given by

$$-k(\partial T/\partial x)|_{x=s}=(1/4)cT_m(\dot{q}+3\dot{s}) \qquad (2.28)$$

Substituting (2.27) into (2.1), integrating from $x=s$ to $x=q-s$, and using the boundary conditions $T|_{x=s}=T_m$ and $T|_{x=q}=0$, we obtain

$$[(11/224)\dot{p}+(1/7)\dot{s}]p=\alpha/2 \qquad (2.29)$$

where

$$p=q-s \qquad (2.30)$$

To find another differential equation, we integrate the second canonical equation in (1.3) over the same space interval, using the temperature field (2.26). Since $Q|_{x=q}=0$ and $Q|_{x=s}=F-\rho L\dot{s}$, we obtain

$$(1/4)\dot{p}+\dot{s}(1+\nu)=F/cT_m \qquad (2.31)$$

where

$$\nu=\rho L/cT_m \qquad (2.32)$$

The initial conditions are $s(0)=0$ and (according to (2.23)) $p(0)=(16/5)T_m\ k/F$. Note that the system of equations (2.29)

Table 2.3 **Dimensionless position of the ablation front $S(\tau)$ and its velocity $dS/d\tau$ versus the melting time τ for $\nu=\sqrt{\pi}/2$**

τ	Present		Goodman	
	$S(\tau)$	$dS/d\tau$	$S(\tau)$	$dS/d\tau$
0.0	0	0.1564	0	0.1563
0.4	0.0884	0.2715	0.0875	0.2682
0.8	0.2090	0.3276	0.2066	0.3231
1.0	0.2763	0.3464	0.2730	0.3417
2	0.6535	0.4008	0.6453	0.3959
6	2.4939	0.4567	2.3796	0.4538
10	4.2553	0.4667	4.2229	0.4653
70	32.4364	0.4698	32.3984	0.4698

and (2.31) possesses a steady-state solution for $t\to\infty$. Namely, by supposing that $p=\text{const}$, it follows from (2.31) that the ablation front moves with a constant velocity $v(s=vt)$, where

$$v=(\alpha F/T_m k)/(1+\nu) \tag{2.33}$$

This value of the ablation speed is identical with the exact asymptotic solution of the same problem given by Landau (1950). Introducing the dimensionless variables

$$P=pF/T_m\,k,\quad S=sF/T_m\,k,\quad \tau=[F^2/\rho LkT_m]t \tag{2.34}$$

the system of equations (2.29) and (2.31) becomes

$$P[(11/224)P'+(1/7)S']=(1/2)\nu,\quad P(0)=16/5$$

$$(1/4)P'+(1+\nu)S'=\nu,\quad S(0)=0 \tag{2.35}$$

where a prime denotes differentiation with respect to the dimensionless time τ.

These equations can easily be integrated. In Table 2.3 we present the position of the ablation front and its velocity as functions of time. The same problem has been solved by Landau (1950), but the results are presented only in graphic form.

The results obtained here compare well with those reported by Landau (1950). The problem has also been discussed by Zien (1978) with a refinement of the integral method, and by Goodman (1964), who combined the classical integral method with Biot's variational principle. Since Goodman's approximate solutions are available in numerical form, they are also given in Table 2.3. The very close agreement between these two approximate solutions is obvious.

3 An Iterative Approximate Method Based on the Canonical Equations

In this section, we shall discuss an iterative procedure for finding approximate solutions of transient heat conduction problems. Essentially, the method is similar to the method of Targ, utilized in the solution of problems in boundary layer theory (see the references cited herein, especially Loitsansky, 1962). The method of successive approximation of ordinary differential equations, proposed by Picard (e.g., Ince, 1956), can serve as an elementary model to which the method presented here can be compared. We begin by selecting a temperature profile in the same way as explained in the introduction with equation (1.4). We also use a basis, the canonical equations (1.2) or (1.3). The method is simple and consists of successive integration of the canonical equations (1.2) or (1.3) with respect to the spatial coordinate x. After each integration, matching with the initial and boundary conditions is necessary in order to determine the arbitrary function of time (which appears as the result of the integration process). After each "cycle" of integration we arrive at an ordinary differential equation of the first order with respect to the generalized coordinate, which should be integrated subject to the given initial condition. Generally, we are able to improve the accuracy by repeating the process of integration, but actually the higher approximations introduce very laborious and tedious calculations. Thus, in practice, only a couple of integrations are needed for a reasonably good approximate solution to the problem. We illustrate the application of the method by the following concrete example.

Example 3.1. Consider a semi-infinite solid, which is initially at its melting temperature. The surface temperature is $T_0=\text{const}$ and the position of the melting line measured from $x=0$ is denoted by $s(t)$. Assuming that the thermophysical coefficients are temperature independent, the behavior of the process can be described by

$$\partial H/\partial x=-\rho cT\qquad 0<x<s(t),\quad t>0 \tag{3.1}$$

$$k(\partial T/\partial x)=-\partial H/\partial t \tag{3.2}$$

$$T(x,\,t)=T_m=0,\qquad x\geq s \tag{3.3}$$

$$T(t,\,0)=T_0=\text{const},\qquad t>0 \tag{3.4}$$

and

$$k(\partial T/\partial x)=-\rho L\dot{s},\qquad \text{at } x=s(t) \tag{3.5}$$

where the melting temperature T_m has been calibrated to zero without loss of generality. We approximate the transient temperature distribution in the liquid phase by a linear profile

$$T=T_0(1-x/s) \tag{3.6}$$

Thus, the boundary conditions (3.3) and (3.4) are identically satisfied. It is clear that the generalized coordinate $s(t)$, which locates the interface between the solid and liquid phases, plays the role of the depth of thermal penetration. Substituting equation (3.6) into (3.1), we find after integration

$$H=(1/2)\rho cT_0 s(1-x/s)^2+K(t) \tag{3.7}$$

where $K(t)$ is an arbitrary function of time. Substituting this into equation (3.2), we obtain

$$-k(\partial T/\partial x)=(1/2)\rho cT_0\dot{s}\,(1-x/s)^2 + \rho cT_0\dot{s}\,(x/s)\,(1-x/s)+\dot{K} \tag{3.8}$$

Matching this equation with the boundary condition (3.5), we find $\dot{K}=\rho L\dot{s}$. Thus,

$$\partial T/\partial x=-(T_0\dot{s}/\alpha)[(1/2)-(1/2)(x/s)^2+(2/\mu)] \tag{3.9}$$

where $\alpha=k/\rho c$ and

$$\mu=2T_0k/\rho L\alpha \tag{3.10}$$

Integrating equation (3.9), and taking (3.4) into account, we obtain

$$T=T_0-(T_0 s\dot{s}/\alpha)[(1/2)(x/s) - (1/6)(x/s)^3+(2/\mu)(x/s)] \tag{3.11}$$

Since $T=0$ for $x=s$, we arrive at the differential equation for s

$$s\dot{s}/\alpha=3\mu/(\mu+6) \tag{3.12}$$

This equation is to be integrated subject to the initial condition $s(0)=0$. Therefore, to a first approximation, the position of the melting line is given by

$$s(t)=s_1(t)=[6\mu/(\mu+6)]^{1/2}(\alpha t)^{1/2} \tag{3.13}$$

Note that the incident heat flux at $x=0$ should be calculated from (3.9). This means that

$$(\partial T/\partial x)_{1|x=0}=-(T_0\dot{s}/\alpha)\,(1/2+2/\mu) \tag{3.14}$$

To improve these results, we substitute equation (3.13) into (3.11) and get

$$T_1=T_0-3\mu T_0/(\mu+6)\{[(\mu+4)/(2\mu)]x/s-(1/6)(x/s)^3\} \tag{3.15}$$

and repeat the same procedure as in the previous step starting from the new temperature profile T_1. Substituting the last expression into (3.1), we have after integration,

$$-H_1=\rho cT_0x-3\mu\rho cT_0 s/(\mu+6)\{[(\mu+4)/4\mu](x/s)^2 -(1/24)(x/s)^4\}+K_1(t) \tag{3.16}$$

where $K_1(t)$ is an arbitrary function of integration. Substituting this into (3.2), and matching with (3.5), we obtain

$$\partial T/\partial x = -[3\mu T_2 \dot{s}/\alpha(\mu+6)]\{-[(\mu+4)/4\mu](x/s)^2 + (1/8)(x/s)^4\} - (3/8)(T_0\dot{s}/\alpha) \times [(\mu+8)/(\mu+6)] - 2T_0\dot{s}/\alpha\mu \qquad (3.17)$$

Integration of this equation, taking (3.4) into account, leads to

$$T = T_0 - [3\mu T_0 s\dot{s}/\alpha(\mu+6)]\{-[(\mu+4)/12\mu](x/s)^3 + (1/40)(x/s)^5\} - (3/8)(T_0 s\dot{s}/\alpha)[(\mu+8)/(\mu+6)](x/s) - 2[T_0 s\dot{s}/\mu\alpha](x/s) \qquad (3.18)$$

By using the boundary conditions (3.3), we arrive at the differential equation for s

$$s\dot{s}(\mu^2+20\mu+60) = 5\alpha\mu(\mu+6) \qquad (3.19)$$

Integrating subject to $s(0)=0$, we find the improved approximate solution

$$s(t) = s_2(t) = [(10\mu^2+60\mu)/(\mu^2+20\mu+60)]^{1/2}(\alpha t)^{1/2} \qquad (3.20)$$

The improved heat flux at $x=0$ is obtained from equation (3.17).

$$(\partial T/\partial x)_{2|x=0} = -(T_0\dot{s}/\alpha)[(3/8)(\mu+8)/(\mu+6) + (2/\mu)] \qquad (3.21)$$

The position of the melt line and the incident heat flux at $x=0$ obtained by the iterations (3.13) and (3.20), and (3.14) and (3.21), are presented in Tables 3.1 and 3.2 for various values of the melting parameter μ. These results are compared with the exact solution of the problem given by Carslaw and Jaeger (1959). It is observed that even for a relatively poor approximate temperature field (3.6), the results to the first approximation are very satisfactory. However, the improvement due to the calculation of a higher approximation can clearly be observed. In fact, as demonstrated in both tables, the error is practically negligible for the second approximation for a wide range of the melt parameter μ.

The reader will also note that a very remarkable improvement upon Goodman's approximate solution has been achieved. By applying the integral method and starting with a quadratic temperature profile, Goodman (1964) reports that for the position of the melt line the percentage error is about 7 percent.

Table 3.1 Dimensionless position of the melt line $s/(\alpha t)^{1/2}$ for various values of the melting parameter μ

μ	Exact $s/(\alpha t)^{1/2}$	First approx. $s_1/(\alpha t)^{1/2}$	% Error	Second approx. $s_2/(\alpha t)^{1/2}$	% Error
0.5	0.6802	0.6794	-0.12	0.6802	0.001
1.0	0.9296	0.9258	-0.40	0.9296	0.000
1.5	1.1042	1.0954	-0.80	1.1043	0.012
2.0	1.2401	1.2247	-1.20	1.2403	0.020
2.5	1.3517	1.3284	-1.70	1.3520	0.020
3.0	1.4464	1.4142	-2.2	1.4467	0.020

Table 3.2 Values of the dimensionless incident temperature flux $-(\partial T/\partial x)|_{x=0}(\alpha t)^{1/2}/T_0$ for various values of the melting parameter μ

μ	Exact	First approx. (3.14)	% Error	Second approx. (3.21)	% Error
0.5	1.5257	1.5286	-0.70	1.5271	-0.02
1.0	1.1533	1.1573	-0.34	1.1537	-0.04
1.5	0.9986	1.0042	-0.55	1.9985	-0.01
2.0	0.9109	0.9186	-0.84	0.9136	-0.30
2.5	0.8536	0.8635	-1.20	0.8539	-0.04
3.0	0.8136	0.8250	-1.40	0.8138	-0.02

4 A Variational Approach Based on the Canonical Heat Conduction Equations

The remainder of this paper will be devoted to some variational aspects of nonlinear heat conduction theory based on the canonical equations. More specifically, we shall employ the general ideas of Gauss' differential variational principle of least constraint and exploit its optimal properties as a tool for finding approximate solutions. Using the heat conduction equation (1.1) as a basis, Gauss' variational principle has been established and used in linear and nonlinear heat conduction analyses (see Vujanović, 1976, Vujanović and Bačlić, 1976, or Vujanović, 1990). Here we try to confirm that the Gaussian method can also be applied to the canonical heat conduction equations. In addition, in this paper as in a previous one (Vujanović et al., 1990), we demonstrate that Biot's variational principle, widely used in thermal engineering and mathematical physics, can be fully interpreted in light of Gauss' variational principle. In the framework of the theory presented here, Biot's principle represents just one of two possibilities for minimizing the Gauss constraint.

Let us consider a nonlinear problem in which the heat capacity is a given function of the temperature $c=c(T)$, while for the sake of simplicity the thermal conductivity k is taken to be a constant. Following the rules suggested by Biot (1970), we introduce the heat content quantity

$$h(T) = \int_0^T \rho c(T)dT, \qquad \rho = \text{const} \qquad (4.1)$$

Let us consider a three-dimensional temperature field $T=T(t, x, y, z)$, and introduce the heat displacement vector $\mathbf{H}=\mathbf{H}(t, x, y, z)$. The canonical equations can now be written in the form

$$h(T) = -\operatorname{div}\mathbf{H} \qquad (4.2)$$

$$\operatorname{grad} T = -(1/k)\dot{\mathbf{H}} \qquad (4.3)$$

Recalling some of the general results of Vujanović (1976), Vujanović and Bačlić (1976), and Vujanović et al. (1990), we form the following Gauss "constraint" in the form of a space integral combined with the differential equation (4.3):

$$Z = (1/2)\int_V k[\operatorname{grad} T - (1/k)\dot{\mathbf{H}}]^2 dV \qquad (4.4)$$

where V denotes the volume of a body whose boundary surface is S^*. By $\mathbf{n}$ we denote the unit vector pointing outward from the boundary surface.

We define the Gaussian variations in the following two ways, which constitute the possible modes of optimization of the Gauss constraint Z:

First possibility:

$$\overset{G}{\delta}\dot{\mathbf{H}} \neq 0, \qquad \overset{G}{\delta}T = 0, \qquad \overset{G}{\delta}(\operatorname{grad} T) = 0 \qquad (4.5)$$

Second possibility:

$$\overset{G}{\delta}(\operatorname{grad} T) \neq 0, \qquad \overset{G}{\delta}\mathbf{H} = 0, \qquad \overset{G}{\delta}\dot{\mathbf{H}} = 0, \qquad \overset{G}{\delta}T = 0 \qquad (4.6)$$

where the symbol $\overset{G}{\delta}$ denotes the Gaussian variations. Gauss' principle of least constraint states that subject to the prescribed variational rules, under the condition that the canonical equation (4.2) is identically satisfied, the Gauss constraint attains its absolute minimum, whose value is equal to zero, "along the actual trajectory" of the process. Namely, the minimum is achieved along the exact solution of the problem. In practical applications of the Gauss principle, we perform the minimization of the Gauss constraint (4.4) with respect to the components of the vectors $\dot{\mathbf{H}}$ or grad T, which can be stated by the following two variational equations:

$$\overset{G}{\delta}Z_{(\dot{\mathbf{H}})} = 0 \qquad (4.7)$$

or

$$\overset{G}{\delta}_{(\operatorname{grad} T)}Z = 0 \qquad (4.8)$$

To employ Gauss's principle as a direct method, we first introduce the approximate temperature field

$$T = T(t, x, y, z, q_1, q_2, \ldots) \tag{4.9}$$

in terms of properly selected generalized coordinates. Also, we assume that the heat displacement vector

$$\mathbf{H} = \mathbf{H}(t, x, y, z, q_1, q_2, \ldots) \tag{4.10}$$

is found as a solution of the differential equation (4.2), and the prescribed initial boundary conditions are satisfied.

According to the variational rules (4.5) and (4.6), we must identify the characteristic complex of parameters (which depend solely on the generalized coordinates) that represent $\dot{\mathbf{H}}$ or grad T, and minimization of Z must be performed with respect to those complexes. For example, since

$$\dot{\mathbf{H}} = (\partial \mathbf{H}/\partial q_\alpha)\dot{q}_\alpha + \partial \mathbf{H}/\partial t \qquad (\alpha = 1, 2, \ldots,) \tag{4.11}$$

Gauss' variation of this quantity is

$$\overset{G}{\delta}\dot{\mathbf{H}} = (\partial \mathbf{H}/\partial q_\alpha)\overset{G}{\delta}\dot{q}_\alpha \tag{4.12}$$

with

$$\overset{G}{\delta}\dot{q}_\alpha \neq 0, \qquad \overset{G}{\delta}q_\alpha = 0 \tag{4.13}$$

Thus, if we wish to minimize Z in accordance with the first possibility (4.5), the variational equation (4.7) implies that $\overset{G}{\delta}Z_{(\dot{\mathbf{H}})} = (\partial Z/\partial \dot{q}_\alpha)\partial \dot{q}_\alpha = 0$, or simply,

$$\partial Z/\partial \dot{q}_\alpha = 0 \qquad (\alpha = 1, 2, \ldots,) \tag{4.14}$$

since the $\overset{G}{\delta}\dot{q}_\alpha$ are completely arbitrary. This result stipulates that the minimization of the Gauss constraint is performed with respect to the generalized velocity. In equation (4.11) and in the subsequent text, repeated Greek indices are summed.

A similar situation arises by applying the second possibility for minimization of Z indicated by (4.6). Since the selection of the optimization parameters is simple and depends mainly on the form of the temperature profile, we will explain this selection afterward by means of a concrete example.

It is important to note that the optimization of Z, in light of the first possibility (4.14), is identical with the relevant equations that stem from Biot's variational principle. To see this we substitute (4.9) and (4.10) into (4.4) and from (4.14) we find

$$\partial Z/\partial \dot{q}_\alpha = \partial/\partial \dot{q}_\alpha\left[\int_V (1/2k)\dot{\mathbf{H}}\bullet\dot{\mathbf{H}}dV\right] - \int_V \mathrm{grad}T\bullet(\partial \mathbf{H}/\partial q_\alpha)dV = 0 \tag{4.15}$$

where we have used the functional relation $\partial \dot{\mathbf{H}}/\partial \dot{q}_\alpha = \partial \mathbf{H}/\partial q_\alpha$, which follows from (4.11). The integration by parts of the last term yields

$$\int_V \mathrm{grad}\ T\bullet(\partial \mathbf{H}/\partial q_\alpha)dV = \int_V - T\mathrm{div}(\partial \mathbf{H}/\partial q_\alpha)dV + \int_{S*} T\mathbf{n}\bullet(\partial \mathbf{H}/\partial q_\alpha)dS^* \tag{4.16}$$

Employing the commutative property of the operators div and $\partial/\partial q_\alpha$ and using the identity (4.2), equation (4.15) can be written as

$$\partial Z/\partial \dot{q}_\alpha = \partial/\partial \dot{q}_\alpha\left[\int_V (1/2k)\dot{\mathbf{H}}\bullet\dot{\mathbf{H}}dV\right] + \int_V T(\partial h/\partial q_\alpha)dV + \int_{S*} T\mathbf{n}\bullet(\partial \mathbf{H}/\partial q_\alpha)dS^* = 0 \tag{4.17}$$

or

$$\partial Z/\partial \dot{q}_\alpha = \partial D/\partial \dot{q}_\alpha + \partial \Pi/\partial q_\alpha - Q_\alpha = 0 \qquad (\alpha = 1, 2, \ldots) \tag{4.18}$$

where D, $\mathbf{H}$, and Q_α denote, respectively, the dissipative function, the thermal potential, and the generalized forces of the thermal process, defined by

$$D = \int_V (1/2k)\dot{\mathbf{H}}\bullet\dot{\mathbf{H}}dV, \quad \Pi = \int_V R\ dV, \quad R = \int_0^h T\ d\ h,$$

$$Q_\alpha = -\int_{S*} T\mathbf{n}\bullet(\partial \mathbf{H}/\partial q_\alpha)dS^* \tag{4.19}$$

However, equations (4.18) are identical with Biot's variational principle (see Biot, 1970, pp. 86–88), which confirms our statement.

The optimization equation $\partial Z/\partial \dot{q}_\alpha = 0$ is equivalent to Biot's variational principle for the case $k = k(T)$, which can be easily demonstrated. It is also important to emphasize that according to our experience, in practical situations it is easier to form the simple equations (4.14) than to calculate the functions D, Π, and Q_α separately as demanded by Biot's theory. Finally, the second possibility for optimization of Z, indicated by (4.8), frequently generates a more accurate approximate solution as pointed out by Vujanović (1990).

Example 4.1. As an illustration, we consider a semi-infinite solid initially at zero temperature. Let the surface $x = 0$ be suddenly raised to temperature $T_0 = \mathrm{const}$ at time $t = 0$. We assume the heat capacity is a linear function of the temperature

$$c = c_0\{1 + G[(T/T_0) - 1]\} \tag{4.20}$$

where G is a given constant. The thermal conductivity k is assumed to be constant. The temperature distribution in the body is assumed to take the form

$$T = T_0(1 - x/q)^2 \tag{4.21}$$

where $q = q(t)$ denotes the penetration depth. From equations (4.1) and (4.2) we find, respectively,

$$h = \rho c_0[T(1 - G) + (1/2)GT^2/T_0] \tag{4.22}$$

and

$$H = \rho c_0 T_0 q[(1/3)(1 - G)(1 - x/q)^3 + (1/10)G(1 - x/q)^5] \tag{4.23}$$

The temperature gradient at $x = 0$ follows from equation (4.3)

$$(\partial T/\partial x)\,|_{x=0} = -(1/k)\dot{H}\,|_{x=0} = -(T_0/\alpha)(1/30)(10 - 7G)\dot{q} \tag{4.24}$$

Let us solve the problem by minimizing the Gauss constraint

$$z = \int_0^q (1/2)k[(\partial T/\partial x) - (1/k)\dot{H}]^2 dx \tag{4.25}$$

in accordance with the two possibilities indicated by equations (4.7) and (4.8). As pointed out earlier, to optimize Z according to the first possibility, we must use equation (4.14). Substituting equations (4.21) and (4.23) into (4.25), we find

$$\bar{Z} = (Z/\rho^2 c_0^2 T_0^2) = q\dot{q}^2[(13/315)(1 - G)^2 + (71/3780)G(1 - G) + (23/9900)G^2] - \alpha\dot{q}[(7/15)(1 - G) + (11/105)G] + (4/3)\alpha^2/q \tag{4.26}$$

To minimize (4.25) in the spirit of the second possibility (4.8), we find from (4.21)

$$\partial T/\partial x = -2T_0 W(1 - x/q) \tag{4.27}$$

where

$$W = 1/q \tag{4.28}$$

is the "complex" representing $\partial T/\partial x$, by means of which the optimization of Z should be performed. Thus, we find

$$\bar{Z} = (Z/\rho^2 c_0^2 T_0^2) = q\dot{q}^2[(13/315)(1 - G)^2 + (71/3780)G(1 - G) + (23/9900)G^2] - \alpha q\dot{q}W[(7/15)(1 - G) + (11/105)G] + (4/3)\alpha^2 qW^2 \tag{4.29}$$

Minimizing (4.26) with respect to $\dot{q}$, i.e., $\partial\bar{Z}/\partial\dot{q} = 0$, we arrive

Table 4.1 Values of the dimensionless incident temperature flux at $x=0$: $Q/k = -(\partial T/\partial x)|_{x=0}\,(\alpha t)^{1/2}/T_0$ obtained by the two methods for optimization of Z and the numerical values given by Aziz and Na (1981). The values of G are taken from Aziz and Na.

G	Numerical	First possibil. Q/k(q$_1$)	% Error	Second possibil. Q/k(q$_2$)	%Error
0	0.5645	0.5664	-0.34	0.5634	0.19
0.0913	0.5476	0.5441	0.64	0.5472	0.07
0.1890	0.5295	0.5260	0.67	0.5292	0.06
0.2951	0.5084	0.5091	-0.13	0.5091	-0.14
0.4131	0.4842	0.4819	0.47	0.4858	-0.33
0.5501	0.4546	0.4529	0.37	0.4576	-0.66
0.7272	0.4126	0.4120	0.15	0.4189	-1.53
0.8613	0.3774	0.3776	-0.05	0.3883	-2.89
0.9021	0.3568	0.3662	-0.11	0.3788	-3.55
-0.0863	0.5795	0.5755	0.69	0.5784	0.18
-0.7321	0.6830	0.6776	0.79	0.6806	0.35
-1.3096	0.7636	0.7574	0.81	0.7607	0.38
-2.2691	0.8814	0.8741	0.83	0.8841	-0.31
-3.0901	0.9709	0.9628	0.83	0.9670	0.40

at a differential equation, whose solution subject to $q(0)=0$ is found to be

$$q_1 = [(97{,}020 - 75{,}240G)/(8580 - 13{,}255G + 5158G^2)]^{1/2}(\alpha t)^{1/2} \tag{4.30}$$

As discussed earlier in this section, the same result follows by applying Biot's variational principle (4.18).

Similarly, the second possibility for optimization, i.e., $\partial \bar{Z}/\partial W = 0$, leads to a solution of the form

$$q_2 = [560/(49 - 38G)]^{1/2}(\alpha t)^{1/2} \tag{4.31}$$

by employing (4.28).

Before proceeding to present the results for the nonlinear case $G \neq 0$, we note that for the linear case $G=0$, the surface temperature gradients obtained by means of equation (4.24) are:

$$(\partial T/\partial x)\,|_{x=0}(q_1) = -0.5664T_0(\alpha t)^{-1/2} \tag{4.32}$$

and

$$(\partial T/\partial x)\,|_{x=0}(q_2) = -0.5634T_0(\alpha t)^{1/2} \tag{4.33}$$

Both agree very well with the exact numerical value of this quantity: $-0.5645\ T_0\ (\alpha t)^{-1/2}$. However, substituting equations (4.30) and (4.31) into (4.26), we find that the square residuals are, respectively,

$$\bar{Z}(t)_{(q_1)} = 0.0164\alpha^{3/2}t^{-1/2} \tag{4.34}$$

and

$$\bar{Z}(t)_{(q_2)} = 0.0042\alpha^{3/2}t^{-1/2} \tag{4.35}$$

Thus, if we take the least value of $\bar{Z}$ to be a measure of the quality of the solution (as proposed, for example, by Citron, 1960), then the second type of optimization is better. The problem discussed here has been solved numerically by Aziz and Na (1981), and the surface heat flux has been calculated for some values of the nonlinear parameter G. In Table 4.1, we present the surface heat fluxes obtained by means of the two methods of optimization of Z. The numerical values of the same quantity are given for comparison. It is evident that the agreement of both approximate solutions with the numerical solution is satisfactory for a rather wide range of the nonlinear parameter G. It is also observed that the results obtained by means of the second method of optimization are in slightly better agreement with the numerical solution for negative values of the nonlinear parameter G.

5 Concluding Remarks

The primary aim of this paper has been to demonstrate that the canonical equations of heat transfer can serve as a useful basis for establishing various methods for approximation. To be specific, we have presented the following three methods:

- A generalization of Goodman's integral method, discussed in Section 2;
- An iterative approximate procedure, similar to the method of Targ, developed in Section 3; and finally
- A variational method based generally on the ideas of Gauss' differential variational principle of least constraint, presented in Section 4.

It was shown that the minimization of the corresponding Gauss constraint Z with respect to the generalized velocities is equivalent to the well-known Biot variational method. However, the second possibility for optimization of the Gauss constraint with respect to the spatial complex also produces very good results in many instances. Illustrative examples have been selected to exemplify the various aspects of each particular method. Agreement of the results obtained by these methods with the known solutions of the various problems is quite satisfactory.

Acknowledgments

This investigation has been supported by the United States–Yugoslavia Joint Board on Technological Cooperation under grant No. JF 805. The award was recommended to the Board by the National Science Foundation. The computer work, ably done by Professor Dragon Spasić, is very much appreciated.

References

Aziz, A., and Na, T. Y., 1981, "A Noniterative Numerical Solution for Step-Heated Semi-infinite Solid With Temperature Dependent Thermal Properties," *Computers and Chemical Engineering*, Vol. 5, pp. 115–117.

Biot, M. A., 1970, "Variational Principles in Heat Transfer," *Oxford Mathematical Monographs*, Clarendon, Oxford, United Kingdom.

Carslaw, H. S., and Jaeger, J. C., 1959, *Conduction of Heat in Solids*, Clarendon, Oxford, United Kingdom.

Citron, S. J., 1960, "A Note on the Relation of Biot's Method in Heat Conduction to a Least-Squares Procedure," *Journal of the Aerospace Sciences*, Vol. 27, No. 4, pp. 317–318.

Glass, D. E., Ozisik, M. N., and Vick, B., 1985, "Hyperbolic Heat Conduction With Heat Surface Radiation," *Int. J. Heat Mass Transfer*, Vol. 28, No. 10, pp. 1823–1830.

Goodman, T. R., 1964, "Application of Integral Methods to Transient Nonlinear Heat Transfer," *Advances in Heat Transfer*, T. Irvine and J. Hartnett, eds., Academic Press, New York.

Ince, E. L., 1956, *Ordinary Differential Equations*, Dover, New York.

Landau, H. G., 1950, "Heat Conduction in a Melting Solid," *Quarterly of Applied Mathematics*, Vol. 8, pp. 81–91.

Loitsansky, L. G., 1962, *Laminar Boundary Layer*, GOSIZDAT F.-M., Moscow [in Russian].

Mennig, J., and Ozisik, M. N., 1985, "Coupled Integral Equations for Solving Melting or Solidification," *Int. J. Heat Mass Transfer*, Vol. 28, No. 10, pp. 1823–1830.

Vujanović, B., 1976, "The Practical Use of Gauss' Principle of Least Constraint," ASME *Journal of Applied Mechanics*, Vol. 43, pp. 491–496.

Vujanović, B., 1989, "A Variational Approach to the Problem of Solidification of a Metal Semi-infinite Thermally Nonlinear Body," *Acta Mechanica*, Vol. 77, pp. 231–240.

Vujanović, B., and Bačlić, B., 1976, "Applications of Gauss' Principle of Least Constraint to the Nonlinear Heat Transfer Problems," *Int. J. Heat Mass Transfer*, Vol. 19, pp. 721–730.

Vujanović, B., Jones, S. E., and Kawaguchi, T., 1990, "On Certain Gaussian Aspects of Biot's Canonical Equations in Heat Transfer Theory," *Tensor*, in press.

Zien, T. F., 1976, "Approximate Calculation of Transient Heat Conduction," *AIAA Journal*, Vol. 14, No. 3, pp. 404–406.

Zien, T. F., 1978, "Integral Solution of Ablation Problems With Time-Dependent Heat Flux," *AIAA Journal*, Vol. 16, No. 12, pp. 1287–1295.

Investigation of Transient Heat Transfer Coefficients in Quenching Experiments

A. M. Osman

J. V. Beck

Heat Transfer Group,
Department of Mechanical Engineering,
Michigan State University,
East Lansing, MI 48824

Methodological and experimental aspects of the estimation of transient heat transfer coefficients in quenching experiments, using inverse heat transfer methods, were addressed and investigated. Beck's method was used for the estimation of the transient heat transfer coefficient history from interior transient temperature measurements during quenching. Experiments involved plunging a high-purity copper sphere into cooling baths without boiling. The sphere was instrumented with several interior thermocouples for measuring the transient temperature response during quenching. Water and ethylene glycol were investigated. The early transient values of the heat transfer coefficient history were found to be about 100–120 percent higher than the values predicted using well-known empirical correlations for free convection. The later time values were in good agreement with those predicted with empirical correlations. The transient inverse technique has the capability of estimating early transients and subsequent quasi-steady-state values of heat transfer coefficient in a single transient experiment.

1 Introduction

During quenching and heat treatment processes, temperatures and cooling rates in the bodies should be controlled within certain limits in order to achieve the desired metallurgical properties. For rapid cooling rates, the heat transfer from the quenched specimen to the cooling bath is not well understood. Understanding of early time transients in heat transfer is important for the optimal design of the quenching and heat treatment processes and the selection of ideal fluid baths. In order to predict the transient temperature distribution and the resultant stress distribution upon quenching, the time-dependent heat transfer coefficient function $h(t)$, is required. To obtain the required $h(t)$ data, experiments with an instrumented prototype or scaled model are necessary for the estimation of $h(t)$.

Although design parts have been quenched for decades, there has been inadequate confirmed analytical and experimental investigation of the associated transient heat transfer coefficient estimation problem. This is particularly true for the experimental investigation of early time transients in heat transfer coefficient during quenching. Stolz (1960) introduced a simple inverse convolution procedure for the determination of the surface heat flux and heat transfer coefficient in quenching experiments; exact matching of the measured and calculated temperatures was used. Stolz's method is restricted to relatively large time steps and is very sensitive to measurement errors. Crosbie and Banerjee (1974) investigated the transient heat conduction in a solid sphere quenched in oil. The Volterra integral equation of the second kind was used for the prediction of the surface temperature from a typical h curve for boiling. Sankaran and Witte (1985) determined the boiling curve for quenching experiments in methanol and water. Irving and Westwater (1986) used the transient quenching method to obtain the boiling curve (q versus ΔT) with spheres made from high-purity metals. The nonlinear parameter estimation procedure of Beck (1970) was used for the estimation of the boiling heat flux distribution around the quenched spheres. Boiling curves were found to be strongly dependent on the metal, size, cooling vessel size, and level of subcooling.

Only now is active work being pursued for the characterization of small-time transient heat transfer coefficients and heat fluxes in quenching experiments. Osman (1987) and Osman and Beck (1989) used Beck's method (Beck et al., 1985) for the estimation of transient heat transfer coefficients in quenching experiments of one- and two-dimensional spheres made from high-purity copper (OFHC). Park et al. (1989) studied the optimal selection of parameters for the calculations of quenching heat flux using Beck's method.

When a body is plunged into a fluid, the instantaneous surface heat flux should start at a very large value and decrease rapidly if the contact between the solid and fluid were perfect. This behavior was not previously observed, however, possibly because sufficiently powerful inverse algorithms were not used and appropriate measurements were not available. The purpose of this paper is: (1) to describe a methodology for the estimation of the surface transient heat transfer coefficient from measured transient temperatures at appropriate points within the quenched body, (2) to aid in more understanding of early transients in heat transfer from the quenched bodies to the cooling bath, and (3) to obtain an accurate estimate of transient heat transfer coefficient during quenching without boiling.

Estimation of the *surface* heat transfer coefficient from *interior* temperature measurements is called an inverse heat transfer coefficient problem (IHTCP). This estimation technique is very appropriate for cases subjected to large and abrupt changes in the time-dependent thermal boundary conditions, such as during quenching. The sequential function specification (SFS) method (Beck et al., 1985) was used for the estimation of $h(t)$ from measured thermocouple data. The quenching experiments involved plunging of a high-purity copper sphere into cooling baths; distilled water and ethylene glycol were investigated.

Experimental facilities and procedures are briefly described in Section 2. A formulation of the IHTCP is given in Section 3. The SFS method for the estimation of the $h(t)$ function is described in Section 4. The experimental results and discussion are given in Section 5. Summary and conclusions are given in Section 6.

Contributed by the Heat Transfer Division for publication in the JOURNAL OF HEAT TRANSFER. Manuscript received by the Heat Transfer Division December 7, 1988; revision received February 22, 1990. Keywords: Conduction, Measurement Techniques, Transient and Unsteady Heat Transfer.

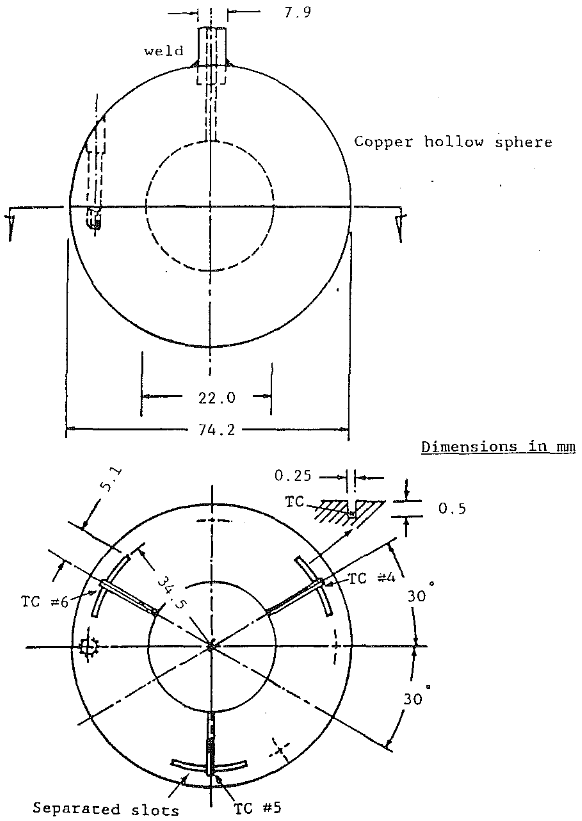

Fig. 1 Schematic diagram of the test sphere

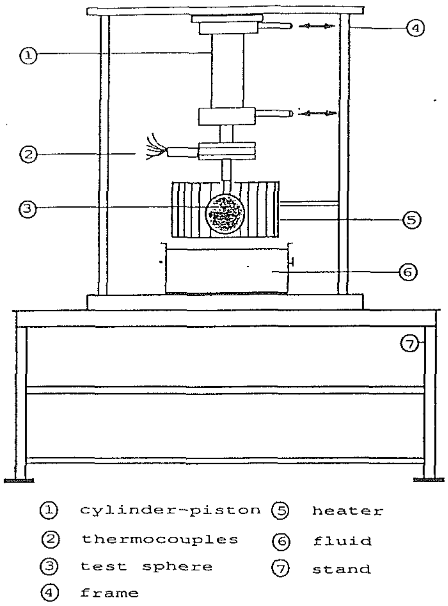

Fig. 2 Schematic diagram of the quenching apparatus

2 Experimental Facilities and Procedures

In this section, the experimental facilities and procedures are briefly described. A hollow copper sphere of 0.0742 m o.d. and 0.0220 m i.d. was machined as two hemispheres. Three thermocouples, TC #4, 5, and 6, were embedded (peened) into separated slots on the flat surface of the lower hemisphere at the same depth of 0.0026 m from the outer surface and $\pi/3$ rad apart. The average of the three thermocouples is used as input to the inverse code. Figure 1 shows a schematic diagram of the test sphere. The thermocouples were made from 30 gage thermocouple wire type "E."

Two separated slots, each 0.25 mm in width, 0.50 mm in depth, and 5.0 mm in length, were machined at each thermocouple location. The measuring (hot) junction was made by inserting each lead into the separated slots and carefully peening 3.8 mm of the lead into each slot. A measuring junction of this type is called a separated junction or intrinsic junction. This installation method was selected because it provides rapid response and good thermal contact between the thermocouples and the test specimen.

The quenching apparatus consists of: (1) a dropping hydraulic system, (2) a tubular heating furnace, (3) a fluid vessel, and (4) a steel frame holder. A schematic diagram of the quenching apparatus is shown in Fig. 2. A cylindrical vessel, 0.22 m in diameter and 0.15 m deep, was used to hold the cooling fluid bath. The transient temperature data acquisition hardware was based on a PDP 11/03 microcomputer. The data acquisition system was tested and calibrated with the present sphere assembly and the results showed that the accuracy of the temperature data was within ±0.2°C. The response time of the amplifiers was determined experimentally by using a step change in the input voltage. The response time (time to achieve 64 percent of the change for a unit step input) was found to be 0.4 s. Since a measurement time step of 0.1 s was used, it was necessary to correct the temperature measurements due to time lag. The procedure for correcting the measured temperatures is outlined in the appendix.

In preparation for the quenching experiments, the surface of the sphere was carefully polished with very fine sandpaper and cleaned with acetone. The sphere was heated in a clamshell heater to the desired temperature, slightly less than the fluid boiling temperature. When a uniform temperature was reached, the data acquisition process was started and then the sphere was plunged into the cooling bath using the cylinder-piston hydraulic system. Data acquisition was started about 0.5 to 1 s before quenching.

3 Formulation of the IHTCP

The mathematical model describing the IHTCP for the estimation of the heat transfer coefficient is given below. During quenching experiments, the outer surface of the hollow sphere is exposed to an external transient convective boundary condition starting at $t = t_0$. The inner surface of the sphere is assumed to be thermally insulated since the thermal capacity

Nomenclature

$h(t)$ = heat transfer coefficient, W/m^2-°C
k = thermal conductivity, W/m-°C
r = number of future time steps
R_{in} = inner radius of sphere, m
R_{out} = outer radius of sphere, m
t = time coordinate, s
$T(r, t)$ = temperature, °C
$T_0(r)$ = initial temperature distribution, °C
$T_\infty(t)$ = fluid temperature, °C
Y = temperature measurements, °C
Z = sensitivity coefficient, °C^2-m^2/W
α = thermal diffusivity, m^2/s

Subscripts

i = future time index
m = time index
M = total number of time steps

Superscripts

n = iteration index
$\hat{}$ = estimated value

of the enclosed air is much smaller than the thermal capacity of the copper sphere. The temperature distribution in the solid body upon quenching is described by the heat conduction equation, assuming constant thermal properties

$$\frac{1}{r^2}\frac{\partial}{\partial r}\left(r^2\frac{\partial T(r,t)}{\partial r}\right)=\frac{1}{\alpha}\frac{\partial T(r,t)}{\partial t},\quad t_0<t\leq t_M,$$
$$R_{in}\leq r\leq R_{\text{out}} \tag{1}$$

with the boundary and initial conditions

$$\left.\frac{\partial T(r,t)}{\partial r}\right|_{r=R_{in}}=0,\quad t_0<t\leq t_M \tag{2}$$

$$-k\left.\frac{\partial T(r,t)}{\partial r}\right|_{r=R_{\text{out}}}=h(t)[T(R_{\text{out}},t)-T_\infty(t)],\ t_0<t\leq t_M \tag{3}$$

$$T(r,t_0)=T_0(r),\ R_{in}\leq r\leq R_{\text{out}} \tag{4}$$

where $T(r, t)$ is the temperature, r is radial position, R_{in} and R_{out} are inner and outer radii of the sphere, respectively, t is time, t_M is final time, α is thermal diffusivity, and k is thermal conductivity. The functions $T_\infty(t)$ and $T_0(x)$ are, respectively, the fluid temperature and the initial temperature distribution.

The time interval $t_0\leq t\leq t_M$ is divided into M equal subintervals, each of length $\Delta t_m=t_m-t_{m-1}$, where Δt_m corresponds to the measurement time step size used in the data acquisition. The discrete interior temperature measurements, $Y_m=Y(t_m)$, denote the value of the transient temperature at sensor location r^* and time t_m. The IHTCP is to estimate the unknown $h(t)$ function from the measurements Y_m, $m=0, 1, 2, \ldots, M$, for the model given by equations (1)–(4).

4 Sequential Function Specification Method

This section derives the sequential function specification method (SFS) for solving the ill-posed inverse heat transfer coefficient problem (IHTCP), originally introduced by Beck et al., (1985). The computational aspects in the SFS methods are outlined below.

The continuous function $h(t)$ is approximated by the following finite vector of discrete values:

$$h(t)=h(h_1, h_2, \ldots, h_{m-1}, h_m, h_{m+1}, \ldots, h_M) \tag{5}$$

It is assumed that the components $h_1, h_2, \ldots, h_{m-1}$ have been estimated one by one and the task is now to estimate h_m. A least-squares criterion is utilized to estimate h_m. Several temperature measurements, $Y_m, Y_{m+1}, \ldots, Y_{m+r-1}$, are used to estimate the component h_m where r is the number of future time steps. A function form over the analysis time interval $t_{m-1}\leq t\leq t_{m+r-1}$ is specified. A "temporary" assumption of constant heat transfer coefficient is used, that is,

$$h_{m+i-1}=h_m,\quad i=1, 2, \ldots, r \tag{6}$$

This temporary assumption is actually much better than one would first think. Beck et al. (1985, p. 196) observe that for the IHCP a comparison of the SFS method with constant heat flux, q, approximation analogous to equation (6) with the regularization method with arbitrary time dependence of q yields nearly equivalent results.

The component h_m is estimated under the condition that the "future-information" least-squares function

$$S_m^{(r)}(h_m)=\sum_{i=1}^{r}[Y_{m+i-1}-T_{m+i-1}(h_m)]^2 \tag{7}$$

is minimized with respect to h_m. Here, Y_{m+i-1} are the experimental data and $T_{m+i-1}(h_m)$ are the corresponding calculated temperatures from the model given by equations (1)–(4). The component h_m obtained from minimizing equation (7) is used only for time interval $t_{m-1}\leq t\leq t_m$. For $r=1$, no "additional" future measurements are used and the SFS method reduces to the exact matching procedure (Stolz, 1960), which has severe stability restrictions for small time steps.

The algorithm is developed by minimizing equation (7) with respect to h_m, replacing h_m by $\hat{h}_m$, and setting the result equal to zero, that is,

$$\sum_{i=1}^{r}[Y_{m+i-1}-T_{m+i-1}(\hat{h}_m)]Z_{m+i-1}(\hat{h}_m)=0 \tag{8}$$

where the quantities $Z_{m+i-1}(\hat{h}_m)=\partial T_{m+i-1}(\hat{h}_m)/\partial h_m$, $i=1, 2, \ldots, r$, are called the sensitivity coefficients (Beck et al., 1985). Equation (8) is a nonlinear algebraic equation of the unknown component $\hat{h}_m$, since the sensitivity coefficient $Z_{m+i-1}(\hat{h}_m)$ is a function of the unknown $\hat{h}_m$. The Gauss-Newton linearization method (Beck and Arnold, 1977) is used for the solution of the above equation. The temperature $T_{m+i-1}(\hat{h}_m)$ is replaced by a first-order Taylor expansion about the nth iteration value $\hat{h}_m^n$ for the unknown $\hat{h}_m$.

$$T_{m+i-1}(\hat{h}_m^{n+1})\approx T_{m+i-1}(\hat{h}_m^n)+\left.\frac{\partial T_{m+i-1}}{\partial h_m}\right|_{\hat{h}_m^n}[\hat{h}_m^{n+1}-\hat{h}_m^n] \tag{9}$$

and the sensitivity coefficient $Z_{m+i-1}(\hat{h}_m)$ is approximated at $\hat{h}_m^n$.

Using equations (8) and (9), the iterative form for the unknown $\hat{h}_m^{n+1}$ is found

$$\hat{h}_m^{n+1}=\hat{h}_m^n+\left[\sum_{i=1}^{r}[Y_{m+i-1}-T_{m+i-1}^n]Z_{m+i-1}^n\right]\left[\sum_{i=1}^{r}(Z_{m+i-1}^n)^2\right]^{-1} \tag{10}$$

where $Z_{m+i-1}^n=Z_{m+i-1}(\hat{h}_m^n)$, and $T_{m+i-1}^n=T_{m+i-1}(\hat{h}_m^n)$. Equation (10) is solved for $\hat{h}_m^{n+1}$, the only unknown. The iteration process continues until negligible changes occur in the $\hat{h}_m^{n+1}$ values. The estimated heat transfer component is retained only over the time interval $t_{m-1}\leq t\leq t_m$. The time index m is increased by one and the process is repeated until the last component h_M is estimated.

The sensitivity coefficients are approximated by using the forward-difference formula

$$Z_{m+i-1}^n=\frac{\partial T_{m+i-1}^n}{\partial h_m}\approx\frac{T_{m+i-1}(\hat{h}_m^n+\delta h_m)-T_{m+i-1}(\hat{h}_m^n)}{\delta h_m},$$
$$i=1, 2, \ldots, r \tag{11}$$

where δh_m is a relatively small quantity such as $0.0001\ \hat{h}_m^n$. A Crank-Nicolson finite control volume method is used for the numerical solution of the direct heat convection problem given by equations (1)–(4). A detailed derivation of the Crank-Nicolson equations is given elsewhere (Osman, 1987). The direct problem and sensitivity coefficient calculations were performed on a VAX-11/750-VMS in double precision. The accuracy of the estimated values obtained for test cases shows that the forward-difference formula, equation (11), is quite satisfactory.

The SFS method described above is an efficient algorithm for solving the IHTCP and can be implemented on personal computers. In the SFS method the computations of the M unknowns reduce to solving only one algebraic equation at each time for M times. This results in a substantial reduction in computation time and computer storage, compared to solving simultaneously for all M components as in the regularization procedure (Beck et al., 1985). Furthermore, the computed values are quite similar. The numerical results of the systematic investigation of the SFS algorithm using simulated data for selected heat transfer coefficient test cases are given by Osman (1987).

5 Experimental Results and Discussion

Several quenching experiments were performed using both

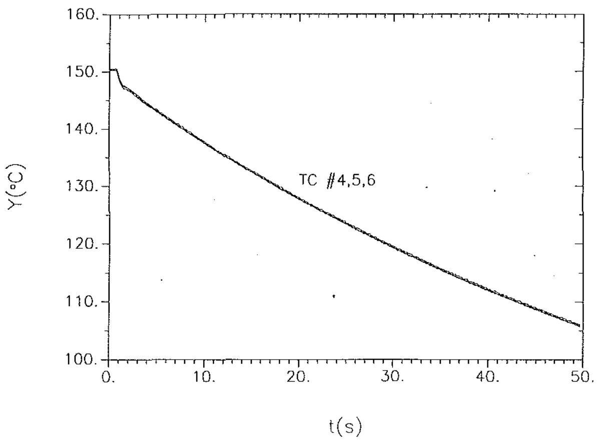

Fig. 3 Measured temperature histories of thermocouples TC #4, 5, and 6

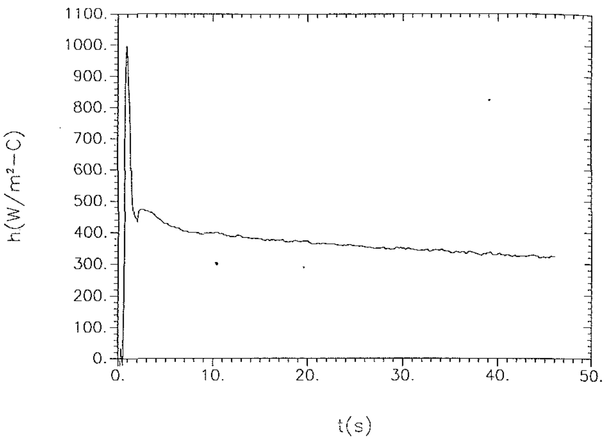

Fig. 4 Estimated heat transfer coefficient, *h(t)*, for run 1 using ethylene glycol

ethylene glycol and water as quenching baths. Temperature data from the thermocouples were acquired at a constant rate of 0.1 s in the time interval from 0 to 50 s. (The nondimensional experimental time step based on the thermocouple depth is 1.62).

5.1 Results for Ethylene Glycol. Ethylene glycol E-178 (boiling range 196–199°C, Fisher Scientific Company) was used. In one test, the test sphere was heated in a cylindrical furnace to a temperature of 170°C. The furnace was then removed and the sphere allowed to reach a uniform temperature of about 150° C (which is below the boiling point of ethylene glycol) before it was quenched into the ethylene glycol bath at 27.5°C. The thermal properties of the copper test sphere were assumed to be constant and the following values were used: $k=377.$ W/m-°C and $\alpha = 1.124 \times 10^{-6}$ m^2/s (Touloukian, 1967). The temperature dependence of k and α is not important here because a small temperature range was covered during quenching. This is particularly true for $t<12$ s where the temperature drop is only about 15°C.

Figure 3 displays the temperature histories of the three thermocouples in the time interval from 0 to 50 s. The bulk temperature of the fluid remained constant, at about 27.5° C, during the experiment. The temperature plots for the three thermocouples are almost identical, indicating that the heat transfer around the sphere is axisymmetric and the measured temperatures are very consistent. A careful examination of the temperature data in Fig. 3 during the important early time stage of quenching shows a sharp decrease in the measured temperatures. An estimate of the standard deviation of the mean measurement is given below.

At any time index m there is a set of three measurement $Y_{m,1}$, $Y_{m,2}$, and $Y_{m,3}$. The estimated variance of the measurements $Y_{m,i}$ is given by

$$s_m^2 = \frac{1}{n-1}\sum_{i=1}^{n}[Y_{m,i} - \bar{Y}_m]^2, \quad m=1, 2, \ldots, M \qquad (12)$$

where $n=3$ and $\bar{Y}_m$ is the estimated mean value. Assuming additive, zero mean, constant variance, and uncorrelated errors, the estimated standard deviation of the mean $\bar{Y}_m$ is (Beck and Arnold, 1977)

$$s_{\bar{Y}_m} = \frac{s_m}{\sqrt{n}}, \quad m=1, 2, \ldots, M \qquad (13)$$

Values of $s_{\bar{Y}_m}$ are calculated using equation (13) for each time index m. The maximum $s_{\bar{Y}_m}$ value is 0.11°C (occurring at $t=1.7$ s) and the minimum value is 0.05°C.

Figure 4 shows the estimated heat transfer coefficient function for run 1 for the entire time of the experiment (from 0 to 50 s). The parameter values used in the SFS method are $r=2$ for times less than 2.5 s and $r=12$ for the rest of the time. The quenching experiments were repeated several times to ascertain the repeatability of the results. The time for complete immersion of the sphere is about 0.2 s. (The estimated data from three different runs are given in Fig. 8.) The plots in Fig. 4 reveal that the $h(t)$) function has three distinct regions. During early time transients, $h(t)$ increases rapidly to a maximum value. The estimated $h(t)$ function has its maximum of about 1000 W/m^2-°C (for run 1) about 0.5 s after immersion; then the heat transfer coefficient decreases with time with a distinct change of the slope at about 2 s. During the early transient, the coupled flow and thermal fields around the sphere are quite complicated due to the sudden immersion of a relatively large-size hot sphere, the travel of the sphere to its final location, and the development of an unsteady coupled field in the cooling bath. Notice that the peak values of the h curves depend on the starting temperature difference between the sphere and the cooling fluid. A better basic understanding of the phenomena associated with initial transient is needed in order to fully characterize the early transient in quenching experiments. Some useful information about the nature of this complicated field can be obtained by flow visualization. A more elaborate way is to solve a coupled system of partial differential equations for the temperature and velocity distributions in the surrounding fluid. The present work uses an inverse method to predict h values using the heat conduction equation in the solid body and transient interior temperature measurements. Notice that the inverse method has permitted estimation of the h values without treating the more complicated temperature and velocity fields in the fluid bath.

Figure 5 shows the sensitivity coefficient for run 1 as a function of time. The absolute value of the sensitivity coefficient multiplied by h increases to a maximum value of 0.65 °C and then decreases. A distinct change of slope occurs at 2 s. The sensitivity coefficient reaches a value of 0.22°C at 10 s when the corresponding drop in measured temperature is about 12°C. Hence, the large-time sensitivity coefficient is small (0.22°C compared to 12°C) and future time steps are therefore necessary for estimating a reasonably smooth curve for the heat transfer coefficient $h(t)$.

The residuals e_m (difference between measured and calculated temperatures) are

$$e_m = \bar{Y}_m - T_m \qquad (14)$$

where $\bar{Y}_m$ is the average of the three thermocouples TC #4, 5, and 6. The residuals e_m are estimates of the random measurement errors and the degree of smoothing introduced by the number of future time steps used in the SFS method. The residuals are plotted in Fig. 6 as a function of time. The re-

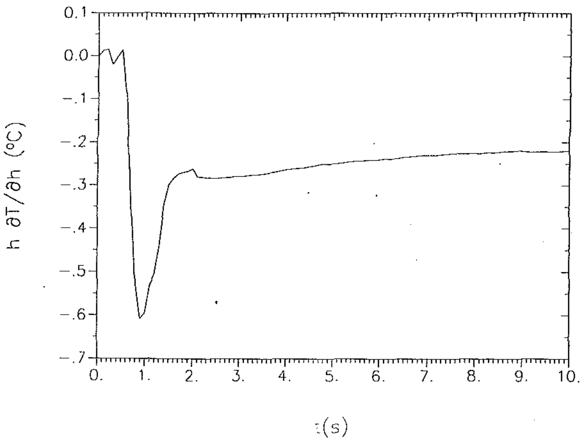

Fig. 5 Sensitivity coefficient function for quenching in ethylene glycol

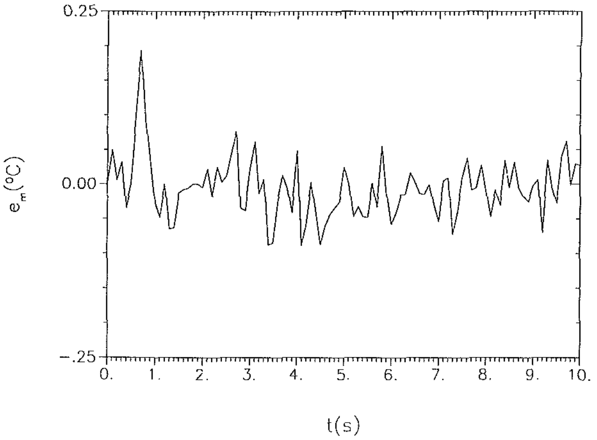

Fig. 6 Residuals, e_m, for quenching in ethylene glycol

siduals are randomly scattered about the zero line with zero mean. After 2 seconds the residuals seem to be uncorrelated. In the time interval from $t=0.5$ s to $t=2$ s, the residuals fall above the zero line. The residuals in this interval are relatively large when compared with the residuals in the rest of the plot. The estimated standard deviation of the residuals, e_m, is 0.034°C.

This standard deviation is approximately equal to those found from averaging the three thermocouple readings (0.034 compared to 0.05°C); the number of future time steps should be chosen to make these deviations roughly equal. The value of the calculated residuals of 0.034 can be increased by using more future temperatures and it can be lowered by reducing the number; it is equal to zero when the number of future time steps is equal to 1. In the 0.5 s to 2 s region, the SFS method deliberately introduces small biases to the estimated values to achieve smaller mean square error (variance + bias^2) than the variance obtained with exact matching unbiased methods. For more information see Beck et al. (1985).

5.2 Results for Water. Experiments were also run for distilled water and similar results were obtained and are given in Fig. 7. The test sphere was heated to 99°C (below boiling point) and then quenched in distilled water at 23°C. The results are very similar to those obtained using ethylene glycol. The main difference is that the heat transfer coefficient reaches higher values, by about a factor of two.

5.3 Comparison With Empirical Correlations. There are no known published results on the transient heat transfer coefficients for the free convection in quenching experiments. However, the obtained experimental results are compared with

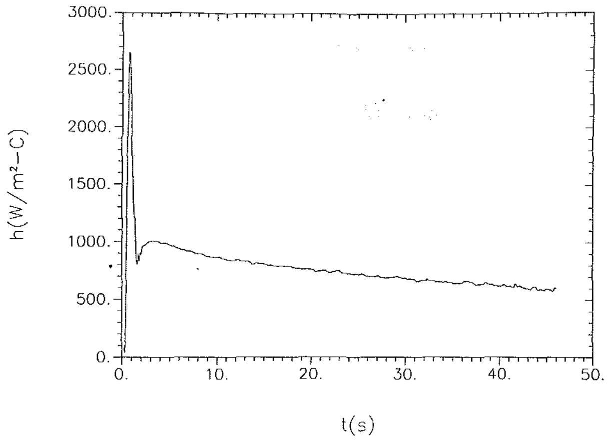

Fig. 7 Estimated heat transfer coefficient, *h(t)*, for run 1 using distilled water

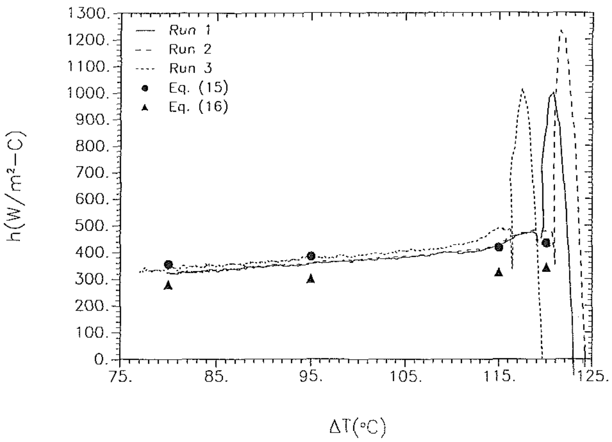

***Fig. 8* Comparison of the estimated results with empirical correlations (ethylene glycol)**

the steady-state published empirical correlations for free convection.

Churchill and Churchill (1975) gave the following correlations between the Nusselt number and Rayleigh number:

$$\mathrm{Nu}^a=\mathrm{Nu}_0^a+(c\ \mathrm{Ra})^b\left[\left\{1+\left(\frac{0.2}{\mathrm{Pr}}\right)^{9/16}\right\}^{16/9}\right]^{-1} \qquad (15)$$

with $a=1$, $b=1/4$, and $c=0.2$ for $10^4<R_a<10^9$ and $a=1/2$, $b=1/6$, and $c=0.00333$ for $\mathrm{Ra}>10^9$. Here Nu $(=hD/k_f)$ is the Nusselt number, Ra $(=g\beta\Delta tD^3/\nu\alpha)$ is the Rayleigh number, Pr $(=\nu/\alpha)$ is the Prandtl number, and $\mathrm{Nu}_0=2$. Equation (15) is a comprehensive correlation for free convection from vertical plates, cylinders, and spheres. Amato and Tien (1972) obtained the following experimental correlation for laminar free convection from isothermal spheres immersed in water:

$$\mathrm{Nu}=2+\mathrm{CRa}^{1/4}, \quad 3\times10^5\le\mathrm{Ra}\le8\times10^8 \qquad (16)$$

where $C=0.5\pm0.009$. They reported a mean standard deviation of less than 11 percent for the range of Ra considered.

Figure 8 shows the estimated heat transfer coefficient function in an expanded scale from 0 to 10 s for runs 1, 2, and 3 as a function of $\Delta T(=T_s-T_f)$ for quenching in ethylene glycol. The predicted results obtained from the above correlations are also shown on the graph (denoted by the solid circles and triangles). The range of Rayleigh number from $5/7\times10^8$ to 1.35×10^9 was covered in the quenching experiments using ethylene glycol. As shown in Fig. 8, equation (16) underestimates the surface heat transfer coefficient with a maximum difference of less than 15 percent, while equation (15) gives estimates that compare well with the estimated values after the

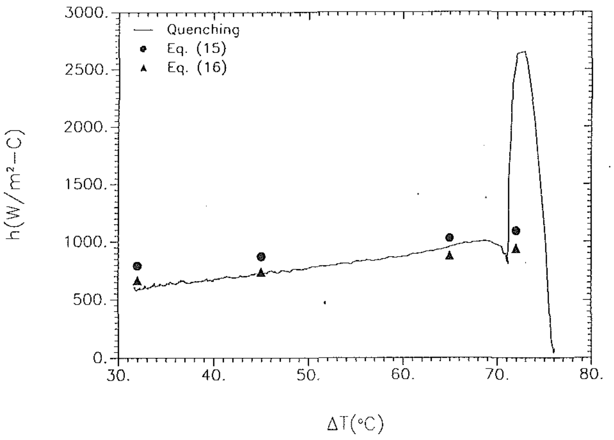

Fig. 9 Comparison of the estimated results with empirical correlations (water)

early transient region, which is poorly predicted (small values) by the empirical correlations. Sudden immersion of hot sphere and subsequent disturbances produces a coupled field, which contributes to fast heat removal rate and high h values.

Figure 9 shows the estimated results for the case of water plotted as a function of ΔT. Also shown are the data from empirical correlations for comparison purposes. The range of Ra number from 5.4×10^8 to 1.92×10^9 was covered in the quenching experiments using water. Notice that the data points obtained by using equation (15) lie slightly above the estimated values with a maximum deviation of less than 20 percent occurring at lower values of ΔT. Equation (16) compares very well with the estimated values, especially at the middle and lower values of Δt.

The conclusion is that this transient inverse estimation technique has the capability of determining the early transients as well as the steady-state results in a single transient experiment.

The data in Fig. 8 for ethylene glycol show that the end of the initial transient period occurs at $\Delta T = 119°\mathrm{C}$. This ΔT value corresponds to a Rayleigh number of about 1.2×10^9, which is close to the transition Rayleigh number. For water (Fig. 9), the transition occurs at $\Delta T = 71°\mathrm{C}$, which corresponds to a Rayleigh number of about 1.7×10^9. Thus, within the accuracy of the estimated values, the vanishing of initial transients appears to depend weakly on the quenching fluid.

6 Summary and Conclusions

Estimation of transient heat transfer coefficients in quenching experiments using inverse heat transfer methods was investigated. Transient heat transfer coefficient values were determined from quenching experiments using water and ethylene glycol without boiling. Substantial variation was found in the time-dependent heat transfer coefficient during the quenching process. These results were compared with well-known steady-state empirical correlations for free convection. The estimated early time transients were about 100–120 percent higher than the values predicted by the empirical correlations. Sudden immersion of the hot sphere produces a coupled field, which initially causes a high heat removal rate and high h values. For later time, the obtained data correlate quite well with the empirical relations. Some of the prominent conclusions of this study can be summarized as follows:

1 Useful data for small-time transients are provided for heat transfer coefficients in quenching experiments without boiling.

2 The well-known steady-state correlations are not appropriate for predicting early transients in quenching experiments.

3 The inverse estimation technique has the capability of estimating the early transients and subsequent steady-state variations of the heat transfer coefficient in a single transient experiment.

4 Early time transient heat transfer in quenching experiments needs more investigation to characterize the heat transfer fully from the quenched solid to the cooling liquid.

References

Amato, W. S., and Tien, C., 1972, "Free Convection Heat Transfer From Isothermal Spheres in Water," *Int. J. Heat Mass Transfer*, Vol. 15, pp. 327–339.

Beck, J. V., and Arnold, K. J., 1977, *Parameter Estimation in Engineering and Science*, Wiley, New York.

Beck, J. V., Blackwell, B., and St. Clair, C. R., Jr., 1985, *Inverse Heat Conduction*, Wiley Interscience, New York.

Churchill, S. W., and Churchill, R. V., 1975, "A Comprehensive Correlating Equation for Heat and Component Transfer by Free Convection," *AIChE J.*, Vol. 21, No. 3, pp. 604–606.

Crosbie, A. L., and Banerjee, S. K., 1974, "Quenching of a Solid in Oil," *Wärme- und Stoffübertragung*, Vol. 7, pp. 113–120.

Irving, M. E., and Westwater, J. W., 1986, "Limitations for Obtaining Boiling Curves by the Quenching Method With Spheres," *Proc. 8th Int. Heat Trans. Conf.*, San Francisco, CA, Vol. 4, pp. 2061–2066, Hemisphere Publishing Corporation, Washington, D.C.

Osman, A. M., 1987, "Estimation of Transient Heat Transfer Coefficients in Multi-dimensional Problems by Using Inverse Heat Transfer Methods," Ph.D. Dissertation, Department of Mechanical Engineering, Michigan State University, East Lansing, MI.

Osman, A. M., and Beck, J. V., 1989, "Nonlinear Inverse Problem for the Estimation of Time-and-Space Dependent Heat Transfer Coefficients," AIAA *J. Thermophysics*, Vol. 3, No. 2, pp. 146–152.

Park, J. E., Childs, K. W., and Ludtka, G. M., 1989, "Quenching Heat Flux Calculated Using Information From Deeply Buried Thermocouples," ASME HTD-Vol. 112.

Sankaran, S., and Witte, L. C., 1985, "Quenching of a Hollow Sphere in Methanol," presented at the National Heat Transfer Conference, Denver, CO, Aug. 4–7.

Stolz, G., Jr., 1960, "Numerical Solutions to an Inverse Problem of Heat Conduction for Simple Shapes," ASME JOURNAL OF HEAT TRANSFER, Vol. 82, pp. 20–26.

Touloukian, Y. S., ed., 1967, *Thermophysical Properties of High Temperature Solid Materials*, Vol. 3, The Macmillan Company, New York.

APPENDIX

Correction of Measurements

This appendix describes the procedure used for the correcting the temperature response of the amplifiers due to time lag. The amplifiers are linear devices since doubling the input results in a doubled output, consequently the convolution (Duhamels) integral can be used. The relation between the amplifier input (true value) and the output (measured value) temperatures are then given by

$$T_{\mathrm{out}}(t) = T_0 + \int_0^t [T_{in}(\lambda) - T_0] \frac{\partial \phi(t-\lambda)}{\partial t} d\lambda \qquad \text{(A1)}$$

where $T_{\mathrm{out}}(t)$ is measured temperature, T_0 is uniform initial temperature, $T_{in}(t)$ is true input temperature, and $\phi(t)$ is the response for a unit step increase in input temperature.

The ϕ function for the amplifiers was determined experimentally. A unit step increase into an amplifier was introduced and the response was recorded as a function of time. Values of ϕ were determined from the response curve. The response time was found to be 0.4 s. The response time is the time (after the application of a step input) for the amplifier to achieve 64 percent of the change for the unit step function. Since a measurement time step of 0.1 s was used in the experiments, it was necessary to correct the temperature measurements. An inverse convolution method (Beck et al., 1985) was used to calculate the correct input temperature $T_{in}(t)$ from the measured temperature $T_{\mathrm{out}}(t)$ by

$$\hat{T}_m = T_0 + \left[\sum_{i=1}^{r} K_i \left(Y_{m+i-1} - \sum_{j=1}^{m-1} \hat{T}_j \Delta\phi_{m-j+i-1} \right) \right] \left[\sum_{j=1}^{r} \phi_j^2 \right]^{-1} \qquad \text{(A2)}$$

where $\hat{T}_m \approx T_{in}(t_m)$, r was 2, $Y_{m+i-1} = T_{\mathrm{out}}(t_{m+i-1}) - T_0$, and $\Delta\phi_n = \phi_{n+1} - \phi_n$.

M. Krarti
Joint Center for Energy Management,
CEAE Department,
University of Colorado,
Boulder, CO 80309-0428

D. E. Claridge
Department of Mechanical Engineering,
Texas A&M University,
College Station, TX 77843-3123

J. F. Kreider
Joint Center for Energy Management,
CEAE Department,
University of Colorado,
Boulder, CO 80309-0428

ITPE Technique Applications to Time-Varying Three-Dimensional Ground-Coupling Problems

Approximate analytical solutions for the three-dimensional heat transfer between slab-on-grade floors and rectangular basements under steady-periodic conditions are developed using the Interzone Temperature Profile Estimation (ITPE) method. The slab-on-grade solution is the first analytical slab-on-grade solution that treats the presence of insulation on/under the floor, while the basement solution is the first analytical solution of the time-dependent three-dimensional problem for basements. Solutions are given for the temperature field and expressions are derived for the annual heat loss. Parametric analysis is used to emphasize the effect of geometric dimensions on the magnitude and phase of heat loss relative to ambient temperature. The results obtained are compared with those from the two-dimensional model, and the three-dimensional characteristics of heat flow from slabs and basements are examined.

1 Introduction

Mathematical complexity has greatly limited the number of three-dimensional analytical and numerical treatments of earth-coupling problems. Most common methods available are based on two-dimensional solutions. The decrement factors of Akridge and Poulos (1983), and the correlations of Yard et al. (1984) and Shipp (1982), were generated from two-dimensional finite difference simulations. Similarly, the Mitalas method (1982, 1983, 1987) was deduced from two-dimensional finite element computer program results. A few computer codes have been developed for three-dimensional earth-coupling heat flow, including those of Kusuda and Achenbach (1969) and Metz (1983).

Lachenbruch (1967) and Delsante et al. (1983) have developed analytical solutions of the three-dimensional slab-on-grade problem. Although their work is a major contribution to earth-coupled heat transfer theory, neither Lachenbruch nor Delsante et al. allow inclusion of any thermal insulation on the floor surface. Both assumed a prescribed slab temperature (i.e., a first-kind boundary condition at the slab surface). For basements, no analytical solution has previously been developed for the three-dimensional heat conduction in soil.

This paper gives three-dimensional solutions for the slab-on-grade and the rectangular basement. The thermal contact between earth and surfaces of a structure are described by a third-kind boundary condition. The Interzone Temperature Profile Estimation (ITPE) technique is used to determine the steady-periodic solutions of the heat conduction equation. However, only approximate analytical solutions are provided since the temperature profiles along the surfaces that divide the ground into zones where the heat conduction equation can be easily solved are estimated based on the two-dimensional results of Krarti et al. (1988). It is possible to determine the *exact* temperature profiles through use of heat continuity conditions. Unfortunately, the calculation procedures are very lengthy and take several hours of mainframe computer time.

In the second section, the three-dimensional ITPE solution for the slab-on-grade problem is developed. The temperature gradient at different sections of the slab is analyzed. An expression for the total annual floor heat loss is given and its dependence on some parameters is discussed.

In the third section, the three-dimensional heat equation for a rectangular basement is treated. Analysis of the temperature gradient as well as the annual heat loss for each basement surface is developed.

2 Slab-on-Grade Three-Dimensional Solution

Consider a slab of width 2*a* and length 2*c*, as shown in Fig. 1. The conductance of the soil–slab contact *h* is assumed uniform over the floor surface. Here also, a water table at temperature T_w is introduced at a depth *d* below the soil surface, which has a temperature fluctuating with time (around a mean T_m with an amplitude T_v). The air above the slab is assumed to be at temperature T_i. As discussed by Krarti et al. (1988), the annual soil temperature fluctuations can be divided into two terms: a steady-state term representing the annual average of the soil temperature and a periodic term from which the amplitude of soil temperature variations can be calculated. Both of these terms can be deduced from the *complex tem-*

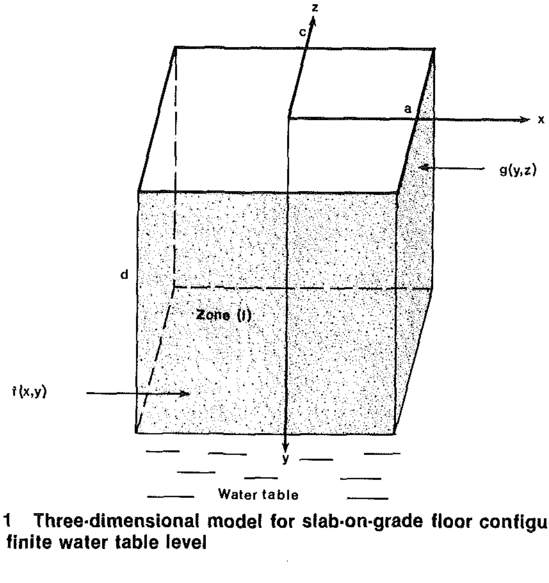

Fig. 1 Three-dimensional model for slab-on-grade floor configuration with finite water table level

---

Contributed by the Heat Transfer Division for publication in the JOURNAL OF HEAT TRANSFER. Manuscript received by the Heat Transfer Division May 9, 1988; revision received October 2, 1989. Keywords: Building Heat Transfer, Conduction, Environmental Heat Transfer.

perature amplitude $\mathfrak{T}(x, y, z)$ solution of the Helmholtz equation associated with the time-dependent heat conduction equation for the the slab-on-grade configuration. Here, we will provide the expression of $\mathfrak{T}(x, y, z)$ only in the zone just beneath the slab floor [i.e., zone (I) in Fig. 1]. The temperature profiles along the surfaces $x = \pm a$ are denoted by $g(y, z)$ and those along the surfaces $z = \pm c$ by $f(x, y)$. Referring to Fig. 1, the complex temperature amplitude $\mathfrak{T}_I(x, y, z)$ in zone (I) is the solution of the following equation:

$$\frac{\partial^2 \mathfrak{T}_I}{\partial x^2}+\frac{\partial^2 \mathfrak{T}_I}{\partial y^2}+\frac{\partial^2 \mathfrak{T}_I}{\partial z^2}=\delta^2 \mathfrak{T}_I \tag{1}$$

where

$$\delta=\sqrt{\frac{i\omega}{\kappa_s}}$$

The boundary conditions are

$$\mathfrak{T}_I=\mathfrak{T}_w \text{ for } y=d$$

$$\mathfrak{T}_I(\pm a, y, z)=g(y, z)$$

$$\mathfrak{T}_I(x, y, \pm c) = f(x, y)$$

$$\frac{\partial \mathfrak{T}_I}{\partial y}=H(\mathfrak{T}_I-\mathfrak{T}_i) \text{ for } y=0 \ \ |x|<a \ \ |z|<c$$

where $H = h/k_s$; h is the equivalent U value of the slab floor; and k_s is the soil thermal conductivity, assumed to be constant in time and space.

We will use the transformation

$$\theta_I(x, y, z)=\mathfrak{T}_I(x, y, z)-\mathfrak{T}_w e^{\delta(y-d)} \tag{2}$$

to simplify the expression of the solution $\mathfrak{T}_I(x, y, z)$. The new unknown temperature $\theta_I(x, y, z)$ satisfies the equations

$$\Delta\theta_I=\delta^2\theta_I \tag{3}$$

with

$$\theta_I=0 \text{ for } y=0$$

$$\theta_I(\pm a, y, z)=g'(y, z)=g(y, z)-\mathfrak{T}_w e^{\delta(y-d)}$$

$$\theta_I(x,y,\pm c)=f'(x, y)=f(x, y)-\mathfrak{T}_w e^{\delta(y-d)}$$

$$\frac{\partial\theta_I}{\partial y}=H(\theta_I-\theta_i) \text{ for } y=0 \qquad |x|<a \qquad |z|<c$$

where $\theta_i=\mathfrak{T}_i-\mathfrak{T}_w e^{-\delta d}(1-\delta/H)$.

Using the separation of variables technique, the solution of the Helmholtz equation (3) in region (I) of the soil medium beneath the slab is found to be (Krarti, 1987)

$$\begin{aligned}\theta_I={}&\frac{4}{dc}\sum_{n=1}^{+\infty}\sum_{m=1}^{+\infty} g'_{n,m}\sin\nu_m y\cos\zeta_n z\,\frac{\cosh\mu''_{n,m}x}{\cosh\mu''_{n,m}a}\\&+\frac{4}{ad}\sum_{n=1}^{+\infty}\sum_{m=1}^{+\infty} f'_{n,m}\cos\mu_n x\sin\nu_m y\,\frac{\cosh\zeta''_{n,m}z}{\cosh\zeta''_{n,m}c}\\&+\frac{4}{ac}\sum_{n=1}^{+\infty}\sum_{m=1}^{+\infty} A_{n,m}\cos\mu_n x\cos\zeta_m z\,\frac{\sinh\nu''_{n,m}(d-y)}{\sinh\nu''_{n,m}d}\end{aligned} \tag{4}$$

Nomenclature

a = half-width of ground-coupled building, m
$A_{n,m}$, $B_{n,m}$ = general term in a Fourier series expansion
b = basement depth, m
C_{ac},C_{bc} = corner length, m
c = half-length of ground-coupled building, m
d = water table depth, m
f, g, l, u, v = functions of two of the space coordinates
$f_{n,m}$, $g_{n,m}$, $l_{n,m}$, $u_{n,m}$, $v_{n,m}$ = Fourier coefficients
H = ratio of surface conductance and soil thermal conductivity, m^{-1}
h = equivalent U value (including surface coefficient) of a floor or wall, W/m^2 K
I = heat flux, W/m^2
$\mathfrak{I}$ = complex heat flux amplitude, $(1+i)$ W/m^2
k_s = soil thermal conductivity, W/(m K)
L = distance from floor center to a boundary where soil temperature is undisturbed, m
Q = total heal loss, W
$\mathfrak{Q}$ = complex total heal loss amplitude, $(1+i)$ W
Re = real part of complex number
T = temperature, K
T_m = annual mean of soil surface temperature, K
T_v = annual amplitude of soil surface temperature variation, K
$\mathfrak{T}$ = complex temperature amplitude, $(1+i)$ K
$\mathfrak{T}_i$ = complex building air temperature amplitude, $(1+i)$ K
$\mathfrak{T}_w$ = complex water table temperature amplitude, $(1+i)$ K
$\mathfrak{T}_1$ = complex soil surface temperature amplitude, $(1+i)$ K
t = time, s
x, y, z = space coordinates, m
δ = complex variable defined in equation (1), $(1+i)$ m
ζ_n, χ_n, ν_n, μ_n = eigenvalues, m^{-1}
ζ'_n, χ'_n, ν'_n, μ'_n = complex eigenvalues, $(1+i)$ m^{-1}
$\zeta''_{n,m}$, $\chi''_{n,m}$, $\nu''_{n,m}$, $\mu''_{n,m}$ = complex eigenvalues, $(1+i)$ m^{-1}
θ = complex temperature amplitude, $(1+i)$ K
κ_s = soil thermal diffusivity, m^2/s
ω = angular frequency for annual cycle = 1.992×10^{-7} rad/s

Subscripts

f = floor
wl = walls
I = zone (I)
II = zone (II)

where

$$\mu_n=\frac{(2n-1)\pi}{2a} \qquad \zeta_n=\frac{(2n-1)\pi}{2c} \qquad \nu_n=\frac{n\pi}{d}$$

$$\zeta''_{n,m}=\sqrt{\delta^2+\mu_n^2+\nu_m^2} \qquad \mu''_{n,m}=\sqrt{\delta^2+\zeta_n^2+\nu_m^2}$$

$$\nu''_{n,m}=\sqrt{\delta^2+\mu_n^2+\zeta_m^2}\,.$$

$$f'_{n,m}=\int_0^a\int_0^a f'(x, y)\cos\mu_n x\sin\nu_m ydxdy \tag{5}$$

$$g'_{n,m}=\int_0^c\int_0^b g'(y, z)\cos\zeta_n z\sin\nu_m ydzdy$$

$$A_{n,m}=\frac{1}{(H+\nu''_{n,m}\coth\nu''_{n,d})}\left[\frac{(-1)^{n+m}H\theta_i}{\mu_n\zeta_m}\right.$$

$$\left.-\frac{2}{d}\sum_{p=1}^{+\infty}\frac{(-1)^n\nu_p\mu_n}{\mu_n^2+\mu''^{\,2}_{m,p}}g'_{m,p}-\frac{2}{d}\sum_{p=1}^{+\infty}\frac{(-1)^m\nu_p\zeta_m}{\zeta_m^2+\zeta''^{\,2}_{n,p}}f'_{n,p}\right] \tag{6}$$

As noted in the introduction, the *exact* determination of temperature profiles $f'(x, y)$ and $g'(y, z)$ is not attempted; instead, the correlation of equation (14) of Krarti et al. (1988) is used to estimate the Fourier coefficients $f'_{n,m}$ and $g'_{n,m}$. To do so, the variation of the temperature with x and z along the surfaces $z = \pm c$ and $x = \pm a$ is approximated by second-order polynomial functions. In other words, it is assumed that

$$f'(x, y)=\left(1-\frac{x^2}{a^2}\right)F'_0(y)+\frac{x^2}{a^2}F'_a(y) \tag{7}$$

with $F'_0(y) = f'(0, y)$ and $F'_a(y) = f'(\pm a, y)$.

This second-order polynomial approximation is justified by the shape of the isotherms below the slab-on-grade floor as obtained in the two-dimensional configuration of Krarti et al. (1988).

Similarly

$$g'(y, z)=\left(1-\frac{z^2}{c^2}\right)G'_0(y)+\frac{z^2}{c^2}G''_c(y) \tag{8}$$

with $G'_0(y) = g'(y, 0)$ and $G''_c(y) = g'(y, \pm c)$.

For $F'_0(y)$ a profile similar to that observed in the two-dimensional solution is adopted. The Fourier coefficients F'_{0_p} of the profile $F'_0(y)$ can then be approximated by

$$F'_{0_p}=\frac{1}{\nu'_p(1+\tanh\nu'_p a)}\,[\theta_1+\theta_i e^{-2\pi/aH}\tanh\nu'_p\,a] \tag{9}$$

where as before, $\nu'_p = \sqrt{\delta^2+p^2\pi^2/d^2}$.

For F'_a a corner effect is introduced by defining a length C_{ac} such that

$$C_{ac}=\frac{ac}{a+c} \tag{10}$$

Note that when $c = +\infty$ (i.e., two-dimensional configuration) the corner length C_{ac} is reduced to the floor half-width a. Unlike the profile $F'_0(y)$, which is affected mostly by the half-width a, the temperature profile just below the slab corners, $F'_a(y)$, is affected by both the width and the length of the floor. The Fourier coefficients of $F'_a(y)$ are assumed to be

$$F'_{ap}=\frac{1}{\nu'_p(1+\tanh\nu'_p C_{ac})}\,[\theta_1+\theta_i e^{-2\pi/C_{ac}H}\tanh\nu'_p C_{ac}] \tag{11}$$

Therefore, from equation (7), the Fourier coefficients of f' can be put in the form

$$f'_{n,m}=\frac{(-1)^n}{\mu_n}\left[\left(\frac{2}{\mu_n^2a^2}F'_{0m}+(-1+\frac{2}{\mu_n^2a^2}\right)F'_{am}\right] \tag{12}$$

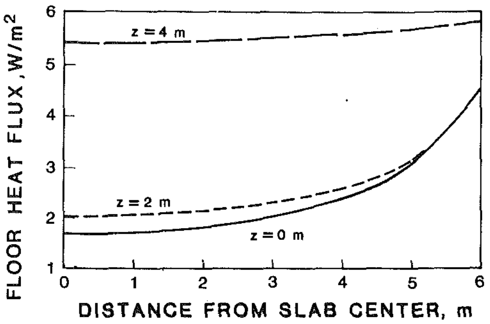

Fig. 2 Heat flux distribution at various z sections of the slab-on-grade floor

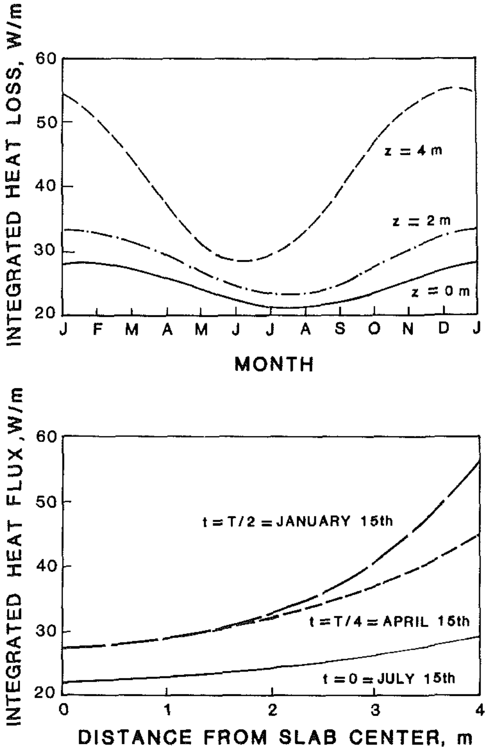

Fig. 3 Integrated z section heat flux variation with (*a*) time for various z sections; (*b*) location for various times

The Fourier coefficients of g' are obtained from the above equation by interchanging the values of a and c. Note that $G'_{cp} = F'_{ap}$.

2.1 Heat Flux Distribution. The complex heat flux $\mathcal{G}(x, z)$, at any point (x, z) of the slab surface, is determined from the expression $\theta_I(x, y, z)$ using the third boundary condition of equation (1) and the transformation equation (2). It is found that

$$\mathcal{G}(x, z)=k_s\delta\mathfrak{I}_w e^{-\delta d}+\frac{4}{ac}h\sum_{n=1}^{+\infty}\sum_{m=1}^{+\infty}$$

$$\times\left[A_{n,m}-\frac{(-1)^{n+m}}{\mu_n\zeta_m}\theta_i\right]\cos\mu_n x\cos\zeta_m z \tag{13}$$

where $A_{n,m}$ can be calculated from equation (6).

For all the results given below, each sum above was truncated to $N = 15$ terms. This provides an accuracy of better than 1 percent in the annual heat flux.

Figure 2 shows the wintertime (Jan. 15) variation of the temperature gradient profile at different z sections of a slab with a = 6 m and c = 4 m. The following parameters are assumed:

$$\kappa_s = 6.45 \times 10^{-7}\ \mathrm{m^2/s} \qquad k_s = 1\ \mathrm{W/m°C}$$

$$h = 0.5\ \mathrm{W/m^2°C} \qquad d = 5\ \mathrm{m}$$

$$T_i = 18°\mathrm{C} \qquad T_1 = 8 + 7\cos\omega t\ (°\mathrm{C}) \qquad T_w = 10°\mathrm{C}$$

Time, t, is in days with t = 0 on July 1, when the soil surface temperature is assumed to reach its maximum.

Note that the heat flow is almost constant in the central floor area. Progressively, the flow increases as the slab perimeter is approached. Heat loss reaches a maximum at the corners. This result indicates that, indeed, heat transfer from a slab to the ground is three dimensional since its pattern differs at each section.

If heat flux at each z section is integrated over the total length $2a$, a cumulative heat flux is obtained, changing with time and location z, as shown in Figs. 3(a) and 3(b). At any time, losses from the slab perimeter are greater than those occurring at the center, as Fig. 3(a) indicates. However, in warm months heat is nearly uniformly lost from the slab surface. Figure 3(b) shows clearly that the slab edges are thermally sensitive to the time fluctuations of soil surface temperature. Both amplitude and mean of the integrated heat flux increase near the slab edges.

2.2 Total Slab Heat Loss. The complex amplitude $\mathfrak{Q}(\delta)$ of total floor heat loss is obtained by integrating the heat flux $\mathcal{G}(x, z)$ over both x and z directions. Its expression is

$$\mathfrak{Q}(\delta) = 4ack_s\delta\mathfrak{I}_w e^{-\delta d} + \frac{4}{ac}h \sum_{n=1}^{+\infty}\sum_{m=1}^{+\infty} \frac{(-1)^{n+m}}{\mu_n\zeta_m}\left[A_{n,m} - \frac{(-1)^{n+m}}{\mu_n\zeta_m}\mathfrak{I}_i\right] \tag{14}$$

with $A_{n,m}$ being given by equation (6).

The time-dependent total heat loss from a slab-on-grade floor, $Q(t)$, is simply given by

$$Q(t) = \mathfrak{Q}(0) + Re\left[\mathfrak{Q}(\delta)\ e^{i\omega t}\right] \tag{14$'$}$$

In the following parametric analysis, the same slab configuration used above will be taken as the base case.

2.2.1 Effect of Soil Thermal Diffusivity. The total heat loss $Q(t)$ for the 8 m × 12 m slab considered earlier is found to be $Q(t) = 178.0 - 10.5\cos\omega(t-20)$ (W), for $\kappa_s = 6.45$ 10^{-7} m^2/s when d = 2m and $Q(t)) = 178.0 - 9.0\cos\omega(t-51)$ (W) for $\kappa_s = 3.255 \times 10^{-7}$ m^2/s. Hence it is seen that the soil thermal diffusivity does not affect the steady-state component of annual heat loss variations but does affect its amplitude and lag time. When thermal diffusivity increases, the time lag of floor loss decreases while its amplitude increases. The earth's capacity to absorb heat lost from the slab decreases with increasing soil thermal diffusivity (which is after all the ratio of thermal conductivity to mass heat capacity).

2.2.2 Effect of Water Table Depth. The total heat loss $Q(t) = 178.0 - 10.5\cos\omega(t-20)$ (W) for d = 2 m becomes $Q(t) = 157.0 - 23.5\cos\omega(t-58)$ (W) when d = 5 m. The deeper the water table, the greater the impact of soil surface temperature fluctuations on floor loss. This effect is shown by an increase in the amplitude of $Q(t)$ variations. The increase in floor loss time delay is attributed to other factors. Knowing that the soil surface temperature is maximum on July 1, it can be seen from Fig. 3 that the central area of the slab needs about one and one-half months to respond to the soil surface temperature fluctuations while near the edges the slab responds almost instantaneously. As a whole the slab takes an intermediate time before responding to the annual soil surface temperature variations. However, as the water table (at constant temperature) gets closer to the slab surface, the central area interacts progressively less with soil surface and the overall slab response is increasingly dominated by edge effects. Hence the phase lag of floor loss increases with water table depth.

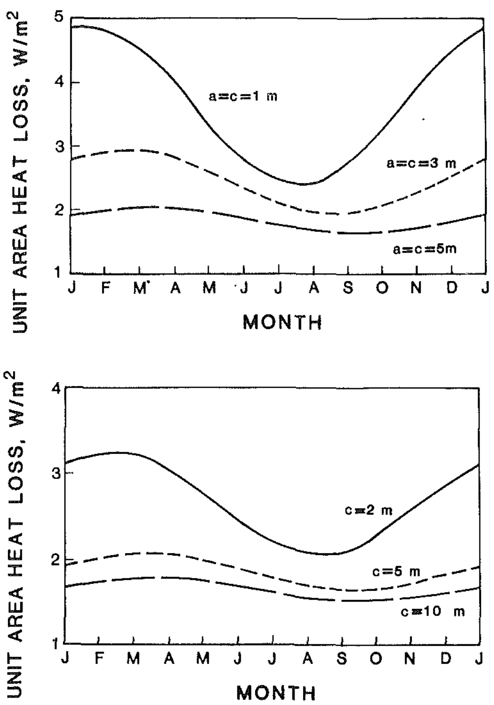

Fig. 4 Effect of floor size on the annual variation of total slab heat loss for (a) square slabs; (b) rectangular slabs

2.2.3 Effect of Floor Size. Figure 4(a) shows annual variations of heat loss per unit area from square slabs of different sizes. Similar results are shown in Fig. 4(b) for slabs of identical width $2a$ = 10 m and different lengths $2c$ ($2c$ = 4 m; $2c$ = 10 m; $2c$ = 20 m). Both figures indicate that the smaller the size of a slab, the greater the heat lost per unit floor area. Both amplitude and mean of the unit area annual loss decrease with increasing floor size. On the contrary, the phase lag between soil surface temperature and floor loss increases with size. This behavior is related to the damping effect of the central zone of the floor discussed above. In fact, as the slab size increases the central zone contribution to the overall floor response to soil surface temperature increases. This contribution is characterized by smaller average heat loss per unit area and longer time delay.

2.3 Comparison With Mitalas Method. Annual average heat loss from several slab-on-grade floors was determined using the ITPE method presented in this paper and the Mitalas method (1987).

The Mitalas method is based on two-dimensional finite element techniques. However, special corner allowance factors are used to account for the three-dimensional heat flow at corners. These corner allowance factors are based on measured heat-loss data.

The following slab-on-grade floor parameters are assumed for this comparison:

$\kappa_s = 6.45 \times 10^{-7}$ m^2/s $\qquad k_s = 0.9$ W/m-°C

$h = 0.45$ W/m^2-°C or R (Mitalas) = 2.0

$d = 100$ m (no water table)

$T_i = 20°$C $\qquad T_i = T_w = 10°$C

The results are given as heat loss per unit area (i.e., W/m^2).

Table 1 Average annual heat loss per unit area of slab-on-grade floor (W/m²)

A x C (mxm)	ITPE	Mitalas* (case #48)	Mitalas** (case #50)
2 x 2	3.725	3.75 (+0.7%)	4.150 (+11.4%)
4 x 4	2.700	2.68 (-2.3%)	2.920 (+8.1%)
6 x 6	2.500	2.39 (-4.4%)	2.500 (0%)
4 x 10	2.525	2.35 (-6.9%)	2.525 (0%)
10 x 10	2.030	2.18 (+7.4%)	2.260 (+11.3%)
10 x 20	1.850	2.03 (+9.7%)	2.090 (+12.9%)

* Case #48 has uniform insulation (R = 2) above the slab floor.

** Case #50 has uniform insulation (R = 2) below the slab floor.

As shown in Table 1, the Mitalas results agree well with the ITPE annual average heat loss. The relative discrepancy between the two methods varies from 0 to about 13 percent for the particular cases of slab-on-grade floors considered in Table 1.

The agreement between the ITPE and Mitalas methods is better in the cases where the insulation is placed above the slab. This result is to be expected, at least for the annual average heat loss calculations (which are the steady-state heat transfer results). The thermal characteristics of the concrete slab are very similar to those of the ground, so when the insulation is placed above the slab, only this insulation layer thermally separates the inside of the building from the ground. However, when the insulation is placed beneath the slab, two layers (the concrete slab and the insulation layer) resist heat transfer between the building and ground.

3 Three-Dimensional Basement Heat Loss

Figure 5 shows a rectangular basement of width $2a$, length $2c$, and depth b. All the walls are assumed to have identical conductance values, h_{wl}. The conductance of the floor is denoted by h_f. As before, a water table is considered at a depth d below the soil surface. To determine heat transfer from the basement to the surrounding earth, the temperature variation in the zone just beneath the floor [zone (*I*) in Fig. 5] and in the regions of soil adjacent to basement walls must be known. Since not all the walls have the same geometric dimensions, their thermal behavior may differ. However, only the temperature solutions near a wall of length $2c$ [zone (*II*) in Fig. 5] is given, since by inverting the values of a and c the soil temperature variation near a wall of length $2a$ can be obtained. The temperature solution in zone (*I*) is used to determine floor heat loss while the solution in zone (*II*) allows all wall heat loss to be calculated. Below, the expressions for the complex temperature amplitudes associated with both solutions are provided.

3.1 Temperature Solution in Zone (II). The complex temperature amplitude $\mathfrak{I}_{II}(x, y, z)$ near the wall is subject to the following equation:

$$\Delta \mathfrak{I}_{II} = \delta^2 \mathfrak{I}_{II} \tag{15}$$

with the boundary conditions

$$\mathfrak{I}_{II}(x, y, \pm c) = l(x, y)$$

$$\mathfrak{I}_{II}(x, b, z) = u(x, z)$$

$$\mathfrak{I}_{II}(x, 0, z) = T_1$$

$$\left.\frac{\partial \mathfrak{I}_{II}}{\partial x}\right|_{x=a} = H_{wl}(\mathfrak{I}_{II} - \mathfrak{I}_i) \text{ for } y < c \text{ and } |z| < b$$

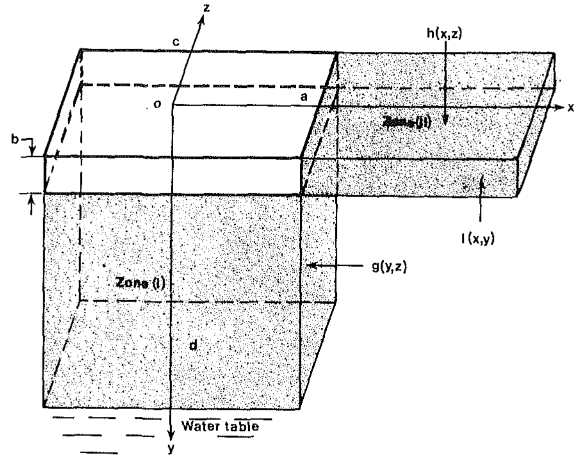

Fig. 5 Three-dimensional model for a rectangular basement configuration with finite water table level

At locations far from the basement, the soil temperature is undisturbed. As shown in Fig. 5, region (*II*) is bounded to the right by the surface $x = L$. Along this surface, the soil temperature is undisturbed and is expressed as

$$\mathfrak{I}_{II}(L, y, z) = v(y) = \mathfrak{I}_w \frac{\sinh \delta y}{\sinh \delta d} + \mathfrak{I}_1 \frac{\sinh \delta(d-y)}{\sinh \delta d}$$

In this paper, L is taken to be 15m. The solution of the Helmholtz equation (15) and the above boundary conditions is

$$\begin{aligned}\mathfrak{I}_{II}(x, y, z) = & -\frac{4}{c(L-a)} \sum_{n=1}^{+\infty} \sum_{m=1}^{+\infty} \frac{(-1)^m[1-(-1)^n]}{\mu_n \zeta_m} \\ & \bullet \sin \mu_n(x-a) \cos \zeta_m z \frac{\sinh \nu''_{n,m}(b-y)}{\sinh \nu''_{n,m} b} \\ & + \frac{4}{c(L-a)} \sum_{n=1}^{+\infty} \sum_{m=1}^{+\infty} u_{n,m} \sin \mu_n(x-a) \cos \zeta_m z \frac{\sinh \nu''_{n,m} y}{\sinh \nu''_{n,m} b} \\ & + \frac{4}{b(L-a)} \sum_{n=1}^{+\infty} \sum_{m=1}^{+\infty} l_{n,m} \sin \mu_n(x-a) \sin \nu_m y \frac{\cosh \zeta''_{n,m} z}{\cosh \zeta''_{n,m} c} \\ & + \frac{4}{bc} \sum_{n=1}^{+\infty} \sum_{m=1}^{+\infty} v_{n,m} \cos \zeta_n z \sin \nu_m y \frac{\sinh \mu''_{n,m}(x-a)}{\sinh \mu''_{n,m}(L-a)} \\ & + \frac{4}{bc} \sum_{n=1}^{+\infty} \sum_{m=1}^{+\infty} B_{n,m} \cos \zeta_n z \sin \nu_m y \frac{\sinh \mu''_{n,m}(L-x)}{\sinh \mu''_{n,m}(L-a)}\end{aligned} \tag{16}$$

where

$$\mu_n = \frac{n\pi}{(L-a)} \qquad \zeta_m = \frac{(2m-1)\pi}{2c} \qquad \nu_m = \frac{m\pi}{b}$$

$$\mu''_{n,m} = \sqrt{\delta^2 + \zeta_n^2 + \nu_m^2} \qquad \zeta''_{n,m} = \sqrt{\delta^2 + \mu_n^2 + \nu_m^2}$$

$$\nu''_{n,m} = \sqrt{\delta^2 + \mu_n^2 + \zeta_m^2}$$

$$u_{n,m} = \int_a^L \int_0^c u(x, z) \sin \mu_n(x-a) \cos \zeta_m dxdz$$

$$l_{n,m} \int_a^L \int_0^b l(x, y) \sin \mu_n(x-a) \sin \nu_m \, ydxdy$$

$$\nu_{n,m} = -\frac{(-1)^n}{\zeta_n} \left[\mathfrak{I}_1 \frac{\nu_m}{\delta^2 + \nu_m^2} - (-1)^m \mathfrak{I}_w \frac{\nu_m}{\delta^2 + \nu_m^2} \right]$$

and

$$B_{n,m}=\frac{1}{[H_{wl}+\mu''_{n,m}\coth\mu''_{n,m}(L-a)]}\left\{-\frac{(-1)^n[1-(-1)^m]}{\zeta_n\nu_m}H_{wl}\mathfrak{I}_i\right.$$

$$-\frac{(-1)^n\nu_m}{\zeta_n\mu''_{n,m}}\mathfrak{I}_1\tanh\mu''_{n,m}\frac{(L-a)}{2}+\frac{\mu''_{n,m}v_{n,m}}{\sinh\mu''_{n,m}(L-a)}$$

$$-\frac{2}{(L-a)}\sum_{p=1}^{+\infty}\frac{(-1)^m\mu_p\nu_m}{\nu''^{\,2}_{p,n}+\nu_m^2}u_{p,n}$$

$$\left.-\frac{2}{(L-a)}\sum_{p=1}^{+\infty}\frac{(-1)^n\mu_p\zeta_n}{\zeta''^{\,2}_{n,m}+\zeta_n^2}l_{p,m}\right\}\tag{17}$$

To determine approximate expressions for the profiles $u(x, z)$ and $l(x, y)$, a procedure similar to that developed in the slab-on-grade section is adopted. For the $u(x, z)$ profile, a second-order polynomial variation with z is assumed similar to equation (8). Therefore, the Fourier coefficients $u_{n,m}$ can be expressed in the form

$$u_{n,m}=\frac{(-1)^m}{\zeta_m}\left[\frac{-2}{\zeta_m^2c^2}U_{0n}+\left(-1+\frac{2}{\zeta_m^2c^2}\right)U_{cn}\right]\tag{18}$$

with

$$U_{0n}=\frac{1}{\mu'_n[\coth\mu'_nb+\coth\mu'_n(d-b)]}\,[B_0+e^{-0.1/H_{wl}c}\mathfrak{I}_i]$$

$$U_{cn}=\frac{1}{\mu'_n[\coth\mu'_nb+\coth\mu'_n(d-b)]}\,[B_0+e^{-0.1/H_{wl}C_{bc}}\mathfrak{I}_i]$$

where $\mu'_n=\sqrt{\delta^2+\mu_n^2}$.

The length $C_{bc}=bc/(b+c)$ is introduced to account for the corner effect. The constant B_0 represents the undisturbed ground temperature at the basement floor level; it is given by

$$B_0=\mathfrak{I}_w\frac{\sinh\delta b}{\sinh\delta d}+\mathfrak{I}_1\frac{\sinh\delta(b-d)}{\sinh\delta d}$$

The correlation above for U_{0n} was established from the basement two-dimensional results by the same manner in which correlation (14) of Krarti et al. (1988) was obtained.

For the profile $l(x,y)$, a similar y variation to that in $v(y)$ [i.e., temperature profile at $x=\pm L$ defined as one boundary condition of equation (15)] is assumed with $\mathfrak{I}_w$ being replaced by $U_c(x)$. Thus, the Fourier coefficients are given by

$$l_{n,m}=\frac{\nu_m}{\nu_m^2+\delta^2}\,[\mathfrak{I}_1-(-1)^mU_{cn}]\tag{18'}$$

3.2 Temperature Solution in Zone (I). The complex temperature amplitude in zone (I) is the solution of

$$\Delta\mathfrak{I}_I=\delta^2\mathfrak{I}_I\tag{19}$$

with the boundary conditions

$$\mathfrak{I}_I(x,d,z)=\mathfrak{I}_w$$

$$\mathfrak{I}_I(\pm a,y,z)=g(y,z)$$

$$\mathfrak{I}_I(x,y,\pm c)=f(x,y)$$

$$\left.\frac{\partial\mathfrak{I}_I}{\partial y}\right|_{y=b}=H_f(\mathfrak{I}_I-\mathfrak{I}_i)\ \text{for}\ |x|<a\ \text{and}\ |z|<c$$

The solution of the above equation is

$$\mathfrak{I}_I(x,y,z)=\frac{4}{c(d-b)}\sum_{n=1}^{+\infty}\sum_{m=1}^{+\infty}g_{n,m}\cos\zeta_nx$$

$$\sin\nu_m(y-b)\,\frac{\cosh\mu''_{n,m}x}{\cosh\mu''_{n,m}a}$$

$$+\frac{4}{a(d-b)}\sum_{n=1}^{+\infty}\sum_{m=1}^{+\infty}f_{n,m}\cos\mu_nx\sin\nu_m(y-b)\,\frac{\cosh\zeta''_{n,m}z}{\cosh\zeta''_{n,m}c}$$

$$+\frac{4}{ac}\mathfrak{I}_w\sum_{n=1}^{+\infty}\sum_{m=1}^{+\infty}\frac{(-1)^{n+m}}{\mu_n\zeta_m}\cos\mu_nx\cos\zeta_mz\,\frac{\sinh\nu''_{n,m}(y-b)}{\sinh\nu''_{n,m}(d-b)}$$

$$+\frac{4}{ac}\sum_{n=1}^{+\infty}\sum_{m=1}^{+\infty}A_{n,m}\cos\mu_n\,x\cos\zeta_mz\,\frac{\sinh\nu''_{n,m}(d-y)}{\sinh\nu''_{n,m}(d-b)}\tag{20}$$

where

$$\mu_n=\frac{(2n-1)\pi}{2a}\qquad\zeta_m=\frac{(2m-1)\pi}{2c}\qquad\nu_m=\frac{m\pi}{(d-b)}$$

$$\mu''_{n,m}=\sqrt{\delta^2+\zeta_n^2+\nu_m^2}\ \ \zeta''_{n,m}=\sqrt{\delta^2+\mu_n^2+\nu_m^2}$$

$$\nu''_{n,m}=\sqrt{\delta^2+\mu_n^2+\zeta_m^2}$$

$$f_{n,m}=\int_0^a\int_b^d f(x,y)\cos\mu_nx\sin\nu_mydxdy$$

$$g_{n,m}=\int_0^c\int_b^d g(y,z)\cos\zeta_nz\sin\nu_mydzdy$$

$$A_{n,m}=\frac{1}{[H_f+\nu''_{n,m}\coth\nu''_{n,m}(d-b)]}\left[\frac{(-1)^{n+m}}{\mu_n\zeta_m}H_f\,\mathfrak{I}_i\right.$$

$$+\frac{(-1)^{n+m}\nu''_{n,m}}{\mu_n\zeta_m\sinh\nu''_{n,m}(d-b)}-\frac{2}{(d-b)}\sum_{p=1}^{+\infty}\frac{(-1)^n\nu_p\mu_n}{\mu''^{\,2}_{n,m}+\mu_n^2}g_{m,p}$$

$$\left.-\frac{2}{(d-b)}\sum_{p=1}^{+\infty}\frac{(-1)^m\nu_p\zeta_m}{\zeta''^{\,2}_{n,m}+\zeta_m^2}f_{n,p}\right]\tag{21}$$

A correlation similar to equation (14) of Krarti et al. (1988) was established to estimate the Fourier coefficients $f_{n,m}$ and $g_{n,m}$. First, the variation of the temperature with x and z along the surfaces $z=\pm c$ and $x=\pm a$ is approximated by second-order polynomial functions. In other words, it is assumed that

$$f(x,y)=\left(1-\frac{x^2}{a^2}\right)F_0(y)+\frac{x^2}{a^2}F_a(y)$$

with $F_0(y)=f(0,y)$ and $F_a(y)=f(\pm a,y)$.

Similarly,

$$g(y,z)=\left(1-\frac{z^2}{c^2}\right)G_0(y)+\frac{z^2}{c^2}+\frac{z^2}{c^2}G_c(y)$$

with $G_0(y)=g(y,0)$ and $G_c(y)=g(y,\pm c)$.

The Fourier coefficients F_{0p} of the profile $F_0(y)$ are determined using the two-dimensional basement solution developed by Krarti et al. (1988). The best correlation found for F_{0p} is

$$F_{0p}=\frac{\nu_p}{(\nu'^{\,2}_p)[\tanh\nu'_pa+\coth\nu'_p(L-a)]}$$

$$\times\{A_{0p}+\mathfrak{I}_ie^{-0.5/(H_fa)+0.1/(H_wlb)]}\}$$

where $\nu'_p=\sqrt{\nu_p^2+\delta^2}$ and

$$A_{0p}=\mathfrak{I}_w\left[\frac{\sinh\delta b}{\sinh\delta d}-(-1)^p\right]+\mathfrak{I}_1\frac{\sinh\delta(d-b)}{\sinh\delta d}$$

For F_a a corner effect is introduced by defining a length $C_{ac}=ac/(a+c)$. The Fourier coefficients of $F_a(y)$ are then given as follows:

$$F_{ap}=\frac{\nu_p}{(\nu'^{\,2}_p)[\tanh\nu'_pa+\coth\nu'_p\,(L-a)]}$$

$$\{A_{0p}+\mathfrak{I}_ie^{-[0.5/(H_fC_{ac})+0.1/(H_wlb)]}\}$$

Therefore, the Fourier coefficients of $f(x,y)$ are

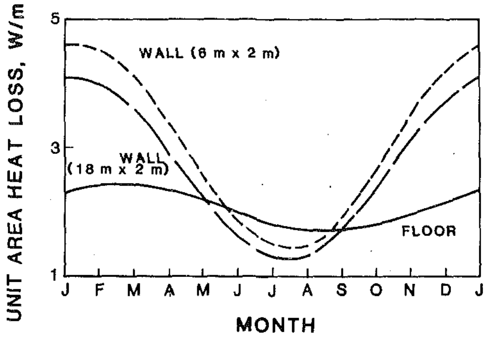

Fig. 6 Annual variation of total heat loss per unit area from each component of the basement envelope

$$f_{n,m}=\frac{(-1)^n}{\mu_n}\left[\left(\frac{2}{\mu_n^2a^2}\right)F_{0m}+\left(-1+\frac{2}{\mu_n^2a^2}\right)F_{am}\right]$$

The Fourier coefficients of $g(y, z)$ are obtained from the above equation by inverting the values of a and c.

3.3 Total Basement Heat Loss. The complex amplitudes of total heat loss from the floor, $\mathfrak{Q}_f(\delta)$, and from one wall of length $2c$, $\mathfrak{Q}_{wl}^c(\delta)$, are given by, respectively

$$\mathfrak{Q}_f(\delta)=\frac{16}{ac}h_f\sum_{n=1}^{+\infty}\sum_{m=1}^{+\infty}\frac{(-1)^{n+m}}{\mu_n\zeta_m}\left[A_{n,m}-\frac{(-1)^{n+m}}{\mu_n\zeta_m}\mathfrak{I}_i\right] \tag{22}$$

and

$$\mathfrak{Q}_{wl}^c(\delta)=\frac{8}{bc}h_{wl}\sum_{n=1}^{+\infty}\sum_{m=1}^{+\infty}\frac{(-1)^n[1-(-1)^m]}{\zeta_n\nu_m}\left\{B_{n,m}+\frac{(-1)^n[1-(-1)^m]}{\zeta_n\nu_m}\mathfrak{I}_i\right\} \tag{23}$$

where $A_{n,m}$ and $B_{n,m}$ are calculated from equations (20) and (17), respectively.

The time-dependent total heat loss from the basement floor, $Q_f(t)$, and from the basement ($b\times 2c$) wall, $Q_{wl}^c(t)$, are deduced from the above expressions as follows:

$$Q_f(t)=\mathfrak{Q}_f(0)+Re[\mathfrak{Q}_f(\delta)e^{i\omega t}] \tag{22'}$$

$$Q_{wl}^c(t)=\mathfrak{Q}_{wl}^c(0)+Re[\mathfrak{Q}_{wl}^c(\delta)e^{i\omega t}] \tag{23'}$$

Note that the total heat loss from the wall of width $2a$ is obtained from equation (23′) by exchanging c and a.

To illustrate use of the above equations, consider a basement with the following parameters:

$$a=5\text{ m}\qquad b=2\text{ m}\qquad c=3\text{ m}\qquad d=5\text{ m}$$

$$T_i=18^\circ\text{C}\qquad T_1=8+7\cos\omega t(^\circ\text{C})\qquad T_w=10^\circ\text{C}$$

$$h_f=1\text{ W/m}^{2\circ}\text{C}\qquad h_{wl}=0.5\text{ W/m}^{2\circ}\text{C}$$

$$\kappa_s=6.45\times 10^{-7}\text{ m}^2/\text{s}\qquad k_s=1\text{ W/m}^\circ\text{C}$$

The annual variation of heat loss, Q_f, from the basement floor is found to be

$$Q_f=3.20-0.39\cos\omega(t-51)\qquad(\text{W/m}^2)$$

while the combined loss, Q_{wl}, from the walls is

$$Q_{wl}=2.58-1.52\cos\omega(t-15)\qquad(\text{W/m}^2)$$

As observed in previous analyses, walls are much quicker than the floor to respond to the soil surface temperature fluctuations. There is nearly two months of time delay (51 days) for the floor and only 15 days for these walls.

When heat loss from each wall is singled out as shown in Fig. 6 (in which the length a is changed to 9 m), the shorter wall (here, c = 3m) is seen to lose more heat per unit area than the longer wall (a = 9m). This result is consistent with the effect of floor size on slab loss observed earlier.

Table 2 Average annual heat loss per unit area of basement walls and floor (W/m²)

a x c	ITPE		Mitalas (Case #99)		Walton	
(mxm)	Walls	Floor	Walls	Floor	Walls	Floor
8.53 x 8.53	13.01	5.40	13.37 (+2.8%)	4.23 (-21.6%)	11.57 (-11.1%)	4.40 (-18.5%)
8.53 x 17.07	12.57	4.54	13.17 (+4.8%)	3.71 (-18.3%)	11.22 (-10.7%)	3.63 (-20.0%)
8.53 x 34.14	12.21	4.15	13.02 (+6.6%)	3.45 (-16.9%)	10.93 (-10.5%)	3.23 (-22.2%)
34.14 x 34.14	11.39	2.06	12.32 (+13.4%)	2.86 (+38.8%)	10.71 (-6.0%)	2.00 (-2.9%)

Finally, the three-dimensional basement floor loss, Q_f (W/m²), is compared with the two-dimensional loss obtained from Krarti et al. (1988) for a floor 6 m wide.

three-dimensional, 10-m length:

$$Q_f(t)=3.15-0.43\cos\omega(t-62)$$

three-dimensional, 18-m length:

$$Q_f(t)=2.96-0.38\cos\omega(t-60)$$

two-dimensional: $Q_f(t)=2.85-0.34\cos\omega(t-58)$

As the length a increases, with c being held constant, the three-dimensional predictions approach those made from two-dimensional solutions. Similar behavior was observed for wall heat loss. It can be shown that the heat loss per unit area (from a basement wall, a basement floor, or a slab-on-grade floor) calculated by the three-dimensional procedure of this paper converges to that determined from the two-dimensional method developed by Krarti et al. (1988), as the building length increases.

3.4 Comparison With Walton and Mitalas Methods. Annual average heat losses from rectangular basement walls and floors of various sizes were calculated using the ITPE method, as presented in this paper, and the Mitalas method. The results of these two methods are compared with those of Walton (1987). In his three-dimensional calculations, Walton used a finite difference method with variable grid spacing. Only uninsulated configurations were treated by Walton.

The basement parameters chosen are those treated by Walton, and are as follows:

$$\kappa_s=6.5\times 10^{-7}\text{m}^2/\text{s}\qquad k_s=1.56\text{ W/m}^\circ\text{C}$$

$$d=100\text{ m (no water table)}$$

$$T_i=22.2^\circ\text{C }(72^\circ\text{F})\qquad T_0=12.8^\circ\text{C }(55^\circ\text{F})$$

$b=1.83$m (6 ft), a and c are variable (see Table 2)

The annual average heat loss per unit area of basement walls and floor, as calculated from ITPE, Mitalas, and Walton, is summarized in Table 2. The Mitalas results correspond to his case #99, an uninsulated basement with soil conductivity $k_{\text{upper}}=1.2$ W/m°C and $k_{\text{lower}}=1.35$ W/m°C.

In general, the agreement between the three methods is reasonable for the cases considered. For small basements, the ITPE results agree better with those of Mitalas. However, for large basements, the ITPE results agree better with those of Walton. This is consistent with the expectation that the accuracy of Walton's method will be higher for larger basements, since the minimum spacing (of 0.3 m) of his finite element grid used to simulate heat conduction in the ground is kept constant, regardless of the size of the basement.

6 Conclusions

The ITPE procedure is used to obtain approximate solutions of the three-dimensional heat conduction equation for a slab-on-grade floor and a rectangular basement. In general, it is found that the heat loss estimated using the three-dimensional solution is greater than that determined from a two-dimensional model, mainly because of the three-dimensional character of heat flow from building corners, specially those which are in contact with soil surface. Furthermore, these corners are the parts of a building most strongly coupled to the earth's surface; therefore they are the most sensitive to variation in soil surface temperature. As a consequence, a significant portion of the heat exchanged between soil and buildings occurs through these corners.

In light of the results presented in the present paper and by Krarti et al. (1988), it can be concluded that in rectangular ground-coupled structures, the heat flow has:

1 one-dimensional nature in the central area of floors (parallel to both the soil surface and the water table).

2 two-dimensional nature along the walls (perpendicular to both the soil surface and water table) and near the floor and roof edges (connecting two perpendicular surfaces).

3 three-dimensional nature near the corners (connecting three perpendicular surfaces).

References

Akridge, J. M., and Poulos, J. F. J., 1983, "The Decremented Average Ground Temperature Method for Predicting the Thermal Performance of Underground Walls," *ASHRAE Transactions*, Vol. 89, Part 2A, p. 49.

Delsante, A. E., Stockes, A. N., and Walsh, P. J., 1982, "Application of Fourier Transforms to Periodic Heat Flow Into the Ground Under a Building," *International Journal of Heat and Mass Transfer*, Vol. 26, pp. 121-132.

Krarti, M., 1987, "Developments in Ground-Coupling Heat Transfer," Ph.D. Thesis, University of Colorado, Boulder, CO.

Krarti, M., Claridge, D. E., and Kreider, J. F., 1988, "The ITPE Method Applied to Time-Varying Ground-Coupling Problems," *International Journal of Heat and Mass Transfer*, Vol. 31, pp. 1899-1911.

Kusuda, T., and Achenbach, T. R., 1963, "Numerical Analysis of the Thermal Environment of Occupied Underground Spaces With Finite Cover Using Digital Computer," *ASHRAE Transactions*, Vol. 69, pp. 439-462.

Lachenbruch, A. H., 1967, "Three-Dimensional Heat Conduction in Permafrost Beneath Heated Buildings," *Geological Survey Bulletin 1052-B*, U.S. Government Printing Office, Washington, DC.

Metz, P. D., 1983, "Simple Computer Program to Model Three-Dimensional Underground Heat Flow With Realistic Boundary Conditions," ASME *Journal of Solar Energy Engineering*, Vol. 105, pp. 42-49.

Mitalas, G. P., 1982, "Basement Heat Loss Studies at DBR/NRC," DBR Paper No. 1045, NRC Canada.

Mitalas, G. P., 1983, "Calculation of Basement Heat Loss," *ASHRAE Transactions*, Vol. 89, Part 1B, pp. 420-438.

Mitalas, G. P., 1987, "Calculation of Below Grade Heat Loss—Low Rise Residential Building," *ASHRAE Transactions*, Vol. 93, Part 1, pp. 743-783.

Shipp, P. H., 1982, "Basement, Crawlspace and Slab-on-Grade Thermal Performance," *Proceedings of ASHRAE/DOE Thermal Envelopes Conference*, Las Vegas, NV, pp. 160-179.

Walton, G. N., 1987, "Estimating 3-D Heat Loss From Rectangular Basements and Slabs Using 2-D Calculations," *ASHRAE Transactions*, Vol. 93, Part 1, pp. 791-798.

Yard, D. C., Gibson, M., and Mitchell, J. W., 1984, "Simplified Relations for Heat Loss From Basements," *ASHRAE Transactions*, Vol. 90, Part 1B, pp. 663-643.

L. S. Fletcher
Dietz Professor of Mechanical Engineering.
Fellow ASME

G. P. Peterson
Professor of Mechanical Engineering.
Mem. ASME

Dept. of Mechanical Engineering,
Texas A&M University,
College Station, TX 77843

C. V. Madhusudana
Senior Lecturer of Mechanical Engineering,
School of Mechanical and Industrial Engineering,
University of New South Wales,
Sydney, Australia
Mem. ASME

E. Groll
Research Assistant,
Dept. of Mechanical Engineering,
Ruhr University,
Bochum, Federal Republic of Germany

Constriction Resistance Through Bolted and Riveted Joints

A correlation relating nondimensional macroscopic thermal resistance to the geometric variables of a bolted joint has been developed. The variables considered include the upper and lower plate thickness, the plate radius, the contact zone radius, and the bolt radius. Experiments were conducted using an electrolytic analog method. The investigation was conducted over a range of variables that include the plate thicknesses, 0.95 to 2.22 cm; the bolt radii, 0.32 to 1.27 cm; the plate radii, 5.1 to 10.2 cm; and the contact zone radii, 1.27 to 8.89 cm. A numerical technique was developed that accurately predicted the experimental results to within ±8 percent. Based on the analysis and experimental data, a correlation was developed that may be used to predict the macroscopic thermal resistance in bolted joints.

Introduction

Heat transfer through junctions composed of metallic plates in contact fastened by bolts, screws, or rivets occurs in a wide range of applications, from spacecraft thermal control to microelectronics cooling. Most contact heat transfer studies deal with solids in which the interface pressure is assumed to be uniform. Sheets and plates fastened by bolts, screws, or rivets, however, are subjected to a nonuniform pressure distribution over the contact area. In such situations there is often a strong interest in optimizing the heat flow through such joints.

When analyzing the heat flow through a single bolted joint, two separate components must be considered: the macroscopic component, which is generally limited to an annular circular contact zone around the bolt hole; and the microscopic component, which includes the actual contact spots. Although for bolted and riveted joints the macroscopic component is typically the most important, no adequate mechanism has been developed that combines these two effects and hence can accurately predict the thermal contact conductance.

The analysis of single microscopic contacts has been reported by a number of different investigators, as noted in recent thermal contact conductance reviews by Madhusudana and Fletcher (1986), Yovanovich (1986), and Fletcher (1988). Specific theoretical or experimental correlations for evaluation of the microscopic resistance would include Malkov (1970), Mikic (1974), Madhusudana and Fletcher (1983), and Yovanovich (1986), assuming that the interface pressure distribution and extent of the contact zone are known. The macroscopic resistance, however, is more complex and depends upon the general condition of the contacting surfaces and the geometric characteristics of the bolted joint. In the present investigation the macroscopic resistance, and consequently the thermal contact conductance, are evaluated using an electrolytic tank analog. A separate numerical analysis was developed to substantiate the analog results.

Literature Review

There have been several theoretical and experimental studies of bolted joints (or plates with circular holes) subjected to axisymmetric loading. A majority of these studies focus on the development of solutions for the interfacial pressure and resulting stress distribution as a means for determining the contact area and associated energy transfer. Although some studies are directed toward analog techniques for ascertaining heat transfer, few investigations deal with the thermal contact conductance of the bolted joint.

A single bolted joint is shown in Fig. 1, which illustrates the geometric parameters of bolt radius a, bolt head radius b, radius of contact c, radius of the plates r_o, and plate thicknesses t_1 and t_2. The pressure distribution and heat flow lines are also shown.

Interfacial Pressure Distribution Studies. Fernlund (1961) investigated the pressure distribution between bolted plates, starting from the fundamental principles of elasticity. The study contains a method for calculating the stress in a plate of finite thickness, loaded by normal and shearing forces in a symmetrically situated hole. The proposed method was designed for use in calculating stresses in a collar and can be used for estimating the stresses in a shrink fit.

In order to define the pressure distribution between the plates in a bolted joint, Bradley et al. (1971) conducted experimental investigations of nine bolted geometries with a three-dimensional photoelastic analysis using a stress freezing technique. The bolted joints were composed of smooth, flat, equal-thickness plates of photoelastic material loaded over an annular area by an aluminum bolt. After freezing the stress in the plates, the load was removed and the plates were sliced to obtain the principal stress differences. A finite-element solution for the midplane stress in a uniform single plate closely

---

Contributed by the Heat Transfer Division and presented at the ASME Winter Annual Meeting, San Franciscco, California, December 10-15, 1989. Manuscript received by the Heat Transfer Division August 24, 1989; revision received February 12, 1990. Keywords: Conduction, Heat Recovery, Modeling and Scaling.

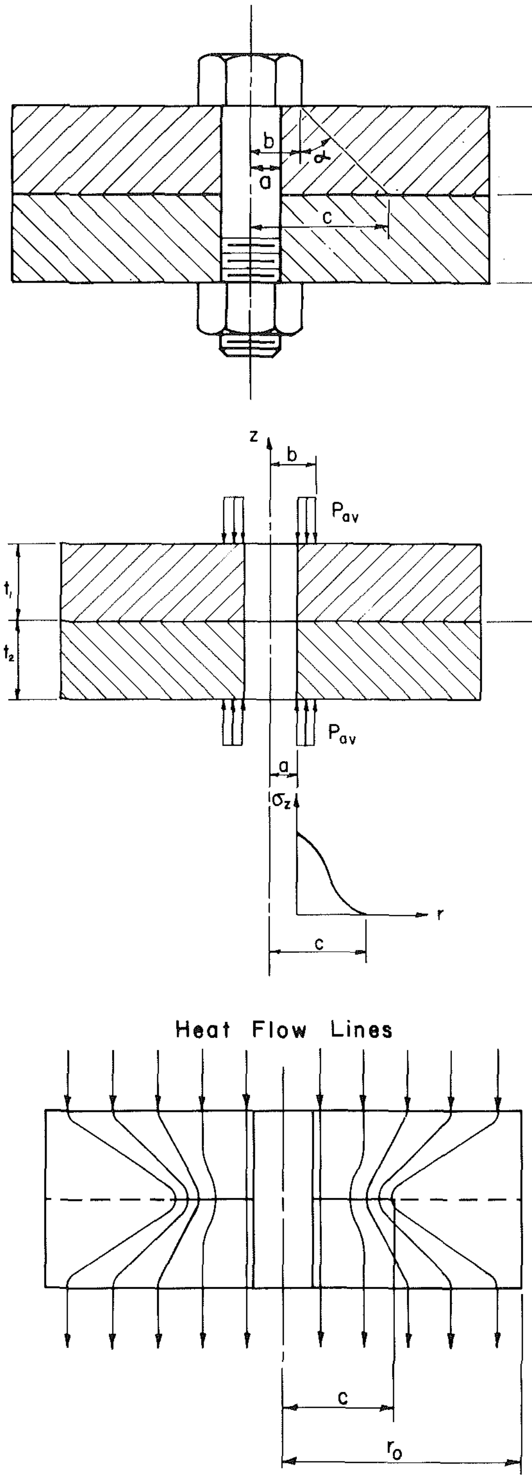

Fig. 1 Bolted joint

approximated the experimental results. When the resulting interface pressure distributions were integrated over the area of contact, the results were within 5 to 10 percent of the applied load.

Gould and Mikic (1972) investigated the area of contact and the pressure distribution in bolted joints using a finite element method. A related experimental investigation of bolted stainless steel plates was also conducted to ascertain the radii of the separation region. Two methods were used: an autoradiographic technique and direct measurement of the polished area around the bolt hole caused by the surfaces sliding under load. A comparison of the computational and experimental results demonstrated excellent agreement. Both the measured and predicted contact areas were considerably lower than those previously reported in the literature.

An expression for the stress distribution and thermal contact resistance of bolted joints in a vacuum was derived by Yip (1972) for rough surfaces of normal height distribution. A simplified solution, which governs the thermal and mechanical properties as well as the metrology of the surface, was proposed for bolted joints. The results suggested that nonuniform stress distributions were not significant in the determination of microcontact resistance across a bolted joint.

The stress and resulting displacements in a junction between a thick plate with a circular hole resting on a smooth rigid surface subjected to an axisymmetric normal load were investigated by Chandrashekhara and Muthanna (1977, 1978a, 1978b). The analysis utilized a Fourier-Bessel series and Love's stress function to provide numerical results in terms of the plate thickness to hole radius ratio. The solution provided results for the pressure and stress distribution in selected bolted joints.

The interface pressure distribution for a bolt-flange assembly was investigated by Ito et al. (1979). A method was developed for converting qualitative pressure at an interface to quantitative pressure and clarified the influence of surface topography, material type, and plate thickness on the interface pressure. Results of the investigation suggested that the surface topography was extremely important in the analysis of pressure distribution in bolt-flange junctions.

Roca and Mikic (1972) noted that the thermal contact resistance of a bolted joint was comprised of two components: a large-scale constriction, which was influenced by the extent of the interfacial pressure distribution, and a small-scale constriction, which was influenced by the magnitude of the local pressure. The presence of asperities was shown to affect the large-scale constriction for certain conditions. The results of the investigation demonstrated that if the pressure distribution was known, it was possible to calculate the interfacial contact conductance and the total joint resistance, which are both a function of the dimensionless surface roughness.

The extension of the contact region and the associated axial stress distribution in bolted joints was evaluated by Curti et al. (1985) through analysis of two circular steel plates of the same thickness, assuming linear, elastic, and isotropic behavior. The evaluation included three different plate thicknesses, two values of the annular loading area, and the external load

Nomenclature

a = bolt radius
a^* = nondimensional radius
A = area, coefficients
b = bolt head radius
c = contact zone radius
h = thermal contact conductance
k = thermal conductivity
L = tank height, length
M = conductivity of electrolyte
P = contact pressure
r = radius
r_o = tank radius
R^* = dimensionless resistance
R = resistance
T = temperature
t = plate thickness
t^* = nondimensional thickness
Y_o = yield stress
Z = axial length
α = cone angle
σ_z = normal stress

Subscripts

1 = Plate 1
2 = Plate 2
0 = without constriction
m = measured

shapes. Results indicated that the contact radius and axial stress distribution both depended upon load shape and plate thickness, and that local stiffness conditions in the contact zone between bolt and plates could influence the results.

The results of these various investigations suggest that:

(*a*) The compressive stress at the interface, i.e., the contact pressure, decreases from a maximum at the bolt edge to zero at a comparatively small distance from the edge;

(*b*) The area of the zone of actual contact is only a fraction of the total area at the interface; and

(*c*) a gap of small but finite thickness exists in the remaining area.

Interfacial Heat Transfer Studies. Heat flow in bolted joints is complex, and depends upon a number of independent parameters including the surface conditions (roughness, waviness, and mean slope of the individual asperities), the mechanical and thermophysical properties of the contacting materials (coefficient of thermal expansion, thermal conductivity, elastic modulus, and material hardness), mean interface temperature, and interfacial contact pressure, as noted by Peterson and Fletcher (1987). In addition, for bolted joints the diameter of the hole, the bolt diameter, the bolt head or washer diameter, and the torque or axial loading on the bolt all contribute to the complexity of the problem.

One of the earliest studies devoted to bolted joints was conducted by Aron and Colombo (1963). A limited experimental program was conducted to investigate the pressure distribution and the temperature profiles at the interface of representative bolted joints. The pressure distribution, which was obtained by stress analysis techniques, compared favorably with results from photoelastic tests. The temperature profiles were obtained from aluminum strips bolted together. The results of the investigation suggest that the transfer of heat is controlled by the pressure distribution at the interface, and may be predicted by an expression that relates the thermal conductance to the pressure-to-yield strength ratio

$$h = 10^4 \left(\frac{P}{Y_o}\right)^{2/3} \text{for} \left(\frac{P}{Y_o}\right) < 0.5 \tag{1}$$

where h is the interface thermal conductance, P is the interface contact pressure, and Y_o is the yield stress at the elastic limit for the plate material.

Elliott (1965) developed a method for calculating the thermal resistance across bolted metallic joints in a vacuum, and experimentally measured the thermal resistance for Aluminum 6061-T6 strips fastened with a No. 10 steel bolt. The experimental results compared favorably with the calculations, which showed that the thermal interface contact resistance approached zero as the bolt torque load was increased to a moderately high level.

The relationship for bolted joint thermal resistance suggested by Aron and Colombo (1963) was modified by Velleux and Mark (1969) to include different materials and surface finishes and was verified by experiment. In this investigation, it was assumed that all conduction takes place in a contact area under the bolt head extending from the shank of the bolt to a radius equal to the loading radius plus two times the plate thickness of the least rigid plate. Experimental tests were conducted in a vacuum for conventional bolting where both sheets were physically held apart. The results of the investigation suggest a reasonable correlation between the prediction method and the experimental data. It was further noted that the resistance at the joint decreased by approximately 50 percent when the joint was assembled and disassembled seven times.

A thermal model for bolted joints was developed by Hewitt et al. (1968) using a general nondimensional differential equation. In order to verify the model, values of joint conductance were determined experimentally for Aluminum 2024-T4 prototype and half-scale models with variable bolt torque and joint temperature. The thermal model predicted the joint conductance to within an accuracy of 30 percent. Increasing the bolt torque generally reduced the resistance to heat flow; however, the effect of increasing the mean junction temperature could not be evaluated. The transient response of the bolted joint was also measured for two different values of torque, and it was noted that the interfacial temperature difference decreased more rapidly for bolted joints than for plain surfaces in contact.

In order to provide a practical analytical method for predicting the interface thermal conductance of a bolted joint from minimal design information, Fontenot (1968) and Fontenot and Whitehurst (1968) conducted an extensive analytical and experimental study of the thermal conductance of bolted joints. The analytical technique employed the method of superposition to describe the deflection of thin circular plates with center holes subject to nonuniform partial loading. The experimental study involved both circular and square plates for steady-state heat transfer across aluminum and stainless-steel bolted joints in air and vacuum. The computed temperature gradients predicted the experimentally measured gradients to within approximately 2°C.

Oehler et al. (1979) conducted a series of experimental tests in a vacuum to establish the thermal contact conductance between two heavy Aluminum 6061-T6 plates attached with stainless steel bolts extending through one plate and threaded into the second plate. Both steady-state and transient tests were conducted with and without silicon grease at the interface. Contact conductance values based on the steady-state tests were found to be somewhat higher than those of the transient tests and conductance values with silicon grease were slightly higher than values for dry surfaces. Based on the experimental data, an analytical solution was derived that simulated the conditions of the transient tests and permitted direct calculation of the transient contact conductance. It was concluded that the transient technique was a viable approach for obtaining contact conductance values, provided that an error analysis was conducted to establish the temperature uncertainty requirements.

Whitehurst and Durbin (1970) extended the work of Fontenot (1968) to develop a simplified, design-oriented approach for predicting the thermal resistance of a bolted lap joint. The study showed that plate deflections in response to the static loading of bolted or riveted joints must be considered. The authors suggested that the simplified technique may be used for joints with any type of bolting or riveting pattern, with any type of interfacial filler material, or any other parameter or combination of parameters. The technique, however, requires knowledge of the temperature gradients on both sides of the joint, information that is not usually available.

Electrolytic Analog. Several investigators have used the electrolytic analog technique for the solution of problems associated with thermal contact conductance. Jeng (1967) and Yip and Venart (1968) defined the analogous processes and used the electrolytic analog method to determine the thermal resistance associated with single and multiple constrictions in a plane. To simulate the contact geometry, Jeng developed an electrolytic tank of a semicylindrical shape with distilled water as the electrolyte and a thin sheet of mylar to simulate the contact plane. The results agreed very closely with the total constriction resistance calculated by Roess (1948).

The electrolytic analog was also used by Yip and Venart (1968) to determine the thermal constriction resistance, including the effects of asperity distribution, roughness, and surface waviness. Results of the investigation demonstrated that the analog technique may be used as an accurate method of predicting the thermal constriction resistance.

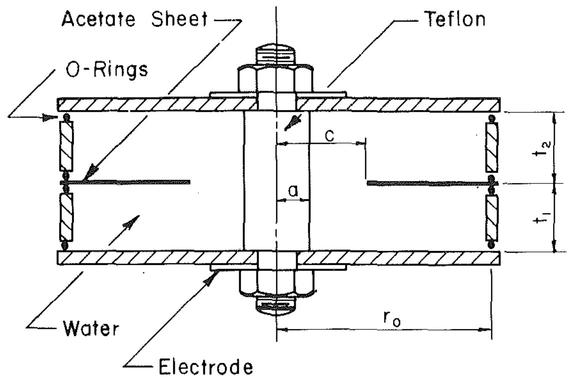

Fig. 2 Electrolytic tank

Yip (1969) developed a thermal analysis of an interface that treats the microcontacts as circular heat flow channels and related the thermal contact resistance to the actual contact configurations. The resulting solution was verified by an electrolytic analog experiment, which included the mutual interaction of the neighboring contacts. The analysis compared favorably for all of the contact configurations considered.

Major and Williams (1979) utilized the electrolytic analog technique to determine the thermal conductance of metallic joints for single spot and conical constrictions. The electrolytic tank was composed of a vertical cylinder with brass plates on the top and bottom to serve as electrodes, and a dilute solution of copper sulfate as the electrolyte. Thin plastic sheets with circular holes simulated the spot constrictions while solid plastic cone frustrums simulated the cone to flat joint configuration. Results of the study indicated that the electrolytic analog could be used to obtain solutions to steady-state conduction heat transfer problems.

The electrolytic analog technique has been used successfully for the study of several different thermal contact conductance configurations, and the results compare favorably with the results of both theoretical and experimental investigations. Based upon the previous work, it appears that the electrolytic analog technique can be used to investigate other configurations and to determine the effect of variations in the physical or geometric parameters of bolted joints.

Experimental Investigation

The objective of the experimental investigation was to determine the macroscopic resistance of a bolted joint with an electrolytic tank and to determine the effect of different bolt radii, contact radii, tank radii, and plate thicknesses. A schematic of the electrolytic tank, which was constructed from PVC pipes with brass endplates as electrodes, is shown in Fig. 2. Distilled water (resistivity 18×10^6 ohm-cm) was chosen as the electrolyte because of the availability and ease of handling. The polished electrodes were coated with graphite, GRAFO 253K6. Since the resistivity of Teflon is several orders of magnitude greater than that of the electrolyte, a Teflon rod was chosen to simulate the central bolt. This is analogous to the condition that there is no heat flow through the bolt; i.e., the bolt is thermally isolated from the plates. An acetate sheet 0.49 mm (0.02 in.) thick, with a central circle cut-out, was used to simulate the adiabatic interface with the contact zone radius c, which is dependent upon the bolt torque. Several acetate sheets with different contact zone radii were prepared. The range of the contact zone radius ranged from 1.27 cm (0.5 in.) to 8.89 cm (3.5 in.) in increments of 0.635 cm (0.25 in.). Four O-rings together with four C-clamps were used to seal the tank and prevent leakage of the electrolyte.

A digital conductivity meter (Cole-Parmer Model J-1481-60) was used to measure the overall conductivity of the assembled tank. This meter together with a dip cell (Cole-Parmer No. J-1481-64) was used to measure the conductivity of the electrolyte (distilled water). The accuracy stated by the manufacturer is 0.1 to 0.2 percent over the entire range applicable to the present measurements. Prior to testing, the meter was calibrated with a 718 micromho standard solution.

Experimental Procedure. The apparatus was assembled with various combinations of tank and bolt radii, and upper and lower plate thicknesses. It was clamped with the C-clamps and the electrodes were connected to the conductivity meter. After measuring the overall thickness of the tank, the tank inlet was connected to a reservoir containing the electrolyte (distilled water) and the tank outlet to a drain. It was noted that after the tank was filled with distilled water, air bubbles could become trapped near the horizontal electrode surfaces. Therefore the tank was shaken and moved to different orientations until there were no air bubbles in the tank. After all the bubbles had been eliminated, measurements of the electrical conductivity were recorded. During the tests, the conductivity of the electrolyte changed slightly each time the apparatus was dismantled and reassembled. This change was the result of the electrolyte coming into contact with a new set of surfaces with associated impurities, such as grease on the O-rings, etc. For this reason some water was siphoned from the tank into a test tube each time, and the conductivity of the distilled water was measured using a standard dip cell. The tank was then disassembled and reassembled with the acetate plastic sheet to simulate the contact radius. Subsequently, the experimental procedure as described above, i.e., measuring the thickness of the tank, filling it with distilled water, eliminating any air bubbles in the tank, recording the data, and measuring the conductivity of the electrolyte with dip cell, was repeated.

Method of Calculation. A nondimensonal resistance, R^*, was defined as

$$R^* = \frac{R-R_o}{R_o} = \frac{R}{R_o} - 1 \tag{2}$$

where R is the resistance of the tank with the constriction, and R_o is the resistance of the tank without the constriction. Thus, R^* represents the fractional increase of the resistance due to the constriction.

The resistance R of the tank with constriction and the resistance R_o of the tank without constriction can be calculated as

$$R = \left(\frac{L}{A}\right)\left(\frac{1}{k_m}\right) \tag{3}$$

$$R_o = \left(\frac{L}{A}\right)\left(\frac{1}{k_o}\right) \tag{4}$$

where k_m is the measured conductivity of the tank with constriction and k_o the measured conductivity of the tank without constriction.

In both equations (3) and (4), L is the thickness of the tank and A is the cross-sectional area of the tank. If R^* is expressed in terms of the conductivity of the electrolyte, two correction factors are required.

The first factor, M/M_o, compensates for the difference between the measurement of the conductivity of the electrolyte in the tank without a constriction and with a constriction. Since the conductivity is directly proportional to the conductivity of the electrolyte in the tank, the measured conductivity of the tank was corrected by multiplying equation (1) by the ratio of these conductivities.

The second factor, L_o/L, compensates for the different thicknesses of the tank due to the presence of the acetate sheet. Again, since the conductivity is inversely proportional to the length, the conductivity reading of the tank was multiplied by the ratio of the two thicknesses.

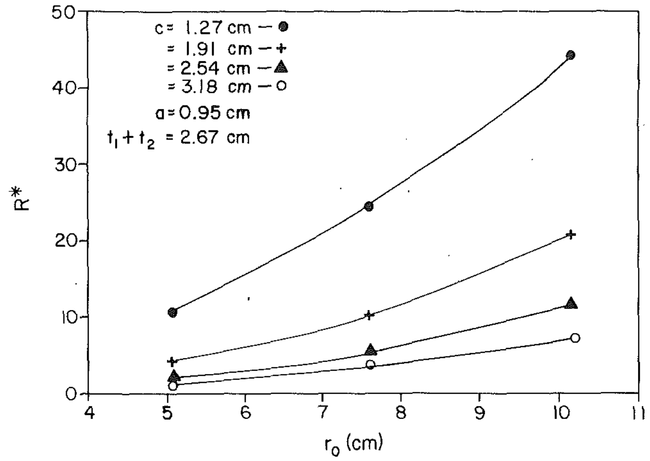

Fig. 3 Nondimensional resistance as a function of tank radius for constant bolt contact radii and constant sum of plate thicknesses

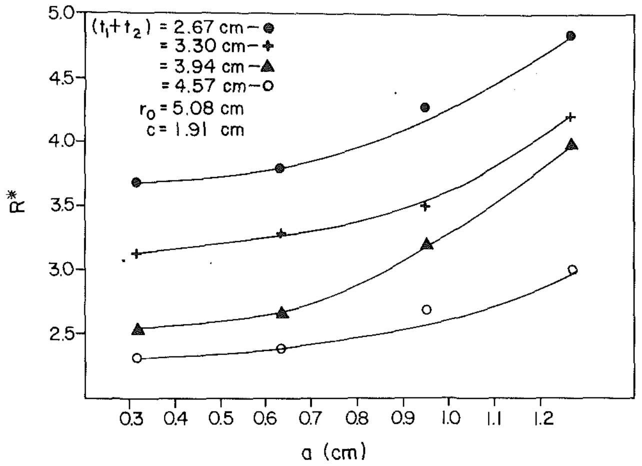

Fig. 4 Nondimensional resistance as a function of bolt radius for constant tank and contact radius and constant sums of plate thicknesses

Combining these two correction factors with equation (1) yields

$$R^* = \left(\frac{k_o}{k}\right)\left(\frac{M}{M_o}\right)\left(\frac{L_o}{L}\right) - 1 \tag{5}$$

The uncertainty analysis of Groll and Madhusudana (1988) indicated the measurements for the nondimensional resistance R^* were accurate within ±5 percent.

Numerical Investigation

The objective of the numerical investigation was to develop a model that could be used to calculate the nondimensional resistance from the geometric parameters of the bolted joint. This model was then used to develop a correlation for a range of variables that included the plate thicknesses, 0.95 to 2.22 cm; the bolt radius, 0.32 to 1.27 cm; the plate radii, 5.1 to 10.2 cm; and the contact zone radius, 1.27 to 8.89 cm.

The heat conduction problem under consideration is one in which axial symmetry exists. Because of this, the Laplace equation in cylindrical coordinates may be written as

$$\frac{\partial^2 T}{\partial r^2} + \frac{1 \partial T}{r \partial r} + \frac{\partial^2 T}{\partial z^2} = 0 \tag{6}$$

The physical domain is a set of rings of radius r, radial dimension Δr, and axial dimension Δz. Hence, the governing equation in discrete form can be written as

$$\frac{T_r + T_l - 2T}{\Delta r^2} + \frac{T_r - T_l}{2r\Delta r} + \frac{T_a + T_b - 2T}{\Delta z^2} = 0 \tag{7}$$

where T equals the temperature of the node under consideration, and the subscripts a, b, r, and l refer to the nodes above, below, right, and left, respectively.

Equation (7) can be modified further to

$$T_b\left(\frac{\Delta r}{\Delta z}\right)^2 + T_l\left(1 - \frac{\Delta r}{2r}\right) + T_r\left(1 + \frac{\Delta r}{2r}\right)$$

$$+ T_a\left(\frac{\Delta r}{\Delta z}\right)^2 - 2T\left(1 + \left(\frac{\Delta r}{\Delta z}\right)^2\right) = 0 \tag{8}$$

or

$$A_b T_b + A_l T_l + A_r T_r + A_a T_a + AT = 0 \tag{9}$$

where

$$A_b = A_a = \left(\frac{\Delta r}{\Delta z}\right)^2 \tag{10}$$

$$A_1 = 1 - \frac{\Delta r}{2r} \tag{11}$$

$$A_r = 1 + \frac{\Delta r}{2r} \tag{12}$$

and

$$A = -2\left(1 + \left(\frac{\Delta r}{\Delta z}\right)^2\right) \tag{13}$$

with boundary conditions

$r = a$	$0 \le z \le (t_1 + t_2)$	$(\partial T/\partial r) = 0$
$r = r_o$	$0 \le z \le (t_1 + t_2)$	$(\partial T/\partial r) = 0$
$c \le r \le r_o$	$z = t_1$	$(\partial T/\partial z) = 0$
$0 \le r \le r_o$	$z = 0$	$T = T_1$
$0 \le r \le r_o$	$z = (t_1 + t_2)$	$T = T_2$

This resulted in a set of simultaneous equations, which were solved using a Gaussian elimination technique. To reduce the computational time, the coefficient array was compressed to a 36 × 13 array using a standard reduction technique. Once completed, a series of different geometries was evaluated to determine the significance of grid size and indicated that the 36 × 13 grid size was adequate with larger grid sizes resulting in changes of less than ±1 percent.

Results and Discussion

Experimental tests were conducted using more than 50 different combinations of tank radii, bolt radii, contact radii, and plate thicknesses as shown in Fig. 2. Numerical results were also computed for the same combinations of geometric parameters. The maximum error between the measured and numerical results was found to be 8 percent; however, a large majority of the results were within ±4 percent. The difference between some of the measured and predicted values was believed to be due to temporary aberrations such as undetected air bubbles, loose contacts, or system transients. Nevertheless, the generally satisfactory agreement between the electrolytic analog and the numerical method indicates that the electrolytic analog is a feasible method for the solution of this type of problem.

For constant bolt and contact radii, and a constant sum of plate thicknesses, the results indicated an increase in the nondimensional resistance as the tank radius increased, as illustrated in Fig. 3. Each curve represents a different contact zone radius. For the case illustrated, the bolt radius was defined as 0.95 cm (0.3 in.), and the sum of the plate thicknesses was 2.67 cm (1.05 in.).

As illustrated in Fig. 4 for a constant tank and contact zone radius and a constant sum of plate thicknesses, the nondimensional resistance also increased as the bolt radius increased. This comparison illustrates the nondimensional resistance as a

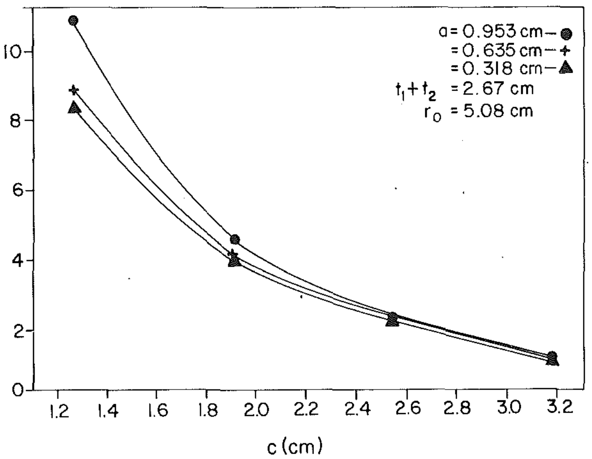

Fig. 5 Nondimensional resistance as a function of contact radius for constant bolt and tank radii and constant sum of plate thicknesses

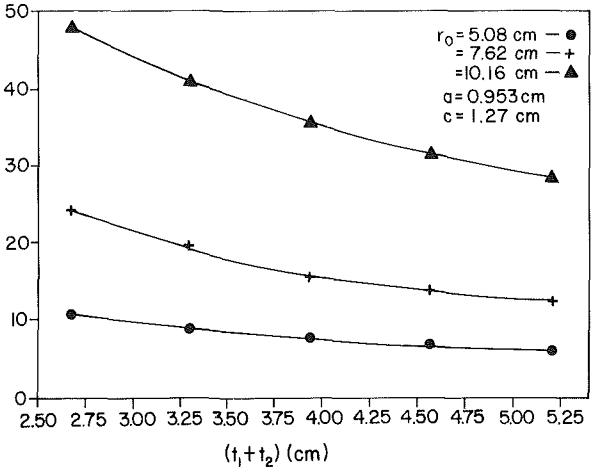

Fig. 6 Nondimensional resistance as a function of sum of plate thicknesses for constant bolt, tank, and contact radii

function of the bolt radius for four different sums of plate thicknesses. For this case the tank radius was equal to 5.08 cm (2.0 in.) and the contact radius was held constant at 1.91 cm (0.75 in.).

The third comparison, Fig. 5, illustrates the relationship between the nondimensional resistance and the contact zone radius. The tank radius and the sum of the plate thicknesses were held constant at 5.08 cm (2.0 in.) and 2.67 cm (1.05 in.), respectively. Each curve, for a constant bolt radius, indicates a decrease of the nondimensional resistance as the contact radius increases.

The nondimensional resistance in relation to the sum of the plate thicknesses is shown in Fig. 6. For a constant tank, bolt, and contact radius, the nondimensional resistance decreases as the sum of plate thicknesses increases. This is illustrated for three different tank radii, a bolt radius of 0.95 cm (0.38 in.), and a contact radius of 1.27 cm (0.5 in.).

Based on these relationships, a nondimensional parameter t^* was developed, which would affect the nondimensional resistance in such a way that an increase or decrease of t^* results in a corresponding increase or decrease of the resistance. An inverse relationship was found between the nondimensonal parameter t^* and the nondimensional radius a^*. The parameter t^* also established that for the investigated values of a^* all curves tend to coalesce. This parameter t^* was termed the nondimensional thickness and was defined as

$$t^* = \frac{t_1 a^4 + t_2 c^4}{0.1 r_o^5} \tag{14}$$

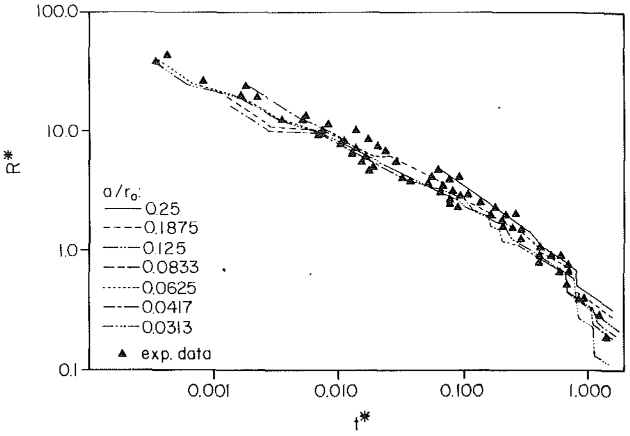

Fig. 7 Experimental and numerical data ($t_1 = t_2$)

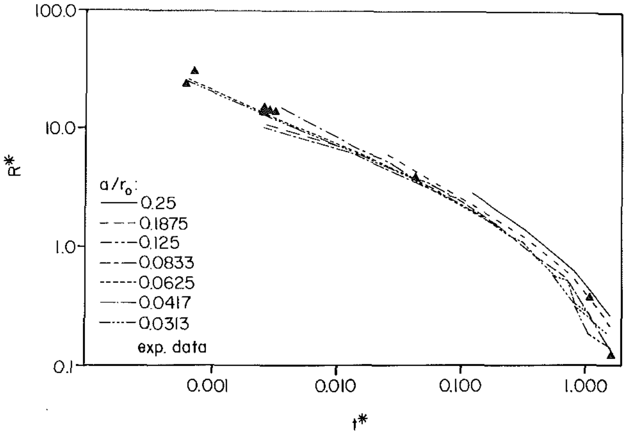

Fig. 8 Experimental and numerical data ($t_1 \neq t_2$)

where t_1 is always the thickness of the thinner plate. This relationship has no specific geometric rationale but contains all the variables that significantly affect the thermal contact conductance.

The numerical and experimental results are compared in Figs. 7 and 8 using the nondimensional thickness as the abscissa, and as mentioned previously are typically within ±4 percent. Figure 7 illustrates the results when the upper plate thickness is equal to the lower plate thickness, and Fig. 8 shows the results when the plate thicknesses are unequal. It can be seen from Figs. 7 and 8 that the computed nondimensional resistance, as predicted by the numerical model, has a linear dependency with t^* on log-log paper, and that all a^* curves tend to fall together. It can be observed from these figures that the numerical model is equally accurate in predicting the nondimensional resistance for both equal and unequal plate thicknesses.

The experimental results were then plotted as a function of $(t^* e^{2t^*})$. As shown in Fig. 9, the nondimensional resistance has a linear dependency with $(t^* e^{2t^*})$. By utilizing the method of least squares for the experimental results, an equation for the nondimensonal resistance was derived as

$$R^* = 0.7524 (t^* e^{2t^*})^{-0.5275} \tag{15}$$

This equation, together with the experimental results, is illustrated in Fig. 9. It can be seen that the equation fits the experimental results satisfactorily. By replacing t^* with its previously defined value, equation (15) can be rewritten as

$$R^* = 0.7524 \left[\frac{t_1 a^4 + t_2 c^4}{0.1 r_o^5}\right]^{-0.5275} e^{-1.055\left[\frac{t_1 a^4 + t_2 c^4}{0.1 r_o^5}\right]} \tag{16}$$

As a result of this equation, the nondimensional resistance of

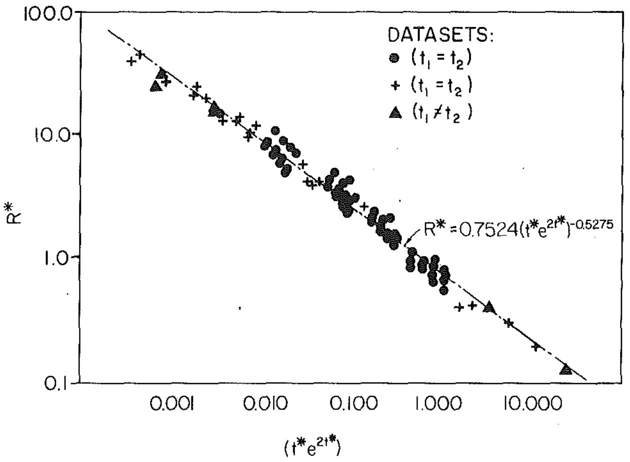

Fig. 9 Nondimensional resistance as a function of t^*

a single bolted joint can be directly calculated from the geometrical parameters of the joint to within ±15 percent.

Summary and Conclusions

An experimental investigation of the macroscopic resistance of single bolted joints was conducted. An electrolytic tank analog was utilized to obtain the experimental data. A numerical method was developed to compare the results with the experimental findings. The two methods, the numerical and the electrolytic analog, compare favorably. Based on these results, a correlation that relates the macroscopic resistance to the geometric parameters of a single bolted joint was developed.

Three conclusions can be derived from the results of this investigation. First, the electrolytic tank analog technique and the finite difference analysis, as reported herein, can be used accurately to ascertain the macroscopic resistance of a single bolted joint. The results show very good agreement indicating that the electrolytic analog method may be used for the solution of problems of this nature. A second related conclusion is that the electrolytic analog could be used for rapid determination of resistances of constrictions on various shapes for which solutions are currently not available in the literature. The final conclusion is that the macroscopic resistance of single bolted joints is influenced by the bolt, contact, and spacing zone radii, and by the plate thicknesses. The resistance increases as bolt and bolt spacing radii increase, but decreases as contact zone radius and the sum of the plate thicknesses increase. A nondimensional correlation was developed that can be used to predict the thermal resistance of bolted joints.

Further work should include the effect of heat tansfer through the bolts, particularly when there is a significant difference between the thermal conductivity of the bolts and the plates. In addition, the microscopic and macroscopic resistances should be combined to obtain the overall joint resistance. This value could then be compared to the results of experimental investigations.

Acknowledgments

This investigation was supported by a grant from the Texas Higher Education Coordinating Board Advanced Technology Program and the Department of Mechanical Engineering of Texas A&M University. Thanks are due to Clark Havis for his work in the development of the numerical analysis reported herein.

References

Aron, W., and Colombo, G., 1963, "Controlling Factors of Thermal Conductance Across Bolted Joints in a Vacuum Environment," ASME Paper No. 63-WA-196.

Bradley, T. L., Lardner, T. J., and Mikic, B. B., 1971, "Bolted Joint Interface Pressure for Thermal Contact Resistance," ASME *Journal of Applied Mechanics*, Vol. 38, No. 2, pp. 542–545.

Chandrashekhara, K., and Muthanna, S. K., 1977, "Stress in Thick Plates With a Circular Hole Under Axisymmetric Loading," *Int. J. Eng. Science*, Vol. 15, pp. 135–146.

Chandrashekhara, K., and Muthanna, S. K., 1978a, "Pressure Distribution in Bolted Connections," *Advances in Reliability and Stress Analysis*, ASME, New York, pp. 117–124.

Chandrashekhara, K., and Muthanna, S. K., 1978b, "Analysis of a Thick Plate With a Circular Hole Resting on a Smooth Rigid Bed and Subjected to Axisymmetric Normal Load," *Acta Mechanica*, Vol. 33, pp. 33–44.

Curti, G., Raffa, F., and Strona, P., 1985, "Analysis of Contact Area and Pressure Distribution by Boundary Element Method," *Wire*, Vol. 35, No. 1, pp. 14–18.

Elliott, D. H., 1965, "Thermal Conduction Across Aluminum Bolted Joints," ASME Paper No. 65-HT-53.

Fernlund, I., 1961, "A Method to Calculate the Pressure Between Bolted or Riveted Plates," Report No. 17, Institute of Machine Elements, Chalmers University of Technology, Gothenburg, Sweden.

Fletcher, L. S., 1988, "Recent Developments in Contact Conductance Heat Transfer," ASME JOURNAL OF HEAT TRANSFER, Fiftieth Anniversary Issue, Vol. 110, No. 4(B), pp. 1059–1070.

Fontenot, J. E., Jr., 1968, "The Thermal Conductance of Bolted Joints," Ph.D. Dissertation, Mechanical, Aerospace and Industrial Engineering Dept., Louisiana State University, Baton Rouge, LA.

Fontenot, J. E., Jr., and Whitehurst, C. A., 1968, "A Method to Predict the Thermal Conductance of a Bolted Joint," NASA CR 96316, Division of Engineering Research, Louisiana State University, Baton Rouge, LA.

Gould, H. H., and Mikic, B. B., 1972, "Areas of Contact Pressure Distribution in Bolted Joints," ASME *Journal of Engineering for Industry*, Vol. 94, No. 3, pp. 864–870.

Groll, E., and Madhusudana, C. V., 1988, "Heat Transfer Through Bolted Joints—The Macroscopic Resistance," Report No. ME-CHTL-70220-6, Texas A&M University, College Station, TX.

Hewitt, H. C., Jr., Smith, A. M., and Nutt, K. W., 1968,, "Thermal Modeling of Bolted Joints," AIAA Paper No. 68-762.

Ito, Y., Toyoda, J., and Negata, S., 1979, "Interface Pressure Distribution in a Bolt-Flange Assembly," ASME *Journal of Mechanical Design*, Vol. 101, No. 2, pp. 330–337.

Jeng, D. R., 1967, "Thermal Contact Resistance in a Vacuum," ASME JOURNAL OF HEAT TRANSFER, Vol. 89, No. 4, pp. 275–276.

Madhusudana, C. V., and Fletcher, L. S., 1983, "Solid-Spot Thermal Conductance of Zircaloy-2/Uranium Dioxide Surfaces," *J. Nuclear Science and Engineering*, Vol. 83, pp. 327–332.

Madhusudana, C. V., and Fletcher, L. S., 1986, "Contact Heat Transfer—The Last Decade," *AIAA Journal*, Vol. 24, No. 3, pp. 1–8.

Major, S. J., and Williams, A., 1979, "The Solution of a Steady Conduction Heat Transfer Problem Using an Electrolytic Tank Analog," *Mech. Engr. Trans.*, The Inst. of Engineers, Australia, pp. 7–11.

Malkov, V. A., 1970, "Thermal Contact Resistance of Machined Metal Surfaces in a Vacuum Environment," *Heat Transfer—Soviet Research*, Vol. 2, pp. 24–33.

Mikic, B. B., 1974, "Thermal Contact Conductance—Theoretical Considerations," *Int. Journal of Heat and Mass Transfer*, Vol. 17, pp. 205–214.

Oehler, S. A., McMordie, R. K., and Allerton, A. B., 1979, "Thermal Contact Conductance Across a Bolted Joint in a Vacuum," AIAA Paper No. 79-1068.

Peterson, G. P., and Fletcher, L. S., 1987, "A Review of Thermal Conductivity in Composite Materials," AIAA Paper No. 87-1586.

Roca, R. T., and Mikic, B. B., 1972, "Thermal Conductance in a Bolted Joint," AIAA Paper No. 72-282.

Roess, L. C., 1948, "Theory of Spreading Conductance," Appendix to Weills, N. D. and Ryder, E. A., "Thermal Resistance Measurements on Joints Formed Between Stationary Metal Surfaces," presented at the Semi-Annual ASME Heat Transfer Division Meeting, Milwaukee, WI.

Velleux, E., and Mark, M., 1969, "Thermal Resistance of Bolted or Screwed Sheet Metal Joints in Vacuum," *J. Spacecraft*, Vol. 6, No. 3, pp. 339–342.

Whitehurst, C. A., and Durbin, W. T., 1970, "A Study of the Thermal Conductance of Bolted Joints," NASA CR-102639, Division of Engineering Research, Louisiana State University, Baton Rouge, LA.

Yip, F. C., 1969, "Thermal Contact—Constriction Resistance," Ph.D. Thesis, Dept. of Mech. Eng., University of Calgary, Alberta, Canada.

Yip, F. C., 1972, "Theory of Thermal Contact Resistance in Vacuum With an Application to Bolted Joints," AIAA Paper No. 72-281.

Yip, F. C., and Venart, J. E. S., 1968, "Surface Topography Effects in the Estimation of Thermal and Electrical Contact Resistances," *Proc. IMechE*, Vol. 182, pt. 3K, pp. 81–91.

Yovanovich, M. M., 1986, "Recent Developments in Thermal Contact Gap and Joint Conductance Theories and Experiments," Keynote Paper, *Proc. 8th Int'l Heat Trans. Conf.*, San Francisco, CA, Vol. 1, pp. 35–45.

T. K. Kang
Research Assistant.
Mem. ASME

G. P. Peterson
Professor.
Mem. ASME

L. S. Fletcher
Dietz Professor of Mechanical Engineering.
Fellow ASME

Mechanical Engineering Department,
Texas A&M University,
College Station, TX 77843

Effect of Metallic Coatings on the Thermal Contact Conductance of Turned Surfaces

An experimental investigation was conducted to determine the degree to which the thermal contact conductance at the interface of contacting Aluminum 6061 T6 surfaces could be enhanced through the use of vapor-deposited metallic coatings. Three different coating materials (lead, tin, and indium) were evaluated using four different thicknesses for each coating material. The results verified the existence of an optimum coating thickness, shown to be in the range of 2.0 to 3.0 μm for indium, 1.5 to 2.5 μm for lead, and 0.2 to 0.5 μm for tin. The enhancement factors for thermal contact conductance were found to be on the order of 700, 400, and 50 percent, respectively. Based upon the experimental data, the hardness of the coating materials appears to be the most significant parameter in ranking the substrate and coating material combinations; however, additional experimental data are needed to substantiate this hypothesis. Finally, it was apparent that the thermal contact conductance enhancement effect was greatest at low contact pressures and decreased significantly with increases in the contact pressure.

Introduction

The use of high-capacity heat pipe radiators for spacecraft thermal control systems was investigated on recent Shuttle flight experiments, including the STS-3 flight of the Thermal Canister (Harwell, 1983) and the STS-8 heat pipe radiator experiment (Alario, 1984). These two flight tests along with numerous ground tests have demonstrated that heat pipe radiators present a feasible alternative to the single-phase fluid radiators presently in use. The heat pipe radiator as it is currently envisioned would be built in orbit from individual heat pipe elements, each with a heat rejection capacity of approximately 2 kW. The evaporator section of each of these heat pipes would be thermally connected to a central heat transport loop designed to collect and transport heat from within the habitation modules to the evaporator section of the heat pipes. In order to maximize system performance and minimize overall system weight, it is desirable to develop a method by which thermal conductance at the interface between the central heat transport loop and evaporator section of the heat pipes can be enhanced.

When two smooth nominally flat surfaces are brought together, they contact in only a few discrete points, due to individual surface roughnesses and microscopic asperities as shown in Fig. 1. Past experimental investigations have demonstrated that for relatively smooth, nominally flat surfaces, the "actual" contact area is between 2 and 5 percent of the apparent contact area (Yovanovich, 1987). Because of this significant area reduction, thermal resistance occurs at the interface, resulting in a temperature discontinuity, as shown in Fig. 2. Heat can be transferred across the interface by conduction through actual metal-to-metal contacts, conduction through the substance in the gaps around the contacts, and radiation across the gap, or a combination of all three. In the heat pipe radiator application, conduction through solid contacts is the dominant mode, since gas conduction is nonexistent due to the vacuum of space, and radiation is negligible due to the relatively low temperature gradient present at the interface.

The most common method of enhancing thermal contact conductance is to increase the apparent contact pressure. Unfortunately, this is not always possible due to design or load restrictions. In situations where the applied load is limited, such as spacecraft radiators, thermal contact conductance can be enhanced through the use of thermally conductive greases, thin metal foils, or a thin metal coating deposited on one or both of the surfaces. In all of these situations, interface ma-

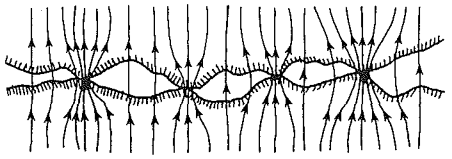

Fig. 1 Two nominally flat surfaces in contact

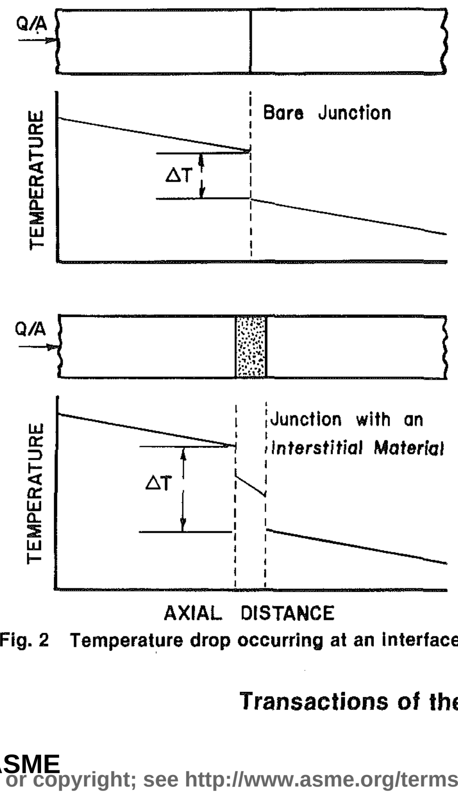

Fig. 2 Temperature drop occurring at an interface

Contributed by the Heat Transfer Division and presented at the 26th National Heat Transfer Conference, Philadelphia, Pennsylvania, August 6-9, 1989. Manuscript received by the Heat Transfer Division April 18, 1989; revision received February 19, 1990. Keywords: Conduction, Measurement Techniques, Thermal Packaging.

terial flows into the gaps between the two surfaces and increases the actual contact area, which in turn increases thermal contact conductance.

Thermal greases are the most desirable of these three techniques for general applications. However, they tend to migrate at high temperatures or vaporize in low pressure or vacuum environments. Once vaporized, they may redeposit on adjoining surfaces. Metal foils are theoretically very attractive but must be very thin to be effective; as a result, they are often difficult to handle. If not properly used or installed, these foils may actually result in decreases in thermal contact conductance due to wrinkles or folds (Peterson and Fletcher, 1988).

Thin metallic coatings have several desirable characteristics. First, they are relatively easy to handle once applied and will not wrinkle or fold; second, under normal operating conditions, they are stable in a vacuum environment; and third, the vapor deposition, sputtering, and/or electroplating processes used to apply these coatings are well understood and allow thin layers of almost any metal or combination of metals to be deposited in any desired thickness. The advantages and disadvantages of each of these three techniques, greases, foils, and coatings, have been presented and discussed by Peterson and Ortega (1989).

Review of Past Investigations

Two interrelated problems must be considered when evaluating thermal contact conductance of surfaces in contact: the thermal problem, which includes physical and thermophysical properties such as hardness and thermal conductivities of the contacting solids and interstitial substances; and the metrological problem, which includes the geometric parameters of the contacting surfaces, such as number, size, shape, and placement of the contacting asperities. The metrological problem can be resolved by measuring surface characteristics of the contacting surfaces, but the thermal problem presents a more difficult challenge.

Most previous studies have assumed that plastic deformation of the surface asperities occurs during the initial loading cycle. This is supported by Greenwood (1967), who analyzed the problem using spherical shaped asperities and demonstrated that, unless the surfaces were carefully polished, deformation would be plastic even at the lightest loads. Mikic (1974) investigated deformation of nominally flat surfaces in contact and identified several modes of deformation. The mode of deformation used in the present investigation was predicted using an index of deformation, given as

$$j = \frac{H}{E' \, |\tan \Theta|} \tag{1}$$

and was found to have an index of deformation of $j = 0.394$, where deformation is predominantly elastic for $j \geq 3$, and plastic for $j \leq 0.33$.

Uncoated Junctions. A review of recent literature on thermal contact conductance has been presented by Madhusudana and Fletcher (1986). The basic governing equation for the constriction resistance for a single contact spot in which radiation and convection have been neglected was first described by Holm (1958) as

$$R_c = \frac{1}{4ka} \tag{2}$$

When both surfaces are considered, and the harmonic mean thermal conductivity is defined as $k_s = (2k_1k_2)/(k_1 + k_2)$, the constriction resistance of the *i*th contact spot becomes

$$R_c = \frac{1}{2k_s a} \tag{3}$$

In order to compute thermal constriction resistance of a junction consisting of many contact spots, a heat flux tube contact model was employed for each spot. The total constriction resistance was obtained by multiplying equation (3) by a constriction parameter, $\Psi(\epsilon)$, to compensate for the thermal effect of neighboring contact points, i.e.,

$$R_c = \frac{\Psi(\epsilon)}{2k_s a} \tag{4}$$

Many shapes have been used to model the contact area, but

Nomenclature

a = mean contact spot radius
A = area
b = mean radius of heat flow channel
c_1 = Vickers microhardness coefficient
c_2 = Vickers microhardness coefficient
C = constriction parameter correction factor
E = modulus of elasticity
E' = $E_1E_2/[E_1(1-\nu_1^2)+E_2(1-\nu_2^2)]$
f = geometric parameter or function
FD = flatness deviation
H = microhardness
H' = effective microhardness of soft layer on hard substrate
h = thermal contact conductance
j = mode of deformation index
K = k_L/k_s
k = thermal conductivity
k' = effective thermal conductivity = $(k_1+k_2)/(k_2C_1+k_1C_2)$
k_s = harmonic mean thermal conductivity = $2k_1k_2/(k_1+k_2)$
m = average absolute asperity slope
m_{rms} = combined average absolute asperity slope = $\sqrt{m_1^2+m_2^2}$
M = effective flow pressure of the softer material
n = constant
P = pressure
r = radius of the test specimen or radial axis
R = thermal resistance
t = coating thickness
T = temperature
w = half-width of the average contact strips
α = coefficient of linear thermal expansion
β = contact angle of a spiral
γ = contact temperature modification factor
δ = surface parameter
Δ = average distance between spiral
ϵ = relative mean contact spot radius = $a/b = \sqrt{P/H}$
σ = rms roughness
σ_{rms} = combined rms roughness = $\sqrt{\sigma_1^2+\sigma_2^2}$
τ = relative layer thickness = t/a
ϕ = layer effect modification factor
ψ = turned surface constriction parameter
Ψ = conforming rough surface constriction parameter
$\tan \Theta$ = absolute asperity slope

Subscripts

1 = one solid in contact
2 = other surface in contact
a = apparent
c = contact or constriction
j = joint
L = layer
m = mean
max = maximum

Superscripts

$'$ = coated
$*$ = dimensionless

as shown by Yovanovich (1987), the constriction parameter is a relatively weak function of the shape of the contact area, and a junction of any shape can be modeled from a circular contact having an equivalent area. The constriction parameter can be solved by overcoming the complexity of the boundary conditions of the contact model.

Cooper et al., (1969) developed an expression for two nominally flat surfaces with Gaussian roughness distributions. The temperature boundary condition at the contacting interface was replaced by a heat flux distribution so that a nearly isothermal boundary condition was achieved. The results, when plotted as a function of ϵ, were approximated by

$$\Psi(\epsilon)=(1-\epsilon)^{1.5} \tag{5}$$

Fletcher and Gyorog (1970) investigated similar metals in contact, both analytically and experimentally. The data from several investigators were compared and analyzed to identify the most significant parameters. The resulting correlation was shown to predict the experimental results from several different materials quite well and was given as

$$\frac{h_j\delta}{k_m}=\sqrt{\pi}\ [3.8\times10^{-6}\delta_o^*+0.026P^*T^*]^{0.56} \tag{6}$$

where

$$\delta=\delta_o e^{(-170\mathrm{P}^*\mathrm{T}^*/\delta_o^*)}$$

$$\zeta=(FD+2\sigma)_{\text{rough surface}}-1/2(FD+2\sigma)_{\text{smooth surface}}$$

$$k_m=(k_1+k_2)/2$$

$$P^*=P/E=\text{ dimensionless pressure}$$

$$T^*=\alpha T_m=\text{ dimensionless temperature}$$

$$\sigma_o^*=\sigma_o/r$$

$$\sigma_o=20.45+8.06\times10^{-2}\zeta-1.58\times10^{-5}\zeta^2+1.36\times10^{-9}\zeta^3$$

Both ζ and δ_o must be expressed in microinches. This correlation clearly shows that thermal contact conductance depends on the mean junction temperature, T_m, and coefficient of thermal expansion, α.

Madhusudana and Fletcher (1983) developed a dimensionless thermal contact conductance correlation for Zircaloy 2 and uranium oxide junctions by utilizing thermal contact conductance data from several investigators. Because of the difficulty in measuring $|\tan\Theta|$, the contribution of the asperity slope was omitted. The dimensionless correlation was obtained after the data points were adjusted to a mean interface temperature of 180°C using the variation of (k_s/M) values with temperature. This correlation was given as

$$\frac{h_j\sigma_{\text{rms}}}{k_s}=12.29\times10^{-3}\left(\frac{P}{M}\right)^{0.66} \tag{7}$$

Negus and Yovanovich (1985) approximated true boundary conditions of surfaces in contact by superimposing Neumann-specified solutions to Laplace's differential equation using a least-square criterion, and solving for the constriction parameter. This resulted in an expression valid over the range $0\leq\epsilon\leq0.9$, with a maximum relative error of 0.02 percent at $\epsilon=0.7$. The results were in excellent agreement with those of other researchers (Gibson, 1976; Smythe, 1953).

Utilizing the geometric analysis of interesting conforming, rough surface results of Cooper et al. (1969), Yovanovich (1982) developed an expression of the form

$$\frac{h_j\sigma_{\text{rms}}}{m_{\text{rms}}k_s}=1.25\left(\frac{P}{H}\right)^{0.95} \tag{8}$$

which has been shown to agree with a previously developed theoretical expression to within ±1.5 percent for $2\leq(Y/\sigma_{\text{rms}})\leq4.75$. Song and Yovanovich (1987) later developed an explicit expression

$$\frac{h_j\sigma_{rms}}{m_{\text{rms}}k_s}=1.25\left(\frac{P}{c_1\left(\frac{\sigma_{\text{rms}}1.62\times10^6}{m_{\text{rms}}}\right)^{c_2}}\right)^{\frac{0.95}{1+0.07c_2}} \tag{9}$$

where σ_{rms} is in μm, c_1 and P are in MPa, and c_2 and m_{rms} are dimensionless.

The thermal contact conductance of a soft turned surface in contact with a hard smooth flat surface was investigated analytically and experimentally by Yovanovich (1971). In this investigation, the solution was composed of the thermal contact conductance due to roughness and to waviness, added in parallel. Utilizing the solution of Cooper et al. (1969), the thermal contact conductance due to roughness was expressed as

$$h_j=f\left(\frac{k_s}{\sigma_{\text{rms}}}\right)\left(P^*\right)^{0.985} \tag{10}$$

where f was a geometric parameter depending upon the slope of the contacting asperities. It was noted that typical values of f were 0.036, 0.175, and 0.290 for flat lapped surfaces, averaged rough, and very rough surfaces, respectively. When the pressure was very large, the number of contact spots increased and these spots merged to form a quasi-continuous spiral. The thermal contact conductance solution due to the waviness (spirals) was described as

$$\frac{1}{h_w}=\Delta\left(\frac{\psi^{w1}}{k_1}+\frac{\psi^{w2}}{k_2}\right) \tag{11}$$

where ψ_{w1} and ψ_{w2} were the geometric factors, defined as

$$\psi=\frac{\left(\frac{w}{b}\cos\beta\right)}{\pi\left(1-\frac{2\beta}{\pi}\right)}[\Theta_2\cosh\Theta_2-\sinh\Theta_2$$
$$-\Theta_1\cosh\Theta_1+\sinh\Theta_1] \tag{12}$$

and the expressions for Θ_1 and Θ_2 were described as

$$\Theta_1=\cosh-1\left(\frac{1}{\cos\beta}\right)\qquad\Theta_2=\cosh-1\left(\frac{b}{w\cos\beta}\right)$$

For small angles ($\beta\leq30$), equation (12) was approximated by

$$\psi=\frac{\left(\frac{w}{b}\cos\beta\right)}{\pi\left(1-\frac{2\beta}{\pi}\right)}[\Theta_2\cosh\Theta_2-\sinh\Theta_2] \tag{13}$$

Coated Junctions. Mikic and Carnasciali (1969) investigated the effects of the thermal conductivity of plating materials. The approximate relative reduction of the thermal contact resistance due to plating was described as

$$\frac{R_{\text{plating}}}{R_{\text{uncoated}}}=f\left(\frac{a}{b},\frac{t}{a},\frac{k_1}{k_2}\right) \tag{14}$$

and was shown to decrease when a/b, t/a, and k_1/k_2 increased. It was noted, however, that the limiting parameter was k_1/k_2 for sufficiently thick plating. The test specimens (stainless steel and copper cylinders) were attached by soldering and thermal contact resistance was measured extrapolating the temperature along the specimens.

The special case of equation (14) where the contact spots are widely separated and do not interact has been considered by Dryden (1983). Snaith et al., (1984) reviewed several previous investigations of interstitial materials used to control thermal contact resistance across metallic contacts.

The most extensive investigation of thermal contact resistance of coated surfaces was performed by Antonetti (1983) who developed a thermomechanical model for nominally flat, conforming rough surfaces. This model demonstrated that a coated joint could be reduced to an equivalent uncoated joint by using an effective hardness. Utilizing k/H to rank the effectiveness as proposed by Yovanovich (1972), the thermal contact resistance for two coated surfaces in contact was given as

$$h_j' = h_j\left(\frac{H}{H'}\right)^{0.93}\left(\frac{k_1+k_2}{k_2C_1+k_1C_2}\right) \tag{15}$$

where C is the ratio of the constriction parameter with a coating to that without a coating, or

$$C=\frac{\psi(\epsilon', \phi)}{\psi(\epsilon)} \tag{16}$$

The constriction parameter of the uncoated contact was modified to account for the influence of the coating, the contact temperature, and the heat flux distribution, and was expressed as

$$\psi(\epsilon', \phi)=\frac{16}{\pi\epsilon'}\sum_{n=1}^{\infty}\frac{J_1^2(\lambda'\epsilon')}{(\lambda')^3 J_0^2(\lambda')}\,\phi\gamma\rho \tag{17}$$

where

$$\phi=K\left(\frac{(1+K)+(1-K)e^{-2\lambda'\epsilon'\tau'}}{(1+K)-(1-K)e^{-2\lambda'\epsilon'\tau'}}\right)$$

$\gamma=1$ (isothermal contact point)

$$\rho=\frac{\sin(\lambda'\epsilon')}{2J_1(\lambda'\epsilon')}$$

For junctions made of the same material and coated on one surface, equation (15) was simplified to

$$h_j' = h_j\left(\frac{H}{H'}\right)^{0.93}\left(\frac{2}{1+C}\right) \tag{18}$$

and shown to compare quite well with results obtained from tests using silver coated and bead blasted nickel surfaces in contact.

Experimental Investigation

An experimental investigation was conducted to determine to what degree thermal contact conductance at the interface of contacting Aluminum 6061 T6 surfaces could be enhanced by vapor deposited metallic coatings. Three different coating materials (lead, tin, and indium) were evaluated using four different thicknesses for each coating material.

Experimental Facility. The experimental apparatus, shown in Fig. 3, consisted of a vertical column composed of a load bellows, a load cell, heat sink, a pair of test specimens, and a heat source. The heat source was a 200-W band heater wrapped around the lower test specimen fixture at the base of the column. The heat sink was maintained at a constant temperature by a constant temperature circulating bath. Radial heat losses from the test specimens were minimized by placing a radiation shield (made of sheet aluminum and asbestos) around the test column and the whole system was enclosed within a bell jar.

Sixteen pairs of samples 9 cm long and 2.54 cm in diameter were made from a single piece of Aluminum 6061 T6 bar stock. The contacting surfaces were all prepared at the same time by turning on a lathe, and the surface parameters were measured to insure similar surfaces. Three additional test specimens were also prepared in order to test the microhardness of the substrate and the effective hardness of the substrate and coating combination. The test specimens were labeled and stored in a vacuum to prevent continued oxidation.

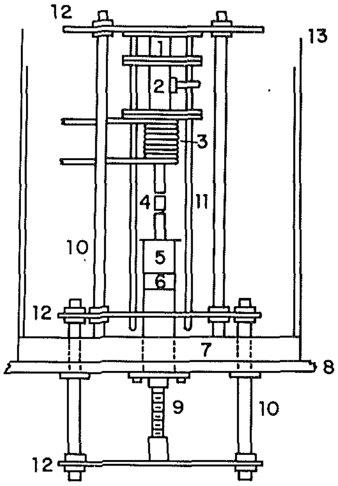

1	LOAD BELLOWS	7	FEEDTHROUGH RING
2	LOAD CELL	8	BASE PLATE
3	HEAT SINK	9	SCREW JACK
4	TEST SPECIMENS	10	SUPPORT RODS
5	HEAT SOURCE	11	GUIDE RODS
6	GUARD HEATER	12	SUPPORT PLATES

13 BELL JAR

Fig. 3 Experimental apparatus

The temperatures along the test specimens were measured using three Chromel-Alumel AWG-30 thermocouples located at 1.27-cm intervals along the specimen centerline. These thermocouples were inserted into the thermocouple wells using a thermally conductive paste. The axial load was applied by bleeding high pressure nitrogen gas into the load bellows. Using a compression load cell located in the test column and a transducer located outside the jar, the load was monitored. The load cell and instrumentation were calibrated with a proving ring to an accuracy of ±4.45 N. In order to reduce the convection effects in the test facility, a vacuum of 7.8×10^{-7} Torr was maintained using a roughing pump in series with an oil diffusion pump.

A vacuum deposition unit equipped with a film thickness monitor was used to vapor-deposit the coating materials (tin, lead, and indium) on the surfaces of the test specimens. Four different thicknesses were selected using the optimum thickness predicted by the analytical solution of Antonetti (1983) as a guide.

Thermal Test Procedure. The experimental tests were conducted to determine the steady-state thermal contact conductance of both uncoated and coated junctions. The uncoated interface of each test pair was tested first to establish a baseline thermal contact conductance value for each pair. The end surface of one sample from each pair was then coated with a thin metallic coating to the desired thickness and the thermal contact conductance was remeasured. Initially, both a thin and thick coating were tested in an attempt to bracket the optimum thickness. A comparison of the thermal contact conductance values was then utilized to select the next coating thickness. A similar approach was used for each of the three types of coating material.

The experimental procedure for all of the thermal experimental tests follows. The fixtures and a pair of test specimens were installed in the test facility and the vertical column was aligned visually to insure that contacting surfaces remained

Table 1 Measured effective microhardness

Tin Coated Aluminum	
$H' = H_S(1\text{-}t/d) + 2.5H_L(td)$	$t/d < 1.0$
$H' = 2.5H_L - 0.3H_L\ (t/d\text{-}1)$	$1.0 \leq t/d \leq 6.0$
Indium Coated Aluminum	
$H' = H_S(1\text{-}t/d) + 4.0H_L\ (t/d)$	$t/d < 1.0$
$H' = 4.0H_L - 0.77H_L\ (t/d\text{-}1)$	$1.0 \leq t/d \leq 4.9$
Lead Coated Aluminum	
$H' = H_S(1\text{-}t/d) + 3.25H_L\ (t/d)$	$t/d < 1.0$
$H' = 3.25K_L - 0.833H_L\ (t/d\text{-}1)$	$1.0 \leq t/d \leq 4.9$

parallel during the tests. A slight load was applied to the test column to insure that fixtures and test specimens would remain properly aligned during evacuation of the test chamber. After the thermocouple readings has been checked, a radiation shield was put in place and the test chamber was evacuated to a vacuum level of 7.8×10^{-7} Torr. After the desired vacuum level was reached, the electrical resistance heater and constant temperature bath were turned on. Before any data were taken, specimens were allowed to outgas for 6–8 hours.

Temperature and pressure test conditions were set by adjusting the heater current and pressurizing the load bellows, respectively. Tests were conducted at an average interface temperature of $25 \pm 1\,^\circ\mathrm{C}$ for uncoated junctions and $25\ \pm 2\,^\circ\mathrm{C}$ for coated junctions. Data were taken when the test specimen temperatures did not vary more than 0.3°C over a one-hour period. The heat flux through the test specimens was computed using the temperature gradient obtained by a linear least-squares curve fit, and thermal conductivities were computed using a previously developed thermal conductivity correlation. Thermal contact conductance was then computed using the average heat flux of the heated and cooled specimens divided by the temperature drop at the interface. The pressure was increased in 100 kPa increments from an initial loading of approximately 100 kPa, to 900 kPa, and 200 kPa increments from 900 kPa to 1600 kPa.

Thermal Conductivity Calibration. In order to determine the heat flux during the tests it was necessary to know the variation of thermal conductivity with temperatures for the Aluminum 6061 T6 test material. A 2.54-cm-dia heat flux meter was fabricated from a standard reference material of a known thermal conductivity (NBS Electrolytic Iron) and mounted between two specimens. The tests conducted using the heat flux meter resulted in a correlation for the thermal conductivity of the tested specimens of

$$k = 0.226T + 111.94 \tag{19}$$

where T was given in degrees Kelvin. Since all test specimens used in this investigation were made of the same bar stock, this thermal conductivity correlation was later utilized for all of the test samples.

Microhardness Testing. Because *work hardening* occurred during the machining process, microhardness of the contacting surface varied with respect to depth. Often, as the depth of indentation increases, contact microhardness decreases, approaching the bulk hardness of the material. Hegazy (1985) investigated the microhardness of Stainless Steel 304, Zr-4, Zr-2.5wt% Nb, and Ni-200 materials, which were ground, lapped, and mechanically polished to a predetermined metal graphic finish. The results showed a trend of decreasing microhardness with respect to an increase of indentation depth. Song and Yovanovich (1987) developed an explicit expression for contact microhardness and the relative contact pressure. It was noted that contact microhardness depended on the mean surface roughness, mean absolute slope of the asperities, the type of material, the method of surface preparation, and applied pressure. Contact microhardness of the surface being penetrated by the harder asperities was assumed to be the same as the Vickers microhardness corresponding to the equivalent Vickers indentation diagonal. Utilizing a power correlation, contact microhardness was expressed as

$$H_c = c_1 d_v^{c2} \tag{20}$$

Using this expression and the mean contact spot radius developed by Mikic (1971), the relative contact pressure can be expressed as

$$\frac{P}{H_c} = \left(\frac{P}{c_1 \left(\frac{1.62 \times 10^6 \sigma_{\mathrm{rms}}}{m_{\mathrm{rms}}} \right)^{c_2}} \right)^{\frac{1}{1+0.071c_2}} \tag{21}$$

In order to rank the combination of the coated material and the substrate using the technique of Yovanovich (1972), the effective Vickers microhardness of the coated material was measured in the same manner as the uncoated material. Several thicknesses were evaluated and results were plotted for tin, indium, and lead coated substrates. Although the full range of effective microhardness was not measured, the trend was that as the load increased (decreased in t/d), the effective microhardness increased, approaching the microhardness of the substrate. This trend was also reported by Antonetti (1983); however, when the indenter began to penetrate the substrate ($t/d = 1$) different microhardness values were observed. Table 1 lists the measured effective microhardness for the three different materials evaluated.

Results and Discussion

In this investigation, approximately 400 data points were obtained. In order to insure that the experimental technique employed was repeatable, the thermal contact conductance was measured for one test pair. The two samples in this test pair were then separated and rotated slightly and retested. This procedure was repeated a total of four times. The data obtained from this series of tests were all within ±2 percent of each other with the highest deviation occurring at light loads between the first and second consecutive tests.

The uncertainty of the measurement technique was comprised of the uncertainty of the temperature measurements, heat flux measurement, temperature distribution accomplished by means of extrapolation, and pressure measurement. Combining these uncertainties with those due to the temperature measurement system, the location of the thermocouple wells, and the thermal conductivity of the materials, overall uncertainty of the experimental data was estimated to be ±7 percent at loads of 1600 kPa to ±21 percent at the lightest loads evaluated.

The uncoated joint results of the experimental test program are presented in Fig. 4. As expected, the results for each pair are different due to minor variations in surface characteristics of the contacting surfaces, listed in Table 2. Also, significant variations in the behavior of pair 8 and pair 11 were observed. These two test pairs were not used in the remaining tests. The measured uncoated thermal contact conductance data for test pair No. 1 are compared in Fig. 5 with several of the models and correlations discussed previously. As shown, the semi-empirical relationship developed by Fletcher and Gyorog (1970) slightly underestimates the measured value of the uncoated junction, while that of Madhusudana and Fletcher (1983), developed for Zircaloy 2 and uranium oxide junctions, and a correlation developed for conforming rough and optically flat

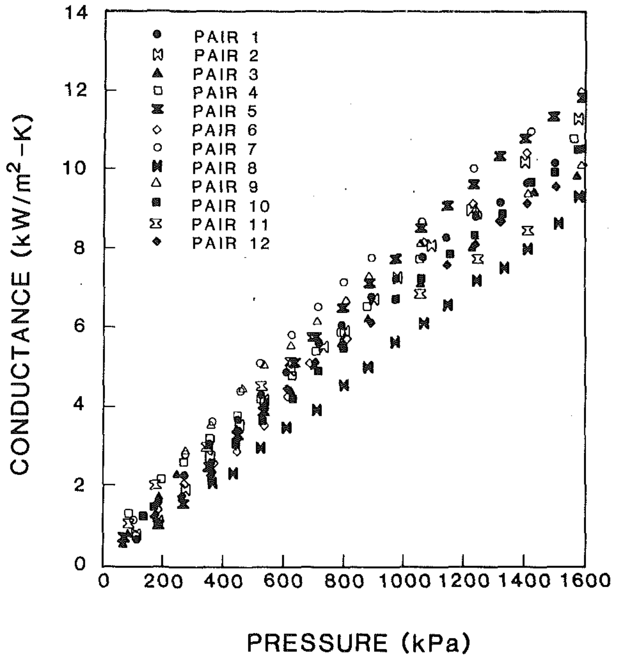

Fig. 4 Uncoated test results

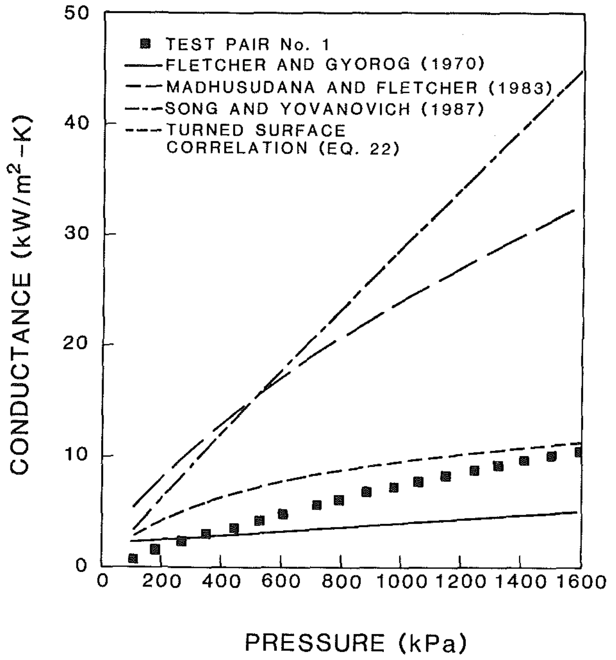

Fig. 5 Comparison of measured bare joint results with predicted values as a function of pressure

smooth surfaces by Yovanovich (1987) greatly overestimate the measured results. The most accurate correlation is one developed as part of this investigation. This correlation, the turned surface correlation, utilizes an analytical model similar to the one developed by Yovanovich (1971) for a flat surface in contact with a turned surface.

In the present investigation, the parameters ψ_{w1} and ψ_{w2} were assumed equal, due to the irregular shape of the waviness of the specimens, and were determined by equation (17). Also due to nonuniform spacing between the waviness, the $\Delta_{\rm rms}$ value used was computed utilizing a combination of the approximated Δ_1 and Δ_2 values. Finally, a combined rms value for β_1 and β_2 was substituted for the single value proposed by Yovanovich (1971). The resulting modified expression can be written as

Table 2 Specimen surface parameters

Specimen No.	R_q (μm)	R_{da}	W_α(μm)	W_t(μm)
1A	0.85598	0.062	2.540	9.779
1B	0.69850	0.066	2.489	10.211
2A	0.69088	0.072	2.235	8.077
2B	0.68580	0.070	2.337	11.811
3A	0.68580	0.063	2.286	7.874
3B	0.74168	0.061	2.489	9.601
4A	0.74168	0.065	2.540	9.652
4B	0.77470	0.063	2.591	9.982
5A	0.72898	0.060	2.540	8.941
5B	0.79248	0.061	2.591	9.855
6A	0.64008	0.067	2.235	7.798
6B	0.68580	0.068	2.337	8.255
7A	0.69850	0.068	2.286	9.144
7B	0.64770	0.065	2.235	8.585
8A	0.65532	0.067	2.489	10.338
8B	0.77470	0.068	2.540	9.982
9A	0.81788	0.057	2.870	10.668
9B	0.36830	0.058	2.737	4.039
10A	0.69850	0.065	2.032	8.255
10B	0.71120	0.070	2.337	8.890
11A	0.71120	0.062	2.413	9.271
11B	0.67818	0.066	2.413	8.712
12A	0.67818	0.066	2.337	8.458
12B	0.78740	0.067	2.667	9.855
13A	0.71628	0.063	2.489	9.474
13B	0.85598	0.058	3.099	11.633
14A	0.72898	0.062	2.489	9.093
14B	0.74168	0.060	2.591	10.668
15A	0.80518	0.063	2.540	10.033
15B	0.71628	0.066	2.337	8.458
16A	0.69088	0.069	2.337	8.001
16B	0.69850	0.069	2.235	7.696

R_q = RMS roughness
R_{da} = Arithmetic average asperity slope
W_α = Arithmetic average waviness height
W_t = Maximum waviness height

$$\frac{1}{h_w} = \frac{2\Delta_{\rm rms}\psi}{k_S} \qquad (22)$$

In order to obtain optimum thicknesses of the layers for different interface pressures, both uncoated and coated junction results were curvefit using a linear regression technique. Using values obtained from this curvefitting technique, the dimensionless thermal contact conductance (defined as the ratio of thermal contact conductance for the coated joint and the uncoated joint at the same pressure) was computed. The results are shown in Figs. 6, 7, and 8, for the lead, tin, and indium-coated interfaces, respectively.

As illustrated in Fig. 6, four different thicknesses of lead coatings were tested and the ratio of coated thermal contact conductance to uncoated thermal contact conductance at eight different pressures was plotted as a function of the coating thickness. Results indicate that the dimensionless thermal contact conductance increases as the coating thickness increases, up to thicknesses of 1.5 to 2.5 μm. At this point, the dimensionless thermal contact conductance decreases with increasing thickness. This phenomenon can be explained as follows: When the coating thickness is increased at constant pressure, the enhancement of thermal contact conductance results from the increase of contact area due to the soft coating material filling the interstitial gaps. If the coating thickness is increased fur-

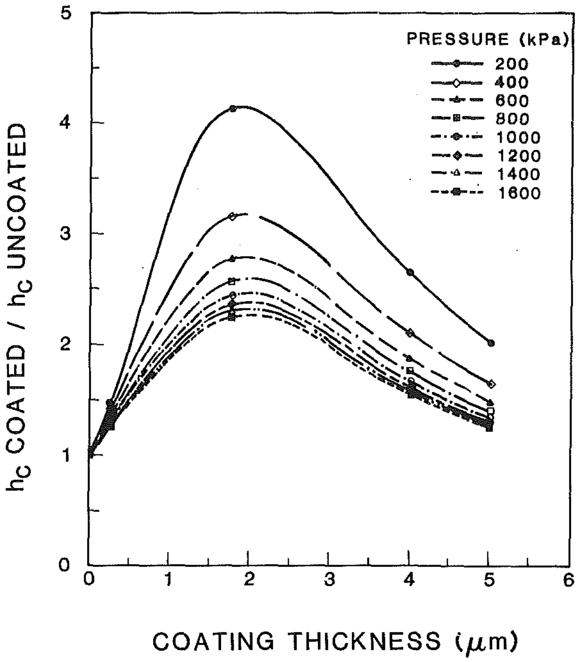

Fig. 6 Improvement in the thermal contact conductance due to lead coatings as a function of thickness

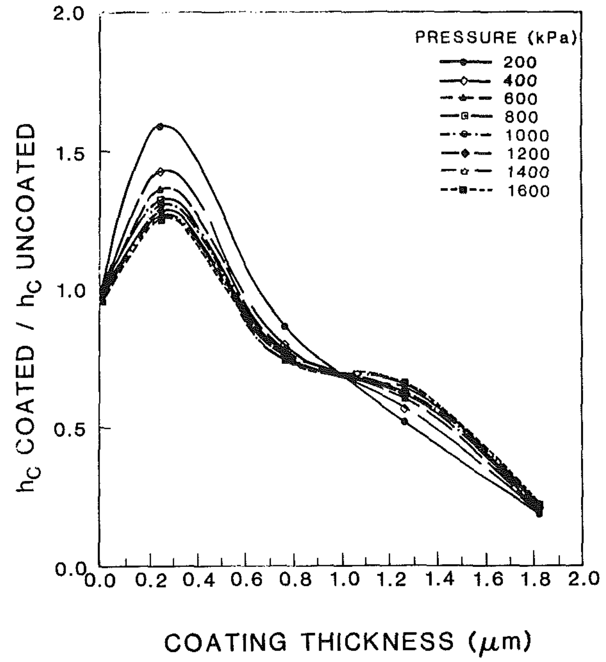

Fig. 7 Improvement in the thermal contact conductance due to tin coatings as a function of thickness

ther, the enhancement due to the increase in area is overshadowed by the increase of the bulk thermal resistance of the coating material. An optimum thickness is reached when the combination of these two effects results in the minimum resistance.

It is also apparent from Fig. 6 that at a constant thickness, the enhancement of thermal contact conductance decreases as the pressure increases. When the pressure is initially increased, the contact area of coated joints increases much faster than for uncoated joints due to the softness of the coating material. As the pressure continues to increase, the rapid increase in contact area is decreased by the aluminum asperities that have penetrated the coating material and are in contact with the other aluminum surface.

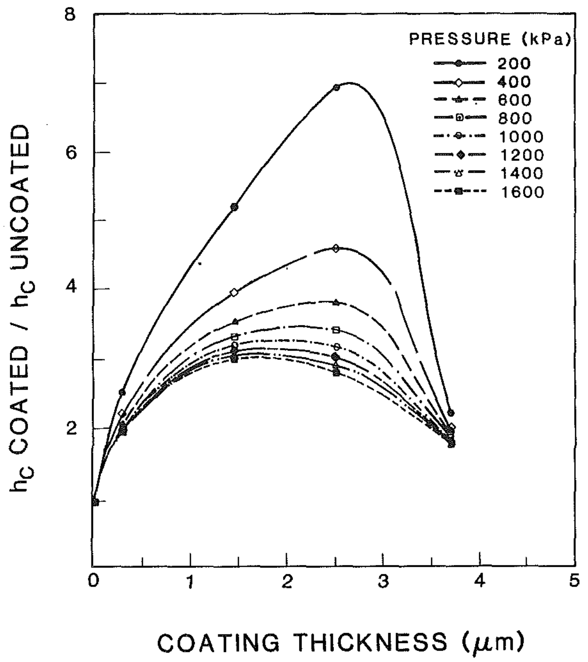

Fig. 8 Improvement in the thermal contact conductance due to indium coatings as a function of thickness

Four different coating thicknesses were evaluated in the investigation of tin-coated junctions. Figure 7 illustrates that the application of tin coatings to the contact interface will slightly improve thermal contact conductance of the joint. For tin, the optimum thickness occurs in a thickness range of 0.2 to 0.5 μm. At a coating thickness, a reversal of the thermal contact conductance with respect to pressure was observed. This particular phenomenon was considered to be an anomaly and was assumed to be due to misalignment of the contacting surfaces at low pressures.

The greatest enhancement of the thermal contact conductance was obtained for an indium coating on the contact surface. Four different thicknesses were tested. The results, illustrated in Fig. 8, indicate that the optimum thickness for indium-coated joints occurs in the thickness range of 2.0 to 3.0 μm and results in an enhancement of thermal contact conductance by a factor of seven. One interesting observation not apparent in the other two materials was that of a shift in optimum thickness as a function of pressure. As shown, the optimum thickness started to shift to the left at a pressure of approximately 1000 kPa.

When test results from the three coating materials are compared, it is apparent that indium is by far the most suitable for thermal enhancement, providing a 700 percent increase in thermal contact conductance. Lead is second, providing a 400 percent increase, followed by tin with a 50 percent increase. Also, the optimum thickness decreased from indium, which was the thickest, to tin, which was the thinnest.

After completion of the tests, different combinations of layer and substrate materials were ranked using the k'/H' method developed by Antonetti (1983). Using the measured Vickers hardness for these combinations and a pressure of 200 kPa, indium was predicted to be the most effective, followed by tin and lead, respectively. Although experimental results indicate that indium is in fact the best of the three combinations evaluated, the measured and predicted enhancement of lead and tin were reversed. This difference between the predicted and measured results may be due to surface parameters (the surfaces evaluated in this investigation were both turned) and/or the relationship of the material hardnesses (the aluminum substrate was harder than some of the coating materials and softer than others). For these reasons, the thermomechancial model of Antonetti (1983) may not be appropriate for all material and surface combinations.

Conclusions and Recommendations

This investigation has demonstrated that thin metallic coatings may be used for thermal enhancement of contacting joints. The experimental results have verified the existence of optimum coating thicknesses, which have been experimentally shown to be in the range of 2.0 to 3.0 μm for indium, 1.5 to 2.5 μm for lead, and 0.2 to 0.5 μm for tin. The enhancement of thermal contact conductance increased by 700, 400, and 50 percent for indium, lead, and tin, respectively. Evidence of a significant shifting of optimum thickness for different coating materials was also presented. Based upon these data, the hardness of the coating material seems to be the most significant parameter in ranking of substrate and coating material combinations. However, additional experimental data are needed to substantiate this hypothesis. Finally, it is clearly apparent that the most effective enhancement of thermal contact conductance occurs at low pressures.

This investigation considered the enhancement of thermal contact conductance for surfaces with similar surface characteristics and it should be noted that optimum thicknesses obtained in this investigation may only be valid for joints in which the contacting surfaces have surface characteristic values similar to those tested in this investigation. In order to maximize heat flow through a given contact interface, further investigation is necessary to determine the effect of variations in surface characteristics on optimum coating thickness.

Acknowledgments

The authors would like to acknowledge the support of NASA Johnson Space Center and The Texas Advanced Technology Program.

References

Alario, J., 1984, "Monogroove Heat Pipe Radiator Shuttle Flight Experiment: Design, Analysis and Testing," SAE Paper No. 840959.

Antonetti, V. W., 1983, "On the Use of Metallic Coatings to Enhance Thermal Contact Conductance," Ph.D. Thesis, Mechanical Engineering Department, University of Waterloo, Waterloo, Ontario, Canada.

Cooper, M. G., Mikic, B. B., and Yovanovich, M. M., 1969, "Thermal Contact Conductance," *Int. J. Heat Mass Transfer*, Vol. 12, pp. 274–300.

Dryden, J. R., 1983, "The Effect of Surface Coating on the Constriction Resistance of a Spot on an Infinite Half-Plane," ASME JOURNAL OF HEAT TRANSFER, Vol. 105, No. 2, pp. 408–410.

Fletcher, L. S., and Gyorog, D. A., 1970, "Prediction of Thermal Contact Conductance Between Similar Metal Surfaces," in: J. W. Lucas, ed., *Progress in Astronautics and Aeronautics: Heat Transfer and Spacecraft Thermal Control*, Vol. 24, MIT Press, Cambridge, MA, pp. 73–88.

Gibson, R. D., 1976, "The Contact Resistance for a Semi-infinite Cylinder in a Vacuum," *Applied Energy*, Vol. 2, pp. 57–65.

Greenwood, J. A., 1967, "The Area of Contact Between Rough Surfaces and Flats," ASME *Journal of Lubrication Technology*, Vol. 89, No. 1, pp. 81–91.

Harwell, W., 1983, "The Heat Pipe Thermal Cannister: An Instrument Thermal Control System," SAE Paper No. 831124.

Hegazy, A. A., 1985, "Thermal Joint Conductance of Conforming Rough Surfaces: Effects of Surface Microhardness Variations," Ph.D. Thesis, Mechanical Engineering Department, University of Waterloo, Waterloo, Ontario, Canada.

Holm, R., 1958, *Electric Contacts Handbook*, Springer-Verlag, Berlin.

Madhusudana, C. V., and Fletcher, L. S., 1983, "Solid Spot Thermal Conductance of Zircaloy-2/Uranium Dioxide Interfaces," *Nuclear Science and Engineering*, Vol. 83, pp. 327–332.

Madhusudana, C. V., and Fletcher, L. S., 1986, "Contact Heat Transfer—The Last Decade," *AIAA Journal*, Vol. 24, No. 3, pp. 510–523.

Mal'kov, V. A., and Dobashin, P. A., 1969, "The Effect of Soft-Metal Coatings and Linings on Contact Thermal Resistance," *Inzhenerno-Fizicheskii Zhurnal*, Vol. 17, No. 5, pp. 871–879.

Mikic, B., and Carnasciali, G., 1969, "The Effect of Thermal Conductivity of Plating Material on Thermal Contact Resistance," ASME Paper No. 69-WA/HT-9.

Mikic, B. B., 1971, "Analytical Studies of Contacts for Nominally Flat Surfaces; Effect of Previous Loading," ASME *Journal of Lubrication Technology*, Vol. 93, No. 4, pp. 451–459.

Mikic, B. B., 1974, "Thermal Contact Conductance; Theoretical Considerations," *Int. J. Heat Mass Transfer*, Vol. 17, pp. 205–214.

Negus, K. J., Yovanovich, M. M., and Thompson, J. C., 1985, "Thermal Constriction Resistance of Circular Contacts on Coated Surfaces: Effects of Contact Boundary Conditions," AIAA Paper No. 85-1014.

Peterson, G. P., and Fletcher, L. S., 1988, "Thermal Contact Conductance in the Presence of Thin Metallic Foils," Paper No. AIAA-88-0466.

Peterson, G. P., and Ortega, A., 1989, "Thermal Control of Electronic Equipment and Devices," in: *Advances in Heat Transfer*, J. Hartnett and T. Irvine, eds., Pergammon Press, Oxford, United Kingdom, in press.

Smythe, W. R., 1953, "Current Flow in Cylinders," *Journal of Applied Physics*, Vol. 24, No. 1, pp. 70–73.

Snaith, B., O'Callaghan, P. W., and Probert, S. D., 1984, "Interstitial Materials for Controlling Thermal Conductance Across Pressed Metallic Contacts," *Applied Energy*, Vol. 6, pp. 175–191.

Song, S., and Yovanovich, M. M., 1987, "Explicit Relative Contact Pressure Expression: Dependence Upon Surface Roughness Parameters and Vickers Microhardness Coefficients," AIAA Paper No. 87-0152.

Yip, F. C., 1975, "Effect of Oxide Films on Thermal Contact Resistance," in: M. M. Yovanovich, ed., *AIAA Progress in Astronautics and Aeronautics: Heat Transfer With Thermal Control Applications*, Vol. 39, MIT Press, Cambridge, MA, pp. 45–46.

Yovanovich, M. M., 1971, "Thermal Contact Conductance of Turned Surfaces," AIAA Paper No. 71-80.

Yovanovich, M. M., 1972, "Effect of Foils Upon Joint Resistance: Evidence of an Optimum Thickness," AIAA Paper No. 72-283.

Yovanovich, M. M., 1982, "Thermal Contact Correlations," in: T. E. Horton, ed., *Progress in Aeronautics and Astronautics: Spacecraft Radiative Transfer and Temperature Control*, Vol. 83, MIT Press, Cambridge, MA, pp. 83–95.

Yovanovich, M. M., 1987, "Theory and Applications of Constriction and Spreading Resistance Concepts for Microelectronic Thermal Control," Keynote Address, *Proceedings of the International Symposium on Cooling Technology for Electronic Equipment*, Honolulu, HI, Mar.

M. I. Flik
Assistant Professor,
Department of Mechanical Engineering,
Massachusetts Institute of Technology,
Cambridge, MA 02139
Mem. ASME

C. L. Tien
A. Martin Berlin Professor.
Department of Mechanical Engineering,
University of California,
Berkeley, CA 94720
Fellow ASME

Size Effect on the Thermal Conductivity of High-T_c Thin-Film Superconductors

Using the kinetic theory approximation and reported data, this study shows that at low temperatures, the phonon mean free path in polycrystalline ceramic $YBa_2Cu_3O_7$ can be of the order of the thickness of thin-film superconductors. In this case, boundary scattering reduces the thermal conductivity with decreasing film thickness. A simple method accounts for the size effect on conduction in thin films. This analysis rests solely on geometric arguments and does not consider the effect of grain boundaries. For conduction along the film, this model approximates well an analytical solution of the Boltzmann transport equation, and is in good agreement with experimental data for thin lead films. The model is also employed to analyze the size effect on conduction across the film and the influence of anisotropy.

Introduction

Early in 1987, $YBa_2Cu_3O_7$ ceramics were found to exhibit superconductivity at temperatures above the boiling point of liquid nitrogen. This discovery initiated an unprecedented spurt of research activity. For the first time, there exists a temperature range in which both superconductors and semiconductors are operative. Powerful hybrid superconductor-semiconductor devices now appear feasible, combining the best features of both technologies. Van Duzer (1988) and Nisenoff (1988) reviewed the prospects of such a development. The basic elements of these hybrid devices are thin films of high-T_c superconductors, deposited on silicon or gallium arsenide substrates. Another promising application of high-T_c thin-film superconductors is the liquid-nitrogen superconducting bolometer. In such a device, a superconducting film operated near the temperature of the midpoint of its transition serves as a radiation absorber and as an electrical resistance thermometer and is coupled to a heat sink through a thermal conductance. Bolometers are infrared-radiation detectors of excellent responsivity, and recently Richards et al. (1989) showed that the noise power of a high-T_c superconducting bolometer could be two orders of magnitude smaller than that of a room-temperature pyroelectric detector.

Flik and Tien (1990a) showed that the thermal conductivity of a thin-film superconductor strongly affects its intrinsic thermal stability. The precise prediction of the stability margin is a prerequisite for the design of actual devices that operate safely under all conditions. Gross et al. (1989) and Huebener et al. (1988) observed that thermal conduction in thin-film superconductors determines the spatial resolution limit of the powerful characterization method of low-temperature scanning electron microscopy (LTSEM). The generation of stable temperature structures in thin-film superconducting bridges is governed by thermal conduction in these devices (Freytag and Huebener, 1985).

The thermal conductivity of ceramic samples of $YBa_2Cu_3O_7$ was measured by Uher and Kaiser (1987) and Jezowski et al. (1987). Fisher et al. (1988) reviewed further measurements of the thermal conductivity and the specific heat of high-T_c superconductors. Recently, Uher (1989) provided a comprehensive review of the mechanisms of heat conduction in high-T_c superconductors. All investigators agree that 80–90 percent of the conduction of heat in ceramic $YBa_2Cu_3O_7$ is brought about by lattice vibrations, except at temperatures below 1 K (Cohn et al., 1988). Kirk et al. (1989) measured the thermal conductivity of hot-pressed $YBa_2Cu_3O_7$ samples and detected anisotropic behavior, presumably due to partial orientation of crystallites. Hagen et al. (1989) experimentally investigated the thermal conductivity of single crystals of $YBa_2Cu_3O_7$. They found the *ab* plane conductivity to be about 5 times higher than the conductivity along the *c* direction. They also observed that electrons play a significant role in *ab* plane heat conduction in the normal state, while their contribution is negligible in the *c* direction. Flik and Tien (1990b) showed that at low temperatures, the phonon mean free path in $YBa_2Cu_3O_7$ is of the order of the thickness of thin-film superconductors. In general, if the carrier mean free path is of the order of the smallest dimension of a given specimen, the transport due to these carriers exhibits a dependence on the specimen size (Ziman, 1960). It is the purpose of this work to analyze the influence of the film thickness on the thermal conductivity of high-T_c thin-film superconductors.

Since the discovery of the size effect on electric conduction along thin gold films at the beginning of this century, numerous experimental and theoretical investigations have been performed and were summarized by Ziman (1960) and, more recently, by Tellier and Tosser (1982). Most of the theoretical studies concerned electric conduction along thin films, but due to the analogy between electronic transport of electric charge and heat, these results are directly applicable to thermal conduction by electrons. Almost all of these works accounted for the size effect by solving the Boltzmann transport equation in the thin film with appropriate boundary conditions at the film surface. Tien et al. (1969) used the solution to the Boltzmann equation given by Fuchs (1938) to predict the thermal conductivity along thin metallic films. Tellier and Tosser (1982) also reported a number of approximate relations, which are mostly used to interpret experimental data without undue computational effort. Since the Boltzmann equation in its appropriate form also governs phonon transport, many of the results on the size effect on electronic conduction can be applied, at least in a modified form, to the conduction of heat by phonons. It was the aim of most investigations to deduce from the comparison of theory and experiment information on the carrier mean free path in the film or on the scattering mechanisms.

Without using the Boltzmann equation and solely resting on geometric arguments, the present work develops a simple

---

Contributed by the Heat Transfer Division and presented as the ASME Winter Annual Meeting, San Francisco, California, December 10–15, 1989. Manuscript received by the Heat Transfer Division June 5, 1989; revision received February 12, 1990. Keywords: Conduction, Cryogenics, Thermophysical Properties.

model for the thin-film size effect, which is valid for both electron and phonon conduction. In several situations, also the heat conduction *across* the film is important, such as in scanning electron microscopy of thin-film superconductors or in the superconducting bolometer. The value of the present model is illustrated by its ability to analyze the size effect on conduction across the film and the size-induced anisotropy in thin films of an otherwise isotropic material. The model is also applied to the combined influence of size effect and material anisotropy, which is relevant to the high-T_c superconductors because of their anisotropic crystal structure. The results of this model for conduction along the plane of the film are compared to experimental data and to the analytical solution of the Boltzmann equation due to Fuchs (1938). Based on reported property measurements for bulk $YBa_2Cu_3O_7$, predictions are made for the thermal conductivity along thin films of this material.

Phonon Mean Free Path

Heat conduction by phonons can be analyzed employing kinetic theory, treating the phonons as carriers moving at an average velocity, the speed of sound, across a distance of a mean free path between collisions and possessing a volumetric capacity of heat. The average velocity corresponds to an average group velocity of the lattice waves, and the specific heat to the kinetic and potential energy of the vibrational modes. The mean free path characterizes the interaction of the different modes with each other due to their not being perfectly harmonic, and with imperfections, electrons, and other scatterers. The application of the kinetic method in formal transport theory of phonon heat conduction yields the familiar expression (Ziman, 1960)

$$k = \frac{1}{3} C v l \tag{1}$$

where C is the specific heat per unit volume of the lattice vibrations, v the sound velocity, and l the phonon mean free path. In the following, this relation and experimental data are used to find the temperature dependence of the phonon mean free path in bulk $YBa_2Cu_3O_7$.

Lang et al. (1988) measured the sound velocity in a ceramic sample of this material, and found that it varies less than 5 percent between 0 and 220 K. Below 100 K, the sound velocity for longitudinal polarization stays approximately constant at 4000 m/s, while the velocity for transverse polarization attains a value of 2500 m/s. Due to the approximate nature of kinetic theory, in the present calculations the longitudinal sound velocity is used in order to establish a lower bound for the phonon mean free path. In the range from 40 K to 130 K, the measurements of Lang et al. (1988) of the specific heat of $YBa_2Cu_3O_7$ are employed, from 10 K to 40 K the data of Ferreira et al. (1988), and from 5 to 10 K the results of von Molnar et al. (1988). The first two measurements were performed with ceramic samples, while the third concerns a single crystal. The absolute values of the specific heat from these sources differ by as much as 50 percent at the temperature interval boundaries. Hence the following matching procedure is employed. The data of Ferreira et al. (1988) are matched to those of Lang et al. (1988) by forming the ratios $C(T)/C(40\ \mathrm{K})$. The data of von Molnar et al. (1988) are matched similarly, using the ratio $C(T)/C(10\ \mathrm{K})$. It was shown by Beckmann et al. (1987) that 97 percent of the specific heat of $YBa_2Cu_3O_7$ is due to lattice vibrations, and thus the measured values are directly applicable to equation (1).

At this point, there are no reported measurements of the thermal conductivity of high-T_c superconducting films. Pohl and co-workers (Cahill et al., 1989) developed two bolometric techniques for the measurement of thin-film thermal conductivity, a transient and a steady-state method. These procedures appear to be very promising for application to high-T_c thin-film superconductors, as well as a very sensitive laser detection scheme developed by Fanton et al. (1989) based on the temperature dependence of the refractive index. Jezowski et al. (1987) measured the thermal conductivity of ceramic $YBa_2Cu_3O_7$ in the entire temperature range from 5 K to 130 K, the range of interest for the operation of high-T_c superconductors. These measurements were performed on a ceramic sample, which reached 80 percent of the theoretical density calculated from the unit cell dimensions of the crystal structure, 6350 kg/m^3. Due to the apparent porosity of this sample, the geometric cross section is different from the cross section available for heat conduction. Therefore the thermal conductivity of a polycrystalline film of $YBa_2Cu_3O_7$ is different from

Nomenclature

a = constant, equation (2)
A = anisotropy of a thick film $= k_1/k_2$
C = specific heat per unit volume
d = film thickness
$f(\lambda)d\lambda$ = distribution function of carrier free paths
$F(\delta)$ = size-effect function $= l_x/l$
$G(\delta)$ = size-effect function $= l_y/l$
h_P = Planck's constant $= 6.62620 \times 10^{-34}$ Js
k = thermal conductivity
k_∞ = thermal conductivity of infinite medium
$k_{a,c}$ = thermal conductivity along a, c axis of crystal
$k_{x,y,z}$ = thermal conductivity in x, y, z direction of thin film
k_B = Boltzmann constant $= 1.38062 \times 10^{-23}$ J/K
$\mathbf{K}$ = thermal conductivity tensor
l = bulk mean free path
l_∞ = exchange length in an infinite medium
$l_{x,y}$ = exchange length in x, y direction of thin film
$\tilde{l}_{x,y}$ = components of individual carrier free path
m = matching parameter, equations (25) and (26)
$\mathbf{q}$ = heat flux vector
S = $(1-\delta^2)^{1/2}$
t_R = relaxation time
T = temperature
v = sound velocity
x = coordinate parallel to the film
y = coordinate normal to the film
z = coordinate normal to xy plane
δ = reduced film thickness $= d/l$
δ_1 = reduced film thickness $= d/l_1$
δ_2 = reduced film thickness $= dA^{1/2}/l_1$
Θ_D = Debye temperature
λ = carrier free path
χ = angle between $d\Omega$ and the positive y axis
χ^*, χ^{**} = angles separating internal scattering regime from boundary scattering regime
ψ = angle between the projection of $d\Omega$ onto the xz plane and the positive x axis
$d\Omega$ = differential solid angle

Subscripts

1, 2, 3 = along the x, y, z direction in a thick film
x = x direction
y = y direction
z = z direction

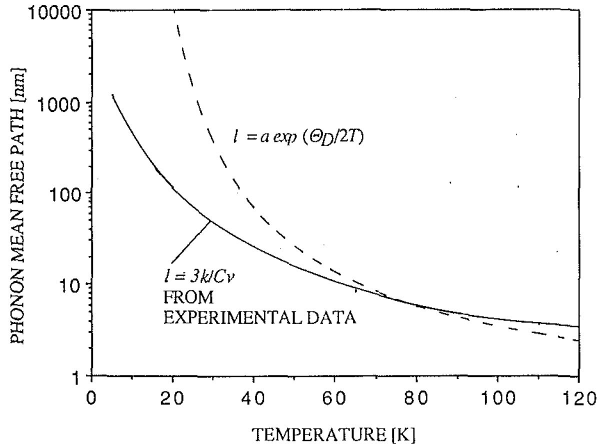

Fig. 1 Phonon mean free path in polycrystalline ceramic $YBa_2Cu_3O_7$

that of a ceramic sample. Presently, detailed information on the microstructure of both configurations is not available, and the ceramic data are used here for thin-film calculations, with a maximum relative error of 20 percent. At 80 K, the specific heat is 144 J kg^{-1} K^{-1}, and the thermal conductivity is 5.5 W m^{-1} K^{-1}.

The solid line in Fig. 1 shows the relation between the phonon mean free path and the temperature as calculated from equation (1). The dashed line in Fig. 1 represents the relation

$$l = a\exp(\Theta_D/2T) \tag{2}$$

where Θ_D is the Debye temperature, which is about 400 K for $YBa_2Cu_3O_7$ (Lang et al., 1988). The constant a was chosen to be $a = 0.48$, such that at 80 K equations (1) and (2) yield the same value for the mean free path. The dependence given by equation (2) would be expected to hold if the resistance to the flow of heat were due solely to phonon-phonon interactions in a perfect crystal, so-called *umklapp* processes (Ziman, 1960). It is seen in Fig. 1, however, that at low temperatures the mean free path calculated from equation (1) is much shorter than that predicted from equation (2). Other processes, such as the scattering of phonons at grain boundaries, impurities, or with tunneling systems (Izbizky et al., 1988) are likely to be responsible for this reduction of the mean free path. It should be noted that the present determination of the mean free path only applies to polycrystalline films, since the conductivity data were found with a ceramic sample. For the determination of the mean free path relevant to size effects in epitaxial or pseudocrystalline films, conductivity data for single crystals must be employed. The $YBa_2Cu_3O_7$ single-crystal data of Graebner et al. (1988), which only cover temperatures below 10 K, indicate that the *ab* plane single-crystal thermal conductivity is about 5 times higher than for the sintered bulk samples. This indicates a larger phonon mean free path in $YBa_2Cu_3O_7$ single crystals than in bulk samples. A similar result was obtained by Morelli et al. (1989), who found that the thermal conductivity of single-crystal $La_2CuO_{4-\Delta}$ is about twice that of a sintered sample. Both of these investigators only observed phonon heat conduction in single crystals, in contrast to the results of Hagen et al. (1989).

The smallest dimension of the sample used by Jezowski et al. (1987) for the conductivity measurements is 1.5 mm, which is much larger than the mean free path at 5 K. Hence it is ensured that the solid curve in Fig. 1 is a true representation of the bulk mean free path in the ceramic sample. If the mean free path exceeded the grain size, then its value determined from equation (1) would become a constant of the order of the grain size due to scattering at the grain boundaries (Klemens, 1958). Since this is not observed in Fig. 1, it can be estimated that the grain size in the sample of Jezowski et al. (1987) was larger than about 2 μm. The mean free path l is of the order of the film thickness d at 5 K for $d = 1$ μm, at 20 K for $d = 0.1$ μm, and around 60 K for films with $d = 10$ nm. If the bulk mean free path is of the order of the film thickness, then, in addition to internal scattering, the phonon free paths in the film are terminated by boundary scattering at the surfaces (Ziman, 1960). This introduces an additional resistance to the flow of heat, and the thermal conductivity decreases with a decreasing ratio of the film thickness to the bulk mean free path. Hence, at temperatures of the order given above or less, the thermal conductivity of a high-T_c superconducting thin film depends on its thickness. In the next section, a simple geometric model is developed to analyze this effect. It should be noted that the phonon mean free path in a bulk sample could be different from that in a layer deposited on a substrate. But in the absence of other information, the use of the bulk mean free path is the best way to investigate the size effect.

Throughout this paper, "thermal conductivity" does not denote a material property describing the diffusion of heat, as it is usually understood. The "thermal conductivity" along the film has to be taken as a parameter that, when multiplied by a temperature gradient along the film, yields a heat flux in the direction of this gradient. Similarly, the "conductivity" across the film determined in the following is a parameter that has to be multiplied by the temperature difference across the film divided by the film thickness to give the heat flux across the film. These "conductivities" are not unique material properties, but depend on the geometry of the specimen under consideration.

Analysis of the Size Effect

Most of the existing theoretical models for the size effect on conduction along thin films belong to one of two classes. The first class is based on the Fuchs-Sondheimer (FS) model (Fuchs, 1938; Sondheimer, 1952), which accounts for the additional resistance due to the scattering of carriers at the film surface. The second class is founded on the Mayadas-Shatzkes (MS) model (Tellier and Tosser, 1982), which also considers the scattering of carriers at grain boundaries by representing them through potential functions. The model developed in the following does not consider the grain boundaries and belongs to the class based on the FS model. Its limit of application is discussed later. The present model relies solely on geometric considerations and is built upon an argument due to Lovell (1936), whose model was valid in the case of very thin films. In addition to the FS model, the present model also considers the size effect on conduction *across* the film.

Exchange Length. If kinetic theory is employed to predict transport properties, it is found that parameters like thermal conductivity, gas viscosity, or coefficient of self-diffusion are proportional to an *exchange length*, the average distance normal to a plane that the carriers crossing this plane travel after their last collisions (Tien and Lienhard, 1979). In the case of an isotropic bulk material, the exchange length is independent of direction. In the present work, the concept of exchange length is employed to analyze the size effect on transport along and across a thin film. This is in contrast to previous geometric theories of the size effect (Lovell, 1936), which only account for the shortening of the absolute magnitude of the carrier free paths, and do not consider the free path components in the direction of transport.

In the following, the distribution of the carrier free paths λ around the mean free path l according to the distribution function (Tien and Lienhard, 1979)

$$f(\lambda)d\lambda = \frac{d\lambda}{l}\exp(-\lambda/l) \tag{3}$$

is not considered in order to achieve a simple solution. Chambers (1950) has shown that if the distribution function of carrier free paths is considered, then the application of kinetic theory to the thin-film size-effect problem is equivalent to the solution of the Boltzmann equation, which can only be given in the form of tabulated functions. In the present case, the exchange length is defined as the average distance a carrier travels normal to a plane without a collision after having experienced a collision within this plane. The carriers either travel a distance l between collisions, or are scattered at a boundary, if they reach this boundary from the point of their last collision in a distance smaller than l. Perfect accommodation is assumed, i.e., that after a scattering event the carrier possesses the energy corresponding to the temperature that prevailed at the position where the scattering occurred. The carrier paths are assumed to originate isotropically, i.e., to leave their point of origination in a direction given by the differential solid angle $d\Omega$ with a uniform probability $d\Omega/4\pi$. If a carrier is scattered at a boundary, it is assumed to be scattered *diffusely*, with probability $d\Omega/2\pi$ to go into any direction $d\Omega$. This means that the carrier scattered at a boundary does not contribute any further to the transport, and under this assumption boundary scattering is equivalent to internal scattering.

For phonon carriers in $YBa_2Cu_3O_7$, the validity of this assumption can be checked by comparing the dominant phonon wavelength to the length scale of the surface roughness of thin films. The dominant phonon wavelength is given by $h_P v/2.7k_B T$, where h_P is Planck's constant and k_B is the Boltzmann constant. Using the measured value of the sound velocity, the dominant phonon wavelength is found to be smaller than 7 nm for temperatures above 10 K. Since micrographs of cross sections of typical $YBa_2Cu_3O_7$ thin films show roughness features of the order of μm (Yee et al., 1988), the dominant phonon wavelength appears to be much smaller than the characteristic roughness features. This lends support to the assumption of diffuse scattering at the boundary. Resently, however, Wu et al. (1988) deposited $YBa_2Cu_3O_7$ films on sapphire at a reduced substrate temperature without annealing; these films possess superior surface morphology. The surfaces of these films appear smooth on a scale of micrometers. The quality and surface structure of high-T_c thin-film superconductors not only depend on the processing conditions, but also on the substrate material, in particular on its lattice structure and its coefficient of thermal expansion. Quantitative studies of the surface structure of films on different substrates resulting from different processes are called for to check the assumption of diffuse boundary scattering rigorously.

If the distribution of free paths around the mean free path is considered according to equation (3), the bulk exchange length is $l_\infty = (2/3)l$ (Rohsenow and Choi, 1961). With the assumptions employed in the present study, the isotropic bulk exchange length becomes

$$l_\infty = \frac{1}{2\pi}\int_{-\pi/2}^{\pi/2} d\psi \int_0^{\pi} d\chi \cos\psi \sin^2\chi = \frac{1}{2} l \tag{4}$$

where χ is the angle of $d\Omega$ with the positive y axis, and ψ the angle of its projection onto the xz plane with the positive x axis. In the case of transport in the x direction, say, l_∞ is the average x component of all carrier free paths contained in the hemisphere whose base is normal to the positive x axis. The reduction of the thermal conductivity in a given direction due to the size effect is found by comparing the resulting exchange length in the film to the bulk exchange length

$$k_{x,y} = k_\infty \frac{l_{x,y}}{l/2} \tag{5}$$

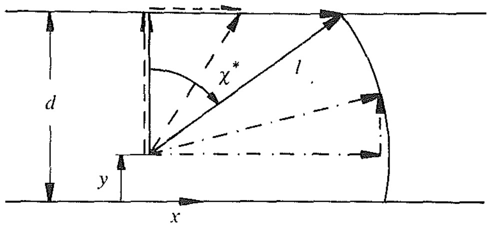

Fig. 2 . Free path components of carriers in a thin layer

Free Path Components in the Film. Figure 2 shows the geometry under consideration in the xy plane. This study concerns a film bounded by the planes $y=0$ and $y=d$, and extending to infinity in the x and z directions. This is a good representation of an actual thin-film superconductor, whose width is typically of the order of tens of microns, which is much larger than the phonon mean free path of $YBa_2Cu_3O_7$ in the temperature range of interest. The free path of a carrier starting at y is terminated by boundary scattering if it starts into a direction χ with $0 \le \chi \le \chi^*$ or $\chi^{**} \le \chi \le \pi$, where

$$\cos\chi^* = \frac{d-y}{l}, \qquad \cos\chi^{**} = -\frac{y}{l} \tag{6}$$

and by internal scattering for directions $\chi^* < \chi < \chi^{**}$. If the carriers are assumed to originate with uniform probability dy/d in the film along the y direction, then the resulting exchange length in the x direction is found by integrating first all individual carrier paths starting at a position y over the solid angle given by $0 \le \chi \le \pi$, $-\pi/2 \le \psi \le \pi/2$, and then integrating over all y positions. Similarly, in the y direction, the exchange length is found by integrating first over $0 \le \chi \le \pi/2$, $0 \le \psi \le 2\pi$, and then over all y positions. Symmetry considerations show that it is sufficient to integrate over the solid angle $0 \le \chi \le \pi/2$, $0 \le \psi \le \pi/2$, from $y=0$ to $y=d$, to obtain

$$l_{x,y} = \frac{2}{\pi d}\int_0^d dy \int_0^{\pi/2} d\psi \int_0^{\pi/2} d\chi \, (\sin\chi)\tilde{l}_{x,y}(\psi, \chi, y) \tag{7}$$

where $\tilde{l}_x$ and $\tilde{l}_y$ are the x and y components of an individual carrier free path originating at y into the (χ, ψ) direction.

For determination of the free path components, one must distinguish between the two cases where the film thickness is larger or smaller than the bulk mean free path.

I. $d > l$

For $d \ge y > d-l$:

$$\tilde{l}_x(\chi, \psi, y) = \begin{cases} \text{for } 0<\chi<\chi^*: & (d-y)\tan\chi\cos\psi \\ \text{for } \chi^*<\chi<\pi/2: & l\sin\chi\cos\psi \end{cases} \tag{8}$$

$$\tilde{l}_y(\chi, \psi, y) = \begin{cases} \text{for } 0<\chi<\chi^*: & (d-y) \\ \text{for } \chi^*<\chi<\pi/2: & l\cos\chi \end{cases} \tag{9}$$

For $d-l \ge y \ge 0$:

$$\tilde{l}_x(\chi, \psi, y) = l\sin\chi\cos\psi \tag{10}$$

$$\tilde{l}_y(\chi, \psi, y) = l\cos\chi \tag{11}$$

II. $d \le l$

If the film thickness is smaller than the bulk mean free path, then the free path components are given by equations (8) and (9).

Substituting equations (8) to (11) into equation (7), the resulting exchange lengths are

I. $d > l$

$$\frac{l_x}{l}=\frac{1}{2}-\frac{1}{3\pi}\frac{1}{\delta} \tag{12}$$

$$\delta=\frac{d}{l} \tag{13}$$

$$\frac{l_y}{l}=\frac{1}{6}\left(3-\frac{1}{\delta}\right) \tag{14}$$

II. $d \leq l$

$$\frac{l_x}{l}=-\frac{1}{3\pi}\frac{1}{\delta}(1-S^3)+\frac{1}{\pi}\delta\ln\frac{1+\delta+S}{1+\delta-S}+\frac{1}{2}-\frac{1}{\pi}\arccos\delta \tag{15}$$

$$S=(1-\delta^2)^{1/2} \tag{16}$$

$$\frac{l_y}{l}=\frac{1}{6}\delta(3-\delta) \tag{17}$$

For $\delta \to \infty$, both l_x and l_y approach $l/2$, which is the bulk value.

Limit of Very Thin Films. The foregoing formulae are based on the assumption that the carrier paths originate uniformly within the film along the y direction. A simple consideration, however, shows that this is not a good assumption for very small film thicknesses, $d/l << 1$. Of all the carrier paths originating at a position y with a positive y component, a fraction

$$\int_0^{\chi^*} d\chi \sin\chi$$

hits the boundary, and only the rest is scattered internally. Approximating

$$\chi^* \approx \arccos\frac{d}{l} \tag{18}$$

this fraction becomes $(1-\delta)$, which is close to unity for $\delta << 1$. Hence, for very thin films, almost all carrier paths originate on the boundaries, in contrast to the assumption of uniform origination. In the following, the resulting exhange lengths are determined for pure boundary origination of the carrier paths, in the case $d < l$. The free path components, now independent of y, become

$$\tilde{l}_x(\chi,\psi)\begin{cases}\text{for } 0<\chi<\chi^*: & d\tan\chi\cos\psi\\ \text{for } \chi^*<\chi<\pi/2: & l\sin\chi\cos\psi\end{cases} \tag{19}$$

$$\tilde{l}_y(\chi,\psi)\begin{cases}\text{for } 0<\chi<\chi^*: & d\\ \text{for } \chi^*<\chi<\pi/2: & l\cos\chi\end{cases} \tag{20}$$

where χ^* is now given by equation (18). The resulting exchange lengths are found in a similar manner as before, but without the integration across the film, and the results are

$$\frac{l_x}{l}=\frac{2}{\pi}\delta\left(-\frac{1}{2}S+\ln\frac{1+\delta+S}{1+\delta-S}\right)+\frac{1}{2}-\frac{1}{\pi}\arccos\delta \tag{21}$$

$$\frac{l_y}{l}=\delta\left(1-\frac{1}{2}\delta\right) \tag{22}$$

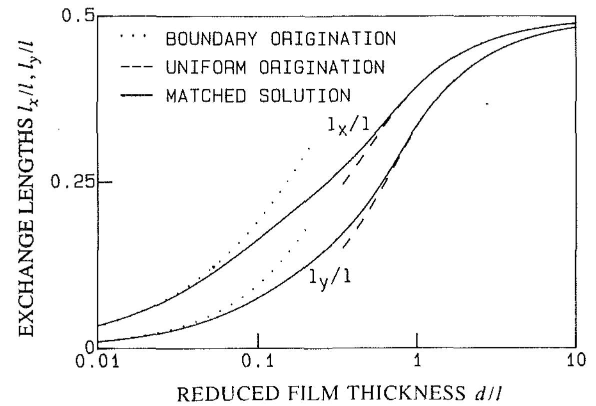

Fig. 3 Matching of the solutions for uniform and pure boundary path origination

Equation (22) simply says that for very thin films, the exchange length across the film is just given by the film thickness, which is intuitive, since practically all carriers travel from one boundary to the other. Lovell (1936) made a similar argument for conduction in the x direction in the case of $\delta \ll 1$. That analysis only considered the absolute magnitude of the free paths, instead of the components, as does the present work. The solution for uniform origination, equations (15)-(17), is now matched with the solution for pure boundary origination, equations (21) and (22), in the following manner. The limiting behavior of the uniform origination solution is

$$\frac{l_x}{l}\sim\frac{1}{2\pi}\delta+\frac{1}{\pi}\delta\ln(2/\delta),\quad \frac{l_y}{l}\sim\frac{1}{2}\delta \text{ for } \delta\to 0 \tag{23}$$

and pure boundary origination yields the limit

$$\frac{l_x}{l}\sim\frac{2}{\pi}\delta\ln(2/\delta),\quad \frac{l_y}{l}\sim\delta \text{ for } \delta\to 0 \tag{24}$$

In equation (23), the logarithmic term is of a higher order than the linear term for $\delta \to 0$. The limiting behavior is governed by the logarithmic term in the case of l_x and by the linear term in the case of l_y. The correct limiting behavior for $\delta \to 0$ can be achieved by multiplying the difference in the governing terms by an exponential negative in δ, and the final formulae for $d < l$ are

$$\frac{l_x}{l}=-\frac{1}{3\pi}\frac{1}{\delta}(1-S^3)+\frac{1}{2}-\frac{1}{\pi}\arccos\delta+\frac{1}{\pi}\delta[1+\exp(-m\delta)]\ln\frac{1+\delta+S}{1+\delta-S} \text{ for } \delta<1 \tag{25}$$

$$\frac{l_y}{l}=\frac{1}{2}\delta[1+\exp(-m\delta)]-\frac{1}{6}\delta^2 \text{ for } \delta<1 \tag{26}$$

where m is the matching parameter. If it is chosen as $m=6$, then the two solutions merge close to $\delta=1$, which is desirable, recalling that the fraction of carriers originating at the boundary is given by $(1-\delta)$. The merit of the present approximate solution is twofold. It is valid over the entire range of δ, and it is in a simple form that is easily evaluated. Figure 3 shows the matched solution, equations (12)-(14), (25), and (26), and the limiting cases of pure boundary and uniform origination.

For comparison, the limiting behavior of the Boltzmann equation solution derived by Fuchs (1938) for electrons, in the case of diffuse boundary scattering, is given by

$$\frac{k_\infty}{k_x}\sim 1+\frac{3}{8\delta}, \text{ for } \delta>>1 \tag{27}$$

$$\frac{k_\infty}{k_x}\sim\frac{4}{3\delta\ln(1/\delta)}, \text{ for } \delta<<1 \tag{28}$$

Determining the limit of equation (12) for $\delta \to \infty$ and using equations (5) and (24) the limiting behavior of the present theory is found as

$$\frac{k_\infty}{k_x} \sim 1 + \frac{2}{3\pi\delta}, \text{ for } \delta >> 1 \qquad (29)$$

$$\frac{k_\infty}{k_x} \sim \frac{\pi}{4\delta \ln(2/\delta)}, \text{ for } \delta << 1 \qquad (30)$$

The agreement can be considered to be very good, keeping in mind the simplicity of the present approach. Apparently, it is much more important to consider the components of the carrier free paths than to account for the free path distribution around the mean. Although the functional dependence in equation (30) is identical to the solution of Fuchs (1938) except for a constant factor, it is interesting to note that for $\delta \rightarrow 0$, equation (23), the relation for uniform origination, yields the better numerical agreement. In fact, equations (15)–(17) serve as an excellent approximation to the theory of Fuchs (1938) over the entire range of δ.

The foregoing analysis employs the idealization that both surfaces of the film are impermeable for the carriers. In reality, thin films are deposited on substrates, and the film–substrate interface can be permeable for the carriers. The extent of the carrier transmission through the interface depends on the nature of the carriers and on the combination of film and substrate materials. For a metallic film on a dielectric substrate, the transmission of electrons can be assumed to be small, and the data for these films agree well with the FS theory. Phonons can be transmitted through an interface between two dissimilar solids, and the rate of transmission depends on the temperatures and elastic properties of film and substrate (Little, 1959). If the temperature difference between film and substrate is small, then the heat transfer coefficient of phonon transmission is proportional to the third power of the substrate temperature. At very low temperatures, where the size effect is strong, the transmission is weak, and at higher temperatures, corresponding to a weak size effect, the transmission is larger. Significant carrier transmission through the film–substrate interface considerably reduces the size effect due to boundary scattering.

Size Effect in an Anisotropic Film

High-T_c superconductors possess orthorhombic or tetragonal crystal structures. When they are orthorhombic, such as in $YBa_2Cu_3O_7$, the *a* and *b* lattice parameters are very close, and it is a very good approximation to consider them tetragonal. This crystal symmetry strongly indicates that the thermal conductivity of single-crystal high-T_c superconductors is anistropic. This was confirmed recently by the measurements of Morelli et al. (1989) on single crystals of $La_2CuO_{4-\Delta}$, which exhibited a thermal conductivity 50 percent higher normal to the copper-oxide planes that parallel to them. The measurements of Hagen et al. (1989) show that the thermal conductivity of $YBa_2Cu_3O_7$ single crystals is about five times higher in the *ab* plane than along the *c* direction, while Fanton et al. (1989) found an anisotropy factor of seven for the $Bi_2Sr_2CaCu_2O_x$ compound.

Due to the strong anisotropy of the electrical properties of the high-T_c superconductors, the best films are achieved by strongly orienting the crystals, with epitaxial films being most desirable. In a thick, highly oriented film, the anisotropy of the film thermal conductivity will be very close to that of the single crystal. In very thin films, however, this anisotropy could be influenced by the size effect. This section presents an approximate treatment of the combined influence of crystal anisotropy and the size effect, which relies on the results derived in the previous section. Kinetic theory yields the expression for the heat flux **q** (Ziman, 1960; Klemens, 1958)

$$\mathbf{q} = C t_R \mathbf{v}\mathbf{v} \cdot \nabla T \qquad (31)$$

where t_R is the relaxation time. In the isotropic bulk case, the average of the tensor **vv** over all directions is $(1/3)v^2$, and using $vt_R = l$, one recovers equation (1). Now consider the case of an anisotropic material. Tetragonal crystals possess a thermal conductivity tensor of the form (Nye, 1985)

$$\mathbf{K} = \begin{bmatrix} k_a & 0 & 0 \\ 0 & k_a & 0 \\ 0 & 0 & k_c \end{bmatrix} \qquad (32)$$

where k_a and k_c are the thermal conductivities along the *a* and *c* axes of the crystal, respectively. The *c* axis possesses a 90 deg rotational symmetry.

Consider a highly oriented film made of such crystals, with the *c* axis normal to the plane of the film, parallel to the *y* axis. This is the preferred orientation in films of high-T_c superconductors, because the *ab* plane possesses superior electrical transport properties. In a thick film, the thermal conductivities along and across the film are then $k_1 = k_a$, and $k_2 = k_c$, where the subscripts 1 and 2 refer to the *x* and *y* directions, respectively. The thick-film material anisotropy $A = k_1/k_2$ is identical to the crystal anisotropy k_a/k_c. In equation (31), *C* are t_R are scalar quantities, and **vv** is a second-order tensor. If one assumes that the relaxation time is independent of direction, then the anisotropy is solely due to different carrier velocities in different directions. Within the kinetic-theory model, the anisotropy of the carrier velocity can be approximated as

$$\frac{v_1}{v_2} = A^{1/2} \qquad (33)$$

A similar approximate approach was employed by Slack (1962), who estimated the anisotropy of the thermal conductivity of pyrolytic graphite from the ratio of the sound velocities and the mean free paths in the different directions. He took the mean free paths to be limited by the crystallite size and achieved very reasonable agreement with experimental data. It follows that

$$\frac{l_1}{l_2} = A^{1/2} \qquad (34)$$

where v_1, v_2 are the carrier velocities along and across a thick film, and l_1, l_2 are the corresponding mean free paths. Using these relations, the conductivities along and across a *thin* film are given by

$$k_x = 2k_1 F(\delta_1) \qquad (35)$$

$$k_y = \frac{2}{A} k_1 G(\delta_2) \qquad (36)$$

$$\delta_1 = d/l_1, \quad \delta_2 = dA^{1/2}/l_1 \qquad (37)$$

where

$$F(\delta) = \frac{l_x}{l}, \quad G(\delta) = \frac{l_y}{l} \qquad (38)$$

which are the solutions for the size effect derived in the previous section. The anisotropy of a thin film is now given by

$$\frac{k_y}{k_x} = \frac{1}{A} \frac{G(\delta_2)}{F(\delta_1)} \qquad (39)$$

The material anisotropy *A* influences the thin-film anisotropy in two ways. First, it enters equation (39) as a constant of proportionality multiplying the ratio of the size-effect functions *F* and *G*. For thick films, *F* and *G* approach unity, and the material anisotropy is recovered. Second, the reduced film thicknesses, δ_1 and δ_2, i.e., the arguments of the size-effect functions, differ from each other by the square root of *A*. This reflects the fact that in the direction of higher conductivity, with larger intrinsic mean free path, the size effect is felt more strongly for the same film thickness *d*. For very small film thickness, the stronger reduction of conduction normal to the

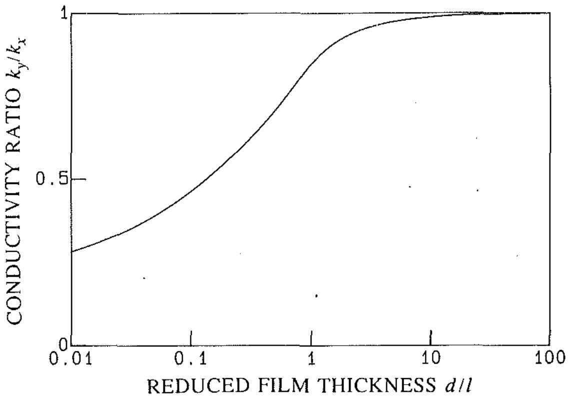

Fig. 4 Size-induced anisotropy in a thin film of an isotropic material

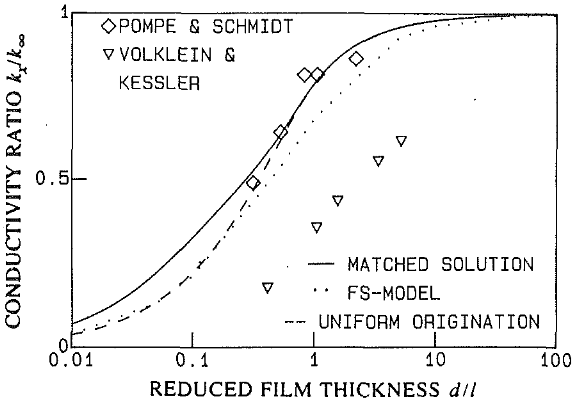

Fig. 5 Comparison of predicted thermal conductivity along a thin film with experimental data

film, as illustrated by Fig. 4, forces k_y/k_x to approach zero for any material anisotropy, as can be seen from the limiting form of equation (39)

$$\frac{k_y}{k_x} \sim \frac{\pi}{2A^{1/2}} \frac{1}{\ln(2l_1/d)}, \text{ for } d/l_1 \to 0 \tag{40}$$

which is derived using equation (24).

If the c axis in a single-crystal film is not parallel to the y axis, but inclined at an angle to it, then there also results an anisotropy in the xz plane. The influence of the size effect on this anisotropy depends on the angle of inclination of the c axis, and approximate (Sondheimer, 1956) and exact (Englman and Sondheimer, 1956) analyses of this phenomenon have been performed.

A special case of practical importance is obtained if the c axis lies within the xz plane, an orientation observed after the deposition of $YBa_2Cu_3O_7$ on certain substrates (Chan et al., 1988). If the c axis is parallel to the x axis, in a thick film the conductivities are $k_1 = k_c$, $k_2 = k_3 = k_a$, where k_3 is measured along the z axis. In this case, $A = k_c/k_a$, and equations (35) and (36) again hold. In addition, the size effect influences conduction along the z direction according to

$$k_z = \frac{2}{A} k_1 F(\delta_2) \tag{41}$$

It should be noted that the application of the present theory to anisotropic epitaxial films of high-T_c superconducting films is not as straightforward as for isotropic polycrystalline films. The recent measurements of Hagen et al. (1989) on a single crystal indicate that the electronic contribution to the thermal conductivity, as estimated from the Wiedemann–Franz law, is significant in the ab plane, while it is negligible along the c direction. It follows that for the determination of the size effect in the ab plane, both electron and phonon carriers must be considered. The present theory can be applied if the total conductivity in the ab plane is assumed to be the sum of the electronic and phonon contribution. The size effects on these two contributions can be determined independently. Electron-phonon scattering, however, appears to be a major factor in limiting the bulk mean free path of both carrier types determining ab plane heat conduction.

Results and Discussion

Figure 4 shows the ratio of the thermal conductivities across and along the film, k_y/k_x, as a function of the reduced film thickness d/l. For films much thicker that bulk mean free path, the two conductivities are equal, corresponding to an isotropic bulk sample. However, it is clearly seen that for film thicknesses of the order of or smaller than the mean free path, the conductivity across the film becomes smaller than that along the film. For a film thickness of $l/10$, k_y is about half of k_x, and for $d = l/100$, it is only one fourth. This size-induced anisotropy is due to the different reduction of carrier free paths along and across the film. It indicates that an otherwise isotropic material becomes an anisotropic conductor, merely due to the fact that it is formed into a thin film. Flik and Tien (1990a) found anisotropy to have a strong influence on the intrinsic thermal stability of thin-film superconductors.

Figure 5 shows a comparison of the results of the present model with the FS model and with experimental data. It presents the ratio of the thermal conductivity along the film to the bulk conductivity as a function of the reduced film thickness. The solid line represents the matched solution, equations (12) and (25), and the dashed line the solution for uniform path origination, equations (12) and (15). It is seen that the present approximate solution agrees well with the FS model. As noted earlier, the uniform origination solution agrees slightly better with the FS model, and it is recommended as a good approximation for the size effect on conduction along thin films.

Pompe and Schmidt (1975) reported data on the thermal conductivity of thin lead films at 7.2 K, the critical temperature of lead. Lead, like any metal, conducts heat through electrons. The good agreement between theory and experiment indicates that the boundary scattering of the electrons was diffuse, and that grain boundaries in the film did not influence conduction appreciably. Pompe and Schmidt (1975) also reported data for very low temperatures, and for $T \sim 16$ K, which cannot be compared to the present theory. For temperatures very close to absolute zero, the electron wavelength becomes very large, and some specular reflection occurs at the boundaries. At temperatures around 16 K, lead films exhibit anomalous electrical and thermal resistances, which overshadow the size effect.

A very different picture is obtained from the data of Völklein and Kessler (1986), which concern phonon heat conduction in thin bismuth films. These data differ strongly from the FS model and the present theory. The reason lies in the microstructure of these films. They exhibited a film-thickness-dependent grain size between 80 and 170 nm, which is of the order of the film thickness, which varied between 30 and 350 nm. In this case, the scattering of carriers at the grain boundaries leads to an additional, substantial reduction of the thermal conductivity, as evidenced by the data in Fig. 5. In addition to the reduced film thickness, another dimensionless parameter becomes important, the ratio of the grain diameter to the mean free path. This parameter is accounted for in the MS model, and Völklein and Kessler (1986) were able to fit a modified MS model to their data, albeit with an adjustable parameter.

Polycrystalline high-T_c films exhibit grain sizes much larger

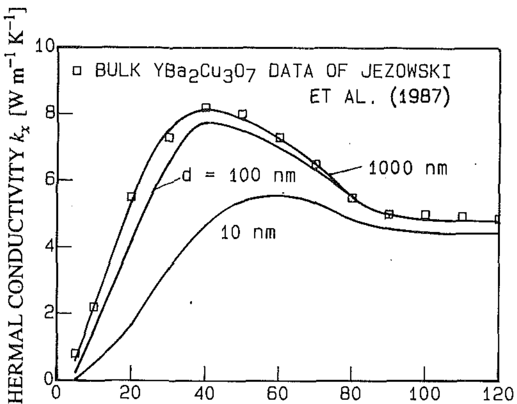

Fig. 6 Predicted thermal conductivity along polycrystalline films of $YBa_2Cu_3O_7$

than those of these bismuth films, with grain diameters about five times the film thickness (Gross et al., 1989), and in epitaxial or pseudocrystalline films, the grain boundaries can be expected to have a very small effect. Hence, the data for polycrystalline high-T_c films are likely to lie between the two sets of data in Fig. 5, but closer to the data of Pompe and Schmidt (1975). The present model can serve as a starting point for the development of a simple model incorporating the grain-boundary scattering and approximating the MS model.

Equations (12) and (25), combined with equation (5), provide a framework to predict the temperature dependence of the thermal conductivity k_x along thin films of $YBa_2Cu_3O_7$, if the temperature dependence of the mean free path is calculated using equation (1). The resulting relation

$$k_x(T) = 2k_\infty(T)F(\delta) \tag{42}$$

$$\delta = d/l(T) \tag{43}$$

is shown in Fig. 6 for various values of the film thickness. These results are obtained using the mean free path data of Fig. 1, and the data of Jezowski et al. (1987) for k_∞. Since these data were measured on ceramic, polycrystalline samples, the results of Fig. 6 only apply to unoriented polycrystalline films of $YBa_2Cu_3O_7$. It is apparent that a film with $d = 1$ μm does not exhibit any size effect, since it has the same thermal conductivity as the bulk material down to 5 K. A film of 100 nm shows a moderate size effect below 80 K, while a 10 nm film experiences a significant reduction of the thermal conductivity, down to half of the bulk value at 30 K. The effect of the superconducting-normal transition is taken into account in these curves, since they are based on data that reflect this influence. The peak in the thermal conductivity at about 40 K in the data of Jezowski et al. (1987) was explained by the following mechanism. Above $T_c = 85$ K, the scattering of phonons by electrons is the governing process limiting the flow of heat. Below T_c, the electrons condense into pairs and do not participate in the phonon scattering any more, which results in an increase of the phonon thermal conductivity. At very low temperatures, the rapidly decreasing phonon population and intragrain scattering processes reduce the thermal conductivity. The combination of these two effects results in a peak at around one half of T_c (Uher, 1989). For decreasing film thickness, the size effect becomes important at higher temperatures, shifting the peak in the thermal conductivity toward higher temperatures. For epitaxial high-T_c films, the mean free path will be much longer, resulting in an increased size effect. Similarly, the effects of grain boundaries in polycrystalline films are likely to lead to a stronger size effect than shown in Fig. 6 if the grain size is of the order of or smaller than the film thickness. Moreover, the use of an average sound velocity in equation (1) will shift the onset of the size effect to higher temperatures.

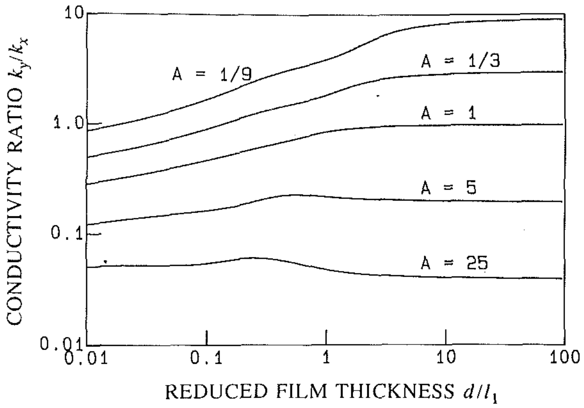

Fig. 7 Combined influence of size effect and material anisotropy

Figure 7 illustrates the result of equation (39) by plotting the ratio of the conductivities across and along the film as a function of the film thickness divided by the bulk mean free path along the x direction l_1, for several values of the material anisotropy A. It shows the combined influence of the material anisotropy and the size effect on the anisotropy of a thin film. The case $A = 1$ corresponds to an isotropic material and is identical to Fig. 4. Due to the size effect, k_y/k_x approaches zero for all values of A if $d/l_1 \rightarrow 0$. If A is smaller than unity, then the size effect is felt more strongly, and for small film thicknesses this limiting behavior occurs rapidlly, thus reversing the material anisotropy when k_y/k_x becomes smaller than unity. Due to the size effect, a film of an anisotropic material can be isotropic, or the material anisotropy can even be reversed. For $A > 1$, conduction in the x direction is more strongly depressed by the size effect than in the y direction due to the larger intrinsic mean free path, $l_1 > l_2$. Hence, for decreasing d/l_1, the ratio k_y/k_x starts to increase, before the reduction of y conduction takes over and forces this ratio to approach zero. These two competing effects yield a maximum of k_y/k_x, which for the given values is observed for d/l_1 between 0.1 and 1.

There is an analogy between heat conduction *across* a thin film, and heat conduction across a thin gas layer. Kennard (1938) provided expressions for the heat flux across gas layers much thicker and much thinner than the molecular mean free path. Assuming an accommodation coefficient of 1, a Prandtl number of 1, and neglecting the difference between the specific heats at constant pressure and volume, for $d \gg l$, Kennard's (1938) analysis yields $k_y/k_\infty = (1 + 2/\delta)^{-1}$. For $\delta = 10$, this relation gives $k_y/k_\infty = 0.83$, while equation (14) predicts a significantly smaller size effect, $k_y/k_\infty = 0.97$. With the same assumptions and using equation (1), Kennard's (1938) result for $d \ll l$ becomes $k_y/k_\infty = (3/4)\delta$, which for the entire region $\delta < 1$ agrees within 25 percent with equation (17), the present result for uniform path origination. In contrast, equation (22), the result for pure boundary path origination, yields a value for k_y/k_∞ that is (8/3) times Kennard's (1938) value for $\delta \ll 1$. The solution for conduction across the film for uniform path origination agrees better with the kinetic theory of gases than the solution for pure boundary path origination.

Concluding Remarks

The present study indicates that below 80 K, the thermal conductivity of polycrystalline $YBa_2Cu_3O_7$ thin-film superconductors is reduced by the size effect if the film thickness is smaller than about 100 nm. This result has a strong impact on the thermal stability of these films, and on the design of thin-film devices, such as bolometers. Measurements of the thermal conductivity of such films are called for to verify the predictions of this study.

The size effect depends on the boundary scattering of the phonons, the carriers of thermal energy in $YBa_2Cu_3O_7$. Whether this scattering is diffuse or specular depends on the surface roughness of the film. Only quantitative experimental studies of the surface structure of high-T_c thin-film superconductors can answer this question. Thin-film superconductors in actual devices are deposited on crystalline substrates. At the film-substrate interface, the phonons are either transmitted or reflected. Since the conductance due to the transmission through such an interface is proportional to the third power of the temperature, at 77 K the corresponding resistance will be very small, and the consideration of this transmission will yield a reduced size effect.

The present analysis of the thin-film size effect rests on purely geometric considerations and applies equally to phonons and electrons. It yields simple relations valid over the entire range of the ratio film thickness-mean free path. For conduction along the film, it agrees well with a solution to the Boltzmann equation, and with experimental data on homogeneous films. This analysis does not consider the effect of grain boundaries and does not agree with experimental data on films with grain sizes smaller than the film thickness. This present work can serve as a starting point for the development of a simple model incorporating this effect. Due to its simplicity, the present model can easily analyze the size effect on conduction across the film and account for the influence of anisotropy.

In summary, the geometric model for the size effect due to boundary scattering presented here is valid for both phonons and electrons. It is not valid for films with grain sizes of the order of or smaller than the film thickness. The calculations based on this model for high-T_c films presented in Fig. 6 are restricted to polycrystalline films, since the phonon mean free path was determined from measurements on sintered bulk samples. The calculations are valid for polycrystalline films with grain diameters greater than the film thickness. If the model for anisotropic films is applied to epitaxial high-T_c films, then transport by both phonons and electrons must be considered.

Acknowledgments

The authors benefited from discussions with Professor C. Uher, Professor R. O. Pohl, M. F. Crommie, and K. E. Goodson.

References

Beckmann, O., Lundgren, L., Hordblad, P., Sandlund, L., Svedlindh, P., Lundström, T., and Rundqvist, S., 1987, "Specific Heat and Magnetic Susceptibility of Single Phase $YBa_2Cu_3O_7$," *Physics Letters A*, Vol. 125, pp. 425-428.

Cahill, D. G., Fischer, H. E., Klitsner, T., Swartz, E. T., and Pohl, R. O., 1989, "Thermal Conductivity of Thin Films: Measurements and Understanding," *J. Vac. Sci. Techn.*, Vol. A7, pp. 1259-1266.

Chambers, R. G., 1950, "The Conductivity of Thin Wires in a Magnetic Field," *Proc. Roy. Soc. A*, Vol. 202, pp. 378-395.

Chan, S. W., Greene, L. H., Feldmann, W. L., Miceli, P. F., and Bagley, B. G., 1988, "The Preparation of Superconducting Thin Films of $YBa_2Cu_3O_{7-x}$ by Co-evaporation With Electron-Beam/Thermal Sources," *Thin Film Processing and Characterization of High-Temperature Superconductors*, J. M. E. Harper, R. J. Colton, and L. C. Feldman, eds., American Institute of Physics Conference Proceedings No. 165, pp. 28-35, New York.

Cohn, J. L., Peacor, S. D., and Uher, C., 1988, "Thermal Conductivity of $YBa_2Cu_3O_{7-\delta}$ below 1 K: Evidence for Normal-Carrier Transport Well Below T_c," *Phys. Rev. B*, Vol. 38, pp. 2892-2895.

Englman, R., and Sondheimer, E. H., 1956, "The Electrical Resistivity of Anisotropic Thin Films," *Proc. Phys. Soc. B*, Vol. 69, pp. 449-458.

Fanton, J. T., Mitzi, D. B., Kapitulnik, A., Khuri-Yakub, B. T., Kino, G. S., Gazit, D., and Feigelson, R. S., 1989, "Photothermal Measurements of High-T_c Superconductors," *Appl. Phys. Lett.*, Vol. 55, pp. 598-599.

Ferreira, J. M., Lee, B. W., Dalichaouchi, Y., Torikachvili, M. S., and Maple, M. B., 1988, "Low-Temperature Specific Heat of the High-T_c Superconductors $La_{1.8}Sr_{0.2}CuO_{4-\delta}$ and $RBa_2Cu_3O_{7-\delta}$ (R = Y, Eu, Ho, Tm, and Yb)," *Phys. Rev. B*, Vol. 37, pp. 1580-1586.

Fisher, H. E., Watson, S. K., and Cahill, D. G., 1988, "Specific Heat, Thermal Conductivity and Electrical Resistivity of High Temperature Superconductors," *Comments on Condensed Matter Physics*, Vol. 14, pp. 65-127.

Flik, M. I., and Tien, C. L., 1990a, "Intrinsic Thermal Stability of Anisotropic Thin-Film Superconductors," ASME JOURNAL OF HEAT TRANSFER, Vol. 112, pp. 10-15.

Flik, M. I., and Tien, C. L., 1990b, "Thermal Phenomena in High-T_c Thin-Film Superconductors," *Annual Review of Heat Transfer*, C. L. Tien, ed., Vol. 3, Hemisphere, New York, pp. 115-166.

Fuchs, K., 1938, "The Conductivity of Thin Metallic Films According to the Electron Theory of Metals," *Proc. Cambridge Phil. Soc.*, Vol. 34, pp. 100-108.

Freytag, L., and Huebener, R. P., 1985, "Temperature Structures in a Superconductor as a Non-equilibrium Phase Transition," *J. Low Temperature Physics*, Vol. 60, pp. 377-393.

Graebner, J. E., Schneemeyer, L. F., Cava, R. J., Waszczak, J. K., and Rietmann, E. A., 1988, "Thermal Conductivity of Single-Crystal and Sintered $RBa_2Cu_3O_7$ at Low Temperatures," *Mat. Res. Soc. Proc.*, Vol. 99, pp. 745-748.

Gross, R., Hartmann, M., Hipler, K., Huebener, R. P., Kober, F., and Koelle, D., 1989, "Spatial Resolution Limit for the Investigation of High-T_c Films by Low Temperature Scanning Electron Microscopy," *IEEE Transactions on Magnetics*, Vol. MAG-25, pp. 2250-2253.

Hagen, S. J., Wang, Z. Z., and Ong, N. P., 1989, "The Anisotropy of the Thermal Conductivity of Single-Crystal $YBa_2Cu_3O_7$," *Phys. Rev. B*, Vol. 40, pp. 9389-9392.

Huebener, R. P., Gross, R., and Bosch, J., 1988, "Low-Temperature Scanning Electron Microscopy for Studying Inhomogeneities in Thin-Film High-T_c Superconductors," *Z. Phys. B*, Vol. 70, pp. 425-430.

Izbizky, M. A., Regueiro, M. N., Esquinazi, P., Duran, C., and Fainstein, C., 1988, "Phonon Transport in Superconducting $EuBa_2Cu_3O_{7-x}$," *Phys. Letters A*, Vol. 129, pp. 71-75.

Jezowski, A., Mucha, J., Rogacki, K., Horyn, R., Bukowski, Z., Horobiowski, M., Rafalowicz, J., Stepien-Damm, J., Sulkowski, C., Trojnar, E., Zaleski, A. J., and Klamut, J., 1987, "Thermal Conductivity and Electrical Resistivity of the High-T_c Superconductor $YBa_2Cu_3O_{9-\Delta}$," *Physics Letters A*, Vol. 122, pp. 431-433.

Kennard, E. H., 1938, *Kinetic Theory of Gases*, McGraw-Hill, New York, pp. 311-327.

Kirk, W. P., Kobiela, P. S., Tsumura, R. N., and Pandey, R. K., 1989, "Thermal Conductivity of Hot-Pressed 123 YBCO Superconducting Oxides: Anisotropic Behavior at High and Very Low Temperatures," *Ferroelectrics*, Vol. 92, pp. 151-157.

Klemens, P. G., 1958, "Thermal Conductivity and Lattice Vibrational Modes," *Solid State Physics*, Vol. 7, pp. 1-98, Academic Press, New York.

Lang, M., Lechner, T., Riegel, S., Steglich, F., Weber, G., Kim, T. J., Lüthi, B., Wolf, B., Rietschel, H., and Wilhelm, M., 1988, "Thermal Expansion, Sound Velocities, Specific Heat and Pressure Derivative of T_c in $YBa_2Cu_3O_7$," *Z. Phys. B*, Vol. 69, pp. 459-463.

Little, W. A., 1959, "The Transport of Heat Between Dissimilar Solids at Low Temperatures," *Can. J. Phys.*, Vol. 37, pp. 334-349.

Lovell, A. C. B., 1936, "The Electrical Conductivity of Thin Metallic Films. I—Rubidium on Pyrex Glass Surfaces," *Proc. Roy. Soc. A*, Vol. 157, pp. 311-329.

Morelli, D. T., Heremans, J., Doll, G., Picone, P. J., Jenssen, H. P., and Dresselhaus, M. S., 1989, "Thermal Properties of Single-Crystal $La_2CuO_{4-\Delta}$," *Phys. Rev. B*, Vol. 39, pp. 804-807.

Nisenoff, M., 1988, "Superconducting Electronics: Current Status and Future Prospects," *Cryogenics*, Vol. 28, pp. 47-56.

Nye, J. F., 1985, *Physical Properties of Crystals*, Clarendon Press, Oxford, United Kingdom.

Pompe, G., and Schmidt, K., 1975, "Vapour-Deposited Lead Films and Their Transport Characteristics at Low Temperatures," *Phys. Stat. Sol. (a)*, Vol. 31, pp. 37-46.

Richards, P. L., Clarke, J., Leoni, R., Lerch, Ph., Verghese, S., Beasley, M. R., Geballe, T. H., Hammond, R. H., Rosenthal, P., and Spielmann, S. R., 1989, "Feasibility of the High-T_c Superconducting Bolometer," *Appl. Phys. Lett.*, Vol. 54, pp. 283-285.

Rohsenow, W. M., and Choi, H. Y., 1961, *Heat, Mass and Momentum Transfer*, Prentice-Hall, Englewood Cliffs, NJ.

Slack, G. A., 1962, "Anisotropic Thermal Conductivity of Pyrolytic Graphite," *Phys. Rev.*, Vol. 127, pp. 694-701.

Sondheimer, E. H., 1952, "The Mean Free Path of Electroncs in Metals," *Advances in Physics*, Vol. 1, pp. 1-42.

Sondheimer, E. H., 1956, "Conductibilite Electrique des Lames Minces Anisotropes," *J. Phys. Rad.*, Vol. 17, pp. 201-203.

Tellier, C. R., and Tosser, A. J., 1982, *Size Effects in Thin Films*, Elsevier, New York.

Tien, C. L., Armaly, B. F., and Jagannathan, P. S., 1969, "Thermal Conductivity of Thin Metallic Films and Wires at Cryogenic Temperatures, *Proceedings of the 8th Thermal Conductivity Conference*, Plenum Press, pp. 13-19.

Tien, C. L., and Lienhard, J. H., 1979, *Statistical Thermodynamics*, Hemisphere, New York, pp. 307-321.

Uher, C., 1989, "Mechanisms of Heat Conduction in High-T_c Superconductors," *Proceedings of the Third Annual Conference on Superconductivity and Applications*, New York State Institute of Superconductivity, Buffalo, NY, Sept. 19-21, Plenum Press, New York.

Uher, C., and Kaiser, A. B., 1987, "Thermal Transport Properties of $YBa_2Cu_3O_7$ Superconductors," *Phys. Rev. B*, Vol. 36, pp. 5680-5683.

Van Duzer, T., 1988, "Superconductor-Semiconductor Hybrid Devices, Circuits and Systems," *Cryogenics*, Vol. 28, pp. 527-531.

Völklein, F., and Kessler, E., 1986, "Analysis of the Lattice Thermal Conductivity of Thin Films by Means of a Modified Mayadas-Shatzkes Model: The Case of Bismuth Films," *Thin Solid Films*, Vol. 142, pp. 169-181.

von Molnar, S., Torressen, A., Kaiser, D., Holtzberg, F., and Penney, T., 1988, "Low-Temperature Specific Heat of Single-Crystal $YBa_2Cu_3O_{7-\delta}$," *Phys. Rev. B*, Vol. 37, pp. 3762-3765.

Wu, X. D., Venkatesan, T., Inam, A., Chase, E. W., Chang, C. C., Jeon, Y., Croft, M., Magee, C., Odem, R. W., and Radicati, F., 1988, "Versatility of Pulsed Laser Deposition Technique for Preparation of High-T_c Superconducting Thin Films," *High-T_c Superconductivity: Thin Films and Devices*, R. B. van Dover, and C. C. Chi, eds., Proceedings of the International Society of Optical Engineering, Vol. 948, pp. 50-65.

Yee, D. S., Gambino, R. J., Chisholm, M. F., Cuomo, J. J., Madakson, P., and Karasinski, J., 1988, "Critical Current and Texture Relationships in $YBa_2Cu_3O_7$ Thin Films," *Thin Film Processing and Characterization of High-Temperature Superconductors*, J. M. E. Harper, R. J. Colton, and L. C. Feldman, eds., American Institute of Physics Conference Proceedings No. 165, pp. 132-140, New York.

Ziman, J. M., 1960, *Electrons and Phonons*, Oxford University Press, Oxford, United Kingdom.

Applying Heat Transfer Coefficient Data to Electronics Cooling

R. J. Moffat
Professor.

A. M. Anderson
Research Assistant.

Department of Mechanical Engineering,
Stanford University,
Stanford, CA 94305

Many electronics cooling applications involve direct air cooling of the components and their heat transfer performance is often estimated, in the design phase, using heat transfer coefficient data from either in-house data or published sources. The agreement between predicted and observed system performance is quite often not acceptable, which means that the cooling system must be developed empirically—an expensive and time-consuming process. The authors believe they have identified one important reason for this state of affairs: the heat transfer coefficient values presented in the literature are being used improperly. Almost all of the published heat transfer coefficient data are from single-active-component experiments, which implicitly define h based on the adiabatic temperature of the component (h_{ad})*, while most users assume h to be defined on the basis of the mean fluid temperature* (h_m)*. This misunderstanding leads to underpredictions of the temperature rise of the components by 20–30 percent or more. This paper reviews the options for defining the heat transfer coefficient, shows how the problem arises, and then describes the steps necessary to properly use the existing heat transfer coefficient data base. There are two options for applying the existing data base to a fully powered array: One can either calculate the adiabatic temperatures of the components from the known heat release distribution in the array or calculate the values of* h_m *that can be used with* T_m*, again using the known heat release distribution. The two options represent different ways to apply the same general method, superposition. The superposition method of Sellars, et al.,* (*1956*) *is adapted to discrete systems and used as a guide to the forms recommended.*

Introduction

This paper addresses the problems faced by the electronics cooling field. Cooling of electronic components has both practical and technical interest, since it relates to technical problems now faced by the electronics industry, yet at the same time it involves one of the most general of heat transfer problems: nonuniform heat release from nonuniform geometries.

The typical modular approach used in the construction of electronic systems results in printed circuit boards, carrying rather dense arrays of components, stacked together so that the more nearly smooth surface of one board faces the rough surface of its neighbor. Cooling air is forced through this passage by a fan or blower. Figure 1 is a typical card-on-board packaging configuration. Figure 2 is a typical printed circuit board. Module shapes and sizes vary according to their function. The electronics cooling industry needs the ability to predict module temperatures accurately in the complex situations depicted in Figs. 1 and 2.

A large fraction of all electronics cooling situations involve direct air cooling of the components. In most cases, preliminary heat transfer designs are made based on simple correlations taken from experimental data on related geometries with only modest expectations of precision. The performance of the system is then confirmed or adjusted by full-scale tests. When the design goals are not met on the first trial, the air flow rate and the air flow path are adjusted until the system operates with an acceptable temperature distribution. This hardware development takes time and costs money and sometimes unexpectedly severe thermal problems will bring a program to a complete halt while a new cooling approach is developed. One might well ask, why are there any surprises in this process? The laws of heat transfer are well known, the mathematics are simple, and there seems to be an adequate data base in the literature related to air cooling. Experience has shown, however, that industrial users have relatively little success in making good designs based on the published data.

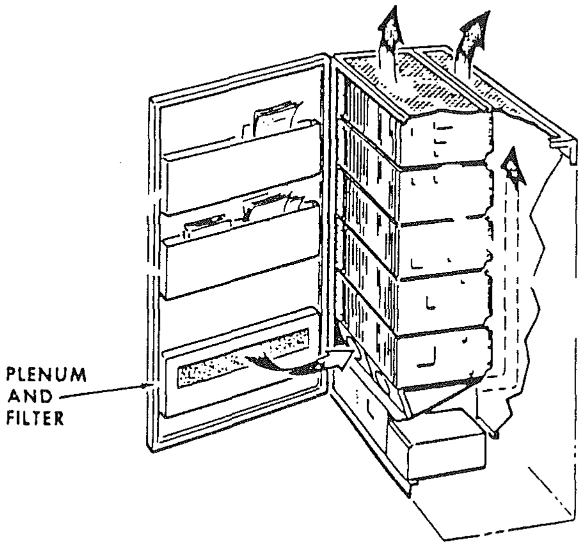

Fig. 1 Typical electronic cabinet illustrating modular arrangement

The present authors believe they have identified one important reason for this state of affairs: The heat transfer coefficient values in the literature are defined (almost always) on the basis of the adiabatic temperature of the component, while users are assuming them to have been defined on the basis of the mean fluid temperature. Such a misunderstanding can lead to underpredictions of component temperatures by 20–30 percent.

This paper reviews the options for defining the heat transfer coefficient, shows how the problem arises, outlines the theory behind the use of the adiabatic temperature as the reference temperature for heat transfer, and discusses some of the consequences of the present state confusion.

Contributed by the Heat Transfer Division and presented at the ASME Winter Annual Meeting, Chicago, Illinois, November 28–December 2, 1988. Manuscript received by the Heat Transfer Division February 21, 1989; revision received February 22, 1990. Keywords: Electronic Equipment, Forced Convection, Thermal Packaging.

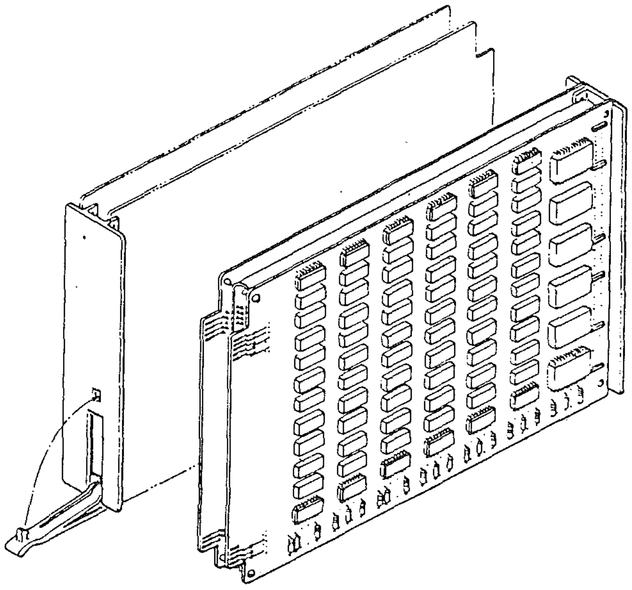

Fig. 2 Typical printed circuit board

Defining the Heat Transfer Coefficient

The heat transfer coefficient is a defined quantity used for convenience to simplify calculation of the surface temperature when the heat flux is known, or vice versa. The definition is

$$h = \frac{\dot{q}''_{\text{conv}}}{(T_e - T_{\text{ref}})} \qquad (1)$$

where h is the heat transfer coefficient in W/m^2 °C, $\dot{q}''_{\text{conv}}$ is the convective heat flux in W/m^2, T_e is the element surface temperature, and T_{ref} is the reference temperature for the fluid.

For a given situation, there are four options that might be used for the reference temperature: the temperature far from the surface T_∞; the mixed mean temperature T_m; the channel inlet temperature T_{in} or the temperature the wall would have attained had it not been heated locally: the adiabatic wall temperature T_{ad}. Each of these options is used by some segment of the professional population involved in electronics cooling. As a consequence, for any given situation with exactly the same heat flux, wall temperature, and fluid temperature distribution, there are four different values that could be assigned to h, depending on which reference temperature was chosen for the fluid. These options are described in the following paragraphs.

Option 1: Using the Temperature Far From the Surface. External boundary layer studies (free or forced convection) and tests of isolated objects in the flow field have traditionally defined the heat transfer coefficient in terms of the gas temperature far from the surface. The far-field temperature is easy to identify and is often constant.

In the electronic cooling area, this option is often used in preliminary heat transfer screening. Power is applied to a single component mounted on a pedestal or board in a large tunnel where the approach velocity is known. The heat transfer coefficient is defined using the temperature difference between the component and the free-stream temperature

$$h_\infty = \frac{\dot{q}''_{\text{conv}}}{(T_e - T_\infty)} \qquad (2)$$

Option 2: Using the Mixed Mean Temperature of the Fluid. The mixed mean temperature has a long history in heat exchangers and process heat transfer. Most (if not all) analytical predictions of h are described in texts and reference works. The mixed mean temperature is convenient because it can be calculated by an energy balance, at any location in the channel, if the flow rate and the heat added up to that location are known.

The mixed mean temperature is defined as

$$T_m = T_{in} + \frac{\dot{W}_{\text{tot}}}{\dot{m}c_p} \qquad (3)$$

W_{tot} is the total power added between the inlet and the location in question.

$$h_m = \frac{\dot{q}''_{\text{conv}}}{(T_e - T_m)} \qquad (4)$$

Option 3: Using the Channel Inlet Temperature. The channel inlet temperature is used by many practitioners in the electronics cooling area because it is part of the environmental description and is unambiguous

$$h_{in} = \frac{\dot{q}''_{\text{conv}}}{(T_e - T_{in})} \qquad (5)$$

Option 4: Using the Adiabatic Temperature. The adiabatic temperature is the name given to the temperature the component achieves when its own power is shut off, but the remainder of the system is "on." The term is not strictly accurate, in the thermodynamic sense, because there may still be heat transfer to or from the component by conduction, convection, or radiation exchanges with its surroundings; i.e., the component may not be truly adiabatic, simply "unpowered." In spite of that defect in nomenclature, the term h_{ad} will still be used here.

The adiabatic wall temperature has traditionally been used in heat transfer analysis in complex situations, e.g., high-ve-

Nomenclature

A = surface area
A_m = eigenvalue of Sellars et al.
B = cube dimension
c_p = specific heat
CPF = cumulative pattern factor
g^* = discrete two-dimensional kernel function
$g(x^+)$ = superposition kernel function of Sellars et al.
G = discrete one dimensional superposition kernel function
h = heat transfer coefficient
H = channel height;
k = thermal conductivity
$\dot{m}$ = mass flow rate
M = number of columns
N = number of rows downstream of a heated component
r_o = pipe diameter of Sellars et al.
$\dot{q}''_{\text{conv}}$ = convective heat transfer rate per unit area
$\dot{q}_o(\xi)$ = wall heat transfer rate of Sellars et al.
S = center-to-center spacing of cubes
T = temperature
UPF = unit pattern factor
V = channel inlet velocity
$\dot{W}_{\text{tot}}$ = total power input
x^+ = dimensionless distance of Sellars et al.
β_1, β_2 = linear coefficients of UPF model, equation (20)
α_1, α_2 = nonlinear coefficients of UPF model, equation (20)
γ_m = eigenvalue of Sellars et al.
θ = thermal wake function
ρ = density

Subscripts

ad = adiabatic
e = element
in = inlet
m = bulk mean
ref = reference
s = surface
∞ = far field

locity heat transfer, discrete-hole injection, and film cooling. In each case, the local heat transfer behavior is described in terms of the temperature rise caused by the local heat transfer. For an electronic component, its adiabatic temperature is typically higher than its mean temperature because components dissipate heat on one side of the channel. If the flow is fully mixed the adiabatic temperature is the same as the mean temperature

$$h_{ad}=\frac{\dot{q}''_{\mathrm{conv}}}{(T_e-T_{ad})} \tag{6}$$

The Misunderstanding and Its Consequences

These definitions look equally attractive and it would appear that one could simply choose any one of them arbitrarily, but that is not the case. If we wish to measure the value of h in the lab and use that value in an application, we must ensure that the measured value will be transferable to the application situation. With h_{in}, h_m, and h_∞ but not with h_{ad}, the value of the heat transfer coefficient at a given point depends on the wall temperature and heat flux upstream of, as well as at, the considered point. If the upstream distributions are different in the application from those in the lab experiment, then the values of h would be different even though the geometry and Reynolds number were the same. Let's examine the conditions under which most heat transfer data are taken in laboratory studies and see what temperature distributions are used.

Almost all the heat transfer data published today come from experiments that use a single active element in an otherwise passive array. The following discussion will be presented in heat transfer terms, but the same comments apply whether the measurement is made directly, using heat transfer, or indirectly using naphthalene sublimation or some other analog method.

When there is only one active component in an otherwise passive array, the air temperature approaching the component is uniform and the mean fluid temperature, the adiabatic temperature, and the inlet temperature are all the same. The heat release from the component raises the surface temperature and the heat flux divided by that temperature rise is used as the measure of h. The value of h is clear enough, but which definition should we say has been used: h_{in}, h_m, h_∞, or h_{ad}? Another way of presenting this same issue is to ask: Which of the four optional reference temperatures will we use with this value of h to calculate the heat transfer in the application?

For a given experiment, if we claim that the measured h represented h_{in}, h_m, or h_∞, then the reported value could only be used with exactly the same upstream distribution of wall temperature or heat flux that was used in the experiment. If the measuring experiment used only a single-heated element, and the value of h was described as h_{in}, h_m, or h_∞, then the value deduced from that experiment could not be used in any situation except a single-heated-element situation. Values of h_{in}, h_m, or h_∞ cannot be transferred from one temperature distribution to another. Those definitions are not useful except for situations of uniform wall temperature or heat flux.

On the other hand, the value of h_{ad} is independent of the upstream thermal boundary conditions, and therefore transferable from single element tests to more complex situations. Thus, if one wishes to uses the experimentally measured value of h from a single-active-element test in an application, one must consider the measured h to represent h_{ad} and use it accordingly.

The transferability of h_{ad} arises from the fact that the energy equation is linear in temperature whenever the fluid properties can be considered independent of temperature. When the energy equation is linear, the temperature distribution in the fluid around a heated component can be regarded as the sum of two distributions, with one being the distribution generated by the upstream thermal effects and the other being the result of the local heat release. The value of h_{ad} is set by the temperature distribution induced by the local heat transfer, which is independent of the incoming distribution. Thus, if a given heat release produces a 10° C rise in surface temperature when the incoming fluid is uniform in temperature (as in a single-element test), it will cause a 10° C rise above the adiabatic surface temperature when the incoming distribution is more complicated, and the value of h_{ad} measured in one situation can be used in the other.

The fundamental physics of the heat transfer process are not simplified by using h_{ad}, but neither are they made more complex. No matter which definition of h is used, the effect of the upstream thermal boundary conditions must still be acknowledged in order to get correct answers. If one uses h_{in}, h_m, or h_∞, then the value of h depends on the upstream temperature distribution but the reference fluid temperature is easy to deduce. If one uses h_{ad}, the value of h is easy to measure, but T_{ad} depends on the upstream temperature distribution. The burden shifts but it doesn't become lighter or heavier.

There are two undeniable facts to keep in mind about trying to use h_m in electronics cooling situations instead of h_{ad}. The first is that situations involving nonuniform wall temperature or heat released require much more effort than situations with uniform wall conditions, for comparable accuracy. The effect of the heating pattern on the value of h_m can only be found using the full superposition method described later. Taking h_m to be a function of Reynolds number and Prandtl number alone is correct only when the wall temperature or wall heat release is uniform along the passage. The second fact is that using a measured heat transfer coefficient from a single-active-element experiment as though it represented h_m will always yield wrong answers in situations where there is heating upstream of the considered component.

The notion that h_m is a function only of geometry, Reynolds number, and Prandtl number is fostered by the many correlations of the sort used in heat exchanger analysis. Heat transfer coefficient data for flows inside pipes and tubes have traditionally been presented as correlations between dimensionless groups such as Nusselt number and Reynolds number for a given geometry, with the effects of fluid properties acknowledged through a Prandtl number term. Equation (7), the well-known Dittus-Boelter equation for turbulent heat transfer in round pipes, is typical

$$\mathrm{Nu}_D=hD/k=0.023\mathrm{Re}_D^{0.8}\mathrm{Pr}^{0.4} \tag{7}$$

Nu_D is the Nusselt number based on tube diameter, Re_D is the Reynolds number based on tube diameter, and Pr is the Prandtl number.

In this equation, h is traditionally referenced to the mixed mean temperature of the fluid, T_m, and treated as though it were a function only of the Reynolds number and Prandtl number. By implication, then, h_m is considered to be constant along the wall and, specifically, to be independent of the wall temperature distribution. Equations like equation (7) are only valid when there is a fully developed, self-similar temperature distribution within the channel—situations with long runs of constant or slowly varying wall temperature or heat flux. In more general situations, the heat transfer coefficient, and hence the Nusselt number, is a function of the temperature or heat flux distribution on the wall and equations like equation (7) cannot be used; one must go to the full superposition approach, which will be discussed later.

To be transferable from the measurements lab to an application, values of h reported from single-element tests must be interpreted as h_{ad} and must be used with T_{ad} to calculate heat transfer rates. This is unfortunate because most users of heat transfer data have been trained to use h_m and almost automatically assume that all h values have that definition.

The distinction between the definitions is of more than academic interest, since misusing h can cause serious errors in

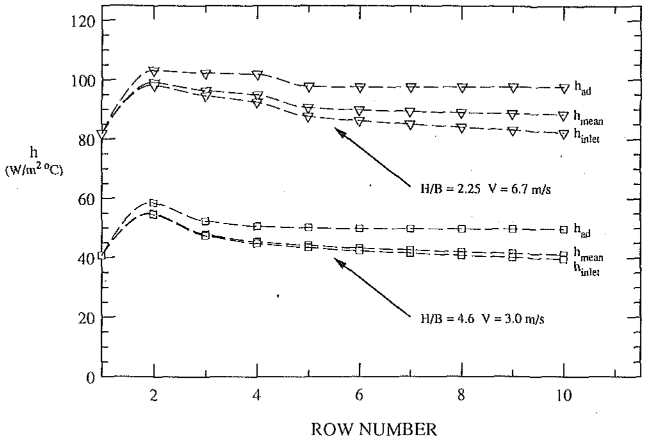

Fig. 3 Three possible descriptions of h, all deduced from the same data

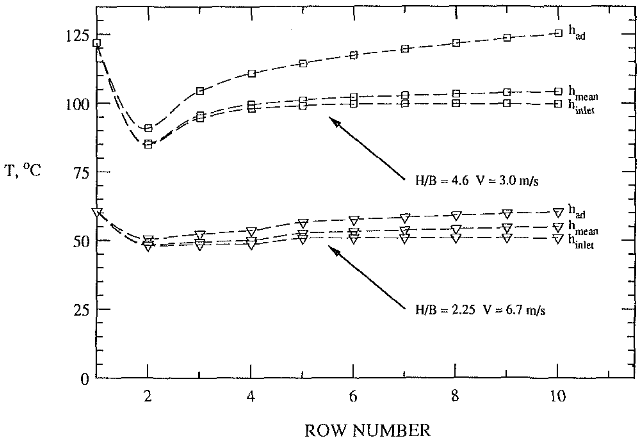

Fig. 4 The element temperatures that would be calculated if h_{ad} data were used as though they represented h_m or h_{inlet}

Table 1 Calculation of heat transfer coefficients for a uniformly heated array of elements and the corresponding temperatures if h_{ad} were used as h_{ad}, h_{mean}, and h_{inlet}

H/B = 4.6, V = 3.0 m/sec

	heat transfer coefficients (W/m ^{2} °C)			temperature rise (°C) calculated using:		
Row	h_{ad}	h_{mean}	h_{inlet}	T_{ad}	T_{mean}	T_{inlet}
1	40.7	40.7	40.7	121.9	121.9	121.9
2	58.5	54.9	54.6	90.9	85.3	84.8
3	52.4	47.9	47.4	104.5	95.7	94.7
4	50.6	45.7	44.8	110.8	99.5	98.0
5	50.1	44.2	43.4	114.4	101.0	99.0
6	49.8	43.2	42.2	117.3	102.1	99.6
7	49.8	42.6	41.5	119.5	102.6	99.6
8	49.8	42.0	40.8	121.5	103.1	99.6
9	49.8	41.6	40.2	123.4	103.6	99.6
10	49.8	41.1	39.6	125.2	104.1	99.6

H/B = 2.25, V = 6.7 m/sec

	heat transfer coefficients (W/m ^{2} °C)			temperature rise (°C) calculated using:		
Row	h_{ad}	h_{mean}	h_{inlet}	T_{ad}	T_{mean}	T_{inlet}
1	81.9	81.9	81.9	60.6	60.6	60.6
2	103.2	99.1	98.2	50.5	48.5	48.1
3	102.3	96.4	94.7	52.3	49.4	48.5
4	101.9	94.9	92.5	53.6	50.1	48.7
5	97.8	90.6	87.7	56.6	52.6	50.7
6	97.6	89.9	86.2	57.5	53.1	50.8
7	97.6	89.4	85.1	58.3	53.6	50.8
8	97.6	89.0	84.1	59.0	54.1	50.8
9	97.6	88.6	83.1	59.7	54.5	50.8
10	97.6	88.3	82.2	60.3	55.0	50.8

predicting component operating temperatures. We have seen that single-element experiments naturally generate h_{ad}. Let us now look at applying those data to predicting the behavior of a uniformly powered array and examine the errors that would result if those values of h_{ad} were used as though they were values of h_m and h_{in}.

Consider an array with 10 rows of elements, each with the same power applied. We first examine the different values of h (h_{in}, h_m, and h_{ad}) that might have been correctly calculated from the measured power, component temperatures, and reference temperatures. The tests were done using the apparatus described by Anderson and Moffat (1988) and included two channel-to-module height ratios, $H/B = 4.6$ and 2.25, at inlet channel velocities of 3.0 and 6.7 m/s, respectively. T_{in} and T_m were easy to obtain; values of T_{ad} were experimentally determined by turning off the power to one row at a time, with the other upstream rows heated, and determining the equilibrium temperature.

Figure 3 shows representative data from these tests, with all three values of h calculated for each test condition. For both channel heights, the value of h_{ad} on the tenth row is 20-25 percent higher than h_{in} and 10-20 percent higher than h_m. Each of these values would yield a true picture of the heat transfer from the components if used with its appropriate reference temperatures. Table 1 lists the values of temperature and h.

Figure 4 shows a different interpretation of this problem the error that results from using h_{ad} with the wrong reference temperature. Such errors are common because, while almost all of the published data are, in fact values of h_{ad}, the usual interpretation of h is as h_m. Figure 4 shows the element temperatures that would be predicted for the same uniformly heated array, in the same flow field, using the same h values (h_{ad}) but with three different reference temperatures, T_{in}, T_m, and T_{ad}. Figure 4 shows that correct use of h_{ad} will predict a final temperature of about 125° C for the elements in the last row, but using h_{ad} with $(T_e - T_m)$ would underestimate the maximum temperature by 20° C and treating h_{ad} as though it were h_{in} would underestimate $T_{\max}$ by 26° C.

Since most of the published data are in the form of h_{ad}, it is obviously important to know how to find T_{ad}, in order to be able to use the data. Alternately, one can calculate h_m from h_{ad}, and that is discussed in a later section of this paper, but there are theoretical advantages to sticking with h_{ad}, and that is our recommendation.

Determining the Adiabatic Temperature

Analytically, convective heat transfer with nonuniform wall heating has usually been dealt with by superposition, taking advantage of the linearity of the energy equation for constant property flow situations. The effect of each heated region on the adiabatic temperature of its downstream neighbors is expressed by a "kernel function" and the effects of several heated strips are summed to find the adiabatic wall temperature at a given point. The key question in applying h_{ad} to practical problems is, "How does one find the distribution of T_{ad}?" One important question for an experimentalist working on this problem is, "How should the experimental superposition kernel be described—what form should be used in representing the data?" It seemed appropriate to look to the early analytical works that used superposition methods for guidance as to the form.

The form described here follows early work by Sellars et al. (1956), who presented a solution for the adiabatic wall temperature in a tube whose wall heat flux varies arbitrarily, although remaining peripherally uniform. Their method was based on the superposition principle, taking advantage of the linearity of the differential equation governing the temperature distribution in the fluid. Their principal result is described by Kays and Crawford (1980) who provide a good conceptual background for the work. Their result is

$$T_{ad}(x^+) - T_{in} = \frac{r_o}{k}\int_0^{x^+} g(x^+ - \xi) q_o''(\xi) d\xi \tag{8}$$

$$g(x^+ = 4 + \sum_m \frac{\exp\{-\gamma_m^2 x^+\}}{\gamma_m^2 A_m} \tag{9}$$

where r_o is the tube radius, k is the thermal conductivity of the fluid, q_o'' is the wall heat flux, x^+ is the nondimensional downstream distance, γ_m and A_m are eigenconstants of the original differential equation, and $g(x^+)$ is the superposition kernel function. In these dimensionless terms, the constant 4 accounts for the rise in mean temperature, while the summation describes the extra temperature rise of the adiabatic wall over the mean temperature and its roll-off in the x direction.

The equations developed by Sellars et al., apply to laminar flow in a round tube or flat duct with a fully developed velocity profile. We can apply their results to the electronics cooling situation because the method of superposition is applicable whenever the governing equations are linear. The particular velocity distribution encountered is unimportant, so long as it is independent of the temperature distribution. The resulting equations are the same for turbulent flow in a pipe but the eigenfunctions will change.

Applying equation (8) to a tube with a single, short heated length (Δx^+, located at ξ) shows a form that can be useful in the present discussion

$$(T_{ad}(x^+, \xi) - T_{in}) = \frac{r_o \dot{q}_o'' \Delta x^+}{k} g(x^+, \xi) \tag{10}$$

Substituting for $\Delta x^+ = \Delta x / r_o \mathrm{RePr}$ and rearranging

$$(T_{ad}(x^+, \xi) - T_{in}) = \frac{\dot{q}_o''}{4\dot{m}c_p} g(x^+, \xi) \tag{11}$$

We can apply equation (11) to the electronics cooling situation. It describes the adiabatic temperature rise at location x^+, caused by heating a single element at location ξ. In the following sections we will discuss the calculation of the adiabatic temperature in arbitrarily heated arrays, in arrays with row-by-row uniform heating, and in arrays with fully uniform heating.

The Arbitrarily Heated Array

We can describe the superposition in a two-dimensional array by equations conceptually similar to equation (11). The situation is discrete and two-dimensional, hence we expect a double summation instead of an integral, but the same differential equation applies.

We propose the following form for the temperature rise of a component in the nth row (a line of elements perpendicular to the flow is a row) and mth column (in the direction of flow), where M is the total number of columns in the array

$$(T_{ad} - T_{in})_{n,m} = \sum_{j=0}^{M} \sum_{i=1}^{n-1} \frac{\dot{q}_{ij}}{\dot{m}c_p} g^*(n-i, m-j) \tag{12}$$

The kernel function, g^*, describes the pattern of adiabatic temperature rise everywhere in the array, as a result of heating a single component. In its general, two-dimensional form, we will call this the discretized two-dimensional superposition kernel function (2D SKF), to distinguish it from two less general functions that we will introduce later. From equations (12) we see that $g^*(n-i, m-j)$ is the ratio of the adiabatic temperature rise to the mean temperature rise at element (n, m) due to heating element (i, j)

$$g^*(n-i, m-j) = \frac{(T_{ad} - T_{in})_{n-i,m-j}}{(T_m - T_{in})_{n-i,m-j}} \tag{13}$$

We can deduce some properties of the $g^*(n-i, m-j)$ function from physical grounds. If an element (n, m) lies far to the left or the right of the source element, (i, j), $g^*(n-i, m-j)$ will approach zero because the thermal wake from the source element does not influence element (n, m). If the element lies far downstream of the source element, $g^*(n-i, m-j)$ approaches unity, because the coolant will be well mixed and at its mean temperature. For simple arrays (regular arrays of uniform components) g^* will not depend on the location of the source element whenever the source element lies in the fully developed region of the array. If the source element lies in one of the first few rows of the array g^* will depend on the location of the source due to entry region effects on the velocity field around the heated element. The kernel function will shown an invariant form for a regular array when the source element lies in the fully developed region of the flow.

We can use equation (12) to convert the adiabatic heat transfer coefficient to the mean heat transfer coefficient

$$h_{m(n,m)} = \frac{h_{ad(n,m)}}{1 + \frac{h_{ad(n,m)}}{\dot{q}_{n,m}} \sum_{j=0}^{M} \sum_{i=1}^{n-1} \frac{\dot{q}_{i,j}}{\dot{m}c_p} (g^*(n-i, m-j) - 1)} \tag{14}$$

For a uniformly heated array, where a simple h_m value suffices, one can use equation (14) to find h_m as a function of position in the array, and then predict the component temperature using the mean fluid temperature as the reference. One can also use equation (14) in more general situations, but it seems better, to the authors, to stay with h_{ad}. Both methods require knowledge of the kernel functions. Regardless of one's preferences, however, it is important to use h_{ad} with T_{ad} and h_m with t_m.

We know of no way (other than full numerical simulation) to find the distribution of T_{ad} in the general case of arbitrary distribution of heat release, other than superposition. We must know each of the $g^*(n-i, m-j)$ to use equation (12). Once we know the adiabatic temperature at each location, we can calculate the operating temperature from the adiabatic heat transfer coefficient. Superposition requires a good heat transfer data base relating to the system, including both h_{ad} and the g^* distribution. Only a few researchers have demonstrated superposition for simple, regular geometries (cubic elements, Arvizu and Moffat, 1981; flatpacks, Wirtz and Dykshoorn, 1985; also Biber and Sammakia, 1986). The theoretical path is clear, but we must assemble much more data before we can accurately handle cases of arbitrary geometry and arbitrary heat release. In the interim, we will make as much use as

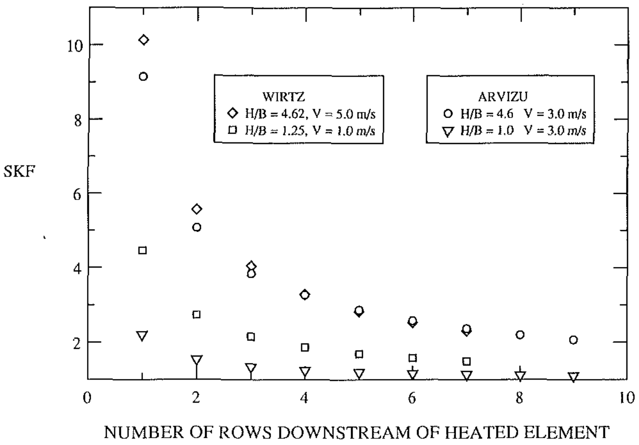

Fig. 5 Comparison of SKF from Wirtz (flat packs) and Arvizu (cubes)

possible of the existing analytical background in seeking a practical way of determining the adiabatic temperature.

Arvizu and Moffat (1981) presented data describing the thermal wake function behind a single heated component in a regular array. They studied cubical components (1.27 cm on a side) in a square, in-line array. They tested two array spacings and three channel heights $S/B=2$ and 3, and $H/B=1.0$, 2.25, and 4.6 over a range of velocities from 1.5 to 6 m/s. They described the thermal wake function in the same column of the heated components as[1]

$$\theta_{n-i,0}=\frac{(T_{ad}-T_m)_{n-i,0}}{(T_s-T_{in})_{n-i,0}}=\frac{1}{N}\theta_{1,0} \tag{15}$$

where $\theta_{1,0}$ is the thermal wake on an element one row downstream and in the same column as the heated element, T_s is the temperature of the source element, and $N=n-i$ is the number of rows behind the heated element. They further found that:

$$\begin{aligned} \theta_{1,0} &= C_1\mathrm{Re}^{-0.28} \\ C_1 &= 0.83 \text{ for } S/B=2.0 \\ C_1 &= 0.59 \text{ for } S/B=3.0 \end{aligned} \tag{16}$$

We can relate the Arvizu and Moffat thermal wake description to the two dimensional function, $g^*(n-i,\ 0)$ by rearranging as follows:

$$g^*(n-i,\ 0)=\frac{\dot{m}c_p}{h_{ad,i}A_i}\,\frac{(T_{ad,n}-T_{in})}{(T_{s,i}-T_{in})}=\theta_{n-i}\,\frac{\dot{m}c_p}{h_{ad,i}A}+1 \tag{17}$$

If we use the model function $\theta_{1,0}/N$ for the wake function we get

$$g^*(n-i,\ 0)=\frac{\theta_{1,0}}{N}\,\frac{(\dot{m}c_p)}{(h_{ad,i}A_i)}+1 \tag{18}$$

$$g^*(n-i,\ 0)=\frac{\theta_{1,0}}{N}\,\frac{1}{5}\,\frac{\rho V c_p}{h_{adi}}\,\frac{H}{B}\,\frac{S}{B}+1 \tag{19}$$

V is the approach velocity in the empty channel, h_{ad} is the adiabatic heat transfer coefficient at the source, H is the channel height, s is the element pitch, and $5B^2$ is the element surface area.

We can rely upon equation (17) strictly, since it describes the kernel function in terms of measurable properties of the system. Equation (19), on the other hand, uses $\theta_{1,0}/N$ as a model for the thermal wake function and is only as good as that approximation. In either equation if we use the actual heat transfer coefficient at the source we will calculate the correct value of g^*. If we use a faulty correlation for h, errors will occur. A 10 percent error in θ or h will cause a 10 percent error in g^*, while a 10 percent error in θ and in h could cause a 20 percent error in g^* (if the two excursions correlate) or 14 percent (an average, if the two excursions do not correlate). There is evidence that θ and h are inversely correlated, suggesting that these errors will generally add.

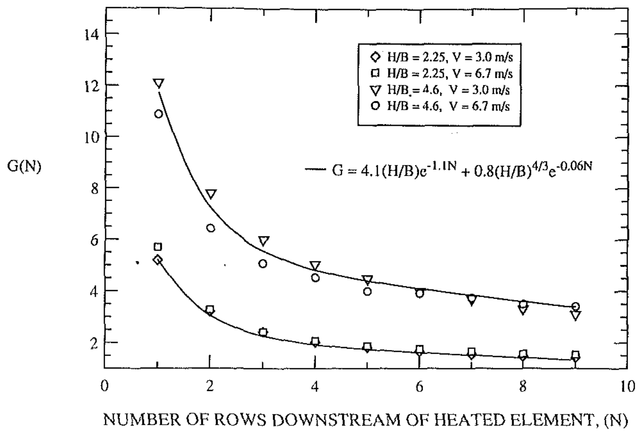

Fig. 6 UPFs for two velocities and two channel heights ($V=3.0$ and 6.7 m/s and $H/B=2.25$ and 4.6)

Table 2 Coefficients for UPF model

$$\mathrm{UPF}=\beta_1 e^{-\alpha_1 N}+\beta_2 e^{-\alpha_2 N}$$

heated row	H/B	V (m/sec)	β_1	β_2	α_1	α_2
1	2.25	3.0	7.81	2.28	0.95	0.05
1	2.25	6.7	10.38	2.33	1.10	0.05
1	4.6	3.0	16.28	6.74	1.01	0.09
1	4.6	6.7	20.01	5.19	1.22	0.05
2	2.25	3.0	13.76	2.20	1.44	0.09
2	2.25	6.7	13.40	2.30	1.66	0.05
2	4.6	3.0	26.87	5.44	1.41	0.10
2	4.6	6.7	34.61	6.38	2.07	0.08
3	2.25	3.0	13.30	2.52	1.33	0.09
3	2.25	6.7	13.72	2.49	1.51	0.05
3	4.6	3.0	29.67	6.46	1.42	0.11
3	4.6	6.7	25.11	6.99	1.38	0.11
4	2.25	3.0	14.98	2.96	1.51	0.10
4	2.25	6.7	16.19	2.91	1.63	0.08
4	4.6	3.0	35.46	6.26	1.65	0.08
4	4.6	6.7	38.26	7.98	1.72	0.12

The parameter $\dot{m}c_p/hA$ is important in determining the adiabatic temperature rise of an element. This parameter is similar to the Ntu parameter used in heat exchanger design ($\mathrm{Ntu}=UA/\dot{m}c_p$). In the present use, it relates the mean temperature rise of the coolant to that of the source element. The Stanton number, $h/\rho v c_p$, also emerges as a natural parameter in this description.

Wirtz and Dykshoorn (1985) also presented data for the thermal wake function in an array of closely packed flat packs. Lehmann and Wirtz (1984) showed that little or no mixing occurs in a channel of flatpacks. Thus we expect that a dense array of flatpacks in a narrow channel would display a relatively large value of g^*. We used the Wirtz and Dykshoorn data for θ, θ_1, and h_{ad} and calculated the kernel functions from equation (17). Figure 5 compares the 2D SKF in the same column as the heated element $g^*(n-i,\ 0)$ from Wirtz and Dykshoorn with those from Arvizu to illustrate this last point.

The Array With Uniform (but Possibly Different) Heating in Each Row

If we apply uniform power to each row of a geometrically uniform array with equal flow through each flow lane (i.e., no interaction occurs between the observed column and its neighbors) then the problem becomes one-dimensional and equation (12) simplifies to

$$(T_{ad}-T_{in})_n=\sum_{i=1}^{n-1}\frac{\dot{q}_i}{\dot{m}c_p}G(n-i) \tag{20}$$

---

[1] Note A: In the original presentation of Arvizu and Moffat's results, they described the temperature wake function data as

$$\frac{T_{ad}-T_{in}}{T_s-T_{in}}=\theta \tag{A1}$$

We now interpret the value of T_{in} in the numerator as T_m rather than T_{in} based on the behavior of θ for large N, while that in the denominator is left unchanged. In their experiments, with only one element of 100 heated, there was no discernible rise in the mean temperature, hence there were only three temperatures to observe: the source, the observed element, and the air temperature. The air temperature was assigned the meaning "inlet temperature," and used in both the numerator and denominator to describe the thermal wake function. We could just as easily define it as T_m. One might ask why not be consistent—why not also interpret the T_{in} in the denominator as T_m? There are two reasons not to do that. First, to do so would complicate the final equation without augmenting its accuracy and, second, such an interpretation would require the heat transfer from the source element to be expressed in terms of h_m instead of h_{ad} and we do not know h_m.

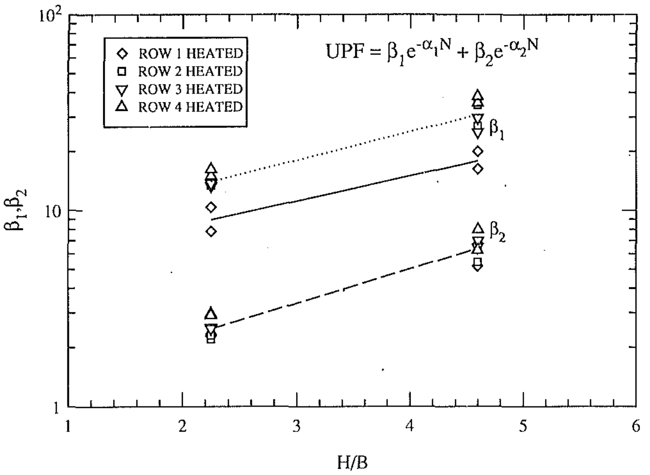

Fig. 7 Linear coefficients of equation (22)

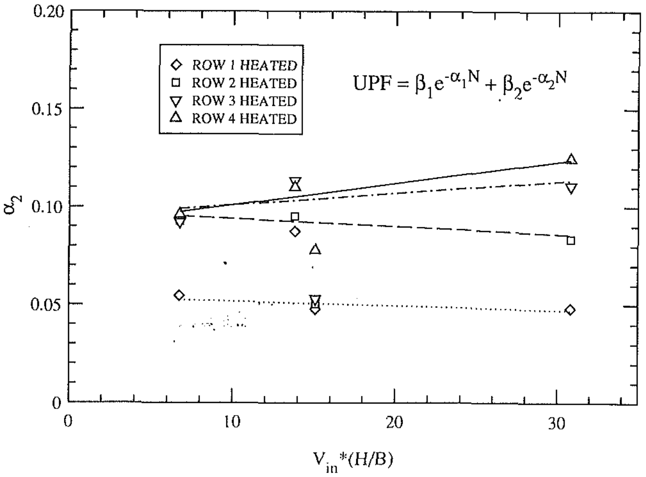

Fig. 9 Nonlinear coefficient α_2 of equation (22)

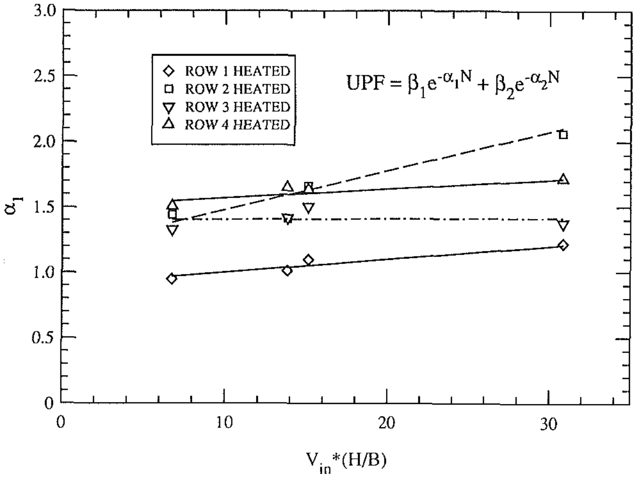

Fig. 8 Nonlinear coefficient α_1 of equation (22)

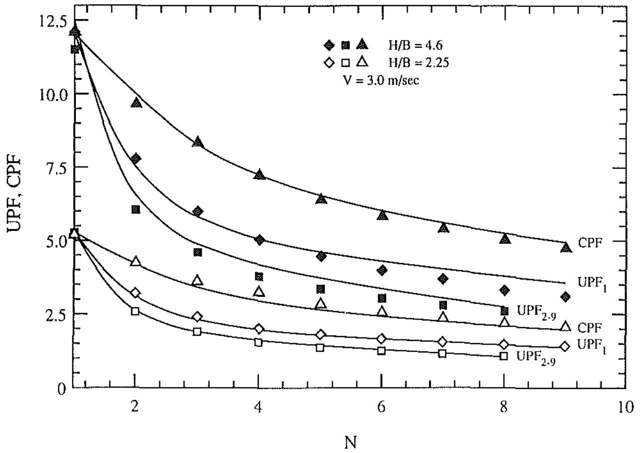

Fig. 10 Calculated and experimental UPFs and CPFs for $V = 3.0$ m/s and $H/B = 2.25$ and 4.6

From equation (20) we see again that the G function describes the ratio of the adiabatic temperature rise to the mean temperature rise at the nth row due to heating the ith row

$$G(n-i)=\frac{T_{ad,n-i}-T_{in}}{T_{m,n-i}-T_{in}} \tag{21}$$

We will call the G function in equation (20) the Unit Pattern Factor (UPF)—the pattern factor that displays the effect of a single uniformly heated row on its downstream neighbors. It is the 1D SKF.

Figure 6 shows the measured UPFs versus row number for several typical situations, from the data of Anderson and Moffat (1988). In these cases we heated the elements in the first row (i.e., $i = 1$) and measured the component temperatures at each downstream row (i.e., $n = 1$-9). We calculated T_m from a global energy balance. The figure shows the UPFs for two channel spacings $H/B = 4.6$ and 2.25, and two velocities, $V = 3$ and 6.7 m/s. The UPF is strongly affected by passage height, but only slightly affected by the approach velocity. If we compare the UPF results to the $g^*(n-i, 0)$ of Arvizu and Moffat (same geometry) we see that the UPFs are higher, which they should be as they include the heating effects of elements in adjacent columns.

Following the solution by Sellars et al. (equation (9)) for the kernel function we modeled the UPF as a sum of exponentials. The model in the last section for $g^*(n-i, 0)$ behaves similarly to a sum of exponentials over a short range where $1/N$ reasonably matches an exponential function. We developed a new model for the UPF based on equation (22) using only two terms of the exponential

$$\mathrm{UPF}(N)=\beta_1 e^{-\alpha_1 N}+\beta_2 e^{-\alpha_2 N} \tag{22}$$

β_1, β_2 are linear coefficients, dependent on H/B and V, while α_1, α_2 are nonlinear coefficients, dependent on H/B and V. N is the number of rows downstream of the heated row $(n-i)$.

The two terms in equation (22) describe different regions of the UPF(N) curve (see Fig. 6). The first term describes the initial near-field ($N = 1$-4) decay in UPF and the second term describes the far field rolloff in UPF ($N = 4$-10).

To determine the coefficients of equation (22) we used a nonlinear least-squares technique to fit 16 sets of data. We varied the channel height H/B from 2.25 to 4.6, the velocity V from 3.0 to 6.7 m/s, and the location of the heated row i from 1 to 4. Table 2 lists the resulting coefficients.

Figure 7 is a plot of the two linear coefficients, β_1 and β_2 versus H/B. The correlation for row 1 heated fits β_1 to within 7 percent and the correlation for rows 2-4 heated fits β_1 to within 6 percent. We correlated β_2 data to within 15 percent, independent of the location of the heated row. This behavior agrees with our intuition because the second term describes the far-field decay and should be independent of the heated row location. β_1 depends on the location of the heated row because it describes the initial decay in UPF.

Figures 8 and 9 plot α_1 and α_2 versus VH/B. To a first approximation α_1 and α_2 are independent of VH/B. They appear to be relatively constant with a slight dependence on the location of the heated row.

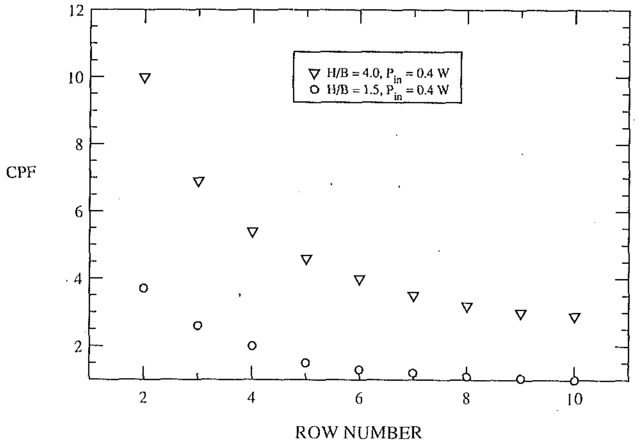

Fig. 11 CPFs measured in a buoyancy-driven channel with a regular in-line array of cubes on one wall

The new model has the form:

For row 1 heated:

$$\mathrm{UPF}(N) = 4.1(H/B)e^{-1.1N} + 0.8(H/B)^{4/3}e^{-0.06N} \tag{23}$$

For rows 2-4 heated:

$$\mathrm{UPF}(N) = 5.8(H/B)^{1.1}e^{-1.5N} + 0.8(H/B)^{4/3}e^{-0.1N} \tag{24}$$

The solid lines in Fig. 6 are from equation (23). Equation (23) fits the data to within 8 percent with the exception of one data point that was 15 percent low. One can use equations (23) and (24) to determine the UPF for similar geometries. Our data are limited to regular arrays of in-line elements, but the method applies to any geometry.

The analysis developed in this section applies to one-dimensional arrays—those with uniform (but possible different) heating in each row. We can use equation (20) to calculate the adiabatic temperatures of elements in an array using the UPFs from equations (23) and (24).

The Array With Uniform Power

If every element in the array dissipates the same power, we can further simplify. Equation (12) reduces to

$$(T_{ad} - T_{in})_n = \frac{\dot{q}}{\dot{m}c_p}\sum_{i=1}^{n-1} G(n-i) \tag{25}$$

We can define a new term, the Cumulative Pattern Factor, as

$$\mathrm{CPF}_n = \frac{1}{(n-1)}\sum_{i=1}^{n-1} G(n-i) \tag{26}$$

We define the CPF_n as (the adiabatic temperature rise in the nth row when all upstream elements are uniformly heated) divided by (the mean temperature rise of the coolant, approaching the nth row, when all upstream elements are uniformly heated). We can calculate the CPF at any location inside a uniformly heated array by summing the UPF from each row upstream of the observed row, as shown by equation (26).

Figure 10 compares Unit and Cumulative Pattern Factors for four cases with cubic elements. The solid lines are calculated values using equations (23) and (24). The symbols are actual data from Anderson and Moffat (1988). The two descriptors differ most markedly for large channel spacing, where the heated fluid does not mix well into the core.

We can apply the Pattern Factor concept developed above to buoyancy-induced channel flows (Moffat and Ortega, 1985) as well as to fan-driven flows. For very low values of $\mathrm{Gr}/\mathrm{Re}^2$, the results should apply directly, since local buoyancy will not affect the flow field. As local buoyancy effects increase, the velocity distribution will change, and the distributions of UPF and CPF will change. We do not yet know the critical value of $\mathrm{Gr}/\mathrm{Re}^2$ above which buoyancy affects the pattern factor. Preliminary results suggest the limit to be around $\mathrm{Gr}/\mathrm{Re}^2 = 0.1$ or smaller, based on measurements of the plume shapes downstream of heated elements (Bejarano, 1986).

In a vertical channel, a buoyancy-driven flow will tend to have higher velocities around the heated elements for a given mean velocity in the channel than fan-driven flows. The direction of entrainment reverses, with core fluid entrained into the near wall region, as opposed to near-wall fluid being extruded out into the core flow. Together, these effects will reduce the cross-channel mixing and should lead to higher values of UPF and CPF.

Figure 11 shows CPFs measured in a buoyancy-induced channel flow over cubes for two channel heights: $H/B = 1.5$ and 4.0. In both cases, the average board power was 0.4 W per element. The adiabatic temperatures were determined by shutting off the power to the rows, one at a time.

Free convection effects may destabilize the flow in a horizontal channel, and thereby improve the mixing. This would reduce both UPF and CPF.

Calculating Element Temperatures Using h_{ad} and T_{ad}

Assuming we know either CPF, for a board with uniform power, or UPF for uniform row heating, or g^*, the power distribution, and h_{ad}, we can then calculate the operating temperature of each element. The working equation depends on the situation.

Equation (27*a*) or (27*b*) is the working equation for calculating the operating temperature of elements in a uniformly heated array, using values of h_{ad}, the power per element, and the values of CPF.

$$(T_e - T_{in})_n = (n-1)\frac{\dot{q}_i}{\dot{m}cp}\sum_{i=1}^{n-1} G(n-i) + \frac{\dot{q}_n}{h_{ad,n}A_n} \tag{27a}$$

$$(T_e - \mathrm{T}_{in})_n = (n-1)\frac{\dot{q}_i}{\dot{m}cp}\mathrm{CPF}_n + \frac{\dot{q}_n}{h_{ad,n}A_n} \tag{27b}$$

If the array is heated on a row-by-row uniform basis, then the working equation is

$$(T_e - T_{in})_n = \sum_{i=1}^{n-1} \frac{\dot{q}_i}{\dot{m}cp} G(n-i) + \frac{\dot{q}_n}{h_{ad,n}A_n} \tag{28}$$

Equation (29) is the working equation for the most general case, where every element may have a different power level.

$$(T_e - T_{in})_{n,m} = \sum_{j=0}^{M} \sum_{i=1}^{n-1} \frac{\dot{q}_{ij}}{\dot{m}c_p} g^*(n-i,\ m-j) + \frac{\dot{q}_{n,m}}{h_{adn,m}A_{n,m}} \tag{29}$$

Conclusions

Almost all researchers in the electronics cooling literature report values of the experimental heat transfer coefficient defined in terms of the adiabatic temperature of the element, as a consequence of the experimental techniques used. In most cases, these values are being used to calculate the temperature rise above the mean fluid temperature, rather than the adiabatic temperature, a procedure that may seriously underpredict the temperature rise of an element in service. The error is caused by the fact that the adiabatic temperature is generally higher than the mean temperature of the coolant, leading to an underestimation of the operating temperature of the element.

Using the analysis presented in this paper, one can either calculate T_{ad} and use h_{ad}, or calculate h_m from h_{ad} and continue to use T_m. Either adjustment will work, but at least one must be made. One cannot use h_{ad} and T_m as is too frequently done at present. The data presented in this paper apply only to regular in-line arrays of elements. We can generalize the method to arbitrary geometries, but we will need new data.

In the present paper, we develop a method for calculating the adiabatic temperature of an element in an array, based on the mean temperature rise, and using information about the thermal wake function of a typical element in the array. The method has sound theoretical footing, being an application of superposition. It requires empirical input, specific to the geometry in question, but the analysis does not require a full array of test data to predict the behavior of elements successfully over a wide range of conditions.

Acknowledgments

This research was supported by IBM Corporation. The authors appreciate the interest and assistance of Richard C. Chu, IBM Fellow.

References

Anderson, A. M., and Moffat, R. J., 1988, "Direct Air Cooling of Electronic Components: Reducing Element Temperatures by Controlled Thermal Mixing," *Symposium on Fundamentals of Forced Convection Heat Transfer*, ASME HTD-Vol. 101, p. 9-16.

Arvizu, D. E., and Moffat, R. J., 1981, "Experimental Heat Transfer From an Array of Heated Cubical Elements on an Adiabatic Channel Wall," Thermosciences Division Report HMT-33, Department of Mechanical Engineering, Stanford University, Stanford, CA.

Bejarano, F., 1986 work in progress, Thermosciences Division, Stanford University, Stanford, CA.

Biber, C. A., and Sammakia, B. G., 1986, "Transport From Discrete Heat Components in a Turbulent Channel Flow," ASME Paper No. 86-WA/HT-68.

Kays, W. M., and Crawford, M. E., 1980, *Convective Heat and Mass Transfer*, McGraw-Hill, New York, p. 124.

Lehmann, G. L., and Wirtz, R. A., 1984, "Convection From Surface Mounted Repeating Ribs in a Channel Flow," ASME Paper No. 84-WA/HT-88.

Ortega, A., and Moffat, R. J., 1986, "Experiments of Buoyancy-Induced Convection Heat Transfer From an Array of Cubical Elements on a Vertical Channel Wall," Thermosciences Division Report HMT-38, Department of Mechanical Engineering, Stanford University, Stanford, CA.

Sellars, J. R., Tribus, M., and Klein, J. S., 1956, "Heat Transfer to Laminar Flow in a Round Tube or Flat Conduit—The Graetz Problem Extended," *Trans. ASME*, Vol. 78, pp. 441-448.

Wirtz, R. A., and Dykshoorn, P., 1984, "Heat Transfer From Arrays of Flat Packs in a Channel Flow," *Proceedings From the Fourth International Electronics Packaging Society*, Baltimore, MD, Oct., pp. 318-326.

Cooling of a Multichip Electronic Module by Means of Confined Two-Dimensional Jets of Dielectric Liquid

D. C. Wadsworth
Graduate Research Assistant.

I. Mudawar
Associate Professor and Director.

Boiling and Two-Phase Flow Laboratory,
School of Mechanical Engineering,
Purdue University,
West Lafayette, IN 47907

Experiments were performed to investigate single-phase heat transfer from a smooth 12.7×12.7 mm^2 simulated chip to a two-dimensional jet of dielectric Fluorinert FC-72 liquid issuing from a thin rectangular slot into a channel confined between the chip surface and nozzle plate. The effects of jet width, confinement channel height, and impingement velocity have been examined. Channel height had a negligible effect on the heat transfer performance of the jet for the conditions of the present study. A correlation for the convective heat transfer coefficient is presented as a function of jet width, heater length, flow velocity, and fluid properties. A self-contained multichip cooling module consisting of a 3×3 array of heat sources confirmed the uniformity and predictability of cooling for each of the nine chips, and proved the cooling module is well suited for packaging large arrays of high-power density chips.

1 Introduction

The current trend of miniaturization of electronic components has given rise to alarmingly high power densities. Future technologies may result in power densities in excess of 100 W/cm^2 at the chip level by the mid-1990s (Bar-Cohen et al., 1986). This trend is complicated by a need for reduction in the dimensions of cooling hardware to facilitate three-dimensional packaging of multichip modules in a minimum volume.

Conventional methods of cooling, such as free and forced air convection, are no longer adequate for the anticipated fluxes. An alternative form of cooling, which has captured much attention in recent years, consists of direct immersion in dielectric liquids. This form of cooling circumvents the problem of high thermal resistance associated with previous technologies and offers the potential for greatly increasing the chip cooling rate. However, poor thermal transport porperties of dielectric liquids make it necessary to augment heat transfer by means of forced convection, surface enhancement, and/or phase change to meet projected chip cooling demands. Recent studies have shown that single-phase forced-convection cooling of chips in a channel is capable of meeting high-power chip cooling requirements (Samant and Simon, 1986; Ramadhyani and Incropera, 1987; Maddox and Mudawar, 1989; Mudawar and Maddox, 1989a, 1989b). Mudawar and Maddox (1989b) dissipated more than 200 W/cm^2 and 300 W/cm^2 using single and two-phase cooling, respectively, from an enhanced surface over which FC-72 (product of 3M) was forced at a moderate velocity while maintaining the chip temperature below 86°C.

Jet impingement, introduction of the cooling fluid perpendicular to the heated surface, has been employed in a variety of environments requiring continuous dissipation of enormous heat fluxes such as cooling of turbine blades, X-ray medical equipment, laser weapons, and annealing of steel. The attractive heat transfer characteristics of an impinging jet make this cooling configuration a viable candidate for the removal of very high power densities encountered in microelectronic devices.

Several jet impingement studies have been conducted using a circular orifice from which the coolant issued (Ma and Bergles, 1983; Jiji and Dagan, 1987). One drawback to such a configuration is the concentration of cooling in the small impingement zone of the heated surface. The use of multiple jets enhances cooling uniformity by creating several impingement zones that cover a significant fraction of the heated area. However, multiple jets promote flow blockage between the jets and complicate fluid distribution downstream from the impingement zone. As indicated in a literature survey by Downs and James (1987), the interference between circular jets leads to a reduction in heat transfer caused by the forma-

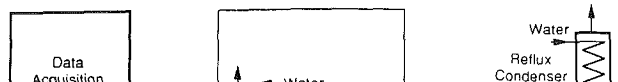

Fig. 1 Schematic diagram of the experimental facility

Contributed by the Heat Transfer Division for publication in the JOURNAL OF HEAT TRANSFER. Manuscript received by the Heat Transfer Division April 12, 1989; revision received February 9, 1990. Keywords: Electronic Equipment, Jets.

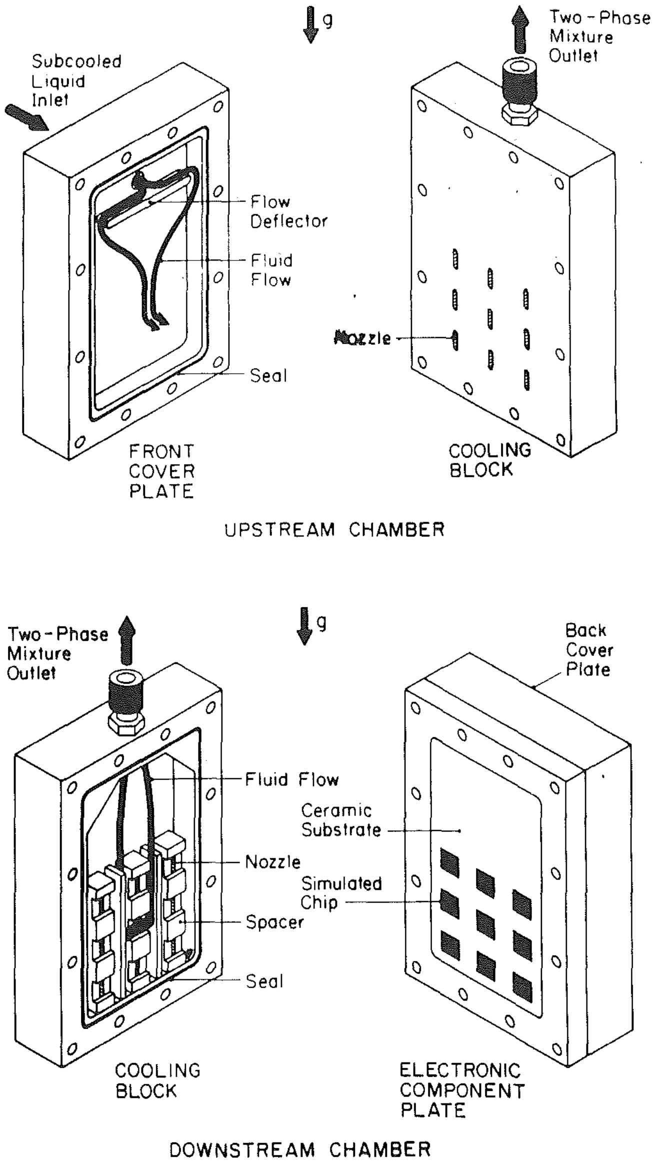

Fig. 2 Schematic diagram of the cooling module

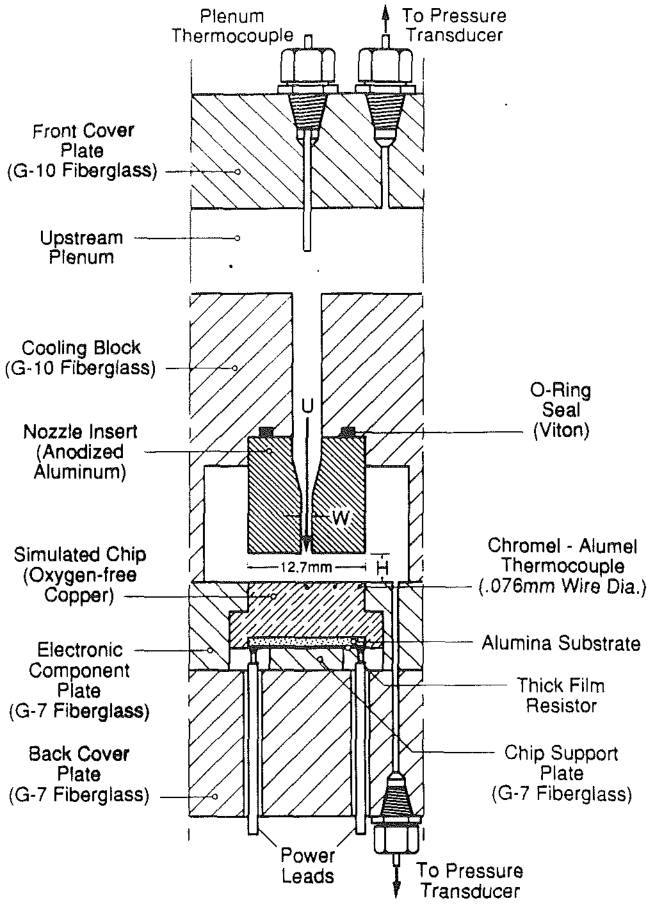

Fig. 3 Sectional view of the cooling module

tion of eddies, and to boundary layer separation, between adjacent jets. The complex spatial variations in the heat transfer coefficient associated with jet interference was illustrated by Goldstein and Timmers (1982) using flow visualization techniques. These problems become very critical in the cooling of multichip modules, which require uniform cooling of a large number of chips and ease of fluid introduction into, the rejection from, the module in the smallest volume possible. A potential solution to this problem is to use two-dimensional or slot jets, which provide a larger impingement zone and insure uniform coolant rejection following impingement.

This paper presents a packaging concept for cooling an array of heat sources (simulated chips) by means of a confined two-dimensional slot jet. Data are correlated for single-phase heat transfer from a smooth 12.7 mm × 12.7 mm chip to a jet of dielectric Fluorinert FC-72 liquid issuing from a thin rectangular slot into a channel confined between the chip surface and the nozzle plate. Information concerning the chemical and thermal properties of FC-72 can be found in previous papers by Mudawar and Maddox (1989a) and Mudawar and Anderson (1989).

Nomenclature

H = height of confinement channel
$\bar{h}_L$ = average heat transfer coefficient based on heater length $= q/(T_s - T_f)$
k = thermal conductivity of liquid based on mean liquid temperature
L = length of heater = 12.7 mm
$\overline{\mathrm{Nu}}_L$ = average Nusselt number based on heater length $= qL/(T_s - T_f)k$
Pr = Prandtl number of liquid based on mean liquid temperature
q = mean surface heat flux
Re = Reynolds number based on nozzle hydraulic diameter $= U(2W)/\nu$
Sc = Schmidt number
$\overline{\mathrm{Sh}}_L$ = mean Sherwood number based on heater length
T_f = liquid temperature at nozzle inlet
T_m = mean liquid temperature $= (T_s + T_f)/2$
T_s = mean temperature of heater surface
ΔT = $T_s - T_f$
U = mean jet velocity at nozzle exit
W = nozzle width
x = horizontal distance along heater surface measured from centerline of impingement zone
ν = kinematic viscosity of liquid based on mean liquid temperature

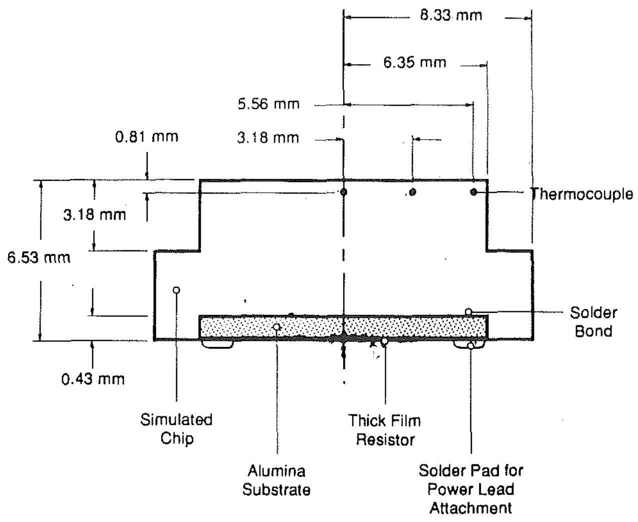

Fig. 4 Test heater construction

2 Experimental Apparatus and Procedure

A schematic diagram of the experimental facility used in this study is shown in Fig. 1. The flow loop was designed to accommodate both single-phase and two-phase experiments. The cooling module was installed between two fluid reservoirs equipped with internal immersion heaters.

Fluid in the system (FC-72) was circulated by a magnetically coupled centrifugal pump. A bypass line from the pump, connected in parallel with the cooling module, made it possible to regulate the flow through the cooling module even for very small flow rates. Flow rate through the test module was measured by a turbine flow meter. Accurate control of fluid temperature was achieved by two immersion heaters coiled in the upstream and downstream reservoirs of the cooling module, and a flat plate water-cooled heat exchanger located downstream from the pump. Two external tanks, shown in Fig. 1, were used for deaeration and for controlling pressure in the system.

Cooling Module. The cooling module accommodated a 3×3 array of 12.7 mm $\times$ 12.7 mm simulated chips. Coolant was supplied to each of the nine chips via a single isolated rectangular slot. As shown in Fig. 2, the module consisted of four parallel attachments: front cover plate, cooling block, electronic component plate, and back cover plate. Fluid was introduced into the module through the front cover plate. A flow deflector downstream from the inlet redistributed the flow and helped create uniform pressure in the chamber formed between the front cover plate and cooling block. The flow was distributed between the nine nozzles, from which fluid impinged onto the simulated chips flush-mounted in the electronic component plate. Fluid impingement was confined to a channel formed between the nozzle face and the simulated chip. After exiting the channel, the fluid was routed vertically upward to the cooling module outlet. The module was designed to insure cooling uniformity among the chips by producing a total pressure drop across the nozzle and confinement channel significantly larger than the pressure drop in the upstream chamber or outlet regions.

Figure 3 shows a detailed sectional view of the cooling module. Located in the front cover plate and extending into the upstream chamber was a single type K thermocouple for measurement of liquid inlet temperature. Also located in the front cover plate was a pressure port to which an absolute pressure transducer was attached. A second pressure port was placed at the confinement channel outlet. Pressure drop through the nozzle and confinement channel was measured by a differential pressure transducer connected between the two pressure ports.

The geometric characteristics of the impinging flow were changed by using different nozzle inserts, which were recessed into the G-10 cooling block. The anodized aluminum nozzle inserts consisted of a 30-deg converging entrance region followed by a straightening section five times the jet width. During single-chip tests, the liquid was injected only through the central nozzle while the other eight nozzles were blocked.

Heater Design. Figure 4 details the construction of the simulated chip. Three type K (chromel-alumel) thermocouples were used to instrument the test heater. Each thermocouple was constructed from 0.13-mm (5-mil) wire and insulated with a two-hole ceramic tube. The thermocouple assemblies were inserted into 0.79-mm (1/32-in.) diameter holes in the copper block to a depth of 6.35 mm. Machining and thermocouple location tolerances were maintained within ±0.03 mm (1 mil). The thermocouple beads were coated with boron nitride thermally conducting epoxy. The thermocouples were located in a plane parallel to the chip surface and perpendicular to the plane of Fig. 4. One of the thermocouples was placed along the centerline of the chip corresponding to the impingement zone while the other two were distributed along the confinement channel flow direction as shown in Fig. 4. The heating element of the simulated chip was a commercially available 90-ohm thick film resistor. The resistor was supplied with a solder coating on the alumina backside for convenient bonding to the copper block. Power to the test heaters was supplied by a 240-vac variac. Power input was measured by means of voltage and current transducers.

Data were taken and recorded using a Keithley series 500 data acquisition system coupled to a Compaq 286 microcomputer. The data acquisition system monitored and processed signals from the current and voltage transducers, pressure transducers, and thermocouples. Thermocouple measurement resolution using this system was approximately 0.1°C.

Experimental Procedure. Deaeration of coolant in the system was necessary to insure consistency of fluid properties for the entire data base. At the onset of each test the coolant was deaerated by energizing the immersion heaters while circulating the fluid through the system. During dearation the fluid temperature was raised to approximately 60°C and maintained at that level for 20 minutes. During this time, air and coolant vapor were released from the upper reservoir into the pressurization tank and secondary condensate tank. A water-cooled reflux condenser connected to the secondary condensate tank permitted air to escape freely into the ambient as coolant vapor was being captured in the condensate tank. Following deaeration the valve connecting the pressurization tank and secondary condensate tank was closed to isolate the system from the ambient, and power input to the pressurization tank immersion heaters was regulated to maintain the desired system pressure.

Single-phase heat transfer data were obtained by operating at the lowest desired jet velocity and adjusting heater power to maintain a ΔT of approximately 10°C. When the system reached steady state the data were recorded and power was reduced by approximately 3 W. A second set of data was obtained in a similar fashion for the reduced power setting. The velocity was then increased slightly and the process repeated until velocities in a range from 0.5 to 12 m/s were covered. This procedure was repeated for a wide spectrum of nozzle inserts having slot widths of $W = 0.127$, 0.254, and 0.508 mm, and nozzle heights $H = 0.127$, 1.27, 2.54 and 5.08 mm. The inserts permitted variations in H/W in the range 1 to 20.

Determination of Temperature Distribution at the Heater Surface. Temperature measurements were obtained at a

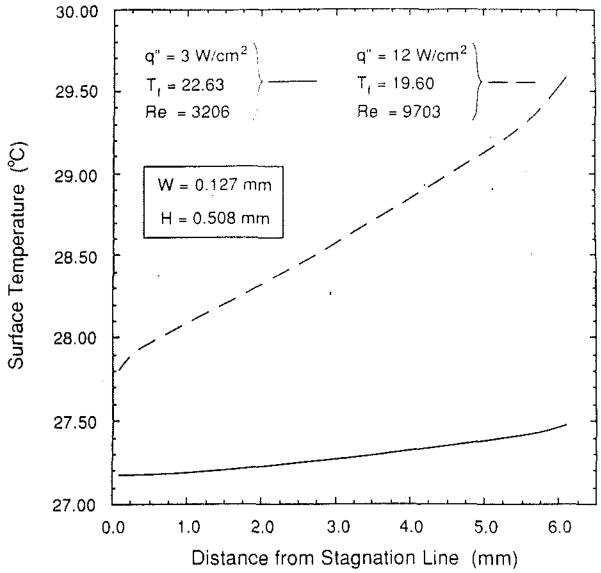

Fig. 5 Variation of chip surface temperature with distance from the impingement centerline

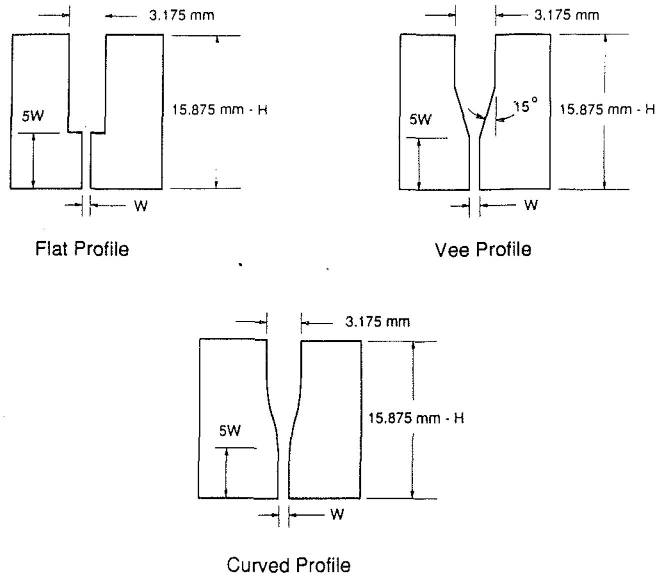

Fig. 6 Nozzle configurations

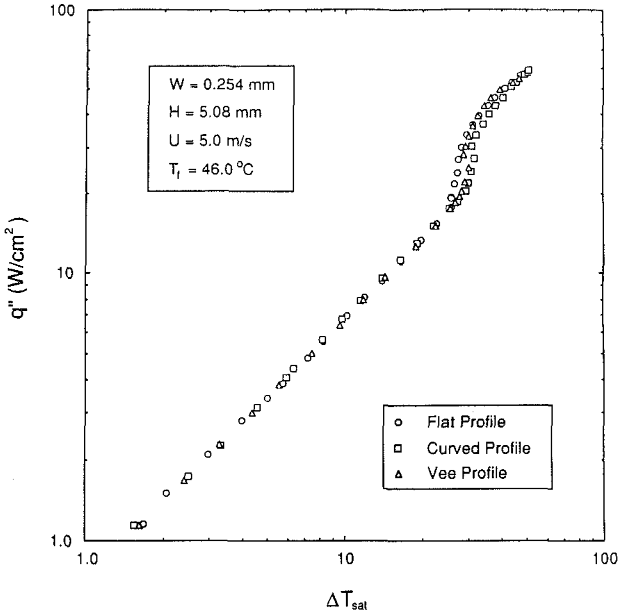

Fig. 7 Effect of nozzle shape on chip cooling performance

plane 0.812 mm below the heat transfer surface; therefore, it was necessary to correct the measured values to determine surface temperature distribution. Two different methods of correction were performed and compared for accuracy. The first method employed a simple one-dimensional correction and the second used a two-dimensional finite difference scheme described by Patankar (1980). For both cases the test heater was modeled to be symmetric about the impingement cenerline.

For the one-dimensional correction the heat flux at the thermocouple plane was assumed uniform, and the test heater was assumed perfectly insulated along its boundaries. Using Fourier's law of conduction, each of three measured temperatures at the thermocouple plane was corrected to its corresponding point on the surface. The average surface temperature was determined as an area-weighted average of the three corrected surface values.

The two-dimensional correction involved a two-step numerical procedure similar to that developed by Jiji and Dagan (1987). First, a temperature profile at the thermocouple plane was fitted to the three temperatures using a Gaussian interpolating polynomial. The temperature profile and heater power input were used in the finite-difference numerical program to predict the temperature field in the domain bound by the thermocouple plane and the back cover plate. Heat fluxes at each nodal point on the thermocouple plane were then computed based on the solved temperature field. One-dimensional conduction was next employed to obtain temperatures at the surface for each corresponding nodal point. The second step was to solve the entire test heater temperature domain (from the actual impingement surface to the back cover plate) using the corrected surface temperatures as a boundary condition in the two-dimensional model. Calculated temperatures at the thermocouple plane were then compared to the measured temperatures at the same locations. The differences between calculated and measured temperatures were within thermocouple measurement accuracy. The mean surface temperature predicted using the one-dimensional correction was within 4 percent of that predicted by the two-dimensional model. Based on these results it was determined that one-dimensional surface temperature correction was adequate.

Heat losses were estimated numerically by assigning zero values for contact resistances between the heater and the fiberglass insulation. This analysis gave an upper bound for the total heat loss since contact resistances reduce heat loss. The analysis showed that the heat loss was a maximum for the lowest heat transfer coefficient, approximately 4 percent, and asymptotically approached 1 percent for higher values of the heat transfer coefficient. Since the contact resistances could not be determined, the authors assumed in their calculations a total heat input equal to the electrical power supplied to the heater uncorrected for heat loss.

Individual measurement uncertainties of the voltage and current transducers, thermocouples, flow meter, geometric parameters, and the one-dimensional temperature correction between the thermocouple plane and the surface were determined and the propagation of these uncertainties to the values of $\overline{Nu}_L/Pr^{1/3}$ and Re were evaluated using the Taylor theorem and the Pythagorean summation of individual uncertainties. These techniques showed maximum uncertainties of 4.5 and 1 percent in determining the values of $\overline{Nu}_L/Pr^{1/3}$ and Re, respectively.

Figure 5 shows the variation of surface temperature with

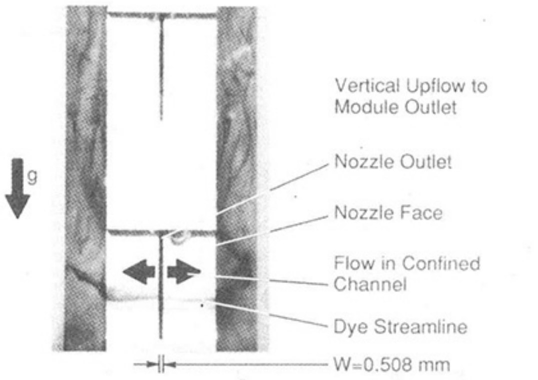

(a) U=.5m/s (Water)

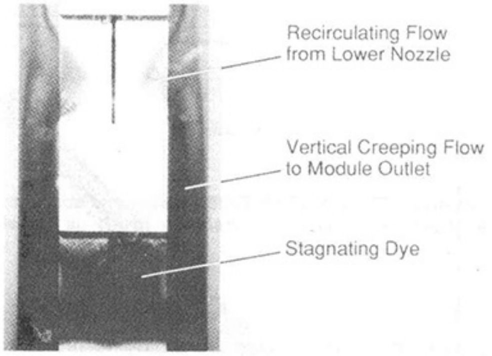

(b) U=.01m/s (Water)

Fig. 8 Visualization of flow in the confinement channel for (*a*) $U = 0.50$ m/s and (*b*) $U = 0.01$ m/s

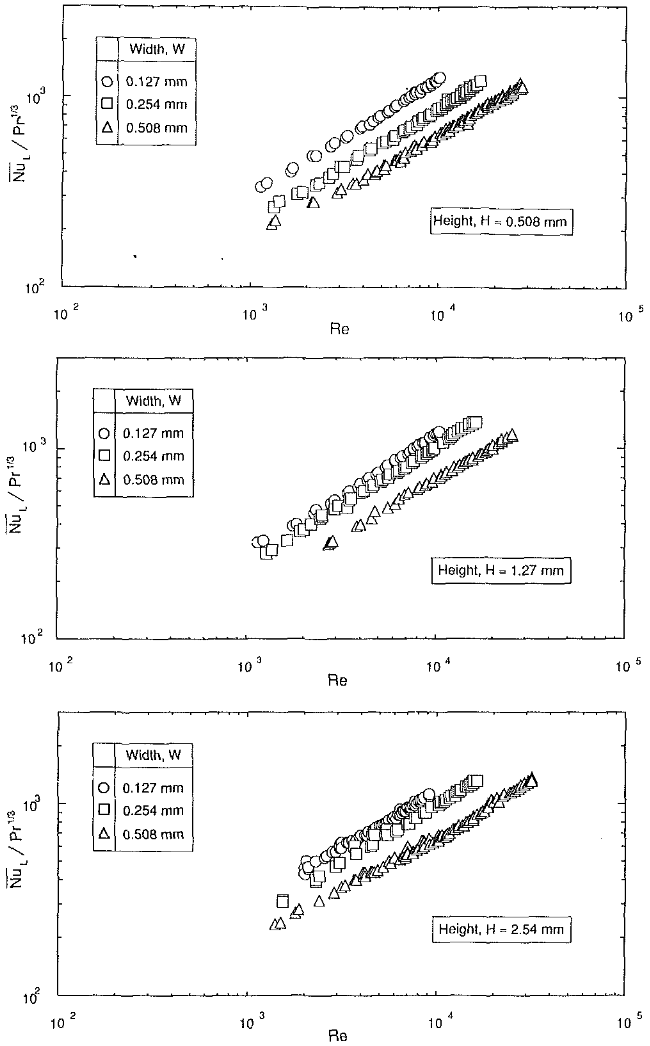

Fig. 9 Effect of Reynolds number and jet width on heat transfer for (*a*) $H = 0.508$ mm, (*b*) $H = 1.27$ mm, and (*c*) $H = 2.54$ mm

distance from the impingement centerline for different flow rates and inlet temperatures as predicted from the two-dimensional correction procedure. Each curve starts with a "cold" point corresponding to the impingement region, followed by a gradual increase in surface temperature with distance along the confinement channel. As expected the temperature gradient increases with increasing heat flux, but the surface temperature variation for the higher heat flux value is within a ±1.8°C temperature band. This result represents strong evidence of the cooling uniformity associated with rectangular jets. This uniformity has, of course, been enhanced by the use of high-purity copper for heater construction. Since copper has approximately twice the thermal conductivity of the silicon used for making chips, multiplying the copper surface temperature variation band by a factor of two would suggest fairly isothermal surface conditions for silicon as well.

3 Results and Discussion

Effect of Nozzle Shape. Tests were conducted to evaluate the influence of the converging section of the nozzle on heat transfer performance. As shown in Fig. 6 three basic shapes were chosen for this comparative study. The width, W, and height, H, were held constant for each nozzle, and the straightening section was set at five times the nozzle width. Figure 7 shows full boiling curves obtained for nozzles with similar H and W, and identical values of jet velocity and inlet temperature. Each boiling curve was initiated in the single-phase region and concluded at the critical heat flux (CHF) point. Figure 7 displays no distinction between the heat transfer characteristics of the three nozzle shapes in the single-phase region. Small deviations occurred only in the boiling region (which is beyond the scope of the present study) until the three curves converged to unique values of critical heat flux and wall superheat. These results indicate that the short straightening section length to nozzle width ratio of five insured uniform flow conditions into the impingement zone and confinement channel. However, the flat and Vee profiles resulted in pressure drops that were, respectively, 15 and 5 percent higher than the curved profile. Thus it was decided that the Vee-profile would be used in the present study since it provided the best compromise between decreased pressure drop and ease of fabrication.

Flow Visualization. Flow uniformity in the cooling module was studied visually and with the aid of still and video photography. The electronic component and back cover plates were replaced with an optical-grade polycarbonate plastic cover, which permitted visual access to the impingement zone. A syringe needle inserted through the front cover plate injected dye into the convergent section of the nozzle. The dielectric fluid was replaced with water for these flow visualization experiments to avoid contamination of the expensive test fluid. The video system traced the path of the streamline of dye as it exited the nozzle, impinged on the polycarbonate window, and proceeded to the module outlet.

Figures 8(*a*) and 8(*b*) display traces of dye at jet velocities of 0.5 and 0.01 m/s, respectively. The dye streamline corresponding to the higher velocity follows a uniform horizontal path unaffected by gravity before exiting into the upflow channel. Close examination of the dye streamline by means of

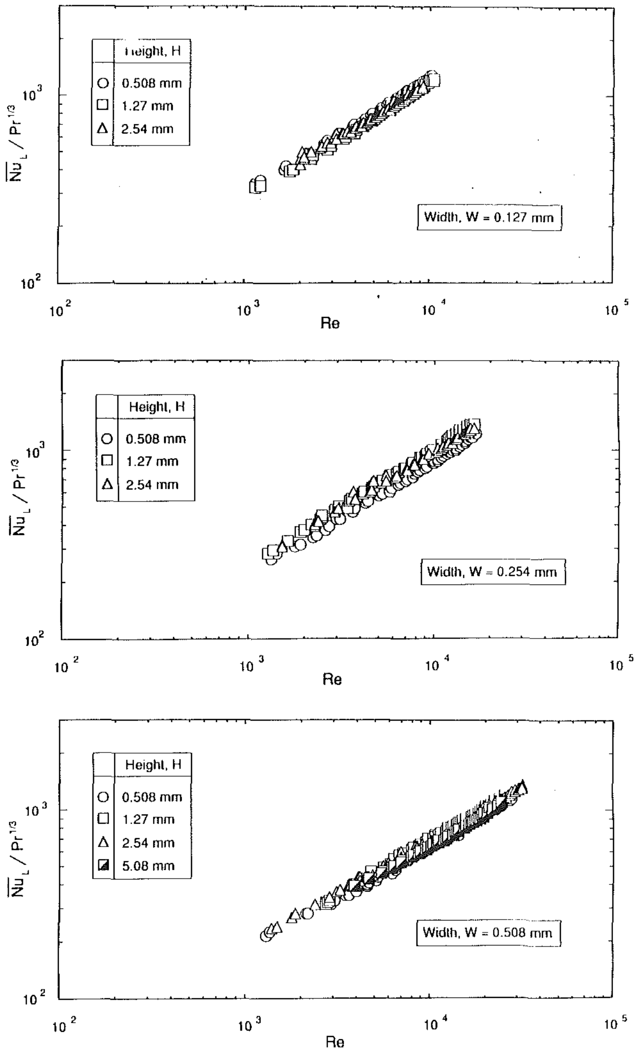

Fig. 10 Effect of Reynolds number and confinement channel height on heat transfer for (*a*) $W = 0.127$ mm, (*b*) $W = 0.254$ mm, and (*c*) $W = 0.508$ mm

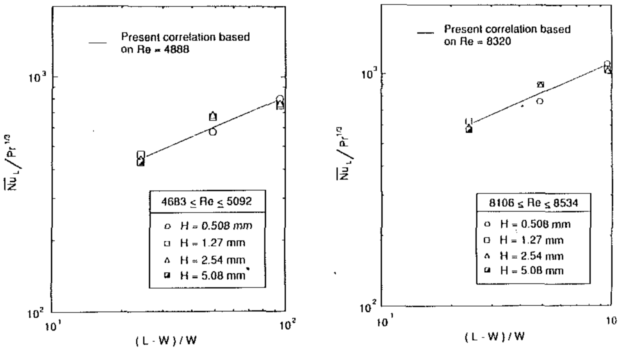

Fig. 11 Variation of the average Nusselt number with the ratio (*L* − *W*)/*W*

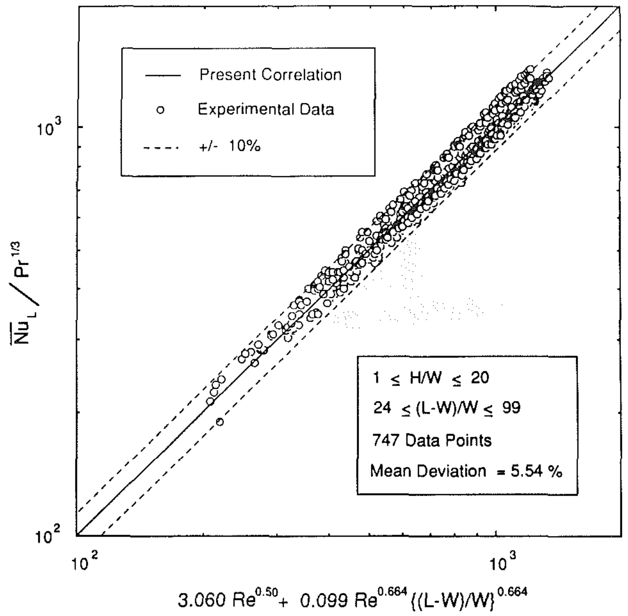

Fig. 12 Correlation of all the present single-phase heat transfer data

both still and video photography showed evidence of strong attachment of the streamline to the transparent cover surface. Figure 8(*b*) shows an extremely small jet velocity (0.01 m/s) inducing stagnation and recirculation in the confinement channel, as well as recirculation from the vertical upflow channel into the confinement channel of the jet vertically above the dyed jet. Transition to the streamlined conditions of the higher velocity case occurred at jet velocities slightly greater than 0.01 m/s.

The flow visualization experiments demonstrate a need for avoiding very small flow velocities to insure uniform and predictable cooling. Fortunately, the need to achieve heat fluxes commensurate with projected cooling loads for high power chips imposed a lower bound on jet velocity of approximately 1.0 m/s, two orders of magnitdue greater than the velocity corresponding to Fig. 8(*b*). This large velocity difference is a partial justification for drawing qualitative conclusions concerning FC-72 flow uniformity from flow visualization experiments performed with water. In any case, the 3×3 chip array was tested for cooling uniformity through heat transfer measurements obtained simultaneously for the nine chips. These multichip results will be discussed later in this section.

Heat Transfer Results. Figures 9 and 10 show data for ten different nozzle configurations. The data are grouped in two different ways, according to height and according to width. The plots reveal a relatively strong heat transfer dependence on nozzle width and virtually no dependence on channel height. This proves that for the conditions of the present study, the flow displays strong attachment to the impingement surface, and the other channel wall plays a minor role in influencing the flow. This statement is further substantiated in Fig. 11, which shows that heat transfer rate is independent of channel height.

The present data were reduced using a superposition technique commonly employed for correlating jet impingement data (Sitharmayya and Raju, 1969; Nakatogawa et al., 1970). This technique involves dividing the heated surface area into two regions: one, directly below the jet, dominated by jet impingement heat transfer, and a second region that extends beyond the impingement region.

The parameter $(L-W)/W$ in Fig. 11 was derived by dividing the heat transfer surface in the present study into two regions: one region, of width W, dominated by jet impingement, and a second region, of width L-W, governed by liquid flow at velocity U parallel to the chip surface. The entire data base of the present study was reduced using this superposition correlation technique. As shown in Fig. 12, the data were fitted by the equation

$$\overline{Nu}_L/Pr^{1/3} = 3.06\ Re^{0.50} + 0.099\ Re^{0.664}[(L-W)/W]^{0.664} \quad (1)$$

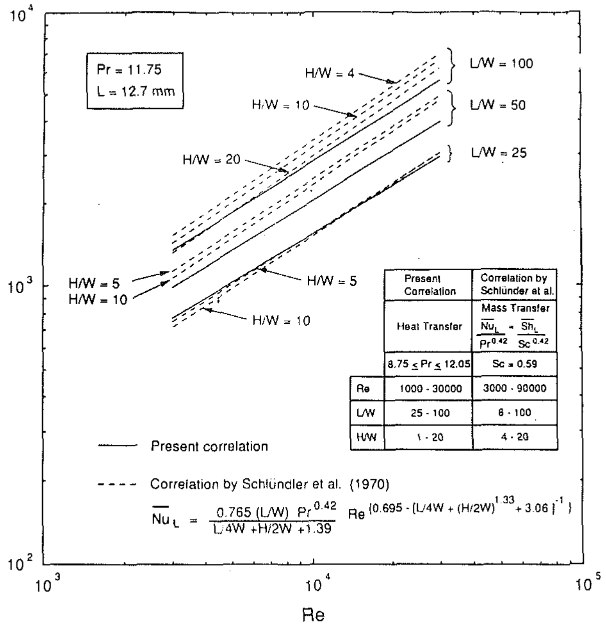

Fig. 13 Comparison of present correlation predictions with those of the Schlunder et al. (1970) correlation for mass transfer to a free gaseous jet

Table 1 Multichip heat transfer results ($W = 0.508$ mm, $H = 2.54$ mm)

Heater Arrangement

1	2	3
4	5	6
7	8	9

Heater Number	Re	$\overline{Nu}_L$	% * Deviation	Re	$\overline{Nu}_L$	% * Deviation	Re	$\overline{Nu}_L$	% * Deviation
1	9529	648.0	-1.36	11876	734.7	-1.79	14374	836.5	-0.13
2	9638	635.1	-3.97	11924	724.4	-3.40	14956	843.8	-1.59
3	9663	663.2	0.12	11915	758.9	1.24	14977	865.0	0.79
4	9699	648.5	-2.76	11937	732.2	-2.42	15079	841.5	-2.34
5	9680	631.2	-4.81	11891	722.3	-3.52	15037	838.1	-2.57
6	9782	623.5	-6.55	11892	719.0	-3.97	15103	815.8	-5.41
7	9702	651.3	-1.91	11798	725.7	-2.62	15069	818.0	-5.03
8	9688	649.8	-2.05	11669	721.1	-2.60	14982	842.0	-1.91
9	9713	645.9	-2.78	11594	698.6	-5.28	15077	820.6	-4.76

* % Deviation = $(\overline{Nu}_L - \overline{Nu}_{L,corr}) / \overline{Nu}_{L,corr} \times 100$; where $\overline{Nu}_{L,corr}$ is the average Nusselt number determined from the present correlation of heater no. 5 data

with a mean deviation (from the correlation) of 5.54 percent. Equation (1) is valid for Reynolds numbers ranging from 1000 to 30,000, and H/W values from 1 to 20. The Prandtl number exponent was fixed at 1/3 due to the limited variation in Prandtl number associated with the data. Dividing the heat transfer surface area into the aforementioned regions actually enhanced correlation accuracy. Attempts at modifying the exponent of the parameter $(L-W)/W$ from that of the Reynolds number in the second right-hand-side term of equation (1) actually increased the magnitude of deviation from the correlation.

It is important to note that, for small values of W, the second term on the right-hand side of equation (1) has a stronger effect on $\overline{Nu}_L$ than the jet impingement term. Hence, for very small values of W (i.e., $W \ll L$), equation (1) yields

$$\bar{h}_L \propto U^{0.664}\,L^{-0.336} \tag{2}$$

independent of jet width.

The EDM machining process utilized in fabricating the nozzle inserts of the present study imposes 0.03 mm as a minimum practical slot width. Using this width as a reference, and a heater length of 12.7 mm, which is typical of electronic chips, shows that the jet impingement term of equation (1) accounts for only 13.9 and 8.4 percent of the sum of the superposition terms for Re = 1000 and 30,000, respectively.

Equation (2) demonstrates that, for given fluid properties and chip length, the cooling rate can be increased by increasing jet velocity. The coolant flow rate may be minimized by reducing jet width without compromising chip cooling as long as jet velocity is set to the desired value. It is important to note that the pressure drop across the jet and confinement channel never exceeded 20 psi for the conditions of the present study. For a fixed flow rate of 0.043 gpm per chip, reducing nozzle width from 0.127 mm ($U = 0.413$ m/s) to 0.127 mm ($U = 1.69$ m/s) increased the pressure drop from less than 0.01 psi to only 0.10 psi. The highest pressure drop value of 20 psi was achieved at a flow rate of 0.38 gpm per chip using the smallest jet with of 0.127 mm (i.e., $U = 15$ m/s).

Figure 13 shows a comparison of predictions based upon the present correlation to those of the Schlunder et al. (1970) correlation for mass transfer to a free gaseous jet. The fair agreement between the two correlations is further evidence that, for conditions of the present study, the nozzle confinement plate has a weak effect on fluid flow and, therefore, the heat transfer is independent of channel height. As the ratio $(L-W)/W$ decreases, which corresponds to an increasing jet width, the heat transfer becomes more dominated by impingement, resulting in better agreement between the two correlations.

Module Cooling Uniformity. The heat transfer results of tests performed using the cooling module with a 3 × 3 array of simulated chips are detailed in Table 1. The heat transfer data for each of the nine chips are compared to values determined from equation (1) for the corresponding Reynolds number. Except for one measurement, the deviations of individual chip data from the correlation were less than the mean deviation associated with generating the correlation itself using heater number 5 data. These results strongly support the feasibility of using the present jet-impingement geometry and cooling module packaging technique to insure cooling uniform for large arrays of chips.

4 Summary

Experiments were performed to investigate single-phase heat transfer from a smooth 12.7 × 12.7 mm^2 simulated chip to a two-dimensional jet of dielectric Fluorient FC-72 liquid issuing from a thin rectangular slot into a channel confined between the chip surface and nozzle plate. Specific findings from the study are also as follows:

1 Cooling via rectangular jets maintains nearly isothermal chip surface conditions.

2 A nozzle straightening second 5 times the nozzle width provides uniform flow into the impingement region regardless of the nozzle inlet geometry. The choice of nozzle shape may therefore be based solely on the considerations of pressure drop and ease of fabrication.

3 The combined jet impingement/confinement channel configuration provides uniform and predictable flow parallel to the chip surface.

4 The chip cooling rate is independent of channel height for the conditions of the present study. The average Nusselt number is more strongly dependent upon jet velocity and jet width.

5 The chip cooling rate is determined by the contributions of a jet impingement region and region of flow parallel to the chip surface. A correlation based upon this superposition scheme was found successful at fitting all the data of the present study with a mean deviation of 5.54 percent. The correlation yields a vanishing effect of jet width on average chip heat transfer coefficient for small values of jet width. Thus, the chip cooling rate may be increased by increasing jet velocity alone. At the same time, the cooling flow rate may be minimized by reducing jet width without compromising chip cooling as long as jet velocity is set to the desired value.

6 The multijet cooling module is very successful in insuring equal flow distribution and heat dissipation from each of the nine simulated chips. The agreement between heat transfer data obtained for each of the nine chips with the correlation based on single chip data is strong evidence that the present module geometry is feasible for cooling large arrays of chips.

Acknowledgments

This material is based upon work supported by the National Science Foundation under Grant No. CBT-8618949. The authors appreciate this support and thank the Industrial Chemical Products Division of 3M for providing test fluid (FC-72) samples for the present study.

References

Bar-Cohen,, A., Mudawar, I., and Whalen, B., 1986, "Future Challenges for Electric Cooling," *Research Needs in Electronic Cooling*, F. P. Incropera, ed., published by the National Science Foundation and Purdue University, pp. 70-77.

Downs, S. J., and James, E. H., 1987, "Jet Impingement Heat Transfer—A Literature Survey," ASME Paper No. 87-HT-35.

Goldstein, R. J., and Timmers, J. F., 1982, "Visualization of Heat Transfer From Arrays of Impinging Jets," *Int. J. Heat Mass Transfer*, Vol. 25, pp. 1857-1868.

Jiji, L. M., and Dagan, Z., 1987, "Experimental Investigation of Single Phase Multi-Jet Impingement Cooling of Array of Microelectronic Heat Sources," *Proc. Int. Symp. on Cooling Technology for Electronic Equipment*, Honolulu, HI, pp. 265-283.

Ma, C. F., and Bergles, A. E., 1983, "Boiling Jet Impingement Cooling of Simulated Microelectronic Chips," *Heat Transfer in Electronic Equipment*, ASME HTD-Vol. 28, pp. 5-12.

Maddox, D. E., and Mudawar, I., 1989, "Single and Two-Phase Convective Heat Transfer From Smooth and Enhanced Microelectronic Heat Sources in a Rectangular Channel," ASME JOURNAL OF HEAT TRANSFER, Vol. 111, pp. 1045-1052.

Mudawar, I., and Anderson, T. M., 1989, "High Flux Electronic Cooling by Means of Pool Boiling—Part I: Parametric Investigation of the Effects of Coolant Variation, Pressurization, Subcooling and Surface Augmentation," *Heat Transfer in Electronics*, R. K. Shah, ed., ASME HTD-Vol. 111, pp. 35-50.

Mudawar, I., and Maddox, D. E., 1989a, "Critical Heat Flux in Subcooled Flow Boiling of Fluorocarbon Liquid on a Simulated Electronic Chip in a Vertical Rectangular Channel," *Int. J. Heat Mass Transfer*, Vol. 32, pp. 379-394.

Mudawar, I., and Maddox, D. E., 1989b, "Enhancement of Critical Heat Flux From High Power Microelectronic Heat Sources in a Flow Channel," *Heat Transfer in Electronics*, ASME HTD-Vol. 111, pp. 51-58.

Nakatogawa, T., Nishiwaki, N., Hirata, M., and Torri, K., 1970, "Heat Transfer of Round Turbulent Jet Impinging Normally on a Flat Plate," *Proc. 4th Int. Heat Transfer Conf.*, Paris-Versailles, France, Vol. 2, pp. 1-11.

Patankar, S. V., 1980, *Numerical Heat Transfer and Fluid Flow*, Hemisphere Publishing Corp., New York.

Ramadhyani, S., and Incropera, F. P., 1987, "Forced Convection Cooling of Discrete Heat Sources With and Without Surface Enhancement," *Proc. Int. Symp. on Cooling Technology for Electronic Equipment*, Honolulu, HI, pp. 249-264.

Samant, K. R., and Simon, T. W., 1986, "Heat Transfer From a Small, High-Heat-Flux Patch to a Subcooled Turbulent Flow," ASME Paper No. 86-HT-22.

Schlunder, E. U., Krotzch, P., and Hennecke, F. W., 1970, "Gesetzmassigkeiten der Warme- und Stoffubertragung bei der Prallstromung aus Rund- und Schlitzdusen," *Chemie Ingenieur Technik*, Vol. 42, pp. 333-338.

Sitharmayya, S., and Raju, K. S., 1969, "Heat Transfer Between an Axisymmetric Jet and a Plate Held Normal to the Flow," *The Canadian Journal of Chemical Engineering*, Vol. 47, pp. 365-368.

Local Convective Heat Transfer From a Heated Surface to a Planar Jet of Water With a Nonuniform Velocity Profile

D. H. Wolf

R. Viskanta

F. P. Incropera

Heat Transfer Laboratory,
School of Mechanical Engineering,
Purdue University,
West Lafayette, IN 47907

Experiments have been conducted on a planar, free surface jet of water to investigate the effects of a nonuniform velocity profile on the local convection coefficient for a uniform heat flux surface. Heat transfer coefficient distributions were measured for heat fluxes ranging from 0.24 to 1.47 MW/m² and for Reynolds numbers (based on the average nozzle velocity and nozzle width) from 15,000 to 54,000. This range of flow conditions yielded turbulent velocity profiles similar to those of channel flow. Results have been obtained for both single-phase convection and nucleate boiling. Relative to results for a uniform velocity profile, the nonuniform profile was found to enhance heat transfer significantly. However, enhancement is attributed primarily to increased levels of turbulence and only secondarily to changes in the velocity profile.

Introduction

Increasing involvement with high heat flux applications requires the design of effective cooling schemes. Often the problem is compounded by restrictions on available space, choice of coolant, and local environmental conditions. The use of liquid jet impingement to dissipate large heat fluxes is being widely considered with the cooling of neutron beam targets, microelectronic components, and primary metals among the many possible applications. This study is concerned with impinging liquid jets characterized by a free surface and, more specifically, on the effect of the jet velocity profile on surface heat transfer.

Despite the existence of turbulence within the impinging jet, the boundary layer that develops along the impingement surface is laminar for some finite distance from the stagnation line. Nevertheless, the presence of turbulence in the free stream of a favorable pressure gradient flow has been known to yield sizable differences between experimental data and predictions for laminar flow. However, in the absence of a more representative model, analytical solutions for laminar, impinging flows have been used to obtain a first-order estimate for the energy and momentum transfer. The Falkner-Skan class of uniform flows past a wedge of included angle $\beta\pi$ typifies such solutions (Falkner and Skan, 1931).

For $\beta=1$, the Falkner-Skan equations describe local transport processes for a flow of infinite extent impinging normal to a surface. However, for jets of finite width, the solution may only be applied to conditions in the stagnation region. Evans (1962) obtained solutions for uniform surface and free-stream temperatures, while Levy (1952) showed that for $\beta=1$, solutions for the heat transfer coefficient are the same, irrespective of whether the boundary condition is one of uniform surface temperature or heat flux. Accordingly, the heat transfer coefficient at the stagnation line of a uniform heat flux surface cooled by a laminar, impinging jet may be expressed as

$$h_0=0.571k\left(\frac{C}{\nu}\right)^{1/2}\mathrm{Pr}^{0.373} \tag{1}$$

where the coefficient (0.571) and the Prandtl number exponent (0.373) were chosen as a best fit of the theoretical results of Evans (1962) for $0.7\leq \mathrm{Pr}\leq 10$. The streamwise velocity gradient (C) for a finite width jet (see Fig. 1) may be expressed as

$$C=\frac{du_\delta}{dx}=b\frac{V_j(0)}{W_j} \tag{2}$$

where b is a coefficient that varies with the shape of the velocity profile, $V_j(0)$ is the local jet velocity on the stagnation line, and W_j is the width of the jet. Hence, for a prescribed fluid (prescribed k, ν, and Pr), heat transfer at the stagnation line is determined by the velocity gradient C. Through the velocity gradient, the effects of the stagnation line velocity and the jet width are apparent. With increasing velocity, the increased

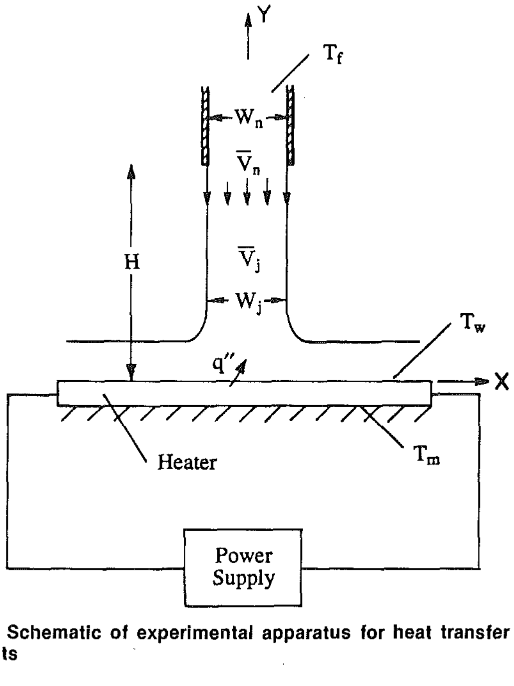

Fig. 1 Schematic of experimental apparatus for heat transfer measurements

---

Contributed by the Heat Transfer Division for publication in the JOURNAL OF HEAT TRANSFER. Manuscript received by the Heat Transfer Division January 16, 1990; revision received April 3, 1990. Keywords: Forced Convection, Jets, Materials Processing and Manufacturing Processes.

advection and thinning of the hydrodynamic and thermal boundary layers enhance heat transfer. Moreover, since complete acceleration of the fluid along the impingement surface normally occurs in less than three jet widths, a decrease in the jet width causes the fluid to accelerate over a shorter distance, thereby increasing the velocity gradient and heat transfer coefficient. Conversely, the effects of the jet velocity profile are not so apparent. Such effects have received only limited consideration, and published work has been restricted to jets for which nozzle Reynolds numbers suggest laminar flow and a parabolic velocity profile.

Experimental investigations (Scholtz and Trass, 1970; Sparrow and Wong, 1975), along with numerous analytical and numerical studies (Scholtz and Trass, 1970; Sparrow and Lee, 1975; van Heiningen et al., 1976; Saad et al., 1977; Abrosimov, 1984; van der Meer, 1987), have consistently shown stagnation line heat or mass transfer coefficients for a parabolic velocity profile that were approximately twice those of a uniform profile for a fixed average velocity. Several studies (van Heiningen et al., 1976; Saad et al., 1977; Deshpande and Vaishnav, 1982) have also shown concurrent enhancements in the wall shear stress for a parabolic profile that range from two to four times that for a flat profile, depending on the Reynolds number.

Augmentation of heat transfer at the stagnation line depends on the manner in which the velocity profile affects the velocity gradient through the coefficient b and the local velocity $V_j(0)$ of equation (2). Sparrow and Lee (1975) have analytically shown that the value of b for a near-parabolic velocity profile (a cosine function was utilized for mathematical simplicity) is 1.93, while Vader et al. (1990b) have shown that, for a uniform profile, b is equal to 0.785. Additionally, for a fixed average velocity, the value of $V_j(0)$ for a near-parabolic profile was shown to be 57 percent larger than for a uniform profile. The combined effect of differences in b and $V_j(0)$ gives a velocity gradient that is nearly four times larger for a near-parabolic profile than for a uniform profile, yielding approximately a twofold enhancement in heat transfer.

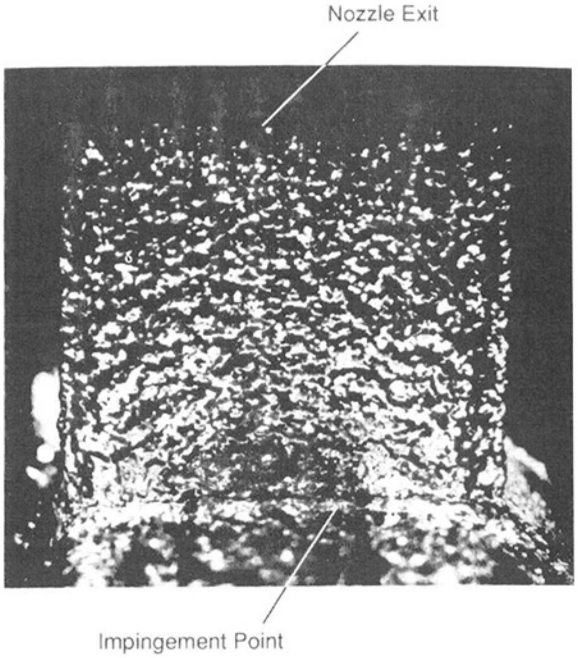

Fig. 2 High-speed photograph revealing the free surface structure of the jet for $\bar{V}_j = 4.5$ m/s, $W_n = 5.1$ mm, and $\mathrm{Re}_n = 27{,}100$

To the authors' knowledge, there has been no prior study of the effects of the velocity profile on impingement heat transfer under turbulent flow conditions. Turbulent and laminar nozzle flows differ in two fundamental ways. First, the fully developed velocity profile for turbulent flow is much more uniform than that for laminar flow. Hence, large differences in the coefficient b and the centerline velocity $V_j(0)$ associated with a parabolic and uniform velocity profile would not be expected for turbulent nozzle flows. A turbulent velocity profile would therefore be expected to yield only moderate enhancements in heat transfer relative to a uniform profile for a fixed flow rate (constant $\bar{V}_j$). Second, equation (1) predicts heat transfer in a laminar boundary layer without free-stream turbulence. It has been shown that free-stream turbulence in a flow with zero pressure gradient affects the transition from a laminar to turbulent boundary layer but has no impact on heat transfer (Kestin et al., 1961). Conversely, free-stream turbulence in the presence of a favorable pressure gradient can induce considerable heat transfer enhancement in a laminar boundary layer (Kestin et al., 1961; Kestin, 1966). Stagnation flow provides ideal conditions for such enhancement due to the strong pressure gradient that accelerates the fluid along

Nomenclature

A_n = nozzle discharge area
b = dimensionless velocity gradient = $CW_j/V_j(0)$
C = velocity gradient = du_δ/dx
COV = coefficient of variation
$f(\bar{x})$ = function described by equation (11)
g = gravitational acceleration
G = volume flow rate
h_x = local heat transfer coefficient $= q''/(T_w - T_f)$
H = distance between the nozzle discharge and the impingement surface
k = thermal conductivity of the fluid
$\mathrm{Nu}_{j,x}$ = local Nusselt number = $h_x W_j/k$
$P(x)$ = local static pressure along the impingement surface
$P_j(x)$ = local stagnation pressure within the jet
$\bar{P}$ = dimensionless static pressure = $P(x)/P(0)$
Pr = Prandtl number
q'' = surface heat flux
Re_c = critical Reynolds number = $u_\delta x/\nu$
Re_j = jet Reynolds number = $\bar{V}_j W_j/\nu$
Re_n = nozzle Reynolds number = $\bar{V}_n W_n/\nu$
T_f = fluid (jet) temperature
T_{film} = film temperature $(T_f + T_w)/2$
T_m = measured temperature
T_w = wall temperature
u_δ = local free-stream value of the x component of velocity
$V_j(x)$ = local fluid velocity within the jet [equation (6)]
$\bar{V}_j$ = average jet velocity at impingement [equation (3)]
$\bar{V}_n$ = average jet velocity at the nozzle discharge [equation (5)]
W_j = width of the jet at impingement [equation (4)]
W_n = discharge width of the nozzle
x = coordinate along the impingement surface with origin at the stagnation point
$\bar{x}$ = dimensionless streamwise distance = x/W_j
y = coordinate perpendicular to the impingement surface with origin at the stagnation point
β = coefficient prescribing included wedge angle for Falkner–Skan type flows
ν = kinematic viscosity
ρ = density of the fluid
σ = sample standard deviation

the surface. For a cylinder in crossflow, it has been shown that an increase in the free-stream turbulence intensity from 0 to 3 percent can yield enhancements in the local heat transfer coefficient by as much as 80 percent (Kestin, 1966; Lowery and Vachon, 1975). Similar trends have been reported for impinging jets (Gardon and Akfirat, 1965; Sparrow and Wong, 1975; Vader et al., 1990b; Zumbrunnen et al., 1989). Clearly, altering the shape of a velocity profile in a high Reynolds number flow will also modify its turbulence characteristics, suggesting that for turbulent jets of differing velocity profile, the enhancement prescribed by equation (1) would be superimposed on that due to free-stream turbulence.

A major source of data obtained for turbulent jets with near-uniform velocity profiles is the recent work of Vader et al. (1990b). The measurements were obtained using the experimental apparatus employed in this investigation, thus providing an excellent basis for a comparison of results. Vader and co-workers employed a planar, converging nozzle, specially designed to produce a low-turbulence jet with a nearly uniform velocity profile. The nozzle for the current investigation was a parallel-plate channel, with no attempts made to abate turbulence.

Experimental Apparatus and Methods

A schematic of the experimental apparatus used to obtain the heat transfer data is shown in Fig. 1. The system was designed to obtain nonintrusive measurements of the local heat transfer coefficient through knowledge of the surface heat flux (q''), free-stream fluid temperature (T_f), and local wall temperature (T_w).

The jet consisted of deionized water that issued into air (Fig. 2) from a rectangular channel 10.2 mm in width (W_n), 102 mm in depth, and with a development length of 895 mm (48.3 hydraulic diameters). The jet descended normal to a uniformly heated strip (Haynes Alloy 230) that was 35.7 mm wide, 260 mm long, and 0.660 mm thick. The plate was subjected to direct current, Joulean heating over 119 mm of its total length by a power supply with peak output of 15 kW (1500 A at 10 V). The nozzle-to-surface spacing (H) was maintained at 89.7 mm for all experiments. The jet (free-stream) temperature was measured with a thermocouple mounted in a plenum chamber that preceded the nozzle entrance and was held constant at 30°C. The average jet velocity ($\bar{V}_j$) and width (W_j) were based on the conditions at the nozzle exit ($\bar{V}_n$ and W_n) but corrected for gravitational acceleration by expressions of the form

$$\bar{V}_j = (\bar{V}_n^2 + 2gH)^{1/2} \tag{3}$$

$$W_j = W_n[\bar{V}_n/\bar{V}_j] \tag{4}$$

where

$$\bar{V}_n = G/A_n \tag{5}$$

The surface heat flux and local wall temperature were inferred from a two-dimensional, finite difference solution of the energy equation within the heater. Boundary conditions were based on temperatures measured at the dry surface of the heater (T_m) using 21 spring-loaded thermocouples emanating from an insulated substrate and positioned at 5.1 mm intervals along the streamwise midline. Measurement of the voltage drop across the heated section and the electrical resistivity of the heater enabled evaluation of the heat generation. Experimental details, including data acquisition and reduction procedures, may be found elsewhere (Vader, 1988; Wolf, 1989; Vader et al., 1990a).

In addition to heat transfer measurements, static and stagnation pressure data were obtained to determine the velocity profile within the jet and the subsequent velocity gradient along the impingement surface. In both regions, a pressure tap was connected to a water manometer and moved through the flow by means of a calibrated translation device (Zumbrunnen, 1988; Wolf, 1989). Simultaneous measurement of local static and stagnation pressures made within the jet yields the local velocity through use of Bernoulli's equation. Independent measurement of the static pressure within the jet revealed that conditions were atmospheric throughout the jet. The stagnation pressure was measured with a probe constructed from stainless steel capillary tubing, with inner and outer diameters of 0.48 mm and 0.79 mm, respectively. The probe was held in a streamlined mount, and its tip was positioned a minimum of five nozzle widths from the nozzle exit. The local fluid velocity was calculated from the stagnation pressure data by the relation

$$V_j(x) = (2P_j(x)/\rho)^{1/2} \tag{6}$$

Measurements were taken at intervals of 0.35 mm and only at locations where the probe was completely within the jet to avoid entrapment of air at the interface. For this reason, velocity data are not reported for the outer 20 percent of the jet's width. Static pressure measurements were taken along the impingement surface with a wall tap located on a flat, acrylic plate. The diameter of the tap was 0.15 mm, and data were obtained at intervals of 1.06 mm.

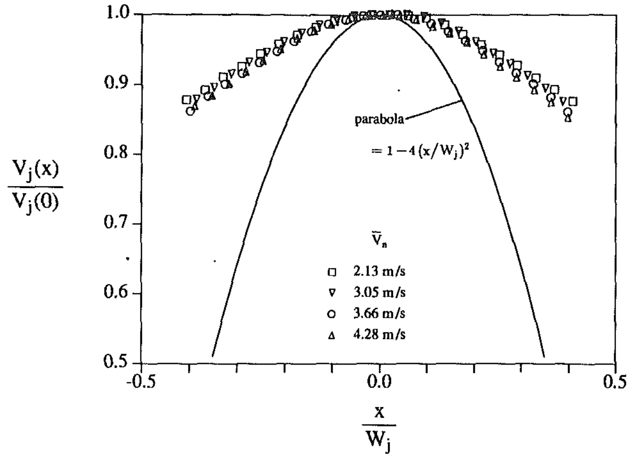

Fig. 3 Nondimensional velocity profile within the jet at an axial distance of 57.2 mm from the nozzle exit and 27,100≤Re_n≤54,300

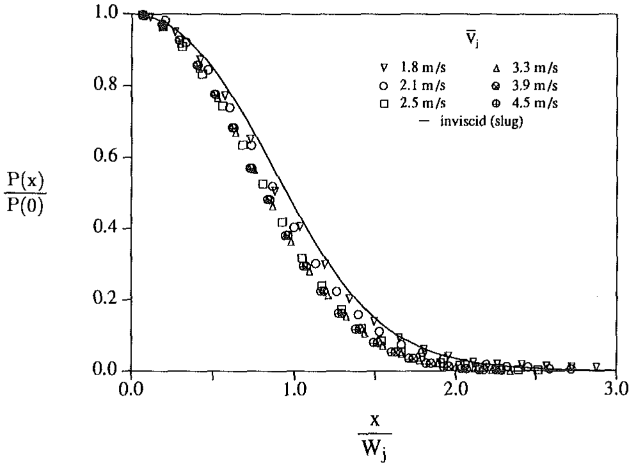

Fig. 4 Static pressure distribution along the impingement surface

An uncertainty analysis performed in accordance with the method suggested by Moffat (1988) for single sample experiments has been applied to the *worst-case* conditions of this study. The results of that analysis are as follows: heat transfer coefficient (h_x), ±28 percent; average jet velocity ($\bar{V}_j$), ±3 percent; jet width (W_j), ±7 percent; Nusselt number ($Nu_{j,x}$) ±28 percent; Reynolds number (Re_j), ±8 percent; stagnation pressure $[P_j(x)]$, ±0.5 percent; and stagnation line velocity $[V_j(0)]$, ±0.3 percent. Repeatability of the heat transfer data was commonly achieved to within ±5 percent. The values of uncertainty for the heat transfer coefficient and Nusselt number are relatively large compared to values quoted by Vader et al. (1990b), which are attributed solely to the uncertainty in the measured temperature difference $(T_m - T_f)$. In order to utilize the results of Vader and co-workers as a baseline condition for a near-uniform jet velocity profile, their operating conditions (q'', $\bar{V}_j$, and T_f) needed to be duplicated. However, the cooling efficiency of the present jet produced temperature differences that were smaller than those of Vader, yielding higher levels of uncertainty. Experimental conditions least susceptible to error had a level of uncertainty in the stagnation line Nusselt number $(\mathrm{Nu}_{j,0})$ of ±10 percent.

Results and Discussion

Hydrodynamic Characteristics. Velocity profile data are presented in Fig. 3 for four representative flow conditions at a distance of 57.2 mm from the nozzle exit. The results reveal a nonuniform profile for which the velocity drops to nearly 85 percent of the centerline value at locations near the air-liquid interface. Although the profile lacks the curvature of a parabola, it contains sufficient nonuniformity to increase the centerline velocity, $V_j(0)$, by as much as 11 percent relative to the average jet velocity. Based on equations (1) and (2), this increase suggests heat transfer enhancement of approximately 5 percent.

Figure 4 shows the surface static pressure data for each of the average velocities examined, as well as the static pressure distribution for a finite width jet of uniform (slug) velocity profile (Milne-Thomson, 1955). Relative to the distribution for a uniform profile, the measured pressures decay more rapidly, implying higher magnitudes of the fluid acceleration (C) away from the stagnation zone. The static pressure data may be used to infer the local free-stream velocity gradient through the relation

$$C = \frac{du_\delta}{dx} = -\frac{dP}{dx}(2\rho[P(0) - P(x)])^{-1/2} \tag{7}$$

derived from Euler's equations (Wolf, 1989). This expression may be nondimensionalized to obtain the following relation for the coefficient b:

$$b = \frac{W_j}{V_j(0)}C = -\frac{1}{2}\frac{d\bar{P}}{d\bar{x}}(1 - \bar{P})^{-1/2} \tag{8}$$

where $\bar{P}$ and $\bar{x}$ are the dimensionless static pressure $[P(x)/P(0)]$ and streamwise distance (x/W_j), respectively.

For a given average velocity, the data of Fig. 4 may be fit with a spline to enable calculation of the pressure gradient. Although differentiation of experimental data is susceptible to error, it may be used to estimate relative magnitudes of the various factors that augment heat transfer. Use of the data for $\bar{V}_j = 4.5$ m/s yields a value of $b = 0.968$, while values for the uniform and near-parabolic profiles are 0.785 and 1.93, respectively. Hence, the value of b corresponding to the experimental conditions of this study is approximately 20 percent larger than that for the uniform profile, which according to equations (1) and (2), translates to roughly an additional 10 percent enhancement in the heat transfer coefficient. Combining the foregoing effects, heat transfer coefficients for the turbulent, nonuniform profile should be at least 15 percent larger than those for a uniform profile.

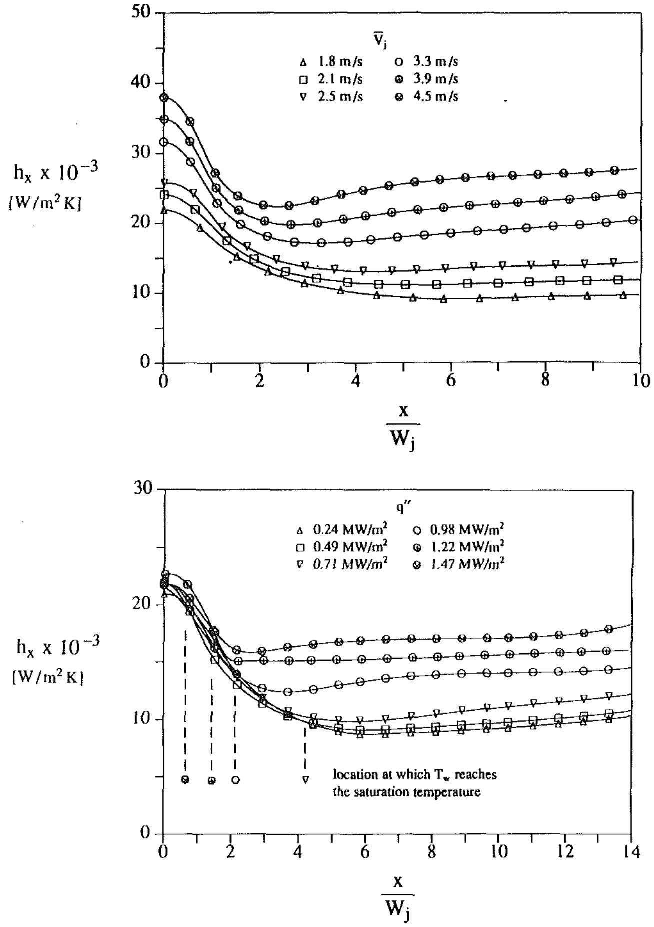

Fig. 5 Distribution of local heat transfer coefficient: (*a*) effect of average jet velocity for q'' = 0.49 MW/m², and (*b*) effect of surface heat flux for $\bar{V}_j$ = 1.8 m/s

Heat Transfer Characteristics. Figure 5(*a*) shows the distribution of the heat transfer coefficient along the heater surface for different jet velocities and a heat flux of 0.49 MW/m². The symbols represent locations of temperature measurement. The measured temperatures were smoothed by a least-squares cubic spline fit prior to solving the heat conduction equation in the heater to determine the local wall temperature (T_w), and the solid lines depict the corresponding curve fits. All of the data in the figure represent single-phase convection over the entire surface.

For a given jet velocity, the heat transfer coefficient is largest at the stagnation line, where the thermal and hydrodynamic boundary layers are thinnest. The fluid begins from rest and is accelerated downstream by the imposed pressure gradient. Concurrently, the hydrodynamic and thermal boundary layer thicknesses increase, with an attendant increase in the thermal resistance between the wall and the low-temperature free-stream fluid (estimates indicate that both boundary layer dimensions fall within the thickness of the liquid layer for all operating conditions investigated). Since the surface heat flux is uniform, the local heat transfer coefficient decreases monotonically (T_w increases) with axial distance until instabilities in the flow bring about a transition to turbulence. At the onset of transition, low-temperature liquid from the free-stream is mixed within the boundary layer, thereby increasing the heat transfer coefficient. The effect becomes more pronounced with increasing jet velocity. Although the heater was not sufficiently long to provide a fully developed turbulent flow, transition to turbulence would eventually be complete, causing a second decrease in the convection coefficient. The figure also reveals that the effect of increasing the average jet velocity is to increase the heat transfer coefficient at all locations on the surface. This result is expected, at least at the stagnation line, from the Falkner-Skan analysis [equation (1)].

Although T_w increases with increasing heat flux, changes in the heat transfer coefficient should be small and attributable

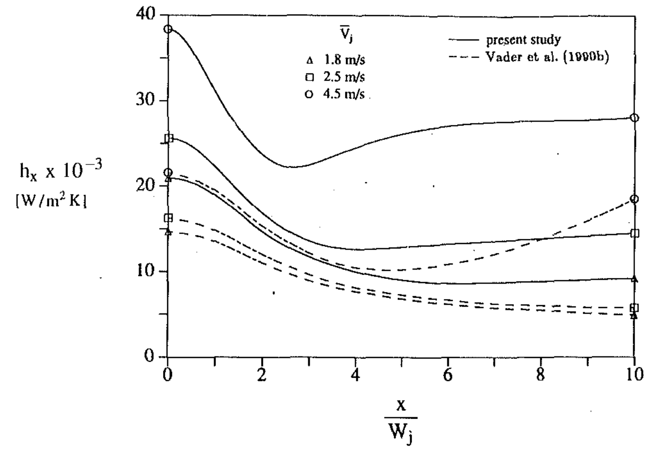

Fig. 6 Comparison of local heat transfer coefficients for nonuniform and uniform (Vader et al., 1990b) jet velocity profiles when $q'' = 0.24$ MW/m²

Table 1 Enhancement of stagnation line heat transfer over that published by Vader et al. (1990b)

q'' (MW/m²)	$\bar{V}_j$ (m/s)	$\frac{Re_n}{10^4}$	$Nu_{j,0}$	$Nu_{j,0_{Vader}}$	$\frac{Nu_{j,0}}{Nu_{j,0_{Vader}}}$
0.24	1.8	1.55	231	160	1.44
0.49	"	"	238	161	1.48
0.71	"	"	231	162	1.43
0.24	2.5	2.71	355	224	1.58
0.49	"	"	351	229	1.53
0.71	"	"	355	229	1.55
0.98	"	"	348	227	1.53
0.24	4.5	5.43	598	335	1.79
0.49	"	"	588	335	1.76
0.98	"	"	553	339	1.63
1.22	"	"	585	347	1.69
0.24	2.1	2.14	295	187	1.58
0.24	3.3	3.88	469	270	1.74
0.98	3.3	3.88	441	278	1.59
0.98	3.9	4.65	497	308	1.61

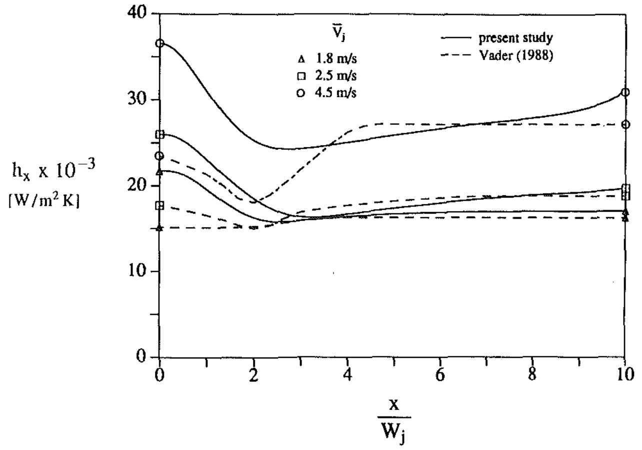

Fig. 7 Comparison of local heat transfer coefficients for nonuniform and uniform (Vader, 1988) jet velocity profiles when $q'' = 1.47$ MW/m²

to variations in the thermophysical properties. Figure 5(*b*) shows the effects of surface heat flux on the heat transfer coefficient for an average jet velocity of 1.8 m/s. As expected, differences in the heat transfer coefficient near the stagnation line are minimal, and for several jet widths downstream, there is reasonable agreement between results for the three lowest heat fluxes. However, for the heat fluxes exceeding 0.71 MW/m², deviations surpass those attributable to thermophysical property variations. Temperature profiles [not shown but reported elsewhere (Wolf, 1989)] reveal that, for fluxes of 0.24 and 0.49 MW/m², heat transfer is solely by single-phase convection, while only minimal local boiling is experienced for 0.71 MW/m². Additional increases in the heat flux cause the onset of local boiling to occur at streamwise locations progressively nearer the stagnation line (Fig. 5*b*).

Comparison With Results for a Uniform Velocity Profile. Figure 6 compares the local heat transfer coefficient distributions obtained in this study with those of Vader et al. (1990b) for several jet velocities at a surface heat flux of 0.24 MW/m². Enhancement of the heat transfer coefficients over those obtained by Vader is considerable and occurs over the entire surface. Table 1 shows stagnation line enhancement factors for a variety of average velocities and heat fluxes.

In addition to the enhancement, it is apparent that the convection coefficient distributions differ in shape. Specifically, the location of the onset of turbulence (a minimum in h_x) occurs at an axial position that is closer to the stagnation line for the nonuniform velocity profile. For example, the minimum in the heat transfer coefficient for the nonuniform profile occurs at $x/W_j \approx 6$ for $\bar{V}_j = 1.8$ m/s. For the uniform profile a minimum is not achieved within ten jets widths. For the higher velocities, a minimum occurs within the heater length but at an x/W_j that is approximately twice that for the nonuniform profile.

Analysis of the pressure data in conjunction with equations (1) and (2) has shown that, for $\bar{V}_j = 4.5$ m/s, enhancements in the stagnation line heat transfer should be approximately 15 percent in the absence of free-stream turbulence. However, the data in Fig. 6 reveal augmentations of nearly 80 percent, suggesting that the additional enhancement must be due to differences in the turbulence characteristics of the impinging jets.

It is well established that subjecting a fluid to rapid acceleration (favorable pressure gradient) induces substantial damping of turbulence. Sizable pressure gradients for internal flows may be achieved through large contraction ratios, for which transition from fully developed turbulent flow to a near-laminar state is known to occur (Hoyt and Taylor, 1985; Vader et al., 1990a). Vader's nozzle was designed to exploit the phenomenon of relaminarization by using a 5:1 contraction ratio over an axial length 6½ times the inlet width. As discussed earlier, the nozzle used in this study was a parallel-plate design that made no attempt to dampen turbulence.

A thorough search of the literature was unable to reveal any type of quantitative velocity or turbulence measurement in a free-surface jet, yet the number of investigations that considered turbulence measurements in submerged jets (free, wall, and impinging) is overwhelming. Clearly, one reason why the free-surface jet has received so little attention is due to the formidable nature of the measurement. In the jet itself, measurements using a laser-Doppler anemometer (LDA) are unacceptable due to the continuously changing and rough contour of the free surface (Fig. 2). The LDA provides turbulence information at the point where the two beams intersect. When the beams cross an optically smooth interface that separates media of differing densities, the location of the beam intersection is highly predictable. The coarse interface of the free surface jet would preclude calculation of the beam intersection, thus causing any measurements to be meaningless. This suggests that the only viable alternative to an LDA would be a hot-film anemometer system. However, the LDA may be better suited along the impingement surface, due to the small thickness and sensitive nature of the liquid layer flowing in the streamwise direction. Azuma and Hoshino (1983) have obtained velocity measurements only in the parallel-flow region of an impinging, axisymmetric jet. The measurement scheme involved positioning of the beams within the liquid film from beneath a glass impingement surface. Measurements of the

Table 2 Average critical Reynolds number data for full range of heat fluxes. [Key: q'' = surface heat flux; sample = number of experiments; $(T_w - T_f)$ = average temperature difference at point of transition; Re_c = average critical Reynolds number; σ = sample standard deviation of Re_c; COV = coefficient of variation = σ/Re_c]

q'' (MW/m^2)	Sample	$(T_w - T_f)$ (°C)	Re_c	σ	COV, percent
0.24	6	18	154,000	19,900	12.9
0.49	6	35	178,000	8480	4.8
0.71	5	45	209,000	7140	3.4
0.98	3	49	245,000	6190	2.5
1.22	3	58	239,000	9610	4.0
1.47	2	65	291,000	7430	2.6

laminar velocity profile were achieved with liquid film thicknesses of less than 1 mm. It is the intention of the authors to address these measurements in the future.

A comparison of the local heat transfer coefficient distributions obtained in this study with those of Vader (1988) for $q'' = 1.47$ MW/m^2 is shown in Fig. 7. It is apparent that the stagnation line heat transfer coefficient for the nonuniform velocity profile is greater than that for the uniform profile, independent of the heat flux. At locations downstream of the stagnation line, the amount of enhancement varies with the degree of heating. For example, with $\bar{V}_j = 4.5$ m/s, enhancement of the stagnation line heat transfer coefficient ranges from 56 percent at 1.47 MW/m^2 to 79 percent at 0.24 MW/m^2. Five jet widths downstream of the stagnation line enhancement varies from 155 percent at 0.24 MW/m^2 to a 5 percent deficit at 1.47 MW/m^2 (Figs. 6 and 7). However, these results are deceiving because of the effects of boiling. The nozzle used in this investigation provided sufficient cooling at 4.5 m/s to prevent boiling at all heat fluxes tested. In contrast, the results of Vader at 4.5 m/s contain finite areas where nucleate boiling occurred (determined from temperature distributions published by Vader, 1988). The onset of nucleate boiling destabilizes the laminar boundary layer and causes premature transition to turbulent flow. The onset of turbulence and mixing due to boiling causes the cooler fluid in the free stream to be advected to regions near the surface, yielding higher rates of heat removal.

Correlation of Data. Correlations have been developed to predict the critical Reynolds number that marks the onset of turbulence (Re_c), the Nusselt number at the stagnation line ($Nu_{j,0}$), and the local Nusselt number for single-phase convection along the surface ($Nu_{j,x}$). All of the thermophysical properties utilized in the following correlations (μ, ρ, k, and c_p) have been evaluated at the local film temperature (T_{film}).

The onset of turbulent flow within the boundary layer is defined as the first streamwise position at which the heat transfer coefficient reaches a minimum. Although the actual transition does not occur exactly at this location, it is commonly used as a means of estimation (Vader et al., 1990b). Correlation of the data has been achieved through a critical Reynolds number ($Re_c = u_\delta x/\nu$), where u_δ has been calculated from the static pressure distribution at the onset of transition (Wolf, 1989). The results for the critical Reynolds number are based on 25 observations for the full range of surface heating conditions and are shown in Table 2. Only those experiments for which the maximum temperature was less than the saturation temperature are given in the table. The results are presented as a function of the surface heat flux and suggest that transition is delayed with increased heating. This behavior is consistent with other observations reported in the literature (Wazzan et al., 1970; Strazisar et al., 1977).

For comparison, Vader et al., (1990b) reported a single critical Reynolds number of $Re_c = 3.6 \times 10^5$. The earlier transition to turbulence for the present investigation can be readily observed in Fig. 6. This accelerated transition may be attributed to the elevated levels of free-stream turbulence in the present jet. Small increases in the level of free-stream turbulence have been shown to cause sizable reductions in the critical Reynolds number, regardless of the pressure gradient (van Driest and Blumer, 1963).

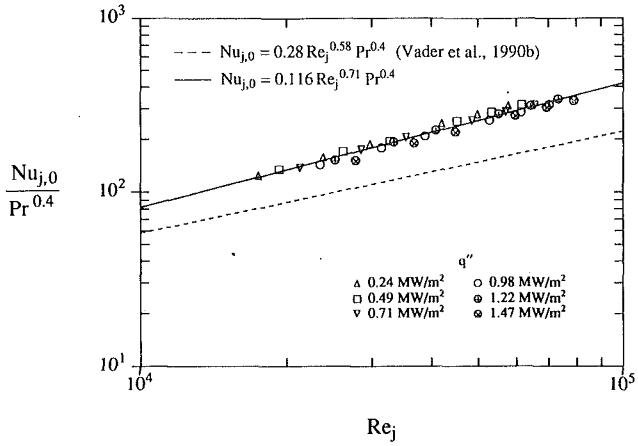

Fig. 8 Correlation of stagnation line heat transfer data for $1.8 \le \bar{V}_j \le 4.5$ m/s

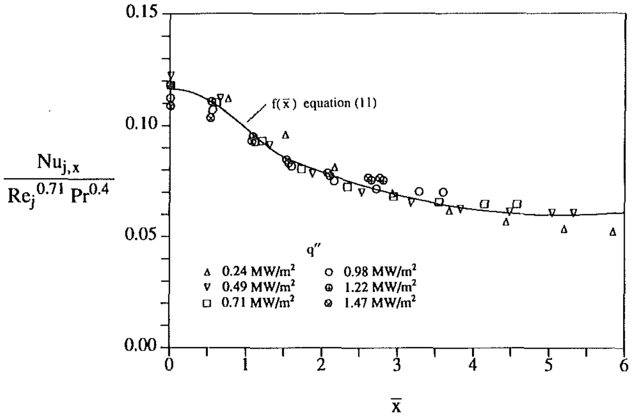

Fig. 9 Correlation of local heat transfer data for $1.8 \le \bar{V}_j \le 4.5$ m/s

Using results from 36 experiments, the stagnation flow Nusselt numbers ($h_0 W_j/k$) were correlated by

$$Nu_{j,0} = 0.116 Re_j^{0.71} Pr^{0.4} \quad (9)$$

Figure 8 shows the data of this study and equation (9), as well as the correlation presented by Vader et al. (1990b) for the near-uniform velocity profile. The correlation is based on Reynolds and Prandtl number ranges of $1.7 \times 10^4 \le Re_j \le 7.9 \times 10^4$ and $2.8 \le Pr \le 5.0$. For prescribed values of Re_j and Pr, equation (9) predicts the data to within 10.6 percent (20:1 odds). The exponent on the Prandtl number (0.4) was chosen to maintain consistency with other correlations (0.33–0.42) for jet impingement (McMurray et al., 1966; Vader et al., 1990b; Zumbrunnen et al., 1989). Based on the limited range of Prandtl numbers, an independent correlation for the exponent would be inappropriate.

Figure 8 shows the enhancement in the stagnation line Nusselt number over that of the near-uniform velocity profile jet of Vader et al. (1990b). Note that the Reynolds number exponent of equation (9) is 22 percent larger than that given by Vader. Such a difference is consistent with the increased levels of free-stream turbulence in the nonuniform profile jet. Zukauskas and Ziugzda (1985) show that, for the impingement of air and transformer oil at the stagnation point of a cylinder, the Reynolds number exponent is a clear function of the free-stream turbulence. For a turbulence intensity of 1 percent, the exponent was 0.5, which agrees with analytical predictions for laminar flow. An increase in the turbulence intensity to 7 percent increased the exponent to 0.6.

The local Nusselt number was correlated by the expression

$$\frac{\mathrm{Nu}_{j,x}}{\mathrm{Re}_j^{0.71}\mathrm{Pr}^{0.4}}=f(\bar{x}) \tag{10}$$

where f is some function of $\bar{x}$ that best fits the experimental data. The exponents on the Reynolds and Prandtl numbers were chosen to conform with the stagnation line results [equation (9)], requiring that $f(0)=0.116$. Figure 9 presents data obtained prior to the onset of transition and for surface temperatures less than saturation. The solid line represents the best fit of the data and is given by

$$f(\bar{x})\Big|_{0\le\bar{x}\le 1.6}=0.116+\bar{x}^2(0.00404\bar{x}^2-0.00187\bar{x}-0.0199) \tag{11a}$$

$$f(\bar{x})\Big|_{1.6\le\bar{x}\le 6}=0.111-0.0200\bar{x}+0.00193\bar{x}^2 \tag{11b}$$

For given values of Re_j, Pr, and $\bar{x}$, equations (10) and (11) predict the data to within 9.6 percent (20:1 odds).

Summary and Conclusions

Local heat transfer coefficient measurements have been made to explore the effects of the velocity profile on jet impingement cooling. Static and stagnation pressure measurements have been obtained along the impingement surface and within the jet, respectively. These data have been used in conjunction with the heat transfer results to assess the effects of the velocity profile.

Comparisons of local heat transfer data for nonuniform and near-uniform velocity profiles show that enhancement is considerable for the nonuniform case at all locations on the impingement surface for which there is single-phase convection. Augmentation diminishes when nucleate boiling is dominant. Over the range of velocities considered, heat transfer enhancement at the stagnation line was as much as 79 percent. Although these results are consistent with those published for laminar flow (≈ 100 percent augmentation), the pressure measurements suggest that enhancement is due to different mechanisms.

Enhancement for a laminar jet characterized by a nearly parabolic profile is due to the large velocity gradient that develops along the surface. In turbulent flow, however, the velocity profile is much more uniform, providing a much smaller surface velocity gradient and, hence, only limited heat transfer enhancement.

It is postulated that the majority of the enhancement is induced by the higher levels of free-stream turbulence in the nonuniform jet. The uniform profile of the previous study (Vader, 1988) was generated by passing the liquid through a converging nozzle with a high contraction ratio, which also provides considerable damping of turbulence. Conversely, the nonuniform profile was generated by passing the liquid through a parallel-plate channel which imparts a level of turbulence in the fluid that is typical of internal, constant-pressure gradient flows. Hence, the majority of the heat transfer enhancement is not due to the shape of the velocity profile but is, instead, a consequence of the higher turbulence levels in the jet.

Acknowledgments

This work was supported in part by the National Science Foundation under grant numbers CPE-8414613 and CTS-8912831.

References

Abrosimov, A. I., 1984, "Internal Peak of Heat-Transfer Coefficient for a Plate Washed by a Normal Jet," *High Temperature*, Vol. 22, No. 3, pp. 417–421.

Azuma, T., and Hoshino, T., 1983, "LDV Measurement in Radial Flow of Thin Liquid Film," *Proceedings of the Osaka Symposium on Flow Measuring-Techniques: The Application of Laser Doppler Velocimetry*, Association for the Study of Flow Measurements, Osaka, Japan, pp. 1–15.

Deshpande, M. D., and Vaishnav, R. N., 1982, "Submerged Laminar Jet Impingement on a Plane," *Journal of Fluid Mechanics*, Vol. 114, pp. 213–236.

van Driest, E. R., and Blumer, C. B., 1963, "Boundary Layer Transition: Freestream Turbulence and Pressure Gradient Effects," *AIAA Journal*, Vol. 1, No. 6, pp. 1303–1306.

Evans, H. L., 1962, "Mass Transfer Through Laminar Boundary Layers—7. Further Similar Solutions to the *b*-Equation for the Case $B=0$," *International Journal of Heat and Mass Transfer*, Vol. 5, pp. 35–57.

Falkner, V. M., and Skan, S. W., 1931, "Solutions of the Boundary-Layer Equations," *Philosophical Magazine and Journal of Science*, Vol. 12, pp. 865–896.

Gardon, R., and Akfirat, J. C., 1965, "The Role of Turbulence in Determining the Heat-Transfer Characteristics of Impinging Jets," *International Journal of Heat and Mass Transfer*, Vol. 8, pp. 1261–1272.

van Heiningen, A. R. P., Mujumdar, A. S., and Douglas, W. J. M., 1976, "Numerical Prediction of the Flow Field and Impingement Heat Transfer Caused by a Laminar Slot Jet," ASME JOURNAL OF HEAT TRANSFER, Vol. 98, No. 4, pp. 654–658.

Hoyt, J. W., and Taylor, J. J., 1985, "Effect of Nozzle Boundary Layer on Water Jets Discharging in Air," *Jets and Cavities—International Symposium*, J. H. Kim et al., eds., ASME, FED-Vol. 31, pp. 93–100.

Kestin, J., 1966, "The Effect of Free-Stream Turbulence on Heat Transfer Rates," *Advances in Heat Transfer*, T. F. Irvine and J. P. Hartnett, eds., Academic Press, New York, Vol. 3, pp. 1–32.

Kestin, J., Maeder, P. F., and Wang, H. E., 1961, "Influence of Turbulence on the Transfer of Heat From Plates With and Without a Pressure Gradient," *International Journal of Heat and Mass Transfer*, Vol. 3, pp. 133–154.

Levy, S., 1952, "Heat Transfer to Constant-Property Laminar Boundary-Layer Flows With Power-Function Free-Stream Velocity and Wall-Temperature Variation," *Journal of the Aeronautical Sciences*, Vol. 19, No. 5, pp. 341–348.

Lowery, G. W., and Vachon, R. I., 1975, "The Effect of Turbulence on Heat Transfer From Heated Cylinders," *International Journal of Heat and Mass Transfer*, Vol. 18, pp. 1229–1242.

McMurray, D. C., Myers, P. S., and Uyehara, O. A., 1966, "Influence of Impinging Jet Variables on Local Heat Transfer Coefficients Along a Flat Surface With Constant Heat Flux," in: *Proceedings of the Third International Heat Transfer Conference*, AIChE, New York, Vol. II, pp. 292–299.

van der Meer, T., 1987, "Heat Transfer From Impinging Flame Jets," Doctoral Thesis, Technical University of Delft, The Netherlands.

Milne-Thomson, L. M., 1955, *Theoretical Hydrodynamics*, 3rd ed., Macmillan Co., New York, pp. 279–289.

Moffat, R. J., 1988, "Describing the Uncertainties in Experimental Results," *Experimental Thermal and Fluid Science*, Vol. 1, pp. 3–17.

Saad, N. R., Douglas, W. J. M., and Mujumdar, A. S., 1977, "Prediction of Heat Transfer Under an Axisymmetric Laminar Impinging Jet," *Industrial and Engineering Chemistry, Fundamentals*, Vol. 16, No. 1, pp. 148–154.

Scholtz, M. T., and Trass, O., 1970, "Mass Transfer in a Nonuniform Impinging Jet," *AIChE Journal*, Vol. 16, No. 1, pp. 82–96.

Sparrow, E. M., and Lee, L., 1975, "Analysis of Flow Field and Impingement Heat/Mass Transfer Due to a Nonuniform Slot Jet," ASME JOURNAL OF HEAT TRANSFER, Vol. 97, No. 2, pp. 191–197.

Sparrow, E. M., and Wong, T. C., 1975, "Impingement Transfer Coefficients Due to Initially Laminar Slot Jets," *International Journal of Heat and Mass Transfer*, Vol. 18, pp. 597–605.

Strazisar, A. J., Reshotko, E., and Prahl, J. M., 1977, "Experimental Study of the Stability of Heated Laminar Boundary Layers in Water," *Journal of Fluid Mechanics*, Vol. 83, Part 2, pp. 225–247.

Vader, D. T., 1988, "Convective and Boiling Heat Transfer From a Heated Surface to an Impinging, Planar Jet of Water," Ph.D. Thesis, Purdue University, West Lafayette, IN.

Vader, D. T., Incropera, F. P., and Viskanta, R., 1990a, "A Method for Measuring Steady, Local Heat Transfer to an Impinging, Liquid Jet," *Experimental Thermal and Fluid Science*, in press.

Vader, D. T., Incropera, F. P. and Viskanta, R., 1990b, "Local Convective Heat Transfer From a Heated Surface to an Impinging, Planar Jet of Water," *International Journal of Heat and Mass Transfer*, in press.

Wazzan, A. R., Okamura, T. T., and Smith, A. M. O., 1970, "The Stability and Transition of Heated and Cooled Incompressible Laminar Boundary Layers," *Fourth International Heat Transfer Conference*, U. Grigull and E. Hahne, eds., Elsevier, Amsterdam, Vol. II, Paper No. FC 1.4.

Wolf, D. H., 1989, "Impingement Heat Transfer From a Heated Surface to a Nonuniform, Planar Jet of Water," MSME Thesis, Purdue University, West Lafayette, IN.

Zukauskas, A., and Ziugzda, J., 1985, *Heat Transfer of a Cylinder in Crossflow*, G. F., Hewitt, ed., Hemisphere, Washington, pp. 85–95.

Zumbrunnen, D. A., 1988, "A Study of Heat Transfer From Stationary and Moving Plates Cooled by Planar Jets of Water," Ph.D. Thesis, Purdue University, West Lafayette, IN.

Zumbrunnen, D. A., Incropera, F. P., and Viskanta, R., 1989, "Convective Heat Transfer Distributions on a Plate Cooled by Planar Water Jets," ASME JOURNAL OF HEAT TRANSFER, Vol. 111, pp. 889–896.

Heat Transfer Across Turbulent Boundary Layers With Pressure Gradients

J. Sucec
Professor of Mechanical Engineering.
Mem. ASME

Y. Lu
Graduate Student.

University of Maine,
Orono, ME 04469

The problem being addressed is steady, constant property, turbulent, thin boundary layer flow over a body with a pressure gradient. To find the local Stanton number distribution, the integral energy equation, cast in inner variables, is solved for the thermal boundary layer thickness. The needed velocity distributions are given by the inner law and by the combined law of the wall and wake. Approximate temperature profiles are based upon thermal inner and outer laws, except for the thermal superlayer, which is modeled by a polynomial distribution of temperature. Comparison of predictions is made with experimental Stanton numbers from the literature. Very good agreement is noted for zero, adverse, and favorable pressure gradients, including very strong accelerations tending toward laminarization, with less satisfactory agreement in regions "relaxing" from acceleration.

Introduction

The problem of calculating heat transfer through turbulent boundary layers with streamwise pressure gradients is encountered in gas turbine vanes and blades as well as in rocket nozzles and other applications.

Often one is confronted by both favorable pressure gradients, perhaps with very strong accelerations, and unfavorable ones on the same surface, and the Stanton number distribution along the surface must be predicted.

Perhaps the easiest to use existing predictive method is that of Ambrok (1957). This method, including the modifications introduced by Moretti and Kays (1965), often gives results of reasonable accuracy. Some of the more modern and accurate predictive techniques involve the finite difference solution of the governing time-averaged partial differential equations of mass, momentum, and energy in the turbulent boundary layer. Cebeci et al. (1970) employ algebraic mixing length models, with a modification to the Van Driest constant A^+ to account for nonzero pressure gradient in the inner region, in their finite difference method. Jones and Launder (1972) use a two-equation model of turbulence, one for turbulent kinetic energy and the other for turbulent dissipation, along with low Reynolds number modeling in their finite difference solutions. However, the 1968 Stanford Conference (Kline et al., 1968) demonstrated that integral methods have not been made obsolete by finite difference methods. In fact, four of the methods that received a "good" rating (the highest of the three possible ratings) at the Conference were integral methods, while three finite difference methods also obtained that rating.

Modern integral methods for solving turbulent boundary layer problems employ velocity and temperature profiles in inner variables, y^+, u^+, and T^+. Sucec (1986) proposed a more complete integral theory for predicting heat transfer across turbulent boundary layers in which the velocity and thermal law of the wall, the inner laws, are used in the inner region, while the combined law of the wall and wake is used in the overlap and outer layers as velocity and temperature profiles. Previous methods of this type had either used only the thermal inner law across the entire thermal boundary layer or else had assumed equal thickness of the velocity and thermal boundary layers. These limitations are not valid for adverse and strong favorable pressure gradients, respectively, and basically limit those solutions to zero or small pressure gradient cases. Although must of the theory developed by Sucec (1986) is for nonzero pressure gradients, predicted results were only for a zero pressure gradient case. Comparison to experimental data yielded very good agreement, especially in the high Prandtl and high Reynolds number regions where other predictive schemes had experienced difficulty.

In the present work, Sucec's (1986) theory is extended and completed for the case of arbitrary pressure gradients, both favorable and adverse. As is also noted in Launder and Lockwood (1969), strong favorable pressure gradients can lead to the condition whereby the thermal boundary layer thickness is much greater than the velocity boundary layer thickness. When this occurs, the region between the two thicknesses, which Launder and Lockwood refer to as the "thermal superlayer," must be modeled with regard to velocity and temperature profiles as well as heat transfer across the layer. The required modeling of the thermal superlayer region is developed here. Using this and profiles of temperature and velocity for other portions of the boundary layers allows us to solve the integral thermal energy equation. With this solution the local Stanton number can be predicted for arbitrary pressure gradients.

Comparison of these predictions is then made to experimental data from the literature for favorable pressure gradients, including strong accelerations in which the flow is tending toward laminarization, for unfavorable pressure gradients, and for "relaxing" regions where a favorable gradient has been abruptly changed to a zero gradient. Predictions of the present work are also compared to available finite difference solutions for some cases. The present integral solution gives the better results.

Analysis

Under consideration is steady (on the average), constant-property, two-dimensional planar, thin boundary layer type, turbulent flow, without appreciable viscous dissipation, over a body with arbitrary streamwise pressure gradient. A schematic of the physical situation for the case when $\delta_t > \delta$ is depicted in Fig. 1. The governing partial differential forms of the x-momentum equation and the thermal energy equation, available from White (1974), are given next.

Contributed by the Heat Transfer Division for publication in the JOURNAL OF HEAT TRANSFER. Manuscript received by the Heat Transfer Division August 15, 1989; revision received February 9, 1990. Keywords: Forced Convection, Turbines, Turbulence.

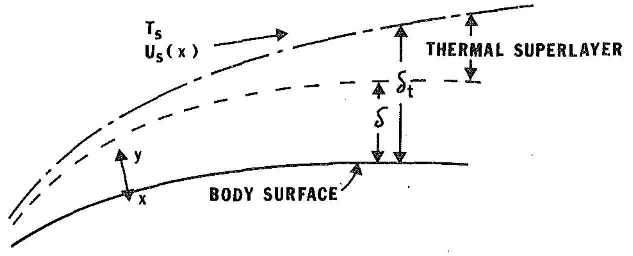

Fig. 1 Sketch of hydrodynamic and thermal boundary layers on body

$$\frac{\partial}{\partial y}\left[(\nu+\epsilon_m)\frac{\partial u}{\partial y}\right]=u\frac{\partial u}{\partial x}+v\frac{\partial u}{\partial y}+\frac{1}{\rho}\frac{\partial p}{\partial x} \qquad (1)$$

$$\frac{\partial}{\partial y}\left[(\alpha+\epsilon_H)\frac{\partial T}{\partial y}\right]=u\frac{\partial T}{\partial x}+v\frac{\partial T}{\partial y} \qquad (2)$$

Now, the following inner variables are introduced:

$$u^*=\sqrt{\tau_w/\rho},\ u^+=u/u^*,\ v^+=v/u^*,\ y^+=u^*y/\nu,$$

$$T^+=\frac{T_w-T}{q_w/\rho c_p u^*}\ P^+=\frac{\partial P/\partial x}{\rho u^{*3}/\nu},\ x^+=\int_0^x\frac{u^*(\xi)}{\nu}d\xi \qquad (3)$$

Substituting these into equation (2), the integral form of the low-speed thermal energy equation is given as follows:

$$\frac{d}{dx^+}\left[\frac{q_w}{u^*}\int_0^{\delta_t^+}u^+(T_s^+-T^+)dy^+\right]=\frac{q_w}{u^*} \qquad (4)$$

The velocity and temperature profiles needed to solve this equation will be discussed next.

Velocity Profiles and Hydrodynamic Solution Procedure. In the inner layer, consisting of the viscous and the buffer sublayers, one has

$$u^+=y^+ \qquad 0\le y^+\le y^+_{\mathrm{sub}}$$

$$u^+=5\ln y^+-3.05 \qquad y^+_{\mathrm{sub}}<y^+\le y_b^+ \qquad (5)$$

In the overlap layer and the outer layer, use is made of the combined law of the wall and wake, which, after representing Cole's wake function by a polynomial due to Moses, can be expressed as (White, 1974)

$$u^+=\frac{1}{K}\ln y^+ + B+\frac{2\pi(x)}{K}\left[3\left(\frac{y^+}{\delta^+}\right)^2-2\left(\frac{y^+}{\delta^+}\right)^3\right] y_b^+<y^+\le\delta^+$$

$$u^+=u_s^+=1/\sqrt{c_f/2} \qquad y^+>\delta^+ \qquad (6)$$

The second equation in (6) is the velocity profile to be used in the thermal superlayer, $\delta^+ < y^+ < \delta_t^+$, when it exists; that is, when $\delta_t^+ > \delta^+$.

Along with these velocity profiles, the hydrodynamic quantities needed here and in the solution of the temperature field problem to get the local Stanton number St_x are δ^+, $c_f/2$, and $\pi(x)$, the wake parameter. These are found from the complete theory advanced by White (1974) in which the following equilibrium boundary layer correlation is used for $\pi(x)$ even when dealing with nonequilibrium flows:

$$\pi\approx 0.8[\beta+0.5]^{3/4} \qquad \beta\ge -0.5$$

$$\pi=0 \qquad \beta<-0.5 \qquad (7)$$

where $\beta=\frac{\delta^*}{\tau_w}\frac{\partial P}{\partial x}$.

The second of equations (7) is used to satisfy the theoretical requirement that, for equilibrium boundary layers, the wake vanishes when β reaches -0.5, which corresponds to a strong favorable pressure gradient (Mellor and Gibson, 1966). The

Nomenclature

a_j = profile parameters defined by equation (14)
B = turbulence constant in the overlap law
C = lag constant in equation (24)
c_f = $2\tau_w/\rho u_s^2$ skin friction coefficient
C_p = constant pressure specific heat
g, g_e = defined by equation (17), and value at δ, respectively
H = δ^*/θ = shape factor
j = an index
k–ϵ = model using turbulent kinetic energy and dissipation equations
K = von Karman turbulence constant
$\bar{K}$ = $(\nu/u_s^2)du_s/dx$ = acceleration parameter
P = local pressure
P^+ = defined in equation (3)
Pr, Pr_t, Pr_{te} = molecular, turbulent, and turbulent value at δ of Prandtl number, respectively
q, q_w = local and wall heat flux, respectively
Re_x, Re_θ = $u_s x/\nu$, $u_s\theta/\nu$, respectively
s_o = $K^4e^{-BK}/6$
St_x = $q_w/\rho C_p u_s\Delta T$ = local Stanton number
T, T_s, T_w = local, free-stream, and wall temperature, respectively
T_b^+, T_s^+, T_δ^+ = T^+ at y_b^+, δ_t^+, δ^+, respectively
u, u_s = local and free-stream mean x component of velocity, respectively
u^* = $\sqrt{\tau_w/\rho}$ = friction velocity
u^+, u_s^+ = u/u^*, u_s/u^*, respectively
v = local mean y component of velocity
v^+ = v/u^*
x^+ = defined by equation (3), with x measured along body surface
y = space coordinate perpendicular to body surface
y^+ = yu^*/ν
y_b^+, y^+_{sub} = values of y^+ at edge of buffer and viscous sublayer, respectively
α = thermal diffusivity
β = defined in equation (7)
γ_e = intermittency factor at edge of velocity boundary layer
δ, δ_t = local hydrodynamic and thermal boundary layer thickness, respectively
δ^+, δ_t^+ = $\delta u^*/\nu$, $\delta_t u^*/\nu$, respectively
δ^* = displacement thickness of boundary layer
ΔT = T_w-T_s
ϵ = small value tending to zero
ϵ_H, ϵ_m = eddy diffusivity for heat and momentum, respectively
θ = momentum thickness
$\bar{\theta}$, $\bar{\theta}_\delta$, $\bar{\theta}_{\delta t}$ = $(T-T_s)(T_w-T_s)$ at a general position, at δ, and at δ_t, respectively
λ = turbulence constant in equation (18)
ν = kinematic viscosity
$\pi(x)$ = Cole's wake parameter
ρ = mass density
τ_w = wall shear stress

pressure gradient parameter β can also be rewritten in the following useful form in which the acceleration parameter $\bar{K} = (\nu/u_s^2)\, du_s/dx$ appears explicitly. $\bar{K}$ is useful as a parameter that measures the tendency toward laminarization (Moretti and Kays, 1965), as well as being a parameter whose invariance with x occurs in asymptotic boundary layers (Thielbahr et al., 1972), and in the "sink flow" equilibrium boundary layer (Launder and Lockwood, 1969)

$$\beta = -2\bar{K}\,\mathrm{Re}_\theta H/c_f \tag{8}$$

The hydrodynamic initial condition given may be the value of θ at x_0, θ_0, or c_f at x_0 or sometimes the boundary layer thickness, δ_o^+, at x_o may be known. If θ_o is known, a Newton-Raphson iteration is used to solve the set of nonlinear algebraic equations of White's complete theory, for $c_f(x_o)$, $H(x_o)$, and $\pi(x_o)$. These are then used in the integral momentum equation to solve for $(d\theta/dx)_{x_o}$ and this, with a simple differencing scheme, leads to $\theta(x_o + \Delta x)$. These steps are now repeated to advance the solution from $x_o + \Delta x$ to the new position, $x_o + 2\Delta x$, and so on until the largest x value of interest is reached. This scheme is stable (Hildebrand, 1968) with a maximum step size found to be about $\Delta x = 0.01$ m. The same procedure is used if $c_f(x_o)$ is known instead of θ_o. If δ_o^+ is given, one must also add equation (6) evaluated at $y^+ = \delta^+$ to the nonlinear algebraic equation set.

Temperature Profiles. Convective transport is neglected in the inner layer so that equation (2) in inner coordinates becomes

$$\frac{\partial}{\partial y^+}\left[\left(\frac{1}{\mathrm{Pr}} + \frac{\epsilon_m}{\nu \mathrm{Pr}_t}\right)\frac{\partial T^+}{\partial y^+}\right] = 0 \tag{9}$$

The eddy diffusivity model developed by Sucec (1986) accounts for pressure gradient explicitly and is relatively simple in form. It is given by $\epsilon_m/\nu = P^+y^+ + K^4 \exp(-BK) y^{+3}\,[1 + P^+y^+]$, $0 \le y^+ < y_b^+$. With this, equation (9) is integrated to yield the thermal inner law

$$T^+(y^+) = \int_0^{y^+} \frac{dy^+}{\dfrac{1}{\mathrm{Pr}} + \dfrac{1}{\mathrm{Pr}_t}\left[s_o y^{+3}(1 + P^+y^+) + P^+y^+\right]} \tag{10}$$

for $0 \le y^+ \le y_b^+$.

For the case when $\delta_t^+ \le \delta^+$, the combined thermal law of the wall and of the wake is developed by Sucec (1986) as

$$T^+ = T_b^+ + \frac{\mathrm{Pr}_t}{K}\left\{\ln\left(\frac{y^+}{y_b^+}\right) + 2\pi(x)\left[3\left(\frac{y^+}{\delta_t^+}\right)^2 - 2\left(\frac{y^+}{\delta_t^+}\right)^3 - 3\left(\frac{y_b^+}{\delta_t^+}\right)^2 + 2\left(\frac{y_b^+}{\delta_t^+}\right)^3\right]\right\} \tag{11}$$

for $y_b^+ < y^+ < \delta_t^+$ and $\delta_t^+ \le \delta^+$.

The heat transfer law is obtained from equation (11) by setting $y^+ = \delta_t^+$ and noting that $T_s^+ = \sqrt{c_f/2}/\mathrm{St}_x$ with T_b^+ given by equation (10) at $y^+ = y_b^+$. Thus

$$\mathrm{St}_x = \frac{\sqrt{c_f/2}}{T_b^+ + \dfrac{Pr_t}{K}\left\{\ln\left(\dfrac{\delta_t^+}{y_b^+}\right) + 2\pi(x)\left[1 - 3\left(\dfrac{y_b^+}{\delta_t^+}\right)^2 + 2\left(\dfrac{y_b^+}{\delta_t^+}\right)^3\right]\right\}} \tag{12}$$

when $\delta_t^+ \le \delta^+$.

Some experimental support for a relationship such as equation (11) is shown in Hoffmann and Perry (1979). They find a thermal law of the wall for the overlap portion of the inner layer as well as a thermal defect law for the outer layer under the experimental condition of a slightly favorable pressure gradient, which gradually became zero. It was found that these thermal laws have the same overall form as the more familiar inner and outer laws of the velocity field. A thermal law of the wake, valid in the overlap portion of the inner layer and in the outer layer, was formed for the case of zero pressure gradient. As a further check on the validity of these experimentally determined thermal laws, they were used to calculate enthalpy thickness and Stanton number distributions that were in good agreement with flat plate data.

Profiles for the Case When $\delta_t^+ > \delta^+$. Here the velocity wake region ends at δ^+, which is less than δ_t^+, so the thermal law of the wall and wake also ends at δ^+ and is taken to be of the following form:

$$T^+ = T_b^+ + \frac{\mathrm{Pr}_t}{K}\left\{\ln\left(\frac{y^+}{y_b^+}\right) + 2\pi(x)\left[3\left(\frac{y^+}{\delta^+}\right)^2 - 2\left(\frac{y^+}{\delta^+}\right)^3 - 3\left(\frac{y_b^+}{\delta^+}\right)^2 + 2\left(\frac{y_b^+}{\delta^+}\right)^3\right]\right\} \tag{13}$$

for $y_b^+ < y^+ < \delta^+$ and $\delta_t^+ > \delta^+$.

For the temperature profile in the thermal superlayer, $\delta^+ < y^+ < \delta_t^+$, we use the following cubic polynomial as an approximating sequence:

$$T = \sum_{j=0}^{3} a_j y^{+j} \tag{14}$$

The profile is forced to satisfy the conjugation conditions of temperature and flux continuity at the interface, δ^+, as well as the zero derivative and collocation condition at δ_t^+, namely,

$$T^+_{\delta^+ - \epsilon} \to T^+_{\delta^+ + \epsilon}, \quad q_{\delta^+ - \epsilon} \to q_{\delta^+ + \epsilon},$$

$$\text{as } \epsilon \to 0, \text{ and } \frac{\partial T^+}{\partial y^+} = \frac{\partial^2 T^+}{\partial y^{+2}} = 0 \text{ at } \delta_t^+ \tag{15}$$

Since the thermal superlayer is beyond the edge of the velocity boundary layer, δ^+, we model it by setting the turbulent transport coefficients equal to zero in it as was also done by Launder and Lockwood (1969). $T^+_{\delta^+ - \epsilon}$ and $q_{\delta^+ - \epsilon}$ are found from equation (13) and, with these, equations (15) determine the profile parameters in terms of δ^+ and δ_t^+. Thus, equation (14) becomes

$$T^+ = T^+_{\delta^+} + \frac{\mathrm{Pr}_t}{K}\, g\left(\frac{y^+ - \delta^+}{\delta^+}\right)\left[1 - \left(\frac{y^+ - \delta^+}{\delta_t^+ - \delta^+}\right) + \frac{1}{3}\left(\frac{y^+ - \delta^+}{\delta_t^+ - \delta^+}\right)^2\right] \tag{16}$$

for $\delta^+ < y^+ < \delta_t^+$ and $\delta_t^+ > \delta^+$.

Here

$$g = \frac{\left[\dfrac{1}{\mathrm{Pr}} + \dfrac{\epsilon_m}{\nu \mathrm{Pr}_t}\right]_{\delta^+ - \epsilon}}{\dfrac{1}{\mathrm{Pr}}} \tag{17}$$

The eddy diffusivity of momentum at the edge of the velocity boundary layer, in equation (17), was taken to be the following common prescription, after modification by the Klebanoff intermittency factor γ_e, evaluated at δ^+, as given by Cebeci et al. (1970):

$$(\epsilon_m/\nu)_{\delta^+ - \epsilon} = \frac{\lambda^2}{K}\,\delta^+\gamma_e \tag{18}$$

In reality, the eddy diffusivity is not zero everywhere in the thermal superlayer. There is some intermittent distribution for small distances beyond δ^+ in the thermal superlayer. However, the quantitative details of this diffusivity distribution are not known. Because of this uncertainty about values of eddy diffusivity in this region just beyond δ^+, equation (16) is used in the integral energy equation (22) to solve for δ_t^+ while the thermal resistance to heat transfer across the thermal superlayer is modeled as being due, as an approximation, simply to molecular conduction across a layer of local thickness $\delta_t - \delta$. This gives

$$\frac{q}{q_w}=\frac{T_s^+ - T_{\delta+}^+}{\Pr(\delta_t^+ - \delta^+)} \tag{19}$$

Setting equation (19) equal to the flux ratio, at $\delta^+ - \epsilon$ as $\epsilon \to 0$, calculated by using equation (13) and rearranging by use of $T_s^+ = \sqrt{c_f/2}\,/\mathrm{St}_x$ gives the heat transfer law

$$\mathrm{St}_x=\frac{\sqrt{c_f/2}}{T_{\delta+}^+ + \dfrac{\Pr_{te}}{K}\, g_e\left[\dfrac{\delta_t^+}{\delta^+}-1\right]}, \quad \delta_t^+ > \delta^+ \tag{20}$$

$T_{\delta+}^+$ is evaluated from equation (13) at $y^+ = \delta^+$ and g_e is found from equation (17) with $\Pr_t$ replaced by $\Pr_{te}$, which is the turbulent Prandtl number at the edge of the velocity boundary layer, at $y^+ = \delta^+$.

It is known (Launder and Spalding, 1972), for example, that in wakes, plane jets, and mixing layers, $\Pr_t$ has a value of about 0.5. Experimental evidence in wall boundary layers (Sepri, 1987, reporting on the data of Blair) indicates a gradual decrease in $\Pr_t$ across the outer layer to a value of about 0.5 at δ^+ for zero pressure gradient circumstances where the wake strength parameter has the value $\pi = 0.5$. This and some numerical experimentation on nonzero pressure gradients forms the basis for our proposal and use of the following at the edge of the velocity boundary layer:

$$\begin{aligned} \Pr_{te}&=0.9 \qquad \pi(x)<0.35 \\ \Pr_{te}&=0.5 \qquad \pi(x)>0.35 \end{aligned} \tag{21}$$

Solution for δ_t^+. As is well known, as long as Pr > 0.5 and the flow is turbulent, the thermal history effect on the local Stanton number is very small; hence, results for constant flux surfaces are practically the same as for the constant temperature surface condition and even for other surface temperature variations. This point is discussed in Kays and Crawford (*1980*) and specifically addressed by Thomas and Al-Shariff (1981). Hence, under this condition, equation (4), the thermal energy equation, can be integrated to yield

$$\int_o^{\delta_t^+} u^+(T_s^+ - T^+)dy^+ = \left(\mathrm{Re}_x - \frac{u_s x_o}{\nu}\right)\sqrt{c_f/2} + \frac{u_s\sqrt{c_f/2}}{\left[u_s\sqrt{c_f/2}\right]_{x_o}} \int_o^{\delta^+{}_{t0}} u^+\,(T_s^+ - T^+)dy^+ \tag{22}$$

where δ_{to}^+ is the thermal boundary layer thickness at the position x_o and is either a given initial value or is estimated from experimental data.

To solve equation (22) for $\delta_t^+(x)$, the appropriate temperature and velocity profiles from equations (5), (6), (10), (11), (13), and (16) are inserted along with the previously determined hydrodynamic quantities, such as c_f. The velocity and temperature profiles being used allow the integrations needed in equation (22) to be carried out analytically, expect for the buffer sublayer, with the result being a nonlinear algebraic equation for δ_t^+. The algorithm used for the numerical quadratures required in the sublayers was IMSL ROUTINE DCADRE, while the root-finding solution used to solve for δ_t^+ was the routine ZREAL2. With $\delta_t^+(x)$ in hand, either equation (12) for $\delta_t^+ < \delta^+$ or equation (20) for $\delta_t^+ > \delta^+$ gives the local Stanton number variation with x.

The values of the turbulence constants used in the calculations were $K=0.41$, $B=5.0$, $y_{\mathrm{sub}}^+=5.0$, $y_b^+=30.0$, $\Pr_t=1.0$ for $0<y^+<30.0$ and $\Pr_t=0.9$ for $30 \le y^+ \le \delta^+$, $\lambda=0.085$, and the Klebanoff intermittency value at the edge of the velocity boundary layer was computed as $\gamma_e=0.154$.

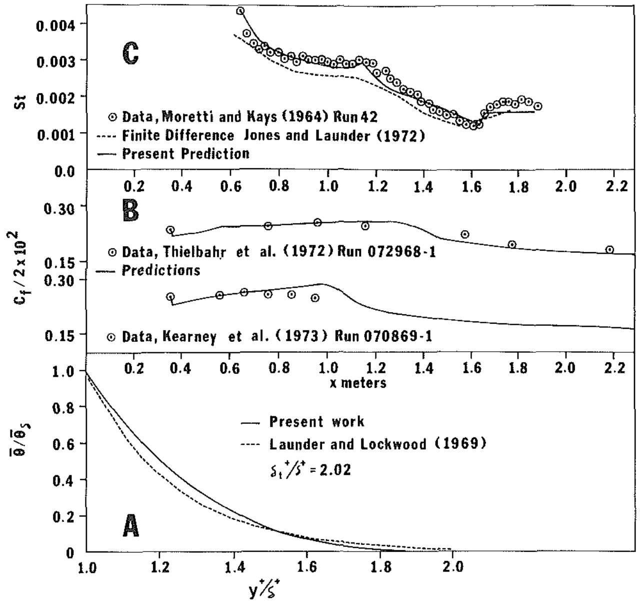

Fig. 2 (A) Comparison of temperature profiles in superlayer; (B) skin friction coefficient predictions versus data; (C) Stanton number predictions and data

Discussion

One qualitative check on the modeling done in the present work within the thermal superlayer, $\delta^+ < y^+ < \delta_t^+$, exists in the predictions of Launder and Lockwood (1969) for sink flow boundary layers in this region. Using a value of $\beta_o = 6.25 \times 10^{-3}$ in their expression $\Delta T \sim u_s^{\beta_o}$, $\Pr = 0.70$, $\bar{K} = 10^{-7}$, and defining the edge of the thermal boundary layer to be at their $\theta_{\delta_t} = (T_{\delta_t} - T_s)/(T_w - T_s) = 0.01$ gives $\delta_t^+ \;/\; \delta^+ = 2.02$. Figure 2(*A*) shows the comparison between their predicted temperature profile and the cubic polynomial profile, equation (16), developed in the present work. The agreement between the two seems reasonable and a similar agreement was also noted for the more extreme case (not shown) where $\delta_t^+/\delta^+ = 7.9$.

Prediction of the Stanton number distribution requires prior calculation of the hydrodynamic quantities, $c_f(x)$, $\pi(x)$, and $\delta^+(x)$. The "complete theory" given by White (1974) was chosen for use because of its accuracy combined with relative simplicity as compared to finite difference methods. This accuracy is demonstrated by comparison with data from three of the flows judged "most difficult" in the Stanford Conference (Coles and Hirst, 1968), flows 1200, 2200, and 3800, in White (1974), where it is also seen that its performance is comparable to the finite difference predictions. Our use of this method was checked by essentially reproducing White's predictions for flows 1200, 2200, and 3800. These check cases are given by Lu (1987). In addition, comparison was made to available c_f data by Thielbahr et al. (1972), and Kearney et al. (1973); this is shown in Fig. 2(*B*) where good agreement is demonstrated.

In Fig. 2(*C*) are shown results for Run 42 of Moretti and Kays (1964), $2.8 \times 10^5 < \mathrm{Re}_x < 2.9 \times 10^6$, which has a zero pressure gradient up to about $x = 1.2$ m, an acceleration zone in which $\bar{K}$ is about constant at 3.2×10^{-6} to $x = 1.6$ m, followed by a relaxation zone where $\bar{K} = 0$. The solid curve of the present predictions agrees very well with the data except for part of the relaxation zone. Also shown (by a dashed line) is the finite difference prediction of Jones and Launder (1972) which is a two-equation, k-ϵ, model of turbulence. The present method is substantially superior in the acceleration zone where the Stanton number depression occurs and in the flat plate region immediately upstream of this zone, while in the relaxation region, $x > 1.6$ m, both methods give about the same results.

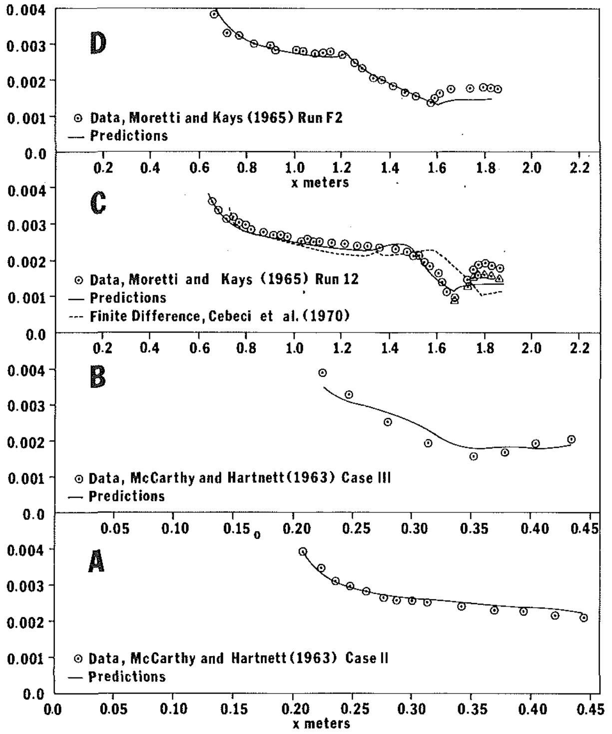

Fig. 3 Stanton number predictions and data; triangular △, symbols in Fig. 3(C) are the circled data points corrected for aerodynamic heating effects

Ambrok's method, as modified by Moretti and Kays (1964), leads to a large overprediction of the Stanton number in severe acceleration regions. Their predictions lead to a maximum error of 60 percent in the Stanton number, at 1.58 m in Run F-2, while the integral solution given here is only 5 percent in error at this point. This failure of the modified Ambrok method for Run F-2 is shown very graphically by Fig. 9 of Moretti and Kays (1965).

Case II of McCarthy and Hartnett (1963), $7\times10^5<\mathrm{Re}_x<2.1\times10^6$, is a mildly accelerated flow with a constant pressure gradient and an unheated starting length $x_o=20.3$ cm (8 in.). The initial values of momentum and thermal boundary layer thickness at x_o were $\theta_o=0.054$ cm (0.0214 in.) and $\delta_{to}^+=0.0$. Predicted Stanton numbers are plotted versus data in Fig. 3(*A*) and very good agreement is apparent. $\bar{K}$ ranged from about 0.55×10^{-6} to 0.25×10^{-6}; hence, the severe depression of the Stanton number due to strong favorable accelerations that was seen in Fig. 2(*C*) was not exhibited here, but will show up again in other data to be discussed. This mild acceleration, combined with the unheated starting lengths, also results in a δ_t^+ that is smaller than δ^+ for most of the test section until an x of 0.417 m is reached.

Case III of McCarthy and Hartnett (1963), $4.8\times10^5<\mathrm{Re}_x<2.1\times10^6$, is a case of a strong acceleration (maximum value of $\bar{K}$ of about 2.6×10^{-6}) followed by a deceleration. As seen in Fig. 3(*B*), the predictions show good agreement with the data for Case III, whereas the six older, simpler predictive methods shown by McCarthy and Hartnett (1963) give very poor results. For example, at $x=0.35$ m, very near the end of the strong acceleration region, Ambrok's (1957) method predicts an St_x that is 64 percent low, while our present integral method is close to 15 percent low.

Runs F-2 and 12 of Moretti and Kays (1965) both have a long initial region of zero pressure gradient followed by strong accelerations, after which the negative pressure gradient is abruptly removed and returned to zero, giving the complex recovery or "relaxing" region. The maximum value of the acceleration parameter, $\bar{K}$, is about 3×10^{-6} for Run F-2 and 3.4×10^{-6} for Run 12. This value for Run 12, in particular, is large enough so that if it were sustained for a great enough distance along the surface, the flow could undergo a complete retransition to a laminar flow. Examination of the experimental data in Fig. 3(*C*) shows the severe depression of the Stanton number between about 1.5 m and 1.67 m caused by the strong acceleration of Run 12. For Run F-2, $8.8\times10^5<\mathrm{Re}_x<3.5\times10^6$ while for Run 12, $1.7\times10^6<\mathrm{Re}_x<5.7\times10^6$. Calculations for these runs were started at the point where the step change in surface temperature had been fully established in the experiments (about 61 cm for Run F-2) using a thermal boundary layer thickness, δ_t^+, of zero. However, the momentum thickness, θ_o at this point was not measured, so it was computed as follows. Since the pressure gradient in the test section is zero in this region, the flat plate solution formula given by White (1974) was used to calculate c_f at this point, namely

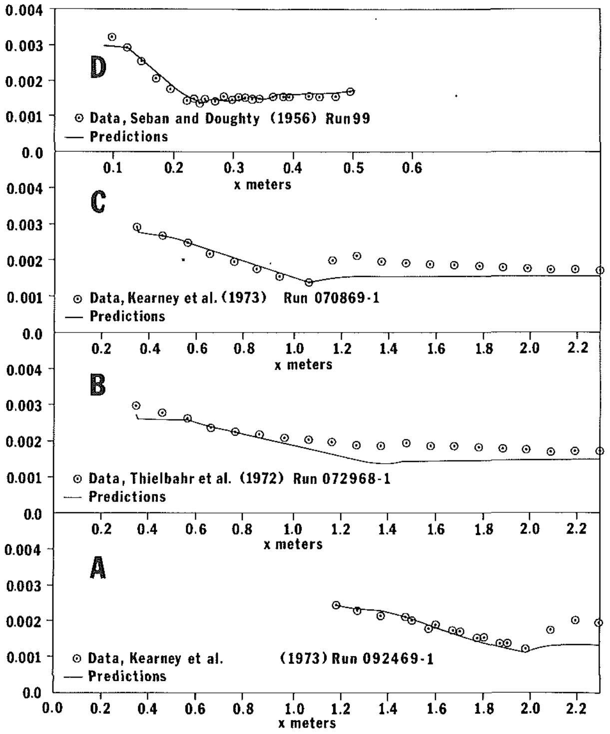

Fig. 4 Stanton number predictions and data

$$c_f=0.455/\ln^2 0.06\,\mathrm{Re}_x \tag{23}$$

Use of the velocity profile, equation (6), in the definition of the momentum thickness then relates θ to c_f and allows the determination of the needed starting value, θ_o. With this, our Stanton number predictions are made and shown as the solid curves in Figs. 3(*C*) and 3(*D*).

As is evident, the agreement is very good in the initial flat plate region and the strong acceleration regions but certainly not anywhere near as good in the relaxation zones beyond about 1.6 and 1.67 m, respectively, for Runs F-2 and 12, where the pressure gradient has been rather abruptly changed back to zero and held there for the rest of the test surface. The agreement of the predictions with data in the relaxation region is much better for Run F-2 than for Run 12. This is due to a smaller value of $\bar{K}$ just before $\bar{K}$ starts returning to zero, namely $\bar{K}\approx2.6\times10^{-6}$ versus 3.4×10^{-6} for Run 12, and a more gradual change of $\bar{K}$ to zero in Run F-2 where the change takes place in about 18 cm as opposed to about 11 cm in Run 12 as depicted by Moretti and Kays (1965).

Also graphed in Fig. 3(*C*) is the prediction of the finite difference solution of Cebeci et al. (1970), which uses algebraic mixing length models. The present predictions are considerably better than the finite difference results in the strong acceleration and recovery (relaxation) regions and are even better in the part of the zero pressure gradient region which immediately precedes the start of acceleration, $1.1 \text{ m} < x < 1.4$ m.

The agreement of our Stanton number predictions with data in the strong acceleration zones in all of the figures, including those yet to be discussed, lends some support to the modeling developed for the thermal superlayer in regards to heat transfer and the cubic polynomial temperature profile.

Runs 092469-1 and 070869-1 from Kearney et al. (1973) have $5.3 \times 10^5 < \text{Re}_x < 2.8 \times 10^6$ and $1.6 \times 10^5 < \text{Re}_x < 3 \times 10^6$, respectively. Both have strong accelerations with the nominal value of $\bar{K} = 2.5 \times 10^{-6}$. However, Run 092469-1 has a very short recovery region, the last 0.3 m of the test surface, while Run 070869-1 has a very long recovery region, namely the last 1.2 m of surface. The predictions shown in Figs. 4(*A*) and 4(*C*) are excellent in the acceleration zone and exhibit the same difficulties in the relaxation zone as in many previous cases. It is seen in Fig. 4(*C*) that the predictions near the end of the surface are much better than for smaller values of x in the relaxing region.

The effect of allowing unequal thermal and hydrodynamic boundary layer thickness, δ_t and δ, was studied with the use of Run 092469-1 results. A few representative calculations were made of St_x by assuming that $\delta_t = \delta$ for $1.7 \text{ m} < x < 2.3$ m. This yielded a Stanton number that averaged almost 90 percent higher than the solid line predictions (in Fig. 4(*A*)) calculated without this restriction of equal thickness. Hence, at least based upon our modeling of the transport process, the thermal superlayer of thickness, $\delta_t - \delta$, plays a significant role in strongly accelerated regions and the recovery zone immediately downstream of them.

Figure 4(*B*) shows results for Run 072968-1 of Thielbahr et al. (1972), where $1.7 \times 10^5 < \text{Re}_x < 3.1 \times 10^6$. Here the nominal $\bar{K}$ is only about 1.47×10^{-6} and there is a long relaxation zone covering the last meter or so of the surface. Predictions for this region mirror those in Fig. 4(*C*) for Run 070869-1. However, unlike all the other cases tested, the analysis underpredicts the data in the second half of the acceleration zone and we have no explanation for this.

Run 99 of Seban and Doughty (1956), $2.6 \times 10^5 < \text{Re}_x < 3.9 \times 10^6$, has a strong acceleration (maximum $\bar{K}$ of 2×10^{-6}) and then a deceleration. Figure 4(*D*) shows the comparison with data for Run 99 and agreement is excellent in this run. In the deceleration regions, $x > 0.28$ m in Run 99 and $x > 0.37$ m for Case III, there are, as expected, large wake contributions and large values of $\pi(x)$, and agreement of our predictions seems particularly good here.

A small number of the experimental data points used in the comparisons had high enough Eckert numbers (as large as 0.2) to introduce some aerodynamic heating effects. Seban and Doughty (1956), used the adiabatic wall temperature to calculate St_x in the data reduction. Hence, this gave the St_x for low-speed flow which is the one our predictions also yield. In run 12 (Moretti and Kays, 1964), for $1.7 \text{ m} < x < 1.9$ m, there are some high-speed flow effects, since the adiabatic wall temperature was apparently not used to compute the experimental St_x. After we corrected the data for this, the St_x were lowered and this moved the circle data points even closer to our predicted line in the recovery region of Fig. 3(C) where the corrected data are shown as triangles. In case III of McCarthy and Hartnett (1963) at 0.38 m, there are also aerodynamic heating effects. These would cause the experimental St_x to shift above our prediction (in Fig. 3(*B*)) by about the same amount as it is presently below. The authors thank the reviewer who brought the possibility of aerodynamic heating to our attention.

As mentioned previously, the method developed is least satisfactory in the recovery, or relaxation, region where the pressure gradient is changed back to zero. But even here, it gives better predictions than the algebraic mixing length model finite difference solution of Cebeci et al. (1970) and does as well as the two equation model of Jones and Launder (1972), Figs. 2(*C*) and 3(*C*). The complexity of the turbulence phenomena in this region is attested to by the difficulty experienced by even the k-ϵ, low Reynolds number model used in the finite difference calculations of Jones and Launder (1972). A number of other investigators handle this imperfectly understood relaxation region by use of the concept of lag, namely that various boundary layer parameters to not "abruptly" change to new equilibrium values when the pressure gradient abruptly changes, but rather require some additional downstream distance to adjust to the new value of pressure gradient. Yet, equation (7), the equilibrium relation, requires that π revert to the flat plate value at the same place where the pressure gradient parameter β changes to zero. This lack of lag between π and β is probably causing part of the difference between our predictions and the data in the recovery region. Thus, Moffat and Kays (1984) and White (1974) use lag equations of the following type:

$$dP_e^+/dx^+ = (P^+ - P_e^+)/C \tag{24}$$

where P_e^+ is the effective value of the pressure gradient parameter P^+, which lags behind the local, at x, value of P^+. P_e^+ would be used, for example, in the calculation of β, and therefore, of $\pi(x)$ in equation (7), would also be used explicitly in the thermal law of the wall, equation (10), and implicitly elsewhere in the calculation of c_f, δ_t^+, and St_x. In fact, Moffat and Kays (1984) indicate that the use of lag is critical in their model if their solution is to follow actual events in the recovery zone. More recently, Sarrough and Ibrahim (1987) used a similar type of lag relation for outer region mixing length and one for effective radius of curvature, and obtained very good results in the recovery region of flows with streamline curvature.

Concluding Remarks

An integral method has been developed to predict the Stanton number distribution in turbulent boundary layer flow with arbitrary pressure gradient. The method makes use of inner laws, and combined laws of wall and wake for both the velocity and temperature profiles, as well as temperature profile and heat transfer modeling in the thermal superlayer.

Comparison of predictions with available experimental data yields good to excellent agreement in zero and favorable pressure gradients, including strongly accelerated flows tending toward retransition, and in adverse pressure gradients. Agreement is not as good in recovery regions.

The method presented yields better predictions than two finite difference methods, yet is more economical and considerably simpler to program and use since nonlinear algebraic equations are solved along with one ordinary differential equation.

In an effort to improve the procedure in recovery regions, work is continuing on the modeling in this region. This work includes the use of lag equations, low Reynolds number modifications, and employment of thermal parameter values different from their hydrodynamic counterparts.

More work also should be done to improve the modeling in the thermal superlayer. In reality, this layer is not one of completely laminar flow and is not a pure conduction region. This should be coupled with sublayer modeling, which accounts for the variable thickness, in y^+, discussed by Moffat and Kays (1984).

References

Ambrok, G. S., 1957, "Approximate Equation for the Thermal Boundary Layer With Variations in Boundary Layer Structure," *Soviet Physics, Technical Physics*, Vol. 2, No. 9, pp. 1979–1986.

Cebeci, T., Smith, A. M., and Mosinskis, G., 1970, "Solution of the Incompressible Turbulent Boundary Layer Equations With Heat Transfer," ASME JOURNAL OF HEAT TRANSFER, Vol. 99, pp. 133-143.

Coles, D. E., and Hirst, E. A., 1968, *Proc. Comput. Turbul. Boundary-Layers Vol. II*, Dept. of Mechanical Engineering, Stanford University, Stanford, CA.

Hildebrand, F. B., 1968, *Finite Difference Equations and Simulations*, Prentice Hall, Englewood Cliffs, NJ, p. 143.

Hoffmann, P. H., and Perry, A. E., 1979, "The Development of Turbulent Thermal Layers on Flat Plates," *Int. J. Heat Mass Transfer*, Vol. 22, pp. 39-46.

Jones, W. P., and Launder, B. E., 1972, "The Prediction of Laminarization With a Two Equation Model of Turbulence," *Int. J. Heat Mass Transfer*, Vol. 15, pp. 301-314.

Kays, W. M., and Crawford, M. E., 1980, *Convective Heat and Mass Transfer*, 2nd ed., McGraw-Hill, New York, pp. 217, 267-268.

Kearney, D. W., Kays, W. M., and Moffat, R. J., 1973, "Heat Transfer to a Strongly Accelerated Turbulent Boundary Layer: Some Experimental Results Including Transpiration," *Int. J. Heat Mass Transfer*, Vol. 16, pp. 1289-1305.

Kline, S. J., Cockrell, D. J., Morkovin, M. V., and Sovran, G., 1968, *Proc. Comput. Turbul. Boundary Layers, Vol. I*, Dept. of Mechanical Engineering, Stanford University, Stanford, CA.

Launder, B. E., and Lockwood, F. C., 1969, "An Aspect of Heat Transfer in Accelerating Turbulent Boundary Layers," ASME JOURNAL OF HEAT TRANSFER, Vol. 91, pp. 229-234.

Launder, B. E., and Spalding, D. B., 1972, *Mathematical Models of Turbulence*, Academic Press, New York, pp. 49, 55.

Lu, Yaning, 1987, "Heat Transfer Across Turbulent Boundary Layers With Pressure Gradients," MS Thesis, University of Maine, Orono, ME.

McCarthy, T. F., and Hartnett, J. P., 1963, "Heat Transfer to Turbulent Boundary Layers With a Pressure Gradient," Tech. Report No. 26, Dept. of Mechanical Engineering, Univ. of Delaware.

Mellor, G. L., and Gibson, D. M., 1966, "Equilibrium Turbulent Boundary Layers," *J. Fluid Mech.*, Vol. 24, Part 2, pp. 225-253.

Moffat, R. J., and Kays, W. M., 1984, "A Review of Turbulent Boundary Layer Heat Transfer Research at Stanford, 1958-1983," *Advances in Heat Transfer*, Vol. 16, Academic Press, New York, pp. 241-365.

Moretti, P. M., and Kays, W. M., 1964, "Heat Transfer to a Turbulent Boundary Layer With Varying Free Stream Velocity and Varying Surface Temperature—An Experimental Study," Stanford Univ. Thermosciences Division, Dept. of Mechanical Engineering, Report No. PG-1.

Moretti, P. M., and Kays, W. M., 1965, "Heat Transfer to a Turbulent Boundary Layer With Varying Free Stream Velocity and Varying Surface Temperature—An Experimental Study," *Int. J. Heat Mass Transfer*, Vol. 8, pp. 1187-1201.

Sarrough, S., and Ibrahim, M., 1987, "Turbulence Modelling for Convective Heat Transfer Over Convexly Curved Surfaces and the Recovery from Curvature," *Heat Transfer in Gas Turbine Engines*, Winter Annual Meeting of the ASME, Boston, HTD-Vol. 87, pp. 25-34.

Seban, R. A., and Doughty, D. L., 1956, "Heat Transfer to Turbulent Boundary Layers With Variable Free Stream Velocity," *Trans. ASME*, Vol. 78, No. 1, pp. 217-223.

Sepri, P., 1987, "Experimental Wake Structure of Heated Turbulent Boundary Layers at Elevated Levels of Free Stream Turbulence," ASME JOURNAL OF HEAT TRANSFER, Vol. 109, pp. 336-344.

Sucec, J., 1986, "Heat Transfer Across the Constant Property Turbulent Boundary Layer," *Heat Transfer 1986*, Proc. Eighth Inter. Heat Transfer Conf., San Francisco, CA, Hemisphere Press, Washington, DC, Vol. 3, pp. 1109-1114.

Thielbahr, W. H., Kays, W. M., and Moffat, R. J., 1972, "The Turbulent Boundary Layer on a Porous Plate: Experimental Heat Transfer With Uniform Blowing and Suction With Moderately Strong Acceleration," ASME JOURNAL OF HEAT TRANSFER, Vol. 94, pp. 111-118.

Thomas, L., and Al-Shariff, M. M., 1981, "An Integral Analysis for Heat Transfer in Turbulent, Incompressible Boundary Layer Flow," ASME JOURNAL OF HEAT TRANSFER, Vol. 103, pp. 772-777.

White, F. M., 1974, *Viscous Fluid Flow*, McGraw-Hill, New York, pp. 464-465, 523, 519, 538-541, 519-520.

S. Kakac
Professor.
Mem. ASME

W. Li
Graduate Student.
Student Mem. ASME

Department of Mechanical Engineering,
University of Miami,
Coral Gables, FL 33124

R. M. Cotta
Programa de Engenharia Mecanica,
COPPE—Universidade
Federal do Rio Janeiro,
Rio de Janeiro, Brazil

Unsteady Laminar Forced Convection in Ducts With Periodic Variation of Inlet Temperature

A theoretical and experimental study of laminar forced convection in the thermal entrance region of a rectangular duct, subjected to a sinusoidally varying inlet temperature, is presented. A general boundary condition of the fifth kind that accounts for both external convection and wall thermal capacitance effects is considered, and an analytical solution is obtained through extending the generalized integral transform technique. The variations of amplitudes and phase lags of centerline and bulk temperatures are determined as functions of modified Biot number, fluid-to-wall thermal capacitance ratio, and dimensionless inlet frequency. An apparatus has been designed, built, and used for the experimental study to provide validation of the mathematical modeling employed. Good agreement is obtained when the nonuniform sinusoidally varying inlet temperature profile obtained by experiments is incorporated into the theoretical model.

Introduction

Unsteady forced convection is an important branch of heat transfer research and technology. Ducts are generally the basic parts of a heat exchanger that may be exposed to a number of planned or unplanned transients. In thermal equipment, transients may also arise due to changes in operating conditions such as time-varying inlet temperature of flow rates. Unsteady behavior of temperature distribution in heat exchange equipment can produce such undesirable effects as reduced thermal performance and severe thermal stress with eventual mechanical failure. Thus, it is highly important to know and predict the transient response of a heat exchanger for time-varying inlet temperature; it is also essential to know its transient response in order to provide an effective control system. Solutions to forced convection problems with periodic variation of inlet temperature lead to eigenvalue problems, which are not of the conventional Sturm–Liouville type: The eigenvalues and the corresponding eigenfunctions are complex numbers and complex-valued function, respectively.

Kardas (1966) studied the heat transfer from parallel flat plates to fluids flowing between them with an inlet temperature varying with time. He actually presented an analytical solution of the unidirectional regenerator problem. Sparrow and De Farias (1968) did an analysis of periodic forced convection with slug flow in a parallel-plate channel with sinusoidally varying inlet temperature and time- and space-dependent wall temperature. The wall temperature was dynamically determined by a balance of the heat transfer rate and the energy storage. Numerical evaluation of the analytical results provided the time and space dependence of the wall and bulk temperatures and the Nusselt number. Kakac and Yener (1973) obtained an exact solution to the transient energy equation for laminar slug flow of an incompressible fluid in a parallel-plate channel with a sinusoidal variation of fluid inlet temperature. Kakac (1975) obtained a general solution to the unsteady energy equation under constant wall temperature or zero heat flux boundary conditions for the decay of inlet and initial temperature distributions of incompressible transient forced convection between parallel plates. Cotta et al. (1987) solved the slug flow problem considered by Sparrow and De Farias (1968) and Kakac and Yener (1973), for both circular tubes and parallel-plate channels, by developing an approach for complex transcendental equations and providing accurate results for the related eigenvalues; this approach was not, however, extended to parabolic flow situations. A second-order accurate finite difference scheme was also developed for transient forced convection resulting from a step change of inlet temperature by Cotta et al. (1986). Cotta and Ozisik (1986) presented an analytical solution to periodic laminar forced convection inside ducts, by making use of the generalized integral transform technique, completely avoiding the complex eigenvalue problem and solving, instead, the resulting coupled system of complex ordinary differential equations. An experimental investigation of transient forced convection in ducts with a timewise variation of inlet temperature is reported by Kakac et al. (1988, 1989*a*).

In the present work, the theoretical analysis given by Cotta and Ozisik (1986) and Ozisik and Murry (1974) is extended for laminar flow inside a parallel-plate channel subjected to timewise variation of inlet temperature, when external convection, wall thermal capacitance, and nonuniformity of the sinusoidal variation of temperature across the duct entrance are no longer negligible effects. The present study is an extension of the analysis presented by Kakac et al. (1989b). The results thus obtained are compared with experimental findings to verify the present modeling approach. Numerical results are also obtained for various combinations of the relevant parameters, such as dimensionless inlet frequency, modified Biot number, fluid-to-wall thermal capacitance ratio, and nonuniform periodic inlet temperature profile, and their effects on the bulk and center temperature amplitudes and phase lags are critically examined.

In practical applications, the inlet temperature of the heat

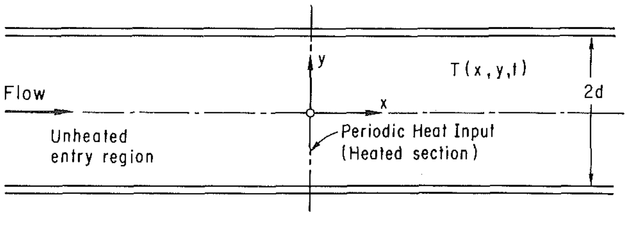

Fig. 1 Geometry of the theoretical analysis

Contributed by the Heat Transfer Division for publication in the JOURNAL OF HEAT TRANSFER. Manuscript received by the Heat Transfer Division September 12, 1989, revision received March 13, 1990. Keywords: Forced Convection, Transient and Unsteady Heat Transfer.

exchanger may vary as a function of time. A general time-dependent inlet condition can be expanded in terms of sine and cosine function by use of Fourier's integral theorem. Therefore, the authors believe that the results of this work are a valuable contribution to the industrially significant problem area of transient response of thermal systems.

Problem Formulation

We consider transient laminar forced convection inside a parallel-plate channel with fully developed flow, which is subjected to a periodic variation of inlet temperature the geometry for the theoretical analysis is shown in Fig. 1. A general boundary condition of the fifth kind that accounts for both external convection and wall heat capacitance effects is considered, while axial conduction and free convection effects are disregarded. Further assuming constant fluid thermophysical properties, the energy equation governing the diffusion in the y direction and the convection in the x direction can be written as

$$\frac{\partial T}{\partial t} + u(y)\frac{\partial T}{\partial x} = \alpha\frac{\partial^2 T}{\partial y^2}, \text{ for } 0<y<d,\ x>0,\ t>0 \qquad (1a)$$

with inlet and boundary conditions given, respectively, by

$$T(0, y, t) = T_\infty + \Delta T(y)e^{i\beta t}, \qquad \text{for } 0<y<d \qquad (1b)$$

$$\frac{\partial T}{\partial y} = 0, \text{ at } y=0, \qquad \text{for } x>0 \qquad (1c)$$

and on the duct walls, the fifth kind of boundary condition is imposed as

$$h_e(T-T_\infty) + k\frac{\partial T}{\partial y} + (\rho C)_w L\frac{\partial T}{\partial t} = 0, \text{ at } y=d, \text{ for } x>0 \qquad (1d)$$

Here the initial condition is not necessary, since we only seek periodic solution to problem (1) stated above.

Problem (1) can now be rewritten in dimensionless form as:

$$\frac{\partial \theta}{\partial \tau} + U(\eta)\frac{\partial \theta}{\partial \xi} = \frac{\partial^2 \theta}{\partial \eta^2}, \qquad \text{for } 0<\eta<1,\ \xi>0 \qquad (2a)$$

$$\theta(0, \eta, \tau) = \Delta\theta(\eta)e^{i\Omega\tau}, \qquad \text{for } 0\le\eta\le 1 \qquad (2b)$$

$$\frac{\partial \theta}{\partial \eta} = 0, \qquad \text{at } \eta=0, \text{ for } \xi>0 \qquad (2c)$$

$$\text{Bi}\,\theta + \frac{\partial \theta}{\partial \eta} + \frac{1}{a^*}\frac{\partial \theta}{\partial \tau} = 0, \qquad \text{at } \eta=1, \text{ for } \xi>0 \qquad (2d)$$

where various dimensionless parameters are defined by
$\eta = y/d$, $\xi = (x/D_e)(D_e/d)^2/(\text{RePr})$,

$$\tau = \alpha t/d^2, \quad \theta = (T-T_\infty)/\Delta T_c,$$

$$\text{Bi} = h_e d/k, \quad \Omega = \beta d^2/\alpha, \quad a^* = (\rho C_p)_f d/(\rho C)_w L$$

and

$$U(\eta) = u(y)/U_m, \quad \Delta\theta(\eta) = \Delta T(y)/\Delta T_c$$

Note that if a^* goes to infinity the wall capacitance effects become negligible. A periodic solution of the form

$$\theta(\xi, \eta, \tau) = e^{i\Omega\tau}\bar{\theta}(\xi, \eta) \qquad (3)$$

can be assumed for the decay of the inlet condition, equation (1b), along the duct. Since only the quasi-steady response is of interest (i.e., initial transients are passed), problem (2) simplifies to the problem for $\bar{\theta}(\xi, \eta)$:

$$\frac{\partial^2 \bar{\theta}}{\partial \eta^2} - U(\eta)\frac{\partial \bar{\theta}}{\partial \xi} - i\Omega\bar{\theta} = 0, \qquad \text{for } 0<\eta<1,\ \xi>0 \qquad (4a)$$

$$\bar{\theta}(0, \eta) = \Delta\theta(\eta), \qquad \text{for } 0\le\eta\le 1 \qquad (4b)$$

$$\frac{\partial \bar{\theta}}{\partial \eta} = 0, \qquad \text{at } \eta=0, \qquad (4c)$$

$$\text{Bi}\,\bar{\theta} + \frac{\partial \bar{\theta}}{\partial \eta} = -\frac{i\Omega}{a^*}\bar{\theta}, \qquad \text{at } \eta=1, \qquad (4d)$$

Method of Solution

A formal solution of this homogeneous problem is through the use of the classical integral transform technique leading to a complex nonclassical Sturm-Liouville problem for which no known direct solution is available. To alleviate such difficulties we choose to follow the approach introduced by Cotta and Ozisik (1986), based on the generalized integral transform technique used by Ozisik and Murry (1974). Here it is extended to include the wall heat capacitance effects to provide solutions under the experimental conditions. The following eigenvalue problem is then considered:

$$\frac{d^2 Y_n}{d\eta^2} + \lambda_n^2 U(\eta) Y_n = 0 \qquad \text{for } 0<\eta<1, \qquad (5a)$$

Nomenclature

a^* = fluid-to-wall thermal capacitance ratio = $(\rho C_p)_f d/(\rho C)_w L$
a^*_{nk} = element of matrix **A**, defined by equation (9b)
A = dimensionless temperature amplitude function
A = $N\times N$ matrix, defined by equation (9b)
A_{nk} = coefficient, defined by equation (9b)
Bi = modified Biot number = $h_e d/k$
c_n = coefficient, defined by equations (9c) and (9d)
C_w = wall specific heat, kJ/kg•K
C_p = specific heat of the fluid, kJ/kg•K
d = half distance between parallel plates, m
D_e = equivalent diameter of rectangular duct = $4A_c/P$, m
E = coefficient, defined by equations (15) and (16)
f_n = coefficient, defined by equation (8c)
h_e = effective heat transfer coefficient = $(1/h_\infty + L/k_w)^{-1}$, between inner wall and ambient fluid, W/m^{2}K
i = imaginary number = $\sqrt{-1}$
Im = imaginary part of the complex value defined by equation (13)
k = fluid thermal conductivity, W/m•K
L = thickness of the wall
N = number of terms in series
N_n = norm of the eigenproblem defined by equation (5)
Pr = Prandtl number = ν/α
Re = Reynolds number = $U_m D_e/\nu$ or real part of the complex value defined by equation (13)
t = time variables, s
T = temperature, K
T_∞ = ambient temperature, K
$u(y)$ = velocity across the test section, m/s
$U(\eta)$ = dimensionless velocity profile

$$\frac{dY_n}{d\eta}=0, \qquad \text{at } \eta=0, \qquad (5b)$$

$$\mathrm{Bi}\, Y_n+\frac{dY_n}{d\eta}=0, \qquad \text{at } \eta=1, \qquad (5c)$$

where $Y_n(\eta)$ is the eigenfunction corresponding to the nth eigenvalue. Equation (5) allows definition of the integral-transform pair for the function $\theta(\xi, \eta)$, given by

$$\bar{\theta}(\xi, \eta)=\sum_{n=1}^{\infty}\frac{1}{\sqrt{N_n}}\tilde{\theta}_n(\xi)Y_n(\eta), \qquad 0<\eta<1 \qquad (6a)$$

and

$$\tilde{\theta}_n(\xi)=\int_0^1\frac{1}{\sqrt{N_n}}U(\eta)Y_n(\eta)\bar{\theta}(\xi, \eta)d\eta \qquad (6b)$$

where a symmetric kernel has been utilized, and the normalized integral is given by

$$N_n=\int_0^1 U(\eta)Y_n^2(\eta)d\eta \qquad (6c)$$

We can operate on equation (4*a*) with $\int_0^1[Y_k(\eta)/\sqrt{N_k}]d\eta$, to obtain

$$\frac{d\tilde{\theta}_k}{d\xi}+\lambda_k^2\tilde{\theta}_k=\frac{1}{\sqrt{N_k}}\left[Y_k(1)\frac{\partial\bar{\theta}(\xi, 1)}{\partial\eta}-\bar{\theta}(\xi, 1)\frac{dY_k(1)}{d\eta}\right]$$
$$-i\Omega\int_0^1\frac{Y_k}{\sqrt{N_k}}\bar{\theta}(\xi, \eta)d\eta \qquad (7a)$$

From manipulation of boundary conditions, equations, equations (4*d*) and (5*c*), one obtains

$$\frac{1}{\sqrt{N_k}}\left[Y_k(1)\frac{\partial\bar{\theta}(\xi, 1)}{\partial\eta}-\bar{\theta}(\xi, 1)\frac{dY_k(1)}{d\eta}\right]=-\frac{i\Omega}{a^*}\bar{\theta}(\xi, 1)\frac{Y_k(1)}{\sqrt{N_k}}$$

or, from inversion formula (6*a*)

$$\frac{1}{\sqrt{N}}\left[Y_k(1)\frac{\partial\bar{\theta}(\xi, 1)}{\partial\eta}-\bar{\theta}(\xi, 1)\frac{dY_k(1)}{d\eta}\right]=-$$
$$\frac{i\Omega}{a^*}\sum_{n=1}^{\infty}\frac{1}{\sqrt{(N_nN_k)}}Y_n(1)\ Y_k(1)\tilde{\theta}_n(\xi) \qquad (7b)$$

Once the integral in equation (7*a*) is evaluated by use of the inversion formula (6*c*), we can obtain the following ordinary differential equation for the transform function $\tilde{\theta}_k$:

$$\frac{d\theta_k}{d\xi}+\lambda_k^2\tilde{\theta}_k+i\Omega\sum_{n=1}^{\infty}\tilde{\theta}_nA_{nk}=0 \qquad (8a)$$

where

$$A_{nk}=A_{kn}=\frac{1}{\sqrt{(N_nN_k)}}\left[\frac{Y_n(1)Y_k(1)}{a^*}+\int_0^1 Y_nY_kd\eta\right] \qquad (8b)$$

due to the symmetric kernel chosen for equation (6).

The inlet condition, equation (4*b*), is also transformed by operating with $\int_0^1[Y_k(\eta)/\sqrt{N_k}]d\eta$ to yield

$$\tilde{\theta}_k(0)=f_k=\int_0^1\frac{1}{\sqrt{N_k}}U(\eta)\Delta\theta(\eta)Y_kd\eta \qquad (8c)$$

System (8) above forms a set of infinite, coupled, first-order linear ordinary differential equations, and a closed form solution is unlikely to be obtainable.

As shown by Cotta and Ozisik (1986), however, it can be truncated to any sufficiently large order, N, and solved to any desired accuracy, once the related eigenvalue problem is solved for the eigenvalues, and eigenvectors, $\{\theta_1^+, \theta_2^+, \ldots, \theta_N^+\}$, of the $\mathrm{N}\times\mathrm{N}$ coefficient matrix $\mathbf{A}$

$$(\mathbf{A}-\mu_nI)\theta_n^+=0 \qquad (9a)$$

where

$$\mathbf{A}=\{a_{nk}^*\}, \text{ and } a_{nk}^*=\delta_{nk}\lambda_n{}^2+i\Omega A_{nk} \qquad (9b)$$

The solution is constructed from the linear combination of independent solutions

$$\tilde{\theta}_k(\xi)=\sum_{n=1}^{N}c_n\theta_{kn}^+e^{-\mu_n\xi}, \qquad k=1, 2, \ldots, N \qquad (9c)$$

where θ_{kn}^+ is the nth component of the kth eigenvector, and the constants c_n are determined by constraining this solution to satisfy the inlet condition equation (8*c*)

$$\sum_{n=1}^{\infty}c_n\theta_{kn}^+=f_k, \qquad k=1, 2, \ldots, N \qquad (9d)$$

Reliable schemes in subroutine packages are readily available for complex problem in equations (9*a*) and 9(*d*) (IMSL, 1979). The inversion formula, equation (6*b*), is then employed to provide the complete solution for $\theta(\xi, \eta)$.

From simple inspection of the coefficient matrix we also observe that, especially for smaller values of the dimensionless

Nomenclature (cont.)

U_m = mean velocity, m/s
x = axial coordinate, m
X = axial coordinate $=x/D_e$
y = normal coordinate, m
Y_n = eigenfunction corresponding to nth eigenvalue, defined by equation (5)
α = fluid thermal diffusivity $=k/\rho C_p$, m/s^2
$\bar{\alpha}$ = dimensional decay index defined in equation (15)
β = inlet frequency, Hz
ΔT_c = centerline inlet temperature amplitude
$\Delta T(y)$ = inlet temperature amplitude profile
$\Delta\theta(\eta)$ = inlet temperature amplitude profile $=\Delta T(y)/\Delta T_c$
δ_{nk} = δ function; for $n=k$ $\delta_{nk}=1$, for $n\neq k$, $\delta_{nk}=0$
ϵ = relative deviation
η = normal coordinate $=y/d$
$\theta(\xi, \eta, \tau)$ = dimensionless temperature
$\bar{\theta}(\xi, \eta)$ = quasi-steady dimensionless temperature defined by equation (3)
θ_n^+ = nth eigenvector for equation (9*a*)
Λ = dimensionless decay index defined in equation (16)
λ_n = eigenvalues of equation (5)
μ_n = eigenvalues of equation (9*a*)
ξ = axial coordinate $=(x/D_e)\ (D_e/d)^2/(\mathrm{RePr})$
ρ_f = fluid density, kg/m^3
ρ_w = equivalent density of the wall, kg/m^3
τ = time $=\alpha t/d^2$
ϕ = phase leg
Ω = inlet frequency $=\beta d^2/\alpha$

Superscripts

l = lowest-order solution

Subscripts

b = bulk value, defined in equation (14*a*)
c = centerline value

frequency Ω, and large values of the heat capacitance ratio a^*, the diagonal elements might be quite dominant over those off the diagonal. This fact suggests a way of obtaining a straightforward approximate solution, i.e., the lowest-order solution, by letting $n=k$ in the summation of equation (8*a*). This corresponds to the decoupling system (8), and shall be a reasonably accurate procedure as long as the diagonal elements of the coefficient matrix do not differ substantially from their eigenvalues. A special case of the present problem with $\mathrm{Bi}=\infty$ and $a^*=\infty$ was solved by Cotta and Ozisik (1986) through this approach, and the accuracy of the lowest-order solution was examined, providing good agreement with the complete solution for the lower frequencies considered ($\Omega<5.0$). In the present case the new parameter a^* is considered, the effects of which will be discussed later. The approximate decoupled system to be solved can then be written as

$$\frac{d\bar{\theta}_n^l}{d\xi} + (\lambda_n^2 + i\Omega A_{nn})\bar{\theta}_n^l = 0 \qquad \text{for } \xi>0 \qquad (10a)$$

$$\bar{\theta}_n^l(0) = f_n, \quad n=1, 2, \ldots \qquad (10b)$$

where the superscript l indicates the lowest-order approximation of the corresponding variables. Equation (10) have the explicit solution as

$$\bar{\theta}_n^l(\xi) = f_n e^{-(\lambda_n^2 + i\Omega A_{nn})\xi} \qquad (11)$$

and the result is inverted by the inversion formula to get

$$\bar{\theta}^l(\xi, \eta) = \sum_{n=1}^{\infty} \frac{1}{\sqrt{N_n}} f_n e^{-(\lambda_n^2 + i\Omega A_{nn})\xi} Y_n(\eta) \qquad (12a)$$

For the purpose of comparison with experimental results, the dimensionless centerline temperature of the duct it given by

$$\bar{\theta}_c^l(\xi) = \sum_{n=1}^{\infty} \frac{1}{\sqrt{N_n}} f_n e^{-(\lambda_n^2 + i\Omega A_{nn})\xi} Y_n(0) \qquad (12b)$$

The result can be expressed in polar coordinates, after the time dependence is incorporated, as

$$\theta_c^l(\xi, \tau) = A_c^l(\xi) e^{i[\Omega\tau + \phi_c^l(\xi)]} \qquad (13a)$$

where the subscript c indicates the value at the centerline of the duct ($\eta=0$). The amplitude $A_c^l(\xi)$ and the phase lag $\phi_c^l(\xi)$ can be obtained from the following expressions:

$$A_c^l(\xi) = [[\mathrm{Re}(\bar{\theta}_c^l(\xi))]^2 + [Im(\bar{\theta}_c^l(\xi))]^2]^{1/2} \qquad (13b)$$

$$\phi_c^l(\xi) = \tan^{-1}\left[\frac{Im(\bar{\theta}_c^l(\xi))}{\mathrm{Re}(\bar{\theta}_c^l(\xi))}\right] \qquad (13c)$$

The other problem of interest is the evaluation of the dimensionless fluid bulk temperature along the length of the duct, computed from its definition as

$$\theta_b(\xi, \tau) = \int_0^1 U(\eta)\, \theta(\xi, \eta, \tau) d\eta \Big/ \int_0^1 U(\eta) d\eta \qquad (14a)$$

or in polar form

$$\theta_b(\xi, \tau) = A_b^l(\xi) e^{i[\Omega\tau + \phi_c^l(\xi)]} \qquad (14b)$$

In order to compare the theoretical and experimental results, the dimensional and dimensionless decay indexes, Λ and $\bar{\alpha}$, are defined by comparing equations (12*b*) and (13*a*) as follows:

$$A_c^l(\xi) = Ee^{-\bar{\alpha}X} \qquad (15)$$

or

$$A_c^l(\xi) = Ee^{-\Lambda\xi} \qquad (16)$$

where $X=x/D_e$, and Λ and $\bar{\alpha}$ are related by

$$\Lambda = \mathrm{Re}\ \mathrm{Pr} \left(\frac{D_e}{d}\right)^2 \bar{\alpha} \qquad (17)$$

A computer program was developed to calculate the timewise variation of inlet temperature, the variation of its amplitude and phase lag along the channel for various values of the Biot number, the heat capacitance ratio, and inlet frequency.

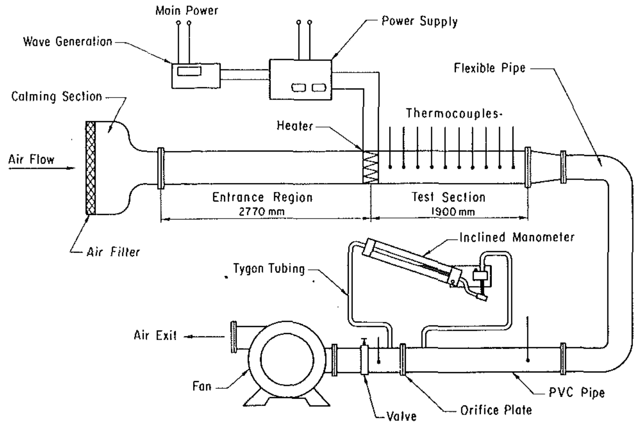

Fig. 2 Schematic diagram of experimental setup

Experiments

An experimental setup has been designed, built, and used to study the behavior of transient forced convection in a duct with a rectangular cross section with a sinusoidal variation of heat input.

The purpose of the experimental setup is to provide a means to study the decay of sinusoidal thermal inlet conditions for laminar and turbulent forced convection in a particular duct geometry described by Kakac et al. (1988, 1989a). The geometry to be used is a rectangular duct with a cross-sectional area measuring 10×1 in.^{2} (254×25.4 mm^2). With this particular geometry, a wide range of Reynolds numbers and inlet frequencies are utilized for the study. A schematic diagram of the experimental apparatus is shown in Fig. 2.

The experimental apparatus is operated in the suction mode. The main components of the apparatus are: air filter, calming section, inlet section, electric heater, test section, thermocouples, convergent section, orifice plate, and a fan.

Air flows from the calming section to the inlet section of the duct (2270 mm) wherein the velocity becomes fully developed.

The duct is constructed with an outer casing made from 6.35 mm (1/4 in.) plywood with outer dimensions of 114.3 mm × 381 mm × 4670 mm. This section incorporates the inlet and test sections. The inside of the casing is lined with 25.4-mm extruded Styrofoam, leaving a cross-sectional flow area of 254 mm × 25.4 mm. The Styrofoam is cemented to the inside of the casing to prevent air leakage. For experiments in the thermal entrance region, the heater is located at a distance of 2270 mm away from the inlet of the duct. Sinusoidal heat input is then applied to the flowing air through the electric heater.

Throughout the study, periodic variation in the heat input is provided by an electric heater constructed so as to fit into the duct. For the assembly of the heater, 0.4-mm-dia nichrome resistance wire is used as heating element, and is threaded between two plates made by insulating material. The heater is powered by a function generator and a power supply.

To measure the variation of temperature along the duct resulting from the sinusoidal heat input, several thermocouples are placed at equal intervals along the test section starting at exit of electric heater. The thermocouples are made from 30-gage, teflon-coated chromel and constantan, E-type thermocouple wires. The junctions of the thermocouples are positioned exactly at the centerline of the duct cross-section.

The measurements made by an E-type thermocouple usually have an uncertainty of $\pm1.7°$C within the range from 0°C to 316°C. The uncertainty associated with the mass flow rate was

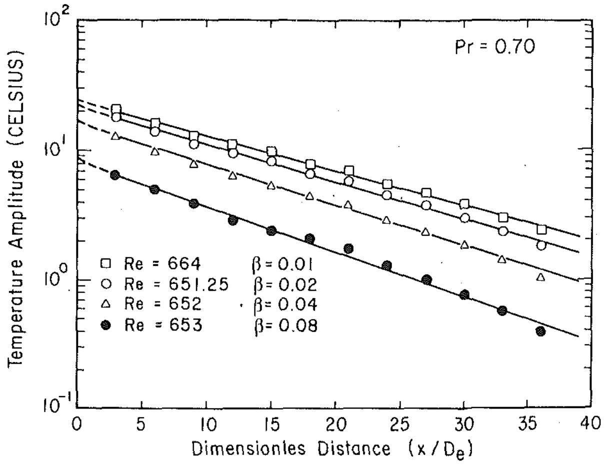

Fig. 3 Variation of centerline temperature amplitude along the duct for Re≃650 and β≃0.01–0.08 Hz

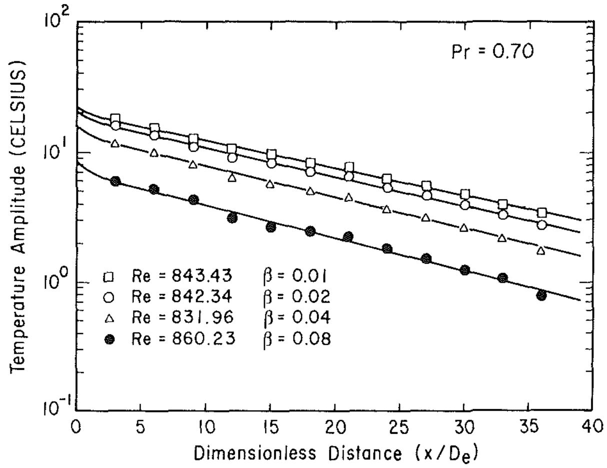

Fig. 4 Variation of centerline temperature amplitude along the duct for Re≃850 and β≃0.01–0.08 Hz

calculated as ±2.64 percent by Ding (1987) according to ASME standards.

During the course of the experimental study, the inlet frequency and the Reynolds number were varied. Figures 3 and 4 show typical experimental results of the decay of the amplitude of the centerline temperature along the duct in the thermal entrance region.

A detailed description of the experimental apparatus, instrumentation, procedure, data reduction techniques, and experimental results for a wide range of Reynolds number and inlet frequencies is given by Ding (1987).

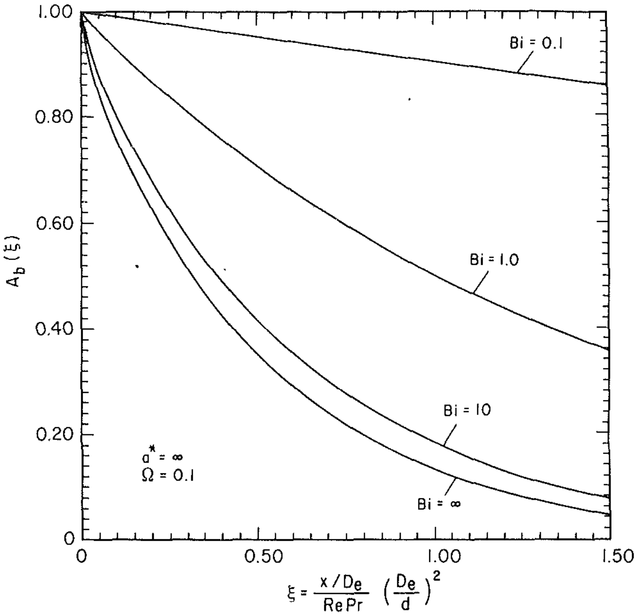

Fig. 5 Amplitudes of dimensionless bulk temperature along the duct for various values of Biot number ($a^* = \infty$, $\Omega = 0.1$)

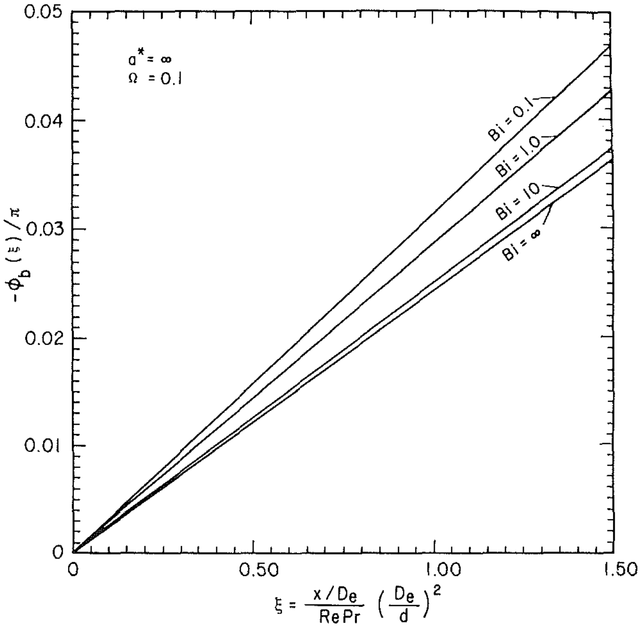

Fig. 6 Phase lag of dimensionless bulk temperature along the duct for various values of Biot number ($a^* = \infty$, $\Omega = 0.1$)

Results and Discussion

Based on the above analysis, a computer program was constructed to calculate the dimensionless bulk and centerline fluid temperatures along the duct, for the parameters Bi, a^*, and Ω specified by experimental conditions. The complete solution is readily obtained from equations (9), through the use of IMSL (1979) subroutines, for complex matrix eigenvalue problems and complex linear systems. The approximate lowest solution was also programmed to assess its range of applicability in terms of the new parameters, namely Bi and a^*. A typical run with $N = 30$ takes less than 60 seconds computing time on the IBM 3090 main frame computer.

In. Figs. 5 and 6, the effects of Biot number on amplitude and phase lag of bulk temperature are presented as functions of dimensionless axial distance ξ, with $a^* = \infty$ (negligible wall thermal capacitance) and $\Omega = 0.1$. It is seen clearly that for Bi ≥ 10, the results will not differ significantly from those for Bi = ∞, especially for the phase lags. Therefore, under experimental air flow situations when Bi is expected to be a large number, its precise determination might be of limited relevance.

Figures 7 and 8 illustrate the effects of fluid-to-wall thermal capacitance ratio on the bulk temperature amplitudes and the phase lags for Bi = 10 and $\Omega = 0.1$. As can be seen, only for large wall thermal capacitances (or small a^*), the storage of heat at the wall itself will be of some importance to the fluid bulk temperature evolution along the duct. The effect will be more significant for the phase lags. It should be noted that amplitudes are practically unchanged for $a^* \geq 0.1$, but some time lag is already present in the fluid temperature behavior

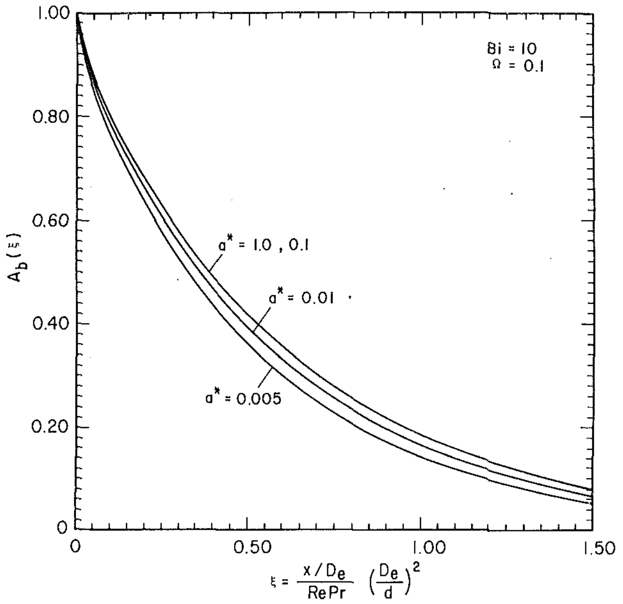

Fig. 7 Amplitudes of dimensionless bulk temperature along the duct for various values of fluid-to-wall thermal capacitance ratio (Bi = 10, $\Omega = 0.1$)

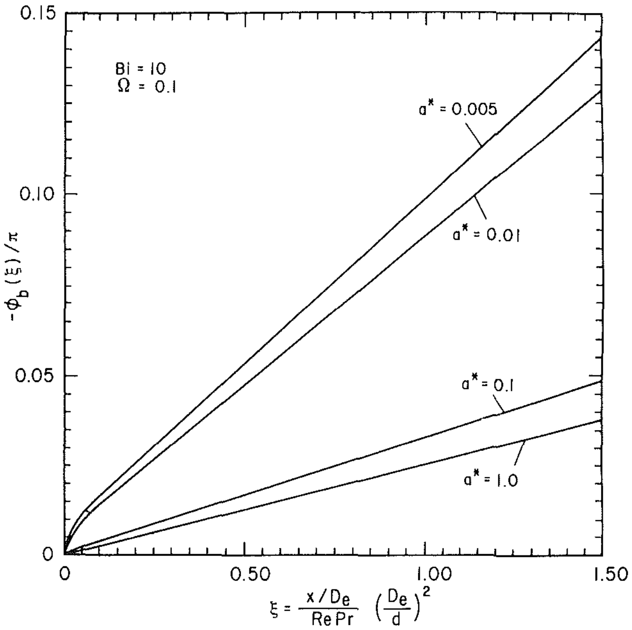

Fig. 8 Phase lag of dimensionless bulk temperature along the duct for various values of fluid-to-wall thermal capacitance ratio (Bi = 10, $\Omega = 0.1$)

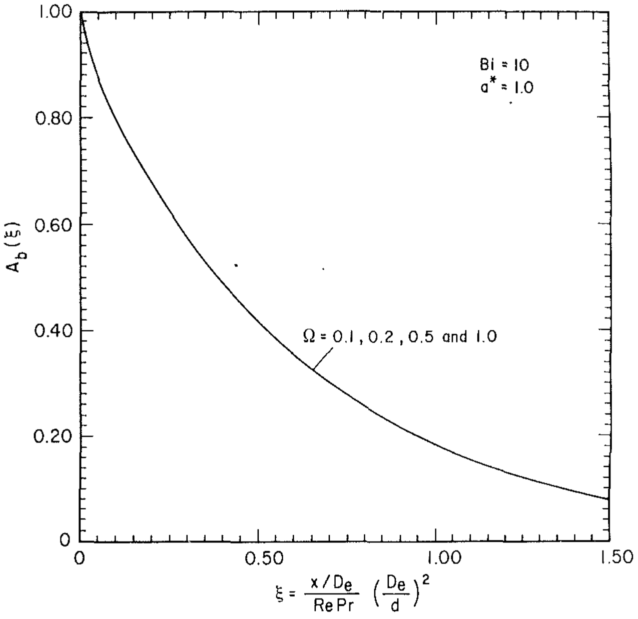

Fig. 9 Amplitudes of dimensionless bulk temperature along the duct for various values of dimensionless inlet frequencies (Bi = 10, $a^* = 1.0$)

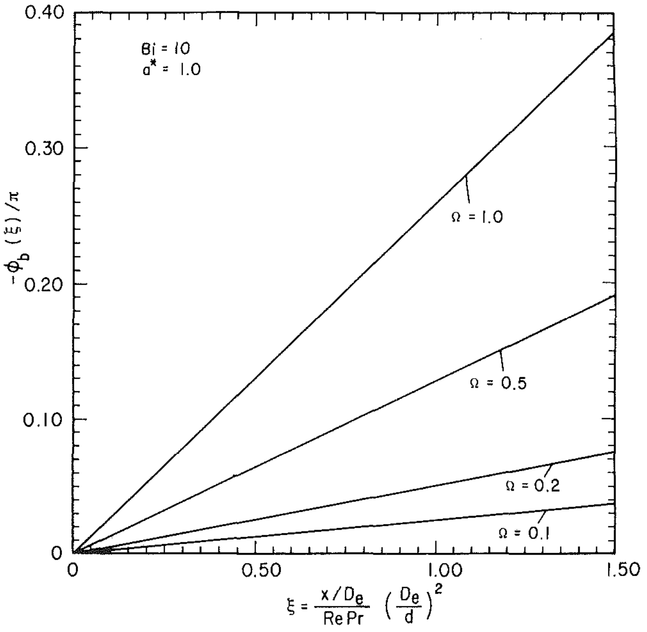

Fig. 10 Phase lag of dimensionless bulk temperature along the duct for various values of dimensionless inlet frequencies (Bi = 10, $a^* = 1.0$)

due to the presence of the wall. From Fig. 7 it can be seen that the effects for a small a^* (below 0.005) are larger than those for the range above 0.01, but the maximum amplitude difference shown on the figure is less than 0.02. The evaluation from the experimental setup shows that a^* is around 5×10^{-5}.

The effect of the dimensionless frequency Ω on the variation of the amplitude and phase lag along the channel is also studied and presented in Figs. 9 and 10, for Bi = 10 and $a^* = 1.0$. The deviations of amplitudes for different frequencies are practically unnoticeable on the graphic scale within this range. The phase lags experience a more significant change, although they have an almost linear relationship with the frequency, since the four curves in Fig. 10 practically collapse together when the phase lag is divided by each value of Ω. This behavior allows one to characterize the thermal response of a system for most practical purposes, subjected to different excitation frequencies in a certain range, by a single set of results; namely, a set of amplitudes and normalized phase lags in terms of duct length.

In order to validate the modeling employed, the present results were compared with experimental findings as described earlier. The comparisons for selected Reynolds number Re, and inlet frequencies β (or Ω), have been listed in Table 1. The present theoretical results have been observed to be consistently higher than the experimental findings for the centerline temperature amplitudes. Dimensionless numerical results at a prescribed Reynolds number and inlet frequency are compared with experimental centerline temperature amplitudes along the channel. For this purpose, Biot number Bi, and fluid-to-wall thermal capacitance a^*, were estimated according to the available data for the experimental setup, and nonuniform variation

Table 1 Comparison of the theoretical and experimental results of the centerline temperature amplitude along the duct for $Bi = 10$ and $a^* = 5 \times 10^{-5}$

x/D_e	$Re = 452.0$, $\beta = 0.01$ Hz		$Re = 680.7$, $\beta = 0.02$ Hz		$Re = 1396.0$, $\beta = 0.01$ Hz	
	exp.	th.	exp.	th.	exp.	th.
0.0	1.000000	1.000000	1.000000	1.000000	1.000000	1.000000
6.0	0.534128	0.637126	0.701328	0.754222	0.837724	0.886241
9.0	0.453329	0.494345	0.538991	0.638410	0.789886	0.822715
12.0	0.380202	0.383413	0.480515	0.539475	0.713192	0.760389
15.0	0.314817	0.297366	0.422120	0.455732	0.674997	0.701399
18.0	0.233740	0.230629	0.369767	0.384966	0.598328	0.647427
21.0	0.167867	0.178870	0.299560	0.325186	0.559772	0.595538
24.0	0.136704	0.138726	0.287885	0.274688	0.502085	0.548565
27.0	0.101692	0.107529	0.229432	0.233032	0.453988	0.505259
30.0	0.086113	0.083446	0.194226	0.196000	0.425066	0.465358
33.0	0.066618	0.064718	0.170859	0.165563	0.396136	0.428601
36.0	0.051009	0.050194	0.147368	0.139853	0.367199	0.394745

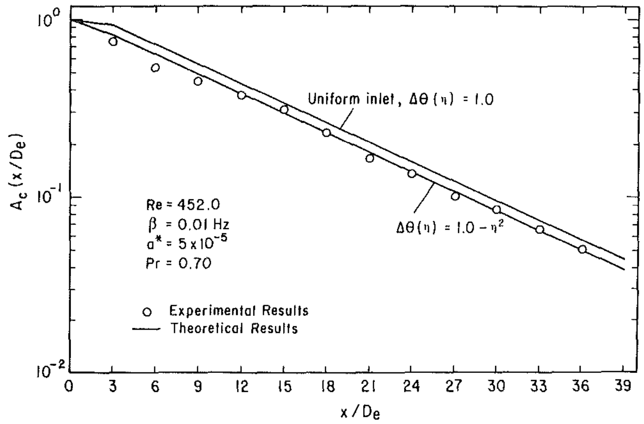

Fig. 11 Comparison of theoretical and experimental results of dimensionless centerline temperature amplitude for $Re = 452.0$, $\beta = 0.01$ Hz ($\Omega = 0.06558$), and $a^* = 5 \times 10^{-5}$

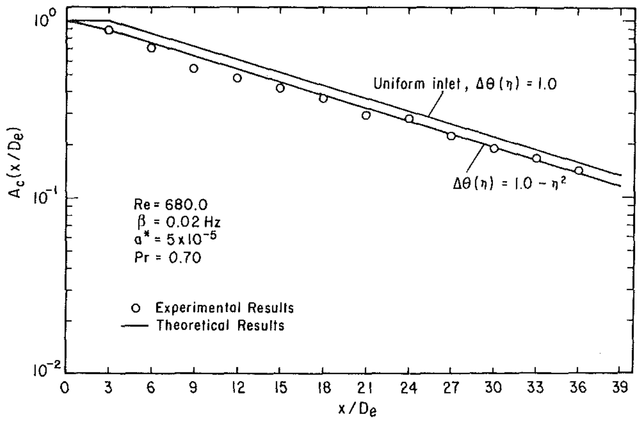

Fig. 12 Comparison of theoretical and experimental results of dimensionless centerline temperature amplitude for $Re = 680.0$, $\beta = 0.02$ Hz ($\Omega = 0.13220$), and $a^* = 5 \times 10^{-5}$

of periodic inlet temperature profile across the duct was obtained experimentally. In Figs. 11, 12, and 13, the experimental results for $Re = 452$, $\beta = 0.01$ Hz ($\Omega = 0.06491$); $Re = 680$, $\beta = 0.02$ Hz ($\Omega = 0.13220$) and $Re = 1396$, $\beta = 0.01$ Hz ($\Omega = 0.07006$) are presented and a representative set of such comparisons is shown.

It is clear from Figs. 11-13 that the effect of an nonuniform inlet temperature profile is quite significant in bringing the theoretical and experimental results to an acceptable agreement when an experimentally obtained nonuniform periodic inlet profile across the duct is considered in place of the theoretical uniform distribution. It should be noted that in Figs. 11-13 the results of the centerline temperature amplitudes are plotted as a function of the axial locations of the temperature readings.

Such a comparison was attempted before by use of the lowest order solution found by Kakac et al. (1989b). With the analysis presented here, advanced effects such as external convection, wall thermal capacitance, and nonuniformity of inlet periodic temperature profile are now incorporated into the analysis.

In Table 2, the dimensionless and dimensional experimental decay indexes, Λ(exp.) and $\bar{\alpha}$(exp.), and the dimensionless and dimensional theoretical decay indexes, Λ(th.) and $\bar{\alpha}$(th.), have been listed and compared. From Table 2 it can be seen that the decay indexes are very close to each other. For Reynolds numbers between 450 and 2000, the maximum relative deviation is less than 12 percent. These results also show an acceptable agreement with the experimental results.

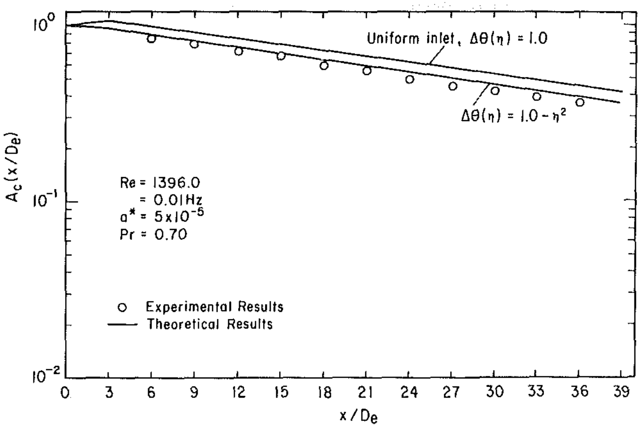

Fig. 13 Comparison of theoretical and experimental results of dimensionless centerline temperature amplitude for $Re = 1396.0$, $\beta = 0.01$ Hz ($\Omega = 0.07006$), and $a^* = 5 \times 10^{-5}$

In Table 3 the results of phase lags, $-\phi_c(\xi)/\pi$, along the duct are presented for different values of Reynolds number at the inlet frequency $\beta = 0.01$ Hz. From this table, one can see that the phase lag decreases with increase in the Reynolds number at a given inlet frequency. Because of the difficulty in measuring the phase lag experimentally, only the numerical values of phase lag are reported.

Concluding Remarks

The analytical solutions to the periodic variation of inlet temperature indicate that the temperature distribution in the fluid may be regarded as the result of the superposition of a series of modes of periodic distribution, each of which decays exponentially with the distance along the duct. At a fixed

Table 2 Decay indexes $\bar{\alpha}$ and Λ for various values of Reynolds number and inlet frequency (Bi = 10 and $a^* = 5 \times 10^{-5}$)

Re	β, Hz	Ω	Λ(exp.)	Λ(th.)	$\bar{\alpha}$(exp.)	$\bar{\alpha}$(th.)	ϵ, percent
452.0	0.01	0.06491	1.98974	2.08334	0.08085	0.08465	4.49
452.0	0.02	0.12930	2.28284	2.08334	0.09276	0.08465	9.58
681.0	0.02	0.13220	1.93138	2.07850	0.05211	0.05608	7.08
842.0	0.02	0.13600	1.94035	2.07311	0.04230	0.04520	6.40
1396.0	0.01	0.07006	1.97736	2.04449	0.02601	0.02690	3.28
1396.0	0.02	0.14030	2.15357	2.04449	0.02833	0.02114	5.34
2088.0	0.01	0.07096	1.76551	1.99338	0.01553	0.01417	11.43
2088.0	0.02	0.14190	2.12625	1.99338	0.01870	0.01753	6.67

Table 3 Theoretical values of phase lag of centerline temperature along the duct for $\beta = 0.01$ Hz, Bi = 10, and $a^* = 5 \times 10^{-5}$

	Re			
x/De	452.0	683.0	965.0	1396.0
0.0	0.000000	0.000000	0.000000	0.000000
3.0	0.001811	0.001204	0.000836	0.000603
6.0	0.003622	0.002487	0.001727	0.001239
9.0	0.005639	0.003785	0.002638	0.001894
12.0	0.007556	0.005084	0.003553	0.002558
15.0	0.009474	0.006384	0.004470	0.003225
18.0	0.011392	0.007684	0.005387	0.003893
21.0	0.013309	0.008984	0.006304	0.004561
24.0	0.015227	0.010284	0.007221	0.005230
27.0	0.017144	0.011585	0.008138	0.005899
30.0	0.019062	0.012855	0.009055	0.006568
33.0	0.020979	0.014185	0.009972	0.007236
36.0	0.022897	0.015485	0.010889	0.007905
39.0	0.024815	0.016785	0.011806	0.008574

frequency, the higher-order modes tend to zero so fast that ultimately only the basic mode remains. The effect has been demonstrated by comparing experimental measurements with the results of the theoretical solution, by giving the comparison of the amplitudes and decay indexes along the duct. For a given value of inlet frequency, the value of the temperature at a point downstream depends on the Reynolds number; when the Reynolds number is increased, the decay decreases. Therefore, the higher the Reynolds number, the slower the decay of the inlet temperature along the duct. From the comparison of experimental results with numerical results, it can be seen that the lowest-order solution is accurate enough in the range of frequencies considered, but it becomes increasingly inaccurate for decreasing a^* when nondiagonal elements in the coefficient matrix are magnified.

Acknowledgments

The authors gratefully acknowledge F. Hatay and M. Padki for their assistance during the preparation of this manuscript. R. M. Cotta wishes to acknowledge the financial support provided by COPPE/UFRJ and CAPES, both from Brazil, during his stay at the University of Miami. This work was also partially supported by NSF through grant No. CBT-860 3997.

References

Cotta, R. M., and Ozisik, M. N., 1986, "Laminar Forced Convection Inside Ducts With Periodic Variation of Inlet Temperature," *Int. J. Heat Mass Transfer*, Vol. 29, p. 1495.

Cotta, R. M., Ozisik, M. N., and McRae, D. S., 1986, "Transient Heat Transfer in Channel Flow With Step Change in Inlet Temperature," *Numerical Heat Transfer*, Vol. 9, p. 619.

Cotta, R. M., Mikhailov, M. D., and Ozisik, M. N., 1987, "Transient Conjugated Forced Convection in Ducts With Periodically Varying Inlet Temperature," *Int. J. Heat Mass Transfer*, Vol. 30, p. 2073.

Ding, Y., 1987, "Experimental Investigation of Transient Forced Convection in Ducts for a Timewise Varying Inlet Temperature," M. S. Thesis, Dept of Mech. Eng., Univ. of Miami, Coral Gables, FL.

IMSL Library, 1987, Edition 7, GNB Building, 7500 Ballaine Blvd., Houston, TX 77036.

Kardas, A., 1966, "On a Problem in the Theory of the Unidirectional Regenerators," *Int. J. Heat Mass Transfer*, Vol. 9, p. 567.

Kakac, S., and Yener, Y., 1973, "Exact Solution of Transient Forced Convection Energy Equation for Timewise Variation of Inlet Temperature," *Int. J. Heat Mass Transfer*, Vol. 16, p. 2205.

Kakac, S., 1975, "A General Analytical Solution to the Equation of Transient Forced Convection With Fully Developed Flow," *Int. J. Heat Mass Transfer*, Vol. 18, p. 1449.

Kakac, S., Ding, Y., and Li, W., 1988, "Experimental Investigation of Transient Laminar Forced Convection in Ducts," *Proc. of the Int. Conf. on Experimental Heat Transfer, Fluid Mechanics and Thermodynamics*, Dubrovnik, Yugoslavia, Sept. 4-9.

Kakac, S., Ding, Y., and Li, W., 1989a, "Transient Fluid Flow and Heat Transfer in Ducts With a Timewise Variation of Inlet Temperature," *Proc. of 3rd Int. Symp. on Transport Phenomena in Thermal Control*, Hemisphere, New York.

Kakac, S., Li., W., and Cotta, R. M., 1989b, "Theoretical and Experimental Study of Transient Laminar Forced Convection in a Duct With Timewise Variation of Inlet Temperature," presented at the ASME Winter Annual Meeting, San Francisco, CA.

Ozisik, M. N., and Murry, R. L., 1974, "On the Solution of Linear Diffusion Problems With Variable Boundary Condition Parameters," ASME JOURNAL OF HEAT TRANSFER, Vol. 96, p. 48.

Sparrow, E. M., and De Farias, F. N., 1968, "Unsteady Heat Transfer in Ducts With Time Varying Inlet Temperature and Participating Walls," *Int. J. Heat Mass Transfer*, Vol. 11, p. 837.

M. Dietrich

R. Blöchl

H. Müller-Steinhagen

Department of Chemical and
Materials Engineering,
The University of Auckland,
Auckland, New Zealand

Heat Transfer for Forced Convection Past Coiled Wires

Heat transfer coefficients were measured for forced convection of isobutanol in crossflow past coiled wires with different coil geometries. Flow rate and heat flux have been varied over a wide range to include laminar and turbulent flow for convective sensible and subcooled boiling heat transfer. To investigate the effect of coil geometry on heat transfer, the wire diameter, coil diameter, and coil pitch were varied systematically. The measured data are compared with the predictions of four correlations from the literature.

1 Introduction

Heat transfer for forced convection past cylinders and straight cylindrical wires has been the subject of numerous investigations, for example, Gnielinski (1984), Fand and Keswani (1973), Whitaker (1972), and Ulsamer (1932). Semi-empirical correlations described in these publications can be used to predict heat transfer coefficients with reasonable accuracy. Coiled wires or helices have a wide practical application as heating elements or fouling monitoring devices. Nevertheless, only Müller-Steinhagen et al. (1986) have reported data on heat transfer from a coiled wire. Heat transfer from coiled wires may be different from straight wires for two reasons: (*i*) the varying angle between flow direction and heat transfer surface, and (*ii*) the effects of helix geometry on the flow profile.

Designing a helix as a heating element is still based on experience or on the use of equations for straight cylindrical wires with the premise that any resulting error will be insignificant.

The aim of the present study is to provide better understanding of heat transfer from coiled wires. A large number of experiments with different wire coils have been carried out within the range of parameters given in Table 1. To establish reference values, heat transfer measurements with straight wires have been performed in addition to the coil measurements.

2 Test Equipment

The test equipment used for the present investigation is similar to that described previously by Müller-Steinhagen et al. (1986). A flow diagram of the setup is given in Fig. 1. The fluid is pumped from the temperature-regulated supply tank via an orifice flow meter to the vertical test section. All measurements were done for upward flow. The complete equipment is made from stainless steel and insulated against heat losses. The test section has a length of 700 mm and a duct cross section of 46 mm × 46 mm. The electrically heated coiled stainless steel wire is mounted horizontally (normal to the flow) at a position 600 mm upstream from the liquid inlet. The coils are held in place by two stainless steel bolts, which also conduct the current from the d-c power supply to the wire. Capillary tube segments were attached to the ends of the coils to improve electrical contact between the coils and the steel bolts and to provide a clearly defined heat transfer surface. Prior to the measurements, the coils were heated to 200°C for 48 h to reduce internal stresses and to provide a stable electrical resistance.

The heat flux supplied by the wire was calculated from the current and the voltage drop. The wire temperature could be determined using the relationship between electrical resistance and temperature of the wire. The bulk temperature around the coil was measured by two thermocouples located upstream and downstream of the coil, respectively. A calibrated orifice meter was used to determine the flow rate in the test section. Isobutanol was chosen as the test fluid, because of its relatively high boiling temperature and its inertness to biofouling.

Altogether, 25 different coils made from NiCr 3020 stainless steel wires with various diameters were investigated. Photographs and dimensions of these coils are shown in Fig. 2. Both helix diameter and pitch were measured between the centerlines of the wires.

3 Test Procedure

Heat transfer coefficients, α, were determined for all the coils illustrated in Fig. 2. All measurements were taken after the system had reached steady-state conditions. Heat transfer coefficients were then measured for 25 different heat fluxes at 6 different flow velocities. The measurements were taken with increasing heat flux.

Table 1 Range of investigations

Wire diameter	0.2 mm	$\leq$	d	$\leq$ 1.0 mm
Helix diameter	1.0 mm	$\leq$	D	$\leq$ 10.0 mm
Diameter to pitch ratio	0.0	$\leq$	s	$\leq$ 5.0
Flow velocity	1.0 cm/s	$\leq$	u	$\leq$ 40.0 cm/s
Heat flux	500 W/m^2	$\leq$	$\dot{q}$	$\leq$ 500 000 W/m^2
System pressure			p	= 1 bar
Fluid bulk temperature			T_b	= 35°C

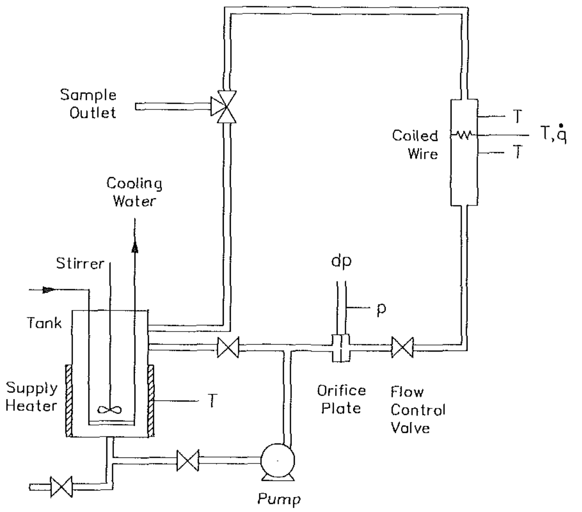

Fig. 1 Test loop

Contributed by the Heat Transfer Division for publication in the JOURNAL OF HEAT TRANSFER. Manuscript received by the Heat Transfer Division June 13, 1988; revision received December 15, 1989. Keywords: Forced Convection, Modeling and Scaling.

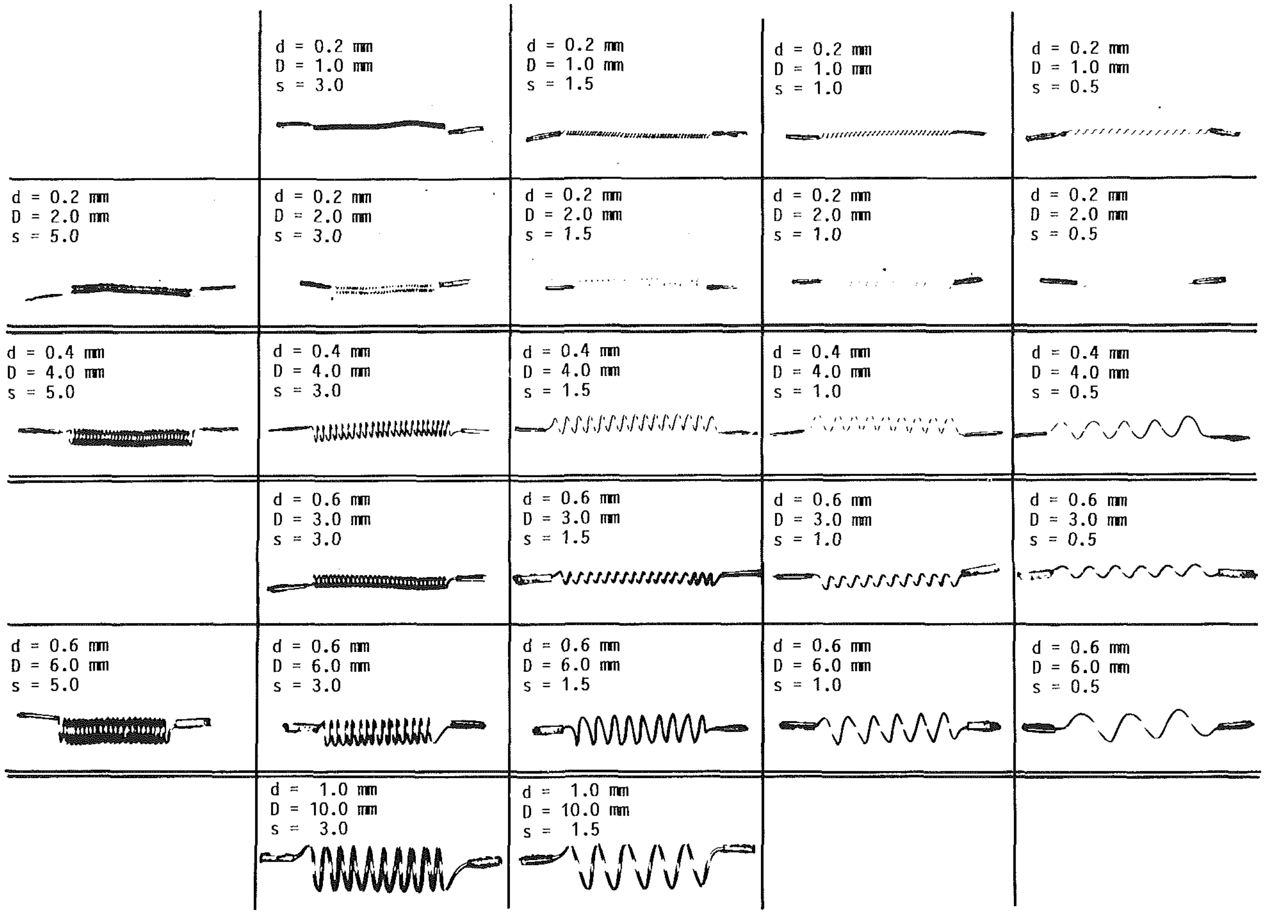

Fig. 2 Wire coils used for comparison

The heat transfer coefficient is calculated from

$$\alpha = \frac{\dot{Q}/A}{T_w - T_b} = \frac{\dot{q}}{T_w - T_b} \tag{1}$$

The heat flow rate $\dot{Q}$ from the wire was calculated from

$$\dot{Q} = I^2 \left(\frac{V}{I} - R_{\text{ext}} \right) \tag{2}$$

where I, V, and R_{ext} are the measured current, the measured voltage drop, and the electrical resistance of the measuring circuit, respectively. The average value of the two thermocouple readings in the test section was taken as the fluid bulk temperature T_b. The wall or surface temperature T_w, which is assumed to be identical to the integral wire temperature, was calculated from

$$T_w = T_0 + \frac{1}{\gamma} \left(\frac{R}{R_0} - 1 \right) \tag{3}$$

In this equation R_0 is the electrical resistance of the coil at the reference temperature T_0 and γ is the temperature coefficient of electrical resistance, which was determined in preliminary measurements with several coils as 0.00040 K^{-1}.

The average flow velocity past the coil was determined considering a flow velocity profile across the test section. Laminar flow in the test section occurs for average flow velocities below 16 cm/s.

4 Experimental Uncertainty

A detailed description of possible sources of error and of the methods used to reduce these errors is given by Dietrich

Nomenclature

A = surface area of wire, m^2
c_p = heat capacity, kJ/(kg K)
d = wire diameter, m
D = helix diameter, m
g = acceleration due to gravity, m/s^2
I = current, A
L = characteristic length, m
$\dot{q}$ = heat flux density, W/m^2
$\dot{Q}$ = heat flow rate, W
r = Nusselt number ratio
R = electrical resistance, V/A
s = helix diameter-to-pitch ratio
T = temperature, K
u = flow velocity, m/s
V = voltage, V
x = pitch, m
α = heat transfer coefficient, W/(m^2 K)
γ = temperature coefficient of electrical resistance, 1/K
λ = thermal conductivity, W/mK
ρ = density, kg/m^3
μ = dynamic viscosity, kg/(m s)
ν = kinematic viscosity, $\text{m}^2\text{/s}$

Subscripts

b = bulk
c = test section or channel
co = coil
eq = equivalent
ext = external
f = film
Hep = heptane
Iso = isobutanol
o = at reference conditions
w = wall
wi = straight wire

Dimensionless numbers

j = $\text{Nu}/\text{Pr}^{1/3}$ = j factor
Nu = $\alpha L/\lambda$ = Nusselt number
Pr = $c_p\mu/\lambda$ = Prandtl number
Re = uL/ν = Reynolds number

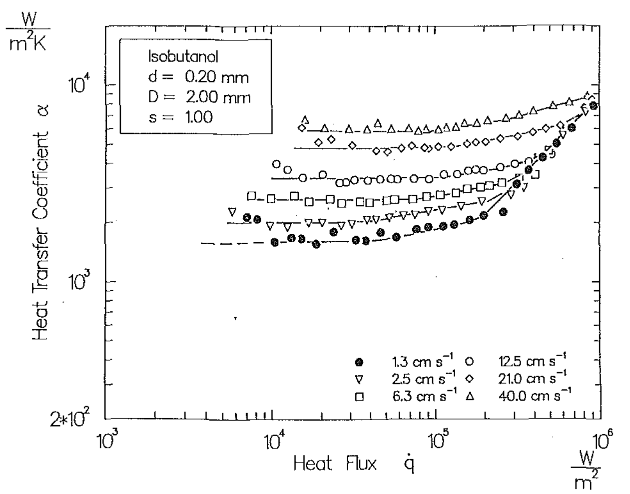

Fig. 3(*a*) Influence of heat flux and flow velocity on the heat transfer coefficient

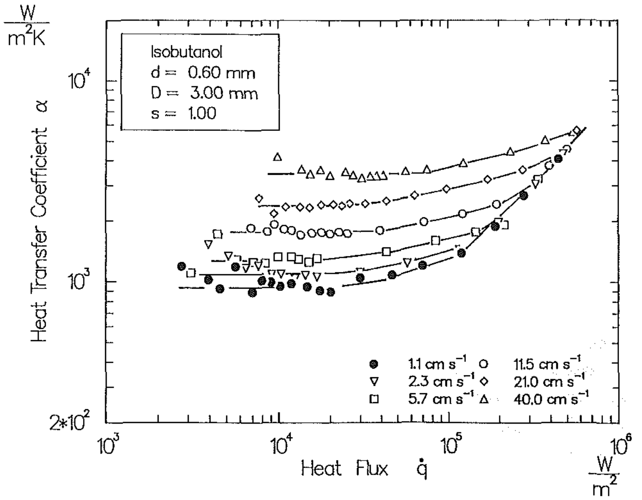

Fig. 3(*b*) Influence of heat flux and flow velocity on the heat transfer coefficient

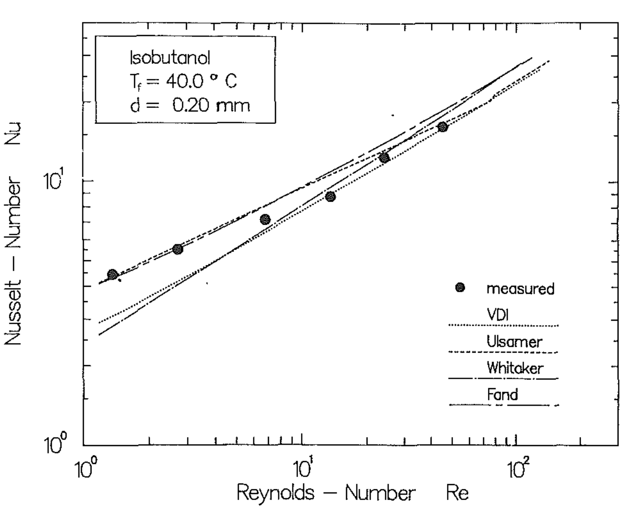

Fig. 4 Comparison between measured and predicted Nusselt numbers for straight wires

(1988). The major uncertainty occurred in the data acquisition system, causing errors in the measured wire temperature between ±0.12°C and ±1.2°C. Since only experiments with a wire superheat in excess of 10°C were considered, the maximum error caused by the data acquisition system is 12 percent. For most experiments, the data acquisition system could be operated in the range where the minimum error occurred. The temperature coefficient of electrical resistance (which is proportional to the wire superheat) could be reproduced in numerous experiments within ±6 percent.

Due to the finite thermal conductivity of the wire, the temperature at the wire surface differs from the average temperature determined via the change of resistance. The maximum deviation for this investigation was 2 percent for the 1-mm wire at the highest heat flux. For smaller wire diameters, the temperature profile within the wire can be neglected.

Since temperature differences rather than absolute temperatures had to be considered, the uncertainty due to the thermocouple reading was only ±0.1° C.

The length of the installed wires could be measured within ±0.5 mm. The resulting uncertainty in the heat transfer surface area was 0.3 and 3 percent for the longest and shortest wires, respectively.

5 Results

In this section, measured data will be shown and compared with the predictions of four correlations from the literature and with experimental results for a flow of *n*-heptane obtained by Müller-Steinhagen et al. (1986). Then, the influence of various parameters on heat transfer from coiled wires will be discussed.

5.1 Heat Transfer as a Function of Heat Flux. The influence of heat flux and flow velocity on the heat transfer coefficient is shown in Figs. 3(*a*) and 3(*b*) for two different helices. In both diagrams, two regimes can be distinguished from the shape of the measured curves: (*i*) the convective heat transfer regime where the heat transfer coefficient is almost independent of the heat flux but dependent on the flow velocity, and (*ii*) the subcooled boiling regime where α increases with increasing $\dot{q}$ but is independent of u. The slight increase of the convective heat transfer coefficient for higher heat fluxes is caused by the effect of film temperature on the physical properties of the fluid and by the additional contribution of natural convection. A small kink is found for some curves at the transition from convective sensible to subcooled boiling heat transfer, indicating boiling hysteresis effects associated with the measurements at increasing heat flux. This phenomenon disappeared for higher flow rates.

For developed *subcooled boiling*, no influence of the coil geometry on the heat transfer coefficients could be detected. Obviously, the microconvection caused by bubble growth and detachment predominates over the macroconvection caused by flow velocity and coil dimensions.

The influence of coil geometry on *convective* heat transfer will be discussed by comparing the heat transfer coefficients for a temperature difference between coil and fluid bulk of 10 K. Thus, effects of film temperature and natural convection are eliminated and experimental inaccuracies in temperature measurement are tolerable.

5.2 Comparison Between Measured and Calculated Heat Transfer Coefficients. To check the reliability of the experimental setup and to provide reference values for the coil heat transfer coefficients, data measured with a straight 0.2-mm-dia wire were compared with the predictions of four correlations from the literature, which are described in detail by Müller-Steinhagen et al. (1986).

The correlations of Fand and Keswani (1973), Whitaker (1972), and Ulsamer (1932) were formulated using the diameter of a cylinder as characteristic length. In analogy to heat transfer from flat plates, the correlation suggested by Gnielinski in the VDI-Wärmeatlas (1984) uses the contact length of a streamline with the cylinder, i.e., $\pi d/2$. Heat transfer coefficients α were calculated using the appropriate diameter. However, to obtain a uniform system, all dimensionless numbers used in the following figures were based on the contact length $\pi d/2$. Figure

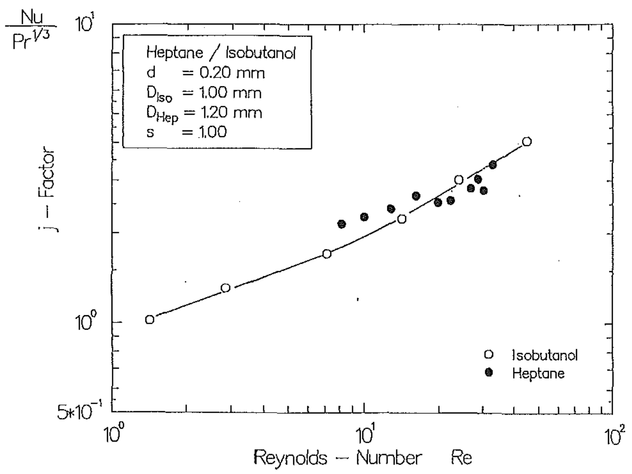

Fig. 5 Comparison between *j* factors for isobutanol and values measured for heptane

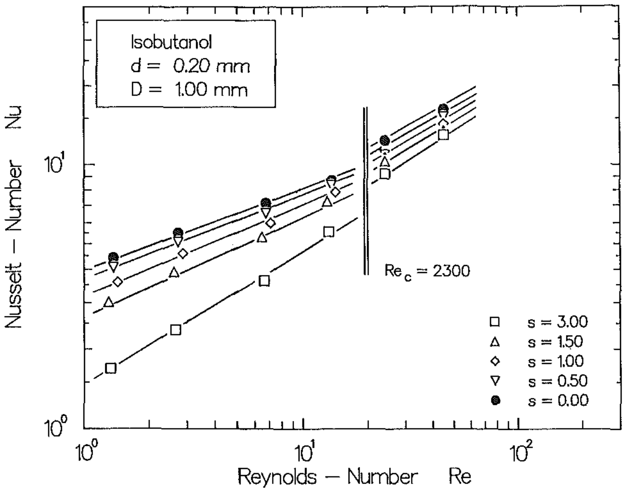

Fig. 6 Nusselt number versus Reynolds number for various coil diameter-to-pitch ratios

4 shows calculated and measured Nusselt numbers for a cylinder with a diameter of 0.2 mm in crossflow. If it is assumed that the flow conditions in the square channel are similar to those in a cylindrical duct, laminar flow occurs in the channel for the four lower flow velocities (Reynolds number based on equivalent channel diameter Re_c < 2300), while turbulent conditions exist for the two highest Reynolds numbers. The agreement between measured and predicted values is satisfactory. For lower Reynolds numbers, predictions of correlations suggested by Whitaker (1972) and in the VDI-Wärmeatlas (Gnielinski, 1984) fall below the measured values.

Figure 5 shows a comparison of the present data for isobutanol with recent data measured with *n*-heptane by Müller-Steinhagen et al. (1986). For easier identification, the isobutanol data are connected by a solid line. Wire coil diameters were 1 mm and 1.2 mm for the isobutanol measurements and the *n*-heptane measurements, respectively. The transition from *n*-heptane to isobutanol was necessary as high grade *n*-heptane was not available at a reasonable price. To compensate for the effect of widely different Prandtl numbers (Pr = 3.9 for *n*-heptane as compared to Pr = 43 for isobutanol), the *j* factor was used as ordinate, rather than the Nusselt number. Considering the difference in the experimental setup, the agreement between the two data sets is satisfactory.

5.3 Influence of Coil Geometry on Heat Transfer.

5.3.1 Effect of Flow Velocity and of Diameter-to-Pitch Ratio. Using the same mode of presentation as in Fig. 4, Fig. 6 shows measured Nusselt numbers for a straight wire as well as the results for different coils having the same wire diameter. The parameter in this diagram is the helix diameter-to-pitch ratio, *s*. Nusselt numbers for the coils are significantly lower than those of the straight wire (*s* = 0).

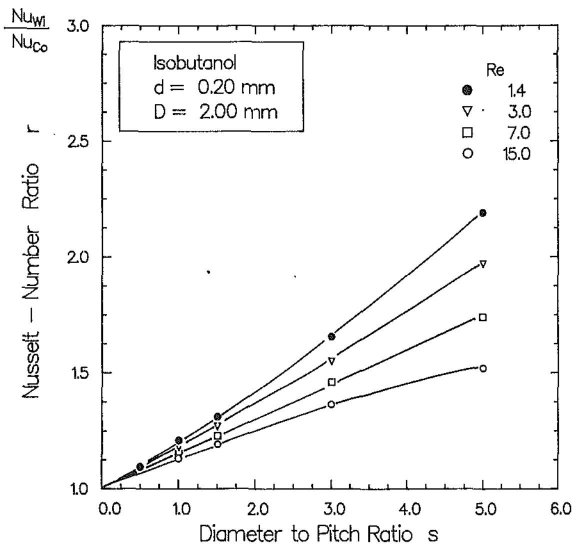

Fig. 7 Nusselt number ratio versus coil diameter-to-pitch ratio for various Reynolds numbers

A clear change in the measured curves can be seen at the transition between laminar and turbulent channel flow. Nusselt numbers in the turbulent flow region are considerably higher and much less affected by the coil geometry than the laminar flow data. Therefore, the following discussion of coil geometry effects will be limited to laminar flow in the channel.

To discuss the influence of the different geometry parameters on heat transfer, a Nusselt number ratio *r* is defined as the ratio of straight wire Nusselt number to coil Nusselt number. The inverse of the Nusselt number ratio can be understood as a correction factor to obtain coil heat transfer coefficients from straight wire correlations.

In Fig. 7, the Nusselt number ratio is presented as a function of the coil diameter-to-pitch ratio for 2-mm helices made from 0.2-mm wire. Heat transfer from the straight wire is up to 2.2 times higher than that of the narrowest coils investigated (highest value of *s*). The difference between coil and straight wire Nusselt numbers decreases continuously with decreasing value of *s*. In addition to the coil geometry, the flow velocity affects the relation between *s* and the Nusselt number ratio. If the Reynolds number is increased, the effect of diameter-to-pitch ratio on the Nusselt number is reduced. This effect is more pronounced for narrow helices than for wide helices.

Due to their low electrical resistance, measurements using larger wire diameter were less accurate than those for fine wires. Nevertheless, the same tendencies were observed.

5.3.2 Effect of Helix Diameter. To reduce the number of experiments, the helix diameter was varied in multiples of the wire diameter, rather than as an absolute value. For a Reynolds number of 1.4, Fig. 8 shows the influence of the helix diameter for 1.0-mm and 2.0-mm coils, all having the same wire diameter *d* = 0.2 mm. While no noticeable influence of the coil diameter is found for wide helices (*s* < 1), narrow helices show significantly lower heat transfer coefficients for *D* = 1 mm as compared to *D* = 2 mm. This result is somewhat surprising, since the heat transfer coefficient for flow past straight cylinders generally increases with decreasing cylinder diameter because of the reduced viscous sublayer thickness.

Comparing coils with identical coil diameter-to-pitch ratio in Fig. 2, one can see that the distance between turns decreases as the coil diameter is reduced. In Fig. 9, the Nusselt number ratio is plotted versus the net pitch, which is defined as distance

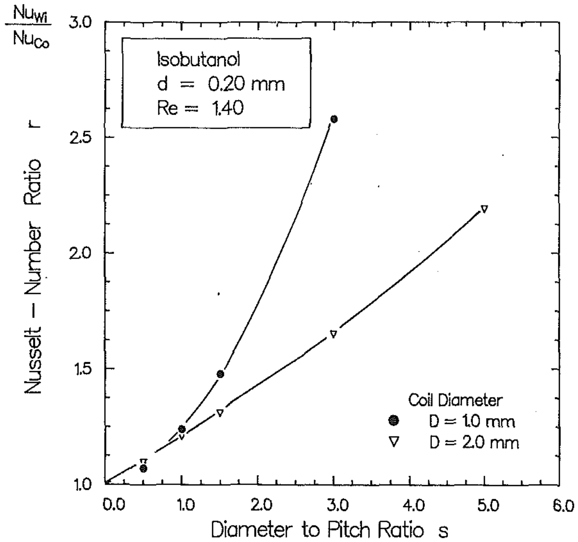

Fig. 8 Nusselt number ratio as a function of coil diameter-to-pitch ratio for two different coil diameters

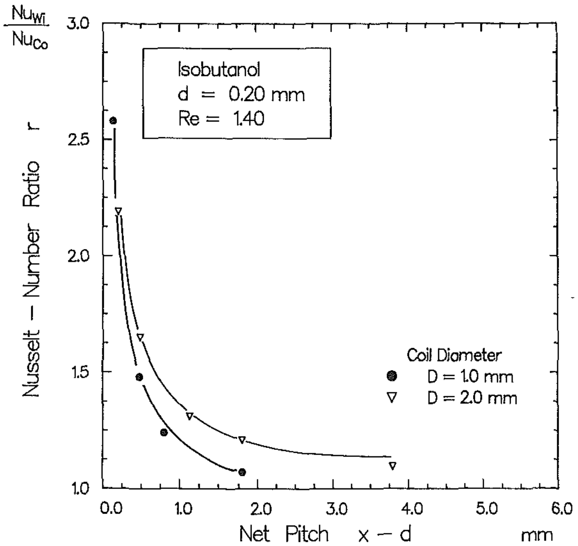

Fig. 9 Nusselt number ratio as a function of the net pitch for two different coil diameters

between turns, obtained by subtracting the wire diameter from the pitch. Opposite to the results described above, Nusselt numbers for 2-mm coils now fall below the values for 1-mm coils, which is consistent with trends known for straight wires. Therefore, the net pitch seems to be a better characteristic parameter for the influence of coil diameter on heat transfer than the diameter-to-pitch ratio.

5.3.3 *Influence of Wire Diameter.* Nusselt number ratios were compared for coils made from 0.2-mm, 0.4-mm, and 0.6-mm diameter wire. In each case, the diameter of the coil was 10 times the wire diameter. For identical coil diameter-to-pitch ratios, no influence of the wire diameter on the Nusselt number ratio was found within the scatter of data.

5.4 Discussion of Results. It was observed that the major changes in heat transfer behavior occur for narrow coils and that this effect is strongly dependent on the Reynolds number. From this result, one may conclude that two situations have to be distinguished:

1 The wide helix in forced convection, where the reduced heat transfer is mostly a result of the angle between the flow direction and the wire surface.

Table 2 Reduction of Nusselt number for various flow angles according to Vornehm (1936)

θ	90°	80°	70°	60°	50°	40°	30°	20°
Nu_θ/Nu_{90}	1.0	1.0	0.99	0.95	0.86	0.75	0.63	0.50

2 Narrow coils in forced convection, where the distance between the coils and the Reynolds number are responsible for the reduced heat transfer.

The effect of the angle between the flow direction and a cylindrical heating element θ was discussed by Vornehm (1936). Table 2 shows his results in the form of reduced Nusselt numbers as a function of θ. Vornehm (1936) did not extend his analysis to the case of helices, where this angle is continuously changing along the coil. To obtain the average coil Nusselt number, an integral average of these values over one turn of the coil has to be calculated or an average angle has to be defined. Nevertheless, this procedure is only useful for wide helices, where no additional effect of Reynolds number is observed, i.e., where no effect of the coil geometry on the flow velocity distribution occurs.

To explain the greatly reduced heat transfer from narrow coils, additional mechanisms have to be considered. It could be observed visually during the experiments that, depending on the net pitch and the flow velocity, the fluid flowed past the total coil rather than past the wire. For this condition, heat transfer is reduced significantly. With increasing distance between turns the fluid will flow through the coil rather than around the coil and the first heat transfer condition will prevail.

5 Conclusion

Heat transfer was investigated for flow of isobutanol past wire coils with various coil dimensions. While no influence of the coil geometry could be found for developed subcooled boiling, the measured convective heat transfer coefficients decreased considerably with increasing coil density. The reduction in heat transfer from coiled wires as compared to straight wires could be as much as 60 percent. The main influence parameters on this effect were the angle of flow inclination for low coil densities and the distance between turns of the coil and the flow velocity for high coil densities.

Acknowledgments

The authors are indebted to the German Research Society (DFG), Bonn, Bad-Godesberg, for financing the fellowship of R. B. and to Prof. E. U. Schlünder, University of Karlsruhe, FRG, for supporting M.D. The test rig was built with financial assistance from New Zealand Forest Products.

References

Dietrich, M., 1988, "Wärmeübergang bei der Umströmung beheizter Drahtspiralen," Diploma-Thesis, University of Karlsruhe, Karlsruhe, Federal Republic of Germany.

Fand, R. M., and Keswani, K. K., 1973, "Combined Natural and Forced Convection Heat Transfer From Horizontal Cylinders to Water," *International Journal of Heat and Mass Transfer*, Vol. 16, pp. 1175–1191.

Gnielinski, V., 1984, "Wärmeübertragung bei der Queranströmung um einzelne Rohre, Drähte und Profilzylinder," *VDI-Wärmeatlas*, Sect. Gf, 4th ed., VDI-Verlag, Düsseldorf, Federal Republic of Germany.

Müller-Steinhagen, H., Watkinson, A. P., and Epstein, N., 1986, "Subcooled-Boiling and Convective Heat Transfer to Heptane Flowing Inside an Annulus and Past a Coiled Wire," ASME JOURNAL OF HEAT TRANSFER, Vol. 108, pp. 922–933.

Ulsamer, J., 1932, "Wärmeabgabe von geheizten Drähten und Rohren," *Forschungsgebiet Ingenieurwesen*, Vol. 3 (referred to in McAdams, W., 1954, *Heat Transmission*, McGraw-Hill, New York).

Vornehm, L., 1936, *Zeitschrift des Verband Deutscher Ingenieure*, Vol. 80, No. 22, p. 702.

Whitaker, S., 1972, "Forced Convection Heat Transfer for Flow in Pipes, Past Flat Plates, Single Cylinders, Single Spheres and for Flow in Packed Beds and Tube Bundles," *AIChE Journal*, Vol. 18, pp. 361–371.

Heat Transfer and Pressure Drop for Short Pin-Fin Arrays With Pin-Endwall Fillet

M. K. Chyu
Department of Mechanical Engineering,
Carnegie Mellon University,
Pittsburgh, PA 15213

The effects of array configuration and pin-endwall fillet on the heat transfer and pressure drop of short pin-fin arrays are investigated experimentally. The pin-fin element with endwall fillet, typical in actual turbine cooling applications, is modeled by a spool-like cylinder. The arrays studied include an in-line and a staggered array, each having seven rows of five pins. These arrays have the same geometric parameters, i.e., $H/D = 1$, $S/D = X/D = 2.5$, *and the Reynolds number ranging from* 5×10^3 *to* 3×10^4. *One of the present results shows that the staggered array always has a higher array-averaged heat transfer coefficient than its in-line counterpart. However, the pressure drop for the staggered array is higher compared to the in-line configuration. These trends are unaffected by the existence of the pin-endwall fillet. Another significant finding is that an array with pin-endwall fillet generally produces lower heat transfer coefficient and higher pressure drop than that without endwall fillet. This leads to the conclusion that pin-endwall fillet is undesirable for heat transfer augmentation. In addition, naive use of the heat transfer results obtained with perfectly circular cylinders tends to overestimate the pin-fin cooling capability in the actual turbine. The effects of endwall fillet on the array heat transfer and pressure drop are much more pronounced for the staggered array than for the in-line array; however, they diminish as the Reynolds number increases.*

Introduction

Pin-fin arrays are commonly used to increase the heat transfer in an internal cooling passage near the trailing section of a turbine blade or vane. They also serve a structural purpose in bridging the narrow span between the suction and pressure surfaces. A pin-fin array usually consists of a number of short circular cylinders attached perpendicular to the endwalls, with the coolant fluid passing in crossflow over the cylinders. The array configuration is either staggered or in-line with respect to the flow direction. Geometrically, an array is determined by the cylinder diameter (D), cylinder height (H), and the spacings between neighboring cylinders in both spanwise (S) and streamwise (X) directions.

Because of the narrow trailing edge for most of turbine blades, the cylinder arrays typically have height-to-diameter ratios of the order of unity. Hence, the cylinder/endwall interaction is strong, and the array total heat transfer must include heat transfer from both the cylinder surface and the uncovered region on the endwall. This presents a fundamental difference from arrays having long cylinders in which the endwall effects are virtually nonexistent, and heat transfer on the cylinder surface is the only concern. Heat transfer with crossflow over a long-cylinder array or a tube bank has been extensively studied in the past. Results from studies prior to 1970 have been compiled in a review paper by Zukauskas (1972).

In the literal sense, the addition of a cylinder array increases the wetted (heat transfer) area and produces higher turbulence levels in the flow. Both effects enhance heat transfer. However, for short pin-fin arrays, the effects of area addition toward the overall heat transfer augmentation are insignificant. This is largely due to the fact that the area of a cylinder surface is comparable to the area covered by the cylinder bases on the blade inner walls. Frequently the addition of a pin-fin array may actually cover up more blade surface area than it added in cylinder surface area. Therefore, in turbine cooling applications, the predominating mechanisms of short pin-fin heat transfer augmentation lies in promoting flow turbulence rather than addition of heat transfer area.

Heat transfer and friction characteristics of short pin-fin arrays specifically directed to the turbine application have been studied extensively since the early 1980s. A significant contribution was made by groups at NASA-Lewis (VanFossen, 1982; Simoneau and VanFossen, 1984; Brigham and VanFossen, 1984) and Arizona State University (Metzger et al., 1982a, 1982b, 1982c, 1984, 1986). They have investigated the effects of pin and array geometries, flow parameters, and thermal conditions. Heat transfer results obtained from these studies include Nu–Re correlations of array-averaged heat transfer and

---

Contributed by the Heat Transfer Division and presented at the 34th International Gas Turbine and Aeroengine Conference and Exhibition, Toronto, Ontario, Canada, June 4–8, 1989. Manuscript received by the Heat Transfer Division March 15, 1989; revision received February 27, 1990. Keywords: Forced Convection, Mass Transfer, Turbines.

row-resolved local heat transfer distributions. It is noted that short pin-fin arrays generally produce lower heat transfer than their long-cylinder counterparts. Hydrodynamically these studies emphasize measurements of friction coefficient and turbulence intensity. The addition of a pin-fin array in a flow channel substantially increases the pressure loss as an inevitable penalty accompanied with the heat transfer augmentation. The measured row-by-row variation of turbulence intensity provides a reference basis for understanding of the transport characteristics in a pin-fin array. Armstrong and Winstanley (1987) have recently reviewed updated information for staggered arrays.

Compared to the aforementioned studies, the present research emphasizes a different aspect, namely the pin-endwall fillet, which exists in blade internal cooling with short pin-fins. Due mainly to the limiting casting technology, a pin-fin element actually manufactured may not be a perfectly circular cylinder. This is specially true near the cylinder endwall where the commonly perceived sharp junction is, in fact, rounded with a fillet. The fillet radius of curvature is of the order of the pin diameter. For crossflow over a perfectly straight cylinder, the flow characteristics near the cylinder–endwall junction are dominated by the well-known horseshoe vortex, which produces high levels of turbulence resulting in a high heat transfer in the region. Besides, for a narrow flow passage, the near-wall turbulence generation has a great influence on the bulk flow and associated transport phenomena. One conjecture is that a rounded junction will affect the local flow fields and friction characteristics in general, and turbulence generation and heat transfer will degrade. Direct use of the results obtained with perfectly straight cylinders may overestimate the heat transfer in actual turbine design. One other concern that may also affect the array heat transfer is the decrease of total heat transfer area due to the fillet presence. To examine the fillet effects on the array heat transfer and flow resistance experimentally is one of the primary objectives of this study.

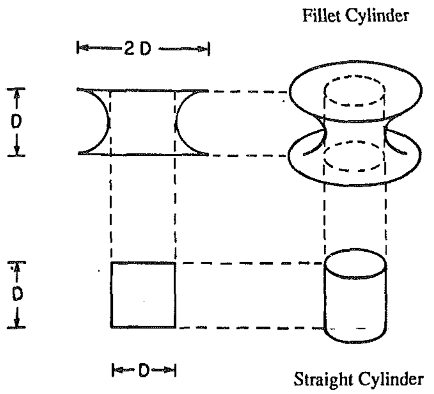

D = 12.7 mm

Fig. 1 Pin-fin elements

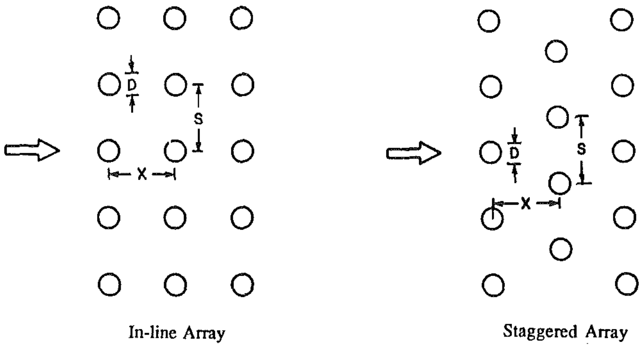

X/D = S/D = 2.5

Fig. 2 Pin-fin arrays

Experimental Apparatus and Procedures

A pin-fin with endwall fillet is modeled by an aluminum, spool-like cylinder, as shown in Fig. 1. Also sketched in the figure is the corresponding straight cylinder. The two cylinders have identical height, $H = 12.5$ mm, and the straight cylinder has a constant height-to-diameter ratio of unity. The fillet is enveloped by a circular profile with a radius of curvature equal to the radius of the straight cylinder. This geometry gives the fillet cylinder varying values of height-to-diameter ratio along

Nomenclature

A = cross-sectional area of unobstructed channel
$A_{\min}$ = minimum cross-sectional area in pin-fin array
A_w = wetted area
D = pin-fin or cylinder diameter or height
D_h = duct hydraulic diameter of unobstructed duct
f = array pressure drop coefficient = $2\Delta p/(\rho U_{\max}^2 N)$
H = pin-fin height
h = heat transfer coefficient
h_m = pin-surface average mass transfer coefficient
K = diffusion coefficient for naphthalene-to-air mass transfer
k = thermal conductivity of fluid
L = channel length
$\dot{m}$ = mass transfer per unit time per unit area
$\dot{M}_j$ = mass transfer per unit time from row j
N = number of pin-fin rows = 7 in the present study
Nu = heat transfer Nusselt number = hD/k
$\overline{\mathrm{Nu}}$ = array-averaged Nusselt number over all pin rows
Nu_D = Nusselt number based on hydraulic diameter = hD_h/k
p = pressure
Pr = Prandtl number = $\mu C_p/k$
Q = volumetric air flow rate
q = heat flux from wall
Re = Reynolds number = $U_{\max}D/\nu$
Re_D = Reynolds number of unobstructed channel = UD_h/ν
S = pin spacing in spanwise direction
Sc = Schmidt number = ν/K = 2.5 for naphthalene-to-air mass transfer
Sh = row-resolved Sherwood number = $h_m D/K$
$\overline{\mathrm{Sh}}$ = array-averaged Sherwood number over all pin rows
T_w = wall temperature
T_b = bulk mean temperature
U = bulk mean velocity
$U_{\max}$ = mean velocity in the minimum flow area $A_{\min}$
X = pin spacing in streamwise direction
ν = kinematic viscosity
ρ = fluid density
$\rho_{v,w}$ = vapor mass concentration or density of naphthalene at wall
$\rho_{b,j}$ = vapor mass concentration or density of naphthalene in bulk mean flow for row j

Subscripts

D = based on hydraulic diameter
EW = endwall
o = fully developed

the cylinder axis. The smallest value ($H/D=0.5$) occurs at both ends and the greatest ($H/D=1.0$) exists at the cylinder midsection, which is the same as that of straight cylinder.

The array geometries studied are the in-line and the staggered; each array has seven rows. Figure 2 gives schematic views of these two arrays; only three rows are shown in the figure. To provide a rational comparison, both arrays have identical geometric parameters, i.e., $S/D=X/D=2.5$. These array configurations can be realized by shifting the even number rows of one array sideways by one-half spanwise fin spacing relative to those of the other array. Note that the total number of pins is different. For the in-line array, each row consists of five pins, giving a total of 35 pins. On the other hand, the number of pins per row in the staggered array alternates with five in the odd-numbered rows and four in the even-numbered rows, giving a total of 32 cylinders.

This study makes use of the naphthalene sublimation mass transfer technique rather than direct heat transfer. The mass transfer results can be transformed into their heat transfer counterparts via a well-established analogy between these two processes (Eckert, 1976). The naphthalene surface sublimes as it is exposed to an air stream. The per-fin resolved mass transfer coefficient is determined by the amount of surface-coated naphthalene sublimed during a wind tunnel exposure. This can be obtained by individually weighing the naphthalene-coated cylinder before and after the test run. One of the most attractive features of this technique is that, by analogy, a naphthalene surface corresponds to a perfectly isothermal wall condition in heat transfer. This implies that the present naphthalene-coated fins have an ideal 100 percent efficiency—a good approximation in actual turbine situations.

The naphthalene coating on a cylinder surface is done by dipping the cylinder, with both ends taped, into a pool of nearly boiling, molten naphthalene. During the dip, the cylinder is held by tweezers at both ends and immersed in the liquid naphthalene for about one second. After the dip, the naphthalene solidifies almost instantly, forming a nearly 2-mm-thick layer on the cylinder surface. This coating process results in a high-quality surface condition, so further machining is unnecessary for the present need. After coating, all fins are stored in a tightly sealed plastic box in the testing room for at least 15 hours before an actual test run. This ensures an attainment of thermal equilibrium with the surrounding air. Since the naphthalene vapor concentration, the primary driving potential of the present mass transfer system, is highly temperature sensitive, an isothermal system throughout the entire test is desirable.

The test channel, made of 12.7-mm-thick aluminum tooling plate, has a rectangular cross section, 159 mm wide and 12.7 mm high, and is 864 mm long. The initial portion of the duct serves as a hydrodynamic development section and delivers the flow to the test section that houses the pin-fin array. The development length ahead of cylinder array is approximately $19D_h$, where $D_h=23.5$ mm is the hydraulic diameter. The distance between the array last row and the channel exit is about $10D_h$. The flow is supplied by a 50 hp compressor, and the compressed air passes through a pressure regulator, a control valve, and an orifice, then reaches the inlet of the test channel. The top wall of the test section is removable. This provision is to accommodate the need for easy access to the test section to install or remove the naphthalene-coated fins. During a test run, the top wall is tightened to the rest of the test section by screws first, then sealed by duct tape.

Also installed on the top wall are six pressure taps for the pressure measurement. The six taps are equally divided into two separate groups. One is located one-half pitch ahead of the first row and the other one-half pitch downstream of the last row. The three taps at each streamwise location are equally spaced across the duct span, and the average of these three pressure readings is taken as the mean pressure at this streamwise location. Using an inclined manometer, the difference among the three pressure readings is found to be very small: about 5 percent downstream of the fin array and virtually zero ahead of the array. The pressure difference between these two streamwise locations is considered as the pressure drop across the entire array.

Before a test run, all fins are separately weighed using an electronic balance with an accuracy of 10^{-2} mg in a 166-g range (Sartorius 2004 MP). Then, according to the array geometry desired, all fins are screw-mounted on the bottom wall of the test section. The entire assembly is completed as the top wall is fastened and sealed. When in place, the inner surface of the channel top wall attaches to the upper endwall of each pin-fin. Thus, all cylinders span the entire channel height. After the assembly is completed, the compressed air is induced to flow through the channel for about 30 minutes. Measurements of air flow rate uses the orifice installed far upstream to the test channel. The flow rate as well as the Reynolds number is varied by the control valve located further upstream of the orifice. During the test run, temperatures on the two endwalls are recorded by readings from four thermocouples embedded in the inner surfaces of these two walls. A valid test requires that the differences among these thermocouple readings be within 0.1°C. Otherwise the particular test is discarded. The average of these four temperatures is used to evaluate the at-wall naphthalene vapor concentration, $\rho_{v,w}$, for all fins. After the test, all fins are removed from the channel and each is weighed again. Because aluminum, the framework of each fin, is inert to the mass transfer process, the weight difference for each individual fin gives the amount of naphthalene mass sublimed during the test period. The mean mass sublimed of each fin is approximately 20 mg.

Heat/Mass Transfer Analogy and Data Reduction

The per-fin mass transfer coefficient h_m is determined from the mass transfer rate, $\dot{m}$, per unit area and the difference in naphthalene vapor concentration between the fin surface and the approaching bulk flow, $\rho_{v,w}-\rho_{n,b}$; i.e.,

$$h_m=\dot{m}/(\rho_{v,w}-\rho_{n,b}) \tag{1}$$

$\dot{m}$ is calculated from the weight change in naphthalene coating in conjunction with duration time of the test run and the exposed area of the pin fin. The wall concentration, $\rho_{v,w}$, is calculated from the vapor pressure-temperature relation for naphthalene (Ambrose et al., 1975) and the ideal gas law.

To evaluate the naphthalene concentration in the bulk flow, $\rho_{n,b}$, it is necessary to note that the increase in bulk concentration of naphthalene vapor within the domain of a specific row j can be expressed as

$$\Delta\rho_{n,b}=\dot{M}_j/Q \tag{2}$$

where $\dot{M}_j$ is the mass transfer per unit time from all fin surfaces of the entire row j, and Q is the volumetric air flow rate. Since the air at the inlet of the test channel is free of naphthalene, it leads to

$$\rho_{n,b}=\sum_{1}^{j-1}\dot{M}_j/Q \tag{3}$$

Once h_m is evaluated, its dimensionless counterpart, the Sherwood number

$$\mathrm{Sh}=h_mD/K \tag{4}$$

can be obtained. D, the characteristic length, is the fin diameter for the straight pin-fin and the midsection diameter for the fillet fin; K is the diffusion coefficient for the naphthalene-to-air mass transfer, which is calculated from the Schmidt number $\mathrm{Sc}=\nu/K=2.5$, where ν is the kinematic viscosity of air. According to the method by Kline and McClintock (1953), the

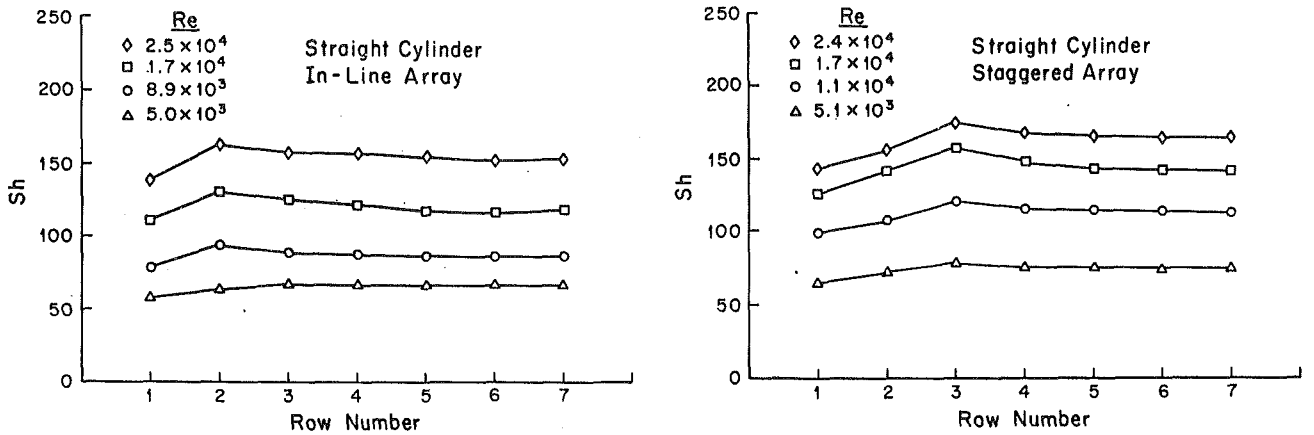

(a). Straight Cylinder, In-lin Array

(c). Straight Cylinder, Staggered Array

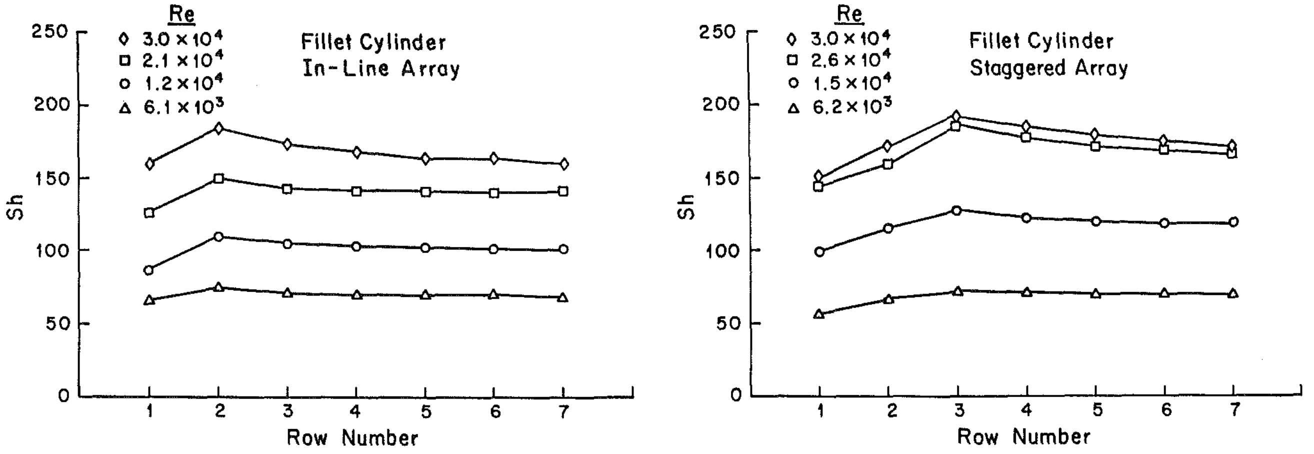

(b). Fillet Cylinder, In-line Array

(d). Fillet Cylinder, Staggered Array

Fig. 3 Row-resolved Sherwood number: *(a)* straight cylinder, in-line array; *(b)* fillet cylinder, in-line array; *(c)* straight cylinder, staggered array; *(d)* fillet cylinder, staggered array

present experimental uncertainty of Sh is estimated at 4 percent, and the repeatability is about the same value.

By analogy, the respective corresponding relationships of equations (1) and (4) in heat transfer are

$$h = q/(T_w - T_b) \qquad (5)$$

and

$$\mathrm{Nu} = hD/k \qquad (6)$$

where q is the heat transfer rate driven by the wall-to-bulk temperature difference, $T_w - T_b$, h is the heat transfer coefficient, k is the fluid thermal conductivity, and Nu represents the Nusselt number. Nu is the dimensionless heat transfer coefficient and corresponds to the Sherwood number in mass transfer as defined in equation (4). The analogy also implies that

$$\mathrm{Sh}/\mathrm{Nu} = (\mathrm{Sc}/\mathrm{Pr})^n \qquad (7)$$

where Pr is the fluid Prandtl number and n is a power index. The value of n is typically equal to 0.4 for turbulent transport with $0.7 \le \mathrm{Pr} \le 2.5$ (Sparrow and Ramsey, 1978). For $\mathrm{Sc} = 2.5$ and $\mathrm{Pr} = 0.7$, equation (7) yields $\mathrm{Nu} = 0.6\ \mathrm{Sh}$.

The Reynolds number Re in the present study is defined as

$$\mathrm{Re} = U_{\max} D/\nu \qquad (8)$$

This definition is chosen to be consistent with heat exchanger practice and most of the pin-fin correlations in the literature. The characteristic velocity, $U_{\max}$, is a superficial maximum velocity defined as

$$U_{\max} = Q/A_{\min} \qquad (9)$$

where Q, as already defined in equations (2) and (3), is the volumetric air flow rate and $A_{\min}$ is the minimum cross-sectional area. As an indication of the hydrodynamic state of the main flow approaching the array, it is also of some interest to evaluate the duct Reynolds number defined as

$$\mathrm{Re}_D = UD_h/\nu \qquad (10)$$

where U is the bulk mean velocity in the channel and D_h is the hydraulic diameter. For a given channel and array geometry, if the mass flow rate in the channel is maintained the same with array and without array present, the two Reynolds number are related by

$$\mathrm{Re}_D = \mathrm{Re} \bullet (D_h/D) \bullet (A_{\min}/A) \qquad (11)$$

where A is the channel unobstructed cross-sectional area.

Results and Discussion

Figure 3 shows the row-by-row distributions of Sherwood number. The figure consists of four plots, and each of the plots corresponds to a specific combination of array configuration and endwall-fillet effect. At any given Reynolds number, the row-resolved variations are confined to the first few rows; beyond these, Sh reaches as asymptotic, fully developed value. The general trend is that Sh increases from the first

Table 1 Comparison of mass transfer between fin surface and endwall

Array	Re	Row number	Sh_{EW}/Sh
In-line	16700	3	0.99
		5	1.02
	4950	3	1.04
		5	1.09
Staggered	17200	3	0.89
		5	0.95
	5060	3	0.99
		5	1.04

row, reaches a maximum, and then decreases toward the fully developed value. The endwall fillet virtually has no effect on this trend.

The maximum Sh is a result of two conflicting phenomena. One of these is the wake shedding behind a cylinder and flow acceleration in the spacing between two spanwise neighboring fins. The mass transfer coefficient increases for a cylinder situated in the region influenced by both local effects. The second phenomenon is the gradual enrichment of naphthalene vapor concentration in the bulk along the streamwise direction. Since the wall concentration is a constant, the driving potential decreases accordingly. As a result, a streamwise decrease in the transfer coefficient is expected. Note that, for each array, the maximum Sh occurs at those rows having the first direct wake shedding, i.e., second row for the in-line array and third row for the staggered array. In addition, the phenomenon of wake shedding and locally accelerated flow becomes more noticeable for cases with high Reynolds numbers. For flow with a low Reynolds number, i.e., $Re \leq 5 \times 10^3$, the local maximum disappears and Sh increases directly to the fully developed value. The present row-by-row transfer distributions show a good agreement with those from earlier studies (Sparrow et al., 1978, 1980; Metzger et al., 1982a, 1986; Simoneau and VanFossen, 1984). Moreover, the locations of maximum Sh observed in the present study correspond perfectly with those with the highest turbulence intensity over the entire array measured by Metzger and Haley (1982b) and Simoneau and VanFossen (1984).

Mass transfer in the first row bears a distinctive feature compared to the downstream rows. Flow field adjacent to the first row generally has lower levels of turbulence and lacks wake shedding. Accordingly low mass transfer coefficients exist. This is evidenced by the results shown in Fig. 3 that, for a given Re, the first row always has the lowest Sh. Meanwhile, the first-row mass transfer is expected to be array-geometry independent and, to a certain extent, affected by the endwall condition. The first-row mass transfer coefficients can be well represented by two least-square fits; i.e., for $5 \times 10^3 \leq Re \leq 3 \times 10^4$,

$$Sh = 0.55\ Re^{0.55} \quad \text{for straight pin-fins} \qquad (12)$$

$$Sh = 0.30\ Re^{0.60} \quad \text{for fillet pin-fins} \qquad (13)$$

A comparison of these two equations shows that pin-fins with fillet have lower mass transfer coefficients than those without fillet by approximately 6 to 13 percent. The difference in Sh decreases as the Reynolds number increases. With analogy, the Nusselt number transformed from the Sherwood number in equation (12), i.e., $Nu = 0.6\ Sh$, agrees well with the measured results in the heat transfer study by Metzger et al. (1982a). The difference is less than 10 percent within the present testing range.

Table 2 Correlation coefficients of array-averaged mass transfer coefficients

Array	Pin-fin shape	A	B
In-line	Straight	0.463	0.537
	Fillet	0.403	0.550
Staggered	Straight	0.690	0.511
	Fillet	0.234	0.608

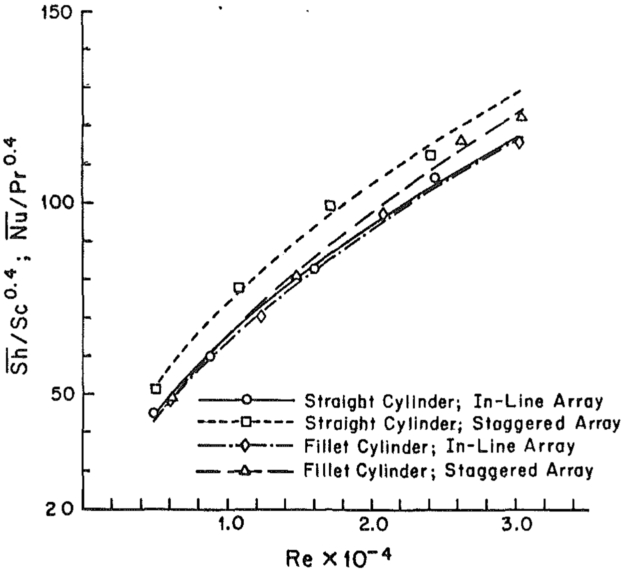

Fig. 4 Array-averaged mass transfer or heat transfer coefficients

As mentioned earlier, for turbine cooling applications, the total heat transfer from a short pin-fin array is the sum of heat transfer from the fin surface and the endwall. It is of interest to examine the individual contribution of each of the two heat transfer components or the ratio between them. However, previous studies have shown contradicting results in this aspect. For geometry similar to the present staggered array with straight pin fins, VanFossen (1981) reported that the pin has a nearly 35 percent higher heat transfer coefficient than the endwall. However, Metzger et al. (1982c) indicated that these two heat transfer coefficients are very comparable, within 10 percent. The latter implies that the heat transfer characteristic obtained solely from the pin-fin surface or the endwall is a sufficient representative for the more complex conditions in reality. In the present study, the investigation is performed by making the endwall of a designated row mass transfer active. This designated endwall region, coated with a strip of naphthalene, spans the entire channel width and, in the streamwise direction, covers a range one-half pitch upstream and downstream from the cylinder axis. During the test, all fins remain mass transfer active. Table 1 shows the sample results for straight cylinders, with the strip located at the third and fifth rows, respectively. The ratio of Sherwood number between endwall and pin surface is very close to unity. This favors the conclusion drawn by Metzger et al. (1982c).

Figure 4 shows the array-averaged mass transfer results for all cases studied. Note that the present mass transfer coefficient averaged over the entire array is almost the same as the corresponding fully developed value. Plotted on the ordinate is the array average Sherwood number, $\overline{Sh}$, scaled by the factor of $Sc^{0.4}$ ($= 1.44$) instead of $\overline{Sh}$ itself. According to the analogy shown in equation (7), the ordinate in Fig. 4 thus has a dual label, i.e., $\overline{Sh}/Sc^{0.4}$ for mass transfer and $Nu/Pr^{0.4}$ for heat transfer. This normalized, array-averaged transfer coefficient is further correlated using the least-square-fitted power form, i.e., $\overline{Sh}/Sc^{0.4} = A \bullet Re^B$. Table 2 lists the correlation coefficients A and B corresponding to each curve plotted in Fig. 4. Compared to similar results reported in the literature, the present

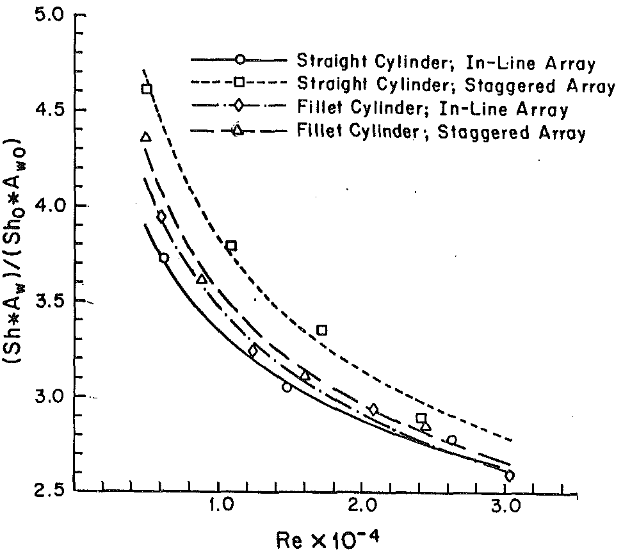

Fig. 5 Total mass transfer augmentation

correlations in general have relatively weak Reynolds number dependency. For $S/D=X/D=2.5$, $H/D=1$, and $10^3 \leq \mathrm{Re} \leq 10^5$, the correlation proposed by Metzger et al. (1982a) is

$$\overline{\mathrm{Nu}}/\mathrm{Pr}^{0.4}=0.080\ \mathrm{Re}^{0.728} \tag{14}$$

The power index of Re is 0.728 compared to the present 0.511. However, despite this difference, equation (14), in fact, gives a very good representation of the present data. The overall deviation is less than 10 percent. A remarkable agreement exists in the midspan of the present testing range; i.e., $1.3 \times 10^4 \leq \mathrm{Re} \leq 2.4 \times 10^4$, where the deviation is less than 5 percent. The difference in the power index is considered to be caused by the correlation range of Reynolds number. Equation (14) has a much higher upper Re limit (10^5) than that of the present study (3×10^4). It has been suggested that the power index value tends to be greater for $\overline{\mathrm{Nu}}$–Re correlations with higher Reynolds numbers (Metzger et al., 1982a).

An examination of the results in Fig. 4 shows that the fillet effect on the array-averaged mass transfer appears to be dependent on the array geometry. One surprising observation is that Sh for the in-line array is virtually uninfluenced by the endwall fillet. For a given Re, the difference of $\overline{\mathrm{Sh}}$ lies in the limits of the present experimental uncertainty, although $\overline{\mathrm{Sh}}$ of the straight pin-fins is always slightly higher. However, this trend changes for the staggered array. $\overline{\mathrm{Sh}}$ with endwall fillet is found to be lower than that without fillet; the difference is about 25, 17, and 8 percent for $\mathrm{Re}=5\times10^3$, 10^4, and 3.0×10^4, respectively. The difference diminishes as the Reynolds number increases.

Further examination of Fig. 4 reveals that array-averaged mass transfer coefficients for the staggered arrays are generally higher than those of the in-line arrays. The difference of $\overline{\mathrm{Sh}}$ is approximately 13 percent for arrays with a straight cylinder and 6 percent for those with a fillet cylinder. Within the present testing range, these differences appear to be Reynolds number independent. This finding suggests that, at least from the standpoint of heat transfer coefficient, it is preferable to use a staggered array than an in-line array. However, if the overall array performance is concerned, other factors such as pressure drop and wetted (heat transfer) area also need to be considered.

Figure 5 shows the combined effects of wetted-area and mass transfer coefficient on the total mass transfer from the entire system surface. The system surface referred to here includes fin surfaces and all inner walls of the channel that houses the array. The wetted area A_w, as defined in hydrodynamic sense, is the size of the system surface. The dimensionless measure of the total mass transfer rate can be expressed by the product of $\overline{\mathrm{Sh}}$ and A_w. This approach assumes that $\overline{\mathrm{Sh}}$ is a rational representative of the area-averaged mass transfer coefficient on all surfaces "wetted" by the fluid. According to the results shown in Table 1, such an assumption appears to be quite reasonable, particularly for the present channel having a large aspect ratio. The scale factor $\mathrm{Sh}_o \bullet A_{wo}$ used for the ordinate is the counterpart of $\overline{\mathrm{Sh}} \bullet A_w$ in smooth channels unobstructed by pin-fin arrays. Sh_o is the Sherwood number with fully developed turbulent flow and A_{wo} is the wetted area in the unobstructed channel. The ratio represents an augmentation index of the overall mass transfer induced by the addition of a pin-fin array.

As expected, the wetted area changes with differences in array geometry and fin shape. The magnitude of A_w for all four arrays studied are higher than the corresponding A_{wo}. For straight pin-fins, A_w is approximately 11.6 percent higher than A_{wo} for the staggered array, and 10.5 percent for the in-line array. The corresponding increases for the fillet pin-fins drop to 3.3 and 2.8 percent. The value of Sh_o is obtained from the Dittus-Boettler equation, i.e.,

$$\mathrm{Nu}_{DO}/\mathrm{Pr}^{0.4}=0.023\ \mathrm{Re}_D^{0.8} \tag{15}$$

Note that Re_D here is the duct Reynolds number as defined in equation (10). Nu_{DO} is the fully developed Nusselt number based on hydraulic diameter, D_h, which equals $1.85D$. To be compatible with the characteristic length used for Sh, equation (15) becomes

$$\mathrm{Sh}_o/\mathrm{Sc}^{0.4}=(D/D_h)\bullet\mathrm{Nu}_{DO}/\mathrm{Pr}^{0.4}=0.0124\ \mathrm{Re}_D^{0.8} \tag{15a}$$

Under the constraint of fixed mass flow rate flowing through the channel with and without the array, Re_D can be substituted by Re using equation (11). Thus,

$$\mathrm{Sh}_o/\mathrm{Sc}^{0.4}=0.0203\bullet[\mathrm{Re}\bullet(A_{\min}/A)]^{0.8} \tag{15b}$$

where $A_{\min}/A$ equals 0.6 for arrays with straight pin-fins and 0.51 with fillet pin-fins.

As seen in Fig. 5, the overall transfer augmentation decreases with Reynolds number, following a decline rate of about $\mathrm{Re}^{-0.2}$ to $\mathrm{Re}^{-0.3}$. $\overline{\mathrm{Sh}}/\mathrm{Sh}_o$ would have a similar dependence on Re, according to the power indices listed in Table 2 and equation (15*b*). A pin-fin array with endwall fillet actually has a better overall transfer capability than that projected by the transfer coefficient shown in Fig. 4. This is evidenced by the fact that, for the in-line arrays, the value of augmentation index $(\overline{\mathrm{Sh}}/\mathrm{Sh}_o)\bullet(A/A_{wo})$ with fillet pins is higher than that with straight cylinders. The difference, however, is very moderate and decreases with an increase in Re, less than 4 percent for $\mathrm{Re}\geq10^4$. This phenomenon is primarily due to the variation of flow area with different fin geometry. According to equation (15*b*), the augmentation index is proportional to the product of two area factors, $(A_{\min}/A)^{-0.8}$ and (A_w/A_{wo}). The presence of endwall fillet increases the value of the former, but decreases the latter to a less extent. The fillet pin-fins thus have a stronger combined contribution of these two area factors toward the overall augmentation than the straight fins. Nevertheless, this contribution for the staggered arrays is insufficient to overcome the difference in the transfer coefficient. As a result, the staggered array still has a higher augmentation index with the straight fins than with the fillet, but the percentage difference reduces to about one-half that of the transfer coefficient.

Figure 6 shows the measured pressure loss coefficients, f, for all arrays studied. f is the dimensionless representation of the pressure drop on a per-row basis, defined as

$$f=2\Delta p/(\rho U_{\max}^2 N) \tag{16}$$

where Δp is the pressure drop across the entire array and N is the number of rows in the array. Note that f is strongly dependent on the array configuration and is much less influenced

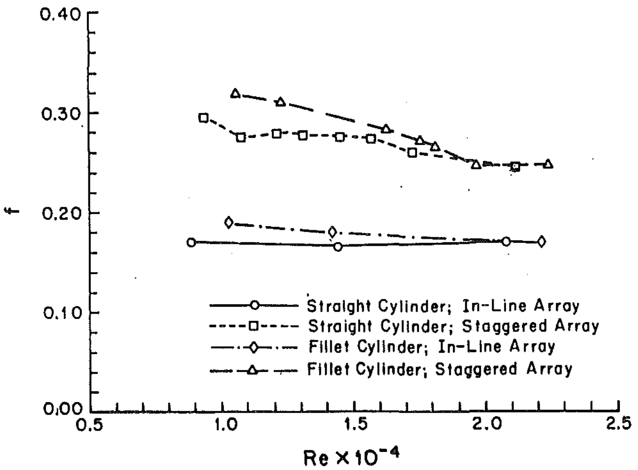

Fig. 6 Pressure loss coefficients

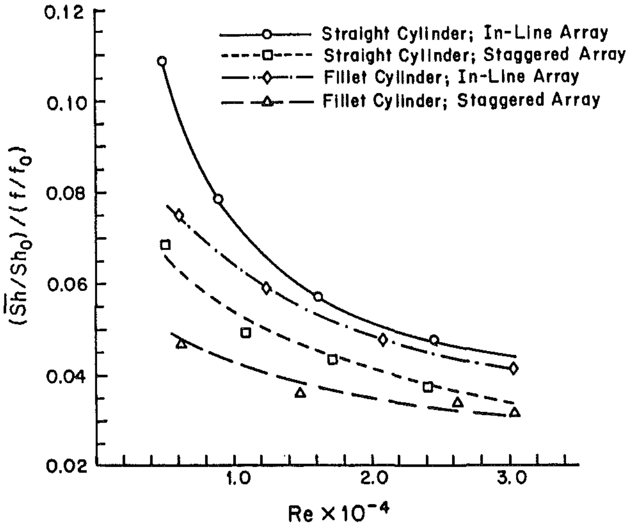

Fig. 7 Performance index; $(\overline{Sh}/Sh_o)/(f/f_o)$

by the endwall-fillet effects. The value of f is larger for the staggered array than for the in-line array, by a factor of nearly 1.5 to 2 depending on the Reynolds number. Arrays with fillet fins generally have slightly larger values of f than those without endwall fillet; however, the difference diminishes as Re increases. The higher mass transfer coefficients for the staggered case are therefore accompanied by higher pressure drops.

The overall performance of a pin-fin array as an augmentation device can be described by a performance index, $\overline{Sh}/f$, which represents mass transfer per unit pressure drop. The ordinate in Fig. 7 is such a performance index normalized by its fully developed, smooth channel counterpart Sh_o/f_o. Similar to Fig. 5, the derivation of this normalized performance index is based on the constraint that the bulk flow rate in the channel is constant, whether the channel is obstructed by the pin-fin array or unobstructed. f_o is the friction factor conventionally defined for fully developed turbulent flow in a smooth duct, i.e.,

$$f_o = 2\Delta p/(\rho U^2)\cdot(D_h/L) \tag{17}$$

where L is the duct length. The value of f_o is calculated from the Blasius Power Law (Kays and Crawford, 1980); i.e.,

$$f_o = 0.078\ \mathrm{Re}_D^{-0.25} \tag{18}$$

The results shown in Fig. 7 indicate that the in-line arrays always have higher performance indices than the staggered arrays, by approximately 50 percent. This is contrary to the general trend found in Figs. 4 and 5. In addition, the endwall fillet consistently results in a degraded performance index for both arrays. This degradation, however, diminishes as the Reynolds number increases.

Conclusions

The present study, using the naphthalene sublimation technique, has effectively investigated the heat transfer characteristics for an in-line and a staggered array, with and without pin-endwall fillet effects. For pins of perfectly cylindrical shape without fillet, the present results agree well with those obtained from earlier heat transfer studies. The general trend of the row-resolved mass (heat) transfer coefficient is uninfluenced by the endwall fillet, but is strongly dependent on the array configuration. The mass transfer coefficient of the first row is lower for fins with endwall fillet than for those without endwall fillet. An auxiliary study shows that mass transfer coefficients on the pin-fin surface and on the fin-attached endwall are comparable.

The staggered array always produces a higher array-averaged mass transfer coefficient ($\overline{Sh}$), mass transfer rate ($\overline{Sh}\bullet A_w$), and pressure drop (f) than the in-line array. The performance index ($\overline{Sh}/f$), however, is lower than that of the in-line array. This general trend prevails for pins with or without endwall fillet. For a given array configuration, the existence of endwall fillet generally results in lower mass transfer coefficient, mass transfer rate, and performance index than without fillet. The effects appear to be much stronger for the staggered array than for the in-line array. The pressure drop is also higher with the endwall fillet than without. All these endwall-fillet effects diminish as the Reynolds number increases. In summary, the endwall fillet is found to be always undesirable if heat transfer augmentation is of concern.

References

Ambrose, D., Lawenson, I. J., and Sprake, C. H. S., 1975, "The Vapor Pressure of Naphthalene," *J. Chem. Thermo.*, pp. 1173–1176.

Armstrong, J., and Winstanley, D., 1988, "A Review of Staggered Array Pin Fin Heat Transfer for Turbine Cooling Applications," ASME *Journal of Turbomachinery*, Vol. 110, pp. 94–103.

Brigham, B. A., and VanFossen, G. J., 1984, "Length-to-Diameter Ratio and Row Number Effects in Short Pin Fin Heat Transfer," ASME *Journal of Engineering for Gas Turbines and Power*, Vol. 106, pp. 241–246.

Eckert, E. R. G., 1976, "Analogies to Heat Transfer Processes," *Measurements in Heat Transfer*, E. R. G. Eckert and R. J. Goldstein, eds., Hemisphere Publishing Corp., New York.

Kays, W. M., and Crawford, M. E., 1980, *Convective Heat and Mass Transfer*, McGraw-Hill, New York.

Kline, S. J., and McClintock, F. A., 1953, "Describing Uncertainties in Single Sample Experiments," *Mechanical Engineering*, Vol. 75, pp. 3–8.

Metzger, D. E., Berry, R. A., and Benson, J. P., 1982a, "Developed Heat Transfer in Rectangular Ducts With Staggered Arrays of Short Pin Fins," ASME JOURNAL OF HEAT TRANSFER, Vol. 104, pp. 700–706.

Metzger, D. E., and Haley, S. W., 1982b, "Heat Transfer Experiments and Flow Visualization for Arrays of Short Pin Fins," ASME Paper No. 82-GT-138.

Metzger, D. E., Fan, C. X., and Shepard, W. B., 1982c, "Pressure Loss and Heat Transfer Through Multiple Rows of Short Pin Fins," *Heat Transfer 1982*, Vol. 3, Hemisphere Publishing Corp., pp. 137–142.

Metzger, D. E., Fan, C. X., and Haley, S. W., 1984, "Effects of Pin Shape and Array Orientation on Heat Transfer and Pressure Loss in Pin Fin Arrays," ASME *Journal of Engineering for Gas Turbines and Power*, Vol. 106, pp. 252–257.

Metzger, D. E., and Shepard, W. B., 1986, "Row Resolved Heat Transfer Variations in Pin Fin Arrays Including Effects of Non-uniform Arrays and Flow Convergence," ASME Paper No. 86-GT-132.

Simoneau, R. J., and VanFossen, G. J., 1984, "Effect of Location in an Array on Heat Transfer to a Short Cylinder in Crossflow," ASME JOURNAL OF HEAT TRANSFER, Vol. 106, pp. 42–48.

Sparrow, E. M., and Ramsey, J. M., 1978, "Heat Transfer and Pressure Drop for a Staggered Wall-Attached Array of Cylinders With Tip Clearance," *Int. J. Heat Mass Transfer*, Vol. 21, pp. 1369–1377.

Sparrow, E. M., Ramsey, J. M., and Altemani, C. A. C., 1980, "Experiments on In-Line Pin Fin Arrays and Performance Comparisons With Staggered Arrays," ASME JOURNAL OF HEAT TRANSFER, Vol. 102, pp. 44–50.

VanFossen, G. J., 1982, "Heat Transfer Coefficient for Staggered Arrays of Short Pin Fins," ASME *Journal of Engineering for Power*, Vol. 104, pp. 268–274.

Zukauskas, A. A., 1972, "Heat Transfer From Tubes in Cross Flow," *Advances in Heat Transfer*, Vol. 8, pp. 116–133.

Heat Transfer Around a Tube in In-Line Tube Banks Near a Plane Wall

S. Aiba
Professor,
Department of Mechanical Engineering,
Akita Technical College,
Akita 011, Japan

Heat transfer in the third cylinder of four circular cylinders above a plane wall has been investigated in a crossflow of air. The turbulent boundary layer thickness along the wall with no cylinder present was about 21 mm. The cylinder diameter (d) was 15 mm, the clearance (c) between the cylinders and the wall was 0.75 ~ 60 mm (c/d = 0.05 ~ 4.0), and the pitch (p) (which denotes the longitudinal spacing between cylinder centers) was 18 ~ 66 mm (p/d = 1.2 ~ 4.4). The Reynolds number (Re) based on the undisturbed uniform flow velocity above the wall ranged from $0.8 \times 10^4 \sim 4 \times 10^4$. *Variations in the characteristic features of local and mean Nusselt number* Nu_m *are discussed in relation to c/d, p/d, and Re.* Nu_m *yielded the compact expression* $Nu_m = 0.103\ (p/d)^{-0.12}(c/d)^{0.23}Re^{0.74}$, *with a spread of ±5 percent in the ranges c/d = 0.18 ~ 0.61, p/d = 1.2 ~ 3.2, and* $Re = 0.8 \times 10^4 \sim 4 \times 10^4$, *except for the case with c/d = 0.18, p/d = 3.2.*

Introduction

A large number of studies have been carried out concerning the features of heat transfer of tube banks. The present author also has investigated heat transfer and flow around tubes in tube banks with crossflow of air (Aiba et al., 1982; Aiba and Tsuchida, 1983). However, the convective heat transfer characteristics around tubes have not been clarified sufficiently for the case when the tubes are arranged in line near a shell wall, as seen in the combustion chamber of the water tube boiler for instance. Also, the convective heat transfer around tubes near the shell wall consisting of the in-line tube bank has not been examined systematically. From this standpoint, the present author has made clear the heat transfer characteristics around a single circular cylinder placed in the plane wall as a first step (Aiba, 1985; Aiba and Tsuchida, 1986). In uniform flow, behavior of flow and heat transfer around the tubes of a single longitudinal row tube bank is quite different from those of a single cyclinder (Zdravkovich, 1977; Eastop and Turner, 1982; Kostić and Oka, 1972; Aiba and Yamazaki, 1976; Aiba et al., 1980). Even the results of the first cylinder (also, the second cylinder) composed of four circular cylinders show quite a complicated variation with the in-line pitch, although it is generally accepted that the heat transfer of the tube in the first row of the tube bank is similar to that of a single cylinder. However, the average heat transfer results of the third and fourth cylinders are not so influenced by the in-line pitch if the pitch is not smaller than the critical one, indicated as follows:

$$(p/d)_c = 7.34\ \mathrm{Re}^{-0.171} \qquad (1)$$

for the ranges $\mathrm{Re} = 10^4 \sim 5 \times 10^4$ and $p/d = 1.15 \sim 3.4$, where p and Re are the pitch between the cylinder centers and Reynolds number based on the cylinder diameter d, respectively (Aiba et al., 1980, 1981). The critical pitch ratio $(p/d)_c$ increases with decreasing Re. At a given value of p/d, the heat transfer rate of all four cylinders is lower than that of the single cylinder in the range of $p/d < (p/d)_c$.

The objective of the present study is to clarify the convective heat transfer characteristics of tubes in a crossflow of air near the plane wall by investigating those of the third of four cylinders aligned at equal intervals, and then comparing the results with those of a single cylinder and with the four cylinders in uniform flow fields.

Experiments and Procedures

The wind tunnel used in the present study is the same as that employed in previous studies (Aiba and Yamazaki, 1976; Aiba, 1985) and the test section is a rectangle 325 mm high and 225 mm wide. The working section was divided by a horizontal partition plate mounted in the tunnel. The plate was 1000 mm long and 5 mm thick and had a round leading edge. A trip wire, 1.4 mm in diameter, was located across the plate 100 mm from the leading edge. The free-stream turbulence of upstream uniform flow $\sqrt{\overline{U'^2}}/U_\infty$ averaged 0.7 percent through the experiments. A constant-temperature hot-wire anemometer with a single tungsten wire of 0.005 mm diameter with a linearizer as the sensing element was used for measuring the distribution of the velocity and turbulence intensity in the flow field around the test section.

The velocity and turbulence intensity in a wake region with low velocity and high turbulence intensity cannot be measured accurately by a single hot-wire method. A single hot wire is the sensing element, and it does not show the direction of flow. Furthermore, even though the velocity of main flow $U = 0$ in a moment, the output from the hot-wire anemometer does not indicate zero, being affected by the other velocity components. Accurate measurements of these flow fields may be conducted by the laser-Doppler anemometer, the pulsed-wire anemometer (Bradbury, 1976), and the flying hot-wire anemometer (Cantell and Coles, 1983), etc. In general, these methods are not always convenient and their apparatus cannot be easily obtained.

In spite of the problems of measurement in such flow fields, a single hot-wire anemometer is useful to examine qualitatively the relationship between the heat transfer and the flow (Aiba and Yamazaki, 1976). The turbulence intensity was calculated from the mean and rms voltage reading from the hot-wire anemometer with a linearizer. No corrections were made for flow direction.

Four cylinders spanned the wind tunnel horizontally as shown in Fig. 1 (which also shows the coordinate system employed). The test cylinder (the third one) was placed 750 mm downstream of the leading edge of the plate. The thickness of the turbulent boundary layer at the test cylinder position (but with all four cylinders removed from the tunnel) was about 21 mm. The boundary layer velocity distribution obtained agrees with

---

Contributed by the Heat Transfer Division for publication in the JOURNAL OF HEAT TRANSFER. Manuscript received by the Heat Transfer Division May 22, 1989; revision received February 9, 1990. Keywords: Forced Convection, Heat Exchangers, Turbulence.

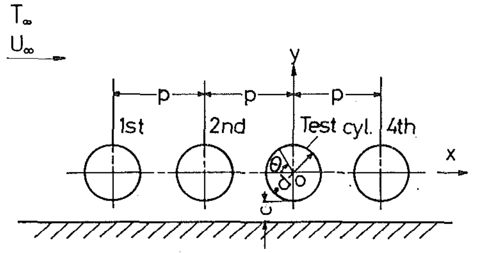

Fig. 1 Arrangement of cylinders and coordinate system

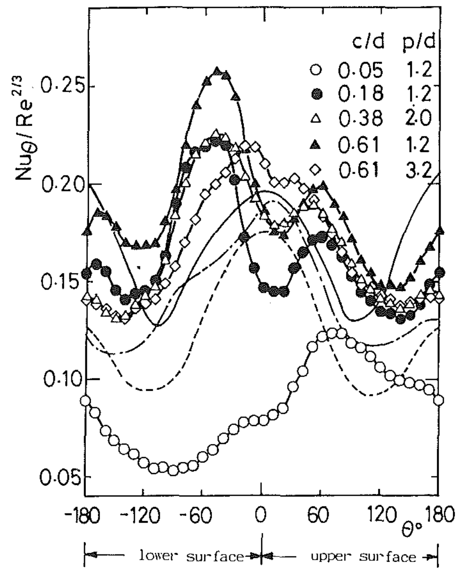

Fig. 2 Variation of local Nusselt number for Re ~ 3.4 × 10⁴ (- - -, *c/d* = ∞; — · —, *c/d* = 0.054; ———, *c/d* = 0.51; at *p/d* = ∞, δ = 16 mm measured by Aiba and Tsuchida, 1986)

that shown by Schubauer and Klebanoff (1956). It was also confirmed that the distribution of turbulence intensity in the wall boundary layer at the test cylinder position was almost identical with that presented by Klebanoff (1955).

Four cylinders, 15 mm in diameter, were located at equal intervals. The clearances between the cylinders and the plate were 0.75, 2.7, 5.7, 9.15, 12, 15, 18.5, and 60 mm. In order to measure the clearance accurately a block gage was used for all experiments. The in-line pitch ratio p/d was varied from 1.2 to 4.4. The Reynolds number Re based on the cylinder diameter and undisturbed uniform flow velocity was varied from 0.8×10^4 to 4×10^4.

For the heat transfer measurement of the test cylinder, a stainless steel ribbon wound helically around the center section of a plexiglass tube was heated electrically. The inside of the tube was filled with rigid urethane foam in order to minimize the heat loss by conduction. The correction of the loss by conduction in the radial direction amounted to less than 1 percent of the electric power input. The wall temperatures were measured with 0.065 mm copper-constantan thermocouples affixed to the back of the stainless sheet at intervals of 10 deg. The maximum temperature of the test cylinder surface was kept under 38°C to reduce the radiative heat loss as much as possible. The heat loss by radiation from the cylinder surface was estimated to be about 0.6 percent of the heat supplied. Thus, the present data were obtained under the condition of constant heat flux (the heat flux q to the test cylinder ranged from 1.0 to 2.7 kW/m^2). The local heat transfer coefficient and the corresponding Nusselt number are defined, respectively, as follows:

$$h_\theta = q/(T_w - T_\infty), \qquad \mathrm{Nu}_\theta = h_\theta d/\lambda \qquad (2)$$

In addition, three dummy cylinders were unheated during the heat transfer measurements.

The experiments should, for practical purposes, be conducted under the condition that all four cylinders are heated. Under such a condition, when evaluating the heat transfer coefficient around the test cylinder, it is necessary to estimate a temperature of the oncoming flow to the test one, although that is not easy. If this temperature of the oncoming flow to the test cylinder is chosen as T_∞ in equation (2), the experimental result for the heat transfer around the test cylinder is almost identical with that obtained under the following conditions: The other three cylinders are unheated, and the oncoming flow temperature is chosen as that in the upstream region of the first cylinder (Aiba and Yamazaki, 1976). Furthermore, when p/d is larger than $(p/d)_c$ in the uniform flow field ($c/d = \infty$), even if all the cylinders are heated and the heat transfer coefficient is defined by equation (2), the heat transfer coefficient of the test cylinder may be smaller by several percent than the coefficient for heating only the test cylinder (Aiba et al., 1981). Of course, the difference cannot be neglected for the condition $p/d < (p/d)_c$.

However, the critical pitch ratio $(p/d)_c$ obtained in the uniform flow field could not be observed in this experiment, as will be shown later. This is caused by the presence of the plane wall in the neighborhood of the four cylinders. Therefore, the difference is not so large for the lower Re and the smaller p/d treated in this experiment.

Measurements of the wall static pressure were made using another unheated cylinder, which had orifices 0.5 mm in diameter at intervals of 10 deg. Oil flow patterns show that the flow field is two dimensional.

Experimental Results and Discussion

Local Heat Transfer Characteristics. Typical distributions of local Nusselt numbers Nu_θ are presented in Fig. 2, including the results for a single cylinder obtained by Aiba and Tsuchida (1986). The results are given as $\mathrm{Nu}_\theta/\mathrm{Re}^{2/3}$ at around $\mathrm{Re} = 3.4 \times 10^4$, noting that the average Nusselt number in the turbulent wake region is proportional to $\mathrm{Re}^{2/3}$. In the case of

Nomenclature

c = distance between the cylinder and the plane wall
C_p = $(P - P_\infty)/(1/2)\rho U_\infty^2$ = static pressure coefficient
d = cylinder diameter
Nu = Nusselt number
P = static pressure
p = longitudinal spacing between cylinder centers
Re = $U_\infty d/\nu$ = Reynolds number
U = flow velocity
$\sqrt{\overline{U'^2}}/U_\infty$ = stream turbulence intensity
δ = thickness of the boundary layer
θ = circumferential angle from forward stagnation point
λ, ρ, ν = thermal conductivity, kinematic viscosity, and density of air at T_∞

Subscripts

m = mean
max = maximum
w = wall
∞ = undisturbed uniform stream

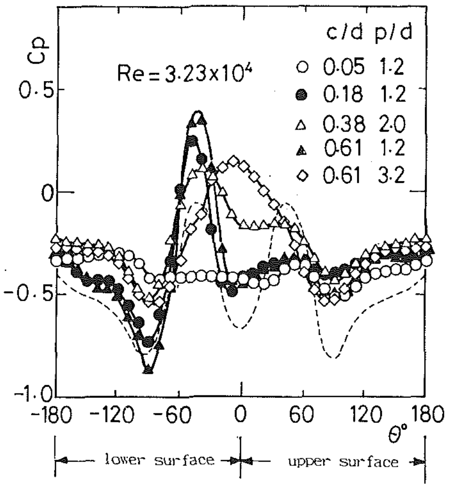

Fig. 3 Variation of local static pressure with c/d, p/d (---, $c/d=\infty$; $p/d=1.2$; $Re=6.7\times10^4$ after Eastop and Turner, 1982)

$c/d=0.05$, Nu_θ of the entire surface of the cylinder is very small compared with that for the single cylinder of $c/d=0.054$ as indicated by the dash-dot line. The maximum Nusselt number Nu_{max} occurs on the upper surface of the cylinder ($0\ deg<\theta<180\ deg$). Although Nu_{max} is located in the vicinity of $\theta=75$ deg for $p/d=1.2$, as shown in Fig. 2, it shifts upstream with increasing p/d. However, the result of $c/d=0.18$ is quite different from that of $c/d=0.05$, although the pitch ratio $p/d=1.2$ is the same. The heat transfer rate around the cylinder increases drastically compared with the case of $c/d=0.05$. Also, it can be observed that Nu_{max} is located on the lower surface of the cylinder ($0\ deg<\theta<-180\ deg$) at around $\theta=-55$ deg. This is due to the effect of the reattachment of the free shear layer shed from the lower surface of the second cylinder. The behavior of this layer is strongly affected by the plane wall mentioned below. Another peak of Nu_θ at around $\theta=60$ deg results from the reattachment of the free shear layer shed from the upper surface of the second cylinder. However, this value of Nu_θ is smaller than that of Nu_{max}, and increases proportionally with increasing c/d. In the case of $c/d=0.61$ for the same pitch ratio $p/d=1.2$, the heat transfer rate around the cylinder increases more than that of $c/d=0.18$.

These results show that the heat transfer phenomena treated herein are closely related to the clearance between the cylinders and the plane wall. For $c/d=0.61$, Nu_{max} is located at around $\theta=-20$ deg when the pitch ratio increases to $p/d=3.2$, as shown in Fig. 2. The other peak, which exists in the neighborhood of $\theta=+30$ deg, is not clear.

In general, it can be said that variations of Nu_θ around the cylinder decrease with increasing p/d, when c/d is constant (see also Fig. 6). These trends may be related to the variations of the free shear layers shed from the second cylinder.

The distributions of the pressure coefficient C_p corresponding to the same conditions in Fig. 2 are shown in Fig. 3 for $Re=3.23\times10^4$. Also included this figure is the result of Eastop and Turner (1982), indicated by a dotted line, which was obtained under the conditions of $c/d=\infty$, $p/d=1.2$, and $Re=6.7\times10^4$.

The distribution of C_p for $c/d=0.05$ and $p/d=1.2$ changes little around the cylinder compared with other results. The flow around the cylinder is rearly stagnant in this case and Nu_θ also becomes small as shown in Fig. 2. For $c/d=0.18$ and 0.61, except when $p/d=3.2$, there exist sharp peaks in the vicinity of $\theta=-45\sim-50$ deg. These C_{pmax} are larger than the results for a uniform flow field obtained by Eastop and Turner (1982). Other C_p peaks on the upper surface of the cylinder are smaller than the results of the lower surface, and the locations of these peaks are not always clear. These results may suggest that the free shear layer shed from the lower surface of the second cylinder is deflected in the upward (say, the y direction) by the existence of the plane wall. The upper side free shear layer shed from the second cylinder is also deflected in the y direction. As a result, based on the flow field measurements, the relatively slow velocity flow in the upper-side shear layer reattaches at these locations.

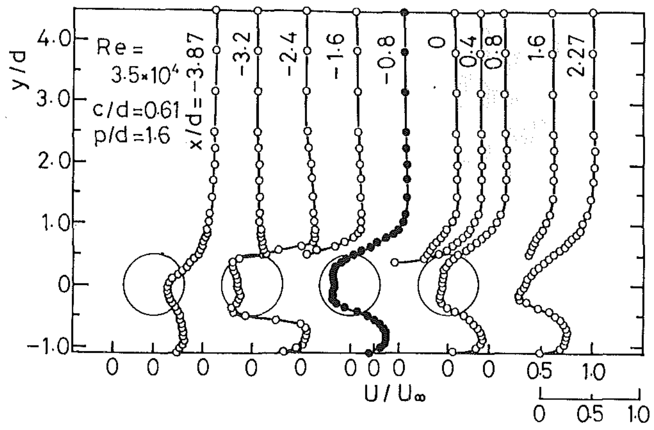

Fig. 4 Distribution of velocity over the test field

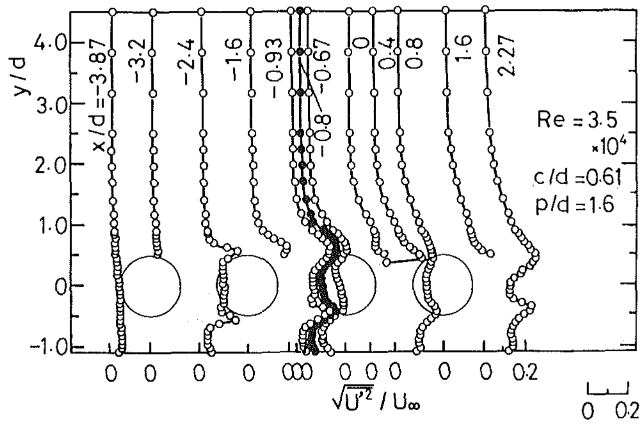

Fig. 5 Distribution of turbulence intensity over the test field

In the case of $p/d=3.2$, C_{pmax} is located at around $\theta=-10$ deg. This indicates that the free shear layer of the plane wall side may be rolled up toward the front surface of the cylinder.

Figure 4 indicates the velocity distributions of the flow field in the case of $c/d=0.61$, $p/d=1.6$, and $Re=3.5\times10^4$. The velocity profile of $x/d=-0.8$ (which is the center section between the second and third cylinders) is similar to that of $x/d=0.8$, although the velocity gradients in the shear layers to the perpendicular to the main flow direction are relatively larger than those of $x/d=0.8$. From this, it is assumed that the behavior of the heat transfer of the fourth cylinder may be nearly identical to that of the test cylinder (Aiba et al., 1981). It can be seen also from the profile of $x/d=-0.8$ that the velocity gradient of the shear layer in the range $y/d<0$ is larger than that for $y/d>0$. Where the velocity gradient of the shear layer is large, the turbulence intensity assumes a large value. In the neighborhood of the largest velocity gradient, maxima occur and are shown in Fig. 5. These peaks of turbulent intensity at $x/d=-0.8$ can be noted at $y/d=0.58$ and -0.43. From these results and oil flow patterns, it appears that the occurrence of Nu_{max} of the lower surface of the cylinder results from the reattachment of the relatively large velocity part of the shear layer with high turbulence intensity, considering also the results of other sections between the second cylinder and the test cylinder. Also, it can be confirmed that the flow velocity

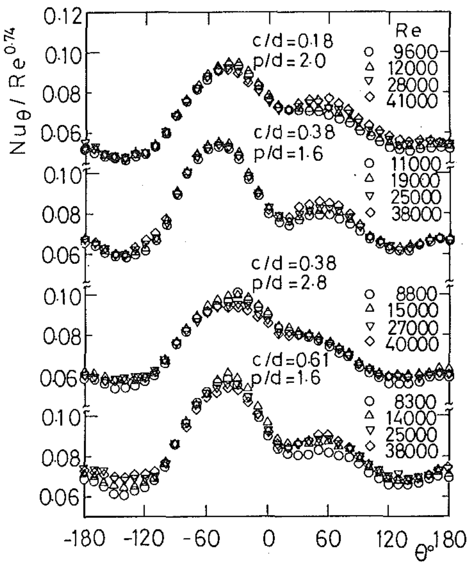

Fig. 6 Local Nusselt number distribution with Reynolds number

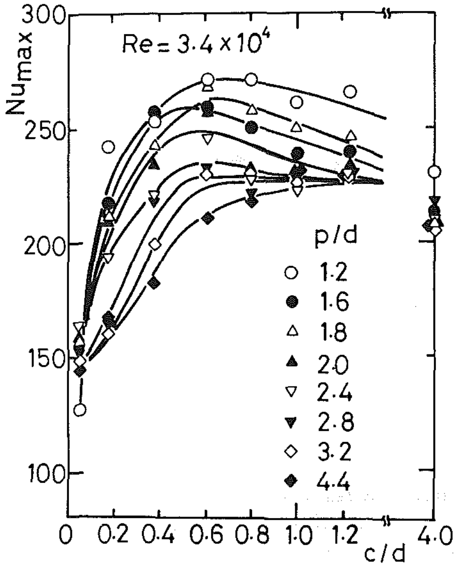

Fig. 7 Correlation of $\mathrm{Nu}_{\max}$ with *c/d*, *p/d*

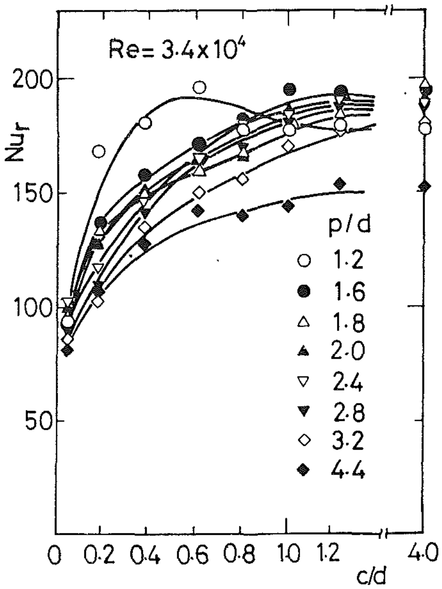

Fig. 8 Correlation of Nu_r with *c/d*, *p/d*

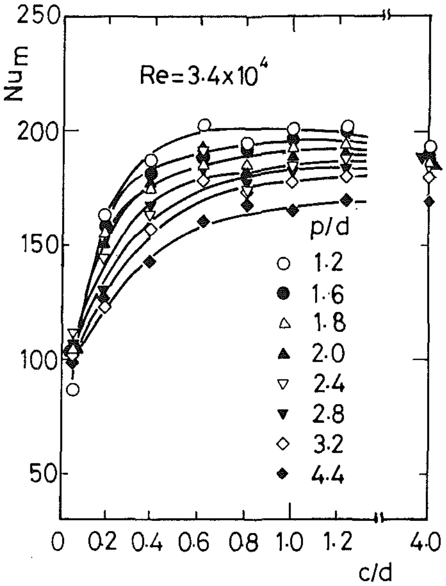

Fig. 9 Variation of Nu_m with *c/d*, *p/d*

of the shear layer that reaches the upper surface is smaller than that to the lower surface.

The distributions of Nu_θ versus Reynolds number are given in Fig. 6. The results are summarized as $\mathrm{Nu}_\theta/\mathrm{Re}^{0.74}$, because the average Nusselt number is proportional to $\mathrm{Re}^{0.74}$ (as shown in Fig. 12) in the ranges $c/d = 0.18 \sim 0.61$, $p/d = 1.2 \sim 3.2$. It can be seen that the local Nusselt number at any angular position is approximately proportional to $\mathrm{Re}^{0.74}$ within an average discrepancy of 5 percent.

Figures 2 and 6 show that $\mathrm{Nu}_{\max}$ on the lower surface plays an important role for the average Nusselt number Nu_m around the cylinder. Therefore, it is important to know the features of $\mathrm{Nu}_{\max}$. Figure 7 illustrates the variations of $\mathrm{Nu}_{\max}$ against c/d with p/d for $\mathrm{Re} = 3.4 \times 10^4$. In the case of $c/d = 0.05$ ($\mathrm{Nu}_{\max}$ is located at the upper side of the cylinder independent of p/d and Re in this case), the results are influenced little by p/d except when $p/d = 1.2$. In the range $c/d > 0.05$, it is confirmed that the value of $\mathrm{Nu}_{\max}$ increases abruptly with increasing c/d. However, for $c/d \geq 0.5 \sim 0.6$, the increasing ratio of $\mathrm{Nu}_{\max}$ versus c/d seems to decrease, and for $p/d \leq 2.8$ the value of $\mathrm{Nu}_{\max}$ decreases with increasing c/d. Moreover, it can be found that $\mathrm{Nu}_{\max}$ has large values when p/d is small for $c/d < 0.61$, except when $c/d = 0.05$. However, they are not as much influenced by p/d with increasing c/d as seen in the case of $c/d = 4.0$.

In order to show the heat transfer characteristics of the rear face of the cylinder, the variations of the Nusselt number of $\theta = 180$ deg, Nu_r, are presented in Fig. 8. The Nu_r values have the same trend as $\mathrm{Nu}_{\max}$, which increases with increasing c/d for $c/d < 0.61$, although Nu_r values do not vary as abruptly with c/d as for $\mathrm{Nu}_{\max}$, except for $c/d = 1.2$. For $c/d \geq 0.61$, increasing ratios of Nu_r for c/d decrease, and in particular the results of $p/d = 1.2$ level out somewhat.

Mean Heat Transfer Characteristics. Figure 9 shows the results for mean Nusselt numbers Nu_m with c/d in the area of $\mathrm{Re} = 3.4 \times 10^4$. From this it can be seen that they increase monotonically with increasing c/d for $c/d < 0.61$, and the increasing ratios of Nu_m for $c/d > 0.61$ decrease (Nu_m changes little with c/d). In the case of $c/d = 0.05$, p/d does not play an important role in the behavior of Nu_m, except when $p/d = 1.2$. The same trends can be seen in the case of c/d =

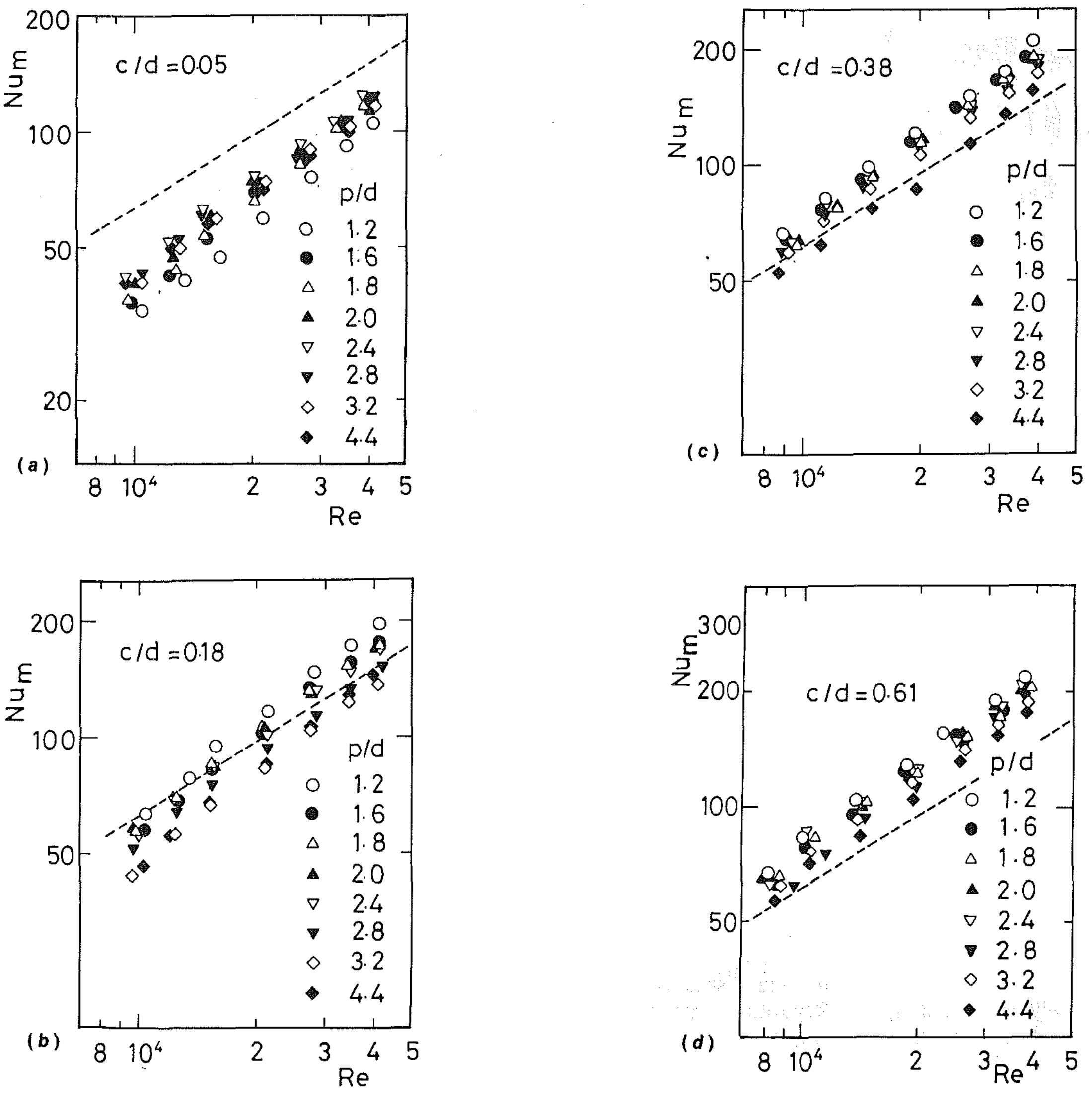

Fig. 10 Variations of mean Nusselt number with Re: *(a)* $c/d = 0.05$; *(b)* $c/d = 0.18$; *(c)* $c/d = 0.38$; *(d)* $c/d = 0.61$; - - -, results of single cylinder in the uniform flow field

4.0, except for $p/d = 4.4$. They had also been observed in the previous work in the uniform flow field (Aiba et al., 1981). In that field, the critical in-line pitch ratio $(p/d)_c$ defined by equation (1) is equivalent to 1.23 for $\mathrm{Re} = 3.4 \times 10^4$ and the critical Reynolds number for $p/d = 1.2$ is 3.9×10^4.

It is obvious that the results shown in Fig. 9 are different from those in the uniform flow field for $c/d > 0.05$. This difference may be a result of the flow structure, which is rolled up toward the front face of the cylinder by being deflected by the plane wall, despite small pitch ratios such as $p/d = 1.2$. In the range $c/d = 0.18 \sim 1.23$, Nu_m generally increases with decreasing p/d (that is, $\mathrm{Nu}_m \propto (p/d)^{-0.12}$ as shown in Fig. 11).

In order to show the dependency of Nu_m with Re, the results are illustrated in Fig. 10 for $c/d = 0.05$, 0.18, 0.38, and 0.61, respectively. It is found that the trends of Nu_m shown in Fig. 9 do not change for the Reynolds numbers range treated in this study. The results of $c/d = 0.05$ are smaller by about 30 to 45 percent at most than that of the single cylinder in the uniform flow field (as indicated by the dotted line). For $c/d = 0.18$, they are also smaller than those of the dotted line in the range $\mathrm{Re} < 1.4 \times 10^4$, independent of p/d. Also, they become larger than that of the single cylinder for $p/d < 2.8$, when $\mathrm{Re} > 2 \times 10^4$. For both cases of $c/d = 0.38$ and 0.61, Nu_m are not smaller than those of the single cylinder except the case of $p/d = 4.4$, in the range $\mathrm{Re} = 0.8 \times 10^4 \sim 4 \times 10^4$, and the increasing ratios of Nu_m increase with increasing Reynolds number (for $p/d = 1.2$, the values of Nu_m become about 1.5 times those for the single cylinder in the uniform flow field for $\mathrm{Re} = 4 \times 10^4$).

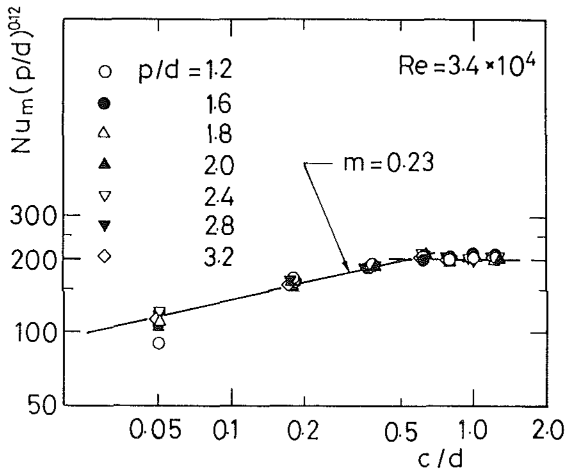

Fig. 11 Correlation of $\mathrm{Nu}_m(p/d)^{0.12}$ with c/d

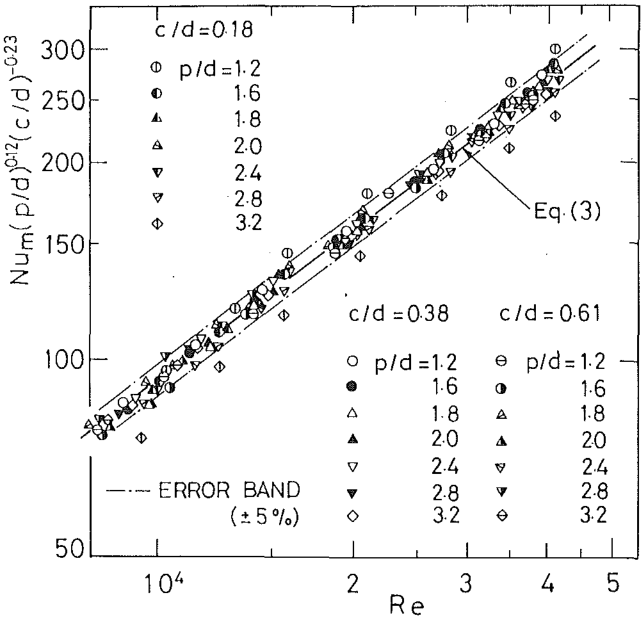

Fig. 12 Mean Nusselt number results

In view of the fact that the average Nusselt numbers are inversely proportional to $(p/d)^{0.12}$, the results of $Nu_m(p/d)^{0.12}$ are demonstrated as a function of c/d in Fig. 11. It appears that the data are better correlated in the ranges $c/d = 0.18 \sim 1.23$ and $p/d = 1.2 \sim 3.2$. In the range of $c/d = 0.18 \sim 0.61$, $Nu_m(p/d)^{0.12}$ increases with increasing c/d and the values are connected in the following relation: $Nu_m(p/d)^{0.12} \propto (c/d)^{0.23}$. As already shown in Fig. 10, the dependency on Nu_m of Re is almost linear.

Considering these facts, the data of $Nu_m(p/d)^{0.12}(c/d)^{-0.23}$ are plotted for those of $c/d = 0.18$, 0.38, and 0.61 as a function of Reynolds number in Fig. 12. The data displayed in this figure are closely correlated against Reynolds number (within a ±5 percent error band) of equation (3), except for $c/d = 0.18$, $p/d = 1.2$ and 3.2. The equation of the fitted line is

$$Nu_m = 0.103(p/d)^{-0.12}(c/d)^{0.23}Re^{0.74} \tag{3}$$

in the ranges $Re = 0.8 \times 10^4 \sim 4 \times 10^4$, $c/d = 0.18 \sim 0.61$, and $p/d = 1.2 \sim 3.2$. However, the data for the cases of $c/d = 0.18$, $p/d = 1.2$ are somewhat larger than the results predicted by equation (3) in the range of $Re > 1.5 \times 10^4$, and the data for the cases of $c/d = 0.18$, $p/d = 3.2$ are lower than those obtained by equation (3) by about $12 \sim 15$ percent independent of Reynolds number. In the cases of $c/d = 0.18$, $p/d \geq 3.2$, the distributions of Nu_θ are similar to that for $c/d = 0.05$, as shown in Fig. 2. That is, it results from the flow stagnation around the cylinder (see Fig. 3 for $c/d = 0.05$). Furthermore, the results of mean Nusselt number Nu_m in the range $0.61 < c/d \leq 1.23$ are relatively independent of c/d, and there exists a correlation such that $Nu_m \propto Re^{0.73}$ (the power of Re is somewhat smaller than that for $c/d \leq 0.61$).

Concluding Remarks

Heat transfer around the third of four cylinders aligned in-line in a crossflow of air near a plane wall have been investigated as a function of c/d, p/d, and Re. When c/d is very small (such as for $c/d = 0.05$), Nu_{max} occurs on the upper surface of the cylinder and Nu_θ around the cylinder is lower than that for $c/d > 0.05$, independent of p/d as a result of the stagnation of the flow around the cylinder. Nu_θ takes maximum values on the lower surface of the cylinder (except the special cases such as $c/d = 0.05$, and $c/d = 0.18$, $p/d = 3.2$) influenced by the free shear layer shed from the second cylinder, which is deflected by the existence of the plane wall. Nu_m increases monotonically with c/d in the range $c/d = 0.05 \sim 0.61$, and changes little with c/d for $c/d > 0.61$ (Fig. 9). Although p/d does not severely affect Nu_m different from c/d, it must be noticed that Nu_m is inversely proportional to p/d, except when $c/d = 0.05$.

A correlation of the overall heat transfer yielded the compact expression $Nu_m = 0.103\,(p/d)^{-0.12}(c/d)^{0.23}Re^{0.74}$, with a spread of ±5 percent in the ranges $c/d = 0.18 \sim 0.61$, $p/d = 1.2 \sim 3.2$, and $Re = 0.8 \times 10^4 \sim 4 \times 10^4$, except the case for $c/d = 0.18$, $p/d = 3.2$. This final correlation will be useful to design the heat exchanger that is of the convective heat transfer type and consists of a single longitudinal row tube bank near a shell wall.

Acknowledgments

The author is grateful to former students Mr. Y. Sasaki and M. T. Ito for their assistance in the experiments.

References

Aiba, S., and Yamazaki, Y., 1976, "An Experimental Investigation of Heat Transfer Around a Tube in a Bank," ASME JOURNAL OF HEAT TRANSFER, Vol. 98, pp. 503-508.

Aiba, S., et al., 1980, "Heat Transfer of Tubes Closely Spaced in an In-Line Bank," *Int. J. Heat Mass Transfer*, Vol. 33, pp. 311-319.

Aiba, S., et al., 1981, "Heat Transfer Around a Tube in a Bank," *Bull. of the JSME*, Vol. 24, No. 188, pp. 380-387.

Aiba, S., et al., 1982, "Heat Transfer Around Tubes in In-Line Tube Banks," *Bull. of the JSME*, Vol. 25, No. 204, pp. 919-926.

Aiba, S., and Tsuchida, H., 1983, "A Criterion for Tube Arrangement and Optimum Tube Spacing in Tube Banks," *Heat Transfer—Japanese Research*, Vol. 12, No. 3, pp. 86-95.

Aiba, S., 1985, "Heat Transfer Around a Circular Cylinder Near a Plane Surface," ASME JOURNAL OF HEAT TRANSFER, Vol. 107, pp. 916-921.

Aiba, S., and Tsuchida, H., 1986, "Heat Transfer Around a Circular Cylinder Near a Plane Boundary," *Heat Transfer—Japanese Research*, Vol. 15, No. 2, pp. 1-25.

Bradbury, L. J. S., 1976, "Measurements With a Pulsed-Wire and a Hot-Wire Anemometer in the Highly Turbulent Wake of a Normal Flat Plate," *J. Fluid Mech.*, Vol. 77, No. 3, pp. 473-497.

Cantwell, B., and Coles, D., 1983, "An Experimental Study of Entrainment and Transport in the Turbulent Near Wake of a Circular Cylinder," *J. Fluid Mech.*, Vol. 136, pp. 321-374.

Eastop, T. D., and Turner, J. R., 1982, "Air Flow Around Three Cylinders at Various Pitch-Diameter Ratios for Both a Longitudinal and Transverse Arrangement," *Trans. IChemE*, Vol. 60, pp. 359-363.

Klebanoff, P. S., 1955, "Characteristics of Turbulence in a Boundary Layer With Zero Pressure Gradient," NACA TR No. 1247.

Kostić, Ž. G., and Oka, S. N., 1972, "Fluid Flow and Heat Transfer With Two Cylinders in Cross-Flow," *Int. J. Heat Mass Transfer*, Vol. 15-2, pp. 278-299.

Schubauer, G. B., and Klebanoff, D. S., 1956, "Contributions on the Mechanism of Boundary Layer Transition," NACA TR No. 1289.

Zdravkovich, M. M., 1977, "Review of Flow Interference Between Two Cylinders in Various Arrangements," ASME *J. Fluids Engng.*, Vol. 99, pp. 618-633.

T.-Y. Wang

C. Kleinstreuer
Mem. ASME

Mechanical and Aerospace
Engineering Department,
North Carolina State University,
Raleigh, NC 27695-7910

Similarity Solution of Combined Convection Heat Transfer From a Rotating Cone or Disk to Non-Newtonian Fluids

A powerful similarity solution of the highly nonlinear, coupled boundary-layer equations has been developed for steady laminar mixed convection heat transfer between a rotating cone/disk and power-law fluids. Of special interest are the effects of the power-law viscosity index, a generalized local Prandtl number, the buoyancy parameter, and the type of thermal wall condition on the velocity and temperature fields and hence the skin friction coefficient and the local Nusselt number. While the momentum boundary-layer thickness increases measurably with decreasing viscosity index n, the thermal boundary-layer thickness is less affected by changes in n. The magnitude and direction of the buoyancy force influence the upward velocity profile near the wall and the temperature profiles significantly. Both Prandtl number and buoyancy parameter have a more pronounced effect on the skin friction group, SFG $\sim c_f$*, than on the heat transfer group, HTG* $\sim$ *Nu.*

Introduction

Convection heat transfer of power-law fluids in rotating systems is important for the thermal design of industrial equipment dealing with molten plastics, polymeric liquids, food stuffs, or slurries. Considering steady laminar flow of a non-Newtonian fluid induced by a rotating heated or cooled cone, the new similarity solution allows an efficient and accurate analysis of the effects of the power-law index, Prandtl number, buoyancy parameter, and the type of thermal wall condition on the velocity and temperature fields and hence on the skin friction coefficient and the Nusselt number.

Simplified forms of the present study have been extensively analyzed in the past. For example, Sparrow and Gregg (1959) obtained a similarity solution over a wide range of Prandtl numbers for a rotating disk. Tien (1960) indicated that the heat transfer results for a rotating disk can also be used for a rotating cone employing boundary-layer approximations. Hartnett and Deland (1961) studied the effects of Prandtl number on heat transfer rates from rotating nonisothermal disks and cones. Hering and Grosh (1963) investigated combined convection from a rotating cone. Oehlbeck and Erian (1979) analyzed heat transfer from axisymmetric heat sources at the surface of a rotating disk. Recently, Himasekhar and Sarma (1986) found a similarity solution for a rotating cone in a stably stratified medium. Lin and Lin (1987) proposed a new similarity variable for the analysis of laminar boundary-layer heat transfer from a rotating cone or disk. For all previous investigations, the fluid considered was Newtonian. The literature on thermal convection of power-law fluids past standard bodies has been reviewed by Shenoy and Mashelkar (1982). Recent contributions dealing with natural convection between power-law fluids and nonrotating bodies have been provided by Shenoy (1983) for a slender vertical cone and by Chang et al. (1988) for two-dimensional or axisymmetric bodies.

In the present analysis, the coupled highly nonlinear boundary-layer equations for combined spin and buoyancy induced flow of a power-law fluid subjected to different thermal boundary conditions have been reduced to ordinary differential equations and then solved with an implicit finite difference scheme.

Analysis

The nonrotating orthogonal coordinate system used is shown in Fig. 1. Assuming steady laminar axisymmetric boundary-layer flow, the velocity and temperature fields are functions of x and y only, and transverse curvature effects can be neglected since $\delta/r \ll 1$. The analysis is valid for cones with a sufficiently large apex half angle. The cone surface is maintained at either a uniform temperature T_w or a uniform heat flux q_w. The actual surface temperature may be above or below T_∞, depending on the operational mode of fluid heating by the cone ($Z=1$) or cooling ($Z=-1$), respectively. Fluid friction, including the no-slip condition, causes a circumferential velocity, w, of fluid elements, which are also subjected to a centrifugal force causing the radial velocity, v. Satisfying mass conservation, outward-moving fluid is being replaced by fluid eventually flowing along the cone surface with velocity u. The buoyancy force will assist the boundary layer flow for a heated surface ($T_w > T_\infty$) and will retard the flow for a cooled cone ($T_w < T_\infty$).

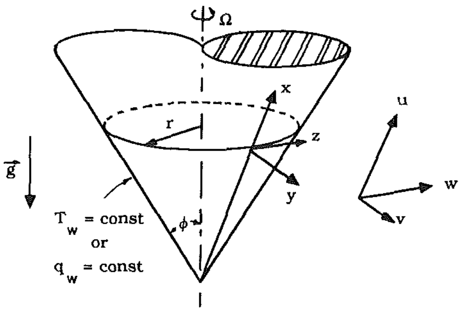

Fig. 1 System schematics with coordinates

Contributed by the Heat Transfer Division for publication in the JOURNAL OF HEAT TRANSFER. Manuscript received by the Heat Transfer Division May 18, 1989; revision received November 27, 1989. Keywords: Mixed Convection, Non-Newtonian Flows and Systems, Rotating Flows.

Neglecting secondary effects, the continuity equation and the boundary-layer equations are

$$\frac{\partial}{\partial x}(ru) + \frac{\partial}{\partial y}(rv) = 0 \tag{1}$$

$$u\frac{\partial u}{\partial x} + v\frac{\partial u}{\partial y} - \frac{w^2}{x} = Zg\beta|T - T_\infty|\cos\phi$$
$$+\frac{K}{\rho}\frac{\partial}{\partial y}\left[\left|\frac{\partial u}{\partial y}\right|^{n-1}\frac{\partial u}{\partial y}\right] \tag{2}$$

$$u\frac{\partial w}{\partial x} + v\frac{\partial w}{\partial y} + \frac{uw}{x} = \frac{K}{\rho}\frac{\partial}{\partial y}\left[\left|\frac{\partial w}{\partial y}\right|^{n-1}\frac{\partial w}{\partial y}\right] \tag{3}$$

and

$$u\frac{\partial T}{\partial x} + v\frac{\partial T}{\partial y} = \alpha\frac{\partial^2 T}{\partial y^2} \tag{4}$$

The boundary conditions are

$$\underline{\text{as } y \to \infty:}\ u = 0, \quad w = 0, \text{ and } T = T_\infty \tag{5a}$$

$$\underline{\text{at } y = 0:}\ u = v = 0, \quad w = r\,\Omega,\ T = T_w = \text{const} \tag{5b}$$

$$\text{or } q_w = -k\frac{\partial T}{\partial y}\bigg|_{y=0} = \text{const}$$

The system equations can be reduced to a set of self-similar equations by using the stream function approach

$$u = \frac{1}{r}\frac{\partial \psi}{\partial y} \text{ and } v = -\frac{1}{r}\frac{\partial \psi}{\partial x} \tag{6a, b}$$

and the transformations (cf. Kleinstreuer, 1990)

$$\eta = \frac{y}{x}\,\mathrm{Re}^{1/(n+1)} \tag{7}$$

$$\psi = r^2 x\,\Omega \mathrm{Re}^{-1/(n+1)} F(\eta) \tag{8}$$

$$u = (r\,\Omega)F'(\eta) \tag{9a}$$

$$v = -(r\,\Omega)\mathrm{Re}^{-1/(n+1)}\left(\frac{3n+1}{n+1}\right)F(\eta)$$
$$+(r\,\Omega)\frac{y}{x}\left(\frac{n-1}{n+1}\right)F'(\eta) \tag{9b}$$

$$w = r\,\Omega G(\eta) \tag{9c}$$

and

$$\theta(\eta) = \begin{cases} (T - T_\infty)/(T_w - T_\infty) & \text{for UWT case} \quad (10a) \\ (T - T_\infty)/[q_w x/(k\mathrm{Re}^{1/(n+1)})] & \text{for UHF case} \quad (10b) \end{cases}$$

where Re is the generalized local Reynolds number, defined as

$$\mathrm{Re} = \rho(r\,\Omega)^{2-n}x^n/K \tag{11}$$

UWT denotes uniform wall temperature and UHF means uniform heat flux.

As a result, the continuity equation is automatically satisfied, and the momentum equations and energy equation are transformed to

$$(|F''|^{n-1}F'')' + \left(3 - \frac{2}{n+1}\right)FF'' - F'^2 + G^2 + Z\lambda\theta = 0 \tag{12}$$

$$(|G'|^{n-1}G')' + \left(3 - \frac{2}{n+1}\right)FG' - 2F'G = 0 \tag{13}$$

and

$$\frac{\theta''}{\mathrm{Pr}} + \left(3 - \frac{2}{n+1}\right)F\theta' - aF'\theta = 0 \tag{14}$$

where Pr is a generalized Prandtl number, i.e.,

$$\mathrm{Pr} = \mathrm{Pr}(x) = x^2\Omega\sin\phi/(\alpha\mathrm{Re}^{2/(n+1)}) \tag{15a}$$

which is a function of fluid properties, body spin, and geometric parameters. An alternative form of Pr(x), which reduces directly to the Newtonian Prandtl number for $n = 1$, is

$$\mathrm{Pr}(x) = [(K/\rho)^{2/(n+1)}(r\,\Omega)^{3(n-1)/(n+1)}x^{(1-n)/(n+1)}]/\alpha \tag{15b}$$

However, the nonrotating cone case, $\Omega = 0$, is excluded here (cf. Shenoy, 1983).

The buoyancy parameter λ is defined for

(*i*) *UWT case:*

$$\lambda = \lambda_T = \mathrm{Gr}/\mathrm{Re}^{2/(2-n)} \tag{16a}$$

where

$$\mathrm{Gr} = \left(\frac{K}{\rho}\right)^{2/(n-2)} g\beta|T_w - T_\infty|x^{(2+n)/(2-n)}\cos\phi \tag{16b}$$

and

(*ii*) *UHF case:*

$$\lambda = \lambda_q = \mathrm{Gr}^*/\mathrm{Re}^{(n+4)/[(n+1)(2-n)]} \tag{17a}$$

where

$$\mathrm{Gr}^* = \left(\frac{K}{\rho}\right)^{2/(n-2)} g\beta|q_w/k|x^{4/(2-n)}\cos\phi \tag{17b}$$

Nomenclature

c_f = local skin friction coefficient
F = dimensionless stream function
Gr = generalized Grashof number (T_w = const)
Gr* = generalized Grashof number (q_w = const)
G = dimensionless velocity
g = gravitational acceleration
h = local heat transfer coefficient
K = fluid consistency index for power-law fluid
k = thermal conductivity
Nu = local Nusselt number
n = power-law viscosity index
Pr = generalized Prandtl number
Re = generalized Reynolds number
r = distance from axis of cone to the surface
T = temperature
U = reference velocity
u = velocity component in x direction
v = velocity component in y direction
w = velocity component in z direction
x = streamwise coordinate
y = coordinate normal to the surface
Z = dimensionless parameter; Z = 1 for heated and Z = − 1 for cooled submerged cone
z = tangential coordinate
α = thermal diffusivity
β = thermal expansion coefficient
θ = dimensionless temperature
θ^* = dimensionless temperature
λ = buoyancy parameter
ρ = density of fluid
τ = shear stress
ϕ = cone apex half-angle
ψ = stream function
Ω = angular velocity

Subscripts

∞ = ambient condition
e = boundary layer edge condition
q = uniform wall heat flux case
T = uniform surface temperature case
w = wall condition

Table 1 Comparison of $Nu/Re^{1/(n+1)}$ for an isothermal rotating disk in a Newtonian fluid; $n=1$, $Z=1$, $\lambda_T=0$

Pr	Present Method	Sparrow & Gregg (1959)	Hartnett & Deland (1961)	Oehlbeck & Erian (1979)	Lin & Lin (1987)
0.01	0.8718(-2)*	0.871(-2)*	—	0.870 (-2)*	0.8708(-2)*
0.1	0.7667(-1)*	0.766(-1)*	0.766(-1)*	0.763(-1)*	0.7659(-1)*
0.72	0.3286	—	0.330	0.341	0.3286
1	0.3962	0.396	0.396	0.394	0.3963
10	1.1335	1.134	1.13	1.131	1.1341
100	2.6865	2.687	2.69	2.684	2.6872
1000	6.0097	—	—	6.002	6.0163

* $(-m) \doteq 10^{-m}$

Table 2 Comparison of the heat transfer results for the Newtonian fluid case; $n=1$, $\lambda=0$

	$-\theta^*(0)'$ $(T_w = const)^+$		$1/\theta^*(0)$ $(q_w = const)^+$	
Pr	Lin & Lin (1987)	Present Method	Lin & Lin (1987)	Present Method
0.01	0.87658	0.87603	0.87658	0.87643
0.1	0.81614	0.81699	0.81613	0.81609
0.72	0.65512	0.65512	0.65514	0.65512
1	0.62902	0.62894	0.62901	0.62898
10	0.56095	0.56066	0.56095	0.56086
100	0.58240	0.58240	0.58278	0.58264
1000	0.60203	0.60139	0.60201	0.60187

+ NOTE:
for $T_w = \text{const}$, $-\theta^{*\prime}(0) = -\theta'(0)\frac{(1+Pr)^{2/3}}{Pr}$
and for $q_w = \text{const}$, $1/\theta^*(0) = [1/\theta(0)]\frac{(1+Pr)^{2/3}}{Pr}$

and

$$a = \begin{cases} 0 & \text{for UWT case} \quad (18a) \\ \dfrac{n-1}{n+1} & \text{for UHF case} \quad (18b) \end{cases}$$

With the definition of the local skin friction coefficient

$$c_f = \tau_w \Big/ \left(\frac{1}{2}\rho U^2\right) \tag{19a}$$

where U is the reference velocity, defined as

$$U = r\,\Omega \tag{19b}$$

A dimensionless skin friction group, SFG, can be formed as

$$\text{SFG} = \frac{1}{2}\, c_f \text{Re}^{1/(n+1)} = [F''(o)]^n \tag{20}$$

Similarly, with the local Nusselt number defined as

$$\text{Nu} = hx/k \tag{21}$$

a dimensionless heat transfer group, HTG, can be formed, i.e.,

$$\text{HTG} = \text{Nu}/\text{Re}^{1/(n+1)} = \begin{cases} -\theta'(0) & \text{for UWT case} \quad (22a) \\ 1/\theta(0) & \text{for UHF case} \quad (22b) \end{cases}$$

Numerical Solution

A two-point finite difference technique (cf. Keller's box method discussed by Cebeci and Bradshaw, 1977) with Newton's linearization method has been used to solve the similarity equations and associated boundary conditions. A mesh of variable density is needed in order to accommodate steep velocity and temperature gradients near the cone surface. The location

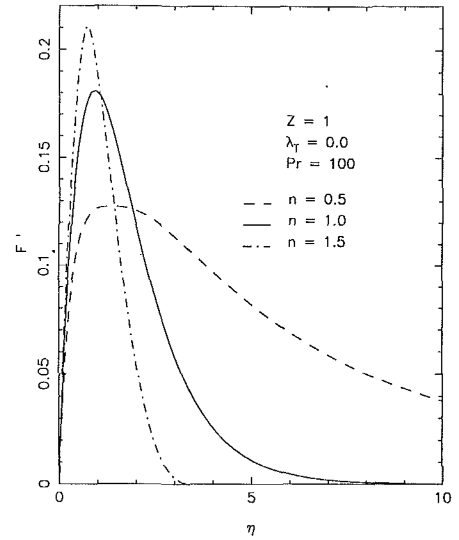

Fig. 2 Effect of power-law viscosity index on dimensionless velocity profiles (*x* component)

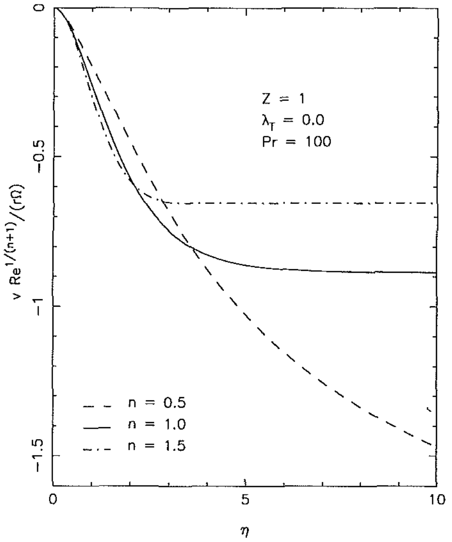

Fig. 3 Effect of power-law viscosity index on dimensionless velocity profiles (*y* component)

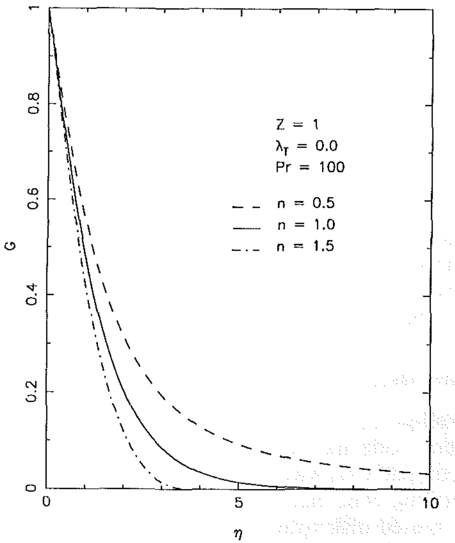

Fig. 4 Effect of power-law viscosity index on dimensionless velocity profiles (*z* component)

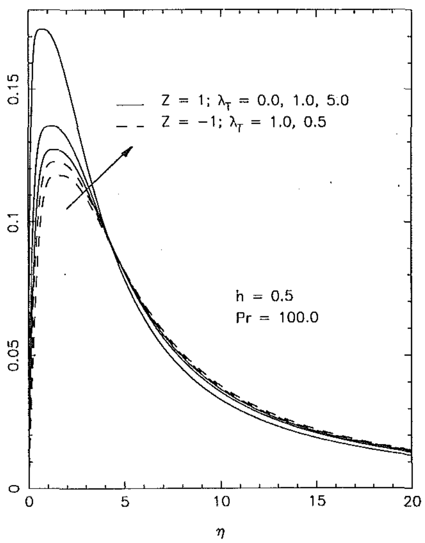

Fig. 5 Effect of buoyancy parameter on dimensionless velocity profiles (*x* component)

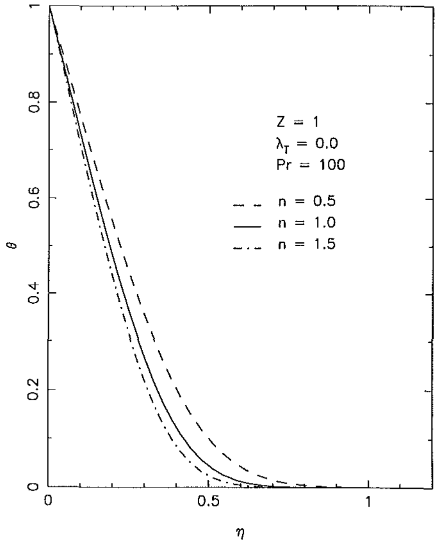

Fig. 6 Effect of power-law viscosity index on dimensionless temperature profiles for isothermal wall case

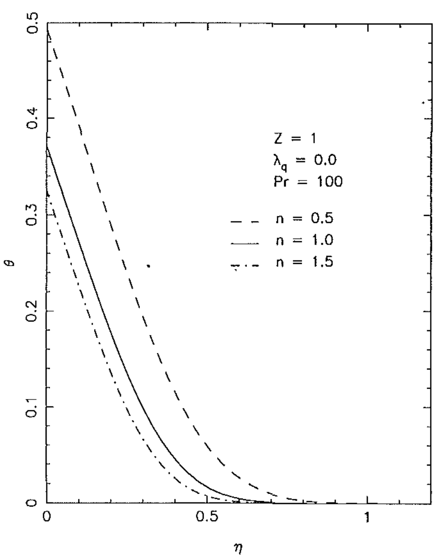

Fig. 7 Effect of power-law viscosity index on dimensionless temperature profiles for constant wall heat flux case

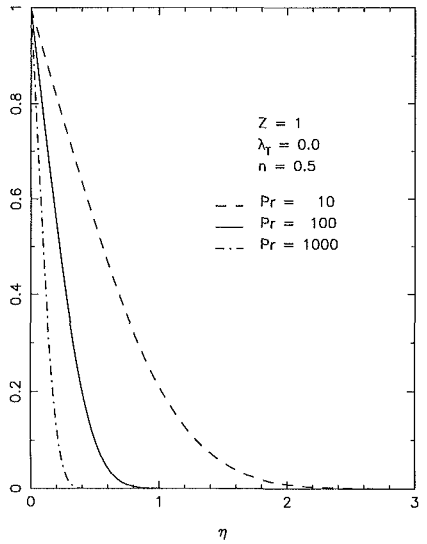

Fig. 8 Effect of Prandtl number on dimensionless temperature profiles for isothermal wall case

of the boundary-layer edge, η_e, is strongly dependent on the generalized local Prandtl number, Pr(x), and the power-law viscosity index, n. For example, $\eta_e(\mathrm{Pr}=1.0,\ n=1.5)\approx 6$ but η_e $(\mathrm{Pr}=1000,\ n=0.5)\approx 150$. For a typical value of $\eta_e=30$, about 100 grid points have been necessary. The independence of the results from the mesh density has been successfully checked by repeat calculations with finer meshes. The program of 530 lines is in double precision and runs 15 seconds on a VAX 11/785. The accuracy of the computer simulation model when compared with established special case studies is discussed in the next section.

Results and Discussion

Model Validation. The accuracy of the predictive results of the present model has been established for Newtonian fluids ($n=1$) by comparisons with the rotating-disk case ($\phi=90$ deg) and the rotating-cone case. Table 1 lists HTG values for an isothermal heated disk rotating in a Newtonian fluid without buoyancy effects. Table 2 compares heat transfer data on isothermal and constant wall heat flux cones rotating in a Newtonian fluid without buoyancy effects. In all cases, the data sets match very well.

Velocity and Temperature Profiles. Representative velocity profiles and temperature distributions as a function of $\eta=y/f(x)$ are shown in Figs. 2-10, exhibiting the effects of the flow index n, the generalized local Prandtl number Pr(x), the heating/cooling mode Z, the buoyancy parameter λ, and the type of thermal boundary condition T_w = const or q_w = const.

Figures 2-4 depict the dimensionless upward flow velocity $u(x)$, the circumferential velocity $w(z)$, and the normal velocity component $v(y)$ for a shear-thinning fluid ($n<1.0$), Newtonian fluids ($n=1.0$), and a shear-thickening fluid ($n>1.0$). The power-law index has a profound effect on the boundary layer thicknesses or radii of influence due to the cone rotation. The velocity normal to the cone surface is negative because upward-moving fluid is being replaced by fluid from the infinite reservoir (cf. Fig. 3). In general, the peak circumferential velocity has the largest values when compared with peak magnitudes of the upward and the radial velocities. For example, for $n=0.5$ and Re = 1000, one obtains $w_{\max}$: $u_{\max}$:

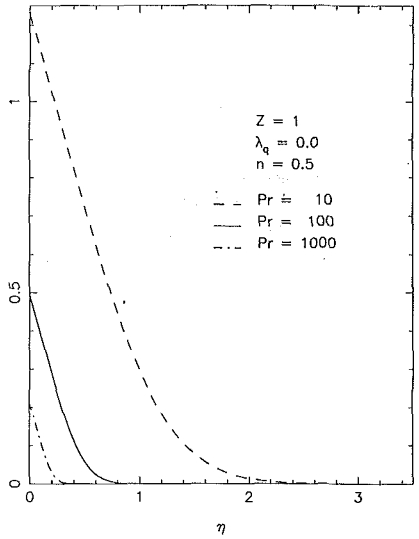

Fig. 9 Effect of Prandtl number on dimensionless temperature profiles for constant wall heat flux case

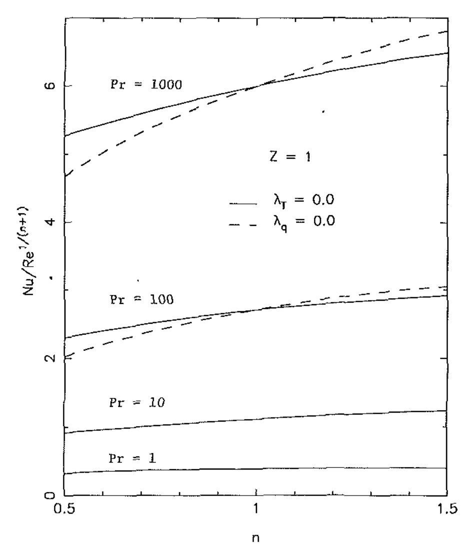

Fig. 11 Heat transfer group as a function of flow index for isothermal wall and constant wall heat flux cases

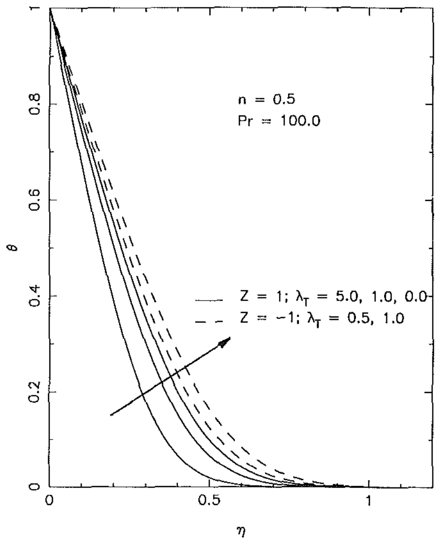

Fig. 10 Effect of buoyancy parameter on dimensionless temperature profiles in heating and cooling mode

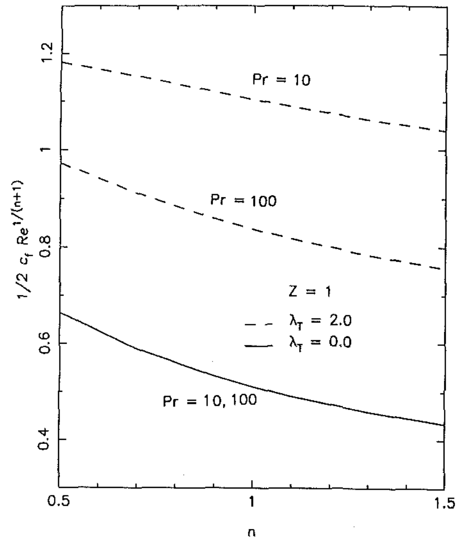

Fig. 12 Effects of buoyancy force and Prandtl number on skin friction group as a function of power-law viscosity index

$|v|_{\max}=1$: 0.13: 0.02 and for $n=1.5$ and Re = 1000, $w_{\max}$: $u_{\max}$: $|v|_{\max}=1$: 0.21: 0.04. Selecting a pseudoplastic ($n=0.5$, with Pr = 100), the effect of heating/cooling mode and buoyancy parameter on the upward velocity is shown in Fig. 5. While $w(z)$, being perpendicular to the buoyancy force, is basically unaffected by changes in Z and λ_T, the upward flow velocity $u(x)$ increases near the cone surface with the aiding buoyancy ($Z=1$ and λ_T increasing) and is reduced because of the retarding buoyancy effect, i.e., when $Z=-1$ and λ_T is increasing.

Complementary to the previous five figures, Figs. 6–10 depict the effects of (the) system parameters on the temperature distribution near the wall. Figures 6 and 7 show the difference in $\theta(\eta)$ resulting from the two different thermal wall conditions for three power-law fluids. The impact of the flow index n is more visible for the uniform wall heat flux case when compared with the isothermal wall case. The thermal boundary-layer thickness is strongly affected by the generalized Prandtl number (Figs. 8 and 9). As expected, the thermal thickness decreases with increasing Prandtl number and as a result, heat transfer is enhanced. Figure 10 shows the flow-aiding and flow-retarding effects of the buoyancy force on the temperature distribution for a pseudoplastic ($n=0.5$, with Pr = 100) near a rotating isothermal cone.

Heat Transfer Group and Skin Friction Group. The variations in HTG = $Nu/Re^{1/(n+1)}$ can be directly deduced from the previous temperature profiles since HTG ~ θ_w^{-1} for the constant wall heat flux case. Specifically, HTG increases with increasing Prandtl number for all power-law fluids. Shear-thickening fluids, because of thinner boundary layers, generate higher HTG numbers than shear-thinning fluids (cf. Fig. 11). The skin friction group SFG ~ τ_w directly reflects the velocity gradient at the cone surface, i.e., SFG = $[F''(0)]^n$. The buoyancy force affects SFG quite strongly, especially for problems with relatively low generalized Prandtl number fluids (Fig. 12). The opposite is the case for HTG(Pr) when buoyancy-assisted flow produces enhanced heat transfer due to steeper fluid temperature gradients at the isothermal cone surface (Fig. 13). Measurable buoyancy effects, i.e., a 10 percent change in HTG or SFG values, come into play when $(\lambda_T)_{\min}=0.83$ for com-

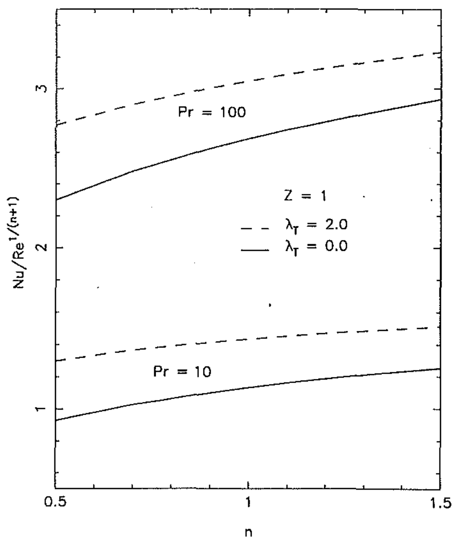

Fig. 13 Effects of buoyancy force and Prandtl number of heat transfer group as a function of power-law viscosity index

puting HTG(n), assuming Pr = 100. These threshold values decrease when the Prandtl number decreases.

Conclusions

A powerful similarity analysis of steady laminar mixed convection heat transfer between a rotating cone and power-law fluids has been presented. The coupled nonlinear boundary-layer equations have been uniquely transformed and the resulting ordinary differential equations have been accurately solved using Keller's box method (cf. Cebeci and Bradshaw, 1977).

While the momentum boundary-layer thickness increases measurably with decreasing fluid flow index n, the thermal boundary-layer thickness is less affected by changes in n. The magnitude and direction of the buoyancy force influence the upward velocity profile near the wall and the temperature profiles significantly. Thus the validated computer simulation model can be used to calculate the velocity and thermal region of influence as a function of thermal wall condition, power-law viscosity index, fluid Prandtl numbers, and buoyancy parameter.

The heat transfer group HTG is, for all generalized Prandtl numbers, consistently lower for shear-thinning fluids ($n < 1.0$) when compared with shear-thickening fluids ($n > 1.0$). The skin friction group, on the contrary, is higher for all Prandtl numbers for pseudoplastics when compared with dilatant fluids. Both Prandtl number and buoyancy parameter have a more pronounced effect on SFG than on HTG: threshold values for the buoyancy parameter, e.g., $(\lambda_T)_{\min}$, increase with increasing Prandtl numbers. The type of thermal boundary condition applied, i.e., T_w = const versus q_w = const, influences the temperature profiles noticeably and generates slightly higher HTG (n) values for the isothermal surface case.

The portable computer simulation model, which runs on minicomputers or scientific workstations, could be used in design applications such as the evaluation of torque and hence power requirements for a given polymer and suitable heat transfer conditions for polymer processing.

Acknowledgments

The authors wish to acknowledge the valuable comments and suggestions made by Prof. P. Mitschka, Institute of Chemical Process Fundamentals, CAS, Prague and the ASME HTD reviewers.

References

Cebeci, T., and Bradshaw, P., 1977, *Momentum Transfer in Boundary Layers*, Hemisphere, Washington, DC.

Chang, T.-Ch. A., Jeng, D. R., and DeWitt, K. J., 1988, "Natural Convection to Power-Law Fluids for Two-Dimensional and Axisymmetric Bodies," *Int. J. Heat Mass Transfer*, Vol. 31, pp. 615–621.

Hartnett, J. P., and Deland, E. C., 1961, "The Influence of Prandlt Number on the Heat Transfer From Rotating Nonisothermal Disks and Cones," ASME JOURNAL OF HEAT TRANSFER, Vol. 83, pp. 95–96.

Hering, R. G., and Grosh, R. J., 1963, "Laminar Combined Convection From a Rotating Cone," ASME JOURNAL OF HEAT TRANSFER, Vol. 85, pp. 29–34.

Himasekhar, K., and Sarma, P. K., 1986, "Laminar Combined Convection From a Rotating Cone to a Thermally Stratified Environment," ASME JOURNAL OF HEAT TRANSFER, Vol. 108, pp. 973–976.

Kleinstreuer, C., 1990, *Engineering Fluid Dynamics—An Interdisciplinary Systems Approach*, in preparation.

Lin, H. T., and Lin, L. K., 1987, "Heat Transfer From a Rotating Cone or Disk to Fluids of Any Prandtl Number," *Int. Comm. Heat Mass Transfer*, Vol. 14, pp. 323–332.

Oehlbeck, D. L., and Erian, F. F., 1979, "Heat Transfer From Axisymmetric Sources at the Surface of a Rotating Disk," *Int. J. Heat Mass Transfer*, Vol. 22, pp. 601–610.

Shenoy, A. V., and Mashelkar, R. A., 1982, "Thermal Convection in Non-Newtonian Fluids," *Adv. Heat Trans.*, Vol. 15, pp. 143–225.

Shenoy, A. V., 1983, "Natural Convection From a Slender Vertical Cone to a Power-Law Fluid," *Can. J. Chem. Eng.*, Vol. 61, pp. 896–902.

Sparrow, E. M., and Gregg, J. L., 1959, "Heat Transfer From a Rotating Disk to Fluids of any Prandtl Number," ASME JOURNAL OF HEAT TRANSFER, Vol. 81, pp. 249–251.

Tien, C. L., 1960, "Heat Transfer by Laminar Flow From a Rotating Cone," ASME JOURNAL OF HEAT TRANSFER, Vol. 82, pp. 252–253.

A. Shabbir
Visiting Assistant Professor.

D. B. Taulbee
Professor.
Mem. ASME

Department of Mechanical
and Aerospace Engineering,
University at Buffalo, SUNY
Amherst, NY 14260

Evaluation of Turbulence Models for Predicting Buoyant Flows

Experimental data for the buoyant axisymmetric plume are used to validate certain closure hypotheses employed in turbulence model equations for calculating buoyant flows. Closure formulations for the turbulent transport of momentum, thermal energy, kinetic energy, and squared temperature used in the k-ε and algebraic stress models are investigated. Experimental data for the mean velocity, mean temperature, and kinetic energy are used in the closure formulation to obtain Reynolds stresses, heat fluxes, etc., which are then compared with their measured values.

1 Introduction

Various turbulence models have been formulated for predicting buoyancy-driven flows. Some of the parameters in these models have been determined by keying the solution of the model equations to experimental data for certain basic flows such as decay of grid turbulence. Other parameters have been determined by calibrating closure formulations directly with experimental data. However, this approach may be somewhat inaccurate due to the lack of quality experimental data for certain correlations, especially dissipation. Finally, certain model parameters have been fine tuned or determined by requiring that the computed solution agree with experimental data for more complex flows, such as shear flows. In addition there have been instances where model parameters have been adjusted or empirical corrective terms added so that agreement with experimental data is accomplished for a particular flow. When model parameters are adjusted to get agreement, say for the mean velocity and temperature fields for a particular flow, little regard is given for the internal integrity of the model. In other words, are the various processes such as diffusional transport, pressure-strain interactions, etc., predicted correctly? Or are there compensating assumptions where one process is overpredicted at the expense of another and yet the end predicted result for the mean flow agrees with experiment? The lack of complete sets of data for higher moments, dissipation, and pressure-velocity correlations for various flows has prevented detailed verification of closure models for the various processes that have to be modeled.

The objective of this paper is to use the recently obtained and comprehensive experimental data of Shabbir and George (1987) and Shabbir (1987) on the axisymmetric buoyant plume to assess the various closure relations proposed for the kinetic-energy/dissipation and the algebraic stress models for buoyancy-dominated flows. The usual approach is to solve the modeled differential equations numerically, and then compare the computations with the experiment. However, this method does not help pinpoint the drawbacks in the various terms of the models. In this paper, instead of the usual approach, correlations obtained from measured velocity and temperature are used directly to verify the closure hypotheses for the turbulent transport of momentum, thermal energy, and turbulent kinetic energy.

2 Experimental Data

The data used were taken in an axisymmetric buoyant plume by Shabbir and George (1987) and Shabbir (1987), who measured velocity and temperature fields at several vertical levels above a heated source of air. Here we briefly summarize their experimental technique and results.

The three-wire probe used consisted of a cross-wire and a temperature wire. Thus the instantaneous values of the two velocity components (vertical and radial) and temperature were measured. The axisymmetry of the flow was established by using an array of 16 thermocouples and also by rotating the cross-wire by 90 deg. Profiles for the correlations between the velocity components and velocity components with temperature through the fourth order were determined from the instantaneous measurements.

Source conditions were continuously monitored in order to calculate the rate at which buoyancy was added at the source. The source Grashof number was 5.5. By integrating the mean energy equation, an integral constraint can be obtained for a buoyant plume. For a neutral environment this constraint implies that the rate at which buoyancy crosses each horizontal section is constant and must equal the rate at which buoyancy is added at the source, i.e., the ratio

$$\frac{F}{F_o} = \frac{1}{F_o}\left[2\pi\int_0^\infty g\beta(U\Delta T+\overline{ut})rdr\right] \tag{1}$$

must be unity (F_o is the source buoyancy). This integral constraint was satisfied within 7 percent.

The correlation profiles at various heights were found to be similar in the coordinate $\eta = r/z$ (z accounted for the virtual origin) when the velocity is scaled by $U_s\ F_o^{1/3}z^{-1/3}$ and the temperature is scaled by $T_s = F_0^{2/3}z^{-5/3}/g\beta$. The measurements agreed well with the earlier study by George et al. (1977), who measured only the temperature and the vertical component of velocity. The scatter in the measurements of higher moments is typical for such flows and is also present in previous experiments, such as those of George et al. (1977). The primary reason for the scatter is that slow time scales of the flow require much longer averaging time for the higher moments in order to obtain the same statistical convergence as for the mean quantities. Other errors in the measurements arise from the flow reversal on the hot wire—a phenomenon most likely to occur toward the outer edges of the flow where local turbulent intensities are considerably higher. These are discussed in Shabbir and George (1987).

The various correlations in similarity variables were fitted with curves using a least-squares fitting procedure. This representation allows easy evaluation of the terms in the governing equations and closure formulations when they are cast in similarity variables. Using these profiles the balances for the mean momentum and energy differential equations were carried out to check whether the flow satisfied the equations of motion it is supposed to represent. Within the thin shear layer and the Boussinesq assumption the mean momentum and energy equa-

---

Contributed by the Heat Transfer Division and presented at the National Heat Transfer Conference, Pittsburgh, Pennsylvania, August 9-12, 1987. Manuscript received by the Heat Transfer Division March 3, 1988; revision received November 10, 1989. Keywords: Modeling and Scaling, Plumes, Turbulence.

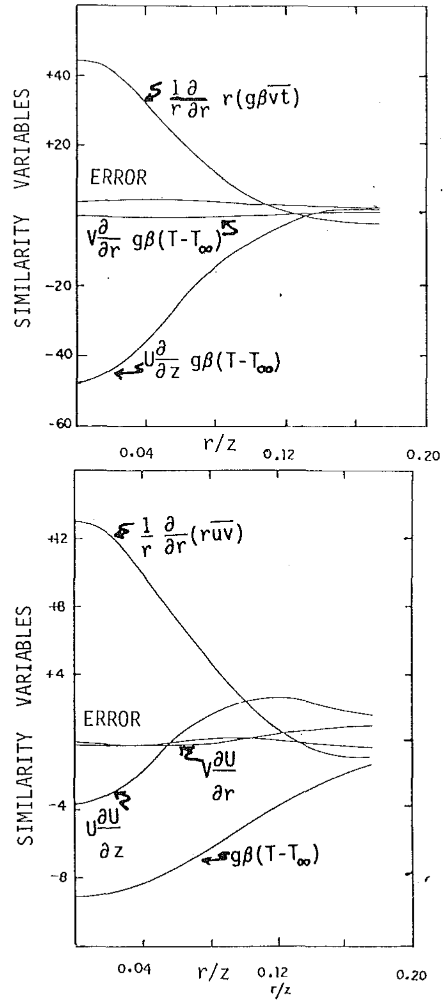

Fig. 1(*a*) Balances of mean energy and momentum equations (taken from Shabbir and George, 1987)

tions can be respectively written as

$$U\frac{\partial U}{\partial z} + V\frac{\partial U}{\partial r} = -\frac{1}{r}\frac{\partial}{\partial r}(r\overline{uv}) - g\beta\Delta T \qquad (2)$$

$$U\frac{\partial \Delta T}{\partial z} + V\frac{\partial \Delta T}{\partial r} = -\frac{1}{r}\frac{\partial}{\partial r}(r\overline{vt}) \qquad (3)$$

Since all the quantities appearing in these equations are measured, their profiles were substituted to see whether the measurements balance the equations. Figure 1(*a*), taken from Shabbir and George (1987), shows that the experiment satisfies this nontrivial test within 10 percent. An error of such magnitude is typical of turbulent shear flows.

The dissipation of mechanical energy was determined by balancing the turbulent energy equation

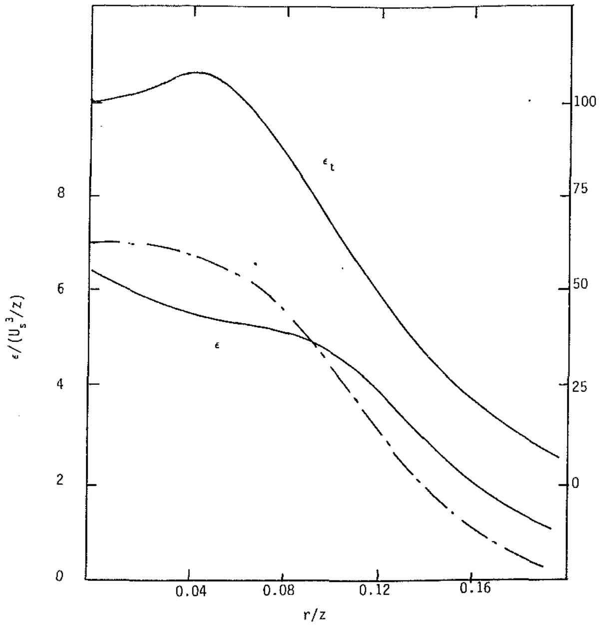

Fig. 1(*b*) Mechanical and thermal dissipation profiles! Full lines are experimental; the chained line is from model equation (10), which was solved for ϵ with all other quantities taken from experiment.

$$U_j\frac{\partial k}{\partial x_j} = -\frac{\partial}{\partial x_j}\left(\frac{1}{2}\overline{q^2u_j} + \frac{1}{\rho}\overline{pu_j}\right) + P + G - \epsilon \qquad (4)$$

where $P = -\overline{u_iu_j}\,\partial U_i/\partial x_j$ is the mechanical production and $G = -\beta g_i\overline{u_it}$ is the production due to buoyancy. Each term except for the dissipation ϵ and the pressure transport $\overline{pu_i}$ is determined from the experimentally determined correlations. The pressure transport was evaluated from $\overline{pu_j}/\rho = -\overline{q^2u_j}/5$, a formula given by Lumley (1978). Although this closure relation has not been verified experimentally, it was felt that since the pressure transport is significant, some correction should be included rather than simply neglecting it, as is often done. The dissipation determined from the balance of the turbulent kinetic energy equation is shown in Fig. 1(*a*) as a solid line.

By a similar procedure the dissipation of the mean-square temperature $\overline{t^2}$ is determined from

$$U_j\frac{\partial \overline{t^2}}{\partial x_j} = -\frac{\partial}{\partial x_j}\overline{u_jt^2} - 2\,\overline{u_jt}\,\frac{\partial T}{\partial x_j} - 2\epsilon_t \qquad (5)$$

All terms are evaluated from experimental data and the resulting thermal dissipation is shown in Fig. 1(*b*).

The time scales $\overline{q^2}/\epsilon$ and $\overline{t^2}/\epsilon_t$ for the relaxation of the mechanical and thermal dissipation, respectively, are shown in Fig. 2, along with their ratio

$$R = (\overline{t^2}/\epsilon_t)/(\overline{q^2}/\epsilon) \qquad (6)$$

Nomenclature

F_o = buoyancy flux, equation (1)
g = acceleration due to gravity
G = turbulence production from buoyancy
k = turbulent kinetic energy
p = fluctuating pressure
P = turbulence production by mean flow
Pr_T = turbulent Prandtl number
r = radial coordinate
R = time scale ratio, equation (4)
t = fluctuating temperature
T = mean temperature
u = fluctuating axial velocity component
U = mean axial velocity component
v = fluctuating radial velocity component
z = vertical coordinate
β = coefficient of thermal expansion
ϵ = dissipation of mechanical energy
ϵ_t = dissipation of mean-square temperature
ν_T = turbulent eddy viscosity
ρ = mean density

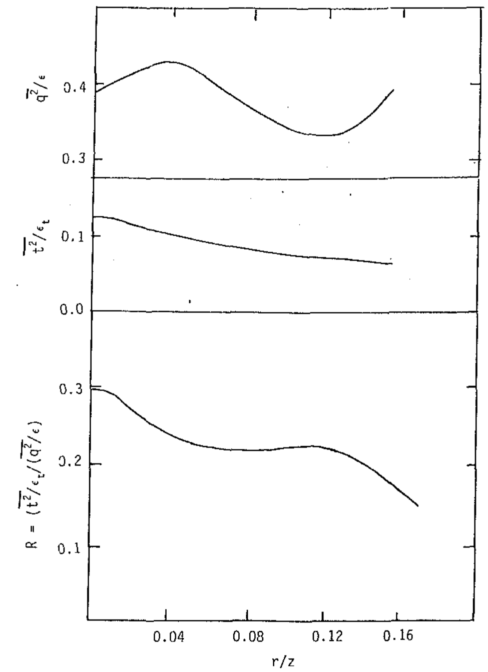

Fig. 2 Mechanical and thermal time scale ratios and variation of *R* as calculated from experimental data

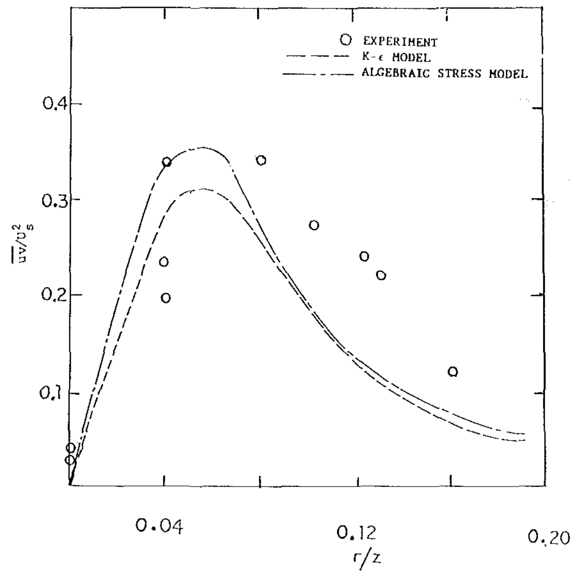

Fig. 3 Shear stress

These time scales appear extensively throughout the model formulations and will be further discussed in the next sections.

3 Assessment of Closure Hypotheses of k-ε Model

The form of the k-ϵ model, which is considered to be the standard one, is that used by Launder and Spalding (1974). In this model the Reynolds stress is given by

$$-\overline{u_i u_j} = \nu_T \left(\frac{\partial U_i}{\partial x_j} + \frac{\partial U_j}{\partial x_i} \right) - \frac{2}{3} k \delta_{ij} \tag{7}$$

and the heat flux by

$$-\overline{u_i t} = \frac{\nu_T}{\mathrm{Pr}_T} \frac{\partial T}{\partial x_i} \tag{8}$$

where $\nu_T = C_\mu k^2/\epsilon$ and $C_\mu = 0.09$ (see Launder and Spalding, 1974).

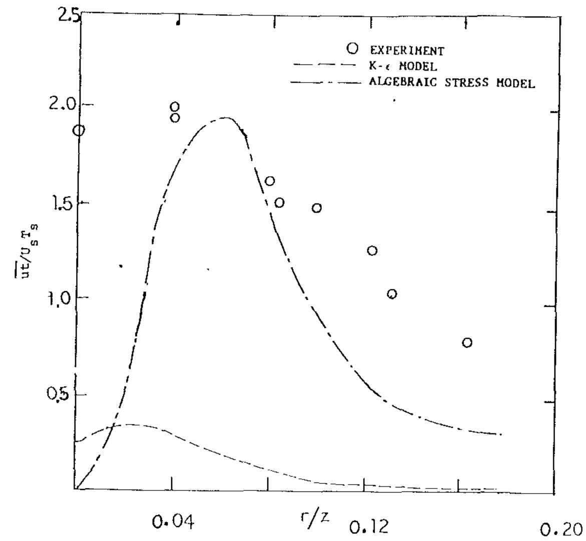

Fig. 4 Axial heat flux

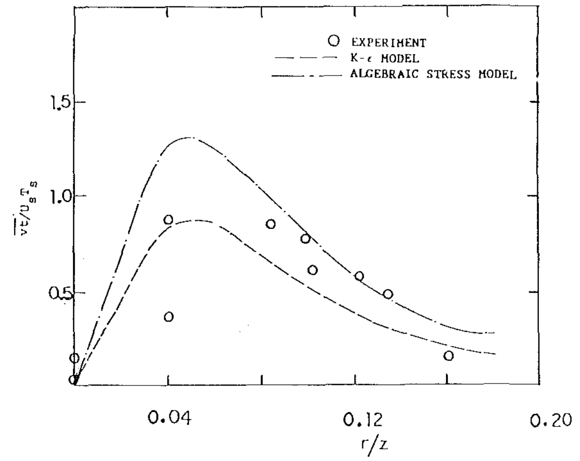

Fig. 5 Radial heat flux

By invoking the thin shear layer assumption for a buoyant plume, the above relations reduce to

$$\overline{uv} = -\nu_T \frac{\partial U}{\partial r}$$

$$\overline{ut} = -(\nu_T/\mathrm{Pr}_T) \frac{\partial T}{\partial z}$$

$$\overline{vt} = -(\nu_T/\mathrm{Pr}_T) \frac{\partial T}{\partial r}$$

Taking $\mathrm{Pr}_T = 1.0$, the right-hand sides of the above equations were evaluated experimentally. These are compared with measured values of $\overline{uv}$, $\overline{ut}$, and $\overline{vt}$ in Figs. 3-5. The points are experimental values and the chain lines are from the model.

The modeled values of $\overline{uv}$ and $\overline{vt}$ compare reasonably with the experimental profiles except in the outer portion of the curves. On the other hand the modeled profile of vertical heat flux $\overline{ut}$ is much smaller than the experimental one. It is well known that the simple gradient models given by equations (7) and (8) with an isotropic eddy viscosity are inadequate for determining streamwise turbulent momentum and heat fluxes. Usually these quantities do not influence the prediction for shear layers since only the radial fluxes are important in these flows. However, in the case of the buoyant plume the flux $\overline{ut}$ is a dominant production term in the turbulent kinetic energy

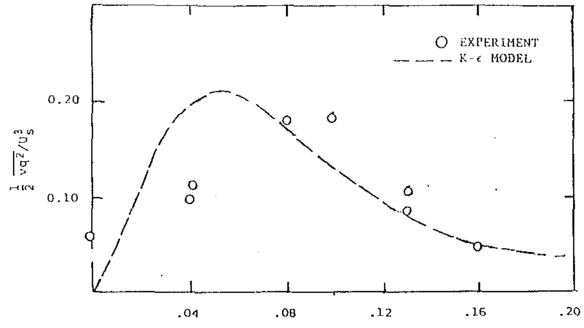

Fig. 6 Transport of kinetic energy

equation and its correct calculation is very important for accurate prediction of k.

The diffusional transport in the kinetic energy equation (4) for a thin shear layer is modeled as

$$\frac{1}{2}\overline{vq^2}+\frac{1}{\rho}\overline{pv}=-\nu_T\frac{\partial k}{\partial r} \tag{9}$$

Using $\overline{pv}/\rho = -\overline{vq^2}/5$ from Lumley (1978) gives $\overline{vq^2}/2 = -(5/3)\nu_T\partial k/\partial r$ from which the result, with the right side evaluated from experimental results, is shown in Fig. 6. It is seen that the predicted and experimental data peak at different radial locations; however, the predicted magnitude is more accurate, which indicates that the pressure diffusion needed to be taken into account.

In the k-ϵ model the dissipation is calculated from

$$U_j\frac{\partial\epsilon}{\partial x_j}=-\frac{\partial}{\partial x_j}\overline{\epsilon' u_j}+C_{\epsilon 1}\frac{\epsilon}{k}(P+G)-C_{\epsilon 2}\frac{\epsilon^2}{k} \tag{10}$$

where $\overline{\epsilon' u_j} = -(\nu_T/\sigma_\epsilon)\partial\epsilon/\partial x_j$ and $\sigma_\epsilon = 1.3$, $C_{\epsilon 1} = 1.44$, and $C_{\epsilon 3} = 1.92$ as given by Launder and Spalding (1974). In order to get an indication of the validity of equation (10), it was numerically solved for the dissipation ϵ with all other quantities needed to evaluate the coefficients determined from the experimental correlations. The result is shown in Fig. 1(*b*) and it is seen that it compares reasonably well with the curve obtained from balancing the turbulent kinetic energy equation with experimental data.

Launder et al. (1972) showed that the standard k-ϵ model yields a solution for the axisymmetric jet that overpredicts the spreading rate by about 30 percent. The standard k-ϵ model also does not correctly predict the axisymmetric buoyant plume (Hossain and Rodi, 1982). Proposals have been made (Pope, 1978; Hanjalic and Launder, 1980) for modifying the dissipation equation, based on arguments concerned with vortex or eddy structures characteristic of axisymmetric flows. The modified equation produces more dissipation, thus decreasing the turbulent eddy viscosity, which results in a smaller spreading rate of the flow. Here we use the empirical correction given by Rodi (1972) where $C_{\epsilon 2} = 1.92\,(1-0.035H)$ with $H = |(y_E/U_m)dU_m/dx|^{0.2}$ and where U_m is the maximum velocity and y_E is the distance from the centerline to the edge of the shear layer. This correction decreases the destruction term in the dissipation equation, hence producing an increased dissipation. However, when this correction is used in equation (10) there is very little change in the solution for ϵ when experimental data are used for the other quantities in the equation. This is probably due to the approach taken here, which does not allow for the nonlinear interactions between the various terms in the closure. If the kinetic energy and dissipation equations are solved simultaneously, then the axisymmetric correction will produce a significant change in the solution of the k-ϵ model.

4 Assessment of Closure Hypotheses for Algebraic Stress Model

Chen and Rodi (1975), Tamanini (1978), Chen and Chen (1979), and Hossain and Rodi (1982) have made predictions for the buoyant jet using algebraic stress models. Many of the ideas used in these models for calculating buoyant flows originated with Launder (1975, 1978). Algebraic stress models are obtained by simplifying the convective transport equations for Reynolds stresses and heat fluxes so they are no longer differential equations. The dynamic equation for the Reynolds stress tensor is

$$\begin{aligned}(C-D)_{\overline{u_iu_j}}&=P_{ij}+G_{ij}-\frac{2}{3}\epsilon\delta_{ij}\\&-C_1\epsilon\left(\frac{\overline{u_iu_j}}{k}-\frac{1}{3}\delta_{ij}\right)-C_2\left(P_{ij}-\frac{2}{3}P\delta_{ij}\right)\\&-\frac{30C_2-22}{5}\left(D_{ij}-\frac{2}{3}P\delta_{ij}\right)-(8C_2-6)k\left(\frac{\partial U_i}{\partial x_j}+\frac{\partial U_j}{\partial x_i}\right)\\&-C_3\left(G_{ij}-\frac{2}{3}G\delta_{ij}\right)\end{aligned} \tag{11}$$

where $P_{ij} = -\overline{u_iu_k}\,\partial U_j/\partial x_k - \overline{u_ju_k}\,\partial U_i/\partial x_k$ is the mechanical production and $G_{ij} = -\beta g_i\,\overline{u_jt} - \beta g_j\,\overline{u_it}$ is the buoyancy production. The left side represents convection minus diffusional transport, the dissipation is assumed isotropic, and the last three lines represent the closure formulation for $\overline{p(\partial u_i/\partial x_j+\partial u_j/\partial x_i)/\rho}$ given by Launder et al. (1975) and Launder (1975, 1978). Launder assumes: (1) an equilibrium situation where convection is balanced by diffusion ($C - D = 0$) and production is balanced by dissipation ($P + G - \epsilon = 0$); (2) the second and third terms (third line) in the rapid part of the pressure-velocity correlation are negligible; the coefficient C_2 is adjusted so that the first term approximates the entire rapid part; (3) the parameter C_3 is taken equal to C_2. After applying all the assumptions

$$\overline{u_iu_j}=\frac{2}{3}\frac{C_1+C_2-1}{C_1}k\delta_{ij}-\frac{1-C_2}{C_1}\frac{k}{\epsilon}(P_{ij}+G_{ij}) \tag{12}$$

where $c_1 = 2.2$ and $C_2 = 0.6$. It should be pointed out that in free shear flows the equilibrium condition ($C - D = 0$ and $P + G - \epsilon = 0$) only applies in the outer portion of the flow. Also, Zeman and Lumley (1976) found $C_3 = 0.3$, after applying all the constraints applicable to determining the contribution of buoyancy to the pressure-strain correlation.

The dynamic equation for the heat flux is

$$\begin{aligned}(C-D)_{\overline{u_it}}&=-\overline{u_iu_j}\frac{\partial T}{\partial x_j}-\overline{u_jt}\frac{\partial U_i}{\partial x_j}-\beta g_i\overline{t^2}\\&-C_{1t}\frac{\epsilon}{k}\overline{u_it}+C_{2t}\overline{u_jt}\frac{\partial U_i}{\partial x_j}-\frac{1}{5}\overline{u_jt}\frac{\partial U_j}{\partial x_i}+C_{3t}\beta g_i\overline{t^2}\end{aligned} \tag{13}$$

where the first line on the right side is the production and the second line is the closure for $\overline{p\partial t/\partial x_i/\rho}$. Neglecting convection and diffusion ($C - D = 0$) and the third term in the second line, equation (13) becomes

$$\overline{u_it}=\frac{1}{C_{1t}}\frac{k}{\epsilon}\left[-\overline{u_iu_j}\frac{\partial T}{\partial x_j}-(1-C_{2t})\overline{u_jt}\frac{\partial U_i}{\partial x_j}-(1-C_{3t})\beta g_i\overline{t^2}\right] \tag{14}$$

where $C_{1t} = 3.0$, $C_{2t} = 0.5$, and $C_{3t} = 0.5$. Zeman and Lumley (1976) show that $C_{2t} = 0.8$ and $C_{3t} = 0.2$ from theoretical considerations.

Neglecting the convection and diffusional transport in equation (5) and eliminating ϵ_t with equation (6) gives

$$\overline{t^2}=-R\frac{k}{\epsilon}\overline{u_jt}\frac{\partial T}{\partial x_j} \tag{15}$$

which was given by Launder (1975, 1978) and used by Hossain and Rodi (1982).

Chen and Rodi (1975) and Chen and Chen (1979) used the differential equation (5), with ϵ_t eliminated by using equation (6) to determine $\overline{t^2}$ rather than using equation (15). In either case R is taken to be a constant equal to 0.8 (Hossain and Rodi, 1982; Chen and Rodi, 1975; Chen and Chen, 1979; Launder, 1975, 1978). It is seen in Fig. 2 that the experimentally determined value of R is much lower with an average value across the profile of roughly 0.25. Launder (1978) cites experimental evidence for R being in the range of 0.5 to 0.8. However, he found that the algebraic stress relations agreed best with an experiment for a stably stratified homogeneous shear flow with $R = 0.8$. Hence, that value has been adopted in the algebraic stress models. The experimental results of Shabbir and George (1987) indicate R is much lower for strongly buoyant flows. When the algebraic stress model is applied to this experiment with $R = 0.8$, the results are very poor for $\overline{t^2}$. Therefore, in the following evaluation of the algebraic stress model, the experimentally determined profile for R (Fig. 2) is used.

Equations (10), (12), and (13) represent a system of *algebraic equations* that can be solved for $\overline{u_iu_j}$, $\overline{u_it}$, and $\overline{t^2}$. Employing the thin shear layer approximation, where only gradients in the radial direction are retained, Hossain and Rodi (1982) give

$$\overline{u^2} = \frac{2}{3}\frac{C_1+C_2-1}{C_1}k + \frac{1-C_2}{C_1}\frac{k}{\epsilon}\left(-2\overline{uv}\frac{\partial U}{\partial r} + 2\beta\overline{gvt}\right) \quad (16)$$

$$\overline{uv} = \frac{1-C_2}{C_1}\frac{k}{\epsilon}\left(-\overline{v^2}\frac{\partial U}{\partial r} + g\beta\overline{vt}\right) \quad (17)$$

$$\overline{v^2} = \frac{2}{3}\frac{C_2+C_2-1}{C_1}k \quad (18)$$

$$\overline{ut} = \frac{1}{C_{1t}}\frac{k}{\epsilon}\left[-\overline{uv}\frac{\partial T}{\partial r} - (1-C_{2t})\overline{vt}\frac{\partial U}{\partial r} + (1-C_{3t})\beta g\overline{t^2}\right] \quad (19)$$

$$\overline{vt} = \frac{-1}{C_{1t}}\frac{k}{\epsilon}\overline{v^2}\frac{\partial T}{\partial r} \quad (20)$$

$$\overline{t^2} = -2R\frac{k}{\epsilon}\overline{vt}\frac{\partial T}{\partial r} \quad (21)$$

from which $\nu_t = C_\mu k^2/\epsilon$ where

$$C_\mu = \frac{2}{3}\frac{(1-C_2)(C_1+C_2-1)}{C_1^2}\left(1 + \frac{1}{C_{1t}}\frac{k}{\epsilon}g\beta\frac{\partial T/\partial r}{\partial U/\partial r}\right) \quad (22)$$

The system of equations (16)–(21) was solved to determine the Reynolds stress and heat flux components with U, T, k, ϵ, and R given by the experiment. The following values for the constants were used:

$$C_1 = 2.2, \quad C_2 = 0.6, \quad C_3 = 0.6$$
$$C_{1t} = 3.0, \quad C_{2t} = 0.5, \quad C_{3t} = 0.5$$

The value of C_μ, which appears in the eddy viscosity relation $\nu_t = C_\mu k^2/\epsilon$ and is given by equation (22), is roughly 0.125 and is reasonably constant across the flow. This value is considerably larger than the value of $C_\mu = 0.09$ in the standard k-ϵ model. Rodi (1972), to correct for the discrepancies in the prediction for the axisymmetric jet, developed an empirical correction to C_μ. The parameter C_μ is replaced by $(1\text{-}0.465H)C_\mu$ where $H = |(y_E/U_m)dU_m/dx|^{0.2}$, U_m is the maximum velocity, and y_E is the distance from the centerline of the edge of the jet. Hossain and Rodi (1982), Chen and Rodi (1975), and Chen and Chen (1979) used this correction in their predictions for turbulent buoyant jets. When the correction is applied, we get approximately 0.09, which is the value of C_μ for the standard k-ϵ model.

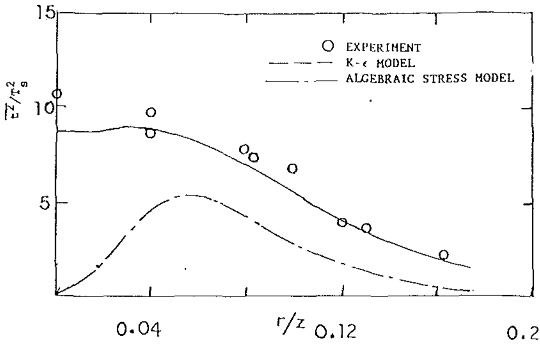

Fig. 7 **Mean square temperature**

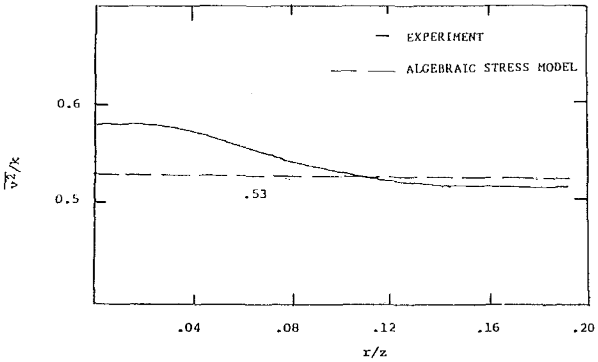

Fig. 8 **Radial Reynolds stress $\overline{v^2}$**

The question we are asking is, "given the turbulent energy, dissipation, velocity, and temperature, does the proposed algebraic stress expression correctly predict the Reynolds stress and heat flux components?" Figure 8 shows the radial Reynolds stress determined from equation (18). It is seen that the predicted value $\overline{v^2}/k = 0.53$ is a little smaller than the experimental curve in the center portion of the plume, but agrees quite well with experiment in the outer portion. The predicted shear stress $\overline{uv}$, the axial heat flux $\overline{ut}$, the radial heat flux $\overline{vt}$, and the mean squared temperature $\overline{t^2}$ are shown in Figs. 3, 4, 5, and 7, respectively. Again the points are experimental data and the broken lines are from the model. It is seen that the shear stress $\overline{uv}$ and radial heat flux $\overline{vt}$ are predicted reasonably. However, the vertical heat flux $\overline{ut}$ and temperature fluctuations $\overline{t^2}$ are predicted poorly and have incorrect shapes; unlike the experimental values they go to zero near the origin.

Equation (21) gives $\overline{t^2}$ proportional to the radial temperature gradient, which is zero at the centerline. Then since $\overline{t^2} = 0$ at $r = 0$, equation (19) gives $\overline{ut} = 0$ at $r = 0$. In order to obtain nonzero values for $\overline{ut}$ and $\overline{t^2}$ at the centerline from the model equations (12), (14), and (15), terms containing the axial gradient, i.e., $\partial U/\partial z$ and $\partial T/\partial z$, were retained. These terms were added to equations (19) and (21) and the system of equations was solved again. Although the centerline values of ut and $\overline{t^2}$ were found to be nonzero, the predictions still decreased to relatively small values near the centerline.

Another possibility for this behavior is the neglect of advection and diffusion terms in the model. Gibson and Launder (1976) have proposed the following model for these terms:

$$(C-D)_{\overline{u_iu_j}} = \frac{\overline{u_iu_j}}{k}(P+G-\epsilon) \quad (23)$$

$$(C-D)_{\overline{u_it}} = \frac{\overline{u_it}}{2\overline{t^2}}(P_t-\epsilon_t) + \frac{\overline{u_it}}{2k}(P+G-\epsilon) \quad (24)$$

where P_t is the production term in the $\overline{t^2}$ equation. These were

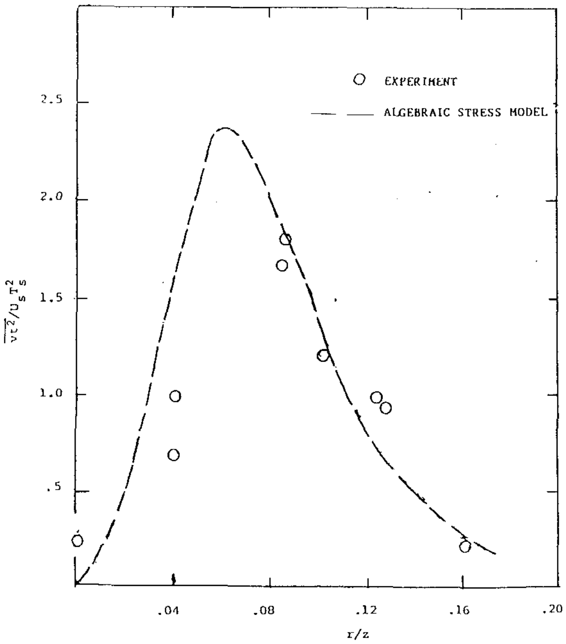

Fig. 9 Transport of temperature variance $\overline{t^2}$

incorporated in equations (16)–(21) and the resulting set of nonlinear coupled algebraic equations was solved simultaneously. The results did improve the prediction for the vertical heat flux $\overline{ut}$ and temperature variance $\overline{t^2}$ but the comparison for radial heat flux and shear stress became worse. As noted by Gibson and Launder (1976), the above model is not good near an axis of symmetry. This is why, by incorporating them in the original model, no overall improvement in the prediction is achieved.

Chen and Rodi (1975), Tamanini (1978), and Chen and Chen (1979) use the differential convective-transport equation (5) to determine $\overline{t^2}$ in their predictions of buoyant jets. Equation (6) was used to eliminate ϵ_t. Thus, the final form of the $\overline{t^2}$ equation becomes

$$U\frac{\partial \overline{t^2}}{\partial z} + V\frac{\partial \overline{t^2}}{\partial r} = \frac{1}{r}\frac{\partial}{\partial r}\left(C_t\frac{k^2}{\epsilon}\frac{\partial \overline{t^2}}{\partial r}\right) - 2\overline{vt}\,\frac{\partial T}{\partial r} - \frac{1}{R}\frac{\epsilon}{k}\,\overline{t^2} \qquad (25)$$

This equation was numerically solved for the temperature variance $\overline{t^2}$ with all other quantities needed to evaluate the coefficients determined from experiments. The value of C_t was taken as 0.13. The best agreement, as shown in Fig. 7, was achieved with $R = 0.35$. When the average experimental value of $R = 0.25$ is used, the prediction peaks at about 6.0 ($\eta = 0.04$) as compared to the experimental value of $\overline{t^2}$ of about 8.0 ($\eta = 0.04$). When the standard value of $R = 0.8$ is used, $\overline{t^2}$ is overpredicted by a factor of four.

When $\overline{t^2}$ is calculated from the convective-transport equation (5), the diffusive transport is given by the simple gradient closure

$$\overline{vt^2} = -C_t\frac{k^2}{\epsilon}\frac{\partial \overline{t^2}}{\partial r} \qquad (26)$$

with $C_t = 0.13$ as given by Chen and Rodi (1980). The prediction for $\overline{vt^2}$, using experimental information to evaluate the right-hand side of equation (26), is shown in Fig. 9. The predicted curve peaks somewhat above and toward the centerline as compared to the data.

Finally, we ask that if the models do not depict the axial heat flux $\overline{ut}$ and the temperature variance $\overline{t^2}$ correctly, then why do the predictions such as made by Hossain and Rodi (1982), Chen and Rodi (1975), Tamanini (1978), and Chen and Chen (1978) show reasonable agreement with the experiment for the mean velocity and buoyancy? The answer to this is that with $R = 0.8$ the temperature variance $\overline{t^2}$ from equation (21) or (25) is too large. This makes the vertical heat flux $\overline{ut}$ from equation (19) large enough so that the mean velocity and buoyancy are reasonably predicted.

5 Summary and Conclusions

The experimental data on buoyant plumes were used to evaluate various closure relations for turbulence transport. The objective was not to propose new models, but to evaluate the closure schemes proposed by other workers for buoyancy-dominated flows. The closures evaluated were those used in the k–ϵ and algebraic stress models. The results are summarized below.

1 The closure relations of the k–ϵ model compare reasonably with experimental data, except for the axial turbulent transport, which is drastically underpredicted. The axial heat flux governs the production due to buoyancy in the kinetic energy and dissipation equations and its correct prediction is very important. This is a probable reason why the results of Hossain and Rodi (1982) from the k–ϵ model underpredict the spreading rate for the plume by 10 percent even when axisymmetric jet corrections are included.

2 The ratio R of the time scales, which is used to determine the dissipation of the mean squared temperature in the algebraic stress model, was found to be considerably different from the accepted value of $R = 0.8$. Apparently R is not a universal constant, but can vary from flow to flow and is influenced by the strength of the buoyancy present. From the experimental data on a plume it appears that $R = 0.25$ for strongly buoyant flows.

3 The closure equations for the shear stress and radial heat flux of the algebraic stress models also compared well with experiment but are not better than the simple gradient closures used in the k–ϵ model. The axial heat flux and mean squared temperature are predicted poorly in the central core of the flow and had incorrect trends. This drawback could be attributed to the assumption of local equilibrium, which resulted in the neglect of convection and diffusion terms in the transport equations for Reynolds stress and heat flux. However, no substantial improvement was achieved by keeping the secondary derivatives or by incorporating the model for the convection and diffusion terms. Therefore, the full dynamic equations for Reynolds stress and heat flux with convection and diffusion are required to predict the axial heat flux and temperature variance properly.

Acknowledgments

This work was partially supported by the National Science Foundation under Grants ATM-8023699 and MSM 8316833.

References

Chen, C. J., and Chen, C. H., 1979, "On Prediction and Unified Correlation for Decay of Vertical Buoyant Jets," ASME JOURNAL OF HEAT TRANSFER, Vol. 101, pp. 532–437.

Chen, J. C., and Rodi, W., 1975, "A Mathematical Model for Stratified Turbulent Flows and Its Application to Buoyant Jets," *Proc. 16th Congress, IAHR*, Sao Paulo, Brazil, pp. 31–37.

George, W. K., Alpert, R. L., and Tamanini, F., 1977, "Turbulence Measurements in an Axisymmetric Buoyant Plume," *Int. J. Heat Mass Transfer*, Vol. 20, pp. 1145–1154.

Gibson, M. M., and Launder, B. E., 1976, "On the Calculation of Horizontal Non-equilibrium Turbulent Shear Flows Under Gravitational Influence," ASME JOURNAL OF HEAT TRANSFER, Vol. 98, pp. 81–87.

Hanjalic, K., and Launder, B. E., 1980, "Sensitizing the Dissipation Equations to Irrotational Strains," ASME *Journal of Fluids Engineering*, Vol. 102, pp. 34–40.

Hossain, M. S., and Rodi, W., 1982, "A Turbulence Model for Buoyant Flows and Its Application to Buoyant Jets," *Turbulent Buoyant Jets and Plumes*, W. Rodi, ed., Pergamon, NY, pp. 121–178.

Launder, B. E., 1975, "On the Effects of a Gravitational Field on the Turbulent Transport of Heat and Momentum," *J. Fluid Mech.*, Vol. 67, pp. 569–590.

Launder, B. E., 1978, "Heat and Mass Transport," *Topics in Physics, Vol. 12: Turbulence*, Springer-Verlag, New York, pp. 231–287.

Launder, B. E., Morse, A. P., Rodi, W., and Spalding, D. B., 1972, "The Prediction of Free-Shear Flows—A Comparison of the Performance of Six Turbulence Models," *Proc. Langley Free Shear Flows Conf.*, Vol. 1, NASA SP 320.

Launder, B. E., Reese, G. J., and Rodi, W., 1975, "Progress in the Development of a Reynolds-Stress Turbulence Closure," *J. Fluid Mech.*, Vol. 68, pp. 537–566.

Launder, B. E., and Spalding, D. B., 1974, "The Numerical Computation of Turbulent Flow," *Comp. Meth. in Appl. Mech. and Engr.*, Vol. 3, p. 269.

Lumley, J. L., 1978, "Computational Modeling of Turbulent Flows," *Advances in Applied Mechanics*, Vol. 18, pp. 123–176.

Pope, S. B., 1978, "An Explanation of the Turbulent Round-Jet/Plane-Jet Anomaly," *AIAA J.*, Vol. 16, pp. 279–281.

Rodi, W., 1972, "The Prediction of Free Turbulent Boundary Layers by Use of a Two-Equation Model of Turbulence," Ph.D. Thesis, Univ. of London, United Kingdom.

Shabbir, A., 1987, "An Experimental Study of an Axisymmetric Turbulent Buoyant Plume and Evaluation of Closure Hypotheses," Ph.D. Dissertation, Univ. at Buffalo, SUNY.

Shabbir, A., and George, W. K., 1987, "Energy Balance Measurements in an Axisymmetric Buoyant Plume," *Sixth Symposium on Turbulent Shear Flows*, Toulouse, pp. 9-3-1 to 9-3-6 (also submitted to *J. Fluid Mech.*).

Tamanini, F., 1978, "The Effect of Buoyancy on the Turbulence Structure of Vertical Round Jets," ASME JOURNAL OF HEAT TRANSFER, Vol. 100, pp. 659–664.

Zeman, O., and Lumley, J. L., 1976, "Modeling Buoyancy Driven Mixed Layers," *J. Atm. Sci.*, Vol. 33, p. 1988.

An Approximate Analysis for Convective Heat Transfer on Thermally Nonuniform Surfaces

S. H. Park[1]

C. L. Tien[2]
A. Martin Berlin Professor.
Fellow ASME

Department of Mechanical Engineering,
University of California,
Berkeley, CA 94720

This paper presents a new, simple, but powerful technique for nonsimilar natural and assisting mixed convection heat transfer problems in which thermal boundary conditions are specified arbitrarily even with step discontinuities. Temperature and velocity fields for natural convection over thermally nonuniform surfaces are formulated in terms of equivalent Grashof numbers defined by the superposition *of* surface heat fluxes *and* velocities *obtained from similarity analyses for isoflux or isothermal surfaces. A local heat transfer rate for assisting mixed convection over thermally nonuniform surfaces is approximated using Nusselt numbers for pure forced and pure natural convection over such surfaces, which are obtained by the superposition method. Comparisons with existing similarity solutions, experimental results, and numerical solutions validate the use of this simple superposition method in many practical situations such as cooling configurations in electronic and manufacturing equipment.*

Introduction

Convective cooling technology is fundamental to the performance and reliability of electronic circuitry. A simple methodology for the estimation of heat transfer in electronic systems is strongly required for practical thermal design. Any attempt to develop such a simple analytical model, however, has been hindered by the complicated temperature and velocity fields and by the complex structure of electronic systems. The objective of this paper, therefore, is to develop a simple analytical technique for the prediction of convective heat transfer in these complicated systems. While the surfaces are assumed to be flat and flow regime is laminar, thermal boundary conditions are specified arbitrarily even with step discontinuities.

Analytical solutions of forced convection heat transfer over a flat plate with arbitrary surface-temperature or heat flux variations can be easily obtained by the superposition method (Kays and Crawford, 1980) because of the linearity of the boundary layer energy equation. On the other hand, due to the nonlinear coupling of flow and energy fields, analytical solutions for natural convection boundary layers are limited to the situations with uniform or simply varying boundary conditions, which yield similarity formulation (Jaluria and Gebhart, 1977; Jaluria, 1980). Moreover, analytical solutions are seldom obtained even for simple thermal boundary conditions in the analysis of mixed convection heat transfer (Churchill and Usagi, 1972; Wilks, 1973; Shai and Barnea, 1986; Lin and Chen, 1988)〉

For the description of natural convection heat transfer along thermally nonuniform surfaces, several approximating techniques have been developed. For surfaces with continuous thermal boundary conditions, the integral method was used by Sparrow (1955) and Scherberg (1964). Kelleher and Yang (1972) employed a Görtler-type series expansion and Kao et al. (1977) developed a general theory with local similarity and universal functions. Natural convection over inclined surfaces with power-law variations of wall temperatures or surface heat fluxes was numerically analyzed by Chen et al. (1986). For thermally discrete surfaces, Schetz and Eichhorn (1964) conducted an experiment with a Mach-Zehnder Interferometer. Kelleher (1971) analyzed the problem using an asymptotic series, Hayday et al. (1967) applied a difference-differential method, and Jaluria (1982) numerically investigated multistep discontinuity cases. Lin and Yu (1988) numerically studied natural convection induced by an isoflux surface with a line source at its leading edge over a wide range of Prandtl numbers using a unified buoyancy parameter. Currently Lee and Yovanovich (1987-89) approximated these nonsimilar natural convection phenomena using an integral and pseudo-transient technique.

For mixed convection heat transfer over a thermally nonuniform surface, almost all the analyses are assisted by numerical computations. Mixed convective flow along thermally nonuniform surfaces was analyzed numerically by Oosthuizen and Hart (1973). A similarity formulation for mixed convection heat transfer can be obtained for a special situation, such as mixed convection over a circular cylinder where mainstream velocity and temperature difference between the surface and the ambient condition vary linearly along the surface (Mahmood and Merkin, 1988).

In spite of extensive efforts to analyze natural and mixed convection heat transfer on thermally nonuniform surfaces, there has been no simple analytic approach reported that is generally applicable for practical engineering calculations. In the present work, a simple analytical technique for the approximation of natural and assisting mixed convective heat transfer for arbitrarily specified boundary conditions will be developed. The superposition method will be employed for the simulation of nonsimilar convection heat transfer in that the superposition method is one of the simplest techniques accommodating arbitrarily varying boundary conditions. Although the superposition method is not rigorously valid for nonlinear cases, the present study attempts to show that such a method can yield very small errors. The superposition technique has rarely been employed for natural or mixed convection heat transfer due to the coupling effects and the nonlinearity of the field equations and, if at all, has been used only for the case

---

[1] Currently Post-Doctoral Research Engineer, University of California, Irvine, CA 92717.

[2] Currently UCI Distinguished Professor, University of California, Irvine, CA 92717.

Contributed by the Heat Transfer Division and presented at the National Heat Transfer Conference, Philadelphia, Pennsylvania, August 6-9, 1989. Manuscript received by the Heat Transfer Division May 10, 1989; revision received October 25, 1989. Keywords: Electronic Equipment, Mixed Convection, Thermal Packaging.

where local buoyancy effects are negligibly small (Ortega and Moffat, 1986).

In this study, temperature and velocity fields for natural convection over thermally nonuniform surfaces are described in terms of equivalent Grashof numbers defined by the superposition of surface heat fluxes and velocities formulated from similarity analyses or correlations for simple boundary conditions. Local heat transfer rates for assisting mixed convection on thermally nonuniform surfaces are expressed by the third root of the sum of the third power of Nusselt numbers for pure forced and pure natural convection on such surfaces. These Nusselt numbers are obtained by the superposition method. This summation method was originally devised for assisting mixed convection over thermally uniform surfaces for practical engineering applications (Churchill and Usagi, 1972; Shai and Barnea, 1986). Various comparisons are made between the results from the proposed technique and those from numerical studies, experiments, and similarity analyses.

Analysis

Figure 1 shows the physical schematic for thermally continuous and discrete vertical surfaces. The superposition method is employed for the analysis of forced, natural, and assisting mixed convection on thermally nonuniform vertical surfaces. The flow is assumed to be a laminar boundary layer flow over a flat plate for the simplicity of the analysis, although the superposition method can also be used for turbulent flow regime.

Forced Convection. It is well known that the method of superposition can give heat transfer solutions for a forced boundary layer flow with arbitrary thermal boundary conditions because of the linearity of the energy equation for this case. Since details of this case are well explained in general textbooks (Kays and Crawford, 1980), only the results are presented in this study.

For arbitrary wall temperature variations with a finite number (j) of step discontinuities, the wall heat flux is modeled as

$$\dot{q}_w'' = \int_0^x h_F(\xi, x)\,\frac{dT_w}{d\xi}\,d\xi + \sum_{i=1}^{j} h_F(\xi_i, x)\Delta T_{w,i} \qquad (1)$$

where $h_F(\xi, x)$ is the local heat transfer coefficient and is given as

$$h_F(\xi, x) = \frac{0.332k}{x}\,\mathrm{Pr}^{1/3}\mathrm{Re}_x^{1/2}\left[1-\left(\frac{\xi}{x}\right)^{3/4}\right]^{-1/3} \qquad (2)$$

Thus, a local Nusselt number is

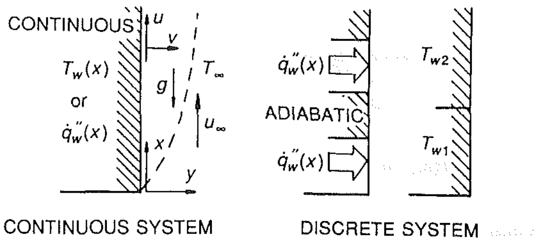

Fig. 1 Coordinate system and thermally nonuniform surfaces

$$\mathrm{Nu}_{x,F} = \frac{0.332\mathrm{Pr}^{1/3}\mathrm{Re}_x^{1/2}}{T_w - T_\infty}\cdot \left\{\int_0^x\left[1-\left(\frac{\xi}{x}\right)^{3/4}\right]^{-1/3}\frac{dT_w}{d\xi}\,d\xi + \sum_{i=1}^{j}\left[1-\left(\frac{\xi_i}{x}\right)^{3/4}\right]^{-1/3}\Delta T_{w,i}\right\} \qquad (3)$$

For arbitrarily specified surface heat fluxes, the wall temperature is formulated as

$$T_w = T_\infty + \frac{0.623}{k}\,\mathrm{Pr}^{-1/3}\mathrm{Re}_x^{-1/2}\int_0^x\left[1-\left(\frac{\xi}{x}\right)^{3/4}\right]^{-2/3}\dot{q}_w''(\xi)\,d\xi \qquad (4)$$

and a local Nusselt number is evaluated as

$$\mathrm{Nu}_{x,F} = \frac{x\dot{q}_w''}{0.623\mathrm{Pr}^{-1/3}\mathrm{Re}_x^{-1/2}\int_0^x\left[1-\left(\frac{\xi}{x}\right)^{3/4}\right]^{-2/3}\dot{q}_w''(\xi)\,d\xi} \qquad (5)$$

Natural Convection. Using the Boussinesq approximation, the boundary layer equations governing laminar natural convection over a vertical plate are given by

Continuity

$$\frac{\partial u}{\partial x} + \frac{\partial v}{\partial y} = 0 \qquad (6)$$

Momentum

$$u\frac{\partial u}{\partial x} + v\frac{\partial u}{\partial y} = g\beta(T - T_\infty) + \nu\frac{\partial^2 u}{\partial y^2} \qquad (7)$$

Energy

$$u\frac{\partial T}{\partial x} + v\frac{\partial T}{\partial y} = \alpha\frac{\partial^2 T}{\partial y^2} \qquad (8)$$

Nomenclature

C_H = constant for the case $\dot{q}_w''$ specified
C_L = constant for the line source case
C_T = constant for the case T_w specified
C_U = constant for velocity $= 2(g\beta)^{1/2}F'(\eta)$
F = dimensionless stream function
g = gravitational acceleration
Gr_x = Grashof number
Gr_x^* = heat flux-based equivalent Grashof number
Gr_x^{**} = momentum-based equivalent Grashof number
h = heat transfer coefficient
j = number of discontinuities
k = thermal conductivity
n = exponent for surface temperature distribution
Nu_x = Nusselt number $= hx/k$
Pr = Prandtl number $= \alpha/\nu$
$\dot{q}_w''$ = surface heat flux
Q_s = thermal energy input per unit length of a line source
Re_x = Reynolds number $= u_\infty x/\nu$
T = temperature
T_∞ = ambient temperature
u, v = velocity components in the x, y directions
$u_{\max}$ = peak velocity
x = vertical coordinate
y = transverse coordinate
α = thermal diffusivity
β = volumetric coefficient of thermal expansion $= 1/T_\infty$
η = dimensionless independent similarity variable
θ = dimensionless temperature
ν = kinematic viscosity
Ψ = stream function

Subscripts

F = forced convection
H = specified surface heat flux
M = mixed convection
N = natural convection
T = specified surface temperature
U = velocity
w = surface
x = x direction
∞ = ambient condition

with the boundary conditions

$$u(x,0)=v(x,0)=u(x,\infty)=0, \qquad T(x,\infty)=T_\infty,$$

$$u(0,y)=0, \qquad T(0,y)=T_\infty,$$

$$T(x,0)=T_w(x) \text{ or } \frac{\partial T(x,0)}{\partial y}=-\frac{\dot q_w''(x)}{k} \tag{9}$$

When $[T_w(x)-T_\infty]$ is proportional to x^n, the governing partial differential equations can be transformed into the corresponding ordinary differential equations (Kays and Crawford, 1980; Jaluria, 1980) as

$$F'''+\theta+(n+3)FF''-(2n+2)F'^2=0 \tag{10}$$

$$\theta''+\mathrm{Pr}[(n+3)F\theta'-4nF'\theta]=0 \tag{11}$$

with the transformed boundary conditions

$$F'(0)=F(0)=F'(\infty)=0, \qquad \theta(0)=1, \qquad \theta(\infty)=0 \tag{12}$$

The solutions are given in terms of the independent similarity variable (η), stream function (ψ), streamwise velocity (u), and dimensionless temperature (θ), which are defined as

$$\eta=\frac{y}{x}\left(\frac{\mathrm{Gr}_x}{4}\right)^{1/4} \tag{13}$$

$$\psi(x,\eta)=4\nu F(\eta)\left(\frac{\mathrm{Gr}_x}{4}\right)^{1/4} \tag{14}$$

$$u(x,\eta)=\frac{4\eta}{x}F'(\eta)\left(\frac{\mathrm{Gr}_x}{4}\right)^{1/2}=C_U x^{1/2}(T_w-T_\infty)^{1/2} \tag{15}$$

$$\theta=\frac{T-T_\infty}{T_w-T_\infty} \tag{16}$$

where Gr_x is the Grashof number defined as

$$\mathrm{Gr}_x=\frac{g\beta x^3(T_w-T_\infty)}{\nu^2} \tag{17}$$

The exponent $n=0$ corresponds to an isothermal vertical surface, $n=1/5$ to an isoflux surface, and $n=-3/5$ to a line thermal source on an adiabatic surface (Jaluria and Gebhart, 1977).

The present analysis utilizes the similarity solutions for both isothermal and isoflux surface cases for the formulation of superposition variables. The local surface heat flux for isothermal vertical surfaces and the local surface temperature differences (T_w-T_∞) for isoflux vertical surfaces are written in terms of the first order of surface temperature difference and surface heat flux, respectively, and given as

$$\dot q_w''=-k(T_w-T_\infty)\frac{\theta_T'(0)}{\sqrt{2}}\frac{1}{x}\mathrm{Gr}_x^{1/4}=C_T(T_w-T_\infty)^{5/4}x^{-1/4} \tag{18}$$

$$(T_w-T_\infty)^{5/4}=-\frac{x^{1/4}\dot q_w''}{k\dfrac{\theta_H'(0)}{\sqrt{2}}\left(\dfrac{g\beta}{\nu^2}\right)^{1/4}}=\frac{x^{1/4}\dot q_w''}{C_H} \tag{19}$$

where the subscripts T and H represent the isothermal and isoflux surface cases, respectively, and

$$C_H=k\frac{\theta_H'(0)}{\sqrt{2}}\left(\frac{g\beta}{\nu^2}\right)^{1/4}, \qquad C_T=k\frac{\theta_T'(0)}{\sqrt{2}}\left(\frac{g\beta}{\nu^2}\right)^{1/4} \tag{20}$$

Local Nusselt numbers are then defined for both cases as

$$\mathrm{Nu}_{x,N}=\frac{x\dot q_w''}{k(T_w-T_\infty)}=-\frac{\theta'_{T\text{ or }H}(0)}{\sqrt{2}}\mathrm{Gr}_x^{1/4} \tag{21}$$

For natural convection heat transfer, both flow and temperature fields are introduced by the sudden change of the thermal boundary condition at $x=0$, as shown in Fig. 1 and independent of the location of the change. The velocity and temperature fields are the direct responses to the variation in the thermal boundary condition. When there is another step discontinuity in the downstream boundary condition, the flow and thermal fields after the second discontinuity are influenced by both the first and the second step discontinuities. Although thermal discontinuities have nonlinear effects on the thermal and momentum fields, those effects are accumulated in the downstream fields. These accumulated effects will be approximated by the superposition method.

In forced convection heat transfer with a nonuniform thermal boundary condition, there is no difference in selecting either surface temperature difference or surface heat flux as a superposition variable, since surface temperature difference is linearly proportional to surface heat flux. But the situation is different for natural convection because surface temperature difference is not linearly proportional to surface heat flux, as in equation (18). Since the results are strongly influenced by the selected variables for superposition, it is important to select appropriate superposition variables to obtain accurate predictions. The present study selects surface heat flux and momentum per unit mass as superposition variables. Surface heat flux appears to be superposable according to the law of energy conservation since a quantitative expression of the energy input for a system is surface heat flux, not surface temperature difference except for linear cases. For the momentum field, momentum per unit mass is superposable since force exerted on unit mass of the system is conserved.

The resulting surface heat flux for isothermal vertical surfaces is proportional to the 5/4 power of the temperature discontinuity at $x=0$ from equation (18). This consideration can be extended to generalized boundary conditions, which specify a continuous variation of surface temperature together with a finite number (j) of step discontinuities. The resulting surface heat flux can be described using a Stieltjes integral as

$$\dot q_w''=C_T\left[\int_0^x(x-\xi)^{-1/4}\frac{d(T_w-T_\infty)^{5/4}}{d\xi}\,d\xi+\sum_{i=1}^{j}(x-\xi_i)^{-1/4}\Delta(T_w-T_\infty)_i^{5/4}\right] \tag{22}$$

For isoflux vertical surfaces the same analogy can be applied and the 5/4 power of surface temperature difference is proportional to the surface heat flux discontinuity at $x=0$ as in equation (19). Hence, for a generalized heat flux boundary condition, the resulting surface temperature difference can be expressed as

$$(T_w-T_\infty)^{5/4}=\frac{1}{C_H}\left[\int_0^x(x-\xi)^{1/4}\frac{d\dot q_w''}{d\xi}\,d\xi+\sum_{i=1}^{j}(x-\xi_i)^{1/4}\Delta\dot q_{wi}''\right] \tag{23}$$

In addition, a heat flux-based equivalent Grashof number Gr_x^* can be defined by

$$\mathrm{Gr}_x^*=\left[\frac{\dot q_w''}{k\left(-\dfrac{\theta'_{T\text{ or }H}(0)}{\sqrt{2}}\right)}\frac{x}{(T_w(x)-T_\infty)}\right]^4 \tag{24}$$

using equation (22) for surface temperature and equation (23) for surface heat flux specified cases, and thus, $\mathrm{Nu}_{x,N}$ and the temperature profile can be calculated from equations (13), (16), and (21) using Gr_x^* instead of Gr_x.

Since the momentum field is not linearly proportional to the temperature field, the heat flux-based Grashof number Gr_x^* cannot describe the velocity field properly. For an improved prediction of the velocity field, a superposed velocity is formulated from equation (15) at η for a generalized boundary condition as

$$u=C_U\left[\int_0^x (x-\xi)^{1/2}\frac{d(T_w-T_\infty)^{1/2}}{d\xi}\,d\xi + \sum_{i=1}^{j}(x-\xi_i)^{1/2}\Delta(T_w-T_\infty)_i^{1/2}\right] \qquad (25)$$

and a momentum-based equivalent Grashof number Gr_x^{**} is obtained from equations (15) and (25) as

$$\mathrm{Gr}_x^{**}=\frac{g\beta x^2}{\nu^2}\left[\int_0^x (x-\xi)^{1/2}\frac{d(T_w-T_\infty)^{1/2}}{d\xi}\,d\xi + \sum_{i=1}^{j}(x-\xi_i)^{1/2}\Delta(T_w-T_\infty)_i^{1/2}\right]^2 \qquad (26)$$

Therefore, the velocity distribution can be calculated from equations (13) and (15) using Gr_x^{**}.

Mixed Convection. Combined effects of forced and natural convection over thermally uniform vertical surfaces on the heat transfer rate were investigated and correlated by Churchill and Usagi (1972) in the form

$$X=[Y^n+Z^n]^{1/n} \qquad (27)$$

where X, Y, and Z represent mixed, forced, and natural convection, respectively. For the case of assisting mixed convection, Churchill (1977) suggested the use of the following correlation based on equation (27):

$$\mathrm{Nu}_{x,M}=[\mathrm{Nu}_{x,F}^n+\mathrm{Nu}_{x,N}^n]^{1/n} \qquad (28)$$

and a theoretical analysis for assisting convection indicates that the third root of the sum gives the best representation (Churchill, 1977; Shai and Barnea, 1986). Hence, using the correlation mentioned above, a local Nusselt number for assisting mixed convection over a thermally nonuniform surface can be modeled as

$$\mathrm{Nu}_{x,M}=[\mathrm{Nu}_{x,F}^3+\mathrm{Nu}_{x,N}^3]^{1/3} \qquad (29)$$

where $\mathrm{Nu}_{x,F}$ and $\mathrm{Nu}_{x,N}$ are obtained from the superposition model of pure forced and pure natural convection over such a surface, respectively.

Results and Discussion

Results of the present study verify the general applicability of the superposition technique for approximating natural or mixed convection heat transfer phenomena over a thermally nonuniform surface. In comparison, similarity solutions, numerical analysis by the STAN 7 code, experimental data taken by Schetz and Eichhorn (1964), and an empirical correlation, equation (29), are used as references. STAN 7 is a finite difference code for solving the boundary layer momentum and energy equations for laminar or turbulent flows over or inside a body of revolution and an abridged version of program STAN 5 (Crawford and Kays, 1976). Its numerical scheme and basic program were developed by Patankar and Spalding (1967). The thermophysical properties of air at room temperature (298 K) and atmospheric pressure (1 atm) are used for extensive comparisons.

Natural Convection Over Thermally Uniform Surfaces. Natural convection over an *isoflux* surface is predicted by the superposition of the similarity solutions for *isothermal* surfaces. It is assumed that the distribution of surface temperature difference is known and given as $T_w-T_\infty \propto x^{1/5}$. Using the known temperature distribution for an isoflux surface, the heat flux-based eqivalent Grashof number (Gr_x^*) is calculated as 1.52 Gr_x from equations (22) and (24) and the momentum-based equivalent Grashof number (Gr_x^{**}) is 0.887 Gr_x from equation (26). In this case, the local heat transfer rates predicted from the superposition method are within a 6 percent error range of those from similarity analyses over a wide range of Prandtl numbers, which is less than the error range from the integral method (Kays and Crawford, 1980). Figure 2 shows a comparison between velocity and temperature distributions from an exact similarity analysis and those from the superposition method. The approximate temperature distribution using Gr_x^* is in excellent agreement with the similarity solution. The velocity distribution is more accurately predicted using the momentum-based equivalent Grashof number (Gr_x^{**}) rather than using the heat flux-based equivalent Grashof number (Gr_x^*).

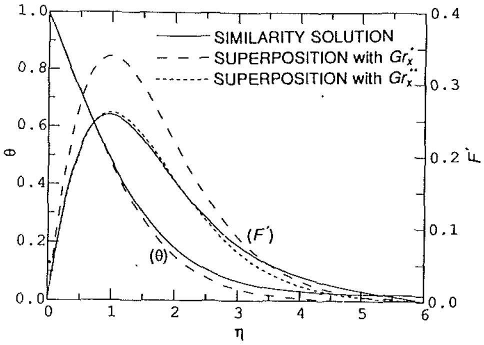

Fig. 2 ***Comparison of dimensionless temperature and velocity profiles for natural convection over isoflux surfaces***

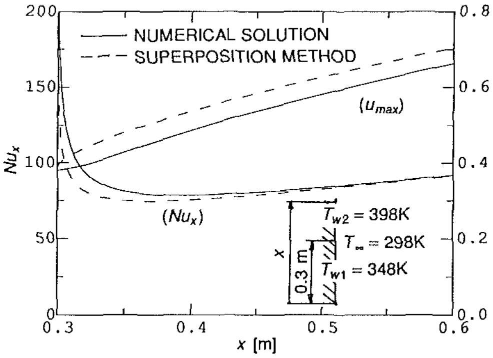

Fig. 3 Comparison of Nu_x and u_{max} for natural convection over a discontinuity in surface temperature

Natural convection over an *isothermal* surface is predicted by the superposition method using the similarity solutions for *isoflux* surfaces, assuming that the distribution of surface heat flux is known and given as $\dot{q}_w'' \propto x^{-1/4}$. Results in this case exhibit an error range similar to that of the isoflux case.

Natural Convection for Discrete Surface Temperature. When there is a discontinuity in the surface temperature distribution, the superposition technique is applied to approximate thermal and momentum fields. Figure 3 shows Nusselt number and the peak velocity ($u_{\max}$) distributions along the vertical axis under the condition $T_{w2} > T_{w1}$. Nusselt numbers are well predicted except for the region very close to the surface temperature discontinuity and $u_{\max}$ is predicted within 10 percent of the numerical calculation. In Fig. 4, approximated downstream temperature profiles based on Gr_x^* are in good agreement with numerical calculations, except for the discontinuity, which induces strong nonsimilar fields. Using similarity formulations, the superposition method does not describe the thermal behavior in strong nonsimilar regions accurately. Figure 5 indicates that downstream velocity profiles can be predicted well using the superposition method with Gr_x^{**}. Figure

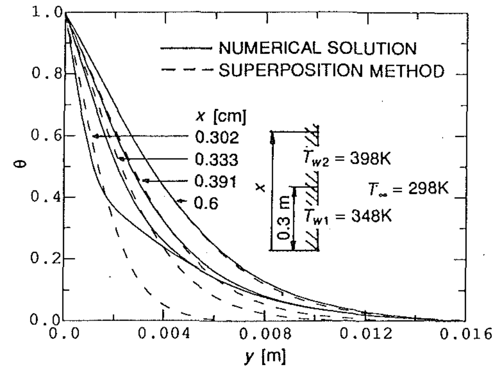

Fig. 4 Comparison of temperature profiles for natural convection over a discontinuity in surface temperature

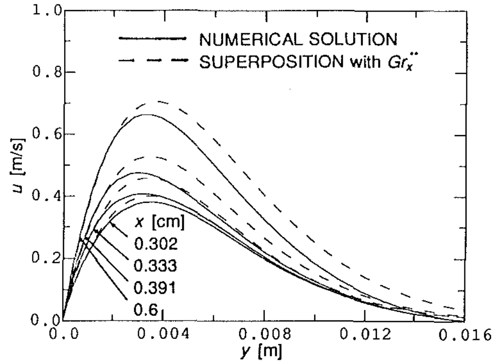

Fig. 5 Comparison of velocity profiles for natural convection over a discontinuity in surface temperature

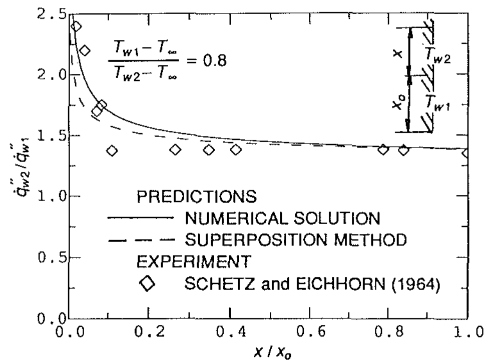

Fig. 6 Comparison of surface heat flux for natural convection over a discontinuity in surface temperature

6 compares calculated surface heat flux variations with experimental results (Schetz and Eichhorn, 1964) as a function of x/x_o, where $\dot q''_{w2}$ is the local heat transfer rate and $\dot q''_{w1}$ is the local heat transfer rate that would be obtained if the surface were maintained at T_{w1}. For the case of $T_{w2} < T_{w1}$, this approximate model cannot predict the fields near the discontinuity due to the inversion of the temperature at the surface. Since this model is based on a negative surface temperature gradient, it cannot be used in the case where there is a positive surface temperature gradient.

Natural Convection for Discrete Surface Heat Flux. The superposition technique is applied for the prediction of the surface temperature and Nu_x distributions, when there is a discontinuity in surface heat flux. The superposition technique predicts surface temperature and Nu_x distributions very well even near the discontinuity, whether the boundary conditions are given by $\dot q''_{w2} > \dot q''_{w1}$ or $\dot q''_{w2} < \dot q''_{w1}$. Figure 7 demonstrates the remarkable applicability of this superposition model for the prediction of heat transfer for electronic systems where heat sources are distributed along an adiabatic surface, which was numerically studied by Jaluria (1982).

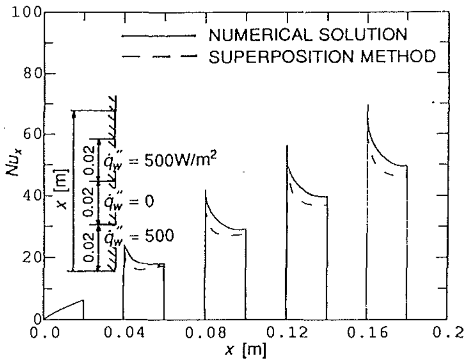

Fig. 7 Comparison of Nu_x for natural convection over distributed heating elements on an adiabatic surface

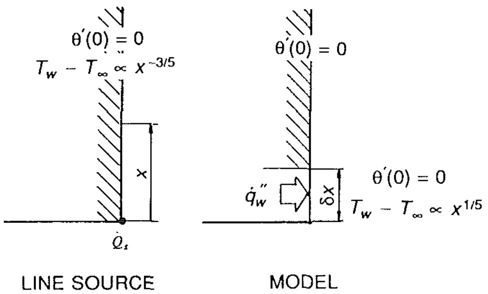

Fig. 8 Natural convection over a line source and a finite size heating element on an adiabatic surface

Natural Convection for a Line Source on a Adiabatic Surface. The physical schematic of an adiabatic surface with an embedded thermal line source and its model for the superposition method are shown in Fig. 8. The model substitutes a finite size heating element for the thermal line source. This example gives a physical insight into the superposition method. The exact solution for a line source on an adiabatic surface has been formulated by Jaluria and Gebhart (1977) and the downstream decay of the surface temperature difference is given by

$$[T_w(x) - T_\infty] = C_L \dot Q_s^{4/5} x^{-3/5} \tag{30}$$

where $\dot Q_s$ is the thermal energy input per unit length of the line source per unit time. To predict the downstream decay of surface temperature difference, the formulation for the isoflux case is used in the superposition method. Using equation (23), approximating boundary conditions for a line source by a finite-size element, and taking the limit of the size of heating element as $\delta x \to 0$ give

$$[T_w(x) - T_\infty]^{5/4} = \lim_{\delta x \to 0} \frac{1}{C_H} [\dot q''_w x^{1/4} - \dot q''_w (x - \delta x)^{1/4}]$$

$$= \frac{\dot q''_w \delta x\, x^{-3/4}}{4 C_H} \tag{31}$$

Assuming that $\dot q''_w \delta x = \dot Q_s$ and rewriting equation (31) give

$$[T_w(x) - T_\infty] = \frac{\dot Q_s^{4/5} x^{-3/5}}{4^{4/5} C_H^{4/5}} \tag{32}$$

which is in the same form as equation (30).

Mixed Convection Over Isoflux Surfaces. A local heat transfer rate for assisting mixed convection over *isoflux* vertical

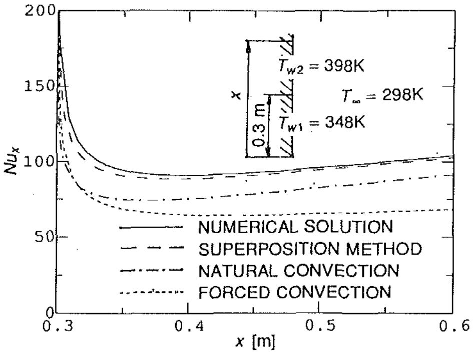

Fig. 9 Comparison of Nu_x for mixed convection over a discontinuity in surface temperature with $u_\infty = 1$ m/s

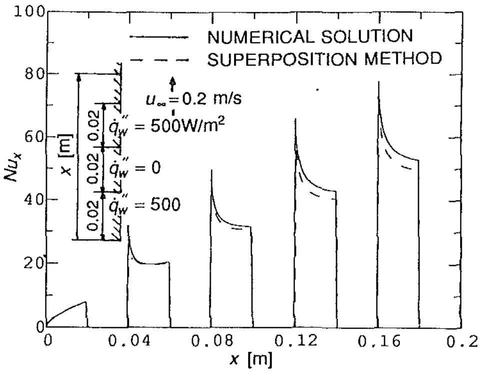

***Fig. 10* Comparison of Nu_x for mixed convection over distributed heating elements on an adiabatic surface with $u_\infty = 0.2$ m/s**

surfaces is predicted using the superposition method. Nusselt numbers in this case are directly obtained from the Nusselt numbers for pure forced convection and pure natural convection over isoflux vertical surfaces. Then, wall temperature distribution is assumed as

$$T_w - T_\infty = \frac{x\dot{q}_w''}{k\mathrm{Nu}_{x,M}} \tag{33}$$

Therefore, it is possible to predict the Nusselt number distribution by the superposition method for pure forced convection and pure natural convection over the surface whose temperature distribution is specified by equation (33). Hence, the approximated Nusselt number for assisting mixed convection is given by equation (29) using the Nusselt numbers obtained by the superposition method. Comparisons are made for various Grashof numbers with the variation of Reynolds number and show a good agreement of this model with numerical solutions.

Mixed Convection for Discrete Surface Temperature. The same boundary condition as for natural convection for the discrete surface temperature case is applied to compare local Nusselt numbers from the superposition method and numerical simulation for mixed convection and those for pure forced convection and pure natural convection. Since the free-stream velocity is 1 m/s and $\mathrm{Gr}_x/\mathrm{Re}_x^2$ varies from 1 to 4 after the discontinuity, both natural and forced convection effects should be included in calculating local heat transfer rates. The superposition method produces a close agreement with the numerical simulation. A comparison of Figs. 4 and 9 indicates that the error of the superposition method is less for the mixed convection case than for the natural convection case, which is due to the thermally linear characteristics of forced convection.

Mixed Convection for Discrete Surface Heat Flux. The same boundary condition as in the case of natural convection for discrete surface heat flux is applied for the comparison of the Nusselt numbers from the superposition method and the numerical simulation. A comparison of Figs. 7 and 10 shows that the local heat transfer rate is increased for the mixed convection case due to the mutual assistances of forced and natural convection. As stated earlier, it is shown that the linearizing tendency in forced convection decreases the error involved in the approximations by the superposition method.

General Applications. The demonstrated predictive ability of the superposition method for natural and mixed convection heat transfer over a thermally nonuniform vertical surface can also be expected in other cases, especially body force-driven motions. Laminar or turbulent flows with a thermally nonuniform boundary condition as well as the flow inside a porous medium can be analyzed by the proposed superposition method, provided that the Nusselt numbers for thermally uniform surfaces are supplied in a closed form, which can be obtained either experimentally or theoretically. Moreover, this method can greatly simplify the analysis of conjugate heat transfer phenomena, since it models the convection part by a similar formulation such as equation (22) or (23).

Conclusions

Despite the coupled and nonlinear nature of the momentum and temperature fields for natural and mixed convections, the superposition method predicts the local heat transfer rates very well on thermally discrete as well as thermally continuous vertical surfaces. The underlying concept for superposition is the linearity of energy, and not that of temperature. Since this method utilizes analytic formulations obtained from similarity analyses or experimental correlations for thermally uniform surfaces, calculations of the local heat transfer rates on thermally complicated surfaces only involve the same degree of difficulty as involved with those of forced convection heat transfer.

When the surface temperature is specified, the superposition method is shown to be useful except for the region very close to the surface temperature discontinuities and the region of positive surface temperature gradients. When the surface heat flux is specified, this method is generally useful even near the discontinuities. An extreme example, natural convection due to a line source on a vertical adiabatic surface, can be estimated well by the superposition method. Local heat transfer rates for assisting mixed convection over thermally nonuniform vertical surfaces are predicted successfully by the superposition method using the Nusselt numbers for pure forced and natural convection over such surfaces. The linearizing effect of the forced convection results in a more accurate prediction of heat transfer rates for assisting mixed convection by the superposition method than those for natural convection.

The present study shows that this superposition method is a simple and powerful tool for the prediction of thermal and momentum fields induced by natural convection phenomena and local heat transfer rates controlled by assisting mixed convection in such systems as electronic circuitry and some manufacturing systems without extensive numerical calculations. This superposition technique can be applied for any body force-induced flow systems with arbitrarily specified thermal boundary conditions, provided that local heat transfer rates for thermally uniform surfaces are supplied. Lastly, this method can simplify conjugate heat transfer problems, which remain for future study.

Acknowledgments

The authors wish to express their appreciation to Professor W. M. Kays of Stanford University for providing the STAN 7.

References

Chen, T. S., Tien, H. C., and Armaly, B. F., 1986, "Natural Convection on Horizontal, Inclined, and Vertical Plates With Variable Surface Temperature or Heat Flux," *International Journal of Heat and Mass Transfer*, Vol. 29, pp. 1465–1478.

Churchill, S. W., 1977, "A Comprehensive Correlating Equation for Laminar, Assisting, Forced and Free Convection," *AIChE Journal*, Vol. 23, pp. 10–16.

Churchill, S. W., and Usagi, R., 1972, "A General Expression for the Correlation of Rates of Heat Transfer and Other Phenomena," *AIChE Journal*, Vol. 18, pp. 1121–1128.

Crawford, M. E., and Kays, W. M., 1976, "STAN 5," NASA-CR-2742.

Hayday, A. A., Bowlus, D. A., and McGraw, R. A., 1967, "Free Convection From a Vertical Flat Plate With Step Discontinuities in Surface Temperature," ASME JOURNAL OF HEAT TRANSFER, Vol. 89, pp. 244–250.

Jaluria, Y., 1980, *Natural Convection Heat and Mass Transfer*, Pergamon Press, New York.

Jaluria, Y., 1982, "Buoyancy-Induced Flow Due to Isolated Thermal Sources on a Vertical Surface," ASME JOURNAL OF HEAT TRANSFER, Vol. 104, pp. 223–227.

Jaluria, Y., and Gebhart, B., 1977, "Buoyancy-Induced Flow Arising From a Line Thermal Source on an Adiabatic Vertical Surface," *International Journal of Heat and Mass Transfer*, Vol. 20, pp. 153–157.

Kao, T. T., Dotomo, G. A., and Elrod, H. G., Jr., 1977, "Free Convection Along a Nonisothermal Vertical Flat Plate," ASME JOURNAL OF HEAT TRANSFER, Vol. 99, pp. 72–78.

Kays, W. M., and Crawford, M. E., 1980, *Convective Heat and Mass Transfer*, McGraw-Hill, New York, pp. 313–331.

Kelleher, M., 1971, "Free Convection From a Vertical Plate With Discontinuous Wall Temperature," ASME JOURNAL OF HEAT TRANSFER, Vol. 93, pp. 349–356.

Kelleher, M., and Yang, K. T., 1972, "A Görtler-Type Series for Laminar Free Convection Along a Non-isothermal Vertical Plate," *The Quarterly Journal of Mechanics and Applied Mathematics*, Vol. 25, pp. 445–457.

Lee, S., and Yovanovich, M. M., 1987, "Laminar Natural Convection From a Vertical Plate With Variations in Wall Temperature," *Convective Transport*, ASME HTD-Vol. 82, pp. 111–119.

Lee, S., and Yovanovich, M. M., 1988, "Laminar Natural Convection From a Vertical Plate With Variations in Surface Heat Flux," ASME HTD-Vol. 96, pp. 197–205.

Lee, S., and Yovanovich, M. M., 1989, "Natural Convection From a Vertical Plate With Step Changes in Surface Heat Flux," *Heat Transfer in Convective Flows*, ASME HTD-Vol. 107, pp. 239–247.

Lin, H.-T., and Chen, C.-C., 1988, "Mixed Convection on Vertical Plate for Fluids of Any Prandtl Number," *Wärme- und Stoffübertragung*, Vol. 22, pp. 159–168.

Lin, H.-T., and Yu, W.-S., 1988, "Free Convection From a Vertical Plate With Concentrated and Distributed Thermal Sources," *Wärme- und Stoffübertragung*, Vol. 22, pp. 231–238.

Mahmood, T., and Merkin, J. H., 1988, "Similarity Solutions in Axisymmetric Mixed-Convection Boundary-Layer Flow," *Journal of Engineering Mathematics*, Vol. 22, pp. 73–92.

Oosthuizen, P. H., and Hart, R., 1973, "A Numerical Study of Laminar Combined Convective Flow Over Flat Plates," ASME JOURNAL OF HEAT TRANSFER, Vol. 60, pp. 60–63.

Ortega, A., and Moffat, R. J,. 1986, "Buoyancy Induced Convection in a Non-uniformly Heated Array of Cubical Elements on a Vertical Channel Wall," *Heat Transfer in Electronic Equipment 1986*, ASME HTD-Vol. 57, pp. 123–134.

Patankar, S. V., and Spalding, D. B., 1967, *Heat and Mass Transfer in Boundary Layers*, First Edition, Morgan-Grampian, London.

Scherberg, M. G., 1964, "Natural Convection From Wall Sections of Arbitrary Temperature Distribution by an Integral Method," *International Journal of Heat and Mass Transfer*, Vol. 7, pp. 501–516.

Schetz, J. A., and Eichhorn, R., 1964, "Natural Convection With Discontinuous Wall-Temperature Variations," *Journal of Fluid Mechanics*, Vol. 18, pp. 167–176.

Shai, I., and Barnea, Y., 1986, "Simple Analysis of Mixed Convection With Uniform Heat Flux," *International Journal of Heat and Mass Transfer*, Vol. 29, pp. 1139–1147.

Sparrow, E. M., 1955, "Laminar Free Convection on a Vertical Plate Prescribed Nonuniform Wall Heat Flux or Prescribed Nonuniform Wall Temperature," NACA TN 3508.

Wilks, G., 1973, "Combined Forced and Free Convection Flow on Vertical Surfaces," *International Journal of Heat and Mass Transfer*, Vol. 16, pp. 1958–1964.

D. L. Littlefield
Post-Doctoral Fellow,
U.S. Army Ballistic Research Laboratory,
Aberdeen Proving Ground, MD

P. V. Desai
Professor,
George W. Woodruff School of Mechanical
Engineering,
Georgia Institute of Technology,
Atlanta, GA

Incipient Buoyant Thermal Convection in a Vertical Cylindrical Annulus

The incipient buoyant thermal convection in a vertical cylindrical annulus when heated from below is examined. The ends are assumed to be free, and the sidewalls perfectly conducting. The temperature needed to initiate fluid motion is expressed nondimensionally in terms of the Rayleigh number. The analytical conflict that arises for annuli of infinite aspects ratios due to insufficient independent boundary conditions is resolved. Calculations for the critical Rayleigh numbers are presented for a variety of geometries, and the corresponding velocity and temperature perturbations are also shown. The number of cells increases as the aspect and radius ratio decrease with a strong bias towards the development of azimuthally varying cells. These changes in cellular behavior are expected based on physical justifications and comparisons with previous studies.

Introduction

The initiation of convection in a pure fluid heated from below and bounded by vertical walls has been the subject of many investigations. The original analytical studies by Hales (1937) and Ostroumov (1947) dealt primarily with incipient buoyant thermal convection in vertical cylinders. The critical temperature gradient needed to initiate fluid motion was expressed nondimensionally in terms of the Rayleigh number. It was determined that at large aspect ratios, convection in cylinders initiates in a bicellular pattern, with two diametrically opposed antisymmetric cells. The analysis was confirmed by the results of experiments conducted for a wide range of thermal conductivities.

The stability of thermally buoyant convective flows in infinite vertical channels was later examined for perfectly insulated sidewalls by Yih (1959). It was discovered that the principle of the exchange of stabilities is valid for this configuration. The critical Rayleigh number, determined by assuming two-dimensional disturbances, was given as $\mathrm{Ra}_c = 31.29$. This analysis was later generalized by Wooding (1960) to include three-dimensional disturbances and sidewalls that were perfectly conducting or insulated. For perfectly insulated sidewalls, the three-dimensional analysis indicated that thermally buoyant convective motion initiates at all temperature gradients, no matter how small. This was attributed to the instabilities associated with insulated sidewalls. For perfectly conducting sidewalls, which is a much more stable configuration, the critical Rayleigh number was determined as $\mathrm{Ra}_c = \pi^4$. A later study by Edwards (1967) included the analysis of vertical channels over a wide range of aspect ratios and sidewall thermal conductivities. Experimental measurements yielded critical Rayleigh numbers slightly lower than the analytical predictions. The differences were attributed to radiation effects.

Sorokina and Chudinov (1955) examined incipient buoyant thermal convection in a vertical cylindrical annulus of infinite aspect ratio with insulated sidewalls. They showed that with the radius ratio of the annulus approaching infinity, the critical Rayleigh number approaches a value corresponding to that for an infinite vertical cylinder. For a fluid-saturated porous medium in an annulus of varying aspect ratio, Bau and Torrance (1981) observed a wide range of preferred convective modes for different geometries. Experiments by Stork and Müller (1975) for an annulus with fixed ends also exhibited various convective modes.

The methodology for the analysis of incipient convection in an annulus of finite aspect ratio follows from the analysis for vertical cylinders by Catton and Edwards (1970) and Littlefield (1989). The difference in boundary conditions leads to a slightly more complicated formulation. However, the methodology does not apply to the limiting case of infinite aspect ratio with sidewalls of ideal conductivity. That problem has not been resolved due to an analytical conflict arising from an insufficient number of boundary conditions.

The present analysis considers incipient buoyant thermal convection in a vertical cylindrical annulus. The sidewalls are assumed to be perfectly conducting, and the ends are assumed to be free and flat. All fluid properties are assumed constant, with the exception of a linear variation of the density with temperature. All effects of viscous dissipation are neglected, as well as any radiation effects. Calculations for the critical Rayleigh numbers are presented over a wide range of aspect and radius ratios. Also resolved is the boundary condition limitation for an annulus of infinite aspect ratio. The critical velocity and temperature profiles corresponding to these critical Rayleigh numbers are also presented, as well as the streamlines.

Analysis

The governing equations for the incipient buoyant thermal convection in vertical geometries are given by Chandrasekhar (1959) as

$$\nabla \cdot \mathbf{V} = 0 \tag{1}$$

$$\frac{\partial \mathbf{V}}{\partial t} = -\frac{1}{\rho}\nabla p + \nu \nabla^2 \mathbf{V} + g\beta \hat{k} T \tag{2}$$

and

$$\frac{\partial T}{\partial t} - \Gamma v_z = \alpha \nabla^2 T \tag{3}$$

where $\mathbf{V}$, v_z, p, and T are the disturbance velocity, its axial component, disturbance pressure, and temperature, respectively, ρ is the density, g is the gravitational acceleration, β is the volumetric coefficient of thermal expansion, ν is the kinematic viscosity, and α is the thermal diffusivity. The equilib-

---

Contributed by the Heat Transfer Division for publication in the JOURNAL OF HEAT TRANSFER. Manuscript received by the Heat Transfer Division June 26, 1989; revision received January 4, 1990. Keywords: Natural Convection.

rium temperature gradient is Γ. It has been demonstrated by Littlefield (1989) that these equations may be combined into one equation for the temperature, given as

$$\nabla^{*6}T^* + \mathrm{Ra}\left[\nabla^{*2} - \frac{\partial^2}{\partial z^{*2}}\right]T^* = 0 \tag{4}$$

where $T^* = T/\Gamma l$, $\nabla^* = \nabla/l$, and $z^* = z/l$; l is an appropriate length scale. The solution to equation (4) is given as

$$T^* = \hat{T}(r^*)\sin mz^*\cos n\theta \tag{5}$$

where m is real and n is an integer, and

$$\hat{T} = C_1J_n(q_1r^*) + C_2Y_n(q_1r^*) + C_3J_n(q_2r^*) + C_4Y_n(q_2r^*) + C_5I_n(q_3r^*) + C_6K_n(q_3r^*) \tag{6}$$

q_1, q_2, and q_3 are determined from the roots δ_1, δ_2, and δ_3 of the polynomial

$$\delta^3 + 3m^2\delta^2 + (3m^4 - \mathrm{Ra})\,\delta + m^6 = 0 \tag{7}$$

which for $\mathrm{Ra} \leq (27/4)m^4$ has two positive real roots and one negative real root. q_1 and q_2 are the square roots of the positive roots and q_3 is the square root of the absolute value of the negative root.

The solution given by equation (5) identically satisfies the boundary conditions on the free ends. The sidewall boundary conditions are used to determine the arbitrary constants in equation (6) and are given as

$$\hat{v}_r = \hat{v}_\theta = \hat{v}_z = \hat{T} = 0 \tag{8}$$

at $r^* = 1$ and $1/R$, where the length scale l is the outer radius r_o, and R is the radius ratio. The velocities in equation (8) are defined from compatibility conditions and are given as

$$v_r^* = \hat{v}_r(r^*)\cos mz^*\cos n\theta$$

$$v_\theta^* = \hat{v}_r(r^*)\cos mz^*\sin n\theta \tag{9}$$

and

$$v_z^* = \hat{v}_z(r^*)\sin mz^*\cos n\theta$$

where $\mathbf{V}^* = \mathbf{V}l/\alpha$. Application of these boundary conditions to equation (6) results in transcendental equations for the critical Rayleigh number, which are given in the Appendix. The corresponding disturbance velocity and temperature are then determined using the scaled variables $\overline{T} = \mathrm{Ra}^{1/2}T$, $\overline{v}_r = \hat{v}_r$, $\overline{v}_\theta = \hat{v}_\theta$, and $\overline{v}_z = \hat{v}_z$ to assure that the profiles are all the same order of magnitude.

Solution for Vanishing Axial Wavenumbers

Littlefield (1989) has shown that when $m = 0$, equations (1) - (3) result in simplified ordinary differential equations for the disturbance amplitudes $\overline{v}_z$ and $\overline{T}$, given as

$$D_n^2\,\overline{v}_z + \overline{T} = 0 \tag{10}$$

and

$$D_n^2\,\overline{T} + \overline{v}_z = 0 \tag{11}$$

where

$$D_n^2 = \frac{1}{\overline{r}}\frac{d}{d\,\overline{r}}\left(\overline{r}\,\frac{d}{d\,\overline{r}}\right) - \frac{n^2}{\overline{r}^2} \tag{12}$$

and $\overline{r} = \mathrm{Ra}^{1/4}r/r_o$. Equations (10) and (11) may be combined into one equation for $\overline{T}$, given as

$$\left[D_n^2 + 1\right]\left[D_n^2 - 1\right]\hat{T} = 0 \tag{13}$$

The appropriate boundary conditions for equation (13) are $\overline{v}_z = \overline{T} = 0$ at $\overline{r} = \mathrm{Ra}^{1/4}$ and $\mathrm{Ra}^{1/4}/R$. The boundary conditions as written, however, are redundant. If $\overline{v}_z = 0$ for any $\overline{r}$, for example, equation (11) requires $D_n^2\overline{T} = 0$. But equation (13) requires $\overline{T}$ to be zero anywhere that $D_n^2\overline{T} = 0$. Therefore, $\overline{v}_z = 0$ automatically implies $\overline{T} = 0$. This redundancy inhibits a formulation of the solution to equation (13) since four independent boundary conditions cannot be written.

This boundary condition limitation was resolved by Littlefield (1989). From the examination of equations (10) and (11) with boundary conditions (14), it is evident that interchanging $\overline{v}_z$ and $\overline{T}$ does not change the formulation of the problem whatsoever. This clearly requires $\overline{v}_z$ and $\overline{T}$ to have solutions that differ only by a multiplicative constant. The substitution of solutions of this form, however, results in only two possible multiplicative constants: 1 and -1. Therefore, the solutions to equations (10) and (11) must conform to either $\overline{v}_z = \overline{T}$ or $\overline{v}_z = -\overline{T}$. $\overline{v}_z = \overline{T}$ corresponds to the situation where positive perturbations in the temperature lead to positive perturbations in the axial velocity. Physical intuition agrees with this situation; a positive perturbation in the temperature will result in a net localized increase in the buoyancy force, which results in a positive perturbation in the axial velocity. However, the same argument requires rejection of the scenario where $\overline{v}_z = -\overline{T}$. Although the mathematical problem related to $\overline{v}_z = -\overline{T}$ has some eigenvalues and corresponding eigenfunctions, they have no significance to the physical problem.

It is concluded that $\overline{v}_z = \overline{T}$. The solutions to equations (10) and (11) are therefore

$$\overline{v}_z = \overline{T} = C_1J_n(\overline{r}) + C_2Y_n(\overline{r}) \tag{15}$$

Application of the boundary conditions to equation (15) yields a transcendental equation for the critical Rayleigh number given as

$$J_n\left(\mathrm{Ra}^{1/4}\right)\,Y_n\left(\mathrm{Ra}^{1/4}/R\right) - J_n\left(\mathrm{Ra}^{1/4}\,R\right)\,Y_n\left(\mathrm{Ra}^{1/4}\right) = 0 \tag{16}$$

Equation (16) does not apply for axisymmetric conditions, because the solution does not identically satisfy the no net flow

Nomenclature

A_r = aspect ratio
C = arbitrary constant
D_n^2 = differential operator
g = gravitational acceleration
J, I, Y, K = Bessel functions
$\hat{k}$ = axial unit vector
l = reference length
m = axial wavenumber
n = azimuthal wavenumber
p = pressure
q = Bessel function argument
R = radius ratio
Ra = $g\beta\Gamma l^4/\nu\alpha$ = Rayleigh number

r = radial direction
r_i = inner radius
r_o = outer radius
T = temperature
t = time
$\mathbf{V}$ = velocity
v_d = velocity difference
v_r = radial velocity
v_s = velocity sum
v_θ = azimuthal velocity
v_z = axial velocity
z = axial direction
α = thermal diffusivity
β = volumetric coefficient of thermal expansion

Γ = equilibrium temperature gradient
δ = characteristic polynomial variable
θ = azimuthal direction
ν = kinematic viscosity
ρ = density

Superscripts

$*$ = dimensionless variable
$\hat{}$ = radial dependence of variable
$\overline{}$ = scaled radial dependence of variable
$'$ = differentiation

Table 1 Ra_c versus A_r for vertical cylindrical annuli at three radius ratios

	R = 1.10		R = 2.00		R = 50.0	
Aspect Ratio	Ra_c	n_{min}	Ra_c	n_{min}	Ra_c	n_{min}
∞	1428130	1	1670.57	1	216.617	1
10	1898030	9	2080.19	1	244.166	1
5.0	2539520	12	2807.43	2	247.725	1
2.0	6161860	19	6816.76	3	453.241	1
1.0	--	--	26480.4	4	1850.45	1
0.5	--	--	213622	7	14839.2	2

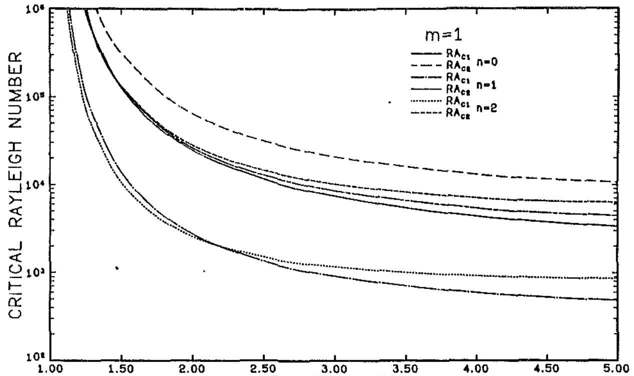

Fig. 1 Ra_c versus R for the first two axisymmetric, diametrically antisymmetric, and quadrametric modes in a vertical cylindrical annulus

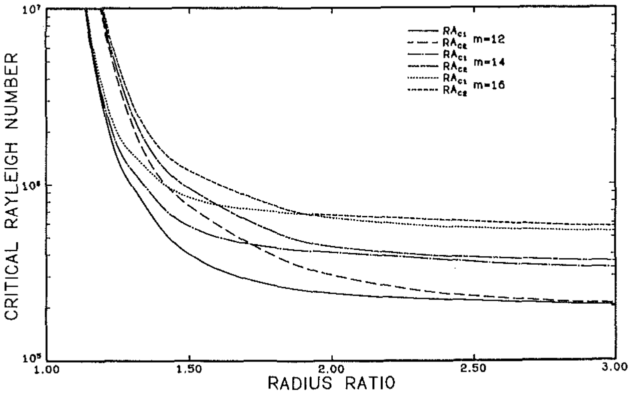

Fig. 2 Ra_c versus R for the primary and secondary modes in a vertical cylindrical annulus at three axial wavenumbers when $n = n_{\min}$

condition. Fortunately, the proper formulation for axisymmetric flow does not have the boundary condition redundancy problem. In fact, its solution is identical to that presented for axisymmetic flow with perfectly insulated sidewalls by Sorokina and Chudinov (1955).

Results and Discussion

Results of calculations for the lowest critical Rayleigh number versus the aspect ratio for three different radius ratios are shown in Table 1. The corresponding azimuthal wavenumber n for each critical Rayleigh number is also shown in Table 1. The axial wavenumber m does not appear because it is related to the geometry of the annulus $\{m = \pi R / A_r(R-1)\}$. This is a consequence of the fact that convection initiates with only one cell in the axial direction.

The limiting cases of Table 1 compare favorably with previous analytical and experimental studies. At large radius ratios, as the effect of the inner wall becomes small, the critical Rayleigh numbers approach the corresponding values for a vertical cylinder; this is reported by Catton and Edwards (1970) and Littlefield (1989). When $A_r = 5$, for example, the critical Rayleigh number for a cylinder is 237.0, as compared to 247.7 for an annulus with $R = 50$. In addition, at small radius ratios, when curvature effects are negligible, the critical Rayleigh numbers approach the values corresponding to those for a vertical channel, as reported by Wooding (1960) and Edwards (1967). When $A_r \rightarrow \infty$, for example, the critical Rayleigh number for a vertical channel is 97.41, as compared to 97.54 for an annulus with $R = 1.1$ (in both cases, the reference length is the gap size for the channel or the annulus). Also, at small aspect ratios the effects of the sidewalls become small. The critical Rayleigh number, when based on the height, approaches $27\pi^4/4$, as reported by Lord Rayleigh (1916).

Qualitative comparisons may also be made between the present study and the experiments of Stork and Müller (1975). Although the difference in end conditions between the two gives lower critical Rayleigh numbers in the former, the preferred convective modes at the incipient point are in good agreement. For example, for $A_r = 1/3$ and $R = 2.2$, Stork and Müller (1975) report a presence of 22 cells. The same result is obtained in the present analysis for $A_r = 0.3$ and $R = 2$.

Table 1 indicates that at large aspect ratios, convection initiates in the diametrically antisymmetric ($n = 1$) mode, which describes a motion for which two counterrotating cells are present when viewed in the r-θ plane. At smaller aspect ratios, however, the initiating mode depends on the radius ratio. At large radius ratios, for example, the initiating mode is mainly diametrically antisymmetric, except at very small aspect ratios. For smaller radius ratios, however, the initiating mode corresponds to increasingly larger azimuthal wavenumbers as the aspect ratio decreases. This trend becomes even more pronounced as the radius ratio decreases.

Figures 1 and 2 also demonstrate the transitions that occur in the initiating mode as the geometry is varied. Figure 1, for example, shows the lowest two critical Rayleigh number versus the radius ratio for three azimuthal wavenumbers when $m = 1$. The tendency toward larger initiating azimuthal wavenumbers at smaller radius ratios is evident from the crossing of the diametrically antisymmetric and quadrametrically symmetric ($n = 2$) modes when $R \approx 2.2$. This behavior was found to be typical of most other small axial wavenumbers. At large axial wavenumbers, on the other hand, the transitions are more complex. Figure 2 shows the lowest two critical Rayleigh numbers versus the radius ratio at three axial wavenumbers. The azimuthal mode crossing that occurs at small axial wavenumbers also occurs at large axial wavenumbers. This trend is not shown on the figure because for large values of m, the critical Rayleigh numbers are nearly coincident at all azimuthal wavenumbers for fixed radius ratio. The frequency of this mode crossing also increases with increasing axial wavenumbers. In addition, Fig. 2 demonstrates that at certain radius ratios the curves for the primary and secondary critical Rayleigh numbers have discontinuous slopes. One example of this behavior occurs at $m = 16$ when $R \approx 1.9$.

The transitions that occur in the critical Rayleigh number, as well as other aspects of incipient convection in vertical cylindrical annuli, may be best interpreted through an examination of the velocity and temperature perturbations. The velocity and temperature disturbance profiles that are typical for annuli of most radius ratios are shown in Figs. 3 and 4. Figure 3 shows representative distributions for $A_r = 2.0$ that are also typical of larger aspect ratios. The only differences in the profiles at larger aspect ratios are the smaller magnitudes in $\bar{v}_r$ and $\bar{v}_\theta$ and the smaller differences between $\bar{v}_z$ and $\bar{T}$. The limiting case of infinite aspect ratio corresponds to the solution when $m = 0$, for which $\bar{v}_z = \bar{T}$ and $\bar{v}_r = \bar{v}_\theta = 0$. The cellular behavior associated with Fig. 3, however, depends on the aspect

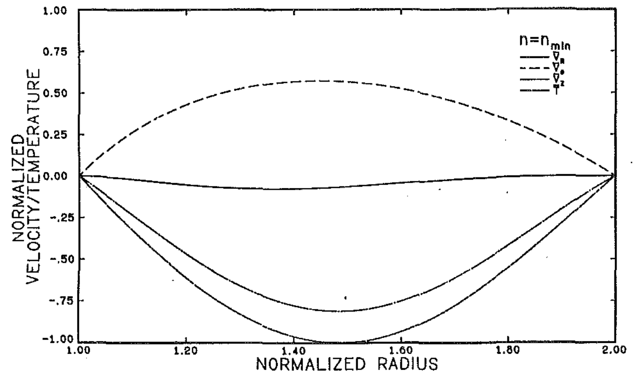

Fig. 3 $\bar{v}_r$, $\bar{v}_\theta$, $\bar{v}_z$, and $\bar{T}$ **versus** Rr^* **for a vertical cylindrical annulus with** A_r = 2.0 **and** $n = n_{\min}$

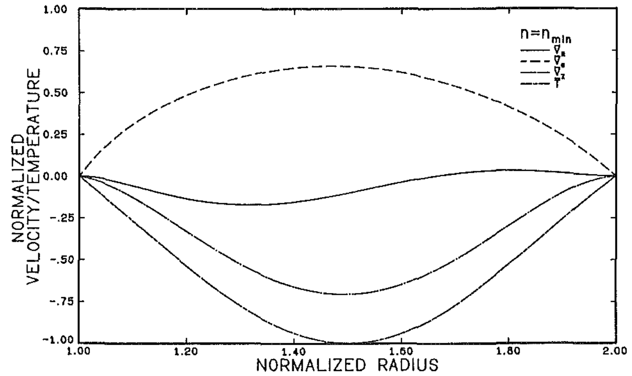

Fig. 4 $\bar{v}_r$, $\bar{v}_\theta$, $\bar{v}_z$, and $\bar{T}$ **versus** Rr^* **for a vertical cylindrical annulus with** A_r = 0.8 **and** $n = n_{\min}$

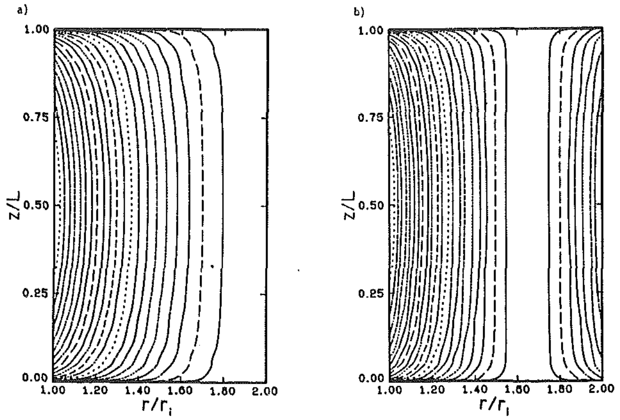

Fig. 5 Streamlines for a vertical cylindrical annulus for (*a*) A_r = 2.0 **and** (*b*) A_r = 0.8 **when** $n = n_{\min}$

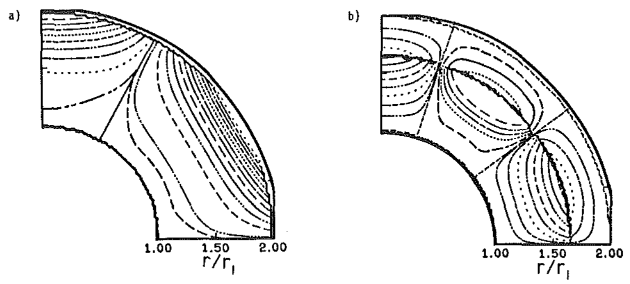

Fig. 6 Streamlines for a vertical cylindrical annulus for (*a*) A_r = 2.0 **and** (*b*) A_r = 0.8 **when** $n = n_{\min}$

ratio, because the azimuthal dependence of the initiating motion is very aspect ratio dependent. When $A_r = 2$, for example, the velocity profiles indicate the presence of six cells, since $n_{\min} = 3$ for these conditions. Figure 4 shows the velocity and temperature perturbations for $A_r = 0.8$. This figure indicates that a transition has occurred, when compared to Fig. 3, because the radial velocity profile exhibits a change in direction near the outer wall. This change in direction indicates the presence of another cell in the radial direction. Since $n_{\min} = 5$ for this aspect ratio, a total of 20 cells are present.

The transition to a larger number of cells in the radial direction occurs more frequently as the aspect ratio decreases, and has been observed by Littlefield (1989) in cylinders. In cylindrical annuli, however, the changes are not quite as rapid, and the effects on the critical Rayleigh number are much different. For vertical cylinders, an increase in the number of cells in the radial direction is accompanied by an oscillation in the initiating motion between the diametrically antisymmetric and axisymmetric modes. For a vertical annulus, however, an increase in the number of cells is accompanied only by increases in the azimuthal wavenumber.

Examination of the streamlines leads to a better understanding of the nature of cell development, as well as the effects on the corresponding critical Rayleigh numbers. In Fig. 5 the streamlines, when viewed in the r–z plane, are shown for aspect ratios 2.0 and 0.8, respectively, at a radius ratio of 2. These profiles are also typical for annuli of different radius ratios. The cell pattern differences indicated previously in Figs. 3 and 4 are clearly evident, but the streamlines are still very similar in appearance. In addition, the gradients in the stream function close to the wall, particularly in Fig. 5(*a*), are small. This characteristic is typical of the initiating motion for any geometry because smaller buoyancy forces are required to overcome the viscous forces when the velocity gradients are minimal. The streamlines in Fig. 6, on the other hand, are very different in appearance. In this figure the streamlines are shown when viewed in the r–θ plane. The difference in the initiating azimuthal wavenumber leads to the different cellular characteristics. Also apparent is the division and recombination of streamlines at cell boundaries. These "stagnation" lines indicate a change in the direction of the flow and are a characteristic of three-dimensional streamlines when shown in a two-dimensional plane.

The changes in cell characteristics that occur as the geometry is changed are a direct consequence of the changes in the corresponding critical Rayleigh numbers. In Fig. 1, for example, the curves corresponding to the lowest critical Rayleigh numbers for the diametrically antisymmetric and quadrametrically symmetric motions crossed each other at $R \approx 2.2$. This crossing is accompanied by a change of the cellular characteristics in the azimuthal direction of the initiating flow, because when $m = 1$ and $R < 2.2$, the initiating motion consists of four cells, but for $R > 2.2$ it consists of two. Likewise, in Fig. 2 the curves for the lowest critical Rayleigh numbers when $m = 16$ and $n = n_{\min}$ had discontinuous slopes at $R \approx 1.9$. This is an indication of a change of the radial variation in the cells of the initiating flow. When $R > 1.9$, for example, two radially varying cells are present and for $R < 1.9$ one radially varying cell exists. The total number of cells depends on $n_{\min}$ in each case.

These changes in the initiating flow also indicate a strong propensity for the formation of azimuthally varying cells in vertical annuli, when compared with radially varying cells. This occurrence can be easily justified by physical arguments. First, cells that form in the azimuthal direction are more uniform in size when compared to radially varying cells. Cells of uniform size always form more easily than nonuniform cells, because they have inherently lower local velocities. These lower velocities lead to lower internal viscous stresses, and consequently

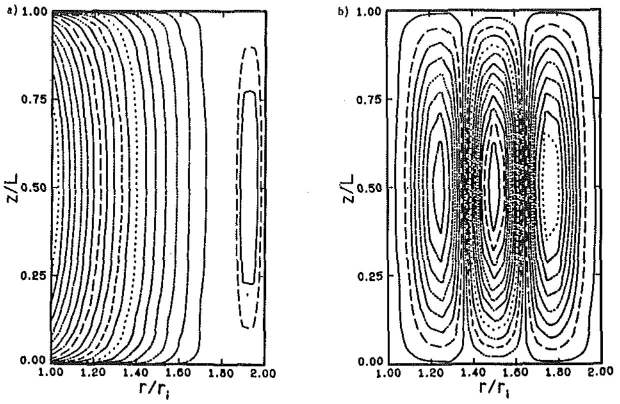

Fig. 7 Streamlines for a vertical cylindrical annulus when $A_r = 0.2$ for (*a*) $n = 16$ and (*b*) axisymmetric conditions

lower critical Rayleigh numbers. Figure 7, which shows streamlines for a limiting geometric configuration, effectively demonstrates this trend. The streamlines on the left correspond to a critical Rayleigh number of about 1.3×10^6 and an azimuthal wave number of 16. The streamlines on the right, on the other hand, correspond to a critical Rayleigh number of about 1.6×10^6 and are for axisymmetric conditions. The former, which indicates the presence of 64 cells, is a more likely condition than the latter, which consists of four cells. It seems almost inconceivable that the motion of 64 cells can occur under a smaller buoyancy force than the motion of four cells. The strong tendency toward azimuthally varying cells, however, permits this condition. Figure 7 also shows that azimuthally varying cells generally have lower wall shear stresses when compared with radially varying cells, because the gradients in the stream function are smaller near the sidewalls. A smaller buoyancy force is required to overcome these lower shear stresses, which result in lower critical Rayleigh numbers for cells forming in the azimuthal direction.

Although the propensity for the formation of azimuthally varying cells has been established, it does not explain why more cells develop in the first place as the aspect and radius ratios decrease. The changes in relative length scales that occur as the geometry is changed may be identified as the primary cause. For example, at large aspect ratios the radial and azimuthal length scales are small. The fluid travels only a short distance before it encounters a sidewall or the boundary of another cell, so no advantage is gained in the formation of new cells. At small aspect ratios, however, the relative azimuthal and radial length scales are larger. It is conceivable that the viscous forces could eventually stop the fluid before it encounters a boundary. This initiates the formation of a new cell, for which the azimuthal variety is the most likely, as explained earlier. Similarly, as the radius ratio decreases, the relative length scale in the azimuthal direction increases, which enhances the azimuthal cell development. At large radius ratios slight increases are found in the radial variation of cells, but these changes are generally overshadowed by the azimuthal variations.

These changes of the cellular characteristics in vertical annuli also follow the expected behavior when compared with the cellular development in horizontal and vertical channels. For example, a vertical annulus of large aspect ratio and small radius ratio displays the characteristics of infinitely tall vertical channels, for which convection initiates with one, large cell. As the aspect ratio decreases, more cells form in the azimuthal direction, which is similar to vertical channels of finite aspect ratio. At small aspect ratios and large radius ratios, the initiating motion in an annulus consists of many longitudinally varying cells, which is similar to the motion in horizontal channels. In every case a change in the number and location of cells is simply an indication of the changes required to minimize the thermal energy needed for fluid motion.

Conclusions

The incipient buoyant thermal convection in a vertical cylindrical annulus with free ends has been examined. Results are presented for the critical Rayleigh number and the corresponding critical temperature and velocity disturbances. The preferred convective modes exhibit a variety of cellular characteristics, with azimuthal cells occurring most frequently. The number of cells generally increases as the aspect and radius ratios decrease; physical arguments support these trends. The analytical results compare favorably with previous experimental results.

References

Bau, H. H., and Torrance, K. E., 1981, "Onset of Convection in a Permeable Medium Between Coaxial Vertical Cylinders," *Phys. Fluids*, Vol. 24, No. 3, pp. 382–385.

Catton, I., and Edwards, D. K., 1970, "Initiation of Thermal Convection in Finite Right Circular Cylinders," *AIChE Journal*, Vol. 16, No. 4, pp. 594–601.

Chandrasekhar, S., 1961, *Hydrodynamic and Hydromagnetic Stability*, Oxford University Press, United Kingdom.

Edwards, D. K., 1967, "Suppression of Cellular Convection by Lateral Walls," ASME JOURNAL OF HEAT TRANSFER, Vol. 91, pp. 145–150.

Hales, A. L., 1937, "Convection Currents in Geysers," *Roy. Astro. Soc. Geophy. Supply.*, Vol. 4, pp. 122–137.

Littlefield, D. L., 1989, "Incipient Buoyant Thermal Convection in Vertical Cylindrical Geometries," Ph.D. Thesis, Georgia Institute of Technology, Atlanta, GA.

Ostroumov, G. A., 1947, "Natural Convection Heat Transfer in Closed Vertical Tubes," *Izv. Estestv. Nauch. Inst. Perm. Univ.*, Vol. 12, No. 4, p. 113.

Rayleigh, Lord, 1916, "On Convective Currents in a Horizontal Layer of Fluid When the Higher Temperature Is on the Underside," *Phil. Mag.*, Vol. 32, pp. 527–546.

Sorokina, A. I., and Chudinov, A. A., 1955, "Steady Free Convection Between Two Vertical Coaxial Cylinders," *Uchen. Zap. Perm. Univ.*, Vol. 9, No. 4, p. 49.

Stork, K., and Müller, V., 1975, "Convection in Boxes: an Experimental Investigation in Vertical Cylinders and Annuli," *J. Fluid Mech.*, Vol. 71, pp. 231–240.

Wooding, R. A., 1960, "Instability of a Viscous Liquid of Variable Density in a Vertical Hele-Shaw Cell," *J. Fluid Mech.*, Vol. 7, No. 4, pp. 501–515.

Yih, C. S., 1959, "Thermal Instability of Viscous Fluids," *Quart. Appl. Math.*, Vol. 17, No. 1, pp. 25–42.

APPENDIX

Application of the Boundary Conditions to Equation (6)

1 Axisymmetric Conditions. For axisymmetric flow the azimuthal perturbation velocity is identically zero and the boundary conditions are

$$\hat{v}_r = \hat{v}_z = \hat{T} = 0 \tag{A1}$$

at $r^* = 1$ and $1/R$. The perturbation velocities may be expressed in terms of the temperature as

$$\hat{v}_r = \frac{m}{r^*} \int r^* \left[D_o^2 - m^2 \right] \hat{T} \, dr^* \tag{A2}$$

and

$$\hat{v}_z = - \left[D_o^2 - m^2 \right] \hat{T} \tag{A3}$$

which gives

$$v_r = -m \left[C_1 \frac{\left(q_1^2 + m^2\right)}{q_1} J_1(q_2 r^*) \right.$$

$$+ C_2 \frac{\left(q_1^2 + m^2\right)}{q_1} Y_1(q_1 r^*)$$

$$+ C_3 \frac{\left(q_2^2 + m^2\right)}{q_2} J_1(q_2 r^*)$$

$$+ C_4 \frac{\left(q_2^2 + m^2\right)}{q_2} Y_1(q_2 r^*)$$

$$- C_5 \frac{\left(q_3^2 - m^2\right)}{q_3} I_1(q_3 r^*) + C_6 \frac{\left(q_3^2 - m^2\right)}{q_3} K_1(q_3 r^*)\Bigg] \tag{A4}$$

and

$$\begin{aligned}\hat{v}_z = {} & C_1\left(q_1^2 + m^2\right) J_o(q_1 r^*) + C_2\left(q_1^2 + m^2\right) Y_o(q_1 r^*) \\ & + C_3\left(q_2^2 + m^2\right) J_o(q_2 r^*) + C_4\left(q_2^2 + m^2\right) Y_o(q_2 r^*) \\ & - C_5\left(q_3^2 - m^2\right) I_o(q_3 r^*) - C_6\left(q_3^2 - m^2\right) K_o(q_3 r^*)\end{aligned} \tag{A5}$$

The boundary conditions require equations (A4), (A5), and (6), for $n = 0$, to be zero when evaluated at $r^* = 1$ and $1/R$. Nontrivial solutions are obtained when the determinant formed from the 6×6 matrix of these equations vanishes, resulting in a transcendental equation for the critical Rayleigh number.

2 Three-Dimensional Conditions. The axial velocity may be determined from the energy equation as

$$\hat{v}_z = -\left[D_n^2 - m^2\right] \hat{T} \tag{A6}$$

which gives

$$\begin{aligned}\hat{v}_z = {} & C_1\left(q_1^2 + m^2\right) J_n(q_1 r^*) + C_2\left(q_1^2 + m\right) Y_n(q_1 r^*) \\ & + C_3\left(q_2^2 + m^2\right) J_n(q_2 r^*) + C_4\left(q_2^2 + m^2\right) Y_n(q_2 r^*) \\ & - C_5\left(q_3^2 - m^2\right) I_n(q_3 r^*) - C_6\left(q_3^2 - m^2\right) K_n(q_3 r^*)\end{aligned} \tag{A7}$$

The radial and azimuthal velocities must satisfy the equations

$$\left[D_{n+1}^2 - m^2\right] \hat{v}_z = \hat{p}' + \frac{n\hat{p}}{r^*} \tag{A8}$$

and

$$\left[D_{n-1}^2 - m^2\right] \hat{v}_d = \hat{p}' - \frac{n\hat{p}}{r^*} \tag{A9}$$

where

$$\begin{aligned}\hat{v}_s &= \hat{v}_r + \hat{v}_\theta \\ \hat{v}_d &= \hat{v}_r - \hat{v}_\theta\end{aligned} \tag{A10}$$

$\hat{p}$ is determined from the axial momentum equation, given by

$$m\hat{p} + \left[D_n^2 - m^2\right] \hat{v}_z + \mathrm{Ra}\hat{T} = 0 \tag{A11}$$

where

$$p = \frac{\hat{p}(r^*)\, l^2}{\rho\nu\alpha} \cos mz^* \cos n\theta \tag{A12}$$

The homogeneous solutions to equations (A8) and (A9) that satisfy the continuity equation are given by

$$\hat{v}_s = C_7 I_{n+1}(mr^*) + C_8 K_{n+1}(mr^*) \tag{A13}$$

and

$$\hat{v}_d = - C_7 I_{n-1}(mr^*) - C_8 K_{n-1}(mr^*) \tag{A14}$$

When combined with the particular solutions, the total solutions for $\hat{v}_s$ and $\hat{v}_d$ are given by

$$\begin{aligned}\hat{v}_s = {} & \frac{q_1\left[\left(q_1^2 + m^2\right) - \mathrm{Ra}\right]}{m\left(q_1^2 + m^2\right)} \left[C_1 J_{n+1}(q_1 r^*) + C_2 Y_{n+1}(q_1 r^*)\right] \\ & + \frac{q_2\left[\left(q_2^2 + m^2\right)^2 - \mathrm{Ra}\right]}{m\left(q_2^2 + m^2\right)} \left[C_3 J_{n+1}(q_2 r^*) + C_4 Y_{n+1}(q_2 r^*)\right] \\ & + \frac{q_3\left[\left(q_3^2 - m^2\right)^2 - \mathrm{Ra}\right]}{m\left(q_3^2 - m^2\right)} \left[C_5 I_{n+1}(q_3 r^*) - C_6 K_{n+1}(q_3 r^*)\right] \\ & + C_7 I_{n+1}(mr^*) + C_8 K_{n+1}(mr^*)\end{aligned} \tag{A15}$$

and

$$\begin{aligned}\hat{v}_d = {} & - \frac{q_1\left[\left(q_1^2 + m^2\right)^2 - \mathrm{Ra}\right]}{m\left(q_3^2 + m^2\right)} \left[C_1 J_{n-1}(q_1 r^*) + C_2 Y_{n-1}(q_1 r^*)\right] \\ & - \frac{q_3\left[\left(q_2^3 + m^2\right)^2 - \mathrm{Ra}\right]}{m\left(q_3^2 + m^2\right)} \left[C_3 J_{n-1}(q_2 r^*) + C_4 Y_{n-1}(q_2 r^*)\right] \\ & + \frac{q_3\left[\left(q_3^2 - m^2\right)^2 - \mathrm{Ra}\right]}{m\left(q_3^2 - m^2\right)} \left[C_5 I_{n-1}(q_3 r^*) - C_6 K_{n-1}(q_3 r^*)\right] \\ & - C_7 I_{n-1}(mr^*) - C_8 K_{n-1}(mr^*)\end{aligned} \tag{A16}$$

Equations (6), (A7), (A15), and (A16), when evaluated at $r^* = 1$ and $1/R$ and set equal to zero, have nontrivial solutions when the determinant formed from the matrix of these equations is zero. This gives a transcendental equation for the critical Rayleigh number.

P. Le Quéré
LIMSI-CNRS
91403 Orsay Cedex, France

A Note on Multiple and Unsteady Solutions in Two-Dimensional Convection in a Tall Cavity

Two-dimensional natural convection in a vertical differentially heated air-filled cavity is investigated numerically from the onset of the multicellular flow structure to the return of the unicellular pattern. Several branches of solutions characterized by different numbers of cells in the flow structure are found. The return to the unicellular flow structure occurs through a gradual decrease in the number of cells and each change in the number of cells is characterized by hysteresis. Also, unsteady solutions are found.

1 Introduction

Convection in tall cavities has been the subject of continuing research since the beginning of the century. Many studies have emphasized the heat transfer side of the problem, while others have concentrated on fluid mechanical aspects. These two aims are in fact closely tied together if one recognizes that the rate of the heat transport depends on the flow structure. In a differentially heated cavity, fluid normally rises along the heated surface, turns in the top end, sinks along the cold wall, and turns again in the bottom end. If the cavity is tall enough and if the Rayleigh number is small, the end regions where the flow turns around are of limited extent and a parallel flow exists in the central portion of the slot. In this region the isotherms are parallel to the vertical walls and heat is transferred by conduction from the hot to the cold wall. This flow regime was first analyzed by Batchelor (1954), who named it the conduction regime. He showed that in the central portion of the slot, the vertical velocity has a cubic profile, and the temperature decreases linearly from the temperature of the hot wall to that of the cold wall. It was subsequently shown that this conduction regime is prone to an instability, which takes different forms depending on the fluid Prandtl number Pr (see, e.g., Hart, 1971; Korpela et al., 1973). In the limit of zero Prandtl number, the instability is purely hydrodynamic owing to the inflection point in the velocity profile. It takes the form of steady cross cells not unlike the "cat's eyes" of Kelvin in shear layers. The secondary cells gain their energy from the shear between the two counterflowing streams. For increasing Prandtl numbers, thermal effects play an increasing role and lead to a traveling wave instability. The value of the Prandtl number that demarcates steady from unsteady perturbations, Pr^c, is approximately 12.5. The values predicted in the early studies of Korpela (1974) ($\mathrm{Pr}^c = 12.7$), Gershuni and Zhukhovitskii (1976) ($\mathrm{Pr}^c = 11.4$) or Bergholz (1978) ($\mathrm{Pr}^c = 12.7$), have been confirmed in the more recent studies of Brenier et al. (1986) ($12 \le \mathrm{Pr}^c \le 12.5$) or Chen and Pearlstein (1989) ($12.4 \le \mathrm{Pr}^c \le 12.5$).

These results correspond to base flow solutions that can only be found in a slot of infinite vertical extent, while real experimental setups have a limited vertical extent and thus a finite aspect ratio. In finite cavities, a new element comes into play in the form of a small but nonetheless important vertical temperature gradient that develops in the core of the cavity. What is the influence of this new parameter on the flow structure and on its stability? It can be shown that there still exists a parallel solution of the Boussinesq equations, provided the stratification is linear and the wall temperatures also increase linearly at the same rate. Along a vertical isolated plate, this solution is known as the buoyancy layer (Prandtl, 1952; Gill, 1966). Elder (1965) showed that if the stratification is large enough, two independent buoyancy layers (one with downward flow and the other with upward flow) can be found between two parallel plates. A more general solution encompassing the whole range of stratification parameters was given by Bergholz (1978), who performed a linear stability analysis of this class of parallel solutions. For large values of the stratification parameter γ ($\gamma \ge 13$) his results reproduced those obtained by Gill and Davey (1969) for the buoyancy layer. Bergholz showed that, in small Prandtl number fluids, the development of steady cat's eyes is delayed by a small amount of stable stratification. Larger stratifications lead to a change of the flow structure, which becomes a boundary-layer type and is then prone to a traveling wave instability. The situation is exactly opposite for fluids of large Prandtl number. A small stratification delays the onset of the traveling wave instability, whereas larger stratifications lead to stationary disturbances.

By blending Bergholz's results with values of the stratification parameter obtained from numerical computations, many authors have then tried to infer the stability characteristics of convective flows of fluids of various Prandtl numbers in finite aspect ratio cavities. One must, however, bear in mind the fact that the base flow solution investigated by Bergholz is characterized by a linear increase of the wall temperatures for nonzero stratification parameter. Needless to say, this is not the case in a cavity with isothermal walls and consequently, application of the stability characteristics inferred from Bergholz's results to differentially heated cavities is probably more questionable as the value of the stratification parameter increases.

In particular, Roux et al. (1980) (see also de Vahl Davis, 1986) showed that the cat's eye regime can only be observed in air-filled cavities of aspect ratio larger than a critical value between 11 and 12. This conclusion has been confirmed by other numerical computations; see, e.g., Lauriat (1980). Likewise, cat's eyes should be seen in finite cavities for all fluids of Prandtl number smaller than Pr^c, but the critical aspect ratio is an increasing function of the Prandtl number and, as noted by Roux et al., observing the cat's eye regime in water would require a cavity of aspect ratio on the order of 100 and no one has undertaken to do that.

In air, steady cat's eyes have been observed by many authors for small supercritical values of the Rayleigh number. For

---

Contributed by the Heat Transfer Division for publication in the Journal of Heat Transfer. Manuscript received by the Heat Transfer Division May 31, 1989; revision received February 8, 1990. Keywords: Enclosure Flows, Flow Instability, Natural Convection.

instance Vest and Arpaci (1969) reported on their appearance in a cavity of aspect ratio 33 for a Grashof value of 8700 ± 10 percent with a wavenumber of 2.74. Most people have noted, however, that these cat's eyes become unsteady upon increasing Rayleigh number (see Schinkel, 1980; Chikhaoui and Marcillat, 1983; Lauriat and Desrayaud, 1985a; Pignatel and Marcillat, 1986; Chikhaoui et al., 1988a). This fact is not explained by the linear stability theory of the two-dimensional base flow solution and has not been observed numerically either, except perhaps by Polezhaev et al. (1985) in a very tall cavity.

Furthermore, Roux et al. (1980) have shown the existence of a reverse transition from multicellular to monocellular flow when increasing the value of the Rayleigh number. This is due to the increasing influence of the stabilizing temperature gradient in the core, which also leads to a boundary layer type flow structure. This reverse transition has been found in numerical computations (Roux et al., 1980; Lauriat and Desrayaud, 1985a). Its experimental evidence is, however, still controversial. Some authors have indicated the return to steady monocellular convection (Pignatel and Marcillat, 1986; Chikhaoui et al., 1988a) while others (Schinkel, 1980; Lauriat and Desrayaud, 1985a) never saw such a return and generally report an increasingly chaotic motion.

Korpela et al. (1982) and Lee and Korpela (1983) have performed extensive computations of the cat's eye regime in cavities of aspect ratio in the range 10–40 for fluids of Prandtl number in the range 0–1000. Lee and Korpela mention that, in some cases, the number of cells depends on the initial condition, which suggests the existence of multiple solutions.

In order to explain the appearance of unsteady cat's eyes, some authors have argued that their steadiness is linked to the odd-symmetry of the base flow velocity and temperature profiles. Any breaking of this odd-symmetry, such as that resulting from variation of thermophysical properties with temperature, would inevitably result in unsteady perturbations. This is the case for instance if the fluid viscosity is allowed to vary with temperature, as was shown by Thangam and Chen (1986). Similarly, Lauriat and Desrayaud (1985b) have shown that, by taking radiative interaction in a gray gas into account, unsteady perturbations are predicted at criticality.

Others have invoked three-dimensional effects. Chikhaoui et al. (1988b) have performed full nonlinear computations in a cavity with finite aspect ratio in the vertical and horizontal directions. They showed that appreciable spanwise effects distort the cross-roll structure. They chose to solve the steady-state equations, which did not allow them to find unsteady solutions.

One other possibility, of course, is that the two-dimensional secondary flows lose their stability to unsteady disturbances. This motivated the studies carried out by Nagata and Busse (1983) and very recently by Chait and Korpela (1989). Nagata and Busse considered a fluid of zero Prandtl number. They showed that, in the (Rayleigh number, wavenumber α) space, the region of stable two-dimensional cat's eyes is bounded on both sides by the Eckhaus instability and from above by a three-dimensional monotone instability. They also found a region corresponding to a three-dimensional oscillatory instability but, for a given wavenumber, this stability curve is never reached first for increasing Rayleigh number. The investigation carried out by Chait and Korpela for a fluid of Prandtl number equal to 0.71 confirms qualitatively, and to a good extent quantitatively, the general picture established by Nagata and Busse, except that the left branch of the Eckhaus curve was found to be restricted by another curve corresponding to a monotone instability. Both studies thus agree on the fact that, for a given wavenumber, the two-dimensional secondary flows do first give up their stability to three-dimensional stationary disturbances for relatively small supercritical values of the Rayleigh number. Whether this instability is weak enough so that the three-dimensional oscillatory instability can eventually play a role is still unknown.

All these discrepancies between experimental observations, numerical computations, and results from linear and nonlinear stability theory indicate that our understanding of convection in tall cavities is not yet complete. The purpose of this paper is to provide some new elements from numerical integration of the time-dependent two-dimensional Boussinesq equations in a cavity of aspect ratio 16. This investigation was motivated by a closely related work in a tall vertical annulus (Le Quéré and Pécheux, 1989). The surprising results we found in the annulus did not fit what was known from the linear stability analysis of the conduction regime in cylindrical coordinates performed by Choi and Korpela (1980). This led us to carry out the computations described below in the Cartesian case to draw a parallel between the Cartesian and cylindrical configurations. We do not claim that these new elements completely elucidate the discrepancies between the experimental and theoretical results. They seem, however, sufficiently new and important (existence of multiple solutions and of unsteady solutions) to be reported herein. It is hoped that they will help to understand better the experimental observations.

This paper is organized as follows. In the next section, we briefly describe the governing equations to help fix the notation and the main features of the numerical algorithm. Results are presented in the third section. A discussion follows. Some heat transfer results are given in section 5.

2 Governing Equations and Numerical Algorithm

2.1 Governing Equations. Consider the flow of a Newtonian fluid of kinematic viscosity ν and thermal diffusivity κ in a vertical cavity of height H and width W. The coordinate system is defined so that the vertical axis (Oz) points upward in the direction opposite to gravity, which is noted g. The x

Nomenclature

A = aspect ratio $= H/W$
g = gravitational acceleration
Gr = Grashof number $= g\beta\Delta T W^3/\nu^2$
$E_s(f, t)$, $E_a(f, t)$ = indicators of breaking of centrosymmetry for dummy variable $f(x, z, t)$
H = height of the enclosure
Nu = Nusselt number
Nu_z = local Nusselt number
P = pressure
Pr = Prandtl number $= \nu/\kappa$
Ra = Rayleigh number $= g\beta\Delta T W^3/\nu\kappa$
S_f = source term of Helmholtz equation for dummy variable f
u, w = velocity components
T = temperature
T_l = Chebyshev polynomial of lth degree
W = width of the enclosure
α = wavenumber
β = coefficient of volumetric expansion
γ = stratification parameter
Δt = time step
ΔT = temperature difference
Θ = dimensionless temperature
κ = thermal diffusivity
λ = constant in Helmholtz equation
ν = kinematic viscosity
Ψ = stream function
ω = vorticity

axis is horizontal. Constant uniform temperatures T_1 and T_2 ($T_2 - T_1 \geq 0$) are imposed at the right and left vertical walls, respectively. The top and bottom walls are assumed perfectly thermally insulated. The temperature difference is assumed small enough so that the Boussinesq approximation holds.

The set of governing equations is made dimensionless by introducing $W/2$ as a reference length, $\nu/(W/2)$ as a reference velocity and related quantities of time and pressure. The scaled temperature Θ is defined as $(T-T_r)/(T_2-T_1)$ with $T_r = (T_1+T_2)/2$. With this set of reference quantities the governing equations in primitive variables read

$$\frac{\partial u}{\partial x} + \frac{\partial w}{\partial z} = 0 \tag{1}$$

$$\frac{\partial u}{\partial t} + u\frac{\partial u}{\partial x} + w\frac{\partial u}{\partial z} = -\frac{\partial P}{\partial x} + \nabla^2 u \tag{2}$$

$$\frac{\partial w}{\partial t} + u\frac{\partial w}{\partial x} + w\frac{\partial w}{\partial z} = -\frac{\partial P}{\partial z} + \nabla^2 w + \frac{\mathrm{Ra}}{8\mathrm{Pr}}\Theta \tag{3}$$

$$\frac{\partial \Theta}{\partial t} + u\frac{\partial \Theta}{\partial x} + w\frac{\partial \Theta}{\partial z} = \frac{1}{\mathrm{Pr}}\nabla^2 \Theta \tag{4}$$

where u and w are, respectively, the horizontal and vertical velocity components and P the deviation from the hydrostatic pressure divided by the product of mean density and characteristic velocity squared. The Rayleigh number Ra is defined by $\mathrm{Ra} = g\beta(T_2-T_1)W^3/\nu\kappa$ and Pr is the Prandtl number ($\mathrm{Pr} = \nu/\kappa$). In the following the value of the Prandtl number is set to 0.71. In the dimensionless coordinates the computational domain extends from -1 to 1 in the x direction and from $-A$ to A in the z direction where A is the vertical aspect ratio of the cavity ($=H/W$). The boundary conditions are then:

- u and $w=0$ on all four walls of the cavity
- $\Theta = 0.5$ on $x=-1$ and $\Theta = -0.5$ on $x=1$, $-A \leq z \leq A$
- $\partial\Theta/\partial z = 0$ on $z=-A$ and A, $-1 \leq x \leq 1$

2.2 Numerical Algorithm. Except for the time discretization, the numerical scheme is that presented in the paper by Le Quéré and Alziary (1985). For the sake of brevity, we simply state here its main features and describe below the third-order time discretization scheme that we actually used to integrate the time-dependent equations.

2.2.1 Space Discretization. The spatial discretization relies on the use of products of Chebyshev polynomials $T_l(x) \times T_m(z/A)$ in each direction as basis expansion functions for the four dependent variables u, w, P, and Θ. Any two-dimensional field $f(x, z, t)$ is thus expressed as a double truncated series of such basis functions:

$$f(x, z, t) = \sum_{l=0}^{L}\sum_{m=0}^{M} f_{lm}(t)T_l(x)T_m\left(\frac{z}{A}\right) \tag{5}$$

2.2.2 Time Discretization. The time discretization scheme is of finite difference type. In the framework of Chebyshev methods, second-order schemes such as the classical Adams–Bashforth/Crank–Nicolson schemes have generally been used (cf. Gottlieb and Orszag, 1977). In order to increase the accuracy of the time integration we propose here a third-order scheme, derived along the lines of the scheme proposed by Vanel et al. (1986). It combines a backward Euler scheme for the diffusive terms with an explicit Adams–Bashforth extrapolation for the nonlinear terms. When applied to a scalar diffusion-advection equation such as

$$\frac{\partial f}{\partial t} + V\cdot\nabla f = \nabla^2 f$$

this third-order scheme reads

$$\frac{11f^{n+1} - 18f^{n} + 9f^{n-1} - 2f^{n-2}}{6\Delta t} + 3V\cdot\nabla f^{n} - 3V\cdot\nabla f^{n-1} + V\cdot\nabla f^{n-2} = \nabla^2 f^{n+1} \tag{6}$$

which can be cast as an Helmholtz equation for the unknown field f^{n+1}

$$\nabla^2 f^{n+1} - \lambda f^{n+1} = -S_f \tag{7}$$

where $\lambda = 11/6\Delta t$. The source term S_f of this equation is made of all the known quantities at previous time levels $n\Delta t$, $(n-1)\Delta t$, and $(n-2)\Delta t$. In particular, the nonlinear terms $V\cdot\nabla f$ are classically evaluated pseudospectrally in a convective form.

When applied to the governing equations, this scheme yields three Helmholtz equations for the unknown fields Θ, u, and w at time $(n+1)\Delta t$, the Helmholtz equations for u and w being coupled by the incompressibility constraint

$$\nabla^2\Theta^{n+1} - \mathrm{Pr}\lambda\Theta^{n+1} = S_\Theta \tag{8}$$

$$\nabla^2 u^{n+1} - \lambda u^{n+1} = S_u + \frac{\partial P}{\partial x} \tag{9}$$

$$\nabla^2 w^{n+1} - \lambda w^{n+1} = S_w + \frac{\partial P}{\partial z} \tag{10}$$

$$\frac{\partial u^{n+1}}{\partial x} + \frac{\partial w^{n+1}}{\partial z} = 0 \tag{11}$$

In these equations each of the symbols S_Θ, S_u, and S_w is given by the expression

$$S_f = c_f\left(\frac{-18f^{n} + 9f^{n-1} - 2f^{n-2}}{6\Delta t} + 3(V\cdot\nabla f)^{n} - 3(V\cdot\nabla f)^{n-1} + (V\cdot\nabla f)^{n-2} - e_f\frac{\mathrm{Ra}}{\mathrm{Pr}}\Theta^{n+1}\right)$$

with the subscript f denoting either u, w, or Θ and with $c_u = c_w = 1$; $c_\Theta = \mathrm{Pr}$ and $e_u = e_\Theta = 0$; $e_w = 1$. Given the solution (u, w, Θ) at the time level $n\Delta t$, the temperature equation (8) can be readily solved to give the temperature field Θ^{n+1}.

2.2.3 Incompressibility Constraint. Equations (9), (10), and (11) constitute an unsteady Stokes problem, which must be solved at each time step and has to be therefore solved efficiently. The influence matrix technique proposed by Kleiser and Schumann (1980) for a one-dimensional Chebyshev problem and extended to a two-dimensional Chebyshev configuration by Le Quéré and Alziary (1982, 1985) has proven particularly efficient and will be used here. This algorithm suffers, however, from a small residual error of the divergence of the velocity field, an error that is directly proportional to the magnitude of the residual tau-terms in the momentum equations.

2.2.4 Accuracy Assessment. The algorithm described in the previous paragraphs was used to compute the benchmark solutions of the GAMM Workshop dedicated to a similar problem on the loss of stability of convection flows in low Prandtl number fluids (Le Quéré, 1988). In particular, we compared therein the solutions obtained with this tau-Chebyshev algorithm with those produced by an algorithm based on a collocation-Chebyshev scheme on a staggered grid (Bernardi and Maday, 1988). The latter method gives velocity fields that are truly divergence free. We showed that the solutions produced by both algorithms converged toward the same solution as the spatial mesh size was reduced and that the residual error on the divergence had virtually no effect on the accuracy of the solutions produced by the tau-Chebyshev algorithm.

An accuracy test was performed on the two-cell steady solution found for a value of the Rayleigh number of 2.4×10^4. Table 1 gives values of selected quantities listed in the caption as a function of spatial resolution. As can be seen, spatial

Table 1 Evolution of selected quantities with $L \times M$ for the two-cell solution corresponding to a Ra value of 2.4×10^4; $\Psi(0, 0)$ is the value of the stream function at the center, $\omega(-1, 0)$ is the value of the vorticity at midheight of the left vertical wall, Nu is the mean Nusselt number; the last column shows the Euclidian norm of residual divergence

L × M	$\Psi(0.,0.)$	$\omega(-1.,0.)$	Nu	div
12 × 72	42.47	415.0	1.9001	1.2×10^{-3}
16 × 90	44.38	428.82	1.9009	6×10^{-4}
20 × 100	44.472	429.02	1.9009	3×10^{-4}
24 × 120	44.477	429.16	1.9009	1.5×10^{-4}
32 × 150	44.477	429.26	1.9009	3×10^{-5}

convergence is obtained for increasing resolution, even for the more sensitive quantity, which is the vorticity at midheight along the hot vertical wall. The numerical results presented below were generally obtained with $L = 16$, $M = 90$. With this resolution, the residual divergence is smaller than 5×10^{-4} for most solutions and the accuracy of the corresponding solutions is certainly better than 1×10^{-2}. In some cases where the results were new or surprising (unsteady solutions, loss of centrosymmetry), the integrations were repeated with an increased spatial accuracy (generally $L = 24$, $M = 120$) and a smaller time step. Despite unavoidable small changes (a few percent) in the solutions (amplitude of the oscillations in the case of unsteady solutions, for example), these integrations at higher spatial resolution confirmed what was found at coarser resolution.

2.3 Numerical Considerations. There are several ways to characterize numerical solutions. When integrating the unsteady equations, it is usual to follow the time evolution by looking at values of quantities such as temperature or velocity components at selected sampling points. One has thus to make a choice of the location of the sampling point; according to the nature of the expected instability in the computations reported below, the sampling point was generally located on the vertical midline of the cavity in the upper middle half.

As will be seen later, symmetry properties play an important role in the discussion. It is well known that for the problem at hand there is at least one solution of the governing equations that satisfies the so-called centrosymmetry property. It is given by the relations

$$\begin{aligned} u(-x, -z, t) &= -u(x, z, t) \\ w(-x, -z, t) &= -w(x, z, t) \\ \Theta(-x, -z, t) &= -\Theta(x, z, t) \\ P(-x, -z, t) &= P(x, z, t). \end{aligned}$$

Owing to the symmetries of the Chebyshev polynomials, this property translates very simply to the spectral coefficients of the independent variables, namely: $\Theta_{lm} = u_{lm} = w_{lm} = 0$ for all couples (l, m) for which $l + m$ is even and $p_{lm} = 0$ for all couples (l, m) for which $l + m$ is odd. It is then possible to characterize this centrosymmetry property by considering, for instance, the quantity $E_s(\Theta, t)$ defined as $\sum_{l+m \text{ even}} \Theta_{lm}^2$. $E_s(\Theta, t)$ should remain equal to zero to the round-off level for all time for those solutions possessing the centrosymmetry property.

3 Results

Solutions were calculated for air flow in a cavity of aspect ratio 16 for values of Rayleigh number up to 4×10^4. For low values of the Rayleigh number (typically less than 6×10^3), the steady-state solution is achieved at a dimensionless time equal to 2. The corresponding temperature and stream-function patterns display the characteristic features of the conduction regime.

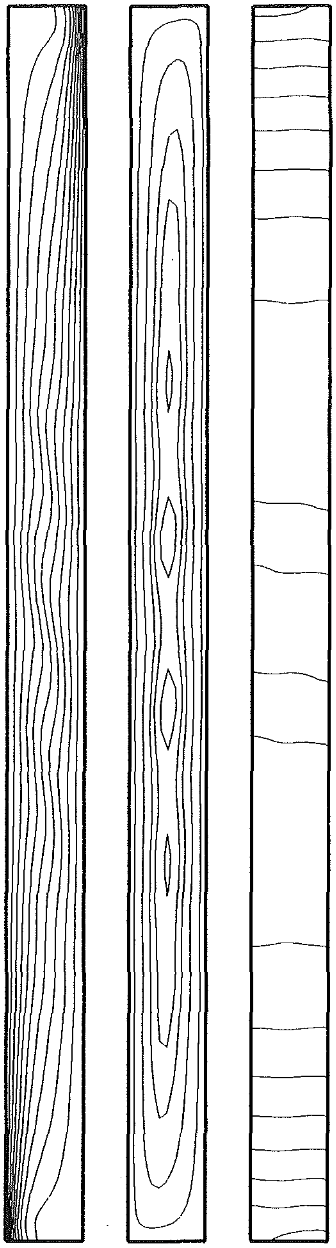

Fig. 1 Temperature (left), stream-function (center), and pressure fields (right); $Ra = 7 \times 10^3$; $L = 16$, $M = 90$; stream-function isovalues are 2, 9, 16, 20, and 24

3.1 Steady Four-Cell Solutions. Achieving the steady-state solution at $Ra = 7 \times 10^3$ takes about five times longer, for then the corresponding solution depicts the characteristic features of the cat's eye instability. The isotherms and stream-function plots (Fig. 1) show the existence of a four-cell pattern characterized by two main central cells and two weaker outer cells. This Ra value corresponds to a Grashof number less than 1×10^4. This value is much lower than the value quoted by Lee and Korpela (1983), who found the cat's eyes appear for Grashof numbers in the range 1×10^4–1.1×10^4 in a cavity of aspect ratio 20. (A larger aspect ratio should give a smaller critical Rayleigh or Grashof number.) It is in better agreement with the critical values found by Roux et al. (1980) and by Lauriat and Desrayaud (1985a). In order to clarify this point the same time integration was repeated with increased spatial resolution ($L = 24$, $M = 120$). Cat's eyes were also found in this

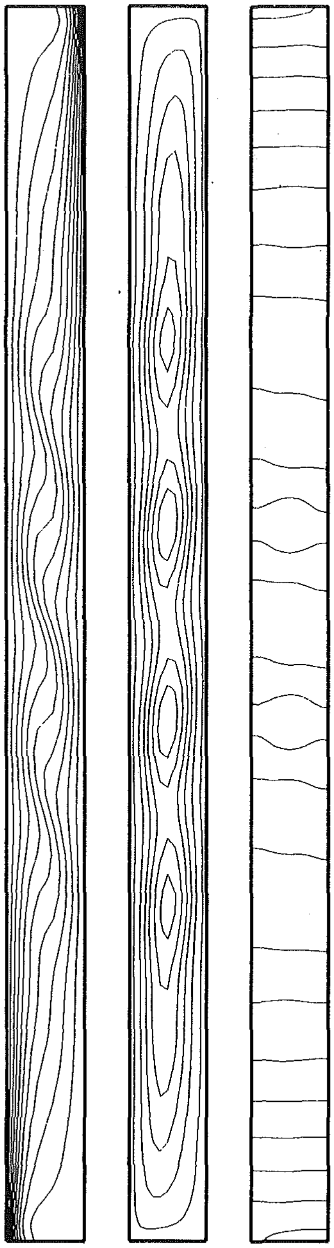

Fig. 2 Temperature (left), stream-function (center), and pressure fields (right); Ra = 1.1×10^4; $L = 16$, $M = 90$; stream-function isovalues are 2, 9, 16, 22, 28, and 33

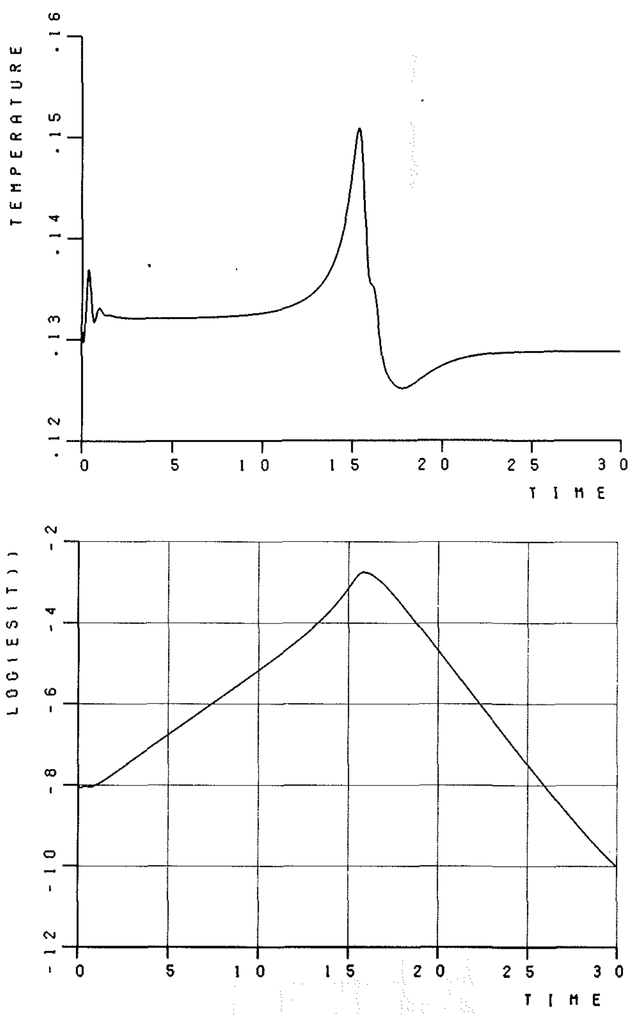

Fig. 3 Time evolution of the temperature at point $x = 0.$, $z/A = 0.53$ (top) and of log ($E_s(\Theta)$) (bottom); Ra = 1.2×10^4; $\Delta t = 0.001$; $L = 16$, $M = 90$

case. Note that in this case the residual divergence is at 1×10^{-5}, which corresponds to the typical accuracy expected for the solution. The reason for obtaining the instability at a value close to that predicted by the linear stability theory is undoubtedly due to the lack of false damping in the spectral method. The wavenumber based on the distance of the central cells is 2.78, which is in good agreement with the value of 2.69 predicted by the linear stability theory, considering that the finite aspect ratio of the cavity will influence the spacing of the cells.

Starting from this solution as the initial condition and increasing the Ra value to 8×10^3, 1×10^4, and 1.1×10^4 in turn results also in steady-state solutions. The cross rolls in these solutions are qualitatively similar but their amplitude is larger. In particular, for the solutions corresponding to 1×10^4 and 1.1×10^4 the two outer weaker cells have almost grown to the same intensity as the central cells (Fig. 2). The spacing between the central cells increases with increasing Ra and the wavenumbers for the solutions corresponding to 8×10^3, 1×10^4, 1.1×10^4 are 2.68, 2.54, and 2.46, respectively.

The conclusion of this first set of computations is that the solution of the Boussinesq equations in a cavity of aspect ratio 16 becomes unstable to a shear instability for a Ra value between 6×10^3 and 7×10^3. We did not try at this stage to determine more precisely the critical value, and it was later found (see paragraph 3.2) that the value of the critical Rayleigh number lies between 6×10^3 and 6.6×10^3. The corresponding flow pattern exhibits a four-cell structure near the condition of criticality.

3.2 Transition to a Three-Cell Pattern. Starting from the four-cell solution corresponding to a Ra value of 1.1×10^4 as the initial condition, the Ra value was next set to 1.2×10^4. The time trace of the temperature at a point located on the vertical midline of the cavity is shown on Fig. 3(*a*). Its evolution can be split into three parts. Up to a dimensionless time of 5, the temperature seems to tend asymptotically toward a steady value, approximately equal to 0.132. It undergoes a large variation at time t around 15 and afterwards tends, in a dimensionless time of 30, to a final steady value smaller than 0.129. The final isotherm and streamfunction plots are shown on Fig. 4. This solution is characterized by a three-cell pattern. The time evolution of $E_s(\Theta, t)$ (Fig. 3*b*) also shows that the transition is linked to a momentary loss of centrosymmetry of the numerical solution. $E_s(\Theta, t)$ starts to develop from a round-off error and increases exponentially in time. A transition

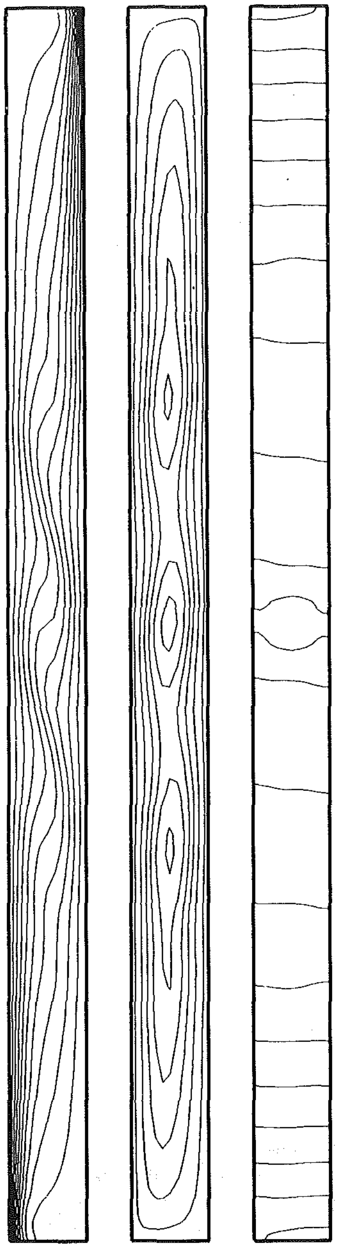

Fig. 4 Temperature (left), stream-function (center), and pressure fields (right); $Ra = 1.2 \times 10^4$; $L = 16$, $M = 90$; stream-function isovalues are 2, 9, 17, 24, 31, and 38

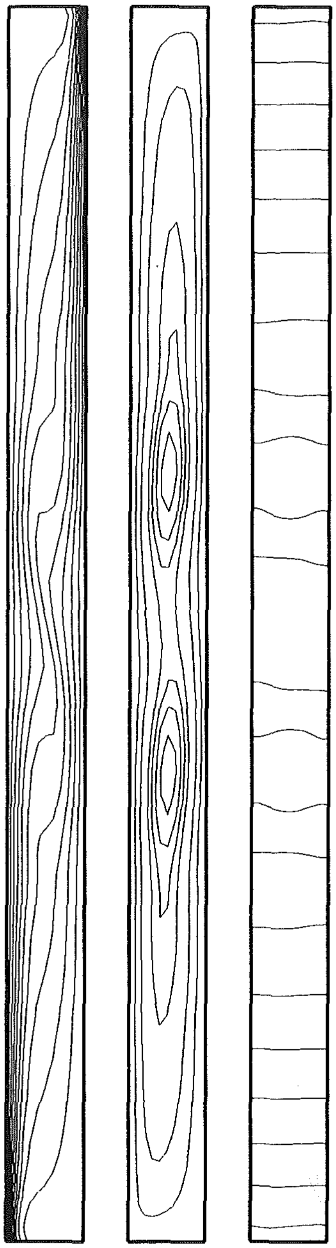

Fig. 5 Temperature (left), stream-function (center), and pressure fields (right); $Ra = 2.4 \times 10^4$, $L = 16$, $M = 90$; stream-function isovalues are 7, 20, 40, 49, 56, and 63

occurs when this quantity reaches quite a large amplitude. After having triggered the transition, it returns to zero exponentially, which restores a final three-cell centrosymmetric solution. This final three-cell solution is characterized by a wavenumber based on the distance of the centers of the cells equal to 2.14.

As can be intuitively expected, this three-cell structure remains stable upon *increasing* or *decreasing* the Rayleigh number. When the Ra value is successively set to 1.6×10^4, 1.9×10^4, and 2×10^4, steady-state solutions are obtained after integrating over a sufficient period of time. These solutions display the same three-cell structure but with an increasing amplitude of flow in the cells. The respective wavenumbers are 2.08, 2.00, and 2.00.

Starting from the three-cell solution corresponding to 1.2×10^4 as the initial condition, the Ra value was next successively decreased to 1×10^4, 9×10^3, 8×10^3, and 7×10^3. Again steady-state solutions are obtained and these solutions remain characterized by a three-cell pattern. The amplitude of the cells decreases with Ra, as does the wavelength of the perturbations. The solutions for the smaller values of 8×10^3 and 7×10^3 exhibit a marked tendency to form a five-cell pattern. The wavenumbers of the solutions corresponding to 1×10^4, 9×10^3, 8×10^3, and 7×10^3 are 2.27, 2.49, 2.63, and 2.88, respectively.

When the Ra value is further decreased to 6.6×10^3, the solution shifts back on the four-cell branch, which was discussed in the previous paragraph. One should note that during this transition the centrosymmetry property is maintained. It was confirmed that this four-cell solution could be obtained by starting the flow from rest and the spatial resolution was either ($L = 16$, $M = 90$) or ($L = 24$, $M = 120$).

3.3 Transition to a Two-Cell Pattern.

Starting from the three-cell solution corresponding to a Ra value of 2×10^4 as the initial condition, the Ra value is set to 2.4×10^4. What appears is qualitatively similar to what was described in the previous paragraph. The time trace of the temperature at the

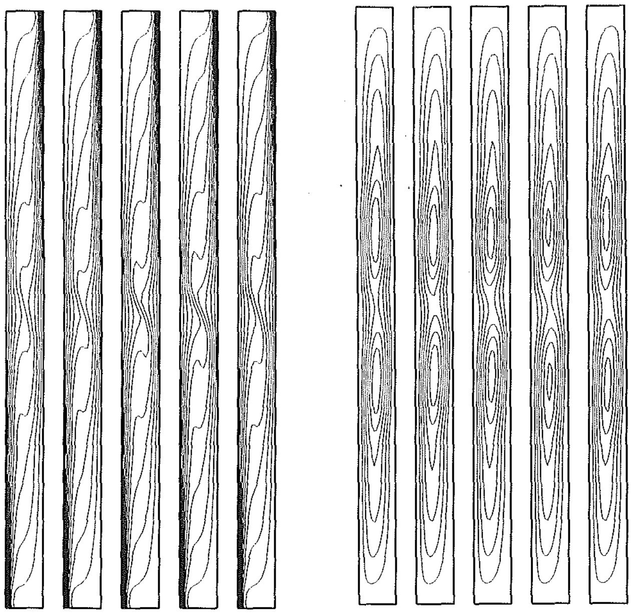

(a) (b)

Fig. 6 Time sequence of temperature field *(a)* and of stream-function field *(b)*, Ra = 3.6×10^4; $L = 24$, $M = 120$; time integration performed with $\Delta t = 4\times10^{-4}$; time interval is 0.172, which corresponds to $\Pi/5$; frame 6 (not shown) is identical to frame 1; stream-function isovalues are 14, 28, 42, 56, 68, and 77

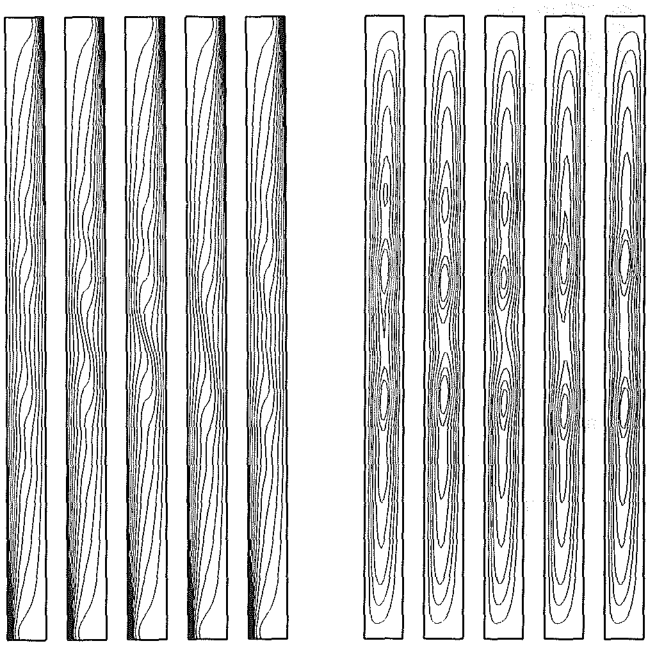

(a) (b)

Fig. 7 Time sequence of temperature field *(a)* and of stream-function field *(b)*, Ra = 1.4×10^4; $L = 24$, $M = 120$; time integration performed with $\Delta t = 1\times10^{-3}$; time interval is 0.228, which corresponds to $\Pi/5$; frame 6 (not shown) is identical to frame 1; stream-function isovalues are 7, 14, 20, 28, 35, 40, and 43

Table 2 Dimensionless oscillation period Π; reference time is $W^2/4\nu$

Ra $\times10^{-4}$	1.2	1.4	1.6	1.7	1.8	3.4	3.6
Π	1.33	1.14	0.99	0.95	0.90	0.74	0.86

sampling point first oscillates with decreasing amplitude up to a dimensionless time of 2 as if it were to settle down at a steady value. It then undergoes a rapid change to another value at t around 2 and afterward the flow tends to its final steady state through decaying oscillations. The final isotherm and stream-function plots are shown in Fig. 5. This solution is now characterized by a two-cell pattern and a wavenumber equal to 1.59. Examination of the quantity $E_s(\Theta, t)$ again shows that the transition is linked to a momentary loss of centrosymmetry of the numerical solution. $E_s(\Theta, t)$ presents an evolution similar to that found in the transition from the four-cell to the three-cell pattern: It starts to develop from a round-off error and increases exponentially in time. After having triggered the transition it returns to zero exponentially yielding the final two-cell solution with centrosymmetry. Again, this two-cell structure remains stable upon *increasing* or *decreasing* the Rayleigh number but new unexpected features are found on this solution branch.

By setting the Ra value successively to 2.8×10^4 and 3.2×10^4, steady-state solutions were obtained after sufficiently long integration. In these cases the transients that lead to the steady solutions are highly oscillatory but the amplitude of the oscillations is damped with increasing time. These solutions display the same two-cell structure with increasing amplitude of the cells and their respective wavenumbers are 1.56 and 1.53.

When the value of the Rayleigh number is further increased to 3.4×10^4 or 3.6×10^4 using the two-cell solution found for 3.2×10^4 as an initial condition, the time evolution of the temperature at the sampling point shows that the numerical scheme predicts a time-periodic asymptotic solution characterized by fluctuations of constant amplitude. Time sequences of the temperature and stream-function fields are shown on Fig. 6. The unsteadiness is seen to correspond to an oscillation of the position of the centers of the cells, which move apart or come closer in phase, in a way that maintains the centrosymmetry of the solution. These unsteady solutions were confirmed at higher resolution ($L = 24$, $M = 120$).

We now describe what happens when the value of Ra is decreased. For a Rayleigh number equal to 1.9×10^4, a steady-state solution was found after an oscillatory transient. As expected this solution is characterized by a two-cell pattern. If the Rayleigh number is now decreased to 1.8×10^4, the amplitude of the oscillations observed during the transient is no longer damped and a time-periodic solution is predicted. This is also the case for the solutions computed for decreasing Ra values of 1.7×10^4, 1.6×10^4, 1.4×10^4, and 1.2×10^4. Table 2 presents the dimensionless periods of oscillations for the various unsteady solutions. For the solutions found in the range 1.2×10^4–1.8×10^4, the oscillation period Π varies like Ra^{-1}.

For the unsteady solutions found in the range 1.2×10^4–1.8×10^4, the unsteadiness mainly corresponds to an oscillation of the two cell centers around their mean location in the same manner as was found for 3.6×10^4. But, whereas the time-dependent solutions for Ra equal to 1.2, 1.6, 1.7, and 1.8×10^4 were found to be centrosymmetric, the solution corresponding to 1.4×10^4 is found to break this symmetry property. For it, $E_s(\Theta, t)$ oscillates periodically at a small but finite amplitude (about 5×10^{-4}). This feature was confirmed by a computation at an increased spatial resolution ($L = 24$, $M = 120$). This solution is also the solution for which the amplitude of the oscillations is maximum among the unsteady solutions in the range of Ra values between 1.2×10^4–1.8×10^4. Figure 7 presents time sequences of the temperature and stream-function fields for the symmetry-breaking solution found at Ra = 1.4×10^4. It is particularly noticeable that, due to the loss of centrosymmetry, the streamline pattern conveys the feeling of a disordered flow structure, even though its evolution is strictly periodic in time.

On the other hand, the local Nusselt number at the wall experiences relatively large local variations in the vertical direction as a result of the presence of cross rolls in the middle part of the cavity. For unsteady solutions, these spatial variations also become time dependent. As an example, evolution of local Nusselt number Nu_z along the heated wall is shown in Fig. 11 for the unsteady solution found on the two-cell branch for a Ra value of 1.4×10^4. The two thick solid lines represent the upper and lower envelopes in time of the local instantaneous Nusselt number when the asymptotic solution is reached. A typical instantaneous Nusselt number distribution is shown by the thin line. Unsteady fluctuations as large as 20 percent can be observed in the central part of the cavity.

6 Conclusion

We have investigated the instability of the conduction regime of two-dimensional natural convection in a tall cavity. We have shown that the return to the unicellular flow structure is more complex than previously analyzed. The number of cells decreases step by step, and each change in the number of cells is characterized by hysteresis. Unsteady solutions are also found. As current research we are studying the stability of these two-dimensional solutions with respect to three-dimensional disturbances.

Acknowledgments

The computations were carried out on the Cray-2 of the CCVR. This work is supported by DRET under contract 88/169. I am very grateful to Professor Seppo Korpela for many stimulating discussions and for his help during the revision of this manuscript.

References

Batchelor, G. K., 1954, "Heat Transfer by Free Convection Across a Closed Cavity Between Vertical Boundaries at Different Temperatures," *Quart. J. of Applied Mathematics*, Vol. 12, pp. 209-233.

Bergholz, R. F., 1978, "Instability of Steady Natural Convection in a Vertical Fluid Layer," *J. Fluid Mech.*, Vol. 84, pp. 743-768.

Bernardi, C., and Maday, Y., 1988, "A Collocation Method Over Staggered Grids for the Stokes Problem," *Int. J. Num. Meth. Fluids*, Vol. 8, pp. 537-557.

Brenier, B., Roux, B., and Bontoux, P., 1986, "Comparison des méthodes tau-Chebyshev et Galerkin dans l'étude de stabilité des mouvements de convection naturelle. Problème des valeurs propres parasites," *J. Mécanique Théorique et Appliquée*, Vol. 5, pp. 95-119.

Chen, Y. M., and Pearlstein, A. J., 1989, "Stability of Free-Convection Flows of Variable Viscosity Fluids in Vertical and Inclined Slots," *J. Fluid Mech.*, Vol. 198, pp. 513-541.

Chikhaoui, A., and Marcillat, J. F., 1983, "Stabilité des régimes thermoconvectifs dans une cavité rectangulaire," *Jour. Int. Transf. Helio.*, Monastir, Tunisie, pp. 521-527.

Chikhaoui, A., Marcillat, J. F., and Sani, R. L., 1988a, "Successive Transitions in Thermal Convection Within a Vertical Enclosure," in: *Natural Convection in Enclosures*, ASME HTD-Vol. 99, pp. 29-35.

Chikhaoui, A., Maslanik, M. K., and Sani, R. L., 1988b, "Steady Three-Dimensional Thermal Convection in a Vertical Rectangular Enclosure," *Comm. Applied Num. Meth.*, Vol. 4, pp. 825-834.

Choi, I. G., and Korpela, S. A., 1980, "Stability of the Conduction Regime of Natural Convection in a Tall Vertical Annulus," *J. Fluid Mech.*, Vol. 99, pp. 725-738.

Eckert, E. R. G., and Carlson, W. O., 1961, "Natural Convection in an Air Layer Enclosed Between Two Vertical Plates With Different Temperatures," *Int. J. Heat Mass Transf.*, Vol. 2, pp. 106-120.

Elder, J. W., 1965, "Laminar Free Convection in a Vertical Slot," *J. Fluid Mech.*, Vol. 23, pp. 77-98.

Gershuni, G. Z., and Zhukhovitskii, E. M., 1976, "Convective Stability of Incompressible Fluids," *Israel Prog. Scient. Transl.*, Jerusalem.

Gill, A. E., 1966, "The Boundary Layer Regime for Convection in a Rectangular Cavity," *J. Fluid Mech.*, Vol. 26, pp. 515-536.

Gill, A. E., and Davey, A., 1969, "Instabilities of a Buoyancy-Driven System," *J. Fluid Mech.*, Vol. 35, pp. 775-798.

Gottlieb, D., and Orszag, S. A., 1977, *Numerical Analysis of Spectral Methods: Theory and Applications*, SIAM, Philadelphia, PA.

Hart, J. E., 1971, "Stability of the Flow in a Differentially Heated Inclined Box," *J. Fluid Mech.*, Vol. 47, pp. 547-576.

Kleiser, L., and Schumann, U., 1980, "Treatment of Incompressibility and Boundary Conditions in Three-Dimensional Numerical Spectral Simulations of Plane Channel Flows," *Notes on Num. Fluid Mech., Vieweg*, Vol. 2, pp. 165-173.

Korpela, S. A., 1974, "A Study on the Effects of Prandtl Number on the Stability of the Conduction Regime of Natural Convection in an Inclined Slot," *Int. J. Heat Mass Transf.*, Vol. 17, pp. 215-222.

Korpela, S. A., Gozum, D., and Baxi, C. B., 1973, "On the Stability of the Conduction Regime of Natural Convection in a Vertical Slot," *Int. J. Heat Mass Transf.*, Vol. 15, pp. 1683-1690.

Korpela, S. A., Lee, Y., and Drummond, J. E., 1982, "Heat Transfer Through a Double Pane Window," ASME JOURNAL OF HEAT TRANSFER, Vol. 104, pp. 539-544.

Lauriat, G., 1980, "Numerical Study of Natural Convection in a Narrow Cavity: an Examination of High Order Accurate Schemes," ASME Paper No. 80-HT-90.

Lauriat, G., and Desrayaud, G., 1985a, "Natural Convection in Air-Filled Cavities of High Aspect Ratios: Discrepancies Between Experimental and Theoretical Results," ASME Paper No. 85-HT-37.

Lauriat, G., and Desrayaud, G., 1985b, "Influences of the Boundary Conditions and Linearization on the Stability of a Radiating Fluid in a Vertical Layer," *Int. J. Heat Mass Transf.*, Vol. 28, pp. 1613-1617.

Lee, Y., and Korpela, S. A., 1983, "Multicellular Convection in a Vertical Slot," *J. Fluid Mech.*, Vol. 126, pp. 91-121.

Le Quéré, P., 1988, "Contribution to the GAMM-Workshop With a Chebyshev Collocation Scheme on a Staggered Grid," GAMM Workshop, *Notes on Num. in Fluid Mech.*, Vieweg, Vol. 27, pp. 227-236.

Le Quéré, P., and Alziary de Roquefort, T., 1982, "Sur une méthode spectrale semi-implicite pour la résolution des équations de Navier-Stokes de'un écoulement bidimensionnel visqueux incompressible," *C. R. Acad. Sci. Paris*, Vol. 294, série II, pp. 941-944.

Le Quéré, P., and Alziary de Roquefort, T., 1985, "Computation of Natural Convection in Two-Dimensional Cavities With Chebyshev Polynomials," *J. Comp. Phys.*, Vol. 58, pp. 210-228.

Le Quéré, P., and Pécheux, J., 1989, "Numerical Simulations of Multiple Flow Transitions in Axisymmetric Annulus Convection," *J. Fluid Mech.*, Vol. 206, pp. 517-544.

Nagata, M., and Busse, F. H., 1983, "Three-Dimensional Tertiary Motions in a Plane Shear Layer," *J. Fluid Mech.*, Vol. 135, pp. 1-26.

Pignatel, J. F., and Marcillat, J. F., 1986, "Transition to Time-Dependent Free Convection in an Inclined Air Layer," *Int. J. Heat and Fluid Flow*, Vol. 7, pp. 169-178.

Polezhaev, V. V., Bune, A. V., and Griaznov, V., L., 1985, "Structure, Characteristics of Transition and of Turbulence in the Thermal Convection Given by the Direct Numerical Modelling," *IUTAM Symp. on Lam. Turb. Transition*, Novosibirsk, Springer, pp. 741-747.

Prandtl, L., 1952, *Essentials of Fluid Dynamics*, Hafner, New York.

Roux, B., Grondin, J., Bontoux, P., and de Vahl Davis, G., 1980, "Reverse Transition From Multicellular to Monocellular Motion in Vertical Fluid Layer," *Phys. Chem. Hydro.*, Vol. 3F, pp. 292-297.

Schinkel, W. M. M., 1980, "Natural Convection in Inclined Air-Filled Enclosures," PhD. Thesis, Pijnacker, Dutch Efficiency Bureau, The Netherlands.

Thangam, S., and Chen, C. F., 1986, "Stability Analysis on the Convection of a Variable Viscosity Fluid in an Infinite Vertical Slot," *Physics Fluids*, Vol. 29, pp. 1367-1372.

de Vahl Davis, G., 1986, "Finite Difference Methods for Natural and Mixed Convection in Enclosures," *8th Int. Heat Transf. Conf.*, San Francisco, Hemisphere Pub. Corp., Vol. 1, pp. 101-109.

Vanel, J. M., Peyret, R., and Bontoux, P., 1986, "A Pseudo-Spectral Solution of Vorticity-Stream Function Equations Using the Influence Matrix Technique," *Num. Meth. Fluid. Dyn. II*, Clarendon Press, Oxford, pp. 463-475.

Vest, C. M., and Arpaci, V. S., 1969, "Stability of Natural Convection in a Vertical Slot," *J. Fluid. Mech.*, Vol. 36, pp. 1-15.

Mixed Convection Heat Transfer From Thermal Sources Mounted on Horizontal and Vertical Surfaces

S. S. Tewari

Y. Jaluria

Department of Mechanical and Aerospace
Engineering,
Rutgers, The State University of
New Jersey,
New Brunswick, NJ 08903

An experimental study is carried out on the fundamental aspects of the conjugate, mixed convective heat transfer from two finite width heat sources, which are of negligible thickness, have a uniform heat flux input at the surface, and are located on a flat plate in the horizontal or the vertical orientation. The heat sources are wide in the transverse direction and, therefore, a two-dimensional flow circumstance is simulated. The mixed convection parameter is varied over a fairly wide range to include the buoyancy-dominated and the mixed convection regimes. The circumstances of pure natural convection are also investigated. The convective mechanisms have been studied in detail by measuring the surface temperatures and determining the heat transfer coefficients for the two heated strips, which represent isolated thermal sources. Experimental results indicate that a stronger upstream heat source causes an increase in the surface temperature of a relatively weaker heat source, located downstream, by reducing its convective heat transfer coefficient. The influence of the upstream source is found to be strongly dependent on the surface orientation, especially in the pure natural convection and the buoyancy dominated regimes. The two heat sources are found to be essentially independent of each other, in terms of thermal effects, at a separation distance of more than about three strip widths for both the orientations. The results obtained are relevant to many engineering applications, such as the cooling of electronic systems, positioning of heating elements in furnaces, and safety considerations in enclosure fires.

Introduction

Natural and mixed convective wakes generated by isolated thermal sources are of interest in many practical problems, such as cooling of electronic circuitry, positioning of heating elements in furnaces, and fires in enclosures. Examples from these applications are considered by Kraus and Bar-Cohen (1983), Jaluria (1984), and Quintiere et al. (1981), among others. A thermal source situated in a stationary medium gives rise to a vertically rising natural convection wake or plume. The idealized plume flows arising from point or line sources have been analyzed, using the similarity method, by Fujii (1963), Gebhart et al. (1970), and Mollendorf and Gebhart (1973). Experimental work has also been done by several researchers; see, for instance, the papers by Forstrom and Sparrow (1967), Schorr and Gebhart (1970), and Fujii et al. (1973). In many applications of practical interest, heat sources are located on horizontal or vertical surfaces, giving rise to wall plumes. The behavior of wall plumes generated by isolated line, point, and finite-width sources has been investigated by many researchers such as Zimin and Lyakhov (1970), Carey and Mollendorf (1977), and Sparrow et al. (1978).

A more complex flow occurs if the ambient medium is not stationary but has an externally induced flow velocity. Depending on the ambient flow velocity and the surface heat flux input by the heat source, the heat transfer from the source could be predominantly due to forced or natural convection. If the natural and forced convection effects are of comparable magnitude, the circumstance is termed mixed convection, as reviewed by Gebhart (1971) and Jaluria (1980), among others.

In the above circumstances, an interesting situation occurs, from a practical standpoint, if a second heat source is placed in the vicinity of a given heat source. In this case, interest lies in determining the thermal interaction between the two heat sources. The interaction of natural convection wakes due to isolated heat sources has been investigated by many workers; see, for instance, the papers by Lieberman and Gebhart (1969), Pera and Gebhart (1975), Jaluria (1982a, 1982b), and Milanez and Bergles (1986). It has been found that an upstream wake strongly affects the heat transfer from a downstream thermal

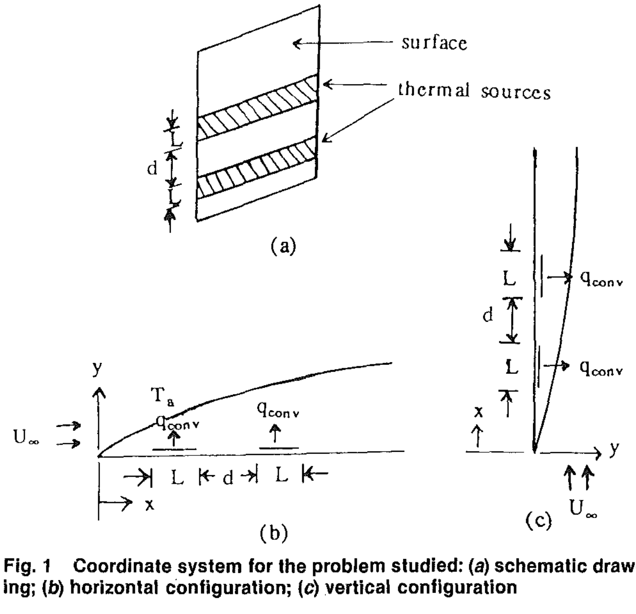

Fig. 1 Coordinate system for the problem studied: (*a*) schematic drawing; (*b*) horizontal configuration; (*c*) vertical configuration

---

Contributed by the Heat Transfer Division and presented at the 25th National Heat Transfer Conference, Houston, Texas, July 24–27, 1988. Manuscript received by the Heat Transfer Division October 31, 1988; revision received February 16, 1990. Keywords: Conjugate Heat Transfer, Electronic Equipment, Mixed Convection.

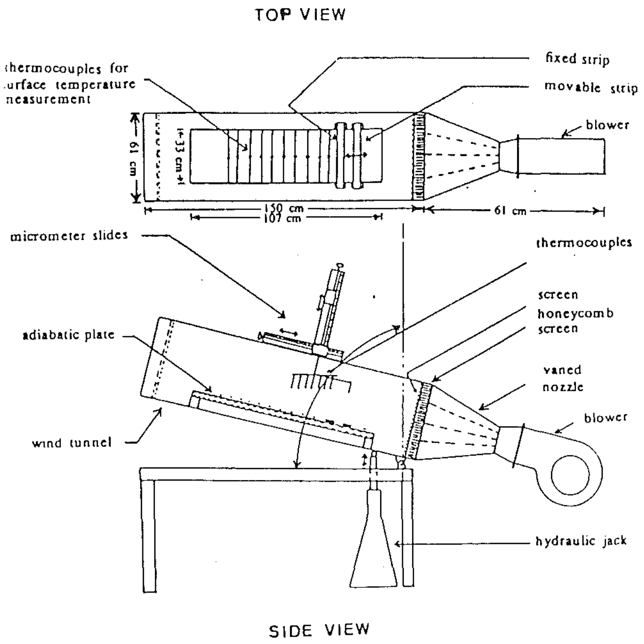

Fig. 2(*a*) Top and side views of the experimental setup

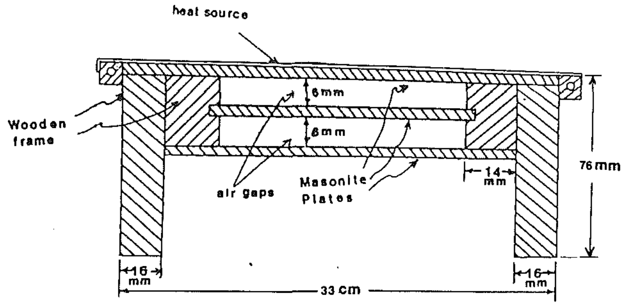

Fig. 2(*b*) End view of the cross-sectional details of the plate on which thermal sources are located

source and that, depending on the distance separating the two sources, the heat transfer coefficient for the downstream source may be increased or decreased. The problem of mixed convection from multiple heat sources has been studied numerically by Jaluria (1985). Tewari et al. (1987) carried out an experimental investigation of the interaction between the wakes arising from two heated strips, with uniform heat flux input, mounted on a flat horizontal surface for the pure natural convection and the buoyancy-dominated flows. The latter circumstance refers to the situation where buoyancy effects are dominant and the forced flow has only a small effect on the thermal transport. The vertical surface orientation was also investigated for the natural convection circumstance. It was found that a relatively stronger heat source significantly increases the temperature of a relatively weaker source located downstream, mainly because of a decrease in its surface heat transfer coefficient, defined in terms of the difference between the source and ambient temperatures.

The present paper concerns the fundamental aspects of the thermal interaction of two heat sources mounted on a flat horizontal or vertical surface; see Fig. 1. It continues and extends the effort presented earlier by Tewari et al. (1987). Experimental results are presented for the pure natural convection, buoyancy-dominated, and mixed convection regimes. Detailed measurements of the heat transfer coefficient and of the effect of source separation are presented. The influence of the upstream source is found to be much stronger in the case of the vertical orientation of the surface, as compared to the horizontal orientation. However, the mixed convection circumstance results in a strong upstream source influence in both orientations. The effect of the upstream source on the temperature of the downstream source is directly related to a reduction in the heat transfer coefficient of the downstream source, since uniform heat flux inputs at the sources are considered in this study.

Experimental Arrangement

An experimental facility was developed to generate a uniform flow with very small turbulence levels in order to obtain steady, accurate heat flux inputs at the sources and to carry out accurate measurements of temperature, heat flux, and flow velocities in a precisely controlled manner. The accuracy of the experimentation was checked by the repeatability of the data and by actual measurements of temperature and velocity in the flow.

The experimental arrangement consists of a long channel with a test section 61 cm × 46 cm in cross-sectional area and 150 cm in length. These dimensions are chosen to ensure that a fairly uniform forced flow is obtained in the test section and that the flow over and the transport from the sources are not significantly affected by the walls. The top and side views of the experimental setup are shown in Fig. 2(*a*). The channel can be inclined at any angle ranging from 0 to 90 deg with the horizontal, by means of a hydraulic jack. A blower attached

Nomenclature

A = surface area of the thermal source
d = separation distance between two isolated heat sources, Fig. 1
D = dimensionless separation distance between two isolated heat sources, equation (1)
g = magnitude of gravitational acceleration
Gr = Grashof number, equation (3)
h = local convective heat transfer coefficient
$\bar{h}$ = average convective heat transfer coefficient, equation (7)
k = thermal conductivity of the fluid
L = height or length of the heated strip, Fig. 1
$\overline{\mathrm{Nu}}_w$ = Nusselt number of the downstream strip when the upstream strip is heated, equation (6)
$\mathrm{Nu}_{w/o}$ = Nusselt number of the downstream strip when the upstream strip is not heated, equation (6)
q_{conv} = heat flux convected from the surface to the flow
Re = flow Reynolds number, equation (5)
q_{in} = uniform surface heat flux input to the heated strip with the smaller heat input, due to the electrical power dissipation
T = local temperature in the flow
T_a = ambient temperature
T_s = local surface temperature
$\overline{T}_s$ = average surface temperature
U_∞ = velocity of the uniform forced flow
x = distance from the leading edge of the plate, Fig. 1
X = dimensionless distance from the leading edge of the plate, equation (1)
y = distance normal to the plate
Y = dimensionless coordinate distance normal to the plate, equations (2*b*) and (4*b*)

to the channel through a vaned nozzle provides a variable flow velocity, ranging from 0 to about 0.5 m/s in the test section. Thus, very low velocities are considered in this work in order to investigate the mixed convection flows of interest. Air enters the test section through a section of honeycomb and a fine-mesh polymer screen. This arrangement provides a fairly uniform flow with negligible turbulence (measured turbulence levels of order 5 percent) over the plate. The uniformity of the flow and the turbulence level were checked by velocity measurements using a hot-wire anemometer.

The isolated heat sources were obtained by electrically heating two highly polished stainless-steel strips, 2.54 cm wide and 0.03 mm thick. The strips were mounted across a test plate (also referred to as plate or surface in this paper), 107 cm long and 33 cm wide. The strips were held taut and flush with the plate surface by means of specially designed clamps. The dimensions of the plate ensured a fairly uniform temperature across the width of the plate. The maximum temperature variation across the plate width was found to be less than 0.5 percent of the midpoint temperature, leading to an essentially two-dimensional conjugate conduction–convection problem. The plate was placed parallel to the forced flow direction and held rigidly inside the test section, with plexiglass end plates to avoid transverse flow over the edges. The change in the orientation, with respect to gravity, is obtained by inclining the channel, as mentioned earlier. The leading edge of the plate was taken as sharp, though a blunt edge was also found to cause negligible disturbance at the low velocity levels considered here. The cross-sectional details of the plate are shown in Fig. 2(*b*). In order to reduce the conduction losses from the heat sources to the plate, the plate was made of three thin (3 mm thick) masonite (of thermal conductivity 0.14 W/m•K at 90°C) boards, separated by two 6-mm air gaps between the boards. The boards were mounted on a wooden platform and sealed at both ends. With this arrangement the conduction loss through the air gaps was estimated to be limited to about 10 percent of the total electrical energy dissipated at the strips. The thermal emissivity of the strips was measured to be of order 0.1 and the radiation heat loss to the ambient was estimated to be less than 10 percent of the total electrical power dissipation (Goel, 1984).

The surface temperature was measured by a set of 24 individually calibrated thermocouples (Copper-Constantan, 0.025-mm-dia wire), attached to the surface by means of a high thermal conductivity cement (Omega, Inc., Omegatherm 201). The thinness of the thermocouples results in negligible disturbance to the boundary layer, as verified by the velocity measurements. The thermocouples were located at various positions in the flow with the junction-bead in each case at the middle and the leads parallel to the leading edge of the plate (Fig. 2(*a*), top view), in order to minimize the conduction error. The temperatures in the flow were measured by a set of seven individually calibrated thermocouples (copper-constantan, 0.050-mm-dia wire), mounted on a rack. The entire thermocouple rack was mounted on a pair of precision micrometer slides (Velmex, Inc.) which provided the desired horizontal and vertical positioning of the rack. The micrometer slides had a least count of 0.154 mm. The error in the temperature measurements was less than 0.5°C, which gave a maximum inaccuracy of about 5 percent in the measured temperature differences.

Three very thin and high-temperature heat flux gages (RdF Corp., Micro-Foil Heat Flow Sensor, Model 270310-20, 5 mm × 15 mm in area and 0.1 mm thick) were mounted on the backside of each heated strip to measure the conductive heat flux from the strips to the plate. This flux is then subtracted from the uniform heat flux input due to the electric power dissipation in the strips to obtain the local convective heat flux from the strips. The electric power dissipation in the strips was obtained by measuring the voltage across the strips and the electric current by means of a precision digital voltmeter and an ammeter, respectively. The experimental error in the heat flux measurements was estimated to be within 10 percent of the measured values. The temperature and the heat flux data were recorded by means of two separate data acquisition systems (Omega, Inc., Whitebox, and Keithley, Series 500). The results were analyzed and graphic outputs obtained using the Sun Microsystems, Series 3/50, microcomputer workstation. Some of the typical results obtained in this study are presented in the next section.

Experimental Results and Discussion

A detailed experimental study was carried out on the thermal interaction between the wakes arising from the two heat sources. Both vertical and horizontal surface orientations were investigated and comparisons were made between the results from the two orientations. A general remark, which was made in our earlier paper and which is worth repeating here, applies to both the orientations. Sharp variations in the surface temperatures are found to occur near the leading and trailing edges of the heated strips. This observation indicates that a substantial conductive transport occurs in the longitudinal (x) direction near the strips, despite the thinness of the masonite boards and their low thermal conductivity. However, almost all of this energy is eventually transferred to the air, though

Nomenclature (cont.)

β = coefficient of thermal expansion of the fluid
$\Delta\theta_{\text{diff}}$ = difference of $\Delta\theta_h$ and $\Delta\theta_v$, equation (14)
$\Delta\theta_h$ = maximum nondimensional temperature increase in the downstream strip due to the presence of the upstream strip, for the horizontal orientation
$\Delta\theta_{\max}$ = maximum value of $\Delta\theta_{\text{diff}}$
$\Delta\theta_v$ = maximum nondimensional temperature increase in the downstream strip due to the presence of the upstream strip, for the vertical orientation
θ = dimensionless local temperature in the flow, obtained from equations (2*a*) and (4*a*) by dropping the subscript s
θ_s = dimensionless surface temperature in the horizontal or vertical orientation, equations (2*a*) and (4*a*)
θ_{s_h} = dimensionless surface temperature for the horizontal orientation, Fig. 19
θ_{s_v} = dimensionless surface temperature for the vertical orientation, Fig. 19
θ_w = maximum value of the nondimensional source temperature in the presence of a neighboring heat source
$\theta_{w/o}$ = maximum value of the nondimensional source temperature in the absence of a neighboring heat source
ν = kinematic viscosity of the fluid

Subscripts

h = horizontal
s = surface
v = vertical
w = in the presence of the upstream source
w/o = in the absence of the upstream source

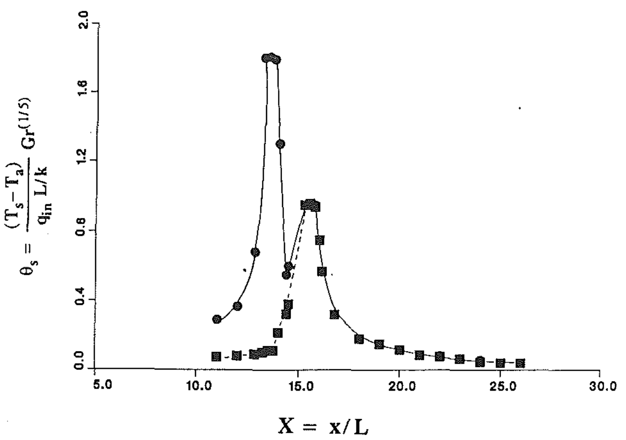

Fig. 3 Effect of a strong heat source on the temperature of a relatively weak neighboring heat source for the horizontal surface orientation in pure natural convection; ———, upstream source at 3200 W/m^2, downstream source at 1300 W/m^2, $D = 1.0$; - - -, isolated heat source at 1300 W/m^2

over an area much larger than the surface area of the heat source. Therefore, the conduction in the plate along the x direction mainly redistributes the heat transfer from the sources. The loss through the air gaps to the backside of the plate is generally less than 10 percent of the energy input, as mentioned earlier. It should also be noted that the effect of longitudinal conduction is limited to only about one strip width and is, therefore, fairly localized (Tewari et al., 1987). Thus, even though around 90 percent of the total energy input is eventually lost to the fluid, conduction effects tend to distort the thermal energy input by spreading it over a much larger surface area and, consequently, lowering the local surface heat flux level.

The thermal interaction between the two heated strips was studied for both the natural and mixed convection circumstances. In a theoretical study of the mixed convection transport from multiple sources located on a vertical surface. Jaluria (1985) obtained $\mathrm{Gr}/\mathrm{Re}^{5/2}$ as the appropriate mixed convection parameter, where Gr and Re are defined later. This parameter was derived from a nondimensionalization of the governing equations and the relevant boundary conditions. As is well known from the available literature, this dimensionless variable plays a key role in establishing different convection regimes for the uniform heat flux circumstances (Jaluria, 1980). Therefore, its significance in the present study would be outlined before the experimental results are discussed. In the absence of an externally induced forced flow velocity ($\mathrm{Gr}/\mathrm{Re}^{5/2} \to \infty$), the circumstance of pure natural convection is obtained. However, when an external flow velocity U_∞ is present, the circumstance is that of mixed convection. For a mixed convection parameter $\mathrm{Gr}/\mathrm{Re}^{5/2}$ around unity, natural and forced convection effects are comparable in magnitude and the circumstance is simply referred to in this paper as that of mixed convection. The mixed convection flow is termed buoyancy dominated if the mixed convection parameter $\mathrm{Gr}/\mathrm{Re}^{5/2}$ is significantly greater than unity, implying a strong natural convection effect. Similarly, if $\mathrm{Gr}/\mathrm{Re}^{5/2}$ is significantly smaller than unity, the mixed convection transport is termed forced flow dominated. In the absence of any heat flux at the surface ($\mathrm{Gr}/\mathrm{Re}^{5/2} = 0$), the circumstance of pure forced convection is obtained. This terminology is employed to demarcate various regimes of flow in the mixed convection transport process.

In the present study, the mixed convection parameter is varied by changing the heat flux and/or the externally induced flow velocity. It was found that about four hours are needed for the surface temperature distribution to reach the appropriate new steady state if one or more of the input parameters, such as the heat flux, flow velocity, or source separation, is changed. This slow transient response is largely due to the conjugate nature of the transport process and severely limits the speed with which different input conditions may be investigated.

The downstream location of the sources, with respect to the leading edge of the plate, is also expected to be an important variable since it determines the local flow characteristics. The location of the leading edge of the upstream source, in terms of the dimensionless downstream distance X, was varied from about 8.0 to 15.0, where X is defined below. It was found that the basic trends in the velocity and temperature fields remained largely unaffected by this change in location, in terms of the dimensionless variables chosen. Consequently, the upstream source was located between $X = 13.0$ and 14.0, and all the results presented here are for this location.

The experimental results are presented in terms of nondimensionalized variables such as the surface temperature θ_s, the local temperature θ in the flow, the distance from the leading edge of the surface X, and the source separation distance D. This nondimensionalization has been frequently applied for convective flows (Jaluria, 1985; Tewari et al., 1987). The nondimensionalized distances along the surface are defined as

$$X = x/L, \qquad D = d/L \tag{1}$$

where L is the height of the heated strip closer to the leading edge (upstream source) in the vertical configuration and the length of the same strip in horizontal configuration. The coordinate system used in the study is shown in Fig. 1. The nondimensional surface temperature, θ_s, is defined for pure natural convection as

$$\theta_s = [(T_s - T_a)/(q_{in}L/k)]\mathrm{Gr}^{1/5} \tag{2a}$$

where q_{in} is the heat flux input at the weaker source, if the two sources have different heat inputs. This value is chosen since, in many cases, interest lies in determining the effect on the transport from the weaker source due to a stronger source in the flow.

The normal distance y away from the surface is nondimensionalized as

$$Y = (y/L)\mathrm{Gr}^{1/5} \tag{2b}$$

where Gr is the Grashof number defined as

$$\mathrm{Gr} = (g\beta q_{in}L^4)/k\nu^2 \tag{3}$$

The nondimensionalized surface temperature in the presence of a forced flow is defined as

$$\theta_s = [(T_s - T_a)/(q_{in}L/k)]\mathrm{Re}^{1/2} \tag{4a}$$

and the normal coordinate distance y is nondimensionalized as

$$Y = (y/L)\mathrm{Re}^{1/2} \tag{4b}$$

where Re is Reynolds number, defined as

$$\mathrm{Re} = U_\infty L/\nu \tag{5}$$

For the local temperature T, the dimensionless temperature is denoted by θ and is obtained from equations (2a) and (4a) by dropping the subscript s. All the symbols used here are defined in the nomenclature. The nondimensionalization used here is the one that arises for the relevant boundary layer flows (Jaluria, 1982a, 1986), since the flow is expected to behave like a boundary layer far from the sources. In this study, U_∞ is varied from 0 to about 0.5 m/s, q_{in} from 400 to 4000 W/m^2, d from 0 to 15 cm, and L from 1 to 3 cm. Consequently, $\mathrm{Gr}/\mathrm{Re}^{5/2}$ was varied from around zero to ∞ (pure natural convection), the combined forced and natural convection results being largely in the range 0.05 to 200. The results for the horizontal surface orientation will be discussed first, followed by those for the case of the vertical orientation. In the discussion that follows, the strong and weak heat sources are heated at the input fluxes of 3200 W/m^2 and 1300 W/m^2,

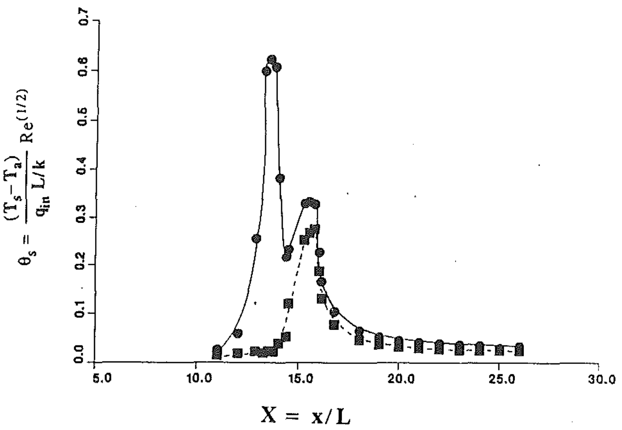

Fig. 4 Effect of an upstream source on the temperature of a downstream source for the horizontal surface orientation in the buoyancy dominated flow regime: $Gr/Re^{5/2} = 47$, $U_\infty = 5$ cm/s; ——— , upstream source at 3200 W/m^2, downstream source at 1300 W/m^2, $D = 1.0$; --- , isolated heat source at 1300 W/m^2

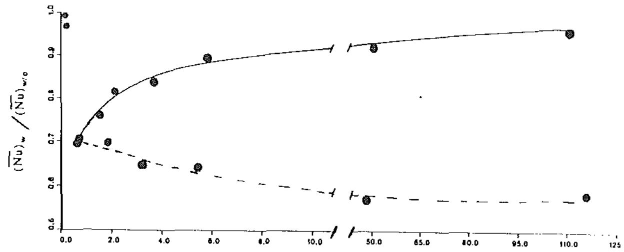

Fig. 5 Effect of an upstream source on the average Nusselt number of a downstream source for a source separation of one strip width; ——— , horizontal surface orientation; --- , vertical surface orientation

respectively. Other heat flux inputs were also considered and these two values are chosen to represent typical heating levels employed in the study. The results presented are well correlated in terms of the dimensionless variables employed. For a consideration of the effect of the heat flux input ratio on the results, see Jaluria (1982a).

Convection From Sources on a Horizontal Surface

Buoyancy-Dominated Flow. The nondimensionalization employed for this case is given by equations (2) and (3). Figure 3 shows the effect of a stronger source on the temperature level of a weaker source placed in its neighborhood. The external flow velocity for this case is zero and, therefore, the circumstance of pure natural convection is obtained. As can be seen in the figure under consideration, the temperature of the weaker source is almost the same as that in the absence of the stronger source. This is an expected result for two essentially independent, vertically rising plumes, indicating that there is essentially no interaction between the two plumes rising from the two sources. In fact, the downstream direction here is not along the plate surface but normal to it, since the free plume rises vertically. At sufficiently small separation distances, these flows will interact (Pera and Gebhart, 1975) and the weaker plume will tilt toward the stronger one, affecting the surface heat transfer, as studied by Gebhart et al. (1976). Although such an interaction was observed at smaller D values, the results obtained are not presented here for brevity. The above references may be consulted for further details on the flow that arises due to the interaction of two-dimensional and axisymmetric plumes.

The effect of a small external flow velocity is investigated next and the results are presented in Fig. 4, for the same heat flux input and separation distance D as used in Fig. 3. The forced flow velocity U_∞ is 5 cm/s for this figure. The mixed convection parameter, $Gr/Re^{5/2}$, is 47.0 for this circumstance. Thus, the situation of a weaker source placed downstream of a stronger source in a buoyancy-dominated circumstance is considered. As mentioned earlier, the heat flux used for calculating the Grashof number Gr is chosen as the smaller of the two heat fluxes, i.e., 1300 W/m^2, so that the resulting effect of varying the upstream source heat input could be determined. As can be seen from this figure, the temperature of the downstream strip is about 20 percent higher than that in the absence of the upstream strip. As expected, an increase in the upstream heat input resulted in an increase in the temperature of the downstream source. This effect is discussed quantitatively later in the paper.

As will be shown later, the corresponding situation for the vertical surface orientation results in a much larger increase (up to 70 percent) in the temperature of the downstream strip. This is largely due to the fact that, in the case of the horizontal configuration, for both the pure natural convection and the buoyancy-dominated flows, the wake from the upstream strip is essentially a vertically rising plume and has only a limited interaction with the plume rising from the downstream strip. Flow visualization by means of smoke indicated that for forced flow velocities of up to around 10 cm/s, the plume from a strip heated at 1300 W/m^2 rises almost vertically before being dissipated by the external flow. The mixed convection parameter, $Gr/Re^{5/2}$, at this value of U_∞ is 8.2. The locations downstream are, therefore, not strongly affected by the upstream wake for the horizontal orientation.

In order to investigate the thermal interaction between the strips in more detail, measurements were undertaken for the heat transfer coefficient at the strip surface. The results for $D = 1.0$ are shown in Fig. 5, using a polynomial best fit of the data. The curves were drawn on the complete graph and a break was then introduced, as shown, in order to reduce the size of the figure. This figure shows the effect of the upstream strip on the average convective heat transfer coefficient for the downstream strip over a wide range of the mixed convection parameter. The ratio of the average Nusselt number in the presence of the upstream strip, $\overline{Nu}_w$, to that without the upstream strip, $\overline{Nu}_{w/o}$ is plotted against the mixed convection parameter, $Gr/Re^{5/2}$. The average Nusselt number is defined here as

$$\overline{Nu}_w \text{ or } \overline{Nu}_{w/o} = \bar{h}\ L/k \tag{6}$$

where $\bar{h}$ is the average heat transfer coefficient over the strip surface, and is measured by two independent methods. In the first approach, $\bar{h}$ is defined in terms of the average surface temperature $\bar{T}_s$ as

$$\bar{h} = q_{\text{conv}}/(\bar{T}_s - T_a) \tag{7}$$

The heat flux q_{conv} is the average of the heat flux values obtained by means of the heat flux gages mounted beneath the strips, as described earlier. The ambient temperature is measured by the rack of thermocouples and the surface temperature by the embedded thermocouples. Here, the heat transfer coefficient $\bar{h}$ is defined in terms of the temperature difference $\bar{T}_s - T_a$, even though the driving temperature difference for convection is altered due to the presence of the upstream thermal wake. A local mixed temperature may be used to characterize the wake effect. However, this temperature is not known and cannot be easily related to the underlying physical process. A better approach will be to employ the adiabatic temperature rise of the source due to the upstream wake, as outlined by Anderson and Moffat (1988) and as also discussed later in the paper.

In the second method, the heat transfer coefficient is obtained by measuring the temperature profile in the flow ad-

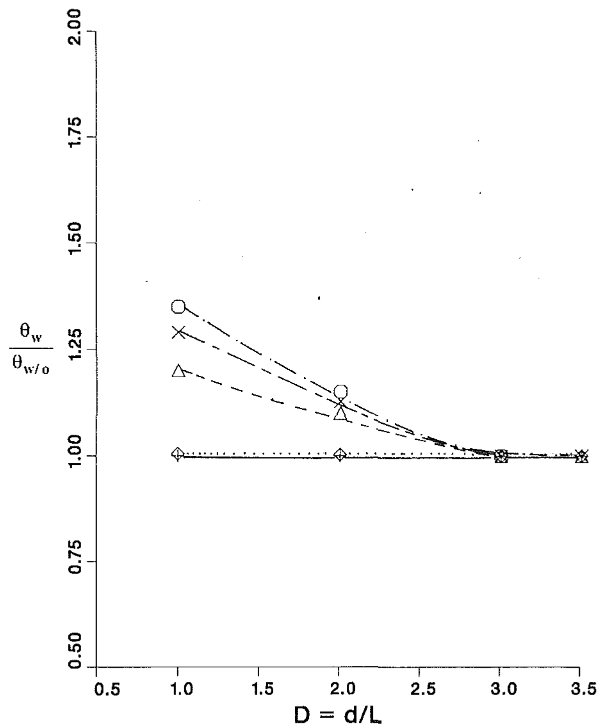

Fig. 6 Effect of a stronger upstream source on the maximum temperature of a weaker downstream source as a function of the source separation distance for the horizontal surface orientation; +, pure natural convection; △, buoyancy dominated ($Gr/Re^{5/2} = 47$); x, mixed convection ($Gr/Re^{5/2} = 3.2$); ○, mixed convection ($Gr/Re^{5/2} = 0.8$); ◇, forced flow dominated ($Gr/Re^{5/2} = 0.13$)

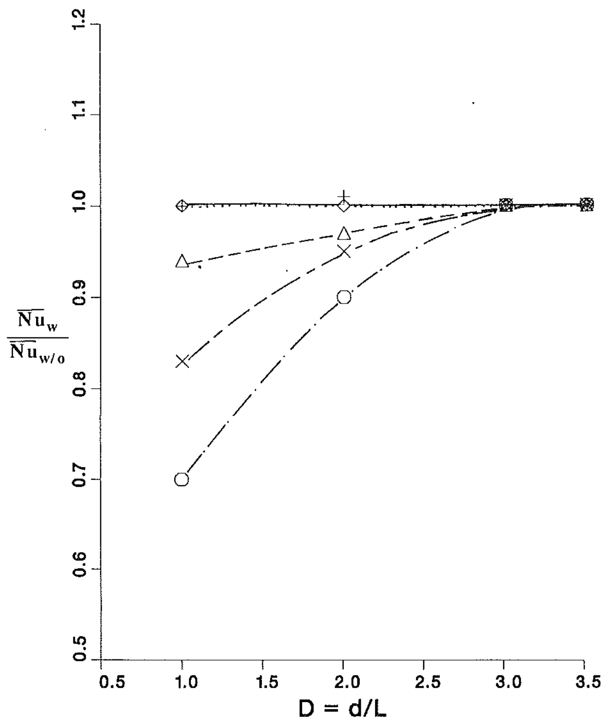

Fig. 7 Effect of a stronger upstream source on the average Nusselt number of a weaker downstream source as a function of the source separation distance for the horizontal surface orientation; +, pure natural convection; △, buoyancy dominated ($Gr/Re^{5/2} = 47$); x, mixed convection ($Gr/Re^{5/2} = 3.2$); ○, mixed convection ($Gr/Re^{5/2} = 0.8$); ◇, forced flow dominated ($Gr/Re^{5/2} = 0.13$)

jacent to the heated strips and calculating the temperature gradient at the strip surface. The temperature gradients are measured at the locations where the heat flux gages are mounted. The local heat transfer coefficient h is calculated from

$$h = -k\frac{dT}{dy}\Big|_{y=0}/(T_s - T_a) \quad (8)$$

The average heat transfer coefficient h is then obtained from

$$h = (1/A)\int h\, dA \quad (9)$$

where A is the surface area of the strip. A close agreement was obtained between the heat transfer coefficients determined by the two independent methods, lending support to the experimental procedures used.

Now consider the results for the horizontal orientation shown in Fig. 5. It can be seen that for the buoyancy-dominated case ($Gr/Re^{5/2}$ significantly greater than unity), there is less than a 10 percent reduction in the average Nusselt number $\overline{Nu}$ of the downstream strip due to the presence of the upstream strip. In the pure natural convection case, which refers to the asymptotic value as $Gr/Re^{5/2} \rightarrow \infty$, the Nusselt number ratio is almost unity, indicating essentially no upstream strip influence at this value of D as well as for larger values of D. These measurements, therefore, lend support to the observations made in Figs. 3 and 4. The results for the vertical orientation in Fig. 5 will be discussed later.

The effect of the separation distance D between the two heat sources will be considered now. The results discussed earlier were for a source separation of one strip width, i.e., $D = 1.0$. Figure 6 is a plot of the ratio of the maximum nondimensional surface temperature of the downstream source, θ_w, in the presence of an upstream source to that without an upstream source, $\theta_{w/o}$, as a function of the source separation distance. Consider the curves for the pure natural convection and the buoyancy-dominated ($Gr/Re^{5/2} = 47$) circumstances. As expected, the influence of the upstream source decreases as the source separation increases. At D of 2.0 and 3.0, the downstream strip temperature increases by 10 and 0 percent, respectively, for the buoyancy-dominated flow. For pure natural convection, the upstream strip has a negligible influence on the downstream strip temperature at D greater than 2.0. The mixed convection regime results shown in this figure are discussed later in the paper.

The above trends in the strip surface temperatures are related to the trends in the convective heat transfer coefficient for the strips, as shown in Fig. 7. This figure shows how the average heat transfer coefficient for a downstream source is affected by the presence of an upstream source at various source separation distances. Consider the curves for the pure natural convection and the buoyancy-dominated flows. At $D = 2.0$ and 3.0, there is an almost negligible change in the downstream strip Nusselt number in the circumstance of pure natural convection. Respective changes of about 3 and 0 percent are obtained for the buoyancy-dominated circumstance ($Gr/Re^{5/2} = 47$).

The reduction in the average heat transfer coefficients for the strip are, thus, related to the increase in its surface temperatures for the uniform heat flux circumstance considered here. As the separation distance D between the strips is increased, the heat transfer coefficient for the downstream strip increases. This is because as the wake from the upstream strip proceeds downstream along with the forced flow, its temperature decreases due to exchange with the cooler ambient. The result is a diminishing upstream source influence on a downstream source and a consequent increase in the heat transfer coefficient.

The effect of a weaker upstream source on a stronger source placed downstream is shown in Fig. 8. In the pure natural convection and the buoyancy-dominated ($Gr/Re^{5/2} = 47$) circumstances, the downstream strip temperature increases by 0 and 5 percent, respectively at $D = 1.0$. Again, the increase is

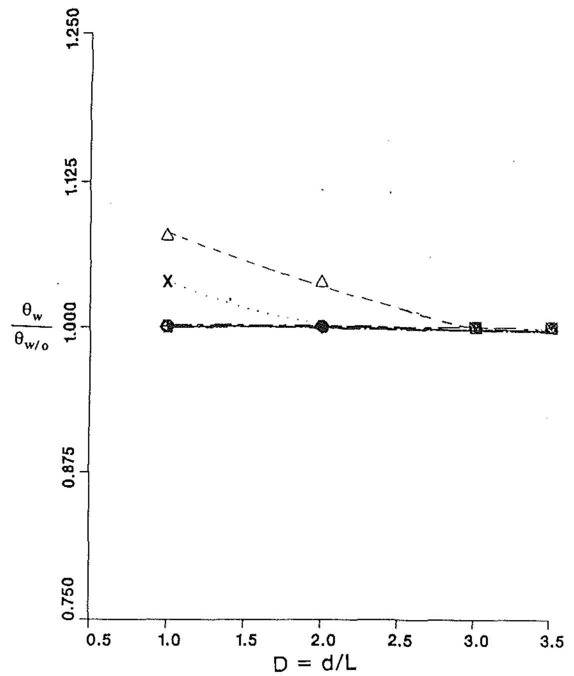

Fig. 8 Effect of a weaker upstream source on the maximum temperature of a stronger downstream source as a function of source separation distance for the horizontal surface orientation; +, pure natural convection; △, buoyancy dominated ($Gr/Re^{5/2} = 47$); x, mixed convection ($Gr/Re^{5/2} = 3.2$); ○, mixed convection ($Gr/Re^{5/2} = 0.8$); ◇, forced flow dominated ($GR/Re^{5/2} = 0.13$)

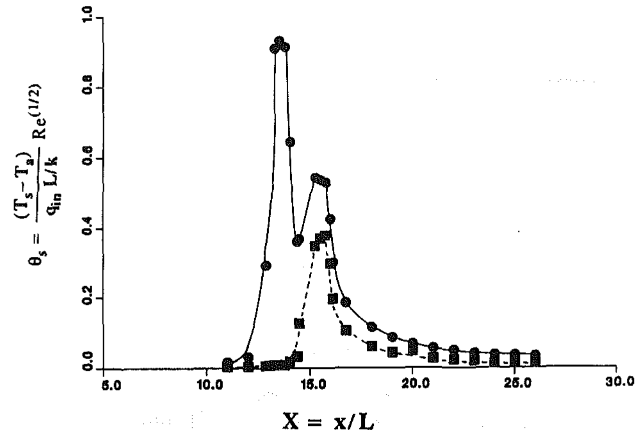

Fig. 9 Effect of a stronger upstream source on the temperature of a weaker downstream source for the horizontal surface orientation in mixed convection; $Gr/Re^{5/2} = 0.8$, $U_\infty = 25$ cm/s; ———, upstream source at 3200 W/m², downstream source at 1300 W/m², $D = 1.0$; - - -, isolated source at 1300 W/m²

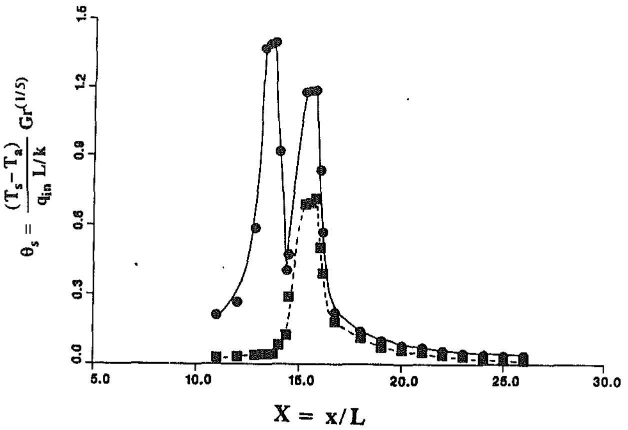

Fig. 10 Effect of an upstream source on the temperature of a downstream source in the vertical surface orientation in pure natural convection; ———, upstream source at 3200 W/m², downstream source at 1300 W/m², $D = 1.0$; - - -, isolated downstream source at 1300 W/m²

almost negligible at larger separation distances. As will be discussed later, this circumstance of a weaker upstream source leads to more interesting results for the vertical orientation.

Figures 6–8 indicate the effect of the upstream source on the thermal transport from the downstream source for the horizontal orientation. Anderson and Moffat (1988) termed the temperature rise at a downstream location due to the thermal wake effect of upstream elements as the adiabatic temperature rise and obtained a heat transfer coefficient based on the difference between the source temperature and the adiabatic temperature. The temperature rise due to the wake, added to the temperature rise due to the internal heating of the downstream element, yields the total temperature rise. Thus, Fig. 6 shows that the temperature of the downstream element increases by almost 34 percent due to upstream wake effect at $Gr/Re^{5/2} = 0.8$ and $D = 1.0$, indicating the importance of the adiabatic temperature rise in this flow. Similarly, Fig. 7 shows the effect on the Nusselt number, defined in terms of the ambient temperature, and Fig. 8 the corresponding results for a stronger source in the wake of a weaker source. Clearly, the wake effect is stronger for a weaker downstream source, as expected. For $D > 3.0$, the wake effect is negligible for all the cases considered here. For the vertical orientation, the wake effects are much stronger, as discussed later.

Mixed Convective Flow. The nondimensionalization employed for this case is given by equations (4) and (5). The mixed convective circumstance is obtained by increasing the external flow velocity U_∞. Figure 9 shows the effect of the heat input at the upstream strip on the temperature of the downstream strip at $D = 1.0$. As can be seen in the figure, for a $Gr/Re^{5/2}$ of 0.8, the temperature of the downstream source is about 40 percent higher in the presence of the upstream source than when the upstream source is absent. This increase in source temperature is considerably higher than the increases obtained for pure natural convection and the buoyancy-dominated flows. At $Gr/Re^{5/2} = 3.2$, a 25 percent increase in the downstream strip temperature is obtained and for $Gr/Re^{5/2} > 50$, and increase of less than 5 percent is observed. Also for $Gr/Re^{5/2} = 0.13$, which is clearly a forced flow dominated circumstance, the effect of the upstream source was found to be essentially negligible. These observations are explained in terms of the underlying flow mechanisms, as outlined below.

It is also interesting to look at the average Nusselt number $\overline{Nu}$ of the downstream source in Fig. 5. A sharp decrease in $\overline{Nu}$ (or heat transfer coefficient) of the downstream strip occurs as the mixed convection parameter decreases from 4.0 to 0.5. This is due to the fact that the upstream plume tilts increasingly in the direction of the flow, affecting the downstream locations, as U_∞ increases or q_{in} decreases. The effect of the upstream plume is to raise the flow temperature directly above the downstream strip and, consequently, to lower its heat transfer coefficient, which is defined in terms of the source temperature difference from the ambient temperature; see equation (7). Once the plume is well aligned with the surface, which is the case at values of $Gr/Re^{5/2}$ around 0.5, a further increase in the flow velocity, or a decrease in the heat input, merely results in a reduction in the temperature level, because of the increased exchange with the ambient or the reduced heat input. As can be seen in this figure, a value of $Gr/Re^{5/2}$ below 0.1 (i.e., in the forced flow dominated region) leads to a negligible influence of the upstream strip on the downstream strip heat transfer coefficient. Thus, both at very small and very large values of $Gr/Re^{5/2}$, the effect of the upstream heat input on the downstream heat source is small.

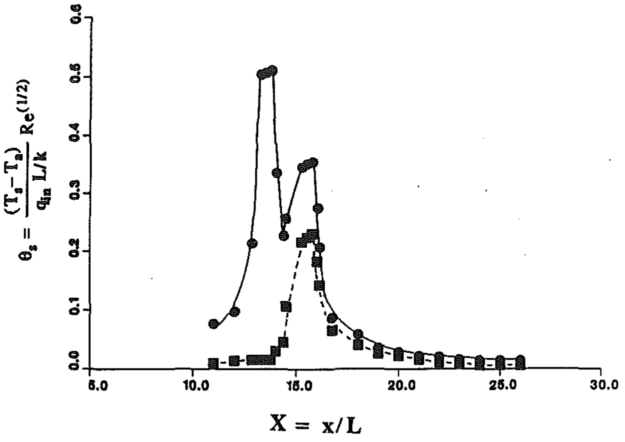

Fig. 11 Effect of an upstream source on the temperature of a downstream source for the vertical surface orientation in the buoyancy-dominated flow; $Gr/Re^{5/2} = 47$, $U_\infty = 5$ cm/s; ——— , upstream source at 3200 W/m^2, downstream source at 1300 W/m^2, $D = 1.0$; --- , isolated downstream source at 1300 W/m^2

As in the case of the buoyancy-dominated flow, the effect of the separation distance D will be discussed next for the case of the mixed convective flow regime. Figure 6 shows that as the source separation is increased beyond one strip width, the influence of the upstream strip on the downstream strip decreases sharply. At a separation of two strip widths, the increase in the temperature of the downstream strip due to the upstream source is less than 20 percent for all the circumstances considered. The change is almost negligible when the strips are separated by a distance D of 3.0 or more, implying a very small adiabatic temperature rise at the downstream source. This increase in the surface temperature can again be related to the decrease in the average heat transfer coefficient for the downstream strip. Figure 7 shows that the average Nusselt number for the downstream strip increases sharply as the source separation distance is increased, indicating a decreased influence of the upstream source on the downstream one. At $D = 2.0$, the Nusselt number of the downstream source is decreased by about 10 percent for the circumstances considered here. Again, the change in $\overline{Nu}$ is almost negligible at $D = 3.0$ or greater.

A relatively weak upstream source has a smaller influence on a relatively stronger source placed downstream. Typical results for this circumstance are shown in Fig. 8. Increasing the ambient flow velocity U_∞ from that corresponding to a buoyancy-dominated circumstance ($Gr/Re^{5/2} = 47$) to that corresponding to a mixed convection circumstance ($Gr/Re^{5/2} = 3.2$) leads to a continuous increase in the upstream source influence, since the upstream plume gets increasingly aligned with the surface. When the velocity is increased, so that $Gr/Re^{5/2}$ becomes 0.8, a decrease in the upstream source influence is observed, since the cooling effect of the flow dominates the effect of the increased local fluid temperature. This trend is obviously different from that obtained when the upstream strip was the stronger source; see Fig. 6. In that case, the upstream source influence was found to increase with velocity up to much higher values of the flow velocity. This result clearly indicates the dominant effect of velocity at relatively smaller heat inputs at the downstream source.

A comparison between Figs. 6 and 8 shows another interesting feature. Both for pure natural convection and for forced flow dominated circumstances, the upstream wake effect is negligible even for a source separation distance D of 1.0. Therefore, since the wake effect is negligible for $Gr/Re^{5/2}$ very small and very large, the maximum effect arises at an intermediate value, being 0.8 in Fig. 6 and 47.0 in Fig. 8. In the former case, the upstream source is stronger and, thus, even at 0.8 a strong effect is felt downstream. In Fig. 8, the upstream source is weaker and a much larger value of $Gr/Re^{5/2}$ is needed for an appreciable effect. These trends arise because of the horizontal orientation, for which the wakes tend to rise vertically, with essentially no interaction at $D = 1.0$ for the natural convection case. The alignment of the wake along the plate due to the forced flow causes the wake effects observed at different values of $Gr/Re^{5/2}$. For the vertical orientation, the wake is always aligned with the plate and the observed trends are, consequently, very different.

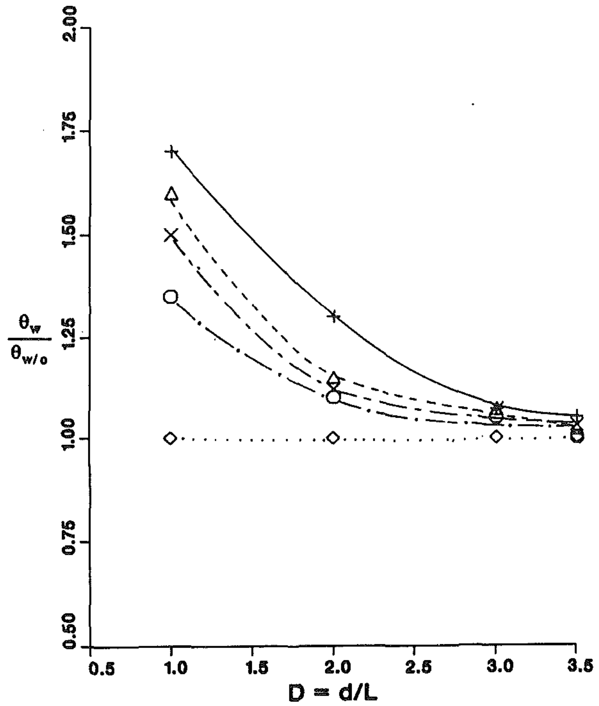

Fig. 12 Effect of a stronger upstream source on the maximum temperature of a weaker downstream source as a function of the source separation distance for the vertical surface orientation; +, pure natural convection; △, buoyancy dominated ($Gr/Re^{5/2} = 47$); x, mixed convection ($Gr/Re^{5/2} = 3.2$); ○, mixed convection ($Gr/Re^{5/2} = 0.8$); ◇, forced flow dominated ($Gr/Re^{5/2} = 0.13$)

Convection From Sources on a Vertical Surface

Buoyancy-Dominated Flow. The nondimensionalization used in this case is given by equations (2) and (3). The circumstance of pure natural convection is obtained when the external velocity U_∞ is zero. Figures 10 and 11 show that for the pure natural convection and the buoyancy-dominated ($Gr/Re^{5/2} = 47$) circumstances, the temperature of a relatively weak downstream source increases by 70 and 60 percent, respectively, at $D = 1.0$. These values may be compared with those obtained earlier for the case of the horizontal configuration, where a much smaller change in the source temperature was obtained. This difference in the horizontal and vertical orientations can be attributed to the difference in the orientation of the wake with respect to the surface. In the vertical configuration, the wake is always aligned with the surface due to the buoyancy force being vertical and, therefore, downstream locations are always under its influence. For the horizontal configuration, the heated wake tends to rise vertically, whereas the forced flow and the surface are horizontal. Thus, the effect of the wake downstream depends very much on the forced velocity and the heat input at the upstream source, as discussed earlier.

Returning to Fig. 5, we see that for $Gr/Re^{5/2}$ significantly greater than unity, the Nusselt number for the downstream strip is reduced by about 40 percent due to the presence of a

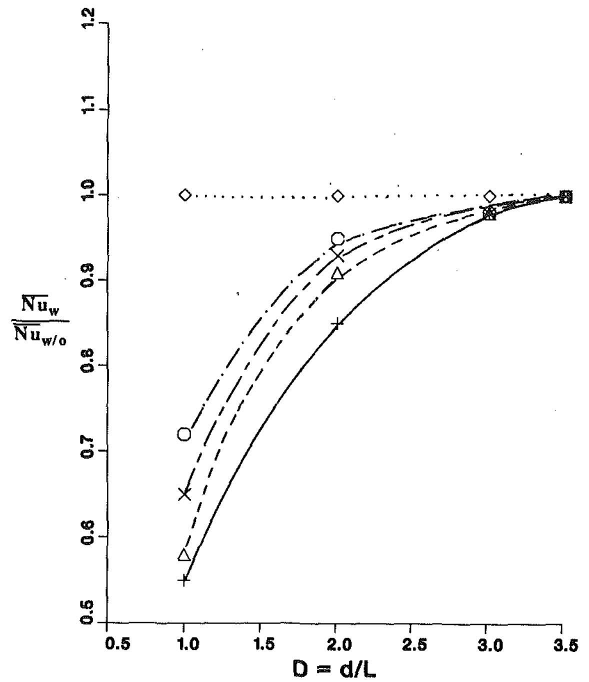

Fig. 13 Effect of a stronger upstream source on the average Nusselt number of a weaker downstream source as a function of the source separation distance for the vertical surface orientation; +, pure natural convection; △, buoyancy dominated ($Gr/Re^{5/2} = 47$); x, mixed convection ($Gr/Re^{5/2} = 3.2$); ○, mixed convection ($Gr/Re^{5/2} = 0.8$); ◇, forced flow dominated ($GR/Re^{5/2} = 0.13$)

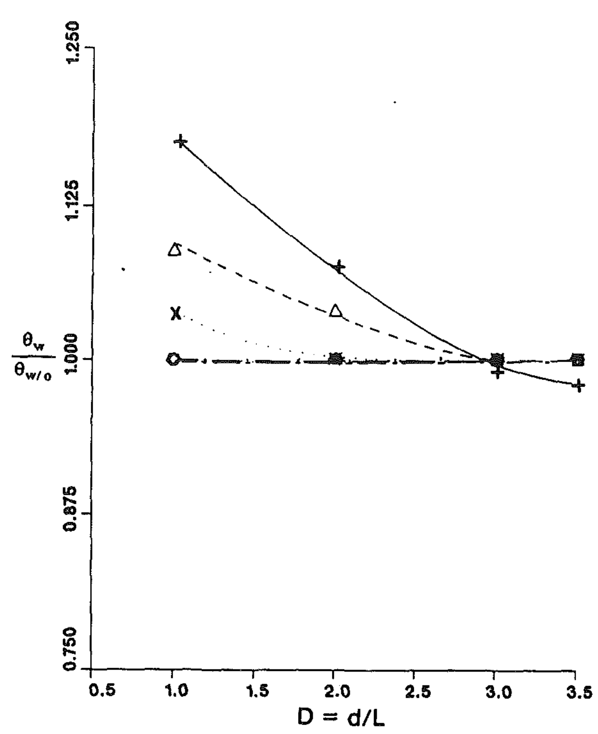

Fig. 14 Effect of a weaker upstream source on the maximum temperature of stronger downstream source as a function of the source separation distance for the vertical surface orientation; +, pure natural convection; △, buoyancy dominated ($Gr/Re^{5/2} = 47$); x, mixed convection ($Gr/Re^{5/2} = 3.2$); ○, mixed convection ($Gr/Re^{5/2} = 0.8$); ◇, forced flow dominated ($Gr/Re^{5/2} = 0.13$)

relatively stronger upstream source for the vertical orientation, whereas it remains essentially unchanged for the horizontal case. Thus, the difference between the horizontal and the vertical configurations can be seen very clearly in this figure. The horizontal configuration leads to a much smaller thermal interaction between the strips as indicated by a significantly smaller reduction in the average Nusselt number of the downstream source as compared to that for the vertical configuration. As $Gr/Re^{5/2}$ increases, the thermal interaction between the sources increases for the vertical case and decreases for the horizontal one. Again, the asymptotic result for $Gr/Re^{5/2} \rightarrow \infty$ refers to the pure natural convection circumstance. Thus, for the vertical orientation, the wake effect is the strongest for natural convection, whereas it is the weakest in the horizontal case. This is expected behavior. An addition of a forced flow velocity U_∞ reduces the effect from the observed asymptotic value of around 0.6, which is close to the corresponding result obtained numerically by Jaluria (1982a).

The effect of the source separation distance D on the temperature of the downstream source in the presence of a strong upstream source can be seen in Fig. 12. At a separation distance of two strip widths, the temperature of the downstream strip increases by 30 and 20 percent for the pure natural convection and the buoyancy-dominated cases, respectively. The influence of the upstream strip on the downstream strip is almost negligible for D greater than 3.0. Figure 13 shows the corresponding decrease in the heat transfer coefficient. At a separation distance of two strip widths, the average Nusselt number of the downstream strip is reduced by about 15 and 10 percent for the pure natural convection and the buoyancy-dominated cases, respectively. A negligible change in the downstream strip heat transfer coefficient is obtained when the separation distance is increased beyond 3.5 strip widths.

An interesting circumstance is that of a relatively strong downstream source placed in the wake of relatively weak upstream source; see Fig. 14. In the pure natural convection circumstance, the temperature of the stronger source is increased due to the upstream source by 15 and 10 percent at D of 1.0 and 2.0, respectively. For $D = 3.0$, the downstream strip temperature actually decreases. At a separation of 3.5 strip widths the decrease is found to be about 2 percent. Jaluria (1982a), in a numerical study of multiple heat sources mounted on an adiabatic vertical plate in the natural convection circumstance, found similar results. The physical explanation is that as the wake proceeds downstream, the temperature in the wake decays downstream due to entrainment and the velocity increases due to buoyancy. Therefore, an increase in the separation distance increases the heat transfer coefficient and, consequently, decreases the temperature of the downstream source. In the presence of a small external flow velocity 5(cm/s), resulting in a $Gr/Re^{5/2}$ of 47, a negligible change is found in the downstream strip temperature and, thus, in the heat transfer coefficient for $D = 3.0$ or more.

The above results may again be compared with those for the horizontal surface orientation, where for the pure natural convection case, a relatively weak source had a negligible influence on a relatively strong heat source located downstream. This is obviously due to the relatively limited interaction between the plumes of the two heat sources in the horizontal surface orientation.

Mixed Convective Flow. The mixed convective regime was studied for $Gr/Re^{5/2}$ values of 3.2, 0.8, and 0.13. Figure 15 shows the effect on the temperature level of the downstream strip due to the presence of an upstream source at $D = 1.0$ and $Gr/Re^{5/2} = 0.8$. When a relatively stronger source is placed upstream of a weaker source, the maximum temperature of the weaker heat source was found to be increased by about 50 and 35 percent, respectively, at $Gr/Re^{5/2}$ values of 3.2 and 0.8. When $Gr/Re^{5/2}$ is reduced to 0.13, which is a forced flow dominated circumstance, the upstream source influence was found to be almost negligible, as shown in Fig. 12. These trends may again be considered in terms of the Nusselt number behavior and the nature of the flow.

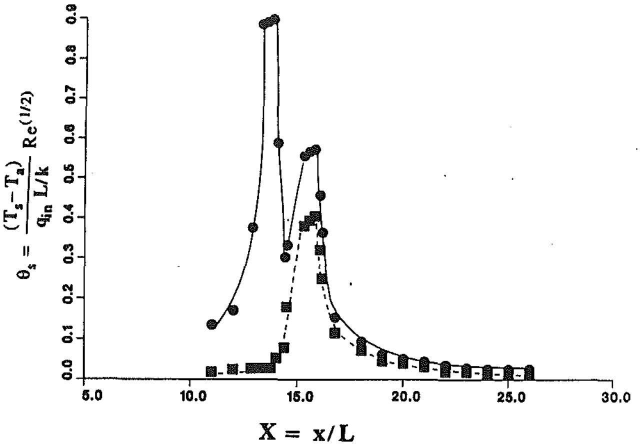

Fig. 15 Effect of an upstream source on the temperature of a downstream source for the vertical surface orientation in mixed convective flow; $Gr/Re^{5/2}=0.8$, $U_\infty = 25$ cm/s; ——— , upstream source at 3200 W/m², downstream source at 1300 W/m², $D=1.0$; --- , isolated downstream source at 1300 W/m²

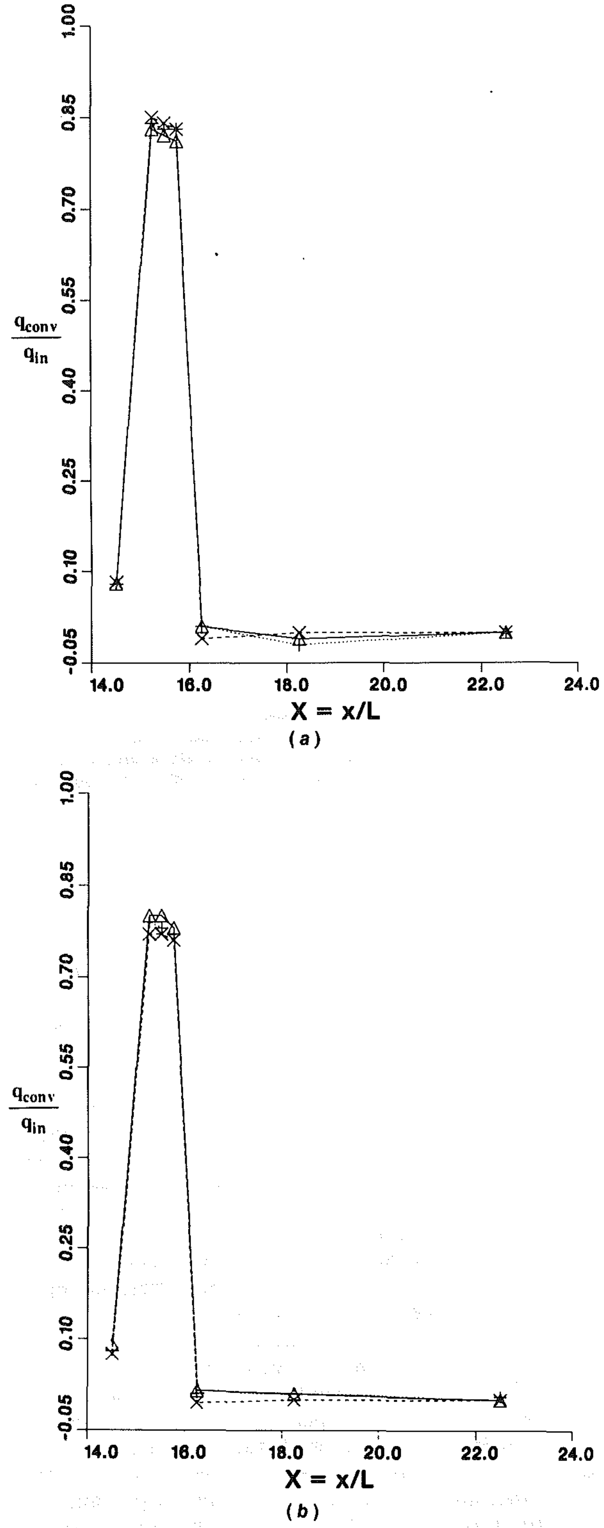

Fig. 16 Effect of the forced flow velocity on the temperature gradient in the flow at the surface; ——— , pure natural convection, --- , buoyancy dominated ($Gr/Re^{5/2}=47$); ..... , mixed convection ($Gr/Re^{5/2}=0.8$): (*a*) horizontal orientation; (*b*) vertical orientation

Figure 5 shows that a relatively sharp change in the average Nusselt number of the downstream strip occurs for a mixed convection parameter, $Gr/Re^{5/2}$, in the range 0.5 to 5.0 for the vertical orientation. However, the change is seen to be less sharp than that in the case of the horizontal configuration. This is because, in the vertical orientation, the main effect of an increase in the velocity is an increase in the entrainment of the ambient fluid. However, in the horizontal orientation, an increase in the velocity may lead to not only an increase in the entrainment but also an increase in the downstream tilting of the plume rising from the upstream source. As the plume aligns with the surface, there is a sharp change in the heat transfer coefficient at the downstream source. These aspects were discussed earlier in connection with flow over a horizontal surface.

As the separation distance between the strips is increased to two strip widths (Fig. 12), the increase in the maximum temperature of the stronger downstream source is around 18, 12, and 0 percent for $Gr/Re^{5/2}$ values of 3.2, 0.8, and 0.13, respectively. This increase becomes almost negligible as the separation distance is increased to $D=3.0$ or higher. Figure 13 shows that the average heat transfer coefficient for the downstream heat source increases toward the value that arises in the absence of the upstream source as D is increased, indicating a decreasing upstream source influence with the separation distance.

Figure 14 shows that a relatively weak source has a very small effect on the temperature of a relatively strong source for $Gr/Re^{5/2}$ of 0.8, and even smaller effect at $Gr/Re^{5/2}$ of 0.13, as expected. This result is similar to that found for the horizontal orientation, indicating a diminishing effect of surface orientation as $Gr/Re^{5/2}$ is decreased to small values.

A further insight into the relationship between the decrease in the heat transfer coefficient and the increase in the surface temperature may be gained by considering the temperature gradients in the flow, at the surface. Even though the heat flux input q_{in} is constant over the surface of each thermal source, the temperature gradient in the fluid at the surface is not necessarily constant because of the conductive transport to the plate. As discussed earlier, the conduction into the plate makes the heat flux input nonuniform over the surface, even though the total energy entering the fluid is not significantly affected because of the insulation arrangement used for the plate; see Fig. 2(*b*). The effect of an external flow velocity U_∞ on the measured temperature gradients in the flow at locations downstream of a heated upstream source are shown in Figs. 16(*a*) and 16(*b*). The nondimensional temperature gradient in the flow, at the surface, can be written as

$$\frac{d\theta}{dY}\Big|_{y=0}=\frac{dT}{dy}\Big|_{y=0}(k/q_{in})-\frac{q_{conv}}{q_{in}} \tag{10}$$

As can be seen in the figure, the temperature gradients in the flow at the strip surface do not change by more than ±5 percent as the flow goes from pure natural convection to the mixed convection circumstance. Therefore, these measure-

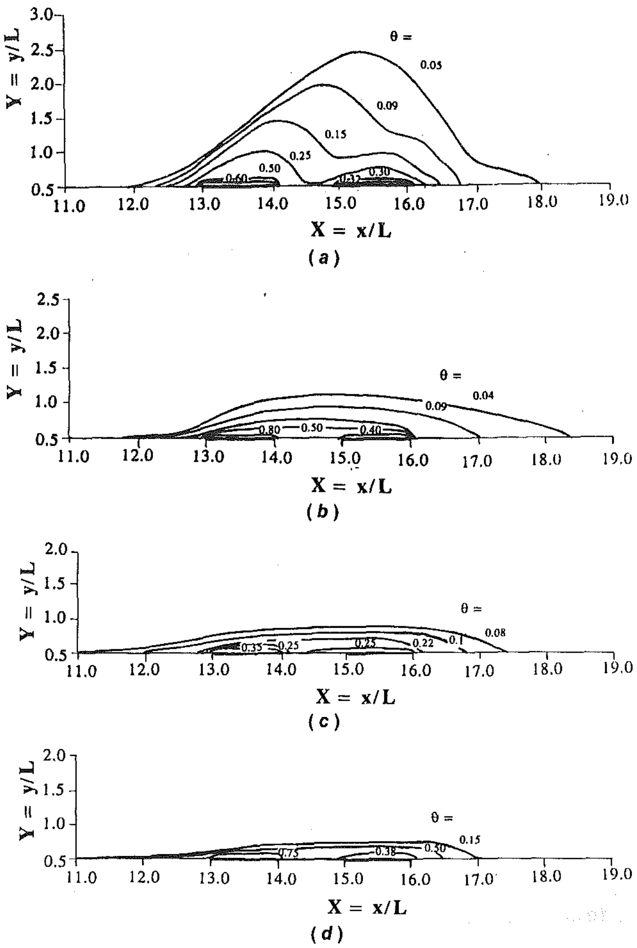

Fig. 17 Isotherm distributions for: (*a*) buoyancy-dominated flow ($Gr/Re^{5/2} = 47$) for the horizontal surface orientation; (*b*) mixed convective flow ($Gr/Re^{5/2} = 0.8$) for the horizontal surface orientation; (*c*) buoyancy-dominated flow ($Gr/Re^{5/2} = 47$) for the vertical surface orientation; (*d*) mixed convective flow ($Gr/Re^{5/2} = 0.8$) for the vertical surface orientation

ments indicate that an increase in the fluid temperature adjacent to the strip is accompanied by a corresponding increase in the strip surface temperature keeping the temperature gradients in the flow, at the surface, largely unaffected. Consequently, the heat convected to the fluid adjacent to the downstream strip remains largely unchanged due to a variation in the flow velocity, in the presence of a heated upstream strip. Therefore, as shown from the following equation, the fraction $(q_{\text{conv}})_w/(q_{\text{conv}})_{w/o}$ remains essentially unaltered as the flow velocity is changed.

$$\frac{(q_{\text{conv}})_w}{(q_{\text{conv}})_{w/o}} = \frac{-k\dfrac{dT}{dy}\Big|_w}{-k\dfrac{dT}{dy}\Big|_{w/o}} \tag{11}$$

Since the electrical heat flux dissipated at the sources is constant and since the conduction heat loss through the air gaps to the backside of the plate is negligible, the above results imply that the heat conduction in the plate along the x direction ($= q_{in} - q_{\text{conv}}$) remains largely unchanged by a change in the external flow velocity, in the presence of a heated upstream source. This result is supported by the constancy (to within ±5 percent) of the experimentally measured heat flux convected from locations downstream of the upstream strip and the fact that the heat conducted in the plate is eventually convected to the flow. Only a small portion of the energy input is lost from the flow across the air gaps. As shown in equation (12) below, the increase in the surface temperature is directly proportional to the decrease in the convective heat transfer coefficient, if q_{conv} is essentially unchanged with varying U_∞.

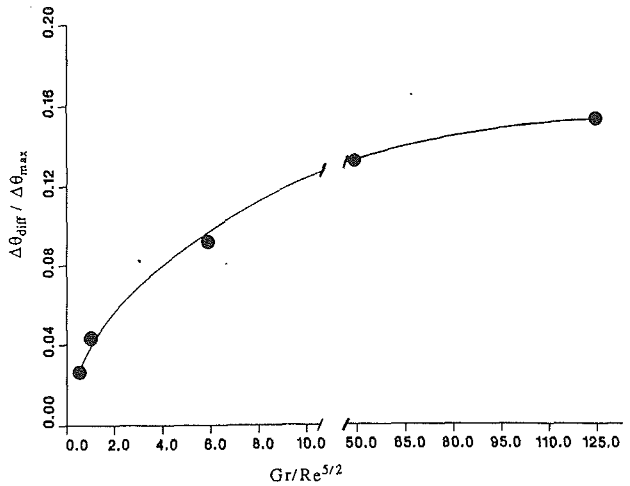

Fig. 18 Effect of surface orientation on the influence of an upstream source on the temperature of a downstream source, as a function of the mixed convection parameter, for a source separation distance of one strip width: upstream source at 3200 W/m², downstream source at 1300 W/m²

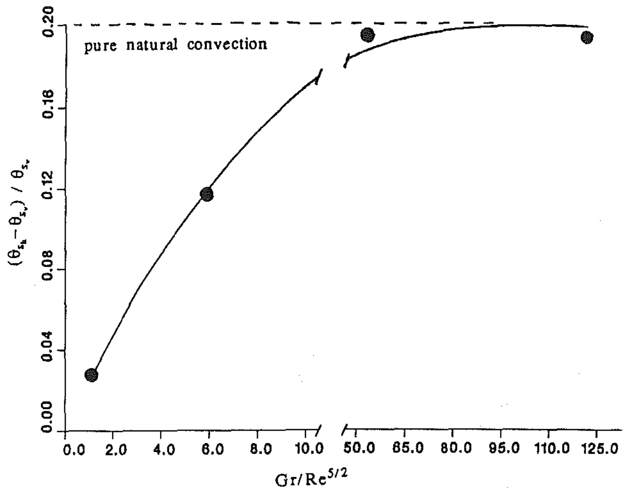

Fig. 19 Effect of surface orientation on the temperature of the downstream heat source as a function of the mixed convection parameter, for a source separation distance of one strip width: upstream source at 3200 W/m² and downstream source at 1300 W/m²

$$q_{\text{conv}} = h(T_s - T_a) \cong \text{const} \tag{12}$$

Therefore, the increase in the surface temperature and a negligible change in the temperature gradient lead to a decrease in $\overline{\text{Nu}}_w/\overline{\text{Nu}}_{w/o}$ due to the presence of an upstream heat source, as shown in the equation given below:

$$\frac{\overline{\text{Nu}}_w}{\overline{\text{Nu}}_{w/o}} = \frac{-k\dfrac{dT}{dy}\Big|_w (T_s - T_a)\Big|_{w/o}}{-k\dfrac{dT}{dy}\Big|_{w/o} (T_s - T_a)\Big|_w} \tag{13}$$

The above discussion is needed since the heat flux input q_{in} is redistributed over the surface due to conduction into the plate. Therefore, the convection heat flux is affected by the conduction effects and an estimate of this effect is being made here.

The fact that the convected energy remains essentially constant with varying U_∞ is not surprising if one looks at the isotherm plots for the various convection circumstances considered, as shown in Figs. 17(*a*) and 17(*b*) for $Gr/Re^{5/2} = 47$ and $Gr/Re^{5/2} = 0.8$, respectively. The surface orientation is horizontal. These isotherms are obtained by applying linear interpolation to the measured thermal field, as presented in the preceding figures, to obtain the locations, on an $X-Y$ plane, at which specific values of the temperature θ are obtained. In general, about 20 locations along the plate surface were employed, with about 15 transverse locations at each X, for temperature measurements that yielded the isotherms shown here. The scale is kept the same for all the isotherm plots to indicate the relative thickness of the flow region. An increase in the forced flow velocity to change the circumstance from a buoyancy-dominated one to that of mixed convection is accompanied by a shift of the relatively higher temperature isotherms closer to the surface, negating the cooling effect of the increased velocity. Thus, the convection from the downstream locations and, hence, the conduction in the x direction remain largely unchanged. Also, the two figures indicate a marked difference in the shape of the isotherms. In Fig. 17(*a*), for the buoyancy-dominated flow, the outlines of the plumes rising from the two heat sources can be clearly seen. The two plumes initially rise independently before interacting with each other. Thus, the flow field adjacent to the downstream strip is not significantly changed. This is the reason for the weak upstream source influence on the downstream source. In Fig. 17(*b*), for the mixed convection circumstance, a complete alignment of the upstream plume along the plate can be clearly seen. This explains the strong upstream source influence. A further increase in the flow velocity leads to a decrease in the average temperature in the upstream plume and a consequent reduced influence on the downstream source. It is seen that no recirculating flow arises, even for the buoyancy-dominated circumstance. It must be remembered that the plate heats up in the neighborhood of the source due to conduction. This leads to a buoyancy input even in the region between the two sources. Thus, the flow is similar to a mixed convection flow over a horizontal surface, where no separation effects arise (Jaluria, 1980).

Isotherms for the pure natural convection and the buoyancy-dominated circumstances, in the vertical surface orientation, are shown in Figs. 17(*c*) and 17(*d*), respectively. A complete alignment of the plumes with the surface can be clearly seen. The boundary layer is thinner than that in the case of the horizontal orientation due to the alignment of buoyancy force with the surface. Also, as expected, an increase in the forced flow velocity leads to a decrease in the boundary layer thickness and a decrease in the upstream source influence.

From the results shown here, it is clear that the horizontal and vertical configurations have very different trends in both the natural convection and the mixed convection modes of heat transfer. The difference due to the surface orientation diminishes as $\mathrm{Gr}/\mathrm{Re}^{5/2}$ is reduced and is almost negligible as $\mathrm{Gr}/\mathrm{Re}^{5/2}$ falls below 0.1, since the flow becomes increasingly forced flow dominated as the parameter is decreased. Figure 18 clearly illustrates this point. This figure shows the effect of the surface orientation on the influence of the upstream source on the temperature of the downstream source at various values of the mixed convection parameter. In this figure, $\Delta\theta_{\mathrm{diff}}$ is defined as

$$\Delta\theta_{\mathrm{diff}} = \Delta\theta_v - \Delta\theta_h \tag{14}$$

where $\Delta\theta_v$ and $\Delta\theta_h$ are the maximum temperature increases in the downstream strip, due to the presence of the upstream strip, in the vertical and the horizontal surface orientations, respectively. In this figure, $\Delta\theta_{\mathrm{diff}}$ is normalized by its maximum value $\Delta\theta_{\mathrm{max}}$, which clearly occurs in the pure natural convection circumstance. As can be seen in the figure, the difference decreases as $\mathrm{Gr}/\mathrm{Re}^{5/2}$ decreases. For a value of $\mathrm{Gr}/\mathrm{Re}^{5/2}$ less than 0.1, the effect of the surface orientation is negligible since the flow becomes forced flow dominated.

This effect of the surface orientation on the temperature of the downstream heat source is shown in Fig. 19. In this figure, $(\theta_{s_h} - \theta_{s_v})/\theta_{s_v}$ is plotted against the mixed convection parameter. Here, θ_{s_h} and θ_{s_v} are the nondimensionalized source surface temperatures in the horizontal and vertical surface orientations, respectively. The temperature difference is maximum in the circumstance of pure natural convection ($\mathrm{Gr}/\mathrm{Re}^{5/2} \rightarrow \infty$). The difference decreases as the value of the mixed convection parameter is reduced and becomes negligible as $\mathrm{Gr}/\mathrm{Re}^{5/2}$ falls below 0.1.

A very important result that may be derived from this paper pertains to the regimes for which the upstream wake effect is not important in the transport from the downstream element. Figures 6, 8, 12, and 14 provide the necessary inputs for a designer in terms of the adiabatic temperature rise due to the wake generated by the upstream source. The results depend strongly on the orientation, as well as on whether the upstream source is stronger or weaker than the downstream source. Considering Fig. 12, for instance, the wake effect is as high as 70 percent for pure natural convection at $D=1.0$. For $D>3.5$, the effect is small for all the $\mathrm{Gr}/\mathrm{Re}^{5/2}$ values considered. However, if a 5 percent effect is taken as significant, the separation distance D for a given value of $\mathrm{Gr}/\mathrm{Re}^{5/2}$ for which the effect is small may be determined. Similarly, Figs. 6, 8, and 14 can be employed to obtain the value of D for a negligible upstream wake effect at a given $\mathrm{Gr}/\mathrm{Re}^{5/2}$. Conversely, if D is fixed, the value of $\mathrm{Gr}/\mathrm{Re}^{5/2}$ at which the effect is small can be determined. This implies adjusting U_∞ or q_{in} to obtain a negligible adiabatic temperature rise in the downstream element.

Conclusions

An experimental study is carried out on the fundamental aspects of the conjugate mixed convective heat transfer from heat sources mounted on vertical and horizontal surfaces. Typical results for the circumstance of pure natural convection are also included. Experiment results are obtianed over a wide range of the mixed convection parameter $\mathrm{Gr}/\mathrm{Re}^{5/2}$, and the dimensionless source separation distance D. Of particular interest in the study was the effect of a strong heat source on the heat transfer from a relatively weak heat source located downstream. It is found that in the horizontal orientation of the surface, even a strong heat source has a negligible effect on the surface temperature of a relatively weak neighboring heat source, for the pure natural convection circumstance at $D=1.0$ or larger. This is attributed to a negligible interaction between the vertically rising wakes from the two heat sources. However, in the presence of a small, externally induced forced flow velocity, the wake from the upstream source is tilted downstream and increases the fluid temperature just above the downstream source. This effect lowers the local connective heat transfer coefficient and increases the source surface temperature.

In the vertical orientation of the surface, the wake from the upstream source is always aligned with the surface and, therefore, the downstream source is always under its influence. The effect of an externally induced flow velocity is a decrease in the average temperature of the wake above the downstream source and a consequent increase in its heat transfer coefficient and decrease in its surface temperature, as compared to the pure natural convection circumstance.

The results indicate that the influence of the upstream source on the downstream source decreases with the separation distance between them, as expected. The surface temperature of an isolated heat source is found to be about 20 percent lower in the vertical orientation than that in the horizontal orientation of the surface, for the circumstance of pure natural convection. This is simply due to the former flow being more vigorous. The effect of the surface orientation gets smaller with an increase in the externally induced flow velocity, and becomes negligible as the flow becomes a forced flow dominated one.

Acknowledgments

The authors acknowledge the support of the National Science Foundation, through Grant No. CBT-84-15364, for this work, and the help of Mr. L. C. Le in conducting the experiments.

References

Anderson, A. M., and Moffat, R. J., 1988, "Direct Air Cooling of Electronic Components: Reducing Component Temperatures by Controlled Thermal Mixing," in: *Symp. Fund. Forced Convection Heat Transfer*, ASME HTD-Vol. 101, pp. 9-16.

Carey, V. P., and Mollendorf, J. C., 1977, "The Temperature Field Above a Concentrated Heat Source on a Vertical Adiabatic Surface," *Int. J. Heat Mass Transfer*, Vol. 20, pp. 1059-1067.

Forstron, R. J., and Sparrow, E. M., 1967, "Experiments on the Buoyant Plume Above a Horizontal Wire," *Int. J. Heat Mass Transfer*, Vol. 10, pp. 321-331.

Fujii, T., 1963, "Theory of the Steady Laminar Natural Convection Above a Horizontal Line Source and a Point Heat Source," *Int. J. Heat Mass Transfer*, Vol. 6, pp. 597-606.

Fujii, T., Morioka, I., and Uehara, H., 1973, "Buoyant Plume Above a Horizontal Line Heat Source," *Int. J. Heat Mass Transfer*, Vol. 16, pp. 755-768.

Gebhart, B., Pera, L., and Schorr, A. W., 1970, "Steady Laminar Natural Convection Plumes Above a Horizontal Line Heat Source," *Int. J. Heat Mass Transfer*, Vol. 13, pp. 161-171.

Gebhart, B., 1971, *Heat Transfer*, 2nd ed., McGraw-Hill, New York.

Gebhart, B., Shaukatullah, H., and Pera, L., 1976, "The Interaction of Unequal Laminar Plane Plumes," *Int. J. Heat Mass Transfer*, Vol. 19, pp. 751-756.

Goel, S., 1984, "An Experimental Study of Non-boundary Layer Effects Due to Finite Sized Thermal Sources on a Flat Unheated Surface," Masters Thesis, Department of Mechanical and Aerospace Engineering, Rutgers, The State University of New Jersey, Dec.

Goel, S., and Jaluria, Y., 1986, "Thermal Transport From an Isolated Heat Source on a Vertical or Inclined Surface," *Proceedings of the Eighth International Heat Transfer Conference*, San Francisco, Hemisphere Pub. Corp., New York, Vol. 3, pp. 1341-1346.

Jaluria, Y., and Gebhart, B., 1975, "On the Buoyancy-Induced Flow Arising From a Heated Hemisphere," *Int. J. Heat Mass Transfer*, Vol. 18, pp. 415-431.

Jaluria, Y., and Gebhart, B., 1977, "Buoyancy-Induced Flow Arising From a Line Thermal Source on an Adiabatic Vertical Surface," *Int. J. Heat Mass Transfer*, Vol. 20, pp. 153-157.

Jaluria, Y., 1980, *Natural Convection Heat and Mass Transfer*, Pergamon Press, United Kingdom.

Jaluria, Y., 1982a, "Buoyancy-Induced Flow Due to Isolated Thermal Sources on a Vertical Surface," ASME JOURNAL OF HEAT TRANSFER, Vol. 104, pp. 223-227.

Jaluria, Y., 1982b, "Natural Convection Flow Due to Line Sources on a Vertical Adiabatic Surface," *Proceedings of the Seventh International Heat Transfer Conference*, Munich, Vol. 2, Hemisphere Pub. Corp., New York, pp. 147-152.

Jaluria, Y., 1984, "Numerical Study of the Thermal Process in a Furnace," *Numerical Heat Transfer*, Vol. 7, pp. 211-224.

Jaluria, Y., 1985, "Interaction of Natural Convection Wakes Arising From Thermal Sources on a Vertical Surface," ASME JOURNAL OF HEAT TRANSFER, Vol. 107, pp. 883-892.

Jaluria, Y., 1986, "Mixed Convection Flow Over Localized Multiple Thermal Sources on a Vertical Surface," *Phys. Fluids*, Vol. 29, pp. 934-940.

Kraus, A. D., and Bar-Cohen, A., 1983, *Thermal Analysis and Control of Electronic Equipment*, Hemisphere Pub. Corp., New York.

Lieberman, J., and Gebhart, B., 1969, "Interactions in Natural Convection From an Array of Heated Elements," *Int. J. Heat Mass Transfer*, Vol. 12, pp. 1385-1396.

Milanez, L. F., and Bergles, A. E., 1986, "Studies on Natural Convective Heat Transfer From Thermal Sources on a Vertical Surface," *Proceedings of the Eighth International Heat Transfer Conference*, San Francisco, Hemisphere Pub. Corp., New York, Vol. 3, pp. 1347-1352.

Molendorf, J. C., and Gebhart, B., 1973, "Thermal Buoyancy in Round Laminar Vertical Jets," *Int. J. Heat Mass Transfer*, Vol. 16, pp. 735-745.

Pera, L., and Gebhart, B., 1975, "Laminar Plume Interactions," *J. Fluid Mech.*, Vol. 68, pp. 259-271.

Quintiere, J. G., Rinkinen, W. J., and Jones, W. W., 1981, "The Effect of Room Openings on Fire Plume Entrainments," *Comb. Sci. and Tech.*, Vol. 26, pp. 193-201.

Schorr, A. W., and Gebhart, B., 1970, "An Experimental Investigation of Natural Convection Wakes Above a Line Heat Source," *Int. J. Heat Mass Transfer*, Vol. 13, pp. 557-571.

Sparrow, E. M., Patankar, S. V., and Abdel-Wahed, R. M., 1978, "Development of Wall and Free Plumes Above a Heated Vertical Plate," ASME JOURNAL OF HEAT TRANSFER, Vol. 100, pp. 184-190.

Steinberg, D. S., 1980, *Cooling Techniques for Electronic Equipment*, Wiley, New York.

Tewari, S. S., Jaluria, Y., and Goel, S., 1987, "Natural and Mixed Convective Transport From Finite-Size Heat Sources on a Flat Plate in Cooling of Electronic Equipment," presented at the Thermofluid Mechanisms in Electronic Thermal Control session of the Annual Winter Meeting of the ASME, Boston, MA, Dec. 13-18; ASME HTD-Vol. 89, pp. 1-9.

Zimin, V. D., and Lyakhov, Y. N., 1970, "Convective Wall Plume," *J. Appl. Mech. Tech. Phys.*, Vol. 11, pp. 159-162.

T.-K. Kim

H. S. Lee

University of Minnesota,
Department of Mechanical Engineering,
Minneapolis, MN 55455

Modified δ-*M* Scaling Results for Mie-Anisotropic Scattering Media

A modified δ-M scaling method, which adjusts the δ-M scaled phase functions to be always positive, is applied to radiative transfer problems in two-dimensional square enclosures. The scaled anisotropic results are compared with the results obtained from an accurate model of the full anisotropic scattering problems using the S-N discrete ordinates method. The modified δ-M anisotropic scaling is shown to improve the isotropic scaled results of a collimated incidence problem, but the required number of terms increases as the phase function complexity and the asymmetry factor increase. For the diffuse incidence problems, even a low-order modified δ-M phase function significantly improves the accuracy of scaled solutions over the isotropic scaling. Significant savings in the computer times are observed when the modified δ-M method is applied.

1 Introduction

Accurate modeling of radiative transfer in scattering media, described by complex phase functions, requires a large number of angular directions when the *S-N* discrete ordinate method is applied. The *N*th order *S-N* discrete ordinate method can be used to model Mie phase functions with up to $2N+1$ terms in a Legendre polynomial expansion (Chandrasekhar, 1960). The order N is equal to the number of ordinate directions for a one-dimensional problem, and $N(N+2)/2$ is the number of ordinate directions for a two-dimensional problem. Since a phase function may require hundreds of terms in a Legendre polynomial expansion, accurate treatment of the complex anisotropic phase functions can be computationally very time consuming.

Isotropic scaling transforms an anisotropic scattering problem to an equivalent isotropic scattering form. The isotropic scaling approximation in two-dimensional square enclosures has been studied by Kim and Lee (1990). It was demonstrated that the isotropic scaling is very accurate in predicting the two-dimensional radiative flux and average incident radiation for low-scattering media with diffuse incidence and for isothermal emission problems. The scaling accuracy tends to decrease a little for diffuse incidence problems as the scattering albedo is increased. The errors in the scaled solution are unacceptably large for collimated incidence problems with highly scattering media.

Anisotropic scaling approximation reduces the number of terms in the phase function expansion series, and it can be used to simplify a complicated anisotropic problem to a simpler anisotropic scattering problem. Although the scaled anisotropic problem requires fewer ordinate directions and less computation time than the full-phase function analysis, the programming effort may be comparable to the full-phase function model.

The simplest form of an anisotropic scaling is the Delta-Eddington method developed by Joseph et al. (1979), which transforms a complicated anisotropic phase function to a linear anisotropic phase function. Wiscombe (1977) suggested the generalized δ-M method, where a full anisotropic phase function could be transformed either to an isotropic ($M=1$) or to a simpler anisotropic ($M>1$) scattering phase function. Crosbie and Davidson (1985) proposed guidelines that are less strict than the δ-*M* method for using a Dirac-delta function approximation to represent complicated scattering phase functions of large spherical particles or voids. Their guidelines are intended to ensure positive scaled phase functions, and the resulting scaled phase functions match the first one or two moments of the original phase functions. Kamiuto (1988) recommended an anisotropic scaling for very large size parameters (>1000), which subtracts the diffraction scattering from a highly anisotropic phase function, leaving only the surface reflection effect in the scaled equation of transfer.

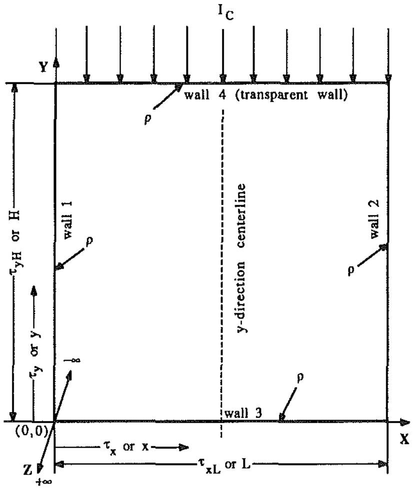

a) Collimated Incidence

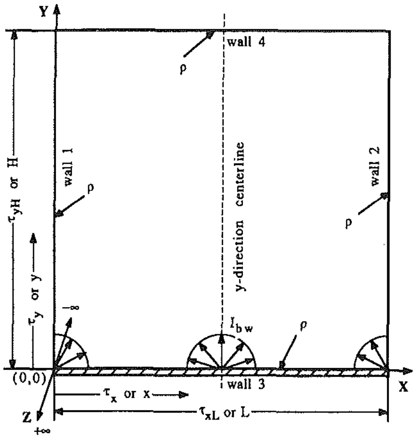

b) Diffuse Incidence

Fig. 1 System geometries

In this study, a modified δ-*M* anisotropic scaling is applied to the equation of transfer to improve the scaled results for

---

Contributed by the Heat Transfer Division for publication in the JOURNAL OF HEAT TRANSFER. Manuscript received by the Heat Transfer Division September 26, 1989; revision received February 13, 1990. Keywords: Radiation.

two-dimensional square enclosures. The modified δ-M scaling ensures positivity in the scaled phase function for all ordinate directions. Accuracy of the modified δ-M scaling scheme is investigated for two-dimensional square enclosure by using the S-14 discrete ordinate method.

Although the anisotropic scaling can be used to improve any isotropic scaling results, we focus on the highly scattering collimated incidence problem (Fig. 1*a*), where the errors in the isotropic scaling were the largest (Kim and Lee, 1990). The accuracy of the modified δ-M anisotropic scaling is also briefly examined for some diffuse incidence problems (Fig. 1*b*) with pure scattering media. Increasingly accurate modified δ-M solutions are compared with the full phase function solutions, which have been previously presented for collimated incidence problems (Kim and Lee, 1989) and for diffuse incidence problems (Kim and Lee, 1988).

2 Anisotropic Scaling

In the δ-M approximation, a full phase function expressed in a $K+1$ term Legendre polynomial series is decomposed into a forward delta function and a simpler scaled phase function as (Wiscombe, 1977)

$$\Phi(\Omega'; \Omega) \cong \sum_{l=0}^{K} C_l P_l(\cos\psi)$$

$$\cong 4\pi f \delta(\Omega' - \Omega) + (1-f)\hat{\Phi}(\Omega'; \Omega) \qquad (1)$$

The scaled phase function $\hat{\Phi}(\Omega'; \Omega)$ is described by M number of terms in the expansion as

$$\hat{\Phi}(\Omega'; \Omega) = \sum_{l=0}^{M-1} \hat{C}_l P_l(\cos\psi) \qquad (2)$$

where M less than K is selected to meet the accuracy requirements of the scaled solutions. $M=1$ corresponds to the isotropic scaling already presented by Kim and Lee (1990).

The expression for the scaled $\hat{C}_l$ is derived by equating the Legendre polynomial moments of equation (1)

$$\hat{C}_l = \frac{C_l - f(2l+1)}{1-f} \qquad (3)$$

Table 1 The full Mie phase function expansion coefficients (C_l)

l	$F0$	$F1$	$F2$	$F3$	$B1$	$B2$
0	1.00000	1.00000	1.00000	1.00000	1.00000	1.00000
1	2.78197	2.53602	2.00917	0.55355	−0.56524	−1.20000
2	4.25856	3.56549	1.56339	0.56005	0.29783	0.50000
3	5.38653	3.97976	0.67407	0.11572	0.08571	
4	6.19015	4.00292	0.22215	0.01078	0.01003	
5	6.74492	3.66401	0.04725	0.00058	0.00063	
6	7.06711	3.01601	0.00671	0.00002		
7	7.20999	2.23304	0.00068			
8	7.20063	1.30251	0.00005			
9	7.03629	0.53463				
10	6.76587	0.20136				
11	6.35881	0.05480				
12	5.83351	0.01099				
13	5.22997					
14	4.47918					
15	3.69000					
16	2.81577					
17	1.92305					
18	1.11502					
19	0.50766					
20	0.20927					
21	0.07138					
22	0.02090					
23	0.00535					
24	0.00120					
25	0.00024					
26	0.00004					
Terms	27	13	9	7	6	3
g	0.92732	0.84534	0.66972	0.18452	−0.18841	−0.40000

Notes:
1 F indicates forward scattering phase functions and B indicates backward scattering phase functions.
2 For information on $F1$, $F2$, $B1$, and $B2$, see Kim and Lee (1988).
3 For information on $F0$, see Lee and Buckius (1982).
4 The coefficients for $F3$ are obtained for a size parameter of 1.0 and refractive index of 1.33.

where $l=0, \ldots, M-1$. $\hat{C}_l$ for $l \geq M$ are set equal to zero, and the forward fraction parameter f is selected as $f = C_M/(2M+1)$.

The scaled parameters, $\hat{\omega}$ and $\hat{\tau}$, are defined as

$$\hat{\omega} = \frac{\omega(1-f)}{(1-\omega f)} \qquad (4)$$

Nomenclature

B = modified δ-M constant
C_l = phase function expansion coefficients
f = forward fraction for scaling
g = phase function asymmetry factor = $C_1/3$
G = average incident radiation; $G^* = 4\pi G/Q_0$
H, L = height and length of the enclosure
I = radiative intensity
$K+1$ = number of terms in the full phase function
M = number of terms in the scaled phase function
MX, MY = number of grid points in x and y directions
$\mathbf{n}$ = inward normal vector to enclosure walls
N = order of S-N discrete ordinate approximation
$P_l(\cos\psi)$ = Legendre polynomial of order l
Q_0 = incident radiative flux = $|\xi_c I_c|$ or πI_{bw}
Q_x^+, Q_x^- = positive and negative $\mathbf{Q}$ in x direction
Q_y^+, Q_y^- = positive and negative $\mathbf{Q}$ in y direction
Q_x, Q_y = net radiative heat fluxes in x and y directions
S = intensity source function
β = extinction coefficient = $\kappa + \sigma_s$
$\delta(\Omega' - \Omega)$ = Dirac-delta function
ϵ_w = wall emissivity
θ = polar angle
κ = absorption coefficient
μ = direction cosine in x direction = $\cos\theta$
ξ = direction cosine in y direction = $\sin\theta \cos\varphi$
ρ = diffuse wall reflectivity
σ_s = scattering coefficient
τ = optical path length
τ_x, τ_y = optical coordinates; $\tau_x = \beta x$; $\tau_y = \beta y$
τ_{xL}, τ_{yH} = overall optical thicknesses; $\tau_{xL} = \beta L$; $\tau_{yH} = \beta H$
$\Phi(\Omega'; \Omega)$ = scattering phase function
φ = azimuthal angle
ψ = scattering angle measured between Ω' and Ω
ω = scattering albedo = σ_s/β
Ω = ordinate direction, (μ, ξ)

Superscripts

$*$ = dimensionless variable
$'$ = incident direction
$\hat{}$ = δ-M scaled value
$\tilde{}$ = modified δ-M scaled value

Subscripts

b = blackbody
c = collimated component
w = wall

$$\hat{\tau}_x = (1-\omega f)\tau_x \tag{5}$$

$$\hat{\tau}_y = (1-\omega f)\tau_y \tag{6}$$

The moments of the δ-M and the original phase functions match up to order M, but the δ-M scaled phase function can be negative in some directions. For example, the δ-M scaled phase function can have negative values for $2 \leq M \leq 21$ for the 27-term phase function $F0$ in Table 1. For this phase function, there is no value of f that can satisfy the equality between moments and still result in a positive scaled phase function when $3 \leq M \leq 19$.

The negative values in the scaled phase function can result in negative intensities. Since the intensity is a positive quantity by definition, the appearance of negative intensities is unacceptable in the S-N discrete ordinate calculation. Most of the discrete ordinate codes use a negative intensity fixup technique (Kim and Lee, 1988, 1989; Lathrop and Brinkley, 1973). Any appearance of negative intensities significantly increases the computation time. The required computation time for a δ-M approximation with a negative scaled phase function can be greater than that required for the corresponding full phase function.

The δ-M phase function given in equation (2) is therefore modified by adding a small positive number B. The resulting phase function, $\hat{\Phi}(\Omega'; \Omega) + B$, is then renormalized by using the S-N quadrature set to obtain the final modified phase function $\tilde{\Phi}$ as

$$\tilde{\Phi}(\Omega'; \Omega) = \frac{\hat{\Phi}(\Omega'; \Omega) + B}{1+B} \tag{7}$$

The positive additive constant B is obtained for the ordinate directions as

$$B = |\min[\hat{\Phi}(\Omega'; \Omega)]| \quad \text{for } \hat{\Phi}(\Omega'; \Omega) \text{ with negative values} \tag{8a}$$

$$B = 0 \qquad \text{for positive } \hat{\Phi}(\Omega'; \Omega) \tag{8b}$$

and

$$1 + B = \frac{1}{4\pi} \int_{\Omega'} [\hat{\Phi}(\Omega'; \Omega) + B] d\Omega' \tag{8c}$$

is the renormalization parameter. The modified δ-M phase function is described by the coefficient $\tilde{C}_l$, which is obtained from the δ-M coefficients as

$$\tilde{C}_l = \frac{\hat{C}_l + B\delta_{0l}}{1+B} \tag{9}$$

The modified phase function $\tilde{\Phi}$ differs only slightly from the original δ-M scaled phase function $\hat{\Phi}$, but a new scaling factor $\tilde{f}$ is needed to account for this difference in equation (1). The modified δ-M phase function approximation is now written as

$$\begin{aligned} \Phi(\Omega'; \Omega) &\cong 4\pi \tilde{f} \delta(\Omega' - \Omega) + (1 - \tilde{f}) \tilde{\Phi}(\Omega'; \Omega) \\ &= 4\pi \tilde{f} \delta(\Omega' - \Omega) + (1 - \tilde{f}) \left[\frac{\hat{\Phi}(\Omega'; \Omega) + B}{1+B} \right] \end{aligned} \tag{10}$$

Matching the moments of $\Phi(\Omega'; \Omega)$ and the modified δ-M phase function results in an expression similar to equation (3) for the expansion coefficients

$$C_l = (2l+1)\tilde{f} + (1-\tilde{f}) \frac{(\hat{C}_l + B\delta_{0l})}{(1+B)} \tag{11}$$

where $\delta_{0l} = 1$ for $l = 0$ and $\delta_{0l} = 0$ for $l \neq 0$. For $l = 1$, the new scaling factor $\tilde{f}$ can be obtained to give the correct first-order moment of $\Phi(\Omega'; \Omega)$. With the asymmetry factors defined from the first-order moment of a phase function as $g = C_1/3$ and $\hat{g} = \hat{C}_1/3$ (Irvine, 1963)

$$\tilde{f} = \frac{(1+B)g - \hat{g}}{(1+B) - \hat{g}} \tag{12}$$

Equation (11) for $l > 1$ gives different results for $\tilde{f}$, but these results are not used since the effect of the asymmetry factor is more important than the higher order moments.

Using the new scaling factor $\tilde{f}$ in equation (12), the new scaled parameters, $\tilde{\omega}$ and $\tilde{\tau}$, are then obtained as

$$\tilde{\omega} = \frac{\omega(1-\tilde{f})}{(1-\omega\tilde{f})} \tag{13}$$

$$\tilde{\tau}_x = (1-\omega\tilde{f})\tau_x \tag{14}$$

$$\tilde{\tau}_y = (1-\omega\tilde{f})\tau_y \tag{15}$$

The modified δ-M phase functions are always positive and the factor B ensures an accurate phase function normalization for the selected angular quadrature set. The accurate phase function normalization results in an accurate overall energy balance, which makes the convergence acceleration by the energy rebalance technique effective (Kim and Lee, 1988, 1989; Lathrop and Brinkley, 1973).

The $\tilde{C}_l$ and $\tilde{f}$ of the modified δ-M phase functions considered for this study fall within the range of acceptable values specified for $1 \leq M \leq 3$ by Crosbie and Davidson (1985). The set of inequalities for $\tilde{C}_l$ and $\tilde{f}$ was not given by Crosbie and Davidson (1985) for $M > 3$. They note that the required relationships must be separately developed for each M, and that the procedure becomes rather tedious for large M. We do expect that the higher order modified δ-M phase functions will meet the requirements set forth by Crosbie and Davidson, since both methods require a positive scaled phase function, and they match the zeroth and first moments of the scaled and full phase functions. The modified δ-M method is a simple method that can easily be generalized to give a higher order scaled phase function.

The accuracy of the current modified δ-M method, Wiscombe's δ-M method, and Crosbie and Davidson's procedure is considered for radiative transfer in simple one-dimensional planar geometry. Pure scattering, net flux results are obtained for a one-dimensional plane parallel slab of a unit optical depth with normal collimated or diffuse incidence. All the phase functions shown in Table 1 are considered for this comparison, and an S-21 approximation is used.

The accuracies of the computed fluxes are comparable to each other, but Wiscombe's δ-M phase functions seem to give the most accurate flux results. The δ-M scaled fluxes are in excellent agreement with the exact full phase function solutions, and the accuracy is seen to improve as M is increased for all the phase functions considered. Although the flux results are excellent for the δ-M method, negative intensities are observed for most of the phase functions for $2 \leq M < K$. The better overall accuracy of the δ-M method is probably due to the fact that the higher order moments of the original phase function are matched by this method, as compared to the modified δ-M method, which matches only the zeroth and first moments. Crosbie and Davidson's positive scaled phase functions seem to result in the largest flux errors when tested for $M = 2$ and 3, although their scaling criteria are similar to those for this study. For $M = 1$, all three methods are identical.

The current modified δ-M method always results in positive intensities. The accuracy of this method is comparable with the δ-M method for relatively simple phase functions with moderate asymmetry factors ($F2$, $F3$, $B1$, and $B2$). For the complex phase functions with large asymmetry factors ($F0$ and $F1$), the modified δ-M solutions are comparable to the δ-M fluxes for $M \leq 3$, but the accuracy of the modified δ-M method does not improve consistently as M is further increased. For some conditions the scaling errors do not decrease monotonically with increasing M, but may increase slightly at some M before decreasing toward zero.

The worst case we have observed during this study is the collimated incidence problem for a pure scattering, unit optical depth medium with the extremely forward peaked $F0$ phase function (asymmetry factor $g=0.92732$). In this case, the modified δ-M method with M increasing from 4 to 10 results in small oscillation in the flux accuracy. The maximum error observed for $4 \leq M \leq 10$ was 1.55 percent, which is still quite small compared to the 2.1 percent flux error for $M=1$. Still, the error for $M=3$ for the same case is only 0.3 percent. For all other phase functions in Table 1 that have asymmetry factors less than 0.85, the modified δ-M method shows increasing accuracy with increasing M.

The flux errors for larger M are mainly due to the fact that the effects of the higher order moments of the scaled phase functions are not included in the selection of $\tilde{f}$. Our understanding is that the selection of $\tilde{f}$ in the modified δ-M scaling plays a more significant role for the accuracy of one-dimensional problems as compared to the two-dimensional problems, where both the selected $\tilde{f}$ and the shape of the scaled phase function affect the accuracy. Therefore, based on our one-dimensional study, we make the following recommendations for applying the modified δ-M method to phase functions with $K+1$ terms. For the phase functions with $g \leq 0.85$ choose a higher M value ($0 \leq M \leq K$) if a more accurate scaled solution is required. For phase functions with $g > 0.9$, we suggest using $M<4$ to obtain approximate solutions, while a significantly larger M (around $K/2$) should be used for a highly accurate solution. For this work, the modified δ-M scaling with $M \leq 4$ is applied to the two-dimensional equation of transfer.

The scaled equation of transfer for the scattered component of the intensity (Kim and Lee, 1990) can be written as

$$\left[\mu \frac{\partial}{\partial \tilde{\tau}_x} + \xi \frac{\partial}{\partial \tilde{\tau}_y} + 1\right] I(\tilde{\tau}_x, \tilde{\tau}_y, \Omega) = S(\tilde{\tau}_x, \tilde{\tau}_y, \Omega) \qquad (16)$$

where the source function is expressed as

$$S(\tilde{\tau}_x, \tilde{\tau}_y, \Omega) = (1-\tilde{\omega}) I_b(\tilde{\tau}_x, \tilde{\tau}_y) + \frac{\tilde{\omega}}{4\pi} \int_{\Omega'} \tilde{\Phi}(\Omega'; \Omega) \mathrm{I}(\tilde{\tau}_x, \tilde{\tau}_y, \Omega') d\Omega' + \frac{\tilde{\omega}}{4\pi} \tilde{\Phi}(\Omega_c; \Omega) I_c \exp(-\tilde{\tau}) \qquad (17)$$

The boundary wall intensity expressions must also be expressed in terms of the transformed parameters. When a collimated beam is incident normally through the top boundary (see Fig. 1), the bottom wall intensity can be expressed as

$$I_w(\tilde{\tau}_x, \tilde{\tau}_y, \Omega) = \epsilon_w I_{bw}(\tilde{\tau}_x, \tilde{\tau}_y) + \frac{\rho}{\pi} \int_{\mathbf{n}\cdot\Omega' \leq 0} |\mathbf{n}\cdot\Omega'| I_w(\tilde{\tau}_x, \tilde{\tau}_y, \Omega') d\Omega' + \frac{\rho}{\pi} |\mathbf{n}\cdot\Omega_c| I_c \exp\{-\tilde{\tau}_{yH}/|\xi_c|\}$$

$$\text{for } \mathbf{n}\cdot\Omega > 0,\ \mathbf{n}\cdot\Omega' \leq 0, \text{ and } \mathbf{n}\cdot\Omega_c < 0 \qquad (18)$$

For all other walls, the boundary intensities are obtained from equation (18) without the I_c term.

Once the intensity field is obtained, the average incident radiation $G(\tilde{\tau}_x, \tilde{\tau}_y)$ and the radiative fluxes Q_x^+, Q_x^-, Q_y^+, and Q_y^- are evaluated as

$$G(\tilde{\tau}_x, \tilde{\tau}_y) = \frac{1}{4\pi}\left[\int_{4\pi} I(\tilde{\tau}_x, \tilde{\tau}_y, \Omega) d\Omega + I_c \exp\{-(\tilde{\tau}_{yH} - \tilde{\tau}_y)/|\xi_c|\}\right] \qquad (19)$$

$$Q_x^+(\tilde{\tau}_x, \tilde{\tau}_y) = \int_{\mu>0} \mu I(\tilde{\tau}_x, \tilde{\tau}_y, \Omega) d\Omega + I_c \mu_c \exp\{-(\tilde{\tau}_{yH} - \tilde{\tau}_y)/|\xi_c|\} \qquad (20a)$$

$$Q_x^-(\tilde{\tau}_x, \tilde{\tau}_y) = \int_{\mu<0} \mu I(\tilde{\tau}_x, \tilde{\tau}_y, \Omega) d\Omega \qquad (20b)$$

$$Q_y^+(\tilde{\tau}_x, \tilde{\tau}_y) = \int_{\xi>0} \xi I(\tilde{\tau}_x, \tilde{\tau}_y, \Omega) d\Omega \qquad (21a)$$

$$Q_y^-(\tilde{\tau}_x, \tilde{\tau}_y) = \int_{\xi<0} \xi I(\tilde{\tau}_x, \tilde{\tau}_y, \Omega) d\Omega + I_c \xi_c \exp\{-(\tilde{\tau}_{yH} - \tilde{\tau}_y)/|\xi_c|\} \qquad (21b)$$

The net radiative fluxes, Q_x and Q_y, are obtained by summing the positive and negative components of $\mathbf{Q}$.

3 Numerical Comparisons

The modified δ-M scaled equation of transfer for two-dimensional square enclosures with Mie-anisotropic scattering media is solved by using the S-14 approximation. Problems with either a collimated incidence or a diffuse incidence are studied to examine the accuracy of the suggested anisotropic scaling. A uniform, normal collimated incidence through the top transparent wall (see Fig. 1a) or a black ($\epsilon_w=1$) emitting bottom wall (see Fig. 1b) are the radiation sources considered. Only the pure scattering media ($\omega=1$) are considered here, since the flux errors for isotropic scaling were largest for these media (Kim and Lee, 1990). The square enclosure walls are nonreflecting ($\rho=0$), and the medium optical thicknesses of 0.1, 1, and 5 are considered for this study. The scattering phase functions $F1$, $F2$, $F3$, $B1$, and $B2$ with the expansion coefficients in Table 1 are considered for this two-dimensional study.

The average incident radiation and the various radiative flux components obtained from the modified δ-M scaling are compared with the full Mie-anisotropic scattering results. Only the results for M from one to three or four are presented to show the improvements in the scaled solutions as the terms in the scaled phase function are increased. The full Mie-anisotropic scattering solutions are marked "EXACT" in the figures (Kim and Lee, 1988, 1989). The flux and average incident results are nondimensionalized by using the incident radiative flux Q_0. The dimensionless results are presented by using the dimensionless coordinates, $\tau_x^* = \tilde{\tau}_x/\tilde{\tau}_{xL} = \tau_x/\tau_{xL}$ and $\tau_y^* = \tilde{\tau}_y/\tilde{\tau}_{yH} = \tau_y/\tau_{yH}$.

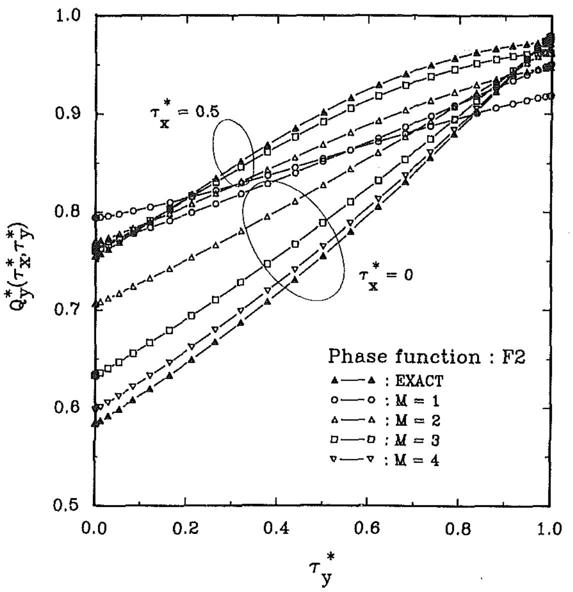

Fig. 2 Centerline and edge net flux comparisons (collimated incidence)

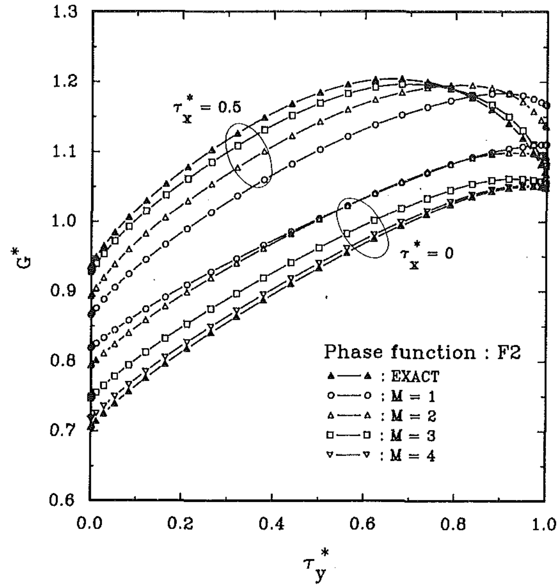

Fig. 3 Centerline and edge average incident radiation comparisons (collimated incidence)

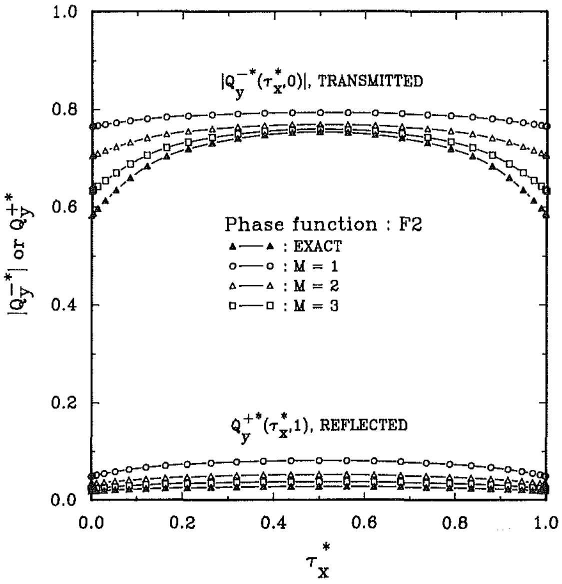

Fig. 4 Transmitted and reflected flux comparisons (collimated incidence)

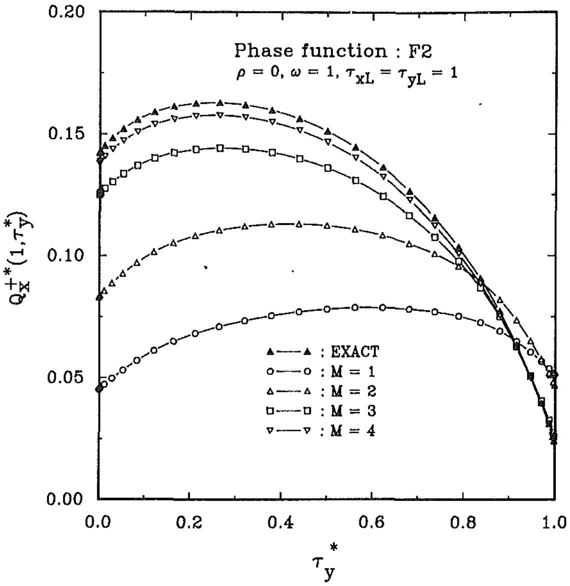

Fig. 5 Side wall energy loss comparisons (collimated incidence)

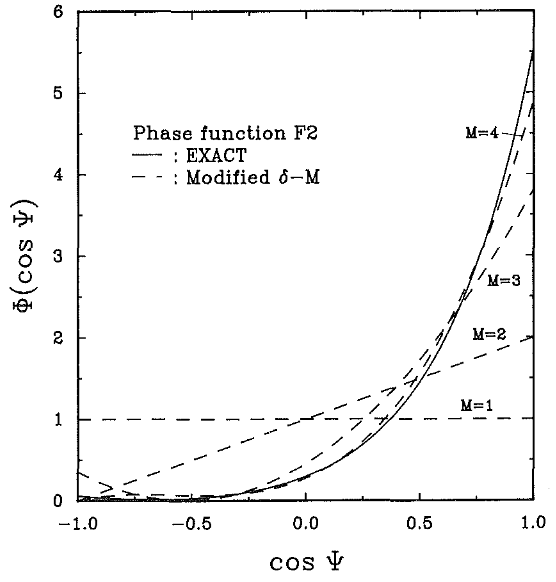

Fig. 6 The modified δ-*M* scaled phase function *F*2

Collimated Incidence Problems. In Fig. 2, increasingly accurate y-direction net radiative fluxes are shown for the *F*2 phase function as M increases. The net flux distributions along the centerline, $\tau_x^* = 0.5$, and the edge, $\tau_x^* = 0$, are shown together in this figure. The $M=1$, or the isotropic scaling approximation at the edge, is lost among the results for the centerline (maximum error of 31.2 percent at the edge), and this illustrates the motivation for seeking improved scaled results. For $M=2$, the flux error from the modified δ-M scaling solution is still large (20.9 percent at the edge), but it is much smaller than that for the isotropic scaling. For $M=3$, the y-direction net flux is predicted with reasonable accuracy. Less than 1.2 percent maximum magnitude in flux error is observed at the centerline of the enclosure, and a maximum flux error of 8.4 percent is observed at the edge region for the $M=3$ scaling. To improve the flux predictions further more terms must be included in the scaled phase function. A maximum flux error of 2.3 percent is found at the edge for $M=4$. The $M=4$ result along the centerline is not presented because it nearly overlaps the exact full phase function solution with a maximum error of 0.4 percent.

Figure 3 shows the centerline and edge variations of the average incident radiation for the phase function *F*2. The anisotropic scaling errors in the average incident radiation are shown to be similar to the net flux error trends discussed above. The average incident radiation is accurately predicted at the edge with 5.9 percent maximum error for $M=3$, and 1.6 percent maximum error with $M=4$.

In Fig. 4, the transmitted (Q_y^{-*} at $\tau_y^* = 0$) and the reflected (Q_y^{+*} at $\tau_y^* = 1$) components of the radiative flux are presented for the *F*2 phase function. The scaled transmitted and reflected fluxes are shown to be very inaccurate for the isotropic scaling cases of $M=1$ (maximum errors of 31.2 and 187.7 percent for the transmitted and the reflected fluxes, respectively). The flux errors with $M=2$ are still large (maximum errors of 20.9 and 86.6 percent, respectively). As M is increased to 3, the flux predictions are significantly improved (maximum errors of 8.4 and 34.6 percent, respectively). Although not shown in the figure, the maximum errors drop to 2.6 and 11.2 percent for the transmitted and the reflected fluxes, respectively, when M is increased to 4.

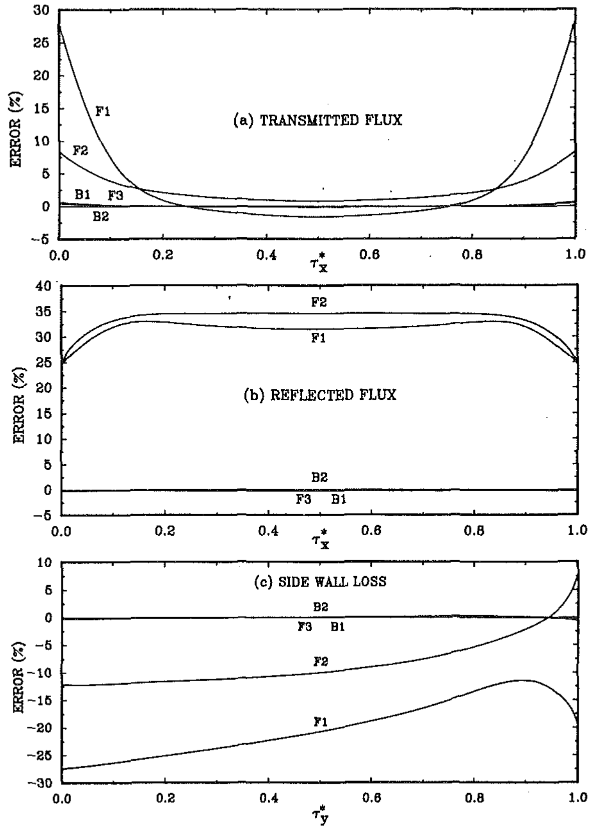

Fig. 7 Effect of phase functions on flux errors for $M=3$ (collimated incidence)

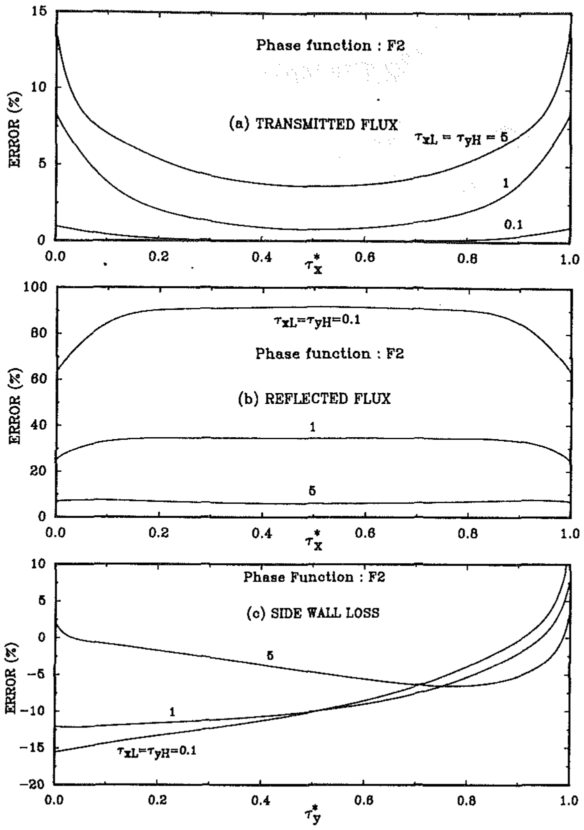

Fig. 8 Effect of optical depths on flux errors for $M=3$ (collimated incidence)

The side wall losses $[Q_x^{+*}(1, \tau_y^*)$ or $-Q_x^{-*}(0, \tau_y^*)]$ for the phase function $F2$ are shown in Fig. 5. The isotropic scaling result of $M=1$ for the side wall loss show an unacceptably large error (maximum error of 113.6 percent in magnitude). As M is increased, the side wall loss error drops rapidly. Maximum error magnitudes for different M values are 95.5, 12.2, and 3.1 percent for $M=2$, $M=3$, and $M=4$, respectively.

The dramatic improvements in the scaling accuracy with increased M can be understood by considering the shape of a scaled phase function. Figure 6 shows the modified δ-M phase functions as compared to the exact $F2$ phase function. The isotropic scaling ($M=1$) that results in the large errors for the collimated incidence problem is very different from the exact phase function. The anisotropic scaled phase functions with $M>2$ show more reasonable representation of the full phase function than the isotropic phase function. For $M=3$, the scaled phase function is very close to the full phase function, and the scaled flux results are very accurate. The $M=4$ scaled phase function nearly overlaps the original full phase function except for the forward direction.

The accuracy of the modified δ-M anisotropic scaling for the two-dimensional collimated incidence problem is further examined for other scattering phase functions $F1$, $F3$, $B1$, and $B2$. Rather than repeating Figs. 2–5 for each phase function, error plots for $M=3$ are used to show the accuracy for the transmitted and reflected fluxes and the side wall losses.

The transmitted flux errors for $M=3$ scaling are shown in Fig. 7(*a*) for the different phase functions. The phase function $F1$ with the largest asymmetry factor ($g = 0.92732$) results in the largest error of 28.5 percent at the corners. The $F2$ phase function ($g=0.84534$), which has been examined in Fig. 4, shows a maximum transmitted flux error of 8.4 percent at the corners. For the phase functions with their asymmetry factors less than 0.2 (phase functions $F3$ and $B1$), the transmitted flux errors are negligibly small (less than 0.6 percent of maximum error). Since the $B2$ phase function has only three terms in the Legendre polynomial series, solution by the $M=3$ scaling is the full phase function solution.

The reflected flux errors for $M=3$ scaling are shown in Fig. 7(*b*). The error for the $F2$ (maximum error of 34.6 percent) is slightly larger than that for $F1$ (31.9 percent maximum), which is opposite the transmitted flux error trends for these phase functions. For the less complex phase functions with small asymmetry factors ($F3$, $B1$, and $B2$), the reflected fluxes are as accurately predicted as the transmitted fluxes with the $M=3$ scaling (less than 0.25 percent maximum error magnitude).

The side wall loss errors shown in Fig. 7(*c*) have error trends similar to the transmitted flux errors. The $F1$ phase function shows the largest error magnitudes with a maximum of 27.5 percent, and the $F2$ phase function shows a maximum error magnitude of 12.2 percent. With $M=3$, the phase functions $F3$, $B1$, and $B2$ show negligibly small side wall loss errors that are smaller than 0.6 percent in magnitude.

Figure 8 shows the error plots for the transmitted, reflected, and side wall loss fluxes, which show the effect of the optical thickness on the scaling accuracy. The $M=3$ scaling with the phase function $F2$ is considered for the plots. The accuracy for predicting the transmitted flux is best for an optically thin medium, while the accuracy for predicting the reflected flux is best for an optically thick medium. The large errors of the reflected and side wall fluxes for optically thin media are due to the small magnitudes of these fluxes. In general, the absolute magnitude of the differences between the exact and scaled fluxes are smaller for the optically thin media than for the optically thick media.

In Table 2, a comparison of the Cray 2 computer times required for the exact analysis and the modified δ-M analysis is made. The medium optical thicknesses of 1 and 5 are considered with $F1$ phase function. For both the exact full phase function analysis and the modified δ-M analysis, the same S-

Table 2 Comparison of computer times ($\rho=0$, $\omega=1$, $F1$, S-14) (unit: seconds)

	Exact	$M=1$	$M=2$	$M=3$	$M=4$
$\tau_{xL}=\tau_{yH}=1$ $(MX=MY=26)$	67.3	8.9	23.5	23.8	24.3
$\tau_{xL}=\tau_{yH}=5$ $(MX=MY=46)$	331.8	49.1	103.7	122.6	157.3

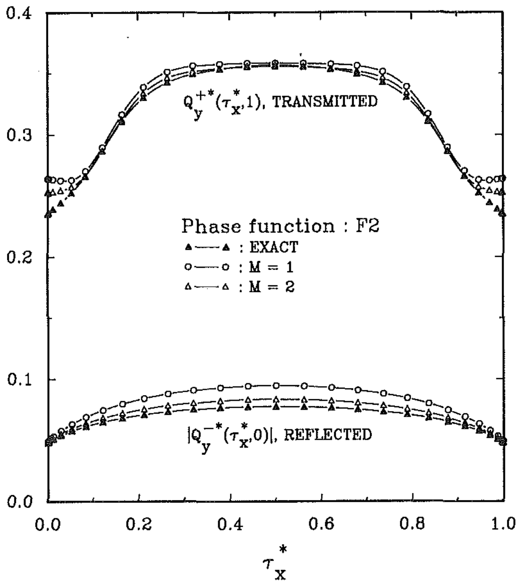

Fig. 9 Transmitted and reflected flux comparisons (diffuse incidence)

14 approximation is used. The isotropic scaling analyses with $M=1$ require less than 15 percent of the c.p.u. times that are required for the full phase function analysis. The dramatic, 85 percent or more savings in c.p.u. times by the isotropic scaling occur because no phase function calculations are needed for this approximation. For the anisotropic scaling approximations with $M=2$, 3, or 4, the c.p.u. times saved ranged between 50 and 70 percent.

Diffuse Incidence Problems. The modified δ-M anisotropic scaling is also applied to the diffuse incidence problem. A two-dimensional square enclosure contains pure scattering medium with the phase function $F2$. Figure 9 shows a comparison between the modified δ-M scaled solutions and the full phase function solutions for the transmitted and the reflected components of the radiative flux. The isotropic scaling results in 12.3 percent maximum error on the the transmitted flux at $\tau_x^*=0.0$ and 22.2 percent maximum error on the reflected flux at $\tau_x^*=0.5$. The anisotropic scaling with $M=2$ generates 7.5 percent maximum error on the transmitted flux and 7.7 percent maximum error on the reflected flux. The linear anisotropic ($M=2$) results show significant improvements over the isotropic scaling, although the exact phase function shape is poorly matched with just two terms (see Fig. 6).

4 Conclusions

Low-order modified δ-M phase functions are used to improve the scaled flux and average incident radiation results for collimated or diffuse incidence problems. The modified δ-M anisotropic scaling guarantees positive phase functions for all directions. It eliminates the negative intensities that are unacceptable for the S-N discrete ordinates method. The modified δ-M phase functions are easily obtained from Wiscombe's δ-M parameters, and the method can be easily generalized to higher order approximations.

For collimated incidence, the low-order anisotropic scaling is very effective for phase functions with moderate asymmetry factors ($F2$, $F3$, $B1$, and $B2$). More terms are needed in the scaled phase functions for complex phase functions with large asymmetry factors ($F1$ for example). The comparisons for $F2$ phase function show that accurate scaled results for collimated incidence problems can only be obtained when the scaled phase function contains enough terms to resemble the exact phase function.

Although the diffuse incidence problem is only briefly examined, the improvements with a low-order modified δ-M phase functions are dramatic. A scaled linear anisotropic phase function will produce significantly better results than the already good isotropic scaled results.

The improvements in solution accuracy with the modified δ-M scaling over the isotropic scaling require a modest increase in the computer time. In general, the phase function scaling helps reduce the order of the S-N approximation that is required for a full phase function analysis and also decreases the optical depth domain for calculation. These factors combine to lower the required computation times. The δ-M method with $M\leq 4$ results in savings of about 50–70 percent in computer times as compared to the full phase function analysis when the same order of the S-N approximation is used.

Acknowledgements

This work was supported in part by the National Science Foundation Grant No. NSF/CBT-8451076. A grant from the Minnesota Supercomputer Institute is also gratefully acknowledged.

References

Chandrasekhar, S., 1960, *Radiative Transfer*, Dover Publications, Inc., New York, pp. 149–150.

Crosbie, A. L., and Davidson, G. W., 1985, "Dirac-Delta Function Approximations to the Scattering Phase Function," *Journal of Quantitative Spectroscopy and Radiative Transfer*, Vol. 33, pp. 391–409.

Irvine, W. M., 1963, "The Asymmetry of the Scattering Diagram of a Spherical Particle," *Bulletin of the Astronomical Institute of Netherlands*, Vol. 17, No. 3, pp. 176–184.

Joseph, J. H., Wiscombe, W. J., and Weinman, J. A., 1979, "The Delta-Eddington Approximation for Radiative Flux Transfer," *Journal of the Atmospheric Sciences*, Vol. 33, pp. 2452–2459.

Kamiuto, K., 1988, "The Diffraction-Scattering Subtraction Method for Highly Anisotropic Scattering Problems," *Journal of Quantitative Spectroscopy and Radiative Transfer*, Vol. 40, pp. 21–28.

Kim, T.-K., and Lee, H. S., 1988, "Effect of Anisotropic Scattering on Radiative Heat Transfer in Two-Dimensional Rectangular Enclosures," *International Journal of Heat and Mass Transfer*, Vol. 31, No. 8, pp. 1711–1721.

Kim, T.-K., and Lee, H. S., 1989, "Radiative Transfer in Two-Dimensional Anisotropic Scattering Media With Collimated Incidence," *Journal of Quantitative Spectroscopy and Radiative Transfer*, Vol. 42, No. 3, pp. 225–238.

Kim, T.-K., and Lee, H. S., 1990, "Isotropic Scaling Results for Two-Dimensional Anisotropic Scattering Media," ASME JOURNAL OF HEAT TRANSFER, Vol. 112, pp. 721–727.

Lathrop, K. D., and Brinkley, F. W., 1973, "TWOTRAN-II: An Interfaced, Exportable Version of the TWOTRAN Code for Two-Dimensional Transport," Los Alamos Scientific Laboratory Report #LA-4848-MS.

Lee, H., and Buckius, R. O., 1982, "Scaling Anisotropic Scattering in Radiation Heat Transfer for a Planar Medium," ASME JOURNAL OF HEAT TRANSFER, Vol. 104, pp. 68–75.

Wiscombe, W. J., 1977, "The Delta-M Method: Rapid Yet Accurate Radiative Flux Calculations for Strongly Asymmetric Phase Functions," *Journal of the Atmospheric Sciences*, Vol. 34, pp. 1408–1442.

Jing-Tang Yang
Professor.

Gwo-Guang Wang
Graduate Student

Hung-Yi Li
Graduate Student

Department of Power Mechanical Engineering,
National Tsing Hua University,
Hsinchu, Taiwan 30043

Modeling of the Convective Thermal Ignition Process of Solid Fuel Particles

This work uses the boundary layer theory to study the thermal ignition process of the solid particle. The theoretical model explores the two-dimensional boundary layer equations in the gaseous phase. The governing equations of mass, momentum, energy, and species in gas phase are first transformed to ordinary differential equations through series expansion with respect to the azimuthal angle. The equations are then quasi-linearized to be the initial value problem and solved using Runge-Kutta method. The minimum heat flux from the gas phase to the fuel is evaluated as the most suitable criterion for the convective thermal ignition. The influences of the heat transfer rate, fluid dynamics, and the gas phase chemical reaction rate on the ignition delay and ignition position are discussed in detail.

Introduction

The phenomena of flame spreading, flame stabilization, and other combustion problems are closely related to the ignition process of solid fuel. In addition, a comprehensive understanding of the mechanism of ignition will benefit the design of combustors and the prevention of hazardous fires. The competing influences among diffusion, reaction, and the flow around the fuel have to be thoroughly analyzed to yield a true description of the ignition mechanism. Moreover, the ignition condition is not a conserved property; it depends not only on the fuel itself, but also on the properties of the surroundings. Due to all these complexities, the development of a generalized ignition criterion is extremely difficult.

According to Birk (1980) there exist three modes of ignition for solid fuels: gas phase ignition, solid phase ignition, and heterogeneous ignition. Among these three categories, gas phase ignition is frequently encountered for most condensed fuel burned in moderate Reynolds number conditions. The ignition criteria previously proposed for the gas phase ignition were summarized by Annamalai and Durbetaki (1977) and Ganhdi and Kanury (1986) as specifications of the gas temperature (Hermance and Kumar, 1970), the rate of gas temperature rise (Price et al., 1966), the rate of energy generated (Kumar, 1983), and the rate of chemical reaction (Kashiwagi and Summerfield, 1973).

Gandhi and Kanury (1986) developed a one-dimensional mathematical model and suggested that the criterion of the gradient reversal of the gas temperature profile at the solid-gas interface is most suitable for the radiantly induced ignition of organic solids. The problem of combustion of solids in a hot gas stream is the most common case and the problem is somewhat similar to the case they examined. Birk (1980) published an in-depth discussion on the theoretical ignition criteria and suggested the new criterion of d(heat flux)$/dt = 0$ and d^2 (heat flux)$/dt^2 > 0$. This criterion is based on the runaway conditions of heat flux at the interface of the propellant and is used and re-examined in this work.

On the aspect of two-dimensional theoretical model, Kashiwagi et al. (1971) used the boundary layer theory to analyze the ignition of a PBAA plate heated by hot air. The similarity theory was assumed to be valid. Kashiwagi and Summerfield (1973) dealt with the same problem but replaced the similarity approach by the nonsimilar approach. The model predicted the ignition delay time and the ignition position for the fuel plate. Sibulkin et al. (1981, 1983) also used the same approach to analyze the burning of a PMMA plate and discussed the differences between the similar and nonsimilar approaches. Fernandez-Pello and Law (1982a, 1982b) used the boundary layer approximation and large asymptotics to study the ignition and extinction in the stagnation point of a fuel particle. Birk (1980) investigated the convective ignition of a cylindrical nitrocellulose-based propellant. He concluded that the ignition occurred in the gas phase and his model could predict the relation among the ignition delay, ignition position, velocity, temperature, and gas concentration, although the model is still limited to the stagnation point zone. Generally there exist very few ignition models for the solid fuels as compared with models for premixed combustible mixtures.

The purpose of this paper is to improve the previous models and to re-examine the suitability of the ignition criteria. The model is developed for an unsteady, reactive boundary layer, and an appropriate numerical scheme is given that can be applied to the whole boundary layer before the separation point. Since the problem analyzed is at points away from the stagnation zone, the present analysis is nonsimilar in nature. The correlation among the ignition condition, the heat flux, and the distributions of the gas temperature, concentrations,

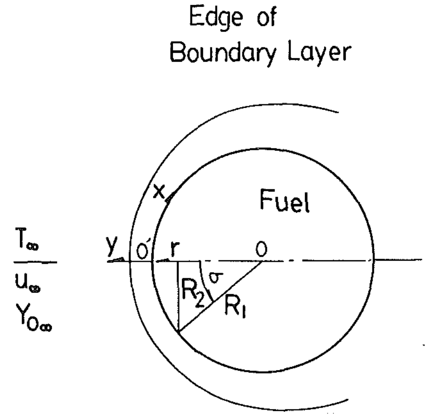

Fig. 1 Configuration and coordinates of the model

Contributed by the Heat Transfer Division for publication in the JOURNAL OF HEAT TRANSFER. Manuscript received by the Heat Transfer Division March 27, 1989; revision received November 22, 1989. Keywords: Combustion, Forced Convection, Transient and Unsteady Heat Transfer.

and velocity are thoroughly investigated. The ignition mechanism is systematically studied.

Theoretical Analysis

The overall sketch of the theoretical model is shown in Fig. 1. Initially, the hot air with a temperature of T_∞, oxygen concentration of Yo_∞, and velocity of u_∞ flows over a spherical solid fuel particle and forms the momentum and the thermal boundary layers. The solid fuel is heated and the pyrolyzed vapor diffuses to the boundary layer in which the chemical reaction occurs. During the reaction, part of the released energy is transferred back to the fuel surface, and thus both the pyrolysis rate and the chemical reaction rate are enhanced. When the runaway chemical reaction occurs somewhere in the boundary layer, the fuel is ignited and the flame starts to spread over the fuel surface.

Due to the chemical reaction and the large temperature variation during the ignition process, the mathematical formulation is complicated and highly nonlinear. The following assumptions are made in order to simplify the problem:

1 The boundary layer is laminar and the boundary layer equations for the gaseous phase are regarded as quasi-steady, even though the solid phase is treated as unsteady.

2 The pyrolysis rate of the fuel $\dot{m}_P''$ obeys the Arrhenius law and is expressed as

$$\dot{m}_P'' = \rho_s A_P \exp(-E_p/R\,T_w) \tag{1}$$

3 The regression distance of the solid fuel prior to ignition is much less than the heat penetration depth and the particle diameter; hence, the surface regression prior to ignition is neglected in this model.

4 The chemical reaction is described by a one-step and second-order Arrhenius kinetics. The volumetric chemical reaction rate $\dot{m}_R'''$ is given as

$$\dot{m}_R''' = A_R \rho^2 Y_o Y_F \exp(-E_R/R\,T) \tag{2}$$

5 The gas mixture obeys the ideal gas law.

6 The volumetric pyrolysis inside the solid fuel is negligible and the specific heat, conductivity, and density are constant.

The origin of the coordinate system of gaseous phase equations is at the front stagnation point of the particle, as depicted in Fig. 1. The x axis is along the fuel surface and the y axis is perpendicular to the x axis. The origin of the formulation of the solid phase is at the center of the fuel.

The equation of conservation of mass is given as

$$\frac{\partial(R_2^j \rho u)}{\partial x} + \frac{\partial(R_2^j \rho v)}{\partial y} = 0 \tag{3}$$

where R_2^j is the radius of the contour of fuel surface. For two-dimensional flows j equals 0 and in axisymmetric flows j equals 1.

The equations of conservation of oxygen and fuel are composed of convective, diffusive, and chemical reaction terms, as interpreted in the following:

$$\rho u \frac{\partial Y_o}{\partial x} + \rho v \frac{\partial Y_o}{\partial y} = \frac{\partial}{\partial y}\left(\rho D \frac{\partial Y_o}{\partial y}\right) - n\rho^2 Y_o Y_F A_R \exp(-E_R/RT) \tag{4}$$

$$\rho u \frac{\partial Y_F}{\partial x} + \rho v \frac{\partial Y_F}{\partial y} = \frac{\partial}{\partial y}\left(\rho D \frac{\partial Y_F}{\partial y}\right) - \rho^2 Y_o Y_F A_R \exp(-E_R/RT) \tag{5}$$

The equation of conservation of momentum is

$$\rho u \frac{\partial u}{\partial x} + \rho v \frac{\partial u}{\partial y} = \rho_e u_e \frac{du_e}{dx} + \frac{\partial}{\partial y}\left(\mu \frac{\partial u}{\partial y}\right) \tag{6}$$

where u_e is the velocity of air external to the momentum boundary layer and can be calculated from the potential flow theory as

$$u_e = \frac{3}{2} u_\infty \sin \frac{x}{R_1} \tag{7}$$

The energy conservation equation is given as

$$\rho u C_p \frac{\partial T}{\partial x} + \rho v C_p \frac{\partial T}{\partial y} = \frac{\partial}{\partial y}\left(K \frac{\partial T}{\partial y}\right) + Q\rho^2 Y_o Y_F A_R \exp(-E_R/RT) \tag{8}$$

The equation of state is given as

$$\rho T = \rho_\infty T_\infty \tag{9}$$

where it is assumed that the pressure change is small across the y direction.

The conservation equation for energy in the solid phase is given as

$$\frac{1}{r}\frac{\partial^2}{\partial r^2}(rT_s) = \frac{1}{\alpha_s}\frac{\partial T_s}{\partial t} \tag{10}$$

where it is assumed that there is no volumetric pyrolysis in the solid.

Since the distributions of velocity, temperature, and concentrations are symmetric at the stagnation point, the boundary conditions at $x=0$ are

$$u = 0 \tag{11a}$$

$$\frac{\partial T}{\partial x} = 0 \tag{11b}$$

Nomenclature

A = pre-exponential factor
C_p = specific heat of gas mixture, cal/g-K
D = mass diffusivity, cm^2/s
E = activation energy, cal/mol
K = thermal conductivity, cal/cm-s-K
L = heat of gasification, cal/g
$\dot{m}_P''$ = pyrolysis rate, g/cm^2-s
$\dot{m}_R'''$ = volumetric chemical reaction rate, g/cm^3-s
n = stoichiometric ratio
Pr = Prandtl number
Q = heat of combustion, cal/g
q = heat flux, cal/cm^2-s
r = radial coordinate
R_1 = fuel particle radius, cm
R_2 = distance from particle surface to symmetric axis
Re = Reynolds number $= \rho u R_1/\mu$
t = time, s
T = temperature, K
u = tangential velocity, m/s
v = radial velocity, m/s
x = peripheral coordinate
Y = mass fraction
y = normal coordinate
α = thermal diffusivity, cm^2/s
η = nondimensional position, defined in equation (18)
μ = dynamic viscosity, g/cm-s
ν = kinematic viscosity, cm^2/s
ρ = density, g/cm^3
σ = azimuthal angle, defined in equation (16)
ψ = dimensionless stream function

Subscripts

e = edge of boundary layer
f = fuel
i = solid phase initial value
o = oxygen
P = pyrolysis
R = reaction
s = solid
w = fuel surface
∞ = free stream

$$\frac{\partial Y_o}{\partial x} = 0 \tag{11c}$$

$$\frac{\partial Y_F}{\partial x} = 0 \tag{11d}$$

On the fuel surface the nonslip condition is fulfilled and the fuel is blown out perpendicular to the surface; hence, the boundary conditions on the fuel surface are

$$u = 0 \tag{12a}$$

$$v = v_w = \frac{\rho_s v_s}{\rho_w} = \frac{\rho_s}{\rho_w} A_p e^{-E_p/RT_w} \tag{12b}$$

$$T = T_w \tag{12c}$$

$$q = K_w \frac{\partial T}{\partial y}\bigg|_w = K_s \frac{\partial T_s}{\partial r}\bigg|_{R_1} + \rho_s v_s L \tag{12d}$$

$$-\rho_w D_w \frac{\partial Y_o}{\partial y}\bigg|_w + \rho_w v_w Y_{ow} = 0 \tag{12e}$$

$$-\rho_w D_w \frac{\partial Y_F}{\partial y}\bigg|_w + \rho_w v_w Y_{Fw} = \rho_s v_s \tag{12f}$$

The boundary conditions on the edge of the boundary layer are

$$u = \frac{3}{2} u_\infty \sin\frac{x}{R_1} \tag{13a}$$

$$T = T_\infty \tag{13b}$$

$$Y_o = Y_{o\infty} \tag{13c}$$

$$Y_F = 0 \tag{13d}$$

The initial condition and the boundary conditions in the solid phase are

$$t = 0: \quad T_s = T_i \tag{14}$$

$$t \geq 0, \quad r = 0: \quad \frac{\partial T_s}{\partial r} = 0 \tag{15a}$$

$$r = R_1: \quad T_s = T_w \tag{15b}$$

The following dimensionless variables are introduced:

$$\sigma = \frac{x}{R_1} \tag{16}$$

$$R_2 = R_1 \sin\sigma \tag{17}$$

$$\eta = \left(\frac{3}{2}\,\mathrm{Re}\right)^{1/2} \frac{1}{R_1} \int_0^y \frac{\rho}{\rho_\infty}\, dy \tag{18}$$

where Howarth transformation is used to reduce the compressible equation into incompressible form.

In addition, a stream function ψ, with $j = 1$, is defined as

$$R_2 \rho u = \mu_\infty \frac{\partial(\psi R_2)}{\partial y} \tag{19}$$

$$R_2 \rho v = -\mu_\infty \frac{\partial(\psi R_2)}{\partial x} \tag{20}$$

With the defined variables and the assumptions, equations (4)–(6) and equation (8) can be transformed into

$$\frac{\partial\psi}{\partial\eta}\frac{\partial Y_o}{\partial\sigma} - \left(\frac{\partial\psi}{\partial\sigma} + \psi\cot\sigma\right)\frac{\partial Y_o}{\partial\eta} = \left(\frac{3}{2}\,\mathrm{Re}\right)^{1/2} \mathrm{Pr}^{-1}\frac{\partial^2 Y_o}{\partial\eta^2} - \left(\frac{3}{2}\mathrm{Re}\right)^{-1/2} \cdot \frac{\rho_\infty^2 R_1^2 n}{\mu_\infty}\frac{\rho}{\rho_\infty} Y_o Y_F A_R \exp(-E_R/RT) \tag{21}$$

$$\frac{\partial\psi}{\partial\eta}\frac{\partial Y_F}{\partial\sigma} - \left(\frac{\partial\psi}{\partial\sigma} + \psi\cot\sigma\right)\frac{\partial Y_F}{\partial\eta} = \left(\frac{3}{2}\,\mathrm{Re}\right)^{1/2} \mathrm{Pr}^{-1}\frac{\partial^2 Y_F}{\partial\eta^2} - \left(\frac{3}{2}\mathrm{Re}\right)^{-1/2} \cdot \frac{\rho_\infty^2 R_1^2}{\mu_\infty}\frac{\rho}{\rho_\infty} Y_o Y_F A_R \exp(-E_R/RT) \tag{22}$$

$$\frac{\partial\psi}{\partial\eta}\frac{\partial^2\psi}{\partial\sigma\partial\eta} - \left(\frac{\partial\psi}{\partial\sigma} + \psi\cot\sigma\right)\frac{\partial^2\psi}{\partial\eta^2} = \left(\frac{3}{2}\mathrm{Re}\right)\frac{\rho_\infty}{\rho}\sin\sigma\cos\sigma + \left(\frac{3}{2}\mathrm{Re}\right)^{1/2}\frac{\partial^3\psi}{\partial\eta^3} \tag{23}$$

$$\frac{\partial\psi}{\partial\eta}\frac{\partial T}{\partial\sigma} - \left(\frac{\partial\psi}{\partial\sigma} + \psi\cot\sigma\right)\frac{\partial T}{\partial\eta} = \left(\frac{3}{2}\mathrm{Re}\right)^{-1/2} \mathrm{Pr}^{-1}\frac{\partial^2 T}{\partial\eta^2} + \left(\frac{3}{2}\mathrm{Re}\right)^{-1/2} \cdot \frac{\rho_\infty^2 R_1^2 Q}{\mu_\infty C_p}\frac{\rho}{\rho_\infty} Y_o Y_F A_R \exp(-E_R/RT) \tag{24}$$

Since the profiles of variables are axisymmetric, the stream function, temperature, and concentration profiles are further expanded with respect to the azimuthal angle σ as

$$\psi = \left(\frac{3}{2}\mathrm{Re}\right)^{1/2} (\sigma f_o(\eta) + \sigma^3 f_1(\eta) + \ldots) \tag{25}$$

$$\frac{T - T_\infty}{T_\infty} = G_o(\eta) + \sigma^2 G_1(\eta) + \ldots \tag{26}$$

$$\frac{Y_o - Y_{o\infty}}{Y_{o\infty}} = H_o(\eta) + \sigma^2 H_1(\eta) + \ldots \tag{27}$$

$$\frac{Y_F}{Y_{o\infty}} = I_o(\eta) + \sigma^2 I_1(\eta) + \ldots \tag{28}$$

Substituting the above expressions into equations (21)–(24) and expanding the triangular functions into azimuthal angles, the following ordinary differential equations, through the comparison of the coefficients of azimuthal angle, are obtained:

$$f_o''' + 2 f_o f_o'' - (f_o')^2 = -1 - G_o \tag{29}$$

$$f_1''' + 2 f_o f_1'' - 4 f_o' f_1' + 4 f_o'' f_1 - \frac{1}{3} f_o f_o'' = \frac{2}{3}(1 + G_o) - G_1 \tag{30}$$

$$\mathrm{Pr}^{-1} G_o'' + 2 f_o G_o' + \left\{\left(\frac{3}{2}\,\mathrm{Re}\right)^{-1} \times \frac{\rho_\infty^2 R_1^2 Y_{o\infty} Q}{\mu_\infty C_p T_\infty} A_R \exp\left[\frac{-E_R}{RT_\infty(1 + G_o)}\right]\right\} \cdot \frac{1 + H_o}{1 + G_o} I_o = 0 \tag{31}$$

$$\mathrm{Pr}^{-1} G_1'' - 2 f_o' G_1 + 2 f_o G_1' + 4 f_1 G_o' - \frac{1}{3} f_o G_o' + \left\{\left(\frac{3}{2}\,\mathrm{Re}\right)^{-1} \cdot \frac{\rho_\infty^2 R_1^2 Y_{o\infty}^2 Q}{\mu_\infty C_p T_\infty} A_R \exp\left[\frac{-E_R}{R\ T_\infty(1 + G_o)}\right]\right\} \cdot \left(\frac{(1 + H_o) I_1 + I_o H_1}{1 + G_o} + \frac{(1 + H_o) I_o G_1 E_R / RT_\infty}{(1 + G_o)^3} - \frac{(1 + H_o) I_o G_1}{(1 + G_o)^2}\right) = 0 \tag{32}$$

$$\mathrm{Pr}^{-1} H_o'' + 2 f_o H_o' - \left\{\left(\frac{3}{2}\mathrm{Re}\right)^{-1} \times \frac{\rho_\infty^2 R_1^2 n Y_{o\infty}}{\mu_\infty} A_R \exp\left[\frac{-E_R}{R\ T_\infty(1 + G_o)}\right]\right\} \cdot \frac{1 + H_o}{1 + G_o} I_o = 0 \tag{33}$$

$$\mathrm{Pr}^{-1} H_1'' - 2 f_o' H_1 + 2 f_o H_1' + 4 f_1 H_o' - \frac{1}{3} f_o H_o' - \left\{\left(\frac{3}{2}\mathrm{Re}\right)^{-1} \times \frac{\rho_\infty^2 R_1^2 n Y_{o\infty}}{\mu_\infty} A_R \exp\left[\frac{-E_R}{RT_\infty(1 + G_o)}\right]\right\} \cdot \left(\frac{(1 + H_o) I_1 + I_o H_1}{1 + G_o} + \times \frac{(1 + H_o) I_o G_1 E_R / RT_\infty}{(1 + G_o)^3} - \frac{(1 + H_o) I_o G_1}{(1 + G_o)^2}\right) = 0 \tag{34}$$

Table 1 The fuel properties and the related parameters adopted in the theoretical model (Kashiwagi and Summerfield, 1973)

$\rho_s = 1.54$ g/cm^3
$L = 120$ cal/g
$Q = 120{,}000$ cal/g
$T_i = 298.2$ K
$L = 120$ cal/g
$u_\infty = 0.2$–330 m/s
$R_1 = 0.05$–1.4 cm

$A_P = 1000$ cm/s
$E_R = 16{,}000$ cal/mol
$E_P = 12{,}000$ cal/mol
$\mathrm{Pr} = 0.7$
$n = 6$
$Y_{o\infty} = 0.05$–0.23
$T_\infty = 1100$–1600 K

$$\left.\begin{array}{l} A_R = 1\times10^{8}\ \mathrm{cm^3/g\text{-}s} \\ \alpha_s = 0.0003\ \mathrm{cm^2/s} \end{array}\right\} \text{ for } u_\infty < 3\ \mathrm{m/s}$$

$$\left.\begin{array}{l} A_R = 1\times10^{10}\ \mathrm{cm^3/g\text{-}s} \\ \alpha_s = 0.0018\ \mathrm{cm^2/s} \end{array}\right\} \text{ for } u_\infty > 10\ \mathrm{m/s}$$

$$\left.\begin{array}{l} K_\infty \\ \rho_\infty \\ \mu_\infty \\ C_p \end{array}\right\} \text{ properties of air at } T = T_\infty$$

$$\mathrm{Pr}^{-1} I_o'' + 2f_o I_o' - \left\{\left(\frac{3}{2}\,\mathrm{Re}\right)^{-1} \frac{\rho_\infty^2 R_1^2 Y_{o\infty}}{\mu_\infty} A_R \exp\left[\frac{-E_R}{RT_\infty(1+G_o)}\right]\right\} \cdot \frac{1+H_o}{1+G_o}\, I_o = 0 \tag{35}$$

$$\mathrm{Pr}^{-1} I_1'' - 2f_o' I_1 + 2f_o I_1' + 4f_1 I_o' - \frac{1}{3} f_o I_o' - \left\{\left(\frac{3}{2}\mathrm{Re}\right)^{-1} \cdot \frac{\rho_\infty^2 R_1^2 Y_{o\infty}}{\mu_\infty} A_R \exp\left[\frac{-E_R}{RT_\infty(1+G_o)}\right]\right\} \cdot \left(\frac{(1+H_o)I_1 + I_o H_1}{1+G_o} + \frac{(1+H_o)I_o G_1 E_R/RT_\infty}{(1+G_o)^3} - \frac{(1+H_o)I_o G_1}{(1+G_o)^2}\right) = 0 \tag{36}$$

Similarly, the boundary conditions are transformed and given as follows:

$$f_o'(0) = 0 \tag{37a}$$
$$f_1'(0) = 0 \tag{37b}$$
$$f_o(0) = \frac{-\rho_s R_1}{2\mu_\infty}\left(\frac{3}{2}\mathrm{Re}\right)^{-1/2} A_p e^{-E_p/RT_w} \tag{37c}$$
$$f_1(0) = \frac{-\rho_s R_1}{24\mu_\infty}\left(\frac{3}{2}\mathrm{Re}\right)^{-1/2} A_p e^{-E_p/RT_w} \tag{37d}$$
$$G_o(0) = \frac{T_w - T_\infty}{T_\infty} \tag{37e}$$
$$G_1(0) = 0 \tag{37f}$$
$$H_o'(0) + 2\mathrm{Pr} f_o(0)(1 + H_o(0)) = 0 \tag{37g}$$
$$H_1'(0) + 2\mathrm{Pr} H_1(0) f_o(0) = 0 \tag{37h}$$
$$I_o'(0) = \frac{2\mathrm{Pr} f_o(0)(1 - Y_{o\infty} I_o(0))}{Y_{o\infty}} \tag{37i}$$
$$I_1'(0) + 2\mathrm{Pr} f_o(0) I_1(0) = 0 \tag{37j}$$
$$f_o'(\infty) = 1 \tag{37k}$$
$$f_1'(\infty) = -\frac{1}{6} \tag{37l}$$
$$G_o(\infty) = 0 \tag{37m}$$
$$G_1(\infty) = 0 \tag{37n}$$
$$H_o(\infty) = 0 \tag{37o}$$
$$H_1(\infty) = 0 \tag{37p}$$
$$I_o(\infty) = 0 \tag{37q}$$
$$I_1(\infty) = 0 \tag{37r}$$

Numerical Method

The governing equations of gaseous and solid phases are coupled and nonlinear. A value of surface temperature is first assumed to decouple the gaseous equations from the equations of the solid. The higher order equations of the gas are transformed into a set of second-order differential equations and then quasi-linearized. Through the process of quasi-linearization (Lee, 1968), these sets of boundary-type equations are transformed into the initial value problems and can be easily solved using the Runge-Kutta method. Finally, the gas phase solutions and the solid phase conditions are matched on the fuel surface. The fuel properties and the related parameters adopted are shown in Table 1 (Kashiwagi and Summerfield, 1973). The accuracy of the numerical solutions were verified by comparing the results with and without the third term of the equations (25) to (28), the error for the temperature profile was found to be less than 1 K; therefore, the first two leading terms of the polynomials are used through the following analysis.

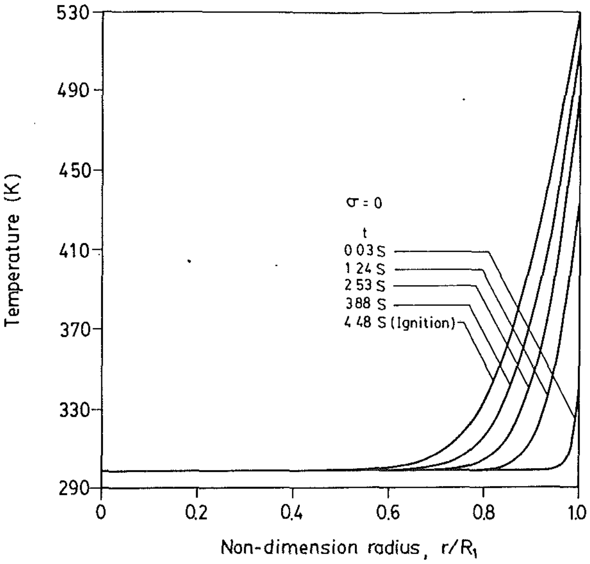

Fig. 2 Temperature distributions in the solid phase at various times ($T_\infty = 1200$ K, $u_\infty = 200$ m/s, $R_1 = 1.0$ cm, $Y_{o\infty} = 0.23$)

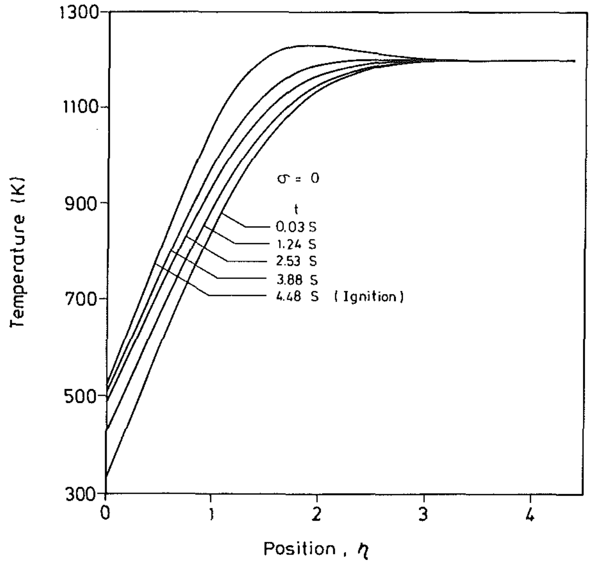

Fig. 3 Temperature profiles at various times around the ignition time ($T_\infty = 1200$ K, $u_\infty = 200$ m/s, $R_1 = 1.0$ cm, $Y_{o\infty} = 0.23$)

Results and Discussion

Figure 2 shows the temperature distributions in the solid phase prior to and right at the ignition time. The thermal wave penetration depth at the ignition time is about half of the particle radius, while the regression distance at ignition time is found to be less than 0.5 percent of the particle radius.

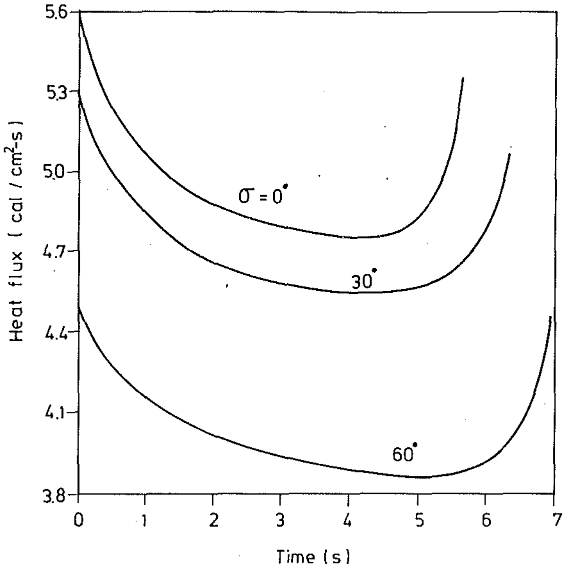

Fig. 4 Histories of the heat flux to the solid fuel at azimuthal angles of 0, 30, and 60 deg ($T_\infty = 1200$ K, $u_\infty = 200$ m/s, $R_1 = 1.0$ cm, $Y_{o\infty} = 0.23$)

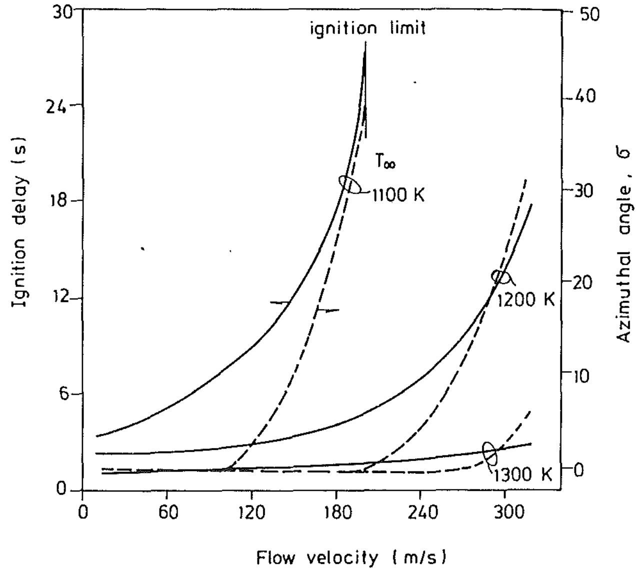

Fig. 6 Initial ignition position and ignition delay versus free-stream air velocity at various gas temperatures ($R_1 = 1.0$ cm, $Y_{o\infty} = 0.23$)

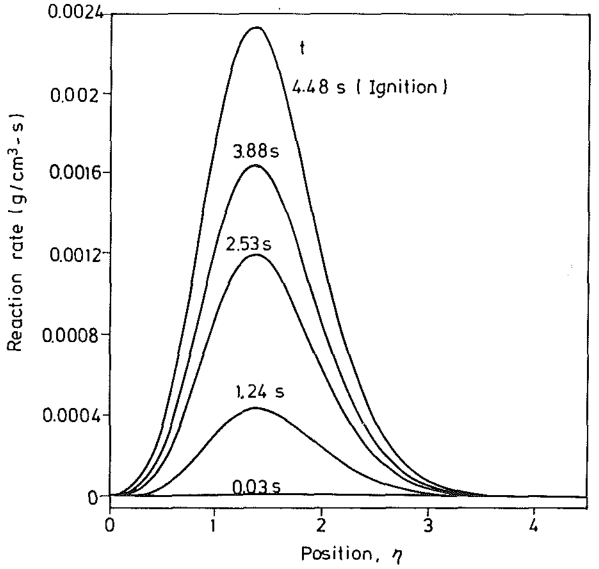

Fig. 5 Reaction rate distributions at various times around the ignition time ($T_\infty = 1200$ K, $u_\infty = 200$ m/s, $R_1 = 1.0$ cm, $Y_{o\infty} = 0.23$)

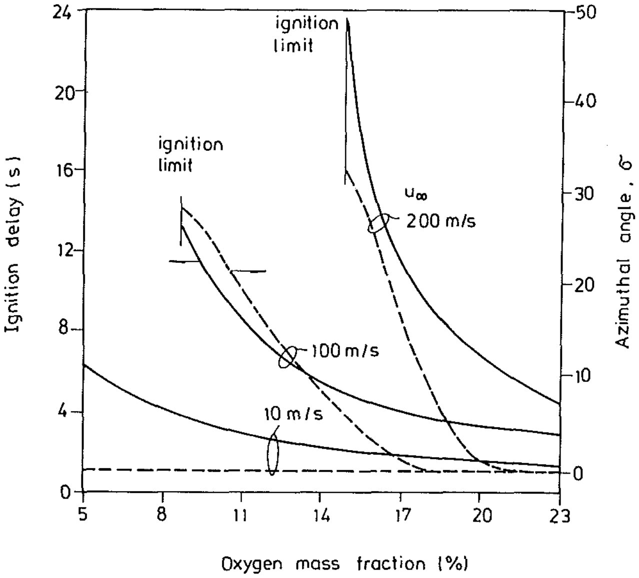

Fig. 7 Effect of oxygen mass concentration on the ignition delay and initial ignition position at various air velocities ($T_\infty = 1200$ K, $R_1 = 1.0$ cm)

Therefore, the thermal wave penetration depth is much larger than the regression distance and the assumption of the neglect of the surface regression is reasonable.

Ignition Criterion. It is reported that the major variables related to the ignition criteria are temperature and concentration of fuel vapor in the gas phase (Mutoh et al., 1979). Since the vapor concentration in this study is within the rich flammability limit, the major variable discussed is the gas temperature. Figure 3 shows the temperature profiles prior to and right at the ignition time. Before ignition, the gas temperature near the stagnation point rises monotonically from the cool wall temperature to the free-stream temperature of 1200 K. At 3.88 s, the first small peak appears near the edge of the boundary layer and propagates inward quickly. The corresponding heat fluxes from the gas phase to the fuel surface at the azimuthal angles of 0, 30 and 60 deg are shown in Fig. 4. As discussed conceptually by Birk (1980), before ignition the heat transfer from the environment to the fuel decreases with time and begins to increase as the ignition occurs and the gas temperature starts to rise. Figure 4 shows that the heat flux from the gas phase to the solid wall, as given in equation (12*d*), is at its minimum value of 4.48 s. At that moment the reaction rate is pretty high, as shown in Fig. 5, and the gas temperature as well as the heat flux begin to run away. In the meantime, the gas temperature at the ignition position is higher than the free-stream temperature. It is therefore judged that the criterion of the inverse point of the slope of the heat flux to the fuel, $dq/dt = 0$, should be able to cover the criterion of the prescribed ignition temperature proposed by Hermance and Kumar (1970) and may also cover the criterion of the critical chemical reaction rate used by Kashiwagi and Summerfield (1973). It fulfills the physical situation of ignition more precisely, and hence is used in the following analysis.

Ignition Mechanism. In the previous theoretical models the ignition is often assumed to begin at the stagnation point. However, this study shows that the ignition point may be swept down to the downstream location for certain ranges of flow

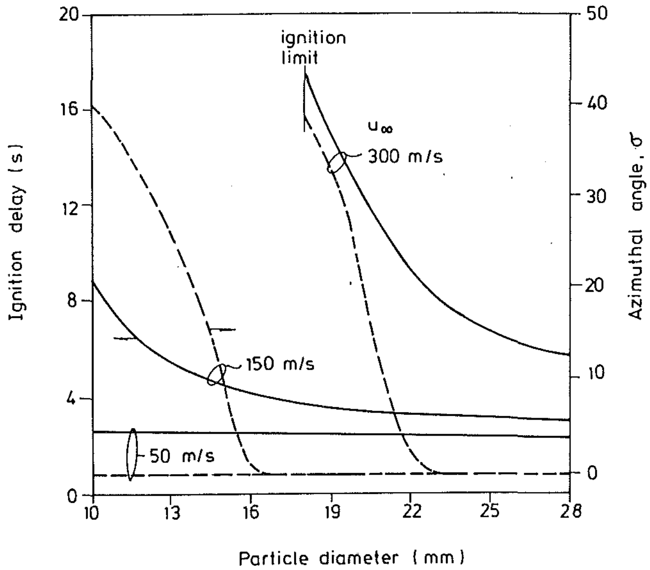

Fig. 8 Effect of initial particle size on the ignition delay and initial ignition position at various air velocities ($T_\infty = 1200$ K, $Y_{o\infty} = 0.23$)

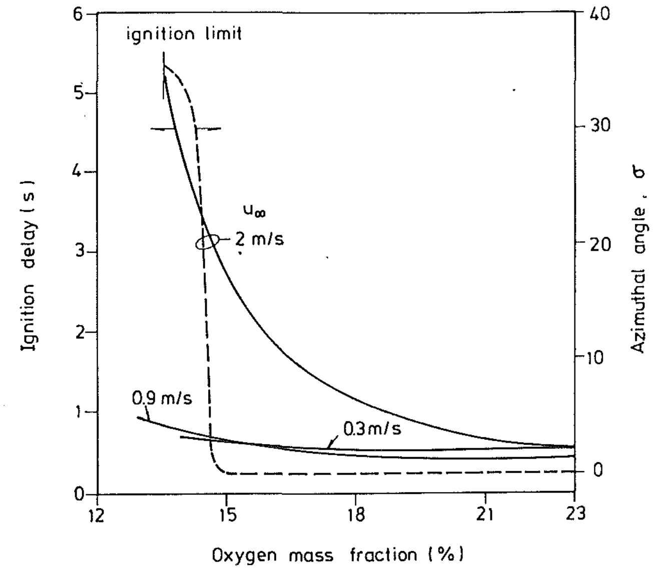

Fig. 10 Effect of oxygen mass concentration on the ignition delay and initial ignition position at various air velocities. ($T_\infty = 1600$ K, $R_1 = 0.2$ cm)

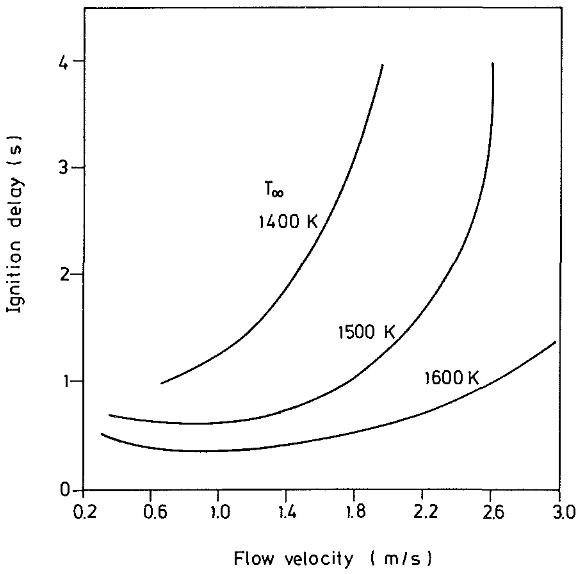

Fig. 9 Effect of air velocity on the ignition delay at various gas temperatures ($Y_{o\infty} = 0.23$, $R_1 = 0.2$ cm)

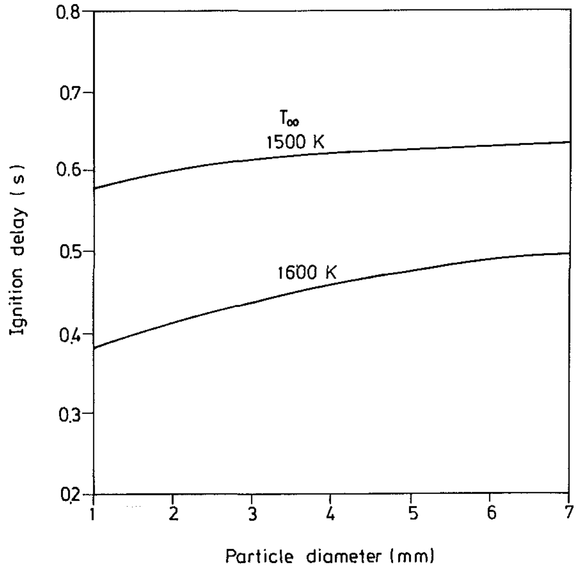

Fig. 11 Effect of initial particle size on the ignition delay at various air temperatures ($u_\infty = 0.7$ m/s, $Y_{o\infty} = 0.23$)

velocity, temperature, and oxygen concentration. Figure 6 shows that when the flow velocity is varied from 100 m/s to 200 m/s and the air temperature is maintained at 1100 K, the ignition point moves from the stagnation point to 35-deg azimuthal angle. Ignition will no longer occur when the velocity is higher than 200 m/s. The case of 1200 K shows a similar tendency. Nevertheless, the flow has only a little influence when the temperature is higher than 1300 K. Figure 6 also shows that the ignition delay increases monotonically with flow velocity when the air temperature is either 1100 K or 1200 K. When the temperature is raised to 1300 K the ignition delay becomes less sensitive to the flow velocity.

Figure 7 shows that both the ignition delay and the initial ignition position are strong functions of the oxygen mass fraction of the N_2/O_2 mixture when the flow velocity is higher than 100 m/s. It is only slightly affected when the flow velocity is 10 m/s. The oxygen mass fractions for the ignition limit are 15 percent and 9 percent for velocities of 200 m/s and 100 m/s, respectively. The ignition can always occur when the oxygen mass fraction is higher than 5 percent and the flow velocity is as low as 10 m/s.

It is then inferred that the gas phase chemical reaction and the fluid dynamics of flow are the two determining steps for convective ignition at high flowing stream. When the flow rate is relatively low, the heat transfer rate, which is maximum at a 0-deg azimuthal angle, dominates the ignition process and thus causes ignition initiates near the stagnation point. As the effect of blow-down of the reactive vapors in the gas phase by the fast flow overcomes the gas phase chemical reaction, the ignition delay is prolonged and the ignition position then shifts to a downstream position. This phenomenon is less profound at higher flow temperature and higher oxygen concentration, since the chemical reaction rate is higher under those conditions.

The effect of the solid fuel particle size on the ignition delay and ignition position is also investigated and the results are shown in Fig. 8. At a velocity of 50 m/s both the ignition delay and the ignition position are scarcely affected by the particle diameter. At a higher flow velocity the trends of ignition delay and ignition position are similar to those of Figs. 6 and 7. The smaller particles take longer to ignite owing to the strong blowdown effect.

Analysis of Low-Velocity Cases. The experiments of Niioka et al. (1981), which were conducted with a flow velocity lower than 10 m/s, indicates the existence of the critical velocity for minimum ignition delay of solid fuel. The boundary layer thickness under these conditions is relatively thick compared with the particle radius, and the accuracy of the boundary layer approximation is reduced to a certain extent. However, a qualitative analysis of the present work is still able to investigate similar phenomena and mechanisms. The prefactor of the chemical reaction rate is adjusted for the analysis of low-velocity cases, as indicated in Table 1.

Figure 9 shows the effect of air velocity on ignition delay in the range of low flow velocity. It is shown that the minimum ignition delays do exist at the critical velocities of 0.9 m/s and 0.8 m/s for 1600 K and 1500 K, respectively. Figure 10 shows that the ignition point is near the stagnation point when the oxygen mass fraction is higher than 14.6 percent. It moves from the 0-deg azimuthal angle to the 35-deg azimuthal angle while the oxygen mass fraction drops from 14.6 percent to 13.5 percent. It also indicates that when the flow velocity is 0.9 m/s the ignition delay is minimum, and the oxygen mass fraction is greater than 15.5 percent at 1600 K. In addition, the influence of the particle size is analyzed in order to judge the controlling factors of the ignition process. Figure 11 indicates that when the velocity is less than 0.9 m/s, the whole ignition process may be dominated by the heat transfer rate. The heat transfer rate for small particles is higher than that for large particles, therefore, the ignition delay increases with the particle diameter.

Conclusions

A two-dimensional, unsteady model is developed to study the convective thermal ignition process of solid fuel particles in the region between the stagnation point and the separation point. The condition of the minimum heat flux from the gas phase to the fuel is investigated and chosen as the ignition criterion. Once this criterion is fulfilled the local gas temperature and the reaction rate are high enough to sustain the combustion flame. This ignition criterion may be able to cover the criteria of the prescribed ignition temperature and chemical reaction rate.

This analysis indicates that the ignition process is mainly controlled by the rate of the gas phase reaction and the fluid dynamics at high flowing stream. When the flow velocity is high, the ignition delay lengthens and the ignition position may shift downstream. This phenomena also occurs under certain ranges of gas temperature and oxygen mass fraction. However, at the environments of high temperature or high oxygen concentration the ignition delay and ignition position are slightly affected by the flow velocity. When the flow velocity is relatively low, the ignition delay is short and the ignition position likely initiates near the stagnation point.

This model is also applied to the flow field of low Reynolds number. The qualitative prediction indicates that a critical velocity exists for convective ignition of solid fuel. Under that velocity the ignition process is mainly controlled by heat transfer from the flow to the fuel. The ignition delay increases with the particle diameter.

Acknowledgments

The authors wish to acknowledge the support of this study by the National Science Council of the Republic of China, under Contract No. NSC78-0401-E007-02.

References

Annamalai, K., and Durbetaki, P., 1977, "A Theory on Transition of Ignition Phase of Coal Particles," *Combust. Flame*, Vol. 29, pp. 193-208.

Birk, A., 1980, "Convective Ignition of Propellant Cylinders in a Developing Cross Flow Field," Ph.D. Thesis, Princeton University, Princeton, N. J.

Fernandez-Pello, A. C., and Law, C. K., 1982a, "On the Mixed-Convective Flame Structure in the Stagnation Point of a Fuel Particle," *19th Symp. (Int.) on Combustion*, The Combustion Institute, Pittsburgh, pp. 1037-1044.

Fernandez-Pello, A. C., and Law, C. K., 1982b, "A Theory for the Free-Convective Burning of a Condensed Fuel Particle," *Combust. Flame*, Vol. 44, pp. 97-112.

Gandhi, P. D., and Kanury, A. M., 1986, "Criterion for Spontaneous Ignition of Radiantly Heated Organic Solids," *Combust. Sci. Tech.*, Vol. 50, pp. 233-254.

Hermance, C. E., and Kumar, R. K., 1970, "Gas Phase Ignition Theory for Homogeneous Propellants Under Shock Tube Conditions," *AIAA Journal*, Vol. 8, pp. 1551-1558.

Kashiwagi, T., MacDonald, B. M., Isoda, H., and Summerfield, M., 1971, "Ignition of a Solid Polymeric Fuel in a Hot Oxidizing Gas Stream," *13th Symp. (Int.) on Combustion*, The Combustion Institute, Pittsburgh, pp. 1073-1086.

Kashiwagi, T., and Summerfield, M., 1973, "Ignition and Flame Spreading Over a Solid Fuel: Non-similar Theory for a Hot Oxidizing Boundary Layer," *14th Symp. (Int.) on Combustion*, The Combustion Institute, Pittsburgh, pp. 1235-1247.

Kumar, R. K., 1983, "Gas Phase Ignition of a Composite Solid Propellant Subjected to Radiant Heating," *Combust. Sci. Tech.*, Vol. 30, pp. 273-288.

Lee, E. S., 1968, *Quasilinearization and Invariant Imbedding*, Academic Press, New York, pp. 73-81.

Mutoh, N., Hirano, T., and Akita, K., 1979, "Experimental Study on Radiative Ignition of Polymethylmethacrylate," *17th Symp. (Int.) on Combustion*, The Combustion Institute, Pittsburgh, pp. 1183-1190.

Niioka, T., Takahashi, M., and Izumikawa, M., 1981, "Gas Phase Ignition of a Solid Fuel in a Hot Stagnation-Point Flow," *18th Symp. (Int.) on Combustion*, The Combustion Institute, Pittsburgh, pp. 741-747.

Price, E. W., Bradely, H. H., Jr., and Dehority, G. L., 1966, "Theory of Ignition of Solid Propellants," *AIAA J.*, Vol. 4, pp. 1153-1161.

Sibulkin, M., Kulkarni, A. K., and Annamalai, K., 1981, "Effects of Radiation on the Burning of Vertical Fuel Surfaces," *18th Symp. (Int.) on Combustion*, The Combustion Institute, Pittsburgh, pp. 611-617.

Sibulkin, M., Kulkarni, A. K., and Malary, S. F., 1983, "Nonsimilar Calculation for Free Convective Diffusion Flames," *Combust. Flame*, Vol. 50, pp. 59-64.

A Skewed PDF Combustion Model for Jet Diffusion Flames

M. M. M. Abou-Ellail
Professor.

H. Salem
Associate Professor.

Department of Mechanical Engineering,
Cairo University,
Cairo, Egypt

A combustion model based on restricted chemical equilibrium is described. A transport equation for the skewness of the mixture fraction is derived. It contains two adjustable constants. The computed values of the mean mixture fraction (f) *and its variance and skewness* (g *and* s) *for a jet diffusion methane flame are used to obtain the shape of a skewed pdf. The skewed pdf is split into a turbulent part (beta function) and a nonturbulent part (delta function) at* f = 0. *The contribution of each part is directly related to the values of* f, g, *and* s. *The inclusion of intermittency in the skewed pdf appreciably improves the numerical predictions obtained for a turbulent jet diffusion methane flame for which experimental data are available.*

Introduction

In many turbulent diffusion flames and combustion systems, the rate of the overall combustion reaction is controlled by the physical rate of turbulent mixing (Lockwood, 1977). Moreover, the fluid-mechanical effect of turbulence gives rise to very large fluctuations of species concentrations, temperature, and density, and hence the whole structure of the flame. At the outer edge of the mixing layer of jet diffusion flames, cold air is engulfed deep into the flame (Bush and Fendell, 1978; Ballantyne and Bray, 1976); at the inner edge pure fuel eddies could also be entrained into the flame zone (Abou-Ellail and Salem, 1988). The intermittency nature of jet diffusion flames causes the probability density function (pdf) of the mixture fraction (f) to be skewed with possible spikes at $f=0$ and/or $f=1.0$.

In the present work, a modeled transport equation for the skewness ($s \equiv \overline{f'f'f'}$) of the mixture fraction is derived. Solution of this equation for a turbulent jet diffusion CH_4–air flame gives the value of s at any point inside the flame. An intermittency factor (γ) is then calculated from the value of s and used to adjust the pdf.

Physical Model

In this section the main modeling assumptions and governing equations are presented.

Mean Flow Equations. The steady-state, time-averaged, conservation equations for mass, momentum, and mixture fraction in Cartesian tensor notation are

$$(\rho \bar{u}_i)_{,i} = 0 \tag{1}$$

$$[\rho \bar{u}_i \bar{u}_j - \mu(\bar{u}_{i,j} + \bar{u}_{j,i} - (2/3)\bar{u}_{m,m}\delta_{ij}) + \bar{p}\delta_{ij}]_{,,i}$$
$$-(\rho - \rho_o)g_j + (\overline{\rho u_i' u_j'})_{,i} = 0 \tag{2}$$

$$(\rho \bar{u}_i \bar{f} - \Gamma_f \bar{f}_{,i} + \overline{\rho u_i' f'})_{,i} = 0 \tag{3}$$

where $\bar{u}_i$ and u_i' are the time-mean velocity and its fluctuating component in the i direction; ρ is density; ρ_o is a reference density; μ is laminar viscosity; $\bar{p}$ is the time-mean pressure; g_j is the j component of the gravitational acceleration; f and Γ_f are the mixture fraction and its molecular diffusion coefficient; and $\rho u_i' u'j$ and $\rho u_i' f'$ are turbulent diffusion fluxes. In the above equations terms involving ρ' were neglected not only because their influence may be insignificant (Gasman et al., 1976) but also because $\bar{f}$ will no longer be a conserved property of the flow, should $(\rho' f' \;\bar{u})_{,i}$, $(\rho' u' \;\bar{f})_{,i}$, and $(\rho' u' f')_{,i}$ be included in the mixture fraction equation. Therefore the above system of equations is equivalent to a Favre-averaged one (Lockwood and Stolakis, 1983).

Separate equations for the stagnation enthalpy (h) and the chemical species mass fraction (m_l) are not required, since under the usual assumption of equal diffusivities, unit Lewis number, and fast chemistry, h and m_l are instantaneously functions of only the mixture fraction (Abou-Ellail et al., 1978).

Turbulence Model. The transport equations for the kinetic energy of turbulence (k) and its dissipation rate (ϵ) are (Launder and Spalding, 1972)

$$(\rho \bar{u}_i k - (\mu_t/\sigma_k)k_{,i})_{,i} - (G - \rho\epsilon) = 0 \tag{4}$$

$$(\rho \bar{u}_i \epsilon - (\mu_t/\sigma_\epsilon)\epsilon_{,i})_{,i} - (C_1 G - C_2 \rho\epsilon)\epsilon/k = 0 \tag{5}$$

where

$$G = \mu_t(\bar{u}_{i,j} + \bar{u}_{j,i})\bar{u}_{i,j} - 2/3\,\bar{u}_{m,m}(\mu_t \bar{u}_{m,m} + \rho k) \tag{6}$$

and μ_t is the turbulent viscosity, given by

$$\mu_t = C_\mu \rho k^2/\epsilon \tag{7}$$

C_1, C_2, and C_μ are constants of the model. σ_k and σ_ϵ are turbulent Prandtl/Schmidt numbers of order unity. The turbulent diffusion fluxes in equations (2) and (3) may be calculated from the following equations (Launder and Spalding, 1972):

$$-\overline{\rho u_i' u_j'} = \mu_t(\bar{u}_{i,j} + \bar{u}_{j,i} - 2/3\,\bar{u}_{m,m}\delta_{ij}) - 2/3\ \rho k\ \delta_{ij} \tag{8}$$

$$-\overline{\rho u_i' f'} = (\mu_t/\sigma_f)\ \bar{f}_{,i} \tag{9}$$

and for any scalar dependent variable ϕ

$$-\overline{\rho u_i' \bullet \phi'} = (\mu_t/\sigma_\phi)\bullet\bar{\phi}_{,i} \tag{10}$$

σ_f and σ_ϕ are further constants of the model.

Combustion Model. Combustion in turbulent jet diffusion flames is characterized by relatively fast chemistry and fast mixture fraction fluctuations. The instantaneous temperature and species concentrations mixture fraction diagram for CH_4 flames is constructed on the basis of a flame zone model, where the turbulent flame may be assumed to consist of a brush of quasilaminar flamelets with restricted chemical equilibrium within zones of finite thickness and frozen reaction outside these zones (Eickhoff and Grethe, 1979). Restricted equilibrium is assumed here to extend the applicability of equilibrium calculations to very rich mixtures beyond the limits imposed by the original flame zone model (Eickhoff and Grethe, 1979). The present combustion model allows for the formation of intermediate hydrocarbon species (C_2H_4), but soot is not included. The mass fractions of CH_4 and C_2H_4 are calculated as described by Bilger and Starner (1983). The intermediate spe-

---

Contributed by the Heat Transfer Division for publication in the JOURNAL OF HEAT TRANSFER. Manuscript received by the Heat Transfer Division March 28, 1989; revision received October 17, 1989. Keywords: Numerical Methods, Reacting Flows, Turbulence.

cies (C_2H_4) starts to appear at stoichiometric mixture fractions while unreacted fuel (CH_4) is taken into account for $f > 0.073$. In the frozen zone, no chemical reaction is allowed; reaction products from the reaction zone may diffuse into the frozen zone and mix intensely with unreacted fuel-air mixture. Figure 1 shows the calculated species mole fractions and temperature plotted against the instantaneous mixture fraction.

The above combustion model is used to obtain the time-averaged value of any property (ϕ) solely dependent on f as follows:

$$\bar{\phi} = \int_0^1 \phi(f)\, P(f)\, df \tag{11}$$

where $P(f)$ is a probability density function, which may be characterized by the mean mixture fraction $\bar{f}$ and its variance g ($\equiv \overline{f'f'}$). The variance g can be computed from its modeled transport equation (Spalding, 1971), namely,

$$(\rho \bar{u}_i g - \mu_t/\sigma_g g_{,i})_{,i} - C_{g1}\mu_t \bar{f}_{,i}\bar{f}_{,i} + C_{g2}\rho g \epsilon/k = 0 \tag{12}$$

where C_{g1}, C_{g2}, and σ_g are additional adjustable constants.

The pfd, characterized by only $\bar{f}$ and g, will have an uncontrollable skewness and thus its shape may not be accurate enough, especially with the equilibrium diagram having very steep gradients near stoichiometric conditions (i.e., near $f = 0.058$ for CH_4 flames). Therefore, a modeled transport equation for the skewness s ($\equiv \overline{f'f'f'}$) is introduced, enabling the shape of the pdf to be accurately determined.

Skewness Tranpsort Equation. In order to obtain a transport equation for the skewness s, the time-dependent conservation equation for the instantaneous mixture fraction f ($\equiv \bar{f} + f'$) is multiplied by f'^2 and then time-averaged. The resulting equation is as follows:

$$\overline{f'^2(\rho(f+f'))_{,t}} + \overline{f'^2(\rho(\bar{u}_i+u_i')(f+f')-\Gamma_f(f+f')_{,i})_{,i}} = 0 \tag{13}$$

where $(\ldots)_{,t}$ denotes time derivative. Rearranging terms in equation (13), the following equation may be obtained:

$$\left(\frac{1}{3}\rho s\right)_{,t} + g(\rho\bar{f})_{,t} + \overline{f'^2(\rho\bar{u}_i f')}_{,i} + g(\rho\bar{u}_i\bar{f})_{,i} + \overline{f'^2(\rho u_i' f)}_{,i} + \overline{f'^2(\rho u_i' f')}_{,i} - g(\Gamma_f\bar{f}_{,i})_{,i} - \overline{f'^2(\Gamma_f f'_{,i})}_{,i} = 0 \tag{14}$$

In the above equation $\overline{f'^2}$ and $\overline{f'^3}$ were replaced by g and s. Under steady-state conditions, the first two terms drop out. By making use of the continuity equations of the mean flow and the fluctuating flow (i.e., $(\rho\bar{u}_i)_{,i} = 0$ and $(\rho u_i')_{,i} = 0$, the third, fifth, and sixth terms on the left-hand side of equation (14) may be modeled as follows:

$$\overline{f'^2(\rho\bar{u}_i f')}_{,i} = \overline{\left(\rho\bar{u}_i\frac{1}{3}f'^3\right)}_{,i} = \left(\frac{1}{3}\rho\bar{u}_i s\right)_{,i} \tag{15}$$

$$\overline{f'^2(\rho u_i' f)}_{,i} = \overline{\rho u_i' f'^2}\bar{f}_{,i} = -(\mu_t/\sigma_g)g_{,i}\bar{f}_{,i} \tag{16}$$

$$\overline{f'^2(\rho u_i' f')}_{,i} = \overline{\rho u_i' f'^2 f'_{,i}} = \overline{\frac{1}{3}\rho u_i'(f'^3)_{,i}}$$

$$= \overline{\left(\frac{1}{3}\rho u_i' f'^3\right)}_{,i} = -\left(\frac{1}{3}(\mu_t/\sigma_s)s_{,i}\right)_{,i} \tag{17}$$

where σ_s is a turbulent Prandtl number of order unity. Equation (10) has been used in equations (16) and (17), i.e., a gradient-type modeling has been used.

The last term on the left-hand side of equation (14) may be modeled as

$$-\overline{f'^2(\Gamma_f f'_{,i})}_{,i} = -\overline{(f'^2\Gamma_f f'_{,i})}_{,i} + \overline{\Gamma_f f'_{,i}(f'^2)}_{,i}$$

$$= -\left(\Gamma_f\left(\frac{1}{3}s\right)_{,i}\right)_{,i} + C_s\rho s\,\epsilon/k \tag{18}$$

where C_s is a constant of the model.

The second term on the right-hand side of equation (18) is modeled in the same manner as the dissipation term of the g transport equation. However, in the present case this term may be positive, negative, or zero, depending on the value of s, which is also true for the original term (which may be written as $2\,\overline{\Gamma_f f' f'_{,i} f'_{,i}}$).

Substituting equations (15)–(18) into equation (14) and multiplying the resulting equation by 3, the final form of the skewness transport equation can be written as

$$(\rho\bar{u}_i s - (\Gamma_f + \mu_t/\sigma_s)s_{,i})_{,i} - [C_{s1}\mu_t g_{,i}\bar{f}_{,i} - 3\,g(\rho\bar{u}_i\bar{f})_{,i} + 3g(\Gamma_f\bar{f}_{,i})_{,i}] + C_{s2}\rho s\,\epsilon/k = 0 \tag{19}$$

Nomenclature

C_1, C_2, C_μ = constants of the k–ϵ model

C_{g1}, C_{g2} = constants of the g equation

C_{s1}, C_{s2} = constants of the skewness equation

d = nozzle diameter

f = mass fraction of nozzle fluid (mixture fraction)

g = variance of mixture fraction

G = production of turbulence kinetic energy

h = stagnation enthalpy

k = turbulence kinetic energy

m = mass fraction of species l

p = pressure

$P(f)$ = probability density function (pdf)

r = radius, radial coordinate

s = skewness $\equiv \overline{f'^3}$

T = temperature

u_i = velocity component in the i direction

u = axial velocity

x = axial coordinate

α, β = exponents of the beta function

γ = intermittency factor

Γ = molecular transport coefficient

δ = Dirac delta function

δ_{ij} = Kronecker delta tensor

$\Delta\bar{u}_c$ = difference between centerline axial velocity and free-stream axial velocity

Δr = width of the jet = r (at $\Delta\bar{u} = 0.9\,\Delta\bar{u}_c$) − r (at $\Delta\bar{u} = 0.1\,\Delta\bar{u}_c$)

ϵ = dissipation rate of k

μ = dynamic viscosity

μ_t = turbulent viscosity

ρ = density

σ = Prandtl/Schmidt number

ϕ = flow variable

Subscripts

c = centerline

f = mixture fraction, fuel

g = variance

i = i direction

J = jet

k = turbulence kinetic energy

s = skewness

t = turbulent

ϵ = dissipation rate of k

Superscripts

$\bar{\ }$ = time-mean value

$'$ = fluctuating components

where C_{s1} is equal to $(3/\sigma_g)$ and C_{s2} is equal to 3 C_s. In the above equation the term involving molecular diffusion of $\bar{f}$ may be neglected as it is very small compared to other terms in the equation. Since s may be positive or negative, the sign of the generation term changes according to the magnitude and sign of each of its terms.

Probability Density Function. Different shapes for the pdf have been used in modeling the turbulent diffusion flame (Abou-Ellail et al., 1978). Clipped Gaussian pdf without intermittency (Lockwood and Naguib, 1975), with intermittency based on empirical relations (Kent and Bilger, 1976), three Dirac delta function pdf (Bockhorn and Lutz, 1984), and beta-function pdf with and without intermittency (Janicka and Kollman, 1980; Correa et al., 1984) are some examples. Recently Chen and Lumley (1984) have proposed a second-order model for intermittency in heated free jets using conditional averaging. Their model was then applied to jet diffusion flames by Chen et al. (1987) and by Chen (1987) yielding reasonable results.

In the present combustion model, a beta function pdf with intermittency is used. $P(f)$ consists of a turbulent part $P_t(f)$ and a delta function $\delta(f)$ at $f = 0$ (nonturbulent part). Therefore, the composite pdf may be written as

$$P(f) = (1-\gamma)\delta(f) + \gamma P_t(f)$$

where γ is the intermittency factor $(1.0 < \gamma > 0)$ and $P_t(f)$ is given by

$$P_t(f) = f^{\alpha-1}(1-f)^{\beta-1} \Big/ \int_0^1 f^{\alpha-1}(1-f)^{\beta-1}df \qquad (20)$$

The exponents α and β are related to the mean mixture fraction and variance, $\bar{f}_t$ and g_t, of the turbulent part of the pdf by

$$\alpha = \bar{f}_t\left[\frac{\bar{f}_t(1-\bar{f}_t)}{g_t} - 1\right] \qquad (21)$$

$$\beta = \alpha(1-\bar{f}_t)/\bar{f}_t \qquad (22)$$

The skewness s_t of $P_t(f)$ may be related to $\bar{f}_t$ and $\bar{g}_t$ by

$$s_t = \frac{2g_t^2(1-2\,\bar{f}_t)}{\bar{f}_t(1-\bar{f}_t)+g_t} \qquad (23)$$

$\bar{f}$, g, and s of the composite pdf are to be calculated from their transport equations (3), (12), and (19). Moreover, f_t, g_t, and γ may be related to $\bar{f}$, f, and s by the following equations:

$$\bar{f} = \gamma\bar{f}_t \qquad (24)$$

$$g = \gamma[g_t + (f_t - \bar{f})^2] + (1-\gamma)\bar{f}^2$$

Substituting the value of $\bar{f}_t$, from equation (24), the above equation yields

$$g = \gamma g_t + (1-\gamma)\bar{f}^2/\gamma \qquad (25)$$

The skewness equation is given by

$$s = \gamma s_t + \gamma(\bar{f}_t - \bar{f})[(\bar{f}_t - \bar{f})^2 + 3g_t] - (1-\gamma)\bar{f}^3$$

using equations (24) and (25); the above equation reduces to

$$s = \gamma s_t + (1-\gamma)\bar{f}[3\gamma g - (2-\gamma)\bar{f}^2]/\gamma^2 \qquad (26)$$

Equation (26) could be used to yield an explicit expression for γ as a function of $\bar{f}$, g, and s. This is done by substituting equations (24) and (25) into equation (23), using the resulting equation into equation (26) and finally solving for γ. The resulting expression for the intermittency factor is

$$\gamma = \frac{2\bar{f}^2 s + \bar{f}[g(4\bar{f}^2 - \bar{f} - g) - \bar{f}^3(1-\bar{f})]}{s(\bar{f}^2 + \bar{f} + g) + g(4\bar{f}^3 + 3\bar{f}g - \bar{f}^2 - 2g) - \bar{f}^4(1-\bar{f})} \qquad (27)$$

Equation (27) is used to calculate γ from the values of f, g, and s. Since g_t must always be greater than (or equal to) zero, equation (25) sets a minimum value for γ given by the following inequality:

$$\gamma \geq \bar{f}^2/(\bar{f}^2 + g) \qquad (28)$$

With γ computed from equation (27), $\bar{f}_t$ and g_t can be calculated from equations (24) and (25), and then α and β may be calculated from equations (21) and (22). The mean value of $\phi(f)$, a thermochemical quantity, is thus given by

$$\bar{\phi}(f) = (1-\gamma)\phi(0) + \gamma\int_0^1 \phi(f)P_t(f)df \qquad (29)$$

The model constants used in the present paper are those given in Table 1. In the table $\bar{u}_c$ is the centerline mean velocity, and Δr and Δu_c are measures of the width and velocity change across the turbulent region (Rodi, 1979). In Table 1, σ_s is taken to be equal to σ_g since they effectively represent the same transport phenomenon. Since C_{s1} is equal to $3/\sigma_g$, then its value is $(3/0.7) = 4.3$. A value of 3.0 for C_{s2} is found to give the best agreement between the predicted intermittency factor and the corresponding experimental data.

Experimental Data and Boundary Conditions

Fortunately, a good number of data sets for turbulent hydrocarbon jet diffusion flames exist. We have mainly restricted the validation of the present combustion model to the Lockwood and Moneib (1982), free jet, undiluted methane flame. The Reynolds number for this flame was 15,000. The burner was a 7.74-mm-dia vertically oriented tube with provision for annular stabilization by hydrogen. Velocity and species concentration measurements of the Lockwood and Moneib stabilized methane flame were reported by El-Banhawy et al. (1983) and by Hassan et al. (1980).

The imposition of the conditions at the boundaries of the above flame is similar to that reported by Abou-Ellail and Salem (1988) except that, in the present study, we use the 1/7 power-law profile for the fuel jet exit velocity.

Solution Procedure

The solution procedure is based mainly on an iterative marching integration algorithm (Abou-Ellail and Morcos, 1983; Abou-Ellail and Salem, 1988). The solution domain is overlaid by a 26 (radial) × 250 (axial) nonuniform axisymmetric grid. Upwind differencing is used to obtain the finite-difference counterpart of the governing transport equations. The usual parabolic flow approximations are used in the governing equations. Due to the large streamwise changes in density and other thermochemical properties, iterations are performed at each cross-stream plane until the error in each equation is less than 0.5 percent before marching downstream to the next plane.

Results and Discussion

Figures 2(*a*) and 2(*b*) depict the predicted profiles of the skewness (s) and the normalized skewness ($s/g^{3/2}$) along the axis and normal to it for the Lockwood and Moneib (1982) methane flame. Also shown in Figs. 2(*a*) and 2(*b*) is the skewness (s_β) of an unmodified beta function pdf without inter-

Table 1 Model constants

C_μ	C_1	C_2	C_{g_1}	C_{g_2}	C_{s_1}
0.09–0.04F	1.44	1.92–0.0667F	2.8	2.0	4.3
C_{s_2}	σk	σ_ϵ	σ_f	σ_g	σ_s
3.0	1.0	1.3	0.7	0.7	0.7

Note: $F = \left|\left(\frac{d\bar{u}_c}{dx} - \left|\frac{d\bar{u}_c}{dx}\right|\right)\Delta r/(1.6\,\Delta u_c)\right|^{0.2}$.

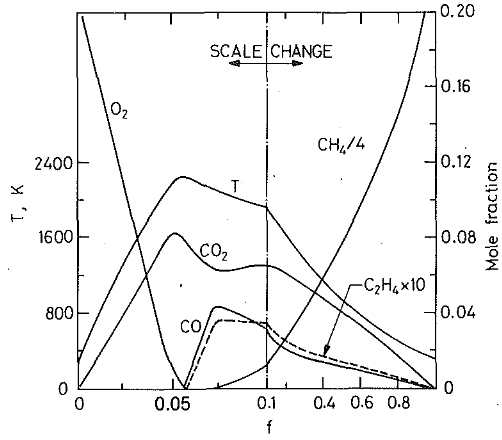

Fig. 1 Variation of temperature and species mole fractions with instantaneous mixture fraction in methane-air jet flame

mittency. It is interesting to notice the similarity between the trend of the profiles of s and s_β, although they differ in magnitude. Along the flame axis s is negative for $x/d < 16$ and positive for $x/d > 16$. Normal to the flame axis, s reaches a maximum value near the inner edge of the shear layer, then decreases gradually toward the outer edge of the shear layer.

The predicted radial profiles of the intermittency factor are shown in Figs. 3(*a*) and 3(*b*). Figure 3(*a*) shows the predicted profiles of γ for a C_3H_8–isothermal jet together with the corresponding experimental data of Schefer and Dibble (1986) at a Reynolds number of 68,000. In this case the fuel jet diameter is 0.502 cm, the fuel exit velocity is 53 m/s; and the surrounding coflowing air velocity is 9.2 m/s. Figure 3(*a*) shows agreement between the predicted profiles of γ for C_3H_8–air isothermal jets and the corresponding data of Schefer and Dibble (1986). Figure 3(*b*) shows the predicted intermittency profiles, with and without combustion, for the Lockwood and Moneib flame (1982). The effect of combustion on the γ profiles is clear; the profiles are shifted to larger radii as a result of the expansion of the hot combustion products. Near the centerline, where γ is close to 1.0, the pdf consists only of a turbulent part approximated by a beta function; while in the outer part of the flame, γ drops sharply and the pdf shape takes on a bimodal profile with a spike at $f=0$, shown in Fig. 4.

The predicted results of the profiles of the mean axial velocity $\bar{u}$ and the rms value of u', $(\sqrt{\overline{u'^2}})$, along the flame axis, are depicted in Fig. 5 together with the data of El-Banhawy et al. (1983) at a Reynolds number of 15,000. The fuel jet exit velocity profile is assumed to follow the "1/7 law" while the turbulence intensity is taken to be about 5 percent, which is equivalent to fully developed pipe flow. Preliminary results indicate that adding ±2 percent to the initial turbulence has little effect on the predicted values for $x/d > 10$. Razdan and Stevens (1985) showed that the effect of the initial conditions diminishes rapidly downstream from the nozzle exit plane. The agreement between the predictions and measurements for $\bar{u}$ and $\sqrt{\overline{u'^2}}$ is fairly good for the whole flame length, as can be seen from Fig. 5.

Figure 6 shows the predicted axial profiles of the temperature, CO, and unburned hydrocarbon concentrations along with the corresponding experimental data (El-Banhawy et al., 1983; Lockwood and Moneib, 1982). The predicted temperature is in general agreement with the thermocouple measurements for most of the flame length; the maximum difference occurs around $x/d_J = 110$, which may be attributed to soot deposition on the thermocouple and to flame radiation. Unburned hydrocarbon levels are underpredicted, specially in the upstream region, which could be attributed to the effect of

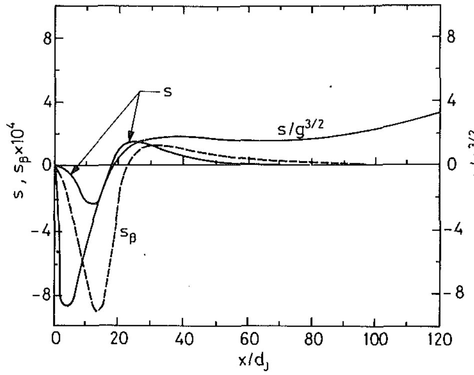

Fig. 2(*a*) Axial variation of skewness *s*, skewness of beta function s_β, and normalized skewness $s/g^{3/2}$

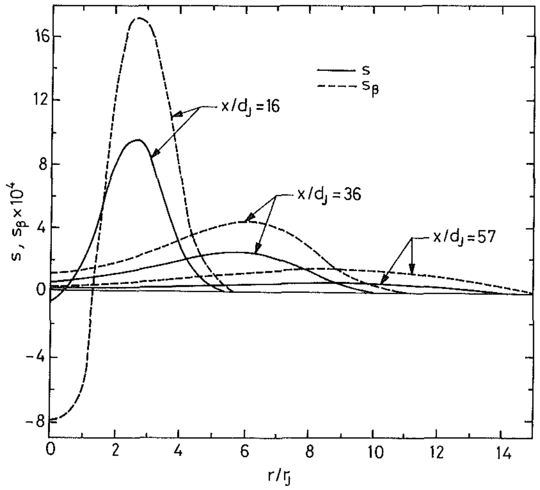

Fig. 2(*b*) Radial distribution of skewness *s*, and skewness of beta function s_β, at x/d_J = 16, 36, and 57

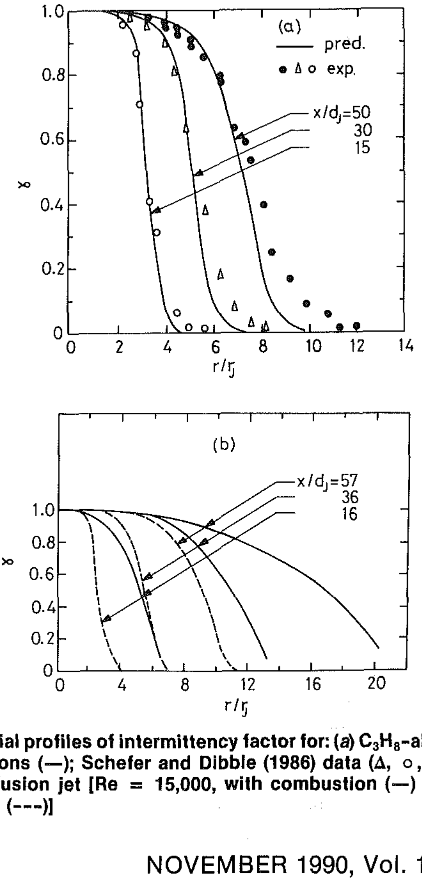

Fig. 3 Radial profiles of intermittency factor for: (*a*) C_3H_8-air isothermal jet [predictions (—); Schefer and Dibble (1986) data (Δ, ○, and ●)]; (*b*) CH_4-air diffusion jet [Re = 15,000, with combustion (—) and without combustion (---)]

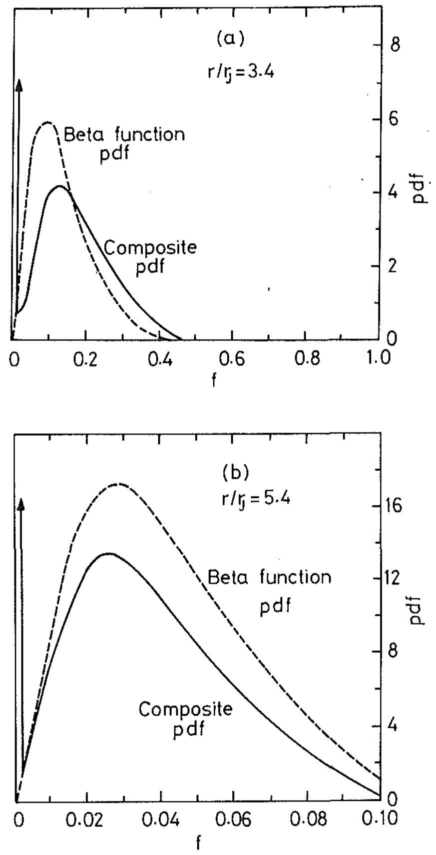

Fig. 4 Comparison of composite and beta probability density functions at x/d_J = 16: (*a*) r/r_J = 3.4, (*b*) r/r_J = 5.4

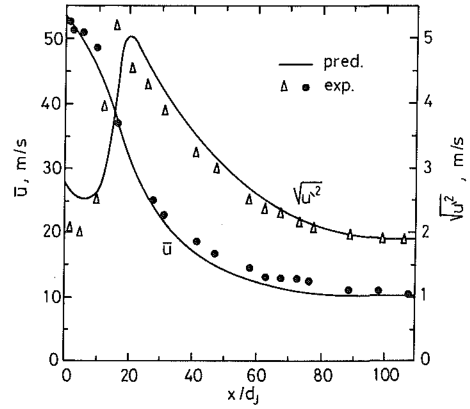

Fig. 5 Axial variation of mean centerline velocity $\bar{u}$, and root mean square fluctuations $\sqrt{u'^2}$, in methane-air jet flame

slow chemistry. This is also consistent with the overpredicted levels of CO concentration for $x/d_J < 80$, as shown in Fig. 6. In addition, Fig. 6 shows that the predictions with the composite (intermittent) pdf are in general better than the corresponding predictions using a simple beta function pdf. However, the small gain in accuracy of the results is to be expected since the greatest value of s is about 1×10^{-3}, as indicated in Fig. 2.

Along the radial direction, Figs. 7 and 8 show that the present physical model accurately predicts the temperature profiles at different axial locations. The slight overprediction of T, near the axis, at $x/d_J = 76$ could be attributed to the effect of radiation from this sooting zone. It should be mentioned here that the present predictions in the outer flame region could be

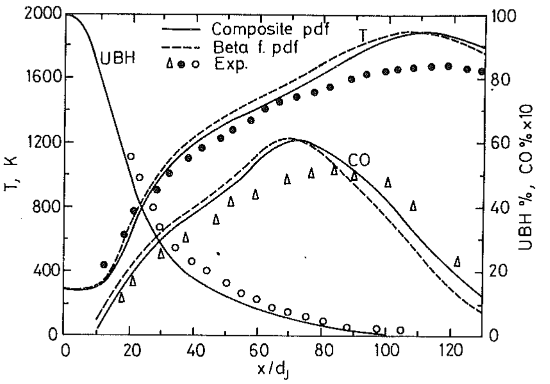

Fig. 6 Axial variation of centerline temperature *T*, carbon monoxide CO, and unburned hydrocarbon UBH, in methane-air jet flame

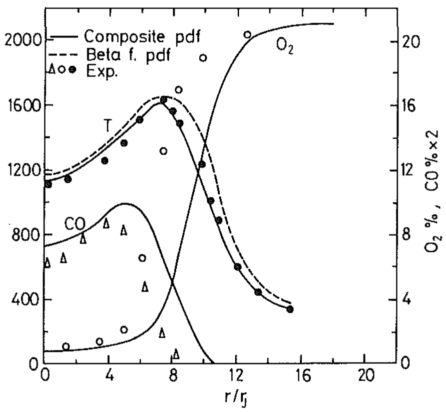

Fig. 7 Radial variation of temperature *T*, carbon monoxide CO, and oxygen O_2, in methane-air jet flame, x/d_J = 36

considered better than the corresponding predictions of Lockwood and Stolakis (1983), although they included thermal radiation; however, they neglected the effect of intermittency on the pdf. Moreover, the O_2 concentration is underpredicted (Figs. 7 and 8), which is consistent with the underpredicted hydrocarbon concentration shown in Fig. 6.

Concluding Remarks

The present physical model presents a new transport equation for the skewness of the mixture fraction in turbulent jet diffusion flames. An intermittency factor can be directly calculated from the computed values of the mixture fraction, its variance and skewness. It is then used to adjust the shape of the pdf by adding a spike at zero mixture fraction. The adjusted pdf is used to compute the mean properties of a turbulent jet diffusion methane flame. The obtained level of agreement between predictions and corresponding experimental data confirms the accuracy of the present combustion model.

References

Abou-Ellail, M. M. M., Gosman, A. D., Lockwood, F. C., and Megahed, I. E. A., 1978, "Description and Validation of a Three-Dimensional Procedure for Combustion Chamber Flows," *Turbulent Combustion*, L. A. Kennedy, ed., Progress in Astronautics and Aeronautics, Vol. 58, pp. 163–190.

Abou-Ellail, M. M. M., and Morcos, S. M., 1983, "Buoyancy Effect in the Entrance Region of a Concentric Annulus With Inner Cylinder Rotation," ASME JOURNAL OF HEAT TRANSFER, Vol. 105, pp. 924–928.

Abou-Ellail, M. M. M., and Salem, H., 1988, "Numerical Predictions of Flow and Heat Transfer in Turbulent Diffusion Flames," *Proc. 1988 National Heat Transfer Conference*, ASME, HTD-96, Vol. 1, Houston, pp. 79–86.

Ballantyne, A., and Bray, K. N. C., 1976, "Investigations Into the Structure

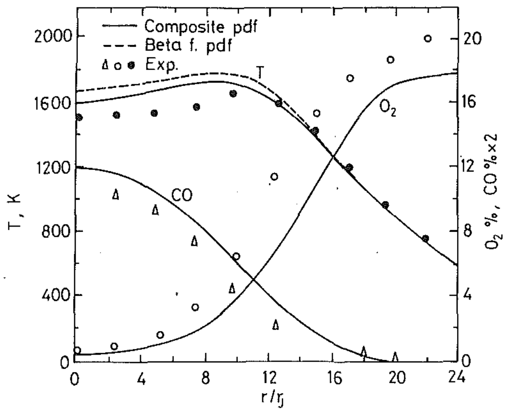

Fig. 8 Radial variation of temperature T, carbon monoxide CO, and oxygen O_2, in methane-air jet flame, $x/d_J = 76$

of Jet Diffusion Flames Using Time-Resolved Optical Measuring Techniques," *16th Symposium (International) on Combustion*, The Combustion Institute, pp. 777–787.

Bilger, R. W., and Starner, S. H., 1983, "A Simple Model for Carbon Monoxide in Laminar and Turbulent Hydrocarbon Diffusion Flames," Combustion and Flames, Vol. 51, pp. 155–176.

Bockhorn, H., and Lutz, G., 1984, "The Application of Turbulent Reaction Models to the Oxidation of CO in a Turbulent Flow," *20th Symposium (International) on Combustion*, The Combustion Institute, pp. 377–386.

Bush, W. B., and Fendell, F. E., 1978, "Analytic Modelling of Turbulent Shear Flow with Chemical Reaction," *Turbulent Combustion*, L. A. Kennedy, ed., Progress in Astronautics and Aeronautics, Vol. 58, pp. 3–18.

Chen, J. Y., 1987, "Second Order Conditional Modeling of Turbulent Nonpremixed Flames With Composite PDF," *Combustion and Flame*, Vol. 69, pp. 1–36.

Chen, J. Y., and Lumley, J. L., 1984, "Second Order Modeling of the Effect of Intermittency on Scalar Mixing," *20th Symposium (International) on Combustion*, The Combustion Institute, pp. 395–400.

Chen, J. Y., Gouldin, F. C., and Lumley, J. L., 1987, "Second Order Modeling of a Turbulent Nonpremixed H_2-Air Jet Flame With Intermittency and Conditional Averaging," *Combustion Science and Technology*, Vol. 53, pp. 235–257.

Correa, S. M., Drake, M. C., Pitz, R. W., and Shyy, W., 1984, "Prediction and Measurement of a Non-equilibrium Turbulent Diffusion Flame," *20th Symposium (International) on Combustion*, The Combustion Institute, pp. 337–343.

Eickhoff, H. E., and Grethe, K., 1979, "A Flame-Zone Model for Turbulent Hydrocarbon Diffusion Flames," *Combustion and Flame*, Vol. 35, pp. 267–275.

El-Banhawy, Y., Hassan, M. A., Lockwood, F. C., and Moneib, H. A., 1983, "Velocity and Unburned Hydrocarbon Measurements in a Vertical Turbulent Free Jet Diffusion Flame," *Combustion and Flame*, Vol. 53, p. 145.

Gosman, A. D., Lockwood, F. C., and Sayed, S. A., 1976, "Prediction of a Horizontal, Free, Turbulent Diffusion Flame," *16th Symposium (International) on Combustion*, The Combustion Institute, pp. 1543–1555.

Hassan, M. M. A., Lockwood, F. C., and Moneib, H. A., 1980, "Fluctuating Temperature and Mean Concentration Measurements in a Vertical Turbulent Free Jet Diffusion Flame," presented at The Italian Flame Days, Milano, Marittina, June 17–21, pp. 357–372.

Janicka, J., and Kollman, W., 1980, "A Prediction Model for Turbulent Diffusion Flames Including NO-Formation," *AGARD Proc.*, No. 275.

Kent, J. H., and Bilger, R. W., 1976, "The Prediction of Turbulent Diffusion Flame Fields and Nitric Oxide Formation," *16th Symposium (International) on Combustion*, The Combustion Institute, pp. 1643–1656.

Launder, B. E., and Spalding, D. B., 1972, *Mathematical Models of Turbulence*, Academic Press, New York.

Lockwood, F. C., 1977, "The Modelling of Turbulent, Premixed and Diffusion Combustion in the Computation of Engineering Flows," *Combustion and Flame*, Vol. 29, No. 2, pp. 111–122.

Lockwood, F. C., and Naguib, A. S., 1975, "The Prediction of the Fluctuations in the Properties of Free, Round-Jet, Turbulent Diffusion Flames," *Combustion and Flame*, Vol. 24, pp. 109–124.

Lockwood, F. C., and Moneib, H. A., 1982, "Fluctuating Temperature Measurements in Turbulent Jet Diffusion Flames," *Combustion and Flame*, Vol. 53, p. 145.

Lockwood, F. C., and Stolakis, P., 1983, "Assessment of Two Turbulence Models for Turbulent Round Diffusion Jet With Combustion," *Proceedings of Turbulent Shear Flow Conference*, pp. 10.25–10.31.

Razdan, M. K., and Stevents, J. G., 1985, "CO/Air Turbulent Diffusion Flame: Measurement and Modeling," *Combustion and Flame*, Vol. 59, pp. 289–301.

Rodi, W., 1979, "Influence of Buoyancy and Rotation on Equations for the Turbulent Length Scale," *2nd Symposium on Turbulent Shear Flows*, London, pp. 10.37–10.42.

Shefer, R. W., and Dibble, R. W., 1986, paper presented at the AIAA 24th Aerospace Science Meeting, Reno, NV, Jan.; also Sandia Report SAND 85-8837.

Spalding, D. B., 1971, "Concentration Fluctuations in a Round, Turbulent, Free-Jet," *Chemical Engineering Science*, Vol. 26, pp. 95–107.

Temperature Measurements of Falling Droplets

M. R. Wells

L. A. Melton

Department of Chemistry,
The University of Texas at Dallas,
Richardson, TX 75083

The temperature of 225-μm-dia decane droplets, which have fallen 100 mm through a hot quiescent, oxygen-free environment, has been measured using exciplex fluorescence thermometry. The droplets were doped with pyrene, and the relative intensities of pyrene monomer and excimer emissions were used to determine the droplet temperatures. The droplet temperature increases approximately 0.4°C per °C increase in the ambient temperature up to an ambient temperature of 200°C. Less than 10 percent evaporation was observed for the droplets at the highest ambient temperatures.

I Introduction

Vaporization in fuel sprays is a complex phenomenon involving heat and mass transfer in a dynamic mixture of droplets, fuel vapor, and ambient gas. Most workers in the field attempt to understand these processes in sprays by treating sprays as aggregates of individual drops, and therefore, understanding the processes that govern vaporization of individual fuel droplets becomes paramount. Many studies, both computational and empirical, of droplet vaporization have been performed, and reviews of the current understanding are available in the literature (Law, 1982; Sirignano, 1988; Faeth, 1983; Abramzon and Sirignano, 1988; Dwyer and Sanders, 1986; Aggarwal et al., 1984; Puri and Libby, 1988; Gogos and Ayyaswamy, 1988; Sirignano, 1983; Law and Sirignano, 1977; Prakash and Sirignano, 1978).

The vaporization of individual fuel droplets is generally studied photographically, a technique that yields only the droplet diameter (Puri and Libby, 1988; Aggarwal and Chen, 1989). A critical parameter in determining droplet evaporation rates is the temperature, specifically the surface temperature, of the droplets, and currently, few measurements of the temperature of vaporizing droplets are available. Charlesworth and Marshall (1959) measured the evaporation rates and temperatures of suspended water droplets by use of microthermocouples placed within the droplets. Trommelen and Crosby (1970), using a similar technique, measured evaporation rates and temperatures of suspended water droplets in various drying media. Abdul-Rahman (1969) measured the evaporation rates and temperature profiles of suspended water droplets by use of microthermocouples placed within the droplets. Hofmeister et al. (1989) measured surface temperatures of falling droplets of molten metals using two-color pyrometry.

Determination of the temperature of a droplet using thermocouples unavoidably perturbs both the droplet and the environment surrounding it and may alter the transfer of heat into or away from the droplet. In addition, suspended droplets are in physical contact with a support structure that may similarly make interpretation of the data uncertain. In this paper we describe the determination of the temperature of a decane droplet falling in a hot, relatively quiescent environment. The optical techniques described here can provide instantaneous, minimally perturbing measurement of even the surface temperatures of freely moving fuel droplets.

The technique used to measure the droplet surface temperature is exciplex fluorescence thermometry (EFT), which exploits the temperature-dependent fluorescence resulting from the reaction of an excited dopant molecule to form an exciplex, or excited-state complex (Murray and Melton, 1985). Room-temperature droplets were allowed to fall into an oven, and after falling 100 mm were intercepted by a laser beam that induced fluorescence of the dopant molecules. Analysis of the resulting fluorescence indicates that the temperature of the droplets increases aproximately 0.4°C per °C of increase in the ambient temperature as the ambient temperature is increased to 200°C.

II Exciplex Photophysics and Thermometry

The use of exciplexes as thermometers for bulk liquids and droplets has been discussed by Murray and Melton (1985), Melton et al. (1986), and Gossage and Melton (1987). More general reviews of the photophysics of fluorescence from exciplexes are available from Forster (1969) and Birks (1970). Recently, Stufflebeam (1989) has applied exciplex fluorescence thermometry to the determination of the temperature of bulk hydrocarbon liquids.

The photophysics of exciplex fluorescence thermometry is summarized in equation (1). A ground state molecule M (the monomer) may be excited by absorption of light to form the first excited singlet state M^*. M^* may react with an appropriately chosen ground state molecule G (which may be another M) to form an excited state complex E^* (exciplex), (excited state dimer or excimer if $G = M$). This reaction is shown by

$$M^* + G(M) \langle = = \rangle E^* \qquad (1)$$

E^* is bound with respect to M^* and G, but ground states M and G have little interaction; thus, fluorescence emission from E^* is red-shifted relative to that from M^*. The emission spec-

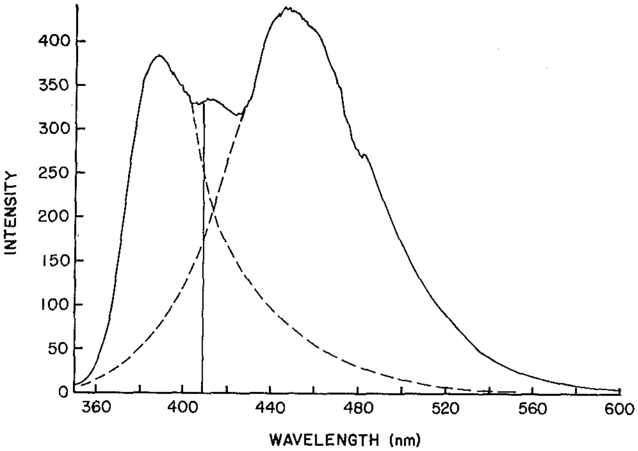

Fig. 1 Fluorescence spectrum of 5 mM pyrene in decane at 80°C, excitation wavelength 337 nm. Dashed lines are estimated extensions of monomer and excimer spectra, respectively. Vertical line at 408 nm is separation between monomer and excimer intensity integrals.

Contributed by the Heat Transfer Division for publication in the JOURNAL OF HEAT TRANSFER. Manuscript received by the Heat Transfer Division October 26, 1989; revision received March 21, 1990. Keywords: Flow Visualization, Measurement Techniques, Sprays/Droplets.

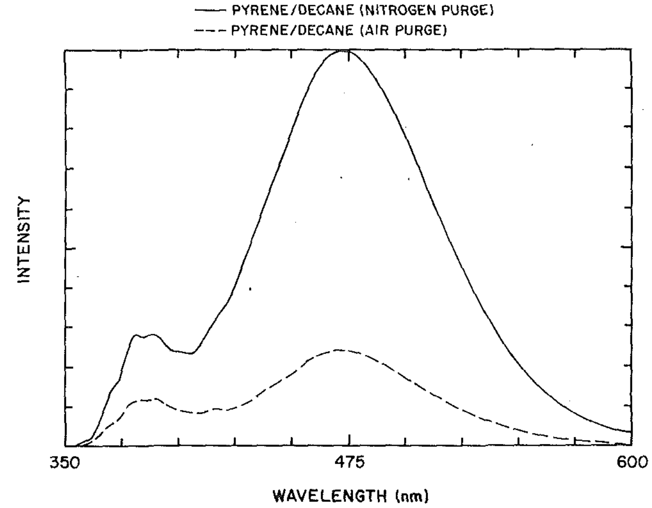

Fig. 2 Fluorescence spectra of 5-nM pyrene in decane, excitation wavelength 337 nm. Solid line is with nitrogen-purged solution; dashed line is with air-saturated solution.

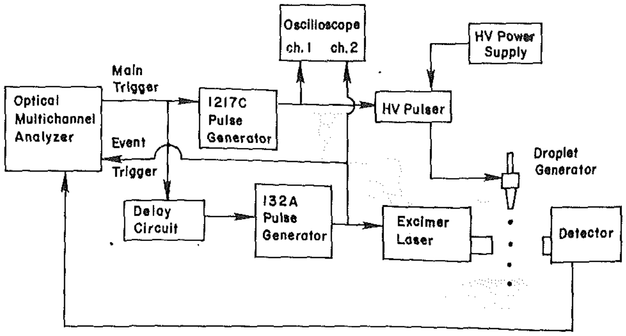

Fig 3 Block diagram of electronics

trum may then exhibit two distinct emission bands, one from M^* and the other from E^*, as shown in Fig. 1. At sufficiently high temperatures, the forward and reverse rates of the reaction shown in equation (1) will be sufficiently fast that the reaction may be treated as a chemical equilibrium, whose position will depend upon the temperature and concentrations. Increasing the temperature will shift the equilibrium toward the monomer; thus, the amount of emission from E^* relative to that from M^* will decrease with increasing temperature. Increasing the concentration of G will shift the equilibrium toward E^*. The temperature-dependent ratio of the exciplex emission intensity (I_E) to the monomer emission intensity (I_M), at constant composition, can therefore be used as the basis for an optical thermometer.

The ratio I_E/I_M can be affected by factors other than temperature and dopant concentrations. Forster (1969) has demonstrated that dissolved molecular oxygen in the system will quench the fluorescence from both the monomer and excimer, the excimer exhibiting greater quenching than the monomer. Shown in Fig. 2 are spectra taken under both nitrogen-purged and air-saturated conditions for the 5.00×10^{-3} (5.00 mM) pyrene in decane solution used in the droplet studies. I_M and I_E are approximately 2 and 4 times greater, respectively, under oxygen-free conditions than under air-saturated conditions. Thus, oxygen-free conditions must be maintained during exciplex thermometry experiments, since the differential quenching of the fluorescence of the pyrene-doped droplets by the oxygen in air could easily result in erroneously high values of the temperature inferred for the droplets.

III Experimental

(A) Chemicals and Solutions. Reagent grade decane (99+ percent purity) was used to model a typical hydrocarbon fuel. It was purchased from Aldrich Chemical Company and used as received. Fluorescence measurements of the decane used indicated no detectable fluorescence. Pyrene was purchased from Aldrich Chemical Company and was sublimed (120°C, 1 torr) before use; unsublimed pyrene did not give reproducible results. A 5.00 mM solution of pyrene in decane was prepared and used both for droplet production and for calibration. Nitrogen gas (99.99 percent purity) was purchased from Big Three Inc. and used as received. The pyrene in decane solution was purged with nitrogen to remove dissolved oxygen in all experiments.

(B) Experimental Apparatus and Procedures. Droplets of a 5.00 mM solution of pyrene in decane were produced using a piezoelectric droplet generator of a design described generally by Shield et al. (1987). The piezoelectric transducer used in the construction of the droplet generator was purchased from E.B.L. Company (East Hartford, CT) and has dimensions of 11 mm × 9.5 mm o.d. × 4.5 mm i.d. The outside and inside surfaces of the transducer are nickel-plated for electrical contact, with the outer surface forming the positive pole. A jeweler's microtorch tip cut from a #3 Little Torch (Tescom Corp, Minneapolis, MN) was used as a nozzle. The microtorch tip has a sapphire insert with a 0.011-in. (approx. 280 μm) laser-drilled orifice. The torch tip was attached to the piezoelectric transducer with quick-setting epoxy. The droplet generator was supplied from a solution reservoir whose height could be adjusted to control the liquid head on the droplet generator. The pyrene in decane solution in the fluid reservoir was maintained under continuous nitrogen purge throughout all experiments. In addition, before each temperature run, enough solution was purged from the fluid system to ensure that only oxygen-free liquid was present in the lines.

A block diagram of the electronics used in the experiment is shown in Fig. 3. Fluorescence data collection, processing, and experimental control were performed by an EG & G PARC OMA III optical multichannel analyzer Model 1460-V consisting of an M1420 intensified photo diode array detector, a Model 1463 detector controller, an M1303 gated pulse interface, and a Jarrell-Ash Monospec 27 monochromator (150 g/mm ruling, dispersion 24 nm/mm). The detector was operated in a feed-back mode so that light integration did not commence until firing of the laser was detected. An output pulse (5 V TTL, 16 μs) from the OMA was amplified to approximately 25 V by a General Radio Model 1217-C pulse generator operated in the external trigger mode. The amplified pulse was sent to a custom-built high-voltage pulser powered by Tennelec Model TC 952 high-voltage power supply and was monitored by a Hitachi Model V-55B 50 MHz oscilloscope. The high-voltage output of the pulser, typically 900 V and 2 ms pulse width, was used to drive the droplet generator. The pulse originating from the OMA was also sent to a custom-built signal delay device (0-300 ms) and then amplified to 40 V (pulse width 2 ms) by an EH Research Model 132A pulse generator operated in the external trigger mode. This pulse was then sent to the Lumonics Model TE 861S pulsed excimer laser, which was operated as an N_2 laser (337 nm, 8 ns FWHM). The pulse energy was typically 1.5 mJ per pulse, as measured with a Scientech Power Energy Meter Model 36-2002 fitted with a Model 36-0001 disk calorimeter. The delayed pulse was also sent back to the OMA to initiate readout of the detector. For the droplet temperature measurements, typical laser pulse rates were 1 Hz.

The droplet generator/heated chamber assembly is shown in Fig. 4. The droplet generator was positioned on a water-cooled cold stage set 15 mm above a 150 mm long × 50 mm diameter cylindrical brass block. The nozzle tube of the droplet

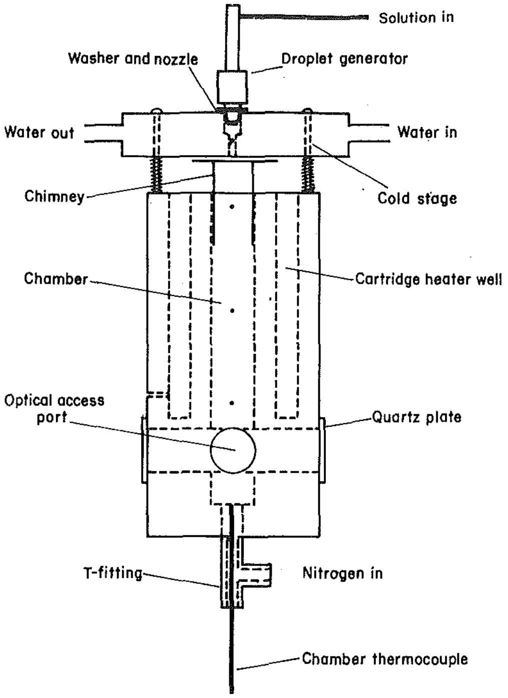

Fig. 4 Diagram of droplet generator/heated chamber assembly

generator was equipped with a snuggly fitting metal washer, which rested on the top of the cold stage. The washer provided good thermal contact between the cold stage and the nozzle tube and sealed the opening around the tube. In this manner, hot gases were prevented from streaming past the tube and heating it. Droplets exited the cold stage through a 1.3-mm orifice in its base. Below the cold stage, droplets entered a 150 mm × 16 mm square channel milled axially through the center of the brass block. A square-section chimney constructed of aluminum sheet (soft drink can, approx. 0.13 mm thick) was inserted into the top of the square channel in the block and was raised within 1 mm of the base of the cold stage. The chimney was lowered to allow photographic measurements of droplets immediately after they emerged from the base of the cold stage. For optical access, four circular ports (approx. 10 mm in. diameter) were positioned with their centers 85 mm from the top of the block. The port were covered with 2-mm-thick quartz windows to reduce convection-induced turbulence within the chamber due to air drawn in through the ports. Four cartridge heaters (each 150 W maximum at 240 V) were inserted into the brass block parallel to its axis and were supplied by a variable autotransformer. Heated nitrogen gas was admitted into the block from the bottom at flow rates from 140 to 180 ml/min, for linear flow velocities of 3.0 to 3.9 cm/s (corrected for thermal expansion within the heated chamber). The Reynolds number, based on the square chamber, for the nitrogen flowing through the chamber was calculated to be 28 at 20°C, and decreased to 13 to 250°C. Care was taken to maintain the temperature of the nitrogen entering the block at the block temperature in order to minimize thermal gradients within the block chamber. The entire block was wrapped with 19-mm-thick ceramic insulation (Kaowool). A type J Omega iron-constantan thermocouple was inserted into the brass block 10 mm above the ports and was read by an Omega HH-70JC meter (±1°C) to monitor the block temperature. In order to determine the temperature profile within the block, an Omega type T copper-constantan thermocouple was inserted into the chamber and was read by an Omega HH-70TC meter (±1°c). The chamber temperature was determined at the ports, 40 mm above the ports, at the top of the block, and immediately below the cold stage. Typically, temperatures within the chamber were within two to three degrees of the temperature at the ports and the temperature of the block itself. The temperature of the ambient on the chamber axis immediately below the cold stage was generally 5–20°C below the average chamber temperature.

The flow of heated nitrogen entering the block from the bottom served two important purposes. First, it prevented the influx of air into the block, which, as shown in Fig. 2, could interfere with the accurate determination of the droplet temperature by differential quenching of the fluorescence. Second, the nitrogen flow reduced the accumulation of decane vapors in the chamber.

After falling 100 mm, a droplet was intercepted by a laser beam focused to an area approximately 4 mm × 6 mm. A delay between the droplet generator firing and triggering of the laser (or strobe) of 160–200 ms was necessary, depending upon the nitrogen flow rate. Fluorescence emission at right angles to the incident laser light was focused with a 50-mm-dia, 100-mm focal length quartz lens onto the 500 μm entrance slit of the spectrometer. Three 350 nm high-pass filters (total $OD_{337} = 4.1$) were positioned in front of the spectrometer entrance slit to suppress the scattered light at 337 nm. The spectrometer was set so that fluorescence from 200–600 nm fell on the intensified portion of the diode array detector.

Droplet emission spectra were digitized by the OMA system and were stored on disk for later analysis. Background light taken without droplets in the chamber was recorded before each experiment and was subtracted from each droplet emission spectrum. Wavelength calibration of the spectrometer was performed with a low-pressure Hg vapor pencil lamp (Hammamatsu Model C-940-001).

The intensities I_E and I_M were determined as integrals over portions of the spectra using the drop-line integration method (see Fig. 1). The vertical line is the declared boundary between the excimer and monomer emissions. The drop-line wavelength chosen for this study was 408 nm. I_M is the integral of the spectrum from 360 to 408 nm, and I_E is the integral from 408 to 600 nm.

In order to account for any possible heating of the droplets by the laser light, droplet emission spectra were recorded at several power levels. The laser beam was attenuated with chemical filters prepared from solutions of potassium chromate in water. Fluorescence spectra were recorded at laser energies, estimated as the fraction of the attenuated laser pulse energy that was intercepted by the droplet, of approximately 11, 6.4, 3.7, and 1.3 μJ per pulse. The quantity ln $[I_E/I_M])$ was plotted versus laser power and was extrapolated to zero laser power in order to remove any effect of heating of the droplets by the laser. The extrapolated values of $\ln[I_E/I_M]$ were determined from a least-squares fit of a straight line to the data. The least-squares program also estimates the standard deviation of the intercept, i.e., the error in the extrapolated value of $\ln[I_E/I_M]$. No laser heating effect on the droplets was found at chamber temperatures higher than 80°C; it was a minor effect at lower chamber temperatures.

A calibration curve for the excimer fluorescence thermometer was constructed from emission spectra taken at known temperatures with the same 5.00-mM pyrene solution and identical optical collection system. A calibration sample cell was constructed from 5-mm Pyrex glass tubing pulled to 1 mm at its narrow section, which was then flame-sealed. Approximately 0.5 mL of the solution was placed in the tubing and was then connected to a vacuum line and degassed with three freeze-pump-thaw cycles. The solution was then flame-sealed at its upper end under vacuum. A second tube, to be used as a background reference for the calibration sample, was drawn from the same Pyrex tubing, filled with 0.5 mL of pure decane, and processed in the same manner. The calibration tube was positioned within the chamber with the narrow section centered

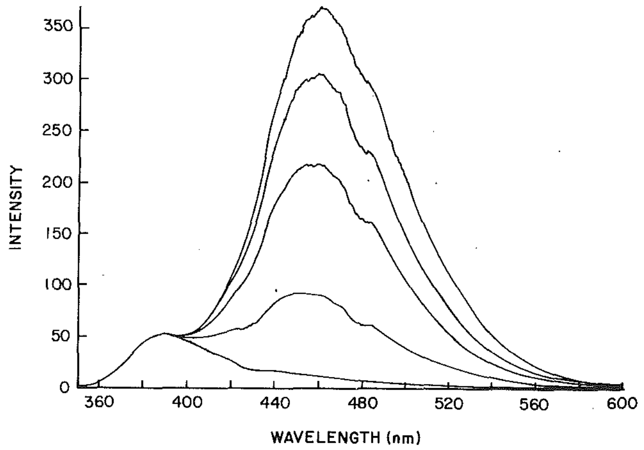

Fig. 5 Fluorescence spectra obtained from 5-mM pyrene in decane calibration sample, excitation wavelength 337 nm. Temperatures, from the top down, are 23, 37, 47, 70-, and 124°C, respectively.

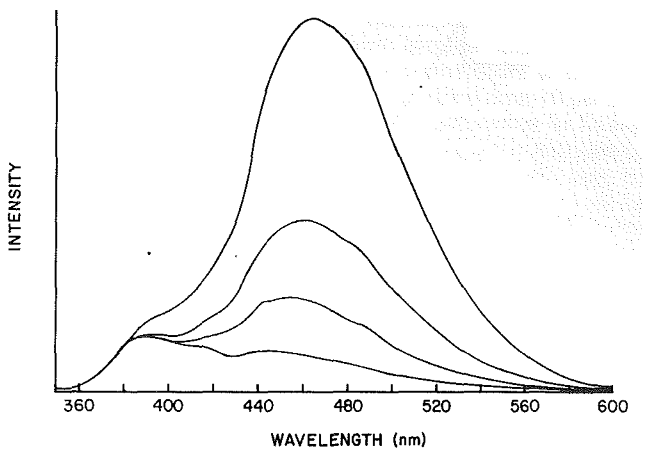

Fig. 7 Fluorescence spectra obtained from 5-mM pyrene in decane droplets, excitation wavelength 337 nm, at chamber temperatures (from top down) of 23, 85, 109, and 257°C

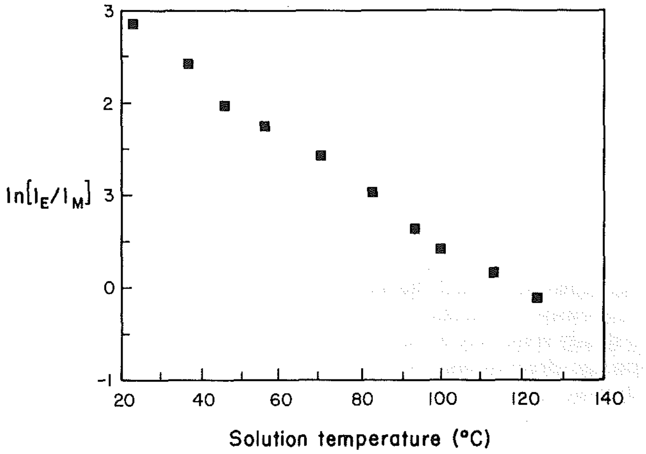

Fig. 6 Calibration curve obtained from data shown in Fig. 5

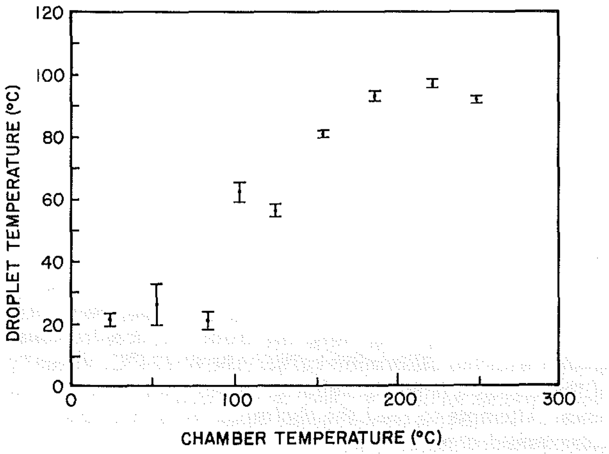

Fig. 8 Droplet temperature as a function of chamber temperature

in the chamber at the port. Due to the large amount of fluorescence available from the calibration sample, it was necessary to attenuate the laser beam with a potassium chromate chemical filter followed by a 1 mm pinhole. Thus, the maximum laser energy falling on the calibration tube was approximately 0.8 μJ per pulse, and no dependence of $\ln[I_E/I_M]$ on laser power was observed for the calibration sample. The calibration sample spectra were corrected for background by subtracting the spectrum obtained with the decane reference sample; no fluorescence was detected from the reference sample. The calibration sample was allowed to equilibrate for 20–30 minutes after the chamber had reached a stable temperature before the spectra at that temperature were collected.

The total emission from the solution decreases approximately a factor of ten as the solution temperature increases from 23°C to 125°C. This does not affect the temperature measurements since the thermometer calibration depends on the ratio I_E/I_M, not the absolute intensities. As long as there is sufficient emitted light available to measure the ratio I_E/I_M accurately, the spectra will yield the temperature of the system accurately.

The droplets were photographed immediately below the cold stage and at the optical access port, with a Ricoh Model KR-30 35 mm SLR camera attached to the eyepiece of a Bausch and Lomb StereoZoom 7 stereomicroscope, which was fitted with a reticle. Droplets were backlighted for photographic measurements via a modified Alpha-M Model 161 stroboscope triggered externally by the pulse, which was otherwise used to trigger the laser. Kodak T-Max 400 Professional B/W film was used to record the negative image of the droplets and was processed in a spiral reel tank with Acufine developer for 13.5 to 14 minutes at 20°C. The processed negatives were cut and mounted as 2×2 in. slides and projected onto a screen for droplet diameter measurements. Absolute sizes were determined by comparison with the photographed reticle. The photographic method has a limit of resolution of droplet diameter of ±5 μm, which corresponds to a volume change of approximately ±7 percent.

Typical vertical instability in the droplet's position at laser interception varied between 0.5 and 5 droplet diameters, depending upon the nitrogen flow rate in the chamber. No lateral instability in the droplet's position occurred at lower temperatures, although at the higher chamber temperatures both vertical and lateral instability resulted, possibly due to turbulence within the chamber. The average velocity of droplets falling through the chamber was 0.6 m/s, resulting in Reynolds numbers for the droplets based on their diameters of between 8.8 at 20°C and 0.3 at 250°C, calculated using the method of Chigier (1981). Every effort was made to maintain the nitrogen flow through the block at a constant rate, but in order to maintain droplet stability, it was occasionally necessary to adjust the flow rate, especially at the higher chamber temperatures.

The spectra in Fig. 2 were taken under front face excitation on a Spex Fluorolog Model DM1B fluorometer. The transmission of the filters was measured with a Hewlett-Packard Model 8450 UV-Vis Spectrophotometer.

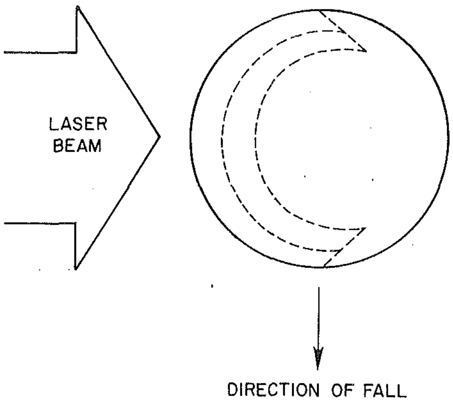

Fig. 9 Penetration of incident laser beam into 225-μm-dia droplet of 5-mM pyrene in decane, excitation wavelength 337 nm. Outer dashed line is the locus of 32 percent transmission ($OD_{337} = 0.5$); inner dashed line is the locus of 10 percent transmission ($OD_{337} = 1.0$).

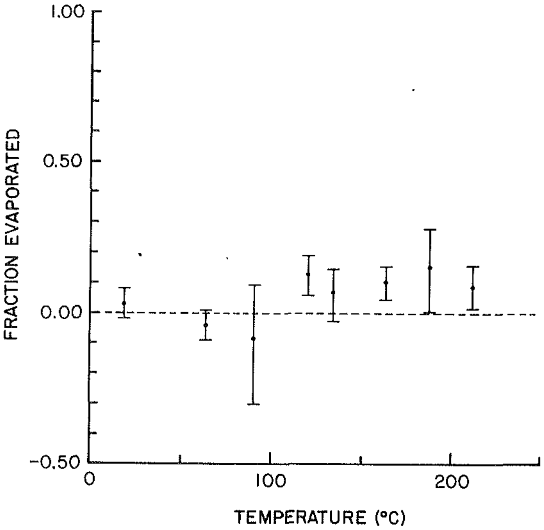

Fig. 10 Fraction of 5 mM pyrene in decane droplet evaporated as a function of chamber temperature. Initial droplet diameter is 225 μm.

IV Results and Discussion

(A) Temperature Calibration. A series of pyrene emission spectra from the calibration sample were collected at temperatures ranging from 23 to 124°C. A stacked plot of selected spectra, normalized to the maximum of the monomer emission, is shown in Fig. 5. A calibration curve was constructed from a plot of $\ln[I_E/I_M]$ versus solution temperature and is shown in Fig. 6. The apparent linearity of the calibration curve is fortuitous, as there is no theoretical reason to expect linearity. The uncertainty in the value of each point was too small to be indicated on the plot, which indicates the reproducibility of the calibration sample data. Droplet temperatures are determined by comparing $\ln[I_E/I_M]$ from the droplet emission spectra with the calibration curve. Above 124°C, virtually all of the emission from the calibration sample is from the monomer. Attempts to read the thermometer above this temperature would contain large errors since the magnitude of the noise in the spectrum approaches the magnitude of the residual emission from the excimer.

(B) Droplet Measurements

1 Temperature Measurements. Figure 7 shows a stacked plot of normalized emission from droplets of the 5.00-mM pyrene in decane solution. The temperature of the decane droplets as a function of chamber temperature is shown in Fig. 8. Since the droplet temperatures were extrapolated to zero laser power, these temperatures represent solely the effect of the heated ambient on the droplet. The uncertainties in each point, indicated by the error bars, were calculated in the two-step process: (1) The measured values of $\ln[I_E/I_M]$ as a function of laser power were fit to a straight line with a linear least-squares program, which also provided a statistical estimate of the uncertainty in $\ln[I_E/I_M]_o$, the value of $\ln[I_E/I_M]$ at the intercept, i.e., with no laser heating, and (2) this estimated uncertainty in $\ln[I_E/I_M]_o$ was used in conjunction with the calibration curve, Fig. 6, to estimate uncertainties in the derived values of the temperature. It is supposed that the error bars obtained with droplets are larger than those obtained with the calibration solutions because of the spatial instability of the droplets, since a comparable number of counts were collected for the droplet and calibration spectra.

The temperatures of the decane droplets increase approximately linearly with an average slope of 0.4°C per degree increase in the chamber temperature up to 200°C. To determine whether the two points at the highest temperatures represent a droplet temperature plateau or simply deviation about the relatively linear temperature trend, more points would be necessary above 250°C; however, severe instability in the position of the droplets prevented collection of either spectral or photographic data above this temperature. There are two reasonable explanations for the decrease in the relatively linear droplet temperature trends. First, evaporation of decane from the droplets may occur at the higher chamber temperatures; thus, pyrene would be concentrated at the droplet surface. The higher concentration of pyrene would shift the monometer-excimer equilibrium toward the excimer, which would result in an erroneously high measured I_E/I_M and a low temperature. Second, a steady state may have been reached in which the heat incident on the droplet results solely in evaporation of liquid at the droplet surface.

It is unlikely that a droplet in a dynamic heat transfer process is at a uniform temperature, and therefore it is necessary to consider how to interpret the temperatures derived from the exciplex fluorescence thermometry experiments. The penetration of the exciting light, and thus the region from which fluorescence is observed, is determined by the optical density of the droplet solution. The molar extinction coefficient of pyrene at 337 nm is approximately 3.6×10^4 M^{-1} cm^{-1} (Berlman, 1971); and thus, for the 5 mM solution used in these droplet experiments, 90 percent (OD = 1) of the light will be absorbed in 56 μm of the solution. A diagram illustrating the penetration of the laser beam into a 225-μm droplet (5 mM pyrene in decane) is shown in Fig. 9. The innermost dotted curve within the droplet represents the locus for absorption of 90 percent (OD = 1) of the incident light; it was constructed by connecting, at 56 μm penetration depth, the light rays refracted into the droplet. The outer dotted line is the locus for penetration to 28 μm, i.e., OD = 0.5; 68 percent of the incident light is absorbed outside of this locus. Note, however, that penetration of the laser light to the full depth occurs only along the axial ray. For off-axis rays, the radial penetration is less because the refracted ray is not along a radius. The actual determination of the radial distribution of the fluorescence reaching the detector is more complicated, since emission from different points within a droplet is refracted into the collecting lens with differing efficiencies. Calculations of the radial distribution of the collected light were made using computer programs, which determine the distribution of absorption within a droplet and the probability of a photon entering a given lens aperture, both within a geometric optics approximation (Melton, 1989). The convolution of these results for a given index of refraction and optical density gives, among other results, the radial distribution of photons entering the lens aperture. Using this program, it was found that for the droplet described in Fig. 3 and for an f/3.5 lens aperture, 46 percent of the collected light originated from the outer 27 μm of the droplet, and an additional 45 percent originated from the next 27 μm. Thus, 91 percent of the light collected from the droplet originates within the outer 46 μm of the droplet. The temperatures reported are, therefore, averages over the outer 50–60 μm on the irradiated side of the droplet.

The penetration of light into the droplet is dependent on the concentration of the absorber but not on the droplet diameter. If these same techniques were applied to droplets 1 mm in diameter, the temperatures thus determined would result from fluoresence from the outer 10 percent of the droplet radius and thus, would probably be interpretable as surface temperatures.

Within the limitations imposed by the averaging described in the previous paragraph, the reported temperatures are believed to be accurate. In the next section, it is argued that, in this experiment, no more than 10 percent of the droplet mass evaporates, and thus distortions of the temperature measurements due to a changing concentration of pyrene in the surface layers is minimized. Thermal expansion of the droplets is expected as the droplet temperatures increase, but in itself it should have no effect on the derived droplet temperatures since the same effect is present in the calibration sample and is accounted for in the calibration curve.

2 Droplet Evaporation Measurements. Photographs of droplets taken immediately below the cold stage and at the optical access port were compared to determine the fraction of liquid evaporated from the droplets. The fraction evaporated is $f = 1 - (d/d_0')^3$, where d is the droplet diameter at the optical access port and d_0' is the droplet diameter measured at the cold stage and corrected for thermal expansion. The fraction evaporated is shown in Fig. 10 as a function of the ambient temperature. Correction for thermal expansion was made by calculating the volume the initial, cold droplet would have if it were simply raised to the measured droplet temperature, with no evaporation, using the thermal expansion coefficient for decane (Riddick and Bunger, 1970). The diameter of that heated, nonevaporating droplet is d_0'. The correction is necessary since, in this experiment, the changes in droplet diameter due to evaporation and thermal expansion are comparable. Using this method, it is estimated that less than 10 percent of the droplet's volume evaporated at the highest chamber temperatures.

3 Future Work. The results presented here demonstrate that temperature measurements can be made on freely falling droplets and lay the groundwork for continuing experiments to determine the surface temperature of fuel droplets exposed to hot, convective environments. Exciplex fluorescence thermometers with higher optical densities (i.e., complete absorption of the incident light within a few microns of the surface), greater temperature range, and lessened dependence on concentration are under development. Further experiments are planned to investigate the transient and steady-state behavior of droplets by providing for optical access to the droplet throughout its trajectory. With the new thermometry systems, exposures to much hotter environments is planned in order to determine the effects of evaporation on the measured droplet temperature.

V Conclusions

The temperature of droplets of decane exposed to a hot, relatively quiescent, oxygen-free environment have been measured using laser-induced exciplex fluorescence thermometry. The measured droplet temperatures increase approximately 0.4°C per °C increase in the ambient temperature as the ambient temperature is increased to 200°C. Less than 10 percent of the droplet's mass was lost due to evaporation in falling 100 mm at a chamber temperatures of 250°C. The decrease in the droplet heating rate at the highest temperatures may be due to concentration of pyrene at the droplet surface due to evaporation or to attainment of a steady-state temperature for the droplets.

Acknowledgments

Funding for this work was provided by the Army Research Office through contract number DAAL03-87-K-0120. We thank W. A. Sirignano for useful comments.

References

Abdul-Rahman, Y. A. K., 1969, "Drying of Drops Containing Dissolved and Dispersed Gases," M.S. Thesis, University of Wisconsin, Madison, WI.

Abramzon, B., and Sirignano, W. A., 1988, "Droplet Vaporization Model for Spray Combustion Calculations," presented at the AIAA 26th Aerospace Sciences Meeting, Reno, NV, Jan. 11–14, Paper No. AIAA-88-0636.

Aggarwal, S. K., Tong, A. Y., and Sirignano, W. A., 1984, "A Comparison of Vaporization Models in Spray Calculations," *AIAA Journal*, Vol. 22, p. 1448.

Berlman, I. B., 1971, *Handbook of Fluorescence Spectra of Aromatic Molecules*, Academic Press, New York, p. 383.

Birks, J. B., 1970, *Photophysics of Aromatic Molecules*, Wiley-Interscience, New York.

Charlesworth, D. H., and Marshall, W. R., 1959, "Evaporation From Drops Containing Dissolved Solids," *AIChE J.*, Vol. 6, p. 9.

Chigier, N., 1981, *Energy, Combustion and Environment*, McGraw-Hill, New York, p. 273.

Dwyer, H. A., and Sanders, B. R., 1986, "A Detailed Study of Burning Fuel Droplets," *21st Symposium (Int.) on Combustion*, Combustion Institute, Pittsburgh, PA, pp. 633–639.

Faeth, G. M., 1983, "Evaporation and Combustion of Sprays," *Prog. Energy Comb. Sci.*, Vol. 9, p. 1.

Forster, T., 1969, *Excimers*, Angew. Chem. Internat. Editions, Vol. 8, p. 333.

Gogos, G., and Ayyaswamy, P. S., 1988, "A Model for the Evaporation of a Slowly Moving Droplet," *Comb. Flame*, Vol. 74, p. 111.

Gossage, H. E., and Melton, L. A., 1987, "Fluorescence Thermometers Using Intermolecular Exciplexes," *Appl. Optics*, Vol. 26, p. 2256.

Hofmeister, W. H., Bayuzick, R. J., and Robinson, M. B., 1989, "Noncontact Temperature Measurement of a Falling Drop," *Int. J. Thermophys.*, Vol. 10, p. 279.

Law, C. K., 1982, "Recent Advances in Droplet Vaporization and Combustion," *Prog. Energy Comb. Sci.*, Vol. 8, p. 171.

Law, C. K., and Sirignano, W. A., 1977, "Unsteady Droplet Combustion With Droplet Heating—II: Conduction Limit," *Comb. Flame*, Vol. 28, p. 175.

Melton, L. A., 1989, "Efficiency of Capture of Fluorescence From Droplets," unpublished results, University of Texas at Dallas, Richardson, TX.

Melton, L. A., Murray, A. M., and Verdieck, J. F., 1986, "Laser Fluorescence Measurements for Fuel Sprays," *Soc. Photo Opt. Instr. Eng.*, Vol. 644, p. 40.

Murray, A. M., and Melton, L. A., 1985, "Fluorescence Methods for Determination of Temperature in Fuel Sprays," *Appl. Optics*, Vol. 24, p. 2783.

Prakash, S., and Sirignano, W. A., 1978, "Liquid Fuel Droplet Heating With Internal Circulation, " *Int. J. Heat Mass Transfer*, Vol. 21, p. 885.

Puri, I. K., and Libby, P. A., 1988, "Droplet Behavior in a Counterflowing Flame," Western States Section/The Combustion Institute 1988 Spring Meeting, Salt Lake City, UT, Mar. 21–22, Paper No. 88-42.

Riddick, J. A., and Bunger, W. B., 1970, *Techniques of Chemistry*, Vol. II, Wiley Interscience, New York, p. 103.

Shield, T. W., Bogy, D. B., and Talke, F. E., 1987, "Drop Formation by DOD Ink-Jet Nozzles: A Comparison of Experiment and Numerical Simulation," *IBM J. Res. Develop.* Vol. 31, p. 96.

Sirignano, W. A., 1983, "Fuel Droplet Vaporization and Spray Combustion Theory," *Prog. Energy Comb. Sci.*, Vol. 9, p. 291.

Sirignano, W. A., 1988, "An Integrated Approach to Spray Combustion Model Development," *Comb. Sci. Tech.*, Vol. 58, p. 231.

Stufflebeam, J. H., 1989, "Exciplex Fluorescence Thermometry of Liquid Fuel," *Appl. Spectrosc.*, Vol. 43, p. 274.

Trommelen, A. M., and Crosby, E. J., 1970, "Evaporation and Drying of Drops in Superheated Vapors," *AIChE J.*, Vol. 16, p. 857.

K. Vafai

M. Sözen

Department of Mechanical Engineering,
The Ohio State University,
Columbus, OH 43210

An Investigation of a Latent Heat Storage Porous Bed and Condensing Flow Through It

In this work the transient analysis of the behavior of a packed bed of encapsulated phase change material (PCM) and the condensing flow through it is presented. The rigorous model used assumes no local thermal equilibrium between the bed particles and the working fluid, and incorporates the inertia effects in the momentum transport by the use of the Ergun–Forchheimer equation. Condensation in the working fluid is investigated. Thermal charging of the packed bed is analyzed and compared for a sensible heat storage material as well as for different latent heat storage materials (PCMs).

1 Introduction

Packed bed heat storage units have been used extensively in a wide variety of applications. Packed beds as storage media are attractive, for they offer a compact structure due to their relatively greater heat storage capacity as compared to systems that utilize energy transporting fluid as the storage medium. Also due to the large surface area offered by packed beds for heat transfer between the energy transporting fluid and the bed particles, the process of energy transfer and storage becomes very efficient.

The earlier forms of packed bed energy storage units relied solely on the sensible heat capacity of solid bed particles for storing thermal energy. This form has been satisfactorily employed for various applications. However, certain applications may impose a limitation on the size and weight of the packed bed system utilized. For instance, in the case of a heat rejection system in pulsed space power supplies that incorporates packed beds, the reduction of mass and volume is of utmost importance. In such cases utilization of only the sensible heat capacity of a certain material for energy storage may not be efficient. The remedy to this can be found in the utilization of latent heat in the process of energy storage. Recently, encapsulated phase-change materials (PCM) have received considerable attention as energy storage materials. The use of an encapsulated PCM is very appealing since it makes the utilization of latent heat storage capacity possible. This is achieved by using a PCM that has a melting temperature within the temperature range of operation of the system incorporating the packed bed. The principal advantage of PCMs in packed beds is that the energy storage density of the bed is increased significantly and thus, the size and mass of the storage system required for a particular application are reduced proportionally.

Different PCMs have been considered for use in packed bed energy storage units in different applications. For applications over 450°C, significant consideration has been given to salts (Marianowski and Maru, 1977). Properties of different PCMs considered for storage of solar energy have been presented by Lane (1986). Ananthanarayanan et al. (1987) investigated the dynamic behavior of a packed bed utilizing encapsulated Al-Si shots, which have a melting temperature of 577°C. Air was used as the energy transporting fluid in their study. Pitts and Ji (1987) presented another study on transient thermal behavior of a latent heat storage packed bed, which utilized the inorganic compound hydrate PCM, $Na_2HPO_3 \cdot 12H_2O$. Torab and Chang (1988) investigated the use of encapsulated PCMs for thermal energy storage units in space power systems. They considered lithium hydride as the PCM and lithium as the transport fluid.

Different models have been developed for analyzing the transient behavior of latent heat storage packed beds. In the majority of these models, the superficial velocity of the working fluid is assumed to be constant. This fact reduces the system of governing equations to a set of energy equations for the working fluid and for the PCM, respectively. Although this is a satisfactory approach when the working fluid is incompressible, it is not so when the working fluid is a gas or vapor under high pressures. Moreover, when the working fluid itself undergoes phase change (condensation), a rigorous model, which consists of the governing energy mass, and momentum balance equations, in addition to the relevant coupling thermodynamic relations, has to be employed for a possible analysis of the phase-change and transport phenomena. In the present work we will undertake the analysis of such a problem with a rigorous model.

Transient behavior of a packed bed of spherical particles under the condensing flow conditions of the working fluid is studied in the present work. The range of temperatures considered in this study is 300–350 K. Refrigerant-12 (R-12, or dichloro-difluoro-methane) is chosen as the energy transport fluid for several reasons. First, it is a highly inert and stable compound and its critical temperature is above the range of temperatures considered in the present problem. Moreover, it has relatively high vapor density and capacitance compared with typical gases such as air. Different bed materials will be considered for the bed particles for qualitative comparison. These include two different encapsulated PCMs (myristic acid and lithium-nitrate-trihydrate) and one sensible heat storage material (1 percent carbon-steel).

The cases considered in the present work involve relatively high fluid velocities and therefore, the Ergun–Forchheimer relation is employed, rather than the Darcy equation, as the vapor phase momentum equation in order to account for the inertia effects. No local thermal equilibrium (LTE) is assumed to be present between the fluid and the solid (or PCM) phases, and the heat transfer between the working fluid and the bed particles is modeled by a convective heat transfer term.

In an earlier work the general characteristics of fluid flow and heat transfer through a porous bed were analyzed in depth (Vafai and Sözen, 1990); a systematic evaluation of the validity of the local thermal equilibrium and one-dimensional transport assumption was made and an assessment of the validity of each of these assumptions was presented in the form of error maps. In another study general characteristics of condensing

---

Contributed by the Heat Transfer Division for publication in the JOURNAL OF HEAT TRANSFER. Manuscript received by the Heat Transfer Division July 11, 1989; revision received January 30, 1990. Keywords: Packed and Fluidized Beds, Phase-Change Phenomena, Thermal Energy Storage.

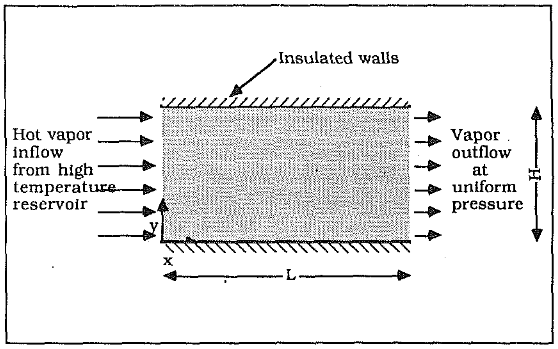

Fig. 1 Schematic diagram of the problem

flow through a porous bed were investigated (Sözen and Vafai, 1990) and it was shown that the pressure difference across the packed bed, the particle diameter, and the heat capacity of the solid phase have a profound effect on the condensation process in the packed bed.

The main objective of the present work is to analyze the thermal charging of a packed bed energy system for different forms of bed particle materials with emphasis on encapsulated phase change material. The time history of the crucial field variables such as the temperature profiles of the working fluid and the bed particles, and the velocity, density, and pressure of the working fluid will be determined. The determination of these quantities is important since the amount of energy flowing into and out of the packed bed, and hence the amount of energy stored in the packed bed as a function of time, can be determined from the time history of these variables.

2 Analysis

A general model has been developed for analyzing the phase change and transport phenomena in the thermal charging process of a packed bed. A schematic diagram of the problem considered in the present study is shown in Fig. 1. The packed bed, which is initially filled with R-12 at a slightly superheated state at uniform temperature and pressure, is subjected to a flow of superheated R-12 from a reservoir that has a higher temperature and pressure than those initially prevailing in the packed bed. Thus the problem becomes one with step change boundary conditions in temperature and pressure. The model developed for the analysis of the problem employs the following assumptions and simplifications:

1 The solid phase (or the PCM) and the liquid phase of the working fluid are incompressible.

2 The packed bed has uniform porosity and is isotropic.

3 Boundary and variable-porosity effects are neglected in the momentum equations.

4 Interparticle and intraparticle radiation heat transfer as well as thermal dispersion effects are neglected.

2.1 Governing Equations. It is customary to use the "local volume averaging" technique in order to develop a rigorous set of governing equations for the transport processes in porous media. It is necessary to make use of the two different averages of a quantity in the governing equations. These are the local volume average and the intrinsic phase average (Vafai and Sözen, 1990). While the local volume average of a quantity Θ associated with phase Ψ is defined as

$$\langle \Phi \rangle = \frac{1}{V} \int_{V_\Psi} \Phi dV \tag{1}$$

the intrinsic phase average of a quantity Φ associated with phase Ψ is defined as (Whitaker, 1977)

$$\langle \Phi \rangle^{\Psi} = \frac{1}{V} \int_{V_\Psi} \Phi dV \tag{2}$$

where V_Ψ represents the volume associated with phase Ψ. In using the volume averaging technique in the governing equa-

Nomenclature

$a_{\sigma\beta}$ = specific surface area common to σ and β phases, m^{-1}
$a_{\sigma\gamma}$ = specific surface area common to σ and γ phases, m^{-1}
A = constant in equation $(11) = 23.485$
B = constant in equation $(11) = 2969.23$, K^{-1}
c_p = specific heat at constant pressure, $\mathrm{J\ kg^{-1}\ K^{-1}}$
d_p = particle diameter, m
Da = Darcy number $= K/H^2$
F = geometric factor defined in equation (13)
$\mathbf{g}$ = gravitational acceleration, $\mathrm{m\ s^{-2}}$
G = mass velocity, $\mathrm{kg\ m^{-2}\ s^{-1}}$
$h_{\sigma\beta}$ = fluid-to-particle heat transfer coefficient between σ and β phases, $\mathrm{W\ m^{-2}\ K^{-1}}$
$h_{\sigma\gamma}$ = fluid-to-particle heat transfer coefficient between σ and γ phases, $\mathrm{W\ m^{-2}\ K^{-1}}$
h_{sf} = specific latent heat of fusion, $\mathrm{J\ kg^{-1}}$
H = height of the packed bed, m
k = thermal conductivity, $\mathrm{W\ m^{-1}\ K^{-1}}$
$k_{r\beta}$ = relative permeability for fluid phase
$k_{\langle T \rangle}$ = coefficient of capillary pressure gradient with respect to temperature, $\mathrm{N\ m^{-2}}$
k_ϵ = coefficient of capillary pressure gradient with respect to liquid volume fraction, $\mathrm{N\ m^{-2}}$
K = permeability, m^2
L = length of the packed bed, m
$\dot{m}$ = condensation rate, $\mathrm{kg\ m^{-3}\ s^{-1}}$
P = pressure, $\mathrm{N\ m^{-2}}$
R_γ = gas constant for Refrigerant-12, $\mathrm{J\ kg^{-1}\ K^{-1}}$
Re_p = particle Reynolds number $= \rho_\gamma v^* d_p / \mu_\gamma$
s = saturation $= \epsilon_\beta / \epsilon$
S = normalized saturation $= (s - s_{im})/(1 - s_{im})$
t = time, s
T = temperature, K
u = velocity component in x direction, $\mathrm{m\ s^{-1}}$
$\mathbf{v}$ = velocity vector, $\mathrm{m\ s^{-1}}$
ϵ = porosity
ϵ_β = volume fraction of liquid phase
ϵ_γ = volume fraction of vapor phase
ϵ_σ = volume fraction of solid phase
Δh_{vap} = latent heat of vaporization for Refrigerant-12, $\mathrm{J\ kg^{-1}}$
Θ = dimensionless temperature $= (T - T_o)/(T_{in} - T_o)$
μ = absolute viscosity, $\mathrm{kg\ m^{-1}\ s^{-1}}$
ρ = density, $\mathrm{kg\ m^{-3}}$
$\rho_{\gamma,s}$ = saturation vapor density, $\mathrm{kg\ m^{-3}}$

Subscripts

f = fluid (liquid + vapor)
feff = effective property for fluid
in = inlet
o = initial
β = liquid
γ = vapor
σ = solid
σeff = effective property for solid

Superscripts

f = fluid (liquid + vapor)
β = liquid
γ = vapor
σ = solid
$*$ = reference

Symbols

$\langle \rangle$ = "local volume average" of a quantity tions, it is very important to distinguish between the properties that are associated with a single phase, such as the solid phase temperature, in which case one should use the intrinsic phase average, and the properties that have a characteristic average value over the averaging volume, such as the so-called "superficial fluid velocity," in which case one should use the spatial average or the local volume average value. These will help in presenting the exact and accurate form of the governing equations

With the assumptions and simplifications previously stated taken into account, the volume-averaged governing balance equations and the coupling relations are established as (Sözen and Vafai, 1990):

Vapor phase continuity equation

$$\frac{\partial}{\partial t}\left(\epsilon_\gamma \langle \rho_\gamma \rangle^\gamma\right) + \nabla \cdot \left(\langle \rho_\gamma \rangle^\gamma \langle \mathbf{v}_\gamma \rangle\right) = -\langle \dot{m} \rangle \tag{3}$$

Liquid phase continuity equation

$$\frac{\partial \epsilon_\beta}{\partial t} + \nabla \cdot \langle \mathbf{v}_\beta \rangle - \frac{\langle \dot{m} \rangle}{\rho_\beta} = 0 \tag{4}$$

Vapor phase equation of motion

$$\nabla \langle P_\gamma \rangle^\gamma = -\frac{\langle \rho_\gamma \rangle^\gamma F \epsilon_\gamma}{K_\gamma^{1/2}} \left[\langle \mathbf{v}_\gamma \rangle \cdot \langle \mathbf{v}_\gamma \rangle\right] \frac{\langle \mathbf{v}_\gamma \rangle}{|\langle \mathbf{v}_\gamma \rangle|} - \frac{\mu_\gamma}{K_\gamma} \langle \mathbf{v}_\gamma \rangle \tag{5}$$

which takes the following form with the second assumption cited above:

$$\frac{\partial}{\partial x} \langle P_\gamma \rangle^\gamma = -\frac{\langle \rho_\gamma \rangle^\gamma F \epsilon_\gamma}{K_\gamma^{1/2}} \langle u_\gamma \rangle^2 - \frac{\mu_\gamma}{K_\gamma} \langle u_\gamma \rangle \tag{5a}$$

Liquid phase equation of motion

$$\langle \mathbf{v}_\beta \rangle = -\frac{k_{r\beta} K}{\mu_\beta} \left\{ k_\epsilon \nabla \epsilon_\beta + k_{\langle T \rangle} \nabla \langle T_f \rangle^f + \left(\rho_\beta - \langle \rho_\gamma \rangle^\gamma\right) \mathbf{g} \right\} \tag{6}$$

Fluid phase energy equation

$$\begin{aligned} &\left[\epsilon_\beta \rho_\beta (c_p)_\beta + \epsilon_\gamma \langle \rho_\gamma \rangle^\gamma (c_p)_\gamma\right] \frac{\partial \langle T_f \rangle^f}{\partial t} - \langle \dot{m} \rangle \Delta h_{\text{vap}} \\ &+ \left[\rho_\beta (c_p)_\beta \langle \mathbf{v}_\beta \rangle + \langle \rho_\gamma \rangle^\gamma (c_p)_\gamma \langle \mathbf{v}_\gamma \rangle\right] \cdot \nabla \langle T_f \rangle^f = \nabla \cdot \left[k_{\text{feff}} \nabla \langle T_f \rangle^f\right] \\ &\qquad + h_{\sigma\beta} a_{\sigma\beta} \left[\langle T_\sigma \rangle^\sigma - \langle T_f \rangle^f\right] + h_{\sigma\gamma} a_{\sigma\gamma} \left[\langle T_\sigma \rangle^\sigma - \langle T_f \rangle^f\right] \end{aligned} \tag{7}$$

Solid phase (PCM) energy equation

$$\begin{aligned} \epsilon_\sigma \rho_\sigma (c_p)_\sigma \frac{\partial \langle T_\sigma \rangle^\sigma}{\partial t} &= \nabla \cdot \left[k_{\sigma\text{eff}} \nabla \langle T_\sigma \rangle^\sigma\right] \\ &\quad - h_{\sigma\beta} a_{\sigma\beta} \left[\langle T_\sigma \rangle^\sigma - \langle T_f \rangle^f\right] - h_{\sigma\gamma} a_{\sigma\gamma} \left[\langle T_\sigma \rangle^\sigma - \langle T_f \rangle^f\right] \end{aligned} \tag{8}$$

Volume constraint relation

$$\epsilon_\sigma + \epsilon_\gamma(t) + \epsilon_\beta(t) = 1 \tag{9}$$

Equation of state for vapor phase

$$\langle P_\gamma \rangle^\gamma = \langle \rho_\gamma \rangle^\gamma R_\gamma \langle T_f \rangle^f \tag{10}$$

Thermodynamic relation for the saturation density of vapor

$$\rho_{\gamma,\, s} = \frac{\exp(A - B/T_f)}{R_\gamma T_f} \tag{11}$$

where A and B are known constants, T_f is in degrees Kelvin, and $\rho_{\gamma,\, s}$ is in kg/m^3. Equations (3)-(11) yield nine equations in nine unknowns, namely, $\epsilon_\beta(t)$, $\epsilon_\gamma(t)$, $\langle \rho_\gamma \rangle^\gamma$, $\langle \mathbf{v}_\gamma \rangle$, $\langle \mathbf{v}_\beta \rangle$, $\langle P_\gamma \rangle^\gamma$, $\langle T_f \rangle^f$, $\langle T_\sigma \rangle^\sigma$, and $\langle \dot{m} \rangle$.

The effective thermal conductivities of the working fluid and for the PCM (or solid phase) were modeled as

$$\begin{aligned} k_{\sigma\text{eff}} &= \epsilon_\sigma k_\sigma \\ k_{\text{feff}} &= \epsilon_\gamma k_\gamma + \epsilon_\beta k_\beta \end{aligned} \tag{12}$$

The permeability for the vapor phase, K_γ, and the geometric factor, F, in the vapor phase momentum equation can be expressed as functions of ϵ_γ and d_p as given by Sözen and Vafai (1990). The relative permeability of the liquid phase is modeled in the form suggested by Udell and Fitch (1985) and given by Sözen and Vafai (1990).

Due to lack of better experimental findings, the value of immobile saturation, s_{im}, used by Kaviany and Mittal (1987), will be used in the present work. With the value of porosity taken to be equal to 0.39 as the average asymptotic value found by Benanati and Brosilow (1962) and s_{im} as 0.1, the critical value of the liquid fraction, $\epsilon_{\beta\text{crit}}$, below which the liquid phase is assumed to be immobile becomes 0.039.

Based on the specific surface area of a packed bed of spheres presented by Dullien (1979) as $a = 6(1-\epsilon)/d_p$, which was obtained from some geometric arguments, where ϵ is the porosity and d_p is the particle diameter, and also due to the fact that ϵ_β takes very small values (less than 0.01) in the problem considered, the specific surface area between the vapor phase and the bed particles can be accurately approximated as

$$a_{\sigma\gamma} = \frac{6(1 - \epsilon_\gamma - \epsilon_\beta)}{d_p} \tag{13}$$

Also from an analysis of the representative length scales and volume scales of the liquid and vapor phases of the working fluid, one may obtain a relation between the specific surface areas $a_{\sigma\gamma}$ and $a_{\sigma\beta}$ as

$$a_{\sigma\beta} = a_{\sigma\gamma} \left(\frac{\epsilon_\beta}{\epsilon_\gamma}\right)^{2/3} \tag{14}$$

and hence

$$a_{\sigma\beta} = \frac{6(1 - \epsilon_\gamma - \epsilon_\beta)}{d_p} \left(\frac{\epsilon_\beta}{\epsilon_\gamma}\right)^{2/3} \tag{15}$$

Empirical correlations found by Gamson et al. (1943) and originally expressed in the form of Colburn-Chilton j_h factors were found to be suitable for use in the present work. This decision was based on the fact that the particle size and particle Reynolds number ranges for these correlations covered the ranges considered in this work. Furthermore, the values of the void fraction and the fluid Prandtl number that were used in the experiments for establishing these correlations were very close to the respective values considered in the present investigation. After some manipulations these correlations can be expressed in the form given by Sözen and Vafai (1990) and repeated here for convenience:

$$\begin{aligned} h_{\sigma j} &= 1.064 (c_p)_j G_j \left[\frac{c_p \mu}{k}\right]_j^{-2/3} \left[\frac{d_p G}{\mu}\right]_j^{-0.41} \\ &\qquad \text{for } \frac{d_p G}{\mu} \geq 350 \quad \text{(turbulent)} \\ h_{\sigma j} &= 18.1 (c_p)_j G_j \left[\frac{c_p \mu}{k}\right]_j^{-2/3} \left[\frac{d_p G}{\mu}\right]_j^{-1} \\ &\qquad \text{for } \frac{d_p G}{\mu} \leq 40 \quad \text{(laminar)} \end{aligned} \tag{16}$$

where G denotes the mass flux of phase j and j stands for β or γ for the liquid or the vapor phase, respectively.

It should be noted that due to the physical conditions of the problem, the liquid phase turned out to be essentially immobile. Therefore, $h_{\sigma\beta}$ practically assumes zero value and there is no need for $a_{\sigma\beta}$. However, for the sake of completeness of the model, these have been included in the model so that it becomes applicable to any condensation problem with funicular condensate.

2.2 Boundary and Initial Conditions. In the problem analyzed, the packed bed is initially filled with R-12 at uniform temperature and pressure and in local thermal equilibrium with the bed particles. Therefore, this condition is mathematically expressed as

$$T_f(x, y, t=0) = T_o$$
$$T_\sigma(x, y, t=0) = T_o \tag{17}$$
$$P_\gamma(x, y, t=0) = P_o$$

There is a continuous flow of high-temperature vapor into the packed bed from a reservoir while the pressure at the exit of the packed bed is maintained at the initial bed pressure. The following mathematical forms express these boundary conditions:

$$T_f(x=0, y, t) = T_{in}$$
$$P_\gamma(x=0, y, t) = P_{in} \tag{18}$$
$$P_\gamma(x=L, y, t) = P_{\text{out}} = P_o$$

where

$$T_o = 300 \text{ K}, \quad P_o = 796 \text{ kPa}, \quad T_{in} = 350 \text{ K}, \quad P_{\text{out}} = 796 \text{ kPa},$$
$$\text{and } P_{in} = 811.2 \text{ kPa}$$

The top and bottom walls of the packed bed are insulated and so we have

$$\left.\frac{\partial T_\sigma}{\partial y}\right|_{y=0,\ y=H} = \left.\frac{\partial T_f}{\partial y}\right|_{y=0,\ y=H} = 0 \tag{19}$$

2.3 Solution. As may be seen from the model outlined in the previous section, the governing equations are strongly coupled and an analytical solution is not possible. Therefore numerical solution by a finite difference technique was employed. Explicit finite difference schemes were found to be more appropriate for solution of this problem. Forward Euler differencing was applied to temporal derivative terms, while central differencing was utilized in spatial derivative terms, except in the convective terms, in which upwind differencing was used instead of central differencing.

It should be noted that depending on whether phase change occurs in the working fluid or the PCM at a given location and instant in the packed bed, the governing equations and the solution format will take different forms. The details of the two-phase solution format algorithm are given in the work of Vafai and Whitaker (1986). It is assumed that condensation occurs when the density of the vapor becomes equal to the saturation vapor density.

When there is no phase change in either the working fluid or the bed particles, the field variables $\langle\rho_\gamma\rangle^\gamma$, ϵ_β, $\langle u_\gamma\rangle$, $\langle \mathbf{v}_\beta\rangle$, $\langle T_f\rangle^f$, $\langle T_\sigma\rangle^\sigma$, ϵ_γ, and $\langle P_\gamma\rangle^\gamma$ are determined from equations (3)-(10), respectively. At the same time $\rho_{\gamma,s}$ is determined from equation (11). This is done to determine when $\langle\rho_\gamma\rangle^\gamma$ determined by equation (3) with a zero $\langle\dot{m}\rangle$ terms exceeds $\rho_{\gamma,s}$. When this happens, $\langle\rho_\gamma\rangle^\gamma$ is replaced by $\rho_{\gamma,s}$ from equation (11), and equation (3) is then used for determining $\langle\dot{m}\rangle$.

On the other hand, the phase-change process in the PCM also needs special consideration. The following physical characteristics of the PCM are built into the solution algorithm. Once the PCM at a certain location and time reaches its melting temperature during the thermal charging of the packed bed, its temperature remains constant until phase change (melting) is complete in the capsules at that location. During this period, the solid phase (or PCM) energy equation should not be used for determining the solid phase (or PCM) temperature. However, the amount of heat that is transferred to the PCM while phase change occurs should be integrated in time in order to determine when the phase change is completed. Once phase change is completed in the PCM at a certain location, determination for the PCM temperature is switched back to solution from the PCM (or solid phase) energy equation with appropriate liquid PCM properties incorporated into the numerical scheme.

At each time step, after the PCM temperature reaches the melting temperature, the convective heat transfer rate from the working fluid to the PCM and conduction heat transfer rates to and from the PCM are all summed up (for node (i, j)) and taken into account. Furthermore, during a given time step both the net energy input to a unit volume of the PCM and the net total energy into the PCM up to the end of that time step were found. This process was carried on until the net total energy into the PCM becomes equal to the net latent heat energy encapsulated within the PCM.

The property values of the materials used in the numerical computations are $k_\gamma = 0.0097$ W/m K, $(c_p)_\gamma = 710$ J/kg K, $\mu_\gamma = 12.6\times10^{-6}$ kg/m s, $R_\gamma = 0.068759$ J/kg K, $\Delta h_{\text{vap}} = 111{,}300$ J/kg, $(c_p)_\beta = 1115$ J/kg K, $\mu_\beta = 179.2\times10^{-6}$ kg/m s, $\rho_\beta = 1190.35$ kg/m^3, $k_\beta = 0.0545$ W/m K.

For myristic acid (PCM1)

$c_p = 1590$ J/kg K, $k = 0.1$ W/m K, $\rho = 860$ kg/m^3, for solid phase

$c_p = 2260$ J/kg K, $k = 0.1$ W/m K, $\rho = 860$ kg/m^3 for liquid phase

For lithium-nitrate-trihydrate (PCM2)

$c_p = 2090$ J/kg K, $k = 0.5$ W/m K, $\rho = 1550$ kg/m^3 for solid as well as liquid phase

For 1 percent carbon-steel

$c_p = 473$ J/kg K, $k = 43$ W/m K, $\rho = 7800$ kg/m^3

In the numerical runs L was chosen as 0.2 m and H as 0.1 m.

2.4 Stability and Accuracy of the Numerical Scheme. We employed a proper combination of Δt, Δx, and Δy in order to assure stability. This was done by a systematic decrease in the grid size until further refinement of the grid size or the Δt showed no more than 1 percent difference in the convergent results. The 41×21 grid configuration (which corresponds to a dimensionless Δx or Δy or 0.025) was found to yield sufficiently accurate solutions.

In order to gain confidence in the validity of the results of the computer program developed, we performed a benchmarking. Since there was no previous effort to solve the present problem with as rigorous a model as we have used, with as many field variables and governing equations, analytical solutions to simpler problems were considered. The benchmarking was carried out for the limiting cases with no phase change in either the working fluid or the PCM. The first check was performed for energy transport by a benchmark against the analytical solution of the Schumann model as presented by Riaz (1977). This was done by reducing the present model to the Schumann model by neglecting some terms in the energy equations. The second benchmark was related to momentum transport in an isothermal flow of an ideal gas through a porous medium. The analytical solution obtained by Kidder and La Habra (1957) by using perturbation methods was for a semi-infinite porous medium. But for small times, before any pressure propagation reaches the exit of the porous medium, the solution is applicable to finite length problems and hence to the present problem. Comparisons of the results from our program with these two analytical solutions are shown in an earlier work (Vafai and Sözen, 1990).

3 Results and Discussion

It is convenient to nondimensionalize some of the field variables in presenting the numerical solutions, and keep others in dimensional form to give a better understanding of the variations of the important parameter. The variables $\langle P_\gamma\rangle^\gamma$, $\langle\rho_\gamma\rangle^\gamma$, and $\langle u_\gamma\rangle$ are nondimensionalized with respect to the corresponding reference quantities P^*, ρ^*, and v^*. However, the pertinent parameters of the thermal charging of the packed bed and the condensation of the working fluid are presented in dimensional form for a unit width of the packed bed as a

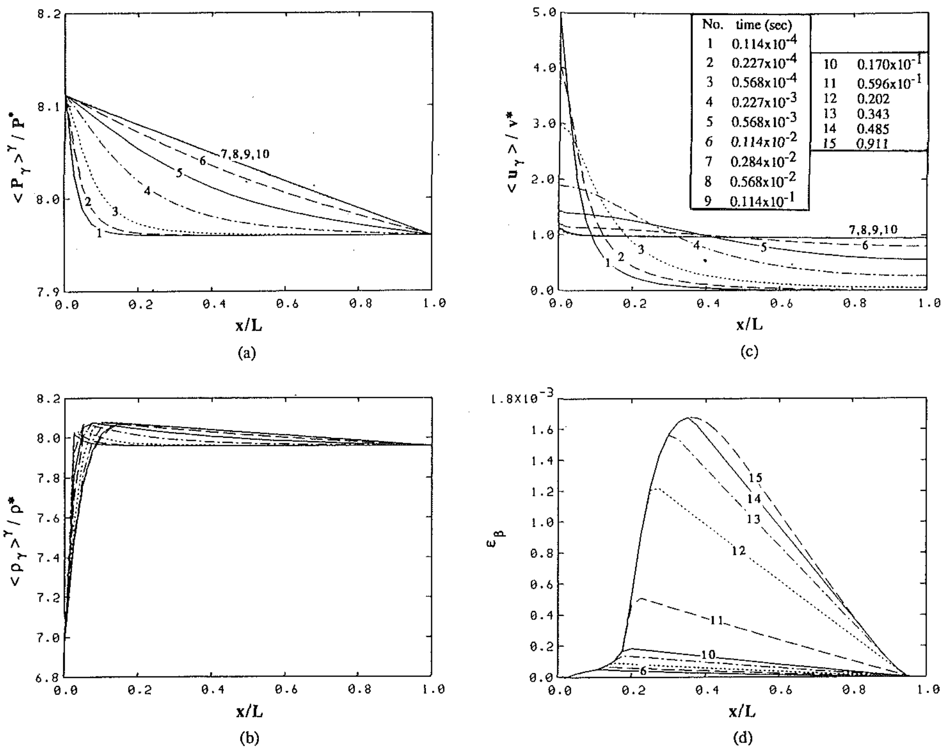

Fig. 2 Distribution of different field variables during the early stage

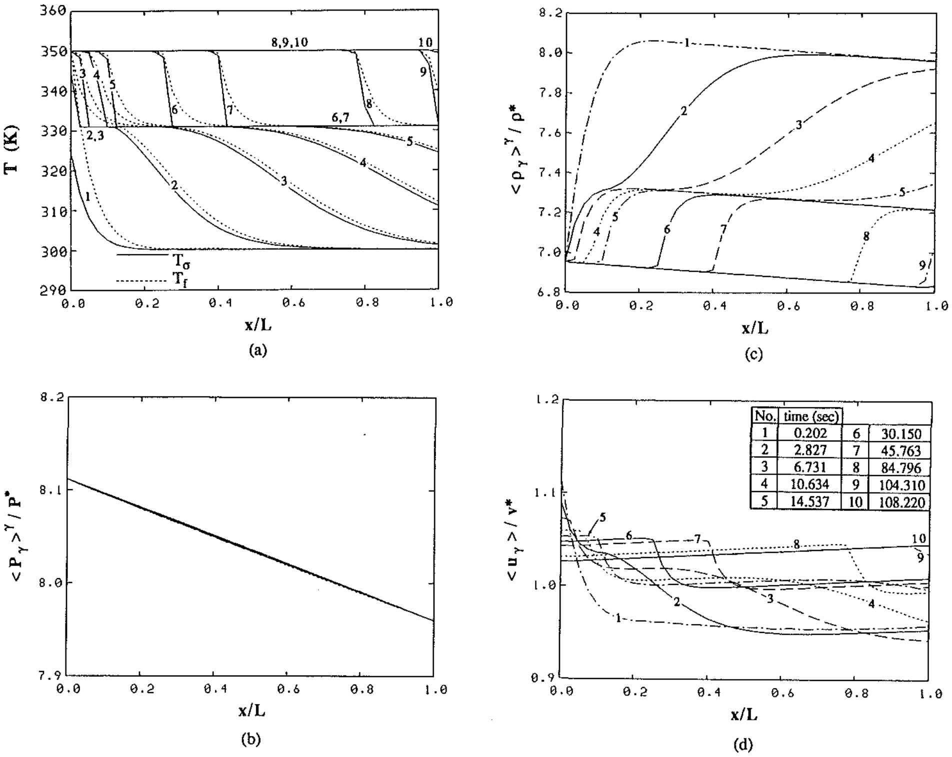

Fig. 3 Distribution of different field variables during the later stage

function of the dimensional time. The value chosen for P^* was 100 kPa, while ρ^* was then computed from the equation of state using P^* and the initial temperature T_o. The calculation of the reference velocity, v^*, was based on the vapor phase momentum equation by incorporating the global pressure difference applied across the packed bed and the vapor density as calculated from the equation of state by using the mean value of the inlet and exit pressures.

It should be noted that due to the nature of the problem it is not feasible to obtain totally generically applicable results for this problem. There are several main reasons for this. The first one is with respect to the condensation process. Since the density of the vapor is a function of temperature and pressure (by the equation of state) and the saturation vapor density is assumed to be a unique function of temperature, the condensation process is sensitive to the boundary and initial conditions of the problem considered. For example, applying a given pressure difference across the packed bed at low operating pressure ranges, say around atmospheric pressure, will not result in any condensation, while applying the same magnitude of pressure difference at higher operating pressure ranges, say around 10 atm, will result in condensation. Therefore, although the pressure difference applied plays an important role in the condensation process, it is also important what ranges of operating pressures we are considering. For different vapors the condensation rate will be different for the same pressure difference applied since they have different heat of vaporization, different equations of state (i.e., gas constants), and different thermodynamic relations giving the saturation vapor density. Storage of energy in the packed bed cannot be scaled either, because thermal charging of the packed bed depends on the transient variation of the vapor exit temperature, which may be different for different PCMs. Also, due to the nature of the problem, the vapor mass flux into the packed bed is not uniform. Nevertheless, the results of this investigation will clearly show the generic qualitative features of transient condensing flow through a packed bed of encapsulated material.

It was found that in all the cases investigated in this study, the maximum local liquid fraction of the working fluid did not exceed the critical value above which the liquid becomes mobile, i.e., the liquid phase was always in a pendular state. This, combined with the fact that only insulated boundary conditions were considered in the present study, made the problem essentially one-dimensional. It was checked through numerical experimentation that the solution of the one-dimensional form of the governing equations did not have any appreciable difference from the solution to the two-dimensional form. Therefore, the two and one-dimensional solutions turned out to be the same. It should be emphasized that for insulated boundary conditions the lateral variations are not significant, and the only physical process that can make the problem two dimensional in this type of forced convective problem is the vertical motion of the liquid due to gravity. For such cases, however, much larger amounts of liquid that would make the liquid phase mobile have to be present.

Two distinct stages can be easily identified in the solution of the problem under consideration. First is an *early stage* with very strong transient effects, i.e., drastic spatial and temporal changes in the field variables, which lasts for a very short time. During the early stage the pressure distribution across the packed bed evolves and assumes an almost linear form, which is maintained afterward during the rest of the charging process, which will be referred to as the *later stage*.

The first PCM employed for the encapsulated bed particles is myristic acid, which has a melting temperature of 331 K. We will refer to this material as PCM1. The results for the case in which this material is used will be presented in detail. Once the high-pressure, high-temperature vapor is applied at the entrance of the packed bed, the vapor moving through the packed bed becomes compressed. Since it gives most of its excess internal energy to the colder PCM particles, its density reaches the saturation vapor density at certain locations and condensation takes place. Most of this condensation occurs in the early stage while the pressure distribution linearizes and the density of the vapor adjusts itself accordingly. Afterward, the vapor reaches superheated conditions at all locations and no more condensation takes place.

The early stage variations of the density, velocity, and pressure of the working fluid and the liquid fraction are shown in Fig. 2. The early stage is extended somewhat to include the period during which more than 99 percent of the condensation in the working fluid is completed. The consequence of the step change boundary condition can easily be seen from the high velocities at the inlet of the packed bed. These high velocities die out as the pressure distribution becomes linear. Except for a short thermal entry region, the changes in the field variables during the early stage are mostly pressure dependent because there is no appreciable thermal penetration. It should be noted that since the liquid fraction never reaches the critical value for becoming mobile, the ϵ_β distribution remains the same throughout the later stage.

The changes in the field variables during the later stage can be attributed to the development of the thermal penetration depth. As may be seen from Fig. 3, the pressure distribution remains linear. Variations of the temperatures of the working fluid and the PCM are very smooth until the PCM reaches its melting temperature. After the onset of melting in the PCM, a distinct discontinuity can be observed in the smoothness of the PCM temperature distribution. This is because for a certain length of the packed bed there is no change in the PCM temperature. In this region the working fluid also adjusts itself accordingly. This can be observed in the temperature profiles for time levels 2–8 in Fig. 3(*a*). This kind of qualitative behavior can also be seen in the vapor velocity and density variations along the packed bed at different time levels. For example, the vapor density variation is precisely and in a physically consistent manner related to pressure and temperature variations. It can also be noticed that there is an inverse relationship between vapor density and vapor velocity. This is due to the fact that the transient term in the vapor continuity equation loses its dominance and the convective term dominates during the later stage. Once the packed bed becomes thermally charged, then the vapor density distribution becomes linear, similar to the pressure distribution explained by the equation of state.

The variations of the average overall condensation rate and the cumulative condensate for a unit width of the packed bed are shown in Fig. 4. The overall condensation rate was computed by integrating the condensation rates at the individual grid points over the associated volumes. Integration of this over time yielded the accumulative condensate for a unit width of the packed bed. The effect of the variation of Δh_{vap} with temperature on condensation was also investigated. In Fig. 4 solid lines show the variations for constant value of Δh_{vap} of R-12, while dashed lines depict the variations for the case with Δh_{vap} varying as a function of temperature. The figure shows that there is a discrepancy of approximately 23 percent. The reason for this was that an average value for Δh_{vap} (for the temperature range of 300–350 K) was used in the results with constant Δh_{vap} value. The actual value of Δh_{vap}, however, drops from 137.78 kJ/kg to 98.35 kJ/kg as the temperature increases from 300 to 350 K. Since most of the condensation for this problem takes place in the early stage during which there is no appreciable thermal penetration in the packed bed, condensation takes place at temperatures close to the initial temperature, i.e., 300 K. Accordingly, the average value for Δh_{vap} for the 300–350 K range was too low and resulted in larger condensation. However, this practically did not have any appreciable effect on the thermal charging of the packed bed since the condensation process lasted only a very short time.

Of interest to the thermal charging of the packed bed are the rates of heat flowing into and out of the packed bed as a function of time. These were also computed for the given cross section of the packed bed for a unit width. The variations of these quantities are depicted in Fig. 5(*a*), except for a very short time section at the beginning of the charging process, which was left out to obtain a better scale on the figure. The variation of the net energy stored for a unit width of the packed bed as a function of time is also depicted in Fig. 5(*b*). At the beginning of the charging process, the vapor flowing out of the packed bed leaves at a low temperature close to the initial temperature, and thus there is a large difference between the heat flow rates at the inlet and at the exit. Hence the rate of energy storage is large. Afterward, for a major portion of the charging process, there is a uniform difference between the rates of heat flowing into and out of the packed bed causing a linear increase in the amount of energy stored. Once the

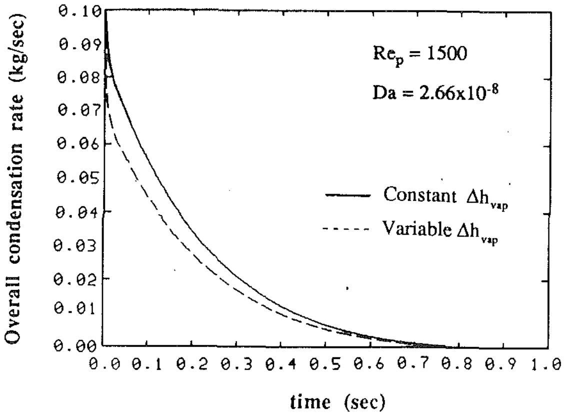

Fig. 4(*a*) Average overall condensation rate in the packed bed

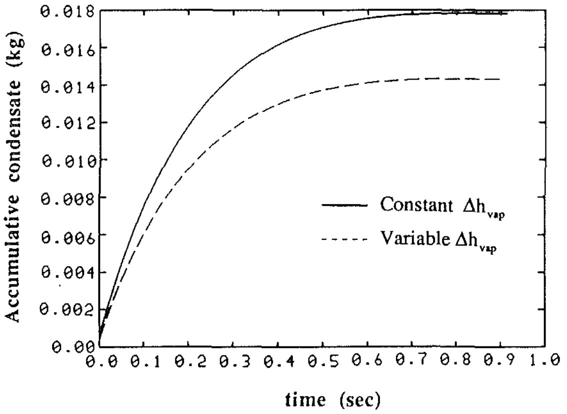

Fig. 4(*b*) Cumulative total condensate in the packed bed

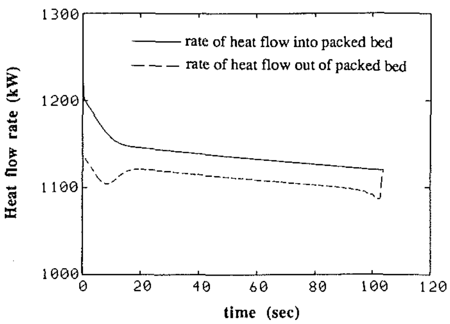

Fig. 5(*a*) Rates of heat flow into and out of the packed bed

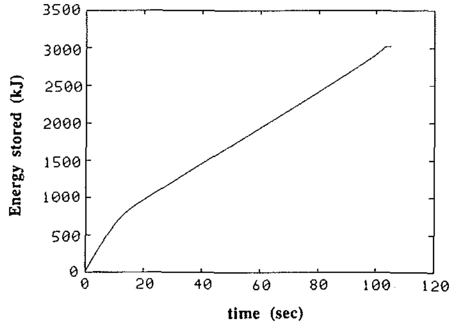

Fig. 5(*b*) Thermal charging of the packed bed

phase change is complete in all particles of the packed bed, both the working fluid temperature and the PCM temperature at the exit of the bed rise rapidly, causing a rapid decrease in the gap between the heat flow rates at the inlet and the exit.

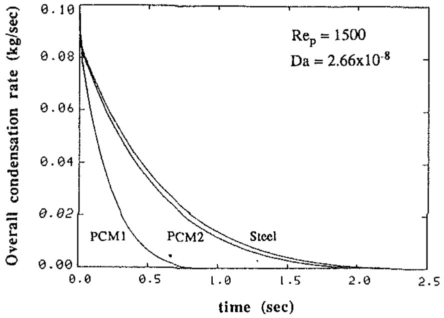

Fig. 6(*a*) Overall condensation rates in the packed bed for cases with different particle materials

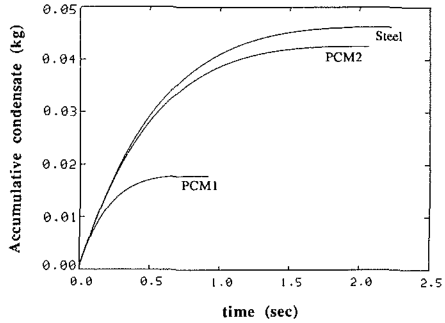

Fig. 6(*b*) Cumulative condensate in the packed bed for cases with different particle materials

3.1 Qualitative Comparison of Condensation in the Working Fluid. In addition to myristic acid (PCM1), two more materials were considered for the particles of the packed bed. These were lithium-nitrate-trihydrate, which we call PCM2, and 1 percent carbon-steel. Runs were made for these cases with the same initial and boundary conditions as in the case of PCM1. Figure 6 depicts the overall average condensation rate and condensate accumulation histories for all three cases. Since condensation in the working fluid takes place in a very short span of time at the beginning, with no significant thermal penetration in the packed bed, the difference in the results for the three materials considered can be attributed mainly to their physical properties. The capacitance of PCM2 differs only by 12 percent from that of steel, whereas that of PCM1 is almost three times smaller than that of steel. Due to this fact and the high heat transfer rate from the working fluid to the solid phase, the temperature propagation in both the solid phase and the working fluid is slower in the cases with steel and PCM2 than in the case with PCM1. Thus, for the former two cases it takes a longer time for condensation to stop. This is as a result of the longer time needed for the vapor to reach a high enough temperature for the vapor density to become lower than the saturation vapor density. Consequently, higher condensation rates are sustained for longer periods and larger condensate accumulations takes place in the case of steel and PCM2.

3.2 Qualitative Comparison of the Thermal Charging Process. The three materials considered for bed particles in this section are the same as those of the previous section. Time histories of the rates of heat flow into and out of the packed bed for the three cases are shown in Fig. 7, while that of the net energy stored in the packed bed for a unit width is shown in Fig. 8. It can be seen that, although at the beginning of the charging process the energy storage rate is almost the same for all three cases, it shows a different variation during later times. While that of the case with steel looks like a conventional

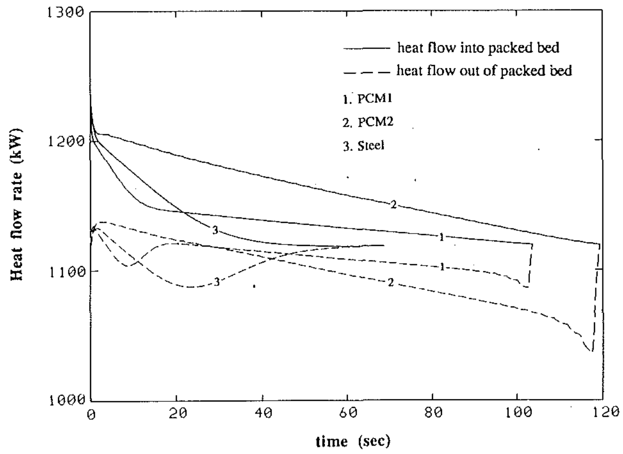

Fig. 7 Rates of heat flow into and out of the packed bed for cases with different particle materials

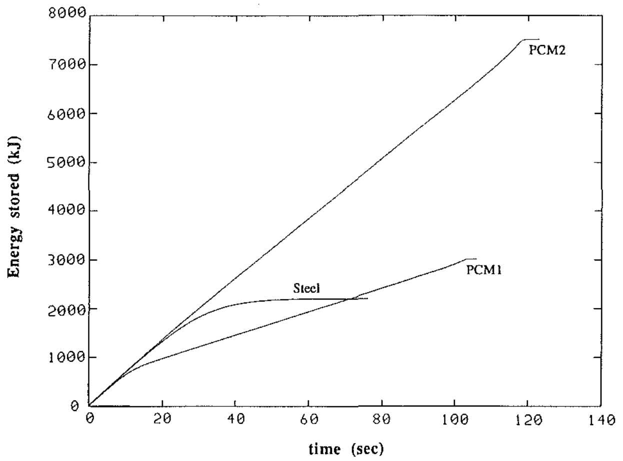

Fig. 8 Thermal charging of the packed bed for cases with different particle materials

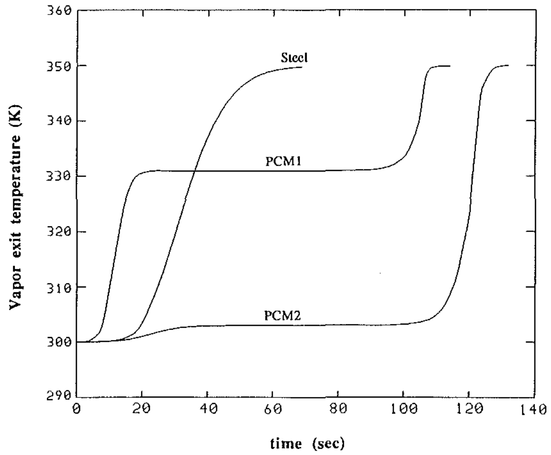

Fig. 9 Vapor exit temperature histories for cases with different particle materials

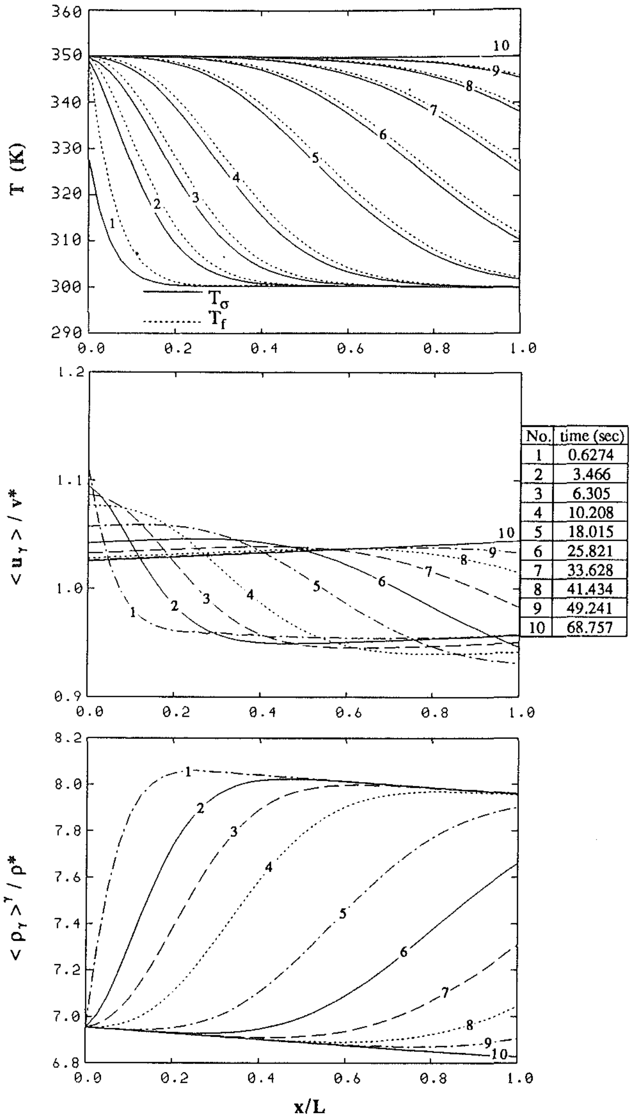

Fig. 10 Distribution of different field variables during the later stage for the case with steel bed particles

charging curve, which decays exponentially with time, the cases with the PCMs have a linear variation for a major portion of the charging period. These linear portions correspond to the time spans during which the temperature of the working fluid at the exit of the packed bed is fairly constant and approximately equal to the melting temperature of the PCM, since once the PCM reaches melting temperature its temperature remains constant until phase change is complete in the PCM. During this period the vapor temperature cannot drop below the melting temperature of the PCM and thus we have a fairly constant vapor exit temperature. In order to illustrate this more clearly, the time history of the vapor exit temperature is presented in Fig. 9 for the three cases.

Figure 8 also shows that using a PCM with a certain melting temperature may not always be a better choice over a sensible heat storage material. For instance, for the boundary conditions and the size considered in the present work, steel seems to perform better than PCM1 if we are interested in the energy storage range of up to 2200 kJ for a unit width. However, since PCM1 weighs significantly less than steel, the weight factor is also another important consideration entering these types of decision.

Figure 10 depicts the temperature profiles of the vapor and the solid phases and the variations of velocity and density of the vapor for the case with steel as the bed particle material. As can be seen, there are no sudden sharp changes in the temperature profiles of either the solid or the working fluid. Comparison of this figure with Fig. 2 explains the different behavior of the vapor exit temperature in the case of steel from those of the PCMs.

4 Conclusions

A rigorous model was developed for analyzing the transient behavior of a latent heat storage packed bed and the condensing flow through it. By this model it was possible to determine the time histories of all the field variables of interest. Qualitative comparisons of the transient behavior of a sensible heat storage and a latent heat storage packed bed have been presented. The difference between the two was very apparent in the thermal charging process. It was found that storage of thermal energy would be most efficient when a PCM with a melting temperature close to the lower limit of the operation temperature range is chosen. It was also found that for a given particle size and nominal particle Reynolds number, the amount of condensation in the working fluid depends principally on the thermophysical properties of the solid phase (or PCM), namely, the thermal capacitance of the packed bed; the larger the thermal capacitance of the bed the larger the amount of condensation in the working fluid. The results of this investigation clearly show the generic qualitative features of transient condensing flow through a porous bed made of encapsulated material.

Acknowledgments

A grant from the Ohio Supercomputer Center is gratefully acknowledged.

References

Ananthanarayanan, V., Sahai, Y., Mobley, C. E., and Rapp, R. A., 1987, "Modeling of Fixed Bed Heat Storage Units Utilizing Phase Change Materials," *Metallurgical Transactions B*, Vol. 18B, pp. 339–346.

Benanati, R. F., and Brosilow, C. B., 1962, "Void Fraction Distribution in Beds of Spheres," *AIChE Journal*, Vol. 8(3), pp. 359–361.

Dullien, F. A. L., 1979, *Porous Media Fluid Transport and Pore Structure*, Academic Press, New York.

Gamson, B. W., Thodos, G, and Hougen, O. A., 1943, "Heat, Mass and Momentum Transfer in the Flow of Gases Through Granular Solids," *Transactions AIChE*, Vol. 39, pp. 1–35.

Kaviany, M., and Mittal, 1987, "Funicular State in Drying of a Porous Slab," *Int. J. Heat Mass Transfer*, Vol. 30, pp. 1407–1418.

Kidder, R. E., and La Habra, 1957, "Unsteady Flow of Gas Through a Semi-infinite Porous Medium," ASME *Journal of Applied Mechanics*, Vol. 24, pp. 329–332.

Lane, G. A., 1986, *Solar Heat Storage: Latent Heat Material*, Vol. II, CRC Press, Inc., Boca Raton, FL.

Marianowski, L. G., and Maru, H. C., 1977, "Latent Heat Thermal Energy Storage Systems Above 450°C," presented at the 12th IECEC, Paper No. 779090, p. 555.

Pitts, D. R., and Ji, S., H., 1987, "Analysis of the Transient Thermal Performance of a Latent Heat Storage Packed Bed," in: *Multiphase Transport in Porous Media*, ASME FED-Vol. 60/HTD-Vol. 91, pp. 51–54.

Riaz, M., 1977, "Analytical Solution for Single- and Two-Phase Models of Packed-Bed Thermal Storage Systems," ASME JOURNAL OF HEAT TRANSFER, Vol. 99, pp. 489–492.

Sözen, M., and Vafai, K., 1990, "Analysis of the Non-thermal Equilibrium Condensing Flow of a Gas Through a Packed Bed," *Int. J. Heat Mass Transfer*, Vol. 33, pp. 1247–1261.

Torab, H., and Chang, W. S., 1988, "High Temperature Thermal Energy Storage for Power Systems," in: *Analysis of Time Dependent Thermal Systems*, ASME AES-Vol. 5, p. 71.

Udell, K. S., and Fitch, J., 1985, "Heat Transfer in Capillary Porous Media Considering Evaporation, Condensation and Non-condensible Gas Effects," in: *Heat Transfer in Porous Media and Particulate Flows*, ASME HTD-Vol. 46, pp. 103–110.

Vafai, K., and Sözen, M., 1990, "Analysis of Energy and Momentum Transport for Fluid Flow Through a Porous Bed," ASME JOURNAL OF HEAT TRANSFER, Vol. 112, pp. 690–699.

Vafai, K., and Whitaker, S., 1986, "Simultaneous Heat and Mass Transfer Accompanied by Phase Change in Porous Insulation," ASME JOURNAL OF HEAT TRANSFER, Vol. 108, pp. 132–140.

Whitaker, S., 1977, "Simultaneous Heat, Mass and Momentum Transfer in Porous Media: A Theory of Drying," *Adv. Heat Transfer*, Vol. 13, pp. 119–203.

Pressure Stratification Effects on Multiphase Transport Across a Vertical Slot Porous Insulation

H. C. Tien

K. Vafai
Mem. ASME

Department of Mechanical Engineering,
The Ohio State University,
Columbus, OH 43210

In this work, thermal stratification effects on heat and mass transfer in a porous insulation are analyzed. The vertical boundaries of the porous system are partially permeable for simulating holes or cracks in wall. Hydrostatic pressure variations are considered on the vertical boundaries and a set of realistic boundary conditions is imposed on the system under consideration. The transient intercoupled equations governing the complicated transport process along with the convective boundary conditions are solved by an efficient numerical scheme. The dependence of the Nusselt number and the field variables on several important parameters is investigated systematically. The results clearly show that infiltration can have a major effect on the overall heat transfer even for small pressure gradients across the insulation slab. Furthermore, it has been found that the opening locations have a pronounced effect on the heat transfer rate across the slab and the corresponding condensation rate. The qualitative information extracted from this investigation can be used to diminish the infiltration and condensation problems in the design of building insulation.

1 Introduction

Usually, a porous material is introduced to reduce the convective and radiative heat transfer. It has been found that, at room temperature, radiation effects on the overall energy transfer are small, as shown in the studies by Verschoor and Greebler (1952), Mumaw (1968), and Lopez (1969). Therefore, convection and conduction are the major modes of heat transfer in porous insulation materials. Since the porous materials are frequently used as building insulation, any basic improvement in the understanding of the thermal performance of these materials will ultimately lead to a reduction in future energy consumption. In addition, water vapor transport by diffusion and convection was shown to have a significant effect on material deterioration. Therefore, it is important, from both applied and basic points of view, to investigate the infiltration and condensation effects on heat and mass transfer in porous insulation materials.

Generally, three phases are present in a wet insulation. These are the solid matrix, the liquid water, and a binary gas phase composed of air and vapor. There is heat conduction in all phases. In the gas phase, there is vapor diffusion due to vapor concentration gradients, and air infiltration due to small pressure differences across the insulation slab. If the liquid is mobile there exists heat convection in the liquid phase. There is also energy transfer due to phase change at the gas–liquid interface. The above-mentioned phenomena represent complex interactions among several different transport mechanisms.

Several experimental studies on the subject of condensation in porous media, such as Tye and Spinney (1979), Stewart (1982) and Langlais et al. (1982), exist. There are also several analytical and numerical studies in the literature. A one-dimensional quasi-steady analytical work was performed by Ogniewicz and Tien (1981). Vafai and Sarkar (1986) studied one-dimensional transient heat and mass transport in insulation materials. Both studies mentioned above accounted for uniform infiltration. Vafai and Whitaker (1986) conducted transient two-dimensional numerical studies with simplifying assumptions. Also, there are two investigations by Burns et al. (1977) and Burns and Tien (1978) dealing with steady-state forced convection (infiltration) and free convection. However, condensation and multicomponent effects are not included.

By design and/or because of holes or cracks in walls, a porous insulation matrix is usually partially exposed to the external environment on one side and the internal environment on the other side. To simulate a true infiltration application for an insulation matrix, one needs to make a three-dimensional analysis of the problem. However, as the present work makes clear, the CPU requirements alone will prevent us from making any significant progress on a three-dimensional model. Therefore, the closest that one can come to simulating the infiltration through a fibrous insulation is the configuration shown in Fig. 1. This figure constitutes the framework for a basic investigation on pressure stratification and infiltration effects on multiphase transport through a porous slab. In this figure the vertical boundaries of the porous insulation are partially permeable to simulate some of these design considerations and/or holes or cracks in the wall, subjected to the external pressure forces. Furthermore, to simulate realistic conditions, the temperature and vapor density boundary conditions for the permeable parts are not specified; rather, convective boundary conditions are applied. Therefore, the numerical results can be utilized for estimating the heat loss due to holes or cracks in the building insulations and other related applications. Since porous materials are frequently used as building insulations, any basic improvement in the understanding of the thermal performance of these materials will ultimately lead to a reduction in future energy consumption. For simulating infiltration through porous insulations, this same configuration has also been used by other investigators (Burns et al., 1977).

In an earlier work (Tien and Vafai, 1990) infiltration effects based on constant pressure distribution on either side of an insulation slab were investigated and the influence of the Biot numbers and the opening locations were demonstrated. The objective of this study is to simulate fully the problem of transient two-dimensional heat and mass transport in fibrous insulation materials accounting for stratification and conden-

---

Contributed by the Heat Transfer Division for publication in the JOURNAL OF HEAT TRANSFER. Manuscript received by the Heat Transfer Division July 21, 1989; revision received March 12, 1990. Keywords: Building Heat Transfer, Multiphase Flows, Porous Media.

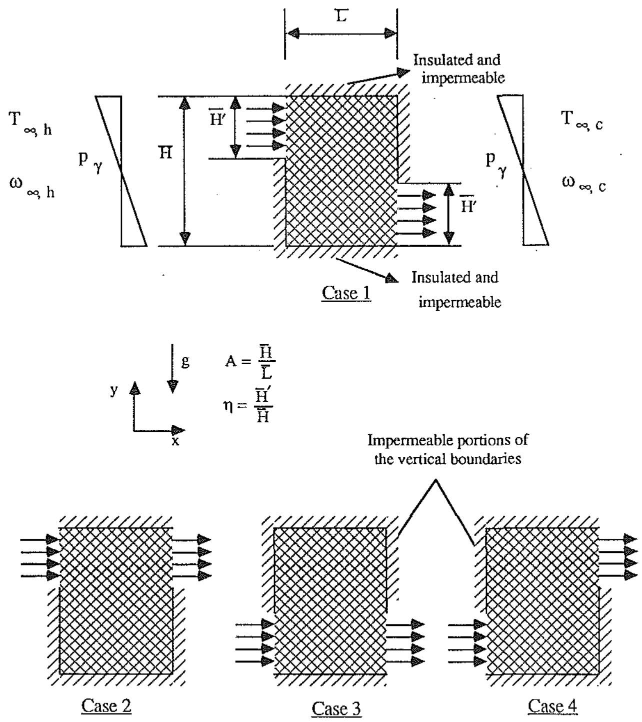

Case 1

Case 2 Case 3 Case 4

Fig. 1 Two-dimensional porous matrix with partially permeable boundaries for four representative opening locations

sation effects without making any significant assumptions. Thus, the common Boussinesq approximation is not invoked. It is found that the pressure stratification has a profound effect on the heat transfer characteristics of different opening locations. Pressure stratification alters the flow field corresponding to a uniform pressure gradient and results in a completely different set of criteria for choosing the optimum opening locations than those found for a uniform pressure gradient.

Figure 1 shows the physical system considered in the present study. The vertical boundaries of the porous matrix are partially permeable to simulate the cracks or holes in the walls. The pressure on the vertical boundaries is assumed to be hydrostatic. The reference zone is set at midheight of the porous system. Due to the pressure difference across the insulation, the fluid flows through the porous insulation. The horizontal boundaries are assumed to be insulated and impermeable. The impermeable parts of the vertical boundaries are also assumed to be adiabatic. The permeable parts of the vertical boundaries are exposed to two different environments, a hot and humid environment on the left-hand side and a cooler environment on the right-hand side. The open portions of the vertical boundaries are exposed to convective temperature and vapor density boundary conditions. In this work, the variations and interactions of the pertinent field variables are analyzed. The effects of the physical parameters such as opening size, heat transfer Biot number, and vapor transfer Biot number are investigated, and detailed physical explanations of all the observed numerical results are given. The influence of the opening locations is examined through studying four typical cases as shown in Fig. 1. The results presented in this work are made more versatile by using a consistent set of symbols and a presentation format similar to the earlier work of Tien and Vafai (1990). The qualitative information extracted from this work can be used to minimize the infiltration and condensation problems in the design of building insulations.

2 Mathematical Formulation

2.1 Governing Equations. The derivation of the governing equations for heat and mass transfer in porous media while accounting for condensation/evaporation effects requires a significant amount of algebraic manipulation. A volume-averaging technique was used to develop the governing equations from the point conservation equations for a continuum. The spatial average for a quantity Ψ is

$$\langle \Psi \rangle = \frac{1}{V}\int_V \Psi dV \tag{1}$$

where V is an averaging volume bounded by a closed surface in a porous medium and the intrinsic phase average is given by

Nomenclature

A = aspect ratio $= \overline{H}/\overline{L}$
B = Biot number referring to heat transfer $= \overline{h}\overline{L}/\overline{k}_{\mathrm{eff},o}$
B^* = Biot number referring to mass transfer $= \overline{h}^*\overline{L}/\overline{\alpha}_{\mathrm{eff},o}$
B_v = Biot number referring to vapor transport $= \overline{h}_v\overline{L}/\overline{\alpha}_{\mathrm{eff},o}$
$\overline{C}_p$ = average heat capacity, W-s/kg-K
$\overline{c}_i$ = dimensional heat capacity for the ith phase at constant pressure, W-s/kg-K
$\overline{c}_o$ = reference heat capacity, W-s/kg-K
$\overline{D}_{v,\mathrm{eff}}$ = effective vapor diffusivity coefficient, m^2/s
$\underline{g}$ = dimensionless gravity vector
$\overline{h}$ = heat transfer coefficient, W/m^2-K
$\overline{h}^*$ = mass transfer coefficient, m/s
$\overline{h}_v$ = species transfer coefficient, m/s
$\Delta\overline{h}_{\mathrm{vap}}$ = enthalpy of vaporization per unit mass, J/kg
$\overline{H}$ = height of porous insulation, m
$\overline{H}'$ = length of opening of porous insulation, m
$\overline{k}_i$ = dimensional thermal conductivity for phase i, W/m-K
$\overline{k}_{\langle\overline{T}\rangle}$ = $-\partial\langle\overline{p}_c\rangle/\partial\langle\overline{T}\rangle$, N/m^2-K
$\overline{k}_\epsilon$ = $-\partial\langle\overline{p}_c\rangle/\partial\epsilon_\beta$, N/m^2
$\overline{k}_{\mathrm{eff}}$ = dimensional effective thermal conductivity, W/m-K
$\overline{K}$ = permeability, m^2
$\overline{K}_\beta$ = effective liquid permeability, m^2
$\overline{K}_\gamma$ = effective gas permeability, m^2
$K_{r\beta}$ = relative permeability for the liquid phase
$K_{r\gamma}$ = relative permeability for the gas phase
$\overline{L}$ = thickness of the insulation, m
Le = Lewis number $= \overline{\alpha}_{\mathrm{eff},o}/\overline{D}_{v,\mathrm{eff}}$
$\dot{\overline{m}}$ = dimensional condensation rate, kg/m^3-s
N_{TETR_h} = the Nondimensionalized Total Energy Transfer Rate, defined in equation (27)
p_a = dimensionless air pressure $= \overline{p}_a/\overline{p}_{a,o}$
$\overline{p}_c$ = capillary pressure $= \overline{p}_\gamma - \overline{p}_\beta$, N/m^2
p_v = dimensionless vapor pressure $= \overline{p}_v/\overline{p}_{v,o}$
p_γ = dimensionless gas phase pressure $= \overline{p}_\gamma/\overline{p}_{\gamma,o}$
Pe = Peclet number $= \overline{v}_{\gamma,o}\overline{L}/\overline{\alpha}_{\mathrm{eff},o}$
$\overline{r}$ = characteristic length of the porous matrix, m
$\overline{R}_a$ = air gas constant, N-m/kg-K
$\overline{R}_v$ = vapor gas constant, N-m/kg-K

$$\langle \Psi_\alpha \rangle^\alpha = \frac{1}{V_\alpha(t)} \int_{V_\alpha(t)} \Psi_\alpha dV \tag{2}$$

where V_α denotes the volume for the α phase within the averaging volume V and Ψ_α is a quantity associated with the α phase. The derivation of the governing equations is based on the work of Whitaker (1977). The dimensionless governing equations originally established by Vafai and Tien (1989) are:

Thermal energy equation

$$\frac{\partial \langle T \rangle}{\partial t} + \frac{P_1 P_2 P_{18}}{P_{19}} \psi_\epsilon \langle \mathbf{v}_\beta \rangle \bullet \nabla \langle T \rangle + \frac{P_3 P_4 P_{18} \mathrm{Pe}}{P_{19}} \langle \rho_\gamma \rangle^\gamma \langle \mathbf{v}_\gamma \rangle \bullet \nabla \langle T \rangle + \frac{P_{18}}{P_{19}} \langle \dot{m} \rangle = P_{18} \nabla^2 \langle T \rangle + \frac{P_{18}}{P_{19}} \nabla P_{19} \bullet \nabla \langle T \rangle \tag{3}$$

Liquid phase equation of motion

$$\langle \mathbf{v}_\beta \rangle = -K_{r\beta} (\nabla \epsilon_\beta + \psi_T \nabla \langle T \rangle - \psi_g \mathbf{g}) \tag{4}$$

Liquid phase continuity equation

$$\frac{\partial \epsilon_\beta}{\partial t} + \psi_\epsilon \nabla \bullet \langle \mathbf{v}_\beta \rangle + \frac{1}{P_1 P_6} \langle \dot{m} \rangle = 0 \tag{5}$$

Gas phase equation of motion

$$\langle \mathbf{v}_\gamma \rangle = P_{20} K_{r\gamma} (-\nabla \langle p_\gamma \rangle^\gamma + P_5 \langle \rho_\gamma \rangle^\gamma \mathbf{g}) \tag{6}$$

Gas phase continuity equation

$$\frac{\partial}{\partial t} (\epsilon_\gamma \langle \rho_\gamma \rangle^\gamma) + \mathrm{Pe} \nabla \bullet (\langle \rho_\gamma \rangle^\gamma \langle \mathbf{v}_\gamma \rangle) - \frac{1}{P_4 P_6} \langle \dot{m} \rangle = 0 \tag{7}$$

Gas phase diffusion equation

$$\frac{\partial}{\partial t} (\epsilon_\gamma \langle \rho_v \rangle^\gamma) + \mathrm{Pe} \nabla \bullet (\langle \rho_v \rangle^\gamma \langle \mathbf{v}_\gamma \rangle) - \frac{1}{P_4 P_6 P_{11}} \langle \dot{m} \rangle = \frac{1}{\mathrm{Le}} \nabla \bullet \left[\langle \rho_\gamma \rangle^\gamma \nabla \left(\frac{\langle \rho_v \rangle^\gamma}{\langle \rho_\gamma \rangle^\gamma} \right) \right] \tag{8}$$

Volume constraint

$$\epsilon_\sigma + \epsilon_\beta + \epsilon_\gamma = 1 \tag{9}$$

Thermodynamic relations

$$\langle p_v \rangle^\gamma = P_9 \langle \rho_v \rangle^\gamma \langle T \rangle \tag{10}$$

$$\langle p_a \rangle^\gamma = P_9 \langle \rho_a \rangle^\gamma \langle T \rangle \tag{11}$$

$$\langle \rho_\gamma \rangle^\gamma = P_{11} \langle \rho_v \rangle^\gamma + P_{12} \langle \rho_a \rangle^\gamma \tag{12}$$

$$\langle p_\gamma \rangle^\gamma = P_{13} \langle p_v \rangle^\gamma + P_{14} \langle p_a \rangle^\gamma \tag{13}$$

$$\langle \rho_{v,s} \rangle^\gamma = \frac{1}{P_9 \langle T \rangle} \exp \left(-\frac{P_{15} + P_{16}}{\langle T \rangle} + \frac{P_{16}}{\langle T_o \rangle} \right) \tag{14}$$

The variable properties in the porous insulation are

$$\overline{k}_{\mathrm{eff}} \cong \epsilon_\sigma \overline{k}_\sigma + \epsilon_\beta \overline{k}_\beta + \epsilon_\gamma \frac{(\overline{k}_v \langle \overline{\rho}_v \rangle^\gamma + \overline{k}_a \langle \overline{\rho}_a \rangle^\gamma)}{(\langle \overline{\rho}_v \rangle^\gamma + \langle \overline{\rho}_a \rangle^\gamma)} \tag{15}$$

$$\overline{\rho} = \epsilon_\sigma \overline{\rho}_\sigma + \epsilon_\beta \overline{\rho}_\beta + \epsilon_\gamma (\langle \overline{\rho}_v \rangle^\gamma + \langle \overline{\rho}_a \rangle^\gamma) \tag{16}$$

$$\overline{C}_p = \frac{\epsilon_\sigma \overline{\rho}_\sigma \overline{c}_\sigma + \epsilon_\beta \overline{\rho}_\beta \overline{c}_\beta + \epsilon_\gamma (\langle \overline{\rho}_v \rangle^\gamma \overline{c}_v + \langle \overline{\rho}_a \rangle^\gamma \overline{c}_a)}{\overline{\rho}} \tag{17}$$

$$\overline{\alpha}_{\mathrm{eff}} = \frac{\overline{k}_{\mathrm{eff}}}{\overline{\rho} \overline{C}_p} \tag{18}$$

The main variables of interest in this study are the temperature $\langle T \rangle$, vapor density $\langle \rho_v \rangle^\gamma$, condensation rate $\langle \dot{m} \rangle$, liquid volume fraction ϵ_β, and the gas density $\langle \rho_\gamma \rangle^\gamma$. The variables with a bar on top refer to dimensional quantities. The controlling parameters P_1, P_2, P_4, P_6, P_9, and P_{11} through P_{14}, defined in the appendix of an earlier work (Tien and Vafai, 1990), are constants and are fixed by the choice of the reference quantities. The controlling parameters P_3, P_{18}, and P_{19} vary with the variation of the properties. The controlling parameter P_5 accounts for the body force, Pe characterizes the infiltration through the porous slab, and P_{20} affects the numerical stability. Only at some points could the physical descriptions be made more effective in terms of dimensional variables. It was found that the controlling nondimensional parameters were indispensable in terms of describing the physics of the problem efficiently and compactly. The dimensionless variables and nondimensional parameters Pe, Le, ψ_ϵ, ψ_g, ψ_T, and P_j and their physical relevance are defined in an earlier work (Vafai and Tien, 1990).

Nomenclature (cont.)

s = scaled fractional liquid saturation $= (s_\beta - s_{\beta p})/(1 - s_{\beta p})$
s_β = fractional liquid saturation $= \epsilon_\beta/(\epsilon_\beta + \epsilon_\gamma)$
$s_{\beta p}$ = saturation for immobile liquid
t = dimensionless time $= \overline{t}/(\overline{L}^2/\overline{\alpha}_{\mathrm{eff},o})$
T = dimensionless temperature $= \overline{T}/\Delta\overline{T}$
$\overline{T}_{\infty,h}$ = hot-side ambient temperature, K
$\overline{T}_{\infty,c}$ = cool-side ambient temperature, K
y_o = reference position in the vertical direction for pressure
$\overline{\alpha}_{\mathrm{eff},o}$ = reference effective thermal diffusivity $= \overline{k}_{\mathrm{eff},o}/(\overline{\rho}_o \overline{c}_o)$, m^2/s
ϵ = volume fraction
η = opening size $= \overline{H}'/\overline{H}$
$\overline{\mu}_\beta$ = liquid dynamic viscosity, kg/m-s
$\overline{\mu}_\gamma$ = gas dynamic viscosity, kg/m-s
$\overline{\rho}$ = dimensional total density defined in equation (16), kg/m^3
ρ_v = dimensionless vapor density $= \overline{\rho}_v/\overline{\rho}_{v,o}$
ρ_i = dimensionless density for phase $i = \overline{\rho}_i/\overline{\rho}_{i,o}$
$\overline{\sigma}_{\beta\gamma}$ = surface tension at the gas and liquid interface, N/m
$\omega_{\infty,h}$ = hot-side ambient relative humidity
$\omega_{\infty,c}$ = cool-side ambient relative humidity

Subscripts

a = denotes air phase
c = denotes cool side of insulation
eff = denotes effective properties
h = denotes hot side of insulation
i = denotes ith phase
o = denotes reference quantities
s = refers to saturation quantities
v = denotes vapor phase
x = denotes component in x direction
y = denotes component in y direction
β = denotes liquid phase
γ = denotes gas phase
σ = denotes solid matrix
∞ = denotes ambient quantities in surroundings

Superscripts

$\overline{}$ = refers to dimensional quantities

Symbols

$\langle\,\rangle$ = denotes "local volume average" of quantity

Two major assumptions were made in arriving at the above governing equations. These are: (1) The porous material is homogeneous and isotropic; and (2) the porous system, which consists of the solid, liquid, and gas phases, is assumed to be in local thermodynamic equilibrium. These assumptions are realistic for a porous insulation matrix. Aside from being a routine assumption (LTE), which is made when dealing with porous insulation, we can substantiate its effectiveness based on the work of Vafai and Sozen (1990). In part of this work, a qualitative and quantitative assessment of the validity of local thermal equilibrium assumption and its use in the energy is made and the findings are presented in an integrated form. The results were presented in terms of entire ranges of Re_p (Reynolds number based on the pore diameter) and Da (Darcy number) for several different porous media. Using typical thermophysical and infiltration data for porous insulation (such as those given in this work) it is found that the use of the LTE assumption in a typical porous insulation will lead to less than 1 percent error. Therefore, the LTE assumption for a porous insulation is justified. Aside from these assumptions, the governing equations are quite general and the results can be applied to a whole class of problems on heat and mass transfer in porous media with phase change.

It is noted that Darcy's flow model is used in describing the motion of the gas phase and the liquid phase. Based on the work of Vafai and Tien (1981) and Vasseur et al. (1984), two conditions representing the inertia and boundary effects should be satisfied to insure that the errors of the results obtained from the Darcy's law are within 10 percent. Based on typical physical data used for porous insulation, these two conditions are satisfied. It should be noted that dispersion effects are not significant in porous insulation.

The effective gas permeability $\overline{K}_\gamma$ and the effective liquid permeability $\overline{K}_\beta$ are related to the permeability $\overline{K}$ and the relative permeabilities, $K_{r\beta}$ and $K_{r\gamma}$, as given in Tien and Vafai (1990). At this time the full tensorial characteristics of $\underset{\approx}{\mathrm{K}}_{r\beta}$ are not known and, hence, we will use

$$\underset{\approx}{\mathrm{K}}_{r\beta} = \underset{\approx}{\mathrm{I}}_{\beta r} K_{r\beta}$$

In the above expression, $\underset{\approx}{\mathrm{K}}_{r\beta}$ denotes the tensor for $K_{r\beta}$ and $\underset{\approx}{\mathrm{I}}$ denotes the identity tensor. The isotropy and homogeneity assumptions for porous insulation are considered to be good assumptions and are routinely made when dealing with such media. It is generally understood that when dealing with a high-porosity medium such as insulation, where the porosities are usually upward of 90 percent, the variations in the porosity near the wall are quite negligible. The relative permeability model used in this work is described in Tien and Vafai (1990).

This model was first suggested by Wyllie (1962), and shows good agreement with the data in the work of Fatt and Klikoff (1959) and has been used by Udell (1985). The liquid is considered to be immobile for $\epsilon_\beta < \epsilon_{\beta p}$, where $\epsilon_{\beta p}$ is the liquid fraction corresponding to the saturation value of $s_{\beta p}$. In this investigation, the value for $s_{\beta p}$ was taken to be 0.1. This value was also used by Kaviany and Mittal (1987). The value for $s_{\beta p}$ was taken from the work of Kaviany and Mittal (1987) due to lack of any other solid information on the value of this quantity. From a practical point of view, there should not be much difference between the actual value of $s_{\beta p}$ and the value that has been used here since $s_{\beta p}$ refers to the saturation of the liquid at the pendular state in the porous medium. Furthermore, it was found that a ∓ 10 percent variation in $s_{\beta p}$ has a negligible effect on the results.

2.2 Boundary Conditions. The vertical boundaries are assumed to be partially insulated and impermeable, and the horizontal boundaries are insulated and impermeable. The convective boundary conditions for the mass, energy, and species at the porous medium–surroundings gas interface in nondimensional form are as those given by Tien and Vafai (1990):

Mass balance:

$$(P_1\psi_\epsilon\langle \mathbf{v}_\beta\rangle + \mathrm{Pe}P_4\langle\rho_\gamma\rangle^\gamma\langle \mathbf{v}_\gamma\rangle)\bullet\mathbf{n} = B^*P_4(\langle\rho_\gamma\rangle^\gamma - \rho_\infty) \tag{19}$$

Energy balance:

$$P_1P_6\psi_\epsilon\langle \mathbf{v}_\beta\rangle\bullet\mathbf{n} + P_{19}\nabla T\bullet\mathbf{n} = B(T_\infty - \langle T\rangle) \tag{20}$$

Species balance:

$$\left[P_1\psi_\epsilon\langle \mathbf{v}_\beta\rangle + \mathrm{Pe}P_4P_{11}\langle\rho_v\rangle^\gamma\langle \mathbf{v}_\gamma\rangle - \frac{P_4P_{11}}{\mathrm{Le}}\langle\rho_\gamma\rangle^\gamma\nabla\left(\frac{\langle\rho_v\rangle^\gamma}{\langle\rho_\gamma\rangle^\gamma}\right)\right]\bullet\mathbf{n}$$
$$= B_vP_4P_{11}(\langle\rho_v\rangle^\gamma - \rho_{v,\infty}) \tag{21}$$

In equations (19)–(21), B^*, B, and B_v are the Biot numbers for the mass transfer, heat transfer, and species transport, and $\mathbf{n}$ is the unit normal vector at the interface between the porous insulation and the surrounding gas phase. For the limiting case with insulated and impermeable boundaries, B, B^*, and B_v are zero and therefore, the right-hand sides of equations (19)–(21) drop out. The horizontal boundaries and the impermeable portions of the vertical boundaries fall within such categories. However, for the permeable portions of the vertical boundaries, B and B_v are nonzero. The pressures at the permeable portions of the vertical boundaries are assumed to be hydrostatic, i.e.,

$$p_\gamma(x, y, t) - p_\gamma(x, y_o, t) = P_5 g_y \int_{y_o}^{y} \rho_\gamma dy \quad \text{for } x = 0, 1 \tag{22}$$

where g_y denotes the dimensionless y component of the gravity vector, and y_o is the reference position in the vertical direction, which in this work is taken at the midheight of the enclosure. The speeds that we are dealing with as a result of the small pressure differences across the insulation are very small. Using Bernoulli's equation, it is found that the deviations from the hydrostatic pressure distributions are negligible. Thus, assuming hydrostatic pressure distributions at the boundaries is realistic. Although these very small speeds have a negligible effect on the hydrostatic pressure distribution at the faces of the insulation slab, they still have a significant effect on the overall energy transfer.

The pressures at the two reference positions at the left and right vertical boundaries are

$$\begin{gathered} p_\gamma(x=0, y_o, t) = 1 + \epsilon \\ p_\gamma(x=1, y_o, t) = 1 \end{gathered} \tag{23}$$

This pressure difference will induce the infiltration through the porous system. In the present work, ϵ is taken as 10^{-5}. Such a value would simulate very small infiltration rates that would exist across a fibrous insulation. Since ρ_γ varies along the vertical boundaries, iterations are needed to make p_γ, ρ_γ, p_v, p_a, ρ_v, and ρ_a satisfy equations (10)–(13), (21), and (22) simultaneously. This results in a highly complex numerical algorithm for analyzing the pressure stratification effects. The temperature and humidity conditions at the ambient environments are specified as

$$\begin{gathered} T_{\infty,h} = 15.4 \\ T_{\infty,c} = 14.65 \end{gathered} \tag{24}$$

and

$$\begin{gathered} \omega_{\infty,h} = 1 \\ \omega_{\infty,c} = 1 \end{gathered} \tag{25}$$

The above nondimensional ambient temperatures correspond to $\overline{T}_{\infty,h} = 308$ K and $\overline{T}_{\infty,c} = 293$ K. These temperatures were chosen based on physical grounds. The initial conditions are specified as

$$\begin{gathered} T(x, y, t=0) = 14.65 \\ \omega(x, y, t=0) = 1 \\ \epsilon_\beta(x, y, t=0) = 0 \end{gathered} \tag{26}$$

$$p_\gamma(x, y, t=0) - p_\gamma(x=1, y_o, t=0) = P_5 g_y \int_{y_o}^{y} \rho_\gamma dy$$

It is noted that the initial pressure condition is also taken to be hydrostatic.

2.3 Heat Transfer Calculation. Based on physical grounds, the ratio given in equation (27), which represents the overall energy transfer across the porous insulation, is called the *Nondimensionalized Total Energy Transfer Rate* (N_{TETR}) for each permeable portion of the walls, and accounts for the contribution from both the heat and mass transfer. N_{TETR} is defined as

$$N_{TETR_h} = \frac{1}{\eta A} \frac{\int_{y^*}^{y^*+\eta A} \left(-P_{19}\frac{\partial T}{\partial x} + P_3 P_4 \mathrm{Pe} \rho_\gamma v_{\gamma_x} T + P_1 P_2 \psi_\epsilon v_{\beta_x} T \right) \Big|_{x=0} dy}{P_{19}(T_{\infty,h} - T_{\infty,c}) + P_3 P_4 \mathrm{Pe} \rho_\gamma^* v_{\gamma_x}^* T_{\infty,h}} \tag{27}$$

where η is the ratio of the opening height to the total height. The N_{TETR} defined in the above equation includes the effects of heat conduction, infiltration, and bulk convection. The numerator denotes the actual energy transfer and the denominator represents a reference heat transfer with infiltration effect included since the dominant mode of the overall energy transfer is due to infiltration (forced convection). It should be noted that the integration in the numerator is done over the permeable portions only.

The physical data used in the numerical experiments are listed in Table 1 of Tien and Vafai (1990). These data represent typical properties for the gas, liquid, and the solid phases of an insulation slab.

3 Method of Solution

3.1 Solution Scheme. An explicit finite difference scheme was employed to solve the complete governing equations associated with the boundary conditions. In this scheme, the spatial derivatives are discretized by central differencing, except for the convective terms. The convective terms are all approximated by an upwind differencing scheme except for the convective term in the gas phase continuity equation. It was found through extensive experimentation that, from a numerical point of view, it would be most efficient to use central differencing for this term. This numerical scheme is composed of two different formats in time and space to account for phase change. Based on the experimental work of Langlais et al. (1982), the liquid content was considered to be part of the adsorbed water for $\epsilon_\beta < 10^{-5}$. Therefore, no bulk condensation was allowed for $\epsilon_\beta < 10^{-5}$ and hence, the condensation rate was set to be zero. For $\epsilon_\beta > 10^{-5}$, the liquid was considered to be part of the condensate. This same criterion was used in the work of Vafai and Whitaker (1986).

Extensive numerical experimentation was conducted for different forms of upwind difference methods such as first-order upwind, third-order upwind, etc., to determine the numerical stability and the accuracy for each scheme. After extensive experimentation, the present scheme was adopted since it resulted in the best numerical stability. This scheme was then compared with several semi-implicit schemes that we had also developed (i.e., in such schemes, the transport equations that have strong advection terms were solved implicitly). It was found that the computational time could not be reduced by employing the semi-implicit schemes. The numerical results from all of the above-mentioned schemes were in good agreement with each other.

3.2 Accuracy Check. The accuracy of the computational scheme was examined rigorously in three different ways. First, for a chosen grid system the time step size was systematically decreased until a time step size was found where any further decrease would not have any significant effect on the field variables or the rates of total energy transfer across the porous slab. In parallel with the former series of tests, the number of grid points was also systematically increased to find the minimum number of grid points required for achieving a reasonable level (with respect to the required CPU time) of accuracy. The effects of the number of grid points on N_{TETR} and the rest of the results were thoroughly checked, rigorously and systematically by increasing the number of grids from 11 × 11 to 15 × 15 and ultimately to 21 × 21. Table 1 illustrates the N_{TETR} results for these three different grid systems (the comparisons for the rest of field variables are not presented here due to space limitations). As shown, the results based on the 15 × 15 and 21 × 21 grid systems are in good agreement. The 15 × 15 grid system does provide enough accuracy if we are willing to tolerate approximately a 1 percent margin of error in our results. Since the results for the 15 × 15 grid system were in good agreement with the 21 × 21 grid system, most of our computations were based on the former. Lastly, good agreement between our explicit and implicit results constituted the third examination of the accuracy of our results.

4 Results and Discussion

In this work, the transient thermal behavior of the porous materials and the interactions of the field variables are studied. The effects of the opening size, heat transfer Biot number B, and the vapor transfer Biot number B_v are also investigated. Four cases corresponding to the four representative opening locations are thoroughly investigated. The surface tension effect has been taken into account in our results. However, based on our numerical results, it was found that usually, surface tension effects are negligible. This fact was also mentioned in the work of Whitaker and Chou (1983). They stated that surface tension presented very little effect on the saturation vapor pressure.

4.1 General Behavior of Field Variables—"Wavelike" Propagation. The distributions for the temperature, vapor density, condensation rate, and liquid content at four different times are illustrated in Figs. 2–5. These results are based on case 1 as shown in Fig. 1 with $B = 1000$, $B_v = 5 \times 10^4$, and an opening size ratio of 1/2. In Fig. 4, positive values denote condensation, whereas negative values represent evaporation. The four different times, t_1, t_2, t_3, and t_4, were chosen to demonstrate clearly the most significant temporal variations of the field variables. As can be seen from Fig. 2, when the left boundary of the porous matrix is suddenly exposed to a higher ambient temperature, the left boundary experiences a rapid increase in temperature. The temperature increase will gradually penetrate into the interior region of the porous system. This wavelike propagating behavior was also observed for the other variables such as the vapor density, the condensation rate and the liquid content shown in Figs. 3–5. It should be mentioned that for brevity, the gas phase density distributions, which showed a similar wavelike behavior, are not presented here. As expected, a larger amount of condensate was formed at the left boundary since it is exposed to a hot and humid environment. This finding was valid for all cases discussed in the present work. As for the gas phase velocity distributions, as expected, due to the pressure difference across the insulation, the fluid is introduced from the upper left opening, flows through the porous matrix, and finally is injected out of the right-hand-side opening. The infiltration speeds were approximately between 10^{-4} and 10^{-3} m/s. Due to these small infiltration speeds, circulation was not observed in the porous

Table 1 Effect of the grid size on the Nondimensionalized Total Energy Transfer Rate, N_{TETR_h}

t	N_{TETR_h} (11×11)	Relative difference between (11×11) and (21×21) grid systems (percent)	N_{TETR_h} (15×15)	Relative difference between (15×15) and (21×21) grid systems (percent)	N_{TETR_h} (21×21)
0.0005	1.7218	4.78	1.7902	1.00	1.8083
0.001	1.6360	2.62	1.6670	0.77	1.6800
0.0015	1.5917	2.31	1.6238	0.34	1.6294
0.002	1.5555	2.87	1.5881	0.84	1.6015
0.0025	1.5373	2.58	1.5660	0.76	1.5780
0.003	1.5186	2.73	1.5487	0.80	1.5612
0.0035	1.5047	2.81	1.5368	0.74	1.5482
0.004	1.4929	3.00	1.5289	0.66	1.5390
0.0045	1.4857	2.90	1.5192	0.71	1.5300
0.005	1.4783	2.90	1.5111	0.74	1.5224

Note: Relative difference $\equiv \dfrac{|N_{TETR_{h,21\times 21}} - N_{TETR_{h,11\times 11 \text{ or } 15\times 15}}|}{N_{TETR_{h,21\times 21}}}$

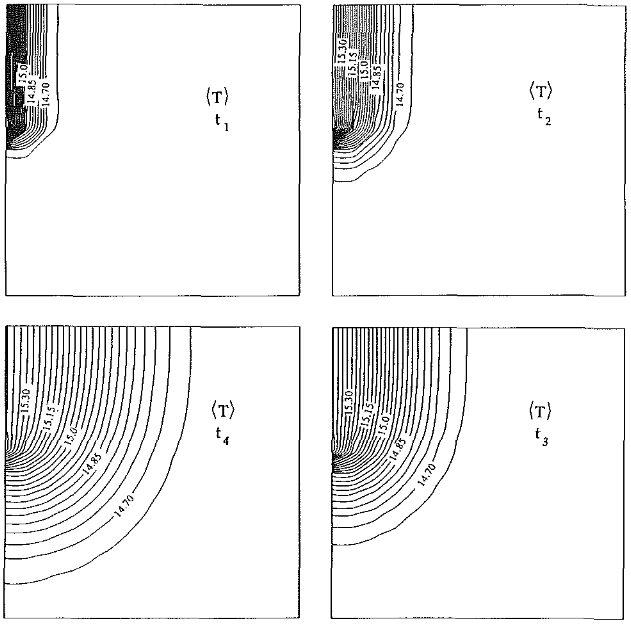

Fig. 2 Variation of temperature inside the porous material for $B=1000$, $B_v=5\times10^4$, and an opening size ratio of 1/2 at four different times: $t_1=0.0005$, $t_2=0.0015$, $t_3=0.005$, $t_4=0.01$

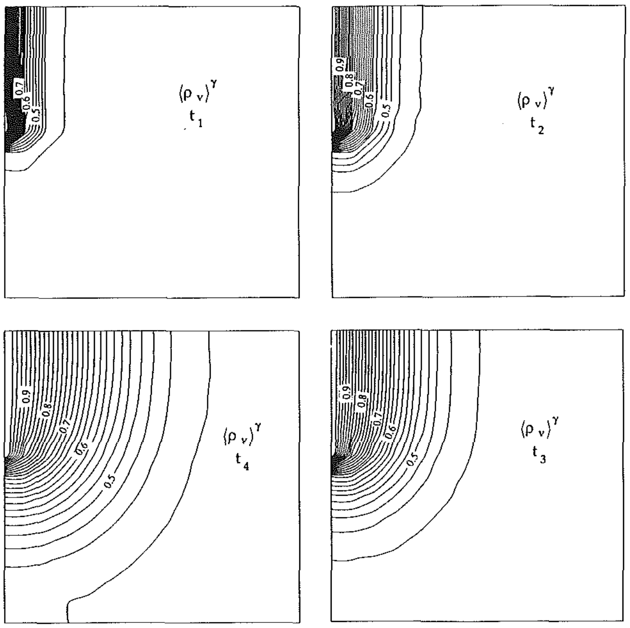

Fig. 3 Vapor density distributions for $B=1000$, $B_v=5\times10^4$, and an opening size ratio of 1/2, at four different times corresponding to Fig. 2

system. However, it should be noted here that although the average gas speed is very small, it still has a significant effect on the overall energy transfer. Since the quality of the velocity fields does not change significantly with respect to time, only the velocity distributions at time t_3 are presented.

The effects of the magnitude of the pressure difference Δp_γ on the heat and mass transfer through porous insulation were investigated. As expected, an increase in the pressure difference causes an increase in the N_{TETR}. Also, an increase in the pressure difference will enhance the thermal penetration, vapor transport, condensation rate, and liquid content.

4.2 Effects of Heat Transfer Biot Number B. The influence of the heat transfer Biot number B on the N_{TETR} and the distributions for the field variables is studied for a selected configuration, namely case 1, while the other parameters are unchanged, i.e., $B_v=5\times10^4$ and the opening size ratio is 1/2. Figure 6 illustrates that increasing the Biot number increases N_{TETR}. However, even though B is increased from 10 to 1000, i.e., two orders of magnitude, the increase in N_{TETR} is not proportional. This is because the energy transfer due to infiltration plays an important role in determining the overall heat transfer. Therefore, the change in the Biot number does not have much influence on N_{TETR}. In Fig. 6, all three curves present some small amplitude oscillations, between $t=0.001$ and $t=0.0015$. This type of oscillating phenomenon was also reported in the work of Patterson and Imberger (1980), Penot (1982), and Staehle and Hahne (1982) on transient natural convection flows.

The effects of the heat transfer Biot number on the field variable, temperature, is illustrated in Fig. 7 for case 1 with $B=10$, $B_v=5\times10^4$, and an opening ratio of 1/2. By comparing Fig. 7 with Fig. 2, it can be seen that a decrease in the Biot number causes a small decrease in the energy transfer rate and so the thermal penetration length decreases. However, the vapor density contours were found almost unchanged since the vapor transfer Biot number B_v was the same in both situations. Since the saturation vapor density is mainly dependent on the temperature, the condensation rate for $B=10$ was found to be higher than that of $B=1000$. This is directly related to the thermal penetration effects. Slower thermal penetration will translate into higher condensation rates. This trend was also observed for the liquid content results. This is because the liquid content is mainly related to the time integration of the condensation rate.

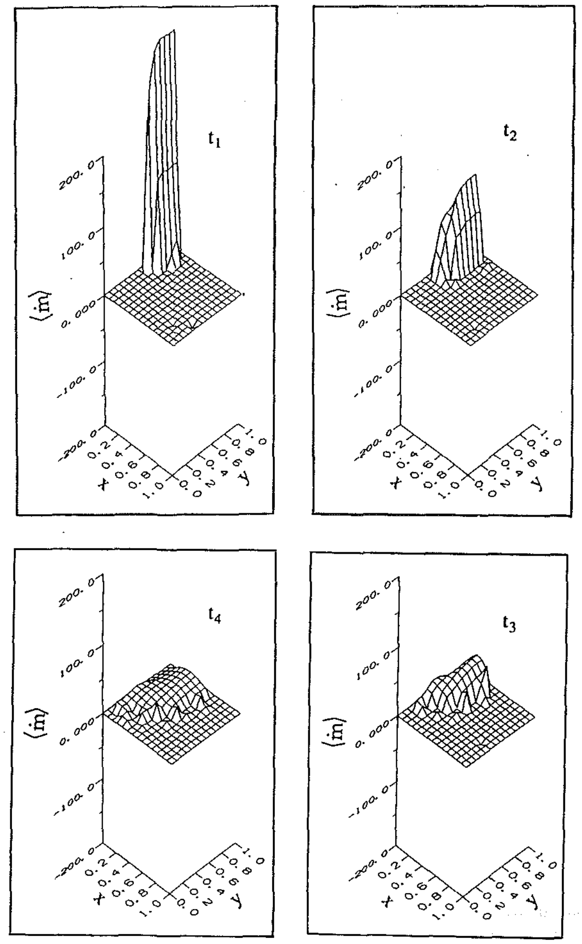

Fig. 4 Condensation rate plots at four different times corresponding to the parameters specified in Fig. 2

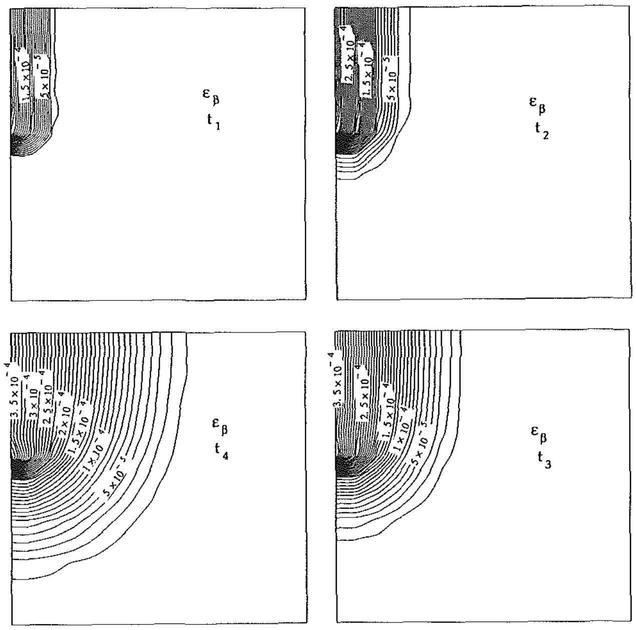

Fig. 5 Liquid content distributions at four different times, corresponding to the parameters specified in Fig. 2

4.3 Effects of the Vapor Transport Biot Number B_v.

To examine the effects of the convective mass transfer boundary conditions, the effects of change in the mass transfer Biot number B_v were examined. Figure 6 presents the N_{TETR} results for two different B_v: $B_v = 5\times 10^4$ and $B_v = 5\times 10^3$ for the same value of heat transfer Biot number, i.e., $B = 1000$. It is observed that at the initial stage, the N_{TETR} for the case with higher B_v is greater than the N_{TETR} for the case with lower B_v, while the reverse trend is true at the later stage. This same phenomenon was also observed when a uniform pressure gradient was imposed across the insulation slab (Tien and Vafai, 1990). As was explained by Tien and Vafai (1990), this phenomenon is due to the fact that initially, the condensation rates close to the left boundary are significantly higher for $B_v = 5\times 10^4$, due to higher rate of vapor transport, than for $B_v = 5\times 10^3$. However, at later times the temperature next to the hot side increases more rapidly for $B_v = 5\times 10^4$, as a result of that extra condensation, than for $B_v = 5\times 10^3$. The effects of B_v on the other field variables were also investigated. It was found that an increase in B_v will lead to an enhancement in vapor transport, condensation rate, and the liquid content.

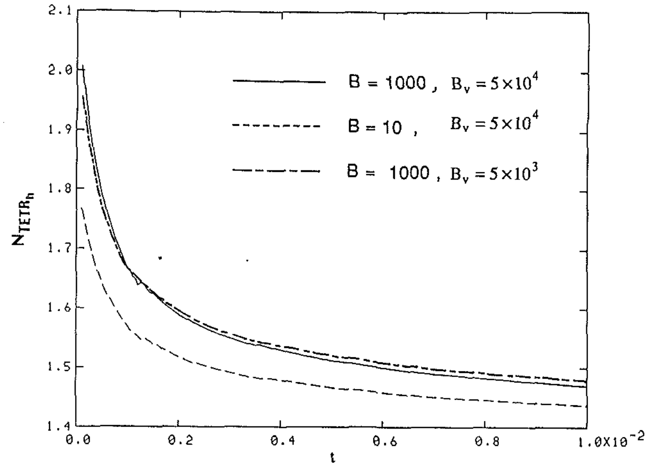

Fig. 6 Effects of the heat transfer Biot number B and the mass transfer Biot number B_v on N_{TETR_h} for an opening size ratio of 1/2

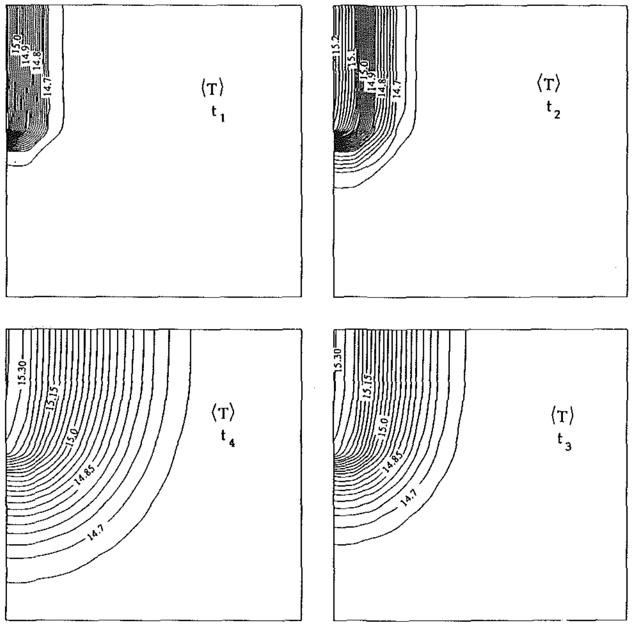

Fig. 7 Variation of temperature inside the porous material for $B = 10$, $B_v = 5\times 10^4$, and an opening size ratio of 1/2 at four different times corresponding to Fig. 2

4.4 Effects of Size of Permeable Area.

The effects of the size of the open region on the N_{TETR} and the field variables

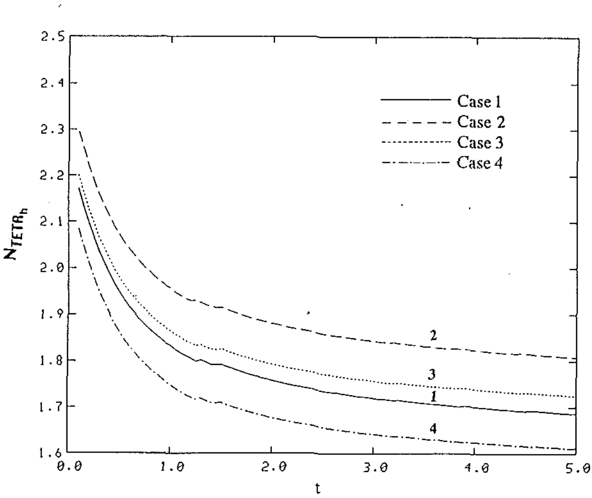

Fig. 8 N_{TETR_h} for the four cases represented in Fig. 1 for $B=1000$, $B_v=5\times10^4$, and an opening size ratio of 1/4

were investigated for all cases; however, due to similarities between all the cases, only the results for case 1 are presented here. It was found that the Nusselt number for a larger opening is less than the N_{TETR} for a smaller opening. This is because the mean air infiltration velocity for the case with a larger opening is lower than that with a smaller opening. This can be explained in terms of the corresponding gas velocity distributions discussed earlier. Therefore, as seen from the definition of N_{TETR} in equation (27), the N_{TETR} for the smaller opening size will become higher than that of the larger opening size. However, it should be clarified that N_{TETR} as defined in this work is based on an averaged heat transfer rate over the permeable area. Therefore, the total heat transfer rate for the larger opening is still greater than that for the smaller opening since the total heat transfer rate is directly dependent on the heat transfer area. The profiles of the field variables for opening = 1/4 are quite similar to the results for opening = 1/2 and hence are not presented here.

4.5 Effects of Opening Locations, Cases 1–4. The effects of the opening locations on transient thermal performance of the porous materials were also investigated in some detail in this work. The N_{TETR} results for the four cases illustrated in Fig. 1 are shown in Fig. 8. Other than the opening locations, other parameters are fixed for the results presented in Fig. 8. That is $B=1000$, $B_v=5\times10^4$, and the opening size is 1/4. It can be seen that case 2 generates the highest N_{TETR}, cases 3 and 1 are next, and case 4 produces the lowest N_{TETR} values. The interesting interrelationship between the N_{TETR} distributions presented in Fig. 8 can be explained as follows. First, it should be noted that although the hydrostatic pressure differences across the porous insulation for the four cases are the same, the gradients across the insulation for cases 2 and 3 are higher than those for cases 1 and 4 due to major differences in the flow paths for these cases, as can be clearly seen in Fig. 9. Next, note that the buoyant effect diminishes the throughflow for case 3 as compared to case 2. This will result in a lower N_{TETR} for case 3 compared to case 2. Finally, the reason for the N_{TETR} for case 1 being higher than case 4 can also be explained in terms of the flow field. In case 1, the flow at the permeable portion of the boundary on the left-hand side essentially enters parallel to the flow field that exists inside the cavity over that portion of the boundary. However, in case 4, the flow at the permeable portion of the boundary enters almost perpendicular to the existing flow field in the cavity. Therefore, this causes the Nusselt number for case 1 to become higher than case 4. The effects of the opening locations on the field variables follow a trend similar to N_{TETR}. The profound qualitative and quantitative effects of the pressure stratification are better crystallized by comparing results shown in Figs. 6, 8, and 9 and Table 1 of the present work with Figs. 11, 15, and 16 and Table 2 of Tien and Vafai (1990). The above results can be utilized for evaluating the heat loss due to cracks and holes in the building insulation.

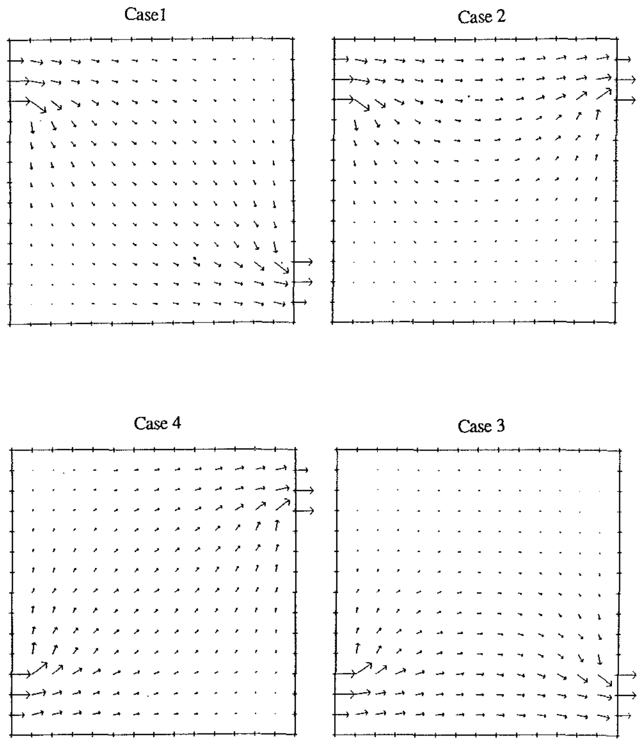

Fig. 9 Velocity distributions at t_3 for the four cases represented in Fig. 1 for $B=1000$, $B_v=5\times10^4$, and an opening size ratio of 1/4

5 Conclusions

Pressure stratification effects on heat and mass transfer in porous insulation materials have been investigated in this work. Proper pressure, temperature, and vapor density boundary conditions were employed to simulate fully the problem of stratified air infiltration in building insulation. The thermal performance of the insulation and the interactions of the field variables were investigated systematically through examining the effects of the Biot numbers, B and B_v, opening area, and the opening locations. The following conclusions were reached:

1 Infiltration was found to have a major effect on the overall heat transfer even when the pressure gradients were small.

2 Only a very large increase in the heat transfer Biot number will lead to a significant increase in the N_{TETR}.

3 Variations in vapor transfer Biot number clearly reveal the complex interactions between the heat and mass transfer fields. The vapor transfer Biot number has an augmenting effect on N_{TETR} during the initial transient heat transfer process; however, the trend is reversed at later times.

4 N_{TETR} decreases with an increase in the size of the permeable area. However, the total heat transfer rate for the larger opening area is still greater than that for the smaller opening area.

5 Pressure stratification had a major impact on the qualitative and quantitative heat transfer characteristics and flow fields corresponding to different opening locations.

Acknowledgments

A grant from the Ohio Supercomputer Center is acknowledged and appreciated.

References

Burns, P. J., Chow, L. C., and Tien, C. L., 1977, "Convection in a Vertical Slot Filled With Porous Insulation," *Int. J. Heat Mass Transfer*, Vol. 20, pp. 919–926.

Burns, P. J., and Tien, C. L., 1978, "Effects of Infiltration on Heat Transfer Through Vertical Slot Porous Insulation," in: *Energy Conservation in Heating, Cooling, and Ventilating Buildings*, C. J. Hoogendoorn and N. H. Afgan, eds., Hemisphere, New York, Vol. 1, pp. 93–105.

Fatt, I., and Klikoff, W. A., 1959, "Effect of Fractional Wettability on Multiphase Flow Through Porous Media," AIME Technical Note No. 2043, *AIME Trans.*, Vol. 216, pp. 426–432.

Kaviany, M., and Mittal, M., 1987, "Funicular State in Drying of a Porous Slab," *Int. J. Heat Mass Transfer*, Vol. 30, pp. 1407–1418.

Langlais, C., Hyrien, M., and Karlsfield, S., 1982, "Moisture Migration in Fibrous Insulating Material Under the Influence of a Thermal Gradient," *Moisture Migration in Building*, ASTM STP, Vol. 779, pp. 191–206.

Lopez, E. L., 1969, "Techniques for Improving the Thermal Performance of Low-Density Fibrous Insulation," *Prog. Astronaut. Aeronaut.*, Vol. 23, pp. 153–172.

Mumaw, J. R., 1968, "Variations of the Thermal Conductivity Coefficient for Fibrous Insulation Materials," M.S. Thesis, The Ohio State University, Columbus, OH.

Ogniewicz, Y., and Tien, C. L., 1981, "Analysis of Condensation in Porous Insulation," *Int. J. Heat Mass Transfer*, Vol. 24, pp. 421–429.

Patterson, J., and Imberger, J., 1980, "Unsteady Natural Convection in a Rectangular Cavity," *J. Fluid Mechanics*, Vol. 100, pp. 65–86.

Penot, J., 1982, "Numerical Calculation of Two-Dimensional Natural Convection in Isothermal Open Cavities," *Numerical Heat Transfer*, Vol. 5, pp. 421–437.

Reddy, G. B., Mulligan, J. C., and Johnson, R. R., 1987, "Analysis of Heat and Mass Transfer in Unsaturated Porous Materials: an Application to Soil With a Heat Source," in: *Multiphase Transport in Porous Media*, ASME FED-Vol. 60, pp. 77–84.

Staehle, B., and Hahne, E., 1982, "Overshooting and Damped Oscillations of Transient Natural Convection Flows in a Cavity," *Proceedings of the Seventh International Heat Transfer Conference*, Vol. 2, pp. 287–292.

Stewart, M. B., 1982, "An Experimental Approach to the Study of Moisture Dynamics in Walls," ASTM STP, Vol. 779, pp. 92–101.

Tien, H. C., and Vafai, K., 1990, "A Synthesis of Infiltration Effects on an Insulation Matrix," *Int. J. Heat and Mass Transfer*, Vol. 33, pp. 1263–1280.

Tye, R. P., and Spinney, S. C., 1979, "A Study of the Effects of the Moisture Vapor on the Thermal Transmittance Characteristics of Cellulose Fiber Thermal Insulation," *J. Thermal Insulation*, Vol. 2, pp. 175–196.

Udell, K. S., 1985, "Heat Transfer in Porous Media Considering Phase Change and Capillarity—the Heat Pipe Effect," *Int. J. Heat Mass Transfer*, Vol. 28, pp. 485–495.

Vafai, K., and Sarkar, S., 1986, "Condensation Effects in a Fibrous Insulation Slab," ASME JOURNAL OF HEAT TRANSFER, Vol. 108, pp. 667–675.

Vafai, K., and Sozen, M., 1990, "Analysis of Energy and Momentum Transport for Fluid Flow Through a Porous Bed," ASME JOURNAL OF HEAT TRANSFER, Vol. 112, pp. 690–699.

Vafai, K., and Tien, C. L., 1981, "Boundary and Inertia Effects on Flow and Heat Transfer in Porous Media," *Int. J. Heat Mass Transfer*, Vol. 24, pp. 195–203.

Vafai, K., and Tien, H. C., 1990, "A Numerical Investigation of Phase Change Effects in Porous Materials," *Int. J. Heat Mass Transfer*, Vol. 32, pp. 1261–1277.

Vafai, K., and Whitaker, S., 1986, "Heat and Mass Transfer Accompanied by Phase Change in Porous Insulations," ASME JOURNAL OF HEAT TRANSFER, Vol. 108, pp. 132–140.

Vasseur, P., Nguyen, T. H., Robillard, L., and Thi, V. K. T., 1984, "Natural Convection Between Horizontal Concentric Cylinders Filled With a Porous Layer With Internal Heat Generation," *Int. J. Heat Mass Transfer*, Vol. 27, pp. 337–349.

Verschoor, J. D., and Greebler, P., 1952, "Heat Transfer by Gas Conduction and Radiation in Fibrous Insulations," *Trans. ASME*, Vol. 74, pp. 961–968.

Whitaker, S., 1977, "Simultaneous Heat, Mass and Momentum Transfer in Porous Media: A Theory of Drying," *Advances in Heat Transfer*, Vol. 13, Academy Press, New York, pp. 119–203.

Whitaker, S., and Chou, W. T. H., 1983, "Drying Granular Porous Media—Theory and Experiment," *Drying Technology*, Vol. 1, pp. 3–33.

Wyllie, M. R. J., 1962, "Relative Permeability," in: *Petroleum Production Handbook*, Frick, ed., Vol. 2, Chap. 25, McGraw-Hill, New York.

Critical Two-Phase Flow in Pipes for Subcooled Stagnation States With a Cavity Flooding Incipient Flashing Model

S. Y. Lee
Research Engineer,
Westinghouse Savannah River Co.

V. E. Schrock
Professor,
Department of Nuclear Engineering,
University of California,
Berkeley CA 94720
Fellow ASME

Analysis of loss of coolant accident (LOCA) scenarios in nuclear reactor safety evaluation depends on knowledge of many complex phenomena. A primary phenomenon controlling the sequence of events, by determining the residual coolant mass inventory within the primary system, is the critical flow process. Critical flow of a flashing liquid is complicated by marked departure from thermal equilibrium. Several complex models have been proposed to represent the non-equilibrium effects, including six-equation two-fluid models. Amos and Schrock (1983) developed a model based on the premise that the two-phase region is homogeneous and that thermal nonequilibrium is the dominant factor causing the departure from the homogeneous equilibrium idealization. Flashing inception was represented by a modification of the Alamgir-Lienhard (1981) pressure undershoot. Exponential relaxation of the metastable liquid was formulated as suggested by Bauer et al. (1976) and the critical flow criterion used the sound speed formulation of Kroeger (1976). Lee and Schrock (1988) extended the Amos-Schrock work by developing an improved correlation for the pressure undershoot correction factor in terms of Reynolds number and subcooling Jakob number. Improvements were also made in the relaxation constant and in the application of Kroeger's formulation. In the present paper a new cavity flooding model is used for the evaluation of pressure undershoot at flashing inception. This model is similar to the one developed by Fabic (1964) for the evaluation of liquid superheat required for boiling on a surface subjected to transient heating. The model contains an experimentally deduced factor, which is correlated against stagnation subcooling using the experimental data of Amos and Schrock (1983, 1984), Jeandey et al. (1981), and the Marviken tests (Anon., 1979). The model was then tested against seven additional data sets and shown to be very accurate in predicted mass flux (standard deviation of 10.9 percent for all data). The cavity flooding model is thought to represent the true physics more correctly than does the earlier model, which had its origin in molecular fluctuation theory.

Previous Work

In recent years, the phenomenon of flashing flow has been studied in relation to the critical flow problem. Models that account for thermal nonequilibrium for initially subcooled or near saturated stagnation states must represent the physics of the nucleation process and the growth of bubbles in a transient pressure environment. Edwards (1968), Ardron (1978), and Richter (1983) are examples of authors who have contributed such detailed mechanistic models. These models involved some adjustable parameters such as initial bubble diameter, bubble number density in the liquid, and initial liquid superheat required to cause bubble nucleation, in order to fit the experimental data. Reviews of these nonequilibrium models have been presented by several authors (for example, Jones and Saha, 1977; Saha, 1978; Abdollahian et al., 1975).

Alamgir and Lienhard (1981) studied the dependence of flashing inception upon the depressurization rate and stagnation temperature in a stagnant liquid. They proposed a semi-empirical correlation for pressure undershoot at the flashing inception point. This correlation was employed by several authors such as Abuaf et al. (1983) and Elias and Chambré (1984) in critical flow modeling.

In an earlier work on nonequilibrium, Henry (1970) introduced a simple correlation for pipes determined from experimental data to represent the lack of thermal equilibrium, and flashing was assumed to occur at $L/D = 12$ for all cases in an arbitrary way. He concluded that the slip ratio for low-quality single-component critical flow should be near unity. It was shown that his model was in good agreement with experimental data obtained by Fauske (1965) and Uchida and Nariai (1966).

Abuaf et al. (1983) presented a study of the nonequilibrium effect on the critical discharge of initially subcooled liquid through nozzles and orifices. Their experimental evidence showed that flashing inception always occurs at or near the nozzle throat. Pressure at the flashing inception was calculated from a modified Alamgir-Lienhard relation. Finally, they obtained a simple correlation for critical mass flux as a function of the pressure drop between the nozzle inlet and the flashing inception. Their empirical model agreed well with data for nozzles.

Levy and Abdollahian (1982) have proposed a model for pipes, which is similar to that of Henry in some respects but less arbitrary in considering the presence of a metastable liquid

---

Contributed by the Heat Transfer Division and presented at the ASME Winter Annual Meeting, Chicago, Illinois, November 28-December 2, 1988. Manuscript received by the Heat Transfer Division July 18, 1989; revision received April 25, 1990. Keywords: Multiphase Flows, Nonequilibrium Flows, Phase-Change Phenomena.

phase using a slight modification to the Alamgir–Lienhard relation rather than specifying a fixed position of flashing inception as in Henry's model. In order to predict the critical flow rate, isentropic and homogeneous flow was assumed. The isentropic assumption in their model makes the model easy to apply, but this assumption still cannot be true. Friction is the only cause of state change in this Fanno-like process. Their comparisons showed overall good agreement with the large-scale Marviken data and some other small-scale experimental data.

Recently, Amos and Schrock (1983) developed a new homogeneous nonequilibrium model (HNEM) with a pressure undershoot at flashing inception. The pressure undershoot relation was obtained from the Alamgir–Lienhard correlation with a modification factor, which was correlated as a function of fluid velocity from the experimental data for their thin slit geometry. Relaxation of the metastable liquid phase produced by flashing delay was assumed to occur exponentially as was suggested by Bauer et al. (1976). The critical flow criterion was taken from Kroeger's (1976) expression for nonequilibrium sound speed in homogeneous flow. The conservation equations were derived from the two-fluid conservation equations with assumption of homogeneous flow. Model predictions showed good agreement with their experimental data for thin slits and with data of Jeandey et al. (1981). John et al. (1988) also carried out experiments on the critical two-phase discharge rate through a slit geometry for subcooled stagnation conditions in order to simulate cracks in the context of leak-before-break philosophy. The experimental data were compared with calculated values from different models.

Approach of Present Work

Most previous works on nonequilibrium models discussed in the previous section used the homogeneous flow model with the assumption of frictionless flow, or a two-fluid model with the assumption of frictionless flow or a detailed mechanistic model (bubble dynamics) including several adjustable parameters. For the critical flow criterion they used either an arbitrarily large pressure gradient or the method of characteristics to obtain a sound speed at the choking plane. They used a fixed flashing position or neglected the detailed influence on pressure undershoot at flashing inception of the stagnation conditions.

However, from the experimental evidence the amount of pressure undershoot due to flashing delay is known to play a strong role in the critical discharge rate (e.g., Reocreux, 1978; Amos and Schrock, 1983; Anon., 1979).

The primary purpose of the work presented here is to extend Amos and Schrock's (1983) model and to describe flashing delay for subcooled stagnation conditions on a more physical basis. Two distinct approaches have been followed. In the first, we have sought to correlate the pressure undershoot correction factor in terms of dimensionless parameters. In the second, we have developed a new cavity flooding mechanistic model of incipient flashing in channel flow. Both approaches are successful in giving accurate critical flow predictions.

Model Formulation

General Set of Governing Equations. Before flashing inception the standard single-phase equation is used. The model for the evaluation of flashing inception after pressure undershoot is described in the next section.

Beyond incipient flashing, two-phase mixture conservation equations are considered with negligible interphase slip, i.e., homogeneous flow. The vapor phase is assumed to be saturated at the local pressure, while the liquid phase is assumed to be superheated (metastable). Vapor properties were calculated from the equations of thermodynamic properties for saturated steam (Ishimoto et al., 1972). Properties of the metastable liquid were evaluated by extrapolating the subcooled liquid properties into the metastable region. The specific heat of superheated water was estimated from the work of Lienhard (1977).

Nomenclature

A = area, m^2
a = sound speed, m/s
c_{p_l} = liquid specific heat, J/kg•K
D_e = equivalent hydraulic diameter, m
f_e = Weisbach friction factor in the entrance region
f = Weisbach friction factor in the fully developed flow region
G = mass flux, kg/m^2•s
g = gravitational acceleration, m/s^2
h = enthalpy, J/kg
Ja = $\rho_l c_{pl} \Delta T_{\text{sub}} / \rho_g h_{fg}$
K_e = entrance loss coefficient associated with kinetic energy change $= 1 -$ (area ratio)^2
K_f = average distributed entrance loss coefficient in the entrance region = $f_e L_e / D_e$
L = channel length, m
L_e = entrance, m
m = mass flow rate, kg/s
p = pressure, Pa
r_c = cavity radius, m
R = channel radius or parameter for sound speed, m
R_1, R_2 = curvature radius of meniscus, m
R_e = $D_e \rho u / \mu$
s = entropy, J/kg•K
T = temperature, K
T_r = reduced temperature
t = transit time, s
t_r = fluid residence time, s
u = fluid velocity, m/s
v = specific volume, m^3/kg
x = flow quality
z = spatial position, m
α = void fraction
β = thermal expansion coefficient and Kroeger's nonequilibrium mass transfer parameter, K^{-1}
β_a = advancing contact angle, deg
β_r = receding contact angle, deg
Δ = difference
ϵ = roughness height of channel surface, m
η = geometric correction factor
θ = total cavity angle at meniscus, deg
κ = isothermal compressibility, Pa^{-1}
μ = viscosity, kg/m•s
ρ = density, kg/m^3
τ = relaxation time, s
σ = surface tension, N/m

Subscripts

act = actual
c = critical
E = equilibrium
ent = entrance
Fl = flashing
f = friction
g = vapor
HF = homogeneous frozen
l = liquid
m = mixture
o = stagnation
p = pressure
r = reduced (divided by critical value)
sat = saturated
sub = subcooled

The steady-state conservation equations were derived by summing the two-fluid phasic equations. The resulting mixture conservation equations do not contain any interphase transfer terms. Heat transfer at the two-phase interface is accounted for in the model by a liquid superheat relation. The following are the governing equations employed for this model (derivation of equations (1) and (3) is given in Appendix):

Mass conservation:

$$\frac{1}{u}\left(\frac{du}{dz}\right) = \frac{(v_g - v_l)}{v_m}\left(\frac{dx}{dz}\right) + \frac{1}{v_m}\left\{x\left(\frac{dv_g}{dp}\right)_{\text{sat}} + (1-x)\left(\frac{\partial v_l}{\partial p}\right)_{T_l}\right\}\left(\frac{dp}{dz}\right) + \frac{(1-x)}{v_m}\left(\frac{\partial v_l}{\partial T_l}\right)_p\left(\frac{dT_l}{dz}\right) \tag{1}$$

Momentum conservation:

$$\frac{u}{v_m}\left(\frac{du}{dz}\right) = -\left(\frac{dp}{dz}\right) - \left(\frac{dp}{dz}\right)_f + \frac{g}{v_m}$$

Energy conservation:

$$\left\{x\left(\frac{dh_g}{dp}\right)_{\text{sat}} + (1-x)\left(\frac{\partial h_l}{\partial p}\right)_{T_l}\right\}\left(\frac{dp}{dz}\right) + (h_g - h_l)\left(\frac{dx}{dz}\right) + (1-x)c_{p_l}\left(\frac{dT_l}{dz}\right) + u\left(\frac{du}{dz}\right) = 0 \tag{3}$$

In order to complete the homogeneous nonequilibrium model, an equation of state is required:

for vapor, assumed saturated,

$$v_g = v_g(p) \quad h_g = h_g(p) \tag{4}$$

for superheated liquid,

$$v_l = v_l(p,\ T_l) \tag{5}$$

$$h_l = h_l(p,\ T_l) \tag{6}$$

The liquid superheat relation is given by a profile-fit-type equation

$$\left(\frac{dp}{dT_l}\right)_{\text{sat}}\left(\frac{dT_l}{dz}\right) - \left(\frac{dp}{dz}\right) + \left(\frac{dp}{dz}\right)_{Fl}\exp\left(-\frac{t_r}{\tau}\right) = 0 \tag{7}$$

where t_r is the residence time of the two-phase mixture after flashing inception. The residence time (t_r) is given by

$$t_r = \int_{z_{Fl}}^{z}\frac{dz'}{u(z')} \tag{8}$$

Metastable liquid properties were obtained by extrapolation of VDI (1974) equations (5) and (6) into the superheat region. The derivatives in equations (1) and (3) are obtained as

$$\left.\frac{\partial v_l}{\partial p}\right|_{T_l} = -v_l\kappa \tag{9}$$

where the isothermal compressibility can be represented by $\kappa = 6.570 \times 10^{-7} v_l$, and

$$\left.\frac{\partial v_l}{\partial T_l}\right|_p = v_l\beta \tag{10}$$

where $\beta = 2.693455 \times 10^1\, e^{T_r} - 9.360687 \times 10^1\, e^{-T_r} - 1.672643 \times 10^1\, T_r^3 + 3.125661 \times 10^1\, T_r^2 - 1.198906 \times 10^2\, T_r + 6.659029 \times 10^1$. For the evaluation of $\partial h_l/\partial p|_{T_l}$, Gibb's equation can be used:

$$\left.\frac{\partial h_l}{\partial p}\right|_{T_l} = T_l\left.\frac{\partial s}{\partial p}\right|_{T_l} + v_l \tag{11}$$

With the use of Maxwell relations, equation (11) becomes

$$\left.\frac{\partial h_l}{\partial p}\right|_{T_l} = (1 - \beta T_l) \tag{12}$$

Finally, in order to provide closure to the differential equations, additional auxiliary equations are needed for the frictional pressure gradient, the location of incipient flashing, and the choking criterion.

In equation (2) the frictional pressure gradient, as proposed by Levy (1960), is given by

$$\left(\frac{dp}{dz}\right)_f = -\frac{f}{(1-\alpha)^2}\frac{G^2(1-x)^2}{2D_e}v_l \tag{13}$$

f is the single-phase friction factor, for which we have used Colebrook's correlation (1939) in the turbulent regime

$$\frac{1}{\sqrt{f}} = -2\log_{10}\left\{\frac{1}{3.7}\left(\frac{\epsilon}{D_e}\right) + \frac{2.51}{\text{Re}\sqrt{f}}\right\};\quad \text{Re} > 4.0 \times 10^3 \tag{14}$$

If the energy equation (3), a specific heat relation for metastable liquid is required. From curve fitting of Lienhard's (1977) graphic estimation of specific heat of superheated water we obtained

$$c_{p_l} = 9.677258 \times 10^7 e^{T_r} - 7.752401 \times 10^6 T_r^4 - 1.081435 \times 10^7 T_r^3 - 5.193637 \times 10^7 T_r^2 - 9.562871 \times 10^7 T_r - 9.691202 \times 10^7 + \frac{4.470480(1 - 1.2p_r^2)}{\left[0.905 + 0.095\left(\frac{T_{\text{sat}}(p)}{T_c}\right)^8 - T_r\right]^{\sqrt{3}}} \tag{15}$$

For the solution of the model the flashing inception position (z_{Fl}) has to be evaluated. This position is evaluated for the given stagnation state (p_o, T_o) by the following procedure:

(*a*) When flashing occurs in the entrance region ($p_{Fl} > p_{\text{ent}}$),

$$z_{Fl} = \frac{L_e\left(p_o - \frac{1}{2}K_e\rho_o u_m^2 - p_{\text{sat}}(T_o) + \Delta p_{Fl}\right)}{\frac{1}{2}K_f\rho_o u_m^2} \tag{16}$$

The average distributed friction factor in the entrance region was evaluated using a relation of Schlichting (1979), giving K_f of about 0.9.

(*b*) When the flashing occurs in the fully developed region ($p_{Fl} < p_{\text{ent}}$)

$$z_{Fl} = L_e + \frac{\left(p_o - \frac{1}{2}(K_e + K_f)\,\rho_o u_m^2 - p_{\text{sat}}(T_o) + \Delta p_{Fl}\right)D_e}{\frac{1}{2}f\rho_o u_m^2} \tag{17}$$

The entrance length for turbulent flow was given by Schlichting, i.e.,

$$\frac{L_e}{D_e} = 1.487\ \text{Re}^{0.25} \tag{18}$$

The solution of the differential equations described in this section depends on the flashing condition

$$\begin{aligned} &\text{at } z = z_{Fl} : x = 0 \\ &p = p_{\text{sat}}\{T_l(z_{Fl})\} - \Delta p_{Fl} \\ &t_r = 0 \\ &T_l = T_o \\ &u = u_{Fl} \end{aligned} \tag{19}$$

where Δp_{Fl} can be found from the model of flashing inception.

In equation (7), the time constant (τ) related to the relaxation was chosen to give the best agreement between the pressure profile predictions and the experimental data. For the present model a value of 1.0 for τ is recommended, whereas Amos chose $\tau = 1.1 \times 10^{-3}$. The influence of τ upon the critical mass flux was found to be weak. When τ is changed from 10^{-5} s to 10^2 s, only a 10 percent increase in predicted mass flux is found. The lower values of τ used by Amos and Schrock resulted in poorer agreement between measured and predicted pressure profiles.

So far there are several criteria for critical flow conditions advanced in the literature. Among these, Kroeger's (1976) sound speed was chosen for the choking criterion by Amos and Schrock and in the present model. The flow is choked when the local fluid velocity is equal to the local sound speed. Kroeger derived the sound speed for nonequilibrium two-phase flow. He used the method of characteristics applied to a four-equation drift flux model, which assumed the vapor phase to be saturated at the local pressure. For zero drift velocity (no slip) the sound speed was given by

$$a = \frac{a_{HF}}{\sqrt{1 - \dfrac{R\beta a_{HB}^2}{v_m}}} \tag{20}$$

In the above equation a_{HF} (homogeneous frozen sound speed) was given by

$$a_{HF} = v_m \left\{ \frac{1}{c_{p_l}} \left(\frac{\partial v_l}{\partial T_l} \right)_p \left[x \left(\frac{dh_g}{dp} \right) - v_m \right] - x \left(\frac{dv_g}{dp} \right) - (1-x) \left(\frac{\partial v_l}{\partial p} \right)_{T_l} \right\}^{-1/2} \tag{21}$$

This sound speed corresponds to that of a particular situation in which no heat or no mass transfer takes place between vapor and liquid; thus, the quality remains constant throughout the wave. R is the nondimensional two-phase mixture compressibility given by

$$R = \frac{1}{V_m} \left\{ (v_g - v_l) - \frac{(h_g - h_l)}{c_{p_l}} \left(\frac{\partial v_l}{\partial T_l} \right)_p \right\} \tag{22}$$

The parameter β accounts for nonequilibrium mass transfer, i.e.,

$$\beta = \beta_{\text{HEM}} \left\{ 1 + \frac{(x_E - x)}{\tau^*} \right\} \tag{23}$$

where β_{HEM} is the factor related to the equilibrium mass transfer due to local pressure change

$$\beta_{\text{HEM}} = \frac{\left\{ v_m - x \left(\dfrac{dh_g}{dp} \right)_{\text{sat}} - (1-x) \left(\dfrac{dh_f}{dp} \right)_{\text{sat}} \right\}}{h_{fg}} \tag{24}$$

x_E is the equilibrium thermodynamic quality corresponding to the local two-phase mixture enthalpy

$$x_E = \frac{(h_m - h_f)}{(h_g - h_f)} \tag{25}$$

The nondimensional parameter, τ^*, was used to characterize the rate of relaxation of metastable liquid at the choking location. The present model was found to be insensitive to the value of τ^* for $\tau^* > 1$. For $\tau^* > 1$, the pressure gradient as well as gradients of the other dependent variables were very large at the channel exit. It was taken as 2.5 in the present work, which results in exit pressure gradients on the order of 10^{12} Pa/m. Larger values of τ^* result in larger gradients. Using $\tau^* < 1$ in the present model results in nearly identical prediction of the critical mass flux (within 0.1 percent).

Equations (1)-(25), with a flashing inception model, fully describe the steady flow from a stagnation reservoir through a constant area channel to the location of choking. Solution of the equation set is accomplished by a numerical marching procedure. Stagnation state and channel dimensions are specified and a first guess mass flux assumed. The solution is then generated marching downstream until the choking condition is reached or the end of the channel is reached with the flow still subcritical. The mass flux is then adjusted accordingly and the calculation repeated until the mass flux that produces choking at the channel exit is found. The procedure is fast running, typically requiring 20 seconds on an IBM 3090.

Models for Flashing Inception

I. Molecular Fluctuation Theory. Little work has been done examining the point of flashing inception. An experimental and theoretical study about flashing delay was performed by Alamgir and Lienhard (1981) and by Jones and Saha (1977). The Alamgir–Lienhard correlation was developed from static depressurization data in a semi-empirical way. They used the theory of homogeneous nucleation, modified to take into account the smaller work required to create a truncated spherical nucleus on the bounding wall. Such a nucleus is created by the inherent molecular energy fluctuations in the superheated liquid state and is not dependent upon trapping of the gaseous phase in the wall cavities.

Amos and Schrock (1983) employed the pressure undershoot relation from the Alamgir–Lienhard (1981) correlation with a modification factor, which was correlated as a function of fluid velocity from the experimental data for their thin slit geometry. Following their work, the Alamgir–Lienhard relation for pressure undershoot was also used as a basis of flashing inception by Lee and Schrock (1988) in previous work. The pressure undershoot at flashing was taken as the Alamgir–Lienhard relation multiplied by the modifying factor S, i.e.,

$$\Delta p_{Fl} = S \frac{0.252\, \sigma^{1.5} T_r^{13.73} \sqrt{1 + 14\Sigma^{0.8}}}{\sqrt{k_B T_c} \left(1 - \dfrac{v_l}{v_g} \right)} \tag{26}$$

The pressure undershoot at flashing inception (Δp_{Fl}) is defined as

$$\Delta p_{Fl} = p_{\text{sat}} \{ T_l(z_{Fl}) \} - p(z = z_{Fl}) \tag{27}$$

Hence, the point at which flashing inception occurs directly affects the initial liquid superheat, and the amount of liquid superheat can be expected to play an important role in vapor generation under flashing critical flow conditions. The factor S (which ranges from 0 to 1) was correlated by Lee and Schrock (1988) in terms of Reynolds number and subcooling Jakob number in the form

$$S = f(\text{Re, Ja}) = f_1(\text{Re})\, f_2(\text{Ja}) \tag{28}$$

Three data sources were used to develop the following correlation. They were those of Amos and Schrock (1983), Schrock et al. (1986), and the Marviken test (Anon., 1979). The data for saturated liquid stagnation states were used to obtain

$$f_1 = \begin{cases} 0.6385\ \text{Re}^{0.1} - 1.689\ (\text{Re} > 5.5 \times 10^5) \\ 0.70\ (\text{Re} < 5.5 \times 10^5) \end{cases} \tag{29}$$

The data for subcooled stagnation states were used to obtain

$$f_2 = 1.40 - 0.40\, e^{-0.28\ \text{Ja}} \tag{30}$$

This correlation was reported previously by Lee and Schrock (1988). It was shown that the HNEM using this flashing correlation was able to predict all the available data for straight channel geometry (nine data sets, including the three used to obtain the S correlation) with a standard deviation of 9.6 percent. Considering the wide range of parameters (D_e, L/D_e,

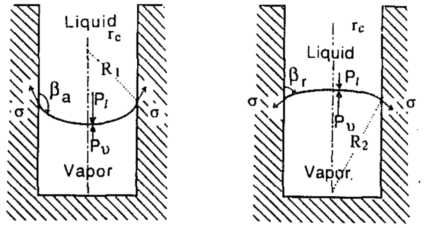

Subcooled liquid advancing into the cavity

Superheated liquid receding from the cavity

Fig. 1 Reference cylindrical cavity for nucleation model

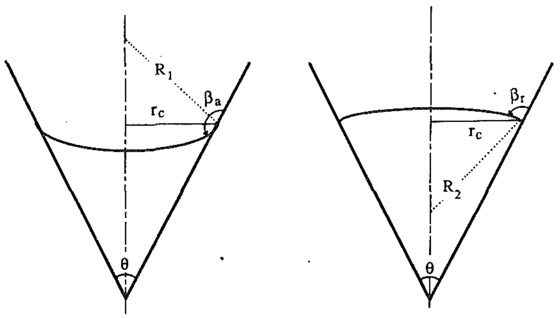

$r_c = R_1 \operatorname{Cos}(\pi - \beta_a + 0.5\theta)$

$r_c = R_2 \operatorname{Cos}(\beta_r - 0.5\theta)$

Subcooled liquid advancing into the cavity

Superheated liquid receding from the cavity

a. Straight Conical Cavity

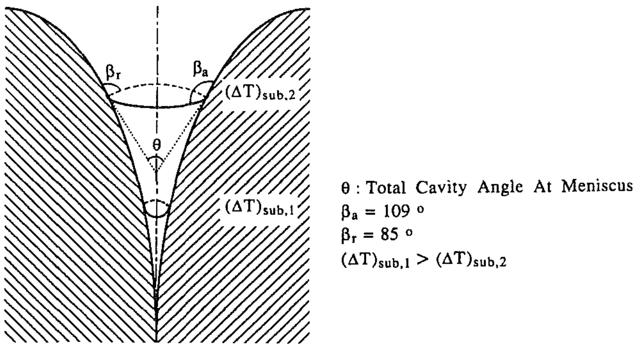

θ : Total Cavity Angle At Meniscus
$\beta_a = 109°$
$\beta_r = 85°$
$(\Delta T)_{sub,1} > (\Delta T)_{sub,2}$

b. More Realistic Cavity

Fig. 2 Interface in conical cavities

p, and Ja) involved in the experimental data base, this is an excellent result and the new HNEM in this form is therefore a highly useful practical (simple and accurate) method to obtain the critical mass flux in straight channels for liquid stagnation states. On the other hand, since the factor S has a value significantly less than unity for much of the data, it appears that the true physics of nucleation at the wall must be gas/vapor trapped in wall cavities rather than molecular fluctuations in the superheated liquid. This has prompted us to seek a flashing inception model based on cavity flooding.

II Cavity Flooding Nucleation Model. It is proposed that incipient flashing is caused by nucleation from wall cavities, similar to nucleate boiling. Liquid superheat is developed by the declining pressure in the isothermal (and adiabatic) single phase flow. At some level of superheat and corresponding pressure undershoot (below saturation), unflooded cavities begin to nucleate.

Fabic (1964) developed a cavity flooding model to predict nucleation on surfaces subjected to transient heating. In his analysis the size of the largest unflooded cavity was related to surface tension, advancing contact angle, and liquid subcooling. Heating causes a rise in vapor pressure, which turns the meniscus until the receding contact angle is reached. Then, further heating causes the meniscus to move out of the cavity. The present problem is similar except that superheating is caused by depressurization rather than heating. Thus, we have adopted this contact angle hysteresis concept for the present model. A different cavity nucleation model was proposed by Shin and Jones (1986). However, their model focused on the nucleation frequency, not upon the incipience of flashing.

When the liquid meniscus enters the nonflooded cavity, a force balance across the liquid-vapor interface yields the following expression:

$$p_l - p_v = \frac{2\sigma}{R_1} \tag{31}$$

This expression relates the radius of curvature to the thermodynamic state (liquid subcooling), which determines the vapor pressure p_v. It is assumed that gas partial pressure is negligible. The radius of curvature is also related to the cavity geometry (angle at the line of contact) and the contact angle. The essence of Fabic's model is that during flooding there exists an advancing contact angle $\beta_a > 90$ deg which can support a pressure difference even when the cavity angle is zero. In the present application, depressurization of the liquid causes a reversal of the pressure difference and the corresponding turning of the meniscus, with the contact line fixed until the receding angle $\beta_r < 90$ deg is reached. The meniscus then begins to move out of the cavity. Figure 1 illustrates the configurations during flooding and at nucleation in a right cylindrical cavity. At nucleation

$$p_v - p_l = \frac{2\sigma}{R_2} \tag{32}$$

in which R_2 is related to the cavity geometry and the receding contact angle. In equation (32) p_v is the saturation pressure corresponding to the stagnation temperature and p_l is the local pressure at incipient nucleation. Fabic suggested, based on data of Stigall (1964) and others for water on stainless steel, that $\beta_a = 109$ deg and $\beta_r = 85$ deg and these values were adopted for numerical work here.

While the contact angles are now known, the details of the cavity shapes remain unknown. Therefore, our approach is to choose a simple reference geometry, a right cylindrical cavity, for the basic model. An empirically based correction factor is then developed to account for the effect of geometry (and perhaps the role of gas). Now, the cavity radius shown in Fig. 1 is related to contact angle, R_1 and R_2, by

$$r_c = R_1 \cos(\pi - \beta_a) = R_2 \cos \beta_r \tag{33}$$

Combining equations (32) and (33) to eliminate R_2 gives

$$p_l = p_v - \frac{2\,\sigma \cos \beta_r}{R_1 \cos(\pi - \beta_a)} \tag{34}$$

This equation gives the flashing inception pressure for use in equation (27). Thus, the basic model predicts the pressure undershoot. We assume that stagnation subcooling governs the flooding condition.

In general, the geometry is not a right cylinder but something more complex. An actual cavity of angle θ (shown in Fig. 2) would require a smaller value of R_2. Therefore, we define

$$\eta = \frac{R_{2,\,\mathrm{act}}}{R_2} \tag{35}$$

Values of η are found from experimental data (Δp_{Fl}) by use of equation (32) to obtain

$$R_{2,\,\mathrm{act}} = \frac{2\,\sigma(T_o)}{\Delta p_{Fl,\,\mathrm{exp}}} \tag{36}$$

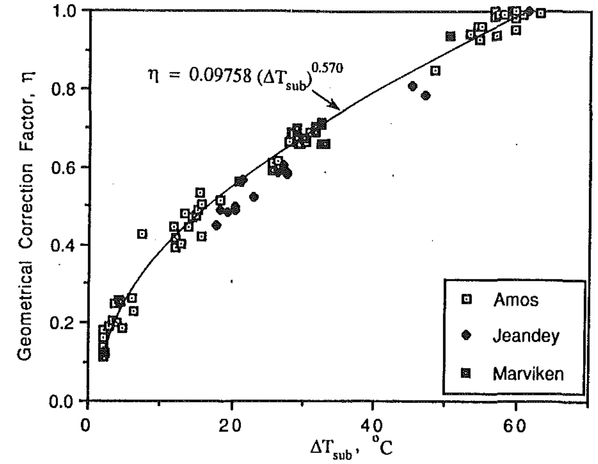

Fig. 3 Correlation of geometric correction factor for subcooled liquid

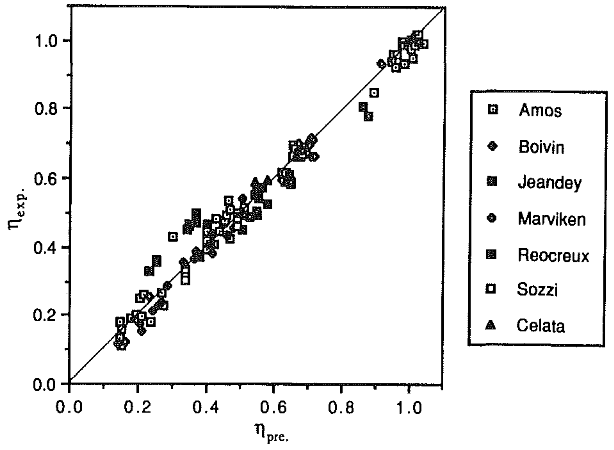

Fig. 4 Comparison of the correlation of geometric correction factor with additional data sets

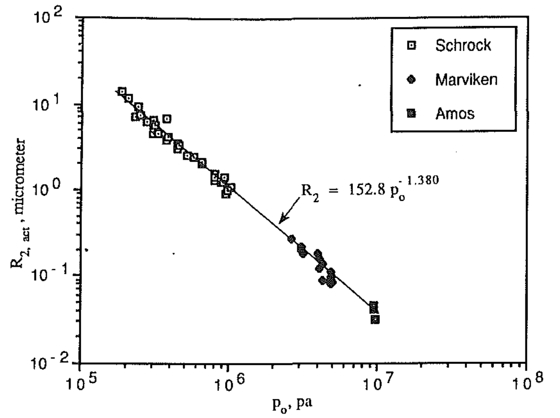

Fig. 5 Correlation of receding meniscus radius for saturated liquid

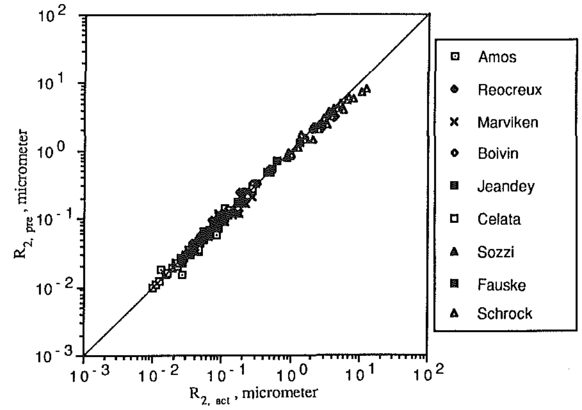

Fig. 6 Comparison of predicted receding meniscus radius with all data sets (saturated and subcooled liquid)

With use of equation (33), equation (35) becomes

$$\eta = \frac{R_{2,\ \mathrm{act}} \cos \beta_r}{R_1 \cos (\pi - \beta_a)} \tag{37}$$

From IAPS (1975) the surface tension may be represented by

$$\sigma = 0.2358(1 - T_r)^{1.256}\{1 - 0.625(1 - T_r)\} \tag{38}$$

When the actual geometry of the cavity is assumed to be conical, the geometric correction factor η can also be expressed by conical angle θ, for the given contact angles with the use of equation (33) and geometric relation for conical cavities as Fig. 2.

$$\eta = \frac{R_{2,\mathrm{act}}}{R_2}$$

$$= \frac{\cos (\pi - \beta_a + 0.5\ \theta) \cos \beta_r}{\cos (\pi - \beta_a) \cos (\beta_r - 0.5\ \theta)} \tag{39}$$

Equation (39) provides a theoretical basis for η if cavities have conical shapes. It shows that η should depend upon subcooling. This dependence is confirmed by plotting η found from experimental results versus subcooling (see Fig. 3). The correlation is found as

$$\eta = \begin{cases} 0.09758\ (\Delta T_{\mathrm{sub}})^{0.570}, & 0 < T_{\mathrm{sub}} \le 59.3\,^\circ\mathrm{C} \\ 1.0, & \Delta T_{\mathrm{sub}} \ge 59.3\,^\circ\mathrm{C} \end{cases} \tag{40}$$

It should be noted that the theoretical limit of $\eta = 1.0$ is also confirmed by the data. Three data sets, Amos and Schrock (1983), Jeandey et al. (1981), and Marviken (Anon., 1979), were used to obtain Fig. 3 and the correlation equation (40). The model was subsequently applied to all data sets with subcooling. The results presented in Fig. 4 show an agreement with a standard deviation of 10.5 percent.

When the liquid is saturated in the stagnation state, the basic cylindrical cavity model becomes indeterminant, i.e., equation (31) gives $R_1 = \infty$. Equation (33) then shows that R_2 is indeterminate. This implies the $\Delta p_{Fl} \rightarrow 0$. However, from the experiment we know that pressure undershoot is not zero even for saturated liquid. In this case the data for $R_{2,\ \mathrm{act}}$ have been correlated against absolute pressure (see Fig. 5). The data sets of Schrock et al. (1986), Amos and Schrock (1983), and Marviken (Anon., 1979) were used to obtain this correlation.

Now using the correlations (saturated and subcooled cases) to calculate $R_{2,\ \mathrm{act}}$, good agreement is found for all the 256 data points (standard deviation of 10.9 percent) as shown in Fig. 6.

In equation (36) we have employed an "experimental" Δp_{Fl}. This quantity is not available as a direct experimental observation in any of the critical flow experiments. In principle it can be found from measured pressure or void fraction profiles, but these methods are quite inaccurate. In this work we have used the flow model, with trial and error procedure, to obtain the values of Δp_{Fl} that produces the best agreement with the measured critical mass flux in each experiment. The data of Reocreux provide the only significant opportunity for comparison with direct measurements (void profiles). As it turns out, there is a consistent bias (about 15 percent) between his data and our correlation for Δp_{Fl}. However, his test section was machined (rather than drawn tubing) in the region of incipient flashing and very likely had unusual characteristics. In any case the comparison of the correlation with Δp_{Fl} obtained from Reocreux's void profiles shows the same trend.

To illustrate further the consistency of the cavity flooding model, we have calculated the equivalent cavity radius at the location of maximum meniscus penetration corresponding to the experimentally inferred Δp_{Fl}. As shown in Fig. 7, the model predicts the cavity radius at the meniscus position corresponding to nucleation in good agreement, showing the dependence upon stagnation conditions, with the values obtained from the experimentally inferred Δp_{Fl}.

Discussion of Results

In the previous section it was shown that the cavity flooding model correlation of the experimentally inferred Δp_{Fl} based on just three data sets also represented well six additional sets of data. The total data base for channels of constant cross-sectional area is given in Table 1. [The last entry in the table, recent data of John et al. (1988), was not used in qualifying the cavity flooding model.] A very wide range of equivalent diameter, *L/D*, and stagnation state is covered by the data. The cavity flooding model correlation of Δp_{Fl} has been used in the critical flow model to predict the results of all ten data sets. The results are compared with experimental data in Fig. 8. The last column in Table 1 gives the standard deviation between predicted and measured mass flux. It varies from 6.6 percent for the data of Boivin (1979) to 15.4 percent for the data of Reocreux (1978) and the overall deviation is 10.9 percent. (Reocreux's was the only data set to show a consistent bias.) This excellent agreement is about the same as obtained previously by Lee and Schrock (1988) using the correlation based upon molecular fluctuation. However, the cavity flooding model is preferred because it more correctly describes the physics of the nucleation process.

A good critical flow model must predict correctly the local state as the fluid progresses from the stagnation state to the critical state. Thus, the pressure at the point of choking is also an important test of the model. Critical pressure ratios are compared in Fig. 9 for all data for which they were reported (five sets). Although the model predicts the data well on the average, the scatter is considerably greater than in the mass flux data. This is due to difficulty in measuring pressure at the point of maximum pressure gradient. It is worth noting

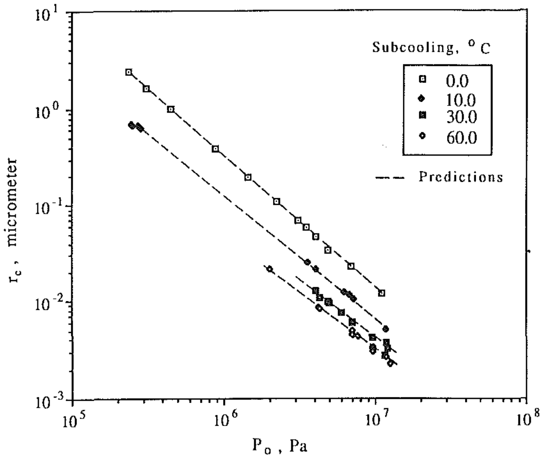

Fig. 7 Cavity radius at point of greatest penetration

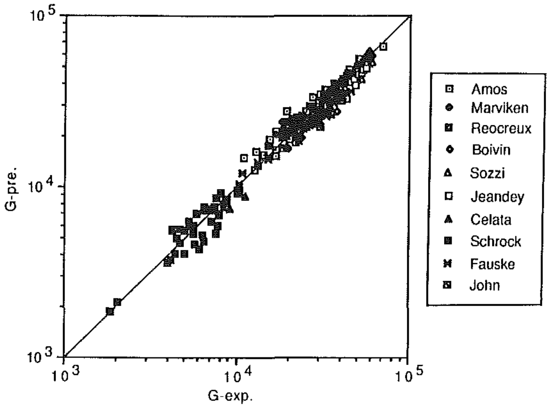

Fig. 8 Comparison of predicted critical mass flux using cavity flooding model with ten experimental data sets

Table 1 Range of stagnation conditions and dimensions for comparison of experiments

Ahthor (Date)	Stagnation Pressure(MPa)	Subcooling Jakob No.	Re	D_c (m x 10^3)	L/D_c	Standard Deviation of Exp. Data and Predictions (%)
Amos & Schrock (1983)	2.73 to 15.70	0 to 18	2.0×10^4 to 5.0×10^5	0.159 to 0.748	85 to 400	11.1
Jeandey et al (1981)	2.0 to 8.39	15 to 44	1.0×10^6 to 4.0×10^6	2.0	17	10.6
Celata et al. (1983)	1.0 to 3.5	0 to 10	5.0×10^5 to 2.0×10^6	12.5	10 to 288	9.16
Reocreux (1978)	0.2 to 0.34	9 to 25	2.0×10^5 to 6.0×10^5	20	134	15.4
Schrock et al. (1986)	0.2 to 1.07	0 to 0.1	2.0×10^4 to 2.0×10^5	3.76 to 6.32	19 to 33	12.0
Marviken (Anon.,1979)	2.6 to 5.2	0 to 10	6.0×10^7 to 3.0×10^8	200 to 509	0.3 to 3.6	11.3
Fauske (1965)	0.79 to 12.07	0	2.0×10^5 to 2.0×10^6	6.35	8 to 40	9.22
Boivin (1979)	1.96 to 10.1	1 to 7	5.0×10^6 to 2.0×10^7	12 to 50	37 to 58	6.60
Sozzi & Sutherland(1975)	6.2 to 6.9	0 to 5	2.0×10^6 to 5.0×10^6	12.7	7 to 143	10.5
John et al. (1988)	4.0 to 10.0	0.1 to 19	6.0×10^4 to 2.0×10^5	0.5	92	10.3

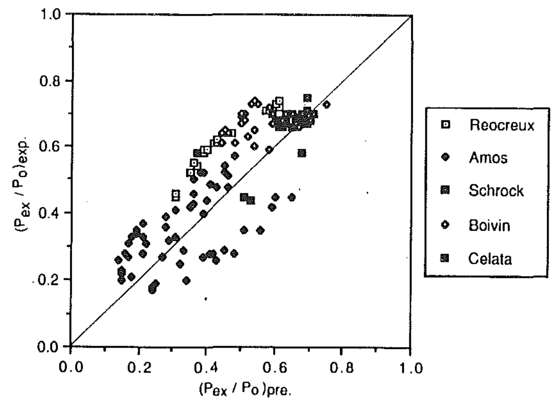

Fig. 9 Comparison of predicted critical pressure ratio with experimental data

that the present prediction gives better results (about 6 percent less scatter) than did the original model by Amos and Schrock.

Conclusion

A model has been developed for the prediction of critical mass flux of water in channels of constant cross sectional area with liquid stagnation states (Fanno-type process). The model is highly mechanistic in that it incorporates the physics of flashing inception caused by nucleation from wall cavities under the influence of declining pressure (pressure undershoot) and the subsequent nonequilibrium two-phase flow to the point of choking. Still the model is quite simple compared with most mechanistic models and incorporates approximations such as homogeneous flow and an ad hoc relaxation relation for thermal nonequilibrium. The model has been shown to be very accurate in predicting critical mass flux for all the available experimental data.

The model, which uses the steady-state form of the conservation equations, must be solved by an iterative numerical procedure, which will be described in a companion paper. The steady-state form is justified for most applications because the stagnation state is practically constant over a time comparable to the fluid transit time through the channel. The problem requires relatively little computer time; a typical evaluation is completed in about 20 seconds on an IBM 3090. This time will be reduced when the model is applied in a quasi-steady systems code because of the improved "first guess" as the evolution of stagnation states is tracked.

References

Abdollahian, D., Healzer, J., Janssen, E., and Amos, C., 1975, "Critical Flow Data Review and Analysis," EPRI NP-13418.

Abuaf, N., Jones, O. C., and Wu, B. J. C., 1983, "Critical Flashing Flows in Nozzles With Subcooled Inlet Conditions," ASME JOURNAL OF HEAT TRANSFER, Vol. 105, Nov.

Alamgir, M. D., and Lienhard, J. H., 1981, "Correlation of Pressure Undershoot During Hot Water Depressurization," ASME JOURNAL OF HEAT TRANSFER, Vol. 103, No. 1, pp. 52–55.

Amos, C. N., and Schrock, V. E., 1983, "Critical Discharge of Initially Subcooled Water Through Slits," NUREG/CR-3475, LBL-16373.

Amos, C. N., and Schrock, V. E., 1984, "Two-Phase Critical Flow in Slits," *Nuclear Science and Engineering*, Vol. 88, pp. 261–274.

Anon., 1979, "The Marviken Full Scale Critical Flow Tests," Summary Report, NUREG/CR-2671, MXC-301.

Ardron, K. H., 1978, "A Two-Fluid Model for Critical Vapor-Liquid Flow," *International Journal of Multiphase Flow*, Vol. 4, pp. 323–337.

Bauer, E. G., Houdayer, G. R., and Sureau, H. M., 1976, "A Nonequilibrium Axial Flow Model and Application to Loss-of-Coolant Accident Analysis: The CLYSTERE System Code," presented at OECD/NEA Specialists' Meeting on Transient Two-Phase Flow, Toronto.

Boivin, J. Y., 1979, "Two-Phase Critical Flow in Long Nozzles," *Nuclear Technology*, Vol. 46, pp. 540–545.

Celata, G. P., Cumo, M., Farello, G. E., and Incalcaterra, P. C., 1983, "Critical Flow of Subcooled Liquid and Jet Forces," *Interfacial Transport Phenomena*, J. C. Chen and S. G. Bankoff, eds., p. 109, ASME New York.

Colebrook, C. F., 1939, "Turbulent Flow in Pipes With Particular Reference to the Transition Region Between the Smooth and Rough Pipe Laws," *Journal of Institution Civil Engineers*, Vol. XX.

Edwards, A. R., 1968, "Conduction Controlled Flashing of a Fluid, and the Prediction of Critical Flow Rates in a One-Dimensional System," UKAEA, ASHB(S) R-147.

Elias, E., and Chambré, P. L., 1984, "A Mechanistic Non-equilibrium Model for Two-Phase Critical Flow," *International Journal of Multiphase Flow*, Vol. 10, No. 1, pp. 21–40.

Fabic, S., 1964, "Vapor Nucleation of Surfaces Subjected to Transient Heating," Ph.D. Thesis, University of California, Berkeley.

Fauske, H. K., 1965, "The Discharge of Saturated Water Through Tubes," *Chemical Engineering Progress Symposium Series*, Vol. 61, No. 59, pp. 210–216.

Henry, R. E., 1970, "The Two-Phase Critical Discharge of Initially Saturated or Subcooled Liquid," *Nuclear Science and Engineering*, Vol. 41, p. 336.

Ishimoto, S., Uematsu, M., and Tanishita, I., 1972, "New Equations for the Thermodynamic Properties of Saturated Water and Steam," *Bulletin of the JSME*, Vol. 15, No. 88, p. 1278–1289.

Jeandey, Ch., Gros D'Aillon, L., Bourgine, L., and Barriere, G., 1981, "Auto Vaporization D'Escoulements Eau/Vapeur," Commisariat a L'Energie Atomique Report, T. T. No. 163.

John, H., Reimann, J., Westphal, F., and Friedel, L., 1988, "Critical Two-Phase Flow Through Rough Slits," *International Journal of Multiphase Flow*, Vol. 14, No. 2, pp. 155–174.

Jones, O. C., and Saha, P., 1977, "Non-equilibrium Aspects of Water Reactor Safety," *Symposium on the Thermal and Hydraulic Aspects of Nuclear Reactor Safety, Vol. 1, Light Water Reactors*, O. C. Jones, Jr. and S. G. Bankoff, eds., ASME, New York.

Kroeger, P. G., 1976, "Application of a Non-equilibrium Drift Flux Model to Two-Phase Blowdown Experiments," CSNI Specialists' Meeting on Transient Two-phase Flow, Toronto.

Lee, S. Y., and Schrock, V. E., 1988, "Homogeneous Non-equilibrium Critical Flow Model for Liquid Stagnation States," *Proceedings of 1988 National Heat Transfer Conference*, H. R. Jacobs, ed., ASME HTD-Vol. 96, pp. 507–513.

Levy, S., 1960, "Steam Slip—Theoretical Prediction From Momentum Model," ASME JOURNAL OF HEAT TRANSFER, Vol. 82, No. 1, pp. 113–124.

Levy, S., and Abdollahian, D., 1982, "Homogeneous Non-equilibrium Critical Flow Model," *International Journal of Heat and Mass Transfer*, Vol. 25, No. 6, pp. 759–770.

Lienhard, J. H., 1977, "Estimation of Specific Heat of Superheated Water," *Nuclear Science and Engineering*, Vol. 62, pp. 302–304.

"Release on Surface Tension of Water Substances," 1975, issued by International Association for the Properties of Steam (IAPS), NBS, Washington, DC.

Reocreux, M., 1978, "Contribution to the Study of Critical Discharge of Steam-Water," Ph.D. Thesis, Medical University of Grenoble, France, NUREG-tr-0002.

Richter, H. J., 1983, "Separated Flow Model: Application to Critical Two-Phase Flow," *International Journal of Multiphase Flow*, Vol. 9, pp. 511–530.

Saha, P., 1978, "A Review of Two-Phase Steam-Water Critical Flow Models With Emphasis on Thermal Non-equilibrium," NUREG/CR-0417.

Schlichting, H., 1979, *Boundary Layer Theory*, translated by J. Kestine, 7th ed., McGraw-Hill, New York.

Schrock, V. E., Revankar, S. T., Mannheimer, R., and Wang, C. H., 1986, "Small Break Critical Discharge—The Roles of Vapor and Liquid Entrainment in a Stratified Two-Phase Region Upstream of the Break," LBL-22024 and NUREG/CR-4671: *International Heat Transfer Conference 1986*, C. L. Tien, ed., Vol. 5, pp. 2207–2311.

Shin, T. S., and Jones, O. C., 1986, "An Active Cavity Model for Flashing," *Nuclear Engineering and Design*, Vol. 95, pp. 185–196.

Sozzi, G. L., and Sutherland, W. A., 1975, "Critical Flow of Saturated and Subcooled Water at High Pressure," General Electric Co., NEDO-13418.

Stigall, J. L., 1964, "Contact Angle Hysteresis," MS Thesis, University of California, Berkeley.

Uchida, H., and Nariai, H., 1966, "Discharge of Saturated Water Through Pipes and Orifices," *Proceedings of the Third International Heat Transfer Conference*, Vol. 5, Chicago, IL, pp. 1–12.

VDI-Warmeatlas, 1974, 2d ed., Dusseldorf, Verein Deutscher Ingenieure, Federal Republic of Germany.

APPENDIX

1 Derivation of Equation (1)

From the steady-state mixed mass conservation equation,

$$\frac{d}{dz}\left(\frac{u}{v_m}\right)=0 \qquad (A1)$$

$$v_m = x v_g(p) + (1-x) v_l(p, T_l) \qquad (A2)$$

From equations (A1) and (A2)

$$\frac{1}{u}\left(\frac{du}{dz}\right) = \frac{(v_g - v_l)}{v_m}\Bigg) + \frac{1}{v_m}\left\{x\left(\frac{dv_g}{dp}\right)_{\text{sat}}\right.$$

$$\left. + (1-x)\left(\frac{\partial v_l}{\partial p}\right)_{T_l}\right\}\left(\frac{dp}{dz}\right) + \frac{(1-x)}{v_m}\left(\frac{\partial v_l}{\partial T_l}\right)_p\left(\frac{dT_l}{dz}\right) \tag{1}$$

2 Derivation of Equation (3)

From the steady-state mixed energy conservation equation

$$\frac{d}{dz}\left(h_m + \frac{1}{2}u^2\right) = 0 \tag{A3}$$

$$h_m = xh_g(p) + (1-x)h_l(p,\ T_l) \tag{A4}$$

From equations (A3) and (A4)

$$\left\{x\left(\frac{dh_g}{dp}\right)_{\text{sat}} + (1-x)\left(\frac{\partial h_l}{\partial p}\right)_{T_l}\right\}\left(\frac{dp}{dz}\right)$$

$$+ (h_g - h_l)\left(\frac{dx}{dz}\right)(1-x)c_{p_l}\Bigg(\frac{dT_l}{dz} + u\left(\frac{du}{dz}\right) = 0 \tag{3}$$

L. M. Schlager
Department of Engineering,
Indiana-Purdue University at Ft. Wayne,
Ft. Wayne, IN 46805

M. B. Pate
Department of Mechanical Engineering,
Iowa State University,
Ames, IA 50011

A. E. Bergles
Department of Mechanical Engineering,
Aerospace Engineering and Mechanics,
Rensselaer Polytechnic Institute,
Troy, NY 12180-3590

Evaporation and Condensation Heat Transfer and Pressure Drop in Horizontal, 12.7-mm Microfin Tubes With Refrigerant 22

Using R-22 as the working fluid, a series of tests was performed to determine the evaporation and condensation performance of three 12.7-mm o.d. tubes having many small, spiral inner fins. The tubes, referred to as microfin tubes, had a 11.7-mm maximum i.d., 60 or 70 fins with heights ranging from 0.15 to 0.30 mm, and spiral angles from 15 to 25 deg. A smooth tube was also tested to establish a basis of comparison. The test apparatus had a straight, horizontal test section with a length of 3.67 m and was heated or cooled by water circulated in a surrounding annulus. Nominal evaporation conditions were 0 to 5°C (0.5 to 0.6 MPa) with inlet and outlet qualities of 15 and 85 percent, respectively; condensation conditions were 39 to 42°C (1.5 to 1.6 MPa) with inlet and outlet qualities of 85 and 10 percent, respectively. Mass flux varied from 75 to 400 kg/m^2·s. The average heat transfer coefficients in the microfin tubes, based on a nominal equivalent smooth tube area, were 1.6 to 2.2 times larger for evaporation and 1.5 to 2.0 times larger for condensation than those in the smooth tube. The pressure drop increased, but by a smaller factor than the heat transfer coefficient.

Introduction

The in-tube augmentation of evaporation and condensation heat transfer for refrigeration and air-conditioning applications has received increasing attention in recent years due to an emphasis on energy efficiency and more compact heat exchanger packaging. This paper deals with tubes having many small, spiralled inner fins, called microfin tubes. Microfin tubes appeared over a decade ago, but there are to date relatively few publications dealing with refrigerant evaporation and condensation in these tubes. Bergles et al. (1983) compiled a bibliography that dealt with various techniques of heat transfer enhancement, including boiling and condensation of refrigerants. Schlager et al. (1987) surveyed the literature with in-tube augmentation of refrigerant heat transfer as a particular emphasis and Schlager (1988) updated the earlier survey. A brief summary of past results using halocarbon refrigerants in microfin tubes is presented in Table 1. The heat transfer enhancement is substantial and often greater than the pressure drop penalty; whereas with other methods of augmentation, the pressure drop penalty can often be significantly higher than the heat transfer enhancement. In Table 1, *EF* is the heat transfer enhancement factor, defined as the ratio of the microfin tube heat transfer coefficient to that of a comparable smooth tube at a similar mass flux, heat flux, pressure level, and inlet and outlet quality. Only one previous paper has reported on results using R-22 in 12.7-mm microfin tubes. Schlager et al. (1989) presented results with 9.52-mm microfin tubes having the same fin shape as the current tubes and manufactured by the same firm. These results will be compared to those of the current investigation.

A drawing of the tube is shown in Fig. 1 and includes definitions of the pertinent geometric parameters. Values for the parameters of the three microfin tubes tested, as well as a smooth tube used for comparison, are presented in Table 2.

Test Facility

The rig used for these tests consisted of the integration of three separate flow loops: (1) a refrigerant loop; (2) a water loop, which heated and cooled the refrigerant in the test section; and (3) a chilled water and glycol loop, which served as a heat sink for the entire rig. A schematic of the test facility is presented in Fig. 2.

Refrigerant Loop. The R-22 loop consisted of a positive displacement pump, a filter dryer, a positive displacement flow meter, two heaters, the test section, an after-condenser, and a bladder-type accumulator. Also included were thermocouples, pressure taps, and control valves, whose locations are included on the schematic. The accumulator was used to set system pressure, to compensate for expansion during two-phase operation, and to help dampen pressure pulses from the pump. The refrigerant was completely isolated from the pump lubricant, so it remained oil-free for all tests.

Test Section. The test section was a straight, horizontal section having an active length of 3.67 m. The test tube was surrounded by an annulus with water flowing counter to the refrigerant. All three microfin tubes were copper, with an outside diameter of 12.7 mm and a maximum inside diameter of 11.7 mm. Instrumentation to measure temperature and pressure was located only at the entrance and exit of the test section, so that reported heat transfer coefficients are average, rather than local values.

Water Loop. The water loop consisted of a centrifugal pump, a magnetic flow meter, a water-to-water heat exchanger, a heater, and the annulus surrounding the test tube. The heat exchanger and heater were used to maintain constant water temperature during testing.

Water and Glycol Loop. A commercial refrigeration unit maintained the water and glycol mixture at −20 to −25°C. The chilled mixture, circulated by a centrifugal pump, was used to condense and subcool the refrigerant leaving the test

---

Contributed by the Heat Transfer Division for publication in the JOURNAL OF HEAT TRANSFER. Manuscript received by the Heat Transfer Division May 22, 1989; revision received January 22, 1990. Keywords: Augmentation and Enhancement, Forced Convection, Refrigeration.

Table 1 Halocarbon heat transfer in microfin tubes

EVAPORATION

Researchers	Tube d_o (mm)	Refrigerant	h [a]	Quality (%)	EF_{max} [b]	Parameters varied [c]
Ito et al. (1977)	?	R-22	avg	?	2.0	ß, f, G
Ito and Kimura (1979)	12.7	R-22	loc	25-90	2.0	p, ß, f, G, q
Kimura and Ito (1981)	6.35	R-12	loc	55	2.0	ß, G, q
Tatsumi et al. (1982)	9.52	R-22	avg	25-95	2.1	n, ß, f, G
Tojo et al. (1984)	9.52	R-22	avg	?	2.0	n, ß, f, G
Shinohara and Tobe (1985)	9.52	R-22	avg	$\bar{X}$=60	2.5	n, ß, s, f, G
Khanpara et al. (1986a)	9.52	R-113	loc	15-85	2.0	n, p, ß, s, f, G
Khanpara et al. (1987a)	9.52	R-113	avg / loc	10-90	2.7	n, p, ß, s, f, G, q
Khanpara et al. (1987b)	9.52	R-22,R-113	loc	5-75	2.2	G, q
Schlager et al. (1988)	9.52	R-22	avg	15-85	2.4	G, q
Schlager et al. (1989)	9.52	R-22	avg	15-85	2.0	ß, f, G, q

CONDENSATION

Researchers	Tube d_o (mm)	Refrigerant	h [a]	Quality (%)	EF_{max} [b]	Parameters varied [c]
Tatsumi et al. (1982)	9.52	R-22	avg	75-10	1.8	n, ß, f, G
Mori and Nakayama (1983)	25.4	R-113	avg / loc	80-20	2.0	p, s, f, G
Tojo et al. (1984)	9.52	R-22	avg	?	1.6	n, ß, f, G
Shinohara and Tobe (1985)	9.52	R-22	avg	100+ - ?	2.4	n, ß, s, f, G
Khanpara et al. (1986b)	9.52	R-113	loc	80-20	2.2	n, p, ß, s, f, G
Schlager et al. (1988)	9.52	R-22	avg	85-15	2.3	G, q
Schlager et al. (1989)	9.52	R-22	avg	85-15	1.9	ß, f, G, q

[a] Heat transfer coefficient: loc = local, avg = average

[b] Maximum reported heat transfer enhancement factor

[c] n = number of fins
ß = spiral angle
f = fin height
q = heat flux
p = pitch of fins
s = fin shape
G = mass flux

section. During evaporation testing, part of the flow cooled the bladder accumulator.

Data Acquisition and Reduction

Data were acquired with an automatic data acquisition system. This system consisted of a controller, a 40-channel scanner, and a digital multimeter. Temperatures were measured with 20 copper-constantan thermocouples, including a redundant pair of thermocouples at the entrance and exit of both the test tube and the annulus. Pressure was measured with a strain-gage type transducer and pressure drop with a variable

Nomenclature

A = area, m^2
c = specific heat capacity, $J/kg \cdot K$
d = diameter, m
EF = heat transfer enhancement factor
F = experimental constant
f = fin height, m
G = mass flux, $kg/m^2 \cdot s$
h = heat transfer coefficient, $W/m^2 \cdot K$
I = current, A
i_{fg} = enthalpy of vaporization, J/kg
LMTD = log mean temperature difference, K
m = mass flow rate, kg/s
n = number of fins
P = pressure, Pa
PF = pressure drop penalty factor
p = fin spacing, m
Q = heat rate, W
q = heat flux, W/m^2
s = fin shape
T = temperature, K
t = wall thickness, m
U = overall heat transfer coefficient, $W/m^2 \cdot K$
V = voltage, V
v = velocity, m/s
X = vapor quality
$\bar{X}$ = average vapor quality
β = angle, deg
Δ = change in quantity

Subscripts

h = heater
i = inside
in = inlet
lat = latent
M = microfin tube
max = maximum
o = outside
out = outlet
r = refrigerant (R-22)
S = smooth tube
sat = saturation conditions
sens = sensible
t = test tube
w = water

reluctance transducer. All voltages and currents were measured with the multimeter. Channels were scanned a total of five times within a two-minute period with the exception of the pressure drop. The pressure drop was sampled a total of 35 times because of the small absolute measurement value and the relatively large observed fluctuations.

A FORTRAN computer code calculated heat transfer coefficients from the arithmetic mean of data samples from a single test run. A summary of the most significant equations is presented below.

The heat transfer in the test section is determined from an energy balance in the annulus

$$Q_t = m_w \cdot c_w \cdot (T_{w_{out}} - T_{w_{in}}) \tag{1}$$

The vapor quality at the entrance to the test section necessitates an energy balance on the two heaters

$$Q_h = F \cdot [(V \cdot I)_{heater\ 1} + (V \cdot I \cdot \cos\beta)_{heater\ 2}] \tag{2}$$

where F (typically around 0.98) is experimentally determined and accounts for energy loss or gain through the insulation; $\cos\beta$ is the power factor. The heat transferred to the refrigerant is

$$Q_h = Q_{sens} + Q_{lat} \tag{3}$$

where

$$Q_{sens} = m_r \cdot c_r \cdot (T_{sat} - T_{h_{in}}) \tag{4}$$

$$Q_{lat} = m_r \cdot i_{fg} \cdot X_{h_{out}} \tag{5}$$

The saturation temperature corresponds to the average pressure in the test tube. From these equations, $X_{h_{out}}$, which is also the test section inlet quality ($X_{t_{in}}$), can be determined.

The quality change in the test section is then calculated from the energy balance

$$\Delta X = \frac{Q_t}{(m_r \cdot i_{fg})} \tag{6}$$

Refrigerant properties are determined at saturation conditions corresponding to the average pressure in the test section. The overall heat transfer coefficient based on the outside area of the test tube is

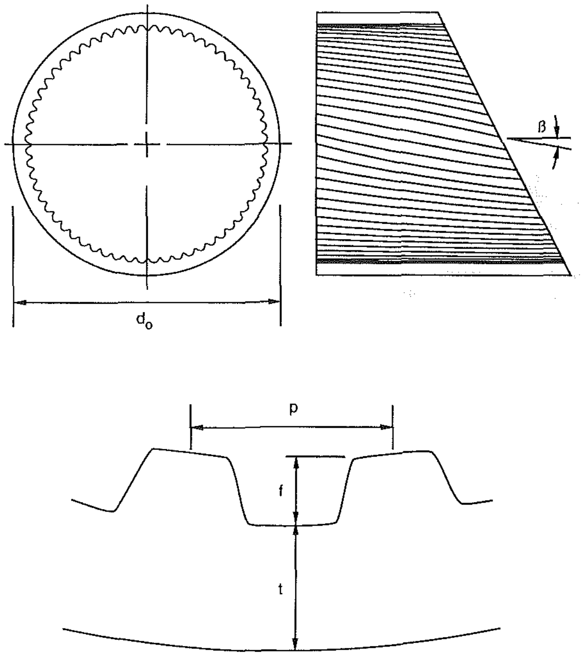

Fig. 1 Drawing of the microfin tube

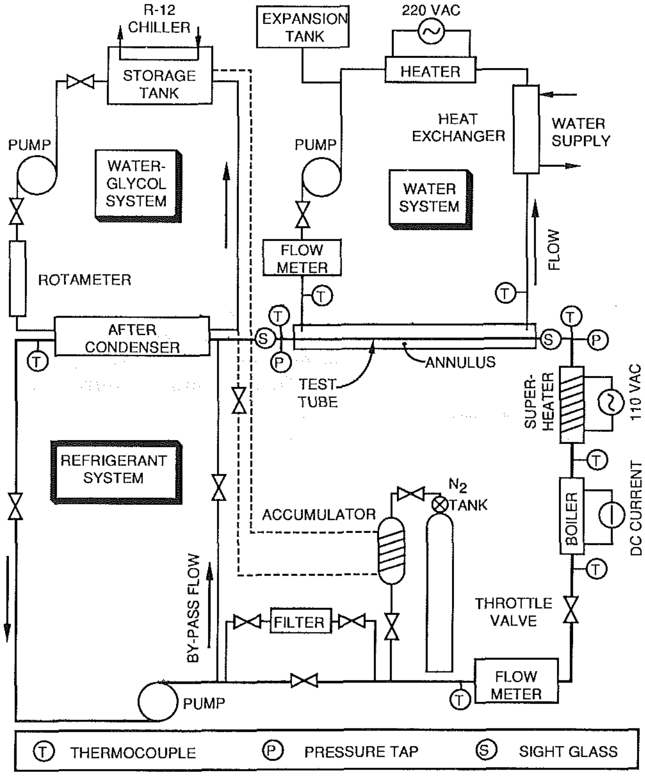

Fig. 2 Schematic diagram of the test facility

Table 2 Dimensions of the tubes tested and previously tested tubes used for comparison

	12.7-mm tubes				9.52-mm tubes		
	Smooth	Micro-fin 1	Micro-fin 2	Micro-fin 3	Micro-fin 1	Micro-fin 2	Micro-fin 3
d_o (mm)	12.7	12.7	12.7	12.7	9.52	9.52	9.52
$d_{i\,max}$ (mm)	10.9	11.7	11.7	11.7	8.92	8.92	8.92
t (mm)	0.90	0.50	0.50	0.50	0.30	0.30	0.30
f (mm)	--	0.30	0.20	0.15	0.20	0.16	0.15
n	--	60	70	60	60	60	60
ß (deg)	--	18	15	25	18	15	25
A_{i_S}/A_{i_M} [a]	--	1.51	1.33	1.39	1.55	1.38	1.43

[a] Ratio of inside surface area of the micro-fin tube to the inside area of a smooth tube having the same maximum inside diameter

$$U_o = \frac{Q_t}{(A_o \cdot \mathrm{LMTD})} \tag{7}$$

and

$$T_{t\mathrm{in}} = T_{t\mathrm{out}} = T_{\mathrm{sat}} \tag{8}$$

Assuming no fouling and a negligible thermal resistance in the copper wall, an expression for h_i is obtained:

$$h_i = \frac{1}{\left(\frac{1}{U_o} - \frac{1}{h_o}\right) \cdot \frac{A_i}{A_o}} \tag{9}$$

where h_o is calculated from an experimentally determined calibration equation obtained by using a modified Wilson plot technique (McAdams, 1942). The inside heat transfer coefficient (h_i) for the microfin tube is based on the area of a smooth tube having an inside diameter equal to the maximum inside diameter of the microfin tube.

The Wilson plot technique involves plotting the overall heat transfer coefficient U versus $1/v_i^{0.8}$, where v_i is the velocity inside the tube. By projecting a line obtained by plotting several values of v_i to the axis at $1/v_i^{0.8} = 0$ (or $v_i = \infty$), and assuming the resistance in the copper to be negligible, an estimate of h_o is obtained. The calibration runs used single-phase flow in both the tube and the annulus.

To quantify the performance of the microfin tubes, a heat transfer enhancement factor (*EF*), mentioned earlier, and a pressure drop penalty factor (*PF*) are defined. These factors are calculated at constant mass fluxes, heat fluxes, pressure levels, and inlet and outlet qualities. The heat transfer enhancement factor was defined earlier (h_M/h_S) and the pressure drop penalty factor is the ratio of microfin tube pressure drop to the pressure drop in a comparable smooth tube ($\Delta P_M/\Delta P_S$). The values of heat transfer coefficients and pressure drops used in the calculation of the enhancement and penalty factors came from least-squares curve fits of the test data, not from individual data points.

The typical uncertainty of the heat transfer coefficients is ±10 percent using a propagation-of-error analysis [technique is based on Kline and McClintock (1953); calculations are shown in Schlager (1988)], while the typical uncertainty of the enhancement factors is ±14 percent. Mass flux has an uncertainty of approximately ±2 percent. The temperature change through the annulus was obtained with redundant, calibrated thermocouples and the uncertainty of ΔT is estimated as 0.05 K. A more complete error analysis for the test rig is contained in Schlager (1988). Pressure drop uncertainties were determined statistically based on all the data samples for a given test run. At a 90 percent confidence level, condensation results are ±1 kPa and evaporation results are ±2 kPa. These uncertainties represent at least ±12 percent of the measured value for evaporation and at least ±25 percent for condensation. For pressure drop in particular, the relative uncertainty (uncertainty as a percentage of measured value) is quite high at low mass fluxes where measured values are the smallest. Because pressure drop becomes small at low mass fluxes, the relative uncertainty of the penalty factor in this region becomes very high. At higher mass fluxes, the relative uncertainty of *PF* remains rather high, generally greater than ±15 percent of the result.

Table 3 Summary of test conditions

		Evaporation	Condensation
G	(kg/m^2·s)	75-300	100-400
P	(MPa)	0.5-0.6	1.5-1.6
T_{sat}	(°C)	0-6	39-42
X_{in}	(%)	10-20	80-90
X_{out}	(%)	80-90	10-20

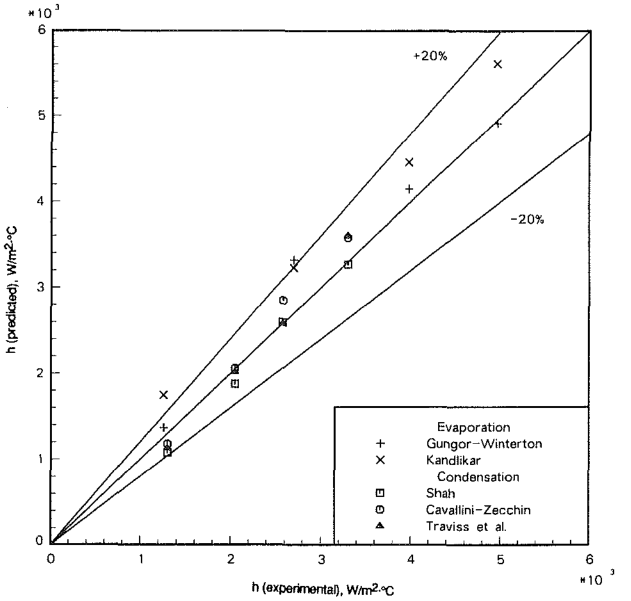

Fig. 3 Comparison of experimental and predicted values of heat transfer coefficient in a smooth tube

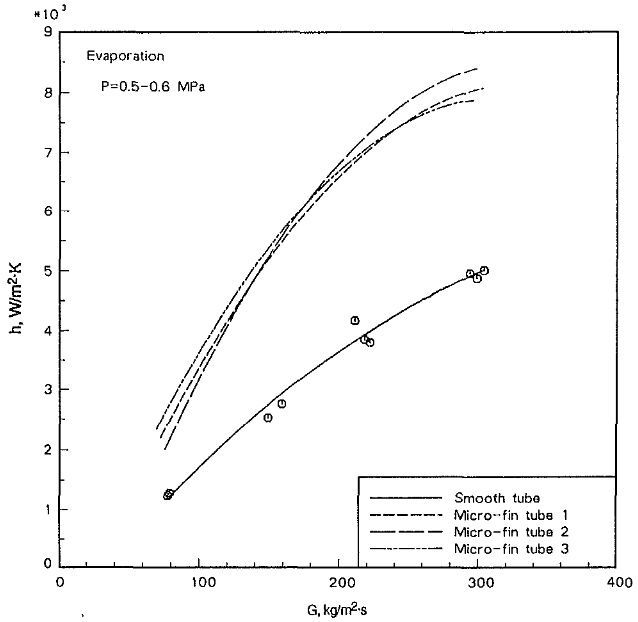

Fig. 4 Evaporation heat transfer results for smooth and microfin tubes

Heat Transfer Results

Evaporation tests were carried out at nominal conditions of 0.5 to 0.6 MPa (0 to 5°C), with mass flux variations of 75 to 300 kg/m^2·s. Nominal vapor qualities at the inlet and outlet were 15 and 85 percent, respectively. For condensation, the pressure was 1.5 to 1.6 MPa (39 to 42°C) and mass flux varied from 100 to 400 kg/m^2·s. Vapor quality ranged from a nominal value of 85 percent at the test section inlet to 10 percent at the outlet. The test conditions are summarized in Table 3.

Smooth Tube. Figure 3 shows smooth tube evaporation and condensation results compared to several correlations from the literature. Evaporation results are compared to the correlations

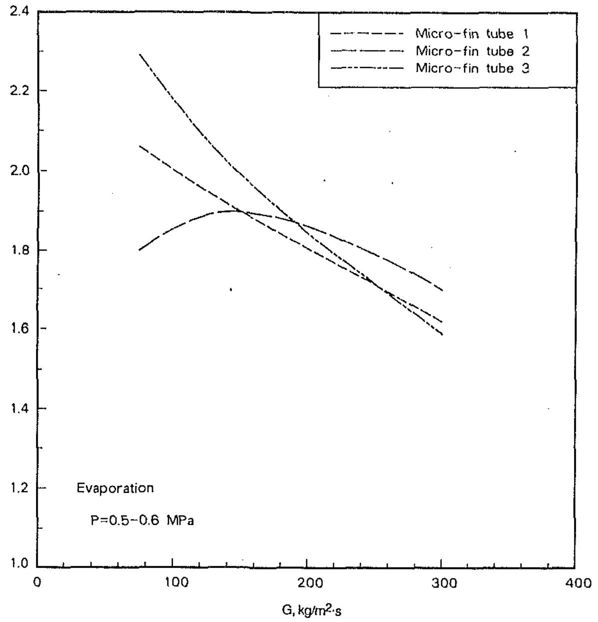

Fig. 5 Evaporation heat transfer enhancement factors for microfin tubes

of Kandlikar (1983) and Gungor and Winterton (1986); condensation results are compared to the correlations of Shah (1979), Cavallini and Zecchin (1974), and Traviss et al. (1972). For correlations that predict local values of the heat transfer coefficient, a numerical integration was carried out to obtain average values. Most of the experimental data lie within ±20 percent of the values predicted by correlations. This agreement lends confidence to the instrumentation and test procedures.

Microfin Tubes. Figure 4 shows evaporation heat transfer results for the three microfin tubes and also includes the results of the smooth tube for comparison. The heat transfer coefficients for the microfin tubes were calculated based on the area of a fictitious smooth tube having an inside diameter equal to the maximum inside diameter of the microfin tube. Individual data points are shown for the smooth tube to indicate typical data scatter for all tubes; for clarity, microfin results are shown only as least-squares curves. As expected, the heat transfer coefficient increases with increasing mass flux, increasing approximately fourfold as mass flux increases from 75 to 300 $kg/m^2 \cdot s$. Compared with the smooth tube, all three microfin tubes show a significant increase in the heat transfer coefficient over the range of mass fluxes tested. The performance of all three tubes is similar, with a deviation among the microfin tubes of only 10 to 20 percent. This is approximately the same magnitude as the uncertainty.

Figure 5 shows the same evaporation data for the microfin tubes, but in the form of heat transfer enhancement factors (*EF*). It is emphasized that the enhancement factors are based on a ratio of the least-squares curve fits of the data and not on a comparison of individual data points. The maximum seen for tube 2 should be considered a result of curve fitting and may not be representative of actual trends. While heat transfer coefficients increase with increasing mass flux, there is a tendency for *EF* to decrease as mass flux increases. At low mass flux, *EF* has a value of 1.8 to 2.3 but falls to around 1.7 for all three microfin tubes at high mass flux. The region of lowest statistical uncertainty for the least-squares curves (and hence for enhancement factors) is at medium mass fluxes. In this region, *EF* has a value of about 1.8 to 1.9. Table 4 presents values of *EF* at medium and high mass fluxes.

Condensation results for all three microfin tubes, as well as for the smooth tube, are presented in Fig. 6. Again, the heat transfer coefficient increases with increasing mass flux and the microfin tubes show a significantly improved heat transfer performance. The magnitude of the heat transfer coefficient is about 30 to 50 percent lower for condensation than for evaporation. Although the curves for all three microfin tubes lie in close proximity, there is a slightly greater spread than was observed with evaporation.

Table 4 Enhancement factors and penalty factors

		Evaporation			Condensation		
Tube size mm	Tube number	G = 100 $kg/m^2 \cdot s$	G = 200 $kg/m^2 \cdot s$	G = 300 $kg/m^2 \cdot s$	G = 200 $kg/m^2 \cdot s$	G = 300 $kg/m^2 \cdot s$	G = 400 $kg/m^2 \cdot s$
12.7	1	2.0 (1.3)	1.8 (1.35)	1.6 (1.2)	1.9 (1.4)	1.8 (1.35)	1.6 (1.3)
12.7	2	1.8 (1.3)	1.9 (1.35)	1.7 (1.2)	1.9 (1.4)	1.7 (1.35)	1.5 (1.3)
12.7	3	2.2 (1.3)	1.9 (1.35)	1.6 (1.2)	1.8 (1.4)	1.7 (1.35)	1.5 (1.3)
—	—	G = 200	G = 300	G = 400	G = 300	G =400	G = 500
9.52	1	1.9 (1.2)	1.8 (1.35)	1.8 (1.4)	1.7 (1.2)	1.6 (1.2)	1.6 (1.25)
9.52	2	1.6 (1.2)	1.6 (1.35)	1.6 (1.4)	1.6 (1.2)	1.5 (1.2)	1.4 (1.25)
9.52	3	2.0 (1.2)	1.9 (1.35)	1.8 (1.4)	1.5 (1.2)	1.5 (1.2)	1.5 (1.25)

The top entry is the heat transfer enhancement factor, EF, and the bottom entry (in parentheses) is the pressure drop penalty factor, PF.

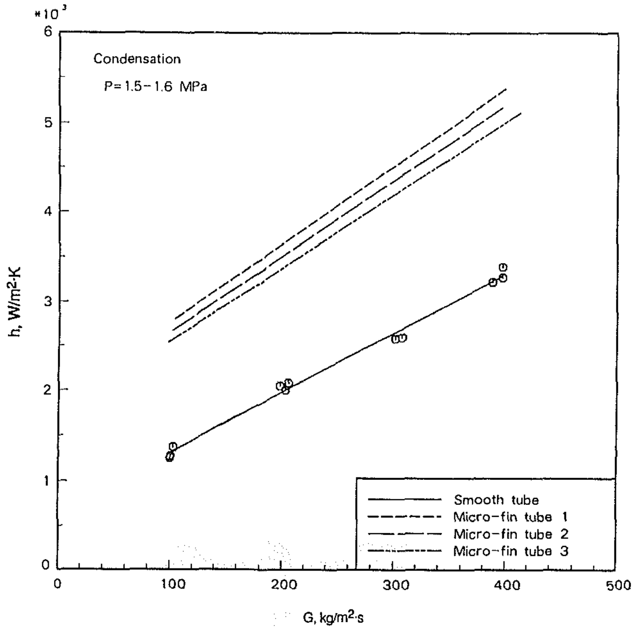

Fig. 6 Condensation heat transfer results for smooth and microfin tubes

Figure 7 depicts the same condensation data as shown in Fig. 6, but as heat transfer enhancement factors (*EF*). As with evaporation, there is a decreasing trend in *EF* as mass flux increases, contrary to the heat transfer coefficient trend. At low mass flux, *EF* has a value of 1.8 to 2.0 and falls to around 1.5 to 1.6 at high mass flux. At medium mass flux, the value of *EF* is about 1.8. The magnitude of the condensation enhancement factor is similar to that shown above for evaporation. Table 4, mentioned above, includes values for *EF* at medium and high mass fluxes.

For both evaporation and condensation data, the maximum values for *EF* in the current study generallly fall within the range of enhancement factors summarized in Table 1.

Pressure Drop Results

Figures 8 and 9 show pressure drop results for evaporation and condensation, respectively. Due to the high uncertainties associated with pressure drop, only one curve is drawn through all the microfin tube values. Individual data points are included to indicate scatter. Pressure drop increases with increasing mass flux, as expected. It is also seen that the pressure drop of the

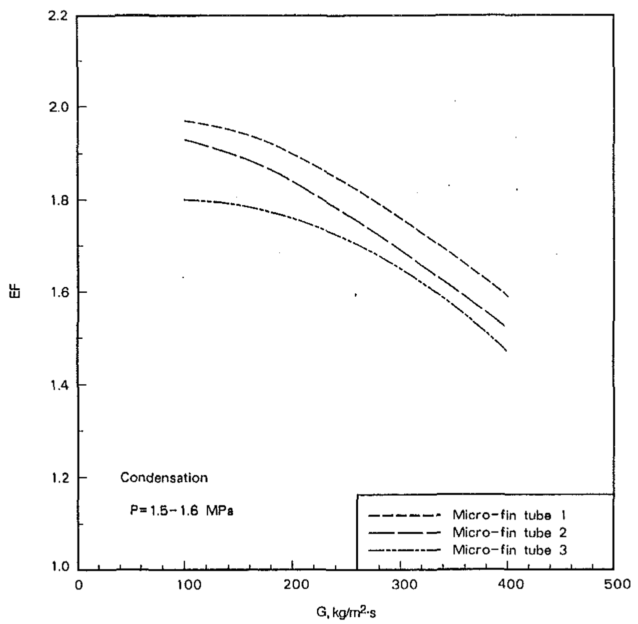

Fig. 7 Condensation heat transfer enhancement factors for microfin tubes

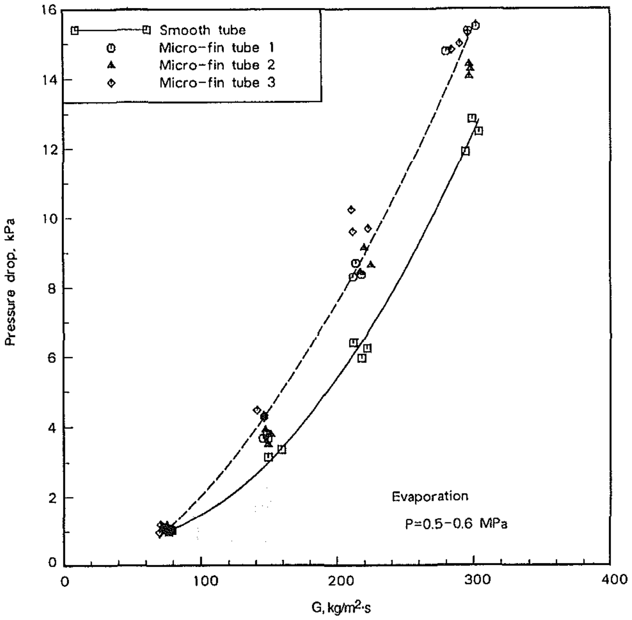

Fig. 8 Evaporation pressure results for smooth and microfin tubes

microfin tubes is somewhat higher than that of the smooth tube for both evaporation and condensation. The magnitude of the pressure drop is higher for evaporation than for condensation. This is due to differing saturation pressures and differing momentum pressure drop components for the two cases. For condensation, the momentum component leads to a pressure recovery, hence the low values for pressure drop seen in Fig. 9.

In terms of pressure drop penalty factors, *PF* is approximately 1.3 ± 0.1 for all three tubes during both evaporation and condensation. There is an apparent tendency for *PF* to fall with increasing mass flux. Table 4 presents calculated values of *PF*.

Discussion

For both evaporation and condensation, heat transfer is enhanced significantly relative to smooth tube values, with *EF* ranging from about 1.5 to greater than 2.0. This increase in heat transfer is generally greater than the increase in internal surface area due to the fins. Pressure drop increases less than heat transfer, with *PF* reaching a maximum of just over 1.4. At the higher mass fluxes, both *EF* and *PF* decrease with increasing mass flux.

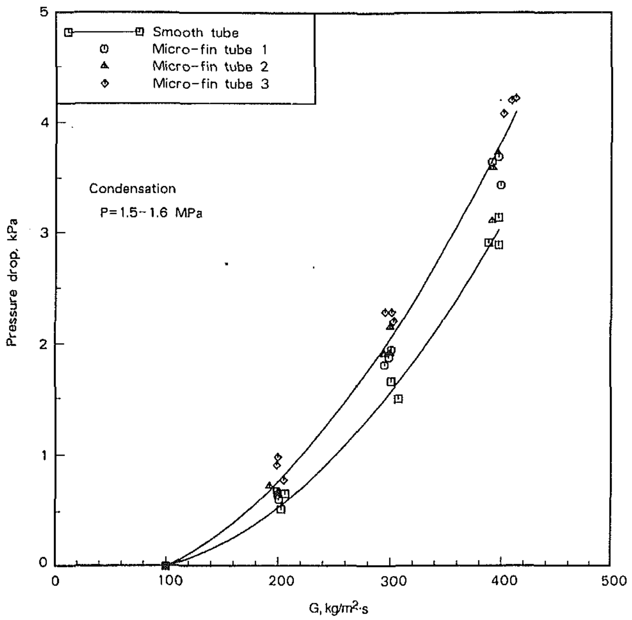

Fig. 9 Condensation pressure drop results for smooth and microfin tubes

A comparison of the current 12.7-mm tube results with those reported earlier for 9.52-mm tubes (Schlager et al., 1989) is presented in the following paragraphs. The earlier results were obtained using the same test facility, but with a different annulus to accommodate the smaller tube diameter. Test conditions were approximately the same as those reported here; however, the range of mass fluxes was somewhat higher in the earlier tests due to the lower flow rates required for a given mass flux. The 9.52-mm tubes had fin shapes similar to those of the 12.7-mm tubes and dimensions of the smaller tubes are also included in Table 1. The comparisons presented are in terms of heat transfer enhancement and pressure drop penalty factors. These factors are included in Table 4, mentioned earlier, along with the values for the 12.7-mm tubes.

Heat Transfer. The trend with both tube sizes is for *EF* to decrease with increasing mass flux during evaporation. Between 200 and 300 kg/m^2·s, where data from the two studies overlap, the data from the 12.7-mm tubes fall approximately in the middle of those of the smaller tubes. Data for the larger tubes are more tightly grouped and the slope appears to be somewhat higher, but results are similar and within the limits of uncertainty (approximately ±14 percent for *EF*). For all six tubes, *EF* fell from 2.1 ± 0.2 at $G \approx 100$ kg/m^2·s to 175 ± 0.1 at $G \approx 400$ kg/m^2·s.

For condensation, like evaporation, both tube sizes exhibit a similar downward trend in *EF* with increasing mass flux. The data from the two investigations overlap between approximately 200 and 400 kg/m^2·s and once more the magnitude of *EF* in both tube sizes is similar. As with evaporation, there are slope variations in this region, but they are not statistically significant. For all of the tubes, *EF* fell from 1.9 ± 0.1 at $G \approx 100$ kg/m^2·s to 1.5 ± 0.1 at $G \approx 500$ kg/m^2·s.

The general downward trend in *EF* as mass flux increases is observed for both evaporation and condensation and with both sizes of tubes. A possible explanation for this phenomenon may be that, as the Reynolds number increases, the turbulence induced by the finned surface becomes less important relative to the level of turbulence in the smooth tube. Therefore, the augmentation of heat transfer due to turbulence decreases.

Pressure Drop. Values of PF for all six tubes are included in Table 4. It should be remembered that pressure drop penalty factors have large uncertainties due to a combination of (1) large statistical fluctuations, (2) small absolute magnitude of pressure drop measurements, and (3) variations due to variable quality change through the test section. At medium to high mass fluxes, where uncertainties are generally smallest, the uncertainty in PF is still ± 15 percent or greater. For all tubes, the value of PF is 1.3 ± 0.1. In light of the uncertainties in calculating pressure drop penalty factors, no firm conclusions regarding a comparison of the two tube sizes can be drawn from these relatively small differences.

Conclusions

This study has investigated the performance of three, 12.7-mm microfin tubes and compared the performance to a comparable smooth tube and to 9.52-mm microfin tubes. The data presented add to a small, but growing, body of microfin tube performance data. These data can be used currently for design purposes. In the future, with a sufficiently broad database, the development of generalized predictive correlations may be possible.

All three 12.7-mm tubes exhibit a significant heat transfer enhancement when compared to smooth tubes. The enhancement factors range from 2.3 to 1.6 for evaporation and from 2.0 to 1.5 for condensation. Pressure drop also increases in the microfin tubes—on the order of 20 to 40 percent at the higher mass fluxes. In general, heat transfer is enhanced more than the pressure drop increases. Because of this, the possible size reduction in a heat exchanger due to heat transfer enhancement could lead to a lower overall pressure drop, in spite of the pressure drop penalty reported for the microfin tubes.

Tube 3 appears to show the best evaporation performance at low mass fluxes and tube 2 the best performance at higher mass fluxes. However, all data lie within a narrow band, which makes a determination of the single best performing tube doubtful. Likewise for condensation, the data are all clustered in a narrow range limiting the differentiation that can be made in tube performance; however, tube 1 appears to have the best performance over the range of mass fluxes tested. Considering the statistical uncertainties, the performance of all three microfin tubes is equivalent for both evaporation and condensation.

When using enhancement factors as a basis of comparison, no significant differences in performance are observed between 9.52-mm and 12.7-mm tubes. This indicates that results for a particular microfin tube can be reasonably applied without modification to a geometrically similar tube having a somewhat different diameter.

Acknowledgments

The authors would like to thank the manufacturer of the microfin tubes, Wieland-Werke AG Metallwerke, Ulm, Federal Republic of Germany, for supplying the tubes and for their support and technical assistance during this research. In particular, special thanks are extended to Mr. Klaus Menze.

References

Bergles, A. E., Nirmalan, V., Junkhan, G. H., and Webb, R. L., 1983, "Bibliography on Augmentation of Convective Heat and Mass Transfer — II," HTL-31, ISU-ERI-Ames-84222, DE-84018484, Iowa State University, Ames, IA.

Cavallini, A., and Zecchin, R., 1974, "A Dimensionless Correlation for the Heat Transfer in Forced Convection Condensation," *Proceedings of the Fifth International Hea Transfer Conference*, Tokyo, Vol. 3, pp. 309-313.

Gungor, K. E., and Winterton, R. H. S., 1986, "A General Correlation for Flow Boiling in Tubes and Annuli," *International Journal of Heat and Mass Transfer*, Vol. 29, No. 3, pp. 351-358.

Ito, M., Kimura, H., and Senshu, T., 1977, "Development of High Efficiency Air-Cooled Heat Exchangers," *Hitachi Review*, Vol. 26, No. 10, pp. 323-326.

Ito, M., and Kimura, H., 1979, "Boiling Heat Transfer and Pressure Drop in Internal Spiral-Grooved Tubes," *Bulletin of JSME*, Vol. 22, No. 171, pp. 1251-1257.

Kandlikar, S. S., 1983, "An Improved Correlation for Predicting Two-Phase Flow Boiling Heat Transfer Coefficients in Horizontal and Vertical Tubes," *Heat Exchangers for Two Phase Flow Applications*, ASME, New York, pp. 3-10.

Khanpara, J. C., Bergles, A. E., and Pate, M. B., 1986a, "Augmentation of R113 In-tube Evaporation With Microfin Tubes," *ASHRAE Transactions*, Vol. 92, Part 2, pp. 506-524.

Khanpara, J. C., Bergles, A. E., and Pate, M. B., 1986b, "Augmentation of R-113 In-tube Condensation With Microfin Tubes," *Heat Transfer in Air Conditioning and Refrigeration Equipment*, HTD-Vol. 65, ASME, New York, pp. 21-32.

Khanpara, J. C., Bergles, A. E., and Pate, M. B., 1987a, "A Comparison of In-tube Evaporation of Refrigerant R113 in Electrically Heated and Fluid Heated Smooth and Microfin Tubes," *Advances in Enhanced Heat Transfer — 1987*, ASME HTD-Vol. 68, New York, pp. 35-46.

Khanpara, J. C., Pate, M. B., and Bergles, A. E., 1987b, "Local Evaporation Heat Transfer in a Smooth Tube and a Microfin Tube Using Refrigerants 22 and 113," *Boiling and Condensation in Heat Transfer Equipment*, ASME HTD-Vol. 85, New York, pp. 31-39.

Kimura, H., and Ito, M., 1981, "Evaporating Heat Transfer in Horizontal Internal Spiral-Grooved Tubes in the Region of Low Flow Rates," *Bulletin of JSME*, Vol. 24, No. 195, pp. 1602-1607.

Kline, S. J., and McClintock, F. A., 1953, "Describing Uncertainties in Single Sample Experiments," *Mechanical Engineering*, Vol. 75, pp. 3-8.

McAdams, W. H., 1942, *Heat Transmission*, 2nd ed., McGraw-Hill, New York.

Mori, Y., and Nakayama, W., 1983, "High Performance Mist Cooled Condensers for Geothermal Binary Cycle Plants," *Heat Transfer in Energy Problems*, Hemisphere, Washington, DC, pp. 211-218.

Schlager, L. M., 1988, "The Effect of Oil on Heat Transfer and Pressure Drop During Evaporation and Condensation of Refrigerant Inside Augmented Tubes," Ph.D. dissertation, Iowa State University, Ames, IA.

Schlager, L. M., Bergles, A. E., and Pate, M. B., 1987, "A Survey of Refrigerant Heat Transfer and Pressure Drop Emphasizing Oil Effects and In-tube Augmentation," *ASHRAE Transactions*, Vol. 93, Part 1, pp. 293-416.

Schlager, L. M., Pate, M. B., and Bergles, A. E., 1988, "Evaporation and Condensation of Refrigerant-Oil Mixtures in a Smooth Tube and a Microfin Tube," *ASHRAE Transactions*, Vol. 94, Part 1, pp. 149-166.

Schlager, L. M., Pate, M. B., and Bergles, A. E., 1989, "Heat Transfer and Pressure Drop During Evaporation and Condensation of R22 in Horizontal Microfin Tubes," *International Journal of Refrigeration*, Vol. 12, pp 6-14.

Shah, M. M., 1979, "A General Correlation for Heat Transfer During Film Condensation Inside Pipes," *International Journal of Heat and Mass Transfer*, Vol. 22, pp. 547-556.

Shinohara, Y., and Tobe, M., 1985, "Development of an Improved 'Thermofin Tube'," *Hitachi Cable Review*, No. 4, pp. 47-50.

Tatsumi, A., Oisumi, K., Hayashi, M., and Ito, M., 1982, "Application of Inner Groove Tubes to Air Conditioners," *Hitachi Review*, Vol. 32, No. 1, pp. 55-60.

Tojo, S., Hosokawa, K., Arimoto, T., Yamada, H., and Ohto, Y., 1984, "Performance Characteristics of Multigrooved Tubes for Air Conditioners," *Australian Refrigeration Air-Conditioning and Heating*, Vol. 38, No. 8, pp. 45, 48, 51, 61.

Traviss, D. P., Rohsenow, W. M., and Baron, A. B., 1972, "Forced Convection Condensation Inside Tubes: A Heat Transfer Equation for Condenser Design," *ASHRAE Transactions*, Vol. 79, Part 1, pp. 157-165.

K. O. Pasamehmetoglu

R. A. Nelson

Nuclear Technology and Engineering
Division,
Los Alamos National Laboratory,
Los Alamos, NM 87544

F. S. Gunnerson

College of Engineering,
University of Central Florida,
Orlando, FL 32816

Critical Heat Flux Modeling in Pool Boiling for Steady-State and Power Transients

Understanding and predicting critical heat flux (CHF) behavior during steady-state and transient conditions is of fundamental interest in the design, operation, and safety of boiling and two-phase flow devices. The results of a comprehensive study specifically conducted to model transient CHF in pool boiling are presented in this paper. The model we developed includes the analysis of thermal energy conduction within the heater coupled with a macrolayer thinning model. Statistical variations in the vapor mass behavior also are incorporated into the model. The resultant model provides new insight into the basic physics of the CHF phenomenon and indicates favorable agreement with the experimental data from cylindrical heaters with small radii.

Introduction

Boiling heat transfer with time-dependent heat input and the prediction of critical heat flux (CHF) under such conditions are of interest in several applications. Some examples are reactivity-initiated accidents (RIAs) in light-water nuclear reactor technology, where sudden increases in power generation are likely, and cooling electronic equipment, where power transients are part of normal operation.

There have been several studies aimed toward providing a fundamental understanding of the transient CHF phenomenon. Using electrically heated flat ribbon heaters, Tachibana et al. (1968), Sakurai et al. (1970), and Kawamura et al. (1970) experimentally studied transient boiling of water. These experiments were conducted at atmospheric pressure. The effect of subcooling also was included in the experiments of Sakurai et al. (1970) and Kawamura et al. (1970).

Sakurai and Shiotsu (1977a, 1977b) obtained transient boiling data using a platinum wire 1.2 mm in diameter in a pool of saturated water. In these experiments, the pressure ranged from atmospheric to 2 MPa, and the exponential period of the heat generation rate ranged from 5 ms to 10 s. Kuroda [as cited by Serizawa (1983)] obtained subcooled pool boiling data using an experimental setup similar to that of Sakurai and Shiotsu. Unfortunately, the data from Kuroda's experiments are not published in the open literature; the only data we could access were those cited by Serizawa (1983). The experimental setup of Kataoka et al. (1983) consisted of a vertical platinum wire of small radius placed in a flow channel. It was designed to study the transient CHF under forced convective boiling. However, a set of data for natural convection boiling also was obtained. In their experiments, Sakurai and Shiotsu, Kuroda, and Kataoka et al. applied an exponential power transient to the heater, where the heat generation rate per unit volume was varied as

$$Q(t) = Q_i \exp(t/\tau) \tag{1}$$

The experiments revealed that the characteristics of the transient boiling curve change with the system pressure and the exponential period of the power generation rate. Regular boiling is defined by Sakurai and Shiotsu (1977a) as transient boiling, where the transient nucleate boiling curve recovers to the steady-state nucleate boiling curve before the steady-state CHF is reached. Beyond the steady-state CHF point, the nucleate boiling curve remains along the extension of the steady-state curve until the transient CHF is reached. In irregular boiling, the transient curve does not recover the steady-state curve before the steady-state CHF is reached. Sakurai and Shiotsu observed that, at atmospheric pressure, the boiling becomes irregular when the exponential period is smaller than 50 ms. However, at pressures higher than 0.6 MPa, the boiling remained regular even for the fastest transient applied ($\tau = 5$ ms). Thus, increasing the pressure for a given exponential period promotes regular boiling, whereas decreasing the exponential period for a given pressure promotes irregular boiling. The transition between regular and irregular boiling is possibly a result of the instantaneous imbalance between the heat transferred to the surface through conduction and the heat removed through convection. Therefore, a universal map for regular and irregular boiling requires heater and fluid properties, geometry, and heating methods as independent variables in addition to the pressure and the speed of the transient.

The first comprehensive, theoretically based modeling of the regular boiling CHF under power transients was presented by Serizawa (1983). However, the proposed model contradicts the physical evidence presented by other investigators. First, Serizawa's steady-state boiling model is based on a continuous liquid supply to the macrolayer. This assumption contradicts the saturated pool boiling model of Haramura and Katto (1983), which will be summarized in the next section. Second, the final quantification of Serizawa's model requires one of its important parameters, the macrolayer thickness, to be correlated empirically. This was done by comparing the model directly with transient CHF data. Therefore, a good agreement between the data and the model is not surprising. However, this empirically correlated magnitude of the macrolayer thickness is almost two orders of magnitude smaller than the macrolayer thicknesses measured by Bhat et al. (1986) and Iida and Kobayasi (1969). In his model, Serizawa neglected the conduction effects within the heater and related the instantaneous surface heat flux to the instantaneous power generation rate through a simple volume-to-surface area ratio. We refer to this approximation as the quasi-steady conduction model.

In this paper, we focus on developing an improved model for CHF in pool boiling for power transients. The model is purely theoretical for saturated pool boiling. For subcooled pool boiling, one empirical constant is required because the dynamics of vapor bubbles are not well understood. First, we will briefly review the pool boiling steady-state CHF models.

Contributed by the Heat Transfer Division and presented at the 24th National Heat Transfer Conference, Pittsburgh, Pennsylvania, August 9-12, 1987, and the 25th National Heat Transfer Conference, Houston, Texas, July 24-27, 1988. Manuscript received by the Heat Transfer Division May 9, 1988; revision received February 2, 1990. Keywords: Boiling, Phase-Change Phenomena, Transient and Unsteady Heat Transfer.

Critical Heat Flux in Steady-State Pool Boiling

A theoretical prediction of the steady-state CHF in saturated pool boiling over horizontal surfaces was first presented in the foundation work of Zuber (1958). Zuber assumed that the collapse of the vapor removal mechanism was responsible for CHF. The final correlation is in the same form as the Kutatelatze correlation (1963). The Zuber and Kutatelatze correlations are extensively used in the international literature. However, various authors recommend different constants for the correlations.

Zuber's model was questioned because of its limited modeling of governing physics (Katto and Yokoya, 1968). Based on a series of studies by Katto and his co-workers (Katto et al., 1970; Katto and Kikushi, 1972; Katto and Yokoya, 1976), Haramura and Katto (1983) presented what is perhaps the most complete formulation of saturated pool boiling CHF. Consistent with experimental observations such as Gaertner's (1965), this model postulates that, near CHF, vapor is removed from the surface as vapor slugs (or vapor mushrooms), not through vapor jets as postulated by Zuber. Note that the vapor slugs have a frequency of 12 Hz or higher and appear to the human eye as vapor jets unless observed using high-speed photography. The model is referred to as a "multistep model" (Katto, 1985) because, in addition to the vapor removal mechanism, it accounts for other mechanisms such as liquid supply, macrolayer formation, and surface dryout. The boiling configuration proposed by the multistep model received much emphasis in recent years as the possible scenario for high-heat-flux boiling [see Bhat et al. (1983) and Chyu (1987)]. Haramura and Katto assumed that the liquid supply to the macrolayer underneath the bubbles is blocked at high heat fluxes. The only time the bulk liquid reaches the surface is when the bubble departs. Based on the experimental observations of Katto and Yokoya (1975), the initiation of the next bubble after departure is almost instantaneous. Furthermore, Haramura and Katto assumed that the surface heat flux is steady and all of it contributes to macrolayer evaporation. Thus, CHF or surface dryout occurs if the heat flux is high enough to evaporate the macrolayer thickness δ before the end of the hovering period of the bubble. This defines the "critical" macrolayer thickness, δ_o, at which CHF occurs. An energy balance yields

$$\tau_d q_{\mathrm{CHF},SS} = \rho_f h_{fg} \delta_o \left(1 - \frac{A_v}{A_w}\right) \qquad (2)$$

where τ_d is the hovering period, δ_o is the critical macrolayer thickness, A_v is the surface area covered by vapor, and A_w is the total surface area. The hovering period (when the heat flux is equal to CHF) can be calculated by using an idealized bubble model as described by Katto and Yokoya (1976) and reported by Katto and Haramura (1983). The critical macrolayer thickness is postulated by Haramura and Katto to be one-fourth of the Helmholtz instability wavelength at the stem interface. The calculation of the Helmholtz instability further assumes that all the evaporation takes place at or near the base of the vapor stems. This postulate is physically plausible as further discussed by Chyu (1987).

The ratio A_v/A_w, which strongly affects the calculation of the initial macrolayer thickness δ_o, must be known to calculate the CHF. Haramura and Katto used an indirect approach in evaluating this quantity. They obtained it by directly comparing equation (2) with the Zuber correlation. Obviously, such an approach invalidates the numerical assessment of the model against experimental data. Instead, we evaluate the parameter A_v/A_w by directly comparing the Helmholtz instability model with the macrolayer thickness data of Bhat et al. (1986). This comparison, which is discussed further in an earlier paper (Pasamehmetoglu and Nelson, 1987), suggests that when considering data, the macrolayer thickness at atmospheric pressure is best predicted if $0.0164 \le A_v/A_w \le 0.0220$.

When these bounding values are used, the multistep model predicts the following range of CHF for saturated water at atmospheric pressure over a horizontal surface: $1.251 \le q_{\mathrm{CHF},SS} \le 1.503$ MW/m^2. For water at atmospheric pressure, the Zuber correlation predicts CHF values ranging from 1.1 to 1.52 MW/m^2 using various constants recommended in the open literature. Thus, the multistep model of Haramura and Katto is in perfect quantitative agreement with the well-assessed Zuber correlation when independently obtained macrolayer thickness data are used for closure.

Unfortunately, similar assessment of the multistep model is not possible at higher pressures because macrolayer thickness data at these pressures do not exist. Therefore, we extrapolated the data of Bhat et al. (1986) by assuming that A_v/A_w follows the form suggested by Haramura and Katto (1983) as follows:

$$\frac{A_v}{A_w} = C_A \left(\frac{\rho_g}{\rho_f}\right)^{0.2} \qquad (3)$$

where the constant C_A is evaluated at atmospheric pressure through the data of Bhat et al., which yields $7.17 \times 10^{-2} < C_A < 9.62 \times 10^{-2}$. Figure 1 in Pasamehmetoglu and Nelson's study (1988) shows the comparison between the multistep model and the Zuber correlation with various con-

Nomenclature

A_v = heater area covered by vapor, m^2
A_w = total heater area, m^2
B_s = switch-over parameter
C = specific heat of the liquid, J/kg-K
C_A = empirical constant
C_B = empirical constant of Rohsenow correlation
d = heater diameter, m
Fo = Fourier number = $\alpha_H \tau / d^2$
g = gravitational constant, m/s^2
h_{fg} = latent heat of evaporation, J/kg
K = empirical constant
k = thermal conductivity, W/m°-C
L_o = Laplace coefficient = $[\sigma / g(\rho_f - \rho_g)]^{1/2}$, m
P = pressure, Pa
Q = heat generation rate, W/m^3
q = surface heat flux, W/m^2
T = temperature, °C
t = time, s
δ = macrolayer thickness, m
δ_o = critical macrolayer thickness, m
ΔT_{sub} = degree of subcooling, °C
η = ratio of transient CHF and steady-state CHF
ρ = density, kg/m^3
σ = surface tension, N/m
τ = exponential period of heat generation rate, s
τ^* = exponential period of surface heat flux, s
τ_d = bubble hovering period in saturated pool boiling, s
τ_g = bubble growth period in subcooled pool boiling, s

Subscripts

B = switch-over point
CHF = critical heat flux
f = saturated liquid
g = saturated vapor
h = heater
i = initial value
SS = steady-state
sat = saturated pool boiling
sub = subcooled pool boiling
TR = transient
w = wall condition

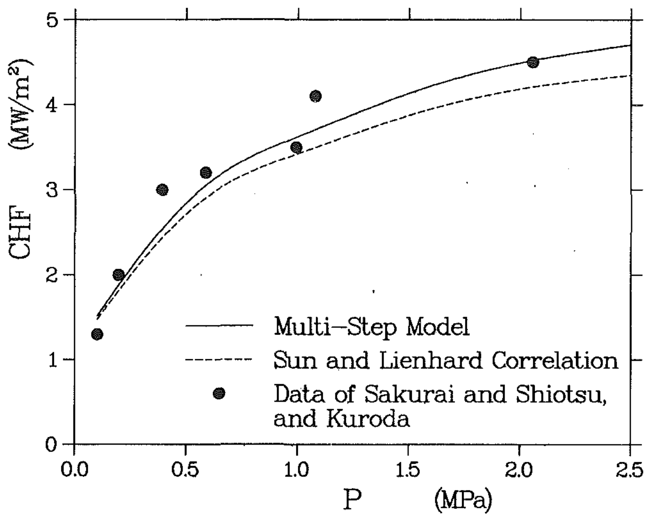

Fig. 1 Comparison of multistep model with the Sun and Lienhard correlation and with the steady-state data of Sakurai and Shiotsu (1977b) and Kuroda (Serizawa, 1983)

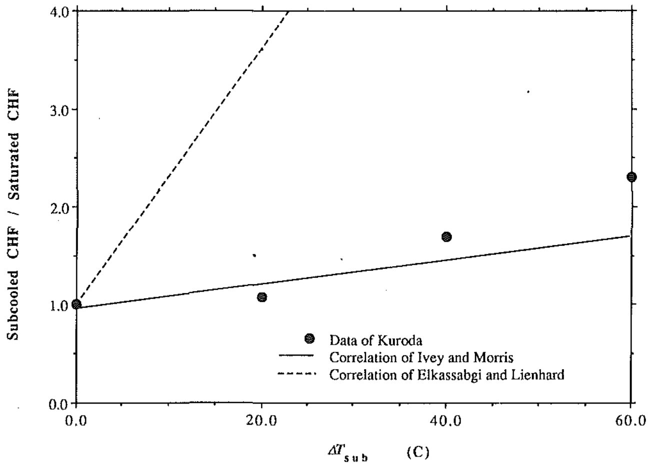

Fig. 2 Comparison of the Ivey-Morris (1962) and Elkassabgi-Lienhard (1988) correlations with the steady-state subcooled boiling data of Kuroda (Serizawa, 1983)

stants up to a pressure of 4 MPa. As shown in this reference, the agreement is quite favorable. This independent assessment of the multistep model provides further confidence in the model and is very important for the present study because the multistep model constitutes the kernel of our transient CHF model.

The multistep model also can be extended to predict the CHF over small-diameter horizontal wires. Including the curvature effects, the energy balance is modified as (Haramura and Katto, 1983; Katto and Haramura, 1983)

$$\tau_d q_{\mathrm{CHS},SS} = \rho_f h_{fg} \delta_o \left(1 - \frac{A_v}{A_w} + \frac{\delta_o}{d}\right) \qquad (4)$$

where d is the heater diameter. In equation (4), the term in parentheses is usually small and thus has little influence on CHF. The major parameter that reflects the influence of small diameter is the hovering period, τ_d. The evaluation of τ_d for small-diameter wires also is described by Katto and Haramura (1983). Decreasing the diameter reduces the hovering period and thus, based on a more frequent resupply of the macrolayer, increases the CHF. When modified for small-diameter wire, the multistep model is in good agreement with the data and also with the empirical correlation of Sun and Lienhard (1970). It can be shown that the comparison between the multistep model and the correlation of Sun and Lienhard is favorable within the application range of the correlation by Sun and Lienhard. The difference is within ±15 percent, which is within the data scatter. The pressure effects formulated by ρ_g/ρ_f, which are not accounted for in the Sun and Lienhard correlation, appear to be negligible. In Fig. 1, the multistep model and Sun-Lienhard correlation are compared with the steady-state CHF data of Sakurai and Shiotsu (1977b) and Kuroda (cited by Serizawa, 1983). All these data were obtained with 1.2-mm-dia platinum wires. The data from the same experiments are used for assessing the transient CHF model. Therefore, it is important that the multistep model favorably predict the steady-state data. As shown in Fig. 1, all the data fall within ±25 percent of the multistep model. The steady-state CHF data shown in this figure are obtained from the transient experiments with $\tau = 10$ s. Thus, actual steady-state CHF values may be slightly smaller than these magnitudes. For example, the experiments of Fontana (1973) reveal that, even with very slow transients, the CHF can be observed at heat fluxes slightly higher than steady-state CHF. The difference in Fontana's experiments is confined within 25 percent, which is also within the data scatter in his experiments. Therefore, it is difficult to reach a strong conclusion from Fontana's experiments. Nevertheless, they may help explain part of the small discrepancy in Fig. 1.

Unfortunately, CHF in subcooled pool boiling is not as well understood as saturated pool boiling. Zuber et al. (1961) extended the hydrodynamic theory to include the effect of subcooling of bulk liquid. They suggested that subcooling will increase CHF because a fraction of the vapor will condense on the jet walls; thus, additional vapor would have to be generated before the Helmholtz instability collapses the vapor removal mechanism. However, the final correlation is not very successful in correlating the available data. A commonly used subcooled boiling CHF correlation is suggested by Ivey and Morris (1962). Ivey and Morris correlated water data for horizontal wires 1.22 to 2.67 mm in diameter and in the subcooling range from 0 to 72°C. This correlation is only accurate within ±25 percent. The models of Zuber et al. (1961) and of Ivey and Morris (1962) suggest that for a given pressure and constant fluid properties, CHF changes linearly with respect to subcooling.

Recently, Elkassabgi and Lienhard (1988) obtained subcooled CHF data over horizontal wires with diameters ranging from 0.8 to 1.54 mm. Their data showed that the linear relation between CHF and ΔT_{sub} is only valid for lower subcoolings. Beyond a limiting subcooling, CHF exhibits a constant behavior independent of subcooling. Between these low and high subcooling regions there is a moderate subcooling range where the CHF is proportional to $(\Delta T_{\mathrm{sub}})^{3/8}$. They postulated different heat transfer mechanisms as being responsible for the behavior in each regime and proposed empirical correlations. The data are scattered within ±25 percent, and the transition from low to moderate subcooling cannot be estimated because their correlations do not intersect. Furthermore, the experiments of Elkassabgi and Lienhard did not include water; thus, there is a question of whether their correlations can be extrapolated to water data. However, their study shows that the low subcooling correlation agrees well with the correlation of Ivey and Morris when the Peclet number for water is evaluated near atmospheric pressure.

The data that are of interest to the present study are the transient CHF data of Kuroda. Figure 2 shows the comparison of the Ivey and Morris and Elkassabgi and Lienhard correlations in comparison with Kuroda's steady-state data. As shown in this figure, at 0.993 MPa pressure, the equation considerably overpredicts the Ivey-Morris correlation and the data. The Ivey-Morris correlation underpredicts the data with

40 and 60°C subcooling by 22 and 43 percent, respectively. This uncertainty is outside the ±25 percent range recommended for the correlation. Therefore, the applicability of the Ivey–Morris correlation at high pressure is questionable. However, we must note that Kuroda's steady-state data correspond to transient data obtained with $\tau = 10$ s. These values may be slightly higher than the actual steady-state values because of a hysteresis similar to the saturated pool boiling case as suggested by Fontana (1973).

To formulate the transient CHF, we need a physical model similar to the multistep model that explicitly includes the time constant of the CHF phenomenon. For this purpose, we have tried to extend the multistep and model to include subcooling effects. Our effort is limited to a simple physical approximation. It is forced empirically to yield the same result as Kuroda's empirical data. Therefore, the current model does not improve the predictive capability for the steady-state CHF in subcooled boiling. Its sole advantage is that it explicitly includes the vapor mass growth period. In subcooled boiling, we use the term "growth period" as an equivalent to the hovering period in saturated pool boiling. Physically, the growth period may be terminated by the collapse of the vapor bubble, whereas the hovering period always terminates by vapor mass departure. Our approximation is based on the following postulates: (*a*) the vapor removal mechanism in subcooled boiling remains similar to that in saturated boiling, as described by the multistep model, at moderate subcoolings; (*b*) the thermodynamic properties of subcooled liquid are very close to the properties at saturation temperature; (*c*) the fraction of the heater area covered by vapor is unaffected by subcooling. This quantity is formulated by Haramura and Katto (1983) as a function of density ratio only. Because of postulate (*b*), this ratio remains independent of subcooling. Furthermore, this ratio is not affected strongly by the surface heat flux and is usually very small even at pressures close to critical pressure (Haramura and Katto, 1983); (*d*) the critical liquid layer thickness δ_o is inversely proportional to the square of the surface heat flux. This assumption requires further analysis because some of the vapor may condense along the vapor stems in subcooled boiling, thus reducing the vapor velocity. In turn, this will increase the Helmholtz instability wavelength, yielding a thicker macrolayer.

Based on these postulates, the energy balance in subcooled boiling can be written as

$$\tau_g q_{\mathrm{CHI},SS,\mathrm{sub}} = \rho_f h_{fg} \delta_{o,\mathrm{sub}} \left(1 - \frac{A_v}{A_w}\right) \left(1 + K \frac{C_{p,f} \Delta T_{\mathrm{sub}}}{h_{fg}}\right) \qquad (5)$$

where τ_g is the growth period, $\delta_{o,\mathrm{sub}}$ is the critical macrolayer thickness, and K is the empirical constant that accounts for the following effects: (1) liquid recirculation resulting from condensation on the vapor bubble interface and along the vapor stems within the macrolayer; (2) possible liquid supply to the macrolayer during the growth period; (3) after the departure or collapse of the vapor bubble, the supplied liquid may be warmer than the far-field subcooled temperature; (4) increase in critical macrolayer thickness resulting from condensation along the stems.

It is a very aggressive assumption to model all these effects with a single empirical constant. However, as mentioned before, the present model is a first-order approximation and is developed merely to analyze the transient CHF. Using postulate (*d*), the critical macrolayer thickness in subcooled boiling can be formulated as

$$\delta_{o,\mathrm{sub}} = \left(\frac{q_{\mathrm{CHF},SS,\mathrm{sat}}}{q_{\mathrm{CHF},SS,\mathrm{sub}}}\right)^2 \delta_{o,\mathrm{sat}} \qquad (6)$$

Substituting equation (6) into equation (5) and combining it with equation (1), we obtain the following relation for the vapor bubble growth period in subcooled boiling:

$$\tau_g = \left(\frac{q_{\mathrm{CHF},SS,\mathrm{sat}}}{q_{\mathrm{CHF},SS,\mathrm{sat}}}\right)^3 \left(1 + K \frac{C_{p,f} \Delta T_{\mathrm{sub}}}{h_{fg}}\right) \tau_d \qquad (7)$$

Unfortunately, there are no independent data for the growth period in subcooled boiling. Also, no simple theoretical model is available to estimate K.

Figure 2 in the study of Pasamehmetoglu et al. (1988) illustrates the growth period, τ_d, as a function of subcooling for the steady-state data of Kuroda and for various values of K. As shown in this figure, the growth period of the vapor bubbles quickly decreases with increasing subcooling. This is in qualitative agreement with the discrete bubble data of Ibrahim and Judd (1985). However, quantitatively, the extrapolation of discrete bubble data to model the vapor slug behavior is questionable.

Transient CHF Modeling

In this section, the multistep model is extended to formulate the CHF during power transients. The multistep model suggests that, when a heat flux equal to steady-state CHF is applied to the surface, dryout can be detected after a certain period of time, τ_d or τ_g, these are the time constants of the CHF phenomena in saturated and subcooled pool boiling, respectively. During power transients, the local heat flux increases during the time constant and the total evaporation of the macrolayer takes place sooner. By the time the surface is essentially dry, the local heat flux reaches a value higher than at steady state. This instantaneous heat flux is referred to as transient CHF, $q_{\mathrm{CHF},TR}$.

No liquid is supplied to the macrolayer during the hovering or growth period; thus, the thinning of the liquid layer is governed by one of two mechanisms: hydrodynamic instability (which dictates the maximum thickness of the stable macrolayer for a given surface heat flux) or evaporation. This may be expressed mathematically as

$$\frac{d\delta}{dt} = \max\left[\left|\frac{\partial \delta_o}{\partial q} \frac{dq}{dt}\right|, \left|\frac{q}{f_2(P, \Delta T_{\mathrm{sub}})}\right|\right] \qquad (8)$$

where

$$f_2(P, \Delta T_{\mathrm{sub}}) = \rho_f h_{fg} \left(1 - \frac{A_v}{A_w}\right) \left(1 + K \frac{C_{p,f} \Delta T_{\mathrm{sub}}}{h_{fg}}\right) \qquad (9)$$

The first term on the right-hand side of equation (8) corresponds to the hydrodynamic-instability-controlled behavior. It is assumed that this instability has a very small time constant; thus, it can be modeled as a quasi-steady process through

$$\delta_o(t) = \frac{f_1(P)}{[q(t)]^2} \qquad (10)$$

where

$$f_1(P) = \frac{\pi}{2} \sigma \left(\frac{\rho_f - \rho_g}{\rho_f \rho_g}\right) \left(\frac{A_v}{A_w}\right)^2 (\rho_g h_{fg})^2 \qquad (11)$$

This formulation assumes a uniform vapor velocity in the vapor stems that accelerates instantaneously to a value dictated by the surface heat flux. This assumption is considered very reasonable because the length of the vapor stems is very small (~10–100 μm). A numerical justification of this assumption for saturated pool boiling is given in an earlier paper (Pasamehmetoglu et al., 1987a). The assumption becomes less plausible for subcooled pool boiling because possible condensation along the stem causes a nonuniform vapor velocity. The second term on the right-hand side corresponds to the evaporation of the macrolayer.

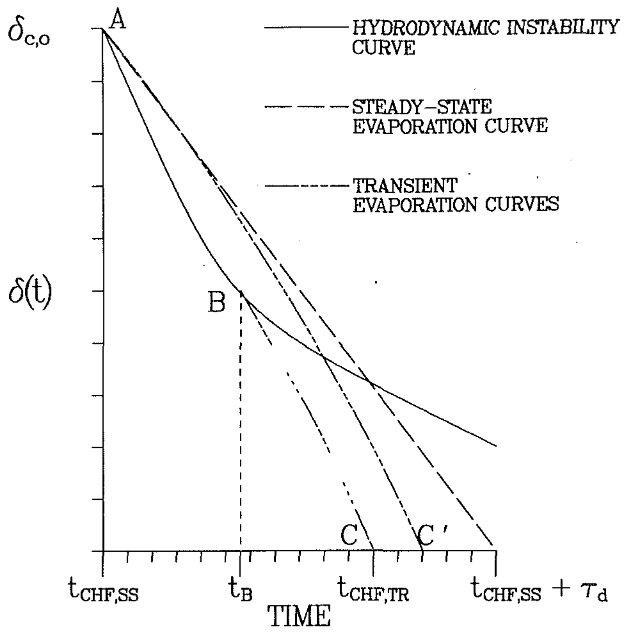

Fig. 3 Schematic of macrolayer thinning mechanisms

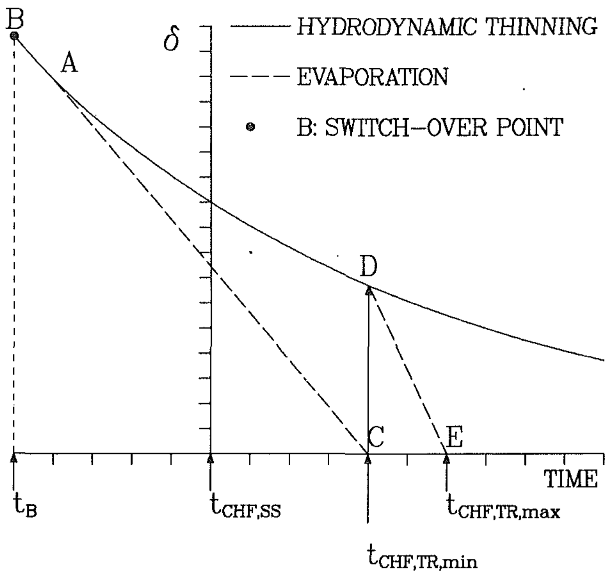

Fig. 4 Schematic of macrolayer thinning during slow transients

Equation (8) is illustrated graphically in Fig. 3. This figure shows that if the heat flux is kept constant at the steady-state CHF level, the macrolayer will evaporate at the end of the hovering period, τ_d. (This figure is describing saturated pool boiling, but the same concepts also apply to subcooled pool boiling if τ_d is replaced by τ_g). However, because the heat flux increases with time, the rate of evaporation also increases as shown by the dotted lines. Thus, the dotted lines correspond to the evaporation mechanism. On the other hand, an increase in heat flux also causes a decrease in the thickness of the stable macrolayer as shown by the solid line, which corresponds to the hydrodynamic thinning mechanism. In Fig. 3, hydrodynamic thinning dominates until $t = t_B$, and from t_B until complete dryout ($t = t_{\mathrm{CHF},TR}$) evaporation dominates. Thus, the instantaneous macrolayer thickness follows the curve ABC, rather than AC′ as suggested by Serizawa (1983). For a monotonically increasing surface heat flux, the transition from one mechanism to the other is unique and determined by the slopes of evaporation and hydrodynamic thinning lines. The switch-over occurs when

$$\left|\frac{\partial \delta_o}{\partial q}\frac{dq}{dt}\right| = \left|\frac{q}{f_2(P,\ \Delta T_{\mathrm{sub}})}\right| \tag{12}$$

which yields

$$q_B = \left[2 f_1(P) f_2(P,\ \Delta T_{\mathrm{sub}}) \left(\frac{dq}{dt}\right)_{q=q_B}\right]^{1/4} \tag{13}$$

Equation (13) can be expressed as a function of the steady-state CHF as

$$q_B = B_s q_{\mathrm{CHF},SS} \tag{14}$$

where the switch-over parameter B_s becomes

$$B_s = \left[\frac{2\tau_d (dq/dt)_{q=q_B}}{q_{\mathrm{CHF},SS}}\right]^{1/4} \tag{15}$$

If the instantaneous surface heat flux changes exponentially according to

$$q(t) = q_i \exp(t/\tau^*) \tag{16}$$

equation (15) reduces to

$$B_s = \left(\frac{2\tau_d}{\tau^*}\right)^{1/3} \tag{17}$$

When B_s is less than or equal to 1, the macrolayer thinning is a result of evaporation only (thermal thinning) beyond steady-state CHF. We refer to these cases as slow transients, where τ^* is greater than $2\tau_d$. On the other hand, when B_s is greater than 1, hydrodynamic thinning exists beyond the steady-state CHF up to the switch-over point. These are the fast transients, where τ^* is less than $2\ \tau_d$. Because the macrolayer thinning mechanisms are different for slow and fast transients, the transient CHF models will be developed separately. First, we consider the slow transients.

CHF Modeling During Slow Transients. During slow transients, B_s is smaller than 1 and evaporation is the dominant mechanism even before the steady-state CHF is reached. The corresponding macrolayer thickness follows the curve BC in Fig. 4. To calculate the minimum possible value of transient CHF, we assume that a vapor mass is formed at time t_A, where $t_B \le t_A \le t_{\mathrm{CHF},SS}$. For the macrolayer underneath this vapor mass to dry out in an evaporation mode at time t_C, the energy deposition must be high enough to evaporate all the liquid during the vapor mass hovering period. Thus, the following inequality must be satisfied:

$$(\delta_o)_{q=q_A} \le \int_0^{\eta^{1/5}\tau_d} \frac{q_A \exp(t'/\tau^*)}{f_2(P,\ \Delta T_{\mathrm{sub}})}\, dt' \tag{18}$$

where $t' = t - t_A$ and η is the CHF ratio given by

$$\eta = \frac{q_{\mathrm{CHF},TR}}{q_{\mathrm{CHF},SS}}$$

The term $\eta^{1/5}\tau_d$ in equation (18) represents the vapor mass hovering period when the surface heat flux is equal to transient CHF. As we showed in an earlier study (Pasamehmetoglu et al., 1987b), the vapor mass hovering period is almost independent of history effects during transient boiling and may be calculated as a function of departure heat flux using a steady-state heat flux model. It is assumed tentatively that the same behavior is correct for subcooled boiling. Using equations (5) and (10), the inequality in equation (18) yields

$$q_A \ge \frac{1}{2^{1/3}} B_s q_{\mathrm{CHF},SS}\left[\exp\left(\frac{\eta^{1/5}\tau_d}{2}\right) - 1\right]^{-1/3} \tag{19}$$

Because this part of the analysis is concerned with slow transients, where $B_s < 1$ and $\eta < 1.5$ (as shown later), we can approximate $\eta^{1/5}$ by 1. Thus, for an exponential increase in the heat flux, we obtain

$$\eta_{\min} = \frac{1}{2^{1/3}} B_s \exp\left(\frac{B_s^3}{2}\right)\left[\exp\left(\frac{B_s^3}{2}\right) - 1\right]^{-1/3} \tag{20}$$

This result is valid for slow transients, where dryout under a given vapor mass occurs because of evaporation during its hovering period. Therefore, q_A must be greater than or equal to the switch-over heat flux q_B, which is defined as $B_s q_{\mathrm{CHF},SS}$. Thus, equation (19) yields

$$\frac{1}{2^{1/3}}\left[\exp\left(\frac{B_s^3}{2}\right) - 1\right]^{-1/3} \geq 1, \tag{21}$$

the solution of which gives $B_s \leq 0.93$. Therefore, the vapor mass that leads to the earliest dryout must be formed when $q \approx 0.93 q_{\mathrm{CHF},SS}$. Any vapor mass formed earlier will depart before dryout, whereas a vapor mass formed after will lead to dryout before departure.

For the same slow transient, the maximum value of transient CHF corresponds to the case where the vapor mass departs before the dryout (at point C) and fresh liquid replenishes the macrolayer. Thus, the macrolayer follows the path ACDE. The corresponding maximum transient CHF may be obtained through the solution of the following integral:

$$(\delta_o)_{q=q_{\mathrm{CHF},TR,\min}} = \int_0^{t'_{\mathrm{CHF},TR,\max}} \frac{q_{\mathrm{CHF},TR,\min}\exp(t'/\tau^*)}{f_2(P, \Delta T_{\mathrm{sub}})}\,dt' \tag{22}$$

where $t' = t - t_{\mathrm{CHF},TR,\min}$. Integrating equation (22) and rearranging the terms, we obtain

$$\eta_{\max} = \eta_{\min} + \frac{B_s^3}{2\eta_{\min}^2} \tag{23}$$

where $\eta_{\min}$ is given by equation (20). It is worth noting that during slow transients, the maximum value of $\eta_{\min}$ corresponds to the case with $B_s = 0.93$, which yields $\eta_{\min} \approx 1.4$. It easily can be shown that the maximum difference between the minimum and maximum values of η is less than 15 percent, which is commonly the data scatter for CHF. Thus, for practical purposes, equations (20) and (23) can be approximated by a single expression given by

$$\eta = 1 + \frac{B_s^3}{2}. \tag{24}$$

It can be shown that this expression is obtained if the vapor mass that leads to dryout is formed when $q = q_{\mathrm{CHF},SS}$ and the macrolayer thinning is a result of evaporation only ($B_s \leq 1$).

CHF Modeling During Fast Transients. During fast transients, the macrolayer leading to the earliest dryout is caused partially by hydrodynamic thinning. For these transients, the macrolayer history in the vicinity of transient CHF is shown in Fig. 5. A vapor mass initiated after the switch-over point will lead to dryout, whereas a vapor mass initiated before the switch-over point ($t = t_B$) may depart before dryout. As shown in Fig. 5, the behavior of vapor mass before $t = t_B$ does not affect the liquid layer thickness. The only time the liquid layer thickness is affected by vapor mass departure is when the departure occurs after t_B. Therefore, the minimum transient critical heat flux can be calculated from the following energy balance:

$$(\delta_o)_{q=q_B} = \int_{t_B}^{t_{\mathrm{CHF},TR}} \frac{q(t)}{f_2(P, \Delta T_{\mathrm{sub}})}\,dt \tag{25}$$

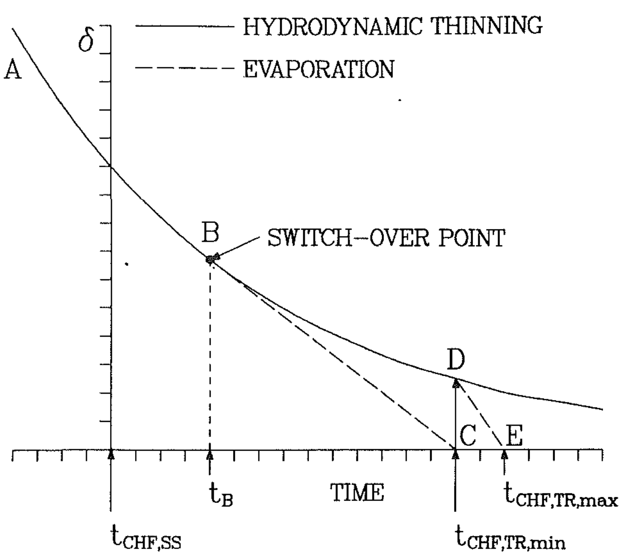

Fig. 5 Schematic of macrolayer thinning during fast transients

Substituting equation (10), (14), (16), and (17) into equation (25), we obtain

$$\eta_{\min} = 1.5 B_s \tag{26}$$

The maximum possible value corresponds to the case where the vapor mass departs just before dryout ($t = t_{\mathrm{CHF},TR,\min}$). Thus, the liquid layer thickness follows the curve ABCDE in Fig. 5. Through an analysis similar to that for slow transients, it can be shown that the maximum heat flux also is given by equation (23), where $\eta_{\min}$ must be obtained from equation (26).

We also must remember that the above analysis is not applicable to very fast transients. If the transient is fast enough so that the very first vapor mass that forms remains on the surface until the transient CHF occurs, the transient CHF becomes a deterministic value rather than a probabilistic one. Actually, in these cases, it is more appropriate to talk about a vapor blanket overlaying the liquid macrolayer rather than vapor masses because, without departure, Taylor wave patterns may not be distinguished. Such rapid transients correspond to the case where

$$\frac{q_{\mathrm{CHF},TR}}{q_{\mathrm{M-B}}} \leq \exp\left(\frac{\tau_d}{\tau^*}\right) \tag{27}$$

where $q_{\mathrm{M-B}}$ represents the heat flux at the first transition point on the boiling curve as formulated by Moissis and Berenson (1963). The Moissis–Berenson correlation is only valid for flat plates. Bhattacharya and Lienhard (1972) suggested a similar equation for circular cylinders. However, their correlation shows a strong dependence on the contact angle, which is typically a *nuisance parameter* with high degree of uncertainty. Furthermore, to the best of our knowledge, the effect of subcooling on the first transition point has never been investigated. In addition, during transient boiling, the first transition may occur at a heat flux lower than what is predicted by the steady-state correlations because of the temperature overshoot at the early stages of the transient. Consequently, it is difficult to solve for τ^* from equation (27). As a first-order guess, we will assume that the solution yields $\tau^* \leq$ 10–20 ms.

Combining the above analysis into a single correlation yields

$$\eta_{\min} = [1 - H(B_s - 0.93)]\frac{1}{2^{1/3}} B_s \exp\left(\frac{B_s^3}{2}\right)\left[\exp\left(\frac{B_s^3}{2}\right) - 1\right]^{-1/3} + [H(B_s - 1)]1.5B_s \tag{28}$$

and

$$\eta_{\max} = \eta_{\min} + \frac{B_s^3}{2\eta_{\min}^2} \qquad (29)$$

where H is the Heaviside step function. The first term with the Heaviside step function corresponds to slow transients, whereas the second term corresponds to fast transients. A simpler deterministic version of this correlation, which was obtained earlier by Pasamehmetoglu (1986), can be written as

$$\eta = [1 - H(B_s - 1)]\left(1 + \frac{B_s^3}{2}\right) + H(B_s - 1)1.5B_s \qquad (30)$$

In this equation, the approximation discussed above for slow transients is used. For fast transients, the minimum value of transient CHF is calculated as a conservative approach. This is a good approximation, especially if the heater is long and where there is more than one vapor mass growing simultaneously. Then, having a vapor mass that will lead to dryout near the minimum transient CHF point becomes more likely.

Effect of the Heater's Thermal Storage on the Transient CHF Model

So far, we have assumed that the surface heat flux is known as a function of time. However, in the experiments, the power generation rate is the controlled parameter and is given as a function of time. Thus, the conduction solution within the heater must be coupled with convection to solve for instantaneous heat flux. To calculate the actual relationship between $q(t)$ and $Q(t)$, we must either model the entire boiling curve theoretically or use the temperature-versus-time data from the transient CHF experiments to solve the transient conduction equation. The former is a difficult task, and the latter are not available in the open literature. Therefore, we have decided to develop an approximate approach using the following assumptions: (1) We restricted the analysis to regular boiling. With this restriction, we are able to approximate the surface heat flux/surface temperature relation between steady-state and transient CHF through the use of an appropriate steady-state nucleate boiling correlation such as the Rohsenow correlation (Rohsenow, 1952). (2) We assumed that, for an exponential increase in power as given by equation (1), the surface heat flux increases exponentially, as given by equation (16), between steady-state and transient CHF. (3) Finally, we assumed that the temperature profile within the heater remains parabolic between steady-state and transient CHF. Although we know that the real temperature profile is time dependent, this assumption allows us to see the effect of temperature profile on the results. A parabolic temperature profile means

$$T(t, r) = T_w(t) + \frac{q(t)d}{4k_h}\left(1 - \frac{r^2}{R^2}\right) \qquad (31)$$

The instantaneous average temperature then can be calculated as

$$T_a(t) = T_w(t) + \frac{q(t)d}{8k_h} \qquad (32)$$

Between steady-state and transient CHF, the total heat generated for an exponential transient is given by

$$E_{\text{total}} = \int_{t_{\text{CHF},SS}}^{t_{\text{CHF},TR}} Q_i \exp\left(\frac{t}{\tau}\right) dt \qquad (33)$$

This integral can be approximated by

$$E_{\text{total}} = \frac{4\tau q_{\text{CHF},SS}}{d}\left[\exp\left(\frac{t_{\text{CHF},TR} - t_{\text{CHF},SS}}{\tau}\right) - 1\right] \qquad (34)$$

The total heat stored per unit volume within the heater is given by

$$E_{\text{stored}} = \rho_h C_h (T_{a,\text{CHF},TR} - T_{a,\text{CHF},SS}) \qquad (35)$$

where the average temperatures can be calculated using equation (32) as

$$T_{a,\text{CHF},TR} - T_{a,\text{CHF},SS} = T_{w,\text{CHF},TR} - T_{w,\text{CHF},SS} + \left[\frac{(q_{\text{CHF},TR} - q_{\text{CHF},SS})d}{8k_h}\right] \qquad (36)$$

Note that if the term in the brackets is dropped from equation (37), the equation corresponds to a lumped system. Near CHF, and Biot number is on the order of zero to unity for a platinum heater with a 1.2-mm diameter. Thus, the lumped assumption is not accurate at high heat fluxes. Because our analysis is restricted to regular boiling, the relationship between the heat flux and the surface temperature can be calculated using a nucleate boiling correlation such as the one given by Rohsenow (1952) as

$$T_w - T_{\text{sat}} = \Phi(P)q^{0.33} \qquad (37)$$

where

$$\Phi(P) = C_B\left(\frac{L_o}{\mu_f h_{fg}}\right)^{0.33}\left(\frac{h_{fg}\mu_f}{k_f}\right) \qquad (38)$$

L_o is the Laplace coefficient and the empirical constant C_B is 0.013 for platinum heaters in water (see Rohsenow, 1973). Substituting equations (36) and (37) into equation (35), we obtain

$$E_{\text{stored}} = \rho_h C_h \Phi (q_{\text{CHF},TR}^{0.33} - q_{\text{CHF},SS}^{0.33}) + \frac{d}{8\alpha_h}(q_{\text{CHF},TR} - q_{\text{CHF},SS}) \qquad (39)$$

Finally, it can be shown that, for an exponential increase in surface heat flux, the convected energy per unit volume is given by

$$E_{\text{convected}} = \frac{4\tau^* q_{\text{CHF},SS}}{d}\left[\exp\left(\frac{t_{\text{CHF},TR} - t_{\text{CHF},SS}}{\tau^*}\right) - 1\right] \qquad (40)$$

Substituting equations (34), (39), and (40) into the energy balance, $E_{\text{total}} = E_{\text{stored}} + E_{\text{convected}}$, and rearranging the terms, we obtain

$$(\eta^{\tau^*/\tau} - 1) - \left(\frac{\tau^*}{\tau} + \frac{1}{32\text{Fo}}\right)(\eta - 1) = \left(\frac{\rho_h C_h d\Phi}{4\tau q_{\text{CHF},SS}^{0.67}}\right)(\eta^{0.33} - 1) \qquad (41)$$

where Fo is the Fourier number.

Equations (30) and (41) compose a set of two nonlinear equations with two unknowns (η and τ^*) that must be solved simultaneously. If the minimum and maximum limits are desired for transient CHF, equations (28) and (29) can be used instead of equation (30). Figure 4 in an earlier publication (Pasamehmetoglu and Nelson, 1988) shows the simultaneous solution of equations (30) and (41) in terms of τ^*/τ for a 1.2-mm-dia platinum wire placed in a pool of saturated water at various pressures that correspond to the experimental conditions of Sakurai and Shiotsu (1977a, 1977b). This reference shows that within the range investigated, τ^* is independent of pressure. Furthermore, for fast transients, τ^* is considerably greater than τ, meaning the rate of increase in the heat flux is smaller than the rate of increase in power generation.

Comparison of Model With Available Data

In this section, the developed model is compared with the data from Sakurai and Shiotsu (1977b), Kuroda (Serizawa, 1983), and Kataoka et al. (1983). Small 1.2-mm-dia platinum

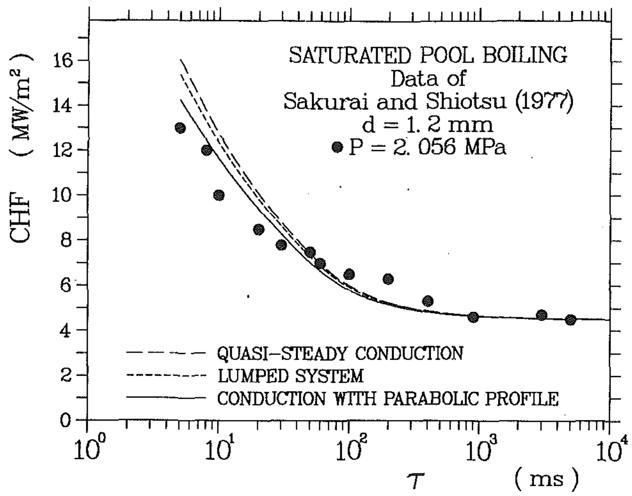

Fig. 6 Comparison of the present model with the data of Sakurai and Shiotsu (1977b) at 2 MPa pressure

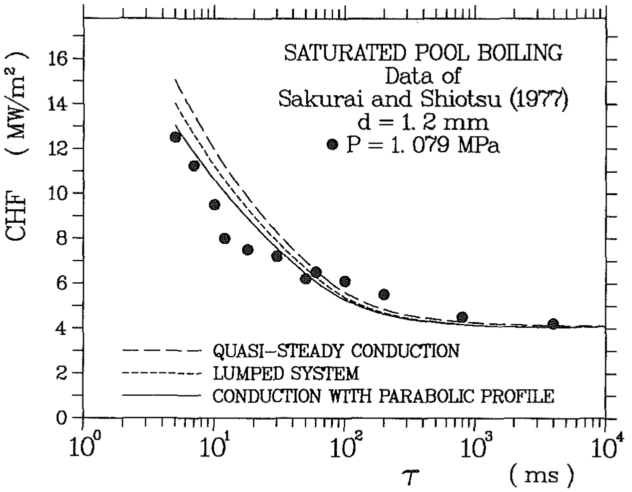

Fig. 7 Comparison of the present model with the data of Sakurai and Shiotsu (1977b) at 1 MPa pressure

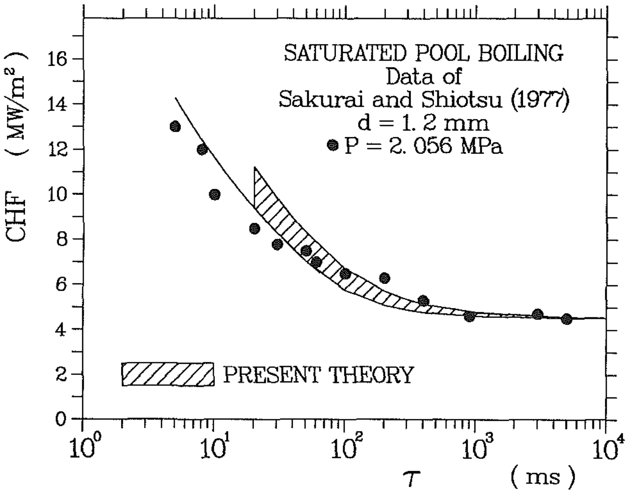

Fig. 8 Comparison of the present model's prediction range with the data of Sakurai and Shiotsu (1977b) at 2 MPa pressure

wires are used in these experiments, and the power generation is increased exponentially in accordance with the developed model.

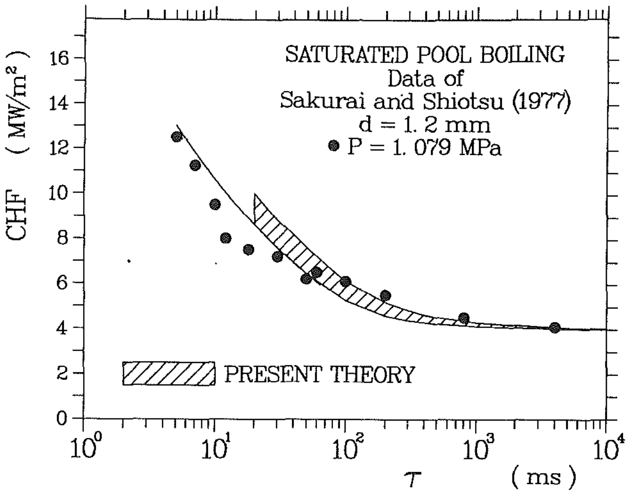

Fig. 9 Comparison of the present model's prediction range with the data of Sakurai and Shiotsu at 1 MPa pressure

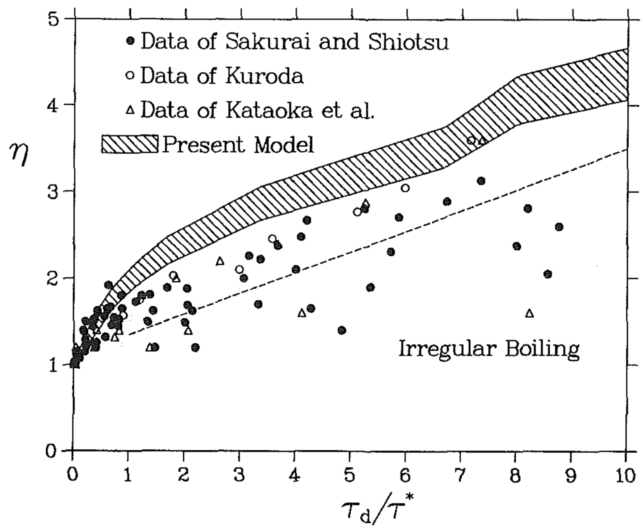

Fig. 10 Comparison of the present model with the reduced data of Sakurai and Shiotsu (1977b), Kuroda (Serizawa, 1983), and Kataoka et al. (1983)

Figures 6 and 7 show the comparison between the model and the data of Sakurai and Shiotsu (1977b) at two pressures. In this case, equations (30) and (41) are solved simultaneously to obtain the transient CHF. As shown in these figures, the quasi-steady conduction solution and the lumped model approximations considerably overpredict the data for fast transients. Even with all its simplifying assumptions, the conduction solution with parabolic profile is in much better agreement with the data. Figures 8 and 9 show the comparison with the same data, this time solving equations (28) and (29) simultaneously with equation (41). As shown in these figures, the current model is in very good agreement with data from slow transients and in favorable agreement with data from fast transients. For transients slower than $\tau = 20$ ms, the maximum limit is not plotted because the transient is too fast in these cases to allow for vapor mass departure and to result in a statistical distribution, as discussed before. These figures further indicate that the envelope covered by minimum and maximum limits is rather narrow, and this feature is also in agreement with the experimental data that show little scatter. This small scatter also verifies the importance of hydrodynamic thinning, without which the scatter would have been much larger during fast transients. All the saturated pool boiling data of Sakurai and Shiotsu and Kuroda and the natural convection data of Kataoka et al. (1983) are shown in Fig. 10 in comparison with the current model using the dimensionless

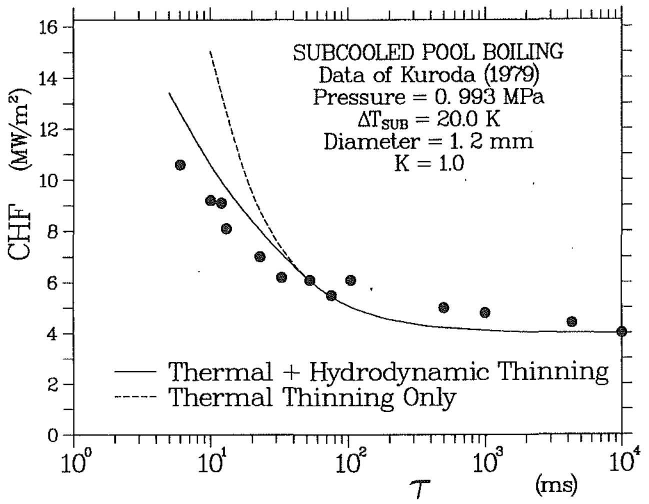

Fig. 11 Comparison of the present model with the data of Kuroda (Serizawa, 1983) with 20°C subcooling

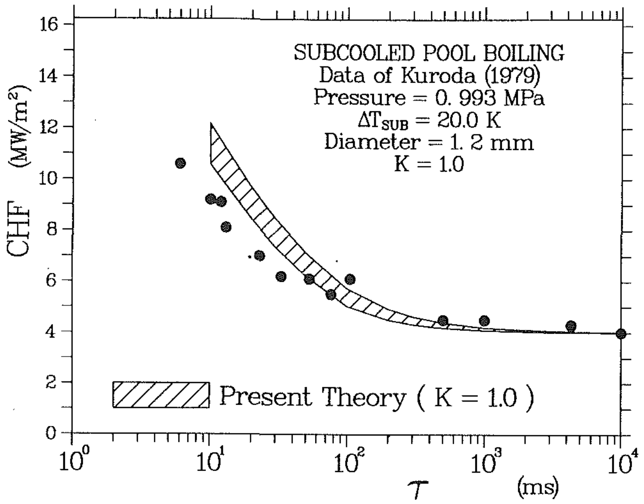

Fig. 12 Comparison of the present model's prediction range with the data of Kuroda (Serizawa, 1983) with 20°C subcooling

coordinates η and τ_d/τ. Likewise, the agreement between the present model and the data from these experiments is quite favorable.

For comparison with subcooled pool boiling data, we neglected the effect of conduction and assumed that a quasi-steady conduction mode applies ($\tau = \tau^*$) because the applicability of the Rohsenow nucleate boiling correlation to subcooled boiling is questionable. Figure 11 shows the comparison between the model and the data with 20° subcooling. The empirical parameter K is set to 1 for this comparison. Even with the quasi-steady conduction assumption, the prediction is quite favorable. This figure also shows the improvement by accounting for hydrodynamic thinning. As shown, if thermal thinning is assumed to be the only mechanism, as suggested by Serizawa (1983), the data for fast transients are considerably underpredicted. Figure 12 shows the minimum and maximum limits of predicted transient CHF in comparison with the same data. Similar to the saturated boiling case, the agreement is favorable, especially for slow transients, and the prediction indicates little data scatter as observed in the experiments. Finally, Fig. 13 shows the comparison between the present model and the 60°C subcooling data of Kuroda. As shown in this figure, the empirical parameter K needs to be increased with increasing subcooling for improved prediction. For successful modeling over a wide range of subcooling, the current theory needs certain adjustments in K. However, because of limited data and limited knowledge of subcooled boiling hydrodynamics, such adjustments could not be quantified in a correlation form. Development of a correlation for K requires additional data at various pressures and subcoolings, as well as identifying the quantitative effect of quasi-steady conduction approximation.

In the above paragraphs, we have shown that even with certain simplifying assumptions, the effect of thermal storage within the heater may considerably improve the final prediction in saturated pool boiling, especially for fast transients. The effect of thermal storage possibly becomes less pronounced with increasing subcooling. Nevertheless, it must be quantified before a strong statement can be made about the parameter K.

One last note on the comparison is that in all cases, the experimentally measured value of steady-state CHF is used when needed. This avoided errors that would be introduced through using steady-state correlations. However, as shown before, the available correlations are in favorable agreement with the steady-state data except for highly subcooled boiling.

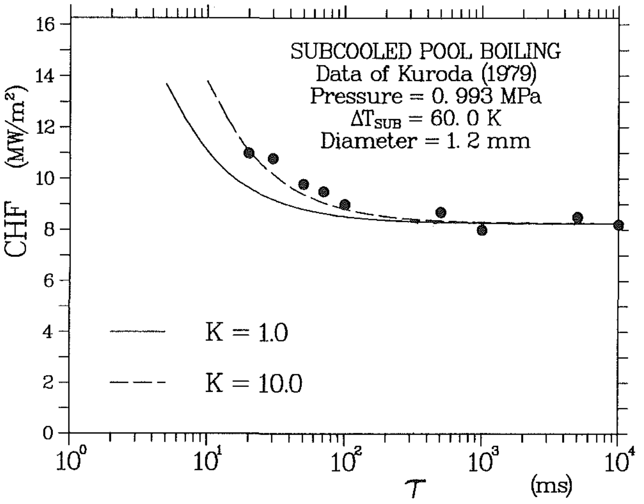

Fig. 13 Comparison of the present model with the data of Kuroda (Serizawa, 1983) with 60°C subcooling

Summary and Conclusions

A model for predicting transient CHF in saturated and subcooled pool boiling is provided in this paper. The model provides considerable improvement over the previous model of Serizawa for the following reasons: (*a*) It is in agreement with the steady-state CHF model of Haramura and Katto (the multistep model), which is in good agreement with visual observations and available steady-state data. An independent assessment of the multistep model also is provided within this study. (*b*) The effect of hydrodynamic thinning of the macrolayer is included in the model, whereas Serizawa assumes thermal thinning as the only mechanism. (*c*) The present model is purely analytical for saturated pool boiling and requires one empirical constant for subcooled pool boiling. Serizawa's model requires an empirical evaluation of the macrolayer thickness using transient CHF data. The value empirically evaluated is not in agreement with the macrolayer thickness measurements reported in the literature. (*d*) The effect of thermal conduction within the heater also is incorporated into the model using some simplifying assumptions. Serizawa assumed quasi-steady conduction even for fast transients.

The results indicate favorable agreement with the available data. The agreement is much better for saturated or near-saturated boiling conditions. As the subcooling increases, an empirical adjustment is needed to improve the predictions. The present model favorably explains the small data scatter observed in the experiments. The remaining discrepancies in the comparison are possibly a result of various simplifying assumptions made in the analysis.

There is considerable room for improvement in the postulated model. Nevertheless, we believe that the new model provides the state of the art for understanding both steady-state and transient CHF and brings new insight into the understanding of CHF phenomena in general.

References

Bhat, A. M., Saini, J. S., and Prakash, R., 1986, "Role of Macrolayer Evaporation in Pool Boiling at High Heat Fluxes," *Int. J. Heat Mass Transfer*, Vol. 29, pp. 1953-1961.

Bhat, A. M., Prakash, R., and Saini, J. S., 1983, "Heat Transfer in Nucleate Pool Boiling at High Heat Fluxes," *Int. J. Heat Mass Transfer*, Vol. 26, pp. 833-840.

Brattacharya, M., and Lienhard, J. S., 1972, "Hydrodynamic Transition in Electrolysis," ASME *Journal of Basic Engineering*, Vol. 94, pp. 804-810.

Chyu, M.-C., 1987, "Evaporation of Macrolayer in Nucleate Boiling Near Burnout," *Int. J. Heat Mass Transfer*, Vol. 30, pp. 1531-1538.

Elkassabgi, Y., and Lienhard, J. H., 1988, "Influences of Subcooling on Burnout of Horizontal Cylindrical Heaters," ASME JOURNAL OF HEAT TRANSFER, Vol. 110, pp. 479-486.

Fontana, D. M., 1974, "Pool Boiling Critical Heat Fluxes in Slowly Variable Transient States," *Int. J. Heat Mass Transfer*, Vol. 17, pp. 1411-1412.

Gaertner, R. F., 1965, "Photographic Study of Nucleate Pool Boiling on a Horizontal Surface," ASME JOURNAL OF HEAT TRANSFER, Vol. 87, pp. 17-29.

Haramura, Y., and Katto, Y., 1983, "A New Hydrodynamic Model of Critical Heat Flux Applicable Widely to Both Pool and Forced Convection Boiling of Submerged Bodies in Saturated Liquids," *Int. J. Heat Mass Transfer*, Vol. 26, pp. 389-399.

Ibrahim, E. A., and Judd, R. L., "An Experimental Investigation of the Effect of Subcooling on Bubble Growth and Waiting Time," ASME JOURNAL OF HEAT TRANSFER, Vol. 107, pp. 168-174.

Iida, Y., and Kobayasi, K., 1969, "Distribution of Void Fraction Above a Horizontal Heating Surface in Pool Boiling," *Bull. JSME*, Vol. 12, pp. 283-290.

Ivey, H. J., and Morris, D. J., 1962, "On the Relevance of the Vapor-Liquid Exchange Mechanism for Sub-cooled Boiling Heat Transfer at High Pressure," UKAEA Report No. AEEW-R 137.

Kataoka, T., Serizawa, A., and Sakurai, A., 1983, "Transient Boiling Heat Transfer Under Forced Convection," *Int. J. Heat Mass Transfer*, Vol. 26, pp. 583-594.

Katto, Y., 1985, "Critical Heat Flux," *Adv. Heat Transfer*, Vol. 17, pp. 1-85.

Katto, Y., and Kikushi, K., 1972, "Study of Forces Acting on a Heated Surface in Nucleate Boiling at High Heat Fluxes," *Heat Transfer, Jpn. Res.*, Vol. 1, pp. 36-46.

Katto, Y., and Haramura, Y., 1983, "Critical Heat Flux on a Uniformly Heated Horizontal Cylinder in an Upward Cross-Flow of Saturated Liquid," *Int. J. Heat Mass Transfer*, Vol. 26, pp. 1199-1205.

Katto, Y., and Yokoya, S., 1968, "Principal Mechanism of Boiling Crisis in Pool Boiling," *Int. J. Heat Mass Transfer*, Vol. 11, pp. 993-1002.

Katto, Y., and Yokoya, S., 1976, "Behavior of Vapor Mass in Saturated Nucleate and Transition Boiling," *Heat Transfer, Jpn. Res.*, Vol. 5, pp. 45-65.

Katto, Y., Yokoya, S., and Yosunama, M., 1970, "Mechanisms of Boiling Crisis and Transition Boiling in Pool Boiling," *Heat Transfer 1970*, Elsevier, Amsterdam, Vol. 5, Paper, No. B3.2.

Kawamura, H., Tachibana, F., and Akiyama, M., 1970, "Heat Transfer and DNB Heat Fluxes in Transient Boiling," *Heat Transfer 1970*, Elsevier, Amsterdam, Vol. 5, Paper No. B3.3.

Kutatelatze, S. S., 1963, *Fundamentals of Heat Transfer*, Academic Press, New York.

Moissis, R., and Berenson, P. J., 1963, "On the Hydrodynamic Transition in Nucleate Boiling," ASME JOURNAL OF HEAT TRANSFER, Vol. 85, pp. 221-229.

Pasamehmetoglu, K. O., 1986, "Transient Critical Heat Flux," Ph.D. dissertation, University of Central Florida, Orlando, FL; EIES Report No. 86-87-1.

Pasamehmetoglu, K. O., and Nelson, R. A., 1987, "The Effect of Helmholtz Instability on the Macrolayer Thickness in Vapor Mushroom Region of Nucleate Pool Boiling," *Int. Comm. Heat Mass Transfer*, Vol. 14, pp. 709-720.

Pasamehmetoglu, K. O., and Nelson, R. A., 1988, "Further Considerations of Critical Heat Flux in Saturated Pool Boiling During Power Transients," in: *ASME Proceedings of 1988 National Heat Transfer Conf.*, Houston, TX, July 24-27, Vol. 2, pp. 395-404.

Pasamehmetoglu, K. O., Nelson, R, A., and Gunnerson, F. S., 1987a, "A Theoretical Prediction of Critical Heat Flux in Saturated Pool Boiling During Power Transients," *Nonequilibrium Transport Phenomena*, ASME HTD-Vol. 77, pp. 57-64.

Pasamehmetoglu, K. O., Nelson, R, A., and Gunnerson, F. S., 1987b, "Study of Hovering Period and Bubble Size in Fully Developed Pool Boiling of Saturated Liquid With a Time-Dependent Heat Source," *Nonequilibrium Transport Phenomena*, ASME HTD-Vol. 77, pp. 39-45.

Pasamehmetoglu, K. O., Nelson, R. A., and Gunnerson, F. S., 1988, "A Theoretical Prediction of Critical Heat Flux in Subcooled Pool Boiling During Power Transients," in: *ANS Proceedings of 1988 National Heat Transfer Conf.*, Houston, TX, July 24-27, pp. 125-134.

Rohsenow, W. M., 1952, "A Method of Correlating Heat Transfer Data for Surface Boiling of Liquids," ASME JOURNAL OF HEAT TRANSFER, Vol. 74, pp. 969-978.

Rohsenow, W. M., 1973, "Boiling," in: *Handbook of Heat Transfer*, W. M. Rohsenow and J. P. Hartnett, eds., McGraw-Hill, New York, pp. 13.1-13.75.

Sakurai, A., Mizukami, K., and Shiotsu, M., 1970, "Experimental Studies on Transient Boiling Heat Transfer and Burnout," in: *Heat Transfer 1970*, Elsevier, Amsterdam, Vol. 5, Paper No. B3.4.

Sakurai, A., and Shiotsu, M., 1977a, "Transient Pool Boiling Heat Transfer, Part 1: Incipient Boiling Superheat," ASME JOURNAL OF HEAT TRANSFER, Vol. 99, pp. 547-553.

Sakurai, A., and Shiotsu, M., 1977b, "Transient Pool Boiling Heat Transfer, Part 2: Boiling Heat Transfer and Burnout," ASME JOURNAL OF HEAT TRANSFER, Vol. 99, pp. 554-560.

Serizawa, A., 1983, "Theoretical Prediction of Maximum Heat Flux in Power Transients," *Int. J. Heat Mass Transfer*, Vol. 26, pp. 921-932.

Sun, K. H., and Lienhard, J. H., 1970, "The Peak Pool Boiling Heat Fluxes on Horizontal Cylinders," *Int. J. Heat Mass Transfer*, Vol. 13, pp. 1425-1439.

Tachibana, F., Akiyama, M., and Kawamura, H., 1968, "Heat Transfer and Critical Heat Flux in Transient Boiling (I)," *J. Nucl. Sci. Technol.*, Vol. 5, pp. 117-126.

Zuber, N., 1958, "Stability of Boiling Heat Transfer," *Trans. ASME*, Vol. 80, pp. 711-719.

Zuber, N., Tribus, M., and Westwater, J. W., 1963, "The Hydrodynamic Crisis in Pool Boiling of Saturated and Subcooled Liquids," *International Developments in Heat Mass Transfer*, ASME, New York, No. 27, pp. 230-236.

K. O. Pasamehmetoglu

R. A. Nelson

Nuclear Technology and Engineering
Division,
Los Alamos National Laboratory,
Los Alamos, NM 87545

F. S. Gunnerson

College of Engineering,
University of Central Florida,
Orlando, FL 32816

Critical Heat Flux Modeling in Forced Convection Boiling During Power Transients

In this paper, a theoretical prediction of critical heat flux (CHF) during power transients in forced convective boiling is presented. The analysis is restricted to departure from nucleate boiling (DNB) type of CHF at low qualities. The developed theory is compared with the experimental data available in the literature. The agreement is exceptionally good. The new model also is compared with the semi-empirical transient CHF model in the literature.

Introduction

Understanding and predicting the critical heat flux (CHF) during steady-state and transient operations are important tasks in nuclear reactor safety. One application involves reactivity-initiated accidents (RIAs), in which a sudden increase in power generation may occur. If such a power surge occurs in nonboiling or subcooled boiling conditions, CHF probably will be caused by the near-wall bubble crowding mechanism commonly referred to as departure from nucleate boiling (DNB). This situation is typical of a RIA in a pressurized water reactor. Presented in this paper is a theoretical model for predicting transient DNB in forced convection. Our companion study (Pasamehmetoglu et al., 1990) was concerned about transient CHF behavior in pool boiling.

The CHF problem during power transients in forced convective boiling has been the subject of previous studies. The theoretical study of Serizawa (1983) and the experimental studies of Kataoka et al. (1983), Aoki et al. (1976), and Celata et al. (1987) are such examples. In the experiments of Kataoka et al. and Aoki et al., a vertical annular flow channel is used. The flowing fluid was water. The power to the test section was increased exponentially, whereas the system pressure and flow velocity were kept constant. Because of the short length of the heater, the data collected correspond to the DNB mechanism and are independent of history effects. In their experiments, Celata et al. introduced stepwise and rampwise power increases to a circular vertical tube using refrigerant-12 as the working fluid. Their steady-state and transient CHF data correspond to an annular flow dryout. Therefore, their results are expected to be strongly influenced by history effects. Serizawa's theoretically based model must be recognized for its unique and original approach to the problem. However, as discussed by Pasamehmetoglu et al. (1990), his model requires heavy empiricism for closure and contradicts some pertinent information on pool boiling mechanisms.

In Serizawa's model, if the surface heat flux is high enough such that the balance between the evaporation and rates shifts in favor of the former, steady-state CHF is postulated to occur. This postulate also constitutes the kernel of our transient model. Mathematically, Serizawa's postulate suggests the following relationship:

$$q_{\mathrm{CHF,SS}} A_w = W_{f,o}(h_{fg} + C_p \Delta T_{\mathrm{sub}}) \qquad (1)$$

where $W_{f,o}$ is the liquid supply rate at CHF. However, during a power transient, when the steady-state CHF value is exceeded, surface dryout is not instantaneous. A certain short but finite period of time must elapse before the liquid layer at the surface completely evaporates. During this time, the surface heat flux continues to increase. Thus, at complete dryout, the surface heat flux is higher than steady-state CHF. This dryout heat flux is referred to as transient CHF.

A mathematical model for transient CHF is developed in the next section.

Transient CHF Model

The rate of change of the liquid layer thickness underneath the bubbly boundary layer on the heater surface is the governing parameter in evaluating transient CHF. Mathematically, the rate change of the liquid layer thickness may be written as

$$\left|\frac{d\delta}{dt}\right| = \max\left\{ \left|\frac{\partial \delta_c}{\partial q}\frac{dq}{dt}\right|,\ \left|\frac{q}{f_2(P,\ \Delta T_{\mathrm{sub}})} - \frac{W_f}{\rho_f(A_w - A_v)}\right| \right\} \qquad (2)$$

where $f_2(P,\ \Delta T_{\mathrm{sub}})$ is given by Pasamehmetoglu et al. (1990) as

$$f_2(P,\ \Delta T_{\mathrm{sub}}) = \rho_f h_{fg}\left(1 - \frac{A_v}{A_w}\right)\left(1 + K\frac{C_p \Delta T_{\mathrm{sub}}}{h_{fg}}\right) \qquad (3)$$

In equation (3), K represents a correction factor for vapor mass behavior in pool boiling with high subcooling. For low subcooling, K may be approximated by 1. Further discussion of this parameter may be found in our companion paper (Pas-

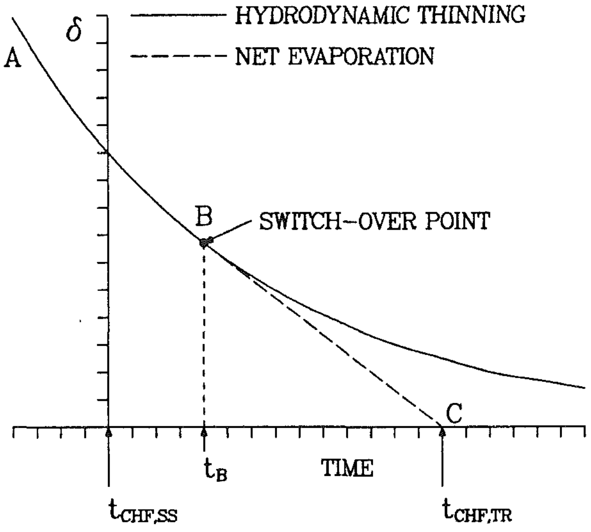

Fig. 1 Schematic description of liquid-layer thickness versus time

---

Contributed by the Heat Transfer Division and presented at the National Heat Transfer Conference, Houston, Texas, July 24–27, 1988. Manuscript received by the Heat Transfer Division May 9, 1988; revision received March 16, 1990. Keywords: Boiling, Phase-Change Phenomena, Transient and Unsteady Heat Transfer.

amehmetoglu et al., 1990). In the present study, we assume $K=1$.

Similar to the rate of change of the liquid layer thickness in pool boiling (Pasamehmetoglu et al. 1990), the first term on the right-hand side of equation (2) represents the liquid layer thinning caused by the hydrodynamic instability. The second term represents the net evaporation rate, which is defined as the difference between the evaporation rate and the liquid-supply rate. Note that W_f was assumed to be zero in pool boiling (Pasamehmetoglu et al., 1990) based on the postulate by Haramura and Katto (1983). Figure 1 shows a graphic representation of the rate-of-change equation and the switch-over point between hydrodynamic and thermal thinning mechanisms.

The hydrodynamic dependence of the liquid layer thickness is related to the Helmholtz instability wavelength of the vapor stems that feed the vapor bubbles. This wavelength is inversely proportional to the square of the instantaneous surface heat flux (Haramura and Katto, 1983; Katto and Haramura, 1983). Thus,

$$\delta_c=\frac{f_1(P)}{q^2} \tag{4}$$

where

$$f_1(P)=\frac{\pi}{2}\sigma\left(\frac{\rho_f+\rho_g}{\rho_f\rho_g}\right)\left(\frac{A_v}{A_w}\right)^2(\rho_g h_{fg})^2 \tag{5}$$

In an earlier publication (Pasamehmetoglu et al., 1987), we showed that, when this relationship is applied to transient heat flux situations in a quasi-steady manner, the error is less than 1 percent for exponential transients that have a time constant greater than 5 ms.

When the transient CHF is reached, the liquid layer thickness becomes zero. Thus, the transient heat flux can be obtained by integrating equation (2) between $t_{\mathrm{CHF,\,SS}}$ and $t_{\mathrm{CHF,TR}}$. One difficulty in the integration of equation (2) is the evaluation of the liquid supply term as a function of time. Serizawa (1983) assumed this term to remain constant beyond steady-state CHF. We developed a simple model to quantify this term, as described below.

Evaluation of the Liquid Supply Term. The liquid supply term W_f is related to the instantaneous radial (perpendicular to the wall) velocity fluctuations $v(t)$, for a given flow field. The radial velocity fluctuations are a function of the distance from the wall and the axial flow velocity outside the boundary layer. The velocity fluctuations that are of interest in the present study are those at the liquid–bubbly layer interface. Weisman and Pei (1983) postulate that the only radial velocity fluctuations that enter the bubble layer are those that are larger than the vapor escape velocity v_v, which, in turn, is directly proportional to the surface heat flux. By its nature, the radial velocity fluctuation is a statistical quantity. Thus, to evaluate W_f, the expected value of the radial velocity fluctuations that are larger than the vapor escape velocity must be computed. It is assumed that the vapor that enters the bubbly layer eventually reaches the heater surface because of high turbulence within the bubbly layer. This assumption is used successfully by Weisman and Pei (1983) in their analytical formulation of steady-state CHF at low qualities. The expected value of $v(t)$ may be expressed as

$$E(v)=\int_{v_v}^{\infty}(v-v_v)dv \tag{6}$$

where $p(v)$ and $E(v)$ are the probability density function and the expected value of radial velocity fluctuations. A normal distribution for v previously was postulated by Weisman and Pei (1983). However, in this study, we assumed a hyperbolic distribution because of its computational convenience. For large positive values of v_v, a hyperbolic distribution represents the same physical trends as a normal distribution. Thus, in the range of interest, the probability density function for v is approximated by the following expression:

$$p(v)=\frac{C_1}{v^{n'}} \tag{7}$$

where C_1 is the proportionality constant and n' is a positive real number greater than or equal to 2. Substituting equation (7) into equation (6), integrating the latter, and expressing the results in terms of heat flux, the following equation may be obtained for the liquid-supply rate near steady-state CHF:

$$W_f(t)=\left[\frac{q_{\mathrm{CHF,SS}}}{q(t)}\right]^n W_{f,o} \tag{8}$$

where $n = n'-2$. For $n=0$, equation (8) yields a constant liquid supply between steady-state and transient CHF, as previously assumed by Serizawa (1983). At the other extreme, when n goes to ∞, the liquid supply rate sharply declines to zero after the heat flux reaches steady-state CHF. For now, n is left as an adjustable empirical quantity, which can assumed any positive real value.

Formulation of the Transient CHF. If the surface heat flux is known as a function of time, equation (2) may be integrated to yield the transient CHF. In the present study, the surface heat flux is assumed to follow an exponential transient given by

$$q(t)=q_{\mathrm{CHF,SS}}\exp\left(\frac{t}{\tau}\right) \tag{9}$$

The switch-over point between the hydrodynamic instability mechanism and the net evaporation mechanism may be calculated by equating their slopes at the switch-over point; thus,

Nomenclature

A_v = heater area covered by vapor, m^2
A_w = heater area, m^2
B_s = parameter for switch-over from hydrodynamic to thermal thinning
C_p = liquid specific heat, J/kg-K
h_{fg} = latent heat transfer of vaporization, J/kg
K = empirical constant
n, n' = empirical exponents
P = pressure, Pa
q = surface heat flux, W/m^2
t = time, s
t_B = switch-over time from hydrodynamic to thermal thinning, s
U = liquid axial velocity, m/s
v = radial liquid velocity, m/s
v_v = vapor escape velocity, m/s
W_f = liquid-supply mass flow rate, kg/s
$W_{f,o}$ = liquid-supply mass flow rate at steady-state CHF, kg/s
ΔT_{sub} = liquid subcooling, K
δ = liquid layer thickness, m
δ_c = maximum liquid layer thickness, m
$\delta_{c,o}$ = maximum liquid layer thickness at steady-state CHF, m
η = ratio of transient and steady-state CHF
ρ = density, kg/m^3
σ = surface tension, N/m
τ = exponential period, s
τ_c = time constant of CHF in forced convection boiling, s
τ_c = vapor mass hovering period in saturated pool boiling, s

Subscripts

f = saturated liquid properties
g = saturated vapor properties
sat = saturated pool boiling

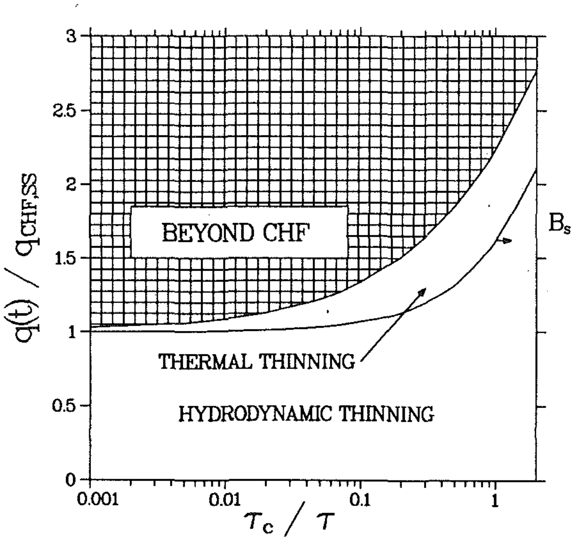

Fig. 2 Liquid-layer thinning map

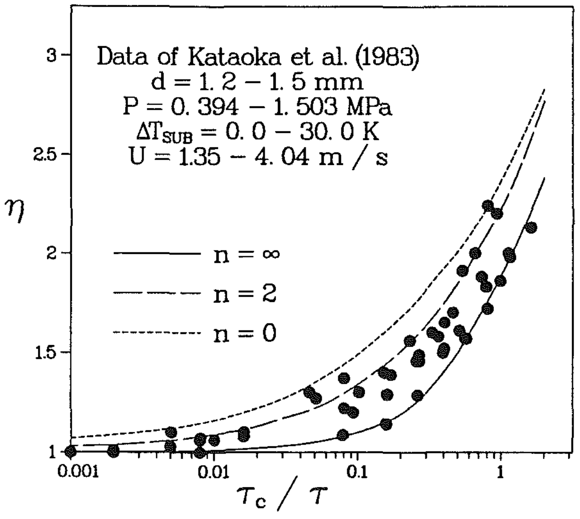

Fig. 3 Comparison of the current model with the data of Kataoka et al. (1983) for different values of *n*

$$\frac{\partial\delta_c}{\partial q}\frac{dq}{dt}=-\frac{q}{f_2(P,\,\Delta T_{\rm sub})}+\frac{W_f}{\rho_f(A_w-A_v)} \tag{10}$$

By setting the surface heat flux at the switch-over point q_B equal to $B_s q_{\rm CHF,SS}$ and defining the time constant of the CHF phenomenon for forced convective boiling, τ_c, as

$$\tau_c=\frac{\delta_{c,o}f_2(P,\,\Delta T_{\rm sub})}{q_{\rm CHF,SS}} \tag{11}$$

and using equation (4), equation (10) may be integrated to yield

$$B_s^{n+1}-\frac{2\tau_c}{\tau}B_s^{n-2}-1=0 \tag{12}$$

When solved for B_s, equation (12) gives $B_s \geq 1$ for any positive real value of n. Figure 2 shows a thinning map for $n=2$. Similar maps can be obtained for different values of n. Having obtained B_s, we can proceed to calculate the transient CHF by evaluating the following integrals:

$$\delta_{c,{\rm o}}=\int_{t_{\rm CHF,SS}}^{t_B}\frac{2f_1(P)}{q^3}\frac{dq}{dt}dt+\int_{t_B}^{t_{\rm CHF,TR}}\left[\frac{q}{f_2(P,\,\Delta T_{\rm sub})}-\frac{W_f}{\rho_f(A_w-A_v)}\right]dt \tag{13}$$

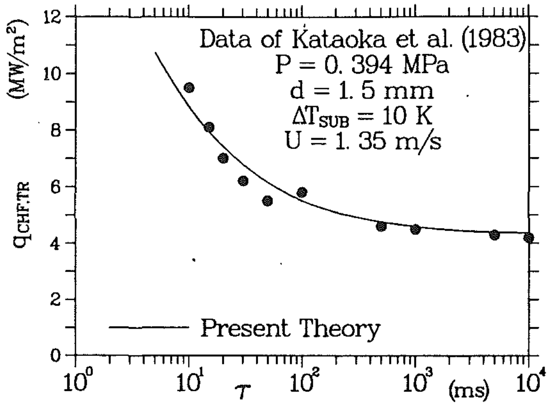

Fig. 4 Comparison of the current model with the data of Kataoka et al. (1983)

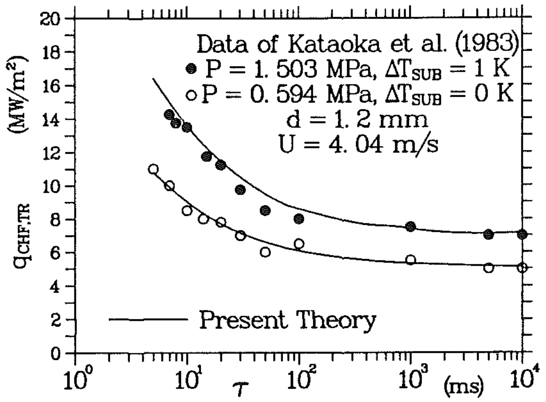

Fig. 5 Comparison of the current model with the data of Kataoka et al. (1983)

Using equations (1), (8), (9), and (11), equation (13) may be integrated to yield

$$\eta^{n+1}-\frac{1}{nB_s^2}\left[\frac{n\tau_c}{\tau}+nB_s^3+B_s^2\right]\eta^n+\frac{B_s^n}{n}=0 \tag{14}$$

where $\eta=q_{\rm CHF,TR}/q_{\rm CHF,SS}$. The time constant of CHF, τ_c, represents the time required for the complete evaporation of a given liquid layer, $\delta_{c,o}$, without any liquid supply. Therefore, it can be related to the vapor mass hovering period, τ_d, in saturated pool boiling, given by Haramura and Katto (1983) as

$$\tau_d=\frac{\delta_{c,o,{\rm sat}}\rho_f h_{fg}(1-A_v)}{A_w q_{\rm CHF,SS,sat}} \tag{15}$$

Combining equations (3), (4), (11), and (15), the following relation between τ_c and τ_d may be obtained:

$$\tau_c=\left(\frac{q_{\rm CHF,SS,sat}}{q_{\rm CHF,ss}}\right)^3\left(1+K\frac{C_p\Delta T_{\rm sub}}{h_{fg}}\right)\tau_d \tag{16}$$

where τ_d mat be obtained from the idealized bubble model of Katto and Yokoya (1976) as described by Haramura and Katto (1983).

To obtain transient CHF, equations (12) and (14) must be solved simultaneously. Both solutions depend on the value of n. Figure 3 shows the comparison of equation (14) with the reduced data on Kataoka et al. (1983) for different values of n. The range of experimental variables for the data is shown in the same figure. As this figure illustrates, a constant liquid supply ($n=0$) overpredicts the data, whereas no liquid supply ($n=\infty$) is a conservative choice. These two extremes provide a rather narrow envelope for the data considered. Therefore, after considering the other uncertainties involved, the choice

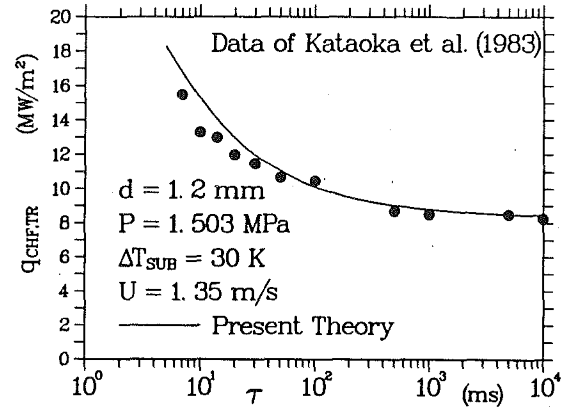

Fig. 6 Comparison of the current model with the data of Kataoka et al. (1983)

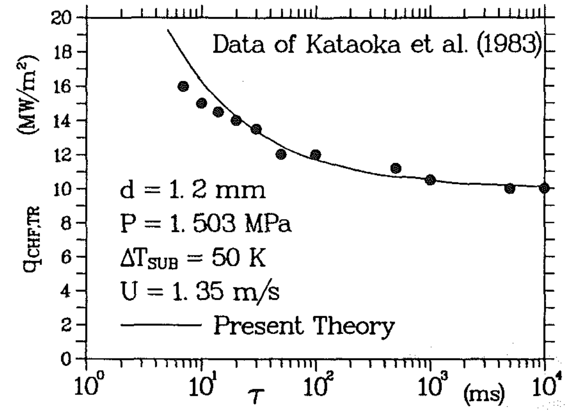

Fig. 7 Comparison of the current model with the data of Kataoka et al. (1983)

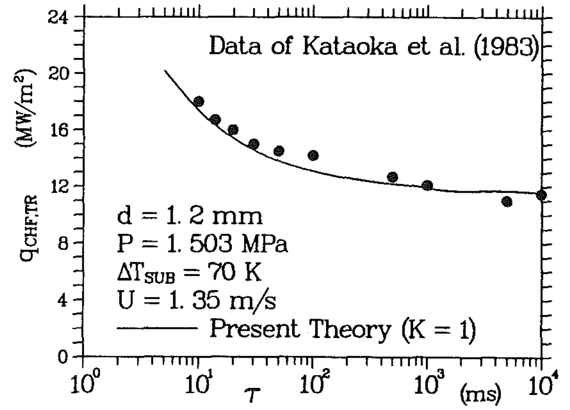

Fig. 8 Comparison of the current model with the data of Kataoka et al. (1983)

of n does not seem to be crucial for the data comparison, even though it is necessary for the theoretical integrity of the study. The comparison of equations (12) and (14) with several sets of data using $n=\infty$ is shown to be reasonably successful by Pasamehmetoglu (1986). In this paper, n is set equal to 2 based on Fig. 3.

Comparison with Data

Setting $n=2$, equations (12) and (14) reduce to

$$B_s = \left(1+\frac{2\tau_c}{\tau}\right)^{1/3} \tag{17}$$

and

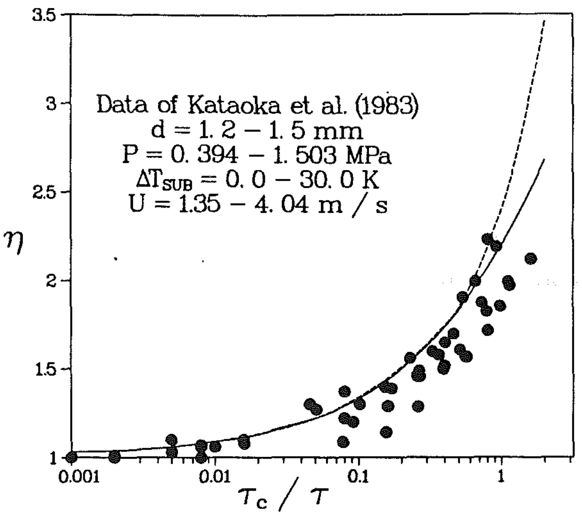

Fig. 9 Effect of hydrodynamic thinning on final prediction

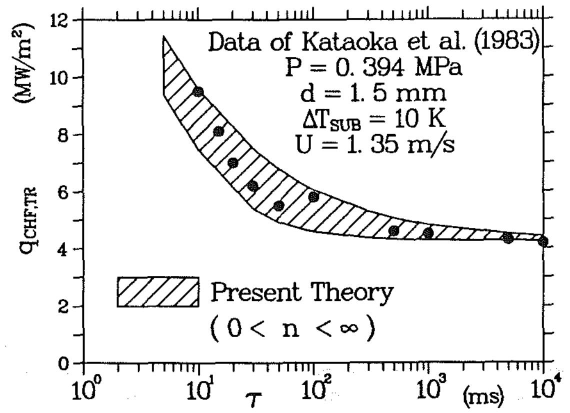

Fig. 10 Comparison of the current model with the data of Kataoka et al. (1983) for all possible values of *n*

$$\eta^3 - \left(\frac{3B_s^3+B_s^2-1}{2B_s^2}\right)\eta^2 + \frac{B_s^2}{2} = 0 \tag{18}$$

respectively.

In equation (17), the time constant τ_c is calculated using equation (16). For data comparison, it is assumed further that the heat generation rate and surface heat flux can be related through a simple volume-to-surface area ratio. This assumption, which is referred to as the quasi-steady conduction mode, is shown to be valid for electrical heaters with small radii (Pasamehmetoglu, 1986). As a result of this approximation, the exponential periods of the heat generation rate and the surface heat flux become the same. The effect of the heater thermal storage on the prediction of transient CHF during saturated pool boiling has been shown to improve the comparison (Pasamehmetoglu et al., 1990). A similar analysis may be applied to forced convection boiling. However, the thermal storage effect is expected to be less than saturated pool boiling with the same heater because the convective heat transfer coefficients near CHF are higher in forced convection boiling.

The solutions of equations (17) and (18) are compared with some sample data of Kataoka et al. (1983) in Figs. 4 to 8. Further data are reported in the papers of Serizawa (1983) and Kataoka et al. (1983). These figures are chosen to represent the effect of various parameters, such as heater diameter, pressure, subcooling, and flow velocity. The figures are self-explanatory in terms of the experimental conditions of each set. As seen in these figures, the comparison between the data and the current theory is exceptionally good. The slight overprediction of the data at small exponential periods is possibly due to the quasi-steady conduction assumption. The worse comparison is in Fig 8, where almost all the data are underpredicted by the current model. This discrepancy possibly is related to the effect of high subcooling on the parameter K, which is set equal to 1 in this study. For further discussion on this parameter, the readers are referred to our companion paper (Pasamehmetoglu et al., 1990).

Summary and Conclusions

In this paper, a novel model to predict CHF during power transients in forced convection boiling is presented. The current model given by equations (17) and (18) is compared with the data available in the literature and the agreement is exceptionally good, as shown in Figs 4-8. The transient CHF problem as investigated earlier by Serizawa (1983). The present model is similar to Serizawa's model in the following aspects:

1 They both use the same steady-state CHF model given by equation (1).

2 They both use the quasi-steady conduction approximation to obtain the exponential period of the surface heat flux.

However, the current model includes additional improvements on Serizawa's transient CHF model. The novelty of the current approach may be itemized as follows:

1 Serizawa extends the same model to correlate the pool boiling data. As discussed by Pasamehmetoglu et al. (1990), this extension has contradictions with other pertinent studies in the literature. The current study provides a similar continuity between different boiling modes, and yet is has a more valid physical basis for pool boiling and forced convection boiling.

2 As opposed to Serizawa's theory, in the present model, the critical liquid layer thickness is not obtained by direct comparison with the transient CHF data.

3 In the present model, the effect of hydrodynamic thinning is added to evaporation, which was assumed to be the only thinning mechanism in Serizawa's model. However, for the data of Kataoka et al. cited in this paper, the time constant of the CHF phenomenon is between 3 and 8 ms. Because the fastest power transients in the experiments have a time constant on the same order of magnitude ($\tau = 5$ ms), the effect of hydrodynamic thinning is hardly noticeable, as shown in Fig. 9. However, as the forced convection velocity and the degree of subcooling approach zero, the time constant of the CHF phenomenon becomes large. In this case, the hydrodynamic thinning mechanism is shown to be very effective (Pasamehmetoglu et al., 1990).

4 Serizawa assumed that the liquid supply rate remained constant between steady-state and transient CHF. In the current model, we modeled the liquid supply rate as a function of time. The comparison with the data shows that the effect of this parameter on transient CHF is minimal, as shown in Figs. 3 and 10; however, a constant liquid supply assumption overpredicts the data. Note that the adjustable liquid supply parameter n reflects the statistical nature of the transient CHF. As shown in Fig. 10, the rather narrow envelope that covers all positive values of n yields a perfect agreement with the data.

The present model still needs further improvements, even though it correlates the existing data well and brings a solid physical explanation to transient CHF phenomenon. The weaknesses of the current model may be listed in three categories:

1 A better transient conduction-convection coupling is necessary. For very fast transients, the quasi-steady conduction approximation may not be accurate.

2 The time constants for the different boiling modes must be quantified better. The effect of subcooling especially requires additional investigation.

3 The radial velocity fluctuations and the liquid supply mechanism require further investigation, possibly through a turbulent flow modeling. These fluctuations are possibly a strong function of the liquid Reynolds number. In the present model, this effect is indirectly included within $W_{f,s}$. However, a more rigorous modeling would be desirable.

References

Aoki, S., Kozawa, Y., and Iwasaki, H., 1976, "Boiling and Burnout Phenomena Under Transient Heat Input," *Bull. JSME*, Vol. 19, pp. 667-675.

Celata, G. P., and Cumo , M., D'Annibale, F., Farello, G. E., and Abou Said, S., 1987, "Critical Heat Flux in Flow Boiling During Power Transients," in: *Nonequilibrium Transport Phenomena*, ASME HTD-Vol. 77, pp. 65-72.

Haramura, Y., and Katto, Y., 1983, "A New Hydrodynamic Model of Critical Heat Flux Applicable Widely to Both Pool and Forced Convection Boiling of Submerged Bodies in Saturated Liquids," *Int. J. Heat Mass Transfer*, Vol. 26, pp. 389-399.

Kataoka, I., Serizawa, A., and Sakurai, A., 1983, "Transient Boiling Heat Transfer Under Forced Convection," *Int. J. Heat Mass Transfer*, Vol. 26, pp. 583-594.

Katto, Y., and Haramura, Y., 1983, "Critical Heat Flux on a Uniformly Heated Horizontal Cylinder in an Upward Cross-Flow of Saturated Liquid," *Int. J. Heat Mass Transfer*, Vol. 26, pp. 1199-1205.

Katto, Y., and Yokoya, S., 1976, "Behavior of Vapor Mass in Saturated Nucleate and Transition Boiling," *Heat Transfer, Jpn. Res.*, Vol. 5, pp. 45-65.

Pasamehmetoglu, K. O., 1986, "Transient Critical Heat Flux," Ph.D. Dissertation, University of Central Florida, Orlando, FL, (also EIES Report No. 86-87-1).

Pasamehmetoglu, K. O., Nelson, R. A., and Gunnerson, F. S., 1987a, "A Theoretical Prediction of Critical Heat Flux in Saturated Pool Boiling During Power Transients," in: *Nonequilibrium Transport Phenomena*, ASME, HTD-Vol. 77, pp. 57-64.

Pasamehmetoglu, K. O., Nelson, R. A., and Gunnerson, F. S., 1990, "Critical Heat Flux Modeling in Pool Boiling for Steady-State and Power Transients," ASME JOURNAL OF HEAT TRANSFER, this issue.

Serizawa, A., 1983, "Theoretical Prediction of Maximum Heat Flux in Power Transients," *Int. J. Heat Mass Transfer*, Vol. 26, pp. 921-932.

Weisman, J., and Pei, B. S., 1983, "Prediction of Critical Heat Flux in Flow Boiling at Low Quality," *Int. J. Heat Mass Transfer*, Vol. 26, pp. 1463-1477.

Analysis of Buoyancy and Tube Rotation Relative to the Modified Chemical Vapor Deposition Process

M. Choi[1]

Y. T. Lin

R. Greif

Department of Mechanical Engineering,
University of California at Berkeley,
Berkeley, CA 94720

The secondary flows resulting from buoyancy effects in respect to the MCVD process have been studied in a rotating horizontal tube using a perturbation analysis. The three-dimensional secondary flow fields have been determined at several axial locations in a tube whose temperature varies in both the axial and circumferential directions for different rotational speeds. For small rotational speeds, buoyancy and axial convection are dominant and the secondary flow patterns are different in the regions near and far from the torch. For moderate rotational speeds, the effects of buoyancy, axial and angular convection are all important in the region far from the torch where there is a spiraling secondary flow. For large rotational speeds, only buoyancy and angular convection effects are important and no spiraling secondary motion occurs far downstream. Compared with thermophoresis, the important role of buoyancy in determining particle trajectories in MCVD is presented. As the rotational speed increases, the importance of the secondary flow decreases and the thermophoretic contribution becomes more important. It is noted that thermophoresis is considered to be the main cause of particle deposition in the MCVD process.

Introduction

The Modified Chemical Vapor Deposition (MCVD) process (MacChesney et al., 1974a, 1974b; Nagel et al., 1982) is the most widely used process in the fabrication of low-loss optical fiber performs. In this process, reactant gases flow through a rotating silica tube heated by an exterior torch, which traverses slowly in the axial direction. The reactant gases are heated as they approach the hot zone of the traversing torch and a homogeneous gas phase reaction takes place, resulting in the formation of submicron particles. Downstream from the reaction zone, some of the particles are deposited on the inner wall of the tube and the particulate deposit is consolidated into a pore-free thin layer by a sintering mechanism as the torch traverses. When the torch reaches the end of its travel, it quickly returns and the process is repeated. After several layers are deposited the tube is collapsed into a solid preform rod and then drawn into a very long thin fiber. The particle deposition mechanism has been established as resulting from thermophoresis (Simpkins et al., 1979; Walker et al., 1980).

The manufacture of the solid preform is very important because it strongly affects the characteristics of the optical fiber. The heat transfer and thermophoretic particle transport during the preform fabrication process are complex and depend on conduction, forced convection, buoyancy, thermal radiation, and chemical reactions. The effects of buoyancy have generally been neglected in analyzing the MCVD process except in studies of laser enhanced MCVD (Wang et al. 1985; DiGiovanni et al., 1985). It is pointed out that buoyancy and tube rotation will result in asymmetric three-dimensional secondary flow fields. In this study, a perturbation analysis is utilized to study the effects of both buoyancy and tube rotation with respect to the MCVD process for small values of $\mathrm{Gr}/\mathrm{Re}^2$. Angular and axial variations of the wall temperature due to torch heating are also included in this study. The important role of buoyancy in determining particle trajectories is identified and compared with thermophoresis.

Analysis

The gas is flowing inside a circular tube of radius a that is rotating with an angular velocity Ω about its axis. The wall of the tube is heated by a torch that is moving with a constant speed U_o in the axial direction. The introduction of a coordinate ξ defined by $\xi = x - U_o t$, together with the polar coordinates r, θ as shown in Fig. 1, results in a steady-state reference coordinate system (r, θ, ξ). Multiple passes of the torch are not included in the analysis. The temperature profile on the surface of the tube is assumed to be steady in the moving reference frame with a Gaussian variation in the axial direction and a periodic cosine variation in the angular direction (Choi et al., 1987, 1989):

$$T_w = (T_M - T_\infty)\exp\left[-\lambda^2\left(\frac{\xi^2}{a^2} + 1 - \cos\theta\right)\right] + T_\infty$$

This variation reflects the effect of the torch heating; the parameter λ characterizes the thickness of the flame; a large value of λ corresponds to concentrated torch heating while a small value of λ refers to a broad heating distribution. A value of 0.5 for λ is taken in this study. Note that the surface temperature is assumed to be independent of the rotational speed.

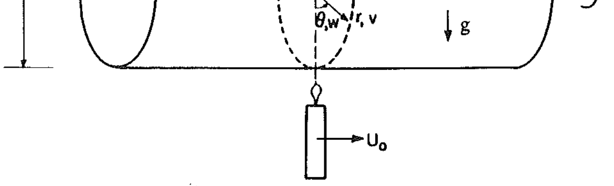

Fig. 1 Sketch of the system

---

[1] Present address: Argonne National Laboratory, Argonne, IL.

Contributed by the Heat Transfer Division for publication in the JOURNAL OF HEAT TRANSFER. Manuscript received by the Heat Transfer Division September 4, 1989; revision received March 21, 1990. Keywords: Materials Processing and Manufacturing Processes, Mixed Convection, Rotating Flows.

The governing equations using the Boussinesq approximation are:

Continuity:

$$\frac{1}{r}\frac{\partial(rv)}{\partial r}+\frac{1}{r}\frac{\partial w}{\partial \theta}+\frac{\partial u}{\partial \xi}=0 \tag{1a}$$

Momentum:

$$v\frac{\partial u}{\partial r}+\frac{w}{r}\frac{\partial u}{\partial \theta}+(u-U_o)\frac{\partial u}{\partial \xi}=-\frac{1}{\rho_\infty}\frac{\partial p_d}{\partial \xi}+\nu_\infty\nabla^2 u \tag{1b}$$

$$v\frac{\partial v}{\partial r}+\frac{w}{r}\frac{\partial v}{\partial \theta}+(u-U_o)\frac{\partial v}{\partial \xi}-\frac{w^2}{r}=-\frac{1}{\rho_\infty}\frac{\partial p_d}{\partial r}-\beta g(T-T_\infty)\cos\theta+\nu_\infty\left(\nabla^2 v-\frac{v}{r^2}-\frac{2}{r^2}\frac{\partial w}{\partial \theta}\right) \tag{1c}$$

$$v\frac{\partial w}{\partial r}+\frac{w}{r}\frac{\partial w}{\partial \theta}+(u-U_o)\frac{\partial w}{\partial \xi}+\frac{vw}{r}=-\frac{1}{\rho_\infty r}\frac{\partial p_d}{\partial \theta}+\beta g(T-T_\infty)\sin\theta+\nu_\infty\left(\nabla^2 w-\frac{w}{r^2}+\frac{2}{r^2}\frac{\partial v}{\partial \theta}\right) \tag{1d}$$

Energy:

$$v\frac{\partial T}{\partial r}+\frac{w}{r}\frac{\partial T}{\partial \theta}+(u-U_o)\frac{\partial T}{\partial \xi}=\alpha_\infty\nabla^2 T \tag{1e}$$

where $p_d=p-p_s$, $p_s=\rho_\infty g\ r\cos\theta$. The boundary conditions are

$$\begin{gathered} u=v=w=0 \text{ at } r=a \\ T_w=(T_M-T_\infty)\exp\left[-\lambda^2\left(\frac{\xi^2}{a^2}+1-\cos\theta\right)\right]+T_\infty \text{ at } r=a \\ u,\ v,\ w,\text{ and } T \text{ are finite at } r=0 \\ u=2U_{av}\left(1-\frac{r^2}{a^2}\right),\ v=0,\ w=r\Omega,\ T=T_\infty \text{ at } \xi=\pm\infty \end{gathered} \tag{1f}$$

u, v, w, T, and their gradients in the angular direction are periodic functions.

The dimensionless variables are defined by

$$u^*=\frac{u}{U_{av}},\quad v^*=\frac{v}{U_{av}},\quad w^*=\frac{w}{U_{av}},\quad r^*=\frac{r}{a},\quad \xi^*=\frac{\xi}{a},$$

$$H^*=\frac{T-T_\infty}{T_M-T_\infty},\quad p_d^*=\frac{p_d}{\rho_\infty U_{av}^2}$$

The governing equations in dimensionless form are then

Continuity:

$$\frac{1}{r^*}\frac{\partial(r^*v^*)}{\partial r^*}+\frac{1}{r^*}\frac{\partial w^*}{\partial \theta}+\frac{\partial u^*}{\partial \xi}=0 \tag{2a}$$

Momentum:

$$v^*\frac{\partial u^*}{\partial r^*}+\frac{w^*}{r^*}\frac{\partial u^*}{\partial \theta}+\left(u^*-\frac{U_o}{U_{av}}\right)\frac{\partial u^*}{\partial \xi^*}=-\frac{\partial p_d^*}{\partial \xi^*}+\frac{1}{\mathrm{Re}}\nabla^{*2}u^* \tag{2b}$$

$$v^*\frac{\partial v^*}{\partial r^*}+\frac{w^*}{r^*}\frac{\partial v^*}{\partial \theta}+\left(u^*-\frac{U_o}{U_{av}}\right)\frac{\partial v^*}{\partial \xi^*}-\frac{w^{*2}}{r^*}=-\frac{\partial p_d^*}{\partial r^*}-\frac{\mathrm{Gr}}{\mathrm{Re}^2}H^*\cos\theta+\frac{1}{\mathrm{Re}}\left(\nabla^{*2}v^*-\frac{v^*}{r^{*2}}-\frac{2}{r^{*2}}\frac{\partial w^*}{\partial \theta}\right) \tag{2c}$$

$$v^*\frac{\partial w^*}{\partial r^*}+\frac{w^*}{r^*}\frac{\partial w^*}{\partial \theta}+\left(u^*-\frac{U_o}{U_{av}}\right)\frac{\partial w^*}{\partial \xi^*}+\frac{v^*w^*}{r^*}=-\frac{1}{r^*}\frac{\partial p_d^*}{\partial \theta}+\frac{\mathrm{Gr}}{\mathrm{Re}^2}H^*\sin\theta+\frac{1}{\mathrm{Re}}\left(\nabla^{*2}w^*-\frac{w^*}{r^{*2}}+\frac{2}{r^{*2}}\frac{\partial v^*}{\partial \theta}\right) \tag{2d}$$

Energy:

$$v^*\frac{\partial H^*}{\partial r^*}+\frac{w^*}{r^*}\frac{\partial H^*}{\partial \theta}+\left(u^*-\frac{U_o}{U_{av}}\right)\frac{\partial H^*}{\partial \xi^*}=\frac{1}{\mathrm{Pe}}\nabla^{*2}H^* \tag{2e}$$

where

$$\mathrm{Re}=\frac{U_{av}a}{\nu_\infty},\quad \mathrm{Gr}=\frac{\beta g(T_M-T_\infty)a^3}{\nu_\infty^2},\quad \mathrm{Pe}=\frac{U_{av}a}{\alpha_\infty}.$$

It is pointed out that $\mathrm{Gr}/\mathrm{Re}^2$ varies over a broad range of values from $O(0.01)$ to $O(10)$ (cf. Simpkins et al., 1979; Walker et al., 1980). The present study is valid for small values of this buoyancy parameter and the dependent variables are expanded as follows:

$$\begin{gathered} u^*=u_0+\epsilon\tilde{u}+\ldots,\quad v^*=v_0+\epsilon\tilde{v}+\ldots, \\ w^*=w_0+\epsilon\tilde{w}+\ldots,\quad p_d^*=p_{d0}+\epsilon\tilde{p}_d+\ldots, \\ H^*=H_0+\epsilon\tilde{H}+\ldots \end{gathered} \tag{3}$$

where

$\epsilon=\dfrac{\mathrm{Gr}}{\mathrm{Re}^2}$

$u_0=2(1-r^{*2})$, Poiseuille flow in the axial direction

$w_0=r^*\Gamma$, rigid body rotation in the angular direction; $\Gamma=\dfrac{a\Omega}{U_{av}}$

$v_0=0$, no velocity in the radial direction for purely forced flow

Nomenclature

a = tube radius
$C_{i,j}$ = complex coefficients in equation (7)
$F(r^*)$ = $2(1-r^{*2})-U_o/U_{av}$
G_+ = $\dfrac{\bar{\bar{H}}_0(r^*,\ n-1,\ z)+\bar{\bar{H}}_0(r^*,\ n+1,\ z)}{2}$ in equations (5) and (6)
G_- = $\dfrac{\bar{\bar{H}}_0(r^*,\ n-1,\ z)+\bar{\bar{H}}_0(r^*,\ n+1,\ z)}{2}$ in equations (5) and (6)
Gr = Grashof number = $\dfrac{\beta g(T_M-T_\infty)a^3}{\nu_\infty^2}$
g = gravitational acceleration
H = dimensionless temperature
i = $\sqrt{-1}$
K = thermophoretic coefficient
N = upper limit of summation in equation (7)
n = Fourier Mode
p = pressure
p_s = static pressure = $\rho_\infty gr\cos\theta$
p_d = dynamic pressure = $p-p_s$
Pe = Peclet number = $U_{av}a/\alpha_\infty$
r = radial coordinate
Re = Reynolds number = $U_{av}a/\nu_\infty$
T = temperature
T_M = maximum temperature on the tube wall
T_W = wall temperature
t = time
u = axial velocity
U_o = torch speed
U_{av} = average velocity of gas in the axial direction
v = radial velocity
V_t = thermophoretic velocity in the radial direction
w = circumferential velocity
x = axial coordinate

$p_{d0} = -\frac{8}{\mathrm{Re}}\xi^* + \frac{1}{2}r^{*2}\Gamma^2$, pressure due to the Poiseuille flow in the axial direction and rigid body rotation in the angular direction

$\tilde{u}$, $\tilde{v}$, $\tilde{w}$, and $\tilde{p}_d$ are the first-order solutions, i.e., the secondary motion due to the buoyancy

H_0 and $\tilde{H}$ are the zeroth and first-order solutions of the energy equation

The leading terms in the expressions, u_0, v_0, w_0, and H_0, correspond to the nonbuoyant problem, i.e., fully developed Poiseuille flow in the axial direction and rigid body rotation in the angular direction. Solutions were obtained for the velocities, $\tilde{u}$, $\tilde{v}$, $\tilde{w}$, which include the effect of buoyancy to order ϵ. However, for the temperature, only the term H_0 was obtained, which does not include the effect of buoyancy. Substituting equations (3) into equations (2) and linearizing the dimensionless equations of motion and energy yields

$$\frac{1}{r^*}\frac{\partial(r^*\tilde{v})}{\partial r^*} + \frac{1}{r^*}\frac{\partial\tilde{w}}{\partial\theta} + \frac{\partial\tilde{u}}{\partial\xi^*} = 0 \tag{4a}$$

$$-4r^*\tilde{v} + \Gamma\frac{\partial\tilde{u}}{\partial\theta} + F(r^*)\frac{\partial\tilde{u}}{\partial\xi^*} = -\frac{\partial\tilde{p}_d}{\partial\xi^*} + \frac{1}{\mathrm{Re}}\nabla^{*2}\tilde{u} \tag{4b}$$

$$\Gamma\frac{\partial\tilde{v}}{\partial\theta} + F(r^*)\frac{\partial\tilde{v}}{\partial\xi^*} - 2\Gamma\tilde{w} = -\frac{\partial\tilde{p}_d}{\partial r^*} - H_0\cos\theta + \frac{1}{\mathrm{Re}}\left(\nabla^{*2}\tilde{v} - \frac{\tilde{v}}{r^{*2}} - \frac{2}{r^{*2}}\frac{\partial\tilde{w}}{\partial\theta}\right) \tag{4c}$$

$$2\Gamma\tilde{v} + \Gamma\frac{\partial\tilde{w}}{\partial\theta} + F(r^*)\frac{\partial\tilde{w}}{\partial\xi^*} = -\frac{1}{r^*}\frac{\partial\tilde{p}_d}{\partial\theta} + H_0\sin\theta + \frac{1}{\mathrm{Re}}\left(\nabla^{*2}\tilde{w} - \frac{\tilde{w}}{r^{*2}} + \frac{2}{r^{*2}}\frac{\partial\tilde{v}}{\partial\theta}\right) \tag{4d}$$

$$\Gamma\frac{\partial H_0}{\partial\theta} + F(r^*)\frac{\partial H_0}{\partial\xi^*} = \frac{1}{\mathrm{Pe}}\nabla^{*2}H_0 \tag{4e}$$

where $F(r^*) = 2(1 - r^{*2}) - U_o/U_{av}$.

The boundary conditions are

$$\tilde{u} = \tilde{v} = \tilde{w} = 0 \text{ at } r^* = 1$$

$$H_0 = \exp[-\lambda^2(\xi^{*2} + 1 - \cos\theta)] \text{ at } r^* = 1$$

$\tilde{u}$, $\tilde{v}$, $\tilde{w}$, $\tilde{p}_d$, and H_0 are finite at $r^* = 0$

$$\tilde{u} = \tilde{v} = \tilde{w} = \tilde{p}_d = H_0 = 0 \text{ at } \xi^* = \pm\infty$$

$\tilde{u}$, $\tilde{v}$, $\tilde{w}$, $\tilde{p}_d$, and H_0 and their gradients in the angular direction are periodic functions

Equations (4*a*–*e*) constitute a linear system that can be solved sequentially. The energy equation, equation (4*e*), may be first solved for H_0, which depends only on the known zeroth-order velocities, u_0, v_0, w_0, which are forced convection contributions. The solution for H_0 was obtained previously by Choi et al. (1989) by applying the double Fourier transformation in the axial and the angular directions. These transformations result in ordinary differential equations, which can be solved by the Frobenius series expansion method. The solutions for the velocities may then be obtained by taking the complex Fourier transformation in the axial direction and the finite Fourier transformation in the angular direction (Miles, 1971), e.g.,

$$\bar{\bar{H}}_0(r^*, n, z) = \int_{-\infty}^{\infty} e^{-i\xi^* z}\int_{-\pi}^{\pi} e^{-in\theta} H_0(r^*, \theta, \xi^*)\,d\theta\, d\xi^*$$

$$\bar{\bar{p}}(r^*, n, z) = \int_{-\infty}^{\infty} e^{-i\xi^* z}\int_{-\pi}^{\pi} e^{-in\theta} \tilde{p}_d(r^*, \theta, \xi^*)\,d\theta\, d\xi^*$$

$$\bar{\bar{u}}(r^*, n, z) = \int_{-\infty}^{\infty} e^{-i\xi^* z}\int_{-\pi}^{\pi} e^{-in\theta} \tilde{u}(r^*, \theta, \xi^*)\,d\theta\, d\xi^*;$$

similar relations for $\bar{\bar{v}}$ and $\bar{\bar{w}}$

Applying the double integral transformation to the equations of continuity and momentum (4*a*–*d*) yields the following ordinary differential equations in r^*:

$$\frac{1}{r^*}\frac{d(r^*\bar{\bar{v}})}{dr^*} + \frac{1}{r^*}in\bar{\bar{w}} + iz\bar{\bar{u}} = 0 \tag{5a}$$

$$F(r^*)iz\bar{\bar{u}} + in\Gamma\bar{\bar{u}} - 4r^*\bar{\bar{v}} = -iz\bar{\bar{p}} + \frac{1}{\mathrm{Re}}(\nabla_1^2\bar{\bar{u}}) \tag{5b}$$

$$F(r^*)iz\bar{\bar{v}} + in\Gamma\bar{\bar{v}} - 2\Gamma\bar{\bar{w}} = -\frac{d\bar{\bar{p}}}{dr^*} - G_+ + \frac{1}{\mathrm{Re}}\left(\nabla_1^2\bar{\bar{v}} - \frac{\bar{\bar{v}}}{r^{*2}} - \frac{2}{r^{*2}}in\bar{\bar{w}}\right) \tag{5c}$$

$$F(r^*)iz\bar{\bar{w}} + in\Gamma\bar{\bar{w}} + 2\Gamma\bar{\bar{v}} = -\frac{1}{r^*}in\bar{\bar{p}} + G_- + \frac{1}{\mathrm{Re}}\left(\nabla_1^2\bar{\bar{w}} - \frac{\bar{\bar{w}}}{r^{*2}} + \frac{2}{r^{*2}}in\bar{\bar{v}}\right) \tag{5d}$$

Nomenclature (cont.)

z = complex transformed coordinate
α = thermal diffusivity
β = coefficient of thermal expansion
Γ = rotation parameter = $a\Omega/U_{av}$
ϵ = small parameter = $\mathrm{Gr}/\mathrm{Re}^2$
θ = angle
λ = parameter in torch heating distribution
ν = kinematic viscosity
ξ = moving coordinate = $x - U_o t$
ρ = density
Ψ_i = test functions
Ω = angular velocity of tube
$\nabla^2 = \frac{1}{r}\frac{\partial}{\partial r}\left(r\frac{\partial}{\partial r}\right) + \frac{1}{r^2}\frac{\partial^2}{\partial\theta^2} + \frac{\partial^2}{\partial\xi^2}$
$\nabla^{*2} = \frac{1}{r^*}\frac{\partial}{\partial r^*}\left(r^*\frac{\partial}{\partial r^*}\right) + \frac{1}{r^{*2}}\frac{\partial^2}{\partial\theta^2} + \frac{\partial^2}{\partial\xi^{*2}}$
$\nabla_1^2 = \frac{1}{r^*}\frac{d}{dr^*}\left(r^*\frac{d}{dr^*}\right) - n^2\frac{1}{r^{*2}} - z^2$
$\nabla_2^2 = \frac{d^2}{dr^{*2}} - \frac{1}{r^*}\frac{d}{dr^*} + \frac{1}{r^{*2}} - n^2\frac{1}{r^{*2}} - z^2$

Subscripts

0 = unperturbed part
∞ = ambient
real = real part
imag = imaginary part

Superscripts

$*$ = dimensionless
$\tilde{}$ = dimensionless (first-order perturbation)
$\bar{\bar{}}$ = double transformation
$\hat{}$ = transformed; $\hat{u} = \bar{\bar{u}}\, r^*$, etc.; cf. equations (6)
$\bar{}$ = transformed, after Fourier inversion

where $G_+ = \dfrac{\bar{\bar{H}}_0(r^*, n-1, z)+\bar{\bar{H}}_0(r^*, n+1, z)}{2}$, $G_- = \dfrac{\bar{\bar{H}}_0(r^*, n-1, z)-\bar{\bar{H}}_0(r^*, n+1, z)}{2i}$

The transformed boundary conditions are

$$\bar{\bar{u}} = \bar{\bar{v}} = \bar{\bar{w}} = 0 \text{ at } r^* = 1;\ \bar{\bar{u}},\ \bar{\bar{v}}, \text{ and } \bar{\bar{w}} \text{ are finite at } r^* = 0$$

To solve equations (5), the variables are changed according to $\hat{u} = \bar{\bar{u}}r^*$, $\hat{v} = \bar{\bar{v}}r^*$, $\hat{w} = \bar{\bar{w}}r^*$. This provides boundary conditions of $\hat{u} = \hat{v} = \hat{w} = 0$ at $r^* = 0$. The equations are then

$$\frac{d\hat{v}}{dr^*} + \frac{1}{r^*}in\hat{w} + iz\hat{u} = 0 \qquad (6a)$$

$$F(r^*)iz\hat{u} + in\Gamma\hat{u} - 4r^*\hat{v} = -ir^*z\bar{\bar{p}} + \frac{1}{\text{Re}}(\nabla_2^2\hat{u}) \qquad (6b)$$

$$F(r^*)iz\hat{v} + in\Gamma\hat{v} - 2\Gamma\hat{w} = -r^*\frac{d\bar{\bar{p}}}{dr^*} - r^*G_+ + \frac{1}{\text{Re}}\left(\nabla_2^2\hat{v} - \frac{\hat{v}}{r^{*2}} - \frac{2}{r^{*2}}in\hat{w}\right) \qquad (6c)$$

$$F(r^*)iz\hat{w} + in\Gamma\hat{w} + 2\Gamma\hat{v} = -in\bar{\bar{p}} + r^*G_- + \frac{1}{\text{Re}}\left(\nabla_2^2\hat{w} - \frac{\hat{w}}{r^{*2}} + \frac{2}{r^{*2}}in\hat{v}\right) \qquad (6d)$$

with boundary conditions

$$\hat{u} = \hat{v} = \hat{w} = 0 \text{ at } r^* = 1;\ \hat{u} = \hat{v} = \hat{w} = 0 \text{ at } r^* = 0$$

The pressure may be eliminated from the above equations and the resulting equations are then solved by the Galerkin method (Fletcher, 1984) with

$$\hat{u} = \sum_{i=1}^{N} C_{1,i}\Psi_i, \quad \hat{v} = \sum_{i=1}^{N} C_{2,i}\Psi_i, \quad \hat{w} = \sum_{i=1}^{N} C_{3,i}\Psi_i \qquad (7)$$

where $C_{1,i}$, $C_{2,i}$, $C_{3,i}$ are constant complex coefficients and $\Psi_i = (1-r^*)r^{*i}$ is the test function to satisfy the boundary conditions. Substituting these relations into the differential equations, multiplying by $r^*\Psi_i$, and integrating from $r^* = 0$ to $r^* = 1$ yields a system of linear algebraic equations, which are then solved for the complex coefficients. The number of test functions, N, was chosen so that using additional functions resulted in changes for $\hat{u}$, $\hat{v}$, $\hat{w}$ that were less than 0.01 percent (N is equal to 24 in this study). The results from the Galerkin method were compared with numerical solutions to equations (6*a*-*d*) and good agreement was obtained.

To obtain the velocities $\tilde{u}$, $\tilde{v}$, $\tilde{w}$ (r^*, θ, ξ^*), it is necessary to invert the transformed velocities $\hat{u}$, $\hat{v}$, $\hat{w}$ (r^*, n, z), which are equal to $r^*\bar{\bar{u}}$, $r^*\bar{\bar{v}}$, $r^*\bar{\bar{w}}$. This is accomplished as follows. First, the Fourier inversion

$$\bar{u},\ \bar{v},\ \bar{w}\ (r^*, n, \xi^*) = \frac{1}{2\pi}\int_{-\infty}^{\infty}\bar{\bar{u}},\ \bar{\bar{v}},\ \bar{\bar{w}}(r^*, n, z)e^{iz\xi^*}dz$$

is utilized and the integration is carried out using a Fast Fourier Transformation (FFT). The upper and lower bounds of the integral and the size of the interval Δz were varied until the changes of less than 1 percent were obtained. The inversion of the finite Fourier transform is accomplished by evaluating the summation

$$\tilde{u},\ \tilde{v},\ \tilde{w}(r^*, \theta, \xi^*) = \frac{1}{\pi}\sum_{n=1}^{\infty}((\bar{u},\ \bar{v},\ \bar{w})_{real}\cos n\theta - (\bar{u},\ \bar{v},\ \bar{w})_{imag}\sin n\theta) + \frac{1}{2\pi}(\bar{u},\ \bar{v},\ \bar{w})_{real,n=0}$$

where $(\bar{u}, \bar{v}, \bar{w})_{real}$ and $(\bar{u}, \bar{v}, \bar{w})_{imag}$ are the real and imaginary parts of the transformed velocities, respectively. The upper limit of the sum was varied until changes of less than 0.01 percent were obtained.

Results and Discussion

Temperature Fields. In the present study, the values of the parameters are U_{av}/U_o = 50, Pe = 50, Re = 50, Γ = 0, 0.7, and 2.0. The values of the dimensionless parameters are in the range of interest for the MCVD process (cf. Simpkins et al., 1979; Walker et al., 1980). The three different values of Γ are

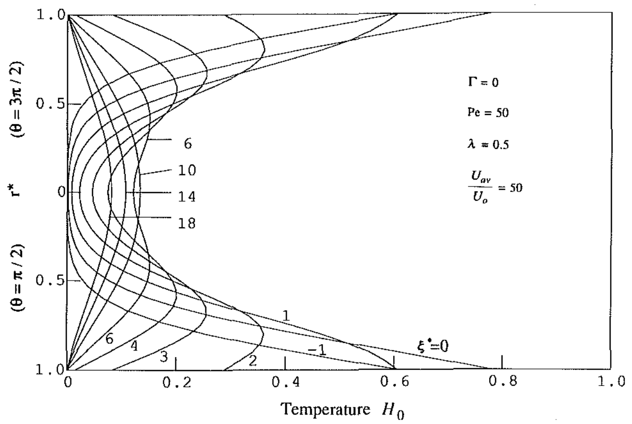

Fig. 2(*a*) Radial temperature distribution along the diameter containing $\theta = \pi/2$ and $3\pi/2$: Γ = 0, Pe = 50, λ = 0.5, U_{av}/U_o = 50

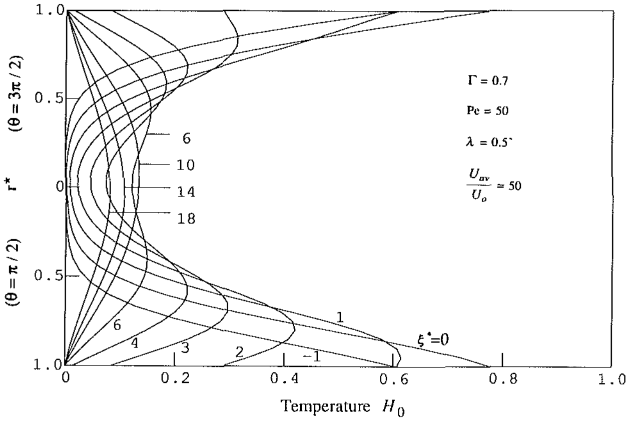

Fig. 2(*b*) Radial temperature distribution along the diameter containing $\theta = \pi/2$ and $3\pi/2$: Γ = 0.7, Pe = 50, λ = 0.5, U_{av}/U_o = 50

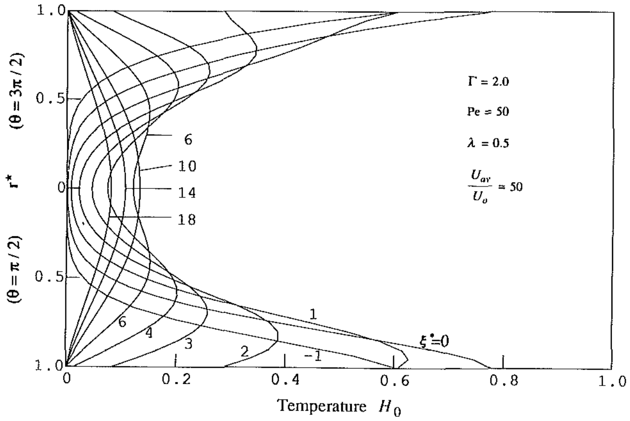

Fig. 2(*c*) Radial temperature distribution along the diameter containing $\theta = \pi/2$ and $3\pi/2$: Γ = 2.0, Pe = 50, λ = 0.5, U_{av}/U_o = 50

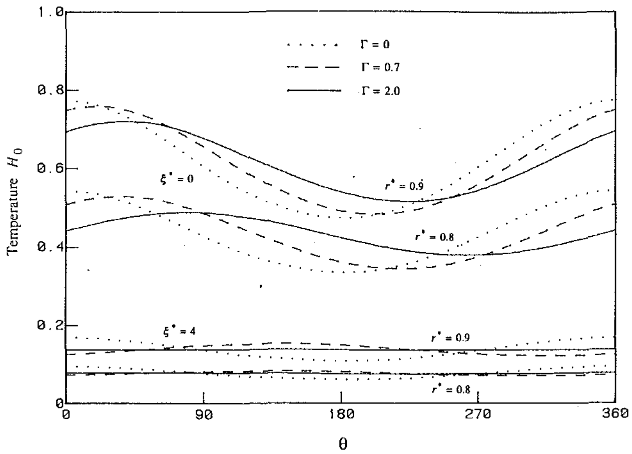

Fig. 3 Variation of the temperature in the θ direction at $\xi^* = 0$ and 4; Pe = 50, $\lambda = 0.5$, $U_{av}/U_o = 50$

chosen to study the effect of tube rotation; $\Gamma = 0.7$ corresponds to a typical value for MCVD.

The radial variation of the temperature along the horizontal diameter, defined along $\theta = \pi/2$ and $3\pi/2$, is shown in Figs. 2(*a–c*) for different axial locations ξ^* with the torch fixed at $\xi^* = (x - U_o t/a = 0$. It is noted that the temperature H_0 is the solution of equation (4*a*), which does not include the effect of buoyancy. For no rotation, $\Gamma = 0$, the temperature profile is symmetric with respect to the vertical diameter (i.e., $\theta = 0$ and π) at all axial locations ξ^*, which results in the symmetry shown in Fig. 2(*a*). Recall the symmetry of the boundary condition for the surface temperature. When rotation (counterclockwise) occurs, i.e., for nonzero values of Γ, the temperature profiles are no longer symmetric (cf. Figs. 2*b* and 2*c*). It is also noted that as rotation is increased the temperature distribution becomes more uniform in the θ direction, as shown in Fig. 3.

It is seen (cf. Figs. 2(*a–c*)) that behind ($\xi^* < 0$), directly above ($\xi^* = 0$), and slightly ahead of (ξ^* near 1) the torch, the temperature decreases monotonically from the hot surface to the cold central region. However, for $\xi^* > 1$, the gas may be at a higher temperature than the surrounding surface. Note that the gas has been strongly heated at $\xi^* = 0$ and moved ahead of the torch ($U_{av}/U_o = 50$), while the surrounding wall temperature (ahead of the torch) is cold because of its large distance from the torch. Thus, hot particles that have been carried downstream ahead of the torch would now move toward the cold tube surface due to the thermophoretic force (discussed later), which acts in the direction of decreasing temperature, i.e., from the hot gas to the cold wall.

Secondary Flow Pattern. An important effect of buoyancy is to alter the flow within the cross section, i.e., in the r^*-θ plane. There is also an effect in the axial direction, which is shown in Fig. 4 for $\Gamma = 0$ (in the vertical r^*-ξ^* plane). As the gas moves downstream, the temperature at the centerline first increases and then, after $\xi^* = 10$ is reached, decreases (cf. Figs. 2*a–c*). Near the torch ($\xi^* < 2$), the heat diffuses from the hot wall, resulting in the increasing centerline temperature. As the gas moves ahead of the torch, the temperature of the gas near the wall becomes higher than that of the wall. This results in a maximum temperature of the gas near the wall; thus, energy is transferred away from this region to both the wall and to the core. As the flow proceeds downstream, the peak temperature moves toward the tube center and there is then a monotonic decrease in the temperature from the center to the wall. Farther downstream, the magnitude of the peak temperature decreases and the profile becomes more uniform. These variations have an effect (due to buoyancy) on both the streamwise velocity, as indicated by the dotted curves in Fig. 4, and the velocities within the different cross sections, as indicated by the dashed vertical lines in Fig. 4.

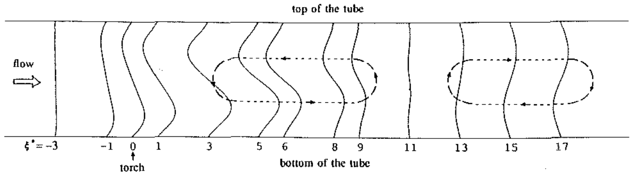

Fig. 4 Axial component of the secondary flow along the diameter containing $\theta = 0$ and π for $\Gamma = 0$

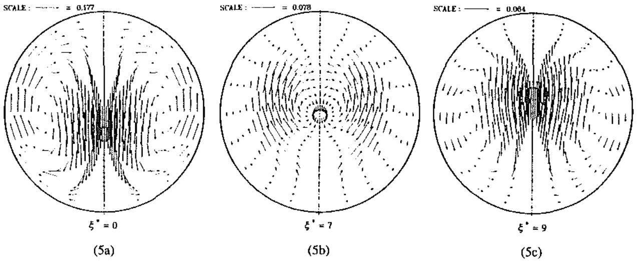

Fig. 5 Secondary flow pattern for $\Gamma = 0$ at $\xi^* = 0$, 7, and 9

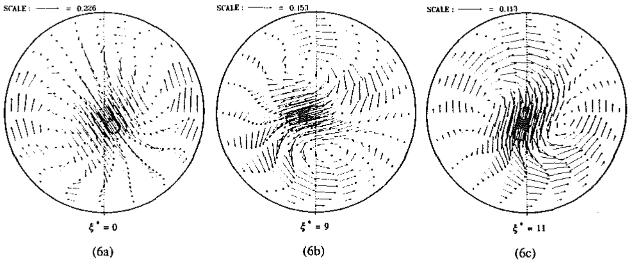

Fig. 6 Secondary flow pattern for $\Gamma = 0.7$ at $\xi^* = 0$, 9, and 11

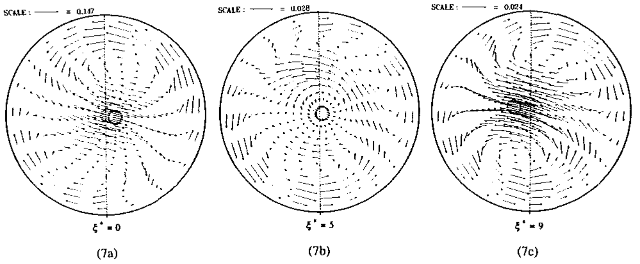

Fig. 7 Secondary flow pattern for $\Gamma = 2.0$ at $\xi^* = 0$, 5, and 9

Figures 5, 6, and 7 represent the deviation from rigid body rotation and show the buoyancy-induced secondary velocity fields $\tilde{v}$ and $\tilde{w}$ at different axial cross sections. For no rotation, i.e., $\Gamma = 0$, there is no angular forced convection and the velocity field, which is affected by buoyancy and axial convection, is symmetric with respect to the vertical plane containing $\theta = 0$ and π (cf. Figs. 5*a–c*). In detail, close to the torch (ξ^* near 0) the wall temperatures are much higher than the gas temperatures near the center (cf. Fig. 2*a*). The secondary flow is therefore symmetrically upward around the wall and continues downward toward the central region. As the flow proceeds downstream (away from the torch) the wall temperature is colder and the peak temperature moves away from the wall toward the central region. The resulting flow field is gradually altered and there then results a downward flow near the wall. Note that at the location $\xi^* = 7$ there are four regions of recirculation present (cf. Fig. 5*b*). At locations farther downstream, the peak temperature occurs near the center of the tube, which causes the secondary motion to be upward at the center and then continues downward around the wall.

For small values of Γ, the effects of angular convection are small in comparison to the effects of axial convection and buoyancy. The results (not shown) resemble the nonrotating condition, with the temperature and velocity profiles being only slightly asymmetric with respect to the vertical plane, which extends from $\theta=0$ to π.

For moderate values of Γ, e.g., $\Gamma=0.7$, angular convection is important everywhere in the tube. In the region near the torch, i.e., ξ^* near 0, the gas is strongly heated over the bottom portion of the tube and angular (counterclockwise) convection, then carries the heated gas into the right half of the cross section, i.e., over $0<\theta<\pi$. The temperature there is higher than that over the left half of the tube (cf. Fig. 2*b*). A typical secondary motion is shown in Figs. 6(*a*–*c*), with the flow appearing to be tilted to the left in Fig. 6(*a*) (directly above the torch). Note the comparison with Fig. 5(*a*), which shows a symmetric flow pattern about the vertical diameter, i.e., no tilt. This secondary flow pattern only exists near the torch where the flow is dominated by buoyancy effects. As the flow proceeds downstream, the gas cools and the effects of buoyancy are reduced. The combined effects of axial convection, rotation, and buoyancy result in a spiraling motion (cf. Figs. 6*b* and 6*c*).

For large values of Γ, the secondary flow results, primarily, from the balance between buoyancy and angular convection. The effect of angular convection on the flow pattern in the region near the torch, i.e., over the interval $-1\le\xi^*\le1$, results in no tilt for $\Gamma=0$ (no rotation), moderate tilt for $\Gamma=0.7$, and strong tilt for $\Gamma=2.0$ (cf. Figs. 5*a*, 6*a*, and 7*a*). In the region far from the torch, the gas temperature near the center is higher than the wall temperature (cf. Fig. 2*c*). This causes the secondary flow pattern far downstream (cf. Fig. 7*c*) to be reversed from that near the torch (Fig. 7*a*). For $\Gamma=2.0$, axial convection makes only a small contribution to the secondary flow field; the secondary flow does not have a spiral pattern in the axial direction as occurred for the case $\Gamma=0.7$. For values of ξ^* near 5 (cf. Fig. 7*b*), there exists a transition region between two different secondary flows (cf. Fig. 7*a* for $\xi^*=0$ and Fig. 7*c* for $\xi^*=9$ and greater). This corresponds to the movement of the peak temperature from the bottom of the tube at the axial location $\xi^*=0$ toward the center of the tube as the flow proceeds downstream.

It is noted that different values of Γ $(0<\Gamma<2.0)$ have only a slight effect on the temperature profiles (cf. Figs. 2 and 3). Thus the buoyancy force terms in the momentum equations vary only slightly for different Γ and increasing Γ results in smaller values of the perturbed velocities (cf. equations (4*b*–*d*) and Fig. 8). Figure 8 also shows that the magnitude of the induced secondary flow decreases as the speed of rotation increases.

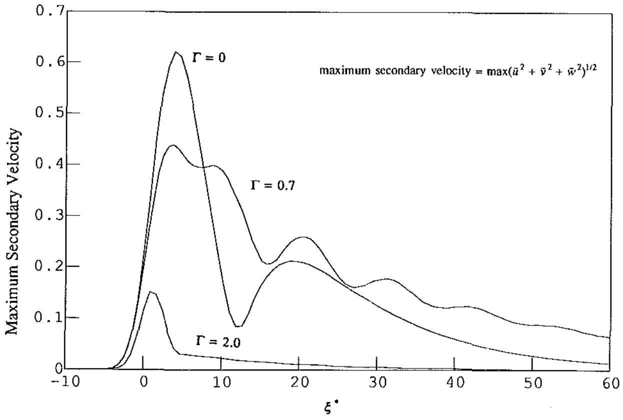

Fig. 8 Variation of maximum secondary velocity

Calculations have also been carried out neglecting the diffusion terms in the axial direction. The resulting flow patterns are virtually the same as when these contributions are included (Pe = 50). Also, for large values of Γ, the large angular convection causes angular diffusion to have only a small effect on the secondary flow.

Contribution of Secondary Flows Compared to Thermophoresis. Figures 9(*a*–*c*) show the importance of the radial velocity component v (the zeroth-order value of v is zero and positive values are toward the wall) with respect to the radial component of the thermophoretic velocity $V_t=-(K\nu_\infty/T)(\partial T/\partial r)$ (Talbot et al., 1980); K is the thermophoretic coefficient, which, for micron and submicron-sized particles, generally varies from 0.5 to 1.1 (Walker et al., 1979). $K=0.9$ is chosen in the present study (Walker et al., 1980) for the MCVD process. Positive values of the ratio v/V_t mean that the secondary (radial) flow is in the same direction as that due to the radial component of thermophoresis (cf. Figs. 9*a*–*c*). The dashed

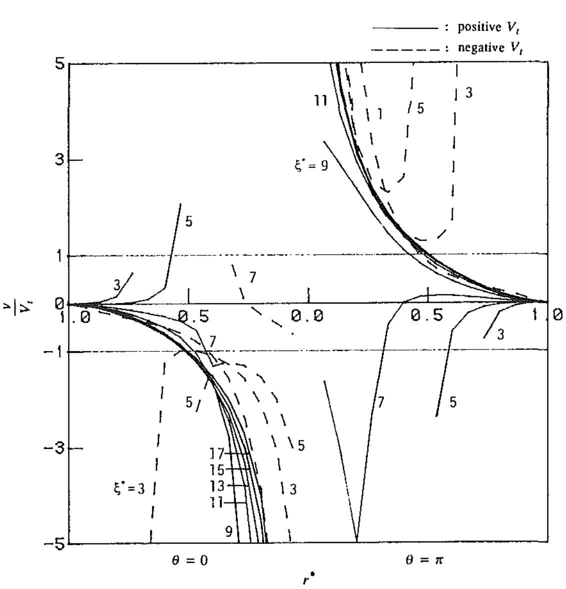

Fig. 9(*a*) Comparison of radial velocity v with radial thermophoretic velocity V_t: $\Gamma=0$, $\epsilon=0.1$, Re = 50, $a=0.01$ m

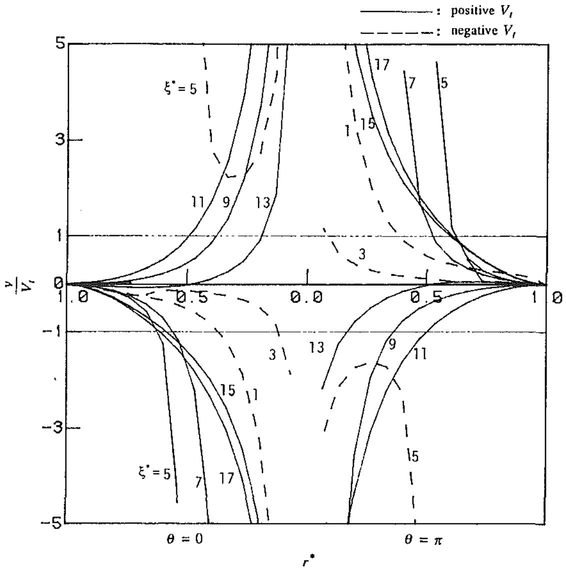

Fig. 9(*b*) Comparison of radial velocity v with radial thermophoretic velocity V_t: $\Gamma=0.7$, $\epsilon=0.1$, Re = 50, $a=0.01$ m

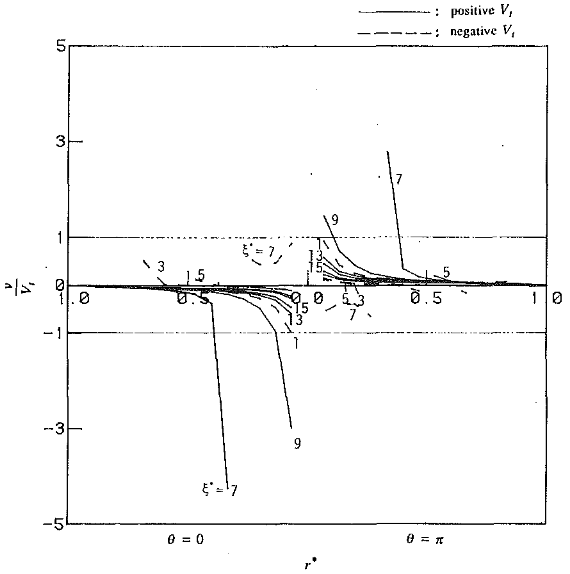

Fig. 9(*c*) Comparison of radial velocity *v* with radial thermophoretic velocity V_t: $\Gamma = 2.0$, $\epsilon = 0.1$, $\mathrm{Re} = 50$, $a = 0.01$ m

curves refer to negative values of V_t, i.e., when the thermophoretic velocity is away from the wall (toward the center of the tube). For $|v/V_t|$ greater than one, the effect of the secondary flow is more important than thermophoresis in determining the particle motion. The ratio $|v/V_t|$ is always less than one in the region near the wall; thus, thermophoresis is dominant in this region. Note that the secondary flow vanishes on the wall but the thermophoretic velocities have nonzero values that depend on the local temperatures and temperature gradients. These results confirm the important role of thermophoresis for particle deposition on the tube wall in the MCVD process. However, in the central region of the tube, for both small and moderate Γ, it is seen that $|v/V_t|$ is larger than one, i.e., here the secondary flows are more important than thermophoresis in determining particle trajectories (cf. Figs. 9*a* and 9*b* for $\Gamma = 0$ and 0.7). For large values of Γ, the secondary flows are very weak and therefore have less influence on particle motion than does thermophoresis except in the region very near the center of the tube (cf. Fig. 9*c* for $\Gamma = 2.0$).

For values of ξ^* greater than 9, the temperatures are higher in the central region than near the wall (cf. Figs. 2*a*–*c*), and the thermophoretic velocity is toward the wall over the entire cross section; i.e., V_t is always positive (cf. Figs. 9*a*–*c*). In the region near the torch ($\xi^* = 1$ in Figs. 9*a*–*c*), the largest temperature is at the wall and the thermophoretic velocity is therefore away from the wall. No particle deposition occurs in this region even though at the bottom of the tube ($\theta = 0$) the radial component of velocity is toward the wall (cf. Figs. 5*a*, 6*a*, and 7*a*).

In the region far from the torch (cf. Figs. 9*a* and 5*c*), for no rotation, i.e., $\Gamma = 0$, the flow is away from the wall at the bottom of the tube ($\theta = 0$) but is toward the wall at the top of the tube ($\theta = \pi$) while the thermophoretic velocity is toward the wall over the entire cross section. For $\Gamma = 0.7$, the secondary flow far downstream is spiraling; at the top of the tube ($\theta = \pi$) the flow is first toward the wall at $\xi^* = 5$, 7, then away from the wall at $\xi^* = 9$, 11, 13 and then again toward the wall at $\xi^* = 15$, 17. At the bottom of the tube ($\theta = 0$) the effects are the opposite (cf. Fig. 9*b*). For $\Gamma = 2.0$ (cf. Fig. 9*c*), the secondary flow far downstream is not spiraling and the variation observed for $\Gamma = 0.7$ does not occur.

Conclusions

The three dimensional secondary flow resulting from buoyancy effects and tube rotation has been studied in respect to the MCVD process. Axial and circumferential variations of the torch heating have been included. The following conclusions are cited.

1 For small rotational speeds, the effects of buoyancy and axial convection are dominant. The secondary flow in the region near the torch is upward near the tube wall and downward in the central region. Far from the torch the opposite secondary flow pattern is present.

2 For moderate rotational speeds, e.g., $\Gamma = 0.7$, buoyancy, axial, and angular convection are all important in the region far from the torch and a spiraling secondary flow occurs in this region. Near the torch, the secondary flow results primarily from buoyancy and angular convection and the flow is tilted with respect to the nonrotating condition.

3 For large rotational speeds, e.g., $\Gamma = 2.0$, the effects of buoyancy and angular convection are dominant everywhere. In the region near the torch, the secondary flow has a greater tilt than that occurring for $\Gamma = 0.7$. In the region far from the torch, no spiraling occurs and the secondary flow pattern differs by 180 deg from the flow near the torch.

4 For the determination of the particle trajectories, thermophoresis is dominant in the region near the wall but the secondary flow is more important near the center of the tube. However, for large rotational speeds, e.g., $\Gamma = 2.0$, thermophoresis is more important almost everywhere because the buoyant secondary flow is small.

Acknowledgments

The authors are deeply indebted to Dr. U. C. Paek, AT&T Engineering Research Center, for providing valuable comments and discussion. Support from the National Science Foundation, the San Diego Supercomputer Center, and the Computing Center of the University of California at Berkeley is gratefully acknowledged.

References

Choi, M., Baum, H.R., and Greif, R., 1987, "The Heat Transfer Problem During the Modified Chemical Vapor Deposition Process," ASME JOURNAL OF HEAT TRANSFER, Vol. 109, pp. 642–646.

Choi, M., Greif, R., and Baum, H. R., 1989, "A Study of Heat Transfer and Particle Motion Relative to the Modified Chemical Vapor Deposition Process," ASME JOURNAL OF HEAT TRANSFER, Vol. 111, pp. 1031–1037.

DiGiovanni, D., Wang, C. Y., Morse, T. F., and Cipolla, J. W., Jr., 1985, "Laser Induced Buoyancy and Forced Convection in Vertical Tubes," *Natural Convection: Fundamentals and Applications*, S. Kakac, W. Aung, and R. Viskanta, eds., Hemisphere, New York, pp. 1118–1139.

Fletcher, C. A. J., 1984, *Computational Galerkin Methods*, Springer-Verlag, New York.

MacChesney, J. B., O'Connor, P. B., DiMarcello, F. V., Simpson, J. R., and Lazay, P. D., 1974a, "Preparational Low-Loss Optical Fibers Using Simultaneous Vapor Phase Deposition and Fusion," *Proc. 10th Int. Congr. Glass*, Kyoto, Japan, pp. 6-40–6-44.

MacChesney, J. B., O'Connor, P. B., and Presby, H. M., 1974b, "A New Technique for Preparation of Low-Loss and Graded Index Optical Fibers," *Proc. IEEE*, Vol. 62, pp. 1278–1279.

Miles, J. W., 1971, *Integral Transforms in Applied Mathematics*, Cambridge University Press, United Kingdom.

Nagel, S. R., MacChesney, J. B., and Walker, K. L., 1982, "An Overview of the Modified Chemical Vapor Deposition (MCVD) Process and Performance," *IEEE J. Quant. Elec.*, Vol. QE-18, No. 4, pp. 459–476.

Simpkins, P. G., Kosinski, S. G., and MacChesney, J. B., 1979, "Thermophoresis: The Mass Transfer Mechanism in Modified Chemical Vapor Deposition," *J. Appl. Phys.*, Vol. 50, pp. 5676–5681.

Talbot, L., Cheng, R. K., Schefer, R. W., and Willis, D. R., 1980, "Thermophoresis of Particles in a Heated Boundary Layer," *J. Fluid Mech.*, Vol. 101, part 4, pp. 737–758.

Walker, K. L., Homsy, G. M., and Geyling, F. T., 1979, "Thermophoretic Deposition of Small Particles in Laminar Tube Flow," *J. Colloid Interface Sci.*, Vol. 69, pp. 138–147.

Walker, K. L., Geyling, F. T., and Nagel, S. R., 1980, "Thermophoretic Deposition of Small Particles in the Modified Chemical Vapor Deposition (MCVD) Process," *J. Am. Ceram. Soc.*, Vol. 63, pp, 552–558.

Wang, C. Y., Morse, T. F., and Cipolla, J. W., Jr., 1985, "Laser Induced Natural Convection and Thermophoresis," ASME JOURNAL OF HEAT TRANSFER, Vol. 107, pp. 161–167.

Optical Determination of Stagnation Temperature Behind a Gas Sampling Orifice

J. R. Herron

R. B. Peterson

Dept. of Mechanical Engineering,
Oregon State University,
Corvallis, OR 97331

A technique has been developed for measuring the temperature during a transient combustion event. It combines the features of atomic resonance absorption and direct sampling to produce a relatively simple, intrusive diagnostic technique to obtain time-resolved measurements. In this study, a propagating hydrogen/air flame was used to provide a rapid temperature increase. A small fraction of krypton was added to the reactants and the absorption of resonant radiation at 123.5 nm was recorded downstream of the sampling orifice within a flow tube. Conversion from absorption measurements to temperature values was performed using a computer model of the radiation source and the absorption by the sample. The model of the source was validated by comparing predicted and recorded spectra of hydrogen Lyman-α emissions, while the absorption model for the sampled gas was tested by comparing the temperatures predicted by krypton absorption measurements with those recorded at a range of known temperatures. The direct sampling atomic resonance technique minimizes time-history distortions inherent in other direct sampling techniques, and is capable of tracking local temperatures during the passage of a propagating flame front.

Introduction

The technique of direct sampling has yielded much new and valuable information concerning combustion and other reactive systems. When coupled with molecular beam formation and mass spectrometry, detailed knowledge of temperature and chemical species is provided, as demonstrated by the works of Deckers and Van Tiggelen (1959), Milne and Green (1966), Peeters and Mahnen (1972), Knuth (1973), and Biordi (1977). Although the technique is a powerful tool for the study of steady-state flame systems, application to transient phenomena has been limited due to the inherent shortcomings associated with molecular beam propagation (Peterson et al., 1984; Lucas et al., 1984a, 1984b). To avoid this problem, we have been investigating several ways of performing species detection immediately behind the direct sampling orifice. Our goal has been the development of a technique to follow temperature and chemical species concentrations on a fast transient basis. Such information is of importance for the study of flame kernel development and other ignition processes, flame propagation, and heat transfer to combustion chamber walls. Recently we have reported on the detection of stable species in a propagating flame (Herron and Peterson, 1988). Measurements of temperature and radical species concentrations are also of considerable value and this paper reports on progress toward this goal.

Description of Technique

The technique described here is a combination of two well-established experimental practices used in combustion studies. The first of these is resonant absorption. It has been extensively applied in shock tube work (Myerson and Watt, 1968; Thielen and Roth, 1987) and flow reactor studies (Morse and Kaufman, 1965; Michael and Weston, 1966) for the detection of H, O, and N atoms. Two important considerations when applying this technique are the concern for absorption by species other than the resonant absorber and the emission characteristics of the light source. In most typical combustion systems, O_2 and H_2O are in concentrations higher than can be tolerated, thus preventing transmission of ultraviolet radiation—a prerequisite for implementing the technique. Furthermore, the desired target species are in concentrations that lead to total absorption when experiments are conducted near atmospheric pressure, especially in and around the reaction zone. These considerations dictate the need to combine resonant absorption with another technique to lower the overall sample density. To accomplish this, direct sampling is used. It has a demonstrated capability for effectively preserving the concentrations of both reactive and nonreactive species by rapidly quenching reactions through gas dynamic expansion. Sampling takes place by extracting gas through a small orifice and passing it into a vacuum chamber, hence reducing the density to such a degree that vacuum ultraviolet radiation can pass through the rarified sample at a specific location downstream from the orifice. By recording the changes in the absorption signal during a transient event, it is possible to determine the sample temperature through an appropriate analysis. The advantages of combining these two techniques include fast time response to local changes in temperature and species concentrations, and good discrimination between atomic species and nonresonant absorbing species.

To obtain temperatures from absorption measurements, both the lamp emission and sample absorption characteristics need to be determined. Many investigators have studied atomic resonance lamps (Maki et al., 1985; Braun et al., 1970; Braun and Carrington, 1969); however, resonant absorption by the sampled gas needs to be addressed. In a free jet, it is difficult to determine unique values for the sample temperature as well as the absorbing atom concentration. This is due to the expansion of the gas in all directions and the speed distribution the gas ultimately attains. To avoid this problem, a flow tube similar to a stagnation temperature probe can be positioned downstream from the orifice in the hypersonic region of the flow. It has been demonstrated that such probes generate a detached normal shock wave, and the temperature behind the shock approaches the stagnation temperature of the flow (Winkler, 1954; Shadday et al., 1978). If an evacuated optical path is provided so that resonant absorption

---

Contributed by the Heat Transfer Division for publication in the JOURNAL OF HEAT TRANSFER. Manuscript received by the Heat Transfer Division September 19, 1989; revision recieved January 29, 1990. Keywords: Combustion, High-Temperature Phenomena, Measurement Techniques.

occurs only across the diameter of the tube, absorption will then take place in a gas of near-uniform temperature and pressure. In this study, a known mole fraction of a monatomic inert gas (krypton) was added to the sample. Only a small percentage of krypton was needed to provide high levels of resonant absorption, while the concomitant effects on the fluid and thermodynamic characteristics of the sample were negligible.

Theory Section

The analysis for obtaining temperatures from absorption measurements requires a detailed knowledge of the frequency dependence of both the UV radiation source and the absorption by the sample. In resonance absorption experiments, UV radiation at the energy of an atom's first electronic ground-state transition is generated by microwave excitation of a gas mixture containing the species of interest. The resulting spectral line profile exhibits broadening due to Doppler effects. If this were the only mechanism affecting line shape, a thermal speed distribution would predict a Gaussian profile with the width at one half maximum given by

$$\Delta\nu_D = \nu_0\sqrt{\frac{8kT\ln(2)}{mc^2}} \tag{1}$$

where ν_0 is the frequency at the center of the emission band, k is Boltzmann's constant, T is the temperature of the gas, m is the atomic mass, and c is the speed of light.

Resonant lamp profiles are not, however, Gaussian in shape. Before the radiation can exit the lamp, it is attenuated by resonant absorption by the same species that generate the radiation—an effect that is termed "self-absorption." If it is assumed that the lamp behaves as an emitting region followed by an absorbing region at the same temperature, Beer's law can be used for finding the emission intensity as a function of wavelength. The resulting profile can be written as

$$I(\nu) = I_D(\nu)\times\exp[-K(\nu)l] \tag{2}$$

where l is the length of the absorbing region. The emitting region's Doppler profile, $I_D(\nu)$, is given by

$$I_D(\nu) = I_D(\nu_0)\,\exp\left[-\left(\frac{\nu-\nu_0}{0.6\Delta\nu_D}\right)^2\right] \tag{3}$$

The function $K(\nu)$ accounts for the wavelength-dependent absorption intensity and is given by

$$K(\nu) = \left[\frac{1}{l}\ln\left(\frac{I(\nu_0)}{I_D(\nu_0)}\right)\right]\times\exp\left[-\left(\frac{\nu-\nu_0}{0.6\Delta\nu_D}\right)^2\right] \tag{4}$$

where $I(\nu_0)/I_D(\nu_0)$ is the transmittance fraction at the center of the emission band. Note that the first quantity in brackets is given the symbol K_0, or the centerline absorption coefficient. The effect of lamp self-absorption on the emission profile produces an intensity spectrum with maxima on either side of ν_0 and a local minimum at ν_0.

The proposed model of lamp emission (an emitting region followed by an absorbing region) is relatively simple. This is an advantage that allows the frequency profile of a specific resonant line to be characterized by two parameters: the emitter-absorber temperature T_L, and the lamp centerline absorption coefficient K_{0L}. The most straightforward way to obtain these two parameters would be to perform a scan of the line with a high-resolution monochromator, then numerically correct the measured profile to account for distortions introduced by the monochromator instrument function. From the actual line profile, the two parameters can be deduced. The problem with this approach is that most resonant lines are too narrow to be resolved. High-resolution scans can yield spectral line shapes from very light atoms such as hydrogen or deuterium (Lifshitz et al., 1979), since their high thermal velocities produce large Doppler line widths. However, the resonant line from krypton is far too narrow to resolve.

Values of the two characterizing parameters must therefore be obtained indirectly. To estimate the emission temperature, the lamp may be operated with a gas containing both hydrogen and krypton, and a spectrum recorded of the Lyman-α line. A mathematical fit to the recorded line shape can be preformed using the proposed model, where T_L and K_{0L} are the parameters of variation. Again, line shape corrections must be made to account for instrument function distortions.

Once the lamp emitter temperature has been found, the lamp centerline absorption coefficient for krypton is obtained from sample absorption measurements. The equations describing sample absorption are the same as those for absorption in the lamp. Thus, for a gas sample extracted from a mixture of known composition under steady-state conditions, temperature is a known or measurable quantity. Using the temperature of the gas in the flow tube, T_s, the centerline absorption coefficient K_{0S} is derived from measurable quantities using the relation

$$K_0 = 2f\left(\frac{\pi}{\ln 2}\right)^{-1/2}\frac{\pi e^2}{mc}\,\frac{n}{\Delta\nu_D} \tag{5}$$

In this relationship, f is the transition oscillator strength, n is the krypton number density, and $\Delta\nu_D$ is the Doppler width of the sample's absorption line. The value of f is obtained from the literature, while $\Delta\nu_D$ and n are calculated from known values of the sample temperature, the krypton mole fraction, and from measurements of the pressure in the flow tube. Thus, a summarized procedure for determining K_{0L} is as follows.

- $K(\nu)$ of the sampled gas in the flow tube is calculated from known quantities.
- A trial $I_D(\nu)$ for the lamp is determined using the temperature found earlier (from the hydrogen line emission) and an assumed value of K_{0L}.
- A trial theoretical absorption value is obtained by solving for the intensity profile after sample absorption by using the known $K(\nu)$ and the assumed K_{0L}, and then integrating the resulting profile.
- The procedure is repeated using refined estimates of K_{0L} until the integrated theoretical absorption corresponds to the measured value.

After K_{0L} is obtained, unknown sample temperatures can be determined by first finding a K_{0S} value for which the measured and predicted absorption values match, then finding a sample temperature that would produce the K_{0S}.

The procedure for determining temperatures may appear involved; however, it is based on relatively few assumptions. The validity of the model can also be checked by comparing experimentally measured temperatures with those predicted numerically from absorption values.

Experimental Section

The experimental apparatus used in this investigation is shown in Fig. 1. The vacuum chamber was a hollow aluminum cube 15.24 cm on a side where each face of the cube provided access to the 12.7-cm-dia, cylindrical interior region. The two side ports used in this investigation contained a microwave discharge lamp and an aperture having a diameter of 0.75 mm that led to the entrance of the monochromator. The vacuum chamber was connected to a 1200-l/s oil diffusion pump through a 90-deg elbow. An insert through the front of the chamber contained either the combustion cell, as pictured in Fig. 1, or the steady-state gas delivery apparatus, pictured in Fig. 2.

The combustion cell was a cylindrical vessel 5.1 cm in length

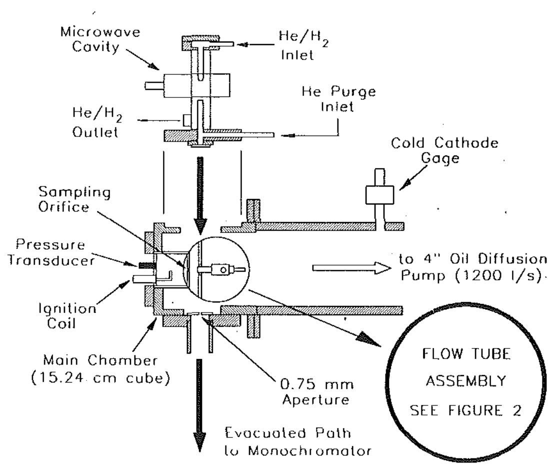

Fig. 1 Diagram of the combustion cell, vacuum chamber, and microwave resonance lamp

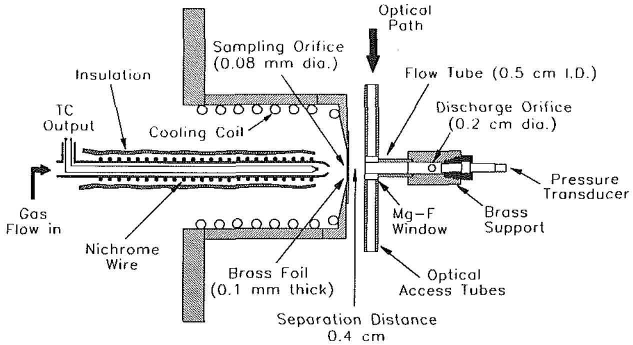

Fig. 2 Flow tube assembly inside vacuum chamber shown with experimental arrangement for the steady-state measurements; gas composition suppied to the heated tube was 1 percent krypton in a balance of nitrogen

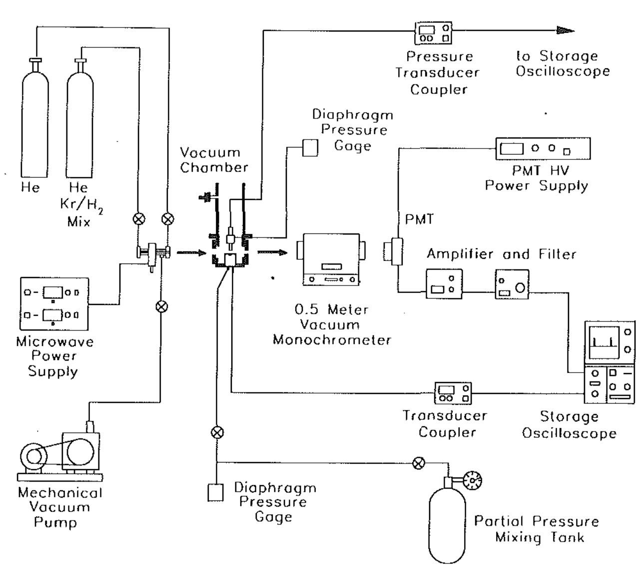

Fig. 3 Schematic diagram of the instrumentation used in the absorption measurements

and 3.2 cm in diameter, with a 0.20-mm sampling orifice in the center of a brass foil endplate. The cell was equipped with a coiled nichrome ignition element, a fill line, and a piezoelectric pressure transducer. Connected to the fill line was a Validyne DP14-44 diaphragm gage to measure initial fill pressure to within 0.3 kPa.

The steady-state gas delivery apparatus consisted of an insert containing a brass foil endplate with a 0.08-mm sampling orifice. Gas samples were supplied through a 1.0-mm orifice in a quartz tube positioned less than 2 mm from the sampling orifice. The insert was open to the atmosphere allowing excess gas supplied by the delivery tube to escape into the surroundings. Reproducible delivery rates were obtained by measuring the pressure in the supply tube. High-temperature gas samples were provided by a resistively heated nichrome wire coiled around the tube. Gas temperatures were recorded with a chromel-alumel thermocouple positioned inside the tube near the exit.

A normal shock was generated by a tube positioned in the flow downstream from the sampling orifice. It had an inner diameter of 0.5 cm and was positioned 0.4 cm from the sampling orifice along the center line. An evacuated path for lamp emission was provided by access tubes mounted perpendicular to the jet centerline at the front of the tube. At the points of intersection, the walls of the quartz tube were ground away and magnesium fluoride windows 2 mm thick were attached. A distance of 0.46 cm was measured between the faces of the windows. A brass mounting supported the tube and contained a Kistler 211B5 piezoelectric pressure transducer and a tube connection (not shown in the figure) leading to a diaphragm gage. Subsonic flow through the flow tube was produced by a 0.2-cm orifice near the end of the brass support.

To begin each transient experiment, the combustion chamber was filled with a flammable mixture of stoichiometric hydrogen and air. A current of 9.7 amps was passed through the ignition coil. Combustion was initiated after approximately 4 s of heating. During the experiment, the chamber pressure was monitored by a Kistler model 211B3 pressure transducer mounted in the wall opposite the sampling orifice. The sharp rise in pressure due to combustion was used to trigger sampling by a digital oscilloscope. All combustible mixtures were prepared 24 h beforehand in a partial pressure mixing tank with convective stirring of the mixture used to ensure a uniform reactant supply.

A schematic diagram of the instrumentation used in this experiment is shown in Fig. 3. The lamp required two gas supplies: one of 5 percent hydrogen and 5 percent krypton in a balance of helium, and the other of pure helium. Needle valves in the supply lines and a mechanical vacuum pump on the exhaust line permitted lamp flow rates and pressures to be adjusted. A 100-W microwave power supply was connected to an Evanson-type cavity (details of the lamp design will be given shortly) that enclosed a section of the lamp discharge tube. The detection side of the apparatus included a 0.5-m vacuum monochromator with an attached 150-l/s turbo-molecular pump. Detection of the vacuum UV radiation was accomplished with a photomultiplier tube with a Mg-F window. The signal output was first amplified by a wide-band video amplifier, then sent through a low-pass filter having a frequency cutoff of 3 kHz. During each experimental run, a dual trace, digital storage oscilloscope simultaneously recorded both the pressure trace from the combustion chamber, and either the absorption signal or the amplified pressure signal from the piezoelectric pressure transducer mounted in the flow tube.

A specially designed lamp was developed for use in this experiment yielding high-intensity output. Design features included a 1.5-cm o.d. quartz outer tube containing two opposing 3-mm o.d. inner tubes. The helium/hydrogen feed line terminated in a 120-μm orifice positioned in the center of the Evanson-type microwave cavity. Typically, pressure upstream of the orifice was in the range of 1 to 5 kPa while downstream it was 0.3 kPa. This configuration provided a high-density gas jet where radiation was generated and a rarefied region that transmitted the generated UV light. Opposing the gas jet was a tube for UV light passage through which helium purge gas flowed. The function of this feature was to reduce absorption of resonant radiation as it passed through the lamp and into the vacuum chamber. A Mg-F window 2 mm thick separated

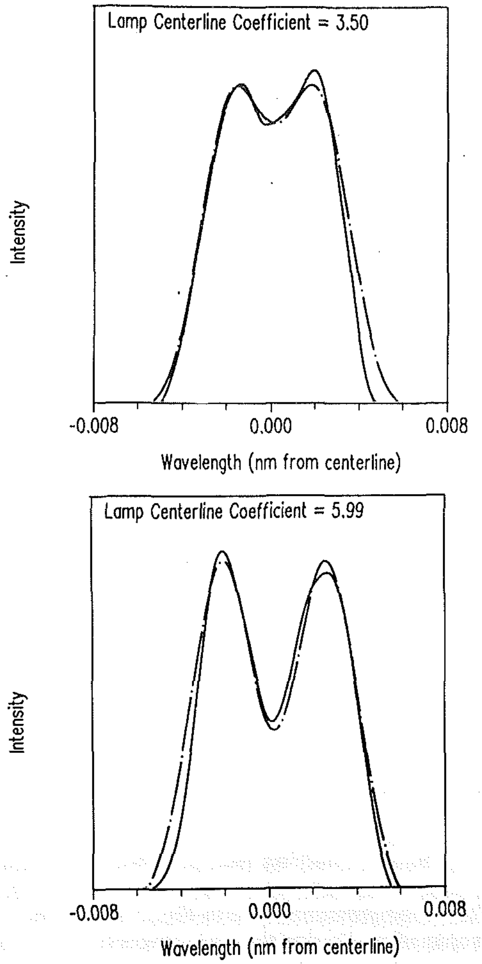

Fig. 4 Recorded (solid line) and predicted (dashed line) spectra of hydrogen Lyman-α lamp emissions: The top curve exhibits moderate *self-absorption, and the bottom exhibits high self-absorption*

the lamp from the vacuum chamber. The helium purge also reduced the amount of lamp self-absorption leading to a net threefold increase in output.

Results and Discussion

(A) Lamp Emission Profiles. A value for T_L was deduced from hydrogen Lyman-α line profiles recorded for six H_2/Kr/He lamp flow rates at a lamp power of 30 W. The necessary resolution was achieved by using a 316 g/mm Eschelle grating in the 0.5-m monochromator. The grating was rotated approximately 60 deg for operation in the 47th order. Two digitally smoothed examples of the spectra are shown by the solid curves in Fig. 4, with the top profile recorded at a moderate flow rate, and the bottom at a high flow rate. Both plots exhibit the self-absorbed profile discussed earlier, and the degree of self-absorption was found to increase at higher flow rates. For all spectra, the frequency scale was calibrated by a measurement of the separation between the 47th order hydrogen and deuterium lines.

The profiles in Fig. 4 are not, however, accurate representations of the actual lines emitted from the lamp. Line broadening and reduction in definition occur due to the instrument function of the monochromator. As with any spectral device, the monochromator does not resolve radiation at specific frequencies, but instead passes radiation in a narrow bandwidth. During a scan of resonant line, the monochromator grating is rotated so that this band moves steadily across the emitting frequencies. If the emission line is much broader than the bandpass of the instrument, little distortion of the spectrum occurs. However, if the line is narrower than the bandpass, the resulting line bears little resemblance to the actual profile.

Table 1 Recorded and predicted temperatures for the steady-state experiment

Recorded temperature	Predicted temperature	Absorption fraction	Flow tube pressure
305 K	305 K	0.417	25.7 Pa
338 K	348 K	0.456	26.6 Pa
384 K	382 K	0.472	24.7 Pa
414 K	409 K	0.485	23.9 Pa
451 K	432 K	0.495	23.3 Pa
523 K	514 K	0.533	22.5 Pa
550 K	554 K	0.548	22.3 Pa
578 K	565 K	0.550	22.0 Pa

In this study, the instrument function was obtained from a scan of a krypton emission line. The actual width of the line was estimated to be approximately an order of magnitude narrower than the bandpass of our monochromator; therefore the shape of the recorded spectrum was primarily dependent on the instrument function. This allowed the measured line shape to be used as a calibration of the instrument function.

Values of T_L were then obtained from fits of the model profiles to the recorded spectra. For reasons of numerical stability and simplicity, computational line shapes were convoluted with the instrument function and fit to measured spectra instead of deconvoluting the experimentally recorded line shapes and performing fits. Two model profiles after convolution, using the best fits of T_L and K_{0L} (for hydrogen), are shown as the dashed lines in Fig. 4.

An analysis of the spectra showed the best fit occurred for a T_L of 1100 K, regardless of lamp flow rates. The constant value is explained by noting that T_L is primarily dependent on the lamp power and gas pressure, both of which were kept constant while the relative flow rates of the two lamp gas supplies were varied. In these fits, it was observed that the most reliable indication of lamp temperature was found in the highly self-absorbed profiles. For these spectra, the frequency separation between the two maxima is very weakly dependent on K_{0L}, and is primarily a function of T_L. This measure was also found to be insensitive to small errors in the evaluation of the instrument function.

It should be stressed that before numerical filtering, recorded spectra exhibited a much higher noise level than those presented. Due to the very low signal levels observed when the monochromator was operated at its highest resolution, high-frequency noise at a signal-to-noise ratio near 3 was observed, in spite of signal conditioning by a low-pass filter with a frequency cutoff of 100 Hz. However, with proper numerical filtering, the shape of the emission profile could be recovered as demonstrated by Fig. 4.

For the krypton lamp emission profile, the second parameter, K_{0L}, was evaluated by resonant absorption measurements and will be discussed in the following section.

(B) Model Validation. The accuracy of the proposed model in evaluating temperatures was confirmed by a series of steady-state absorption measurements. The steady-state apparatus described earlier was used to deliver a gas composed of 1 percent Kr in N_2. Resonant absorptions at the Kr emission line of 123.5 nm, along with the pressure in the flow tube, were recorded for eight gas temperatures between 305 K and 580 K. Temperatures above ambient were generated by heating the gas delivery tube. Thermocouples provided an independent measurement of the gas temperature delivered to the sampling orifice.

Table 1 shows a comparison of the thermocouple temperatures with the temperatures predicted from krypton absorption measurements. The predictions were made using a value of 0.16 for the oscillator strength (Zaidel, 1970), a lamp temperature of 1100 K, and a K_{0L} of 4.2. This latter value was obtained by matching the predicted and measured absorption at 305 K. With these values, the measured absorption levels along with the flow tube pressure at each of the seven elevated thermocouple readings were used to generate a corresponding temperature using the model.

The absorption fraction shown in Table 1 was observed to increase with increasing temperature. This runs contrary to the decrease in absorbing atom density caused by the temperature rise. The absorption increase can be explained by noting that, due to the high emission temperature, the lamp profile is much broader than the sample absorption line width. As a consequence, effective absorption only occurs at the center of the emission band, leaving the wings relatively unaffected. Increasing absorption with temperature is therefore observed because, as the sample temperature increases, the width of the absorption line expands and a larger portion of the emission line is subject to absorption.

Another observed trend was a decrease in flow tube pressure with increasing temperature. Such a decrease is expected, since gas dynamic theory predicts a $1/\sqrt{T}$ dependence of the mass flow rate through a sonic orifice. An exception to this pattern is found in the first pressure value. The low reading was caused by a reduction in flow rate through the gas delivery tube to avoid overloading the diffusion pump. This resulted in a slightly lower stagnation pressure at the sampling orifice and a corresponding low pressure reading in the flow tube. Higher flow rates were used with heated gases to ensure a uniform gas temperature at the orifice.

Table 1 shows predicted and recorded temperatures remain relatively close throughout the temperature range studied. Deviations do not appear to be systematic, and can be attributed to uncertainty in the absorption measurement. The necessity of passing radiation through three Mg-F windows caused attenuation to the point where noise from the PMT was significant. Even after time averaging, variations as large as 1 percent were seen between consecutive data sets (absorption values presented in Table 1 are the result of averaging three sets of 2500 data points, each collected at a sampling rate of 2000 Hz). Variations are important because small deviations in absorption lead to significant changes in the predicted temperature. For example, the model temperature of 432 K rises to 450 K when an absorption fraction of 0.503 is used in place of the recorded value of 0.495.

(C) Transient Combustion Temperatures. The capability of this new diagnostic technique to track rapid changes in temperature was demonstrated by experiments in which a propagating flame was studied. To produce such a flame, the combustion chamber described earlier was filled to a pressure of 25 kPa with a stoichiometric hydrogen-air mixture containing a 0.20 percent mole fraction of krypton. Ignition of the mixture was initiated at the nichrome coil, producing a flame that propagated throughout the combustion chamber. Absorption in the flow tube during many repetitions of the combustion event was measured using three different lamp profiles. Plots of absorption and flow tube pressure during combustion are presented in Fig. 5. Each absorption curve is the result of signal averaging 10 experimental runs and the pressure trace is an average of 5 runs.

The combustion event occurring near the sampling orifice can be divided into periods before and after the arrival of the flame front. Before the front's arrival, the chamber pressure increases due to compression caused by the flame propagation; however, during this period the sampled gas is comprised of coal, unburned reactants. The flame front's arrival at the orifice is responsible for an extremely abrupt rise in temperature, after which hot product gases are sampled. This localized temperature increase has little effect on the overall chamber pressure, implying that an abrupt drop in density occurs.

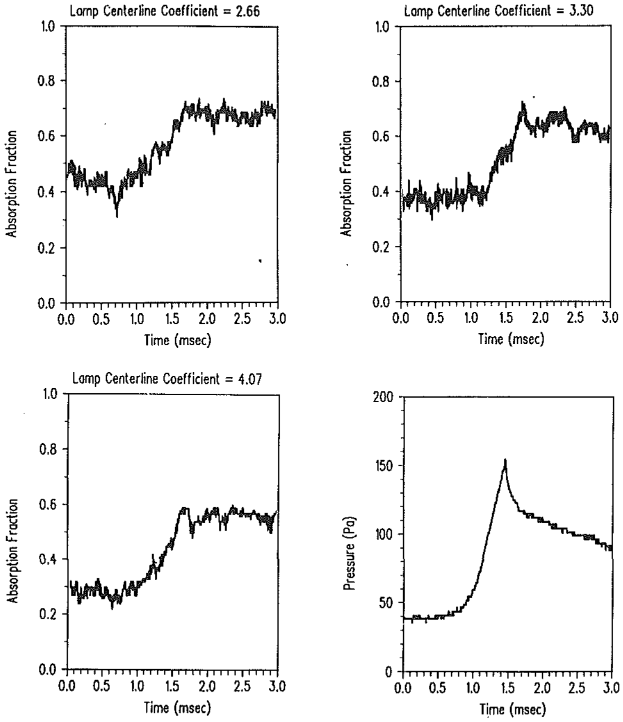

Fig. 5 Three plots of krypton absorption recorded during combustion using three lamp emission profiles; last plot gives the pressure in the flow tube during combustion

The flow tube pressure curve in Fig. 5 shows the effects of flame propagation. During the early stages of combustion, the rise in pressure was similar to that in the chamber. However, at 1.5 ms, an abrupt decrease occurred. This drop coincided with the arrival of the flame front and was caused by the decrease in mass flow through the orifice induced by the rapid increase in the sample temperature. The gradual decrease in pressure after 1.6 ms was due to cooling of the product gases inside the chamber.

Absorption measurements were recorded using three lamp emission profiles in order to obtain independent estimates of temperature during combustion. Agreement between the predicted temperature–time histories was used to provide further confirmation of the validity of the technique. In this analysis, T_L was set to 1100 K, and K_{0L} values were obtained by the procedure described earlier. In obtaining K_{0L}, it was assumed that the sample initially had a temperaure of 300 K, and that the initial absorption and flow tube pressure could be approximated by their averages over the first 0.5 ms of the recorded event (before ignition). Employing the derived lamp parameters, temperatures were calculated by first taking an average of the absorption signal within a 0.1 ms interval (ten data points), then using the model-fitting procedure to convert these averaged absorption measurements into temperature values. The results are shown in Fig. 6. It should be noted that, due to the chemical reaction, the Kr mole fraction of the product gases was taken to be 0.23 percent.

Temperatures in Fig. 6 remain around 300 K until the arrival of the flame front, at which time a jump to approximately 1800 K occurs. The low scatter in the time period before the flame arrival is a result of averaging adjacent absorption measurements as described above, and it is also due to the relative insensitivity of the model to noise at the lower absorption values. The highest temperature is observed about 0.3 ms after the arrival of the front, which can be explained by flame quenching. Boundary layer effects cause the flame to be ex-

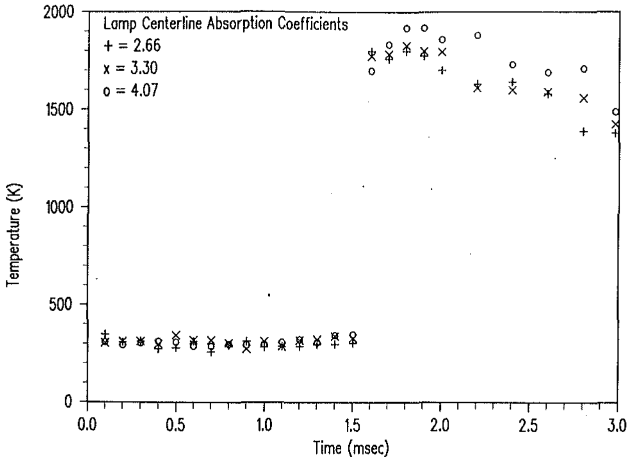

Fig. 6 Temperatures during combustion as predicted by an analysis of the krypton absorption curves; lamp emission profiles correspond to those used to obtain the data shown in Fig. 5

tinguished before passing through the orifice, so immediately after the flame's arrival, much of the sampled gas is drawn from the unburned layer near the chamber wall. The temperature then rises as this layer is depleted. Boundary layer effects, as well as radiative heat transfer from the flame, account for the measured temperature being lower than the adiabatic flame temperature.

Agreement between the three temperature time histories is relatively good, considering the noise levels found in the absorption signals. The variations in the product gas temperatures are not caused by an increase in absorption fluctuations, but instead were caused by the increased sensitivity of the model at these temperatures to changes in absorption.

Temperature values during the passage of the flame front are not presented. Reliable absorption values in this region were not obtained due to the high noise level and uncertainties in signal averaging. For individual runs, it was very difficult to determine the exact time of the flame's arrival, and errors of up to 50 μs were possible. This led to a loss in resolution of the averaged absorption signal.

Conclusions

Direct sampling is an important technique in the study of combustion processes. Extending it to transient events would provide a valuable tool for the study of a larger class of problems. In the work presented here, an optical technique has been described that provides a measure of the sample temperature. Determining this stagnation property is part of characterizing the sample and is required before quantitative determination of radical species concentrations can take place. Results of both the steady-state and transient experiments have shown that quantitative data has been obtained, although the transient results suffered in time resolution due to signal averaging. Before achieving the ultimate time response from this technique, useful single event data must be acquired. Toward this end, future experimental development will be directed toward improving the signal-to-noise ratio.

Acknowledgments

We would like to acknowledge support for this project from the National Science Foundation, Grant No. CBT-8713328. Also, support has been provided from the Air Force Office of Scientific Research.

References

Biordi, J. C., 1977, "Investigating the Fundamental Chemistry of Flames With Molecular Beam Mass Spectrometry," in: *Progress in Aeronautics and Astronautics*, AIAA, New York, Vol. 53, pp. 125-152.

Braun, W., Bass, A. W., and Davis, D. D., 1970, "Experimental Test of a Two Layer Model Characterizing Emission Line Profiles," *J. Opt. Soc. Am.*, Vol. 60, pp. 166-170.

Braun, W., and Carrington, T., 1969, "Line Emission Sources for Concentration Measurements and Photochemistry," NBS-TN476, National Bureau of Standards, Washington, DC.

Deckers, J., and Van Tiggelen, A., 1959, "Ion Identification in Flames," *7th Symp. (Int.) Combust.*, pp. 254-255.

Herron, J., and Peterson, R., 1988, "Time Resolved Concentration Measurements of Nitrogen, Oxygen, and Water in a Freely Propagating Hydrogen/air Flame by Direct Sampling Electron Impact Fluorimetry," *ASME Collected Papers in Heat Transfer*, Vol. 2, pp. 25-31.

Knuth, E. L., 1973, *Engine Emissions: Pollutant Formation and Measurement*, K. Springer and R. B. Peterson, eds., Plenum Press, New York, p. 319.

Lifshitz, A., Skinner, G. B., and Wood, D. R., 1979, "Resonance Absorption Measurements of Atom Concentrations in Reacting Gas Mixtures. I. Shapes of H and D Lyman-α Lines From Resonance Sources," *J. Chem. Phys.*, Vol. 70, pp. 5607-5613.

Lucas, D., Peterson, R., Brown, N. J., and Oppenheim, A. K., 1984a, "Molecular Beam Mass Spectrometer Sampling of Flash Ignited Combustion," *20th Symp. (Int.) Combust.*, pp. 1205-1211.

Lucas, D., Peterson, R., Hurlbut, F. C., and Oppenheim, A. K., 1984b, "Effects of Transient Combustion Phenomena on Molecular Beam Sampling," *J. Phys. Chem.*, Vol. 88, pp. 4548-4552.

Maki, R. G., Michael, J. V., and Sutherland, J. W., 1985, "Lyman-α Photometry; Curve of Growth Determination, Comparison to Theoretical Oscillator Strength, and Line Absorption Calculations at High Temperature," *J. Phys. Chem.*, Vol. 89, pp. 4815-4821.

Michael, J. V., and Weston, R. E., 1966, "Determination of Hydrogen Atom Concentrations by Lyman-α Photometry," *J. Chem. Phys.*, Vol. 45, pp. 3632-3641.

Milne, T. A., and Green, F. T., 1966, "Mass Spectrometric Studies of Reactions in Flames. II. Quantitative Sampling of Free Radicals From One-Atmosphere Flames," *J. Chem. Phys.*, Vol. 44, pp. 2444-2449.

Morse, F. A., and Kaufman, F., 1965, "Determination of Ground-State O, N, and H by Light Absorption and Measurement of Oscillator Strengths," *J. Chem. Phys.*, Vol. 42, pp. 1785-1790.

Myerson, A. L., and Watt, W. S., 1968, "Atom Formation Rates Behind Shock Waves in Hydrogen and the Effect of Added Oxygen," *J. Chem. Phys.*, Vol. 49, pp. 425-433.

Peeters, J., and Mahnen, G., 1973, "Reaction Mechanisms and Rate Constants of Elementary Steps in Methane-Oxygen Flames," *14th Symp. (Int.) Combust*, pp. 133-141.

Peterson, R., Lucas, D., Hurlbut, F. C., and Oppenheim, A. K., 1984, "Molecular Beam Overrun in Sampling Transient Combustion Processes," *J. Phys. Chem.*, Vol. 88, pp. 4746-4749.

Shadday, M. A., Kauzlarich, J. J., and Lowry, R. A., 1978, "Total Temperature Probe Calibration in Supersonic Rarified Flows," ASME Paper No. 78-WA/HT-1.

Thielen, K., and Roth, P., 1987, "Resonance Absorption Measurements of N, O, and H Atoms in Shock Heated HCN/O_2/Ar Mixtures," *Combust. Flame*, Vol. 69, pp. 141-154.

Winkler, E. V., 1954, "Design and Calibration of Stagnation Temperature Probes for Use at High Supersonic Speeds and Elevated Temperatures," *J. Appl. Phys.*, Vol. 25(2), pp. 231-232.

Zaidel, A. N., 1970, *Vacuum Ultraviolet Spectroscopy*, Ann Arbor-Humphrey Scientific Publishing, MI, p. 312.

Journal of Heat Transfer

Technical Notes

This section contains shorter technical papers. These shorter papers will be subjected to the same review process as that for full papers.

One-Dimensional Heat Conduction in a Semi-infinite Solid With the Surface Temperature a Harmonic Function of Time: A Simple Approximate Solution for the Transient Behavior

P. Burow and B. Weigand[1]

1 Introduction

Consider the temperature distribution $\vartheta(x, t)$ in a semi-infinite solid extending from the surface $x=0$ to $+\infty$. For $t<0$ the solid has the constant temperature $\vartheta=0$. For $t\geq 0$ the temperature at the surface $x=0$ is assumed to be a periodic harmonic function of time. The temperature distribution in the medium is governed by the following equations:

$$\frac{\partial\vartheta}{\partial t} = a\frac{\partial^2\vartheta}{\partial x^2} \qquad \text{(heat conduction equation)} \quad (1)$$

$$t=0 \text{ and } x>0\text{: } \vartheta=0 \qquad \text{(initial condition)} \quad (2)$$

$$t\geq 0 \text{ and } x=0\text{: } \vartheta=\vartheta_o\cos(\omega t-\epsilon) \qquad \text{(boundary condition)} \quad (3)$$

where a is the thermal diffusivity of the solid, ϑ_o represents the amplitude, ω the angular frequency, and ϵ the phase displacement of the temperature distribution at the surface.

The solution of equation (1) with the boundary condition (3) and the initial condition (2) is discussed in many classical books dealing with the theory of heat conduction in solids, e.g., Carslaw and Jaeger (1973), Eckert and Drake (1972), Özişik (1980), and Boelter et al. (1965). The resulting solution can be split off in two parts:

$$\vartheta=\vartheta_p-\vartheta_t \quad (4)$$

ϑ_p represents the periodic part of the solution, which is a steady oscillation with the frequency given by the boundary condition, reading

$$\vartheta_p=\vartheta_o e^{-x\sqrt{\frac{\omega}{2a}}}\cos\left[\omega t-x\sqrt{\frac{\omega}{2a}}-\epsilon\right] \quad (5)$$

This part is treated extensively in the literature and needs no further discussion.

The second term ϑ_t in equation (4) describes the transient behavior of the temperature in the solid from the beginning of the surface temperature oscillation at time $t=0$ to the steady oscillation ϑ_p at large times ($t\rightarrow\infty$):

$$\vartheta_t=\frac{2\vartheta_o}{\sqrt{\pi}}\int_o^{\frac{x}{2\sqrt{at}}}\cos\left[\omega\left(t-\frac{x^2}{4a\,\mu^2}\right)-\epsilon\right]e^{-\mu^2}d\mu \quad (6)$$

ϑ_t is of importance only for small times and vanishes at large times. The knowledge of the behavior of the transient part ϑ_t is necessary in some engineering problems such as the prediction of the transient behavior of recuperators or hardening furnaces, when modeling as a semi-infinite solid with a harmonic boundary condition holds. Therefore, and also to satisfy theoretical requirements, a detailed investigation of ϑ_t is presented, particularly because there exists none in the literature.

2 A Short-Time Solution for the Temperature Distribution

To simplify the considerations, the following dimensionless quantities are introduced:

$$\text{dimensionless time:} \qquad \tau=\omega t \quad (7)$$

$$\text{dimensionless coordinate:} \qquad \eta=x\sqrt{\frac{\omega}{2a}} \quad (8)$$

$$\text{dimensionless temperature:} \qquad \theta=\vartheta/\vartheta_o \quad (9)$$

After inserting these variables into equations (5) and (6), the following dimensionless expressions for ϑ are obtained:

$$\theta_p=e^{-\eta}\cos(\tau-\eta-\epsilon) \quad (10)$$

$$\theta_t=\frac{2}{\sqrt{\pi}}\int_o^{\frac{\eta}{\sqrt{2\tau}}}\cos\left[\tau-\frac{\eta^2}{2\mu^2}-\epsilon\right]e^{-\mu^2}d\mu \quad (11)$$

In order to get a short-time solution for the temperature field, equation (11) should be integrated. However, an analytical treatment would be very difficult and a numerical integration procedure cannot show the functional dependence of the solution on the variables. Therefore, another method will be employed to find a solution that is valid for short times.

After introducing the dimensionless quantities into equation (3) we get

$$\tau\geq 0 \text{ and } \eta=0\text{: } \theta=\cos(\tau-\epsilon) = \cos\epsilon\cos\tau+\sin\epsilon\sin\tau \quad (12)$$

Equation (12) can be expanded into a power series in τ

$$\theta=\cos\epsilon\sum_{n=0}^{\infty}(-1)^n\frac{\tau^{2n}}{(2n)!}+\sin\epsilon\sum_{n=0}^{\infty}(-1)^n\frac{\tau^{2n+1}}{(2n+1)!} \quad (13)$$

The solution of equations (1), (2), and (13) can be received by

---

[1] Institut für Technische Thermodynamik, Technische Hochschule Darmstadt, Federal Republic of Germany.

Contributed by the Heat Transfer Division for publication in the JOURNAL OF HEAT TRANSFER. Manuscript received by the Heat Transfer Division March 6, 1989; revision received November 21, 1989. Keywords: Conduction, Transient and Unsteady Heat Transfer.

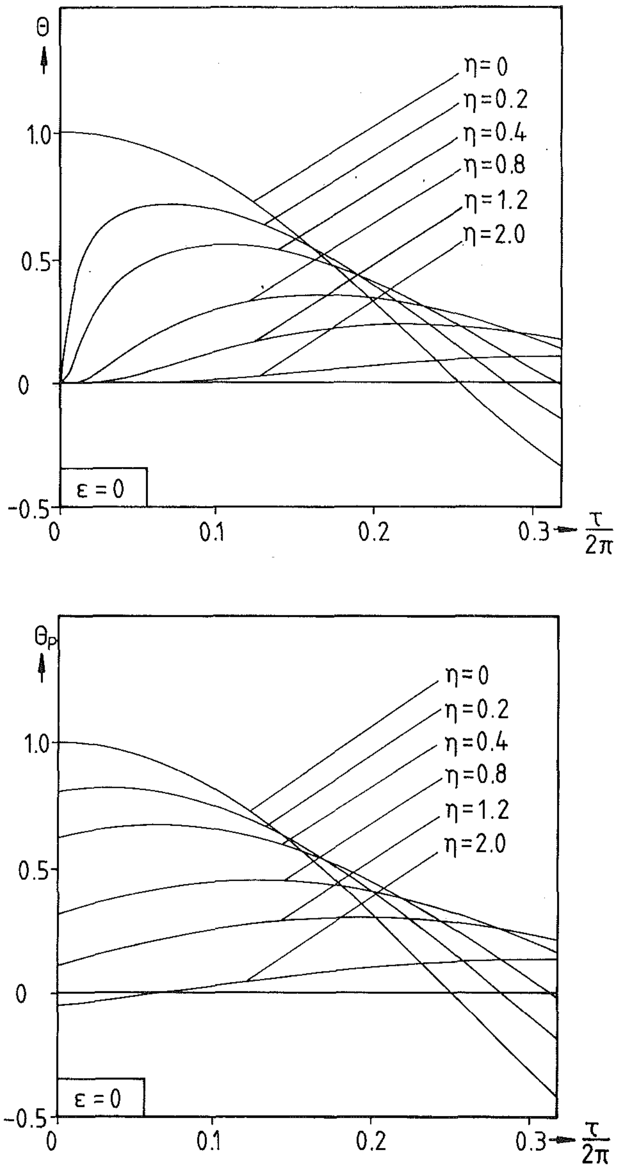

Fig. 1 Temperature distribution in the solid for $\epsilon = 0$ with the coordinate η as parameter

applying the superposition principle. The temperature field in the semi-infinite solid is found to be

$$\theta=\cos\epsilon\sum_{n=0}^{\infty}(-1)^n(4\tau)^{2n}i^{4n}\text{erfc}\left[\frac{\eta}{\sqrt{2\tau}}\right]$$
$$+\sin\epsilon\sum_{n=0}^{\infty}(-1)^n(4\tau)^{2n+1}i^{2(2n+1)}\text{erfc}\left[\frac{\eta}{\sqrt{2\tau}}\right]\qquad(14)$$

The repeated integrals of the error function complement appearing in equation (14) are defined according to Spanier and Oldham (1987)

$$i^n\text{erfc}(\xi)=\int_{\xi}^{\infty}i^{n-1}\text{erfc}(\mu)d\mu=\frac{1}{2^n}\sum_{j=0}^{\infty}\frac{(-2\xi)^j}{j!\Gamma\left(1+\frac{n-j}{2}\right)}\qquad(15)$$

which is equivalent to

$$\frac{d}{d\xi}\left[i^n\text{erfc}(\xi)\right]=-i^{n-1}\text{erfc}(\xi)\qquad(16)$$

where Γ denotes the gamma function.

Equation (14) represents the exact solution of equations (1), (2), and (3) in a new formulation. For large times τ the numerical evaluation of this formulation becomes disadvantageous, but it can be used advantageously as a short-time solution for the temperature field. By restricting equation (14) to terms including $n=2$ and observing that (14) is an alternating series, it follows that the truncation error in equation (14) is less than

$$F_{\theta\max}=|\cos\epsilon|(4\tau)^6i^{12}\text{erfc}\left(\frac{\eta}{\sqrt{2\tau}}\right)$$
$$+|\sin\epsilon|(4\tau)^7i^{14}\text{erfc}\left(\frac{\eta}{\sqrt{2\tau}}\right)\qquad(17)$$

The maximum values of the repeated integrals of the error function complement occur at $\eta/\sqrt{2\tau}=0$ (i.e., at the surface $\eta=0$) and are given by

$$i^k\text{erfc}(0)=\left[2^k\Gamma\left(1+\frac{k}{2}\right)\right]^{-1}\qquad(18)$$

Introducing equation (18) into (17) yields

$$F_{\theta\max}=\frac{\tau^6}{6!}|\cos\epsilon|+\frac{\tau^7}{7!}|\sin\epsilon|$$

in accordance with equation (13). For $\tau=\pi/2$ we get

$$F_{\theta\max}\left(\tau=\frac{\pi}{2}\right)=\left(\frac{\pi}{2}\right)^6\frac{1}{6!}\left[|\cos\epsilon|+\frac{\pi}{14}|\sin\epsilon|\right]<0.0214$$

This indicates the accuracy of the short-time solution (14) taking into account terms including $n=2$, provided we restrict our attention to the interval $0\le\tau\le\pi/2$. Figure 1 shows the temperature distribution in the solid for $\epsilon=0$ with the coordinate η as parameter. The two figures represent the solution given by equation (14), compared with the periodic solution given by equation (10). It can be seen that the difference between equations (10) and (14) disappears faster for smaller values of η than for greater ones. This means that the transient terms dies away more rapidly close to the surface than it does for large distances.

3 Heat Flux

The dimensionless heat flux is defined as

$$\psi=\frac{\dot{q}}{\lambda\vartheta_o\sqrt{\frac{\omega}{a}}}=\frac{-\lambda\frac{\partial\vartheta}{\partial x}}{\lambda\vartheta_o\sqrt{\frac{\omega}{a}}}=-\frac{1}{\sqrt{2}}\frac{\partial\theta}{\partial\eta}\qquad(19)$$

where $\dot{q}$ denotes the dimensional heat flux and λ the thermal conductivity. Introducing equation (14) into equation (19) and using equation (16) gives

$$\psi=\frac{\cos\epsilon}{2\sqrt{\tau}}\sum_{n=0}^{\infty}(-1)^n(4\tau)^{2n}i^{4n-1}\text{erfc}\left(\frac{\eta}{\sqrt{2\tau}}\right)$$
$$+\frac{\sin\epsilon}{2\sqrt{\tau}}\sum_{n=0}^{\infty}(-1)^n(4\tau)^{2n+1}i^{4n+1}\text{erfc}\left(\frac{\eta}{\sqrt{2\tau}}\right)\qquad(20)$$

Again restricting to terms $n\le2$, equation (20) represents a short-time solution. An error analysis analogous to that performed for the temperature field results in a truncation error less than

$$F_{\psi\max}=\frac{|\cos\epsilon|}{1\cdot3\cdot5\cdot7\cdot9\cdot11}\frac{(2\tau)^6}{\sqrt{\pi\tau}}+\frac{|\sin\epsilon|}{1\cdot3\cdot5\cdot7\cdot9\cdot11\cdot13}\frac{(2\tau)^7}{\sqrt{\pi\tau}}$$

where the maximal values occur at the surface $\eta=0$. For $\tau = \pi/2$ we get

$$F_{\psi_{\max}}<0.043$$

In many technical problems the main interest is focused on the heat flux ψ^0 at the surface. Therefore, this case will be analyzed in detail. Introducing equation (18) into equation (20) yields

$$\psi^0=\frac{\cos\epsilon}{\sqrt{\pi\tau}}\sum_{n=0}^{\infty}(-1)^n\frac{(2\tau)^{2n}}{(4n-1)!!}+\frac{\sin\epsilon}{\sqrt{\pi\tau}}\sum_{n=0}^{\infty}(-1)^n\frac{(2\tau)^{2n+1}}{(4n+1)!!} \tag{21}$$

with $k!! = 1$ for $k = -1$ and $k!! = k(k-2)(k-4)\ldots\bullet 5\bullet 3\bullet 1$ for $k = 1, 3, 5, \ldots$ resulting from relations for special arguments of the gamma function. Similar to equation (14), the numerical evaluation of equation (21) becomes disadvantageous for large times τ, but it is useful as a short-time solution. Truncating the series at $n = 2$ gives the forementioned error bound $F_{\psi_{\max}}$.

In order to find a formulation for the heat flux showing favorable numerical properties also for large times, the periodic part ψ_p and the transient part ψ_t are treated separately. Introducing equations (10) and (11), respectively, into equation (19) yields

$$\psi_p=-\frac{1}{\sqrt{2}}\frac{\partial\theta_p}{\partial\eta}=e^{-\eta}\cos\left(\tau-\eta-\epsilon+\frac{\pi}{4}\right) \tag{22}$$

$$\psi_t=-\frac{1}{\sqrt{2}}\frac{\partial\theta_t}{\partial\eta}=$$

$$-\sqrt{\frac{2}{\pi}}\left\{\cos(\tau-\epsilon)\frac{\partial}{\partial\eta}\int_o^{\frac{\eta}{\sqrt{2\tau}}}\cos\left(\frac{\eta^2}{2\mu^2}\right)e^{-\mu^2}d\mu\right.$$
$$\left.+\sin(\tau-\epsilon)\frac{\partial}{\partial\eta}\int_o^{\frac{\eta}{\sqrt{2\tau}}}\sin\left(\frac{\eta^2}{2\mu^2}\right)e^{-\mu^2}d\mu\right\} \tag{23}$$

Partial differentiation and using the substitution $z = \eta/\sqrt{2\mu}$ leads to

$$\psi_t=\cos(\tau-\epsilon)\left[-\frac{2}{\sqrt{\pi}}\int_{\infty}^{\sqrt{\tau}}(\sin z^2)e^{-\frac{\eta^2}{2z^2}}dz-\frac{\cos\tau}{\sqrt{\pi\tau}}e^{-\frac{\eta^2}{2\tau}}\right]$$
$$+\sin(\tau-\epsilon)\left[\frac{2}{\sqrt{\pi}}\int_{\infty}^{\sqrt{\tau}}(\cos z^2)e^{-\frac{\eta^2}{2z^2}}dz-\frac{\sin\tau}{\sqrt{\pi\tau}}e^{-\frac{\eta^2}{2\tau}}\right] \tag{24}$$

Again we restrict the considerations to the surface $\eta=0$ and introduce the Fresnel integrals according to Spanier and Oldham (1987)

$$S(\xi)=\sqrt{\frac{2}{\pi}}\int_o^{\xi}(\sin z^2)dz \text{ and}$$

$$C(\xi)=\sqrt{\frac{2}{\pi}}\int_o^{\xi}(\cos z^2)dz \tag{25}$$

with the limiting values $S(\xi\rightarrow\infty) = C(\xi\rightarrow\infty) = 1/2$ into equation (25). This results in

$$\psi_t^o=\cos(\tau-\epsilon)\left[\sqrt{2}\left(\frac{1}{2}-S(\sqrt{\tau})\right)-\frac{\cos\tau}{\sqrt{\pi\tau}}\right]$$
$$+\sin(\tau-\epsilon)\left[\sqrt{2}\left(-\frac{1}{2}+C(\sqrt{\tau})\right)-\frac{\sin\tau}{\sqrt{\pi\tau}}\right] \tag{26}$$

Equation (26) represents the transient part of the dimensionless heat flux ψ_t^o at the surface and may be simplified with the help of the auxiliary Fresnel integrals

$$\mathrm{Fres}(\xi)=\left[\frac{1}{2}-S(\xi)\right]\cos(\xi^2)-\left[\frac{1}{2}-C(\xi)\right]\sin(\xi^2)$$

and (27)

$$\mathrm{Gres}(\xi)=\left[\frac{1}{2}-S(\xi)\right]\sin(\xi^2)+\left[\frac{1}{2}-C(\xi)\right]\cos(\xi^2)$$

according to Spanier and Oldham (1987). This results in

$$\psi_t^o=F(\tau)\cos\epsilon+G(\tau)\sin\epsilon \tag{28}$$

where the functions $F(\tau)$ and $G(\tau)$ stand for

$$F(\tau)=\sqrt{2}\,\mathrm{Fres}(\sqrt{\tau})-\frac{1}{\sqrt{\pi\tau}} \text{ and}$$

$$G(\tau)=\sqrt{2}\,\mathrm{Gres}(\sqrt{\tau}) \tag{29}$$

At the surface $\eta=0$ the periodic part of the heat flux from equation (22) simplifies to

$$\psi_p^o=\cos\left(\tau-\epsilon+\frac{\pi}{4}\right)=\frac{1}{\sqrt{2}}[\cos(\tau-\epsilon)-\sin(\tau-\epsilon)] \tag{30}$$

The total dimensionless heat flux at the surface is found from equations (30) and (28), analogously to equation (4) as

$$\psi^o=\psi_p^o-\psi_t^o \tag{31}$$

The comparison of equation (31) with equation (21) leads to power series expansions for the functions $\mathrm{Fres}(\sqrt{\tau})$ and $\mathrm{Gres}(\sqrt{\tau})$, which are also given by Spanier and Oldham (1987). This may be considered as a proof for the correctness of our method.

For engineering applications simple approximations of the functions $F(\tau)$ and $G(\tau)$ might be helpful in using equation (28). The following approximations are recommended:

$$F(\tau)=-\left[\sqrt{\pi\tau}\left(\frac{1+\sqrt{\frac{\pi}{2}\tau+2\tau}}{1+0.1\,\tau}+\frac{4}{3}\tau^2\right)\right]^{-1}$$

$$G(\tau)=\left[\sqrt{2}\,\frac{1+2\sqrt{\frac{2}{\pi}\tau+3\tau}}{1+\tau}+\sqrt{\pi\tau}\,2\tau\right]^{-1} \tag{32}$$

These approximations show the same asymptotic behavior as equation (29). For short times this can be shown from equation (21), whereas at large times the relations

$$F(\tau)=-\frac{3}{\sqrt{\pi\tau}\,4\tau^2} \text{ and } G(\tau)=\frac{1}{\sqrt{\pi\tau}\,2\tau} \tag{33}$$

hold (see Spanier and Oldham, 1987).

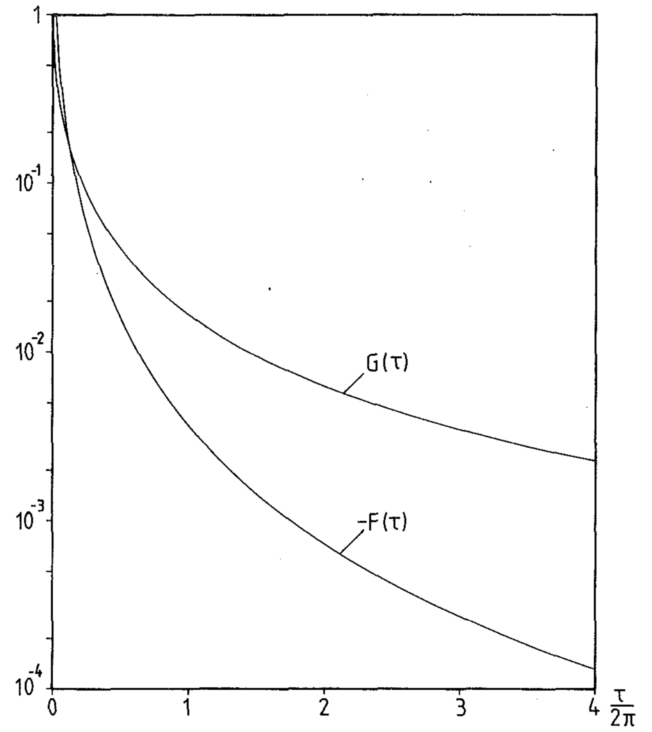

Fig. 2 Functions $F(\tau)$ and $G(\tau)$ from equation (29) representing the transient part of the heat flux ψ_t^o at the surface corresponding to equation (28)

In Fig. 2 the functions $F(\tau)$ and $G(\tau)$ are plotted according to equation (29). After the first period of the oscillation has passed ($\tau/2\pi = 1$), the values $F(2\pi) = -0.0036\ldots$ and $G(2\pi) = 0.0166\ldots$ are found, i.e., the transient part of the heat flux ψ_t^o at the surface from equation (28) has decreased to less than 2.4 percent of the periodic part ψ_p^o. In most cases, the transient part can be neglected for times larger than the first period.

The relative deviation of the approximation (32) from the exact expression (29) is less than 2.1 percent. So equation (32) represents a rather simple approximation for calculating the heat flux at the surface for arbitrary times.

Finally, it should be mentioned that the problem treated before can be adapted to the analogous problem of fluid flow in the vicinity of an oscillating flat plate (second Stokes problem). If ϑ is replaced by the flow velocity parallel to the plate, and λ is replaced by the kinematic viscosity, the heat flux at the wall $\dot{q}^o$ changes to the wall shear stress. So equation (32) represents a simple approximation to calculate the wall shear stress at any time. The periodic part of the second Stokes problem is discussed extensively by Schlichting (1982).

References

Boelter, L. M., Cherry, V. H., Johnson, V. A., and Martinelli, K. C., 1965, *Heat Transfer Notes*, McGraw-Hill, New York, pp. 218–229.

Carslaw, H. S., and Jaeger, J. C., 1973, *Conduction of Heat in Solids*, Clarendon Press, Oxford, United Kingdom.

Eckert, E. R., and Drake, R. M., 1972, *Analysis of Heat and Mass Transfer*, McGraw-Hill, New York.

Özişik, M. N., 1980, *Heat Conduction*, Wiley, New York.

Schlichting, H., 1982, *Grenzschicht-Theorie*, Braun, Karlsruhe, Federal Republic of Germany.

Spanier, J., and Oldham, K. B., 1987, *An Atlas of Functions*, Springer, Berlin.

Thermal Stresses Induced by Water Solidification in a Cylindrical Tube

S. Lin,[1] D. Y. Gao,[1] and X. C. Yu[1]

Nomenclature

C_p = specific heat at constant pressure, kJ/kg°C
E = Young's modulus, Pa
k = thermal conductivity, W/m°C
L = latent heat of water freezing, kJ/kg
r = radial coordinate, m
R_1 = outside radius of the brass tube, m
R_2 = inside radius of the brass tube, m
t = time, s
T = temperature, °C
T_b = outside surface temperature of the brass tube, °C
T_f = freezing temperature of water, °C
ΔT = temperature difference $= (T - T_f)$, °C
u = displacement, m
X = interface position between ice and water, m
z = axial coordinate, m
α = thermal diffusivity, m^2/s
α^* = linear thermal expansion coefficient, 1/°C
β = $\Delta V/(3V)$ = initial strain of ice, caused by volume expansion during water solidification, where V is the volume of ice
ν = Poisson ratio
ρ = density, kg/m^3
σ = stress, Pa

Subscripts

1 = brass tube
2 = ice
r = radial direction
t = circumferential direction
z = axial direction

Introduction

Thermal stresses caused by the volume expansion of water during the freezing process are important not only for industrial processes, such as freezing of food and production of ice, but also for damage of water containers or pipes in cold regions. Unfortunately, a theoretical analysis for the thermal stress cannot be readily conducted because of the following primary difficulties:

1 The mechanical properties of ice are not clearly known. They are greatly affected by many factors, such as the temperature of ice (Dantl, 1969), the internal structure of the ice

---

[1] Department of Mechanical Engineering, Concordia University, Montreal, Quebec, H3G 1M8, Canada.

Contributed by the Heat Transfer Division and presented at the National Heat Transfer Conference, Philadelphia, Pennsylvania, August 6–9, 1989. Manuscript received by the Heat Transfer Division May 10, 1989; revision received August 27, 1989. Keywords: Moving Boundaries, Phase-Change Phenomena, Transient and Unsteady Heat Transfer.

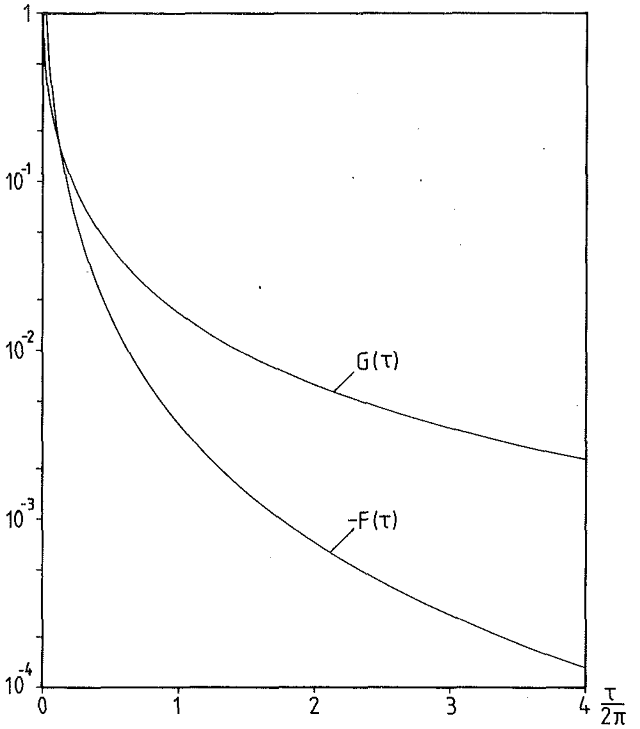

Fig. 2 Functions $F(\tau)$ and $G(\tau)$ from equation (29) representing the transient part of the heat flux ψ_t^o at the surface corresponding to equation (28)

In Fig. 2 the functions $F(\tau)$ and $G(\tau)$ are plotted according to equation (29). After the first period of the oscillation has passed ($\tau/2\pi = 1$), the values $F(2\pi) = -0.0036\ldots$ and $G(2\pi) = 0.0166\ldots$ are found, i.e., the transient part of the heat flux ψ_t^o at the surface from equation (28) has decreased to less than 2.4 percent of the periodic part ψ_p^o. In most cases, the transient part can be neglected for times larger than the first period.

The relative deviation of the approximation (32) from the exact expression (29) is less than 2.1 percent. So equation (32) represents a rather simple approximation for calculating the heat flux at the surface for arbitrary times.

Finally, it should be mentioned that the problem treated before can be adapted to the analogous problem of fluid flow in the vicinity of an oscillating flat plate (second Stokes problem). If ϑ is replaced by the flow velocity parallel to the plate, and λ is replaced by the kinematic viscosity, the heat flux at the wall $\dot{q}^o$ changes to the wall shear stress. So equation (32) represents a simple approximation to calculate the wall shear stress at any time. The periodic part of the second Stokes problem is discussed extensively by Schlichting (1982).

References

Boelter, L. M., Cherry, V. H., Johnson, V. A., and Martinelli, K. C., 1965, *Heat Transfer Notes*, McGraw-Hill, New York, pp. 218–229.

Carslaw, H. S., and Jaeger, J. C., 1973, *Conduction of Heat in Solids*, Clarendon Press, Oxford, United Kingdom.

Eckert, E. R., and Drake, R. M., 1972, *Analysis of Heat and Mass Transfer*, McGraw-Hill, New York.

Özişik, M. N., 1980, *Heat Conduction*, Wiley, New York.

Schlichting, H., 1982, *Grenzschicht-Theorie*, Braun, Karlsruhe, Federal Republic of Germany.

Spanier, J., and Oldham, K. B., 1987, *An Atlas of Functions*, Springer, Berlin.

Thermal Stresses Induced by Water Solidification in a Cylindrical Tube

S. Lin,[1] D. Y. Gao,[1] and X. C. Yu[1]

Nomenclature

C_p = specific heat at constant pressure, kJ/kg°C
E = Young's modulus, Pa
k = thermal conductivity, W/m°C
L = latent heat of water freezing, kJ/kg
r = radial coordinate, m
R_1 = outside radius of the brass tube, m
R_2 = inside radius of the brass tube, m
t = time, s
T = temperature, °C
T_b = outside surface temperature of the brass tube, °C
T_f = freezing temperature of water, °C
ΔT = temperature difference $= (T-T_f)$, °C
u = displacement, m
X = interface position between ice and water, m
z = axial coordinate, m
α = thermal diffusivity, m^2/s
α^* = linear thermal expansion coefficient, 1/°C
β = $\Delta V/(3V)$ = initial strain of ice, caused by volume expansion during water solidification, where V is the volume of ice
ν = Poisson ratio
ρ = density, kg/m^3
σ = stress, Pa

Subscripts

1 = brass tube
2 = ice
r = radial direction
t = circumferential direction
z = axial direction

Introduction

Thermal stresses caused by the volume expansion of water during the freezing process are important not only for industrial processes, such as freezing of food and production of ice, but also for damage of water containers or pipes in cold regions. Unfortunately, a theoretical analysis for the thermal stress cannot be readily conducted because of the following primary difficulties:

1 The mechanical properties of ice are not clearly known. They are greatly affected by many factors, such as the temperature of ice (Dantl, 1969), the internal structure of the ice

---

[1] Department of Mechanical Engineering, Concordia University, Montreal, Quebec, H3G 1M8, Canada.

Contributed by the Heat Transfer Division and presented at the National Heat Transfer Conference, Philadelphia, Pennsylvania, August 6-9, 1989. Manuscript received by the Heat Transfer Division May 10, 1989; revision received August 27, 1989. Keywords: Moving Boundaries, Phase-Change Phenomena, Transient and Unsteady Heat Transfer.

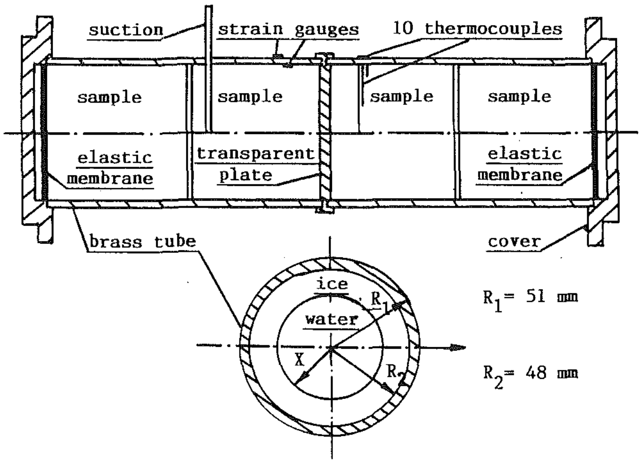

Fig. 1 Schematic diagram of the equipment used for the one-dimensional water freezing process in the brass tube

crystal (Michel, 1978), and the strain rate inside ice (Duval et al., 1981). It is difficult to develop general constitutive relations for ice.

2 The initial strain of ice is difficult to predict because the volume expansion of ice during solidification is dependent on the ice internal structure, which is often unknown and affected by many factors (Kuon and Jonas, 1973).

Due to these difficulties, simplifications have to be made for the thermal stress analysis of ice during the water freezing process. In this paper, a thermal stress analysis model for the one-dimensional water freezing process taking place inside a cylindrical brass tube is presented. Numerical results generated by the model agree well with experimental data.

Experimental Equipment and Method

The experimental apparatus was specifically designed for testing a one-dimensional water freezing process in a cylindrical brass tube, as shown in Fig. 1. Eight copper-constantan thermocouples were assembled inside the tube in the radial direction. Two thermocouples were fixed on the inside and outside surfaces of the tube wall. The thermal strains in the axial and circumferential directions on the inside and outside surfaces of the tube wall were measured by four strain gages. The two ends of the long brass tube were sealed by two thermal insulation covers. Each cover had an elastic membrane, which allowed the ice to expand freely in the axial direction. A transparent plastic plate was assembled at the central cross section of the brass tube. The tube could be opened at the central cross section and the ice-water interface positions could be measured or photographed directly through the transparent plastic plate. The interface position could also be determined from the measured temperature distributions. Before starting a test, the brass tube was filled with distilled water and precooled in a tank filled with ice-water mixture (0°C). Then the tube was quickly immersed into a stirred and temperature-controlled ethanol bath. The outside surface temperature of the brass tube was controlled at a constant value. The absolute error of the thermocouples was ± 0.1°C. The absolute error of the strains measured by the strain gages was $\pm 0.5 \times 10^{-6}$ (nondimensional unit).

Mathematical Formulation

Heat Transfer Process. It is assumed that the thermal properties of brass, ice, and water are constant; the density change during the water freezing may be neglected. However, the density change is considered in thermal stress analysis. Under these assumptions, the one-dimensional water freezing process taking place inside the brass tube, initially at the freezing temperature of water, can be formulated in two time periods separated at a specific time t^* at which the water inside the brass tube starts freezing.

Period 1. Before time t^*:

Governing equation:

$$\frac{\partial^2 T_1}{\partial r^2} + \frac{1}{r}\frac{\partial T_1}{\partial r} = \frac{1}{\alpha_1}\frac{\partial T_1}{\partial t} \quad \text{for } R_2 < r < R_1,\ 0 < t < t^* \tag{1}$$

Boundary conditions:

$$T_1(R_1, t) = T_b \tag{2}$$

$$T_1(R_2, t) = T_f \tag{3}$$

Initial condition:

$$T_1(r, 0) = T_f \tag{4}$$

Period 2. After time t^*:

Governing equations:

$$\frac{\partial^2 T_i}{\partial r^2} + \frac{1}{r}\frac{\partial T_i}{\partial r} = \frac{1}{\alpha_i}\frac{\partial T_i}{\partial t} \quad t > t^* \tag{5}$$

$i = 1$ for $R_2 < r < R_1$; $i = 2$ for $X < r < R_2$.

Boundary conditions:

$$T_1(R_1, t) = T_b \tag{6}$$

$$T_1(R_2, t) = T_2(R_2, t) \tag{7}$$

$$k_1 \frac{\partial T_1(R_2, t)}{\partial r} = k_2 \frac{\partial T_2(R_2, t)}{\partial r} \tag{8}$$

$$T_2(X, t) = T_f \tag{9}$$

Initial conditions:

$$T_1(r, t^*) = f(r, t^*) \text{ (known from Period 1)} \tag{10}$$

$$X(t^*) = R_2 \tag{11}$$

At the interface position:

$$L\rho_2 \frac{dX}{dt} = k_2 \frac{\partial T_2(X, t)}{\partial r} \tag{12}$$

In the above formulation, $T_f = 0$°C, and T_b is a constant.

Thermal Stress Analysis. It is assumed that (*a*) the brass tube is considered to be infinitely long; (*b*) the test system is mechanically in a quasi-equilibrium state during the freezing process; (*c*) the shear stress between the tube and the ice may be neglected; (*d*) the mechanical properties of ice are constant; and (*e*) the characteristics of the isotropic polycrystalline ice may be applied to the analysis as a first approximation. For the isotropic polycrystalline ice, the brittle behavior is characterized by the elastic deformation followed by a sudden crush (Michel, 1978; 1980). Therefore, the elastic theory may also be applied to the polycrystalline ice before its crush occurs. After the crush of the ice, the strains and stresses in the ice and in the brass tube would be redistributed. These redistributions cannot be predicted by the model. When the ice is crushed inside the tube, a sudden decrease of the strains on the tube wall can be observed from the strain gage record. From the literature, the crush strength of ice varies in the range from 4×10^5 to 130×10^5 Pa (Michel, 1978). Comparing the experimental data with the numerical results, it was found that the ice was indeed crushed when the maximum thermal stress in the ice reached the range. In the thermal stress analysis, the crush of the ice is therefore defined to be bound by the upper and the lower limits as follows: upper limit: maximum $\sigma_2 = 130 \times 10^5$ Pa; lower limit: maximum $\sigma_2 = 4 \times 10^5$ Pa.

Table 1 Thermal and mechanical properties of brass and ice

	k, W/m°C	C_p, kJ/kg°C	L, kJ/kg	ρ, kg/m^3	E, Pa	ν	α^*, 1/°C	β
Brass	52.0	0.385		8800	1.0×10^{11}	0.36	1.6×10^{-7}	
Ice	2.0	4.180	333.84	910	2.5×10^{9}	0.31	5.5×10^{-7}	0.01

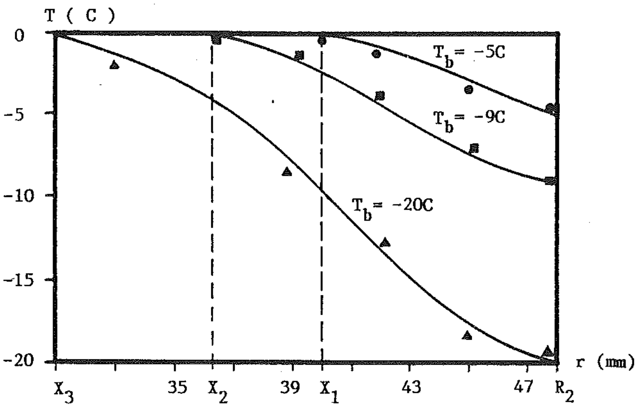

Fig. 2 Numerical and experimental results for the temperature distributions in the ice at the time when the ice starts to be crushed at the interface positions X_1, X_2, and X_3, respectively: ●: test data for $T_b = -5$ C; ■: test data for $T_b = -9$°C; ▲: test data for $T_b = -20$°C; —: numerical result

For this axial symmetric plane-strain problem, only the main components of the strain and stress of the system are considered. The following equations can be derived from the stress equilibrium equations, the strain-displacement relations, and Hooke's Law (Boley and Weiner, 1962):

$$\frac{d}{dr}\left[\frac{1}{r}\frac{d(ru_{ri})}{dr}\right] = \frac{1+\nu_i}{1-\nu_i}\alpha_i^*\frac{dT_i(r)}{dr} \quad (i=1,\ 2) \tag{13}$$

$$\sigma_{rri} = \frac{E_2}{1+\nu_i}\left[\frac{1-\nu_i}{1-2\nu_i}\frac{du_{ri}}{dr} + \frac{\nu_i}{1-2\nu_i}\left(\frac{u_{ri}}{r} + \frac{du_{zi}}{dz}\right)\right] - \frac{\alpha_i^* E_i}{1-2\nu_i}[T_i(r)+\phi] \quad (i=1,\ 2) \tag{14}$$

where $\phi = 0$ if $i=1$, $\phi = \beta/\alpha_2^*$ if $i=2$.

$$\frac{du_{zi}}{dz} = k_{zi} = \text{const} \quad (i=1,\ 2) \tag{15}$$

Equations (13) to (15) are subject to the following boundary conditions:

$$\sigma_{rr1}(R_1) = 0 \tag{16}$$

$$\sigma_{rr1}(R_2) = \sigma_{rr2}(R_2) \tag{17}$$

$$u_{r1}(R_2) = u_{r2}(R_2) \tag{18}$$

$$\sigma_{rr2}(X) = 0 \tag{19}$$

Under the assumption of no shear stress between the tube and ice, the moment balance equations for the brass tube and ice can be obtained, respectively, as follows:

$$2\pi\int_{R_2}^{R_1} r\sigma_{zz1}dr = 0 \tag{20}$$

$$2\pi\int_{X}^{R_2} r\sigma_{zz2}dr = 0 \tag{21}$$

Integrating equation (13) yields

$$u_{r1} = \frac{1+\nu_1}{1-\nu_1}\frac{\alpha_1^*}{r}\int_{R_2}^{r} T_1(r)rdr + C_1 r + \frac{C_2}{r} \tag{22}$$

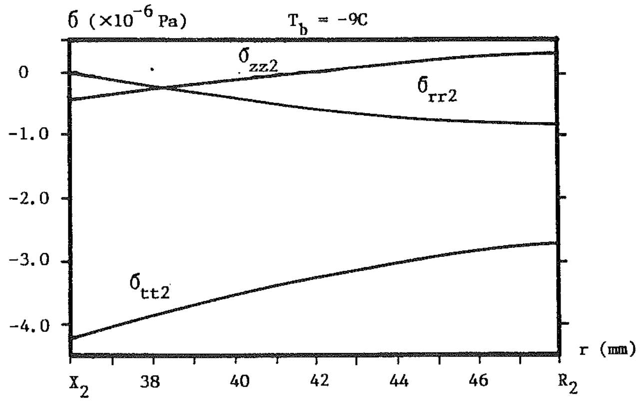

Fig. 3 Stress distributions in the ice with $T_b = -9$°C at the time when the ice starts to be crushed at X_2

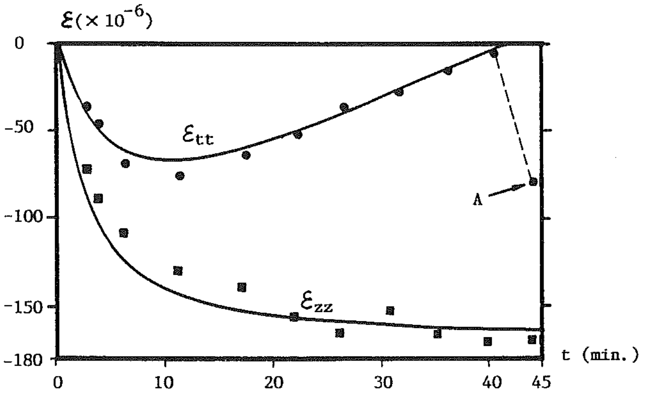

Fig. 4 Numerical and experimental results for the variations of the axial and circumferential strains on the outside surface of the test tube during the freezing process with $T_b = -9$°C; Point A indicates a sudden drop of the circumferential strain, which implies the crushing of the ice inside the tube

$$u_{r2} = \frac{1+\nu_2}{1-\nu_2}\frac{\alpha_2^*}{r}\int_{X}^{r}\left[T_2(r) + \frac{\beta}{\alpha_2^*}\right]rdr + C_3 r + \frac{C_4}{r} \tag{23}$$

Six unknown constants, C_1, C_2, C_3, C_4, k_{z1}, and k_{z2}, can be determined from equations (16)-(21). The stresses and strains in both the tube wall and the ice can then be determined from Hooke's Law and the strain-displacement relations.

Numerical Method

The Finite Difference Method was used to solve the one-dimensional freezing process by using the Crank-Nicholson scheme and the Variable Space Grid technique (Murray and Landis, 1959). The number of nodes set in the ice was varied from 11 to 51 and in the tube wall, 5 to 15. The small time step was adjusted in the range from 10 s to 10 min depending on the rate of the freezing process until the solution of the program was converged. A numerical integral method (Simpson's Rule) was applied to equations (22) and (23). In the computer simulation, Young's Modulus of ice, E_2, and the initial strain of the ice, β, were varied as control factors because they vary over certain ranges, i.e., 0.2×10^9 Pa $< E_2 < 9.8 \times 10^9$ Pa (Michel, 1978) and $\beta < 0.03$. The values of E_2 and β in Table 1 were determined by computer simulations in order to reach the best matching of the numerical results with experimental data.

Results and Discussion

Selected numerical and experimental results are shown in Figs. 2-4. Figure 2 shows the transient temperature distributions in the ice, at the time when the ice starts to be crushed at the interface positions X_1, X_2, and X_3, respectively, with T_b as a parameter. Figure 3 shows the distributions of the stresses in the ice, just before the ice is crushed with $T_b = -9°\mathrm{C}$. Figure 3 also indicates that the circumferential stresses inside the ice are much larger than the radial and axial stresses. The maximum circumferential compressive stress is located at the interface position between the ice and water. Therefore, it is expected that the compressive crushing of the ice should first take place at the interface, and then propagate outward along the radial direction. A great number of the ice crush lines in the radial directions were observed when the brass tube was opened at the central cross section after the experimental tests. Figure 4 shows the transient variations of the axial and circumferential strains on the outside surface of the brass tube. Point A in Fig. 4 indicates a sudden drop of the circumferential strain, which implies crushing of the ice. It was found that the boundary temperature T_b is an important factor that strongly affects the ice thickness at which the ice crushes. When the ice inside the brass tube crushes, the thickness of the ice formed with a slow freezing process is thinner than that with a quick freezing process ($X_1 < X_2 < X_3$, as shown in Fig. 2).

References

Boley, B. A., and Weiner, J. H., 1962, *Theory of Thermal Stress*, Wiley, New York.

Dantl, G., 1969, "Elastic Moduli of Ice," *Physics of Ice*, Plenum Press, pp. 223-230.

Duval, P., Maitre, M., Manouvrier, A., Marec, G., and Jay, J. C., 1981, "Primary Creep and Experimental Method for Testing Ice in Various Conditions of Strain Rates and Stress," *Proceedings of International Symposium on Ice*, Vol. 11, pp. 596-602.

Kuon, L. G., and Jonas, J. J., 1973, "Effect of Strain Rate and Temperature on the Microstructure of Polycrystalline Ice," *Physics and Chemistry of Ice*, The Royal Society of Canada, University of Toronto Press, pp. 370-376.

Michel, B., 1978, *Ice Mechanics*, Laval University Press, Canada.

Michel, B., 1980, "The Strength of Polycrystalline Ice," *Can. J. of Civil Eng.*, Vol. 5, No. 3, pp. 285-300.

Murray, W. D., and Landis, F., 1959, "Numerical and Machine Solutions of Transient Heat-Conduction Problems Involving Melting and Freezing," ASME JOURNAL OF HEAT TRANSFER, Vol. 81, pp. 106-112.

A Comparative Study of the Effect of Inlet Conditions on a Free Convection Flow in a Vertical Channel

P. R. Chappidi[1,2] and B. E. Eno[1]

Nomenclature

b = width of the channel
g = acceleration due to gravity
k = thermal conductivity of the fluid
l = dimensional length of the channel
p' = local dimensional pressure at any axial station x in the channel
p_∞ = ambient pressure at any elevation x
P_i = pressure defect at the inlet
Pr = Prandtl number of the fluid
PVP = parabolic velocity profile = $6U_0(Y - Y^2)$
q_H = heat flux at the "hot" wall
q_C = heat flux at the "cold" wall
R_H = channel wall heat flux ratio = (q_C/q_H)
R_T = channel wall temperature ratio = $(T_C - T_0)/(T_H - T_0)$
Ra = Rayleigh number = GrPr
T = temperature of the fluid
T_C = temperature of the "cold" wall
T_H = temperature of the "hot" wall
T_0 = ambient temperature of the fluid
U_0 = nondimensional "uniform" velocity at the inlet of the channel = $u_0 b^2/l\nu\mathrm{Gr}$
u_M = dimensional mean velocity = $\left(\int_0^b u dy\right)/b$
U_M = nondimensional mean velocity = $(u_M b^2)/l\nu\mathrm{Gr}$
UVP = uniform velocity profile = U_0
$\theta_{X,H}$ = nondimensional local temperature of the hot wall
$\theta_{X,C}$ = nondimensional local temperature of the cold wall
ν = kinematic viscosity of the fluid
ρ = density of the fluid

Introduction

Free convection between heated vertical plates has been the focus of the several studies due to its application in the cooling of electronic components, heating of buildings via Trombe walls, and many other engineering processes. On the theoretical side, which is the focus of this note, the computational strategy for the solution of the developing free convective boundary layer flow within a vertical channel (Aung et al., 1972; Azevedo and Sparrow, 1986; Bodoia and Osterle, 1962) features a marching technique, which mandates the specification of the inlet conditions. As a result, the numerical results may be sensitive to the assumption of inlet conditions.

This note discusses the influence of inlet conditions on the natural convection boundary layer flow within an asymmetrically heated vertical channel. Both uniform heat flux (UHF) and uniform surface temperature conditions (UST) are considered. Inlet conditions examined include a uniform velocity profile with/without inlet pressure defect and a parabolic velocity profile with/without inlet pressure defect. The inlet pressure defect is accounted by applying the Bernoulli equation at the inlet. Numerical results are compared with available experimental results to assess the sensitivity of the thermal performance parameters (local and overall average Nusselt numbers) to the change in inlet condition specifications.

Analysis

The governing equations of the natural convection (steady, laminar, and two-dimensional) flow with Boussineq approximation through an asymmetrically heated parallel plate vertical channel (Fig. 1) in nondimensional form are (Aung et al., 1972)

---

[1] Department of Mechanical Engineering, University of Central Florida, Orlando, FL 32816.

[2] Current address: Los Alamos National Laboratory, Engineering and Safety Analysis Group, Los Alamos, NM 87544.

Contributed by the Heat Transfer Division and presented at the National Heat Transfer Conference, Houston, Texas, July 24-27, 1988. Manuscript received by the Heat Transfer Division August 10, 1989; revision received April 19, 1990. Keywords: Enclosure Flows, Natural Convection, Numerical Methods.

to reach the best matching of the numerical results with experimental data.

Results and Discussion

Selected numerical and experimental results are shown in Figs. 2-4. Figure 2 shows the transient temperature distributions in the ice, at the time when the ice starts to be crushed at the interface positions X_1, X_2, and X_3, respectively, with T_b as a parameter. Figure 3 shows the distributions of the stresses in the ice, just before the ice is crushed with $T_b = -9°\mathrm{C}$. Figure 3 also indicates that the circumferential stresses inside the ice are much larger than the radial and axial stresses. The maximum circumferential compressive stress is located at the interface position between the ice and water. Therefore, it is expected that the compressive crushing of the ice should first take place at the interface, and then propagate outward along the radial direction. A great number of the ice crush lines in the radial directions were observed when the brass tube was opened at the central cross section after the experimental tests. Figure 4 shows the transient variations of the axial and circumferential strains on the outside surface of the brass tube. Point A in Fig. 4 indicates a sudden drop of the circumferential strain, which implies crushing of the ice. It was found that the boundary temperature T_b is an important factor that strongly affects the ice thickness at which the ice crushes. When the ice inside the brass tube crushes, the thickness of the ice formed with a slow freezing process is thinner than that with a quick freezing process ($X_1 < X_2 < X_3$, as shown in Fig. 2).

References

Boley, B. A., and Weiner, J. H., 1962, *Theory of Thermal Stress*, Wiley, New York.

Dantl, G., 1969, "Elastic Moduli of Ice," *Physics of Ice*, Plenum Press, pp. 223-230.

Duval, P., Maitre, M., Manouvrier, A., Marec, G., and Jay, J. C., 1981, "Primary Creep and Experimental Method for Testing Ice in Various Conditions of Strain Rates and Stress," *Proceedings of International Symposium on Ice*, Vol. 11, pp. 596-602.

Kuon, L. G., and Jonas, J. J., 1973, "Effect of Strain Rate and Temperature on the Microstructure of Polycrystalline Ice," *Physics and Chemistry of Ice*, The Royal Society of Canada, University of Toronto Press, pp. 370-376.

Michel, B., 1978, *Ice Mechanics*, Laval University Press, Canada.

Michel, B., 1980, "The Strength of Polycrystalline Ice," *Can. J. of Civil Eng.*, Vol. 5, No. 3, pp. 285-300.

Murray, W. D., and Landis, F., 1959, "Numerical and Machine Solutions of Transient Heat-Conduction Problems Involving Melting and Freezing," ASME JOURNAL OF HEAT TRANSFER, Vol. 81, pp. 106-112.

A Comparative Study of the Effect of Inlet Conditions on a Free Convection Flow in a Vertical Channel

P. R. Chappidi[1,2] and B. E. Eno[1]

Nomenclature

b = width of the channel
g = acceleration due to gravity
k = thermal conductivity of the fluid
l = dimensional length of the channel
p' = local dimensional pressure at any axial station x in the channel
p_∞ = ambient pressure at any elevation x
P_i = pressure defect at the inlet
Pr = Prandtl number of the fluid
PVP = parabolic velocity profile = $6U_0(Y-Y^2)$
q_H = heat flux at the "hot" wall
q_C = heat flux at the "cold" wall
R_H = channel wall heat flux ratio = (q_C/q_H)
R_T = channel wall temperature ratio = $(T_C-T_0)/(T_H-T_0)$
Ra = Rayleigh number = GrPr
T = temperature of the fluid
T_C = temperature of the "cold" wall
T_H = temperature of the "hot" wall
T_0 = ambient temperature of the fluid
U_0 = nondimensional "uniform" velocity at the inlet of the channel = $u_0 b^2/l\nu\mathrm{Gr}$
u_M = dimensional mean velocity = $\left(\int_0^b u\,dy\right)/b$
U_M = nondimensional mean velocity = $(u_M b^2)/l\nu\mathrm{Gr}$
UVP = uniform velocity profile = U_0
$\theta_{X,H}$ = nondimensional local temperature of the hot wall
$\theta_{X,C}$ = nondimensional local temperature of the cold wall
ν = kinematic viscosity of the fluid
ρ = density of the fluid

Introduction

Free convection between heated vertical plates has been the focus of the several studies due to its application in the cooling of electronic components, heating of buildings via Trombe walls, and many other engineering processes. On the theoretical side, which is the focus of this note, the computational strategy for the solution of the developing free convective boundary layer flow within a vertical channel (Aung et al., 1972; Azevedo and Sparrow, 1986; Bodoia and Osterle, 1962) features a marching technique, which mandates the specification of the inlet conditions. As a result, the numerical results may be sensitive to the assumption of inlet conditions.

This note discusses the influence of inlet conditions on the natural convection boundary layer flow within an asymmetrically heated vertical channel. Both uniform heat flux (UHF) and uniform surface temperature conditions (UST) are considered. Inlet conditions examined include a uniform velocity profile with/without inlet pressure defect and a parabolic velocity profile with/without inlet pressure defect. The inlet pressure defect is accounted by applying the Bernoulli equation at the inlet. Numerical results are compared with available experimental results to assess the sensitivity of the thermal performance parameters (local and overall average Nusselt numbers) to the change in inlet condition specifications.

Analysis

The governing equations of the natural convection (steady, laminar, and two-dimensional) flow with Boussineq approximation through an asymmetrically heated parallel plate vertical channel (Fig. 1) in nondimensional form are (Aung et al., 1972)

---

[1] Department of Mechanical Engineering, University of Central Florida, Orlando, FL 32816.

[2] Current address: Los Alamos National Laboratory, Engineering and Safety Analysis Group, Los Alamos, NM 87544.

Contributed by the Heat Transfer Division and presented at the National Heat Transfer Conference, Houston, Texas, July 24-27, 1988. Manuscript received by the Heat Transfer Division August 10, 1989; revision received April 19, 1990. Keywords: Enclosure Flows, Natural Convection, Numerical Methods.

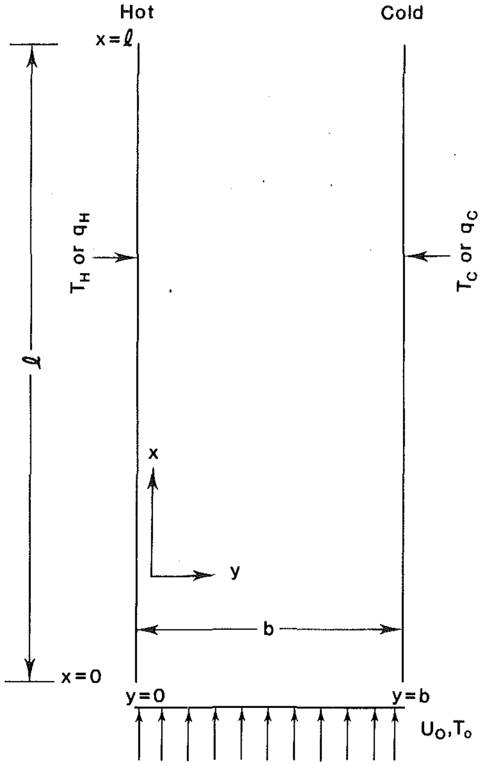

Fig. 1 Physical model

$$\frac{\partial U}{\partial X}+\frac{\partial V}{\partial Y}=0 \tag{1}$$

$$U\frac{\partial U}{\partial X}+V\frac{\partial U}{\partial Y}=-\frac{dP}{dX}+\frac{\partial^2 U}{\partial Y^2}+\theta \tag{2}$$

$$U\frac{\partial \theta}{\partial X}+V\frac{\partial \theta}{\partial Y}=\frac{1}{\Pr}\frac{\partial^2 \theta}{\partial Y^2} \tag{3}$$

Volumetric flow rate:

$$Q=\int_0^1 U dY \tag{4}$$

Inlet conditions:

At $X<0$: $U=U_1$ (i.e., UVP)

$=6U_0(Y-Y^2)$ (i.e., PVP)

$V=\theta=0$; $P_i=-\frac{1}{2}U_M^2$

Boundary conditions:

At $X\geq 0$; $Y=0$, $U=V=0$, $\theta=1$ (UST)

$\frac{\partial\theta}{\partial Y}=-1$ (UHF)

$Y=1$, $U=V=0$, $\theta=R_T$ (UST)

$\frac{\partial\theta}{\partial Y}=R_H$ (UHF)

Exit condition:

At $X=L=\frac{1}{\mathrm{Gr}}$; $P=0$

The *nondimensional* variables and parameters in the above equations are defined as:

Grashof number (Gr): $\mathrm{Gr}=(g\beta\Delta Tb^4)/(l\nu^2)$ (UST) or $(g\beta q_H b^5)/(l\nu^2 k)$ (UHF)

Temperature of the fluid (θ): $\theta=(T-T_0)/(T_H-T_0)$ (UST) or $(T-T_0)/\left(\frac{q_H b}{k}\right)$ (UHF)

Table 1 Grid sizes

ΔX (Axial step size)	X (Stream-wise coordinate)
1.0×10^{-6}	$X < 1.0 \times 10^{-5}$
2.0×10^{-6}	$1.0 \times 10^{-5} \leq X < 3.0 \times 10^{-5}$
1.0×10^{-5}	$3.0 \times 10^{-5} \leq X < 8.0 \times 10^{-5}$
1.5×10^{-5}	$8.0 \times 10^{-5} \leq X < 2.0 \times 10^{-2}$
5.0×10^{-4}	$2.0 \times 10^{-2} \leq X < 5.0 \times 10^{-2}$
5.0×10^{-3}	$5.0 \times 10^{-2} \leq X < 2$

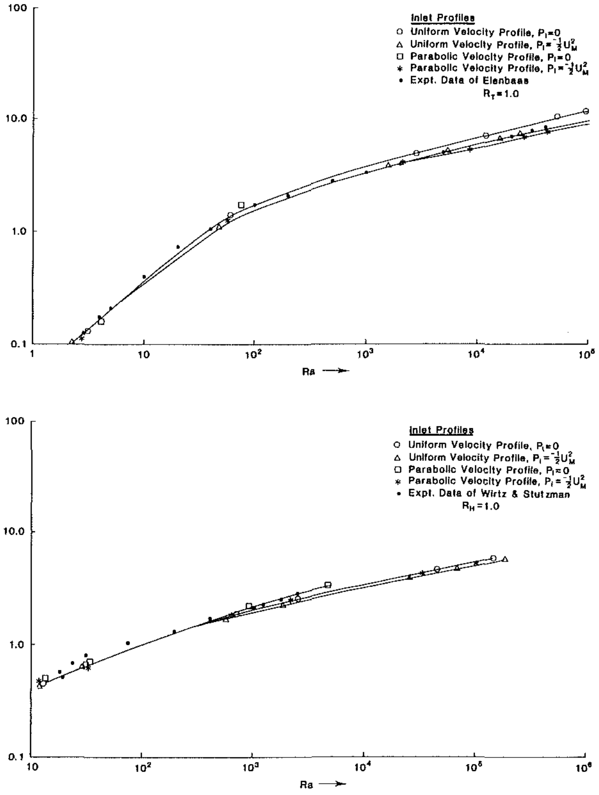

Fig. 2 Influence of inlet conditions on the overall Nusselt number

Streamwise (X) and normal (Y) coordinates: $X=(x)/(l\mathrm{Gr})$; $Y=y/b$

Streamwise (U) and normal (V) components of velocity: $U=(ub^2)/(l\nu\mathrm{Gr})$; $V=(\nu b)/(\nu)$

Pressure defect (P) and volumetric flow rate (Q): $P=((p'-p_\infty)b^4)/(\rho l^2\nu^2\mathrm{Gr})$; $Q=\left(\int_0^b udyb\right)/(l\nu\mathrm{Gr})$

The local Nusselt numbers based on hot ($\mathrm{Nu}_{X,H}$) and cold ($\mathrm{Nu}_{X,C}$) walls are

$$\mathrm{Nu}_{X,U}=-\frac{\partial\theta}{\partial Y}\bigg|_{Y=0}\text{(UST)},\quad \mathrm{Nu}_{X,C}=-\frac{\partial\theta}{\partial Y}\bigg|_{Y=1}\text{(UST)}$$

$$\mathrm{Nu}_{X,U}=\frac{1}{\theta_{X,H}}\text{(UHF)},\quad \mathrm{Nu}_{X,C}=\frac{R_H}{\theta_{X,C}}\text{(UHF)}$$

The overall Nusselt numbers for "UST" and "UHF" conditions are defined below. For the UHF conditions, the overall

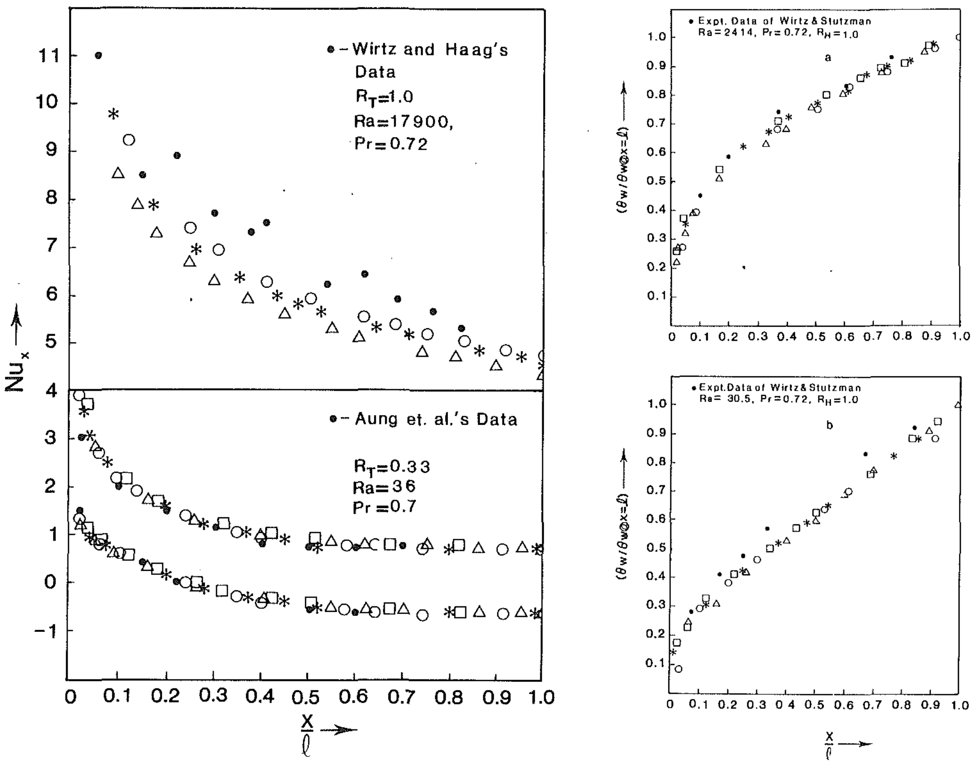

Fig. 3 Influence of inlet conditions on the local Nusselt numbers (UST) and channel wall temperature variation (UHF)

Nusselt number (Nu_E) is based on the channel wall exit temperature.

$$\overline{\mathrm{Nu}}=\frac{\mathrm{Ra}}{1+R_T}\int_0^1 U\theta dY\ \text{(UST)},\qquad \mathrm{Nu}_E=\frac{(1+R_H)}{(\theta_{H@X=L}+\theta_{C@X=L})}$$

Discussion of Results

The solution of methodology is briefly described here but more details can be found from Chappidi and Eno (1988). The finite-difference expansion is of the same implicit form as described by Aung et al. (1972). An implicit, forward marching, finite-difference scheme is used to obtain the solution of the governing equations. After experimenting with several grid sizes, for the calculations reported within this note, 41 grid points were used across the channel width and the axial grid size varied along the length of the channel (Table 1). When the pressure defect within the channel starts increasing, convergence was accelerated by increasing the grid size to 0.02 times the local nondimensional length (X). Using the grid sizes listed in Table 1, good agreement within the bounds of interpolation error was achieved with Bodoia and Osterle (1962) and Aung et al. (1972). For the sake of brevity, these details are not reported.

The numerical results (obtained with different inlet conditions) are compared with the experimental data of various investigators in Figs. 2 and 3. The following pointers are helpful to understand the graphic plots: "O" refers to "UVP" with $P_i=0$ and "Δ" refers to "UVP" with $P_i=-\frac{1}{2}U_M^2$. "□" refers to "PVP" with $P_i=0$ and "*" refers to "PVP" with $P_i=-\frac{1}{2}U_M^2$. More details of this analysis can be found from Chappidi and Eno (1988).

In Fig. 2, the overall Nusselt number predictions at various Rayleigh numbers are compared with experimental data of Elenbass (1942) (UST, $R_T=1.0$) and Wirtz and Stutzman (1982) (UHF, $R_H=1.0$). The maximum deviation of numerical predictions from the experimental data is about 15 percent with Elenbaas' data (1942) and approximately 20 percent in the case of symmetrically heated isoflux plates (Wirtz and Stutzman, 1982). These deviations include the experimental uncertainty, inlet assumptions, variable fluid property effects, numerical approximation errors, boundary layer approximation, and the interpolation error.

The lower left panel of Fig. 3 compares the local Nusselt number variation at low Rayleigh number (Ra = 36 with asymmetric heating $R_T=0.33$). It should be noted that the the current numerical program accepts the nondimensional volumetric flow rate (Q) as the input and gives the dimensional channel length $\left(L=\frac{1}{\mathrm{Gr}}\right)$ as one of the outputs. Thus, the Grashof number matching the experimental value was determined by trial and error assuming various values of the parameter Q. The maximum deviation of theoretical Gr from the experimental value is less than 0.3 percent. All the inlet conditions (lower left panel of Fig. 3) produce results that are very much in agreement with the experimental data, implying that inlet conditions are not of much concern in the numerical solution of low Grashof number flows. However, at a higher Rayleigh number (upper left panel of Fig. 3), the scatter among numerical solutions is relatively noticeable and all the inlet conditions underpredict the local Nusselt number variation. The right panel of Fig. 3 compares the normalized nondimensional wall temperature variation along the channel for uniform heat flux conditions ($R_H=1.0$). All the inlet conditions seem to slightly underpredict the wall temperature variation.

Concluding Remarks

Results of a computational study of free convective boundary layer flow in a heated vertical parallel plate channel indicate that the inlet conditions may not be of much concern in the numerical solution of low Grashof number flows, which are dominated by viscous forces. However, the numerical results are sensitive to inlet conditions at higher Grashof numbers (Figs. 2 and 3). The assumption of zero pressure defect at the inlet always results in higher values of local and overall Nusselt numbers than those obtained by considering the pressure defect. Overall and local comparisons on a comprehensive level do not favor any specific inlet flow assumptions. Additional information may become available with future experimental efforts and/or the solution of the Navier-Stokes equations covering a wide range of Grashof numbers dealing with inlet conditions.

References

Aung, W., Fletcher, L. S., and Sernas, V., 1972, "Developing Laminar Free Convection Between Vertical Flat Plates With Asymmetric Heating," *International Journal of Heat and Mass Transfer*, Vol. 15, pp. 2293-2308.

Azevedo, L. F. A., and Sparrow, E. M., 1986, "Natural Convection in a Vertical Channel Vented to the Ambient Through an Aperture in the Channel Wall," *International Journal of Heat and Mass Transfer*, Vol. 29, pp. 819-830.

Bodoia, J. R., and Osterle, J. F., 1962, "The Development of Free Convection Between Heated Vertical Plates," ASME JOURNAL OF HEAT TRANSFER, Vol. 84, pp. 40-44.

Chappidi, P. R., and Eno, B. E., 1988, "Natural Convection in a Heated Parallel Plate Vertical Channel; Influence of Inlet Conditions," ASME *Proceedings of the 1988 National Heat Transfer Conference*, Houston, TX, Vol. 2, pp. 135-144.

Elenbaas, W., 1942, "Heat Dissipation of Parallel Plates by Free Convection," *Physica*, Vol. 9, pp. 1-28.

Wirtz, R. A., and Haag, T., 1985, "Effect of an Unheated Entry on Natural Convection Between Vertical Parallel Plates," presented at the ASME Winter Annual Meeting Miami Beach, FL, Nov. 17-21.

Wirtz, R. A., and Stutzman, R. J., 1982, "Experiments on Free Convection Between Vertical Plates With Symmetric Heating," ASME JOURNAL OF HEAT TRANSFER, Vol. 104, pp. 501-507.

An Asymptotic Approach to Natural Convection Momentum and Heat Transfer in Saturated Highly Porous Media

H. Herwig[1] and M. Koch[1]

Nomenclature

c_f = skin friction coefficient
d = particle diameter, equation (3)
$\tilde{d}$ = particle diameter, equation (15)
b, d = heat transfer parameters, equation (12)
$D_{\mathrm{I}}, D_{\mathrm{II}}$ = differential operators, equations (23) and (24)
f = dimensionless stream function
$F, \tilde{F}$ = Forchheimer constant, equations (5) and (8)
g = gravitational constant
Gr = Grashof number, Table 1
$K, \tilde{K}$ = permeability, equations (3) and (8)
L = reference length
n = porosity
Nu = Nusselt number
T = temperature
u, v = velocity components
x, y = coordinates
β = expansion coefficient, Table 1
ϵ = perturbation parameter, equation (13)
η = similarity variable
Θ = dimensionless temperature, Table 1
λ = thermal conductivity
μ = viscosity
ν = kinematic viscosity
ρ = density
τ_w = wall shear stress
φ = auxiliary variable, equation (17)
ψ = stream function, Table 1

Subscripts

D = Darcian
e = effective
f = fluid
p = pore
R = reference
W = wall
∞ = at infinity (outside the boundary layer)

1 Introduction

The simplest model for flow in porous media is the Darcy law. For pure free convection it states a balance of buoyancy and friction forces; see Cheng (1978). In dimensional quantities it reads

$$\frac{\mu_f^*}{K^*} u_D^* = \rho_{f\infty}^* \beta_f^* [T^* - T_\infty^*]\, g^* \sin \alpha \tag{1}$$

Here u_D^* is the average velocity over a cross section of the porous medium, which is also called the Darcy velocity. Its relation to the so-called pore velocity—the local average velocity of the fluid in the pores—is simply

$$u_D^* = n u_p^* \tag{2}$$

with n being the so-called porosity ($n = 1$:clear flow, no solid matrix). The empirical constant K^* is the permeability with dimensions $[K^*] = \mathrm{m}^2$. It is a property of the solid matrix and is often related to an average particle diameter by the correlation (3). According to Ergun (1952)

$$K^* = \frac{d^{*2} n^3}{150(1-n)^2} \tag{3}$$

It is quite obvious that equation (1) is more and more insufficient when n becomes larger. In the limit $n = 1$ there is no longer any solid matrix and the clear flow natural convection boundary layer will be observed at the heated wall. The most pronounced difference is that now the no-slip condition at the wall must hold.

The complete system of equations with a momentum equation improved by so-called non-Darcy terms reads (see for example Kaviany and Mittal, 1987)

Table 1 Nondimensional quantities: $\mathrm{Gr} = (\rho_f^* U_R^* L^* / \mu_f^*)^2$; $U_R^* = L^* | g^* \sin \alpha\beta^* \Delta T^* |)^{1/2}$

x	y	u	v	ψ	θ
$\frac{x^*}{L^*}$	$\frac{y^*}{L^*} \mathrm{Gr}^{1/4}$	$\frac{u^*}{U_R^*}$	$\frac{v^*}{U_R^*} \mathrm{Gr}^{1/4}$	$\frac{\psi^*}{U_R^* L^*} \mathrm{Gr}^{1/4}$	$\frac{T^* - T_\infty^*}{(T_w^*(L^*) - T_\infty^*)_{n=1} x^b}$

---

[1] Institut für Thermo- und Fluiddynamik, Ruhr-Universität, D-4630 Bochum, Federal Republic of Germany.

Contributed by Heat Transfer Division for publication in the JOURNAL OF HEAT TRANSFER. Manuscript received by the Heat Transfer Division March 15, 1989; revision received February 5, 1990. Keywords: Natural Convection, Porous Media.

are sensitive to inlet conditions at higher Grashof numbers (Figs. 2 and 3). The assumption of zero pressure defect at the inlet always results in higher values of local and overall Nusselt numbers than those obtained by considering the pressure defect. Overall and local comparisons on a comprehensive level do not favor any specific inlet flow assumptions. Additional information may become available with future experimental efforts and/or the solution of the Navier-Stokes equations covering a wide range of Grashof numbers dealing with inlet conditions.

References

Aung, W., Fletcher, L. S., and Sernas, V., 1972, "Developing Laminar Free Convection Between Vertical Flat Plates With Asymmetric Heating," *International Journal of Heat and Mass Transfer*, Vol. 15, pp. 2293-2308.

Azevedo, L. F. A., and Sparrow, E. M., 1986, "Natural Convection in a Vertical Channel Vented to the Ambient Through an Aperture in the Channel Wall," *International Journal of Heat and Mass Transfer*, Vol. 29, pp. 819-830.

Bodoia, J. R., and Osterle, J. F., 1962, "The Development of Free Convection Between Heated Vertical Plates," ASME JOURNAL OF HEAT TRANSFER, Vol. 84, pp. 40-44.

Chappidi, P. R., and Eno, B. E., 1988, "Natural Convection in a Heated Parallel Plate Vertical Channel; Influence of Inlet Conditions," ASME *Proceedings of the 1988 National Heat Transfer Conference*, Houston, TX, Vol. 2, pp. 135-144.

Elenbaas, W., 1942, "Heat Dissipation of Parallel Plates by Free Convection," *Physica*, Vol. 9, pp. 1-28.

Wirtz, R. A., and Haag, T., 1985, "Effect of an Unheated Entry on Natural Convection Between Vertical Parallel Plates," presented at the ASME Winter Annual Meeting Miami Beach, FL, Nov. 17-21.

Wirtz, R. A., and Stutzman, R. J., 1982, "Experiments on Free Convection Between Vertical Plates With Symmetric Heating," ASME JOURNAL OF HEAT TRANSFER, Vol. 104, pp. 501-507.

An Asymptotic Approach to Natural Convection Momentum and Heat Transfer in Saturated Highly Porous Media

H. Herwig[1] and M. Koch[1]

Nomenclature

c_f = skin friction coefficient
d = particle diameter, equation (3)
$\tilde{d}$ = particle diameter, equation (15)
b, d = heat transfer parameters, equation (12)
$D_{\mathrm{I}}, D_{\mathrm{II}}$ = differential operators, equations (23) and (24)
f = dimensionless stream function
$F, \tilde{F}$ = Forchheimer constant, equations (5) and (8)
g = gravitational constant
Gr = Grashof number, Table 1
$K, \tilde{K}$ = permeability, equations (3) and (8)
L = reference length
n = porosity
Nu = Nusselt number
T = temperature
u, v = velocity components
x, y = coordinates
β = expansion coefficient, Table 1
ϵ = perturbation parameter, equation (13)
η = similarity variable
Θ = dimensionless temperature, Table 1
λ = thermal conductivity
μ = viscosity
ν = kinematic viscosity
ρ = density
τ_w = wall shear stress
φ = auxiliary variable, equation (17)
ψ = stream function, Table 1

Subscripts

D = Darcian
e = effective
f = fluid
p = pore
R = reference
W = wall
∞ = at infinity (outside the boundary layer)

1 Introduction

The simplest model for flow in porous media is the Darcy law. For pure free convection it states a balance of buoyancy and friction forces; see Cheng (1978). In dimensional quantities it reads

$$\frac{\mu_f^*}{K^*} u_D^* = \rho_{f\infty}^* \beta_f^* [T^* - T_\infty^*]\, g^* \sin \alpha \tag{1}$$

Here u_D^* is the average velocity over a cross section of the porous medium, which is also called the Darcy velocity. Its relation to the so-called pore velocity—the local average velocity of the fluid in the pores—is simply

$$u_D^* = n u_p^* \tag{2}$$

with n being the so-called porosity ($n = 1$:clear flow, no solid matrix). The empirical constant K^* is the permeability with dimensions $[K^*] = \mathrm{m}^2$. It is a property of the solid matrix and is often related to an average particle diameter by the correlation (3). According to Ergun (1952)

$$K^* = \frac{d^{*2} n^3}{150(1-n)^2} \tag{3}$$

It is quite obvious that equation (1) is more and more insufficient when n becomes larger. In the limit $n = 1$ there is no longer any solid matrix and the clear flow natural convection boundary layer will be observed at the heated wall. The most pronounced difference is that now the no-slip condition at the wall must hold.

The complete system of equations with a momentum equation improved by so-called non-Darcy terms reads (see for example Kaviany and Mittal, 1987)

Table 1 Nondimensional quantities: $\mathrm{Gr} = (\rho_f^* U_R^* L^* / \mu_f^*)^2$; $U_R^* = L^* \, | g^* \sin \alpha \beta^* \Delta T^* |)^{1/2}$

x	y	u	v	ψ	θ
$\frac{x^*}{L^*}$	$\frac{y^*}{L^*}\,\mathrm{Gr}^{1/4}$	$\frac{u^*}{U_R^*}$	$\frac{v^*}{U_R^*}\,\mathrm{Gr}^{1/4}$	$\frac{\psi^*}{U_R^* L^*}\,\mathrm{Gr}^{1/4}$	$\frac{T^* - T_\infty^*}{(T_w^*(L^*) - T_\infty^*)_{n=1}\, x^D}$

---

[1] Institut für Thermo- und Fluiddynamik, Ruhr-Universität, D-4630 Bochum, Federal Republic of Germany.

Contributed by Heat Transfer Division for publication in the JOURNAL OF HEAT TRANSFER. Manuscript received by the Heat Transfer Division March 15, 1989; revision received February 5, 1990. Keywords: Natural Convection, Porous Media.

$$\frac{\partial u^*}{\partial x^*} + \frac{\partial v^*}{\partial y^*} = 0 \tag{4}$$

$$\rho_f^*\left(u^*\frac{\partial u^*}{\partial x^*} + v^*\frac{\partial u^*}{\partial y^*}\right) = \mu_f^*\frac{\partial^2 u^*}{\partial y^{*2}} - \frac{\mu_f^* n}{K^*}u^* + \rho_{f\infty}^*\beta_f^*(T^* - T_\infty^*)g^*\sin\alpha - \frac{F}{K^{*1/2}}n^2\rho_{f\infty}^* u^{*2} \tag{5}$$

$$\rho_{f\infty}^* c_p^*\left(u^*\frac{\partial T^*}{\partial x^*} + v^*\frac{\partial T^*}{\partial y^*}\right) = \lambda_e^*\frac{\partial^2 T^*}{\partial y^{*2}} \tag{6}$$

The physical properties ρ, μ, and c_p are those of the fluid (subscript f) while the thermal conductivity λ_e is taken to be a so-called effective quantity $n\lambda_f + (1-n)\lambda_s$.

In the limit $n \to 1$ equations (4)–(6) reduce to those for a clear flow with no solid matrix provided that $K^* \to \infty$. Equation (3) shows that K^* goes to infinity for $n \to 1$ when the average particle diameter d^* does not vanish like $(1-n)$. This is no serious restriction with respect to an asymptotic theory for $n \to 1$, which is the scope of this study.

The nondimensional momentum equation, in terms of the dimensionless stream function f, reads according to Table 1:

$$f''' + (3+d)ff'' - (2+2d+4n^2FK^{-1/2}x)f'^2 - 2nK^{-1}\mathrm{Gr}^{-1/2}x^{(1-d)/2}f' + x^{b-d}\Theta = 4x(f'\partial f'/\partial x - f''\partial f/\partial x) \tag{7}$$

The constant b comes in through nondimensionalizing Θ; it is a fixed value for a specific thermal boundary condition. The dimensionless permeability is $K = K^*/L^{*2}$. In the framework of the boundary layer theory (asymptotic theory for $\mathrm{Gr} \to \infty$), K^{-1} must be of the order $O(\mathrm{Gr}^{1/2})$ since the term $2nK^{-1}\mathrm{Gr}^{-1/2}x^{(1-d)/2}f'$ in equation (7) must be a term of order $O(1)$ asymptotically. To express this formally we introduce $\tilde{K}$ and $\tilde{F}$ by setting

$$\frac{1}{\tilde K} = \frac{1}{K\mathrm{Gr}^{1/2}} = O(1), \quad \tilde F = F\mathrm{Gr}^{1/4} = O(1) \tag{8}$$

The asymptotic meaning of equation (8) is that $\tilde K^{-1}$ may become zero as it will with $K \to \infty$ and $\mathrm{Gr} \to \infty$, but it always must be bounded in the limit of infinite Grashof numbers.

The basic equations for a subsequent regular perturbation procedure with respect to n are now

$$f''' + (3+d)ff'' - (2+2d+4n^2\tilde F\tilde K^{-1/2}x)f'^2 - 2n\tilde K^{-1}x^{(1-d)/2}f' + x^{b-d}\Theta = 4x(f'\partial f'/\partial x - f''\partial f/\partial x) \tag{9}$$

$$\mathrm{Pr}_\infty^{-1}\Theta'' + (3+d)f\Theta' - 4bf'\Theta = 4x(f'\partial\Theta/\partial x - \Theta'\partial f/\partial x) \tag{10}$$

with the associated boundary conditions

$$\eta = 0{:}\ f = f' = \Theta - 1 = 0; \quad \eta \to \infty{:}\ f' = \Theta = 0 \tag{11}$$

and the heat transfer parameters

$$b = d = 0 \text{ for } T_w = \text{const}; \quad b = d = \frac{1}{5} \text{ for } q_w = \text{const} \tag{12}$$

2 Asymptotic Approach

The basic idea of the asymptotic approach is to analyze the flow with high porosity, i.e., $n \to 1$, as a (regular) perturbation of the clear flow, i.e., $n = 1$. What follows is an asymptotic theory for $\epsilon \to 0$ with

$$\epsilon = 1 - n \tag{13}$$

It should be pointed out that with this approach it is not claimed that the physical situation described by the continuum approach actually exists for $K^* \to \infty$ (the boundary layer then may be smaller than an average pore size). It only claims that it is a rational approximation for finite (but large values) of K^*. This is comparable to the situation with the laminar boundary layer: It does not exist for arbitrarily large Gr numbers but nevertheless is a rational approximation for large values of Gr.

Based on the Ergun correlation, equation (3), the permeability for $\epsilon \to 0$ is

$$\tilde K^{-1} \equiv \frac{150(n-1)^2}{d^{*2}n^3}\frac{L^{*2}}{\mathrm{Gr}^{1/2}} = \frac{\epsilon^2}{(1-\epsilon)^3}\tilde d^{-2} \tag{14}$$

with an average particle diameter $\tilde d$ defined by

$$\tilde d = 150^{-1/2}\frac{d^*}{L^*}\mathrm{Gr}^{1/4} = O(1) \text{ with respect to } \epsilon \tag{15}$$

With the series expansions in $\epsilon = 1 - n$ (assuming $\tilde F$ is not linked to $\tilde K$ asymptotically) the momentum equation now reads

$$f''' + (3+d)ff'' - \left[2 + 2d + \underbrace{4\tilde F\tilde d^{-1}\left[\epsilon - \frac{1}{2}\epsilon^2 + O(\epsilon^3)\right]x}_{\mathrm{I}}\right]f'^2 \underbrace{-2\tilde d^{-2}(\epsilon^2 + O(\epsilon^3))x^{(1-d)/2}f'}_{\mathrm{II}} + x^{b-d}\Theta = 4x(f'\partial f'/\partial x - f''\partial f/\partial x) \tag{16}$$

For $\epsilon = 0$, equation (16), together with the energy equation (10), holds for a clear flow boundary layer. The influence of a solid matrix comes in through the perturbation parameter ϵ and can be described by a regular perturbation approach to the problem. Within the framework of the boundary layer theory the leading term with respect to the influence of porosity is the "Forchheimer term" I. It is of order $O(\epsilon)$, whereas the "Darcy term" II is of order $O(\epsilon^2)$. To include both terms in the subsequent asymptotic analysis, it will be carried out to the asymptotic order $O(\epsilon^2)$ with the asymptotic error being $O(\epsilon^3)$.

For $\epsilon \neq 0$ the flow is no longer self-similar because an explicit x dependence comes in through term I in equation (16). However, this x dependence is a higher order effect with respect to ϵ. The zero-order, or basic flow, is still the self-similar clear flow boundary layer. In this sense the flow may be called "quasi-self-similar," which will be accounted for in the subsequent expansions for the dependent variables, i.e., f and Θ. In these expansions the two parameters $\tilde F$ and $\tilde d$ can be separated so that the final asymptotic equations are left with the Prandtl number as the only explicit solution parameter, as with the clear flow.

The expansions for f and Θ, given by a general function $\varphi = f$, Θ, read

$$\varphi = \varphi_0 + \epsilon A_1\varphi_1 + \epsilon^2[A_{21}\varphi_{21} + A_{22}\varphi_{22} + A_{23}\varphi_{23}] + O(\epsilon^3) \tag{17}$$

with

$$A_1 = \frac{4\tilde F}{\tilde d}x, \quad A_{21} = \frac{2\tilde F}{\tilde d}x, \quad A_{22} = \frac{2}{\tilde d^2}x^{(1-d)/2}, \quad A_{23} = \frac{16\tilde F^2}{\tilde d^2}x^2 \tag{18}$$

In equation (17) all functions φ_i ($i = 0$, 1, 21, 22, 23) depend on the similarity variable η alone. Inserting f and Θ according to equation (17) into equations (16) and (10) and collecting terms of equal magnitude, i.e., $O(1)$, $O(\epsilon A_1)$, $O(\epsilon^2 A_{21})$, . . . results in a hierarchy of ordinary differential equation systems. The first two of them, for example, read

$$O(1){:}\quad f_0''' + (3+d)f_0f_0'' - (2+2d)f_0'^2 + x^{b-d}\Theta_0 = 0 \tag{19}$$

$$\mathrm{Pr}_\infty^{-1}\Theta_0'' + (3+d)f_0\Theta_0' - 4df_0'\Theta_0 = 0 \tag{20}$$

Table 2 Wall values for the flat plate; $T_w^*=\mathrm{const}$

Pr	f_0''	$-\theta_0'$	$-f_1''$	θ_1'	f_{21}''	$-\theta_{21}'$	$-f_{22}''$	θ_{22}'	f_{23}''	$-\theta_{23}'$
0.1	0.8592	0.2302	0.0503	0.0089	0.0503	0.0089	0.1765	0.0304	0.0046	0.0005
1.0	0.6422	0.5672	0.0183	0.0127	0.0183	0.0127	0.1051	0.0687	0.0011	0.0006
5.0	0.4818	0.9540	0.0070	0.0114	0.0070	0.0114	0.0683	0.1053	0.0003	0.0004
10.0	0.4192	1.1693	0.0044	0.0103	0.0044	0.0103	0.0569	0.1247	0.0002	0.0004
50.0	0.2953	1.8238	0.0015	0.0075	0.0015	0.0075	0.0376	0.1843	0.0001	0.0002
100.0	0.2517	2.1914	0.0009	0.0065	0.0009	0.0065	0.0318	0.2201	0.0000	0.0002

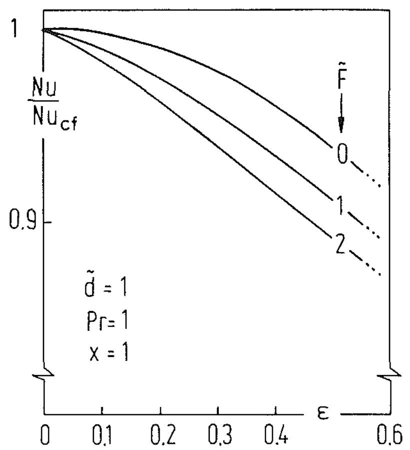

Fig. 1 Influence of $\tilde{F}$ on $\mathrm{Nu}/\mathrm{Nu}_{cf}$

$$O(\epsilon A_1):\quad D_{\mathrm{I}}(f_1,\,\Theta_1)+4(f_0''f_1-f_0'f_1')-f_0'^2=0 \tag{21}$$

$$D_{\mathrm{II}}(f_1,\,\Theta_1)+4(\Theta_0'f_1-f_0'\Theta_1)=0 \tag{22}$$

The differential operators D_{I} and D_{II} are

$$D_{\mathrm{I}}(f,\,\Theta)=f'''+(3+d)\,(f_0f''+f_0''f)-(4+4d)f_0'f'+x^{b-d}\Theta \tag{23}$$

$$D_{\mathrm{II}}(f,\,\Theta)=\mathrm{Pr}_\infty^{-1}\Theta''+(3+d)\,(f_0\Theta'+f\Theta_0')-4b\,(f_0'\Theta+f'\Theta_0) \tag{24}$$

The boundary conditions (11) hold for the zero-order equations for f_0 and Θ_0 with the consequence that all corresponding higher order boundary conditions are zero.

3 Results

From the numerical solutions only the results at the wall are of interest. In Table 2 as an example wall values of the flat plate for six different Prandtl numbers and the thermal boundary condition $T_w=\mathrm{const}$ are given. The skin friction coefficient $c_f=2\tau_w^*/(\rho_{fw}^*U_R^{*2})$ in dimensionless variables reads

$$c_f\mathrm{Gr}^{1/4}=2\sqrt{2}x^{(3d+1)/4}f_w'' \tag{25}$$

Together with the expression (17) for f the ratio of skin friction in a porous medium to that in a clear flow is ($cf \mathrel{\hat{=}}$ clear flow)

$$\frac{c_f}{c_{fcf}}=1+(1-n)A_1\frac{f_{1w}''}{f_{0w}''}+(1-n)^2\left[A_{21}\frac{f_{21w}''}{f_{0w}''}+A_{22}\frac{f_{22w}''}{f_{0w}''}+A_{23}\frac{f_{23w}''}{f_{0w}''}\right]+O[(1-n)^3] \tag{26}$$

Table 3 Comparison with results of Kaviany and Mittal (1987); $K^*=10^{-5}\mathrm{m}^2$, $\epsilon=0.1$

Nu/Nu$_{cf}$:		Kaviany Mittal	asymptotic only O(ϵ)		asymptotic O(ϵ) and O(ϵ^2)	
F	$\tilde{F}$			%		%
0.01	0.56	0.473	0.486	2.75	0.459	− 2.96
0.05	2.8	0.422	0.432	2.34	0.423	0.24
0.1	5.6	0.384	0.364	− 5.21	0.409	6.51
0.5	28	0.264	—	—	—	—

For the Nusselt number $\mathrm{Nu}=q_w^*L^*/\lambda^*\Delta T^*$ we likewise get the following correction formula ($T_w^*=\mathrm{const}$):

$$\frac{\mathrm{Nu}}{\mathrm{Nu}_{cf}}=\frac{q_w^*}{q_{wcf}^*}=1+(1-n)A_1\frac{\Theta_1'}{\Theta_0'}+(1-n)^2\left[A_{21}\frac{\Theta_{21}'}{\Theta_0'}+A_{22}\frac{\Theta_{22}'}{\Theta_0'}+A_{23}\frac{\Theta_{23}'}{\Theta_0'}\right]+O[(1-n)^3] \tag{27}$$

4 Discussion

The advantages of the asymptotic method compared to a purely numerical approach are:

1 The final results are more general; all parameters of the problem (except the Prandtl number) could be separated by introducing equation (17).

2 The influence of the various parameters can be analyzed in the final results.

As mentioned before it turned out that the "Forchheimer term" (I in equation (16)) is the leading term in the asymptotic analysis. Within the framework of boundary layer theory the constant F in the "Forchheimer term" must be of the asymptotic order $O(\mathrm{Gr}^{-1/4})$, see equation (8), which is equivalent to $\tilde{F}=O(1)$.

In Fig. 1 the influence of $\tilde{F}$ on the heat transfer result $\mathrm{Nu}/\mathrm{Nu}_{cf}$ is shown. For a specific situation [$x=\tilde{d}=\mathrm{Pr}=1$, $T_w^*=\mathrm{const}$ (equation (27))] three values of $\tilde{F}$ are shown ($\tilde{F}=0$, 1, and 2).

In the porous media literature there are only few examples that are documented detailed enough to allow for a direct comparison with our asymptotic results. One of these examples can be found from Kaviany and Mittal (1987). For a porosity of $n=0.9$ ($\epsilon=0.1$) they have listed heat transfer results (their Table 2) for several values of K^* and F representing some foams. For this special situation [$x=1$, $\tilde{d}=0.2084$, ($K^*=10^{-5}\mathrm{m}^2$, $\mathrm{Gr}=10^7$), $\mathrm{Pr}=0.7$, $T_w^*=\mathrm{const}$] equation (27) reads

$$\frac{\mathrm{Nu}}{\mathrm{Nu}_{cf}}=1\underbrace{-2.721F}_{O(\epsilon)}\underbrace{+0.1360F-0.0565+13.344F^2}_{O(\epsilon^2)} \tag{28}$$

In Table 3 the asymptotic results according to equation (28) are compared to those of Kaviany and Mittal (1987) with deviations given in percent. Only for $\tilde{F}=28$ were deviations unacceptably high. This case, which was called by Kaviany and Mittal "unrealistically high," obviously no longer meets the asymptotic requirement of being a quantity of $O(1)$.

References

Bear, J., 1972, *Dynamics of Fluids in Porous Media*, Elsevier, New York.

Cheng, P., 1978, "Heat Transfer in Geothermal Systems," *Adv. Heat Transfer*, Vol. 14, pp. 1-105.

Ergun, S., 1952, "Fluid Flow Through Packed Columns," *Chem. Eng. Progress*, pp. 89-94.

Herwig, H., Wickern, G., and Gersten, K., 1985, "Der Einfluss variabler Stoffwerte auf natürliche laminare Konvektionsströmungen," *Wärme- und Stoffübertragung*, Vol. 19, pp. 19-30.

Hong, J. T., Tien, C. L., and Kaviany, M., 1985, "Non-Darcian Effects on Vertical-Plate Natural Convection in Porous Media With High Porosities," *Int. J. Heat Mass Transfer*, Vol. 28, pp. 2149-2157.

Kaviany, M., and Mittal, M., 1987, "Natural Convection Heat Transfer From a Vertical Plate to High Permeability Porous Media: An Experiment and an Approximate Solution," *Int. J. Heat Mass Transfer*, Vol. 30, pp. 967-977.

On the Stability of Salt-Finger Convection in Superposed Fluid and Porous Layers

Falin Chen[1]

Nomenclature

a, a_m = wavenumber in fluid and porous layers

d, d_m = thickness of fluid and porous layers

$\hat{d}$ = depth ratio $= d/d_m$

D_f, D_m = mass diffusivity in fluid and porous layers

g = gravitational acceleration

K = permeability

Ra = $g\alpha(T_u-T_0)d^3/(\nu\lambda_f)$ = thermal Rayleigh number in the fluid layer

Ra_m = $g\alpha(T_0-T_l)d_mK/(\nu\lambda_m)$ = thermal Rayleigh number in the porous layer

Ra_s = $g\beta(S_u-S_0)d^3/(\nu D_f)$ = solute Rayleigh number in the fluid layer

Ra_{sm} = $g\beta(S_0-S_l)d_mK/(\nu D_m)$ = solute Rayleigh number in the porous layer

S = salinity

T = temperature

W = normalized dimensionless vertical velocity

α = $-(\partial\rho/\partial T)/\rho_0$

β = $(\partial\rho/\partial S)/\rho_0$

δ = $\sqrt{K}/d_m$ = Darcy number

ϵ_T = λ_f/λ_m = thermal diffusivity ratio

ϵ_s = D_f/D_m = solute diffusivity ratio

Λ = Beavers-Joseph constant

λ_f, λ_m = thermal diffusivities of fluid and porous layers

ν = kinematic viscosity

ρ = density of fluid

Subscripts

f, m = fluid and porous layers

l, u = lower and upper boundaries

0 = interface

Introduction

In the directional solidification of binary alloys, when the mold is cooled from below, the solid frozen region at the bottom is separated from the liquid region above by a mushy zone consisting of dendrites immersed in the melt. The dendritic mushy zone has been regarded as a porous layer with variable permeability in theoretical and computational investigations (Hills et al., 1983; Maples and Poirier, 1984). When the solidification is from below, and the lighter species is ejected from the solid, the concentration distribution is a stably stratifying influence, while the temperature distribution is destabilizing. Simultaneous occurrence of temperature and solute gradients through the melt and mushy zone may be conducive to the occurrence of salt-finger convection, which may in turn cause adverse effects such as channel segregation or freckles. These have been observed by Copley et al. (1970) and Sample and Hellawell (1984). In this work, we study the hydrodynamic stability problem of salt-finger convection in superposed fluid and porous layers by means of linear stability analysis.

Thermal convection, when the system is heated from below, in a fluid layer overlying a porous layer has been studied by several investigators. Sun (1973) was the first to consider the problem, and used a shooting method to solve the linear stability equations. He also performed experiments to verify his predictions. Nield (1977) included surface-tension effects at the deformable upper surface. He obtained asymptotic solutions for small wavenumbers for a constant-heat-flux boundary condition. Somerton and Catton (1982) included the Brinkman extension in the Darcy equation to consider the viscous effect in the porous layer. The importance of the geometric parameter depth ratio $\hat{d}$ (defined as the depth of the fluid layer divided by the depth of the porous layer) was first elucidated by Chen and Chen (1988). They found that for $\hat{d}\leq 0.12$, convection is observed in both the fluid and porous layers, and the wavelength is approximately the distance between the top and bottom boundaries; when $\hat{d}\geq 0.13$, the convection is confined to the fluid layer and the convective scale is the depth of the fluid layer. These results have been verified by experimental investigation (Chen and Chen, 1989).

Chen and Chen (1988) also extended the analysis to include salt-finger convection in the superposed fluid and porous layer by considering mass transfer in both layers. A fourth-order Runge-Kutta (Forsythe et al., 1977) shooting method is applied to solve the linear stability equations. It was noted by them that the shooting method fails when the differential equations become stiff (the coefficients of an equation differ by orders

---

[1] Institute of Applied Mechanics, National Taiwan University, Taipei, Taiwan 10764.

Contributed by the Heat Transfer Division for publication in the JOURNAL OF HEAT TRANSFER. Manuscript received by the Heat Transfer Division September 26, 1989; revision received February 21, 1990. Keywords: Double Diffusion Systems, Flow Instability, Porous Media.

$$\frac{\mathrm{Nu}}{\mathrm{Nu}_{cf}} = 1 - \underbrace{2.721F}_{O(\epsilon)} + \underbrace{0.1360F - 0.0565 + 13.344F^2}_{O(\epsilon^2)} \tag{28}$$

In Table 3 the asymptotic results according to equation (28) are compared to those of Kaviany and Mittal (1987) with deviations given in percent. Only for $\tilde{F}=28$ were deviations unacceptably high. This case, which was called by Kaviany and Mittal "unrealistically high," obviously no longer meets the asymptotic requirement of being a quantity of $O(1)$.

References

Bear, J., 1972, *Dynamics of Fluids in Porous Media*, Elsevier, New York.

Cheng, P., 1978, "Heat Transfer in Geothermal Systems," *Adv. Heat Transfer*, Vol. 14, pp. 1-105.

Ergun, S., 1952, "Fluid Flow Through Packed Columns," *Chem. Eng. Progress*, pp. 89-94.

Herwig, H., Wickern, G., and Gersten, K., 1985, "Der Einfluss variabler Stoffwerte auf natürliche laminare Konvektionsströmungen," *Wärme- und Stoffübertragung*, Vol. 19, pp. 19-30.

Hong, J. T., Tien, C. L., and Kaviany, M., 1985, "Non-Darcian Effects on Vertical-Plate Natural Convection in Porous Media With High Porosities," *Int. J. Heat Mass Transfer*, Vol. 28, pp. 2149-2157.

Kaviany, M., and Mittal, M., 1987, "Natural Convection Heat Transfer From a Vertical Plate to High Permeability Porous Media: An Experiment and an Approximate Solution," *Int. J. Heat Mass Transfer*, Vol. 30, pp. 967-977.

On the Stability of Salt-Finger Convection in Superposed Fluid and Porous Layers

Falin Chen[1]

Nomenclature

a, a_m = wavenumber in fluid and porous layers

d, d_m = thickness of fluid and porous layers

$\hat{d}$ = depth ratio $= d/d_m$

D_f, D_m = mass diffusivity in fluid and porous layers

g = gravitational acceleration

K = permeability

Ra = $g\alpha(T_u - T_0)d^3/(\nu\lambda_f)$ = thermal Rayleigh number in the fluid layer

Ra_m = $g\alpha(T_0 - T_l)d_m K/(\nu\lambda_m)$ = thermal Rayleigh number in the porous layer

Ra_s = $g\beta(S_u - S_0)d^3/(\nu D_f)$ = solute Rayleigh number in the fluid layer

Ra_{sm} = $g\beta(S_0 - S_l)d_m K/(\nu D_m)$ = solute Rayleigh number in the porous layer

S = salinity

T = temperature

W = normalized dimensionless vertical velocity

α = $-(\partial\rho/\partial T)/\rho_0$

β = $(\partial\rho/\partial S)/\rho_0$

δ = $\sqrt{K}/d_m$ = Darcy number

ϵ_T = λ_f/λ_m = thermal diffusivity ratio

ϵ_s = D_f/D_m = solute diffusivity ratio

Λ = Beavers–Joseph constant

λ_f, λ_m = thermal diffusivities of fluid and porous layers

ν = kinematic viscosity

ρ = density of fluid

Subscripts

f, m = fluid and porous layers

l, u = lower and upper boundaries

0 = interface

Introduction

In the directional solidification of binary alloys, when the mold is cooled from below, the solid frozen region at the bottom is separated from the liquid region above by a mushy zone consisting of dendrites immersed in the melt. The dendritic mushy zone has been regarded as a porous layer with variable permeability in theoretical and computational investigations (Hills et al., 1983; Maples and Poirier, 1984). When the solidification is from below, and the lighter species is ejected from the solid, the concentration distribution is a stably stratifying influence, while the temperature distribution is destabilizing. Simultaneous occurrence of temperature and solute gradients through the melt and mushy zone may be conducive to the occurrence of salt-finger convection, which may in turn cause adverse effects such as channel segregation or freckles. These have been observed by Copley et al. (1970) and Sample and Hellawell (1984). In this work, we study the hydrodynamic stability problem of salt-finger convection in superposed fluid and porous layers by means of linear stability analysis.

Thermal convection, when the system is heated from below, in a fluid layer overlying a porous layer has been studied by several investigators. Sun (1973) was the first to consider the problem, and used a shooting method to solve the linear stability equations. He also performed experiments to verify his predictions. Nield (1977) included surface-tension effects at the deformable upper surface. He obtained asymptotic solutions for small wavenumbers for a constant-heat-flux boundary condition. Somerton and Catton (1982) included the Brinkman extension in the Darcy equation to consider the viscous effect in the porous layer. The importance of the geometric parameter depth ratio $\hat{d}$ (defined as the depth of the fluid layer divided by the depth of the porous layer) was first elucidated by Chen and Chen (1988). They found that for $\hat{d} \leq 0.12$, convection is observed in both the fluid and porous layers, and the wavelength is approximately the distance between the top and bottom boundaries; when $\hat{d} \geq 0.13$, the convection is confined to the fluid layer and the convective scale is the depth of the fluid layer. These results have been verified by experimental investigation (Chen and Chen, 1989).

Chen and Chen (1988) also extended the analysis to include salt-finger convection in the superposed fluid and porous layer by considering mass transfer in both layers. A fourth-order Runge-Kutta (Forsythe et al., 1977) shooting method is applied to solve the linear stability equations. It was noted by them that the shooting method fails when the differential equations become stiff (the coefficients of an equation differ by orders

---

[1] Institute of Applied Mechanics, National Taiwan University, Taipei, Taiwan 10764.

Contributed by the Heat Transfer Division for publication in the JOURNAL OF HEAT TRANSFER. Manuscript received by the Heat Transfer Division September 26, 1989; revision received February 21, 1990. Keywords: Double Diffusion Systems, Flow Instability, Porous Media.

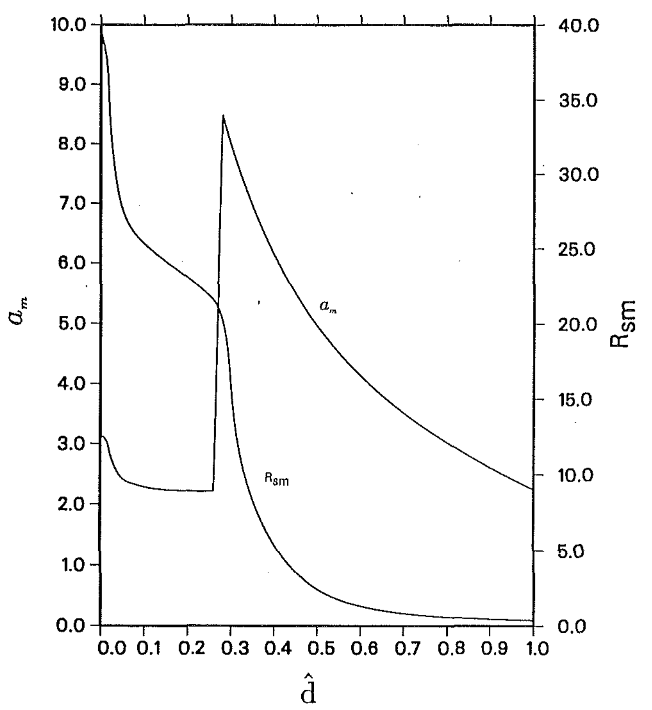

Fig. 1 Variation of critical Ra_{sm} and a_m with $\hat{d}$ for salt-finger convection at $Ra_m = 0.01$

of magnitude; see Antar, 1976). According to Forsythe et al. (1977), the shooting method works well for mildy stiff equations; however, no clear definition of "mildy stiff" was given.

In the salt-finger case, the stiffness problem may become severe when $\hat{d}$ and Ra_m, the thermal Rayleigh number of the porous layer, are large. As an example, for $\hat{d} = 1$ and $Ra_m = 50$, the thermal Rayleigh number Ra in the fluid layer is 1.13×10^7. If the other coefficients are of order one in magnitude, the coefficients in the momentum equation of the fluid layer, therefore, will differ by up to seven orders of magnitude or more. It turns out that the Runge–Kutta shooting code used by Chen and Chen (1988) fails to give accurate results in this case. As a result of discretization and rounding error, the determinant oscillates wildly. Thus, the bisection used by Chen and Chen (1988) cannot locate the zeros of the determinant.

In this study, we employ the code LSODE (Livermore Solver for Ordinary Differential Equations) to perform the salt-finger stability analysis. This solver treats the stiff case by using the Backward Differentiation Formula (BDF), and the nonstiff case by the Adams method. Because many stiff problems are nonstiff over certain ranges of the independent variable, integrating through the entire range using a stiff method is very expensive. The code LSODE automatically switches between an Adams method and BDF method whenever appropriate. The overhead of making the switching decisions is small (Petzold, 1983). In this problem, we find that stiffness occurs only in the fluid layer; the equations in the porous layer are nonstiff.

This improved computational approach allows us systematically to investigate the onset of finger convection in superposed fluid and porous layer configurations, previously considered by Chen and Chen (1988) for a limited range of parameters. Instead of restricting the analysis to $Ra_m = 50$ (as in Chen and Chen 1988), we examine the entire range $0.01 \le Ra_m \le 50$. A wide range of $\hat{d}$ is also considered. The critical solute Rayleigh number Ra_m and the corresponding wavenumber a_m serve to characterize the onset of convection. Finally, a comparison is made to the results obtained earlier by Chen and Chen (1988).

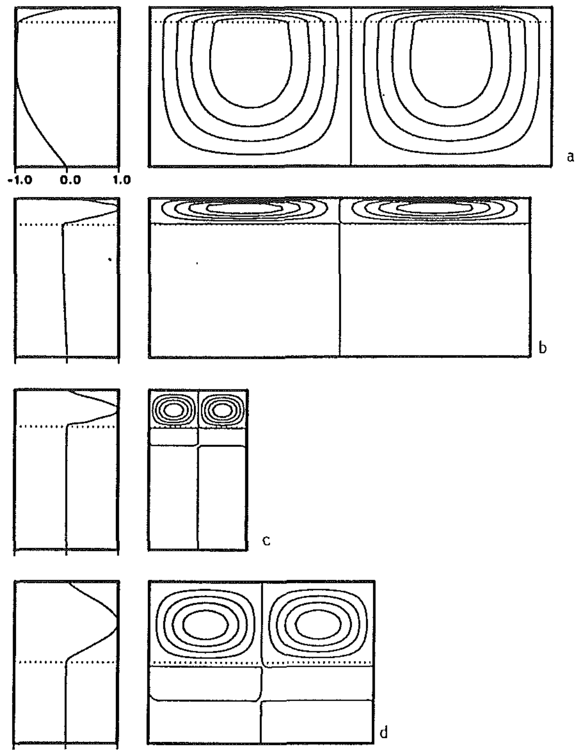

Fig. 2 Streamline pattern and W for salt-finger convection at $Ra_m = 0.01$: (*a*) $\hat{d} = 0.1$; (*b*) $\hat{d} = 0.2$; (*c*) $\hat{d} = 0.5$; (*d*) $\hat{d} = 1$

Table 1 The critical solute Rayleigh numbers Ra_{sm} and corresponding wavenumbers a_m of the case of $Ra_m = 0.01$ obtained by the present study and the critical thermal Rayleigh numbers $-Ra_m$ and wavenumbers of Chen and Chen (1988)

			$R_m = 0.01$ (present)			
$\hat{d}$	10^{-4}	0.1	0.2	0.3	0.5	1.0
R_{sm}	39.49	25.32	23.06	15.60	2.40	0.37
a_m	3.14	2.29	2.22	7.99	4.95	2.25
			Thermal Convection (Chen and Chen, 1988)			
$-R_m$	39.47	19.63	4.29	0.86	0.113	0.0071
a_m	3.14	2.17	14.07	9.48	5.71	2.86

Problem Formulation

The formulation and computational procedure used in this study are essentially the same as those in Chen and Chen (1988). We choose a Cartesian coordinate system with the origin at the interface between the porous and fluid layers and the z axis vertically upward. The governing equations in the fluid layer are conservation laws for mass, momentum, energy, and concentration. In the momentum equation, the Boussinesq approximation has been applied. In the porous layer, the same equations are applied except that the momentum equation is replaced by the Darcy equation. The boundary conditions at the top boundary are no-slip, constant temperature, and salinity. The temperature and salinity are held constant on the bottom, lower than at the top, and the vertical velocity vanishes. At the interface, we require continuity of temperature, salinity, heat flux, salt flux, vertical velocity, and normal stress. Due to use of the Darcy equation in the porous layer, continuity of the horizontal velocity and shear stress cannot be enforced. Instead, we will use the Beavers–Joseph condition (Beavers and Joseph, 1967), which relates the shear in the fluid to the

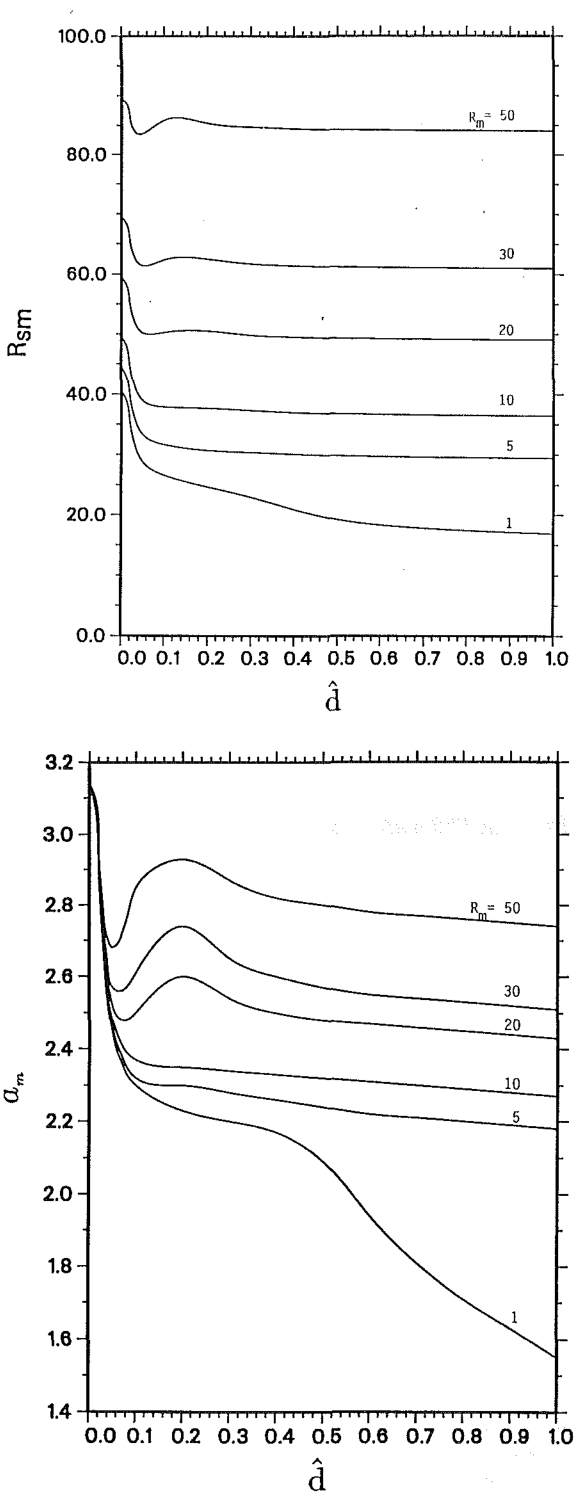

Fig. 3 (*a*) Variation of critical Ra_{sm} with $\hat{d}$ for various Ra_m; (*b*) variation of critical a_m with $\hat{d}$ for various Ra_m

slip velocity at the interface. In rendering the equations nondimensional, separate length scales are chosen for the fluid and porous layers so that both are of unit depth, as was done by Nield (1977). The selection of other characteristic scales to nondimensionalize the corresponding quantities is generally based on this procedure. The details are given by Chen and Chen (1988).

Several important nondimensional parameters appearing in the equations and boundary conditions are the depth ratio $\hat{d}$, thermal Rayleigh number in the fluid layer Ra, thermal Ray-

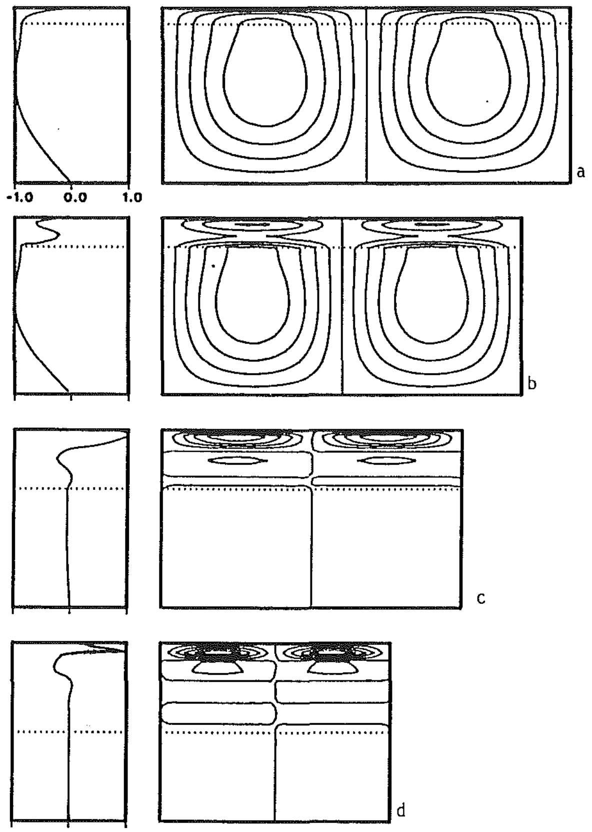

Fig. 4 Streamline pattern and W for salt-finger convection at $Ra_m = 1$: (*a*) $\hat{d} = 0.1$; (*b*) $\hat{d} = 0.2$; (*c*) $\hat{d} = 0.5$; (*d*) $\hat{d} = 1$

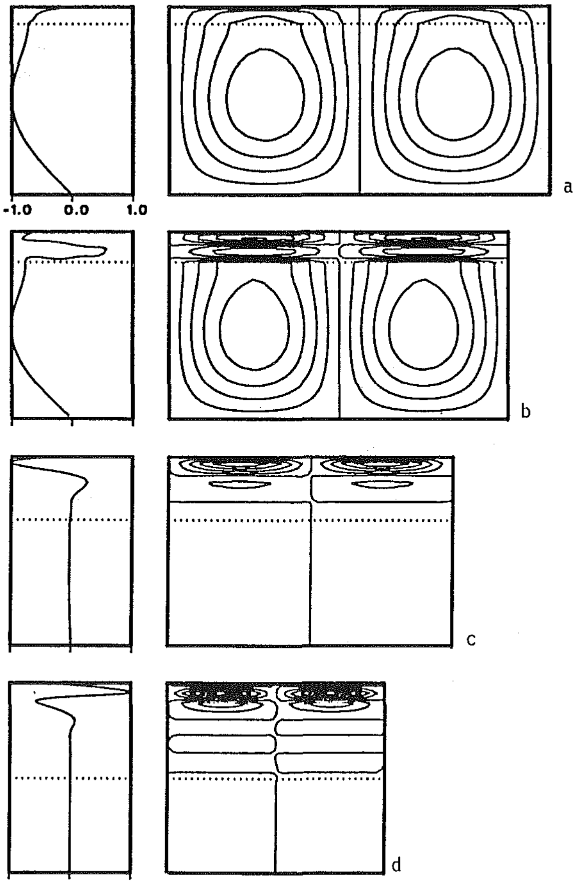

Fig. 5 Streamline pattern and W for salt-finger convection at $Ra_m = 20$: (*a*) $\hat{d} = 0.1$; (*b*) $\hat{d} = 0.2$; (*c*) $\hat{d} = 0.5$; (*d*) $\hat{d} = 1$

Table 2 The critical solute Rayleigh numbers Ra_{sm} and corresponding wavenumbers a_m of the case of $Ra_m = 50$ obtained by the present study (A) and Chen and Chen (1988) (B)

$\hat{d}$		10^{-4}	0.1	0.2	0.3	0.5	1.0
R_{sm}	A	89.48	85.95	85.39	84.75	84.30	84.06
	B	89.45	85.59	97.23	102.37	103.96	104.34
a_m	A	3.14	2.85	2.93	2.85	2.80	2.75
	B	3.14	2.80	3.62	3.96	4.32	4.45

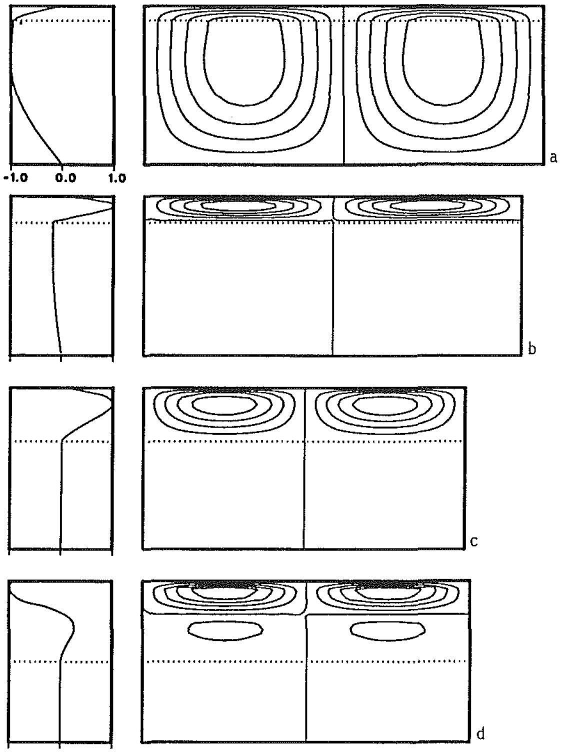

Fig. 6 Streamline pattern and W for salt-finger convection at $Ra_m = 50$: (a) $\hat{d} = 0.1$; (b) $\hat{d} = 0.2$; (c) $\hat{d} = 0.5$; (d) $\hat{d} = 1$

leigh number in the porous layer Ra_m, solute Rayleigh number in the fluid layer Ra_s, and solute Rayleigh number in the porous layer Ra_{sm}. The constants a and a_m are nodimensional horizontal wavenumbers. Since the dimensional horizontal wavenumbers must be the same for the fluid and porous layers if matching of solutions in the two layers is to be possible, one must have $a/d = a_m/d_m$, and hence, $\hat{d} = a/a_m$. The thermal Rayleigh number Ra of the fluid layer is proportional to its counterpart in the porous layer Ra_m; a similar relation exists for Ra_s and Ra_{sm}. The values of the parameters needed in the computation, such as the Darcy number δ, thermal diffusivity ratio ϵ_T, solute diffusivity ratio ϵ_S, and Beavers–Joseph constant Λ, are same as those used by Chen and Chen (1988).

We apply a normal mode expansion to the dependent variables, and assume that the principle of exchange of instabilities holds for the onset of the salt-finger convection in the superposed fluid and porous layers (i.e., that the critical disturbance grows monotonically in time). The resulting eigenvalue problem consists of an eighth-order ordinary differential equation (ODE) system in the fluid layer and a sixth-order ODE system in the porous layer, with 14 boundary conditions. One may regard Ra, Ra_m, $\hat{d}$, and all properties of the fluid and porous layers as given, and the eigenvalues Ra_{sm} (and Ra_s) to be sought for given a_m (and a). The eigenvalue problem is solved by using LSODE, as discussed above.

Results and Discussions

We first used our numerical method to consider the thermal convection case studied by Chen and Chen (1988). The results obtained are identical with those found earlier. This verifies that the BDF method is able to deal with the nonstiff case (e.g., the thermal convection case) as did the shooting method of Chen and Chen (1988); also, the correctness of the BDF computer code is thus confirmed. A parametric study of the salt-finger convection case with Ra_m ranging from 0.01 to 50 and $\hat{d}$ from 10^{-4} to 1 was then carried out. The critical Ra_{sm} and the corresponding a_m were sought. The eigenfunction of the vertical velocity W and the corresponding streamline pattern are presented to illustrate the onset of salt-finger convection in this two-layer system.

The first case examined is $Ra_m = 0.01$. Since Ra_m is small, the stability characteristics are expected to be similar to those of thermal convection. We calculate the critical Ra_{sm} and the corresponding wavenumber a_m for $\hat{d}$ varying from 10^{-4} to 1; the results are shown in Fig. 1. It is seen that a_m jumps from 2.3 to 8.7 when $\hat{d}$ increases from 0.26 to 0.27. Also, Ra_{sm} decreases with increasing $\hat{d}$ and an inflection point occurs in the range $0.26 < \hat{d} < 0.27$, where the sudden jump in a_m occurs. We also examine the eigenfunction w and the corresponding streamline patterns for various values of $\hat{d}$, as shown in Fig. 2. For $\hat{d} = 0.1$, convection is predicted to occur in both the fluid and porous layers. The convection cells are nearly square with the flow passing through both layers as a single cell. As $\hat{d}$ approaches the value at which the jump in a_m occurs, the flow is increasingly confined within the fluid layer. For larger $\hat{d}$, the wavelength of the convection cell is reduced to the scale of the fluid layer depth, so that the cells are nearly square again. To compare these results quantitatively with those for thermal convection, we present in Table 1 the critical Rayleigh numbers and corresponding wavenumbers for $Ra_m = 0.01$ and for the thermal convection case. A sevenfold jump in a_m occurs between $0.1 \leq \hat{d} \leq 0.2$ for the thermal convection case, and a fivefold jump between $0.2 \leq \hat{d} \leq 0.3$ for $Ra_m = 0.01$. Nonetheless, as a whole, it is evident that for small Ra_m, the stability characteristics of fingering convection are qualitatively similar to those for thermal convection.

We then increase Ra_m from 1 to 50; the critical Ra_{sm} and a_m depend on $\hat{d}$ as shown in Figs. 3(*a*) and (*b*), respectively. For $Ra_m = 1$, the critical values of Ra_{sm} and a_m decrease as $\hat{d}$ increases. For $0.3 < \hat{d} < 0.4$, the wavenumber varies more slowly with $\hat{d}$ than for other $\hat{d}$. Unlike the thermal convection case, no precipitous change of wavelength is found. For $Ra_m = 5$ or $Ra_m = 10$, the critical Ra_{sm} decreases sharply when $\hat{d}$ is small and remains almost constant as $\hat{d}$ increases. The critical wavenumber decreases as $\hat{d}$ increases. For $Ra_m = 20$, the critical a_m has a local minimum and a local maximum in the range $\hat{d} < 0.3$. In the same range of $\hat{d}$, the critical Ra_{sm} also develops a local minimum and local maximum. The local extrema of Ra_{sm} and a_m are enhanced at higher Ra_m, as shown for $Ra_m = 30$ and 50. To illustrate the difference between the present results and those of Chen and Chen (1988), we show the critical Ra_{sm} and a_m of the case for $Ra_m = 50$ in Table 2. It is found that the results are in good agreement when $\hat{d} \leq 0.1$ and differ considerably for $\hat{d} \geq 0.2$. It is known that the equations become more stiff for larger $\hat{d}$. The shooting method, accordingly, is shown to be inappropriate to deal with the larger $\hat{d}$.

In order to gain more physical insights into the instability, the z-dependence of the vertical velocity W and the corresponding streamline patterns are shown in Fig. 4 for four depth ratios with $Ra_m = 1$. One can see that convection occurs in both the fluid and porous layers for small $\hat{d}$ (0.1) and is confined to the fluid layer for $\hat{d} \geq 0.2$. For $\hat{d} = 1$, bicellular convection occurs in the fluid layer, with the upper cell being stronger. For higher Ra_m, say 20, Fig. 5 shows that the convection penetrates into the porous layer for $\hat{d} = 0.1$ and 0.2. For $\hat{d} = 0.5$, the convective motion in the porous layer virtually vanishes and bicellular convection occurs in the fluid layer. The upper cell remains stronger. For $\hat{d} = 1$ four convection cells occur in the fluid layer with the strongest one at the top. For $\mathrm{Ra}_m = 50$ and $\hat{d} = 0.2$, Fig. 6 shows that multicellular convection occurs in the fluid layer and convection still occurs in the porous layer. The number of convection cells in the fluid layer increases as $\hat{d}$ increases. For $\hat{d} = 1$, five cells exist in the fluid layer with the uppermost one the strongest.

From the flow patterns, one sees a correlation of high aspect ratio convection with increased stability of the two-layer system. It is interesting to re-examine Figs. 3-6 again with this perspective. For $\mathrm{Ra}_m = 1$, three depth ratio ranges can be discerned on the basis of the predicted convective flow. They are: $\hat{d} < 0.1$, in which a single high aspect ratio cell occurs; $0.2 < \hat{d} < 0.5$, in which a single high aspect ratio cell occurs in the fluid layer; and $\hat{d} = 1$, for which multiple high aspect ratio cells are predicted. For $\hat{d} < 0.1$, Figs. 3(*a*) and 3(*b*) show that the critical Ra_{sm} and a_m decrease as $\hat{d}$ increases. When multicellular convection occurs, the critical Ra_{sm} remains almost constant as $\hat{d}$ increases. By looking at the Ra_{sm} curve in Fig. 3(*a*) and the corresponding streamline patterns in Fig. 6, it is found that for $\hat{d} = 0.2$, when multiple cells appear in the fluid layer and convection in the porous layer still persists, the system is more stable than for $\hat{d} = 0.1$, when the single low aspect ratio cell dominates the system.

Acknowledgment

The author would like to thank Professors C. F. Chen and A. J. Pearlstein for their helpful discussions. The critical reading and correction of the manuscript by AJP is greatly appreciated.

References

Antar, B. N., 1976, "On the Solution of Two-Point Linear Differential Eigenvalue Problems," *J. Computational Physics*, Vol. 20, pp. 208-219.

Beavers, G. S., and Joseph, D. D., 1967, "Boundary Conditions at a Naturally Permeable Wall," *J. Fluid Mech.*, Vol. 30, pp. 197-207.

Chen, F., and Chen, C. F., 1988, "Onset of Finger Convection in a Horizontal Porous Layer Underlying a Fluid Layer," ASME JOURNAL OF HEAT TRANSFER, Vol. 110, pp. 403-409.

Chen, F., and Chen, C. F., 1989, "Experimental Investigation of Convective Stability in a Superposed Fluid and Porous Layer When Heated From Below," *J. Fluid Mech.*, Vol. 207, pp. 311-321.

Copley, S. M., Giamei, A. F., Johnson, S. M., and Hornbecker, M. F., 1970, "The Origin of Freckles in Unidirectionally Solidified Castings," *Metall. Trans.*, Vol. 1, pp. 2193-2204.

Forsythe, G. E., Malcolm, M. A., and Moler, C. B., 1977, *Computer Methods for Mathematical Computations*, Prentice-Hall, Englewood Cliffs, NJ.

Hills, R. N., Loper, D. E., and Roberts, P. H., 1983, "A Thermodynamically Consistent Model of Mushy Zone," *Q. J. Mech. Appl. Math.*, Vol. 36, pp. 505-539.

Maples, A. L., and Poirier, D. R., 1984, "Convection in the Two-Phase Zone of Solidifying Alloys," *Metall. Trans. B.*, Vol. 15, pp. 162-172.

Nield, D. A., 1977, "Onset of Convection in a Fluid Layer Overlying a Layer of a Porous Medium," *J. Fluid Mech.*, Vol. 81, pp. 513-522.

Petzold, L. R., 1983, "Automatic Selection of Methods for Solving Stiff and Nonstiff Systems of Ordinary Differential Equations," *SIAM J. Sci. Stat. Comput.*, Vol. 4, pp. 136-148.

Sample, A. K., and Hellawell, A., 1984, "The Mechanism of Formation and Prevention of Channel Segregation During Alloy Solidification," *Metall. Trans. A.*, Vol. 15, pp. 2163-2173.

Somerton, C. W., and Catton, I., 1982, "On the Thermal Instability of Superposed Porous and Fluid Layers," ASME JOURNAL OF HEAT TRANSFER, Vol. 104, pp. 160-165.

Sun, W. J., 1973, "Convective Instability in Superposed Porous and Fluid Layers," Ph.D. Dissertation, Univ. of Minnesota, Minneapolis, MN.

The Effect of Air on Condensation of Stratified Horizontal Concurrent Steam/Water Flow

T. S. Chan[1] and M. C. Yuen[1,2]

Nomenclature

A = constant in equation (11)
B = constant in equation (11)
b = channel width
C = constant in equation (11)
C_p = heat capacity
G = mass velocity
h_{fg} = latent heat of evaporation
h_g = specific enthalpy of steam
h = heat transfer coefficient
L = channel length
$\dot{m}$ = mass flow rate
Nu = Nusselt number
Pr = Prandtl number
q = condensation heat flux
Re = Reynolds number
T = temperature
t = thickness
x = axial coordinate
α = defined in equation (4)
β = defined in equation (5)
μ = viscosity
ρ = density
ω = air mass fraction

Subscripts

a = air
c = condensate
l = water
m = steam-air mixture
o = inlet
s = saturation
v = pure steam
w = wall

1 Introduction

Recently, there has been considerable interest in studies of direct-contact mode condensation on a fairly thick layer of subcooled liquid. Several experiments (Lim et al., 1984; Jensen and Yuen, 1982; Kim et al., 1985; Thomas, 1979) have been reported and a number of empirical correlations on heat transfer coefficients have been developed. These experiments concentrate on the correlation of pure vapor where the condensation rates are controlled by the rate at which the latent heat is transported from the interface to the bulk of the liquid. However, when noncondensible gas is present, the thermal resistance in the gas phase is no longer negligible.

It is well known that when a small amount of noncondensible gas is present in the vapor, the condensation rate can be appreciably reduced. This is true not only for cold wall conden-

---

[1] Department of Mechanical Engineering, Northwestern University, Evanston, IL 60208.

[2] Mem. ASME; presently on leave at the division of Engineering & Geosciences, DOE.

Contributed by the Heat Transfer Division for publication in the JOURNAL OF HEAT TRANSFER. Manuscript received by the Heat Transfer Division December 10, 1987; revision received February 22, 1990. Keywords: Condensation, Multiphase Flows, Stratified Flows.

the fluid and porous layers for small $\hat{d}$ (0.1) and is confined to the fluid layer for $\hat{d} \geq 0.2$. For $\hat{d}=1$, bicellular convection occurs in the fluid layer, with the upper cell being stronger. For higher Ra_m, say 20, Fig. 5 shows that the convection penetrates into the porous layer for $\hat{d}=0.1$ and 0.2. For $\hat{d}=0.5$, the convective motion in the porous layer virtually vanishes and bicellular convection occurs in the fluid layer. The upper cell remains stronger. For $\hat{d}=1$ four convection cells occur in the fluid layer with the strongest one at the top. For $\mathrm{Ra}_m=50$ and $\hat{d}=0.2$, Fig. 6 shows that multicellular convection occurs in the fluid layer and convection still occurs in the porous layer. The number of convection cells in the fluid layer increases as $\hat{d}$ increases. For $\hat{d}=1$, five cells exist in the fluid layer with the uppermost one the strongest.

From the flow patterns, one sees a correlation of high aspect ratio convection with increased stability of the two-layer system. It is interesting to re-examine Figs. 3-6 again with this perspective. For $\mathrm{Ra}_m=1$, three depth ratio ranges can be discerned on the basis of the predicted convective flow. They are: $\hat{d}<0.1$, in which a single high aspect ratio cell occurs; $0.2<\hat{d}<0.5$, in which a single high aspect ratio cell occurs in the fluid layer; and $\hat{d}=1$, for which multiple high aspect ratio cells are predicted. For $\hat{d}<0.1$, Figs. 3(*a*) and 3(*b*) show that the critical Ra_{sm} and a_m decrease as $\hat{d}$ increases. When multicellular convection occurs, the critical Ra_{sm} remains almost constant as $\hat{d}$ increases. By looking at the Ra_{sm} curve in Fig. 3(*a*) and the corresponding streamline patterns in Fig. 6, it is found that for $\hat{d}=0.2$, when multiple cells appear in the fluid layer and convection in the porous layer still persists, the system is more stable than for $\hat{d}=0.1$, when the single low aspect ratio cell dominates the system.

Acknowledgment

The author would like to thank Professors C. F. Chen and A. J. Pearlstein for their helpful discussions. The critical reading and correction of the manuscript by AJP is greatly appreciated.

References

Antar, B. N., 1976, "On the Solution of Two-Point Linear Differential Eigenvalue Problems," *J. Computational Physics*, Vol. 20, pp. 208-219.

Beavers, G. S., and Joseph, D. D., 1967, "Boundary Conditions at a Naturally Permeable Wall," *J. Fluid Mech.*, Vol. 30, pp. 197-207.

Chen, F., and Chen, C. F., 1988, "Onset of Finger Convection in a Horizontal Porous Layer Underlying a Fluid Layer," ASME JOURNAL OF HEAT TRANSFER, Vol. 110, pp. 403-409.

Chen, F., and Chen, C. F., 1989, "Experimental Investigation of Convective Stability in a Superposed Fluid and Porous Layer When Heated From Below," *J. Fluid Mech.*, Vol. 207, pp. 311-321.

Copley, S. M., Giamei, A. F., Johnson, S. M., and Hornbecker, M. F., 1970, "The Origin of Freckles in Unidirectionally Solidified Castings," *Metall. Trans.*, Vol. 1, pp. 2193-2204.

Forsythe, G. E., Malcolm, M. A., and Moler, C. B., 1977, *Computer Methods for Mathematical Computations*, Prentice-Hall, Englewood Cliffs, NJ.

Hills, R. N., Loper, D. E., and Roberts, P. H., 1983, "A Thermodynamically Consistent Model of Mushy Zone," *Q. J. Mech. Appl. Math.*, Vol. 36, pp. 505-539.

Maples, A. L., and Poirier, D. R., 1984, "Convection in the Two-Phase Zone of Solidifying Alloys," *Metall. Trans. B.*, Vol. 15, pp. 162-172.

Nield, D. A., 1977, "Onset of Convection in a Fluid Layer Overlying a Layer of a Porous Medium," *J. Fluid Mech.*, Vol. 81, pp. 513-522.

Petzold, L. R., 1983, "Automatic Selection of Methods for Solving Stiff and Nonstiff Systems of Ordinary Differential Equations," *SIAM J. Sci. Stat. Comput.*, Vol. 4, pp. 136-148.

Sample, A. K., and Hellawell, A., 1984, "The Mechanism of Formation and Prevention of Channel Segregation During Alloy Solidification," *Metall. Trans. A.*, Vol. 15, pp. 2163-2173.

Somerton, C. W., and Catton, I., 1982, "On the Thermal Instability of Superposed Porous and Fluid Layers," ASME JOURNAL OF HEAT TRANSFER, Vol. 104, pp. 160-165.

Sun, W. J., 1973, "Convective Instability in Superposed Porous and Fluid Layers," Ph.D. Dissertation, Univ. of Minnesota, Minneapolis, MN.

The Effect of Air on Condensation of Stratified Horizontal Concurrent Steam/Water Flow

T. S. Chan[1] **and M. C. Yuen**[1,2]

Nomenclature

A = constant in equation (11)
B = constant in equation (11)
b = channel width
C = constant in equation (11)
C_p = heat capacity
G = mass velocity
h_{fg} = latent heat of evaporation
h_g = specific enthalpy of steam
h = heat transfer coefficient
L = channel length
$\dot{m}$ = mass flow rate
Nu = Nusselt number
Pr = Prandtl number
q = condensation heat flux
Re = Reynolds number
T = temperature
t = thickness
x = axial coordinate
α = defined in equation (4)
β = defined in equation (5)
μ = viscosity
ρ = density
ω = air mass fraction

Subscripts

a = air
c = condensate
l = water
m = steam-air mixture
o = inlet
s = saturation
v = pure steam
w = wall

1 Introduction

Recently, there has been considerable interest in studies of direct-contact mode condensation on a fairly thick layer of subcooled liquid. Several experiments (Lim et al., 1984; Jensen and Yuen, 1982; Kim et al., 1985; Thomas, 1979) have been reported and a number of empirical correlations on heat transfer coefficients have been developed. These experiments concentrate on the correlation of pure vapor where the condensation rates are controlled by the rate at which the latent heat is transported from the interface to the bulk of the liquid. However, when noncondensible gas is present, the thermal resistance in the gas phase is no longer negligible.

It is well known that when a small amount of noncondensible gas is present in the vapor, the condensation rate can be appreciably reduced. This is true not only for cold wall conden-

---

[1] Department of Mechanical Engineering, Northwestern University, Evanston, IL 60208.

[2] Mem. ASME; presently on leave at the division of Engineering & Geosciences, DOE.

Contributed by the Heat Transfer Division for publication in the JOURNAL OF HEAT TRANSFER. Manuscript received by the Heat Transfer Division December 10, 1987; revision received February 22, 1990. Keywords: Condensation, Multiphase Flows, Stratified Flows.

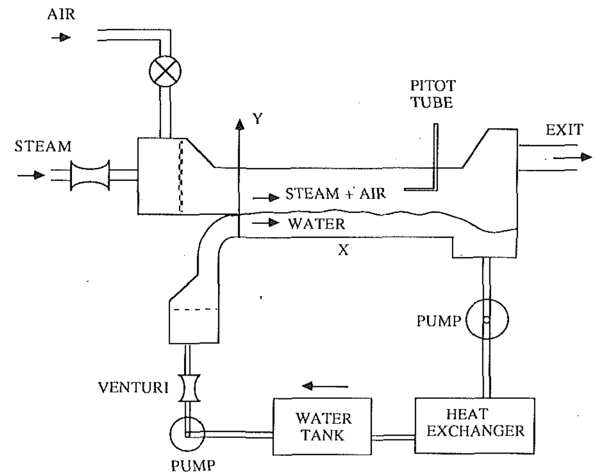

Fig. 1 Schematic of the experiment

sation but also for direct-contact condensation. For cold wall condensation, the solutions of Minkowycz and Sparrow (1966) and Sparrow et al. (1967) include all the important aspects of the problem except that of ripples at the interface. Taitel and Tamir (1969) were the first to consider theoretically the effects of noncondensible gas for direct-contact condensation on a sheet of coolant. Experimentally, Hasson et al. (1964) found that the average heat transfer coefficient could be reduced up to 50 percent when 1 percent of air was present during condensation of steam on a fan jet of water. Sadek (1968) studied the condensation of stagnant steam on a laminar water stream in a tray. He found that the overall heat transfer coefficient was reduced ten times for a concentration of 3 percent air. Jacobs and Nadig (1987) studied the effect of noncondensible gas on condensation on jets and sheets. Other related works can be found in a recent review by Jacobs (1988) on direct-contact heat transfer. However, the authors know of no previous study that considers the effect of noncondensible gas on direct-contact condensation on a fairly thick concurrent turbulent flowing stream.

The present note reports a continuation of a systematic experimental study on direct-contact condensation of concurrent steam/water flow. Data for pure steam condensation have been published by Lim et al. (1984). New data including the noncondensible gas effect are given here. Previous correlations are also extended to include the noncondensible gas effect.

2 Experiment

The experimental setup including the data acquisition system has been described by Lim et al. (1984). The data were shown to repeat to within ±3 percent of each other. The apparatus was modified by the addition of an air line to the steam inlet plenum. The air was supplied from a tank of compressed air and the flow rate was measured by a rotameter. A schematic of the experimental setup is shown in Fig. 1. Local steam–air mixture velocity profiles were obtained by traversing the pitot tubes from the water–steam interface to the top of the channel. The local steam–air mixture flow rate was obtained at each station by integrating the velocity profile at that station. In calculating the mass flow rate, average local air concentration was used. Detailed calculation shows that the effect of nonuniform (more air concentrates at the interface) air distribution is unimportant in deducing mass flow rate because the nonuniformity occurs only in the boundary layer. Measurements were performed by varying the inlet air mass fraction from 0 to 3.4 percent for different steam and water inlet flow rates. The flow regime is concentrated on the condition where both phases are turbulent, and the interface appears to have a pebblelike structure, which corresponds to the regime of wavy interface as reported by Lim et al. (1984).

Table 1 Data matrix; $T_l(0) = 25°C$

$\dot m_v(0)$ kg/s	0.065	0.065	0.09	0.09	0.09	0.13	0.13	0.16
$\dot m_l(0)$ kg/s	1.0	1.36	0.7	1.0	1.36	0.7	1.0	1.0
Inlet air mass fraction %	0.02	0.02	0.02	0.02	0.02	0.02	0.02	0.02
	0.15	0.15	0.15	0.15	0.15	0.13	0.15	0.14
	0.55	0.58	0.55	0.57	0.55	0.36	0.55	0.57
	1.5	1.4	1.5	1.4	1.5	1.6	1.5	1.36
	3.3	3.4	3.0	3.3	3.3	☒	☒	☒

When air is present, thermal resistance on the steam–air mixture is no longer negligible. We shall define the local heat transfer coefficient as we did for the case of pure steam as

$$h = q/(T_s - T_l) \tag{1}$$

where q is the condensation heat flux, T_s is the saturation steam temperature, and T_l is the bulk water temperature, which is a function of distance from the entrance.

The value q can be obtained from the condensation data as

$$q = \frac{\beta}{b}\frac{d\dot m_c}{dx} \tag{2}$$

and T_l is obtained from energy balance

$$T_l(x) = [h_g - \alpha \dot m_l(0)/\dot m_l(x)]/C_{p,l} \tag{3}$$

where $\dot m_l$ is the liquid mass flow rate, $\dot m_c$ is the condensate flow rate, h_g is the steam enthalpy, b is the width of channel, and

$$\alpha = h_g - C_{p,l}T_l(0) \tag{4}$$

$$\beta = h_{fg} + C_{p,v}(T_m - T_s) \tag{5}$$

The average heat transfer coefficient can then be shown to be

$$\bar h = \frac{1}{x}\int_0^x h\,dx = \frac{C_{p,l}}{bx}\left[\dot m_l(0) - \dot m_l(x) - \dot m_l(0)\frac{\alpha}{\beta}\ln\left(\frac{\alpha \dot m_l(0) - \beta \dot m_l(x)}{C_{p,l}\dot m_l(0)(T_s - T_l(0))}\right)\right] \tag{6}$$

The following definitions are used in determining the average Reynolds number. The average steam–air mass velocity $\bar G_m$ is

$$\bar G_m = [G_m(0) + G_m(x)]/2 = \left[\frac{\dot m_m(0)}{t - t_l(0)} + \frac{\dot m_m(x)}{t - t_l(x)}\right]\Big/ 2b \tag{7}$$

where t is the channel height and t_l is the liquid layer thickness. Thus, the average steam–air Reynolds number is

$$\overline{\mathrm{Re}}_m = x\bar G_m/\mu_m \tag{8}$$

The average air mass fraction is defined as

$$\bar\omega(x) = [\omega(0) + \omega(x)]/2 \tag{9}$$

where

$$\omega(x) = \dot m_a/\dot m_m(x) \tag{10}$$

3 Results

A total of 60 experiments have been performed by varying the inlet steam and water flow rate as well as the air mass fraction as shown in Table 1. The steam flow rates varied from

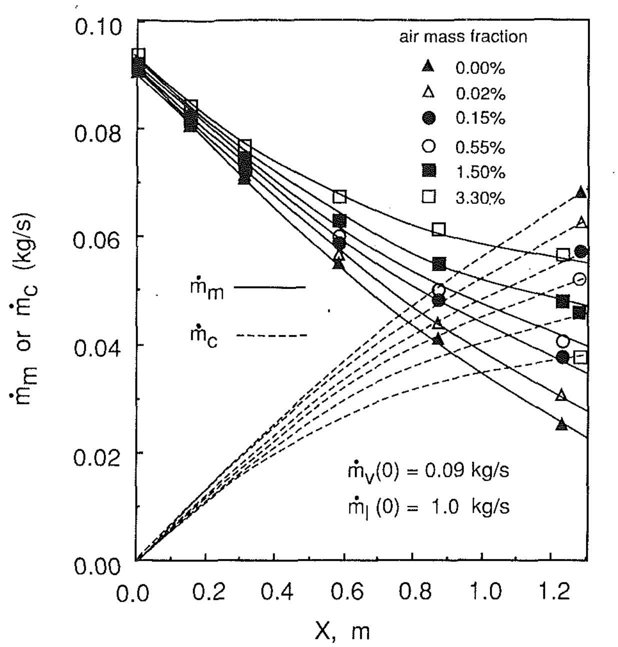

Fig. 2 Axial steam-air mixture and condensation rate profiles as a function of inlet air mass fraction

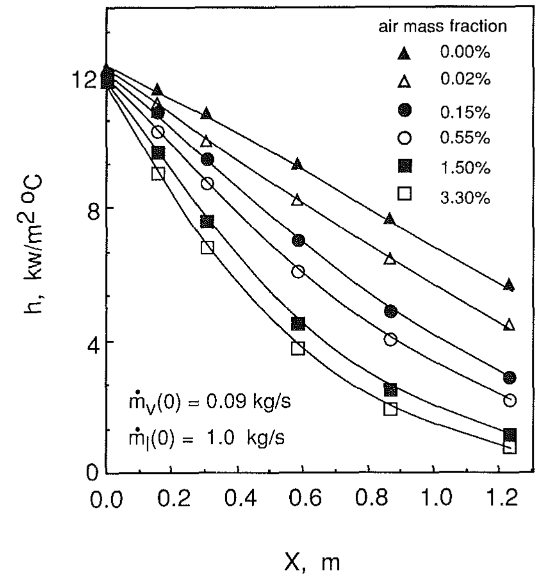

Fig. 3 Local heat transfer coefficient profiles as a function of inlet air mass fraction (corresponding to data in Fig. 2)

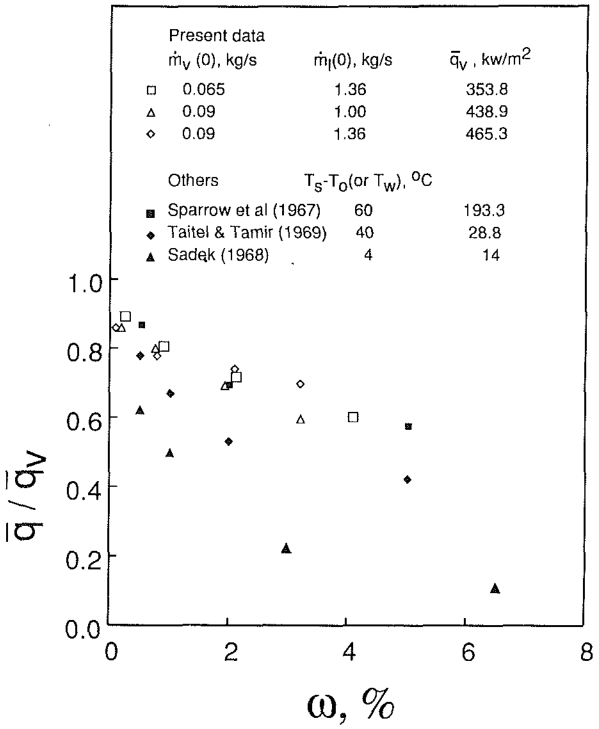

Fig. 4 Comparison of the average heat flux ratio with theories and other data

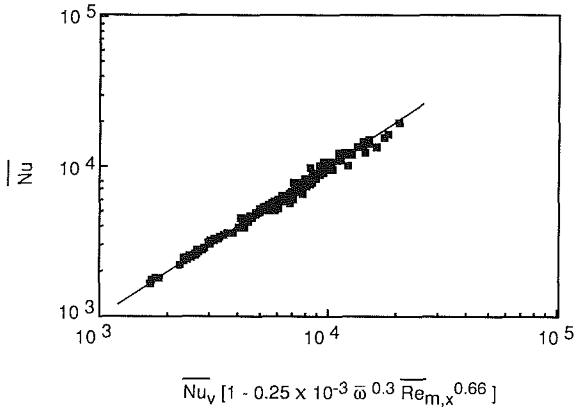

Fig. 5 Correlation of average Nusselt number ratio as a function of steam-air Reynolds number and air mass fraction (equation (13))

0.065 kg/s to 0.16 kg/s and the water flow rate varied from 0.7 kg/s to 1.36 kg/s. The inlet air mass fraction varied from 0 to 3.4 percent. The inlet water temperature was at 25°C and the steam temperature varied from 105°C to 120°C. The effect of small superheat in this case is insignificant because the latent heat of vaporization is large. It was found that the mixture temperature remained constant in the test channel.

Typical data of steam-air mixture flow rate with different inlet air mass fraction are shown in Fig. 2. For the same steam and liquid inlet flow rate, the figure shows that the condensation rate decreases as the inlet air mass fraction increases. As steam condenses, the air concentration increases. Thus in the downstream region, the accumulated air layer at the interface significantly reduces the condensation rate. This effect is especially pronounced for high inlet air concentration.

The local heat transfer coefficient is proportional to the slope of the steam condensate curve as shown in Fig. 2. In order to obtain consistent results, it was decided to best fit the steam-air mixture flow rate curves with the following equation:

$$\dot m_m(x) = Ae^{-Bx} + C \qquad (11)$$

where A, B, and C are constants to be determined. Figure 3 shows the calculated local heat transfer coefficients from the data of Fig. 2. The repeatability of h using the above method of interpretation of data is within ±5 percent.

An attempt is made to compare the present data with others. The comparison as shown in Fig. 4 includes the calculation of Sparrow et al. (1967) of laminar convective condensation heat flux on a flat plate and the calculation and experimental data of condensation heat flux of stagnant steam and air of Taitel and Tamir (1969) and Sadek (1968). Since in the above work, the results are expressed in term of heat flux rather than heat transfer coefficient, the comparison will therefore be in terms of the heat flux ratio $\bar q / \bar q_v$ where

$$\bar q = \frac{1}{L} \int_0^L q\,dx$$

and $\overline{q}_v$ is the average heat flux for pure steam condensation.

Figure 4 shows that the heat flux ratio decreases with increases of air mass fraction as expected. The effect of air is more pronounced for stagnant steam condensation. This is due to the fact that for stagnant conditions, the noncondensible gas tends to accumulate at the interface more than the convective case. The heat flux ratio as a function of air mass fraction is about the same for the calculation of Sparrow et al. (1967) and the present data. However, the absolute values of $\overline{q}$ for the present data are much higher. Since the calculation is for laminar flow past a flat plate and the present data are for turbulent flow, the agreement seems surprising at first glance. A plausible explanation is that in the calculation of Sparrow et al. (1967) the free-stream velocity is constant, whereas in the present case of channel flow, the average velocity is decreasing due to condensation. Thus the effect of turbulent mixing, which should decrease the effect of noncondensible gas, is counterbalanced by the decreasing effect of convection by reducing free-stream velocity in the channel.

A correlation for the average Nusselt number was obtained. The average Nusselt number is defined as

$$\overline{\mathrm{Nu}} = \bar{h}x/\bar{k}_l \tag{12}$$

where $\bar{k}_l = [\bar{k}_l(0) + \bar{k}_l(x)]/2$. The following correlation was obtained:

$$\frac{\overline{\mathrm{Nu}}}{\overline{\mathrm{Nu}}_v} = [1 - 0.25 \times 10^{-3}\overline{\omega}^{0.3}\overline{\mathrm{Re}}_{m,x}^{0.66}] \tag{13}$$

where $\overline{\mathrm{Nu}}_v$ is the average Nusselt number for pure steam condensation taken from Lim et al. (1984). In equation (13), the ratio of the Nusselt number is almost identical to $\bar{h}/\bar{h}_v$ because the changes in $\bar{k}_l$ with and without air are at most 6 percent for the present study. Equation (13) shows that the ratio of Nusselt number not only decreases with average air concentration but also with distance downstream as exemplified by the steam-air Reynolds number. This dependence on steam-air Reynolds number is a result of the decrease of velocity downstream by condensation. The result of the correlation is shown in Fig. 5, where all the data fall within ±20 percent of equation (13).

4 Conclusion

Condensation of atmospheric steam with noncondensible gas (air) on subcooled water flowing concurrently in a horizontal channel was measured and heat transfer coefficients were deduced. The average Nusselt number ratio were correlated with the average steam-air Reynolds number and air concentration. It was found that for high condensing flow, the effect of noncondensible gas is significant. A reduction in heat transfer rate was found to be as high as 40 percent.

Acknowledgments

This research was partially supported by the National Science Foundation.

References

Hasson, D., Luss, D., and Navon, V., 1964, "An Experimental Study of Steam Condensing on a Laminar Water Street," *Int. J. Heat Mass Transfer*, Vol. 7, pp. 983-1001.

Jacobs, H. R., and Nadig, R., 1987, "Condensation on Coolant Jets and Sheets Including the Effects of Noncondensible Gases," ASME JOURNAL OF HEAT TRANSFER, Vol. 109, pp. 1013-1020.

Jacobs, H. R., 1988, "Direct-Contact Heat Transfer for Process Technologies," ASME JOURNAL OF HEAT TRANSFER, Vol. 110, pp. 1259-1270.

Jensen, R. J., and Yuen, M. C., 1982, "Local Heat and Mass Transfer Correlation in Horizontal Stratified Concurrent Flow," *Proceedings, 7th International Heat Transfer Conference*, U. Grigull et al., eds., Hemisphere Publ. Corp., Washington, DC, Vol. 5, Cs-16.

Kim, H. J., Lee, S. C., and Bankoff, S. G., 1985, "Heat Transfer and Interfacial Drag in Countercurrent Steam-Water Stratified Flow," *Int. J. Multiphase Flow*, Vol. 11, No. 5, pp. 593-606.

Lim, I. S., Tankin, R. S., and Yuen, M. C., 1984, "Condensation Measurement of Horizontal Concurrent Steam/Water Flow," ASME JOURNAL OF HEAT TRANSFER, Vol. 106, pp. 425-432.

Minkowycz, W. J., and Sparrow, E. M., 1966, "Condensation Heat Transfer in the Presence of Noncondensible, Interfacial Resistance, Superheating, Variable Properties, and Diffusion," *Int. J. Heat Mass Transfer*, Vol. 9, pp. 1125-1144.

Sadek, S. E., 1968, "Condensation of Steam in the Presence of Air," *I/EC Fundamentals 7*, pp. 321-324.

Sparrow, E. M., Minkowycz, W. J., and Saddy, M., 1967, "Forced Convection Condensation in the Presence of Noncondensibles and Interfacial Resistance," *Int. J. Heat Mass Transfer*, Vol. 10, pp. 1829-1845.

Taitel, Y., and Tamir, A., 1969, "Condensation in the Presence of a Noncondensible Gas in Direct Contact," *Int. J. Heat Mass Transfer*, Vol. 12, pp. 1157-1169.

Thomas, R. M., 1979, "Condensation of Steam on Water in Turbulent Motion," *Int. J. Multiphase Flow*, Vol. 5, pp. 1-15.

A Theoretical Study of Induction Electrohydrodynamic Pumping in Outer Space

J. Seyed-Yagoobi[1]

Nomenclature

a = pipe radius, m

E = electric field intensity, V/m

g = gravitational acceleration = 9.81 m/s^2

P = pressure, N/m^2

r, z = cylindrical coordinates

u, w = dimensional velocities in r and z directions, m/s

ϵ = electrical permittivity, F/m

μ = viscosity, kg/m-s

ρ = density, kg/m^3

$\langle \tau_e \rangle$ = time-averaged electrical shear stress, N/m^2

Subscripts and Superscripts

bo = bulk mean value at entrance condition

op = zero to peak value

$*$ = nondimensional value

Introduction

The challenge for designers of a space station is to meet requirements of weight, reliability, power, and maintainability. Several new technologies must be developed to insure the success of the space station. Electrohydrodynamic (EHD) pumping may have an impact on the design of novel pumping devices for space stations or other space-related operations.

The principal advantage of EHD pumping is that it is nonmechanical; therefore, it has neither moving mechanical parts nor the need for external pressure for operation. Typical applications of EHD pumping include cooling of underground cables (Crowley and Chato, 1983), transformers (Seyed-Yagoobi et al., 1989a, 1989b), and similar electrical equipment. An EHD pump uses electric fields acting on electric charges

---

[1] Assistant Professor, Department of Mechanical Engineering, Texas A&M University, College Station, TX 77843.

Contributed by the Heat Transfer Division and presented at the ASME Winter Annual Meeting, Chicago, Illinois, November 28–December 2, 1988. Manuscript received by the Heat Transfer Division March 13, 1989; revision received November 22, 1989. Keywords: Augmentation and Enhancement, Heat Exchangers, Space Power Systems.

and $\overline{q}_v$ is the average heat flux for pure steam condensation.

Figure 4 shows that the heat flux ratio decreases with increases of air mass fraction as expected. The effect of air is more pronounced for stagnant steam condensation. This is due to the fact that for stagnant conditions, the noncondensible gas tends to accumulate at the interface more than the convective case. The heat flux ratio as a function of air mass fraction is about the same for the calculation of Sparrow et al. (1967) and the present data. However, the absolute values of $\overline{q}$ for the present data are much higher. Since the calculation is for laminar flow past a flat plate and the present data are for turbulent flow, the agreement seems surprising at first glance. A plausible explanation is that in the calculation of Sparrow et al. (1967) the free-stream velocity is constant, whereas in the present case of channel flow, the average velocity is decreasing due to condensation. Thus the effect of turbulent mixing, which should decrease the effect of noncondensible gas, is counterbalanced by the decreasing effect of convection by reducing free-stream velocity in the channel.

A correlation for the average Nusselt number was obtained. The average Nusselt number is defined as

$$\overline{\mathrm{Nu}} = \overline{h}x/\overline{k}_l \qquad (12)$$

where $\overline{k}_l = [\overline{k}_l(0) + \overline{k}_l(x)]/2$. The following correlation was obtained:

$$\frac{\overline{\mathrm{Nu}}}{\overline{\mathrm{Nu}}_v} = [1 - 0.25\times10^{-3}\overline{\omega}^{0.3}\overline{\mathrm{Re}}_{m,x}^{0.66}] \qquad (13)$$

where $\overline{\mathrm{Nu}}_v$ is the average Nusselt number for pure steam condensation taken from Lim et al. (1984). In equation (13), the ratio of the Nusselt number is almost identical to $\overline{h}/\overline{h}_v$ because the changes in $\overline{k}_l$ with and without air are at most 6 percent for the present study. Equation (13) shows that the ratio of Nusselt number not only decreases with average air concentration but also with distance downstream as exemplified by the steam-air Reynolds number. This dependence on steam-air Reynolds number is a result of the decrease of velocity downstream by condensation. The result of the correlation is shown in Fig. 5, where all the data fall within ±20 percent of equation (13).

4 Conclusion

Condensation of atmospheric steam with noncondensible gas (air) on subcooled water flowing concurrently in a horizontal channel was measured and heat transfer coefficients were deduced. The average Nusselt number ratio were correlated with the average steam-air Reynolds number and air concentration. It was found that for high condensing flow, the effect of noncondensible gas is significant. A reduction in heat transfer rate was found to be as high as 40 percent.

Acknowledgments

This research was partially supported by the National Science Foundation.

References

Hasson, D., Luss, D., and Navon, V., 1964, "An Experimental Study of Steam Condensing on a Laminar Water Street," *Int. J. Heat Mass Transfer*, Vol. 7, pp. 983-1001.

Jacobs, H. R., and Nadig, R., 1987, "Condensation on Coolant Jets and Sheets Including the Effects of Noncondensible Gases," ASME JOURNAL OF HEAT TRANSFER, Vol. 109, pp. 1013-1020.

Jacobs, H. R., 1988, "Direct-Contact Heat Transfer for Process Technologies," ASME JOURNAL OF HEAT TRANSFER, Vol. 110, pp. 1259-1270.

Jensen, R. J., and Yuen, M. C., 1982, "Local Heat and Mass Transfer Correlation in Horizontal Stratified Concurrent Flow," *Proceedings, 7th International Heat Transfer Conference*, U. Grigull et al., eds., Hemisphere Publ. Corp., Washington, DC, Vol. 5, Cs-16.

Kim, H. J., Lee, S. C., and Bankoff, S. G., 1985, "Heat Transfer and Interfacial Drag in Countercurrent Steam-Water Stratified Flow," *Int. J. Multiphase Flow*, Vol. 11, No. 5, pp. 593-606.

Lim, I. S., Tankin, R. S., and Yuen, M. C., 1984, "Condensation Measurement of Horizontal Concurrent Steam/Water Flow," ASME JOURNAL OF HEAT TRANSFER, Vol. 106, pp. 425-432.

Minkowycz, W. J., and Sparrow, E. M., 1966, "Condensation Heat Transfer in the Presence of Noncondensible, Interfacial Resistance, Superheating, Variable Properties, and Diffusion," *Int. J. Heat Mass Transfer*, Vol. 9, pp. 1125-1144.

Sadek, S. E., 1968, "Condensation of Steam in the Presence of Air," *I/EC Fundamentals 7*, pp. 321-324.

Sparrow, E. M., Minkowycz, W. J., and Saddy, M., 1967, "Forced Convection Condensation in the Presence of Noncondensibles and Interfacial Resistance," *Int. J. Heat Mass Transfer*, Vol. 10, pp. 1829-1845.

Taitel, Y., and Tamir, A., 1969, "Condensation in the Presence of a Noncondensible Gas in Direct Contact," *Int. J. Heat Mass Transfer*, Vol. 12, pp. 1157-1169.

Thomas, R. M., 1979, "Condensation of Steam on Water in Turbulent Motion," *Int. J. Multiphase Flow*, Vol. 5, pp. 1-15.

A Theoretical Study of Induction Electrohydrodynamic Pumping in Outer Space

J. Seyed-Yagoobi[1]

Nomenclature

a = pipe radius, m

E = electric field intensity, V/m

g = gravitational acceleration = 9.81 m/s^2

P = pressure, N/m^2

r, z = cylindrical coordinates

u, w = dimensional velocities in r and z directions, m/s

ϵ = electrical permittivity, F/m

μ = viscosity, kg/m-s

ρ = density, kg/m^3

$\langle \tau_e \rangle$ = time-averaged electrical shear stress, N/m^2

Subscripts and Superscripts

bo = bulk mean value at entrance condition

op = zero to peak value

$*$ = nondimensional value

Introduction

The challenge for designers of a space station is to meet requirements of weight, reliability, power, and maintainability. Several new technologies must be developed to insure the success of the space station. Electrohydrodynamic (EHD) pumping may have an impact on the design of novel pumping devices for space stations or other space-related operations.

The principal advantage of EHD pumping is that it is nonmechanical; therefore, it has neither moving mechanical parts nor the need for external pressure for operation. Typical applications of EHD pumping include cooling of underground cables (Crowley and Chato, 1983), transformers (Seyed-Yagoobi et al., 1989a, 1989b), and similar electrical equipment.

An EHD pump uses electric fields acting on electric charges

---

[1] Assistant Professor, Department of Mechanical Engineering, Texas A&M University, College Station, TX 77843.

Contributed by the Heat Transfer Division and presented at the ASME Winter Annual Meeting, Chicago, Illinois, November 28-December 2, 1988. Manuscript received by the Heat Transfer Division March 13, 1989; revision received November 22, 1989. Keywords: Augmentation and Enhancement, Heat Exchangers, Space Power Systems.

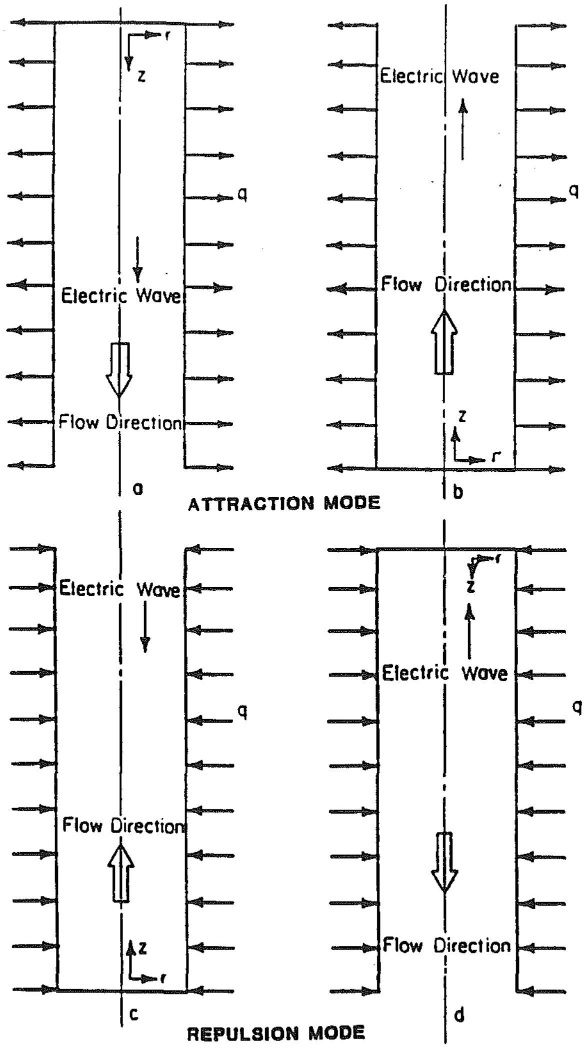

Fig. 1 The EHD pump

Table 1 Reference operating characteristics

Heat Flux	$q = \pm 100$ W/m^2
Temperature at the Center of the Pipe at the Entrance	$T_c = 60$°C
Peak Electric Potential at the Wall	$\phi_{e,\bar{o}p} = 10^4$ V
Frequency	$f = 5$ Hz
Wavelength	$\lambda = 0.04$ m
External Pressure Drop or Gain Per Unit Length of the Pump	$dP/dz = 0$ Pa/m
Pipe Radius	$a = 0.01$ m

embedded in a fluid to move that fluid. One way of setting up the free charges is induction charging, based on establishing an electrical conductivity gradient perpendicular to the desired direction of fluid motion. This gradient can be established in the presence of a temperature gradient.

There are two basic kinds of induction EHD pump: attraction (forward) and repulsion (backward) pumps. In the attraction pump, the pipe is cooled at the wall, giving a negative electric conductivity gradient. In the repulsion pump, the pipe is heated at the wall, causing a positive electric conductivity gradient. In the attraction pump, the fluid is pumped in the same direction as the traveling electric wave. In this mode, the fluid velocity is limited by the speed of the moving electric field (synchronous speed), which depends on frequency and on the spacing of the electrodes (wavelength) along the channel.

Table 2 Properties of pure Sun #4 transformer oil

Conductivity	$k = 0.126$ W/m°C
Density	$\rho = 906.70 - 0.63571T$ Kg/m^3
Specific Heat	$C_p = 1587.3 + 3.3186T$ J/kg°C
Kinematic Viscosity	$\nu = (4.7681 - 0.1836T + 2.7038 \times 10^{-3} T^2 - 1.3750 \times 10^{-5} T^3) 10^{-5}$ m^2/s
Permittivity	$\varepsilon = 2.2135 \times 10^{-11}$ F/m
Electric Conductivity	$\sigma = 1.05 \times 10^{-3} \exp(-5553/T_k)$ S/m

Note: T is in °C and T_k is in °K.

This limit exists regardless of the magnitude of the applied voltage, so that the EHD attraction pump cannot be made to operate faster merely by increasing the voltage. Unlike the attraction pump, a repulsion pump has no velocity limit. In the repulsion mode, the fluid is pumped in the opposite direction to the traveling electric wave.

Theoretical Background

Figure 1 shows the electrohydrodynamically pumped fluid in a pipe in the attraction and repulsion modes. The research reported here is the continuation of a previous study (Seyed-Yagoobi et al., 1989a) that dealt with the induction EHD pump in the attraction mode in the presence of gravity in a vertical configuration. This technical note presents the results for both attraction and repulsion modes in the absence of gravity using the theoretical model given in the above reference with a slight change in the axial momentum equation. The axial momentum equation for a Newtonian, steady, and laminar fluid at the entrance region of the pipe in the absence of gravity can be expressed as follows:

$$\rho\left(u\frac{\partial w}{\partial r} + w\frac{\partial w}{\partial z}\right) = -\frac{dP}{dz} + \frac{1}{r}\frac{\partial}{\partial r}\left(\mu r\frac{\partial w}{\partial r}\right) + \frac{1}{r}\frac{\partial}{\partial r}\langle r\tau_{e,rz}\rangle$$

Although the equations in the above reference were derived for a vertical configuration, the direction has no meaning in the absence of gravity.

Numerical Results

The numerical solution is detailed in the work by Seyed-Yagoobi et al. (1989a). A finite difference technique is used to solve the theoretical model. A convergence criterion of the order of 10^{-4} (m/s) is applied to the axial velocity. The number of nodes in the radial direction is chosen to be eleven. The results differ by less than 2 percent when a greater number of nodes are tested. The step size in the axial direction is on the order of 1×10^{-4} (m), and no significant difference in the results is observed when the step size is further decreased.

The reference operating characteristics are given in Table 1. The acceleration of gravity is assumed to be zero. The working fluid is Newtonian and is Sun #4 transformer oil; its properties are given in Table 2.

It is assumed that the flow enters the pump with a known temperature profile. A known temperature profile is assumed at the entrance of the pumping section because the pumping forces are generated solely due to the temperature gradient in the fluid. Figure 2 shows the fully parabolic temperature profile considered at the entrance of the pump. In the attraction mode, the fluid is warmer in the center and colder close to the wall; in the repulsion mode the opposite holds true.

Figure 3 shows the nondimensional electric shear stress distribution (driving force) for attraction and repulsion modes. The electric shear stress is zero in the center of the pipe but

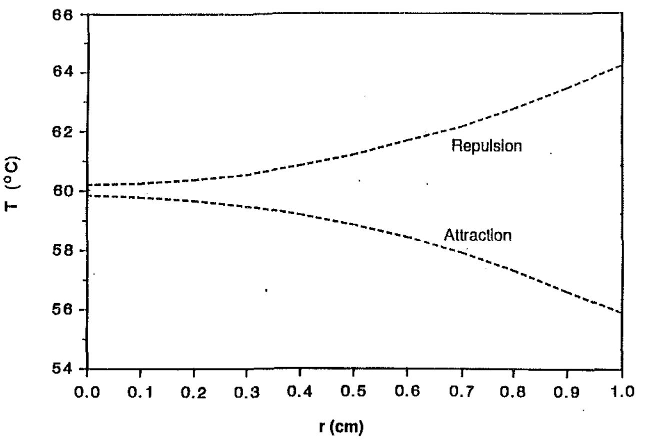

Fig. 2 Temperature profile at the pump entrance

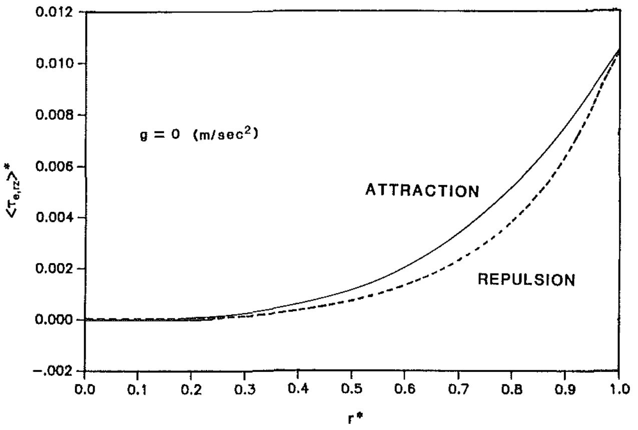

Fig. 3 Nondimensional electric shear stress distribution at the pump entrance

increases toward the pipe wall. The nondimensional electric shear stress is defined as follows (Seyed-Yagoobi et al., 1989a):

$$\langle \tau_{e,rz} \rangle^* = \frac{\langle \tau_{e,rz} \rangle}{\epsilon E_{op}^2/2}$$

The electric shear stress is a function of the electric conductivity gradient that is established in the presence of a temperature gradient. Because of this fact the electric shear stress distribution shown in Fig. 3 corresponds to the temperature profile given in Fig. 2.

A comparison of nondimensional axial velocity profiles in Fig. 4 reveals that the velocities are higher in the attraction mode than in the repulsion mode. This is because the electric shear stress is higher in the attraction mode under the reference operating characteristics specified in Table 1 (see Fig. 3). The nondimensional axial velocity w^* is defined as follows (Seyed-Yagoobi et al., 1989a):

$$w^* = \frac{w}{W_c}$$

where

$$W_c = \frac{a}{\mu_{bo}} \frac{\epsilon}{2} E_{op}^2$$

The absence of the gravity acceleration affects the axial velocity profile slightly. Figure 4 also shows the effect of gravity acceleration on the axial velocity profiles. The profile is almost flat in the central region when gravity is absent; when gravity is present, w^* first increases slowly and then decreases with respect to radius. The difference between the two profiles results from the absence of natural circulation when the gravitational acceleration is equal to zero.

Figure 5 illustrates the fluid velocity at several levels of gravity in attraction and repulsion modes. The fluid velocity increases linearly with gravitational acceleration because of an increase in the natural circulation. The fluid velocity is increased by 17 and 10 percent when the gravity acceleration is increased from 0 to 9.81 m/s^2 in attraction and repulsion modes, respectively.

The effects of the rest of the controlling factors (thermal, electrical, and physical) on the pump performance in the absence of gravity were studied but are not presented in this technical note. Comparison of the results with those of the previous study (Seyed-Yagoobi et al., 1989a) reveals that the operation of the EHD pumping in space is similar to that when gravity is present. In addition, the EHD pump operates similarly in the attraction and repulsion modes. Velocities are slightly higher in the attraction mode under the specified reference operating characteristics. Higher velocity in the repulsion mode than in the attraction mode is easily achievable if the pump is operated under the proper conditions.

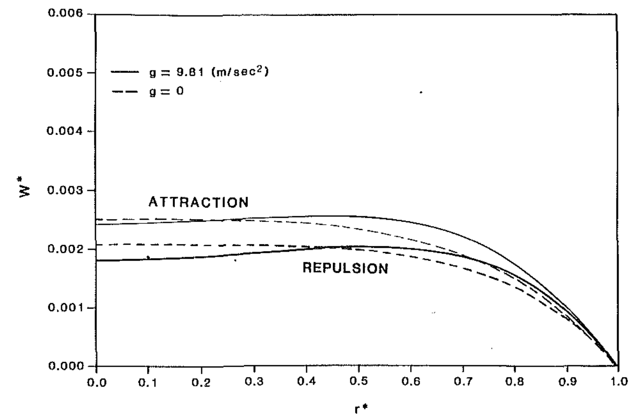

Fig. 4 Effect of gravitational acceleration on the nondimensional axial velocity at the pump entrance

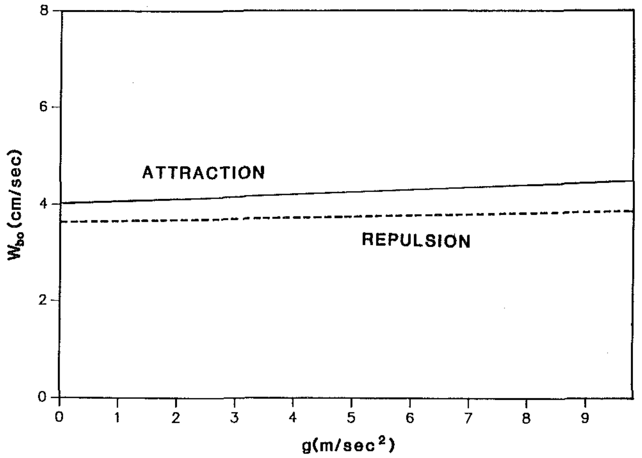

Fig. 5 Effect of gravitational acceleration on the bulk velocity

Acknowledgments

This work was supported in part by Grant No. 32123-70060 APG from the Texas Higher Education Coordinating Board.

References

Crowley, J. M., Chato, J. C., et al., 1983, "Electrohydrodynamic Pumping in Cable Pipes," EPRI EL-2834, Project 7871-1, Final Report.

Seyed-Yagoobi, J., Chato, J. C., Crowley, J. M., and Krein, P. T., 1989a, "Induction Electrohydrodynamic Pump in a Vertical Configuration: Part 1 — Theory," ASME Journal of Heat Transfer, Vol. 111, pp. 664-669.

Seyed-Yagoobi, J., Chato, J. C., Crowley, J. M., and Krein, P. T., 1989b, "Induction Electrohydrodynamic Pump in a Vertical Configuration: Part 2 — Experimental Study," ASME Journal of Heat Transfer, Vol. 111, pp. 670-674.

ERRATA

Errata for the technical paper "A General Correlation for Pool Film Boiling Heat Transfer From a Horizontal Cylinder to Subcooled Liquid: Part 1—A Theoretical Pool Film Boiling Heat Transfer Model Including Radiation Contributions and Its Analytical Solution," by A. Sakurai, M. Shiotsu, and K. Hata, JOURNAL OF HEAT TRANSFER, Vol. 112, pp. 430–440, May 1990.

Equation (16) of the referenced paper contained typographic errors as published. The correct equation is

$$\eta_v = N_v \frac{\gamma(x)}{r} \int_0^y \frac{\rho_v}{\rho_{vs}}\, dy, \qquad \eta_l = N_l \frac{\gamma(x)}{r} \int_0^y \frac{\rho_l}{\rho_{ls}}\, dy \tag{16}$$

where ρ_l for $0 \le y \le \delta$ is taken to be equal to ρ_{ls}.